

FINAL TECHNICAL REPORT FOR

OFFICE OF NAVAL RESEARCH

GRANT NO. N00014-97-1-0880

**Development of a Mesoscale Solid-State
Servo-Hydraulic Actuator**

DISTRIBUTION STATEMENT A
Approved for Public Release
Distribution Unlimited

Grant Period: July 1, 1997 to Feb. 28, 2001

PRINCIPAL INVESTIGATOR

Dr. Nesbitt W. Hagood, IV
nwh@ContinuumPhotonics.com
(978) 670-4910

Department of Aeronautics and Astronautics
Massachusetts Institute of Technology
Cambridge, MA 02139

20030929 120

REPORT DOCUMENTATION PAGE

Form Approved
OMB NO. 0704-0188

Public Reporting burden for this collection of information is estimated to average 1 hour per response, including the time for reviewing instructions, searching existing data sources, gathering and maintaining the data needed, and completing and reviewing the collection of information. Send comment regarding this burden estimates or any other aspect of this collection of information, including suggestions for reducing this burden, to Washington Headquarters Services, Directorate for Information Operations and Reports, 1215 Jefferson Davis Highway, Suite 1204, Arlington, VA 22202-4302, and to the Office of Management and Budget, Paperwork Reduction Project (0704-0188), Washington, DC 20503.

| | | | | |
|--|---|--|---|--|
| 1. AGENCY USE ONLY (Leave Blank) | | 2. REPORT DATE 09/16/2003 | 3. REPORT TYPE AND DATES COVERED Final Technical Report: July 1, 1997 to Feb. 28, 2001 | |
| 4. TITLE AND SUBTITLE Development of a Mesoscale Solid-State Servo-Hydraulic Actuator | | | 5. FUNDING NUMBERS N00014-97-1-0880 | |
| 6. AUTHOR(S) J. Lodewyk Steyn and Nesbitt W. Hagood IV | | | | |
| 7. PERFORMING ORGANIZATION NAME(S) AND ADDRESS(ES) Massachusetts Institute Of Technology 77 Massachusetts Ave. Cambridge, MA 02139 | | | 8. PERFORMING ORGANIZATION REPORT NUMBER | |
| 9. SPONSORING / MONITORING AGENCY NAME(S) AND ADDRESS(ES) Office of Naval Research Ballston Centre Tower One 800 North Quincy St. Arlington, VA 22217-5660 | | | 10. SPONSORING / MONITORING AGENCY REPORT NUMBER | |
| 11. SUPPLEMENTARY NOTES The views, opinions and/or findings contained in this report are those of the author(s) and should not be construed as an official Office of Naval Research position, policy or decision, unless so designated by other documentation. | | | | |
| 12 a. DISTRIBUTION / AVAILABILITY STATEMENT Approved for public release; distribution unlimited. | | | 12 b. DISTRIBUTION CODE | |
| 13. ABSTRACT (Maximum 200 words) This report is a compilation of work related to the development of a high-pressure high flow rate piezoelectric micropump. Such a pump would be at the heart of a small servohydraulic actuation system. The objective of this project was to determine the feasibility such an actuation system. One of the biggest challenges facing small-scale servohydraulic systems is the development of a high performance micro pumping device. To achieve the final result, a) detailed mathematical models of the micropump as well as the micro - servohydraulic system were constructed, b) a micropump was designed, taking into account all the relevant limitations related to the current state-of-the-art microfabrication techniques and c) a micropump was built and tested. The final micropump was a seven-layer microfabricated device consisting of 4 silicon and 3 glass layers. The silicon layers were fabricated using Deep Reactive Ion Etching (DRIE). The glass layers were made using conventional diamond drilling. The final device was assembled using a sequence of Silicon-silicon fusion bonds and silicon-glass anodic bonds. The maximum performance attained from this device was a maximum flow rate of 2700 microliters/min and a maximum differential pressure of 450kPa at a piston drive frequency of 12.5kHz. | | | | |
| 14. SUBJECT TERMS Piezoelectric, micropump, microvalve, servohydraulic, actuation system, micro-servohydraulic, MicroHydraulic Transducer (MHT), microfabrication, Deep Reactive Ion Etching (DRIE), flow rate, fluidic resonance, electrokinetic, electrochemical, microelectromechanical. | | | 15. NUMBER OF PAGES 1088 | |
| | | | 16. PRICE CODE | |
| 17. SECURITY CLASSIFICATION OF REPORT UNCLASSIFIED | 18. SECURITY CLASSIFICATION ON THIS PAGE UNCLASSIFIED | 19. SECURITY CLASSIFICATION OF ABSTRACT UNCLASSIFIED | 20. LIMITATION OF ABSTRACT UL | |

NSN 7540-01-280-5500

Standard Form 298 (Rev.2-89)
Prescribed by ANSI Std. Z39-18
298-102

"Development of a Mesoscale Solid-State Servo-Hydraulic Actuator"

O.N.R. Grant No. N00014-97-1-0880

Abstract

This report is a compilation of work related to the development of a high-pressure high flow rate piezoelectric micropump. Such a pump would be at the heart of a small servohydraulic actuation system. The objective of this project was to determine the feasibility such an actuation system. One of the biggest challenges facing small-scale servohydraulic systems is the development of a high performance micro pumping device. To achieve the final result, a) detailed mathematical models of the micropump as well as the micro - servohydraulic system were constructed, b) a micropump was designed, taking into account all the relevant limitations related to the current state-of-the-art microfabrication techniques and c) a micropump was built and tested. The final micropump was a seven-layer microfabricated device consisting of 4 silicon and 3 glass layers. The silicon layers were fabricated using Deep Reactive Ion Etching (DRIE). The glass layers were made using conventional diamond drilling. The final device was assembled using a sequence of Silicon-silicon fusion bonds and silicon-glass anodic bonds. The maximum performance attained from this device was a maximum flow rate of 2700 microliters/min and a maximum differential pressure of 450kPa at a piston drive frequency of 12.5kHz.

"Development of a Mesoscale Solid-State Servo-Hydraulic Actuator"

O.N.R. Grant No. N00014-97-1-0880

1. Overview

This document is a compilation of work performed to investigate the feasibility of small-scale servohydraulic actuation systems. The goal of these systems would be two-fold:

1. To exploit the nature of new piezoelectric materials with high specific power. This high specific power is only realized at high frequencies of operation, due to the inherently small stroke attainable with piezoelectric materials.
2. To mate the requirement for high frequency operation and small devices with microfabrication technologies, therefore harnessing the benefits of microfabricated systems, such as: batch fabrication, large scale production, use of superior materials such as single crystal silicon, and the ability to fabricate small devices with a large degree of precision.

The work presented here started with a feasibility study in the form of a Master's thesis at MIT (Pulitzer), and continued with the development of a micropump device presented by Li et. al. Additional work is presented in the form of theses by Roberts, Steyn and Yaglioglu.

2. Approach

Initial studies by Pulitzer and Hagood suggested that MHT technology could indeed be a feasible means of small-scale servohydraulic actuation. Continued theoretical studies were augmented by fabrication short-loop experiments to prove the manufacturability of such a device. These experiments eventually yielded both the first piezoelectric drive piston which formed the basis for the first micropump device. In parallel with the fabrication experiments were also experiments on a macrovalve (Carretero) and fluid filling and sealing (R. Mlcak, Boston Microsystems).

3. Results

The final result of the project was the delivery of a high pressure high flow rate micropump. This pump eventually delivered a maximum flow rate of 2600 ml/min and a maximum differential pressure of 450kPa at a drive voltage of 1200Vpp on the piston at an electrical frequency of 12.5kHz. The pump was operated under bias pressures ranging from 300 to 800kPa to prevent cavitation when the piston oscillates at high frequency. One pump failed due to broken valves, while two others had broken pistons and a third one had a broken pressure sensing membrane.

Fluidic resonances were observed during the operation of the pump, and it is presumed that these resonances can be used to enhance the performance of a micropump device at a given frequency.

The micropump that was built performed significantly better than other micropumps reported in the literature up until the time the pump was demonstrated. At the time of writing this report, the only micropumps matching and/or exceeding the performance of this micropump were electrokinetic (EK) pumps. Although EK pumps are much simpler to fabricate than a piezoelectric micropump, they suffer from a finite lifetime, due to the electrochemical reaction that results as part of the operation of the pump.

4. Conclusions

The results, both analytical and experimental, suggested that small-scale microhydraulic transducer devices do show promise for small-scale servohydraulic actuation. The devices appeared to have an acceptable lifetime. The drive pistons of the devices went through at least $O(10^6)$ cycles per device, indicating that fatigue would probably not be a concern for these devices.

Fabrication of such MicroHydraulic Transducer (MHT) devices remains a key challenge. The multi-wafer fabrication process presented several unique problems when considering the fabrication of high performance microhydraulic devices. Challenges such as (1) fillet radius control at the bottom of an etched trench (2) piezo sizing and tolerancing to match the thickness of the glass insulating layer plus the etched recess or "piezo seat" (3) wafer care during fabrication with eventual fusion bonding in mind.

5. Recommendations

Further research was proposed and also undertaken in a formal development of MHT technology through follow-on programs¹. The future goals for MHT technology were the development of an active valve MHT device with bi-directional capabilities, also giving the MHT the ability to generate energy by rapidly cycling the valves to create a pulsing pressure on the main piston.

It is further recommended that the manufacturability of MHT devices be addressed further, as well as integration of such device into a system that could serve as a prototype for a real-world application.

¹ The reader is also referred to the report for ONR grant N00014-01-1-0857, which contains more detailed information on the specifics of MHT technology.

6. Publications

Research performed under this grant was documented in publications that are included as part of this report, following this summary.

Technical Papers (3)

H.Q. Li, D.C. Roberts, J.L. Steyn, K.T. Turner, J. A. Carretero, O. Yaglioglu, Y.-H. Su, L. Saggere, N.W. Hagood, S.M. Spearing, and M.A. Schmidt, R. Mlcak & K. Breuer, "A High Frequency High Flow Rate Piezoelectrically Driven MEMS Micropump," presented at the Transducers Research Foundation Solid-State Sensor and Actuator Workshop, Crowne Plaza Resort, Hilton Head Island, SC, June 2000.

L. Saggere, N. W. Hagood, D. C. Roberts; H-Q. Li; J. L. Steyn; K. Turner, J.A. Carretero, O. Yaglioglu, Y-H. Su, R. Mlcak, S. M. Spearing, K. S. Breuer, M. A. Schmidt, "Design, Fabrication, and Testing of a Piezoelectrically Driven High Flow Rate Micro-Pump," Proceedings of the 2000 12th IEEE International Symposium on Applications of Ferroelectrics IEEE, Piscataway, NJ, USA; p. 297--300 vol. 1, 2001.

D. C. Roberts, H-Q. Li, J. L. Steyn, O. Yaglioglu, S.M. Spearing, M. A. Schmidt and N.W. Hagood, "A Piezoelectric Microvalve for Compact High Frequency High Differential Pressure Micropumping Systems," Journal of Microelectromechanical Systems, 12(1): 81-92, February 2003.

Theses (5)

Pulitzer, Seward Webb, "Feasibility Assessment and Design of Micro Hydraulic Solid-State Transducers," MIT Mechanical Engineering, Master's Thesis, June 1998.

Carretero Benignos, Jorge Alejandro, "Measurement and Modeling of the Flow Characteristics of Micro Disc Valves," MIT Aeronautics and Astronautics, Master's Thesis, February 2001.

Roberts, David C. (David Christopher), "Design, Modeling, Fabrication and Testing of a Piezoelectric Microvalve for High Pressure, High Frequency Hydraulic Applications," MIT Mechanical Engineering, Doctoral Thesis, February 2002.

Steyn, J. Lodewyk (Jasper Lodewyk), "Hydraulic Amplification for Actuation in Microelectromechanical Systems," MIT Aeronautics and Astronautics, Master's Thesis, February 2002.

Yaglioglu, Onnik, "Modeling and Design Considerations for a Micro-Hydraulic Piezoelectric Power Generator," MIT Mechanical Engineering, Master's Thesis, February 2002.

7. Personnel

Faculty and Staff

Prof. Nesbitt W. Hagood, Principal Investigator
Dr. Mauro J. Atalla, Scientific Staff
Mr. Paul H. Bauer, Scientific Staff
Dr. Hanqing Li, Scientific Staff
Mr. David C Robertson, Scientific Staff
Dr. Laxminarayan Saggere, Su Scientific Staff

Graduate Students

Jorge A. Carretero, - S.M. in Aeronautics and Astronautics, 2001.
Seward W. Pulitzer III, - S.M. in Mechanical Engineering, 1998.
David C. Roberts, - Ph.D. in Mechanical Engineering, 2002.
J. Lodewyk Steyn, - S.M. in Aeronautics and Astronautics, 2002.
Onnik Yaglioglu, - S.M. in Mechanical Engineering, 2002.

A HIGH FREQUENCY HIGH FLOW RATE PIEZOELECTRICALLY DRIVEN MEMS MICROPUMP

H.Q. Li, D.C. Roberts, J.L. Steyn, K.T. Turner, J. A. Carretero, O. Yaglioglu,
Y.-H. Su, L. Saggere, N.W. Hagood, S.M. Spearing, and M.A. Schmidt
Massachusetts Institute of Technology

Cambridge, MA 02139

R. Mlcak
Boston Microsystems, Inc.
Woburn, MA 01801

K.S. Breuer
Brown University
Providence, RI 02912

ABSTRACT

A piezoelectrically driven fluidic micropump was fabricated and tested. Microelectromechanical systems (MEMS) fabrication technology was used. Small cylindrical piezoelectric material elements were integrated with microfabricated silicon, silicon on insulator (SOI), and glass chips using eutectic bonding and anodic bonding processes. SOI wafers were used to form the thin membranes within the moving parts (a drive element and two passive valves). The design, microfabrication process, and assembly of the device are described in this paper. Fabrication issues such as control of fillet radii at the feet of the Si membranes for stress reduction and simultaneous eutectic and anodic bonding were discussed. A flow rate as high as 3000 $\mu\text{l}/\text{min}$ was recorded. Experimental and simulation results of the dependences of the pump flow rate on the voltage and frequency applied on the piezoelectric material are shown and discussed.

INTRODUCTION

This paper presents the fabrication and testing of a high pressure, high flow rate piezoelectrically driven fluidic micropump with passive valves. In comparison to other piezoelectrically driven micropumps in the literature [1-4], this device incorporates the integration of bulk piezoelectric material with MEMS microfabrication techniques to allow for high structural driving frequencies in the tens of kHz range and implements novel methods of anodic and eutectic bonding to join silicon, glass, and piezoelectric components, enabling minimal device mass and therefore high power density. It requires a compact design that brings about challenging fabrication issues such as multi-layer wafer bonding, multiple lithography and deep reactive ion etch (DRIE) steps for the SOI wafers, use of nested oxide masks, and integration of small piezoelectric material elements. The need for high frequency and high flow rate calls for precisely micro-machined Si membranes capable of large deflection as the moving components in the pump chamber and the passive valves of the micropump. SOI wafers are good choices for this purpose because they have a uniform thin Si layer, their buried oxide can be used as the etch stop during DRIE processes, and the fillet radii of the membranes that are critical to the strength of the membranes are easier to control in the presence of the buried oxide. Another advantage of SOI wafers is that separate electrodes can be formed in the SOI layer during microfabrication, with the buried oxide as the insulator. Eutectic bonding has been used to integrate the piezoelectric elements into the MEMS devices. For this micropump it is necessary to choose low melting point eutectic bonding alloys so that the eutectic bonding can be performed simultaneously with the anodic bonding of the Si and SOI layers to the glass layer that encloses the piezoelectric material for

insulation. The successful fabrication of the micropump is a major step toward the realization of high power density transducer devices for micro-robotic actuation and heel-strike power generation applications [5, 6].

MICROPUMP STRUCTURE

The micropump has a multi-layer structure, schematically shown in Figure 1. It includes one fluid pump chamber and two identical passive check valves [7]. The volume change in the fluid chamber is achieved by the vertical motion of the double layer cylindrical piston-like drive element (layers 4 and 5) attached to annular Si membranes and driven by a ceramic piezoelectric cylinder (layer 3) 1 mm in diameter and 1 mm in height. When a voltage is applied to the piezoelectric cylinder, it pushes the drive element piston up, producing a high pressure in the fluid chamber that closes the inlet valve and opens the outlet valve so that fluid can flow out of the fluid pump chamber. Next, when the voltage is

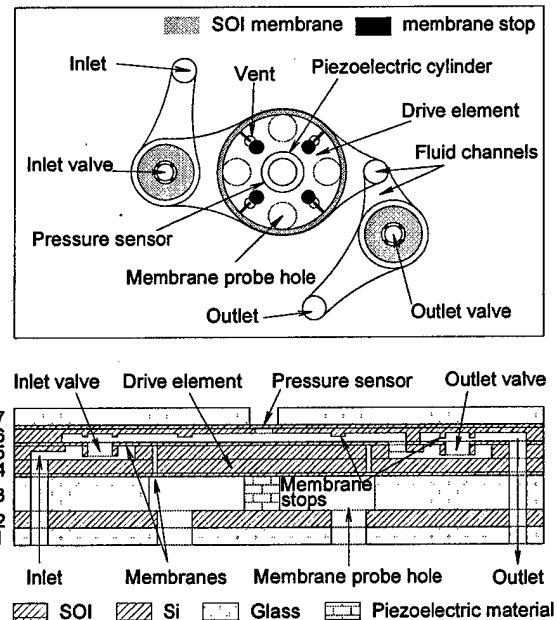


Figure 1. Top view and cross-section view of the micropump. The cross-section view is from a zig-zag cut to show all the features. reduced the piezoelectric cylinder contracts and the drive element piston moves down, resulting in a low pressure in the fluid chamber that closes the outlet valve and opens the inlet valve so

that fluid can flow into the chamber. The pump works by repeating these steps at high frequency.

The drive element piston is 3.6 mm in diameter and each of the two SOI layers 4 and 5 forming the piston is about 400 μm thick. The annular drive element SOI membranes are 150 μm wide and 10 μm thick in the lower layer and 15 μm thick in the upper layer which also includes the valves. SOI wafers (layers 4, 5, and 6) were chosen to construct the membranes in the device for two reasons: 1) to control precisely the membrane thickness by using the buried oxide in the SOI as an etch stop in the DRIE process, and 2) to use the lower SOI (layer 4) as an electrode to the piezoelectric cylinder and the buried oxide as an insulator between the piezoelectric cylinder and the remaining part of the micropump. The thickness of the SOI membranes in layer 5 was determined mainly by the design specifications of the passive valves that were subject to much larger deflections than the drive element piston membrane. Venting channels in layer 5 and holes in layer 4 (not shown in Fig. 1) were formed to release pressure in the cavity between the drive element membranes during the wafer diffusion bonding. The passive valves consist of a 0.5 mm center hole and a 15 μm thick annular SOI membrane with an inner diameter of 0.70 mm and an outer diameter of 1.65 mm. When not deflected the valves are only 0.5 μm from layer 4 to minimize back leaking.

The fluid chamber above the drive element piston and fluid channels to and from the valves are located in layer 6. Small cylindrical motion stops about 8 μm from the drive element and about 18 μm from the valves respectively were also formed in layer 6 to prevent the membranes from excessive deflections. A pressure sensor in the shape of a circular membrane 0.8 mm in diameter and 20 μm thick was formed in the fluid chamber for on-site pressure measurement. A ceramic PZT-5H piezoelectric cylinder 1 mm in diameter and 1 mm in height was incorporated in the middle glass layer 3 as the active drive component of the micropump. The Si layer below the piezoelectric cylinder was used as the other electric contacts to the piezoelectric cylinder. 3 mm thick borosilicate glass was used in the top and bottom layers 1 and 7 for structural strengthening of this bench top device.

MICROFABRICATION PROCESSES

To minimize the size of the device, a compact design requiring a minimum number of layers, efficient use of the both surfaces in each layer, and therefore multiple lithography steps for the SOI wafers was implemented. As an example, Figure 2 shows the fabrication process flow for layer 5. The first step is the selection of the SOI wafer that has a 15 μm thick SOI layer, a 0.4 μm thick buried oxide, and a 380 μm thick handle layer. Secondly, positive photoresist was coated on both sides of the wafer and the SOI side was patterned using standard lithography procedures. The photoresist on the handle side is to protect the handle surface from scratching in the lithography steps. This back surface protection method was used throughout the micro-fabrication processes. The wafer was then put in a DRIE machine until the SOI layer was etched through. This step formed the fluid through holes in the SOI layer. Next, the wafer was cleaned and coated with positive photoresist on both sides again. The handle side was patterned with photoresist and etched down about 0.5 μm in a RIE etcher to form the clearance between the valves and their seating surfaces. In the fourth step the wafer was oxidized at 1100°C for 5 hours to form 2 μm of thermal oxide that is to be used as a nested mask and back surface protection from DRIE etching later on. The thermal oxide was etched in step 5 to form the nested mask and then another lithography process was

performed on handle side to define the membranes in the drive element and in the passive valves in step 6. The wafer was etched first by DRIE about halfway through its thickness with photoresist as seen in step 6. Then the photoresist pattern was stripped and the nested thermal oxide mask was exposed for another DRIE step until it stopped at the buried oxide, as seen in step 7. The nested oxide mask was necessary to construct the 200 μm deep venting channels in the drive element and the fluid channels to the valves. Finally, the thermal oxide was stripped using BOE wet etching.

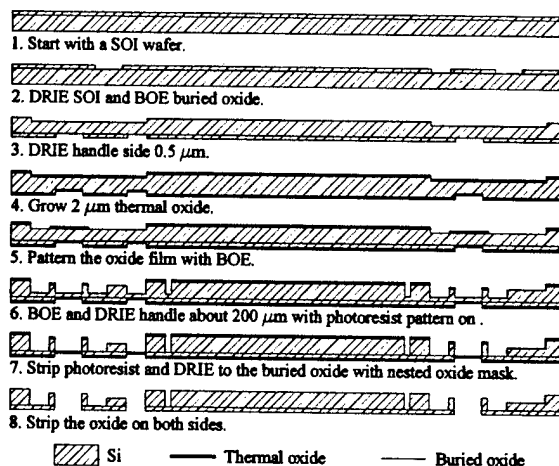


Figure 2. Fabrication flow of an SOI layer (layer 5 in Fig. 1) with the passive valves and half of the drive element piston.

Since all the membranes in this device have to operate under high stress and at high frequency, it is important to have a membrane structure with minimal stress concentration. A significant challenge in the micropump fabrication was controlling fillet radii in the range of 20–40 μm for stress reduction at the feet of the membranes. In the DRIE machine Si is etched at a rate of about 2–4 $\mu\text{m}/\text{min}$, depending on the feature size and exposed Si area. The etch front is usually a gradual curve in cross-section but varies depending on the etch conditions. An SOI membrane fillet radius is formed after the etch front reached the buried oxide and then the Si edges retreat horizontally to the side wall at a rate of about 70–100 $\mu\text{m}/\text{minute}$ as more oxide is exposed. There is a time window of only about 2–4 minutes to control the fillet radius in the desired range after about 2 hours etch of the handle side. Therefore careful monitoring in the final stage of the DRIE is critical. Figure 3 shows a 150 μm wide drive element membrane with a gradual fillet about 25 μm long horizontally.

ASSEMBLY OF THE DEVICE

After the final DRIE etch and cleaning, the three SOI wafers were aligned using an Electronic Visions system and fusion bonded at 1100°C in nitrogen for 1 hour. The bonded wafer stack was cut into 16.7 mm by 15.7 mm chips with a die-saw, cleaned in water, acetone, methanol, and isopropanol successively, and finally dried in air. The glass wafers were processed with diamond drills and die-saw cut into small chips. All the interfaces between Si and glass were anodically bonded at about 300°C. The Si and the piezoelectric material interfaces were eutectically bonded.

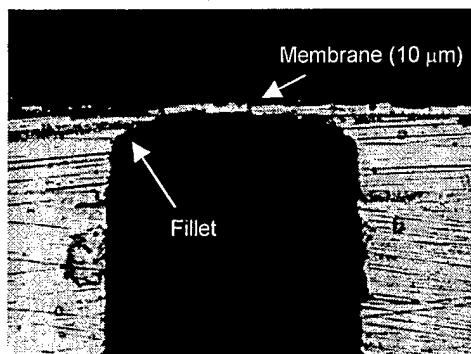


Figure 3. Optical cross-section picture of a drive element membrane, the membrane thickness is about 10 μm .

To prepare for the eutectic bonding, 500 Å of Ti film and 5000 Å of Pt film were deposited on the Si surfaces through a shadow mask by e-beam and 2 μm of an Au-Sn (80-20% wt.) alloy films were deposited on the piezoelectric surfaces by sputtering. The composition of the metal films were chosen for surface wetting (Ti) and low eutectic bonding temperature (Au-Sn) so that the eutectic bonding and the last anodic bonding can be done simultaneously as required by the pump design. The height of the piezoelectric cylinders were designed to be 2-3 μm larger than the height of the middle glass piece (layer 3 in Fig. 1) so that the drive element piston is preloaded and when the chamber is expanded there is no pulling of the drive element piston by the piezoelectric cylinder that might delaminate the eutectic bonding. For this reason, an oxide mask that defines the piezoelectric seating was left on each Si chip below the piezoelectric (layer 2 in Fig. 1) for height compensation by individually trimming etch of the Si chips. Finally wires were soldered on the Ti/Pt electrode pads that were deposited at the same time as the eutectic bonding films were deposited. Figure 4 shows a picture of an assembled micropump.

The key components of this bench top device were built in an area of about 8.6 mm by 7.7 mm, while the electric contacts and

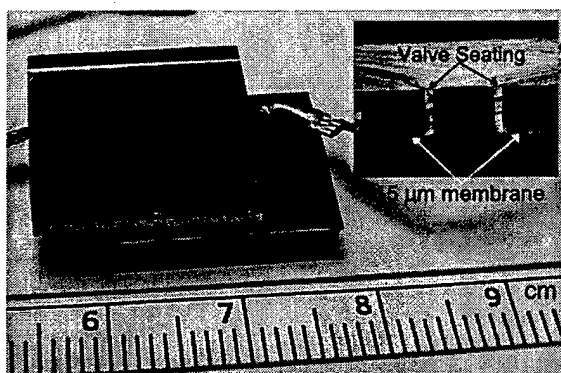


Figure 4. An assembled micropump with electric leads. Small graduations are in mm. The inset is a cross-section picture of a passive valve with 15 μm thick membrane. The supporting glass pieces take most space of this bench-top device. The inset of Fig. 4 is a cross-section photograph of a passive check valve with 15 μm thick membrane.

TEST RESULTS

The assembled device was tested with an experimental setup that includes fluid reservoirs, valves, pressure sensors, and flow meters, as shown in Figure 5. The inset in Fig. 5 is an picture of the test jig with a micropump sealed in it by rubber O-rings. The system was first evacuated and then filled with 1 centistoke silicone oil. The piezoelectric cylinders were driven by AC signals with peak to peak voltages in the range of 0-1600 V, bias voltages in the range of 300-600 V, and frequencies in the range of 1-12.5 kHz. The inlet pressure was maintained at 850 kPa in all the tests. The highest flow rate recorded is 3000 $\mu\text{L}/\text{min}$ at 1200 V peak to peak voltage, 600 V bias voltage, and 4.5 kHz, and zero differential pressure.

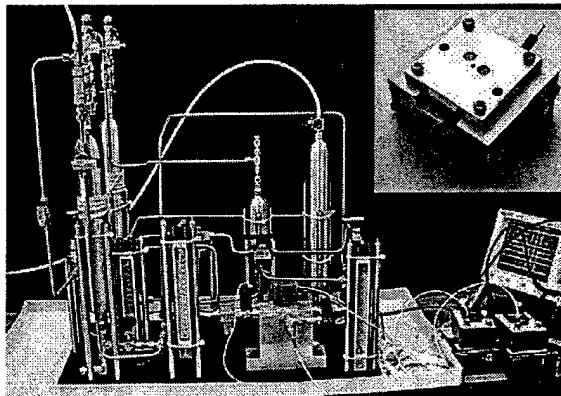


Figure 5. The experimental setup for micropump test. The inset is the package jig holding the micropump.

Figure 6 shows the experimental and quasi-static simulation results of the dependence of flow rate on peak to peak voltage. This test was done at a drive frequency of 3.5 kHz, a bias voltage of 600 V, and zero differential pressure. The flow rate increases with the voltage monotonically but not linearly. In Simulation 1 a rigid chamber structure was assumed. It is believed that the flow rate of Simulation 1 is higher than the experimental results because the micropump has, as part of the fluid chamber, flexible SOI

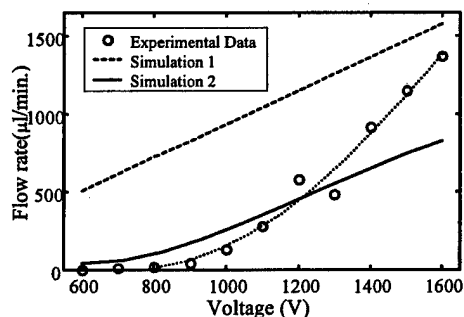


Figure 6. Flow rate vs. piezo peak to peak voltage at 3.5 kHz drive frequency. The results of two quasi-static simulations with different chamber compliance are also shown.

membranes attached to the drive element piston and the two passive check valves (see Fig. 1). An increased fluid chamber compliance was included in Simulation 2 and its results are closer to the experimental data as can be seen from Fig. 6. However, at high drive voltage the experimental flow rate increased with the drive voltage much faster than the results of Simulation 2. This is

probably because the membranes deflect more and become stiffer as the drive voltage increases, resulting in a faster increase in flow rate, while in Simulation 2 this increase of membrane stiffness was not accounted for.

Figure 7 shows the relation between the inlet-outlet differential pressure and the flow rate. In this experiment the piezoelectric cylinder was driven at 1200 V peak to peak voltage, 600 V bias voltage, and 3.5 kHz.

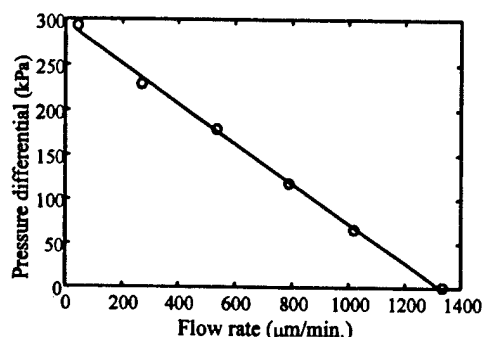


Figure 7. Inlet to outlet differential pressure vs. flow rate.

The flow rate vs. piezoelectric cylinder drive frequency curve of the same device and a quasi-static simulation result are shown in Figure 8. Other experimental conditions of this test were: peak to peak voltage at 1200 V, bias voltage at 300 V, and zero differential pressure. Figure 8 clearly shows some form of resonance effect that is not present in the simulation. We found that changing the bias voltage to the piezoelectric material and changing the pressure difference between the inlet and outlet have an influence on the value of the flow rate but not on the resonance peak positions. The flow resonance could be due to the pressure wave effects at abrupt corners of the package of the micropump or due to the internal structure of the device. A systematic study of the micropumps is under way to better understand their behavior and to improve their performance.

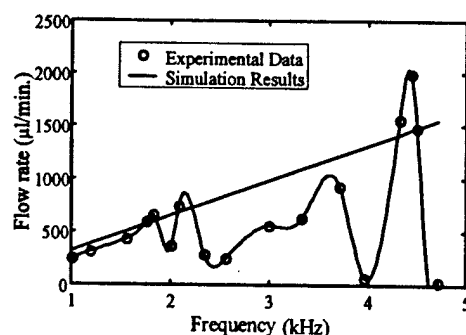


Figure 8. Flow rate vs. drive frequency of the micropump.

CONCLUSIONS

The work in this paper is part of a larger effort to develop high power density transducer devices [5] for micro-robotic actuation and human heel-strike power generation applications. The successful fabrication of the micropump has validated the MEMS process design and bonding techniques to be used for these

devices. Since device power is generally proportional to flow rate, higher flow rate micropumps with larger drive elements and multiple piezoelectric cylinders are currently being developed. A further increase in flow rate can be realized by using newly developed single crystal piezoelectric materials [8]. A performance improvement of 10 times is expected in micropumps that combine larger drive elements and single crystal piezoelectric materials. In order to examine the effect of resonance on the performance of the micropump, the internal device structure and external test set-up are under investigation. In addition, it may be possible to use this resonance behavior to maximize the flow rate by tuning the device to a desired resonance frequency.

ACKNOWLEDGEMENT

We would like to thank the staff members of the Microsystems Technology Laboratories at MIT, especially Kurt Broderick, for their help in the microfabrication of the micropumps. We also thank Dr. Arturo Ayon of MIT for his help with the diffusion bonding of the SOI wafers. This work was funded by DARPA and the ONR.

REFERENCES

1. S. Shoji and M. Esashi, "Microflow Devices and Systems", *Journal of Micromechanics and Microengineering*, 4, 157, (1994).
2. M. Koch, A.G.R. Evans, and A. Brunnschweiler, "The Dynamic Micropump Driven with a Screen Printed PZT Actuator", *Journal of Micromechanics and Microengineering*, 8, 119, (1998).
3. M. Esashi, S. Shoji, and A. Nakano, "Normally Closed Microvalve and Micropump Fabricated on a Silicon Wafer", *Sensors and Actuators*, vol. 20, pp 163-169, 1989.
4. D. Maillefer, H. Van Lintel, G. Rey-Mermet, R. Hirschi, "A High Performance Si Micropump for an Implantable Drug Delivery System", *Technical Digest, IEEE International MEMS'99 Conference*, pp. 541-6, (1999).
5. Nesbitt W. Hagood IV, *et al.* "Micro-hydraulic Transducer Technology for Actuation and Power Generation", submitted to SPIE 7th International Symposium on Smart Structures and Materials, Newport Beach, CA, March 5-9, 2000.
6. D.C. Roberts *et al.* "Design of Piezoelectrically-driven Hydraulic Amplification for High Pressure, High Frequency Applications", submitted to SPIE 7th International Symposium on Smart structures and Materials, Newport Beach, CA, March 5-9, 2000.
7. H.T.V. Van Lintel, F.C.M. Van De Poll, and S. Bouwstra, "A Piezoelectric Micropump Based on Micromachining of Silicon", *Sensors and Actuators* 20, 163, (1989).
8. Seung-Erg Park and Thomas R. Shrout, "Characteristics of Relaxor-Based Piezoelectric Single Crystals for Ultrasonic Transducers", *IEEE Trans. Ultrasonics, Ferroelectrics, and Frequency Control*, 44, 1140 (1997).

Design, Fabrication, and Testing of a Piezoelectrically Driven High Flow Rate Micro-Pump

L. Saggere¹, N. W. Hagood¹, D. C. Roberts¹, H.-Q. Li¹, J. L. Steyn¹, K. Turner¹, J. A. Carretero¹,
O. Yaglioglu¹, Y.-H. Su¹, R. Micak², S. M. Spearing¹, K. S. Breuer³, M. A. Schmidt¹

¹Massachusetts Institute of Technology, Cambridge, MA 02139 USA

²Boston Microsystems, Inc., Woburn, MA 01801 USA

³Brown University, Providence, RI 02912 USA

Abstract — Towards the development of novel class of miniature transducers with very high specific power, a high frequency and high flow rate hydraulic micro-pump with passive check valves was fabricated and tested. The micro-pump features a small piezoelectric (PZT-5H/PZT-PT) cylinder integrated into micromachined silicon and pyrex chips. The piezoelectric cylinder bonded to a thick circular disk serves as the drive element in the pump chamber, and two axisymmetric silicon membranes with hollow annular bosses serve as system check valves. Using silicone oil as the working fluid, the performance of the micro-pump was tested by varying voltages from 0 to 1600V and frequencies from 1 kHz to 12 kHz. The micro-pump with PZT-5H element achieved a high flow rate of 2.5 ml/min at 1200 V and 4.5 kHz.

INTRODUCTION AND MOTIVATION

Recent advances in active materials technology has led to the development of many new solid-state actuators. However, the specific power (power per unit mass) output of these solid-state actuators is fairly limited. A major program with the broad goal of developing miniaturized transducers, called Micro-Hydraulic Transducers (MHT), with very high specific power in the order of 1 kW/kg is currently underway at MIT [1]. This program derives its impetus from an evolving realization that attractive output power densities are achievable by active materials with decreasing size and high frequency operation, and exploits from the integration of the piezoelectric technology with the micro-machining (MEMS) technology and micro-hydraulic concepts. The essential building unit of the MHT is a micro-pump with actively controlled valves that rectify fluid-flow from one pressure potential to another at very high frequencies and high flow-rates against high pressures, yielding a high power output. These operating requirements of the micro-pump are more demanding than any micro-fluidic device developed so far. Several micro-pumps based on different principles have been reported, however, mostly they feature either small flows or low output pressures [2,3].

Development of an active valve micro-pump for MHT involves several critical challenges in design, fabrication and system level integration. The motivation for the work

presented in this paper stemmed mainly from the need to demonstrate the technical feasibility and to minimize the risks involved in the development of an active valve micro-pump for MHT. This purpose was accomplished through a successful development of a slightly simpler version of the device, that is, a micro-pump with passive (check) valves, with similar performance goals of high flow and high pressure. This paper reports the design, modeling, fabrication and testing of the passive valve micro-pump.

WORKING PRINCIPLE AND DESIGN

The micro-pump is comprised of the following generic components: pump chamber, a piezoelectric element, a low-pressure fluid reservoir (LPR), a high-pressure fluid reservoir (HPR), and two check valves—one operating between the LPR and the pump chamber and the other one operating between the pump chamber and the HPR—as schematically shown in Figure 1. An electric voltage applied to the piezo induces a strain in the element resulting in a net volume change in the pump chamber. The two valves transform the volume oscillations of the chamber into a net fluid flow from LPR to HPR. The accumulation of fluid in the HPR increases the pressure and performs useful work on the load. After the actuator travels its full stroke, the flow direction is reversed (not illustrated in Figure 1) and the actuator is evacuated as it returns to its initial position, completing the actuation cycle. In this way the high frequency, small displacements of the piezoelectric are rectified into low frequency, large stroke actuation.

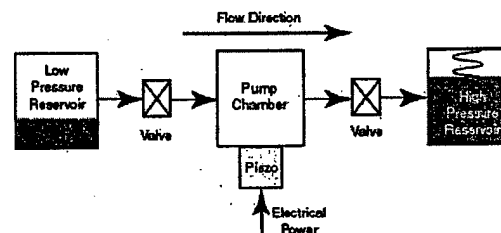


Figure 1. Working principle of the micro-pump.

The micro-pump configuration is shown in Figure 2. The pump chamber at the center encloses a piezo element sandwiched between a moveable thick circular disk and the rigid bottom. The moveable disk is tethered to the chamber wall through thin flexible membranes around the circumference. The moveable plate and the piezo together effectively constitute a piston-like structure that can move vertically up and down when the piezo is strained by applying electric voltage across its ends. The volume between the chamber ceiling and the piston surface encloses the working fluid that is pumped. Two axisymmetric silicon micromachined membranes with hollow annular bosses serve as system check valves between the inlet/outlet port and the pump chamber.

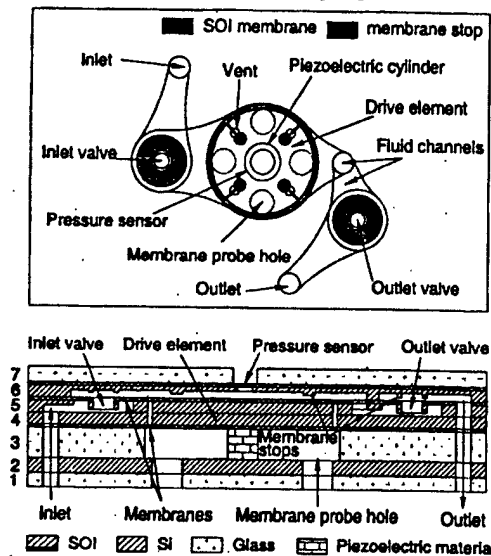


Fig. 2: Top view and cross-sectional view (along a zig-zag cut in the top view) of the micropump.

The approximate dimensions of the piezo cylinder and the chamber were first determined analytically to satisfy the requirement of an average flow rate of 1 ml/s at 20 kHz operating frequency. The dimensions of passive valves were chosen such that their first natural frequency is well above the valve operating frequency, and the membranes stresses are within allowable limits at a maximum stroke of about 20 μm , and other dimensions were chosen suitably. The design was then verified and dimensions adjusted for best performance through computer simulations. The primary transduction element in the device, PZT-5H piezo cylinder is about 1 mm in diameter and 1 mm in height. The diameter of the pumping chamber is 3.6 mm, and its height from the piston surface is 200 μm . The width of the tethers membrane around the piston is 150 μm and their thickness is about 15 μm . The membranes comprising the passive valves are 15 μm thick, and have an inner diameter of 0.70 mm and an outer diameter of 1.65 mm. The hole at

the center of the rigid boss through which the fluid can pass through when the valve is open is 0.5 mm in diameter. When not in motion, the valves are normally closed with a minimal 0.5 μm gap between the valve and the seating to minimize any back flows.

MODELING AND SIMULATION

Dynamic simulations of the micro-pump system were carried out to gain insight into the performance of the micro-pump. Detailed analytical models of the canonical components of the system and the fluid-flow models including fluid inductance and fluidic and structural compliances were built in the Matlab/Simulink® application and system level simulations were carried out by numerically integrating the coupled governing equations. The entire system is highly coupled as can be seen in the block diagram of the system in Figure 2.

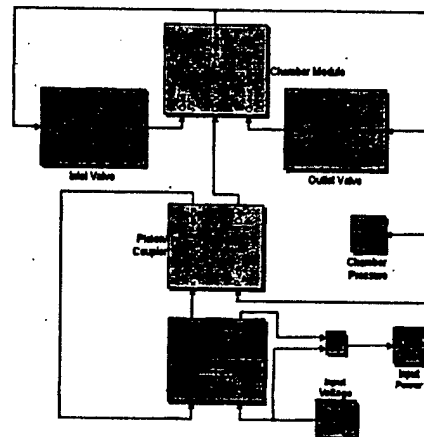


Figure 2: Flow chart of the simulations.

The key components in the micro-pump are: *drive element*, *pump chamber*, *passive valves*, and *flow channels*. All the structural components were modeled as lumped single DOF, and this is adequate since the operational frequency of the device is well below the first natural frequency of any structural component. The liquid in the pump chamber is assumed to be quasi-statically compressible. Further, the interior pressure distributions in the system cavities are assumed to be uniform and the flow is assumed to be steady.

Drive Element: The equations describing the dynamic motion of the drive element which includes piezo and piston is as follows:

$$M\ddot{x} + b\dot{x} + kx - p_c A_{pe} = F$$

$$x = d_{33}V_e - \frac{F}{k}$$

$$\Delta V = x A_{pe}$$

where x = piston displacement, M = effective mass of the piston element, b = damping coefficient, k = stiffness of the tethers attached to the piston, F = internal force at the

interface of piston and the piezo, d_{33} = dielectric constant of the piezo, A_{pis} = area of the piston, p_c = pressure in the chamber, V_e = applied voltage across the piezo, and ΔV = change in volume of the pump chamber.

Pump Chamber: The following equation, obtained by the application of continuity to the control volume, governs the pressure variation in the pump chamber.

$$\dot{p}_c = \left(\frac{V_0 - \Delta V}{C_f} + \frac{1}{K_f} \right)^{-1} (Q_{in} - Q_{out} + \Delta V)$$

where V_0 is the volume of fluid initially contained within the chamber when the volume source is undeformed, K_f is the bulk modulus of the fluid, and C_f is the hydraulic capacitance of the chamber structure.

Check Valve and Channel Dynamics: The check valves rectify the fluid flow by opening or closing the fluid flow path from the reservoir to the chamber in response to the pressure differential between the two sides. The valve opening is modeled as a quasi-static linear function of the pressure differential across the valve. The flow rate Q , and the pressure drop across the valve, ΔP , are related as:

$$\Delta P = \frac{1}{2} \rho \zeta \left(\frac{Q}{A} \right)^2 + I \dot{Q}$$

where ρ = density of the fluid, I = channel inductance, A = surface area of the valve opening for flow across the valve, ζ = the loss coefficient, a function of Reynold's number corresponding to the instantaneous flow rate, determined from a standard look-up table.

FABRICATION

The micro-pump is fabricated as a multi-layer structure as schematically illustrated in Figure 1. The device is assembled from seven layers—3 SOI wafers, 1 Si layer and 3 pyrex layers—as shown numbered in the cross-section figure in Fig. 1. To achieve a compact design using minimum number of layers, both surfaces of each layer were efficiently utilized by implementing multiple lithography steps for the SOI wafers. For complete details on the microfabrication of the layers, interested readers may refer [4]. After the microfabrication process, the top three SOI wafers (layers 4, 5, and 6) were aligned using an Electronic Visions system and fusion bonded at 1100°C in nitrogen for 1 hour. The bonded wafer stack was cut into chips of size 16.7 mm by 15.7 mm chips using a die-saw, cleaned in water, acetone, methanol, and isopropanol successively, and finally dried in air. The glass wafers were processed with diamond drills and die-saw cut into small chips. Then, the Si and glass interface in the bottom stack (layers 1, 2, and 3) and in top stack (layer 7 and the bonded stack 4, 5, 6) were separately anodically bonded at about 300°C. A ceramic PZT-5H piezoelectric cylinder 1 mm in diameter and 1 mm in height was manually placed in the middle of the glass layer 3 in the bottom stack, and the piezo-Si interfaces were eutectically bonded using a Ti-Pt and Au-Sn alloys. Figure 4 shows a picture of a fully assembled

micropump with electrical leads. The packaged device has dimensions 22.7 mm × 15.7 mm × 8.6 mm. However, the packaging volume is not optimized and as such, the total volume of the device could be much smaller.

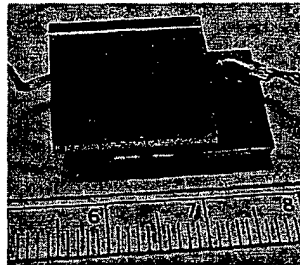


Figure 4. Assembled micro-pump with electrical leads.

TESTING AND MODEL CORRELATION

An experimental rig (Figure 5) that includes low and high-pressure reservoirs, control valves, pressure, voltage, and current sensors and flow meters was constructed to test the micro-pump. The micro pump device is placed in a specially designed aluminum jig (shown in the inset in Figure 5) with O-rings for connection to the inlet and outlet fluid channels. Static and dynamic pressure sensors are placed directly before and after the device to monitor the LPR and HPR pressures. A micromachined membrane within the top structure of the device pump chamber allows for measurement of the internal pressure as a function of the membrane deflection using an MTI laser probe deflection sensor. In order to avoid any air bubbles in the device, the fluid channels and cavities in the micro pump were first evacuated with the aid of a vacuum pump followed by a few cycles of purging the channels with a solvable gas (N_2) and evacuating. Finally, the device was filled with the degassed fluid at a controlled rate.

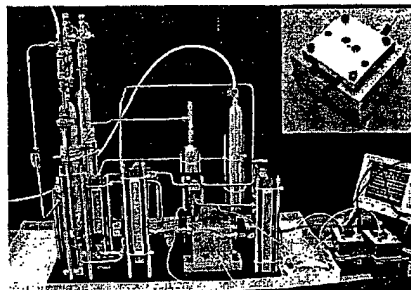


Figure 5. The experimental rig for testing micro-pump. The inset shows packaging jig holding the micro-pump.

The performance of the micro-pump was evaluated by varying voltages across the piezo from 0 to 1600V with bias voltages in the range of 300-600 V, and frequencies from 1 kHz to 12 kHz. The inlet pressure was maintained at 850 kPa, and the differential pressure across the pump

was varied from 0 to 500 kPa. Flow rates were measured using fluid rotameters directly before and after the device, and pressure signals were acquired using the Lab View data acquisition system. Highest flow rate recorded was 2500 $\mu\text{L}/\text{min}$ at 1200 V peak-to-peak voltage, 600 V bias voltage, and 4.5 kHz, and zero differential pressure.

Figures 6, 7, and 8 show the model correlation curves illustrating the performance characteristics of the micro-pump. In Figure 6, the plot of flow rate as a function of drive frequency at zero pressure differential is shown. It can be seen that a good correspondence between the model and experiment was achieved in low frequency regime, however, in the high frequency regime, fluidic resonance effects that were not predicted in the simulation were observed. The resonance effects are attributed to the geometry of the experimental rig.

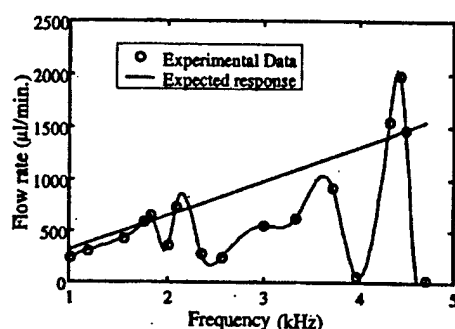


Figure 7. Flow rate versus drive frequency at 1200 V peak-to-peak voltage, and zero differential pressure.

Figure 7 shows the plot of the flow rate versus the pressure differential across the inlet-outlet at 3.5 kHz and 1200 V P-P drive voltage and 600 V bias voltage.

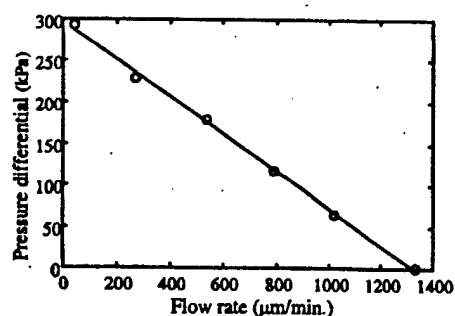


Figure 7. Pressure differential versus flow rate.

Figure 8 shows the relation between the flow rate and the peak-to-peak voltage across the piezo element at a drive frequency of 3.5 kHz, a bias voltage of 600 V, and zero differential pressure. The flow rate increases with the voltage monotonically but not linearly. The slight difference in the slopes of the model and experimental curves is attributed to the non-linear behavior of the tethers that was not modeled in the simulation.

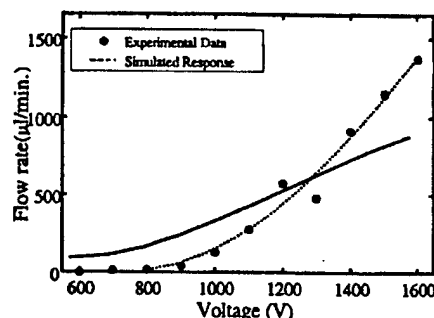


Figure 8. Flow rate vs. piezo peak to peak voltage at 3.5 kHz drive frequency

CONCLUDING REMARKS

A piezoelectrically driven passive valve hydraulic micro-pump operating at very high frequencies and yielding a high flow rate of 2.5 ml/min has been successfully fabricated and tested. This work has demonstrated the technical feasibility of critical micro-fabrication processes, bulk piezo-silicon integration, and fluid-filling techniques, and thus offers exciting prospects for accomplishing high specific power micro-hydraulic transducers, a new technology under development at MIT. A more rigorous and systematic study is under way to better understand the behavior and to improve the micro-pump performance by either eliminating or exploiting the fluidic resonance effects. The next generation micro-pumps, currently under development, will feature active valves and the single crystal piezo (PZT-PT) element for drive both in the pump chamber and the valves. As a result, a ten-fold increase in the performance is expected.

ACKNOWLEDGEMENTS

This research was sponsored by DARPA under Grant # DAAG55-98-0361 and by ONR under Grant # N00014-97-1-0880.

REFERENCES

- [1] Hagood, N., et al. "Micro-hydraulic Transducer Technology for Actuation and Power Generation", *Proceedings of SPIE*, Vol. 3985(2000), Newport Beach, CA, March 5-9, 2000, pp. 680-688.
- [2] Gravesen, P., Branebjerg, J., Jensen, O. S., 1993, "Microfluidics-A Review," *J. Micromech. Microeng.*, 3 (1993), pp. 168-182.
- [3] Shoji, S., and Esashi, M., "Microflow Devices and Systems," *J. Micromech. Microeng.* 4 (1994), pp. 157-171.
- [4] Li, H.-Q. et al., "A High Frequency High Flow Rate Piezoelectrically Driven MEMS Micropump," *Proceedings (CD ROM), Solid State Sensor and Actuator Workshop*, Hilton Head Island, SC, June 4-8, 2000, pp. 69-72.

A Piezoelectric Microvalve for Compact High-Frequency, High-Differential Pressure Hydraulic Micropumping Systems

David C. Roberts, Hanqing Li, J. Łodewyk Steyn, Onnik Yaglioglu, S. Mark Spearing, *Member, ASME*, Martin A. Schmidt, *Senior Member, IEEE*, and Nesbitt W. Hagood

Abstract—A piezoelectrically driven hydraulic amplification microvalve for use in compact high-performance hydraulic pumping systems was designed, fabricated, and experimentally characterized. High-frequency, high-force actuation capabilities were enabled through the incorporation of bulk piezoelectric material elements beneath a micromachined annular tethered-piston structure. Large valve stroke at the microscale was achieved with an hydraulic amplification mechanism that amplified ($40 \times -50 \times$) the limited stroke of the piezoelectric material into a significantly larger motion of a micromachined valve membrane with attached valve cap. These design features enabled the valve to meet simultaneously a set of high frequency (≥ 1 kHz), high pressure (≥ 300 kPa), and large stroke ($20-30 \mu\text{m}$) requirements not previously satisfied by other hydraulic flow regulation microvalves. This paper details the design, modeling, fabrication, assembly, and experimental characterization of this valve device. Fabrication challenges, such as deep-reactive ion etching of the piston and valve membrane structures, wafer-level silicon-to-silicon fusion bonding, wafer-level and die-level silicon-to-glass anodic bonding, preparation and integration of piezoelectric material elements within the micromachined tethered piston structure, and filling of degassed fluid within the hydraulic amplification chamber are detailed. [829]

Index Terms—Hydraulic amplification, MEMS, micropump, microvalve, piezoelectric.

I. INTRODUCTION

THE development of a fluidic microvalve, capable of high-frequency control of high-differential pressure liquid fluid flows, is a key task in the realization of compact high performance micropumping technology. Currently, many research efforts around the world are underway to develop compact liquid micropumping systems, the term “micro” referring to devices which are created with fabrication procedures capable of μm -size tolerances and which produce overall micropump dimensions on the order of a few millimeters to a few centimeters. However, the vast majority of these systems are designed for low pressure and low flow rate applications (i.e., drug dispensing and microdosing) [1]–[8]. The higher performing

of these systems are capable of pumping liquids with flow rates on the order of $1000-3000 \mu\text{L}/\text{min}$ ($0.017-0.050 \text{ mL}/\text{s}$) against differential pressures of no more than $10-50$ kPa.

In an effort to develop higher differential pressure and higher flow rate micropumping systems for both actuation and power generation applications, a novel class of micro-hydraulic transducer (MHT) devices has been introduced [9]–[13]. These devices, which integrate bulk piezoelectric materials within stiff micromachined structures to form a fluid pumping chamber and two active valves, are designed to enable high frequency pumping of fluid ($1-10$ kHz) against pressure differentials on the order of $\sim 0.4-1$ MPa, creating flow rates near or in excess of $0.5 \text{ mL}/\text{s}$. The performance of these MHT systems is directly governed by the pressurization, stroke, and frequency capabilities of the active valves employed. The development of a microvalve for use within these MHT systems is the subject of this paper.

Although a significant amount of literature is available describing the development of active valve devices and technology, few if any have been designed for high frequency control of high differential pressure liquid fluid flows. Microvalve designs using thermopneumatic actuation [14], [15], thermal bimetallic actuation [16], SMA actuation [17], electrostatic actuation [18], [19], electromagnetic actuation [20], [21], piezoelectric bender-type actuation (both thin-film and thick film) [22], [23], and piezoelectric stack-type actuation [24]–[26] have been presented. All of these microvalves share a common operational geometry in that a valve cap is affixed to a diaphragm or membrane structure which carries the cap through a predetermined stroke. Based on the reported capabilities, none of these valves is capable of simultaneously satisfying the set of high frequency, high differential pressure, and large stroke requirements needed within full MHT liquid micropumping systems.

The thermal actuation designs (based on thermopneumatic, thermal bimetallic, and shape memory alloy principles) potentially can achieve large stroke and reasonable actuation force. However, these devices exhibit excessive power consumption and poor response times on the order of seconds. High-frequency actuation in the kHz range is unachievable. The electrostatic devices are limited in their deflection and pressure generation capabilities, since the electrostatic force generated between two parallel plates scales inversely with their spacing and since electrical breakdown across the gap must be avoided. The electromagnetic concepts are impeded by the overall size of external solenoid and housing structures

Manuscript received March 18, 2002; revised July 12, 2002. This research was assisted by the staff at the Microsystems Technology Laboratory at MIT and supported by DARPA under Grant #DAAG55-98-1-0361 and by ONR under Grant #N00014-97-1-0880. Subject Editor H. Fujita.

D. C. Roberts and N. W. Hagood are with the Continuum Photonics, Inc., Billerica, MA 01821 USA (e-mail: droberts@continuumphotonics.com).

H. Li, J. L. Steyn, O. Yaglioglu, S. M. Spearing, and M. A. Schmidt are with the Massachusetts Institute of Technology (MIT), Cambridge, MA 02139 USA. Digital Object Identifier 10.1109/JMEMS.2002.807471

needed to actuate the valve structure. Piezoelectric thin-film and thick-film bender-type designs are limited in their ability to generate both high force and large deflection output. The work in [24]–[26] aimed at solving this limited valve stroke problem through the use of a stack-type piezoelectric actuator material attached directly to the valve membrane. In order to achieve a reasonable stroke of $8\text{ }\mu\text{m}$, however, the piezoelectric stack material was required to be quite long ($\sim 9\text{ mm}$), and the valve membrane structure was designed to be relatively compliant to compensate for the tolerance mismatch between the stack and the surrounding structure. These characteristics resulted in limited differential pressure ($< 50\text{ kPa}$) and limited frequency ($< 50\text{ Hz}$) capabilities for the valve device.

A promising concept for achieving high frequency operation ($\geq 1\text{ kHz}$) in conjunction with large differential pressure ($\geq 300\text{ kPa}$) and large valve stroke ($20\text{--}30\text{ }\mu\text{m}$) capabilities involves the use of miniature-sized bulk piezoelectric elements (for example 1 mm in thickness—almost an order of magnitude smaller in length than those in [24]–[26]), actuating a stiff micromachined piston-type structure, with an integrated area-ratio hydraulic amplification mechanism for amplifying the limited deflection of the piezoelectric material into a significantly larger valve cap stroke. This concept for microscale systems has been introduced in [12] and [13]. Numerous macroscale piezoelectric hydraulic amplification mechanisms have been presented in the literature. In an application for active vibration control, a piezoelectric actuator uses the volume change of a piezoelectric ring to create a large deflection of a smaller area contact surface [27]. In an application for vibration control of a rotary dynamic system, the deflection of a stack-type piezoelectric actuator is coupled through an hydraulic line to a smaller size piston, which helps to control the motion of a rotating shaft [28]. These and other [29] piezoelectric hydraulic amplification mechanisms are novel in design, yet do not face the difficult fabrication, assembly, and tolerancing challenges inherent in the development of microscale systems.

This paper details the development of a compact piezoelectric hydraulic amplification microvalve to enable the realization of high frequency, high differential pressure micropumping systems. The paper is organized as follows. Section II describes the microvalve geometry and its principle of operation. Section III presents modeling tools and dynamic simulations that were developed to design the valve structure. Section IV outlines the fabrication and assembly procedures developed to create the active valve device. Section V details the results of two sub-component studies carried out to validate the concept of the active valve. Section VI outlines the final active valve design geometry. Section VII presents an overview of the measurement set-up and experimental test plan to evaluate the valve performance. Section VIII discusses the experimental results and provides model-experiment correlation for the quasistatic and dynamic performance of the active valve device. Last, Section IX presents conclusions for this research work.

II. PRINCIPLE OF OPERATION

The microvalve geometry is shown in Fig. 1. The active valve consists of three primary components: a piezoelectric drive ele-

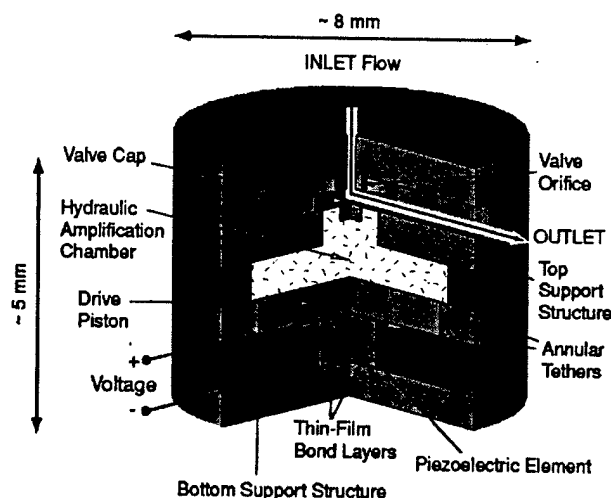


Fig. 1. A schematic of the piezoelectrically driven hydraulic amplification microvalve. The primary structural components are designated with arrows. External hydraulic system pressure loading is applied on the top surface of the valve cap and membrane.

ment, an enclosed hydraulic amplification chamber (HAC), and a membrane with attached valve cap. The drive element incorporates a circular piston structure supported from beneath by one or more small bulk piezoelectric cylinders and is suspended circumferentially from a surrounding support structure by thin annular micromachined tethers. This novel compact “piston-type” design enables high frequency actuation against a large external pressurization due to the high stiffness of the piston structure and integration of miniature bulk piezoelectric elements beneath the piston using a thin-film bond layer.

The lateral dimensions of the tethers are designed to make the tethers compliant enough to allow for rigid piston motion up and down, yet stiff enough to resist bowing under pressurization caused by the hydraulic fluid above the tether during actuation. The tethers provide a seal between the hydraulic fluid above the piston and the piezoelectric chamber below the piston, and also provide a path for electrical contact to the top surface of the piezoelectric cylinders. The fluid chamber resides between the top surface of the drive element piston and the bottom surface of a thin, smaller diameter silicon micromachined valve cap membrane. In response to applied piezoelectric voltage, the piezoelectric material strains. The resulting deflection of the drive element piston generates a pressure within the hydraulic amplification chamber which in turn deflects the valve cap and membrane against a fluid orifice, thereby regulating fluid flow through the external hydraulic system. The pressure loadings on the valve cap and membrane during device operation depend on the external microfluidic system application. The piezoelectric material capabilities, the ratio of the piston diameter to the valve membrane diameter, the compliances of the fluid and structural elements in the chamber, the severity to which the valve cap membrane experiences nonlinear behavior, and the nature of the external loading all contribute to the performance of this microvalve device.

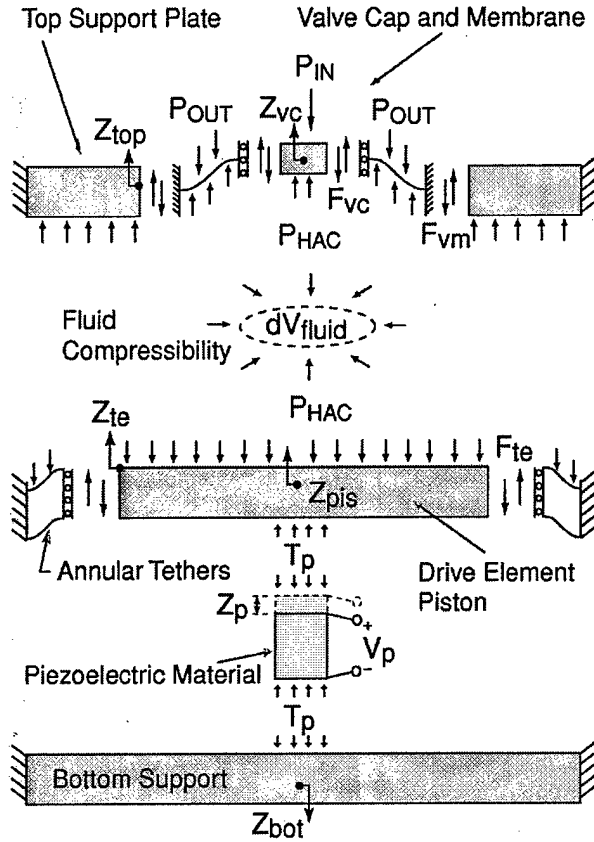


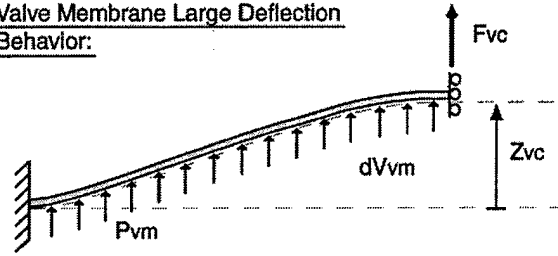
Fig. 2. Structural components included within active valve analytical model. All structures were modeled using linear theory, except for the valve cap and membrane structure, which required the development of nonlinear numerical modeling tools.

III. MODELING AND SIMULATION

Comprehensive quasistatic and dynamic analytical modeling tools were developed in an effort to design the valve structure based on operational requirements and subsequently to predict the valve behavior in response to applied piezoelectric material voltage and external pressure loading. As shown in Fig. 2, the piezoelectric material behavior, the bending of the drive element piston and deformation of the annular tethers, the hydraulic amplification chamber fluid compressibility, the structural compliance of the top support plate, the structural deformation of the bottom support plate, and the deformation of the valve cap and membrane structure were captured by these modeling tools (see Fig. 3).

The deformations of the plate structures were modeled using bending and shearing relations to determine the structural deflections and fluid swept volumes. Detailed discussions of these active valve modeling procedures are found in previous publications [12], [13]. Although the majority of structural deformations within the valve could be evaluated using linear plate theory, the modeling of the valve cap and membrane structure had to include in-plane tensile relations to properly capture the nonlinear large deflection behavior associated with valve cap deflections in excess of the membrane thickness. Associated

Valve Membrane Large Deflection Behavior:



Look-Up Tables:

| | | | |
|----------------------|---|----------------------------|-----------------------------|
| Table F_{vc} | → | Given: Z_{vc} , P_{vm} | Interpolate: F_{vc} |
| Table dV_{vm} | → | Given: Z_{vc} , P_{vm} | Interpolate: dV_{vm} |
| Table σ_{max} | → | Given: Z_{vc} , P_{vm} | Interpolate: σ_{max} |

Fig. 3. Numerical modeling tools were used to generate look-up tables for the nonlinear large deflection behavior of the valve cap and membrane. Given a prescribed valve cap displacement Z_{vc} and pressure loading across the membrane P_{vm} , a look-up table for each of F_{vc} , dV_{vm} , and σ_{vm} was generated.

numerical modeling tools, detailed in [30], were incorporated into the overall active valve structural model for this purpose.

To capture the nonlinear effects of the valve membrane deformation at high frequency, and to include important dynamic effects, such as the drive element piston inertia and the valve cap inertia and damping, a Simulink simulation architecture was developed. The structural compliances within the active valve simulation were based upon the linear and nonlinear modeling tools discussed above. Look-up tables were implemented within the simulation to enable efficient calculation of the valve membrane deflections and stresses at every time step. Taking as inputs the valve cap displacement Z_{vc} and the net pressure across the valve membrane $P_{vm} = P_{HAC} - P_{OUT}$, a lookup table was employed for each of the following output variables: the valve cap force on the membrane F_{vc} , the swept volume beneath the valve cap and membrane dV_{vm} , and the maximum radial stress in the membrane σ_{vm} .

Dynamic relations for the valve cap and drive element piston, schematically shown in Fig. 4, were also implemented to incorporate structural mass and damping. The dynamic behavior of the drive piston structure and the valve cap structure can be described by the following relations, respectively,

$$M_{pis}\ddot{Z}_{te} + C_{pis}\dot{Z}_{te} = A_p T_p - A_{pis} P_{HAC} + F_{te} \quad (1)$$

$$M_{vc}\ddot{Z}_{vc} + C_{vc}\dot{Z}_{vc} = A_{vc}(P_{HAC} - P_{IN}) + F_{vc} \quad (2)$$

where A_{pis} is the piston area, M_{pis} is the piston mass, A_p is the piezoelectric material area, A_{vc} is the valve cap area, and M_{vc} is the valve cap mass. The damping coefficient C_{pis} is a lumped parameter that includes the effects of structural damping in the tethers and damping due to fluid-structural interaction within the hydraulic amplification chamber. The damping coefficient C_{vc} is a lumped parameter that includes the effects of structural damping in the valve membrane and potential squeeze film

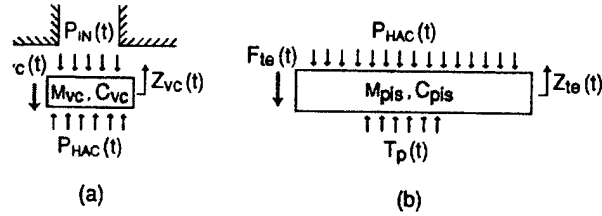


Fig. 4. Dynamic modeling of the valve cap and drive element piston structures: (a) valve cap mass, M_{vc} , and damping, C_{vc} ; (b) piston mass, M_{pis} , and damping, C_{pis} . Values for the damping coefficients were estimated, then verified through experimentation.

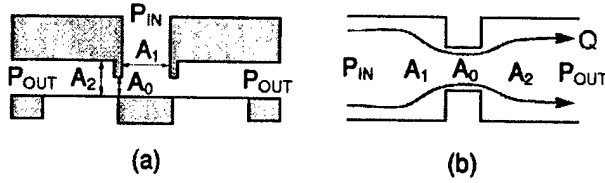


Fig. 5. Valve orifice representation: (a) valve cap geometry and fluid flow areas and (b) representation of flow through valve as a flow contraction followed by a flow expansion.

damping due to the valve cap motion as it closes against the fluid orifice.

Pressure-flow relations through the valve orifice were included in the overall valve simulation, with the orifice structure being represented by a flow contraction followed by a flow expansion. An integral analysis gives a relationship for the combined effect of this flow expansion and contraction. The loss coefficient $\zeta_{orifice}$ is defined as the total pressure drop $\Delta P = P_{IN} - P_{OUT}$ over the dynamic pressure based on the orifice local mean velocity ($\bar{u} = Q/A_0$),

$$\zeta_{orifice} = \frac{\Delta P}{\frac{1}{2} \rho \bar{u}^2} = \left[\frac{1}{2} \left(1 - \frac{A_0}{A_1} \right)^2 + \left(1 - \frac{A_0}{A_2} \right)^2 \right] \quad (3)$$

where the upstream flow area is defined as A_1 , the throat area is defined as A_0 , and the downstream flow area is defined as A_2 (see Fig. 5).

This approximation holds only for Reynolds numbers in excess of 10 000 (i.e., fully turbulent flow). In high-performance micropumping systems, Reynolds numbers fluctuating between 10 and 20 000 are expected as the valve cap opens and closes [31]. For this reason, empirical correction factors were employed to obtain better estimates for the loss coefficients of the laminar and turbulent flow regimes within this range [31]. These higher order loss effects were represented with a Reynolds number dependent coefficient $C(Re)$ as a multiplier of $\zeta_{orifice}$, thereby altering the pressure-flow relation for the orifice,

$$\Delta P = P_{IN} - P_{OUT} = \frac{1}{2} \rho C(Re) \zeta_{orifice} \left(\frac{Q^2}{A_0^2} \right). \quad (4)$$

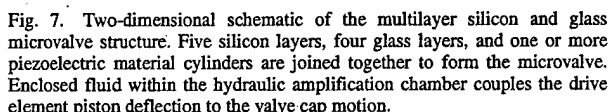
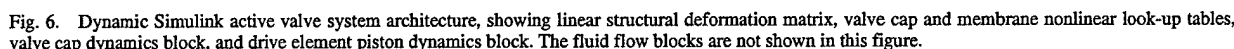
The structural and fluidic modeling tools presented in this section were combined to form a system-level Simulink simulation that was then used to design the active valve geometry

to satisfy performance requirements and to provide model correlation for subsequent experimental results. The simulation architecture for the structural components of the active valve consisted of four major subsystems, as shown in Fig. 6: a matrix of linear coefficients describing the active valve structural behavior, including that of the piezoelectric material, a collection of nonlinear look-up tables that captures the large-deflection valve membrane deformation and stress behavior, a valve cap dynamics block, and a drive piston dynamics block.

IV. FABRICATION AND ASSEMBLY

The fabrication process flow for the microvalve involved the micromachining and assembly of three silicon-on-insulator layers, two silicon layers, and four glass layers. A cross-section schematic of the microvalve device is shown in Fig. 7. The drive element tethered-piston structure was created through deep-reactive ion etching of Layers 4 and 5 separately, followed by wafer-level fusion bonding of the two wafers together to form a double-layer piston structure. During etching of the annular tethers in each of Layers 4 and 5, control of the fillet radii at the oxide etch-stop was critical, in order to minimize stress concentrations [32], [33]. Fig. 8 presents scanning-electron micrograph (SEM) images of a Layer 4 piston structure with well-controlled fillet radii, prior to bonding with Layer 5. The valve cap and membrane structure was also created using deep-reactive ion etching, with a similar requirement for good dimensional control of the fillet radii.

The middle glass layer (Layer 3) forms the drive element support structure and the top (Layer 9) and bottom (Layer 1) glass layers provide structural support. The bottom silicon layer (Layer 2) and drive piston silicon layers (Layers 4,5) provide a path for electrical contact to the piezoelectric cylinders. The top four silicon layers (Layers 4,5,7,8) and glass layer (Layer 6) house the hydraulic amplification chamber, valve cap and membrane structure, and fluid inlet and outlet channels. In order to provide a bottom structural stop for the valve cap as it moves away from the orifice, the Layer 6 glass layer was designed with a series of small through holes to connect the bottom portion of the hydraulic amplification chamber above the drive element piston to the top portion of the chamber directly beneath the valve cap and membrane. Although not shown in Fig. 7, a small fluid channel connecting the valve HAC chamber to an external pressure regulator was micromachined in Layer 7. This channel enabled control of a bias pressure P_{bias} within the chamber during device testing, however, due to its flow impedance characteristics, effectively allowed high frequency P_{HAC} pressure oscillations about the bias pressure during active valve operation. All glass wafers were machined ultrasonically. All silicon-silicon wafer interfaces were bonded with a wafer-level high-temperature ($\sim 1300^\circ\text{C}$) fusion bonding procedure, and all silicon-glass layer interfaces were bonded using a low temperature ($\sim 300^\circ\text{C}$) anodic bonding process (either at the wafer-level or die-level depending on the process step) with an applied voltage of 1000 V. Thin venting channels were etched in Layers 4 and 5 to prevent pressurization and potential plastic deformation or fracture of the piston tethers during the high temperature fusion bonding procedure. Attachment of the



A four layer film structure on the piezoelectric material and a three layer film structure on each of the adjoining silicon layers was deposited in preparation for bonding. The four layer structure on the piezoelectric material consisted of 50 nm Ti, 250 nm Pt, 4000 nm AuSn, and 50 nm Au. The Ti served as an adhesion layer, the Pt as a diffusion barrier, and the final Au as a capping layer to prevent oxidation of Sn in the AuSn alloy. The AuSn layer, chosen to be thick enough (4 μm) to compensate for

One of the critical issues during integration of the piezoelectric material elements was guaranteeing an upward deflection of the drive element piston large enough to ensure a preload on the eutectic alloy interface during bonding, yet small enough to ensure that stresses in the piston tethers during bonding and subsequent high-frequency operation were below critical levels. Typically, for the active valve structures developed in this research, limiting tether stresses near 1 GPa [33] were reached for piston deflections approaching 10 μm . With a conservative safety factor taken into account, the devices were therefore toleranced such that a "piston push-up" of $\sim 2 \mu\text{m}$ could be guaranteed. This tolerancing, shown in Fig. 9, was achieved by plasma etching shallow seats (typically 30–40 μm in depth) beneath the piezoelectric element location in Layer 2.

Following the assembly of the active valve device, a procedure was carried out to pole the piezoelectric material within the drive element structure. This was done by heating the device to 70 °C and applying an electric field across the piezoelectric element of 1000 V/mm. Once poled, the hydraulic amplification chamber of the device was filled and sealed with degassed silicone oil, as detailed in [35]. The active valve device was, at this point, ready for testing. A photograph of a completed nine-layer microfabricated valve is shown in Fig. 10, as part of a full chip-level MHT micropumping system.

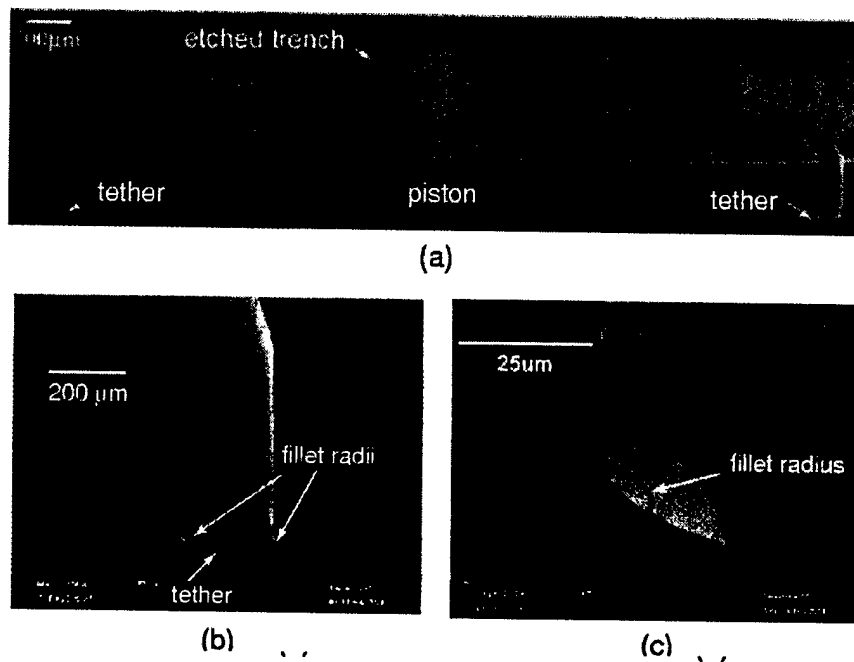


Fig. 8. SEM images of a Layer 4 etched drive element piston: (a) a cross section of the SOI piston structure, (b) a close-up of the etched trench, and (c) a further close-up of the fillet radius. In this structure, a 20–25 μm fillet radius was achieved. Debris in background was generated during die-saw procedures.

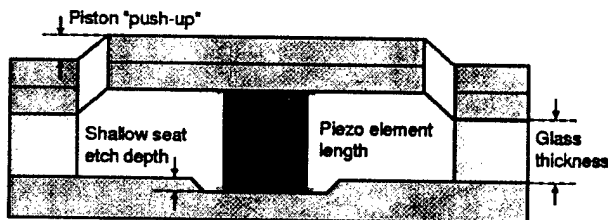


Fig. 9. Tolerancing of the piezoelectric element within the drive element structure was accomplished by etching shallow seats in the top surface of Layer 2. Precise control of the etch depth was necessary to achieve a controlled "push-up" of the drive element piston during bonding operations.

V. VALVE SUBCOMPONENT VALIDATIONS

The development program for this active valve device involved the validation of two primary subcomponent device platforms prior to assembly and characterization of the complete active valve device. These two subcomponent platforms were 1) the piezoelectric drive element structure, encompassing the challenge of integrating the miniature piezoelectric element(s) beneath the micromachined tethered piston structure and 2) the hydraulic amplification unit, as a means to prove the capability to fill the HAC chamber with degassed fluid and to achieve amplification of the piston motion into a significantly larger valve cap deflection.

A. Drive Element Subcomponent Validation

The purpose of this effort was to evaluate the fabrication and assembly process flow for integrating piezoelectric material elements within the micromachined drive element structure and to obtain quasistatic and high-frequency experimental data on the

completed actuator structures. The previously published work [11] provides a comprehensive overview of this subcomponent study. In general, this study, through the assembly and testing of a series of drive element devices, proved the ability to integrate both single and multiple (three) piezoelectric material elements beneath double-layer micromachined tethered-piston structures, as shown in Fig. 11. The presence of three elements spread out beneath the piston enabled higher stiffness actuation capabilities by eliminating tilting and bending behavior of the piston structure. Additionally, this study verified that high-strain capability single-crystal (PZN-PT) piezoelectric material [36], in addition to standard polycrystalline PZT-5H material, could be successfully incorporated. Three-cylinder PZN-PT devices were experimentally characterized up to a frequency of 200 kHz for drive voltages between 50 V and 1000 V. Results showed that these microactuator structures exhibited negligible bending and tilting for quasistatic operation up to 15 kHz and that first modal behavior did not occur until frequencies in excess of 80 kHz [11].

B. Hydraulic Amplification Validation

The purpose of this effort was to validate the concept of hydraulic amplification between the piston and valve cap structures. HAC devices, consisting of Layers 4 through 9, were constructed to validate fluid filling and device operation without the effects of piezoelectric material integration beneath the piston structure. The previously presented work [35] provides a comprehensive overview of this subcomponent study. The assembled devices were successfully filled with degassed silicone oil (hexamethyldisiloxane, produced by Dow Corning under the trade name DC200 0.65 centistoke) and device amplification ratios up to 40 \times were measured.

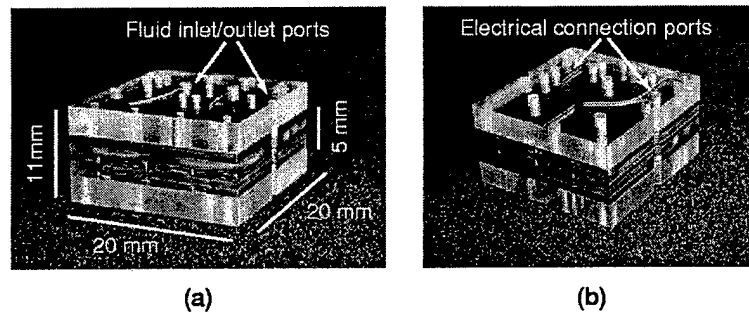


Fig. 10. Photograph of a nine-layer silicon and glass piezoelectrically driven hydraulic amplification microvalve, as part of a full MHT system. Dimensions of the valve structure within the full MHT chip are $8\text{ mm} \times 8\text{ mm} \times 5\text{ mm}$.

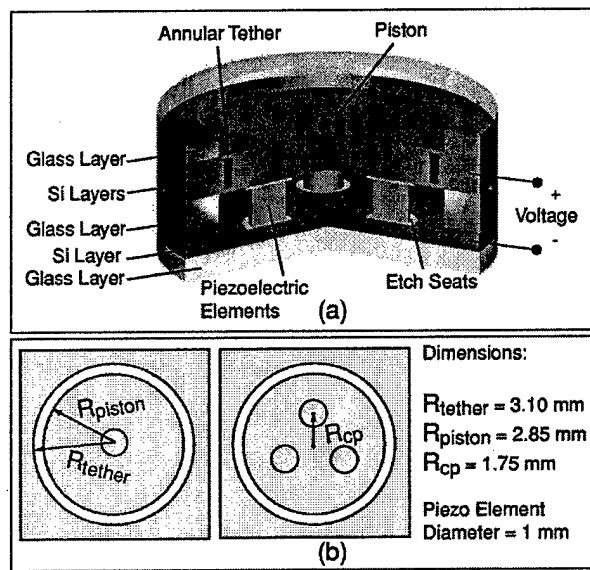


Fig. 11. Three-dimensional schematic of a piezoelectric drive element device. Three piezoelectric cylinders are sandwiched between a lower support silicon layer and an upper double silicon layer tethered-piston structure. Voltage is carried along the upper and lower silicon layers.

VI. FINAL ACTIVE VALVE DIMENSIONS

The dimensions of the fabricated final active valve device are illustrated in Fig. 12. The device incorporated three PZN-PT piezoelectric square elements (each with cross-sectional area $1.06\text{ mm} \times 1.06\text{ mm}$) beneath a double-layer tethered piston structure. The top and bottom tethers of the piston were each $250\text{ }\mu\text{m}$ in width and each had a thickness of $8\text{ }\mu\text{m}$. A valve cap and membrane structure was positioned above the hydraulic amplification chamber, with a structural stop (formed by the glass Layer 6 within the HAC chamber) $\sim 16.5\text{ }\mu\text{m}$ below the equilibrium position of the valve cap. Glass Layer 6 contained a series of "HAC through-holes" to carry the fluid from the lower to upper portion of the HAC chamber. The valve cap had a diameter of $500\text{ }\mu\text{m}$ and the valve membrane had an outer diameter of $1400\text{ }\mu\text{m}$ and thickness of $6\text{ }\mu\text{m}$. A valve orifice was located $\sim 16.5\text{ }\mu\text{m}$ above the valve cap equilibrium position. The orifice had an inner diameter of $450\text{ }\mu\text{m}$.

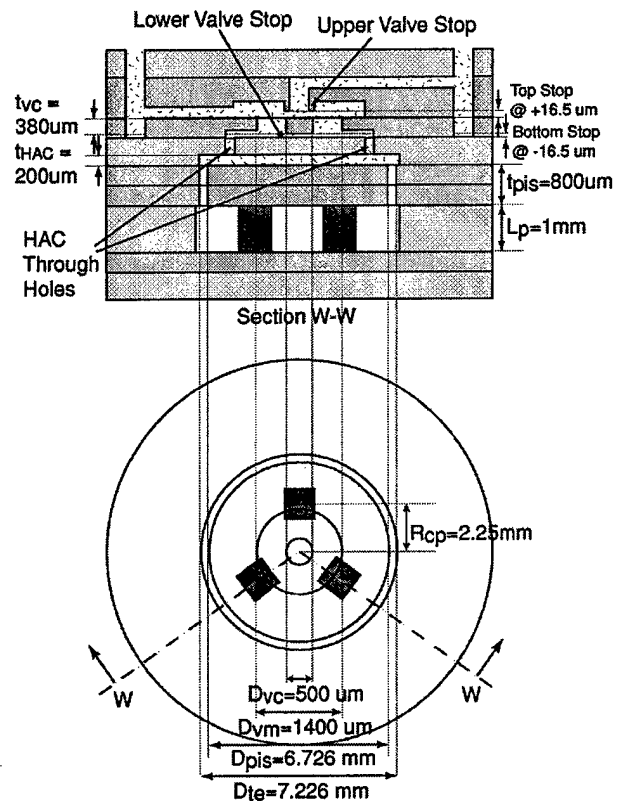


Fig. 12. Dimensions of the fabricated active valve devices. Three square PZN-PT elements were incorporated beneath a double-layer tethered piston. A valve cap and membrane structure interacts with the fluid orifice structure at $Z_{vc} = +16.5\text{ }\mu\text{m}$ and with the glass Layer 6 structure within the HAC chamber at $Z_{vc} = -16.5\text{ }\mu\text{m}$.

VII. EXPERIMENTAL TEST PLAN

Testing of the active valve device was divided into two primary efforts. The first effort focused on characterizing the actuation capabilities of the valve structure without the effects of differential pressure and flowing fluid above the structure. In this effort, the dynamic behavior of the active valve device was evaluated and the range of driving frequency for which the valve behaved in a quasistatic manner was determined. Additionally, at the determined maximum quasistatic operational frequency,

the structural amplification ratio of the valve device was characterized as a function of applied voltage to the piezoelectric drive element. Once the device was proven to be a successful actuator, the second effort focused on evaluating its flow regulation capabilities and limitations. In this effort, the flow regulation capability of the valve device at the maximum quasistatic operational frequency of the structure was evaluated as a function of increasing differential pressure across the valve orifice. In this manner, the valve performance limitations could be determined as the differential pressure was increased.

The aforementioned tests required the development of testing rigs and experimental procedures to measure accurately the drive element piston and valve cap structural vibrations within the multilayered device. A laser vibrometer system, with a micro-lens attachment, was used for these vibration measurements [37]. The active valve chip-level device was mounted in a test-jig which included fluid inlet and outlet ports to the chip, as well as through-holes for alignment of the vibrometer laser beam on the key structural components within the device. The accompanying fluids testing rig was comprised of fluid reservoirs, absolute and differential pressure sensors for measuring the inlet and outlet pressures into the device, and a calibrated real-time flow sensor for measuring flow rates through the valve. Additionally, a data-acquisition system was implemented to enable real-time drive signals to the device and measurements from the device and testing rig.

VIII. RESULTS AND DISCUSSION

A. Device Actuation Capabilities

To characterize the frequency-dependent behavior of the active valve device, a low-voltage ($0\text{ V} \pm 5\text{ V}$) sweep signal from 500 Hz to 100 kHz was applied to the piezoelectric drive element structure. The valve cap and piston velocities were measured using the laser vibrometer system. The corresponding displacements were obtained through post-process integration of the velocity signals. Fig. 13 overlays the frequency response of the drive element piston with that of the valve cap, for the case in which oil is present above the valve structure but for which no differential pressure or flowing fluid occurred across the valve orifice. These tests were performed with $P_{\text{bias}} = 500\text{ kPa}$ to eliminate the possibility of cavitation within the HAC chamber. Additionally, the pressures above the valve cap and membrane were maintained at $P_{\text{IN}} = P_{\text{OUT}} = 500\text{ kPa}$.

The piston and valve responses both followed the same patterns across the frequency range. The valve first modal frequency was observed to occur at $\sim 5\text{ kHz}$. The additional peaks in the response were most likely a result of fluid-structure interactions between the oil and the experimental test-jig flow tubes external to the device or between the oil and the flow channels internal to the device. The increase in piston displacement amplitude at frequencies below 1 kHz was due to measurement limitations in the vibrometer system. Below 1 kHz, the measured velocities were of the same order as the noise floor, whereas at higher drive frequencies, the measured velocities were sufficiently above the noise floor to provide accurate measurements. The results indicate that the amplification ratio of the valve device was steady (between $40 \times - 50 \times$) over the range of frequencies below resonance.

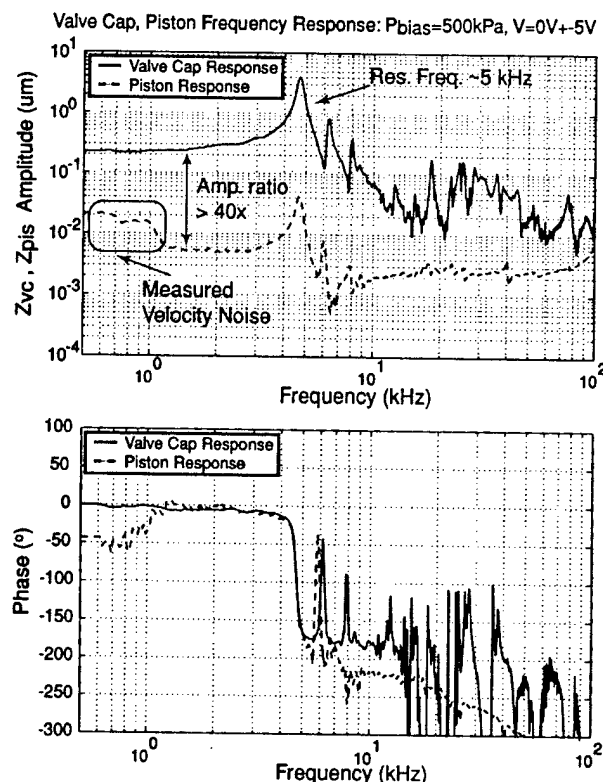


Fig. 13. Low-voltage ($0\text{ V} \pm 5\text{ V}$) piston and valve cap frequency responses from 500 Hz to 100 kHz, with oil present above the valve structure. The top figure plots the valve cap and piston amplitudes, while the bottom figure plots the corresponding phase. The bias pressure in these tests was maintained at $P_{\text{bias}} = 500\text{ kPa}$. An amplification ratio between $40 \times - 50 \times$ is observed for frequencies below 5 kHz.

The previous frequency sweep experimental tests found the 1st modal frequency of the device to be $\sim 5\text{ kHz}$. In order to evaluate the quasistatic performance of the structure under the larger drive voltage levels at which the valve was designed to operate, a frequency of operation of 1 kHz was chosen. Fig. 14 plots the valve cap and piston displacement time histories, respectively, at this drive frequency over a range of applied voltages from 50 Vpp to 800 Vpp. In Fig. 14(a), the dotted lines at $\pm 16.5\text{ }\mu\text{m}$ indicate the position of the upper and lower valve stops, respectively. For an applied voltage of 50 Vpp, the response of the valve cap was purely sinusoidal.

As the voltage was increased to 800 Vpp, the resulting valve cap displacement time history contained small amplitude higher frequency ($\sim 5\text{ kHz}$) oscillations due to the nonlinear nature of the valve membrane structure. These oscillations became more pronounced as the voltage was increased. In Fig. 14(b), the drive element deflection time histories were somewhat rough in nature due to the noise level of the measurement system. As the deflections increased in amplitude, the effect of this noise floor diminished. It is important to note that for a voltage of 800 V, the valve was not deflected sufficiently to close against the valve orifice. This was due to the fact that the actual piezoelectric material coefficient was only $\sim 75\%$ of the expected value used for the original valve design (see further discussion in subsequent paragraphs).

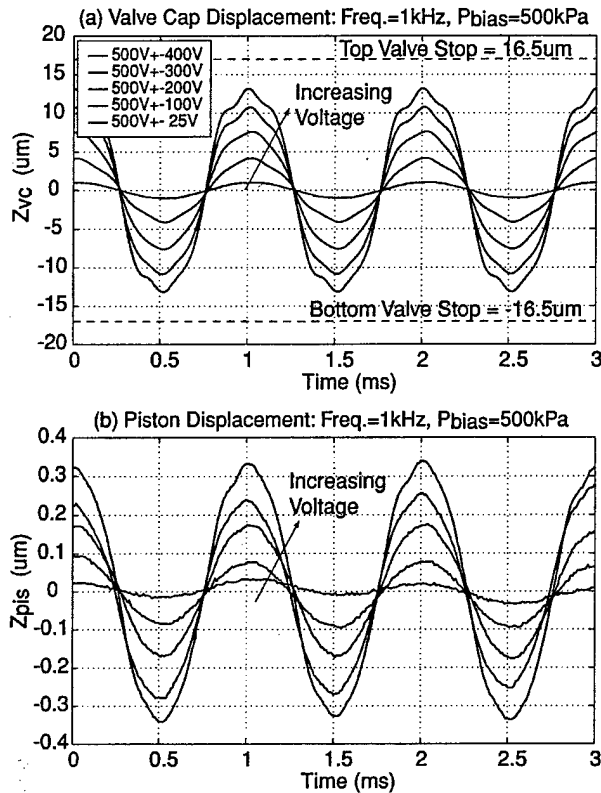


Fig. 14. Experimental valve cap and piston deflection time histories for a series of 1 kHz sinusoidal drive voltage levels. As the voltage was increased, small amplitude 5 kHz oscillations appeared in the deflection responses. Note that a voltage of 800 Vpp was not sufficient to close valve cap against the valve orifice.

Fig. 15 takes these deflection time histories and plots the valve cap peak-peak displacement, piston peak-peak displacement, and corresponding device amplification ratio as a function of applied voltage to the piezoelectric drive element. The amplification ratio was observed to decrease from 50 to 40 as the voltage was increased, as illustrated in Fig. 15(c).

If the structural system was composed of elements operating only in their linear deformation regimes, this amplification ratio would remain constant over the voltage range. Due to the nonlinear stiffness of the valve membrane, however, constant incremental changes in voltage result in increased incremental changes in the chamber pressure and reduced incremental changes in valve cap deflection, as shown in Fig. 15(a). A similar result for the piston deflection is shown in Fig. 15(b). This curve, however, exhibits slightly more linearity than the valve cap deflection curve, due to the increased incremental changes in compressed fluid volume change and structural chamber deformation as the voltage is increased. In essence, as the voltage is increased, a smaller percentage of the piston swept volume is transformed into valve membrane swept volume, thereby resulting in a decreasing amplification ratio.

Fig. 15 also includes model predictions for this behavior. Shown on this plot are three curves generated from the active valve simulation tools discussed previously. The first curve is the predicted response based on the assumed piezo-

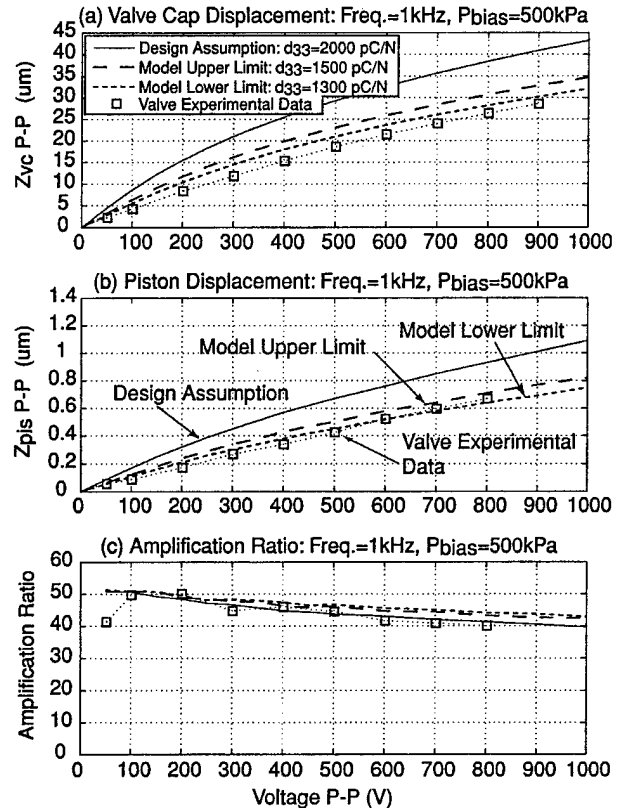


Fig. 15. Active valve quasistatic 1 kHz model correlation for increasing applied voltage: (a) the valve cap deflection curve was 5–10% below the limiting bounds for $d_{33} = 1300 - 1500 \text{ pC/N}$, (b) the piston deflection curve fell within the limiting bounds for large voltage, and (c) the device amplification ratio (between 40 \times and 50 \times) agreed very closely with the predicted limiting bounds.

electric material coefficient value of $d_{33} = 2000 \text{ pC/N}$ used in the original design of the active valve device. The second two model curves are based on limiting values of $d_{33} = 1300 - 1500 \text{ pC/N}$ determined by measuring a large number of individual piezoelectric elements and observing the range of piezoelectric coefficients. Active valve performance was therefore compared to these limiting model cases rather than the ideal case since the piezoelectric elements were determined to be inferior to original design assumptions. The model correlation indicates that the experimental valve cap deflection curve falls slightly short (at 800 Vpp for example, the cap deflection was $26 \text{ }\mu\text{mP-P}$ versus the predicted $31 \text{ }\mu\text{mP-P}$) of the prediction limits for $d_{33} = 1300 - 1500 \text{ pC/N}$, while the experimental piston deflection curve falls within these limits for large enough applied voltage. Based on these results, it can be concluded that an additional compliance mechanism must exist within the HAC chamber, most likely due to a smaller than expected value of fluid bulk modulus. A fluid bulk modulus of $K_f = 2 \text{ GPa}$ was assumed in the active valve models and simulations [37]. The corresponding device amplification ratio, as shown in Fig. 15(c) decreased slightly from $\sim 50\times$ for a low voltage of 100 Vpp to $\sim 40\times$ for a high voltage of 800 Vpp, consistently within 5–10% of the limiting model predictions.

TABLE I
ACTIVE VALVE ACTUATION CAPABILITIES

| Performance Characteristics | Experimental Results | Model Predictions |
|--------------------------------------|-----------------------|-----------------------|
| 1st Modal Frequency | 5 kHz | 14 kHz |
| Piston Deflection (@1kHz, 800Vpp) | 0.65 μm pp | 0.72 μm pp |
| Valve Cap Deflection (@1kHz, 800Vpp) | 26 μm pp | 31 μm pp |
| Amplification Ratio (@1kHz, 800Vpp) | 40x | 43x |

Table I summarizes the critical actuation capabilities of the active valve device in comparison to model predictions. As discussed previously, the valve 1st modal frequency occurred at ~ 5 kHz. Finite-element models of this valve structure had predicted a 1st modal frequency of 14 kHz, however, these models did not include the presence of oil above the valve cap and membrane structure. It was this added mass of the oil that reduced the 1st modal frequency of the valve structure. Future modeling of the valve should more carefully include this added mass effect when predicting modal behavior. As for quasistatic operation at 1 kHz, as already discussed, the measured device valve cap deflection fell slightly short of predictions. However, the amplification ratio was in excellent agreement with model predictions. Overall, this encouraging device performance enabled further investigations into the valve's flow regulation capabilities.

B. Device Flow Regulation Capabilities

To evaluate the capability of the active valve device to regulate flow at 1 kHz, a series of tests was carried out for increasing imposed differential pressure across the valve orifice. Flow regulation tests were performed for differential pressures $P_{\text{IN}} - P_{\text{OUT}} = 24$ kPa, 95 kPa, 145 kPa, 200 kPa, 260 kPa, and 340 kPa. A volatile silicone oil (hexamethyldisiloxane, produced by Dow Corning under the trade name DC200 0.65 centistoke) was used as the flow regulation fluid. By controlling P_{HAC} with respect to the magnitude of P_{IN} and P_{OUT} (using the high-frequency channel and corresponding bias pressure regulator set-up discussed previously), the valve cap was displaced statically upward to a deflection of $Z_{\text{vc}} = 11 \mu\text{m}$. A sinusoidal voltage of 500 Vpp was then applied to the piezoelectric drive element at 1 kHz to actuate the valve cap upward against the valve orifice and downward toward the original equilibrium position of the valve cap. In all test runs, it was desired to just barely close the valve cap against the orifice at its maximum displacement, and to maintain $Z_{\text{vc}} = 0$ at its minimum displacement. In other words, it was desired to always ensure a valve opening stroke of 16.5 μm .

Fig. 16 plots the experimentally measured flow rates for each of the differential pressure test cases. An applied voltage of 500 Vpp was held constant for all of the test cases, and the corresponding measured stroke of the valve cap during actuation is printed inside of each data bar. Fig. 16 also plots the experimental results versus the model expectations obtained using the active valve simulation tools detailed previously. Model predictions for chosen limiting valve strokes of $Z_{\text{vc}, \text{PP}} = 13 \mu\text{m}$ and $Z_{\text{vc}, \text{PP}} = 17 \mu\text{m}$ are shown. The model correlation indicates that the active valve regulates flow in excellent correlation

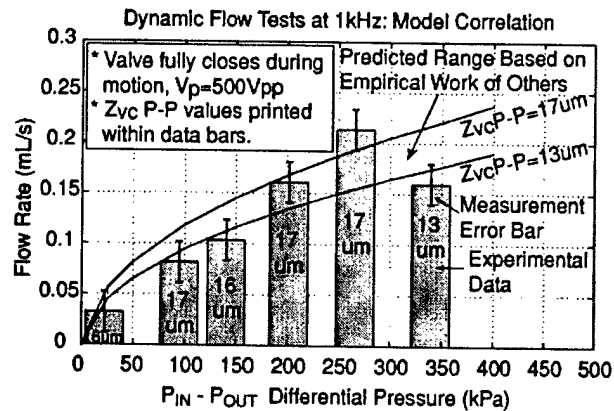


Fig. 16. Dynamic flow regulation model correlation at 1 kHz for varying differential pressures. Correlation is good over range of differential pressures. Error bars on the data indicate the measurement error, which was estimated based on the flow sensor calibration error and the accuracy of the applied differential pressure.

with the model predictions. Since the flow loss coefficients used within the models discussed previously were based on a compilation of empirical Re data from other researchers, the line of predicted behavior in Fig. 16 is understood to be of only "limited accuracy," in other words, it is not based on exact theory.

Subsequent test runs at differential pressures in excess of $P_{\text{IN}} - P_{\text{OUT}} = 340$ kPa resulted in unstable oscillatory motion of the valve cap structure, and eventually fracture of the valve membrane. The nature of the flow behavior (based on Reynolds number) was investigated for a variety of valve opening situations in subsequent studies. The results indicated that these self-excited valve cap oscillations were most probably a result of transitional flow (between laminar and turbulence) through the valve orifice structure, a regime which limited the valve operation to relatively low differential pressures of no more than 340 kPa. A comprehensive overview of these unstable oscillatory valve cap experiments is detailed in [37]. Future research work should focus on a better understanding of the flow regimes through these microscale orifice structures, especially as a function of different viscosity fluids, and on a redesign effort to develop a valve geometry which is less sensitive to the flow behavior passing through the orifice. Additionally, this redesign should include an effort to increase the 1st modal frequency of the device, to potentially enable operation at or above a frequency of 10 kHz. With these redesign efforts, a higher frequency, higher flow rate microvalve could be achieved.

IX. CONCLUSION

A compact piezoelectrically-driven hydraulic amplification microvalve was successfully fabricated and tested for the first time. This concept of hydraulically amplifying the limited stroke of a miniature bulk piezoelectric material into a significantly larger motion of a valve cap structure enables the valve to simultaneously meet a set of high frequency (≥ 1 kHz), high pressure (≥ 300 kPa), and large stroke (20–30 μm) requirements not previously satisfied by other hydraulic flow regulation microvalves. The active valve structural behavior and flow regulation capabilities were evaluated over a range

of applied piezoelectric voltages, actuation frequencies, and differential pressures across the valve. For applied piezoelectric voltages up to 500 Vpp at 1 kHz, the valve devices demonstrated amplification ratios of drive element deflection to valve cap deflection of $40 \times -50 \times$. These amplification ratios correlated within 5–10% of the model expectations. Flow regulation experiments proved that a maximum average flow rate through the device of 0.21 mL/s for a 1 kHz sinusoidal drive voltage of 500 Vpp, with valve opening of 17 μm , against a differential pressure of 260 kPa could be obtained. Tests revealed that fluid-structural interactions between the valve cap and membrane components and flow instabilities (due to transition between the laminar and turbulent flow regimes through the valve orifice) limited the valve performance capabilities. This work has proven this valve technology as a viable component within compact high performance hydraulic micropumping systems.

ACKNOWLEDGMENT

The authors are grateful to the following individuals who have supported this research work: K. Turner, for issues related to fillet radius control and eutectic bonding; J. Carretero and Dr. K. Breuer, for fluid flow modeling at the microscale; Dr. R. Micak, for fluid filling and sealing procedural development; Dr. Y.-H. Su, for nonlinear structural modeling contributions; and Dr. K.-S. Chen and Dr. L. Saggere, for additional structural modeling work. Additionally, the authors wish to acknowledge Dr. S.-H. Liou at the University of Nebraska for his generous support in the deposition of AuSn eutectic alloys and associated films on the piezoelectric materials used in this work.

REFERENCES

- [1] H. Van Lintel, F. van de Pol, and A. Bouwstra, "Piezoelectric micropump based on micromachining of silicon," *Sens. Actuators*, vol. 15, pp. 153–167, 1988.
- [2] M. Stehr, S. Messner, H. Sandmaier, and R. Zengerle, "The VAMP—a new device for handling liquids or gases," *Sens. Actuators, Phys. A*, vol. 57, pp. 153–157, 1996.
- [3] V. Gass, B. van der Schoot, S. Jeanneret, and N. de Rooij, "Integrated flow-regulated silicon micropump," *Sensors and Actuators A*, vol. 43, pp. 335–338, 1994.
- [4] S. Shoji and M. Esashi, "Microflow devices and systems," *J. Micromech. Microeng.*, vol. 4, pp. 157–171, 1994.
- [5] K. Ikuta, T. Hasegawa, and T. Adachi, "The optimized SMA micro pump chip applicable to liquids and gases," in *Proceedings of the 2001 International Conference on Solid-State Sensors and Actuators (Transducers '01)*, 2001.
- [6] M. Koch, N. Harris, R. Maas, A. Evans, N. White, and A. Brunnenschweiler, "Novel micropump design with thick-film piezoelectric actuation," *Measure. Sci. Technol.*, vol. 8, no. 1, pp. 49–57, Jan. 1997.
- [7] P. Watler and M. Sefton, "A piezoelectric driven controlled release micropump for insulin delivery," *Trans. Amer. Soc. Artif. Intern. Organs*, vol. XXXVI, pp. 70–77, 1990.
- [8] B. Wagner, H. Quenzer, S. Hoerschelmann, T. Lisec, and M. Jueress, "Micromachined bistable valves for implantable drug delivery systems," in *Proc. 18th Annu. Int. Conf. IEEE Engineering in Medicine and Biology Society*, 1997, pp. 254–255.
- [9] N. W. Hagood, D. C. Roberts, L. Saggere, K. S. Breuer, K.-S. Chen, J. A. Carretero, H. Q. Li, R. Micak, S. Pulitzer, M. A. Schmidt, S. M. Sparing, and Y.-H. Su, "Micro hydraulic transducer technology for actuation and power generation," in *Proc. SPIE 7th Annu. Int. Symp. Smart Structures and Materials*, vol. 3985, Newport Beach, CA, Mar. 5–9, 2000, pp. 680–688.
- [10] H. Q. Li, D. C. Roberts, J. L. Steyn, K. T. Turner, J. A. Carretero, O. Yaglioglu, Y.-H. Su, L. Saggere, N. W. Hagood, S. M. Sparing, M. A. Schmidt, R. Micak, and K. S. Breuer, "A high frequency high flow rate piezoelectrically driven MEMS micropump," in *Proc. IEEE Solid-State Sensor and Actuator Workshop*, Hilton Head, SC, June 4–8, 2000, pp. 69–72.
- [11] D. C. Roberts, J. L. Steyn, H. Q. Li, K. T. Turner, R. Micak, L. Saggere, S. M. Sparing, M. A. Schmidt, and N. W. Hagood, "A high-frequency, high-stiffness piezoelectric micro-actuator for hydraulic applications," in *Proc. 11th Int. Conf. Solid-State Sensors and Actuators (Transducers '01)*, Munich, Germany, June 10–14, 2001, pp. 686–689.
- [12] D. C. Roberts, N. W. Hagood, Y.-H. Su, H. Q. Li, and J. A. Carretero, "Design of a piezoelectrically-driven hydraulic amplification microvalve for high pressure, high frequency applications," in *Proc. SPIE 7th Annu. Int. Symp. Smart Structures and Materials*, vol. 3985, Newport Beach, CA, Mar. 5–9, 2000, pp. 616–628.
- [13] D. C. Roberts, O. Yaglioglu, J. Carretero, Y.-H. Su, L. Saggere, and N. W. Hagood, "Modeling, design, and simulation of a piezoelectric microvalve for high pressure, high frequency applications," in *Proc. SPIE 8th Annu. Int. Symp. Smart Structures and Materials*, vol. 4327, Newport Beach, CA, Mar. 4–8, 2001, pp. 366–380.
- [14] K. Henning, "Liquid and gas-liquid phase behavior in thermopneumatically actuated microvalves," *Proc. SPIE—The Int. Soc. Optic. Eng.*, vol. 3515, pp. 53–63, 1998.
- [15] C. Rich and K. Wise, "A thermopneumatically-actuated microvalve with improved thermal efficiency and integrated state sensing," in *Proc. IEEE Solid-State Sensor and Actuator Workshop*, Hilton Head, SC, 2000, pp. 234–237.
- [16] H. Jerman, "Electrically-activated, micromachined diaphragm valves," in *Proc. 1991 Int. Conf. Solid-State Sensors and Actuators (Transducers '91)*, 1991, pp. 1045–1048.
- [17] M. A. Huff and W. L. Benard, "Thin film titanium-nickel shape memory alloy microfluidic devices," in *Proc. Third Int. Symp. Microstructures and Microfabricated Systems*, 1997, pp. 26–38.
- [18] M. A. Huff, "Silicon Micromachined Wafer-Bonded Valves," Ph.D. dissertation, Massachusetts Institute of Technology, Cambridge, 1993.
- [19] M. Shikida, K. Sato, S. Tanaka, Y. Kawamura, and Y. Fujisaki, "Electrostatically driven gas valve with high conductance," *J. Microelectromech. Syst.*, vol. 3, no. 2, pp. 76–80, June 1994.
- [20] F. Pourahmadi, L. Christel, K. Petersen, J. Mallon, and J. Bryzek, "Variable-flow micro-valve structure fabricated with silicon fusion bonding," in *Proc. IEEE Solid-State Sensor and Actuator Workshop*, Hilton Head, SC, 1990, pp. 78–81.
- [21] A. Meckes, J. Behrens, and W. Benecke, "Electromagnetically driven microvalve fabricated in silicon," in *Proc. 1997 Int. Conf. on Solid-State Sensors and Actuators (Transducers '97)*, 1997, pp. 821–824.
- [22] J. G. Smits, "Piezoelectric micropump with microvalves," in *Proc. Eighth Bienn Univ Gov Ind Microelectron Symp. (IEEE n 89CH2769-8)*, Piscataway, NJ, pp. 92–94.
- [23] S. Kluge, G. Neumayer, U. Schaber, and M. Wackerle, "Pneumatic silicon microvalves with piezoelectric actuation," in *Proc. 2001 Int. Conf. on Solid-State Sensors and Actuators (Transducers '01)*, 2001.
- [24] M. Esashi, S. Shoji, and A. Nakano, "Normally closed microvalve and micropump fabricated on a silicon wafer," *Sens. Actuators*, vol. 20, pp. 163–169, 1989.
- [25] M. Esashi, "Integrated micro flow control systems," *Sens. Actuators*, vol. A21–A23, pp. 161–167, 1990.
- [26] S. Shoji, B. Van der Schoot, N. de Rooij, and M. Esashi, "Smallest dead volume microvalves for integrated chemical analyzing systems," in *Proc. 1991 Int. Conf. Solid-State Sensors and Actuators (Transducers '91)*, 1991, pp. 1052–1055.
- [27] J. Garcia-Bonito, M. J. Brennan, S. J. Elliot, A. David, and R. J. Pinnington, "A novel high-displacement piezoelectric actuator for active vibration control," *Smart Mater. Struct.*, vol. 7, pp. 31–42, 1998.
- [28] P. Tang, A. Palazzolo, A. Kascak, G. Montague, and W. Li, "Combined piezoelectric-hydraulic actuator based active vibration control for rotor-dynamic system," *J. Vibration Acoust.*, vol. 117, pp. 285–293, 1995.
- [29] W. Tsukamoto, "Piezo-actuator's displacement magnifying mechanism," U.S. Pat. 5 233 834, 1993.
- [30] Y. H. Su, K. S. Chen, D. C. Roberts, and S. M. Sparing, "Large deflection analysis of a pre-stressed annular plate with a rigid boss under axisymmetric loading," *J. Micromech. Microeng.*, vol. 11, pp. 645–653, 2001.
- [31] J. A. Carretero and K. S. Breuer, "Measurement and modeling of the flow characteristics of micro disk valves," in *Proc. 1994 Int. Mechanical Engineering Congress and Exposition: Microfluidics Symposium*, Orlando, FL, Nov. 2000.

- [32] K. S. Chen, A. A. Ayon, and S. M. Spearing, "Controlling and testing the fracture strength of silicon on the Mesoscale," *J. Amer. Ceramic Soc.*, vol. 83, no. 6, pp. 1476-1484, 2000.
- [33] K. T. Turner, "An evaluation of critical issues for microhydraulic transducers: silicon wafer bonding, strength of silicon on insulator membranes and gold-tin solder bonding," S. M. thesis, Massachusetts Institute of Technology, Cambridge, June 2001.
- [34] K. T. Turner, R. Micak, D. C. Roberts, and S. M. Spearing, "Bonding of bulk piezoelectric material to silicon using a gold-tin eutectic bond," in *2001 MRS Fall Meeting*, Boston, MA.
- [35] J. L. Steyn, H. Q. Li, D. C. Roberts, R. Micak, K. T. Turner, O. Yagliglu, Y.-H. Su, M. A. Schmidt, S. M. Spearing, and N. W. Hagood, "Hydraulic amplification devices for microscale actuation," in *Solid-State Sensor, Actuator and Microsystems Workshop*, Hilton Head Island, SC, June 2-6, 2002.
- [36] S. E. Park and T. R. Shrout, "Characteristics of relaxor-based piezoelectric single crystals for ultrasonic transducers," *IEEE Trans. Ultrason., Ferroelect., Freq. Contr.*, vol. 44, pp. 1140-1147, Sept. 1997.
- [37] D. C. Roberts, "Design, modeling, fabrication, and testing of a piezoelectric microvalve for high pressure, high frequency hydraulic applications," Ph.D. dissertation, Massachusetts Institute of Technology, Cambridge, Feb. 2002.
- [38] O. Yagliglu, Y. H. Su, D. C. Roberts, J. Carretero, and N. W. Hagood, "Modeling, simulation and design of piezoelectric micro-hydraulic transducer devices," in *Proc. Fifth Int. Conf. on Modeling and Simulation of Microsystems*, San Juan, Puerto Rico, Apr. 21-25, 2002.



David C. Roberts received the S.B., S.M., and Ph.D. degrees in mechanical engineering from the Massachusetts Institute of Technology (MIT), Cambridge, in 1995, 1998, and 2002, respectively. His doctoral research in the Active Materials and Structures Laboratory at MIT was focused on the development of high-performance piezoelectrically driven microvalve and microactuator devices for hydraulic applications.

His research areas of interest include mechanical design and structural dynamics, as they relate to the development of microfabricated actuators and systems. He is employed as a mechanical engineer at Continuum Photonics, Inc., in Billerica, MA.



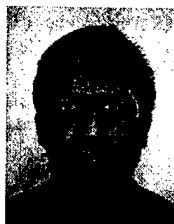
Hanqing Li received the B.S. degree in physics from Peking University, Beijing, China, in 1982 and the M.S. degree in material science at the General Research Institute for Non-ferrous Metals, Beijing, China, in 1985. He received the Ph.D. degree from the University of Nebraska-Lincoln, in 1998.

He was a Guest Scientist at NIST-Boulder, CO, from 1995 to 1998, a Postdoc at MIT between 1998-1999, and is currently a Research Scientist at Massachusetts Institute of Technology (MIT), Cambridge. His primary research interests are in

MEMS fabrication and testing and superconducting devices.



Lodewyk Steyn received the B.Eng. degree in mechanical engineering from the Department of Mechanical and Aeronautical Engineering, University of Pretoria, in 1998. He is currently pursuing a Doctoral degree in the Department of Aeronautics and Astronautics at the Massachusetts Institute of Technology (MIT), Cambridge. His research interests include the fabrication, packaging, instrumentation, and testing of piezoelectrically driven microfluidic devices for actuation and power generation applications.



Onnik Yagliglu received the S.B. degree in mechanical engineering from Bogazici University, Istanbul, in 1999 and the S.M. degree in mechanical engineering from the Massachusetts Institute of Technology (MIT), Cambridge, in 2002. His Master's research in the Active Materials and Structures Laboratory at MIT was focused on the modeling, simulation and design of piezoelectric microhydraulic transducer devices. He is currently working towards the Ph.D. degree in the Mechanical Engineering Department at MIT.

His research areas of interest include power MEMS, RF MEMS, power generation from ambient vibration, and microfluidics.



S. Mark Spearing received the Ph.D. degree from the Engineering Department at Cambridge University, U.K., in 1990.

From 1990 to 1992, he worked as a research engineer at University of California, Santa Barbara, where he produced analytical models for the failure of high-temperature ceramic materials and for Carborundum Microelectronics, where he was a member of the electronic packaging technology development team from 1992 to 1994. He is an Associate Professor of Aeronautics and Astronautics

at the Massachusetts Institute of Technology (MIT), Cambridge, where he has been since 1994. His technical interests include materials and structural analysis and design of MEMS, development of wafer bonding technologies, electronic packaging and advanced composites. Since 1995, he has been responsible for materials, structural design, and packaging tasks of the MIT MicroEngine, MicroRocket, Micro-chemical power, and MicroHydraulic transducer projects as well as conducting cross-cutting underpinning technology development.

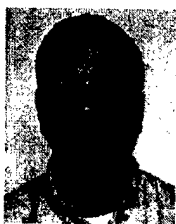
Dr. Spearing is a Member of the ASME.



Martin A. Schmidt (S'88-M'88-SM'00) received the B.S.E.E. degree in electrical and computer engineering from Rensselaer Polytechnic Institute, Troy, NY, in 1981. He received the S.M. and Ph.D. degrees in electrical engineering and computer science from Massachusetts Institute of Technology (MIT), Cambridge, in 1983 and 1988, respectively.

In addition to his professorship in the Department of Electrical Engineering, he is the Director of the Microsystems Technology Laboratories at MIT. He investigates microfabrication technologies for inte-

grated circuits, sensors, and actuators; design of micromechanical sensor and actuator systems; mechanical properties of microelectronic materials, with emphasis on silicon wafer bonding technology; integrated microsensors; and microfluidic devices. His current research projects involve novel applications of MEMS technologies to a variety of fields, including miniature gas turbines, miniature chemical reactors, microswitches, biological applications and sensors monolithically integrated with electronics.



Nesbitt W. Hagood received the S.B., S.M., and Ph.D. degrees from the Department of Aeronautics and Astronautics from Massachusetts Institute of Technology (MIT), Cambridge, in 1985, 1988, and 1991, respectively.

He is co-founder and currently Chief Technology Officer of Continuum Photonics, Inc. He was formerly a tenured Associate Professor of Aeronautics and Astronautics at MIT and Director of the Active Materials and Structures Laboratory. He specializes in the analysis, design and development of solid

state actuation devices, microfabricated systems, and applications. Dr. Hagood is an ONR Young Investigator and has received the Presidential Early Career Award in Science and Technology.

Measurement and Modeling of the Flow Characteristics of Micro Disc Valves

by

Jorge Alejandro Carretero Benignos

B.S. Mechanical Engineering

Universidad de las Americas- Puebla, 1996

Submitted to the Department of Aeronautics and Astronautics
in partial fulfillment of the requirements for the degree of

Master of Science in Aeronautics and Astronautics

at the

MASSACHUSETTS INSTITUTE OF TECHNOLOGY

February 2001

©Jorge Alejandro Carretero Benignos, ASME International, MMI.

All rights reserved.

The author hereby grants to MIT permission to reproduce and to
distribute publicly paper and electronic copies of this thesis document
in whole or in part.

Author

Department of Aeronautics and Astronautics

Jan 19, 2001

Certified by

Kenneth S. Breuer

Visiting Associate Professor of Aeronautics and Astronautics, MIT

Associate Professor Division of Engineering Brown University

Providence, RI

Thesis Supervisor

Accepted by

Wallace E. Vander Velde

Chairman, Department Committee on Graduate Students

MASSACHUSETTS INSTITUTE
OF TECHNOLOGY

SEP 11 2001

Aero

Measurement and Modeling of the Flow Characteristics of Micro Disc Valves

by

Jorge Alejandro Carretero Benignos

Submitted to the Department of Aeronautics and Astronautics
on Jan 19, 2001, in partial fulfillment of the
requirements for the degree of
Master of Science in Aeronautics and Astronautics

Abstract

The head losses in microfluidic systems such as micropumps are dominated by losses in microvalves, where microfabrication constraints limit significantly possible microvalve designs. This makes them quite different from conventional valves. In particular, flow characteristics in the laminar and low-Reynolds turbulent regimes are not understood clearly, and detailed information about the flow losses is lacking. This work addresses this issue by using a scaled-up (10:1) valve experiment to measure pressure losses in typical microfabricated valve geometries. The macroscale model is fully instrumented and discharge coefficients and sensitivities to stroke, seat width and Reynolds number are presented.

Thesis Supervisor: Kenneth S. Breuer

Title: Visiting Associate Professor of Aeronautics and Astronautics, MIT

Associate Professor Division of Engineering Brown University Providence, RI

Acknowledgments

Two roads diverged in a yellow wood... and I, I took the one less traveled by, and that has made all the difference. I have come to understand that in many cases life presents many possible paths for us and that none of them is better than the others, they are only different. The paths I've taken I took because I wanted, it has been my choice and I have no regrets.

My time at MIT has been both the best and the worst. I have met wonderful people and learned a lot from them. I have also gone through very hard times and it has been during those times that I feel that I have matured the most. The path hasn't been easy, but the help of my friends has made it a lot easier. I dedicate this thesis to my family, friends and all the people who have been there when I needed them the most.

First of all I would like to thank my advisor Prof. Kenny Breuer. I thank him for trusting me with this project, for his unending support and infinite patience. Kenny believed and supported me in those times when everything was falling apart. I greatly appreciate his technical expertise, his attention to detail and quality in research and above all his support. Kenny has been not only my advisor but a good friend. Thanks Kenny I am very grateful for all you've done for me. I would also like to thank Professors Mark Spearing, Nesbitt Hagood and Marty Schmidt for their continued support and guidance throughout this time.

The MHT guys, what a group! It has been amazing to work with such a wonderful and diverse group of people. Dave, Rick, Farid, Hanqing, Kuo-Shen, Su, Laxman, Lodewyk, Onnik and Kevin. Guys it has been a pleasure to work with you and one of the best experiences I've had.

Special thanks are due to Dave Robertson and Fred Cote for all their help setting up the experiments. I should also thank James Lu, Todd Oliver and Daniel Sandoval for their hard work and patience.

I would also like to thank my friends at the different aero/astro labs: FDRL (the only lab staffed 24 hours a day), AMSL, Man-vehicle, SSL and the whole aero gang.

The mexican guys, all my friends who have had the patience to hang out with me. We have shared beers, late night movies and coffees they have made my time at MIT both enjoyable and unforgettable. Special thanks to the core group : Ante, Rodrigoq, Raymundo, Mescobar, AB, Juliocc, Joseicv, Kate, Jordi, Dara, Magdalena, Mhurtado, Belen, Anap and Mhadis. You guys have made me feel at home away from home. Thanks guys and I wish everyone the best of the best.

Finally, thinking about home... my friends at home. First of all Edgar, thanks for your support throughout this time. Those late night email sessions we had really made a difference. Thanks for all your help. Special thanks are in order for Diana, Yuria, Gabriel, Samuel, Ramon (aka Livingston), Caro, Karla, Pliego and my aunt Beatriz. Les doy las gracias, sepan que los aprecio y que siempre los he extrañado. Estaremos lejos fisicamente, pero siempre han estado cerca de mi pensamiento.

Casi para terminar, queda el espacio para aquellas ninas que he querido. Como se dijo por ahi... hay anecdotas que contare, y otras que no... estas mejor las dejaremos asi. A ellas tengo mucho que agradecerles aun cuando las cosas no hayan funcionado. A mi asesorada estrella, siento que no hayamos coincidido, pero te agradezco el que me hayas hecho pensar sobre muchas cosas y ello ha tenido un profundo impacto en mi vida. A su tocaya, solo me queda decirle que aunque las cosas no salieron siempre tendra un lugar muy especial en mi corazon y le deseo la mejor de las suertes en su vida.

Finally, my family. My mom, dad, and brother. I have missed you these years so much and I cherish every moment I have been able to share with you. Ustedes han sido mi inspiracion para seguir adelante y una fuente inagotable de amor. Si he llegado hasta aca ha sido por ustedes. Gracias de todo corazon. Muy especialmente dedico esta tesis a mis abuelos Herman, Olga Alicia, Alfonso y Evita.

This research would not have been possible without the generous of DARPA under grant # *DAAG55-98-1-0361* and ONR under Grant # *N00014-97-1-0880*. I would like to acknowledge CONACYT for supporting me throughout my first year at MIT.

| | |
|----------------|------------------------------------|
| C_m | Modified discharge coefficient |
| C_q | Discharge coefficient |
| d_0 | Inlet diameter |
| d_{sys} | Characteristic length |
| d_v | Valve cap diameter |
| f | Driving frequency |
| h^* | h_v/h_p |
| h_p | Plate separation |
| h_v | Valve opening |
| k | Isothermal bulk modulus |
| K | Stiffness |
| l_o | Channel length |
| M | mass |
| Q | Volumetric flow rate |
| Re | Reynolds number |
| s | Seat width |
| \bar{u} | Local flow velocity |
| A_o | Throat flow area |
| A_1 | Upstream flow area |
| A_2 | Downstream flow area |
| ΔP | Pressure drop |
| ϵ | Loss coefficient correction factor |
| λ | Acoustic wavelength |
| μ | Dynamic viscosity |
| ν | Kinematic viscosity |
| ρ | Fluid density |
| σ | h_v/s |
| ζ_{quad} | Turbulent loss coefficient |
| ζ_ϕ | Loss coefficient correction factor |

| | |
|--------------|--|
| E | Young's modulus |
| I_A | Moment of Inertia |
| A_c | Cross-sectional area |
| l | Generic length scale |
| ω_n | circular natural frequency |
| P | Pressure |
| C | Capacitance |
| ΔV_f | Fluid volume change |
| ΔV_s | Structural volume change |
| R | Fluid Resistance |
| $\dot{\Phi}$ | Heat transfer rate |
| e | Internal energy |
| h | Enthalpy |
| D | Channel Diameter |
| n | Scaling power |
| \hat{n} | Unit normal vector |
| \dot{W} | Work rate |
| m | Scaling power |
| C_d | Orifice discharge coefficient |
| β | Diameter ratio d/D |
| d | Orifice diameter |
| A_r | Orifice correction factor |
| M_2 | Orifice correction factor |
| C_∞ | Ultimate Orifice discharge coefficient |
| ΔP_+ | Forward pressure drop |
| ΔP_- | Backflow pressure drop |
| Di | Diodicity |
| S | Strouhal number |

| | |
|-------------|--|
| Fr | Froude number |
| g | gravity |
| t | orifice thickness |
| I | Lumped element Inductance l/A |
| F | Force |
| \vec{v} | Fluid velocity vector |
| u | x-direction absolute velocity |
| u_r | Normal exterior relative velocity to the control surface |
| u_c | Normal exterior fluid velocity in the x -direction |
| x_1 | Wafer thickness |
| x_s | Valve displacement |
| a | area |
| \dot{V}_p | Volume rate of change due to piston movement |
| V_0 | Initial piston chamber volume |
| d_h | Hydraulic diameter |

Contents

| | | |
|----------|--|-----------|
| 1 | Introduction | 15 |
| 1.1 | Overview of the Micro-Hydraulic Transducer | 15 |
| 1.2 | Motivation | 16 |
| 1.3 | Challenges | 17 |
| 1.4 | Contributions | 17 |
| 2 | Literature Background | 18 |
| 2.1 | MEMS Scaling Issues | 18 |
| 2.2 | Microsystems Fluidic Modeling Strategies | 19 |
| 2.3 | Micro Scale Valves | 21 |
| 2.3.1 | Passive Microvalves | 21 |
| 2.3.2 | Active microvalves | 24 |
| 2.4 | Macro-scale Valves | 28 |
| 2.5 | Summary | 30 |
| 3 | Modeling of Hydraulic Microsystems | 31 |
| 3.1 | The MHT Hydraulic Model | 32 |
| 3.1.1 | Valve Cap Force Calculation | 34 |
| 3.1.2 | Capacitance modeling | 36 |
| 3.1.3 | Inductance in fluid channels | 38 |
| 3.1.4 | Resistive Elements | 39 |
| 3.2 | SIMULINK Model Implementation | 43 |
| 3.3 | Summary | 46 |

| | | |
|----------|---|-----------|
| 4 | Experimental Setup | 47 |
| 4.1 | Experiment Design | 47 |
| 4.1.1 | Scale Effects | 49 |
| 4.2 | Macro-scale setup | 51 |
| 4.2.1 | Fluid Delivery Section | 51 |
| 4.2.2 | Test Section | 52 |
| 4.2.3 | Valve Geometry | 54 |
| 4.2.4 | Experimental Procedure | 55 |
| 4.2.5 | Calibration Experiments | 55 |
| 4.3 | Summary | 57 |
| 5 | Experimental Results and Correlations | 58 |
| 5.1 | Experimental Results | 58 |
| 5.1.1 | Valve Opening Dependence | 62 |
| 5.1.2 | Valve Seat Width Dependence | 64 |
| 5.1.3 | Comparison of Lumped Model to Data | 67 |
| 5.2 | Modified model | 67 |
| 5.2.1 | Detailed orifice model background | 67 |
| 5.2.2 | Modified valve model | 70 |
| 5.3 | Summary | 73 |
| 6 | Conclusions and Recommendations | 74 |
| A | Valve Plots and Summary of Model Equations | 76 |

List of Figures

| | | |
|------|--|----|
| 1-1 | Conceptual Diagram of Bidirectional Microdevice | 16 |
| 2-1 | Typical Architectures of Passive Microvalves [37] | 22 |
| 2-2 | NMP Passive Microvalves, Olsson [22] and Forster[4] | 23 |
| 2-3 | Thermopneumatic Active Microvalve [7] | 25 |
| 2-4 | Electrostatically Actuated Microvalve [30] | 26 |
| 2-5 | Electromagnetic Actuated microvalve [9] | 27 |
| 2-6 | MHT Amplification Chamber,[27] | 28 |
| 3-1 | Cross-sectional view of a multiple wafer energy harvester with active valves | 32 |
| 3-2 | Schematic of the MHT hydraulic system | 32 |
| 3-3 | Hydraulic Systems Control Volume Representation | 33 |
| 3-4 | Schematic of the inlet valve section | 33 |
| 3-5 | Valve Sections: Lumped Model Equivalents | 34 |
| 3-6 | control volume for valve cap force calculation | 35 |
| 3-7 | Energy Harvesting Chamber Representation | 37 |
| 3-8 | Valve schematic for the order-of-magnitude model | 41 |
| 3-9 | Order of magnitude valve model. Results are shown for different valve openings h_v | 42 |
| 3-10 | Comparison of component loss coefficients vs Re_s | 43 |
| 3-11 | Generic Architecture of Fluidic resistances in Simulink | 44 |
| 3-12 | Simulink Representation of the Flow Rate Equation 3.20 | 45 |

| | | |
|------|---|----|
| 3-13 | Time histories of chamber pressure, inlet valve flow rate, outlet valve flow rate and valve openings for the resonance condition of an Energy Harvester,[36]. Continuous lines are for inlet parameters | 45 |
| 4-1 | Schematic of the macro-scale test facility layout. | 51 |
| 4-2 | Test section detail of the macro scale test facility. | 53 |
| 4-3 | Valve geometry detail. | 53 |
| 4-4 | Test orifice for calibration | 56 |
| 4-5 | Test orifice discharge coefficient vs Reynolds number. | 57 |
| 5-1 | Discharge Coefficient vs. Reynolds number for different percentages of valve opening (h^*) for valve 1. The plate separation (h_p) was $450\text{ }\mu\text{m}$ | 59 |
| 5-2 | Transition Reynolds number vs valve opening ratio, h^* | 61 |
| 5-3 | Discharge coefficient (C_q) for valve #1 vs modified Reynolds number (Re_m) | 61 |
| 5-4 | Discharge coefficient (C_q) vs. non-dimensional valve opening (h^*) for the three valves; plate separation (h_p) $450\text{ }\mu\text{m}$ | 62 |
| 5-5 | Modified discharge coefficient (C_m) vs. Reynolds number for valve #1 and plate separation $h_p = 450\text{ }\mu\text{m}$ | 63 |
| 5-6 | Discharge coefficient vs. non-dimensional seat width (σ). The plate separation was $h_p=450\text{ }\mu\text{m}$ | 64 |
| 5-7 | Seat width effect on discharge coefficient from Johnston <i>et al</i> [14] . . | 65 |
| 5-8 | Loss coefficient vs. Reynolds number comparison between experimental results and the lumped model for various valve opening percentages (h^*). | 66 |
| 5-9 | Sharp edged orifice discharge coefficient vs Reynolds number | 69 |
| 5-10 | Long orifice $t/d=0.5$ from Lichtarowicz [16] | 71 |
| 5-11 | Long orifice $t/d=0.5$ from Lichtarowicz [16] | 71 |
| 5-12 | Scaled data for valve #1 and valve #3 | 72 |
| 5-13 | Curve fitting using 5.14 for valve #1 | 73 |

| | | |
|-----|--|----|
| A-1 | Reynolds number vs Discharge coefficient for valve 2 ($d_v=11.10$ mm) | 77 |
| A-2 | Reynolds number vs Discharge coefficient for valve 3 ($d_v=14.24$ mm) | 77 |

List of Tables

| | | |
|-----|---|----|
| 4.1 | Valve diameters (d_v) with corresponding seat widths (s) and non-dimensional seat widths (σ) | 54 |
|-----|---|----|

Chapter 1

Introduction

Many definitions exist to describe what are commonly known as Micro-Electro Mechanical Systems (MEMS). In general MEMS devices are those that fall within the range of $1\text{ }\mu\text{m} - 1\text{ mm}$ in size. These devices are typically made out of Silicon wafers and machined using Integrated Circuit (IC) manufacturing techniques. A distinctive feature of MEMS is that they operate outside the realm of IC circuits, finding applications in solid mechanics, fluids, optics, magnetics and others. The focus of this work is on integrated microfluidic systems, particularly on the fluid mechanics aspect of these systems. This thesis discusses the fluid mechanics modeling strategy undertaken as part of the development effort for the MIT Micro Hydraulic Transducer project. The approach and results, however, are by no means limited to this particular system, they are relevant to fluidic microsystems in general.

1.1 Overview of the Micro-Hydraulic Transducer

The immediate application of this work is to the Micro-hydraulic Transducer (MHT) program, although the phenomena described applies to micropumps in general. The concept of the MHT, as shown schematically in Figure 1-1, integrates the large single-stroke force of an hydraulic system with the high-frequency small stroke available from a piezoelectric element. The combination is used to create high-performance transducers (Hagood *et al*, [6]). The device can operate as an actuator (transforming

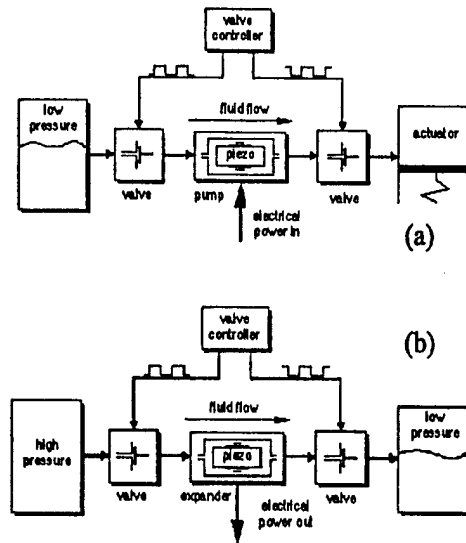


Figure 1-1: Conceptual Diagram of Bidirectional Microdevice

electrical to mechanical energy, (Figure 1-1,a) or as an energy harvester (converting mechanical to electrical energy), Figure 1-1,b. The MHT architecture resembles that of a reciprocating internal combustion engine cylinder. The fluid at high pressure comes into the cylinder chamber through an inlet valve, compresses the piston and in turn the piezoelectric crystal. The cycle is completed when the piezo expands driving the piston up and forcing the fluid out through the outlet valve. In the current design, the piston is approximately 8 mm in diameter, and the valves are poppet type disc valves (\varnothing 500 μ m) with strokes of less than 40 μ m operating at approximately 20 kHz. In order to obtain this stroke at such high frequencies the valve is actuated by a piezoelectric element aided by an amplification chamber as detailed by Roberts *et al* [27].

1.2 Motivation

The rapid increase in the development of complex microfluidic devices has revealed a need for more accurate modeling of fluid behavior in small-scale microfabricated geometries. Microvalves tend to be one of the dominating elements in such systems, but

at the same time their detailed behavior remains poorly understood and systematic studies of microvalve fluid mechanics are lacking.

In the case of the Micro Hydraulic Transducer program at MIT, the requirements on valve modeling take a different perspective. In this case the valve and head loss models are used as design tools. Typical orifice models will not capture geometry related sensitivities necessary for design and optimization. Furthermore, one of the goals of the MHT project is to harvest energy with this device, for this reason, and considering that the valve is the dominating head loss, it becomes critical to determine accurately the corresponding head losses and sensitivities. Only then will it be possible to design a more efficient valve.

1.3 Challenges

The major fluid mechanics challenge is to model the steady and unsteady fluid behavior in these micron-scale geometries. The Reynolds number during one cycle varies between 1 and 20,000 with a Strouhal number of order 1. In this regime both inertial and viscous forces are important and unsteady effects cannot be ignored. The model needs to be accurate, yet implemented in a flexible manner suitable for design purposes and integration into full system simulations. Unfortunately, such models do not presently exist, and where partial models are available, they are typically neither calibrated nor validated for the small scales and unique geometries that are found in microfluidic systems. The purpose of this thesis is to provide such calibration and validation.

1.4 Contributions

An hydraulic model for the Micro-Hydraulic Transducer was constructed based on a low-order lumped element model. The valve flow characteristics were investigated experimentally and parametric studies were carried out to obtain the flow dependencies and allow for a better estimation of the head losses.

Chapter 2

Literature Background

2.1 MEMS Scaling Issues

The miniaturization of systems presents several interesting performance advantages. One of the major advantages that comes with miniaturization is that as a system is scaled down its mass (M) reduces like the third power of the length scale (l), (ie $m \propto l^3$). This dramatic mass reduction increases the natural frequency (ω_n) of a system as shown for a simple cantilever beam:

$$\omega_n = \sqrt{\frac{K}{M}} = \sqrt{\frac{3EI_A}{l^4 \rho A_c}} = c \frac{1}{l} \quad (2.1)$$

where k is the stiffness and m the mass of the beam. The stiffness (K) is given by Young's modulus (E), the area moment (I_A) and the beam length (l). The mass (M) is given by the length (l), the cross-sectional area (A_c) and the material density (ρ). As it can be appreciated in equation 2.1 the natural frequency (ω_n) scales like $1/l$. This allows for a significant increase in operating frequencies for micromachined devices as described in detail by Burgess [3]. The previous argument has been one of the major driving forces towards the development of MEMS. However, not all phenomena scale as favorably as inertia, for instance viscous effects and other surface-driven phenomena become relatively more important as scale decreases. In our case we are particularly interested on Microfluidic MEMS and for this reason, we

will study in detail the fluidic behavior at these scales.

Microfluidic systems encompass many different applications from on-chip chemical systems to micro-mixers, micropumps and microtransducers to name a few. As scale decreases the surface-to-volume ratio increases making such effects as viscosity, Van der Waals forces, electrostatic forces, etc. important and in some cases detrimental to system performance. An introductory discussion of such scaling effects can be seen in Ho and Tai's microfluidics review paper,[10].

In particular the focus of this work is on modeling the fluidic behavior in microfluidic transducers. One of the major questions is to understand how hydraulic systems and their components behave at the micro-scales and how macro-scale results scale down.

In the first part of this chapter a brief literature review of existing modeling approaches for micro-hydraulic systems is presented. The second part of the chapter focuses on microvalves due to their importance in micro-hydraulic MEMS. The main purpose of this chapter is to set the stage for this thesis work by presenting what has been done by other researchers in the field.

2.2 Microsystems Fluidic Modeling Strategies

Several modeling approaches have been proposed for integrated microsystems. From the fluids point of view there are several options: Navier-Stokes simulations, Characteristic equations, impedance models (distributed models), and electrical analogy or lumped models.

The direct simulation of the flow in these systems by solving the Navier-Stokes equations is not feasible due to the complicated geometries, moving boundaries, fluid/structure interactions, and the unsteady nature of the phenomena described making them at best impractical.

A second approach is to use the characteristic equations method. This approach transforms the flow's partial differential equations, into ordinary differential equations significantly simplifying the problem. These equations can then be integrated forward

in time to obtain a solution. This method will give a solution that usually would only be surpassed in accuracy by a direct simulation of the Navier-Stokes equations[35]. However, localized head losses like elbows, valves, etc. still need to be characterized separately and fed to the model. The quality of the model will thus depend on how well these localized losses are modeled. Two important disadvantages of this approach is that integration to structural and electrical models is not straightforward and that a full-system simulation becomes computationally expensive.

A third option is comprised by distributed parameter models or impedance-based models. This approach is part of the so-called electrical analogy methods used traditionally in acoustics. This approach assumes that the pressure is analogous to electrical voltage and that the flow rate is analogous to electrical current. The impedance is defined as the ratio of the dependent variables pressure (P) and flow rate (Q) respectively for each section. In such manner the system may be solved as an eigenvalue problem.

In those cases in which pipe lengths are short the distributed parameter model can be simplified even further to a "lumped" element model. Previous experiences by Olsson[23], Bourouina[2], and Gravesen[5] have proven that the lumped element model is useful for the analysis of microfluidic systems. The advantage of lumped models is that they are easily integrated to full system simulations which may also include structural and electrical components. The intrinsic modularity of this type of model makes it easy to modify and build up on. The lumped model has the added advantage that due to its similarity with circuit system-analysis existing software, such as SPICE and SIMULINK, can be used to obtain solutions.

In this case as in previous approaches the behavior of localized components needs to be characterized separately. Thus the results of a given simulation will be a function of how accurately the system is modeled and how well the subcomponent's behavior is known.

Microvalves are in most cases the most difficult subcomponents to characterize in microhydraulic systems. Incidentally microvalves are also the main dissipative elements of these hydraulic systems. A literature review of existing microvalves is

presented next to set the context for this thesis experimental work.

2.3 Micro Scale Valves

Microvalves may be classified as active (with an actuator) or passive (without actuator). Many different examples of both types of microvalves exist in the literature. A review by Shoji and Esashi [31], and Gravesen [5] indicates that most microvalves have been designed for gas control, while not many have been demonstrated for liquid applications due to their low conductance.

The low conductance of microvalves is directly related to microfabrication constraints, which limits available geometries to low aspect ratio, prismatic elements due to the line-of-sight nature of microfabrication techniques. This greatly limits the available geometries of fluidic devices. For instance valves cannot have three-dimensional structures such as 45° poppets, rounded edges and fillets (although some limited fillet capabilities have been demonstrated in highly stressed MEMS structures; Ayon, et al.[1]). The high temperatures required for wafer bonding preclude the use of polymers and soft materials for the valve seats. Available actuation options are limited in stroke and control authority further constraining valve response time and performance. The above-mentioned constraints have made typical microvalve designs quite different from macro scale valves and yielded highly suboptimal microvalves.

In most cases valves are fabricated and then characterized experimentally, primarily because detailed analysis of the flow characteristics and sensitivities to different relevant parameters is lacking. One of the main reasons for this is that instrumenting a microvalve to measure both flow rate and pressure as functions of the valve position is very difficult.

2.3.1 Passive Microvalves

Passive valves may be subdivided into moving parts valves and No Moving Parts (NMP) valves. The first group mainly has valves which open and close in response to a net force acting on them. These microvalves usually have a micromachined

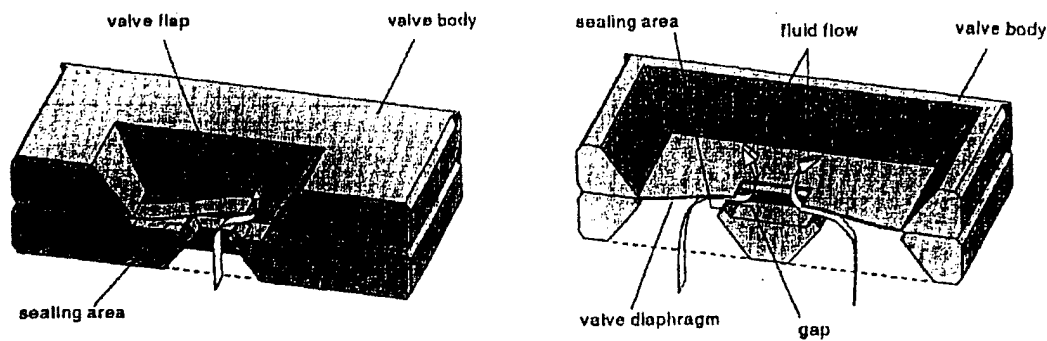


Figure 2-1: Typical Architectures of Passive Microvalves [37]

Silicon membrane that is free to deflect in one direction. The resulting behavior is equivalent to that of a macro-scale check valve. The moving membranes have been fabricated in many different sizes and thicknesses, with annular shapes, cantilever type flaps and tethered structures. This class of micro-valves, however, have some generic characteristics: one way flow, limited stroke, and in many cases they are susceptible to clogging.

A survey of existing micro-check-valves by Shoji [31] shows that typical passive check valves range in size from $800\text{ }\mu\text{m}$ to about 7 mm , and only one valve in the $100\text{ }\mu\text{m}$ range has been reported. All of these valves were Silicon micromachined valves and were either cantilever or circular membrane type check valves as shown in Figure 2-1. The Reverse flow rates (leak flow) of these valves were in the order of $1\text{ }\mu\text{l/min}$ for water. The forward flow rate was generally two to three orders of magnitude higher than the reverse (leak) flow rate. It should be observed, though, that these comparisons suffer from the fact that the reported results for each valve were based on different applied pressures but they do convey the general capabilities of such systems.

One of the contributing factors to the low conductance of microvalves is the limited stroke. In the case of passive valves, the stroke depends on the surrounding fluid pressure, membrane thickness and valve size. In some cases the valve deflection is larger than the membrane thickness resulting in nonlinear behavior and therefore



Figure 2-2: NMP Passive Microvalves, Olsson [22] and Forster[4]

smaller displacements per applied pressure.

From the fluid mechanics point of view the flow characterization of these valves is difficult since the valve position and capacitance are pressure dependent.

The second major type of passive valves are No-Moving-Parts (NMP) valves. These valves are carefully contoured so that flow is preferential in one direction. The aim, as in the case of the micro-check-valves is to obtain a high conductance in one direction and a comparatively low conductance in the reverse flow condition. Several examples of these valves exist, the geometries are different but the operating principle is the same as seen in Figure 2-2. In-depth studies have been carried out by Stemme and Olsson [22] with a diffuser/nozzle design and Forster *et al*[4] with Tesla type valves. These valves are characterized by high reverse flow rates (compared to moving part check valves), however these designs are compensated by their ease to manufacture, robustness, and their ability to transport particle laden fluids.

A figure of merit used to estimate the quality of a given design is the diodicity. The diodicity (Di) is defined as

$$Di = \frac{\Delta P_-}{\Delta P_+} \quad (2.2)$$

where the ΔP_+ is the pressure drop in the forward (or positive direction) and ΔP_- is the pressure drop in the reverse (leak) direction. NMP valves or fluidic diodes

usually have a diodicity of about 1.1- 1.3. Considering that for laminar flow the flow rate (Q) is a linear function of the pressure drop, we can estimate that micro check valves with moving parts would have a diodicity roughly two orders of magnitude higher than NMP valves. It has been suggested, though, that probably a better figure of merit would be reverse pressure differential per flow rate which for very low flow rates should be a constant.

2.3.2 Active microvalves

The microvalve actuator plays a fundamental role in determining the efficiency and overall design of a valve. Many designs and actuation principles have been proposed the most common options are electrical, thermal, magnetic, and piezoelectric.

Ideally an actuator system should be easy to miniaturize, efficient, have a large stroke and fast response time. Currently, no actuation system fulfills the previously mentioned characteristics of the "ideal actuator". Considering this certain types of actuators are better suited to some applications than others. The strengths and weaknesses of the most common actuation systems are outlined next.

Thermal based systems can be categorized into thermopneumatic, bimetallic, and Shape-Memory-Alloys (SMA) actuators. Thermopneumatic based actuators for microvalves have been investigated by Zdeblick, Henning and coworkers [8],[7] resulting in a commercially available microvalve (Redwood microsystems) . The thermopneumatic normally-open valve as shown in Figure 2-3 has a cavity which is filled with Fluorinert. The orifice size as reported varies from 25 to 500 μm , with membrane diameter of roughly 6 mm. The Fluorinert is heated with a Platinum resistor deflecting the cavity membrane and closing the valve. The response time is in the order of 0.1-1 sec, with maximum reported strokes of 50 μm . It is suggested that a change of heat transfer mode from conduction to phase change may reduce the response time down to tenths of milliseconds. Cycling the valve, however, poses a greater challenge, for the system would have to be heated and cooled rapidly. The advantage of this type of actuation is that it has the widest temperature range from -20°C to 70°C . Applications for the control of refrigerant liquids have been suggested.

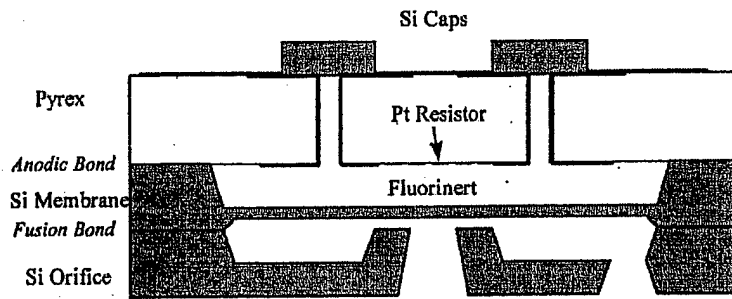


Figure 2-3: Thermopneumatic Active Microvalve [7]

The second thermal actuation system found in the literature are bimetallic systems. The bimetallic actuator usually consists of a circular Silicon membrane connected to a thin annular metallic ring. The system is heated and the effect is such that due to the dissimilar thermal expansion coefficients the membrane deflects. Theoretical estimates by Jerman[13] suggest that for a 2.5 mm diameter, 8 μm thick Si membrane with 5 μm of deposited Aluminum and b/a ratio of 0.5 displacements in the order of 25-30 μm with symmetrical vertical travel are achievable. This actuation mechanism, however, is limited in its response time due to the heating and cooling of the bimetallic materials. The response time oscillates between 1 msec and 1 sec depending on the details of the configuration. For the previously described configuration Jerman has shown experimentally response times of 100 to 300 msec. Bimetallic actuated valves have been proposed for systems in which proportional valve control is required. They have approximately the same operating range of thermopneumatic valves but without the further complication of sealing liquid in a cavity.

Shape-memory-alloy based systems have the ability to produce large strokes, however due to their non-linear response to temperature are difficult to control and response times are in the order of 10 seconds. These valves may have large stroke but are difficult to control and therefore have only been used as on-off valves.

Electrostatically actuated valves typically rely on two Silicon wafers to act as electrodes. The Silicon plates are insulated by grown oxide and separated by another layer usually of pyrex in a "sandwich" fashion as seen on Figure 2-4. The

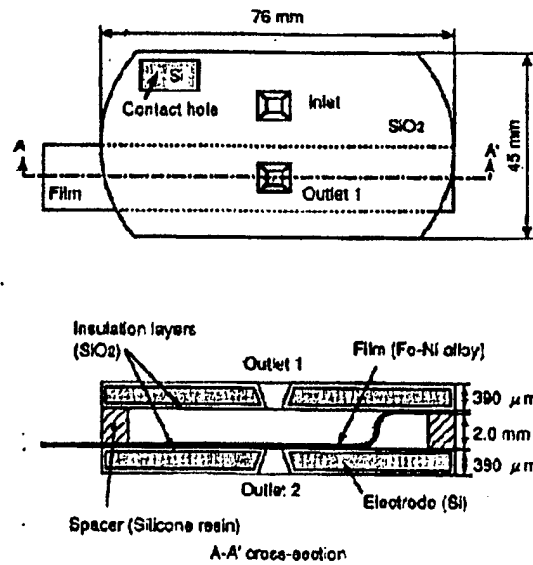


Figure 2-4: Electrostatically Actuated Microvalve [30]

moving part of the valve is a metallic flapper which is attracted either to the lower or upper electrode depending on the field direction. The fundamental limitation of these systems is that the actuation force is inversely proportional to the square of the distance between the flapper and the electrode. These limits the field of usage of this valves to low pressures and relatively short strokes. Experimental results by Shikida[30] showed a maximum block force of ~ 20 mN. The major advantage of this architecture is that fast response times of the order of 0.1 msec can be attained. This actuation system can provide actuation for large strokes but low forces. It has been successfully employed for the control of rarefied gas systems such as Molecular Beam Epitaxy (MBE).

Electromagnetic actuation has been explored by Hirano, Yanagisawa and coworkers[9]. The major problem of this actuation system is the requirement for a miniaturized coil as seen in Figure 2-5.

Piezoelectrically based actuators represent one of the fastest options for opening and closing a microvalve. Piezoelectric actuators however, have very small strokes and this has significantly limited their use for microvalves. Active microvalves with piezoelectric actuators have been proposed by Shoji and Esashi [31] and Roberts *et*

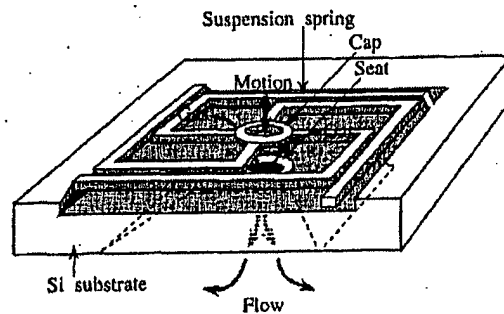


Figure 2-5: Electromagnetic Actuated microvalve [9]

al,[27]. Shoji and Esashi have shown experimentally response times of the order of 1 msec with gas flows of 40 ml/min. The design proposed by Roberts, Figure 2-6, uses an amplification chamber to obtain more stroke out of a piezoelectric while retaining the force and rapid reaction available with a piezoelectric.

Lessons Learned from Existing Microvalves

One can observe from reviewing the existing literature on microvalves and integrated microsystems that virtually all the proposed valve flow models make the following assumptions:

The valve is the dominating flow loss in the system. This means that in most cases the only flow resistance or head loss needed to describe a system is the valve.

The unsteady state head losses are modeled with steady state head loss models. This approximation is made because in many cases the frequency dependent resistance term is difficult to model and experimental results are lacking.

Microvalves are approximated as variable area orifices. This approximation is based on the assumption that inertial losses ($\Delta P \propto Q^2$) are the dominating loss mechanisms in the valves. It should be pointed out that although such approximations do capture the physical flow behavior they will be only order of magnitude models.

Valve stroke, as seen in the literature is one of the key elements required of an actuation system in order to obtain high conductance.

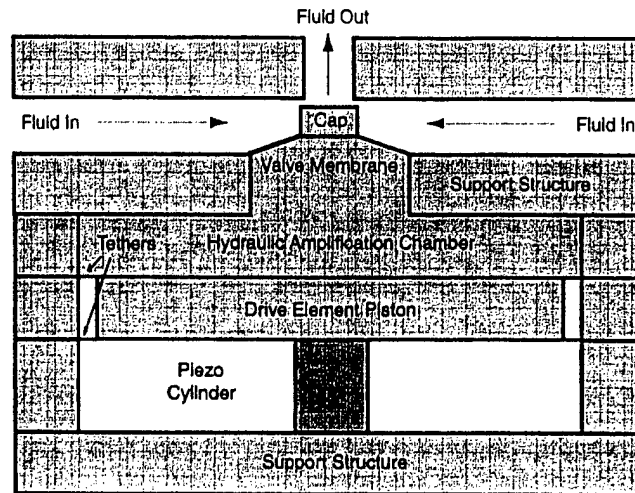


Figure 2-6: MHT Amplification Chamber,[27]

The closing force, leakage, and response times are important but their requirements are heavily dependent on the application at hand.

Microvalves for gas flow applications are characterized by low Reynolds numbers of order 100-1000, but the flows may approach Mach 1. For this reason choked flow in the valve orifice is observed in many cases. The most common flow model is a quasi 1-d gas flow model for subsonic flow and in certain cases for choked flow.

In the case of liquids such as water and Silicon oils, the situation is not much different. Flow models reduce the valve behavior again to a variable area orifice. In most cases these models are used to analyze obtained experimental results. Corrected discharge coefficients are computed and curves fitted to the data.

The systematic study of the valve behavior and sensitivities of the different flow parameters is usually not performed.

2.4 Macro-scale Valves

Macro-scale poppet and disc valves have many applications most notably in internal combustion engines, pressure control and relief valves, compressor valves and even for homogenizing milk.

In contrast to microvalves, much research has been conducted on "normal"-sized valves. However, the complex geometries make the flow in valves very complicated and valve-dependent. Thus comparison between different experimental measurements and numerical simulations is difficult, even impractical. In the past, researchers have investigated such flows using a variety of analytical techniques such as potential flow analysis (Von Mises, [17]), his work predicted the flow contraction but ignored the reattachment and pressure recovery phenomena. Other experimental results have shown that the flow behavior is highly dependent on the details of the valve geometry and the separated jet. The effects of these two parameters are very difficult to model mathematically.

Numerical techniques have been employed to analyze the flow behavior of poppet and disc valves, but as Vaughan [33], points out typical turbulence models (such as the $\kappa - \epsilon$ model) have been shown to give inaccurate results. Vaughn and coworkers concluded that numerical simulations can show qualitative trends but the results may be quantitatively inaccurate. They further point out that the popular $\kappa - \epsilon$ model is inadequate for solving this flows and suggest that a Reynolds-stress based model should give a better approximation to the real flow. It follows from their conclusions that numerical simulations need to be validated against experiments whenever possible.

In summary all these techniques suffer from the fact that flow separation, cavitation, transition, reattachment and relaminarization are difficult to model mathematically and expensive numerically.

The preferred approach to this type of problem is experimental. Previous work on macro-scale valves traces back to the work of Schrenk (1925), Stone,[32] and Johnston[14]. Schrenk reported discharge coefficients on poppet and disc valves. Stone concentrated on sharp edged poppet valves and low turbulence flows. His results however show considerable scatter and as he suggests more research is needed. Johnston and coworkers concentrated on measuring the discharge coefficients and force acting on poppet and disc type valves. Their work concentrated on the fully turbulent regime (i.e. $Re \gg 2500$). Johnston makes no reference to transition effects

or low turbulence behavior.

One important conclusion that can be obtained from these efforts is that, for small openings, poppet valves behave like long orifices, a suggestion that supports the thought that the effects of flow separation and subsequent reattachment dominate the valve dynamics.

A second important conclusion is that although qualitatively the flow behavior may be analogous to that of a long orifice the actual value of the discharge coefficients is a strong function of the valve geometry and the upstream and downstream conditions. For this reason, it is important to investigate experimentally the fluidic behavior for the particular geometry under study.

2.5 Summary

In this chapter a literature review of the most common micro-hydraulic system modeling strategies was undertaken. The main advantages and disadvantages of the different approaches were shown. It was concluded that most of these strategies required separate submodels for their subcomponents (i.e. valves, elbows, etc.). Considering that microvalves are in most cases the dominant dissipative element a separate literature review was undertaken.

The microvalve review showed, as pointed before, that there is very little information regarding the flow characteristics of reported microvalves. Most flow models identified the valve as an orifice correlating adequately with the results. These models gave, however, little insight to the flow sensitivity to valve geometry and Reynolds number. The third part of the chapter concentrated on macro-scale valves that may be similar to those found in microsystems. The complication, as it was pointed out, is that there is a lack of information for disc valves operating at low turbulence and transition regimes. As a conclusion, two decisions were made: to construct an order of magnitude model for the valve based on available orifice information and to explore experimentally, via a macro-scale valve, the valve flow characteristics at low turbulent Reynolds numbers.

Chapter 3

Modeling of Hydraulic Microsystems

Based on the literature review, for initial designs and system analysis, the hydraulic system of the MHT has been modeled using lumped elements. As mentioned in the literature review the lumped model is limited to short channels. Wylie and Streeter[35] have proposed a conservative rule-of-thumb criterion in which they suggest that the maximum channel length (l) should be less than 4% of the acoustic wavelength (λ) as shown by :

$$l \leq 0.04\lambda = \left(\frac{0.04}{f}\right) \sqrt{\frac{k}{\rho}}. \quad (3.1)$$

Equation 3.1 assumes that the flow channel has rigid walls, and therefore the acoustic wavelength (λ) is only a function of the frequency of the pressure oscillations (f), the fluid bulk modulus (k) and the fluid density (ρ).

The lumped model breaks up the hydraulic system into subcomponents or elements. The subcomponent's behavior is described by three 'properties': inductivity, resistivity and capacity. The inductivity represents the fluid mass or inertia. The resistivity is related to the dissipative characteristics of the element. Finally the capacity describes the fluid storage capability of a given component. Different elements will have different combinations of these properties and in some cases the effect of

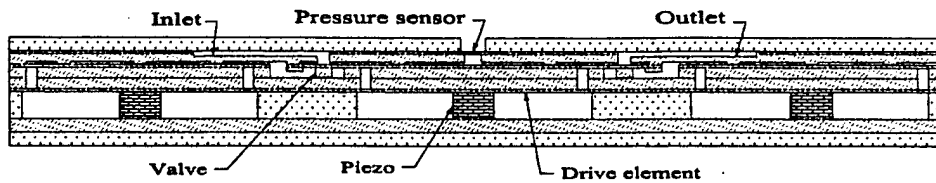


Figure 3-1: Cross-sectional view of a multiple wafer energy harvester with active valves

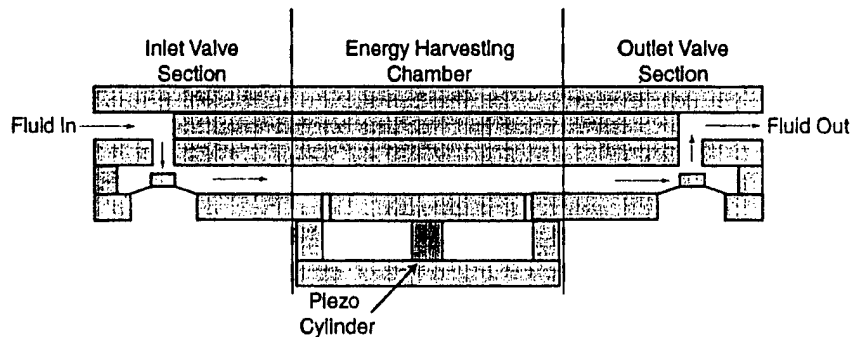


Figure 3-2: Schematic of the MHT hydraulic system

some will be negligible compared to others. The end effect is a system of equations that resembles those used for electrical circuit analysis.

3.1 The MHT Hydraulic Model

The MHT's hydraulic system to be modeled is shown in figure 3-1. A schematic representation of the flow path can be seen in Figure 3-2. The flow paths are rather tortuous being characterized by sudden expansions, contractions, 90° turns, short tubes and valves. The hydraulic system is divided into three main sections: the inlet valve section, Energy Harvesting Chamber (EHC) section, and Outlet valve section as shown schematically in Figure 3-2 and 3-3.

As mentioned before the lumped element model classifies the fluidic components into equivalent capacitances, resistances and inductances. The lumped element representation of the inlet and outlet valve sections is presented in Figure 3-5. The inlet

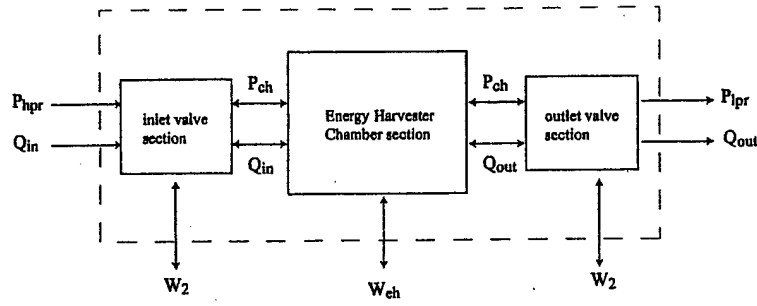


Figure 3-3: Hydraulic Systems Control Volume Representation

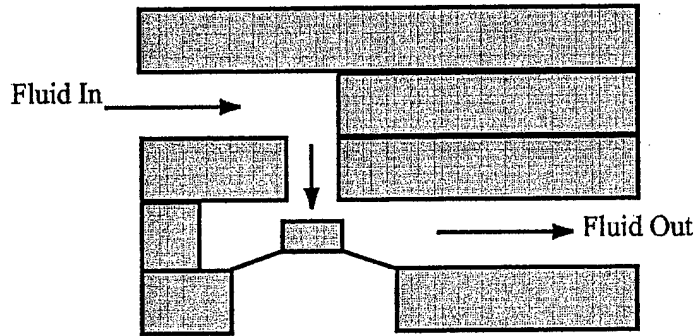


Figure 3-4: Schematic of the inlet valve section

and outlet valve sections are presented schematically in Figure 3-4 and in lumped element representation in Figure 3-5 showing that the dominating effects are of inductive (I_i) and resistive nature ($R_i(Q)$). The channel capacitance is neglected on the grounds that the channels have rigid walls and the fact that the fluid is nearly incompressible.

The lumped model equation for the inlet valve is given by :

$$P_{hpr} - P_{ch} = (I_1 + I_2)\dot{Q} + (R_1(Q) + R_{v1}(Q) + R_2(Q))Q + \Delta P_{vp} \quad (3.2)$$

where as seen in Figure 3-5 there are two inductance elements I_1 and I_2 , and three major groups of resistive elements shown as R_i . It should be pointed out that these resistive terms are in general non-linear which may make the numerical solution more difficult. In the case of the outlet valve the flow equation is similar :

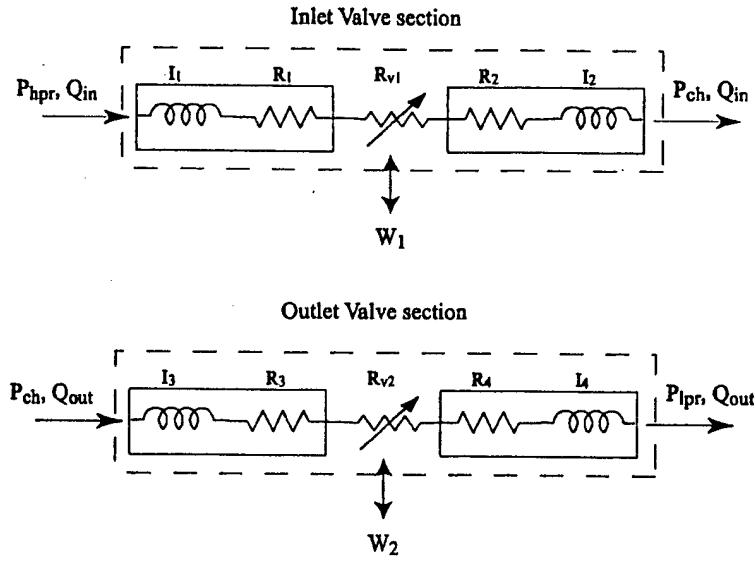


Figure 3-5: Valve Sections: Lumped Model Equivalents

$$P_{ch} - P_{lpr} = (I_1 + I_2)\dot{Q} + (R_1(Q) + R_{v1}(Q) + R_2(Q))Q + \Delta P_{vp}. \quad (3.3)$$

The major difference found in this model relative to other models available in the literature comes from the term ΔP_{vp} which describes the work done by the valve cap on the fluid and viceversa. This term is of the form:

$$\Delta P_{vp} = \frac{\dot{W}}{Q} = \frac{1}{Q} \frac{d \left(\int \vec{F} \cdot d\vec{x} \right)}{dt} \quad (3.4)$$

where the change in pressure ΔP_{vp} is equal to the rate of work (\dot{W}), done on the system by the valve cap, over the instantaneous flow rate (Q).

3.1.1 Valve Cap Force Calculation

The fluid force acting on the valve cap is calculated using the unsteady integral momentum equation given by

$$\vec{F} = \frac{\partial}{\partial t} \int (\rho \vec{v}) dV + \oint (\rho \vec{v} \cdot d\vec{S}) \vec{v} \quad (3.5)$$

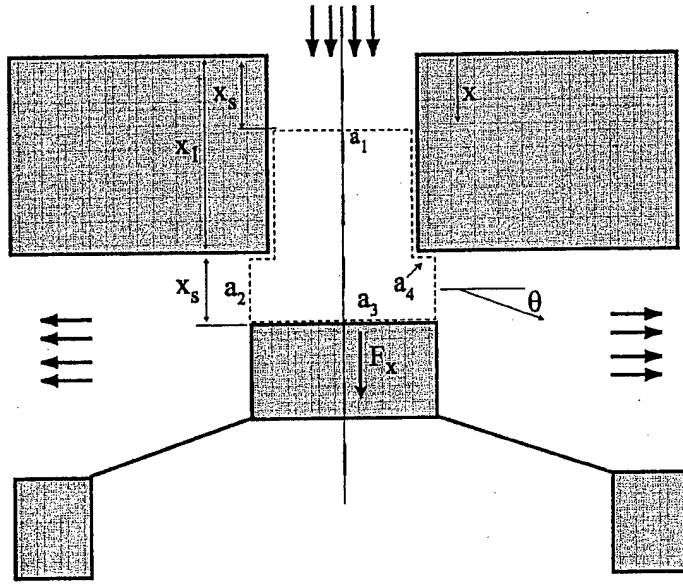


Figure 3-6: control volume for valve cap force calculation

where \vec{F} is the resultant force acting on the control volume, ρ is the fluid density, and \vec{v} is the fluid velocity vector. A schematic of the valve and the control volume used to calculate the force is shown in Figure 3-6. The valve force calculation, as seen in Figure 3-6, only requires the use of the x -direction momentum equation. The calculation assumes that the control volume moves with the valve cap, that friction forces are negligible, and that the fluid is incompressible. Following Ikebe's[12] method we obtain the x -direction momentum equation :

$$F_x = \rho \left\{ \frac{d}{dt} \oint x u_c dS + \oint u u_r dS \right\} \quad (3.6)$$

where F_x is the x -direction force acting on the fluid, ρ is the fluid density, u_c is the normal exterior fluid velocity in the x -direction, and u_r is the normal exterior relative velocity to the control surface. Applying equation 3.6 to all the control surfaces in Figure 3-6 we obtain:

$$\frac{F_x}{\rho} = (x_1 + x_s) \ddot{x}_s + (\dot{x}_s)^2 a_3 + (x_1 - \frac{x_s}{2}) \dot{Q} + \frac{\dot{x}_s}{2} Q + \left(\frac{\tan \theta}{a_2} - \frac{1}{a_1} \right) Q^2 \quad (3.7)$$

where F_x is the x -direction force, ρ is the fluid density, x_s is the valve displacement, x_1 is the height of the control volume, Q is the instantaneous flow rate, θ is the fluid jet angle, and a_i are the control surfaces. The surface areas are given by

$$\begin{aligned} a_1 &= \frac{\pi}{4} d_0^2 \\ a_2 &= \pi x_s d_v \\ a_3 &= \frac{\pi}{4} d_v^2 \end{aligned}$$

where d_0 is the inlet diameter, d_v is the valve diameter, and x_s is the valve displacement.

A simplification of the equation can be obtained if we assume that $x_1 \gg x_s$ in that case we obtain:

$$\frac{F_x}{\rho} = (x_1)\ddot{x}_s + (\dot{x}_s)^2 a_3 + (x_1)\dot{Q} + \frac{\dot{x}_s}{2}Q + \left(\frac{\tan \theta}{a_2} - \frac{1}{a_1} \right) Q^2. \quad (3.8)$$

This result allows us to calculate the unsteady force on the valve cap (F_x) as a function of the flow rate (Q) and valve displacement (x_s). Experimental results by Nakada and Ikebe[21] have shown that for spool valves this modeling approach gives reasonably accurate results.

3.1.2 Capacitance modeling

The Piston chamber or EHC is the dominant capacitance of the system. The compliance of the piston chamber results from the compression of the fluid (ΔV_f), the structural compliances (ΔV_s) and the oscillatory movement of the piston. The change in pressure (\dot{P}) due to capacitive effects is defined as :

$$\dot{P} = \frac{1}{C} (Q_{in} - Q_{out} - \dot{V}_p) \quad (3.9)$$

where C is equivalent capacitance, Q_{in} is the flow rate into the control volume,

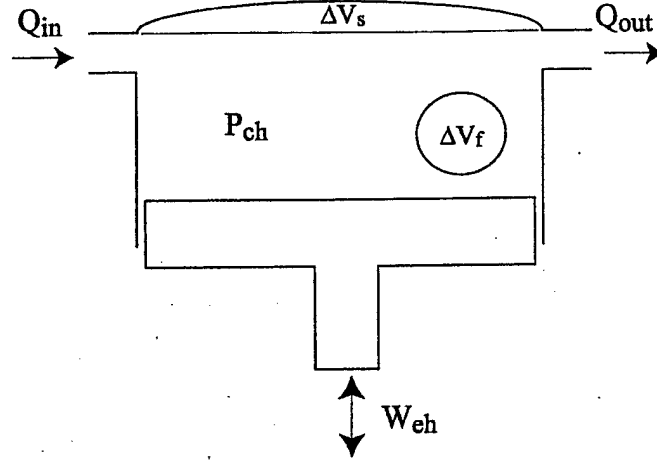


Figure 3-7: Energy Harvesting Chamber Representation

Q_{out} is the flow rate leaving the control volume and \dot{V}_p is the change of volume due to the piston movement. In general the equivalent capacitance for the piston chamber is of the form :

$$C = \frac{\partial V_s}{\partial P} + \frac{\partial V_f}{\partial P} \quad (3.10)$$

where the first term refers to the change in volume by the structure for a given pressure. This relation is obtained from structural calculations and FEA analyses (outside the scope of this thesis). The second term describes fluid compressibility which can be estimated using the isothermal bulk modulus. The underlying assumption here is that the temperature is nearly constant, making the thermal expansion coefficient effect negligible.

The fluidic capacitance (C_f) is related to the isothermal bulk modulus (k) by the following equation:

$$C_f = \frac{V_0}{k} \quad (3.11)$$

where V_0 is the initial volume.

3.1.3 Inductance in fluid channels

The compliance in the fluid channels is usually much smaller than that of the piston chamber due to the fact that the channels are surrounded by rigid walls and that their fluid volume is smaller than that of the chamber.

The inductance element is the fluid mass contained in the channels of the system and it has been modeled by assuming inviscid flow (i.e. $R_1 = R_2 = 0$). For an unsteady constant area channel flow the energy equation can be written as

$$\dot{\Phi} - \dot{W} = \int \int \int_{cv} \left(e + \frac{1}{2}u^2 \right) \rho dV + \int \int_s \left(h + \frac{1}{2}u^2 \right) \rho (\vec{u} \cdot \vec{n}) dS \quad (3.12)$$

where $\dot{\Phi}$ is the heat transfer into the system, \dot{W} is the work done by the system, e is the internal energy, u is the flow velocity, ρ is the fluid density and h is the fluid enthalpy. For an adiabatic, inviscid flow in a constant area channel the expression reduces to :

$$\Delta P = \frac{1}{Q} \int \int \int_{cv} \left(e + \frac{1}{2}u^2 \right) \rho dV \quad (3.13)$$

further assuming a uniform velocity profile we obtain the following result:

$$\Delta P = I \dot{Q} = \left(\frac{\rho l}{A} \right) \dot{Q} \quad (3.14)$$

where I is defined as the inductance which is a function of the fluid density (ρ), the channel length (l) and the channel cross-sectional area (A).

The approximation is now compared to cases where we have fully developed viscous velocity profiles. In those cases where the flow is laminar it has been shown by Morris *et al*[19] that the formula underestimates the correct value by about 30%. This can be easily explained if we consider that in deriving the inviscid Inductance (I), the underlying assumption is that of a uniform velocity profile. For laminar flow this approximation is inaccurate since the velocity profile is parabolic. Using the parabolic velocity profile to compute the change of the kinetic energy in the system we obtain the correct inductance value which is $\frac{4}{3}$ times higher than the inviscid case

as shown by Olsson [23]. For turbulent flows, assuming a velocity profile (u):

$$u \simeq u_0 \left(1 - \frac{2r}{D}\right)^n \quad (3.15)$$

where u_0 is the maximum axial velocity, r is the radial location, D is the pipe diameter and n is the scaling power. The scaling power n is set to $\frac{1}{7}$. Compared to the constant velocity profile the correction factor is only 1.02.

3.1.4 Resistive Elements

For the resistive elements the microvalves have been identified as the major fluidic resistance of most existing micropumps. Gravesen [5] notes that the valves are usually the dominant loss element due to the fact that the entire flow has to pass through the small valve openings. For a first approximation to the valve head loss they were modeled as a simple orifices.

The flow resistance of each element (R_i = elbows, contractions, channels,etc.) is modeled using published experimental loss coefficients (Idelchik [11]), which were corrected according to the local Reynolds number (Re).

The quadratic loss coefficient (ζ) is defined by :

$$\zeta_{quad} = \frac{\Delta P}{\frac{1}{2}\rho\bar{u}^2} \quad (3.16)$$

where ΔP is the total pressure drop, ρ is the fluid density and \bar{u} is the local bulk flow velocity. Published values of the loss coefficient (ζ) for different components such as elbows, expansions and contractions are reported usually for fully turbulent regimes. In this regime pressure losses are inertially dominated and qualitatively behave like ($\Delta P \propto \bar{u}^2$). This clearly shows that the reported loss coefficients will tend to be weak functions (or independent) of the Reynolds number. This approximation, however, only holds for Reynolds numbers of order $Re > 10,000$. Microfluidic systems, like the MHT, usually operate at lower Reynolds numbers. For this reason correction factors or experimental results are employed to obtain better estimates of the loss coefficients for low turbulence flows.

Idelchik modifies the quadratic loss coefficient (ζ_{quad}) with two empirical correction factors (ζ_ϕ and ϵ) based on the local Reynolds number (Re), and with this, a modified loss coefficient (ζ) can be defined:

$$\zeta = \zeta_\phi(Re) + \epsilon(Re)\zeta_{quad}. \quad (3.17)$$

In this manner the flow resistances of the different components were estimated. In order to establish a uniform system model, the different resistive components were referenced to a characteristic system length with which a system-wide Reynolds number (Re_{sys}) is defined. The characteristic length chosen was the valve inlet diameter (d_{sys}).

Order of Magnitude Valve Model for the MHT

For initial estimates an order-of-magnitude valve model was constructed. This model also gave a starting point for designing the valve experiments. As mentioned above, previous work (Schrenk [29]; Stone [32]; Johnston [14]) has suggested that the valve can be modeled as an orifice. The initial order-of-magnitude model was constructed based on an orifice analogy. The disk valve to be modeled can be seen in Figure 3-8. The valve is characterized by three areas : A_1 the upstream flow area, A_0 the throat flow area and A_2 the downstream area.

Most of the information gathered on orifices is based on experiments carried out in pipes of 2in diameter and higher[25]. It has been noted that orifices in pipes of smaller diameter have higher discharge coefficients due to second-order effects, such as surface tension (Ramamurthi [24]).

Thus, the orifice model should be able to capture the flow physics, but should be considered only as an approximation to the correct values.

To certain extent the orifice itself may be thought of as a contraction of the flow and a subsequent expansion. An integral analysis gives a relationship for the combined effect of the flow expansion and contraction. The quadratic local loss coefficient (ζ_{quad}) is defined as the total pressure drop (ΔP) over the dynamic pressure based on the

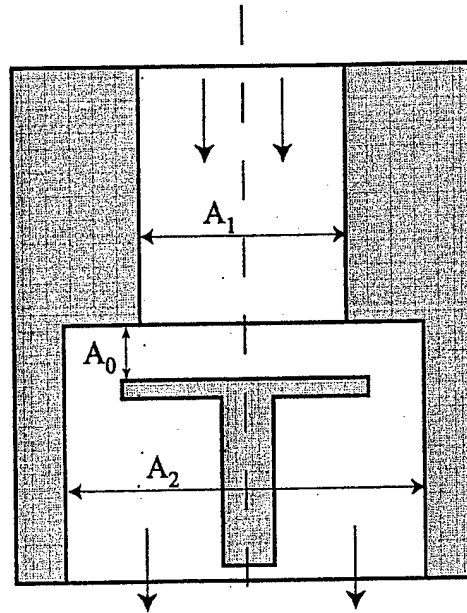


Figure 3-8: Valve schematic for the order-of-magnitude model

orifice local mean velocity (\bar{u}):

$$\zeta_{quad} = \frac{\Delta P}{\frac{1}{2}\rho\bar{u}^2} = \left[\frac{1}{2} \left(1 - \frac{A_0}{A_1} \right)^{\frac{3}{4}} + \left(1 - \frac{A_0}{A_2} \right)^2 \right] \quad (3.18)$$

The loss coefficient, ζ_{quad} , is a function of both the ratio of the orifice throat area to the upstream area (A_0/A_1) and the ratio of the orifice throat area to downstream area (A_0/A_2).

For the initial model, experimental correlations published by Idelchik [11] were used to compute the loss coefficient for a variety of geometries. The order of magnitude valve model is shown in Figure 3-9 where the x -axis represents the Reynolds number and the y -axis represents the loss coefficient (ζ) values for different valve openings (h_v). The model shows that in the turbulent regime the loss coefficient is a weak function of the Reynolds number (as expected). As the Reynolds number decreases, transition to the laminar regime starts and eventually for sufficiently low Reynolds numbers the flow becomes laminar. Figure 3-9 also shows the significant dependence of the loss coefficient (ζ) to the valve opening (h_v)

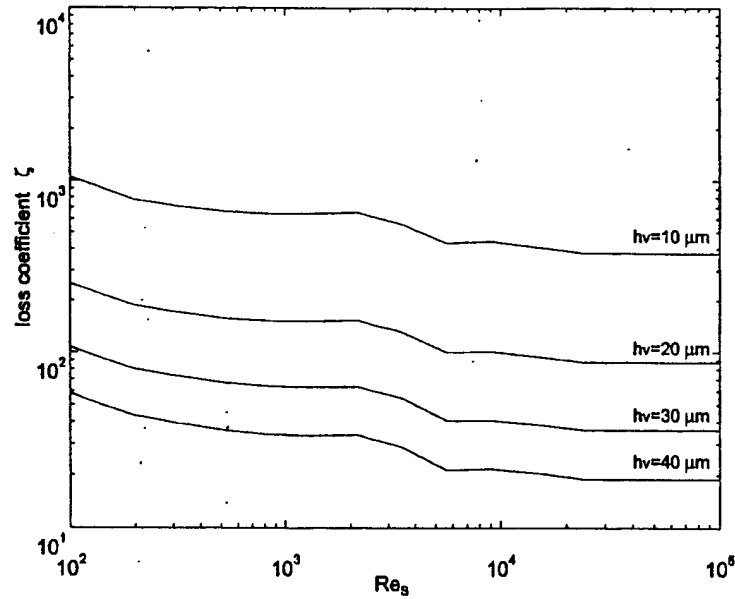


Figure 3-9: Order of magnitude valve model. Results are shown for different valve openings h_v

This order of magnitude model aims to capture the flow physics of the valve and establish within an order of magnitude the head losses. The model takes into account such effects as valve opening (h_v , valve cap diameter (d_v) and downstream chamber height (h_p). This model, however will not be able to capture the effect of the seat width (s).

Comparison of Resistive Elements

The comparison of loss coefficients (ζ) versus a system wide Reynolds number. The system-wide-Reynolds-number (Re_s) is based on one representative reference length for the whole system. In the MHT case the selected reference length is the valve inlet diameter (d_0). The local Reynolds numbers are converted to the system-wide-Reynolds-number by using:

$$Re_s = \frac{d_h}{d_0} Re \quad (3.19)$$

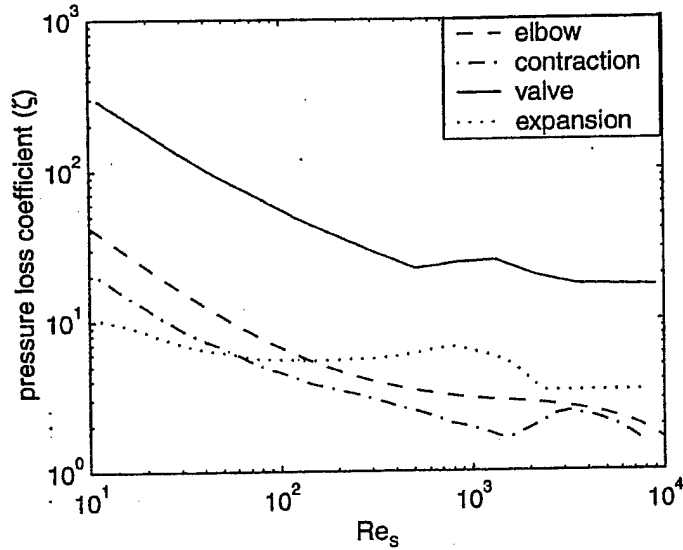


Figure 3-10: Comparison of component loss coefficients vs Re_s

where d_h is the local hydraulic diameter, d_0 is the reference length for the system, and Re is the local Reynolds number.

is shown in Figure 3-10. It should be pointed out that because flow correlations at these low Reynolds numbers are not always reliable they need to be validated through experiment and computations.

Initial results shown in figure 3-10 indicate (confirming previous assumptions) that the valves are the dominant loss element in the hydraulic system. For this reason the valve design and analysis required special attention.

3.2 SIMULINK Model Implementation

SIMULINK is a graphical interface (based on the MATLAB architecture) for modeling, simulating and analysing dynamical systems. SIMULINK allows the user to break-up a system into smaller interchangeable modules giving flexibility without sacrificing performance.

The implementation of the hydraulic lumped model into SIMULINK is divided into two major areas: the implementation of the previously described fluidic resis-

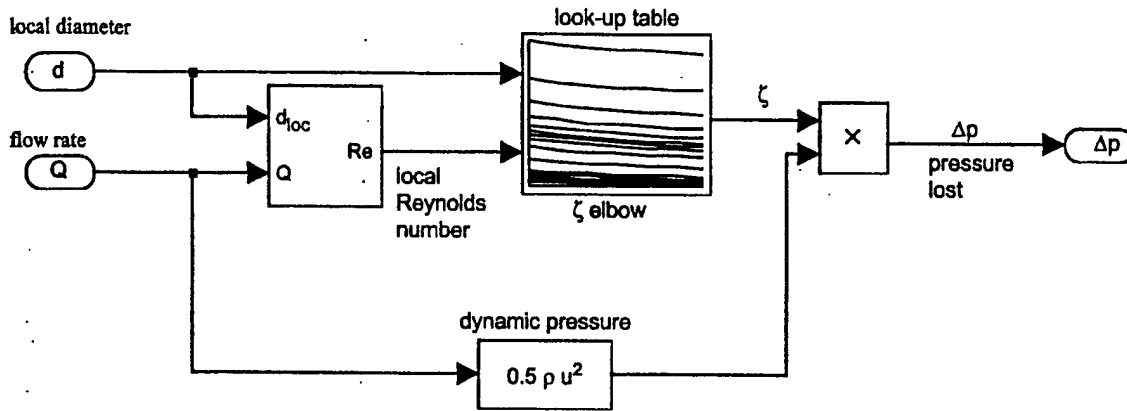


Figure 3-11: Generic Architecture of Fluidic resistances in Simulink

tances and the coding of the flow rate equations.

Each fluidic resistance was coded into a generic fluidic resistance module. Considering that the pressure losses due to fluidic resistances undergo significant qualitative changes for different flow rates the values for each element were coded as two-dimensional look-up tables. The advantage of doing this is that SIMULINK only has to interpolate the correct head loss value from given local flow conditions from the look-up table. This operation is computationally inexpensive and more accurate than using correlation formulas. The look-up tables have as input the local Reynolds number which is computed from the instantaneous flow rate and the dimensions of the element (i.e. diameter, length, etc.) The result is given as a loss coefficient (ζ) which is then converted to a pressure loss by substituting the loss coefficient into equation 3.16. A typical fluidic resistance block is shown in Figure 3-11.

The flow rate equations 3.2 and 3.3 were coded in the following manner to accommodate for SIMULINK's architecture:

$$Q = \int \left(\frac{P_{hpr} - P_{ch} - \Delta P_v(Q) - \Delta P_1(Q) - \Delta P_2(Q)}{I} \right). \quad (3.20)$$

In equation 3.20 Q is the flow rate, P_{hpr} is the upstream pressure (Pressure in the high pressure reservoir), P_{ch} is the downstream pressure (pressure in the chamber),

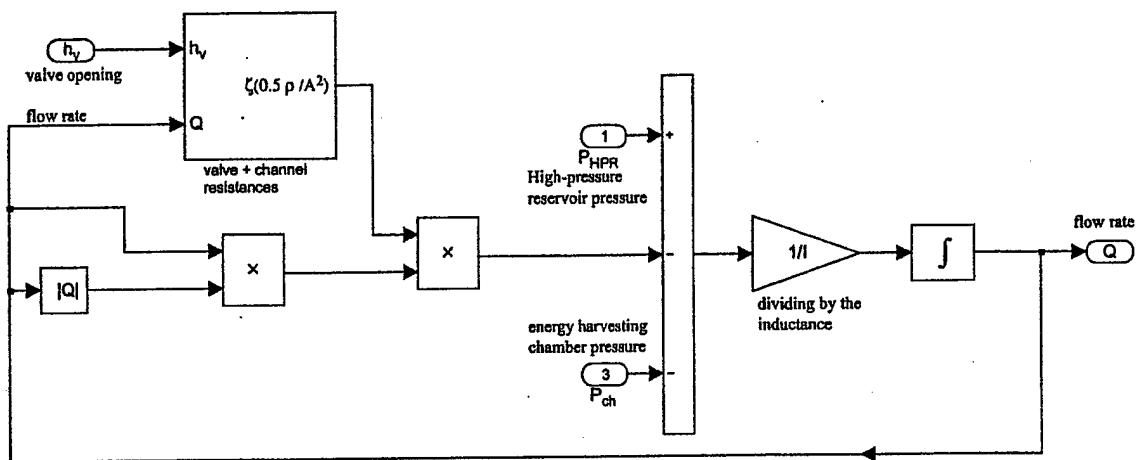


Figure 3-12: Simulink Representation of the Flow Rate Equation 3.20

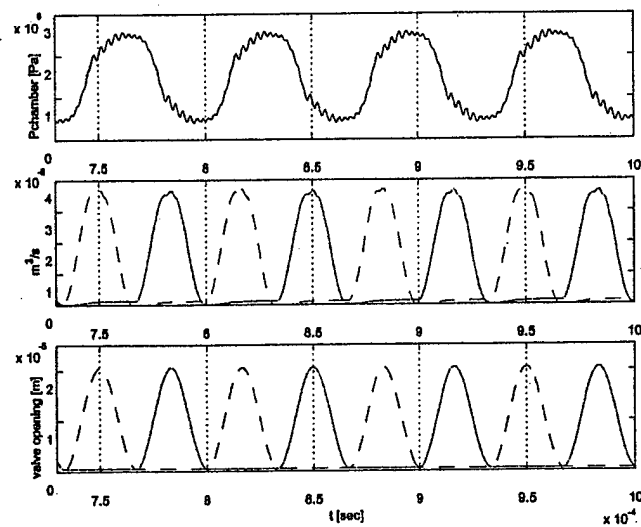


Figure 3-13: Time histories of chamber pressure, inlet valve flow rate, outlet valve flow rate and valve openings for the resonance condition of an Energy Harvester,[36]. Continuous lines are for inlet parameters

$\Delta P_v(Q)$ is the head lost at the valve and I is the fluid inductance defined by equation 3.14. It should be noted that the head loss across the valve is also a function of the flow rate (Q) and that the equation is solved iteratively by SIMULINK. Equation 3.20 is shown in its SIMULINK representation in figure 3-12.

Plots of sample simulations are shown in Figure 3-13. The high frequency ripples of the chamber pressure signal are due to piston dynamics included in the model.

3.3 Summary

This chapter described the lumped parameter model chosen for initial designs and calculations. A detailed explanation of the lumped model structure for the Micro-Hydraulic Transducer was formulated. The dominating components were identified and order of magnitude comparisons between components were made. The microvalve was identified as the dominating resistance suggesting the need of a more accurate model to optimize the valve. The SIMULINK version of the model was presented and sample time histories have been included.

Chapter 4

Experimental Setup

The research strategy previously discussed called primarily for an experimental approach to study the microvalve behavior. As mentioned before, even partial instrumentation of a microvalve is not trivial, for this reason a scaled up version, a macro-scale valve experiment was considered.

In this chapter, the geometrical and dynamic similarity concepts employed to relate the macro to micro-scale results are discussed. The relevant non-dimensional numbers are defined and the scaling effects are explored. The second section of the chapter will cover the experimental macro-scale facility. Fabrication, instrumentation, and setup capability issues are addressed. Finally, the experimental methodology and data validation tests are presented.

4.1 Experiment Design

The flow conditions between a model and a prototype are similar if geometric, kinematic and dynamic similarity is achieved. Once similarity is achieved the results obtained with the model can be related to the prototype via previously defined scaling laws.

Geometrical similarity is attained by replicating the geometry of the full scale (microvalve) at the macro-scale. Kinematic similarity is obtained if the model and prototype have homologous length-scale ratio and time-scale ratio. A result of the

temporal and spatial ratio equivalence will be a similar velocity ratio and therefore a kinematic similarity. Dynamic similarity refers to a model/prototype system with equivalent force-scale ratio throughout. Dynamic and kinematic similarity are attained by matching the Reynolds and Strouhal numbers [34].

The Reynolds number

$$Re = \frac{l\bar{u}}{\nu} \quad (4.1)$$

represents the ratio of inertial to viscous forces and is a function of the length scale (l), the local mean flow velocity (\bar{u}), and kinematic viscosity (ν). Expressing the Reynolds number as a function of a flow rate (Q), we obtain

$$Re = \frac{Q}{\nu l}. \quad (4.2)$$

For a fixed flow rate (Q), the Reynolds number scales linearly with the length scale (l).

The Strouhal number is used to describe the unsteadiness of a flow, and it is defined as:

$$S = \frac{fl}{\bar{u}} \quad (4.3)$$

where f is the oscillatory frequency of the flow, l is the characteristic length scale, and \bar{u} is the local flow velocity. For a fixed Reynolds and Strouhal number, the driving frequency (f) scales as the reciprocal of the length scale squared ($f \propto l^{-2}$).

The pressure drop in a scaled-up model of the micro-valve is also a function of the length scale. In this case, assuming that the head loss across a microvalve is characterized by a loss coefficient as defined by equation 3.16. Replacing the flow velocity (\bar{u}), by the Reynolds number, and solving for the pressure drop we obtain:

$$\Delta P = \frac{\zeta}{2} \rho \left(\frac{Re \cdot \nu}{l} \right)^2 \quad (4.4)$$

which shows that the pressure drop (ΔP) is inversely proportional to the square

of the length scale (l).

4.1.1 Scale Effects

One disadvantage of scaling up a system is that some parameters are difficult, or impossible to scale properly. In the present case, the most obvious parameter that was not matched was that of the surface finish, but this is thought to be less important. However, one attribute of microfabrication that is important to match is the sharp corners that define MEMS-fabricated edges. Care was taken to ensure that this feature was preserved in the macro-rig.

Another disadvantage of scaling up a system is that some effects that may be considered negligible in the full scale (micro-scale) system do have an important effect as the system is scaled up. An important scale effect observed in the macro-scale facility was that of gravity. The Froude number is defined as

$$Fr = \frac{(Re \cdot \nu)^2}{l^3 g} \quad (4.5)$$

where the Re is the Reynolds number, ν is the kinematic viscosity, l is the length scale and g is the gravitational constant. For a fixed Reynolds number Froude is inversely proportional to the third power of the length scale. In the micro-scale $Fr \approx 30000$ which tells that gravity effects are negligible. For the macro-scale experiment the Froude number becomes about 30 which shows that gravity effects are important.

Once the scaling relations were known, it was important to relate these parameters to practical experimental considerations. In choosing a convenient scale factor several issues needed to be addressed :

- Machining limitations
- Instrumentation
- Actuation frequency
- Flow rates
- Expected pressures

A scaled up version of the microvalve should be machined using traditional methods such as milling and turning. The use of standard machine shop technology significantly reduced lead times and allowed for quick modifications of parts.

A properly scaled macrovalve would permit the use of off-the-shelf instrumentation such as pressure sensors, flowmeters and temperature sensors. A fundamental advantage of the scaled-up system is that there is enough space for instrumenting the valve test section and monitoring the flow rates, pressures, valve position and temperature of the fluid at the same time. The ability to measure all these parameters gives a clearer picture of the flow behavior.

The actuation frequency (f) of the valve is an important factor for the sizing of the macro-scale experiment. It should be pointed out that although this parameter has no effect on steady-state measurements, the same setup will be employed for future unsteady macro-scale experiments and therefore should be considered as a design requirement. The intent is to lower the operational frequency so that a conventional actuator may be employed to drive the valve.

Considering all the above listed requirements and issues, a scaling factor of ten was chosen for the macro-scale experiment, resulting in a valve of approximately 1 cm in diameter. The stroke of the valve is 400 μm . The size of the setup allowed for complete instrumentation. The driving frequency for an actuated valve would be in the range of 100 Hz. The maximum flow rate needed was in the order of 3 liters-per-minute. The expected pressures were in the range of 1000 to 20,000 Pa. These were the functional requirements that drove the experimental setup design.

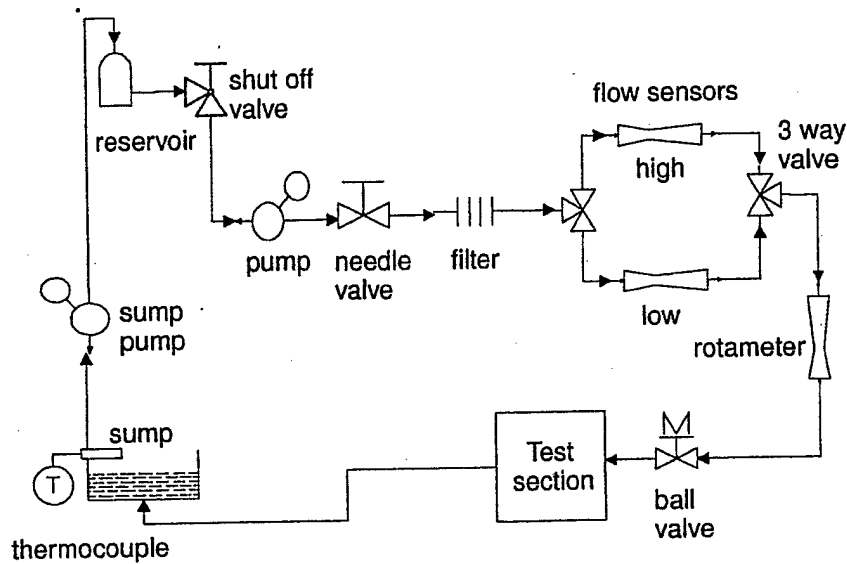


Figure 4-1: Schematic of the macro-scale test facility layout.

4.2 Macro-scale setup

4.2.1 Fluid Delivery Section

A schematic of the experimental setup is shown in Figure 4-1. The fluid used for the experiments is deionized water which flows from the reservoir to a 1/15 HP centrifugal pump passing through a control needle valve and into a 50 μm particulate filter. The purpose of the filter is to remove any particulates that could clog the flowmeters and doubles as a settling chamber for the incoming fluid.

The range of flowrates explored in the experiments required the use of multiple pressure sensors and flowmeters in order to accurately monitor the spectrum of test conditions. The setup includes two Cole-Palmer differential pressure liquid flowmeters (Cole-Parmer model 32916-16 and 14) each with an uncertainty of 3% (full scale). The low discharge flowmeter has a maximum flow rate of 1 liter/min and the high discharge flowmeter has a maximum discharge of 5 liters/min. Both flowmeters have a 0-5 volt output to the data acquisition system. A rotameter was placed in series with the flowmeters to ensure consistency in the measured flowrates. The calibration of each flowmeter was checked gravimetrically prior to the experiments.

The water then flowed into the test section and to the sump where the temperature of the water was measured. The temperature was measured using an Omega K-type submersible thermocouple and corroborated with a regular thermometer. The Temperature (T) data was used to correct the dynamic viscosity (μ) of the deionized water according to:

$$\mu = \left\{ \frac{0.1}{-120 + 2.1428 (T[^\circ C] - 8.435 + \sqrt{8078.4 + (T[^\circ C] - 8.435)^2})} \right\} \quad (4.6)$$

obtained from Richter [26]. Once in the sump, the water was pumped back to the reservoir using an automatic sump pump completing the circuit.

4.2.2 Test Section

The test section, illustrated in Figure 4-2, is axisymmetric with the test fluid flowing in from the center tube and exhausting radially outward. The test section may be subdivided into three subsections: inlet, valve and positioning section. The inlet section consists of a 3/8in Aluminum tube, 36in (96 diameters) long. The tube is connected to the valve section and special care was taken to ensure that the inside surface was free of gaps and steps.

The valve section has two cylindrical plates, which were ground flat to a specified planarity of less than 1 mil (checked with dial gauge). Accurate control of the separation of the two plates is critical to the experiment, and so, to ensure that the plates were parallel, they were separated by three thickness gauges placed 120° apart, and tightened with screws. The separation was then re-checked with thickness gauges and a depth micrometer. Dowel pins ensured the concentricity of the upper and lower plates. The upper plate also serves as guide for the valve, which slides up and down inside a sleeve.

The valves, as well as the seats, were fabricated such that all the edges remained sharp with no appreciable fillets (checked under a microscope). This is important

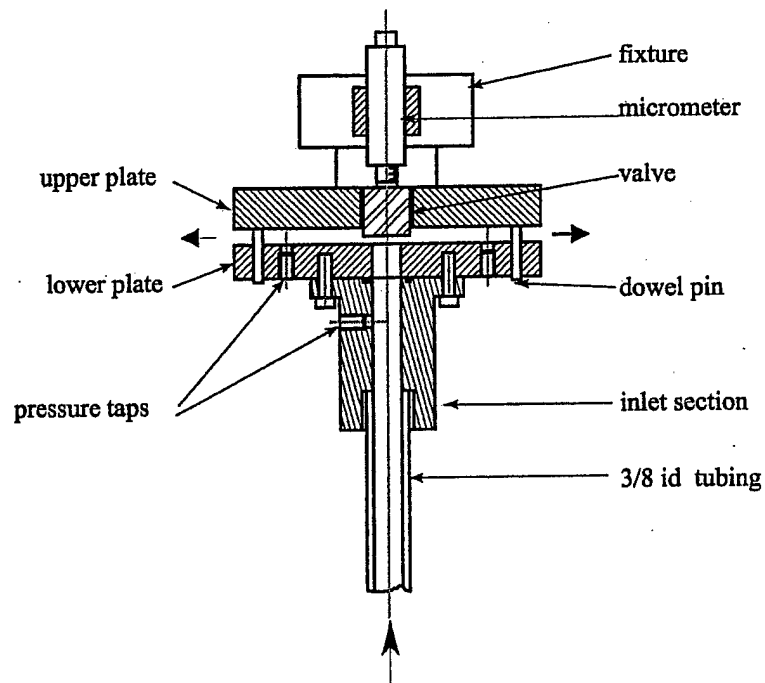


Figure 4-2: Test section detail of the macro scale test facility.

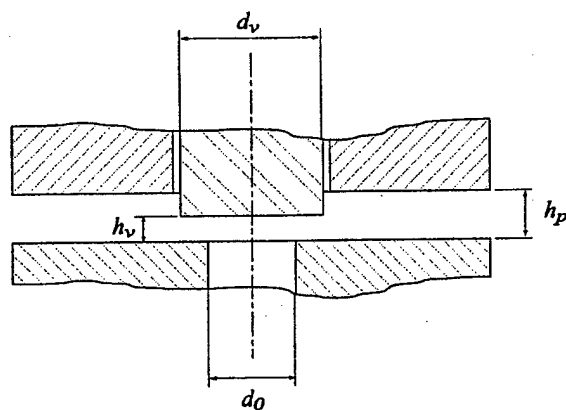


Figure 4-3: Valve geometry detail.

Table 4.1: Valve diameters (d_v) with corresponding seat widths (s) and non-dimensional seat widths (σ)

| | Valve diameter (d_{sys}) | Valve seat width (s) | σ |
|---|------------------------------|--------------------------|----------|
| 1 | 0.383 in (9.72 mm) | 0.004 in (0.10 mm) | 0.01 |
| 2 | 0.437 in (11.10 mm) | 0.031 in (0.78 mm) | 0.08 |
| 3 | 0.562 in (14.24 mm) | 0.093 in (2.36 mm) | 0.25 |

because, as mentioned above, the flow is quite sensitive to rounded edges which would not be present in a MEMS-fabricated fluidic system. Pressure was sensed both upstream and downstream of the valve. Two pressure-sensing ports, 180° apart, were used downstream, to ensure that the flow was symmetric. Pressure sensing both upstream and downstream of the valve was performed using two wet-wet differential pressure transducers. The low-side transducer was a Setra model 230 with a pressure range of 0-2 psid and accuracy of $\pm 0.25\%$ (FS). The high-side sensor was a sensotec model FP2000FDW1VJ with a range from 0-150 psid. The accuracy of this sensor is quoted as 0.1%(FS).

The valve head was positioned using a micrometer (accuracy $\pm 5 \mu\text{m}$) with a special non-rotating head, bonded to the valve. The valve position was measured before and after each measurement with a thickness gauge.

4.2.3 Valve Geometry

The valve geometry employed for the experiments is detailed in Figure 4-3. The inlet diameter (d_0) was 3/8 in (9.525 mm), plate separation (h_p) was set at 450 μm . The valve opening (h_v) was varied from fully-closed to fully-open. Three valve diameters were employed, as shown in Table 4.1. For each of these configurations, the loss coefficient was measured as function of the Reynolds number, valve stroke ($h^* = h_v/h_p$) and seat width (s).

4.2.4 Experimental Procedure

The experimental procedure followed for each experimental run is detailed next. The idea behind such a methodology is to minimize the probability of externally induced variations in the test conditions and to minimize the effect of known disturbances such as bubbles, instrument tare offset and temperature transients.

The setup is energized, and the tare of the flowmeters is reset. The position of the valve is set with the micrometer and checked with the corresponding feeler gauge. The valves are then opened and the pump started. In order to dislodge any existing bubbles the flow rate is stepped up to its maximum value. The readout of the flowmeter is checked with the rotameter to assure the consistency of the flow measurements.

The wet-wet differential pressure sensor is purged via the drain screws and the signal is observed in the oscilloscope. The system runs for 5 minutes before any measurement is taken in order to ensure steady state conditions.

The data acquisition system was a National Instruments board and the software employed was LABVIEW release 5.1. The data was sampled at 2 kHz with an oversampling of 10 points, averaged over 4 periods of 5 seconds each resulting in a total of 10,000 points per reported point. Multiple runs were made cycling from lower to higher flows and viceversa in order to establish if any hysteretic behavior was present.

The data points were converted using the conversions functions provided with each sensor. For each data point the time average and standard deviation were calculated. This information was then saved for further analysis.

4.2.5 Calibration Experiments

In order to ascertain if the test setup and data acquisition systems were properly installed a test experiment was performed. The test experiment was a simple orifice experiment. The test section in this case was substituted by that shown in figure 4-4. This orifice test setup is made of Aluminum and is comprised of 3 parts the upstream section, the orifice plate and the downstream section. The pipe diameter (D) is

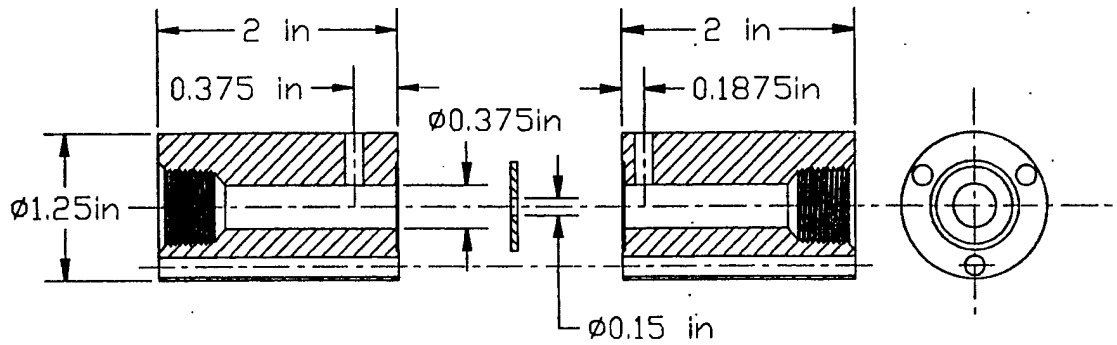


Figure 4-4: Test orifice for calibration

$D = 3/8$ in. The orifice diameter (d) is $d = 0.15$ in and the plate is $t = 1/16$ in thick. The upstream pressure tap is located $1D$ diameters from the orifice plate and the downstream pressure tap is located $1/2 D$ diameters from the orifice plate.

The results of the experiment are shown in Figure 4-5 where the x-axis shows the Reynolds number based on pipe diameter (D) and the y-axis is the orifice discharge coefficient. The orifice discharge coefficient C_d is defined by :

$$C_d = \frac{Q}{A_o} \sqrt{\left(\frac{\rho(1 - \beta^4)}{2\Delta P} \right)} \quad (4.7)$$

where Q is the flow rate, A_o is the orifice area, β is the orifice to pipe diameter ratio, ρ is the fluid density and ΔP is the static pressure drop across the orifice. The orifice tested is classified as a thick orifice ($t^* = 0.425$) as opposed to thin orifices which have a $t^* \leq 0.02$. For thick orifices the separation bubble created at the orifice leading edge tends to reattach to the orifice walls thus reducing the head loss.

Figure 4-5 shows that the experimental values obtained are approximately 3% higher than those expected for small orifices with reattached flow from published data by Lichtarowicz[16].

As it can be appreciated the data shown is nearly independent of the Reynolds number consistent with the known behavior of orifices for turbulent flow. Another important factor to be noted for this test experiment is that the data shows good

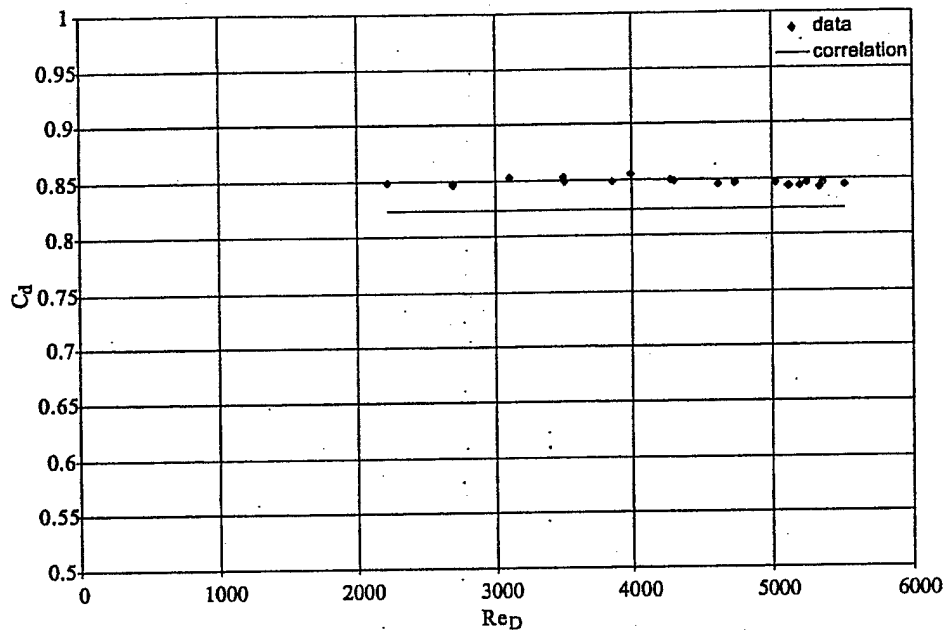


Figure 4-5: Test orifice discharge coefficient vs Reynolds number.

repeatability.

4.3 Summary

In this chapter the scaling issues associated with a macro-scale experiment have been discussed. The relevant non-dimensional numbers were defined and scaling powers derived. Practical considerations of scaling up a system were addressed and finally a scaling factor of ten was chosen for the macro-scale facility.

The second part of the chapter focused on the experimental setup of the macro-scale facility. The general architecture of the system was described, and the sensing capabilities of the system were discussed. Finally calibration data is presented and compared to published results.

Chapter 5

Experimental Results and Correlations

In this chapter the experimental results for the three valves described previously are reported. The characteristics and sensitivities to various parameters are reported and finally the modified valve model is presented.

5.1 Experimental Results

The flow is characterized by a discharge coefficient (C_q) which is a function of the volumetric flow rate (Q), the inlet diameter (d_0), the fluid density (ρ), and the static pressure difference (ΔP) as shown by:

$$C_q = \frac{4Q}{\pi d_0 h_p} \sqrt{\frac{\rho}{2\Delta P}} \quad (5.1)$$

This represents the measured flow rate, normalized by the ideal flow rate based on the applied pressure drop and an equivalent area. The Reynolds number is a function of the volumetric flow rate (Q), the kinematic viscosity (ν) and the valve opening (h_v) and is defined as:

$$Re^* = \sqrt{\frac{Q}{\nu h_v}} \quad (5.2)$$

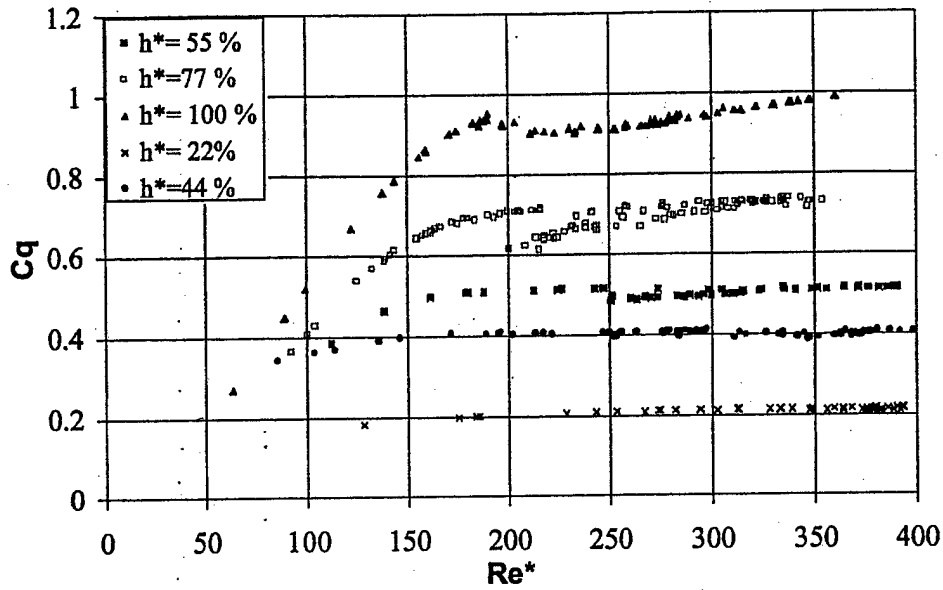


Figure 5-1: Discharge Coefficient vs. Reynolds number for different percentages of valve opening (h^*) for valve 1. The plate separation (h_p) was $450 \mu\text{m}$

This scaling is chosen so that, in the laminar flow regime where the flow rate is proportional to the pressure drop, the discharge coefficient is proportional to the Reynolds number. In Figure 5-1 the discharge coefficient C_q is plotted versus the Reynolds number Re^* for different percentages of valve opening (h^*). It is observed that in the turbulent regime, as expected, the discharge coefficient (C_q) becomes a weak function of the Reynolds number and therefore remains almost constant.

In the laminar regime the pressure drop (ΔP) becomes proportional to the flow rate ($\Delta P \propto Q$). The discharge coefficient is then directly proportional to the square root of the flow rate and linearly proportional to the Reynolds number, as defined above. It should be pointed out that closer analysis of the data presented in Figure 5-1 indicates that only the curves for 77% and 100% aperture achieved laminar flow. The remaining curves show a transition regime behavior with $\Delta P \propto Q^{1.6-1.8}$ depending on the case. Drawing an analogy to pipe flow this is reminiscent of classical low-Reynolds number turbulent behavior as described by Blasius[34]. The qualitative change in the transition point from laminar to turbulent as the percentage of valve opening (h^*)

changes can be explained if we consider that we have two competing flows. The first one is the parallel plate axisymmetric radially divergent flow that undergoes a continuous deceleration. This flow shows a transition at Reynolds numbers $Re_0 \approx 2000$, as shown by Moller[18]. The second flow is an orifice-type flow, which remains turbulent at much lower Reynolds numbers. This explains the fact that as the valve closes the orifice-type effect becomes dominant and turbulent flow continues, even for $Re_0 < 2000$.

It should also be pointed out that, in some cases, hysteresis was observed as measurements were taken cycling from lower to higher flow rates (Q) and viceversa. Hysteresis is clearly visible for the 77% (h^*) curve, and is consistent with observations of Schrenk[29].

Inspection of figures A-2, A-1 and 5-1 shows that the transition Reynolds number varies with valve opening (h_v) and seat width (s). Observation of the Reynolds number behavior for the different valves suggests that for a given valve the transition Reynolds number is nearly a linear function of the valve opening ratio (h^*) as seen in Figure 5-2. Observing that the slopes are similar, a unified formula for the transition Reynolds number is proposed. The transition Reynolds number is described as a function of the valve opening ratio (h^*) and the valve diameter (d^*) ratio. Having an expression that predicts the transition Reynolds number for different valves and openings we can define a modified Reynolds number (Re_m) such that all curves will experience transition at the same point. The curve is empirical in nature and no attempt is made to relate it to physical variables. The modified Reynolds number (Re_m) is defined as

$$Re_m = Re_0 - h^* \left(\frac{1 - 0.692d^*}{2.483e^{-3} - 2.818e^{-3}d^*} \right) + \left(\frac{2942 - 2205d^*}{1 - 1.88d^*} \right) \quad (5.3)$$

where Re_0 is the Reynolds number based on the valve inlet diameter (d_0), h^* is the valve opening ratio and d^* is the valve diameter ratio. The results of the scaling can be seen in Figure 5-3.

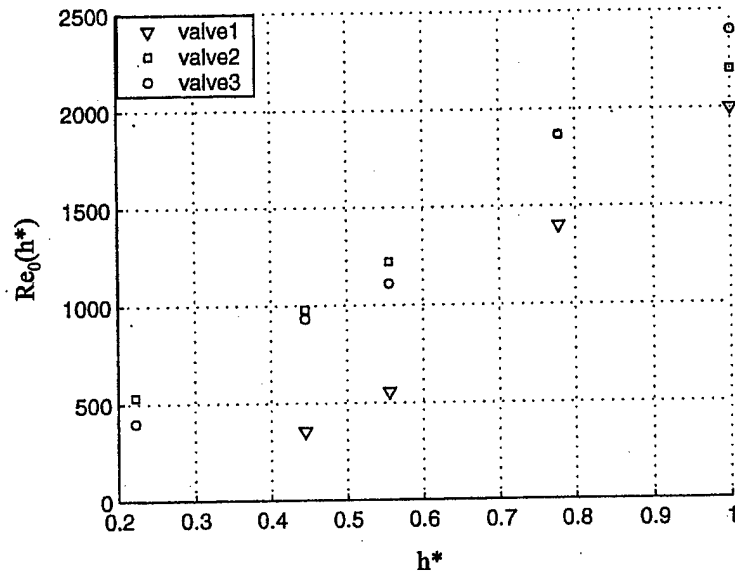


Figure 5-2: Transition Reynolds number vs valve opening ratio, h^*

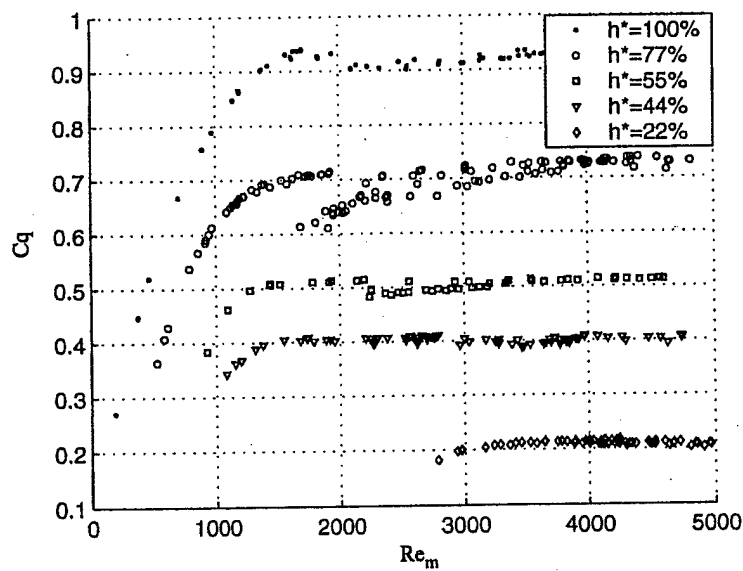


Figure 5-3: Discharge coefficient (C_q) for valve #1 vs modified Reynolds number (Re_m)

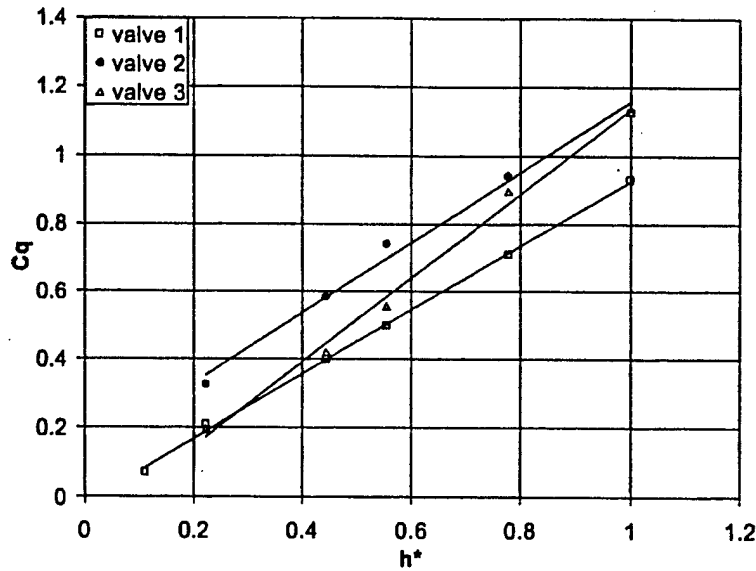


Figure 5-4: Discharge coefficient (C_q) vs. non-dimensional valve opening (h^*) for the three valves; plate separation (h_p) $450\ \mu\text{m}$.

5.1.1 Valve Opening Dependence

The pressure drop vs. valve opening relationship for turbulent flow was explored further and the results are shown in Figure 5-4, where the discharge coefficient, C_q , is plotted versus the percentage of valve opening (h^*) for the three different valves. The discharge coefficient, C_q , is observed to vary linearly with the valve opening, and to be more-or-less independent of the valve geometry, and shows that, based on the definition of C_q in equation 5.1, the static pressure difference is proportional to the square of the non-dimensional valve opening (h^*). This result emphasizes the importance of maximizing the stroke for these valves in system designs.

Knowing the dependence of the discharge coefficient (C_q) to the non-dimensional valve opening (h^*) allows us to define a modified discharge coefficient (C_m) such that all the curves can be collapsed onto one band for the turbulent flow regime. This modified discharge coefficient is based on the valve opening (h_v) raised to some power m , and on the inlet diameter (d_0) having the form:

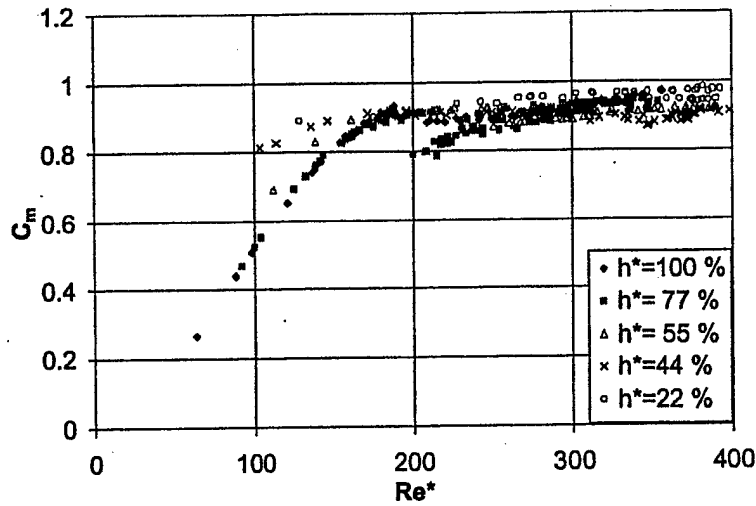


Figure 5-5: Modified discharge coefficient (C_m) vs. Reynolds number for valve #1 and plate separation $h_p = 450\mu\text{m}$

$$C_m = \frac{Q}{\pi d_0 h_p^m} \sqrt{\frac{\rho}{2\Delta P}}. \quad (5.4)$$

The advantage of doing this is that a valve may be modeled rather accurately using a single corrected discharge coefficient formula. Such a scaling can be seen in Figure 5-5 where, for valve #1, the scaling power (m) had a value of one. Here, we see that, for all valve openings, the modified discharge coefficient (C_m) lies between 0.88 – 0.93. It should be noticed that as transition effects start to become important this approximation fails and should therefore be employed with caution. This behavior also supports the analogy between poppet disc valves and orifices. The same behavior was also observed in the other valves, although the proper scaling coefficient varied slightly. A numerical curve fit indicated that, for valves #2 and #3, a value of $m = 0.8$ provided a better collapse of the data in the high-flow regime. The change in the value of m is a consequence of flow reattachment to the valve seat as the valve opening to seat width ratio becomes smaller. This effect is addressed in detail in the following subsection.

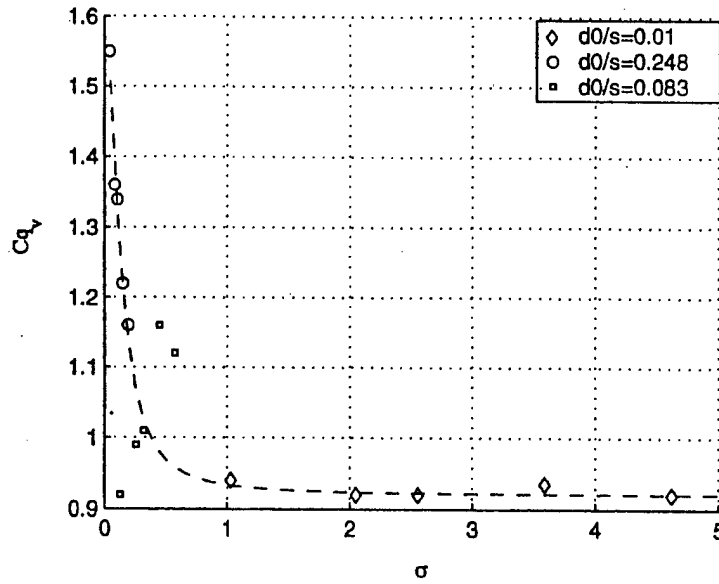


Figure 5-6: Discharge coefficient vs. non-dimensional seat width (σ). The plate separation was $h_p=450 \mu\text{m}$.

5.1.2 Valve Seat Width Dependence

The effect of the valve seat width was investigated with three valves of different seat widths (s). The results are shown in Figure 5-6 where the x -axis shows the ratio of valve opening (h_v) to seat width (s), defined as (σ). The y -axis uses the modified discharge coefficient (C_m) with a scaling power $m=1$. One interesting result is that for values of $\sigma > 1$ the modified discharge coefficient is not affected by the seat width, s . Once this threshold is passed, however, the discharge coefficient becomes very sensitive to the seat width and rises rapidly. Significant pressure recovery is observed, even surpassing $C_m=1$. This increase in discharge coefficient may be explained by drawing an analogy to thick orifices. For a thick orifice, the separation bubble tends to reattach within the throat area as shown by Sahin et al.[28]. The reattachment reduces the flow losses across the orifice. For the case where the non-dimensional seat width $\sigma < 1$ the same phenomenon is observed and we theorize that the separated flow undergoes reattachment with the accompanying pressure recovery.

The results shown in Figure 5-6 are consistent with those obtained by Johnston *et*

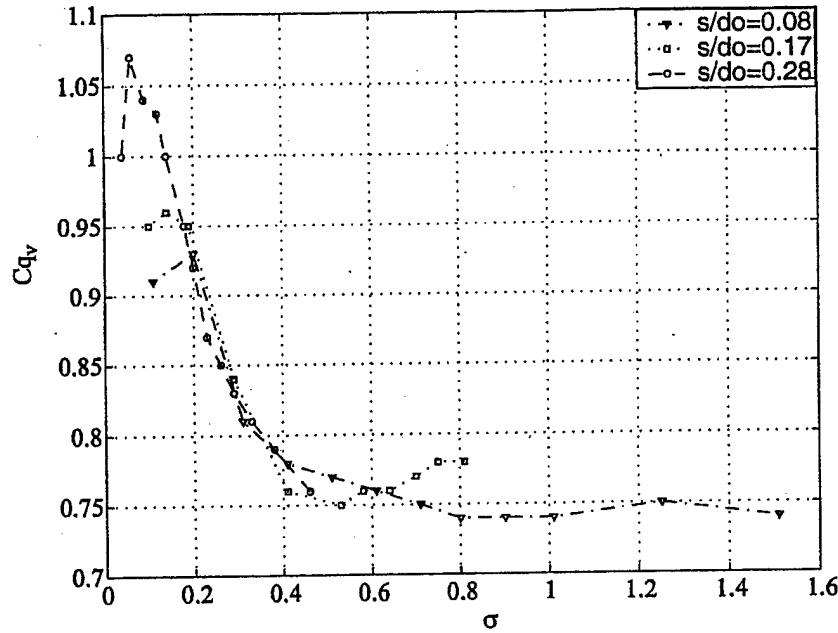


Figure 5-7: Seat width effect on discharge coefficient from Johnston *et al* [14]

al[14], shown in Figure 5-7, and Lichtarowicz[15]. The main difference seen, though, is that Johnston observed a minimum C_m of 0.75 where we observed a higher value of approximately 0.9. The reason for this difference is attributed to geometrical differences in the valve test setup. However it is recognized that although the trends are similar to those of other researchers more experiments are required to fully characterize this behavior. A curve fit for the discharge coefficient (C_m) as a function of σ , the valve opening over seat width ratio, is given by

$$C_m = \left\{ 0.9203 + \frac{0.6755}{1 + \left(\frac{\sigma}{0.1327} \right)^{1.9361}} \right\} (h^*)^{-b}. \quad (5.5)$$

where b is given by

$$b = \frac{\frac{0.1}{1 + \exp\left(\frac{Rem - 2050}{200}\right)}}{1 + 10^{\left(\frac{\ln(s/0.25)}{0.5}\right)}} \quad (5.6)$$

which is a function of the valve seat width (s) and the modified Reynolds number. The value of b oscillates from 0 to 0.1 depending on flow conditions. The valve opening

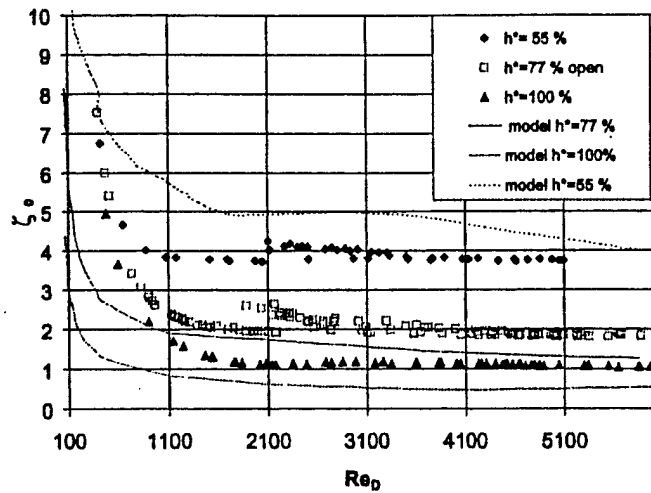


Figure 5-8: Loss coefficient vs. Reynolds number comparison between experimental results and the lumped model for various valve opening percentages (h^*).

dependence changes slightly as the Reynolds number decreases reaching the transition zone changing the exponent b from 0 to 0.1. The effect is related to the Reynolds number dependence of the reattachment point as pointed out by Nakabayashi and Ichikawa[20].

One important factor to mention is the behavior observed with valve #2, this valve shows a flow reattachment similar as that shown by valve #3. The behavior of valve # 2, however reaches a maximum and then a sharp decrease of the discharge coefficient is observed. In this case it is hypothesized that surface friction forces become important diminishing the effect of the pressure recovery product of the flow reattachment as pointed out by Lichtarowicz[15]. More experiments are required in the future to map and understand this behavior and available data from other researchers shows considerable scatter making more difficult the task of identifying the point where the maximum is reached.

5.1.3 Comparison of Lumped Model to Data

A comparison of the original lumped model and the data for valve #1 is presented in Figure 5-8, where the x -axis is the Reynolds number based on the inlet flow area (A_1), as defined by:

$$Re_0 = \left(\frac{4Q}{\pi d_0 \nu} \right) \quad (5.7)$$

and the y -axis is a loss coefficient ζ_0 defined by:

$$\zeta_0 = \frac{\Delta P_0}{\frac{1}{2} \rho \left(\frac{Q}{\pi d_0 h_v} \right)^2} \quad (5.8)$$

where ΔP_0 is the total pressure drop, ρ is the fluid density, Q is the volumetric flow rate, d_0 is the inlet diameter and h_v is the valve opening. It is observed that the original order-of-magnitude flow model captures correctly the flow physics of the valve although the numerical values are off by a factor of 2 with respect to experimental values. In addition, the original model does not accurately capture the transition point.

5.2 Modified model

It may be argued that the valve flow cycles from a dominant axisymmetric radially divergent parallel plate flow to an orifice flow depending as a function of the valve opening. In order to establish a more accurate prediction for the start of transition regime a closer look at the flows is important.

5.2.1 Detailed orifice model background

The thin sharp edged orifice flows have been studied in detail by many researchers. The turbulent behavior of orifices is heavily documented and because of its use as flowmeter, standard empirical correlations exist. Transition in this flows is observed for Reynolds numbers (based in the orifice diameter) in the range of 3000 – 4500 as

reported by Reader-Harris[25]. Reader-Harris and coworkers presented a new correlation for the enlarged EEC/API database. The database includes data for orifices from 50 and 600 mm pipes. The improved orifice discharge (C_d) equation[25] is given by:

$$\begin{aligned}
C_d = & 0.5934 + .0232\beta^{1.3} - 0.2010\beta^8 + .000515 \left(\frac{1e^6\beta}{Re_D} \right)^{0.7} \\
& + (0.0187 + 0.04A_r)\beta^{3.5} \max \left\{ \left(\frac{1e^6}{Re_D} \right)^{0.3}, 23.1 - 4800 \frac{Re_D}{1e^6} \right\} \\
& + (0.043 + (0.090 - A_r) \exp^{-10l_1} - (0.133 - A_r) \exp^{(-7l_1)})(1 - A_r) \left(\frac{\beta^4}{1 - \beta^4} \right) \\
& - 0.031(M_2 - 0.8M_2^{1.1}) \left[1 + 8 \max \left\{ \log \left(\frac{3700}{Re_D} \right), 0.0 \right\} \right] \beta^{1.3} \\
& + 0.0015 \max \left(\frac{0.05}{\beta D} - 1, 0 \right)
\end{aligned} \tag{5.9}$$

where

$$M_2 = \frac{2l_2}{1 - \beta} \tag{5.10}$$

and

$$A_r = \left(\frac{2100\beta}{Re_D} \right)^{0.9} \tag{5.11}$$

The orifice discharge coefficient (C_d) is seen to be a function of the orifice to pipe diameter ratio (β), the Reynolds number (Re_D) based on the pipe diameter (D), the distance between the upstream pressure tap to pipe diameter ratio (l_1) and the distance between the downstream pressure tap to pipe diameter ratio (l_2).

The discharge coefficient for orifices at lower Reynolds numbers ($Re_d < 1000$) is not as well known. Results by Mills[34] and Sahin[28] suggest that for Reynolds numbers up to $Re_d \approx 25$ the orifice discharge coefficient for laminar flow[34] is given by:

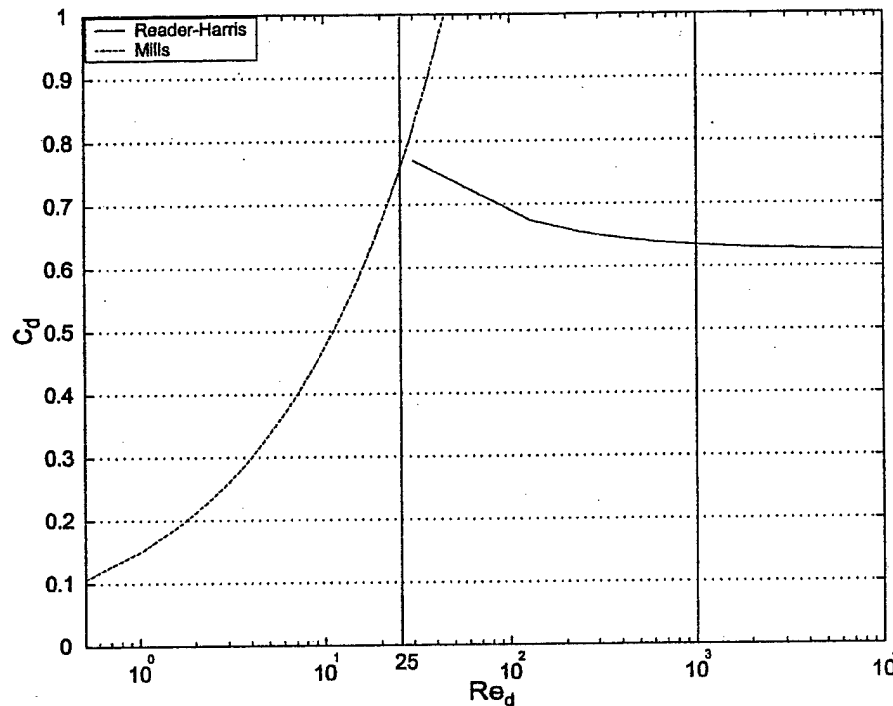


Figure 5-9: Sharp edged orifice discharge coefficient vs Reynolds number

$$C_d = 0.15\sqrt{Re}. \quad (5.12)$$

Combining the known turbulent behavior described by equation 5.9 and the laminar flow behavior of equation 5.12 a map for the behavior of the behavior of a simple thin sharp edged orifice is shown in figure 5-9. The transition region ranges from $Re \approx 25$ to $Re \approx 4500$.

For Reynolds less than 10^4 , the discharge coefficient has to be corrected for Reynolds dependency and surface conditions, and these correlations are less common and less reliable than those for fully rough turbulent regime.

In the case of long orifices results by Lichtarowicz[16] showed that the discharge coefficients are significantly higher than those predicted for thin sharp edged orifices. In particular for non-cavitating long orifices for $1 \leq Re \leq 10000$ he proposes a curve fit

based on a modified Reynolds numbers (Re_h):

$$Re_h = \left(\frac{2\Delta P}{\rho} \right)^{0.5} \frac{d}{\nu} \quad (5.13)$$

which is based on the pressure drop across the orifice (ΔP), the fluid density (ρ), the orifice diameter (d) and the kinematic viscosity (ν). Lichtarowicz[16] curve fit for the orifice discharge coefficient is given by:

$$\frac{1}{C_d} = \frac{1}{C_\infty} + \frac{20}{Re_h} \left(1 + 2.25 \frac{l}{d} \right) - \frac{0.005 \frac{l}{d}}{1 + 7.5(\ln(0.00015 Re_h))^2} \quad (5.14)$$

where C_∞ is the discharge coefficient for $Re_h > 10000$, l is the thickness of the orifice, and (d) is the orifice diameter. The curve fit is very good and describes accurately the results obtained by various researchers for Reynolds numbers between 1 and 10000. Beyond this value the discharge coefficient becomes independent of the Reynolds number (or nearly so) and is described by the equation[16]:

$$C_\infty = 0.827 - 0.0085 \frac{l}{d} \quad (5.15)$$

becoming only a function of length (l) to orifice diameter (d) ratio. The higher discharge coefficients are attributed to flow reattachment and the subsequent pressure recovery that this brings. For $l/d = 0.5$ Lichtarowicz found that the orifice discharge coefficient rose rapidly, reaching a peak at about $Re_h \approx 700$ and then falling rapidly to the ultimate discharge coefficient (C_∞). For longer orifices, the sharp change smoothes out and the irregularity almost disappears.

5.2.2 Modified valve model

The similarity between the orifice results of Lichtarowicz (see Figure 5-10 and 5-11) and the present investigation valve results (Figure 5-1) is striking. It is interesting to note how the shape of the curve varies as the length to diameter ratio of the orifice varies. Analogously the valve curve profile varies in the same manner as the opening changes. Qualitatively, as was originally hypothesized, the valve can be seen to behave

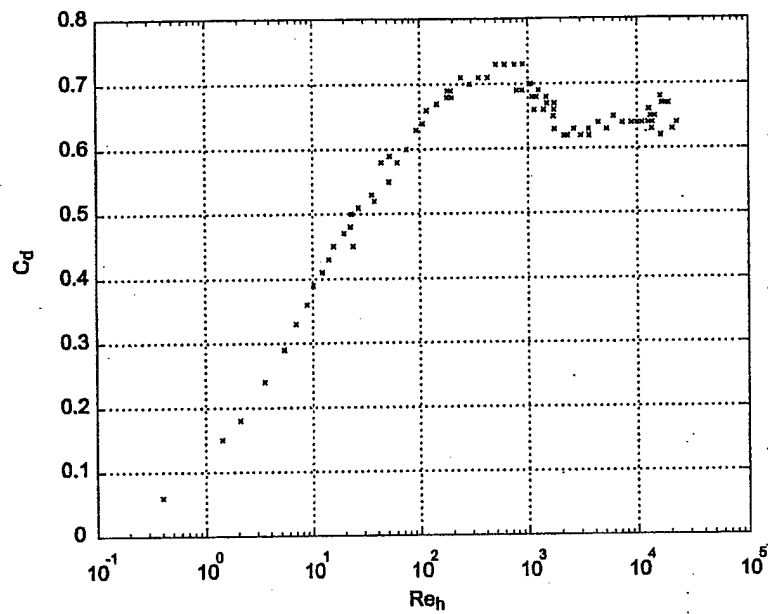


Figure 5-10: Long orifice $t/d=0.5$ from Lichtarowicz [16]

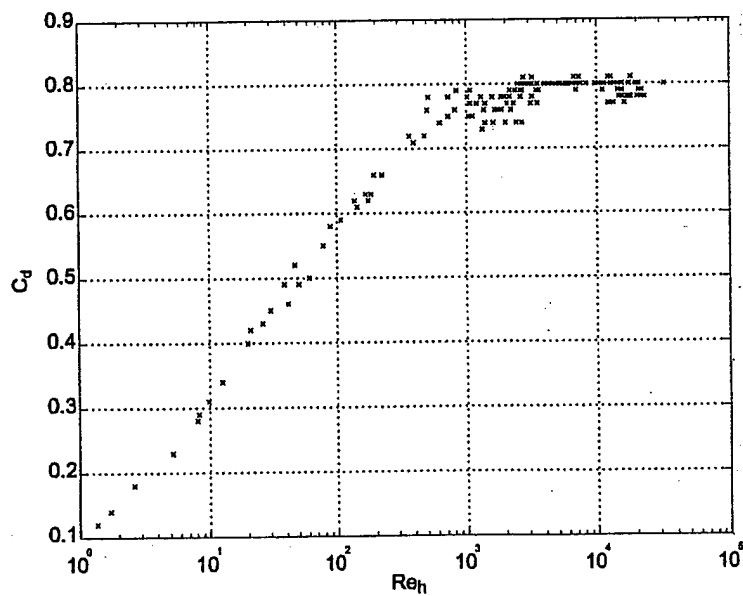


Figure 5-11: Long orifice $t/d=0.5$ from Lichtarowicz [16]

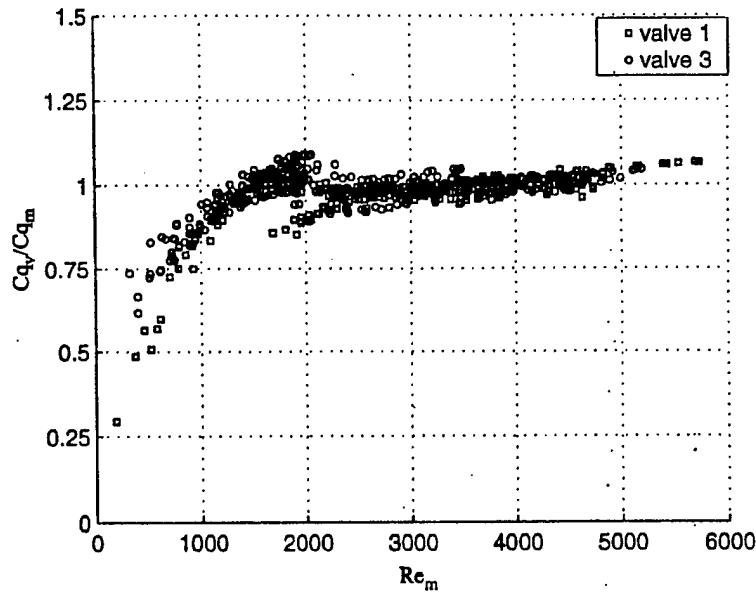


Figure 5-12: Scaled data for valve #1 and valve #3

just as a long orifice but the analogy may be extended to the laminar regime.

Considering the resemblance between the orifice and valve model it is tempting to attempt to correlate the current valve data with an equation similar to Lichtarowics equation 5.14. Using a curve fitting program (DATAFIT by Oakdale Engineering) it is seen that the curves of individual experiments correlate well. In the interest to obtain only one curve for all experiments the current data is scaled using equations 5.3, 5.5 and 5.6. Using this scaling functions the transformed data collapses into one curve as seen in Figure 5-12

The curve shown in Figure 5-12 can be approximated by using equation 5.14 as suggested by Lichtarowicz. The curve however requires different coefficients which were obtained using the curve fitting program DATAFIT. The equation is then given by :

$$\frac{1}{Cq} = 0.956 + \frac{364.89}{Re_m} - \frac{0.194}{1 + 2.608(\ln(0.000718Re_m))^2} \quad (5.16)$$

The results for valve #1 can be seen in Figure 5-13. The corresponding plots for valves #2 and #3 and a summary of the equations can be found in Appendix A.

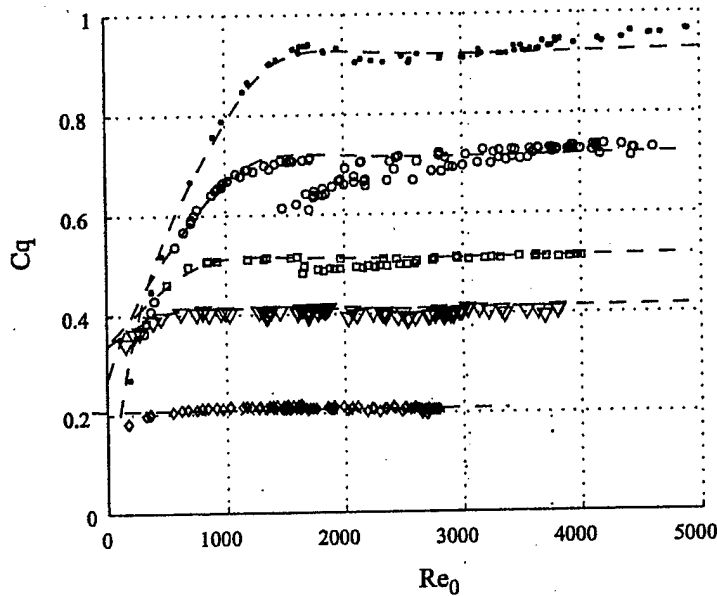


Figure 5-13: Curve fitting using 5.14 for valve #1

5.3 Summary

In this chapter the steady state experimental results for three valves of different diameters have been presented. Parametric studies were done for the Reynolds number dependency, valve aperture dependence, and seat width dependence. The results were compared to those the original order of magnitude valve model and found a factor of 2 difference. More detailed analysis revealed that the valve behavior approximated that of a long orifice even in the transition and laminar regimes. For comparison curve fits using an empirical formula for orifices was employed with good results further confirming the analogy in this low turbulence regimes. Finally a generalized coefficient formula as function of valve opening and valve diameter was obtained.

Chapter 6

Conclusions and Recommendations

From the outset of this research, the goal has been to generate a model that describes accurately the hydraulic behavior of microsystems. A low-order lumped model was constructed and integrated to a full system simulation. The need to obtain a better representation of microvalve behavior led to experiments to characterize their behavior.

The flow characteristics of a poppet type disc valves with geometries defined by standard microfabrication techniques have been studied employing a 10:1 scale experimental facility. The experiments have shown that the commonly used orifice analogy is a good approximation in the turbulent regime. Transition effects, however are not properly captured by such model. This is attributed to the competing nature of the axisymmetric divergent flow between two parallel plates and the small orifice flow for different valve openings.

The sensitivity to valve stroke has been characterized for the turbulent regime and it was shown that ΔP becomes proportional to the square of the valve opening to plate separation ratio (h^*).

The valve seat width effect has been investigated showing that for the turbulent regime the modified discharge coefficient, C_m , is independent of the valve opening to seat width ratio, σ . It has also been seen that for s less than one, the modified discharge coefficient rises significantly, presumably due to reattachment.

What is particularly encouraging, however, is that the simple model does capture

both the character and (with a factor of about two), the numerical values of the loss-coefficients. This is extremely valuable for the complex design in which many trade-offs need to be balanced to ensure a functional, robust and efficient micro-hydraulic transducer.

A more detailed analysis of the data showed that qualitatively the flow behavior is strikingly similar to that of long orifice for the transition and laminar regimes. The present results were fitted to empirical orifice correlations for Reynolds numbers $Re_h \leq 10000$. The resulting model is comprised of two scaling formulas : a modified Reynolds number formula and a discharge coefficient formula (as function of the valve opening to seatwidth ratio). These two formulas allow the re-scaling of the curves into one similarity curve. This curve may in turn be fitted to an orifice empirical orifice formula as in Lichtarowicz[16].

More experiments will be pursued in the near future, including unsteady measurements and measurements in the full-scale (micro) device. A second step in the systematic study of the valve will be unsteady measurements to obtain a better understanding of the unsteady behavior at high frequencies valves. Finally the experiments will be taken to the full-scale prototype microvalves. In this experiments comparisons between the results obtained with the macro-scale valve will be evaluated for the steady and unsteady state.

Appendix A

Valve Plots and Summary of Model Equations

The model used for predicting the flow losses is comprised of three main formulas: a Reynolds number scaling, a discharge coefficient scaling and the equation that relates the scaled Reynolds number to the scaled discharge coefficient.

$$Re_m = Re_0 - \frac{1}{h^*} \left(\frac{1 - 0.692d^*}{2.483e - 3 - 2.818e - 3d^*} \right) + \frac{2942 - 2205d^*}{1 - 1.88d^*} \quad (A.1)$$

$$b = \frac{0.1}{1 + \exp\left(\frac{Re_m - 2050}{200}\right)} \left\{ \frac{1}{1 + 10^{\left(\frac{\ln(\sigma) - \ln(0.25)}{0.5}\right)}} \right\} \quad (A.2)$$

$$C_f = \left[0.9203 + \frac{0.6755}{1 + \left(\frac{\sigma}{0.1327}\right)^{1.9361}} \right] (h^*)^{-b} \quad (A.3)$$

$$\frac{1}{C} = \frac{C_f}{C_m} = 0.956 + \frac{364.89}{Re_m} - \frac{0.194}{1 + 2.608(\ln(0.000718Re_m))^2} \quad (A.4)$$

$$C_m = \frac{Q}{\pi h_v d_0} \sqrt{\frac{\rho}{2\Delta P}} \quad (A.5)$$

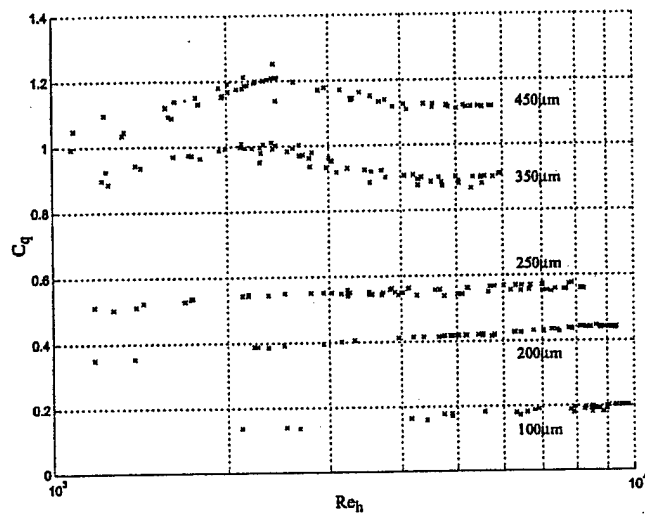


Figure A-1: Reynolds number vs Discharge coefficient for valve 2 ($d_v = 11.10$ mm)

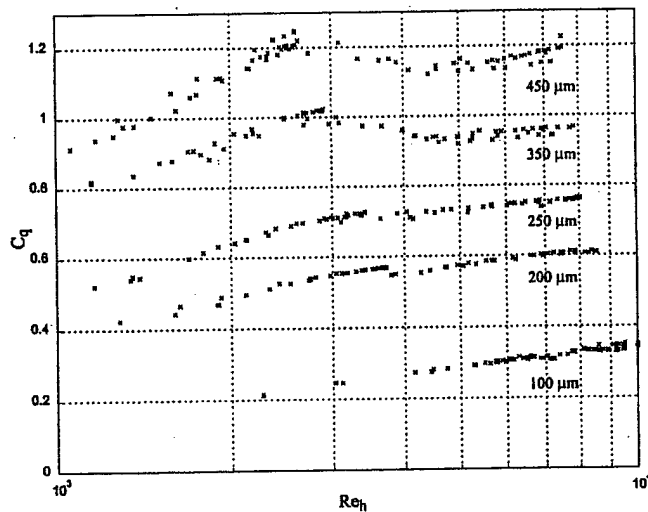


Figure A-2: Reynolds number vs Discharge coefficient for valve 3 ($d_v = 14.24$ mm)

Bibliography

- [1] A. Ayon, K.-S. Chen, K. A. Lohner, S. M. Spearing, H.H Sawin, and M. A. Schmidt. Deep reactive ion etching of silicon. *Proceedings of the 1998 MRS Fall Meeting - Symposium AA, Materials Science of Microelectromechanical Systems (MEMS)*. Boston, MA, USA, 1998.
- [2] T. Bourouina and J. P. Grandchamp. Modeling micropumps with electrical equivalent networks. *Journal of Micromechanics and Microengineering*, pages 398-404, 1996.
- [3] S. C. Burgess, D. F. Moore, D. E. Newland, and H. L. Klaubert. A study of mechanical configuration optimization in micro-systems. *Research in Engineering Design*, 9:46-60, 1997.
- [4] F. K. Forster, R. L. Bardell, M. A. Afromowitz, N. R. Sharma, and A. Blanchard. Design, fabrication and testing of fixed-valve micro-pumps. *Proceedings of the ASME Fluids Engineering Division, ASME*, 234:39-44, 1995.
- [5] P. Gravesen, J. Branebjerg, and O. Sondegard. Microfluidics - a review. *Journal of Micromechanics & Microengineering*, 3:168-182, 1993.
- [6] N. W. Hagood, D. C. Roberts, L. Saggere, K. S. Breuer, K.-S Chen, J. A. Carretero, H. Q. Li, R. Mlcak, S. Pulitzer, M. A. Schmidt, S. M. Spearing, and Y.-H. Su. Micro hydraulic transducer technology for actuation and power generation. *Smart Structures and Materials 2000: Smart Structures and Integrated Systems*, Newport Beach, CA, 3985, March 2000.
- [7] A. K. Henning. Microfluidic mems. *IEEE Aerospace Applications Conference Proceedings, Los Alamitos, CA*, 1:471-486, 1998. This is a full ARTICLE entry.
- [8] A. K. Henning, J. S. Fitch, J. M. Harris, E. B. Dehan, B. A. Cozad, L. Christel, Y. Fathi, Jr. D. A Hopkins, L. J. Lilly, w. McCulley, W. A. Weber, and M. Zdeblick. Microfluidic mems for semiconductor processing. *IEEE Transactions on Components Packaging & Manufacturing Technology Part B-Advanced Packaging*., 21(4):329-337, November 1998.
- [9] M. Hirano, K. Yanagisawa, H. Kuwano, and S. Nakano. Microvalve with ultra-low leakage. *Proceedings of the IEEE Micro Electro Mechanical Systems (MEMS) 1997. IEEE, Piscataway, NJ*, pages 323-326, 1997.

- [10] C.-M. Ho and Y.-C. Tai. Micro-electro-mechanical-systems (mems) and fluid flows. *Annual Review of Fluid Mechanics*, 30:579–612, 1998.
- [11] I. E. Idelchik. *Handbook of Hydraulic Resistance*. CRC Press, Boca Raton, FL, 1994.
- [12] Y. Ikebe and H. Ohuchi. Generalized formulation of momentum theory. *Fluidics Quarterly*, 10(4):27–46, 1978.
- [13] H. Jerman. Electrically-activated, normally-closed diaphragm valves. *Journal of Micromechanics & Microengineering*, 4(4):210–216, December 1994.
- [14] D. N. Johnston, K. A. Edge, and N. D. Vaughan. Experimental investigation of flow and force characteristics of hydraulic poppet and disc valves. *Proceedings of the Institution of Mechanical Engineers, Part A: Power & Process Engineering*, 205(3):161–171, 1991.
- [15] A. Lichtarowicz. Flow and force characteristics of flapper valves. *Third International Symposium on Fluid Power Turin*, pages B1–1, 1973.
- [16] A. Lichtarowicz, R. K. Duggins, and E. Markland. Discharge coefficients for incompressible non-cavitating flow through long orifices. *Journal of Mechanical Engineering Science*, 7(2):210–219, 1965.
- [17] R. Von Mises. The calculation of flow coefficient for nozzle and orifice. *VDA*, 61:21–23, 1917.
- [18] P. S. Moller. Radial flow without swirl between parallel discs. *Aeronautical Quarterly*, 14:163–185, 1962.
- [19] C. J. Morris and Fred K. Forster. The design-fix for fixed-valve micropumps. *Late News Poster Session, Solid-State Sensor and Actuator Workshop. Hilton Head Is. SC*, pages 11–12, June 2000.
- [20] K. Nakabayashi and T. Ichikawa. Annular separation bubble near the inlet corner and viscous radial flow between two parallel disks. *Nippon Kikai Gakkai Ronbunshu, B Hen.*, 56(525):1267–1273, May 1990.
- [21] T. Nakada and Y. Ikebe. Measurement of the unsteady axial flow force on a spool valve. *Pneumatic and Hydraulic Components and Instruments in Automatic Control, Proceedings of the IFAC Symposium, Warsaw, Pol.*, pages 193–198, 1980.
- [22] A. Olsson, G. Stemme, and E. Stemme. Simulation studies of diffuser and nozzle elements for valve-less micropumps. *Transducers '97 and International Conference on Solid-State Sensors and Actuators and Chicago*, pages 1039–1042, June 1997.

- [23] A. Olsson, G. Stemme, and E. Stemme. A numerical design study of the valveless diffuser pump using a lumped-mass model. *Journal of Micromechanics and Microengineering*, 9:34–44, 1999.
- [24] K. Ramamurthi and K. Nandakumar. Characteristics of flow through small sharp-edged cylindrical orifices. *Flow measurement and Instrumentation*, 10:133–143, 1999.
- [25] M. J. Reader-Harris, J. A. Sattary, and E. P. Spearman. The orifice plate discharge coefficient equation- further work. *Flow Measurement and Instrumentation*, 6(2):101–114, 1995.
- [26] M. Richter, P. Woias, and D. Weib. Microchannels for applications in liquid dosing and flow rate measurement. *Sensors and Actuators A*, 62:480–483, 1997.
- [27] D. C. Roberts, N. W. Hagood, Y. H. Su, H. Q. Li, and J. A. J. A. Carretero. Design of a piezoelectrically-driven hydraulic amplification microvalve for high pressure, high frequency applications. *Smart Structures and Materials 2000: Smart Structures and Integrated Systems*, Newport Beach, CA, 3985, March 2000.
- [28] B. Sahin and H. Ceyhan. Numerical and experimental analysis of laminar flow through square-edged orifice with variable thickness. *Transactions of the Institute of Mechanical Engineers*, 18(4):166–174, 1996.
- [29] E. Schrenk. Disc valves, flow patterns, resistance and loading. *BHRA T*, (547), 1957. Translation from German.
- [30] M. Shikida, K. Sato, S. Tanaka, Y. Kawamura, and Y. Fujisaki. Electrostatically driven gas valve with high conductance. *Journal of Microelectromechanical Systems*, 3(2):76–80, June 1994.
- [31] S. Shoji and M. Esashi. Microflow devices and systems. *Journal of Micromechanics & Microengineering*, 4(4):157–171, December 1994.
- [32] J. A. Stone. Discharge coefficients and steady-state flow forces for hydraulic poppet valves. *Transactions ASME, Journal of Basic Engineering*, pages 144–154, 1960.
- [33] N. D. Vaughan, C. Johnston, and K.A. Edge. Numerical simulation of fluid flow in poppet valves. *Proceedings of the Institution of Mechanical Engineers, Part C: Mechanical Engineering Science.*, 206(2):119–127, 1992.
- [34] F. White. *Fluid Mechanics*. McGraw-Hill, Inc., New York, 1994.
- [35] E. B. Wylie, V. L. Streeter, and L. Suo. *Fluid Transients in Systems*. Prentice-Hall Inc., Englewood Cliffs, New Jersey, 1993.
- [36] O. Yaglioglu, Y.-H. Su, J. A. Carretero, D. C. Roberts, and L. Saggere. Mht:energy harvester simulink simulation. in-project design tool, August 2000.

- [37] R. Zengerle and M. Richter. Simulation of microfluid systems. *Journal of Micromechanics and Microengineering*, 4:192-204, 1994.

64

Feasibility Assessment and Design of Micro Hydraulic Solid-State Transducers

by

Seward Webb Pulitzer III

B.S., Mechanical Engineering
Rensselaer Polytechnic Institute, 1996

SUBMITTED TO THE DEPARTMENT OF MECHANICAL ENGINEERING
IN PARTIAL FULFILLMENT OF THE DEGREE OF

MASTER OF SCIENCE IN MECHANICAL ENGINEERING

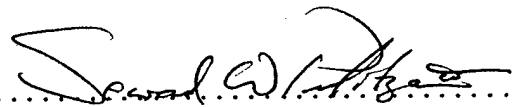
at the

MASSACHUSETTS INSTITUTE OF TECHNOLOGY

June 1998

© 1998 Massachusetts Institute of Technology
All rights reserved

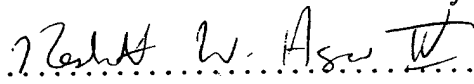
Signature of Author



Department of Mechanical Engineering

May 8, 1998

Certified by

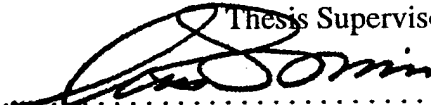


Nesbitt W. Hagood IV

Associate Professor of Aeronautics and Astronautics

Thesis Supervisor

Certified by

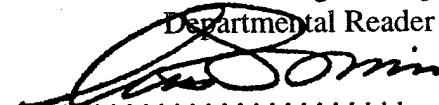


Ain A. Sonin

Professor of Mechanical Engineering

Departmental Reader

Accepted by



Ain A. Sonin

Chairman, Department Committee on Graduate Students

MASSACHUSETTS INSTITUTE
OF TECHNOLOGY

AUG 04 1998

LIBRARIES

Eng

Feasibility Assessment and Design of Micro Hydraulic Solid-State Transducers

by

Seward Webb Pulitzer III

Submitted to the Department of Mechanical Engineering
on May 8, 1998 in Partial Fulfillment of the
Requirements for the Degree of Master of Science in
Mechanical Engineering

ABSTRACT

The performance of a number of mechanical applications could be greatly improved by the introduction of transducers that are capable of exploiting the inherent power densities of piezoelectric materials. The ability of these solid-state materials to exert large forces at high frequencies engenders them with specific power levels (mass normalized) that are often several orders of magnitude greater than conventional transducers, but their utility is offset by their small achievable strains. A novel concept for a device capable of improved solid-state transduction, *Micro Hydraulic Solid-State Transducers* (MHSTs), is introduced and explored in this thesis. The concept is comprised of two core principles: (1) utilization of a hydraulic system consisting of a pump, valves, and a working fluid to rectify the high frequency reciprocations of a piezoelectric drive element into unidirectional motion, and (2) performance enhancement through miniaturization. The goal is a transducer possessing high power densities that is useful in conventional applications.

Feasibility of the MHST concept is evaluated by designing, modeling, and simulating a prototype mechanism. The effects of miniaturization on device performance are investigated and an optimal scale is determined. Concept feasibility is based on predicted system performance, existing issues, and manufacturing constraints. It is concluded that the concept is feasible and warrants further development.

Thesis Supervisor: Nesbitt W. Hagood IV

Title: Associate Professor of Aeronautics and Astronautics

ACKNOWLEDGMENTS

Funding for this research was provided by the Office of Naval Research (ONR), under contract N00014-97-1-0880, and monitored by Wallace Smith.

I could not have accomplished this goal without the help of many people. First and foremost, I wish to thank my family for their love, patience, and encouragement. Their unwavering confidence in my abilities sustained me through those times when I had no confidence in myself. My parents have been overheard asking, half-jokingly, how did a son of ours get to MIT? The answer is in the question.

I am grateful to my "extended family", Johnny and Tee, for their support, hospitality, and the promise of a haven should things get tough.

I would like thank my advisor, Prof. Hagood.

And finally, heartfelt thanks are extended to my comrades in AMSL and SSL who offered, in addition to friendship, their time and assistance. In the midst of exams and pressing deadlines they lent a collective hand to help me over my obstacles, and the successful completion of this thesis is due in no small measure to them. I especially want to thank Brian, Michael, Kamyar, Tim, John H., Alex M., Alex P., Eric, John R., Patrick, and Jeremy. I doubt I will remember the title of my thesis 20 years from now, but I will remember you. I also want to thank John and Margee for watching out for (and feeding) the "new grad students."

TABLE OF CONTENTS

| | |
|--|-----------|
| Abstract | 3 |
| Acknowledgments | 5 |
| Table of Contents | 7 |
| List of Figures | 11 |
| List of Tables | 15 |
| Nomenclature | 17 |
| Chapter 1. Introduction | 21 |
| 1.1 Motivation | 22 |
| 1.2 Objectives | 26 |
| 1.3 Background | 26 |
| 1.4 Approach | 32 |
| 1.4.1 Displacement Rectification Concept | 32 |
| 1.4.2 Actuator Concept | 33 |
| 1.4.3 Power Harvester Concept | 34 |
| 1.4.4 Physical Implementation | 36 |
| 1.4.5 Miniaturization Concept | 42 |
| Chapter 2. Conceptual Design and Manufacturing Issues | 49 |
| 2.1 Introduction | 49 |
| 2.2 Procedure | 51 |
| 2.2.1 Strategy | 51 |
| 2.2.2 Design Drivers | 52 |
| 2.3 Components | 54 |
| 2.3.1 Displacement Amplifier | 54 |
| 2.3.2 Drive Mechanism | 56 |
| 2.3.3 Valves | 57 |
| 2.3.4 Reservoirs and Gas Chamber | 61 |
| 2.3.5 Flow Channels | 62 |
| 2.4 Materials | 63 |

| | |
|---|------------|
| 2.5 Circuitry | 66 |
| 2.6 Manufacturability | 67 |
| 2.7 Summary | 74 |
| Chapter 3. Modeling | 75 |
| 3.1 Introduction | 75 |
| 3.2 Theoretical Model | 76 |
| 3.2.1 Requirements | 76 |
| 3.2.2 Issues | 77 |
| 3.2.3 Assumptions | 81 |
| 3.2.4 Canonical Components | 83 |
| 3.2.5 Prototype System Model | 91 |
| 3.3 Finite Element Analysis | 102 |
| 3.4 Summary | 107 |
| Chapter 4. Optimization and Analysis | 109 |
| 4.1 Introduction | 109 |
| 4.2 Geometry Optimization | 111 |
| 4.2.1 Canonical Hydraulic Coupler | 111 |
| 4.2.2 Prototype | 116 |
| 4.3 System Analysis | 121 |
| 4.3.1 Linear Approximation | 121 |
| 4.3.2 Energy Tracking | 125 |
| 4.4 Summary | 130 |
| Chapter 5. Simulation Results | 133 |
| 5.1 Introduction | 133 |
| 5.2 System Behavior | 134 |
| 5.3 Parameter Studies | 143 |
| 5.4 Final Design | 161 |
| 5.5 Summary | 167 |
| Chapter 6. Conclusions and Recommendations | 169 |
| 6.1 Summary | 169 |
| 6.2 Conclusions | 173 |
| 6.3 Recommendations for Future Work | 175 |

| | |
|--|------------|
| References | 179 |
| Appendix A. Piezoelectric Actuator Dynamics | 185 |
| Appendix B. System Block Diagrams | 189 |
| Appendix C. Simulations | 197 |
| Appendix D. ANSYS Finite Element Code | 215 |

LIST OF FIGURES

| | | |
|------|--|----|
| 1.1 | Upper Bound on Specific Work vs. Frequency for Various Actuation Media . . | 28 |
| 1.2 | Piezoelectric effect | 31 |
| 1.3 | Generalized solid-state hydraulic actuation system | 38 |
| 1.4 | Generalized solid-state hydraulic power harvesting system | 39 |
| 1.5 | Possible system configurations | 40 |
| 1.6 | Prototype microsystem design | 41 |
| 1.7 | System timing | 43 |
| 1.8 | Valve operation | 44 |
| 2.1 | MHST design process | 57 |
| 2.2 | Displacement amplifier | 59 |
| 2.3 | Pump diagram | 61 |
| 2.4 | Valve diagram | 62 |
| 2.5 | Valve cap designs | 64 |
| 2.6 | Pressure balanced valve design | 65 |
| 2.7 | Power harvesting circuit | 71 |
| 2.8 | Mesoscale drive mechanism components | 72 |
| 2.9 | Microfabrication sequence for top SOI wafer | 73 |
| 2.10 | Assembly sequence for device components | 74 |
| 2.11 | SEM micrographs of the DRIE etched prototype drive pistons | 76 |
| 2.12 | MHST layers | 77 |
| 3.1 | 32 microfluidic devices presented in the literature | 82 |
| 3.2 | Canonical volume source and pressure transducer | 88 |
| 3.3 | Canonical pump chamber | 89 |
| 3.4 | Canonical channel | 90 |
| 3.5 | Effects of scale on fluid phenomena | 92 |
| 3.6 | Canonical valve | 94 |
| 3.7 | Spring force function | 95 |
| 3.8 | Drive piston assembly | 96 |

| | | |
|------|---|-----|
| 3.9 | Lumped pressure zones | 99 |
| 3.10 | Detail of valve geometry and flow velocity distribution | 99 |
| 3.11 | Integrated system model | 106 |
| 3.12 | Finite element model of valve (axisymmetric) | 108 |
| 3.13 | Substructures used for stress analysis. Key nodes are highlighted. | 109 |
| 4.1 | Canonical hydraulic coupler | 115 |
| 4.2 | Mechanical efficiency versus the coupler design parameters | 119 |
| 4.3 | Primary valve design dimensions | 122 |
| 4.4 | Dependence of valve actuation energy density on the design parameters | 123 |
| 4.5 | First structural (a) and acoustic (b) modes of the valve mechanism | 124 |
| 4.6 | Maximum pump chamber pressure dependence on chamber stiffness | 126 |
| 4.7 | Equivalent mechanical system during linear interval | 127 |
| 5.1 | System timing | 141 |
| 5.2 | Simulation of actuator configuration A | 143 |
| 5.3 | Actuator configuration A: energy tracking | 144 |
| 5.4 | Simulation of actuator configuration B | 145 |
| 5.5 | Actuator configuration B: energy tracking | 146 |
| 5.6 | Parameter study 2: performance of configuration B versus drive frequency, f . . | 151 |
| 5.7 | Harmonic analysis | 152 |
| 5.8 | Parameter study 3: performance of configuration B versus valve phase, ϕ . . . | 153 |
| 5.9 | Simulation 3a energy tracking | 154 |
| 5.10 | Parameter study 4: perf. of configuration B versus chamber compliance, C_c . . | 155 |
| 5.11 | Parameter study 5: performance of configuration B versus pressure load . . . | 156 |
| 5.12 | Parameter study 5: performance of configuration C versus pressure load . . . | 157 |
| 5.13 | Parameter study 6: performance of configuration B versus γ | 158 |
| 5.14 | Parameter study 9: performance of configuration B versus $ddisc$ | 161 |
| 5.15 | System frequency and damping ratio of configuration B versus scale, λ | 162 |
| 5.16 | Performance of configuration B versus system scale, λ | 163 |
| 5.17 | Parameter study 11: performance of configuration A versus f_v | 164 |
| 5.18 | Simulation of final (mesoscale) design | 169 |
| 5.19 | Performance of the final design versus system scale, λ | 170 |

| | | |
|------|--|-----|
| 5.20 | Electrical power flow in the power harvester | 171 |
| B.1 | Organizational chart for the Simulink block diagrams. | 194 |
| B.2 | Top level | 195 |
| B.3 | Chamber continuity | 195 |
| B.4 | Drive dynamics for the actuator | 196 |
| B.5 | Drive dynamics for the power harvester | 196 |
| B.6 | Diode bridge for the power harvester | 197 |
| B.7 | Inlet valve dynamics | 198 |
| B.8 | Outlet valve dynamics | 199 |
| B.9 | Pressure/flow relations for the (a) inlet and (b) outlet valves | 200 |
| C.1 | Simulation 1a: actuator configuration B | 203 |
| C.2 | Simulation 1b: actuator configuration B | 204 |
| C.3 | Simulation 2a: actuator configuration B | 205 |
| C.4 | Simulation 2b: actuator configuration B | 206 |
| C.5 | Simulation 2c: actuator configuration B | 207 |
| C.6 | Simulation 2d: actuator configuration B | 208 |
| C.7 | Simulation 3a: actuator configuration B | 209 |
| C.8 | Simulation 4a: actuator configuration C | 210 |
| C.9 | Simulation 7a: actuator configuration B using Mercury | 211 |
| C.10 | Simulation 7b: actuator configuration D using Mercury | 212 |
| C.11 | Simulation 8a: actuator configuration B using Carbon tetrachloride | 213 |
| C.12 | Simulation 8b: actuator configuration E using Carbon tetrachloride | 214 |
| C.13 | Simulation 9a: actuator configuration F | 215 |
| C.14 | Simulation 10a: actuator configuration G | 216 |
| C.15 | Simulation 11: power harvester | 217 |

LIST OF TABLES

| | | |
|-----|---|-----|
| 1.1 | Estimated performance and characteristics of various actuators | 29 |
| 1.2 | Performances of active microvalves in the literature | 33 |
| 1.3 | Properties of miniaturized conventional and micromachinable actuators | 35 |
| 1.4 | Comparisons of existing micropumps reported in the literature | 36 |
| 1.5 | Effect of scale on mechanical behavior | 49 |
| 2.1 | Engineering properties of common micromechanical materials | 67 |
| 2.2 | Comparison of polycrystalline and single crystal piezoelectrics | 68 |
| 2.3 | Performance index for diaphragm materials | 69 |
| 2.4 | Comparison of working liquid properties | 70 |
| 3.1 | Flow models for incompressible liquids at various Reynolds numbers | 83 |
| 3.2 | Model parameter values obtained from finite element analysis | 111 |
| 4.1 | Mechanical efficiencies of hypothetical coupler using various materials | 119 |
| 4.2 | Comparisons of six considered valve designs | 121 |
| 4.3 | Frequencies of the first four valve modes | 124 |
| 4.4 | Sub- and superscripts for energy notation | 130 |
| 5.1 | MHST baseline design characteristics - configuration A | 140 |
| 5.2 | Summary of parameter study | 148 |
| 5.3 | MHST final design characteristics (mesoscale) | 166 |
| 5.4 | MHST final design characteristics (microscale) | 167 |
| 5.5 | Performance of the final MHST design | 168 |
| C.1 | Summary of simulation performance | 201 |
| C.2 | Summary of electrical input characteristics used in simulations | 202 |
| C.3 | Summary of mechanical characteristics used in simulations | 202 |

NOMENCLATURE

| | |
|------------|--|
| a | valve travel [m] |
| A | area [m ²] |
| b, B | damping [N/m/s] |
| B_f | mechanical forcing |
| B_q | electrical forcing |
| c | constant |
| c_{33}^E | piezoelectric stiffness constant [Pa] |
| C | hydraulic capacitance [m ³ /Pa] |
| C_d | drag coefficient |
| C_p | piezoelectric capacitance [C/m] |
| d | diameter [m] |
| D | drag [N] |
| d_h | hydraulic diameter [m] |
| DOF | degree of freedom |
| E | Young's modulus [Pa] |
| e^* | non-dimensional ratio of actuator-to-coupler elastic modulus |
| e_{33} | piezoelectric coupling constant [C/m ²] |
| ED | energy density [J/kg] |
| f | frequency [Hz] |
| F | force [N] |
| f_c | flow friction coefficient |
| F_f | fluid momentum force [N] |
| F_p | pressure force [N] |
| f_n | natural frequency [Hz] |
| F_s | spring force [N] |
| F_v | valve actuation force [N] |
| g | gravitational acceleration [m/s ²] |
| h | height [m] |
| i | current [A] |
| I_f | fluid inductance [kg/m ⁴] |

| | |
|------------|---|
| k^* | non-dimensional ratio of actuator elastic modulus to fluid bulk modulus |
| k, K | stiffness [N/m] |
| K_f | bulk modulus [Pa] |
| l^* | non-dimensional ratio of coupler-to-actuator length |
| l, L | length [m] |
| L_e | entrance length [m] |
| m, M | mass [kg] |
| n | generalized displacement |
| N | generalized force |
| p | pressure [Pa] |
| P | power [W] |
| PD | power density [W/kg] |
| q | charge [C] |
| Q | volumetric flow rate [m ³ /s] |
| r | radius [m] |
| R | viscous flow resistance [Pa/m ³ /s] |
| R_b | internal battery resistance [Ω] |
| r^* | non-dimensional ratio of coupler inner radius to wall thickness |
| Re | Reynolds number |
| t | time [s] |
| T | period [s] |
| t_w | thickness [m] |
| u | flow velocity [m/s] |
| U | energy [J] |
| V | volume [m ³] |
| V_{batt} | battery voltage [V] |
| V_e | electrical potential [V] |
| V_o | rest (initial) volume of pump chamber [m ³] |
| V_p | voltage across piezoelectric element [V] |
| V_d | volume displacement of a single pump cycle [m ³] |
| w | width [kg] |
| x | valve displacement [m] |
| y | pump displacement [m] |
| ϵ | mechanical strain |

| | |
|---------------------|---|
| ϵ_{nn} | piezoelectric dielectric constant [F/m] |
| ϵ_0 | permittivity of free space [F/m] |
| ϕ | valve phase (with respect to pump signal) [deg] |
| γ | valve gap [m] |
| λ | scale factor |
| μ | viscosity [Pa s] |
| Θ | electromechanical coupling coefficient [C/m] |
| ρ | density [kg/m ³] |
| σ | stress [Pa] |
| σ_y | yield stress [Pa] |
| ζ | damping ratio |
| $(-)_a$ | composite piezoelectric-coupler actuator |
| $(-)_{act}$ | actuator |
| $(-)_b$ | blocked |
| $(-)_{batt}$ | battery |
| $(-)^c$ | elastic |
| $(-)_c$ | chamber |
| $(-)_{cp}$ | coupler |
| $(-)_{fc}$ | flow channel |
| $(-)^d$ | dissipated |
| $(-)^e$ | electrical |
| $(-)_{eff}$ | effective |
| $(-)_f$ | fluid |
| $(-)_{fr}$ | free |
| $(-)_h$ | high |
| $(-)_{hpr}$ | high pressure reservoir |
| $(-)_i, (-)^i$ | in |
| $(-)_{inert}$ | inertial |
| $(-)_{iv}$ | inlet valve |
| $(-)_I$ | channel section one |
| $(-)_{II}$ | channel section two |
| $(-)_l$ | low |
| $(-)^k$ | kinetic |
| $(-)_{lpr}$ | low pressure reservoir |
| $(-)^m, (-)_{mech}$ | mechanical |

| | |
|------------------|-----------------|
| $(-)_{o}, (-)^o$ | out |
| $(-)_{ov}$ | outlet valve |
| $(-)_{p}$ | piezoelectric |
| $(-)_{ph}$ | power harvester |
| $(-)_{pis}$ | piston |
| $(-)_{s}$ | structure |
| $(-)^s$ | stored |
| $(-)_{seat}$ | valve seat |
| $(-)_{sys}$ | system |
| $(-)_{t}$ | tube |
| $(-)^T$ | transpose |
| $(-)_{v}$ | valve |
| $(-)_{ve}$ | valve excursion |
| $(-)_{visc}$ | viscous |

Chapter 1

INTRODUCTION

Electromechanical transducers are those devices that convert electrical energy to mechanical energy (or electrical to mechanical). Examples of such transducers include solenoids, microphones, loudspeakers, accelerometers, motors, and generators [Crandall et al., 1982]. Two important classes of electromechanical transducers are *actuators*, mechanisms that convert electrical input energy into mechanical forces to perform work on an interfacing structure (or other mechanical load) to alter its state, and *power generators*, mechanisms that extract potential mechanical energy from an interfacing system and convert it into electrical energy that can be consumed or stored.

Power generators range greatly in size and commonly operate in the 1-100 Watt range (e.g. portable gasoline internal combustion generators and solar panels) to the MegaWatt level (e.g. hydroelectric and nuclear power plants), but relatively recent advances in active material and micromachining technologies have given rise to a new subclass of power generators, called *power/energy harvesters*, that generate power on the subWatt to Watt range. The principal objective of power harvesters is to exploit environmental energy sources (natural and man-made) for applications such as sensor, communications, and navigations circuits. Examples of ambient environmental energy sources include chemical and thermal gradients, sound, vibration, mechanical motion, wind, fluid flow, solar, radio frequency, plant material, organic matter, and human movement [DARPA, 1997].

There are a number of ways to compare potential transducers. Common measures of actuator performance include bandwidth, stroke, and induced force or stress. Energy-based comparisons offer a convenient way to combine several of these performance metrics. A useful indicator is the actuation *Energy Density* (J/kg), or Specific Work, which is the maximum amount of work that can be delivered to an ideal load, normalized by the mass of the actuator [Bent, 1997]. Energy density is defined as

$$ED = \frac{\frac{1}{2}\sigma_b\epsilon_f}{\rho_{act}} \quad (1.1)$$

where σ_b is the blocked stress of the actuator, ϵ_f is the free strain, and ρ_{act} is the actuator density. However, the bandwidth, or number of actuation cycles per second, of the device is ignored by this metric and fast actuators are not favored over slow ones in evaluation. Since in many applications it is the *rate* of mechanical energy transfer, which is to say the total energy imparted over a given time interval, that determines actuator effectiveness, a more useful indicator is actuation *Power Density* (W/kg)

$$PD \sim ED \cdot f \quad (1.2)$$

where f is the frequency of actuation. *Efficiency*, defined in this work to be the ratio of output to input energy or average power, is also a powerful comparison tool as it indicates the effectiveness of the transduction. These performance metrics, although described here in the context of actuation, are equally applicable to power generators if the direction of energy transfer is taken to be in the opposite sense, *out* of the interfacing system (see Figure 1.4).

1.1 Motivation

One of the main objectives in the design of transducers is to increase the response of the device, which can be achieved by increasing the rate at which the device converts electrical energy into mechanical, or vice-versa [Nelli Silva et al., 1997]. Applications with

weight and geometry constraints further require a minimization of the transducer mass and size. Examples of such applications include sensing and actuation of air and space structures, transducers for autonomous robotic systems as well as remotely operated vehicles (ROVs), and drivers for underwater acoustic transducers. In many cases the effectiveness, and even feasibility, of these systems depends largely on the abilities of their transducers.

Solid-state, or active, materials possess characteristics that make them well suited to transducer applications. "Piezoceramics are perhaps the most widely used active materials because of their ease of implementation and use... Actuation and sensing is applied through electrical signals, and their low field linear behavior has aided in modeling for transducer applications" [Bent, 1997]. Figure 1.1 compares the energy, bandwidth, and maximum theoretical power densities of some common transducers. The corresponding data and assumptions are listed in Table 1.1. It can be seen that active materials possess power densities that are, in some cases, several orders of magnitude greater than more customary devices such as electromagnetic motors. Specifically, the relatively high bandwidths of piezoelectrics give them peak power densities on the order of 100 kW/kg, while electromagnetic transducers are limited to roughly 10 kW/kg. Also noticeable is that hydraulic actuators possess extremely high single stroke energy densities but are typically capable of only low frequency actuation.

Although piezoelectrics are capable of superior performance their abilities remain largely unexploited in most engineering applications. Since the transducer's optimal power output is the product of its single stroke energy and its bandwidth, it is necessary to operate the device at its maximum frequency to realize this power. Referring to Figure 1.1, the frequency range is 1-100 kHz for common piezoelectric transducers. Unfortunately, most applications require much slower actuation speeds and, as a result, do not utilize the full potential of the material.

The recent development of single-crystal piezoelectric material (PZN:PT) offers remarkable advantages in transducer design. As shown in Figure 1.1, PZN:PT is capable of

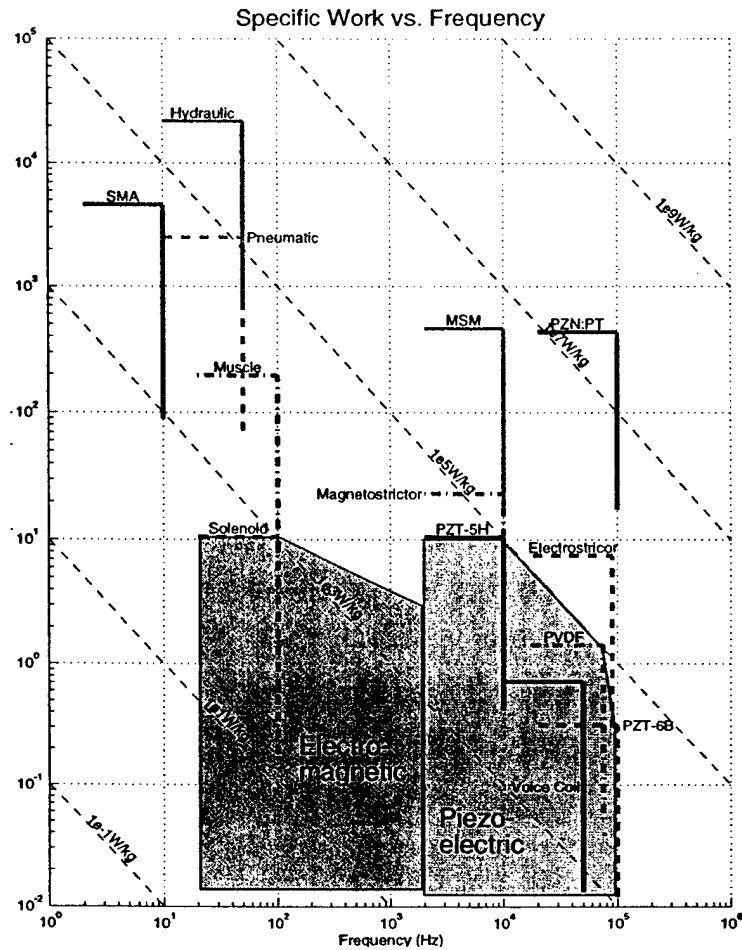


Figure 1.1 Upper Bound on Specific Work vs. Frequency for Various Actuation Media; SMA is shape-memory alloy; PZN:PT is the new single-crystal piezoelectrics; MSM is magnetic shape memory materials [Hollerbach et al., 1992; Huber et al., 1996; Hagood, 1997].

inducing strains which are ten times greater than the best conventional (polycrystalline) piezoelectrics with equal or greater increases in power densities. They also exhibit low hysteresis which leads to greater efficiency. Although researchers have not yet demonstrated effective techniques for manufacturing large single-crystals, small crystal (less than 1 cm) manufacturability has been achieved and such crystals are commercially available¹. *The result of this development is the existence of an active material that has superior performance characteristics which can have a profound impact on actuation technologies.*

1. The single-crystal piezoelectric material TRS-A is available from TRS Ceramics, Inc., Suite J, 2820 East College Avenue, State College, Pennsylvania

TABLE 1.1 Estimated performance and characteristics of various actuators^a. The number sets represent the expected range of values.

| | Clamped stress (MPa) | | Free strain | | Density (kg/m ³) | | Bandwidth (kHz) | | Stroke work coefficient | | Cyclic power coefficient | | Maximum power limit (W/m ³) | |
|-----------------------|----------------------|------|-------------|-------|------------------------------|------|-----------------|------|-------------------------|-----|--------------------------|------|---|------|
| Hydraulic | 14 | 70 | 0.1 | 0.5 | 2000 | 1600 | 0.01 | 0.05 | 1 | 1 | 0.4 | 0.5 | 5e8 | 5e8 |
| Pneumatic | 0.18 | 0.9 | 0.1 | 0.5 | 250 | 180 | 0.01 | 0.05 | 1 | 1 | 0.4 | 0.5 | 5e6 | 5e6 |
| Muscle | 0.08 | 0.4 | 0.14 | 0.7 | 1100 | 1000 | 0.02 | 0.1 | 0.5 | 0.7 | 0.25 | 0.35 | 5e5 | 5e5 |
| SMA | 140 | 700 | 0.014 | 0.07 | 6600 | 6400 | 0.002 | 0.01 | 0.3 | 0.6 | 0.05 | 0.08 | 7e5 | 7e5 |
| Electrostrictor | 23.4 | 117 | 2e-4 | 0.001 | 7800 | 7800 | 18 | 90 | 0.5 | 0.5 | 1 | 1 | 1e10 | 5e9 |
| Magnetostrictor | 30 | 150 | 4e-4 | 0.002 | 9100 | 6500 | 2 | 10 | 0.5 | 0.5 | 1 | 1 | 1e8 | 1e9 |
| MSM | 150 | 750 | 0.002 | 0.01 | 8130 | 8130 | 2 | 10 | 0.5 | 0.5 | 1 | 1 | 1e8 | 1e9 |
| PZN:PT | 60 | 300 | 3.4e-3 | 0.017 | 5882 | 5882 | 20 | 100 | 0.5 | 0.5 | 1 | 1 | 1e10 | 5e10 |
| Electromagnetic Range | 0.01 | 0.1 | 0.02 | 0.4 | 7600 | 3800 | 0.02 | 50 | 0.5 | 1 | 0.25 | 0.5 | 1e4 | 4e4 |
| Voice Coil | 0.01 | 0.05 | 0.02 | 0.1 | 7600 | 7000 | 10 | 50 | 0.5 | 1 | 0.25 | 0.5 | 5e5 | 2e6 |
| Solenoid | 0.02 | 0.1 | 0.08 | 0.4 | 4400 | 3800 | 0.02 | 0.1 | 0.5 | 1 | 0.25 | 0.5 | 1e4 | 4e4 |
| Piezoelectric Range | 1 | 157 | 4e-5 | 0.001 | 7800 | 7500 | 2 | 200 | 0.5 | 0.5 | 1 | 1 | 9e7 | 5e8 |
| PZT-5H (Soft) | 31.4 | 157 | 2e-4 | 0.001 | 7500 | 7500 | 2 | 10 | 0.5 | 0.5 | 1 | 1 | 9e7 | 5e8 |
| PZT-6B (Hard) | 4.68 | 23.4 | 4e-5 | 2e-4 | 7800 | 7500 | 20 | 100 | 0.5 | 0.5 | 1 | 1 | 9e7 | 5e8 |
| PVDF | 1 | 5 | 2e-4 | 0.001 | 1900 | 1750 | 15 | 75 | 0.5 | 0.5 | 1 | 1 | 3e8 | 3e8 |

a. Hollerbach et al., 1992; Huber et al., 1996; Hagood, 1997

The current limitation of PZN:PT crystal size is believed to be temporary and is, as will be seen, not relevant to this thesis.

"MicroElectroMechanical Systems (MEMS) represents a new multi-disciplinary technology field with enormous potential for new commercial, industrial, medical, and defense applications. MEMS are fabricated by integrated circuit processing methods and commonly include sensors and actuators with physical dimensions of less than 1 mm on a side" [Polla et al., 1994]. Demonstrated MEMS devices include a wide variety of actuators, sensors, fluidic systems, and many others. The ability to fabricate microelectromechanical devices has inherent benefits which make the technology extremely attractive. Batch fabrication permits the simultaneous manufacture of large numbers of mechanisms at low cost, and contributes functionality benefits by enabling distributed sensor and actuator arrays, redundant components, and complex system structures. The close similarities

between integrated circuit and MEMS fabrication techniques enable the merger of the mechanical and electrical components into a fully integrated device. Additionally, the behavior of a micromechanical transducer is sometimes different than its macro counterpart (e.g. resonant frequencies are higher) leading to potential performance advantages. As a result of these properties, (1) batch fabrication, (2) distributed sensor/actuator arrays, (3) component redundancy, (4) electronics integration, and (5) high frequency operation, *it is possible to create an array of micromechanical transducers that is capable of greater rates of energy conversion than a single macro transducer of equal mass, leading to higher power density.*

1.2 Objectives

The major goal of this work is to assess the feasibility of a new transducer comprised of a microhydraulic pump, valves, and pressure reservoirs that is capable of efficiently exploiting the power densities of active materials, specifically, single-crystal piezoelectrics. The devices are hereafter referred to as Micro Hydraulic Solid-State Transducers (MHSTs). The supporting objectives are:

1. Development of a prototype design
2. Derivation of an analytical system model
3. Identification of the key issues and trade-offs in the design process
4. Investigation of the effects of scale on performance
5. Investigation of the effects of design parameter changes on system performance

1.3 Background

Active Materials

Active materials are materials that have some property which is controllable by the application of an external excitation. The simplest example is metals which change shape when exposed to variable temperature levels. Other examples of controllable properties are stiff-

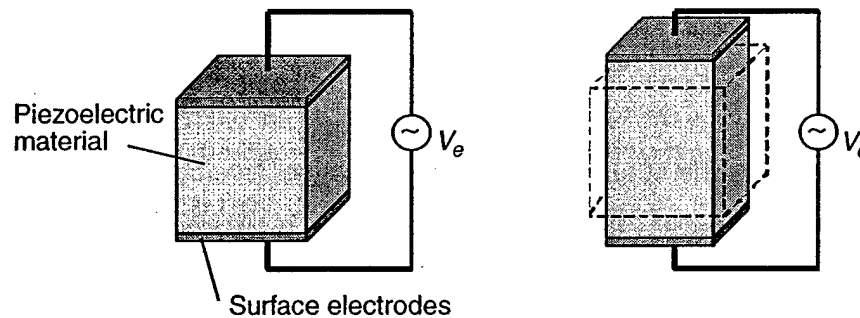


Figure 1.2 Piezoelectric effect

ness (shape memory alloys [Beuller and Wiley, 1965; Hurtado et al., 1995]) and viscosity (electrorheological fluid [Wang et al., 1994]). There are a number of external excitations which cause shape changes, but the most important are electrical and magnetic excitations. For this study, the interest is in piezoelectric materials [Du Plessis, 1996].

Originally discovered by the Curie's in the 1880's, piezoelectricity is the ability of certain crystalline materials to develop an electrical charge proportional to an applied mechanical stress. The converse effect can also be observed in these materials where strain is developed proportional to an applied electrical field (see Figure 1.2) [Jaffe et al., 1971]. Today, industrial piezoelectric materials are lead based ceramics available with a wide array of properties. Maximum actuation strains of conventional materials are on the order of 0.1% [Chan and Hagood, 1994]. Piezoelectric materials have high actuation authority due to the high Young's modulus. Another advantage of piezoelectric ceramics is the high associated bandwidth which enables dynamic control applications. The biggest drawbacks of these materials are their brittleness and high densities. Piezoelectric materials are the most well known active material typically used for transducers as well as in adaptive structures [Du Plessis, 1996].

Microvalves

"Microvalves and micropumps are among the most promising of micromachining devices" [Shoji and Esashi, 1994]. "The development of miniaturized fluid pumping systems started in 1980 with the work of Smits and Wallmark at Stanford University with a peri-

static micropump using piezoelectric bimorphs. Because micropumps can be used for many possible applications in such diverse areas as medicine, office automation, chemical analysis or industrial process control, up to now there have been many efforts to improve these devices" [Zengerle et al., 1992]. The result is the development of a wide variety of pump actuation principles, valve designs, and manufacturing techniques.

The design of microvalves has attracted much attention in the field of MEMS. Quoting Gravesen et al., 1993:

Micromachined valves have a number of advantages over traditional valves. They benefit from small size in terms of response time, power consumption, small dead volume and improved fatigue properties. However, in some applications, the small size can turn out to be an Achilles heel, where flow demands cannot be met. The majority of micromechanical valves have been designed for gas flow control. Only a limited number are intended for liquid applications.

Microvalves, like traditional valves, can be either passive or active. Passive valves require no external power and function by utilizing the energy present in the fluid. Their behavior is governed by their structural geometry and the fluid flow/pressure characteristics. The use of passive valves is beneficial because they are simple and easy to micromachine, and they consume no power. The primary disadvantage of the mechanisms is that they are typically one-way check valves so that fluid can be pumped in one direction only. Active valves derive benefits by using external power, and often employ the same type of actuator as the pump. Their advantages include bidirectional fluid flow, faster response times, and flow control. The design penalties are increased complexity, mass, power consumption, and additional circuitry for valve drive and control.

Due to the planar nature of the fabrication process, design of micromechanical valves is restricted. This constraint, and the matured process for silicon diaphragm fabrication, has favored designs incorporating diaphragms as the moving elements. However, valves with cantilevers as moving parts and various types with perforated diaphragms have also been constructed. Very small cantilever types can be fabricated, making them suitable for passive check valves in micropumps. These valves are surrounded entirely by liquid, which can contribute to failures by clogging or sedimentation of the

narrow gaps encountered in these designs. This is normally overcome in the [active] diaphragm valves, where the diaphragm separates the fluid side from the actuation side... [Gravesen et al., 1993]

Due to their diverse sizes, functions, and operating conditions, it is difficult to compare the performance of existing microvalves. An excellent discussion of demonstrated mechanisms, passive and active, can be found in Shoji and Esashi, 1994, as well as detailed descriptions their functionality. As will be seen later in this section, this thesis is concerned primarily with active valves, and no further discussion of passive devices is necessary. Table 1.2 summarizes the capabilities of some active microvalves in the literature. It can be inferred from the response times that the frequencies of these devices are, with the exception of the microheater valve, roughly 100 Hz to 1 kHz.

TABLE 1.2 Performances of active microvalves in the literature (taken from Shoji and Esashi, 1994).

| Type | Actuator | Size | Flow range | Response time | Ref. ^a |
|-----------------------------------|------------------------------------|---------------------------|--|------------------------|-------------------|
| Bulk silicon (normally closed) | stack type piezoelectric | 10 mm x 10 mm x 10 mm | 40 ml/min (N ₂ :0.5 kgf/cm ²) | 1 msec | [1] |
| Silicone rubber seat | cantilever type piezoelectric | 24 mm x 12 mm x 5 mm | 9 ml/min (H ₂ O:0.2 kgf/cm ²) | 1 msec | [2] |
| Silicone rubber seat | shape memory alloy and bias spring | 3 mm ϕ x 8 mm | | 10 sec | [3] |
| Cantilever | electrostatic | 3.6 mm x 3.6 mm | 150 ml/min (Air:0.25 kgf/cm ²) | | [4] |
| Pressure balance | electrostatic | 1 mm x 1.8 mm x 1.4 mm | 160 ml/min (Air:1.34 kgf/cm ²) | | [5] |
| Microheater | thermopneumatic | 3 mm x 3 mm | 60 ml/min (N ₂ :0.35 kgf/cm ²) | 5 msec (calculated) | [6] |
| Active check | electromagnetic/ electrostatic | 3 mm x 8 mm | 3 ml/min (Air:0.16 kgf/cm ²) | 0.4 msec | [7] |
| Diaphragm | bimetallic | 2.5 mm | 300 ml/min (Air:7 kgf/cm ²) | | [8] |

a. [1] Esashi, 1990; [2] Shoji and Esashi, 1988; [3] Shoji et al., 1988; [4] Ohnstein et al., 1990; [5] Huff et al., 1993; [6] Zdeblick and Angell, 1987; [7] Bosch et al., 1992; [8] Jerman, 1990.

MHSTs require valves with better performance than those found in the literature. Although it is difficult to quantify the flow specifications, except to say that greater flow will always lead to better performance, it is expected that the requirements in MHSTs will be on the order of 100 ml/min. The bandwidth requirement is approximately 10-100 kHz (for a 6 mm valve); it will be shown that the valve bandwidth is one of the primary factors limiting system performance. In summary, some of the current microvalve designs meet the flow requirements but all fall short of the needed bandwidth.

Micropumps

Micropump actuators may be loosely classified into two categories: miniaturizable and micromachinable. Miniaturizable actuators are those conventional devices or materials that are typically employed in macro applications, but find use in MEMS devices by external insertion or bonding techniques. The use of miniaturizable actuators in micropumps is beneficial because of the increased freedom in materials and geometry, but severely restricts the minimum pump size to that which will permit mechanical assembly. Micromachinable actuators are those that are fabricated along with the other pump structures. Their most important benefits are the absence of separate assembly steps, thus permitting batch fabrication, and the potential for creating much smaller devices. Table 1.3 compares the relative characteristics of most pump actuators reported in the literature. For a description of the operational principles behind these actuators, the reader is referred to Shoji and Esashi, 1994.

Most micropumps hitherto demonstrated have been designed for low-pressure, low-flow applications such as microdosing of liquids, fluid transport in chemical analysis systems, and drug delivery, and are therefore inadequate for use in hydraulic actuation systems where high fluidic power is required. Table 1.4 compares the characteristics of several reported designs. In most cases the pump mass was not reported and it is difficult to calculate the power density, but since all of the mechanisms are essentially planar it is possible to make rough comparisons by normalizing the power output to the surface area. Using this metric the best design is a high frequency piezoelectric pump capable of $2 \mu\text{W}/\text{mm}^2$.

TABLE 1.3 Properties of miniaturized conventional and micromachinable actuators (taken from [Shoji and Esashi, 1994])

| Actuators | Pressure | Stroke (displacement) | Response time | Reliability |
|-------------------------------------|------------|--------------------------|------------------|-------------------|
| MINIATURIZABLE | | | | |
| Solenoid plunger | small | large | medium | good |
| Piezoelectric disc | small | medium | fast | good (hysteresis) |
| Piezoelectric stack | very large | very small | fast | good (hysteresis) |
| Pneumatic | large | large | slow | good |
| Shape memory alloy % bias spring | large | large | slow | poor |
| MICROMACHINABLE | | | | |
| Electrostatic | small | very small | very fast | very good |
| Thermopneumatic | large | medium | medium | good |
| Electromagnetic | small | large | fast | good |
| Bimetallic | large | small | medium | enough |

The mechanism achieves high bandwidth operation because it has no mechanical check valves; instead, it incorporates nozzles, or diffusers, that "transform kinetic energy (flow velocity) into potential energy (pressure)" [Olsson et al., 1996]. Such pumps have the added advantage of a highly simplified design. However, the lack of valves precludes a zero-power holding force, and the nozzle elements allow for unidirectional pumping only (although fluid can freely return if an external reverse bias pressure is applied). Also, the pump requires high Reynolds number flow to operate, suggesting a lower limit on the scale at which it may be fabricated [Gravesen et al., 1993]. The remaining pumps possess significantly lower power.

TABLE 1.4 Comparisons of existing micropumps reported in the literature. *N/r* indicates that the data was not reported in the reference. *Power* represents the hydraulic output capability and is calculated based on the maximum reported simultaneous flow and pressure. *Area* denotes the footprint of the device.

| Pump type | Valve type | Working fluid | Freq. | Max flow ($\mu\text{L}/\text{min}$) | Max pres. (kPa) | Power (μW) | Area (mm^2) | Power/area ($\mu\text{W}/\text{mm}^2$) | Ref. ^a |
|------------------------------|-----------------------|---------------|----------|---------------------------------------|-----------------|-------------------------|------------------------|--|-------------------|
| reciprocating piezo. disc | passive diffuser | water | 3-4 kHz | 2300 | 74 | 491 | 255 | 2.0 | [5] |
| reciprocating piezo. beam | active elastic buffer | water | 1-150 Hz | 1600 | 17 | 25 | 35 | 0.7 | [2] |
| reciprocating piezo. disc | passive diffuser | methanol | 10 kHz | 300 | 7 | 7 | 25 | 0.3 | [7] |
| reciprocating piezo. disc | passive check | water | 40 Hz | 100 | 10 | 9 | 784 | 0.01 | [6] |
| flexural wave piezo. plate | valveless | water | 35 kHz | n/r | n/r | 5 | 1000 | 0.005 | [3] |
| reciprocating piezo. disc | passive check | water | 0.1-1 Hz | 8 | 10 | 0.3 | 2000 | 0.0001 | [4] |
| reciprocating piezo. element | active reciprocating | gas | 1-30 Hz | 20 | 8 | 0.04 | 400 | 0.0001 | [8] |
| reciprocating electrostatic | passive check | water | 25 Hz | 70 | 3 | n/r | 49 | n/r | [1] |

a. [1] Zengerle et al., 1992; [2] Stehr et al., 1996; [3] Miyazaki et al., 1991; [4] van Lintel et al., 1988; [5] Olsson et al., 1996; [6] Bass et al., 1994; [7] Gerlach and Wurmus, 1995; [8] Esashi et al., 1989.

1.4 Approach

1.4.1 Displacement Rectification Concept

The approach adopted in this work was to develop advanced actuators (and power harvesters) by using hydraulics to rectify the displacements of a piezoelectric element. This rectification is accomplished through the use of valves and a working fluid (most likely liquid) in what constitutes a piezoelectric pump. The vibrating element enables electromechanical energy conversion as the fluid flows from one pressure potential to another. If electrical power is supplied to the system from an external source a pump is realized that provides fluidic power (pressure and flow) to drive a hydraulic actuator. Conversely, with slight changes in the mode of operation the system functions as a power harvester that extracts

energy from ambient pressure sources as fluid, flowing in the reverse direction, travels from a high pressure source (with correspondingly high potential energy) to a lower one.

The energy conversion rate of the mechanism depends on several factors, including the properties of the piezoelectric material and its frequency of operation. Since piezoelectric properties are limited by the current state of materials technology, the strategy adopted in this work was to target frequency. The power output of the element depends on the application frequency, but successful harnessing of the power density capability of the piezoelectric derives from the ability to operate it at its maximum frequency. Most structural actuation scenarios, however, require bandwidths significantly lower than these frequencies. Likewise, few such high frequency mechanical phenomena exist in nature that can act as suitable energy sources for a power harvesting mechanism. By rectifying the piezoelectric's reciprocations into unidirectional flow, a transformer is realized that reduces the frequency of the active material to a level more suitable for application, thereby maximizing the system's electromechanical energy conversion by allowing the piezoelectric to operate at high frequency. *In this way it is possible to operate along the maximum power curve by trading frequency for stroke* (see Figure 1.1.)

1.4.2 Actuator Concept

A generalized solid-state hydraulic actuator is shown in Figure 1.3. A piezoelectric element and two valves comprise a pump which drives fluid from a low pressure reservoir to an actuator (for immediate usage) or high pressure reservoir (for energy storage). A voltage applied to the piezoelectric induces strain in the element resulting in a net volume change of the fluid chamber. A controller synchronized with the pump signal cycles the active valves out of phase with each other in a specified duty cycle, transforming the volume oscillations of the chamber into a net flow rate. The accumulation of fluid in the actuator increases the pressure and performs useful work on the load. After the actuator travels its full stroke the flow direction is reversed and the actuator is evacuated as it returns to its initial position, completing the actuation cycle. In this way the high frequency, small dis-

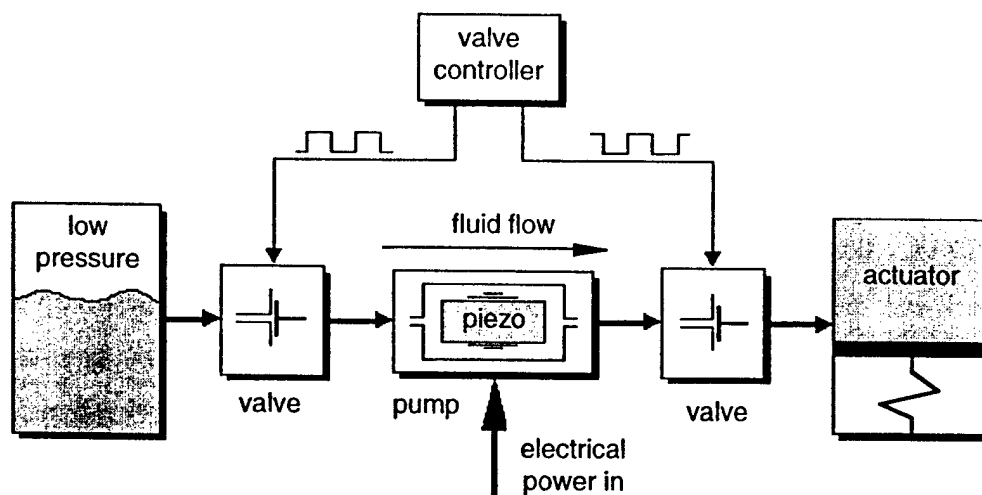


Figure 1.3 Generalized solid-state hydraulic actuation system

placements of the piezoelectric are rectified into low frequency², large stroke actuation. The extent to which the power density of the active material is preserved in the final actuator depends on the mass and efficiency of the design. If the application requires bidirectional actuation then the pump is driven throughout the full actuation cycle; flow reversal is affected by shifting the phasing of the valves with respect to the drive signal.

1.4.3 Power Harvester Concept

Figure 1.4 illustrates a generalized power harvesting system which is capable of extracting the energy that exists in any ambient static or pseudostatic³ pressure source. The controller toggles the valves, transforming the static fluid pressure into high frequency pulses on the piezoelectric. Valve actuation at the natural frequency of the system will resonate the element and create a near sinusoidal voltage signal, inducing a current in the coupled circuitry (not shown) and resulting in an electrical power flow that may be rectified and

2. Because there are typically many (~1000) pump cycles per actuation cycle, the actuator is said to be low frequency *in comparison*. It should be noted, however, that the actuator frequency may in fact be in the kHz range or higher.

3. Low frequency with respect to the pump reciprocations.

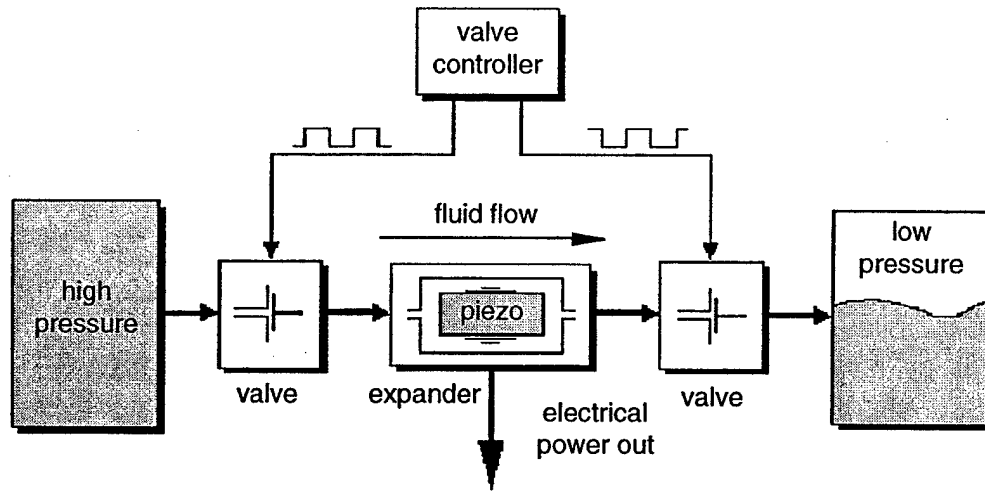


Figure 1.4 Generalized solid-state hydraulic power harvesting system

stored. Exciting the piezoelectric at resonance will maximize the amplitude of the element's deflection and optimize the power output.

Although these diagrams illustrate single systems for simplicity, they may be comprised of any combination of series or parallel units to achieve different goals (see Figure 1.5). Cascaded pumps, for instance, will provide greater ultimate pressure than a single pump is capable of. Similarly, the net flow rate of a power harvester can be tailored by arranging the appropriate number of pumps in parallel. Force and power requirements as well as redundancy criteria dictate the appropriate system configuration.

Although actuator functionality can be achieved using passive check valves (e.g. cantilevered) they have limitations. The high bandwidth requirement necessitates valves that are extremely stiff, leading to significant pressure losses as viscous fluid is forced between the valve disk and seat. Also, because passive valve systems are only capable of unidirectional fluid flow, auxiliary fluid return lines are required for multiple actuation cycles. The applied force present in active valves solves these problems and offers additional advan-

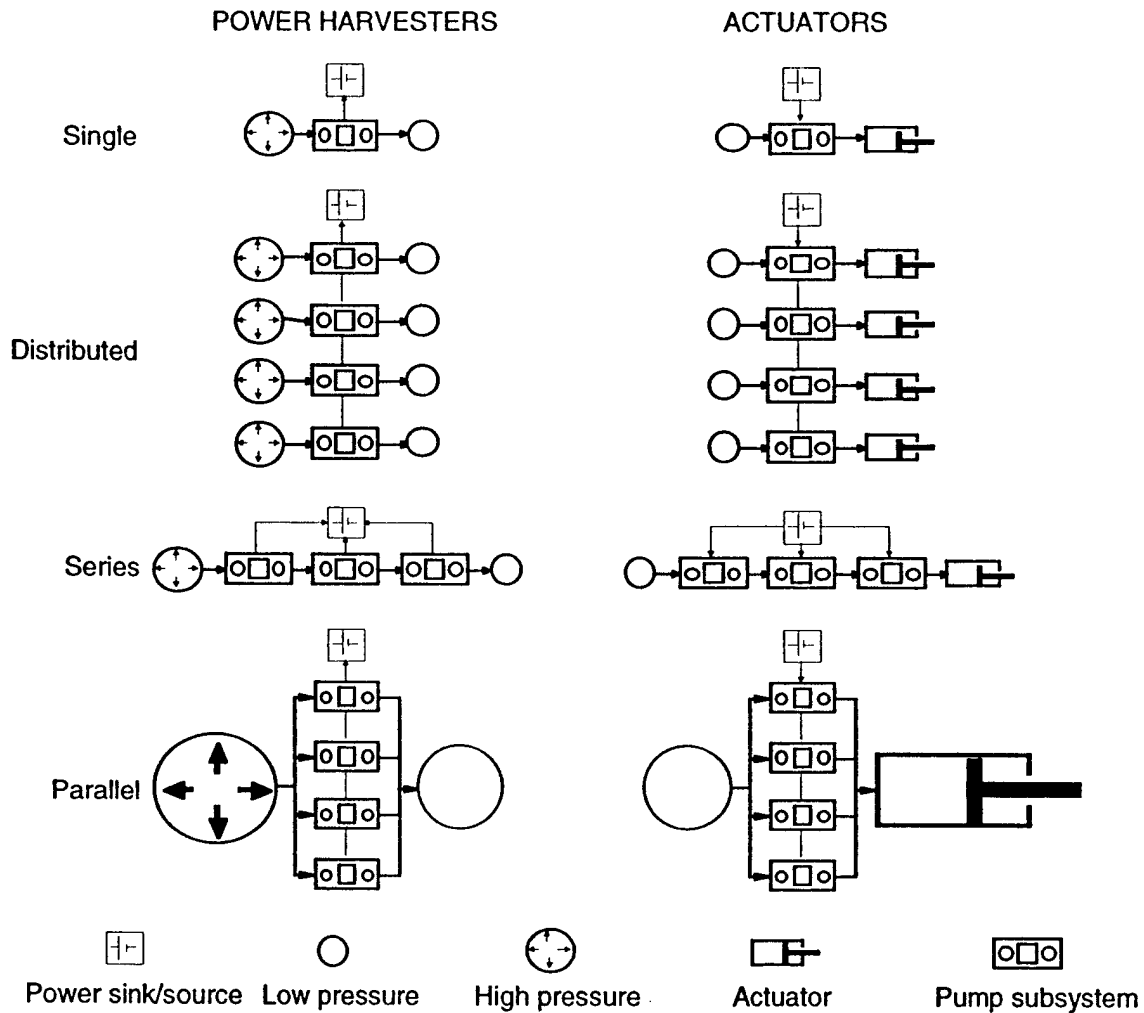


Figure 1.5 Possible system configurations

tages including flow control and improved sealing. Active valves are *required* in the power harvester to transform the static pressure into dynamic forcing.

1.4.4 Physical Implementation

Geometry

A prototype design that provides both actuator and power harvester functionality was created and is shown in Figure 1.6. The constituent components are a pump, two active valves, a low pressure reservoir (LPR), a high pressure reservoir (HPR) (or actuator), a gas

volume compensation chamber, flow channels, a working fluid (liquid), and circuitry. All geometric features are essentially planar to facilitate microfabrication.

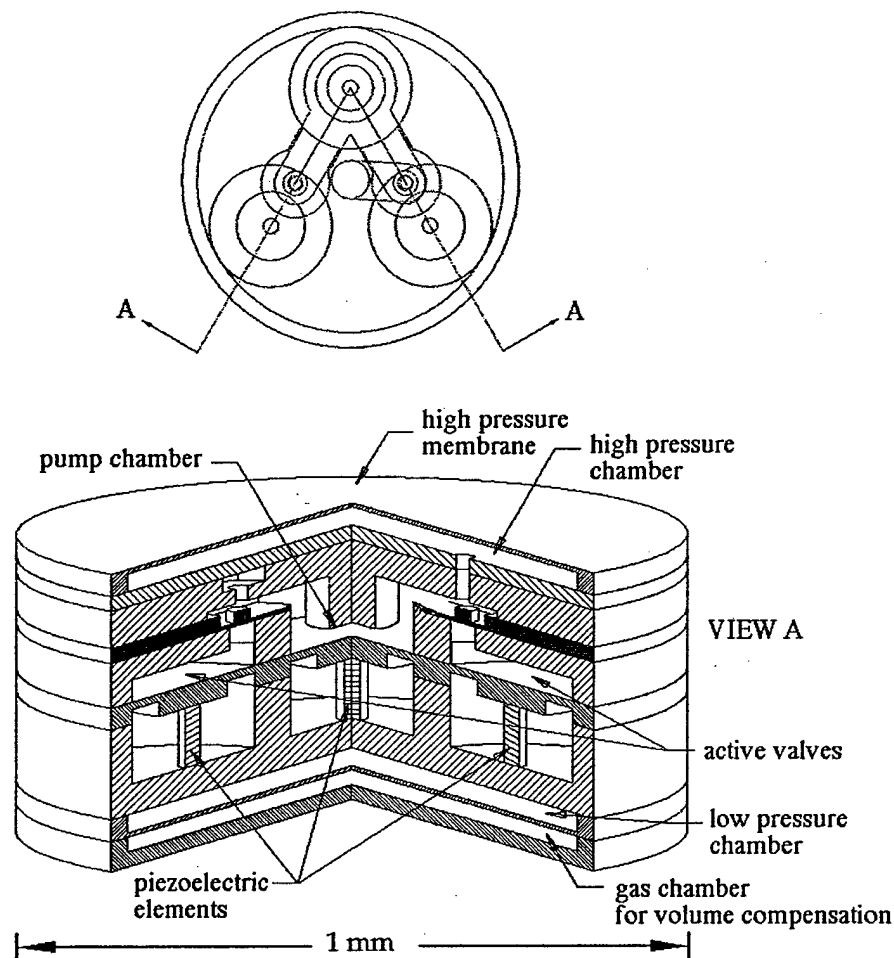


Figure 1.6 Prototype microsystem design

The mechanism is comprised of three piezoelectric elements, each sandwiched between a fixed plate and a flat cylinder. The central piezoelectric element is the actuator for the pump, while the flanking elements serve to actuate the valves. Flexible diaphragms extend radially from the outer diameters of the cylinders to the chamber walls, encasing the elements in sealed chambers. The cylinders are significantly thicker than the diaphragms in order to be rigid; the structures, then, constitute effective pistons when charge is applied to the piezoelectric elements. For compactness, the structure consisting of the central piezo-

electric element and piston will hereafter be referred to as the *drive*, regardless of its role in either the actuation or power harvesting scenarios. Fluid travels between the LPR and the connected valve via a cylindrical vertical channel located in the center of the mechanism (not visible in the cutaway view), while three other channels exist to connect the valves, pump, and HPR.

Two valves are used in the system to rectify the pump reciprocations. A detailed discussion of the valve design is presented in Chapter 2. In addition to the piston diaphragm, a second valve diaphragm is situated above and encloses a hydraulic amplification chamber. A rigid valve cap is situated above this diaphragm and is the component responsible for flow obstruction.

Principle of Operation

Actuator

The system functions as an actuator when the valve drive signals are synchronized with the input pump signal such that each valve is open when the pressure difference across it is positive (sign convention for the pressure difference is chosen to be positive when the upstream pressure is greater than the downstream) and flow is in the direction shown in Figure 1.3. A single pump cycle is described below for different times, t , during the cycle period, T . The corresponding pump and valve drive signals are shown in Figure 1.7. The initial conditions for the cycle are: inlet valve closed, outlet valve open, no pump deflection.

Actuator pump cycle:

| | |
|-------------------|--|
| $t = 0$ | : pump is extending, fluid flowing out of chamber to HPR |
| $t = T/4 - \tau$ | : outlet valve closes |
| $t = T/4$ | : pump begins to retract |
| $t = T/4 + \tau$ | : inlet valve opens, fluid flows into chamber from LPR |
| $t = 3T/4 - \tau$ | : inlet valve closes |
| $t = 3T/4$ | : pump begins to extend |
| $t = 3T/4 + \tau$ | : outlet valve opens, fluid flows out of chamber to HPR |

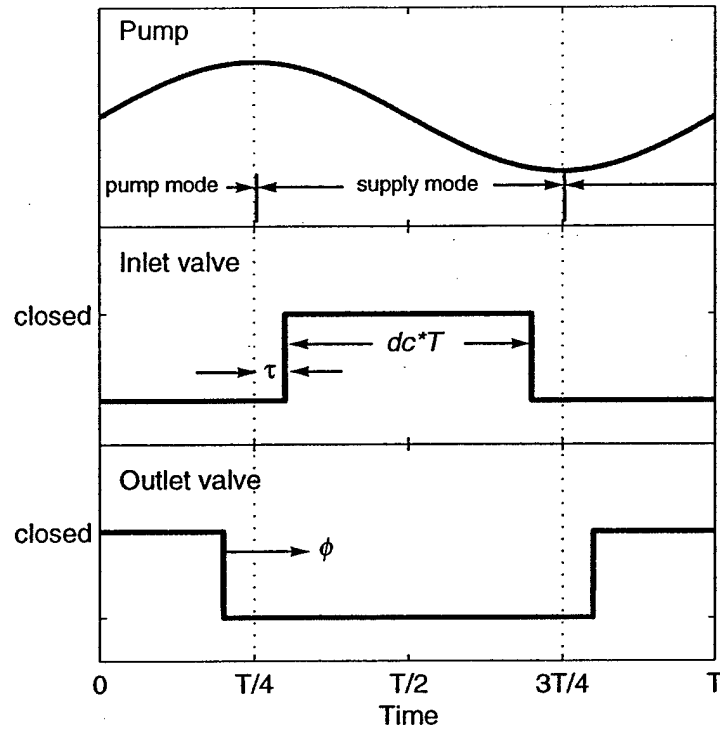


Figure 1.7 System timing. The pump drive signal may be any periodic function (sinusoidal shown for simplicity).

The parameter τ denotes a time delay in the valve actuation, with respect to the pump signal, and is related to the valve duty cycle, dc , by

$$\tau = T \left(\frac{1}{4} - \frac{dc}{2} \right) \quad (1.3)$$

A duty cycle less than 50% ensures that, for sufficiently fast valve response times, at least one valve will always be closed and a pressure short from the HPR to the LPR will not occur. The valve phase, ϕ , indicates the timing between the valve signals and the pump; the valves are always 180° out of phase with each other.

Figure 1.8 illustrates the valve cap in the open and closed states. When no electric field is applied to the valve actuator the cap is in the rest (open) position, allowing fluid to flow between pump chamber and the adjoining reservoir. Application of an electric field parallel to the piezoelectric's poling vector forces the piston upward, pressurizing the hydraulic

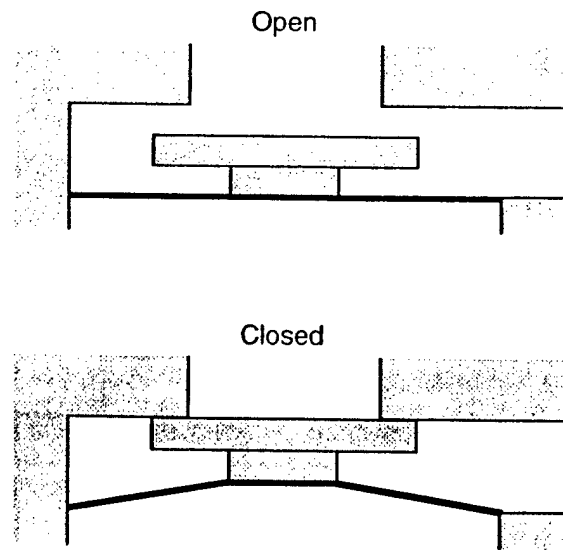


Figure 1.8 Valve operation

chamber and forcing the cap up, where contact with the valve seat blocks the flow. It is also possible for the valve to be forced open by applying an oppositely polarized electric field, thereby pulling the valve cap downward and creating a larger area for fluid flow. Due to the capacitive nature of the piezoelectric no power is drawn when the valve is stationary. Energy is therefore only consumed during valve excursion when work must be performed to overcome the resistance of the fluid on the cap face.

When the system components are driven in the manner described fluid is pumped from the LPR to the HPR where the hydraulic energy is either utilized or stored. The maximum pumping frequency is limited by the resonances of the pump and valves, whichever is lower. It will be demonstrated that, for small scale systems, there is significant dynamic coupling between the fluid and the structure, and the nature of the system's operation depends on several factors including the shape and frequency of the drive signal and the phasing of the valves.

The operation of the actuator consists of two phases: extension and retraction. During extension, the pump operates as described above and fluid is pumped from the LPR to the HPR, expanding the HPR diaphragm and performing work on the load. Similarly, the

retraction of the actuator in the second phase occurs when the pump is driven in the opposite direction, by changing the phase of the valves, returning fluid to the LPR and recycling the actuator. If actuation is required in one direction only, and the load is primarily elastic, then the energy stored in the load may be partially recovered during the actuator-return phase by operating the system as a power harvester (described below), where the percentage of the expended energy that may be recovered depends on the efficiency of the mechanism.

Power Harvester

The system functions as a power harvester when the HPR is maintained at some elevated pressure (relative to the LPR) and the valves are toggled out of phase with one another, as shown in Figure 1.7. Instead of a drive signal being applied to the pump, a periodic voltage across the piezoelectric is induced by the impinging pressure pulses. A typical power harvester cycle is described below:

Power harvester pump cycle:

- $t = 0$: fluid flowing into chamber from HPR, compressing pump
- $t = T/4 - \tau$: outlet valve closes
- $t = T/4 + \tau$: inlet valve opens, fluid flows out of chamber to LPR,
pump expands under decreasing pressure
- $t = 3T/4 - \tau$: inlet valve closes
- $t = 3T/4 + \tau$: outlet valve opens, fluid flows into chamber from HPR,
compressing pump

If the valves are actuated at the resonance of the system a roughly sinusoidal pump displacement will be excited.

The manner in which the mechanical energy imparted to the piezoelectric is extracted depends on the harvesting circuitry used. For example, simple shunting of the element with a resistor will dissipate heat as current oscillates through it, creating a mechanical to thermal conversion. In most applications, though, it is advantageous to store the energy as an electrical potential in a battery where it can be accessed when needed. In this case, the

attached circuitry typically consists of a diode bridge, or equivalent, that rectifies the electrical power flow and charges the battery.

If the high pressure source is purely static (infinite energy potential), then the energy extraction process is continuous. But in the more practical case of a pseudostatic pressure source that oscillates between its high and low values at a frequency much smaller than the power harvester pump frequency, the energy extraction process is divided into two phases: harvesting and recycling. Although the time history of the pressure source may be any periodic function, in many applications (e.g. the heel strike harvester) it will toggle between high and low pressure. For example, consider a power harvester submerged in a pressurized medium that changes in this way. In the harvesting phase, the pressure of the medium is high and compresses the HPR diaphragm, raising the pressure inside it. Since $p_{hpr} > p_{lpr}$, fluid flows from the higher potential to the lower one and the mechanism functions as described above to extract energy. During this phase, the volumes of the HPR and LPR change accordingly. The gas chamber allows the LPR diaphragm to expand with a minimal increase in its internal pressure. The design of the power harvester should be such that the time required to evacuate the HPR coincides with the duration of the high pressure state of the medium (one half of the period of the medium's pressure cycle). After the HPR has been evacuated the pressure of the medium toggles to its low state and works to expand the HPR diaphragm, causing the pressure inside it to fall below the pressure of the LPR. Energy is now further extracted as the fluid flows in the reverse direction from the LPR (now the higher potential) to the HPR. The system cycle is complete at the end of this phase.

1.4.5 Miniaturization Concept

Motivation

The performance of the MHST is enhanced when the system is miniaturized. The scale on which the system is fabricated greatly affects its behavior, and several crucial benefits are realized when the overall size is reduced, most importantly, increased power density. To

determine the relation between power density and system scale, we first note in equations (1.1) and (1.2) that σ_b , ϵ_f and ρ are intensive properties, which is to say that they are scale invariant. For the purpose of assessing the PD capability of an actuator, frequency may be taken to be the maximum bandwidth of the device. Considering the simplified case of a single degree-of-freedom (DOF) mechanism, the natural frequency is given by

$$f_n = \frac{1}{2\pi} \sqrt{\frac{k}{m}} \quad (1.4)$$

where m and k are the mass and stiffness, respectively. Because inertia scales with component volume and pressure scales with component area, the resonance is inversely proportional to scale. For instance, in the case of a clamped-free rod vibrating along its longitudinal axis, the mass and stiffness are given by

$$m = \frac{1}{3} \rho A l \quad k = \frac{EA}{l} \quad (1.5)$$

where E is the elastic modulus of the rod material, A is the cross-sectional area of the rod, and l is the length. Defining the scale factor, λ , as the ratio of the new scaled dimensions divided by the nominal, the dependence of the component's mass and stiffness on its scale is

$$m \sim \lambda^3 \quad k \sim \lambda \quad (1.6)$$

The natural frequency of a mechanical component is then related to its size by

$$f_n = \frac{1}{2\pi} \sqrt{\frac{k}{m}} \Rightarrow \sqrt{\frac{\lambda}{\lambda^3}} = \lambda^{-1} \quad (1.7)$$

And the relation between power density and scale becomes

$$PD \sim \lambda^{-1} \quad (1.8)$$

suggesting that the power density of an electromechanical transducer is increased when it is miniaturized. Although the mass and stiffness equations presented above are for a specific example, the relation to λ is general [Burgess et al., 1997].

General Scaling Effects

Structural mass and elasticity, however, are not the only properties of the MHST that change with scale. It is therefore necessary to consider the general effects of miniaturization on mechanical devices. Table 1.5 shows the scaling laws for some important aspects of fluid and mechanical behavior. The power of the scale factor, n , indicates the strength of the dependence on scale; a positive power means that the quantity will be less as the system scale is decreased. The ramifications of some these effects on MHST systems are briefly discussed below. For a more detailed discussion of scaling effects on mechanical and fluid behavior the reader is referred to [Burgess et al., 1997]; for the effects of scaling on electromagnetic actuation, see [Trimmer and Jebens, 1989].

Friction

The effects of miniaturization on friction forces is difficult to quantify because the nature of the force may change through the scale reduction. For example, consider a mass sliding along a plane and experiencing Coulomb friction. The acceleration experienced by this mass is independent of scale, suggesting that friction is effectively scale-invariant. However, friction forces on the microscale are not governed by the same equations that describe the macro phenomenon. Contacting surface area, which makes no contribution to macro friction forces, has been found to greatly affect MEMS mechanisms [Tai and Muller, 1989]. For this reason, micromachines with rigid body motions must, in most cases, have little or no sliding contact to be efficient. The scientific nature of these surface forces is largely unknown and no analytical expression for them exists [Ho and Tai, 1996].

Additional friction effects must also be considered, such as *atomic friction*: the contact forces caused by the surface adhesive force of liquids. For example, the condensation of water molecules on micromachined surfaces gives rise to capillary effects. These atomic

TABLE 1.5 Effect of scale on mechanical behavior^a (taken partially from [Burgess et al., 1997] and [Trimmer and Jebens, 1989]).

| | Application | Property | Equation | Scale relation | n | |
|----------------------|------------------------------------|---------------------------------------|--|------------------------------|----------------------------|----------------------------|
| Struct. | Mass-spring system | Frequency | $f = \frac{1}{2\pi}\sqrt{\frac{k}{m}}$ | $f \propto \lambda^n$ | -1 | |
| Friction | Sliding mass (gravitational force) | Coulomb friction / inertia | $\frac{F}{m} = \frac{mg\mu_f}{m}$ | $F/m \propto \lambda^n$ | 0 | |
| | | Atomic friction / inertia | $\frac{F}{m} = \frac{C}{m}$ | $F/m \propto \lambda^n$ | -3 | |
| Actuation | Pressure (piston) | Force / inertia | $\frac{F}{m} = \frac{pA}{m}$ | $F/m \propto \lambda^n$ | -1 | |
| | Magnetic | Force / inertia (constant J) | $\frac{F}{m} = \frac{il \times B}{m}$ $\nabla \times B - \frac{1}{c^2} \frac{\partial E}{\partial t} = \mu_o J$ | $F/m \propto \lambda^n$ | 1 | |
| | | Force / inertia (constant heat flow) | | 1 | | |
| | | Force / inertia (constant temp. rise) | | -1 | | |
| | Electrostatic | Force / inertia (constant E) | | -1 | | |
| | | Force / inertia (constant V_e) | | -3 | | |
| Fluid mechanics | Fluid propulsion | Reynolds number | $Re = \frac{\rho l u}{\mu}$ | $Re \propto \lambda^n$ | const. ^b u | scaled ^c u |
| | | | | | 1 | 1 |
| | Fluid propulsion (Stokes' law) | Viscous drag / inertia | $\frac{D}{m} = \frac{C\mu l u}{m}$ | $D/m \propto \lambda^n$ | -2 | 1 |
| | Fluid propulsion | Inertial drag / inertia | $\frac{D}{m} = \frac{\rho A C_d u^2}{2m}$ | $D/m \propto \lambda^n$ | 1 | 2 |
| | Pipe flow (Hagen-Poiseuille law) | Viscous pressure drop | $\Delta p = \frac{32\mu l u}{d^2}$ | $\Delta p \propto \lambda^n$ | -1 | -1 |
| Pipe flow (Inertial) | Inertial pressure drop | $\Delta p = \rho l \dot{u}$ | $\Delta p \propto \lambda^n$ | n/a | 0 | |

a. A = area; B = magnetic field; c = speed of light; C = constant; C_d = drag coefficient; d = diameter; D = drag; E = electric field; f = frequency; F = force; g = gravitational acceleration; i = current; l = mass moment of inertia; J = current density; k = stiffness; l = length; m = mass; p = pressure; q = charge; r = radius; t = time; T = torque; u = flow velocity; v = velocity; V_e = electrical potential; x = distance between electrodes; ϵ_o = dielectric constant; λ = scale factor; μ = viscosity; μ_f = friction coefficient; μ_o = permittivity of free space; ρ = density

b. Constant flow velocity throughout scaling

c. Indicates the dependence of the quantities on scale for a reciprocating pump where the pumping frequency scales according to the relation in the first row

forces remain constant at 10^{-8} - 10^{-7} N, meaning that, on some scales, they may dominate other forces. As a result, the lubrication of sliding parts in micromechanisms may, in fact, increase frictional forces rather than reduce them [Burgess et al., 1997].

For these reasons, (1) contact area dependency and (2) atomic forces, the MHST design has no sliding surfaces. Rather, elastic deformation has been used to effect mechanical motion within the mechanism.

Actuation

The MHST uses pistons to force fluid flow. The pressures that are generated by these components are scale invariant, such that a micropump is capable of generating the same pressures as a macropump. Since the areas on which the pressures act scale with λ^2 , so do the resulting forces. If the focus of the consideration, however, is on how well the force is able to move a mass some given distance, which is to say the achievable acceleration, then the quantity scales with λ^{-1} . The conclusion is that smaller pistons are capable of moving proportional loads at faster speeds.

Fluid Mechanics

Fluid behavior depends strongly on system scale. Because MEMS structures have very small dimensions, the Reynolds numbers for microflows are normally very low. For example, water flowing through a 1 mm diameter channel at 1 mm/s has a Reynolds number of approximately 1. At this level, the flow is laminar and is governed by the Hagen-Poiseuille law, and Stokes' law is applicable for calculating the drag force on objects in the flow stream (Table 1.5). Scale reduction leads to an increase in the viscous friction forces acting on the fluid, resulting in higher pressure drops across flow channels. For this reason, pumping in micropipes is often very difficult [Burgess et al., 1997].

MHST systems, however, are designed to operate at very high frequencies (with correspondingly high flow velocities) and may not conform to these generalizations. Certain designs could have Reynolds numbers high enough that inertial effects dominate. Simi-

larly, high frequency flow transients can lead to pressure differences across flow channels that are dominated by the inertia of the fluid slug rather than its viscosity.

Implications on Design

The effects of miniaturization suggest several things about MHST design and behavior. First, the nature of friction in micromechanisms precludes the use of sliding parts. Second, the maximum pump pressure is a property of the design and not its scale. Finally, the effects of scale reduction on fluid behavior suggest the existence of an *optimal system scale* for the mechanism. As will be shown in subsequent sections, the increased viscous effects encountered when the MHST is miniaturized past this size offset the power density increase, and overall performance becomes scale invariant. Consideration of the increased difficulties of fabrication at increasingly smaller scales suggests that the optimal scale is that at which the performance enhancement resulting from miniaturization begins to roll off.

Chapter 2

CONCEPTUAL DESIGN AND MANUFACTURING ISSUES

2.1 Introduction

The goal of the design process was to create a single transducer that could function as either an actuator or a power harvester, depending on the manner in which it was operated. Although the nature of the problem permits this without difficulty, the retainment of dual functionality in the discussion is somewhat clumsy (e.g. a reference to the *inlet* valve is unclear due to ambiguity in the flow direction). Therefore, *this thesis describes the design of a MHST in the context of a structural actuator*, with the exception of the circuitry discussions.

This chapter deals with the geometry and materials selection for the prototype actuator, and the rationale behind it. A discussion of design optimization is deferred until component models and parameters have been presented (Chapter 3). The objectives of this chapter are:

- Presentation of the strategy used in the design process
- Statement of the goals and constraints as design drivers
- Introduction of the system components and explanation of their function and geometries
- Discussion of materials selection
- Discussion of system electronics

- Discussion of manufacturability based on experience gained from fabrication of prototype drive element

The MHST design was created for the purposes of testing and model correlation as well as eventual implementation. Although the optimal size for the system was unknown when design work began, intuition and behavior estimates suggested dimensions on the order of microns. However, a necessary first step toward implementation on this scale is the fabrication of a larger, *mesoscale*, prototype with the following objectives:

1. Demonstration of the use of micromachining techniques to fabricate a MHST system
2. Validation of the analytical model
3. Investigation of microfabrication issues such as insertion of the piezoelectric element, fluid encapsulation, and multilayer bonding
4. Demonstration of concept feasibility through integrated system operation and testing

Requirements (1) and (2) suggest the size of the prototype system. Since conventional micromachining techniques were to be used an upper bound was set on the scale because the total system diameter must be less than the diameter of a standard Si wafer (4 in). Similarly, to obtain the experimental data necessary for model correlation the prototype must be large enough to permit instrumentation using conventional macro sensors, leading to a corresponding lower bound on system size. It was determined that a system approximately 1 cm in diameter would meet these requirements. To use micromachining techniques the geometry of the prototype was made essentially planar and as simple as possible. The use of wafers with "standard" ($\sim 500\text{ }\mu\text{m}$) thicknesses for most layers of the prototype reduced the cost and time of fabrication (such wafers are commonly kept in stock by vendors) and simplified the design. Although a mesoscale device is described, the above constraints permit the translation to the microscale with few design changes.

2.2 Procedure

2.2.1 Strategy

The design strategy adopted in this work consisted of six tasks:

1. Definition of performance metrics, system level requirements, and design drivers (Chapter 2)
2. Concept generation and selection (Chapter 2)
3. Derivation of a canonical analytical model (Chapter 3)
4. Development of a prototype design (Chapters 2 and 4)
5. Parameter studies (Chapter 5)
6. Final design identification (Chapter 5)

The definition of suitable performance metrics, both for the integrated system and for each of its constituent components, suggested device concepts and provided the framework for physical implementation. Most metrics were based on energy and efficiency principles, enabling their application to different MHST designs. In the concept generation and selection phase, various ideas were considered that met the criteria previously outlined. Evaluations of these concepts was based on manufacturability (with particular attention to microfabrication) and overall versatility (e.g. passive valve pumps are inherently simpler than active valve mechanisms, but have limited functionality). Subsequent to concept selection, work began on the identification of the generalized fluidic elements required to realize the full system, the nature of their governing equations, and the significant design variables. These canonical components, although simple, captured all aspects of mechanical behavior believed to impact MHST performance (based on information found in the relevant literature) and were adaptable to various designs. Using the knowledge gained from the canonical components, prototype designs were created. These were developed by first applying the general model to the subject design, then numerically simulating the system's behavior. Following convergence of the designs on definite trends, a baseline design was established that demonstrated the potential for good performance. Parameter studies were then performed as perturbations of these designs, and data was collected that

reflected the impact of these variations on system performance. The results of the study led to a final design which may be said to represent, to some degree, the actuator performance levels attainable with this concept. Figure 2.1 summarizes the design procedure.

2.2.2 Design Drivers

The components of the system were designed to maximize deliverable power density and efficiency, subject to the material and geometric constraints of microfabrication technology. To facilitate the investigation of system behavior, the extent to which the components could be analytically modeled and characterized was an additional consideration. Furthermore, a core design was sought that could provide both actuator and power harvester functionality. An explicit list of the design drivers appears below:

Deliverable power density

- maximum component bandwidths
- maximum pressure
- minimal chamber compliance
- minimal fluid compressibility
- minimal system mass

Energy loss

- no sliding seals
- low fluid viscosity
- low flow resistances
- minimal backflow
- minimal valve leakage
- energy recovering drive circuitry

Microfabrication

- planar geometry constraints
- materials constraints

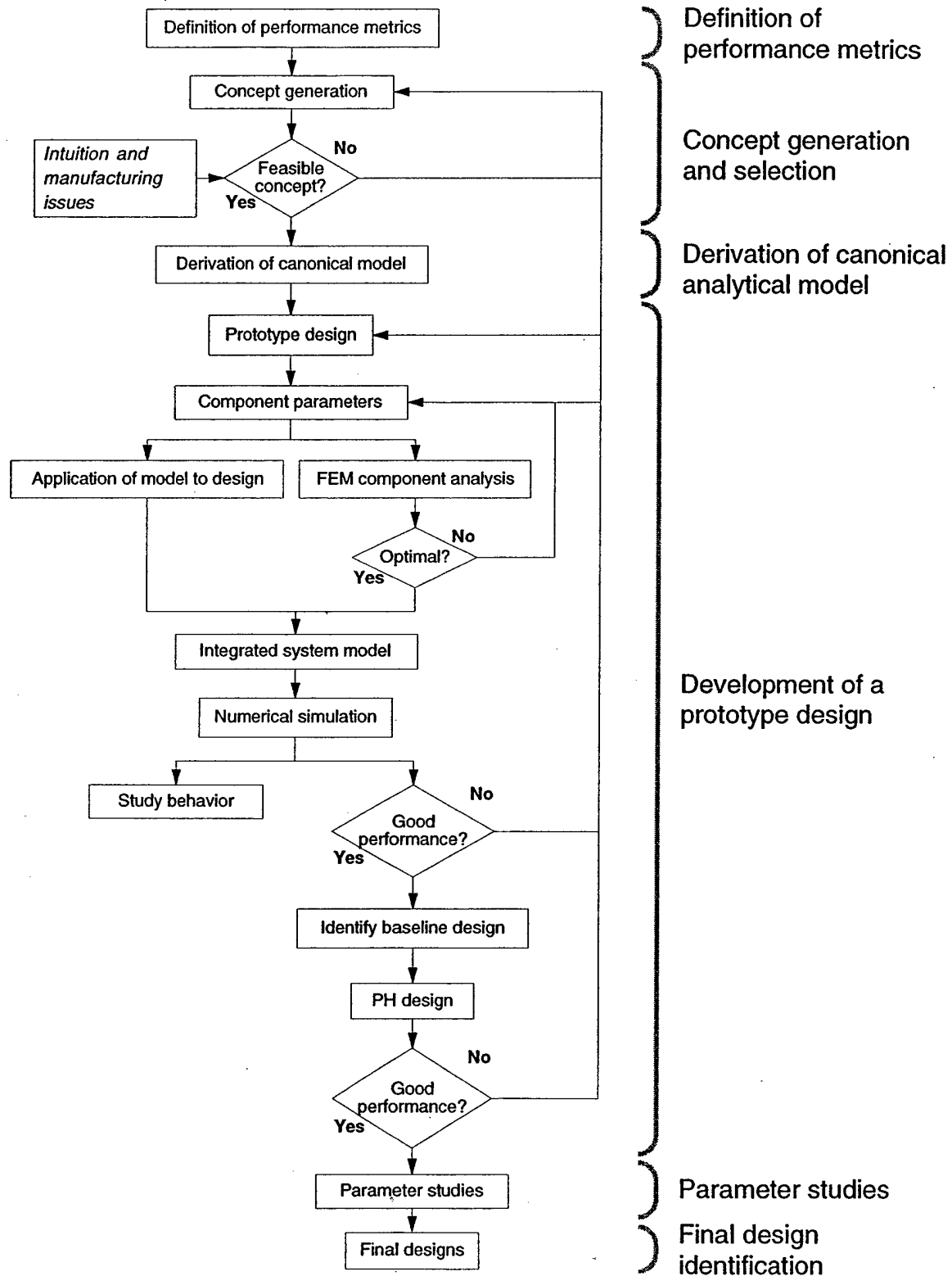


Figure 2.1 MHST design process

Prototype Issues

- common geometries among components where feasible
- size small enough to use micromachining methods
- size large enough to permit conventional instrumentation

The design chosen consists of a drive mechanism and chamber, two active valves, a low pressure reservoir (LPR), gas chamber, and elastic actuator. The valves and drive share a common axisymmetric geometry. The area of the drive piston is larger than that of the piezoelectric element's cross-section and, when strain is induced in the element, amplifies its volume displacement.

2.3 Components

2.3.1 Displacement Amplifier

Function

The purpose of the displacement amplifier is to facilitate an impedance match between the piezoelectric element and the load (HPR). The output power of the actuator is a product of the fluid flow rate into the HPR and the HPR pressure. The pressures seen by the HPR range from zero to the blocked pressure of the piezoelectric. Operation of the actuator with the HPR at either extremum pressure results in zero power output. For example, if the HPR pressure is zero, then the product of pressure and flow will be zero. Likewise, if the HPR pressure is equal to the blocked (maximum) pressure of the pump, then there will be no flow and the product is again zero. In most cases, the piezoelectric will be far stiffer than the load, and would, if no piston were present, be capable of high hydrostatic pressures but small fluid flow. The function of the piston is to make the actuator more compliant (as seen by the HPR) and improve the energy transfer rate. In the power harvester, the piston acts to amplify the stress levels in the piezoelectric thereby increasing the charge and hence the electrical power generated. In a similar manner, the purpose of the valve pis-

ton is to facilitate an impedance match between the valve actuator and the valve structure (further discussed in Chapter 4).

Geometry

The valves and the drive both utilize a displacement amplifying piston and share a common axisymmetric geometry, shown in Figure 2.2, wherein a cylindrical piezoelectric element is situated between a fixed base plate and a flat, relatively rigid cylinder. A flexible diaphragm extends radially from the outer diameter of the cylinder to the chamber wall, encasing the element in a sealed chamber. The cylinder is rigid compared to the diaphragm and, when strain is induced in the piezoelectric, constitutes an effective reciprocating piston.

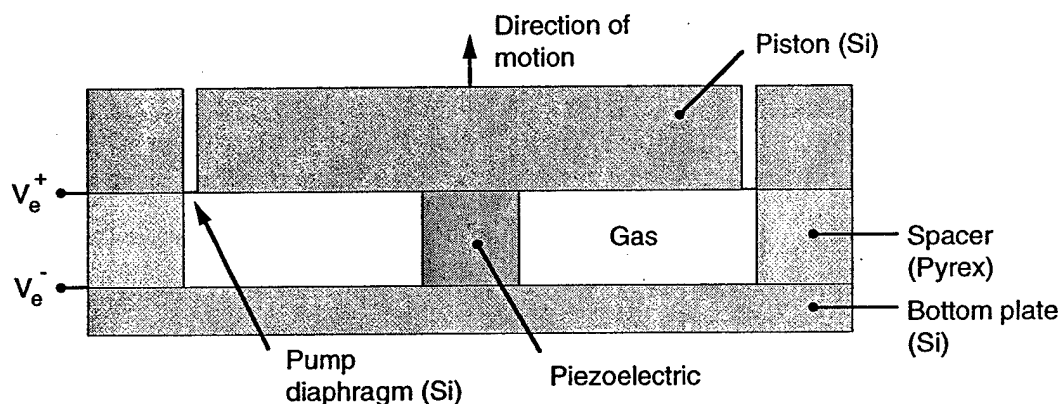


Figure 2.2 Displacement amplifier (prototype materials; axisymmetric)

Ideally, the piston cylinder would be perfectly rigid, thin (to reduce mass and increase natural frequency), and the diameter would be large enough that a perfect impedance match between the piezoelectric and the load could be obtained. In practice, however, the geometry is constrained. A thin flexible piston would contribute to the chamber elasticity and reduce the performance of the system by limiting the maximum pump pressures. Likewise, if the ratio of diameter to thickness was too large, the piston would no longer operate as a rigid body because the first radial vibration mode of the cylinder would be excited and

the pump diaphragm, which is tethered at the maximum deflection point of the piston, could fracture.

Electrical contact between the piezoelectric and the external power source (or sink, in the power harvester case) is established either through electrodes mounted to the interior surfaces of the base plate and cylinder, or by these components themselves if they are conductive. In either case, the spacer must be an insulator.

If separate electrodes are used, the diaphragm is joined to the piston at the cylinder's lower surface, as shown in Figure 2.2, to provide a flat pathway for the upper electrode. Although this creates an annular space above the diaphragm which traps fluid, thereby increasing chamber compliance, inversion of the piston, such that the diaphragm is tethered at the top surface, would force the electrode to travel into and across the annular ring, making it susceptible to cracking at the corners during actuation. If no separate electrodes are used, the geometry may be inverted.

The cavity containing the piezoelectric serves no useful function but must be carefully analyzed in the design. To prevent the accumulation of pressure in the cavity as the piston moves it is filled with a compressible gas. Actuation of the element requires the application of a high electric field across it (approximately 1 kV/mm) and, in cases where the electrodes are exposed in the cavity, introduces the risk of dielectric breakdown of the enclosed medium. To prevent this, an inert gas such as argon can be chosen to withstand the expected electric fields. Manufacturing issues must also be considered. For instance, the elevated temperatures required for the anodic bonds will expand the gas in the cavity, leading to pressures that could force the wafers apart and compromise the bond.

2.3.2 Drive Mechanism

Function

The drive mechanism is the primary transduction mechanism in MHST systems. In the actuator, the drive converts the electrical energy supplied to the piezoelectric into mechan-

ical (hydraulic) energy by moving fluid from a low to a high pressure potential. In the power harvester, the opposite result is achieved as mechanical energy is converted to electrical.

Geometry

The drive consists of a piezoelectric drive piston assembly adjoining a fluid chamber. Inlet and outlet ports permit flow into and out of the chamber when the drive is actuated. The solid structure extending downward from the ceiling of the chamber exists to reduce the volume of fluid in the chamber, increasing the stiffness of the system. The walls of the chamber are relatively thick to reduce the compliance of the chamber structure. The total compliance of the chamber is a function of the chamber structure and the fluid inside it.

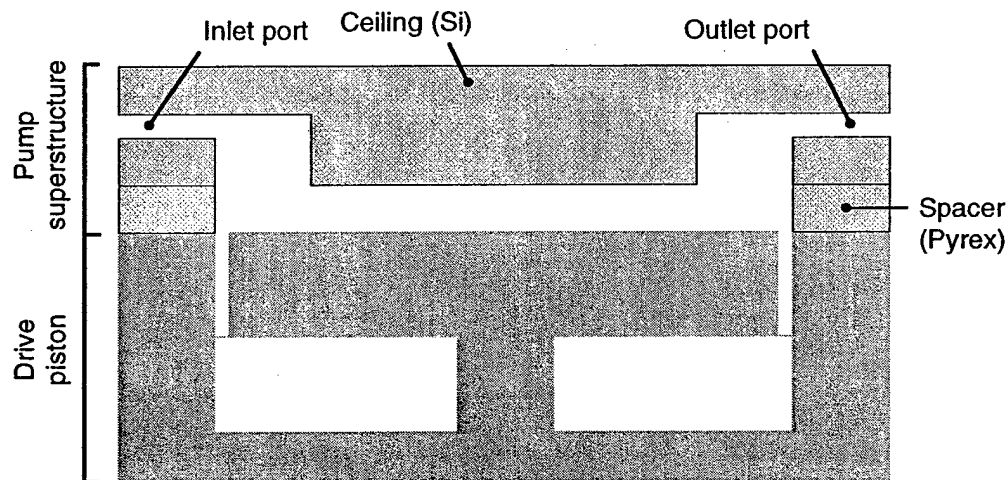


Figure 2.3 Pump diagram (prototype materials)

2.3.3 Valves

Function

In the actuator, the purpose of the valves is to rectify the reciprocations of the drive into unidirectional fluid flow. In the power harvester, the valves exist to transform a static pres-

sure source into high frequency pressure pulses on the drive. The design of the valve for both applications is identical.

Geometry

The active valve design is shown in Figure 2.4. In addition to the drive piston, a second diaphragm is situated above and encloses a hydraulic amplification chamber containing an incompressible fluid. The valve cap and diaphragm are located away from the axis of symmetry of the hydraulic amplifier at a point where the valve diaphragm is tangential to the hydraulic chamber. This is done to minimize the length of the flow channel connecting the valve to the drive so as to reduce inertial and viscous pressure drops. A rigid valve cap exists on top of the valve membrane and contacts the valve seat during actuation, thereby sealing the fluid pathway. The diameter of the valve diaphragm is significantly smaller than the piston diameter so that the vertical strain of the piezoelectric element is amplified and the valve has a longer stroke.

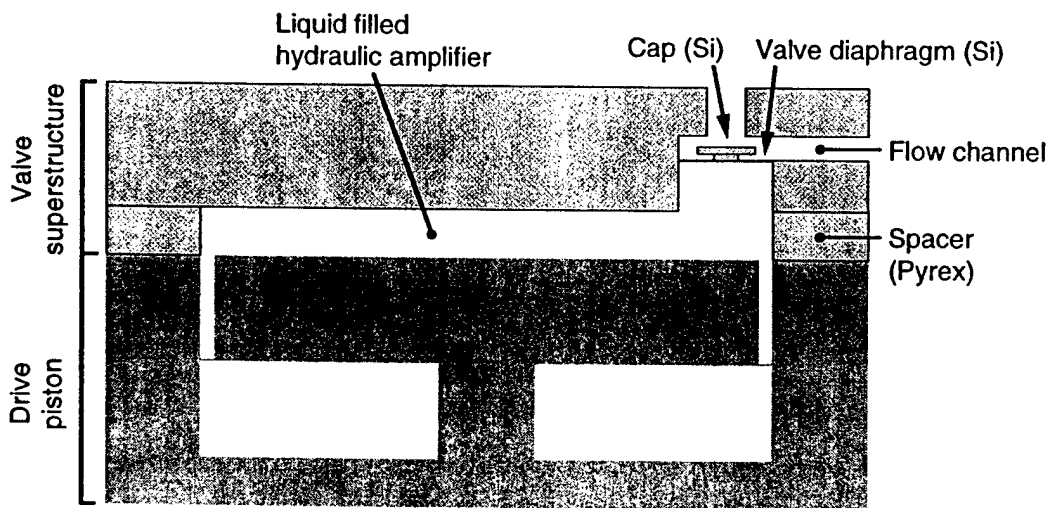


Figure 2.4 Valve diagram (prototype materials)

Actuation of the element forces the piston upwards, pressurizing the fluid in the hydraulic chamber and deforming the valve diaphragm outward. The clamped boundary conditions of the valve diaphragm enforces a cubic deflection which displaces less volume than a

rigid piston, leading to a displacement amplification that is greater than the ratio of the valve to piston diaphragm areas. The fluid encapsulated within the chamber exists solely to transmit pressure from the piston to the valve diaphragm; no flow across chamber boundaries occurs during operation.

The fundamental challenge faced in the design of the valve is the need to make a structure that is extremely stiff yet flexible enough to allow large deflections. A stiff structure is needed to prevent energy losses in the chamber compliance and to provide the required bandwidth. The key to effective system performance, however, lies in the ability to design a valve with a large stroke, which requires a very compliant diaphragm. A successful design balances these factors.

Preliminary valve designs incorporated a simple, flat valve cap located on the upper surface of the valve diaphragm, shown in Figure 2.5(a). Although this feature adds manufacturing steps to the implementation of the design, inclusion of the geometry is necessary to ensure that a flat sealing surface is brought into contact with the valve seat during actuation.

Initial computer simulations of the system indicated that the valve performance was sensitive to the design of the cap structure. During quasistatic operation of the pump using the design shown in Figure 2.5(a), the high chamber pressures generated during the pump mode (ref. Figure 1.7) acted on the inlet valve diaphragm and forced it open. Since the drive and valve share a common design, they are capable of similar pressures, and a situation arises where the valve authority is never enough to overpower the drive pressures. To overcome this problem a *pressure assisted design*, shown in Figure 2.5(b), was introduced to the inlet valve (the outlet valve remained unchanged) wherein a disc was added on top of the cap. The lower surface of the disc provides an additional surface on which the chamber pressure can act when the valve is closed. The pressure acting on the diaphragm creates a force that is partially transmitted to the valve cap, and partially to the remaining valve structure at the tether points of the diaphragm. The lower surface area of the disc is

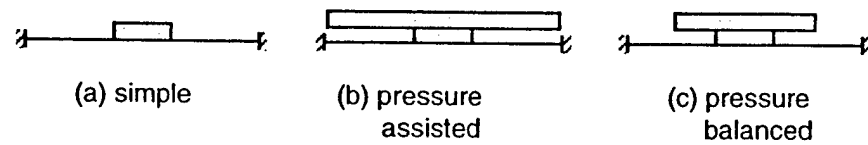


Figure 2.5 Valve cap designs

equal to that of the exposed diaphragm, yet all of the force on it is transmitted to the cap. The result is that when the chamber pressure is high, the inlet valve is forced closed. Likewise, the low pressures generated during the supply mode pull the valve open. The absence of the disc on the outlet valve causes the opposite to happen - valve closure during the supply mode, valve opening during the pump mode. In this manner a system can be created that guarantees proper valve functioning during quasistatic operation.

Simulations of the pressure assisted design showed, however, that problems were caused by the interaction of the fluid with the cap when the system was operated at resonance and the valve reaction time was fast compared to the system dynamics. When the valves were forced shut, fluid flow through the valve was abruptly stopped. Although the volume of fluid contained within the flow channel at this time was small, the slug was moving with a high velocity and possessed much kinetic energy. The sudden velocity change converted the fluid inertia into a high pressure at the valve site which acted to open the valve. For example, at the completion of the pump mode, the outlet valve, which was open during the mode, was actuated and forced closed. The fast moving fluid then impinged against the valve cap, causing a high pressure spike. Since the outlet valve was designed to open during high pressure, the spike popped the valve open, allowing backflow. A similar effect was observed on the inlet valve, where closure caused a low pressure spike that acted to pop the valve open. Although the pressure spikes caused the valves to open for only a brief moment, the deterioration in system performance was large enough to warrant a new design.

The solution reached was a *pressure balanced* valve design, conceptually similar to that used by Huff et al., 1993, wherein a disc was also added to the outlet valve. The size of the

discs, however, was different from that used in the pressure assisted method. Recognizing that a structure that biased the valve to the proper state in both quasistatic and dynamic operation was not feasible, a design was sought that would completely eliminate both effects. Figure 2.5(c) shows the pressure balanced design that was chosen for the prototype design. A detail of the geometry appears in Figure 2.6. Here A_{pb} is the additional surface area created by the inclusion of the valve disc, and A_{eff} is the effective area of the valve diaphragm that relates the ambient pressure, p , to the force seen by the valve cap. The condition for pressure balancing of the valve can be expressed by

$$A_{pb} = A_{eff} \quad (2.1)$$

where A_{eff} may be determined through finite element analysis of the valve structure. When this condition is met, the forces generated by the ambient pressure acting on either surface are balanced and the valve dynamics become decoupled from the drive and inertial pressures when the valve is closed. Pressure balancing also simplifies the analysis and design of the remaining valve structure since, in many cases, only the upstream (in the case of the inlet valve) or the downstream (in the case of the outlet valve) pressures must be considered when computing the valve authority required to hold the valve closed.

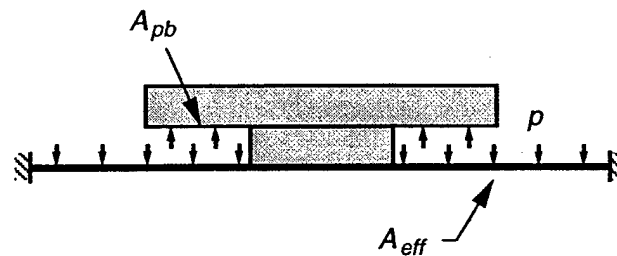


Figure 2.6 Pressure balanced valve design

2.3.4 Reservoirs and Gas Chamber

The purpose of the LPR and gas chamber is to house the working fluid for the system while maintaining the reservoir at a low pressure during fluid transfer either into or out of the chamber. The LPR is located beneath the pump and is comprised of a cylindrical

chamber with a rigid wall and ceiling. The floor of the chamber is a thin flexible diaphragm adjoining a chamber containing a compressible gas which exists to compensate for volume changes. When the fluid is pumped out of the LPR the volume of the reservoir is decreased, causing the membrane to flex upwards, thereby avoiding the accumulation of significant back pressures. Because the volume of gas is relatively large compared to the expected LPR volume change, the developed back pressures are negligible.

The function of the HPR depends on the application of the device. In some cases the HPR diaphragm is the actuation mechanism, performing useful work on a load as it expands outward. In other cases, the HPR acts to accumulate energy by storing the fluidic power generated by the pump as elastic strain energy in the diaphragm, until the energy is required by an external actuator (e.g. a hydraulic piston). In the power harvester application, the external pressure source acts on the diaphragm and increases the internal pressure. The HPR is located above the drive and valve structures and is comprised of a cylindrical chamber with a rigid wall and floor, and a flexible diaphragm ceiling.

2.3.5 Flow Channels

The purpose of the flow channels is to permit fluid flow from one component to another. Four channels exist in the design: (1) LPR to inlet valve, (2) inlet valve to drive, (3) drive to outlet valve, and (4) outlet valve to HPR. As will be shown in Chapter 4, to reduce viscous and inertial losses the flow channels should be as short as possible and have large cross-sectional areas. Observing the mechanism from the top (see Figure 1.6), the drive and the valves are arranged in a triangular fashion to minimize the lengths of the channels joining them. Channel 1 rises vertically through the center of the mechanism (it is not visible in the cutaway view) from the LPR, then runs radially where it connects with the inlet valve. Channels 2 and 3 extend horizontally from the drive to the valves. Channel 4 travels vertically from the outlet valve to the HPR. The vertical channel sections are cylindrical because they are etched directly into the silicon. The horizontal sections are rectangular

because they are created by etching a rectangular feature into the lower wafer, then bonding the upper wafer to it, sealing the flow channel.

2.4 Materials

The primary constraint from materials on the design of micromechanisms is the small number and variety of materials available [Burgess et al., 1997]. Some of them, however, possess outstanding mechanical properties. The engineering properties of some common micromechanical materials are shown in Table 2.1, taken partially from Burgess et al., 1997. Here it can be seen that silicon (Si), the most common MEMS material, has a yield

TABLE 2.1 Engineering properties of common micromechanical materials^a (stainless steel and aluminum are included for comparison).

| Material | Density (kg/m ³) | Young's modulus (GPa) | Poisson's ratio | Yield strength (GPa) | Toughness (MN/m ^{3/2}) | Thermal expansion (10 ⁻⁵ /°C) |
|--|---------------------------------|-----------------------------|--------------------|----------------------------|-------------------------------------|--|
| Single crystal silicon (Si) | 2300 [2] | 196 [1] | 0.250 [8] | 7 [3] | 1-2 [4] | 0.233 [3] |
| Single crystal silicon carbide (SiC) | 3200 [3] | 700 [3] | 0.192 [6] | 21 [3] | 4.8-6.1 [4] | 0.33 [3] |
| Pyrex | 2520 [7] | 70 [7] | 0.200 [7] | 0.069 [7] | 0.75 [8] | 0.46 [7] |
| Diamond (crystalline ceramic) | 3500 [5] | 1000 [2] | 0.100 [9] | 50 [2] | 2.3-3.4 [4] | 1 [5] |
| Stainless Steel (polycrystalline metal) | 7900 [2] | 200 [5] | 0.305 [5] | 2.1 [3] | 40 [10] | 17.3 [5] |
| Aluminum | 2700 [2] | 70 [5] | 0.330 [5] | 0.17 [5] | 100-350 [4] | 25 [5] |

a. [1] Sze, 1988; [2] Gardner, 1994; [3] Peterson, 1982; [4] Ashby, 1992; [5] Avallone and Baumeister, 1987; [6] Lide, 1995; [7] Schneider, 1992; [8] Bloor et al., 1994; [9] Kelly, 1973; [10] Bryzek et al., 1994.

strength more than twice that of stainless steel. The elastic modulus of Si is roughly the same as steel's, but at one-third the density. Its excellent mechanical properties, combined with its well studied and documented use in the field of integrated circuit fabrication, makes it extremely popular in MEMS applications [Mehregany and Huff, 1995]. The emergence of silicon carbide (SiC), an even stiffer and stronger material, in micromachining has also introduced new possibilities in MEMS design. Its strong covalent bonds leads

to an elastic modulus much higher than that of Si. And while silicon's elastic modulus decreases at elevated temperatures (above $\sim 600^{\circ}\text{C}$) SiC retains its mechanical characteristics well above 1000°C . Also included in the table are the properties of diamond, a material whose application to MEMS is currently under development [Burgess et al., 1997].

Piezoelectric

The performance of recently developed single crystal piezoelectrics makes them the clear choice for use as the transduction elements in the MHST design. Table 2.2 compares TRS-A, a commercially available single crystal piezoelectric, with PZT-5H, a common polycrystalline ceramic. It can be seen that the d constants are approximately four times greater for TRS-A than for PZT-5H, indicating a roughly equal increase in performance. It is expected that the ongoing research will soon yield single crystals capable of ten times the performance. For the purpose of system simulation in this work, the properties of TRS-A were used to model the piezoelectric and provide conservative estimates of system performance.

TABLE 2.2 Comparison of polycrystalline and single crystal piezoelectrics

| Piezoelectric | Density (kg/m^3) | d_{33} (pC/N) | d_{31} (pC/N) | k_{33} | k_{31} | k_t |
|---------------------|--------------------------------|-------------------------------|-------------------------------|----------|----------|-------|
| TRS-A ^a | 8000 | 2200 | -1000 | 0.92 | 0.56 | 0.43 |
| PZT-5H ^b | 7500 | 593 | -274 | 0.75 | -0.39 | 0.51 |

a. TRS Ceramics, Inc., Suite J, 2820 East College Avenue, State College, Pennsylvania

b. Mattiat, O.E., 1971

Structure

Two concepts governed materials selection for the structure: (1) creating fluid chambers that were as stiff as possible and (2) diaphragms capable of large deflections. SiC was clearly suited for use in the chamber structures of the MEMS device because of its high elastic modulus and yield strength. To facilitate fabrication of the mesoscale system, Si was selected. The diaphragms required a material that was strong yet capable of large

strains, suggesting the use of the *ratio of yield strength to elastic modulus* as the performance index. Table 2.3 shows this index for the materials mentioned above. It can be seen that Si and SiC possess the best properties for diaphragm fabrication (among conventional MEMS materials), with Si having a slight advantage. Si was therefore selected for use in the device diaphragms. Pyrex wafers were also used in the structure to permit anodic bonding of the layers.

TABLE 2.3 Performance index for diaphragm materials

| Material | Strain to yield ^a |
|--|------------------------------|
| Single crystal silicon (Si) | 0.036 |
| Single crystal silicon carbide (SiC) | 0.030 |
| Pyrex | 0.001 |
| Diamond (crystalline ceramic) | 0.050 |
| Stainless Steel (polycrystalline metal) | 0.011 |
| Aluminum | 0.002 |

a. Strain to yield = σ_y/E

Working Fluid

The working fluid selection was based on finding a substance that had low viscosity (to reduce viscous energy losses), high bulk modulus (to reduce elastic energy losses), and low density (to reduce inertial pressure drops and overall system mass). The non-compressibility requirement immediately precluded using a gas as the working fluid. Table 2.4 compares the mechanical properties of several potential working liquids.

Water was selected as the working fluid for the initial design because it has favorable properties and is the most common liquid used in micropumps. It will be shown in the parameter study (Chapter 5) that, with respect to performance, mercury and carbon tetrachloride are also viable liquids.

TABLE 2.4 Comparison of working liquid properties^a

| Fluid | Density (kg/m ³) | Viscosity (N/m ² ·s) | Bulk modulus (GPa) | Sonic speed (m/s) | Vapor pressure (Pa) |
|----------------------|---------------------------------|------------------------------------|--------------------------|-------------------------|---------------------------|
| Water | 1000 | 1.0e-3 | 2.24 | 1485 | 2339 |
| Mercury | 13,570 | 1.5e-3 | 25.0 | 1450 | n/a ^b |
| Carbon tetrachloride | 1590 | 0.97e-3 | 0.96 | 939 | 13,790 ^c |

a. Avallone and Baumeister, 1987

b. Mercury has no vapor pressure at room temperature

c. Yaws, 1994

2.5 Circuitry

Power and Control Electronics

The system control circuitry is responsible for synchronizing the components and actuating them in such a way that the command signals input to the system are obeyed. The specific duties of the control electronics are:

1. Synchronize valve actuation and duty cycle with the pump drive signal
2. Affect fluid flow direction changes by shifting the valve phasing
3. Operate drive and valves in power harvesting mode if unidirectional actuation and energy recovery are required

Other functionality may be included in the circuitry for specialized applications (e.g. servo valve operation for precise control of flows).

Power Harvesting Electronics

Energy extraction from the piezoelectric in the power harvester may be accomplished using rectified DC voltage source shunting in the manner described by Warkentin and Hagood, 1997. In this concept, the piezoelectric element is shunted by a four-diode full-wave rectifier which is connected to a rechargeable battery. The circuit is illustrated in Figure 2.7. When the piezoelectric element experiences large deformations, the accumulated charge causes the diodes to become forward biased and current flows from the element to the energy storage electronics and the voltage across the element is effectively

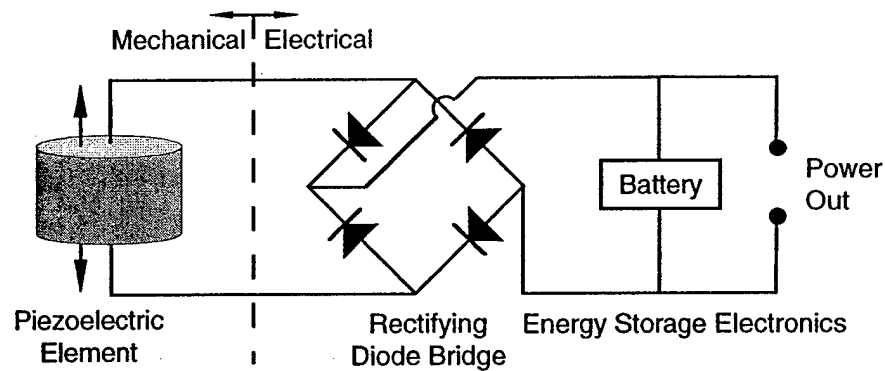


Figure 2.7 Power harvesting circuit

clipped at \pm the DC battery voltage. The diode bridge ensures that current always flows into the battery. Use of this circuit stores the energy harvested from the piezoelectric as an electrical potential across the battery terminals where it can be accessed by external circuitry when needed. It is also possible to include an inductor in parallel with the piezoelectric element to create a resonant circuit tuned to the excitation frequency.

Circuit Integration

The circuitry for the prototype design is external to the system to simplify construction and testing. In the ultimate MEMS transducer both the drive and energy harvesting electronics can be integrated with the MHST system, using IC fabrication techniques, by packaging them in the gas chamber adjoining the LPR. The electronics are thus completely insulated and shielded from the transducer's environment, and the mechanism becomes totally self-contained with the exception of two leads connecting it to the power source/sink.

2.6 Manufacturability

Process

Fabrication of a mesoscale mechanism can be accomplished with conventional micromachining techniques and mechanical assembly. The currently envisioned assembly process

is illustrated below for the drive piston. A diagram of the layers comprising the packaged device is shown in Figure 2.8. The top layer is a 500 μm thick commercially available Silicon-On-Insulator (SOI) wafer consisting of a thin (~ 300 nm) SiO_2 insulating layer sandwiched between a thick layer and a thinner 10 μm layer, both of single crystal Si. The cylindrical piezoelectric element has a diameter and length of 1 mm, with 500 nm thick chrome/gold electrodes at either end. The Pyrex layer is the same thickness as the active element, with a 6 mm hole drilled in it to form the cavity. The bottom layer is a 500 μm thick single crystal Si wafer. Multiple units can be batch fabricated; the mask for etching the annular rings in the SOI wafer is shown Figure 2.8. The units are separated by dicing the wafer along the horizontal and vertical lines on the mask using a rotating diamond saw. Although separation is not necessary it permits individual fabrication and testing and thus greater experimental flexibility.

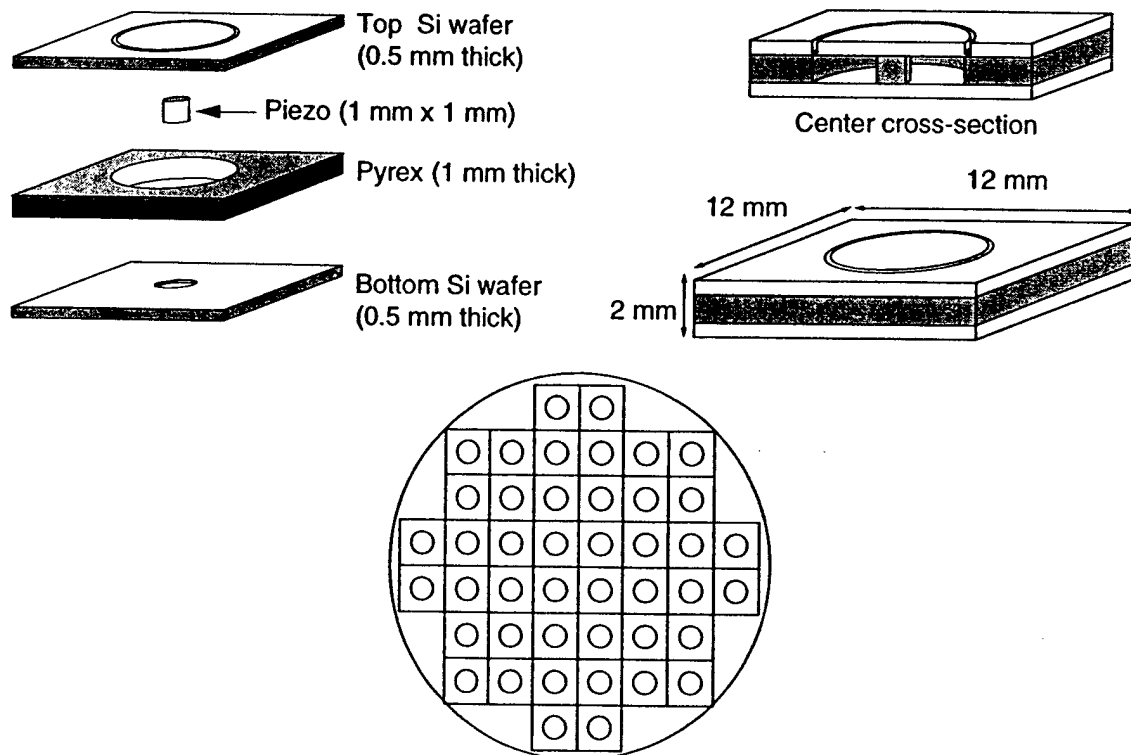


Figure 2.8 Mesoscale drive mechanism components. Clockwise from top left: exploded components, assembled unit, wafer mask. The hole in the Pyrex is 6 mm in diameter. The annular ring in the top wafer has 5.7 mm I.D. and 6 mm O.D.

The manufacturing steps can best be divided into two stages: fabrication of the piston, and assembly of the device components. In the first stage, detailed in Figure 2.9, the top SOI wafer is etched to form the piston and diaphragm. Deep Reactive Ion Etching (DRIE) is used so as to achieve near vertical walls. The Si/SiO₂ selectivity of the process is 100:1 so that the insulating layer forms an effective etch stop. After the material in the annulus has been etched away a 10 μm thick diaphragm remains connecting the piston to the outer structure.

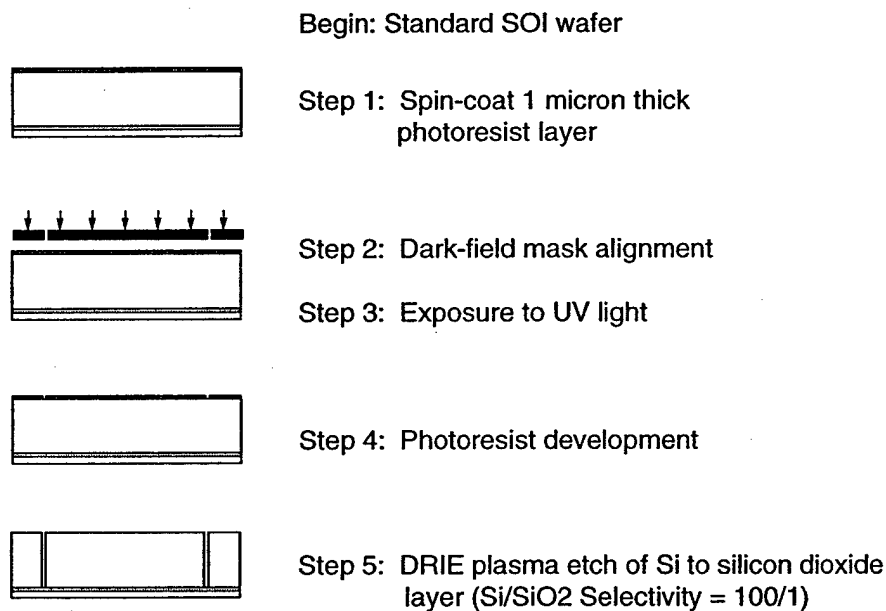


Figure 2.9 Microfabrication sequence for top SOI wafer

The second assembly stage is illustrated in Figure 2.9. First, the piezoelectric element length and the Pyrex layer thickness are measured and compared. Since the allowable mismatch is significantly smaller than the manufacturer's tolerances for the components ($\sim 10 \mu\text{m}$ will fracture the diaphragm), it is necessary to etch a seat for the active element in the bottom wafer after precise measurement of the element's thickness. The seat serves the dual functions of compensating for dimension mismatches (it is possible to control the etch depth to much greater accuracy) and alignment of the element. Since the seat "lowers" the element, the tolerances specified to the manufacturers must ensure that the length

of the piezoelectric is nominally greater than the thickness of the Pyrex. The next step is to anodically bond the pyrex to the bottom wafer. The piezoelectric is then inserted into the seat and captured by the placement of the top SOI wafer. The SOI wafer is then anodically bonded to the Pyrex. Next, the temperature is raised to the eutectic temperature of the chrome/gold electrodes ($\sim 360^{\circ}\text{C}$) and the piezoelectric element becomes bonded to the top and bottom Si layers. Since the eutectic temperature is greater than the Curie temperature of the piezoelectric, depolarization of the active element occurs. Therefore, the final step is to repole the element by applying a strong coercive electric field via voltages at the top and bottom Si wafers.

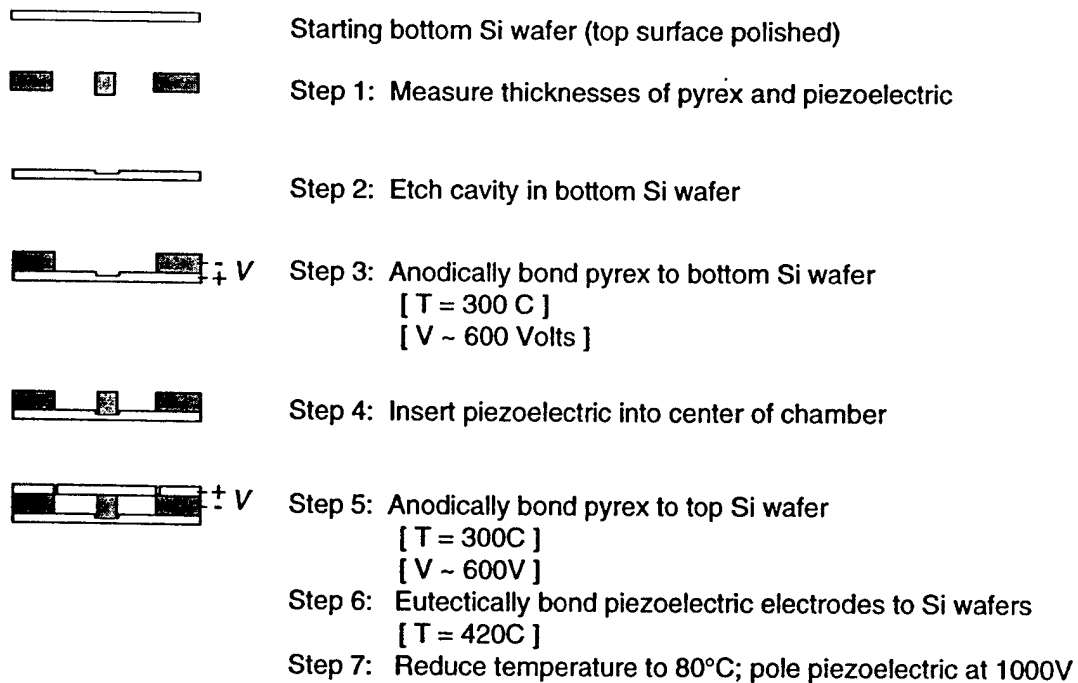


Figure 2.10 Assembly sequence for device components

To test the feasibility of this process, prototype pistons were manufactured¹. Some were examined after a single DRIE etch, while others underwent an additional wet hydrofluoric (HF) etch to improve the surface finish. Scanning Electron Microscope (SEM) micrographs of the devices appear in Figure 2.11. To obtain cross sectional images the devices were broken in half along an Si cleavage plane. Normally, the DRIE process produces an undercut in the walls when the ions reach the SiO₂ etch stop. However, the etch that generated the features seen in micrographs (a) and (b) was stopped prematurely and a fillet is present in place of the expected undercut. Thin vertical features can also be seen in these images - although the majority of them were a result of the incomplete etching, the striated surface visible on the wall is indicative of the DRIE process. Close inspection of the Si-SiO₂ interface revealed fillet radii of approximately 3-4 μm . Images (c) and (d) show the results obtained from the additional HF etch. Image (c) shows a smoother surface, as well as the undercut that is caused by a complete DRIE etch. A detail of the corner geometry appears in image (d), where it can be seen that the HF etch enlarged the pre-existing undercut, and generated an additional one in the underlying SiO₂ layer.

Implementation of a reduced scale microsystem will be similar to the mesoscale fabrication, with some differences. For example, Si-Si wafer bonding will be used in place of the more convenient Si-Pyrex anodic bonding used in the mesoscale prototype. Additionally, smaller wafer thicknesses ($\sim 50 \mu\text{m}$) and diaphragm thicknesses ($\sim 1 \mu\text{m}$) may call for different fabrication techniques.

The currently envisioned 9-layer structure of the microsystem is shown in Figure 2.12. Layer 1 serves as the base of the structure. A large diameter cavity is etched into this layer that serves as the gas chamber used for volume compensation of the LPR. Layer 2 is a thin Si membrane that, when bonded to Layer 1, forms the gas chamber. Layer 3 is a relatively thick layer, housing the internal structural chambers for the two valves and drive. Bonding Layer 3 to Layer 2 results in the formation of the LPR. The piezoelectric elements are

1. Fabrication of the prototypes was performed jointly by the *Active Materials and Structures Lab* and *Boston Microsystems*.

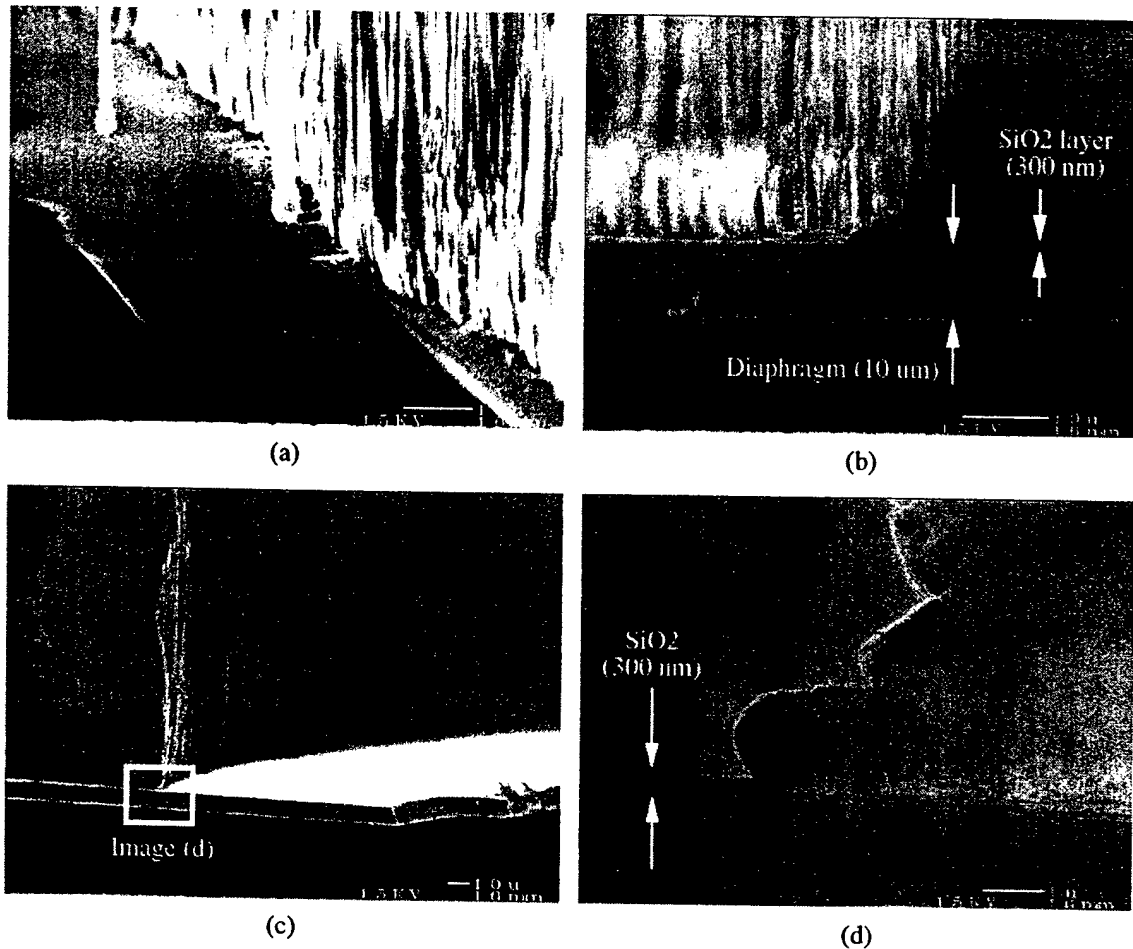


Figure 2.11 SEM micrographs of the DRIE etched prototype drive pistons. The top two show the results provided by the single DRIE process. The bottom two were obtained after a secondary wet etch performed to improve surface finish. Image (a) views the diaphragm-chamber wall interface at an angle. Image (b) is a cross section of the diaphragm-chamber tether point. The darker area at right is the cleavage plane and is normal to the viewing direction. Image (c) shows the diaphragm-chamber wall interface in the wet etched sample. Image (d) details the corner features in image (c).

deposited into Layer 3. Layer 4 contains the flexible diaphragms for the drive pistons. Etched into the underside of Layer 5 are the top portions of the valve chambers and the drive. Layer 6 includes the valve diaphragms for the valves. Through the centers of Layers 3 through 6 is a circular channel that connects the fluid in the LPR to Layer 7. In Layer 7, a horizontal channel is etched that directs this fluid from the outlet of the low-pressure valve to this central vertical channel. Layer 8 seals the horizontal channel and provides an orifice for flow from the HPR to the inlet of the high pressure valve. Layer 9 incorporates a thin membrane that together with Layer 8 forms the HPR.

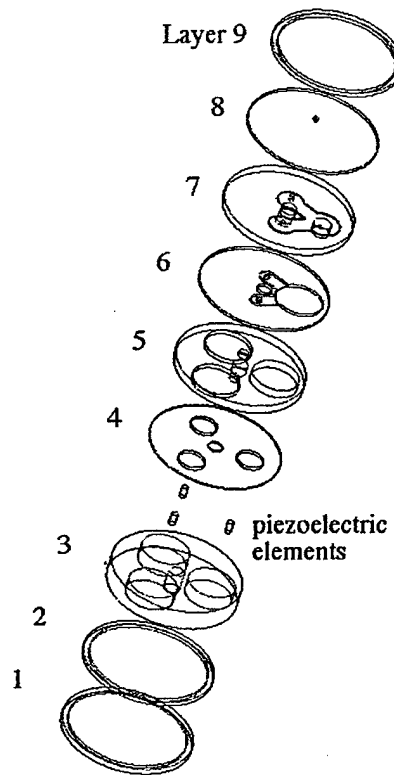


Figure 2.12 MHST layers

Microfabrication Issues

Realization of a system smaller than the mesoscale is contingent on the resolution of several key issues. They are listed below:

1. *Integration of the piezoelectric material:* In the mesoscale system the active element is large enough to be manually inserted into the cavity, but this is both difficult and tedious. Current methods of piezoelectric deposition techniques such as thin-film sputtering are not capable of providing the structure needed. New techniques are therefore required.
2. *Fluid encapsulation:* The procedure whereby the working fluid is encapsulated within the hydraulic chambers of the valves, as well as the priming of the pump chamber and channels, is another area requiring research. Specific issues include the degassing (removal of air bubbles) of the encapsulated fluid, electrical isolation of the fluid (unless a nonconductive fluid is used), and the overcoming of surface tension when priming the pump.
3. *Alignment and bonding:* Although each layer shown in Figure 2.12 is relatively simple to fabricate, the alignment and bonding of a MEMS structure

with so many layers will require the development of new techniques. Currently, conventional MEMS structures are typically limited to approximately 5 layers. Research is also needed to determine the effects of the elevated bonding temperatures on the piezoelectric element. If it is found that such temperatures are damaging, then low temperature bonding techniques must be explored.

2.7 Summary

This chapter described the conceptual development of the MHST design. The strategy used in the design process was presented as well as the existing goals and constraints. A description of the system components was begun by explaining the function and geometry of the hydraulic amplifier mechanism. The design of the drive, valves, reservoirs, gas chamber, and flow channels was then addressed. The considerations and results of the materials selection process were set forth, followed by a discussion of the function and integration of the system electronics. Finally, manufacturability of the system was addressed by considering the current state of micromachining technology as well as information gained from the fabrication of prototype piston mechanisms.

Chapter 3

MODELING

3.1 Introduction

Although quasistatic models of macro hydraulic systems are commonplace, since system scale changes the relative importance of physical effects (e.g. the impact of fluid inertia on behavior is more prominent on the micro scale), a dynamic formulation of the equations is necessary. Unfortunately, little work has hitherto been done to model the dynamic interactions of microfluidic system components [Zengerle and Richter, 1994].

This chapter presents a modeling methodology combining theoretical and numerical techniques that may be used to describe a variety of dynamic hydraulic systems, and applies it to the prototype MHST design. The objectives of this chapter are:

- Definition of the requirements of the model with respect to feasibility assessment and design of MHSTs
- Discussion of the issues involved with modeling microhydraulic systems
- Description of the assumptions used
- Introduction of generalized fluidic system component models
- Application of the general model to derive a theoretical model of the prototype design
- Discussion of the use of finite element analysis to augment the theoretical model

Explicit requirement definition is fundamental to any modeling process but is particularly crucial for fluidic systems where the model's accuracy depends greatly on the assumptions concerning fluid behavior. An understanding of the issues arising from miniaturization is necessary to create a model that is, to the extent possible, valid over all scales of interest, thus permitting studies of performance versus scale. The establishment of canonical system components provides the tools with which an integrated system model may be assembled, as well as highlights significant design parameters. Derivation of the prototype model yields the primary tool for feasibility assessment of the prototype design. Finite element analysis of the drive and valve structures facilitates exploration of geometry and material options, predicts static and modal component responses, and provides numerical values for parameters such as modal masses and structural compliances.

3.2 Theoretical Model

3.2.1 Requirements

Dynamics

Since the operational frequency, and therefore performance, of a MHST system is limited primarily by the resonances of the member components, a dynamic formulation of the component equations is necessary. Furthermore, strong interactions between fluid and structural elements often exist in microhydraulic systems, dictating the inclusion of fluid inductance and chamber compliances (fluidic and structural) [Bourouina and Grandchamp, 1996].

Energy Loss Mechanisms

Most of the energy dissipation in MHST systems is due to viscous fluid flow through valves and channels. Although primary losses will, in most cases, stem from forward flow, backflow resulting from valve leakage as well as dynamic oscillations may be a significant source of energy dissipation. In addition, some of the energy supplied to the valves is dissipated as drag acting on the valve disc throughout its stroke. This is particularly important

when evaluating the power harvester because some fraction of the generated power must be reserved to drive the valves.

System Compliance and Fluid Compressibility

The performance of MHST systems depends strongly on the compliance of the surrounding structure and the compressibility of the working fluid. In the limiting case of an infinitely stiff structure and incompressible fluid, the maximum chamber pressure is equal to the blocked stress of the piezoelectric (accounting for the hydraulic amplification). Chamber and fluid elasticities act as springs between the drive and the load, reducing the actual pressure generated. In the actuation system the effect is to reduce the outlet pressure and therefore the output power; the power harvester suffers a decreased chamber pressure, resulting in lower stress levels in the drive element and lower induced charges. Although liquids in hydraulic systems are often modeled as incompressible, it will be seen that, for MHST systems, fluid compressibility is an important factor and must be included.

3.2.2 Issues

Fluid Behavior

The precondition for successful analytical modeling of the fluid behavior in microhydraulic systems relies on correct assumptions as to the type of flow [Gravesen et al., 1993]. Most flow regime characterizations, however, are based on flow speed and channel geometry, neither of which remain constant during the investigation of MHST feasibility. The reciprocating action of the drive means that flow will transition from zero to maximum velocity every cycle, indicating unsteady flow, and cannot be adequately described with a single Reynolds number. Furthermore, the intended studies of system performance versus scale require a model that, to the extent possible, consistently describes the fluid behavior for all scales of interest. Both requirements present challenges because, as shown in Chapter 1, system scale and frequency affect the flow regimes and therefore the forms of the governing equations. An alternative to a theoretical model exists if numerical methods are employed, either by linking finite element analysis with computational fluid dynamics

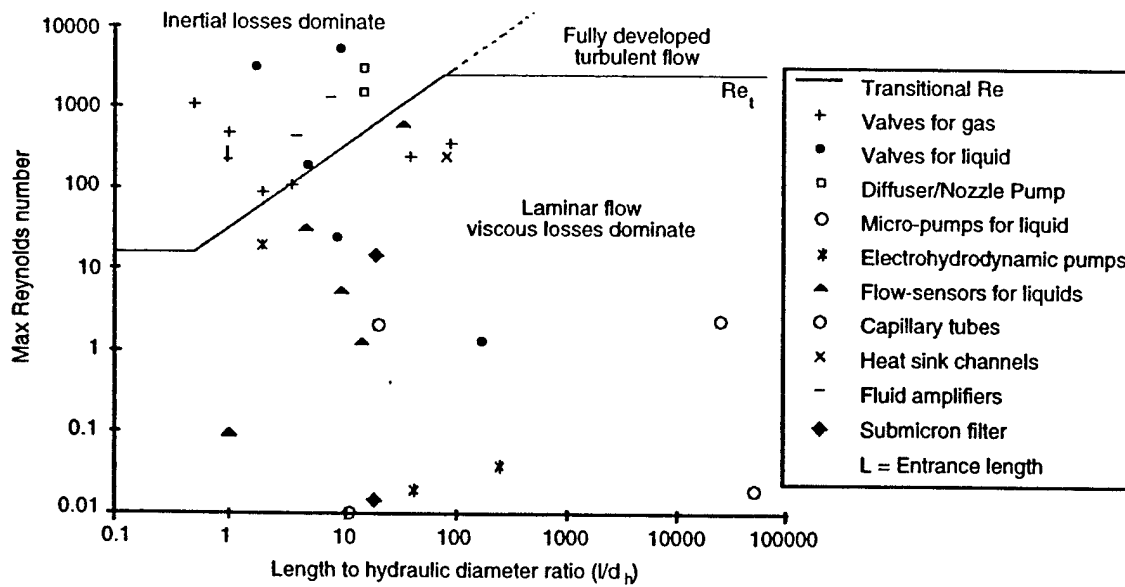


Figure 3.1 32 microfluidic devices presented in the literature, plotted in Reynolds number versus (L/d_h) map. The points plotted represent the largest flow reported [taken from Gravesen et al., 1993].

(CFD) algorithms via interface programs [Koch et al., 1996], or by using software with coupled structural-fluid analysis capabilities [Ulrich et al., 1995]. However, the computational intensity of these numerical methods makes design changes time consuming and leads to very lengthy simulations [Bourouina and Grandchamp, 1996].

It is necessary to identify what flow regimes are to be expected and what equations should describe them. Paraphrasing from Gravesen et al., 1993: in order to determine whether a flow pattern is laminar or turbulent, it is common practice to evaluate the Reynolds number and compare it to the transitional number 2000 or 2300. However, many microfluidic systems cannot be categorized in this way because the length of the flow channel is shorter than the entrance length, L_e , for fully developed laminar or turbulent flow

$$L_e \cong 0.06 d_h Re \quad (3.1)$$

Figure 3.1 shows the operational Reynolds numbers for selected microfluidic devices presented in the literature; the plotted line represents the transitional Reynolds number defined in the following manner: for small L/d_h ratios, the value for a slit-type orifice is

used; for large ratios the commonly accepted $Re_t \sim 2300$ is used; for values in between, Re_t is taken to be the ratio at which

$$(\Delta p)_{inert} = (\Delta p)_{visc} \quad (3.2)$$

Gravesen concludes that, "...none of them was operated in the region of fully developed turbulent flow, and that the [customary] transitional Reynolds number 2300 seems to have little relevance to microfluidics."

TABLE 3.1 Flow models for incompressible liquids at various Reynolds numbers^{ab}.

| Type of restriction | Definition | Viscous losses dominate laminar flow ($Re \ll Re_t$) | Re_t | Inertial losses dominate ($Re \gg Re_t$) |
|---|------------------|--|-------------|--|
| Orifice | $l/d_h < 0.5$ | $Q = A \frac{2}{C_f} \frac{d_h}{\mu} \Delta p$ | 15 | $Q = \frac{A}{\sqrt{\xi}} \sqrt{\frac{2}{\rho}} \Delta p$ |
| Short channel | $2 < l/d_h < 50$ | $Q = A \frac{2}{C_f} \frac{d_h^2}{l \mu} \Delta p$ | $30(l/d_h)$ | orifice: $\xi \cong 2.6$ channel: $1 < \xi < 1.5$ |
| Long channel | $l/d_h > 100$ | | 2300 | $Q = A \sqrt{\frac{d_h}{l}} \frac{1}{f_c} \frac{2}{\rho} \Delta p$ |
| Diffuser inlet (d_h) outlet (d_h) (A is the smallest area) | $5 > l/d_h > 50$ | $Q = A \frac{2}{C_f} \frac{d_h^2}{2\mu} \frac{3(d_h^3/d_h^3 - 1)}{1 - d_h/d_h} \Delta p$ | $30(l/d_h)$ | $Q = \frac{A}{\sqrt{\xi}} \sqrt{\frac{2}{\rho}} \Delta p$ $0.2 < \xi < 1$ |

a. Taken partially from [Gravesen et al., 1993]

b. A = cross-sectional area of flow channel; C_f = friction coefficient ($= fRe$; = 64 for circular cross-section; = 96 for rectangular cross-section; ~ 41 for slit-type orifice); d_h = hydraulic diameter; Δp = pressure drop; f_c = friction factor ($\sim 0.14Re^{-0.18}$ for fully developed turbulent flow); Q = volumetric flow rate; μ = viscosity; ρ = density.

Table 3.1 summarizes the commonly used flow models for incompressible liquids at various Reynolds numbers. According to this table (where the flow channels in the MHST prototype design may be classified as *short channels*), for Reynolds numbers below the transition value, the flow is fully developed laminar, viscous losses dominate, and the left

equation governs flow (the Hagen-Poiseuille law). For values greater than the transition, the inertial pressure drop dominates and the right equation is used.

Several problems exist, however, when these equations are applied to the prototype design. Firstly, the equations for inertial pressure drops are derived assuming that kinetic energy is not transferred from one fluidic element to the next, which is to say that the channels are terminated with a sudden expansion in the flow path cross-section. This assumption is highly dependent on the geometry of the channel ends and, for the most part, is not applicable to the MHST design. Secondly, no account is taken of the acceleration of the fluid slug due to the flow velocity changes (which are extreme in high frequency pumps).

Numerical Integration

Computer simulations of hydraulic systems are difficult to integrate if the ordinary differential equations are numerically stiff, which is common if the system contains compliances of different orders of magnitude. For example, changing valve states cause the pump to experience enormous changes in the stiffness of its load. For such systems, a poorly chosen integration algorithm will require excessively small time steps and simulations will be extremely slow [Piché et al., 1995]. In fact, numerical integration of the model presented in this work using normal Runge-Kutta methods is not feasible. The model was simulated using MATLAB with the SIMULINK¹ dynamic system simulation toolbox, partly because of the versatility of SIMULINK and the ease with which design changes can be made, but also because the package contains several integration routines designed specifically to solve numerically stiff problems; the solver chosen was based on a modified Rosenbrock formula of order 2. Several other integration options exist, such as a modified Runge-Kutta method proposed by Piché et al. in 1995.

1. MATLAB version 5.2; SIMULINK version 2.1; The MathWorks, Inc., 24 Prime Park Way, Natick, MA 01760-1500

3.2.3 Assumptions

Single DOF Component Dynamics

Since drive frequencies significantly exceeding the first natural frequency of any structural component will most likely result in poor system performance, single vibration modes were assumed for all structural elements resulting in lumped, single DOF component models. In most cases, the surrounding structures (e.g. chambers and flow channel walls) will have resonances much greater than the operational frequency and may therefore be treated quasistatically.

Structural Expansion

Due to the structural compliance of the pump chamber, interior pressures will cause the structure to deform, changing the control volume size. It is assumed that this volume change is small compared to the undeformed volume of the chamber, with the result that the control volume may be taken to be constant. Since the flow channels are to be etched or otherwise micromachined in Si or SiC wafers, the volume of material surrounding the channels is large compared to their cross-sectional areas. This fact, combined with the high stiffness of silicon, suggests that the deformation of the channels may be neglected and the cross-sectional areas assumed constant. The channels are therefore assumed to be infinitely stiff, which is to say that they have infinite hydraulic capacitance.

Fluid Compressibility

The liquid in the pump chamber is quasistatically compressible, which is to say that a finite bulk modulus relates pressure to volume change, but wave propagation is ignored. In most cases, the volume of fluid in the flow channels and valves is small compared to the chamber and the added compliance is negligible. Fluid in these regions is therefore modeled as incompressible.

The interior pressure distributions of the system cavities are assumed to be uniform. This assumption is valid when the acoustic wavelength of the working fluid (at the operating

frequency) is significantly greater than the maximum cavity dimension, as it true for the prototype system.

Steady Flow

Steady flow is assumed in the derivation of the viscous resistances of the components. Although this scenario cannot truly occur in high frequency reciprocating pumps, it is a necessary approximation because little *a priori* knowledge exists about the dynamics of the flow in the irregular geometries of the design.

Inertial Pressure Drops

Two sources for inertial pressure drops exist in MHST flow channels. The first is caused by the acceleration of a fluid particle as it enters a channel, and is described by the Bernoulli equation. The second is due to the acceleration of the fluid slug in the channel caused by the corresponding acceleration of the pump piston. It is assumed in this work that the inertial pressure drops caused by the high frequency reciprocation of the pump will dominate the former effect.

Cavitation

Cavitation must be considered in all mechanical pump designs. Cavitation is the formation and subsequent collapse of vapor-filled cavities in a liquid due to dynamic action [Olsson et al., 1996]. In the MHST, the high frequency reciprocations of the pump may induce cavitation at the piston-liquid interface. The phenomenon is, however, difficult to incorporate into the theoretical model. The two passive diffuser pumps discussed in Chapter 1 are the only reciprocating micropumps with operational frequencies approaching that of the MHST. Olsson et al. reported that they measured the best performance of their pump, operating at 3-4 kHz, just below the level of electrical excitation that caused cavitation, concluding that "maximum pump diaphragm excitation is therefore limited by cavitation" [Olsson et al., 1996]. Gerlach and Wurmus reported successful operation of a pump with an 11 x 11 mm² membrane up to its mechanical resonance of 10 kHz, but observed that when a smaller pump was driven at its correspondingly higher resonance "the dynamic

passive valves did not work anymore" [Gerlach and Wurmus, 1995]; the source of the performance reduction was not determined. With this information in hand, it is concluded that it is possible for a mechanical pump to operate in the kHz range, but that cavitation may be a limiting factor.

Several possible solutions exist to the cavitation problem. Firstly, it is possible to bias the chamber pressure, perhaps by using auxiliary piezoelectric elements, such that the chamber pressure never falls below the vapor pressure of the fluid. Secondly, the choice of working fluid is extremely important. For example, it will be seen that mercury, which has no vapor pressure at room temperature, is a viable liquid. Therefore, cavitation will not be addressed in subsequent sections of this report and is, rather, emphasized as a subject for future experimental study. Accordingly, it must be stressed that the pressures predicted by simulation results are meant as *pressure differentials only*, and implementation of the subject design must include measures, such as those mentioned above, to avoid cavitation.

3.2.4 Canonical Components

The definition of canonical system components aids the modeling process and sheds insight into the system's key parameters. The elements required to realize a MHST system are *volume source*, *pump chamber*, *active valve*, and *flow channel*. In order to capture the dynamics of the integrated system, the static and dynamic characteristics of each element must be specified [Zengerle and Richter, 1994].

Volume Source (Piezoelectric Drive Element)

The volume source is piezoelectric and is the primary transduction element in the system. When employed in an actuator its function is to strain under an applied voltage, changing the size of a control volume and forcing fluid flow. In power harvesting applications the reverse process is used: pressurized fluid entering the control volume induces compressive strain in the element and generates a voltage signal. Pressure oscillations will cause similar voltage fluctuations across the material and induce current flow; the resulting electrical power is harvested via coupled rectifying circuitry. Figure 3.2 illustrates the volume

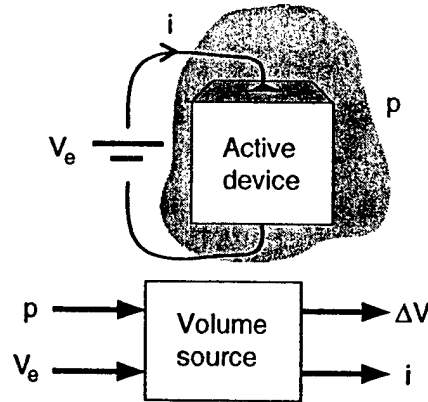


Figure 3.2 Canonical volume source and pressure transducer

source and the nature of its transfer function which relates the pressure of the surrounding fluid, p , and the applied electric field, E_f , to the change in volume of the element, ΔV .

Transduction in piezoelectrics stems from their coupled mechanical and electrical dynamics, the modeling of which has been the subject of much research. Typically the electrical dynamics of the piezoelectric are ignored when it is used as an actuator; the mechanical dynamics are likewise neglected when it is used as a sensor. Although such simplified formulations can fully describe the mechanical behavior of the MHST actuator (because a voltage is applied), the functionality of the power harvester lies in the coupling of the volume source with the attached circuitry and fully coupled equations are therefore necessary. A methodology for deriving the coupled equations of motion has been presented by Hagood et al. using the well-known piezoelectric constitutive relations and Hamilton's Principle [Hagood et al., 1990], and is summarized in Appendix A. The resulting equations are

$$(M_s + M_p)\ddot{n} + (B_s + B_p)\dot{n} + (K_s + K_p)n + \Theta V_e = B_f F \quad \text{Actuator Equation} \quad (3.3)$$

$$\Theta^T n + C_p V_e = B_q q \quad \text{Sensor Equation} \quad (3.4)$$

where $M_{s,p}$ are the mass matrices, $B_{s,p}$ are the damping matrices, $K_{s,p}$ are the stiffness matrices, C_p is the piezoelectric capacitance matrix, Θ is the electromechanical coupling

matrix, B_f is the mechanical forcing matrix, and B_q is the electrical forcing matrix. The subscripts s and p refer to the structure and piezoelectric, respectively.

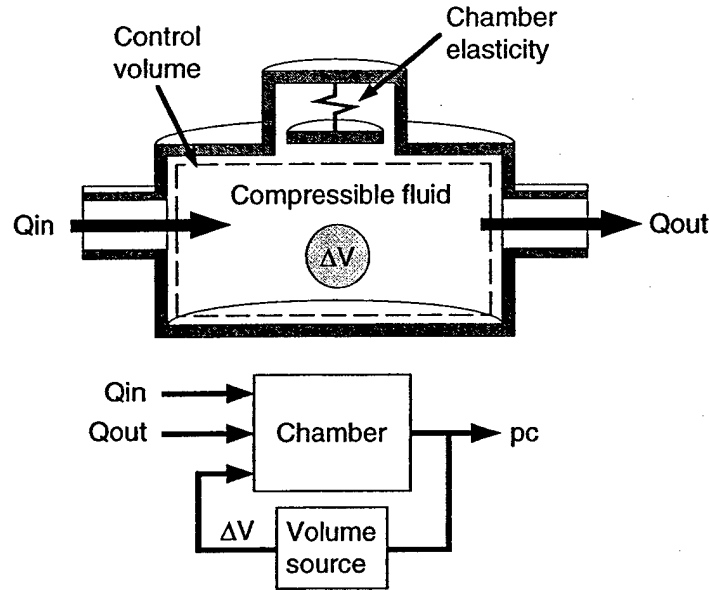


Figure 3.3 Canonical pump chamber

Pump Chamber

The pump chamber, shown in Figure 3.3, is a structure surrounding the volume source that permits the accumulation of fluid pressure. Its transfer function relates the size change of the volume source, ΔV , the volumetric flow in, Q_i , and the volumetric flow out, Q_o , to the pressure in the chamber, p_c . The governing equation for the element may be obtained by the application of continuity to the control volume. Integrating over the control volume surface yields

$$\dot{p}_c = \left(\frac{V_o - \Delta V}{K_f} + \frac{1}{C_s} \right)^{-1} \cdot (\Delta \dot{V} + Q_i - Q_o) \quad \text{Pump Chamber Equation (3.5)}$$

where V_o is the volume of fluid initially contained within the chamber when the volume source is undeformed, K_f is the bulk modulus of the fluid, and C_s is the hydraulic capacitance of the chamber structure. It is assumed that $\Delta V < V_o$. The premultiplying term

relates the deformation of the control volume to the chamber pressure and constitutes the *effective hydraulic capacitance* of the chamber

$$C_c(\Delta V) = \left(\frac{V_o - \Delta V}{K_f} + \frac{1}{C_s} \right)^{-1} \approx C_c \quad (3.6)$$

where the capacitance contributions of the chamber structure and the working fluid act as springs in series. It can be seen that, as the size of the volume source increases, the overall capacitance of the component decreases as fluid leaves the chamber. In many cases where the deformation of the volume source is very small compared to the volume of fluid initially in the chamber, $\Delta V \ll V_o$, C_c is approximately constant.

When considering equation (3.5) it must be remembered that the chamber pressure, p_c , is implicit in ΔV . For example, in the limiting case of an incompressible fluid and a rigid structure, (3.5) suggests that p_c is unbounded, when, in fact, the magnitude of ΔV is limited by the chamber pressure. The result is that, in the limiting case, p_c will be equal to the blocked pressure of the volume source.

Flow Channel

Flow channels are the fluid pathways connecting the other components together. The canonical channel is shown in Figure 3.4 along with its transfer function relating pressure difference to flow.

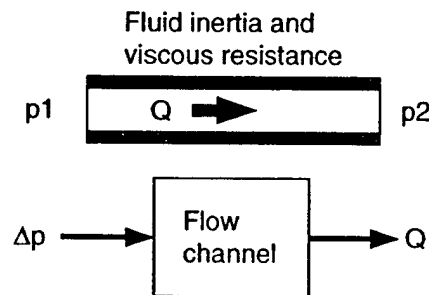


Figure 3.4 Canonical channel

Much of the modeling of fluid behavior occurs in the flow channel. Unfortunately, a fundamental challenge exists: a truly accurate model of MHST fluid behavior requires empirical data, but such data can only be obtained through the design and fabrication of a prototype which, in turn, requires a system model. The strategy chosen was to derive a channel model that would capture both viscous and inertial effects, yet be as simple as possible so as to facilitate correlation with experimental data. The result was an equation incorporating lumped viscous and inductance terms. Such a scheme was used by Zengerle and Richter, 1994, in the modeling of a micropump, where good agreement with experimental data was obtained.

If steady laminar flow in a circular pipe is assumed, under the arguments previously discussed, then the viscous pressure drop is given by the Hagen-Poiseuille law

$$(\Delta p)_{visc} = \frac{128\mu l}{\pi d_h^4} Q \quad (3.7)$$

where d_h and l are the hydraulic diameter and length of the channel, respectively, and μ is the viscosity of the fluid. This can be generalized as

$$(\Delta p)_{visc} = RQ \quad (3.8)$$

where R is defined as the viscous flow resistance of the channel. Considering Newton's equation for inert and incompressible fluids, the inertial pressure drop across the channel is of the form [Zengerle and Richter, 1994]

$$(\Delta p)_{inert} = \rho I_f \dot{Q} \quad (3.9)$$

where ρ is the density of the fluid, \dot{Q} is the acceleration of the fluid slug in the channel, and I_f is the inductance of the channel and is given by

$$I_f = \frac{l}{A} \quad (3.10)$$

where A and l are the cross-sectional area and length of the channel, respectively. Summing over the pressure drops, the governing equation for the channel becomes

$$\Delta p = \rho l_f \dot{Q} + RQ \quad \text{Canonical Flow Channel Equation} \quad (3.11)$$

Insight into the relative magnitudes of these terms may be gained by considering a representative channel and pump system. The volumetric flow rate of the pump can be approximated by

$$Q \sim V_d \cdot f \quad (3.12)$$

where V_d is the expected volume displacement (single-cycle) of the device and f is the pumping frequency. Making use of the relations in Table 1.5, the trends in flow regime versus pump scale can be determined; the results are shown in Figure 3.5. Here, all dimen-

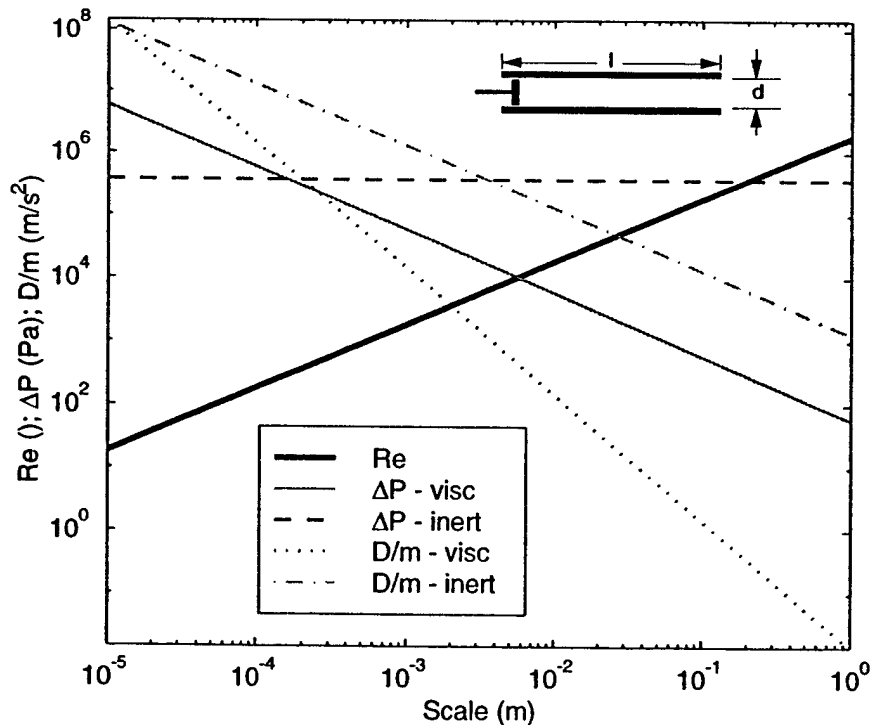


Figure 3.5 Effects of scale on fluid phenomena where pumping frequency varies according to $f \propto \lambda^{-1}$. The representative system is a straight tube with $l = 5$ mm, $d = 0.25$ mm; fluid is water; $V_d = 3.57 \times 10^{-11} \text{ m}^3$. D/m represents the drag force on a flat disc of arbitrary mass, m , with $d = 0.25$ mm oriented normal to the flow direction. The equations used to generate the curves are listed in Table 1.5.

sions are scaled equally and pumping frequency is assumed to increase according to equation (1.3). The equations used to generate the curves can be found in Table 1.5. Most noticeable in the plot and table is the scale invariance of the inertial pressure drop, which delineates a fundamental limit of microhydraulic systems. It suggests that, for a given MHST design with some maximum operational frequency, the same inertial pressure differential will be experienced at all scales, and may not be reduced without modifying the design (or lowering the frequency further below the limit). Also, a transition from inertial to viscous dominated pressure drops is seen as the scale is miniaturized below $\sim 10^{-4}$ m. The transition, combined with the constant inertial contribution, suggests that miniaturization beyond the transition point will eventually lead to a system where flow is entirely dominated by viscous effects. Two conclusions can be drawn: (1) both viscous and inertial terms must be included in the formulation of the flow equations if a consistent and versatile model is to be obtained, and (2) miniaturization past some scale will result in behavior that is dominated by viscous effects rather than inertial.

Active Valve

The valves are the means by which the flow is rectified. Figure 3.6 shows a diagram of the canonical component and its transfer function which relates the applied force and pressure difference to the flow. Valves are typically modeled with experimentally obtained quasistatic pressure-flow curves and, in some cases, by a bode plot of the flow gain [Isacsson et al., 1994], but because the performance of the MHST depends heavily on its component dynamics, valves especially, a fully dynamic model is required. Furthermore, as was the case for the channel model, the use of experimental data is precluded in the initial model formulation.

We begin by summing the forces hypothesized to act on the valve

$$m_v \ddot{x} + D_v(\dot{x}) + F_s(x) + F_p(\Delta p) + F_f(Q) + F_v = 0 \quad \text{Canonical Valve Equation} \quad (3.13)$$

where m_v is the modal mass of the valve, D_v represents the drag force on the valve due to its absolute velocity through the fluid, F_p is the force on the valve caused by the surround-

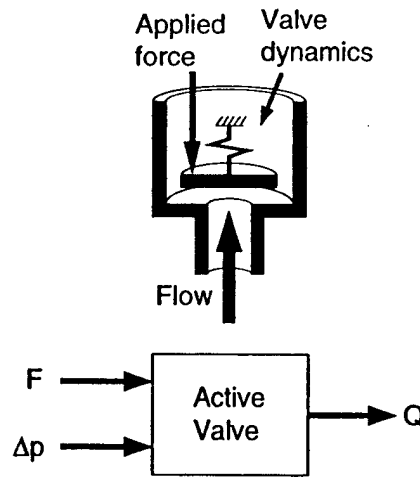


Figure 3.6 Canonical valve

ing pressures, F_f is the force resulting from the momentum transfer from the impinging fluid, and F_v is the externally applied actuation force. Contact between the valve and valve seat may be modeled via a spring force function

$$F_s(x) = \begin{cases} k_v(x - a) & x \geq \gamma \\ k_v(x - a) + k_{seat}(x - \gamma) & 0 < x < \gamma \end{cases} \quad (3.14)$$

where k_v is the stiffness of the valve, a is the valve travel (the distance from the valve disc to the seat when the valve is in its rest position), and k_{seat} is the estimated stiffness of the valve seat. It is assumed that $k_{seat} \gg k_v$. Since perfect sealing between the disc and seat is impossible because of material and manufacturing imperfections, the parameter γ represents the gap that exists when the valve is closed; estimating γ based on known surface finish or fabrication tolerances provides a means of estimating leakage. The spring force function is illustrated in Figure 3.7

In most cases the volume of fluid contained within the valve element is small compared to that within the flow channels, so that its corresponding inertia may be neglected. Valves do, however, contribute significantly to the viscous resistance encountered by the fluid.

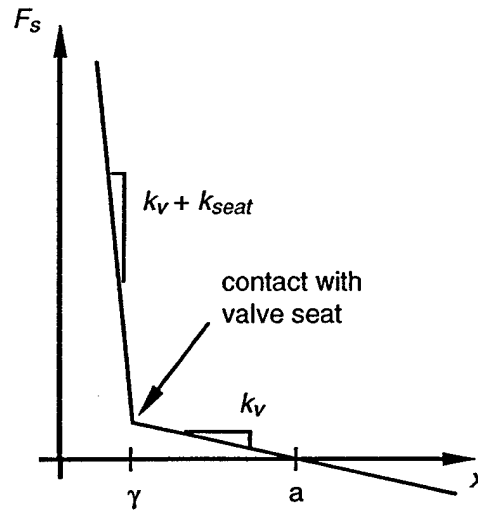


Figure 3.7 Spring force function

The operating frequency of the system is, in many cases, close to the valve resonance, meaning that the response time of the valve is of the same order of magnitude as the pump period. In such cases, a significant percentage of the flow cycle can occur while the valve is transitioning from a closed to an open position, or vice versa. The viscous resistance, then, must be taken to be a function of the valve deflection, and the equation governing flow through the valve is of the form

$$(\Delta p)_v = R_v(x)Q \quad (3.15)$$

where x is the position of the valve. The resistance function, $R_v(x)$, depends greatly on the valve geometry. The nature of the valve forcing functions appearing in (3.13) depend entirely on the valve geometry and will be further discussed in the following section.

3.2.5 Prototype System Model

This section deals with the application of the defined canonical component models to the MHST prototype design to arrive at a set of nonlinear ordinary differential equations that represent the integrated system.

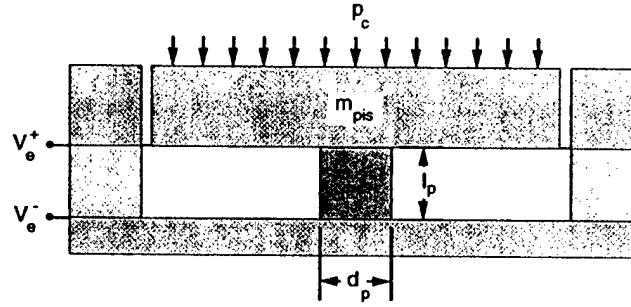


Figure 3.8 Drive piston assembly

Volume Source (Piezoelectric Drive Assembly)

The volume source in the prototype design is a cylindrical piezoelectric element bonded between a silicon plate and flexible membrane, as shown in Figure 3.8, with the poling vector parallel to the longitudinal axis. Using a Rayleigh-Ritz formulation (first extensional mode only) the piezoelectric sensor and actuator terms are found to be

$$\begin{aligned}
 m_p &= \frac{\rho_p A_p l_p}{3} & k_p &= \frac{c_{33}^E A_p}{l_p} \\
 \Theta &= \frac{e_{33} A_p}{l_p} & C_p &= \frac{A_p \epsilon_{33}}{l_p} \\
 B_f F(t) &= -p_c(t) A_{pis} & B_q &= 1
 \end{aligned} \tag{3.16}$$

where l_p and A_p are the length and cross-sectional area of the piezoelectric cylinder, respectively, ρ_p is the active material density, ϵ_{33} is a piezoelectric dielectric constant, c_{33}^E is a piezoelectric stiffness constant, e_{33} is a piezoelectric coupling constant, and A_{pis} is the area of the piston. The mass of the piston, m_{pis} , may be added to the modal mass of the piezoelectric cylinder, m_p , to obtain the effective mass of the drive mechanism

$$M = m_p + m_{pis} \tag{3.17}$$

Substituting these parameters into (3.3) and (3.4) yields the equations of motion for the pump subsystem and its circuitry

$$M\ddot{y} + b_p\dot{y} + k_py - \Theta V_p = -p_c A_{pis} \quad \text{Pump Actuator Equation} \quad (3.18)$$

$$\Theta y + C_p V_p = q_p \quad \text{Pump Sensor Equation} \quad (3.19)$$

where y is the deflection of the element (positive upward) and is related to the change in the control volume by

$$\Delta V = A_{pis}y \quad (3.20)$$

One percent structural damping was assumed for b_p . In the actuator case the voltage across the element is dictated, and (3.19) is not needed for simulation. It can be used, however, for post-simulation analysis of the electrical power flow to the element.

In the power harvester, voltage is a free variable and the sensor equation is required. The nature of the constituent terms depends on the power harvesting circuit used. In this work, the circuit shown in Figure 2.7 was modeled. It is assumed that the battery voltage is positive. Due to the nature of the diode bridge, three different cases must be considered based on the relative voltages across the piezoelectric element and the battery terminals. The resulting equations are

$$\begin{aligned} |V_p| \leq V_{batt} & \quad \dot{q}_{batt} = \dot{q}_p = 0 \\ V_p > V_{batt} & \quad \dot{q}_{batt} = -\dot{q}_p = \frac{V_p - V_{batt}}{R_b} \\ V_p < -V_{batt} & \quad \dot{q}_{batt} = \dot{q}_p = \frac{-V_p - V_{batt}}{R_b} \end{aligned} \quad (3.21)$$

where V_{batt} is the battery voltage, q_p is the charge on the piezoelectric, q_{batt} is the charge on the battery, and R_b is the internal resistance of the battery. For simplicity the bias voltage of the diodes has been omitted. The sign convention chosen in (3.2) is such that $\dot{q}_p, \dot{q}_{batt} > 0$ denotes current *into* the piezoelectric and battery, respectively. In the first case the voltage across the active element is less than the battery voltage and the diodes do not conduct. In the second case, the piezoelectric voltage is greater than that of the battery

and charge is transferred from the element to the battery. The same thing occurs in the third case, where the current follows a different path across the diode bridge. At all times during operation, the current into the battery is either zero or positive.

Pump Chamber

It is useful to derive an expression for the maximum, or blocked, pressure of the pump. The pump chamber equation requires no modification from the canonical form. Consider the case when there is no flow into or out of the pump chamber, and the volume source is statically pushing against the contained fluid. For simplicity we assume that there is no initial pump displacement. In this case the volume of fluid in the chamber is constant and we can neglect the ΔV term in the chamber capacitance. Integrating the remaining expression with respect to time we have

$$p_c = C_c \cdot \Delta V \quad (3.22)$$

If (3.18) is substituted into this expression by making use of the compatibility relation (3.20), an expression for the maximum pressure of the pump, p_{max} , is obtained

$$p_{max} = \left(\frac{\frac{\Theta/A_{pis}}{k_p} + 1}{C_c A_{pis}^2} \right) (V_p)_{max} \quad (3.23)$$

Here, the effects of chamber capacitance and hydraulic amplification on achievable pressure are visible in (3.23). In the limiting case of an infinitely stiff structure and an incompressible fluid, the expression reduces to the blocked stress of the piezoelectric, attenuated by the hydraulic amplification of the piston

$$(p_{max})_{ideal} = \frac{\Theta}{A_{pis}} (V_p)_{max} \quad (3.24)$$

Valves

To quantify the pressure forces acting on the valve, the pressure distribution surrounding it was lumped into discrete zones (Figure 3.9). Sections I and II are sections of the channels where the flow is governed by (3.11). The zone p_I may be either the low or high pressure reservoir, depending on which valve is being modeled; p_4 is the pressure in the chamber, p_c . Using this formulation, the total pressure difference from reservoir to chamber is

$$\Delta p_{14} = (\Delta p_{12})_{inert} + (\Delta p_{12})_{visc} + (\Delta p_{23})_{visc} + (\Delta p_{34})_{inert} + (\Delta p_{34})_{visc} \quad (3.25)$$

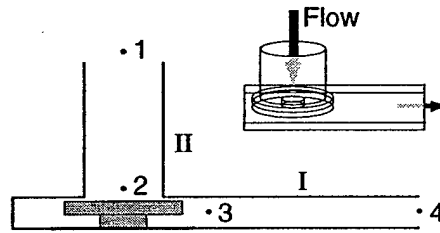


Figure 3.9 Lumped pressure zones

The volume of fluid between zones 2 and 3 is small compared to the other channels, and $(\Delta p_{23})_{inert}$ may be neglected.

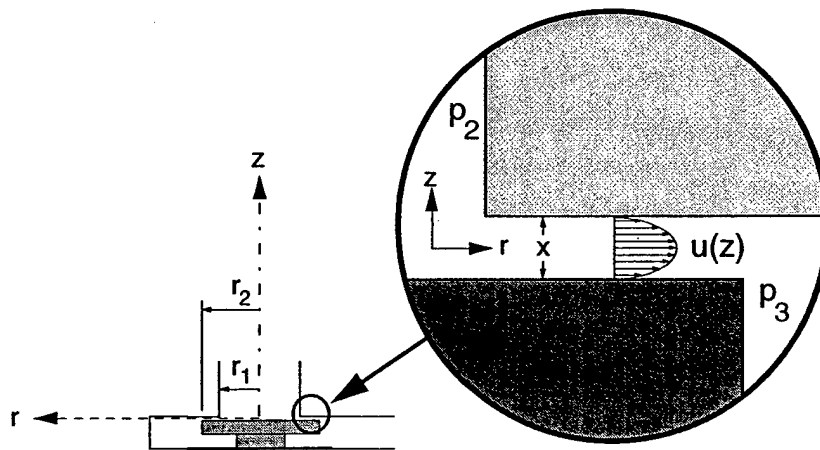


Figure 3.10 Detail of valve geometry and flow velocity distribution

The viscous flow resistance of the valve is derived by applying the Navier-Stokes equations to the region between the valve disc and seat. Referring to Figure 3.9, fluid moving in the direction shown must, after exiting section II, flow radially outward between the valve disc and seat until reaching point 3. Details of the geometry, the coordinate system used, and the flow velocity distribution are shown in Figure 3.10.

The radial component of the Navier-Stokes equation in polar coordinates (assuming constant density) is

$$\begin{aligned} & \rho \left(\frac{\partial u_r}{\partial t} + u_r \frac{\partial u_r}{\partial r} + \frac{u_\theta}{r} \frac{\partial u_r}{\partial \theta} - \frac{u_\theta^2}{r} + u_z \frac{\partial u_r}{\partial z} \right) \\ &= \rho g_r - \frac{\partial p}{\partial r} + \mu \left\{ \frac{\partial}{\partial r} \left(\frac{1}{r} \frac{\partial}{\partial r} [r u_r] \right) + \frac{1}{r^2} \frac{\partial^2 u_r}{\partial \theta^2} - \frac{2}{r^2} \frac{\partial u_\theta}{\partial \theta} + \frac{\partial^2 u_r}{\partial z^2} \right\} \end{aligned} \quad (3.26)$$

The equation simplifies greatly if a steady flow approximation is made by setting the time derivative equal to zero. Additionally, flow in the θ and z directions may be neglected because of symmetry. Equation (3.26) then reduces to

$$\rho u_r \frac{\partial u_r}{\partial r} = - \frac{\partial p}{\partial r} + \mu \frac{\partial^2 u_r}{\partial z^2} \quad (3.27)$$

The continuity equation in polar coordinates is given by

$$\frac{1}{r} u_r + \frac{\partial u_r}{\partial r} = 0 \quad (3.28)$$

Because the flow is radial and viscous it is logical to guess that the velocity is a function of r and z . If a separable function $u(r, z) = R(r)Z(z)$ is introduced, and a parabolic velocity profile is assumed that satisfies the no slip conditions at the vertical boundaries

$$Z(z) = \left(z^2 - \left[\frac{x}{2} \right]^2 \right) \quad (3.29)$$

then substitution of (3.28) and (3.29) into (3.27) yields an expression for the pressure gradient. Integrating with respect to r we obtain

$$p(r, z) = 2\mu c_1 \ln(r) - \frac{\rho c_1^2}{2r^2} \left(z^4 - 2z^2 \left[\frac{x}{2} \right]^2 + \left[\frac{x}{2} \right]^4 \right) + \Psi(z) + c_2 \quad (3.30)$$

where $\Psi(z)$, c_1 , and c_2 are unknown. Because $x/2 \ll 1$, higher powers of the quantity may safely be neglected. Furthermore, if the pressure is assumed constant across z , so that $p = p(r)$, then (3.30) simplifies to

$$p(r) = 2\mu c_1 \ln(r) + c_2 \quad (3.31)$$

Applying the pressure boundary conditions at points 2 and 3, and solving for c_1 and c_2 , the pressure distribution is obtained

$$p(r) = p_3 + \frac{(p_2 - p_3) \ln(r/r_2)}{\ln(r_1/r_2)} \quad r_1 \leq r \leq r_2 \quad (3.32)$$

and the velocity profile is

$$u(r, z) = \frac{(p_2 - p_3)}{2\mu r \ln(r_1/r_2)} \left(z^2 - \left[\frac{x}{2} \right]^2 \right) \quad (3.33)$$

The velocity profile may be integrated over x to obtain the volumetric flow rate

$$Q = 2\pi r \int_{-x/2}^{x/2} u(r, z) dz = \frac{\pi x^3}{6\mu \ln(r_2/r_1)} (p_2 - p_3) \quad (3.34)$$

Comparison of (3.34) with (3.15) provides the viscous flow resistance of the valve

$$R_v(x) = \frac{6\mu \ln(r_2/r_1)}{\pi x^3} \quad (3.35)$$

The total force on the valve disc may then be obtained by integrating the pressure distribution on the disc over its area

$$\begin{aligned}
 F_p(p_2, p_3) &= \int_{A_{r_1}} p_2 dA + \int_{A_{r_1-r_2}} p(r) dA \\
 &= \left(\pi r_2^2 + \frac{(r_1^2 - r_2^2)\pi}{2 \ln(r_2/r_1)} \right) p_3 - \left(\frac{(r_1^2 - r_2^2)\pi}{2 \ln(r_2/r_1)} \right) p_2
 \end{aligned} \tag{3.36}$$

Pressures p_2 and p_3 can be calculated during system simulation by utilizing the known states p_1 and/or p_4 , Q , \dot{Q} , and equation (3.11). Due to the pressure-balanced valve design there is no net force on the valve resulting solely from p_3 .

The fluidic drag acting on the valve is the most difficult force to model because the nature of the local fluid behavior is unknown. Luckily, the use of actuated valves reduces the model's sensitivity to error. What follows is considered to be the best possible approximation, and must be updated with experimental data when possible. Referring to Table 1.5, the drag force on the valve may be either Stokes (viscous) or pressure (inertial) dominated, depending on the Reynolds number. Because the valve may traverse a wide range of velocities through a single cycle, both terms are retained, ensuring that the dominant force (i.e. the force that limits the valve's performance) is present. The inertial drag force is given by

$$D_{inert} = \frac{1}{2} \rho A_v C_d \dot{x}^2 \tag{3.37}$$

where C_d is the drag coefficient for a disc perpendicular to the flow direction ($C_d \sim 1.17$), and A_v is the area of the disc. The corresponding viscous (Stokes) drag force is

$$D_{visc} = 8\mu d_v \dot{x} \tag{3.38}$$

where d_v is the diameter of the disc. The total approximated drag force is then

$$D_v = D_{inert} + D_{visc} \tag{3.39}$$

where it can be seen that, because (3.37) is a function of the square of the velocity, but (3.38) is linear, for $\dot{x} \ll 1$ the viscous term will dominate. Likewise, higher velocities (cor-

responding to higher Reynolds numbers) will cause the disc to experience primarily the inertial term.

Initial simulations showed, however, that under certain conditions lightly damped, high frequency oscillations were observed in the valve's time history. Although the oscillations, which occurred when the valve was open, were normally of small amplitude and did not affect the overall system behavior, it was felt that, in the physical system, the fluid surrounding the valve cap would, in fact, heavily damp the oscillations through some mechanism not captured by (3.39). For this reason, critical damping ($\zeta = 1$) was added to the valve by augmenting D_{visc} .

Referring to Figure 3.9 and equation (3.13), the momentum transfer force, F_f , arises when the fluid flows around the corner near the valve. To evaluate the force, a control volume may be drawn around the valve disc and seat, and conservation of momentum applied. For the case when the flow direction in section II is antiparallel to the valve surface normal (i.e. fluid is flowing down section II toward the valve cap), the fluid impinges against the cap and the resulting force (assuming steady flow conditions) is given by

$$F_f = \frac{\rho}{A_{II}} Q^2 \quad (3.40)$$

where A_{II} is the cross-sectional area of channel section II. While it is possible to include unsteady flow effects in this formulation, their presence gives rise to numerically sensitive acceleration terms which, it was found, led to errors when the equations were integrated. Comparison of results with and without these added terms showed that they are not required and may, in this case, be neglected. When the flow in section II is parallel to the surface normal (i.e. flowing up section II away from the cap) then the change in momentum of the fluid is reacted by the wall to the left of the valve, and the valve disc does not experience a significant force. Therefore, the total momentum force can be written as

$$F_f = \begin{cases} \frac{\rho}{A_{II}} Q^2, & \text{antiparallel flow} \\ 0, & \text{parallel flow} \end{cases} \quad (3.41)$$

Flow Channels

Equation (3.25) can be used to derive the governing equations for the inlet and outlet channels. Making multiple substitutions of equation (3.11) into this expression, we obtain an expression for the total pressure drop across the channel

$$\Delta p = \rho I_f \dot{Q} + R Q \quad (3.42)$$

where the channel inductance is now

$$I_f = \frac{l_I}{A_I} + \frac{l_{II}}{A_{II}} \quad (3.43)$$

and where $(-)_I$ and $(-)_{II}$ refer to the channel sections described Figure 3.9, and R is the total viscous resistance of the channel

$$R = R_I + R_{II} + R_v(x) \quad (3.44)$$

Integrated System Model

The above component equations can be assembled, using compatibility and equilibrium relations, to create a model of the prototype MHST, represented in Figure 3.11. For completeness, the equations comprising the system model are summarized below:

Pump Chamber Continuity:

$$\dot{p}_c = \left(\frac{V_o - \Delta V}{K_f} + \frac{1}{C_s} \right)^{-1} \cdot (\Delta \dot{V} + Q_i - Q_o)$$

$$\Delta V = A_{pis} y$$

Drive Piston Dynamics:

$$M\ddot{y} + b_p\dot{y} + k_py - \Theta V_p = -p_c A_{pis}$$

$$m_p = \frac{\rho_p A_p l_p}{3} \quad k_p = \frac{c_{33}^E A_p}{l_p}$$

$$\Theta = \frac{e_{33} A_p}{l_p} \quad C_p = \frac{A_p \epsilon_{33}}{l_p}$$

$$M = m_p + m_{pis}$$

Inlet (i) and Outlet (o) Valve Dynamics:

$$\begin{aligned} m_i \ddot{x}_i + D_v(\dot{x}_i) + F_s(x_i) + F_p(\Delta p_i) + F_f(Q_i) + F_{v_i} &= 0 \\ m_o \ddot{x}_o + D_v(\dot{x}_o) + F_s(x_o) + F_p(\Delta p_o) + F_f(Q_o) + F_{v_o} &= 0 \end{aligned}$$

$$D_v = \frac{1}{2} \rho A_v C_d \dot{x}^2 + 8 \mu d_v \dot{x}$$

$$F_s = \begin{cases} k_v(x-a) & x \geq \gamma \\ k_v(x-a) + k_{seat}(x-\gamma) & 0 < x < \gamma \end{cases}$$

$$F_p = \left(\pi r_2^2 + \frac{(r_1^2 - r_2^2)\pi}{2 \ln(r_2/r_1)} \right) p_3 - \left(\frac{(r_1^2 - r_2^2)\pi}{2 \ln(r_2/r_1)} \right) p_2$$

$$F_f = \begin{cases} \frac{\rho}{A_{II}} Q^2, & \text{antiparallel flow} \\ 0, & \text{parallel flow} \end{cases}$$

Inlet (i) and Outlet (o) Channel Dynamics:

$$p_{lpr} - p_c = (\rho I_f \dot{Q}_i + R_i Q_i)$$

$$p_c - p_{hpr} = (\rho I_f \dot{Q}_o + R_o Q_o)$$

$$I_f = I_I + I_{II} = \frac{l_I}{A_I} + \frac{l_{II}}{A_{II}}$$

$$R_{i,o} = R_I + R_{II} + R_{v_{i,o}}(x) = \frac{128\mu l_I}{\pi d_{h_I}^4} + \frac{128\mu l_{II}}{\pi d_{h_{II}}^4} + \frac{6\mu \ln(r_2/r_1)}{\pi x_{i,o}^3}$$

Rectification Circuit (power harvester only):

$$\begin{aligned} \Theta y + C_p V_p &= q_p \\ |V_p| \leq V_{batt} \quad \dot{q}_{batt} &= \dot{q}_p = 0 \\ V_p > V_{batt} \quad \dot{q}_{batt} &= -\dot{q}_p = \frac{V_p - V_{batt}}{R_b} \\ V_p < -V_{batt} \quad \dot{q}_{batt} &= \dot{q}_p = \frac{-V_p - V_{batt}}{R_b} \end{aligned}$$

The actuator model has 9 states and the power harvester has 10. The block diagrams used to implement the equations in Simulink are included in Appendix B.

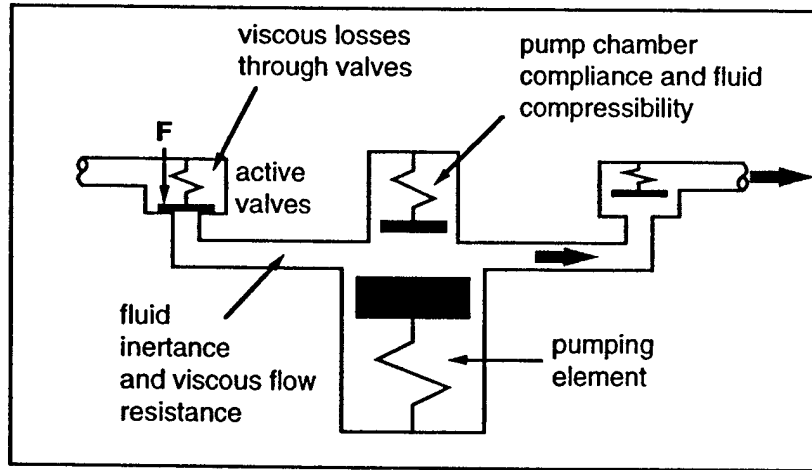


Figure 3.11 Integrated system model

3.3 Finite Element Analysis

Finite element models of the MHST subsystems were created and analyzed to augment the theoretical model. The specific objectives of the analysis were:

- Subsystem design

- Investigation of static and modal responses (structural and acoustic)
- Stress analysis
- Provide numerical values for model parameters

Prototype geometries for the drive and valve subsystems were analyzed to determine crucial design parameters, and eventually to optimize the designs with respect to the performance metrics. Optimization was concurrent with an investigation of the modal responses of the component structures and the acoustic modes in the fluid chambers. Stress analyses were performed on all relevant structural members to ensure design feasibility. After design finalization, numerical values were obtained for the unknown model parameters (e.g. chamber elasticity, valve stiffness and modal mass, and valve actuation force) and fed into the integrated system simulation.

2-D axisymmetric finite element models for the drive and valve subsystems were created and analyzed using the ANSYS² analysis package. The mesh used for the valve is shown in Figure 3.12. To model the pump subsystem a similar mesh is used, with the only difference being the absence of the valve diaphragm and cap structures. The model employed 4-node coupled-field solid plane elements for the active element, 4-node structural solid plane elements for the chamber and piston structures, 4-node acoustic fluid elements for the enclosed fluid, and 2-node axisymmetric structural shell elements for the diaphragms. The code (batch files) used to create and analyze the mesh is included in Appendix D of this report. Four batch files were used: (1) valve (and drive piston) geometry and mesh definition code, (2) static analysis code, (3) pump diaphragm substructure geometry and mesh definition and analysis code, and (4) valve diaphragm substructure geometry and mesh definition and analysis code.

Since the critical stress regions for the design are the diaphragms and their tether points, it is desirable to model them using plane elements through the thickness so that data may be obtained indicating the stresses in the members and at the corner stress concentrations.

2. ANSYS version 5.3, Swanson Analysis Systems, Inc., P.O. Box 65, Johnson Road, Houston, PA 15342-0065

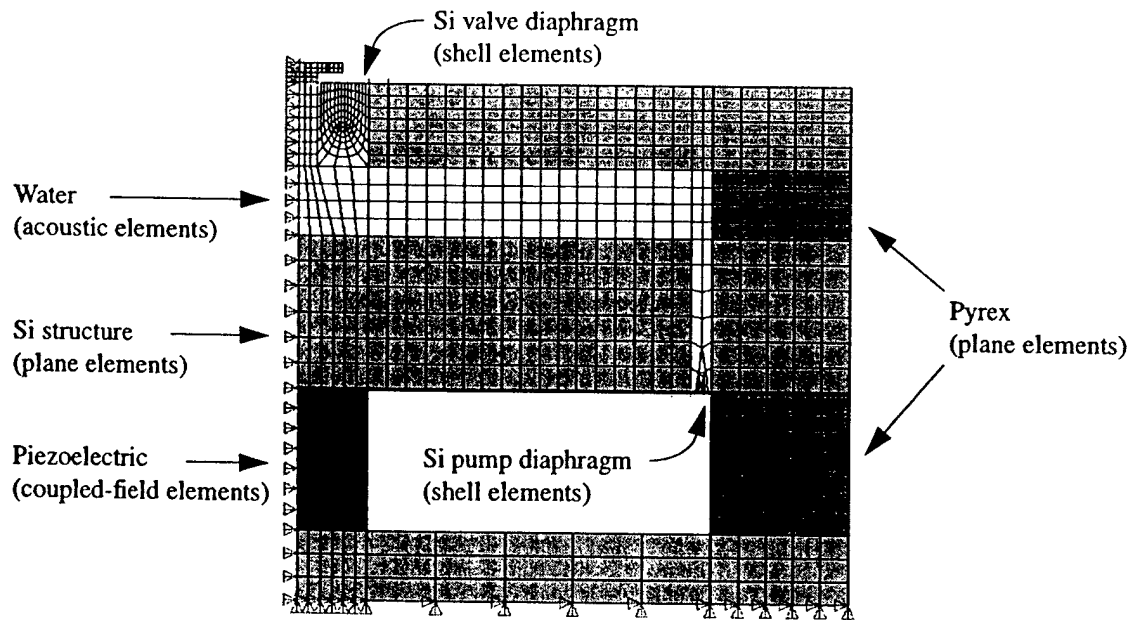


Figure 3.12 Finite element model of valve (axisymmetric)

However, the high aspect ratios of these components makes them difficult to mesh without generating an enormous number of DOFs, resulting in analyses that are time consuming and, in some cases, impossible (given computer memory limitations). Axisymmetric shell elements exist in ANSYS that can be used to model the diaphragms more accurately and with fewer degrees of freedom, but they are incapable of predicting stress concentrations.

The solution used in this work was to create a substructured model, wherein a mesh was created of the full valve structure using shell elements for the diaphragms. In addition, separate submodels of only the diaphragms and their attachment regions were constructed using plane elements. The full model sufficed for modal analyses. For static stress analyses, the full model was first employed to obtain nodal solutions. This data, specifically, the translations of the nodes of the elements adjoining the diaphragm shells and the hydrostatic chamber pressure, were then imported to the submodels and applied as DOF constraints. Detailed stress concentration results are thus obtainable while maintaining model efficiency.

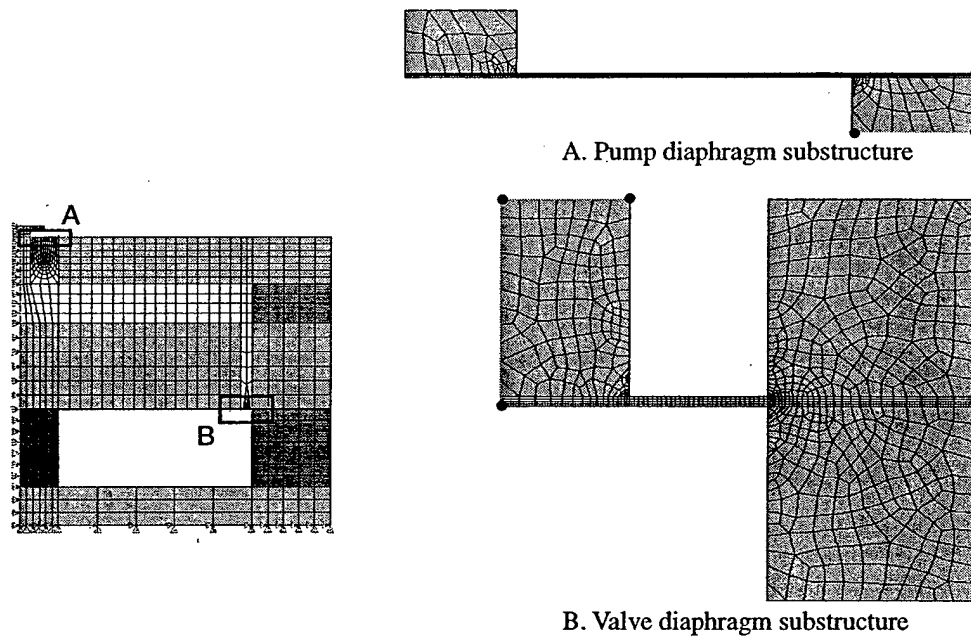


Figure 3.13 Substructures used for stress analysis. Key nodes are highlighted.

Creation of the full model in this manner involved the formulation of additional constraint equations because each node of the shell elements had 2-D translation and rotation DOFs, while the plane elements of the adjoining structure had only translation. By extending the shell elements into the structure, and coupling the rotational degrees of freedom of adjacent shell nodes together, the variables were eliminated and the diaphragms became effectively cantilevered.

Geometric consistency was maintained between full- and submodels by meshing them such that the nodes of the elements coupled to the shells in the full model corresponded geometrically to key nodes of the submodels. The constraints were applied at these nodes, with the intermediate nodes subject to a linear interpolation.

Numerical experiments using the finite element model provided values for those model parameters that are difficult to estimate. They are are

1. structural pump chamber capacitance, C_s
2. valve stiffness, k_v
3. valve modal mass, m_v
4. effective area of valve diaphragm, A_{eff}

The pump chamber capacitance was computed by applying a voltage to the piezoelectric element in the pump model, with fluid contained within the closed chamber, and measuring the resulting pressure, p_c . Since there is no flow ($Q_i = Q_o = 0$), and the volume of fluid in the chamber, V_o , is known from the geometry, then equations (3.5, 3.18, 3.20) can be used to solve for C_s :

$$C_s = \left(\frac{A_{pis} \Theta V_p - A_{pis}^2 P}{k_p p_c} - \frac{V_o}{K_f} \right)^{-1} \quad (3.45)$$

The effective valve stiffness, k_v , can be computed either directly or indirectly from the valve model; both were performed to check consistency. To calculate k_v directly, an external force was applied to the valve by applying a pressure to the nodes comprising the surface of the valve cap and measuring the resulting deflection. To calculate k_v indirectly the free stroke and blocked force of the valve were used. The free stroke, x_{fr} , was computed by applying a voltage across the piezoelectric and observing the deflection. The blocked force, F_b , was obtained using a similar procedure: the vertical displacement of the valve cap was constrained to zero, and the reaction force on the cap was measured. The stiffness of the valve was then derived using the relation

$$k_v = \frac{F_b}{x_{fr}} \quad (3.46)$$

The modal mass of the valve, m_v , was obtained by comparing f_n , the frequency at which the first vibration mode occurred (using an eigenvalue solution), with the valve stiffness, k_v . The mass is then given by

$$m_v = \frac{k_v}{(2\pi f_n)^2} \quad (3.47)$$

The effective area of the diaphragm, A_{eff} , was calculated by applying a pressure, p , to the fluid in the valve hydraulic chamber, with the valve cap blocked, and measuring the reaction force, F_b , on the valve vap. Since the total reaction force is the sum of the forces acting on the cross-sectional area of the valve stem (the short cylinder between the cap and the diaphragm, see Figure 2.6) and the effective area of the diaphragm, A_{eff} , was computed as

$$A_{eff} = \frac{F_b}{p} - A_{stem} \quad (3.48)$$

Although the numerical characteristics of the 1 cm and 1 mm prototype mechanism designs are discussed in Chapters 4 and 5 of this report, the values that were obtained using the preceding methods are listed below

TABLE 3.2 Model parameter values obtained from finite element analysis.

| System scale (λ) | C_s (Pa/m ³) | k_v (N/m) | m_v (g) | A_{eff} (mm ²) |
|----------------------------|----------------------------|-------------|-----------|------------------------------|
| Mesoscale (1) | 7.09e17 | 2727 | 1.26e-4 | 0.25 |
| Microscale (0.1) | 7.09e20 | 272.2 | 1.26e-7 | 0.0025 |

3.4 Summary

This chapter presented the derivation of generalized fluidic component models, then showed the application of these models to the prototype design to arrive at an integrated system model. The first section of the chapter discussed the requirements of the model and the issues involved, especially the dependence of fluid behavior on system scale. The relevant assumptions were then set forth, from which canonical fluidic component models were derived which highlighted the relations of important design parameters such as chamber capacitance, fluid inertia, flow resistance, and so forth. The canonical models were then applied to the design to arrive at a set of equations that fully describe the

dynamic behavior of the MHST. Finally, the creation of a finite element model for the purposes of design optimization and augmentation of the theoretical model was detailed.

Chapter 4

OPTIMIZATION AND ANALYSIS

4.1 Introduction

MHSTs are extremely nonlinear systems capable of complex fluid-structure dynamic coupling. For this reason the performance of a given design is difficult to determine without numerical simulation of the entire system model. Such simulations are computationally intensive and, in some cases, provide results that are of limited usefulness without a deeper understanding of the fundamentals involved. For these reasons the design of the constituent components is difficult. The goal of this chapter is to present methods, both static and dynamic, whereby the behavior of the system can be understood and evaluated, and to apply these methods with the intent of optimizing the design described in Chapter 2. The objectives of this chapter are:

- Definition of a canonical hydraulic coupler to identify the important parameter involved and illustrate their associated trends
- Introduction of *Mechanical Efficiency* as a static analysis and design tool
- Optimization of the chosen design
- Derivation of the equations of motion for time intervals where the system behavior is nearly linear in order to predict dominant frequencies
- Presentation of the equations necessary for energy tracking with respect to the simulation results
- Definition of the energy-based metrics that will be used to evaluate performance during the subsequent parameter study

The first steps in component design optimization is the identification of important parameters and the definition of suitable performance functions based on these variables. Insight into the procedure is sometimes gained if a representative section is introduced that permits a more straightforward analysis yet captures the essential behavior of the actual device. The principle function of the fluid and structural elements in the MHST is to couple the piezoelectric elements to their respective loads. For example, the fluid and chamber comprising the valve hydraulics couple the piezoelectric element to the valve cap and diaphragm. The representative section is therefore a hydraulic coupler that uses a working fluid to connect a piezoelectric actuator to its mechanical load. The first section of this chapter deals with the definition and analysis of a generalized hydraulic coupler, identification of the key parameters, and evaluation based on mechanical coupling efficiency. Trends are shown relating the mechanical efficiency of the device to nondimensional parameters describing the relative physical parameters of the actuator-coupler mechanism. It is shown that the performance of the coupler is highly dependent on its structural elasticity.

The middle section of the chapter deals with the optimization of the valve geometry (the drive piston geometry is identical). Several potential designs are introduced and a final is chosen for the prototype. The performance of the pump is then examined from a static standpoint by comparing the maximum achievable pressure to the ideal.

The latter part of the chapter presents tools with which the integrated system can be analyzed from a dynamic standpoint. A derivation of the governing state-space equations during time intervals when the system behaves linearly is performed, permitting calculation of the dominant system resonances. A discussion of energy tracking in MHSTs follows, along with equations quantifying the input, output, dissipated, and stored energies in the devices. The primary performance metrics, namely, power density and efficiency, are then defined in terms of the energy equations.

4.2 Geometry Optimization

4.2.1 Canonical Hydraulic Coupler

The generic hydraulic coupler, illustrated in Figure 4.1, consists of two rigid pistons, an elastic tube, and a contained compressible working fluid. The tube has an inner radius, r , a wall thickness, t_w , a length, L , a density, ρ_t , and a modulus of elasticity, E_t . The contained fluid column has a density, ρ_f and bulk modulus, K_f . We define the active material element to be a cylinder with a length, l , a density, ρ_{act} , and a radius that is equal to the inner radius of the tube. For simplicity no hydraulic amplification is present and the pistons are of equal area.

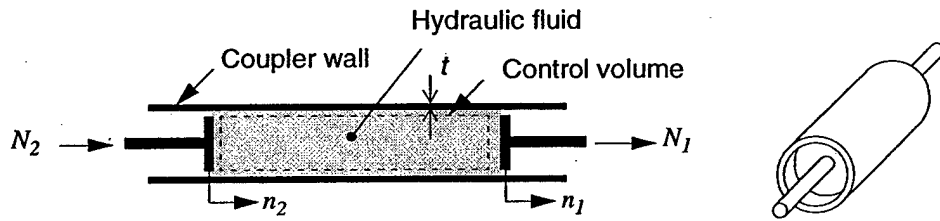


Figure 4.1 Canonical hydraulic coupler

The device has two generalized displacements, n_1 and n_2 , and two corresponding generalized forces, N_1 and N_2 . The forces and displacements in the coupler are related by

$$N = \begin{bmatrix} N_1 \\ N_2 \end{bmatrix} = \begin{bmatrix} k_{11} & k_{12} \\ k_{21} & k_{22} \end{bmatrix} \begin{bmatrix} n_1 \\ n_2 \end{bmatrix} = Kn \quad (4.1)$$

The coupler is connected to the load at DOF 1, and the piezoelectric actuator is connected to the coupler at DOF 2. The piezoelectric actuator characteristics are given by

$$N_{act} = k_{act}n_{act} + N_b \quad (4.2)$$

where N_{act} is the force on the actuator, k_{act} is the stiffness of the actuator, n_{act} is the actuator displacement, and N_b is the blocked force capability of the actuator. By compatibility and equilibrium

$$\begin{aligned} n_{act} &= n_2 \\ N_{act} &= -N_2 \end{aligned} \quad (4.3)$$

Actuation Energy

The actuation energy of the actuator-coupler mechanism is defined as

$$U_{act} = \frac{1}{2}(N_1)_b \cdot (n_1)_{fr} \quad (4.4)$$

where $(N_1)_b$ and $(n_1)_{fr}$ are the blocked force and free deflection capabilities of the mechanism, respectively. Use of actuation energy as a valve performance metric provides a convenient means to favor those designs possessing both large valve deflections and high actuation authority.

Mechanical Efficiency

The effectiveness of the coupler depends on the stiffness of the tube structure and the compressibility of the working fluid. Any compliance that exists in the system will absorb energy during actuation and reduce the force at the output. In 1997 Precht and Hall presented a method for evaluating actuator-load couplers by defining the mechanical coupling efficiency of the mechanism as

$$\eta_{mech} = \frac{k_{12}^2 k_{act}}{k_{11}(k_{act} + k_{22})^2 - k_{12}^2(k_{act} + k_{22})} \quad (4.5)$$

where k_{act} is the stiffness of the piezoelectric actuator and is given by

$$k_{act} = \frac{E_{act} A}{l} \quad (4.6)$$

The quantity represents the ratio of actuation energy output to the work supplied by the actuator. If mass conservation is applied to the coupler control volume using the same assumptions stipulated for the pump chamber in Chapter 3, an expression for the force at the output is obtained

$$N = \left(\frac{AL}{K_f} + \frac{1}{C_s} \right)^{-1} (A^2 n_1 - A^2 n_2) \quad (4.7)$$

where A is the cross-sectional area of the tube bore and the actuator. The pistons are of equal area so the force, N , is the same at both. An expression for the structural tube capacitance, C_s , can be obtained by considering the hoop stress in the shell

$$C_s = \frac{Et}{2\pi L r^3} \quad (4.8)$$

The stiffness terms for the coupler (tube and fluid) are obtained by comparing (4.7) with (4.1)

$$\begin{aligned} k_{11} &= k_{22} = C_a A^2 \\ k_{12} &= k_{21} = -C_a A^2 \end{aligned} \quad (4.9)$$

where C_a is the total capacitance of the system corresponding to the premultiplying term in (4.7). Recognizing that the actuator and coupler constitute springs in series, we can write the equivalent stiffness of the coupler-actuator mechanism, k_{eff} as

$$k_{eff} = \frac{k_{11} k_{act}}{k_{11} + k_{act}} = \frac{E_{act} A^2 C_a}{E_{act} + A I C_a} \quad (4.10)$$

Inserting (4.9) into (4.5) the mechanical efficiency becomes

$$\eta_{mech} = \frac{1}{\frac{k_{act}}{k_{11}} + 1} \quad (4.11)$$

where it can be seen that the mechanical efficiency can be made arbitrarily close to unity by making the coupler arbitrarily stiff. Expanding (4.11) in terms of the design variables we obtain

$$\eta_{mech} = \left[E_{act} \left(\frac{L}{l} \right) \left(\frac{1}{K_f} + \frac{2r}{E_t t_w} \right) + 1 \right]^{-1} \quad (4.12)$$

If we define the following non-dimensional parameters

$$l^* = \frac{L}{l} \quad r^* = \frac{r}{t_w} \quad e^* = \frac{E_{act}}{E_t} \quad k^* = \frac{E_{act}}{K_f} \quad (4.13)$$

then (4.12) may be recast as

$$\eta_{mech} = [l^*(k^* + 2e^*r^*) + 1]^{-1} \quad (4.14)$$

Figure 4.2 shows the dependence of mechanical efficiency on the design parameters. It can be seen in plot (a) that, for cases when the actuator, structure, and fluid are of comparable stiffness, it is impossible to achieve a reasonable efficiency using a thin-walled tube unless the coupler is extremely short. However, as r^* becomes small (corresponding to the case of a fluid channel embedded in a rigid solid medium) the requirements on l^* become somewhat relaxed. Additionally, plot (b) indicates the need for extremely stiff coupler materials to achieve high efficiencies, even when the geometry aspect ratios approach unity.

Further insight may be gained by looking at the effects that different materials have on the mechanical efficiency of a hypothetical coupler design. Consider a cylindrical piezoelectric actuator with a diameter and length of 1 cm, and a coupler tube with a length of 1 cm, an inner diameter of 1 cm, and a wall thickness of 1 mm. Table 4.1 shows the mechanical efficiencies of the hypothetical design using different engineering materials and liquids. It is clear that the mechanism has an inherently low efficiency, a result of the high stiffness of the piezoelectric actuator.

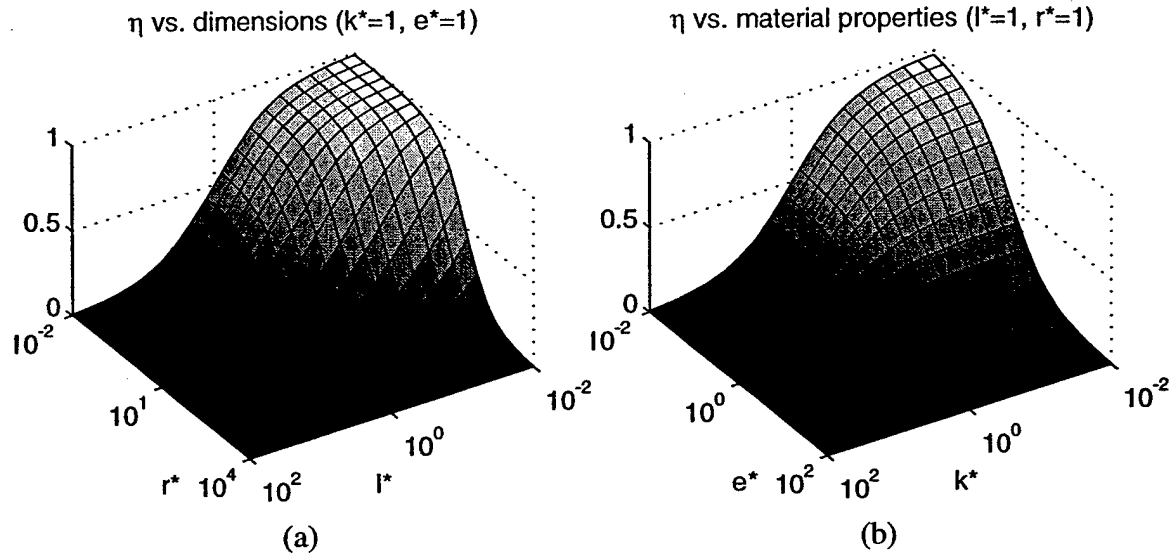


Figure 4.2 Mechanical efficiency versus the geometric parameters l^* and r^* and the material parameters e^* and k^* . Plot (a) varies l^* and r^* while keeping the material parameters arbitrarily fixed at $e^*=k^*=1$. Plot (b) varies e^* and k^* while keeping the geometric parameters arbitrarily fixed at $l^*=r^*=1$.

TABLE 4.1 Mechanical efficiencies of hypothetical coupler using various materials (%).

| Liquid | Tube material | | | |
|------------------|---------------|-----------------|-----|------|
| | Al | Stainless steel | Si | SiC |
| H ₂ O | 1.4 | 1.7 | 1.7 | 1.8 |
| Hg | 4.5 | 8.6 | 8.6 | 13.6 |

Although no dynamic effects were considered in their formulation, the actuation energy and coupling efficiency of a hydraulic component are effective tools for initial MHST design optimization. High bandwidth microhydraulic systems possess an inherent design conflict: in cases where component actuation occurs through elastic deformation of a structural member it is desirable to make the member very compliant, thereby maximizing the deflection, but minimum bandwidth specifications place a lower bound on structural stiffnesses. The insight gained from the analysis of the canonical coupler is useful when evaluating the valve mechanism as a hydraulic coupler between the active valve element and the fluidic load it acts against. In this instance, the valve superstructure acts as a spring in parallel with the active element and restricts the piezoelectric's deflection. If the coupler is made completely rigid a perfect efficiency is possible, but this would prevent motion at

the output (the valve cap) and U would be zero. Likewise, a flexible superstructure would permit large output deflections but possess very little closing force, resulting in a poor efficiency. Precht and Hall show that an optimum coupling efficiency exists, η_{mech}^* , when there is a mechanical impedance match between the active element and the coupler; this optimal value is given by [Precht and Hall, 1997]

$$\eta_{mech}^* = \frac{\bar{k}_{12}^2}{2 - \bar{k}_{12}^2 + 2\sqrt{1 - \bar{k}_{12}^2}} \quad (4.15)$$

where

$$\bar{k}_{12} = \frac{k_{12}}{\sqrt{k_{11}k_{22}}} \quad (4.16)$$

Although design restrictions stemming from dynamic effects may prohibit attainment of this optimum, the use of U_{act} and η_{mech} as performance metrics, in conjunction with other considerations, constitutes a useful design methodology for MHST valves.

4.2.2 Prototype

Valve

The objective in designing MHST valves is to create an efficient mechanism capable of large deflections, large actuation forces, and high bandwidth. Because of the importance of nonlinear dynamic effects, ultimate evaluation of any valve design must be made by considering its performance in the system simulation. The valve design procedure, then, is an iterative process whereby a geometry is created based on estimates of the required parameters, modeled and evaluated using finite element methods, simulated in the system model to assess performance, then modified for improvement.

Performance Optimization

The goal for the prototype was to design a valve, based on the size and geometry described in Chapter 2, that was capable of at least 20 μm free deflection and 20 kHz operation (values arrived at through estimation and intuition). The design procedure was then translated into an optimization of the actuation energy and mechanical efficiency subject to these constraints. After several random iterations, six potential valve designs were selected for closer study. Table 4.2 summarizes the best performance of each design. The procedure used to identify the optimum values is presented below using Design 6, the one selected, as an example.

TABLE 4.2 Comparisons of six considered valve designs^a

| VALVE DESIGN | 1 | 2 | 3 | 4 | 5 | 6 | |
|--------------------------------------|------|------|------|------|------|------|---------------|
| Variables | | | | | | | |
| diameter - outer | 8.0 | 8.0 | 4.0 | 4.0 | 8.0 | 8.0 | mm |
| diameter - piston (db) | 5.7 | 5.7 | 2.8 | 2.8 | 5.7 | 5.7 | mm |
| height - hydraulic chamber | 0.6 | 0.6 | 0.6 | 0.6 | 0.6 | 1.1 | mm |
| height - piezoelectric | 1.0 | 0.5 | 1.0 | 0.5 | 1.0 | 1.0 | mm |
| diameter - piezoelectric | 2.0 | 2.0 | 1.0 | 1.0 | 1.0 | 1.0 | mm |
| diameter - hydraulic chamber | 6.0 | 6.0 | 3.0 | 3.0 | 6.0 | 6.0 | mm |
| diameter - valve membrane (dv) | 1.0 | 1.0 | 0.7 | 0.7 | 1.0 | 1.0 | mm |
| Structure | | | | | | | |
| Valve mechanism mass | 0.32 | 0.28 | 0.08 | 0.07 | 0.30 | 0.36 | g |
| Hydraulic amplification | 38 | 29 | 25 | 26 | 48 | 60 | |
| First resonance | 27 | 27 | 66 | 66 | 23 | 27 | kHz |
| Performance | | | | | | | |
| Applied electric field | 1.0 | 1.0 | 0.7 | 1.0 | 1.0 | 0.8 | kV/mm |
| Valve deflection | 65 | 20 | 29 | 18 | 77 | 78 | μm |
| k_p/k_{11} | 38 | 49 | 12 | 19 | 12 | 8 | |
| Actuation energy density, U_{act} | 20 | 2 | 54 | 26 | 23 | 23 | mJ/kg |
| Mechanical efficiency, η_{mech} | 1.2 | 0.3 | 6.8 | 4.0 | 5.9 | 10.6 | % |

a. Design 6 selected for the baseline system

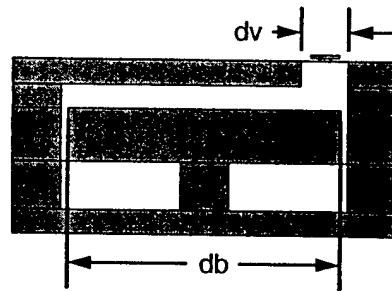


Figure 4.3 Primary valve design dimensions

The valve was designed with prototype fabrication in mind and many of the initial dimensions were arbitrarily chosen (see Chapter 2). Initial FEM analyses indicated that the valve performance was particularly sensitive to two dimensions: the piston diameter, db , and the valve membrane diameter, dv , shown in Figure 4.3. Optimization of the geometry with respect to these variables was performed assuming all other dimensions were fixed. The results are shown in Figure 4.4. When dv is made small, the clamped boundary conditions caused by the adjoining structures restrict its deflection and the resulting actuation energy is reduced. When dv is made large, the valve deflection is again small because the ratio of piston to diaphragm areas is reduced and because the larger, more flexible diaphragm deforms outward and relieves the internal pressure, lowering the amplifier stiffness. Figure 4.4 shows that an optimal value of $dv = 1$ mm exists where these effects are balanced. Similar behavior is seen when db is varied. A small db means that the flexible pump diaphragm is large and relieves the hydraulic pressure. When db is large it becomes clamped near the diaphragm tether point and no longer moves as a rigid piston when actuated. The resulting volume displacement is smaller resulting in a smaller valve deflection. The optimal value was found to be $db = 5.7$ mm.

FEM Stress Analysis

The design of the hydraulic amplification valve is limited by the maximum stresses allowable in the structure, especially the membranes. Single crystal Si is a brittle material with a fracture strength that depends on its orientation and surface finish. "Since the surface flaw population depends on the micromachining process, it is important to obtain strength data

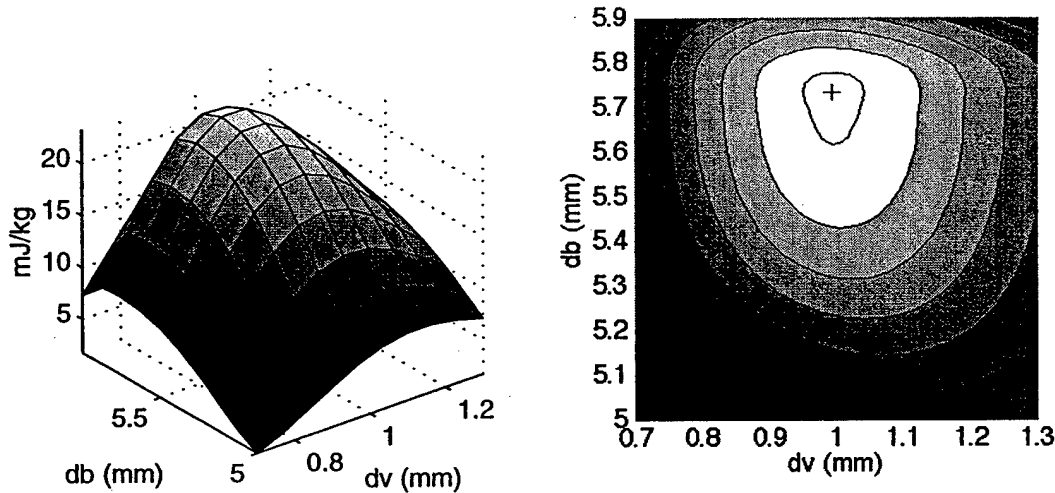


Figure 4.4 Dependence of valve actuation energy density on the design parameters dv and db .

from specimens produced by the relevant fabrication route" [Spearing and Chen, 1997]. Unfortunately, detailed fabrication data is not available at this stage in the feasibility study. The most important missing information is the achievable surface finish and the radii of the corners at the diaphragm tether points, where the stress concentrations are expected to be greatest. Since the purpose of this feasibility study is to quantify the performance of a hypothetical MHST, estimates of the Si fracture strength were made, based on available data, with the intent of approximating the performance achievable after significant micro-fabrication research. Spearing and Chen found that chemically polished Si exhibited a reference strength, σ_0 , greater than 4 GPa. Based on material strength tests, they conclude that "an allowable stress of 1 GPa is a conservative value for structural design purposes," and that "achieving adequate fillet radii to limit stresses to this level is a key fabrication task." The final valve design experienced a maximum principle stress of $\sigma_{\max} \sim 0.8$ GPa in the valve diaphragm during full actuation. The achievable fillet radii, and therefore stress levels, at the tether points is unknown at this time. Determination of this data is a principal objective of prototype fabrication and testing.

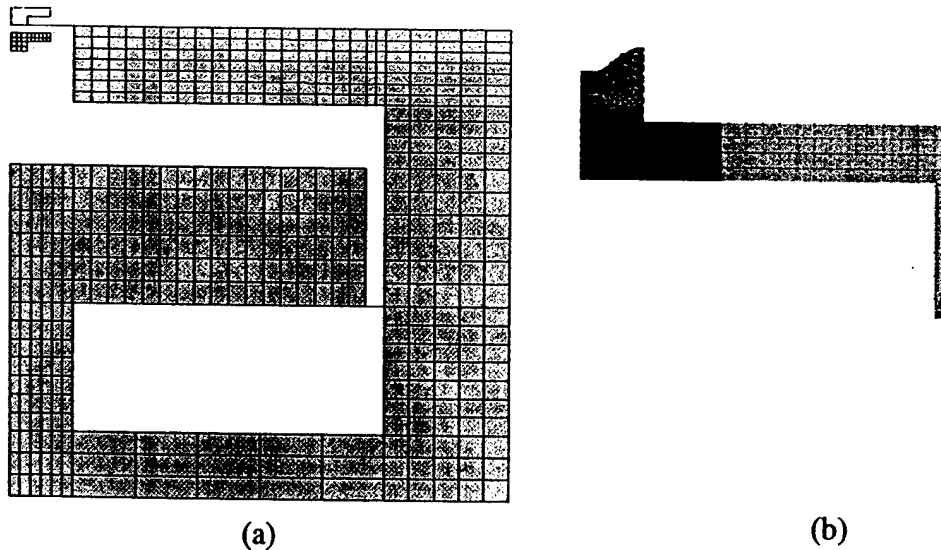


Figure 4.5 First structural (a) and acoustic (b) modes of the valve mechanism. The deflection of the piston in (a) is so small compared to the valve disc displacement that it is not visible.

A modal analysis of the valve was performed to determine the shapes and frequencies of the relevant modes. Figure 4.5 shows the structural and acoustic shape of the first mode. The frequencies of the first four are listed in Table 4.3. The structure was designed such that the first mode corresponded to movement of the valve cap, and not the radial mode of the piston.

TABLE 4.3 Frequencies of the first four valve modes.

| Mode: | 1 | 2 | 3 | 4 |
|------------------|------|------|-------|-------|
| Frequency (kHz): | 23.4 | 68.6 | 151.0 | 198.1 |

Pump Chamber

Since the displacement amplifier geometry is the same for the valve as for the drive mechanism, the components differ only in the ceiling structure. The pump chamber has a solid ceiling and is therefore stiffer than the valve. A good method for evaluating the effectiveness of the chamber is to compare the maximum pressure of the pump with the ideal pressure resulting from an infinitely stiff structure and fluid. With respect to equation (3.23), the stiffness of the chamber as seen by the piezoelectric is

$$k_c = C_c A_{pis}^2 \quad (4.17)$$

If we redefine the non-dimensional parameter e^* to be the ratio of piezoelectric-to-chamber stiffness

$$e^* = \frac{k_p}{k_c} \quad (4.18)$$

then (3.23) can be recast as

$$p_{max} = \left(\frac{\Theta / A_{pis}}{e^* + 1} \right) (V_p)_{max} \quad (4.19)$$

Figure 4.6 below plots equation (4.19) versus e^* for the prototype design, where the pressure has been normalized to the ideal pressure described by equation (3.24), repeated here for clarity

$$(p_{max})_{ideal} = \frac{\Theta}{A_{pis}} (V_p)_{max} \quad (4.20)$$

The maximum pressure of the prototype design is 1.2 MPa (44% of the ideal value of 2.6 MPa) and is indicated by the circle on the plot.

4.3 System Analysis

4.3.1 Linear Approximation

If the valve response times are significantly fast compared to the drive frequency then the system is nearly linear in those intervals where one valve is completely open and the other is completely closed. During these intervals the closed valve decouples the dynamics of its flow channel from the rest of the system, and the viscous resistance of the open valve remains constant. The result is a scenario where the drive inertia interacts with the fluid inertia though the hydraulic capacitance of the chamber. This condition is illustrated in

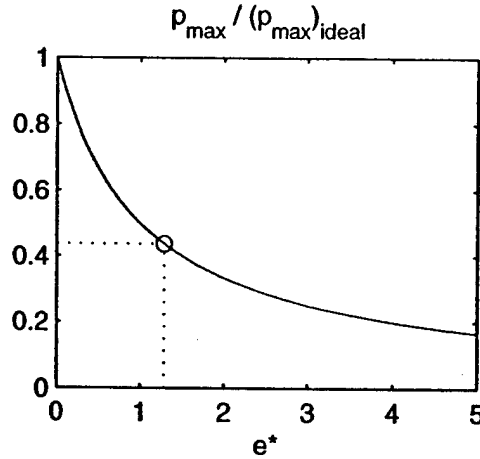


Figure 4.6 Maximum pump chamber pressure versus the ratio of piezoelectric-to-chamber stiffnesses. The pressure has been normalized to the ideal pressure of an infinitely stiff chamber and fluid. The maximum pressure of the prototype design, p_{\max} , is indicated by the circle.

Figure 4.7, along with an equivalent mechanical system. Referring to equations (3.11) and (3.18), the generalized displacements are defined as

$$n_1 = y \quad (4.21)$$

$$n_2 = \int Q dt$$

where n_1 is the deflection of the piezoelectric element and n_2 is the volumetric displacement, or the volume of fluid that has flowed from the chamber into the channel during the interval. The hydraulic amplification caused by the piston is modeled as a pinned lever in the mechanical analogy, where the ratio of the moment arms, r_2/r_1 , represents the amplification magnitude.

The natural frequencies of the system may be calculated by deriving the linear equations of motion for the system during the interval, placing them in state-space form, and solving for the eigenvalues of the system matrix. To illustrate, the state-space equations of motion for the MHST actuator during the linear interval are derived below. The analysis of the power harvester is identical but results in an additional equation, corresponding to the sensor equation (3.4), because the piezoelectric voltage state is a free variable.

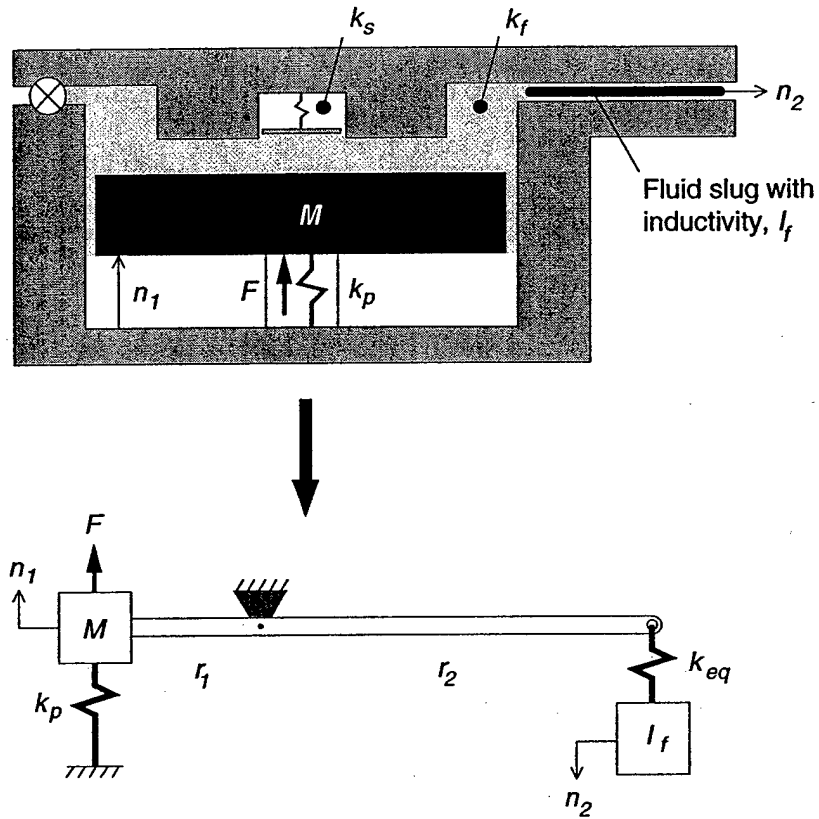


Figure 4.7 Equivalent mechanical system during linear interval

Consider the case when, during actuator operation, the inlet valve is open and the outlet valve is closed. The resistance of the outlet valve can be derived by approximating its position during the interval as

$$x \sim a + \frac{F_v}{k_v} \quad (4.22)$$

where F_v is the opening force applied to the valve and a is the valve stroke. Equation (3.35) can then be used to calculate R_v , and the total resistance seen by the fluid is given by (3.44).

Q_i is then arbitrarily set equal to zero in (3.5) to enforce the closure of the inlet valve (Q_o may just as easily be selected). Recognizing that the volume of fluid in the system during the interval is now a constant, and that

$$V_o \gg \Delta V \quad (4.23)$$

(which is valid for those designs where the chamber height is significantly greater than the deflection of the piezoelectric), the total hydraulic capacitance of the chamber also becomes constant. Integrating equation (3.5) with respect to time, we have

$$p_c = C_c \cdot (\Delta V - \int Q_o dt) \quad (4.24)$$

where the constant hydraulic capacitance is

$$C_c = \left(\frac{V_o}{K_f} + \frac{1}{C_s} \right)^{-1} \quad (4.25)$$

Substituting (3.20) and (4.24) into (3.18) and (3.42) to eliminate p_c and ΔV yields the linear equations of motion for the system

$$\rho I_f \dot{Q}_o + R Q_o + C_c \int Q_o dt - C_c A_{pis} y + p_{hpr} = 0 \quad (4.26)$$

$$M \ddot{y} + (k_p + C_c A_{pis}^2) y - A_{pis} C_c \int Q_o dt - \Theta V_p = 0 \quad (4.27)$$

Using the generalized displacements defined in (4.21) the above equations can be put into state-space form,

$$\begin{bmatrix} \dot{n}_1 \\ \dot{n}_2 \\ \dot{n}_3 \\ \dot{n}_4 \end{bmatrix} = \begin{bmatrix} 0 & 0 & 1 & 0 \\ 0 & 0 & 0 & 1 \\ \frac{(k_p + C_c A_{pis}^2)}{M} & -\frac{C_c A_{pis}}{M} & 0 & 0 \\ \frac{C_c A_{pis}}{\rho I_f} & -\frac{C_c}{\rho I_f} & 0 & -\frac{R}{\rho I_f} \end{bmatrix} \begin{bmatrix} n_1 \\ n_2 \\ n_3 \\ n_4 \end{bmatrix} + \begin{bmatrix} 0 & 0 \\ 0 & 0 \\ \frac{\Theta}{M} & 0 \\ 0 & -\frac{1}{\rho I_f} \end{bmatrix} \begin{bmatrix} V_p \\ p_{hpr} \end{bmatrix} \quad (4.28)$$

System resonance during the linear interval can then be determined by numerically solving for the eigenvalues of the system matrix. The first mode typically corresponds to the interaction of the fluid inductance with the chamber compliance, while second mode

describes the higher frequency oscillation of the drive structure. *Hereafter in this report, the natural frequency of the system, f_n , will refer to the first mode.*

4.3.2 Energy Tracking

Tracking of the power flow through the system during operation is one of the most effective tools for understanding its behavior and provides the basis for performance evaluation. To enable complete energy tracking, equations are needed that describe the electromechanical energy conversion in the piezoelectric, the potential energy stored in the system elasticities, the kinetic energy stored in component momentum, the energy dissipated due to viscous forces, and the hydraulic and electrical energy transfer across the system boundaries. If only steady-state performance over many pump cycles is sought (e.g. the hydraulic power output compared to the electrical power input for the actuator), then the total transferred and dissipated energies will most likely be large compared to potential and kinetic energies stored in the system at the end of the cycles, and the latter need not be considered. However, numerical simulation of stiff fluidic systems is often computationally expensive and permits the integration of only a few pump cycles. In this case, and during investigation of dynamic transients during start-up, the potential energy of the system may be large and must be included in the simulation analysis to verify that the model is thermodynamically conservative. The equations needed to adequately track the system energies, along with the mathematical definitions of the energy based performance metrics, are presented below.

Convention

The discussion of energy tracking is greatly simplified if a notation is introduced which is capable of compactly describing the exact nature of the energy. The convention adopted in this work is as follows

$$Energy = (\mathbf{x})_3^{1,2} \quad (4.29)$$

The quantity in brackets is either energy, U , power, P , energy density, ED, or power density, PD. The subscript 1 refers to the energy type, 2 to the energy behavior, and 3 to the component involved.

TABLE 4.4 Sub- and superscripts for energy notation

| (1) Type | | (2) Behavior | | (3) Component | |
|----------|------------|--------------|------------|---------------|-------------------------|
| <i>m</i> | mechanical | <i>i</i> | into | <i>drive</i> | drive mechanism |
| <i>e</i> | electrical | <i>o</i> | out of | <i>v</i> | valve |
| <i>k</i> | kinetic | <i>s</i> | stored | <i>p</i> | piezoelectric |
| <i>c</i> | elastic | <i>d</i> | dissipated | <i>f</i> | fluid |
| | | | | <i>ve</i> | valve - excursion |
| | | | | <i>hpr</i> | high pressure reservoir |
| | | | | <i>s</i> | chamber structure |
| | | | | <i>sys</i> | total system |

For consistency all quantities reflecting the energy being accumulated in the system are expressed as energies at some instant in time, while the quantities expressing rates of energy transfer remain in their natural states as power. For all cases of power flow, the total energy transferred or dissipated over a time interval, t , is given by

$$U = \int_t^{t+\tau} P dt' \quad (4.30)$$

Stored Elastic Energy

The high pressures experienced by MHST systems can cause significant deformations in the device components and store elastic energy in them. The equations quantifying the stored elastic energies at any instant in time during the simulation are listed below.

$$U_p^{c,s} = \frac{1}{2} k_p y^2 \quad (4.31)$$

$$U_v^{c,s} = \frac{1}{2} k_v x^2 \quad (4.32)$$

$$U_s^{c,s} = \frac{1}{2} C_s p_c^2 \quad (4.33)$$

$$U_f^{c,s} = \frac{1}{2} \left(\frac{V_o - A_{pis} y}{K_f} \right) p_c^2 \quad (4.34)$$

$$U_{hpr}^{c,s} = \frac{1}{2} C_{hpr} p_{hpr}^2 \quad (4.35)$$

Electromechanical Energy Conversion

An expression for the electrical power supplied to the piezoelectric element can be derived using the sensor and actuator equations. If (3.18) and (3.19) are differentiated with respect to time and then combined to eliminate \dot{y} , an expression for the current, i , is obtained. The electrical power input to the element is given by

$$P_p^{e,i} = V_p \cdot i \quad (4.36)$$

Substituting our expression for i into this relation we obtain expression for the electrical power into the piezoelectric.

$$P_p^{e,i} = V_p \left\{ \left(C_p + \frac{\Theta^2}{k_p} \right) \dot{V}_p - \frac{\Theta A_{pis}}{k_p} p_c \right\} \quad (4.37)$$

The mechanical power output from the piezoelectric is the product of the force and velocity of the piston,

$$P_p^{m,o} = p_c A_{pis} \dot{y} \quad (4.38)$$

Eliminating \dot{y} using (3.18) this expression becomes

$$P_p^{m,o} = p_c \left(\frac{\Theta A_{pis}}{k} \dot{V}_p - \frac{A_{pis}^2}{k} \dot{p}_c \right) \quad (4.39)$$

Stored Kinetic Energy

High frequency pump operation can cause high flow velocities, resulting in large momentums for the fluid slugs in the channels. The kinetic energy stored in this momentum, as well as that stored in the motion of the drive and the valves, is quantified below.

$$U_{drive}^{k,s} = \frac{1}{2}M\dot{y}^2 \quad (4.40)$$

$$U_v^{k,s} = \frac{1}{2}m_v\dot{x}^2 \quad (4.41)$$

$$U_{f_{i,o}}^{k,s} = \frac{1}{2}\rho I_f Q_{i,o}^2 \quad (4.42)$$

The subscripts i and o in the last equation indicate that it may be applied to either the inlet or outlet channels.

Dissipated Energy

The flow of viscous fluid in MHSTs converts mechanical into thermal energy. The extraction of mechanical energy from the system manifests itself as a pressure drop across the flow channel, while the conversion to thermal energy results in an increase in the temperature of the fluid and surrounding medium. For most practical cases the conversion is irreversible and the energy is considered lost. This viscous energy dissipation is the primary energy loss mechanism in microhydraulic systems.

The dominant dissipation sites correspond to the areas where the largest viscous pressure drops occur, namely, the flow channel sections and the valve gap. Equations describing the dissipation in these regions may be derived by performing an energy balance on each section. The result is that the mechanical power dissipated in any flow region can be expressed as

$$P^{m,d} = Q \cdot \Delta p \quad (4.43)$$

where Q is the flow through the section, and Δp is the pressure drop across it.

Energy is also expended during valve actuation. The valve structure itself is entirely conservative. The piezoelectric is, from an electrical standpoint, a capacitor and expends no energy when stationary. Dissipation occurs, however, during valve excursion because of the viscous resistance of the fluid on the valve cap and diaphragm. While this energy expenditure is relatively small in the actuator case (compared to the primary power flows) it is an important consideration when evaluating the power harvester. The mechanical power dissipated during the valve excursion is given by

$$P_{ve}^{m,d} = F_v(t)\dot{x} \quad (4.44)$$

Although this relation is exact, it must be remembered that the natures of the motion-dependent fluidic forces experienced by the valve are largely unknown. Equation (4.44) is therefore of limited usefulness in predicting the power requirements of the valve until the fluidic forces are experimentally characterized.

Power and Energy Density

The HPR diaphragm is very flexible and stores little energy, so the hydraulic power output from the mechanism is assumed to be the same as the hydraulic power supplied to the HPR and is expressed as

$$P_{sys}^{m,o} = P_{hpr}^{m,i} = Q_o \cdot p_{hpr} \quad (4.45)$$

The mass-normalized power density, or specific power, of the actuator is then defined as the hydraulic power transferred to the HPR divided by the overall system mass

$$PD = \frac{P_{hpr}^{m,i}}{M_{sys}} \quad (4.46)$$

Power density for the power harvester is defined to be the electrical power out of the piezoelectric divided by the system mass

$$PD = \frac{P_p^{e,o}}{M_{sys}} \quad (4.47)$$

In both cases, the power density changes greatly throughout a single pump cycle as flow ranges between its minimum and maximum values. For evaluation purposes it useful to define the average power density

$$PD_{avg} = \frac{\int_t^{t+nT} PD(\xi) d\xi}{nT} \quad (4.48)$$

where n is an integer number of pump cycles, T is the cycle period, and ξ is a dummy variable of integration. The quantity represents the average rate of energy transfer during the n cycles. Further discussions involving PD in this report will be referring to this definition.

The expressions for energy density, ED, are obtained by making use of the relation between power and energy expressed in (4.30).

Efficiency

Efficiency, η , is defined to be the useful energy output from the system divided by the energy input to it over some time interval. For the actuator

$$\eta_{act} = \frac{U_{sys}^{m,o}}{U_{sys}^{e,i}} \quad (4.49)$$

Efficiency for the power harvester is similarly defined to be

$$\eta_{ph} = \frac{U_{sys}^{e,o}}{U_{sys}^{m,i}} \quad (4.50)$$

4.4 Summary

This chapter presented the tools with which a microhydraulic system can be analyzed, both statically and dynamically. The first section dealt with the definition of a canonical

hydraulic coupler as a representative section for the valves. Mechanical efficiency was then introduced as a static analysis and design tool for the coupler. The valve was then optimized with respect to mechanical efficiency using the finite element model, and a final design was chosen. The equations of motion for the system in the time intervals where the behavior is nearly linear were derived and cast in state-space form in order to predict dominant frequencies. The equations needed for energy tracking in the system were presented. Finally, the performance metrics of average power density and efficiency were defined in terms of the energy equations to evaluate performance during the subsequent parameter study.

Chapter 5

SIMULATION RESULTS

5.1 Introduction

A realistic prediction of MHST behavior can only be gained by numerically integrating the coupled governing equations for the full system. Such system simulations can help to predict the dynamic effects that will be seen during operation of the device, and shed insight into which design parameters are most responsible for the observed behavior.

A better understanding of the dependence of system performance on various design variables can be obtained by first selecting an arbitrary design, then perturbing those constituent parameters that are suspected to have the greatest discernable influence on behavior. Evaluation of the results of these perturbations often provides information that can lead to better designs. A large number of primary parameters (e.g. geometric dimensions and material properties) are required to fully describe a MHST design and many of them affect multiple secondary characteristics (e.g. flow resistance and inertia). As a result, it is not practical to study variations in every parameter. However, the information gained in previous chapters, combined with data from initial computer simulations, suggest which parameters should be targeted for closer study.

This chapter presents the results of the integrated system simulations and a parameter study of selected design variables. It begins with the definition of a baseline design, then explains the behavior observed in the simulation of that design. A parameter study is then

performed on selected design variables for the purposes of characterizing changes in response, acknowledging model limitations, and deducing what modifications will lead to an effective final design. The objectives of this chapter are:

- Definition of a baseline system for the parameter study
- Simulation of the baseline design and characterization of its behavior
- Examination of the changes in system behavior resulting from parameter perturbations
- Application of the parameter study results to create a final design for consideration in feasibility assessment

The first section of this chapter deals with the definition of a baseline design, simulation of its performance, and discussion of the results. Plots of the time histories of the states resulting from the first two simulations are central to the discussion and are therefore included in the text. In some cases the plots of simulation results obtained during the parameter study exhibit interesting behavior; these plots are included in Appendix C of this report and are referenced by their simulation number. Although the baseline design was used as the reference point in the study, several variations of the design were considered in the process. These variations (e.g. a system using a different working fluid) are referred to as different *configurations* of the baseline. Only performance during steady-state operation is considered. The stored elastic and kinetic energies are therefore not addressed, and the performance values reported represent the averages over an integer number of simulated cycles. Also, since only the actuation system is simulated, the energy lost as a result of valve actuation is not considered.

5.2 System Behavior

It is necessary to define a nominal design that will serve as a baseline throughout the parameter study. After many random iterations a configuration was found that demonstrated the fundamental characteristics of MHSTs and was robust to changes in those parameters (robust with respect to integration of the equations). Table 5.1 summarizes the properties of the baseline design, *configuration A*: a mesoscale system with 6 mm diame-

ter pistons using water as the working fluid. The most salient entry in the table is the long lengths of sections I of the flow channels (10 cm). It was found that when short channels were used the natural frequency of the system was significantly higher than the bandwidth of the valves due to the high chamber stiffness and small fluid inductance. It was also found that excitation of the pump near or above the valve resonance results in loss of flow rectification because the valve reaction time is too slow (delayed valve closure results in backflow). Therefore, the short-channel system must be run quasistatically with respect to the fundamental system frequency. However, as will be seen later in this chapter, *adequate pump performance can only be achieved by exciting the pump near the system resonance*. If the valve bandwidth is taken to be a fixed limit, as is the case for most designs, then a potential solution is to lower the system frequency either by decreasing its stiffness (e.g. increase chamber compliance) or by increasing its mass (e.g. increase fluid inductance). Initial investigations showed that increasing the chamber compliance significantly reduced power output. Therefore, the approach used was lengthen section I of the channels. It was found that, at the mesoscale, the increase in viscous flow resistance incurred by this change was nominal. Furthermore, since resonant operation is a prerequisite for effective operation, the added inertia does not hinder system performance. Although eventual MHST implementation will have shorter channels, the long-channel baseline design is acceptable for the parameter study.

A computer simulation of the steady-state operation of baseline configuration A, shown below in Figure 5.2, illustrates the steady-state behavior of the design. The calculated performance for the system was: $PD = 1280 \text{ W/kg}$; $\eta = 21\%$; $Q = 236.0 \text{ ml/min}$. Several comments can be made on the behavior and the information gained while leading up to the design. As previously mentioned, it was found that good performance could only be gained by forcing the system near its resonance. In fact, excellent performance was achieved by driving the pump at $f = 1.11f_n$ (a relation found by iteration). As will be seen, complications arise when the system is driven precisely at resonance. It was also found that, for this geometry, the best performance was obtained by tuning the system such that the natural frequency (and hence the driving frequency) was roughly 1/3 of the valve reso-

TABLE 5.1 MHST baseline design characteristics - configuration A.

| Drive | | Valve | | Valve Seat | |
|---------------------|---------------------------|---------------|----------------------|---------------------------|------------------------------|
| m_p | 2e-3 g | m_v | 1.26e-4 g | k_{seat} | 2.73e9 N/m |
| m_{piston} | 0.06 g | k_v | 2727 N/m | γ | 1 μ m |
| k_p | 9.22e7 N/m | f_n | 23.39 kHz | Valve stroke ^a | 0.25 |
| C_s | 7.09e17 Pa/m ³ | k_v/k_{cp} | 8 | Channel Section I | |
| k_p/k_c | 0.20 | A_{eff} | 0.25 mm ³ | | |
| f_{drive}^b | 161.59 kHz | Field | 0.8 kV/mm | | |
| f_{drive}^c | 151.74 kHz | F_b | 0.21 N | | |
| y_{fr} | 1.4 μ m | x_{fr} | 77 μ m | height | 0.5 mm |
| Field | 1 kV/mm | p_b | 696.79 kPa | width | 6 mm |
| p_{max} | 926.13 kPa | p_{fr} | 232.69 kPa | length, L_I | 100 mm |
| p_{max}/p_{ideal} | 44% | η_{mech} | 10.6% | R | 6.60e10 Pa/m ³ /s |
| V_d | 0.09 μ l | ED | 23 mJ/kg | I_f | 1.57e4 m ⁻¹ |
| System | | | | Channel Section II | |
| | | | | diameter | 0.59 mm |
| | | | | length, L_{II} | 0.5 mm |
| | | | | R | 1.70e8 Pa/m ³ /s |
| | | | | I_f | 1.84e3 m ⁻¹ |
| $f_1 = f_n^d$ | | | | Materials | |
| f_2^e | | | | piezoelectric | PZN:PT |
| M_{sys} | | | | structure | Si, Pyrex |
| p_{hpr}/p_{max} | | | | fluid | water |

a. Stroke = allowed deflection / free deflection

b. Frequency of the drive with no fluid in the chamber

c. Frequency of the drive with closed, fluid filled chamber

d. First mode of the coupled structural-fluid system

e. Second mode of the coupled structural-fluid system

nance. When excited at a higher frequency the valve response rolls off, they are not able to close, and the flow is not rectified. If operated quasistatically the valve response will closely resemble the square wave actuation voltage signal shown below in Figure 5.1 (repeated from Chapter 1). Dynamic effects, though, are clearly visible in plots (b) and (e) of Figure 5.2. The differences in the trajectories of the inlet and outlet valves, as well as their relative phasing with respect to the pump (recall that they are actuated 180° out of

phase with each other), is due to the fact each experiences different forcing. Although pressure balancing eliminates the forces resulting from the pressure acting on the diaphragm and lower surface of the disc, the upper surface of the inlet disc sees a pressure level between that of the LPR and the chamber, while the outlet valve experiences a pressure level between that of the chamber and the HPR. In addition, the fact that the inlet valve experiences a force resulting from the momentum transfer of the inflowing fluid impinging on the valve disc, while the outlet valve does not, also contributes to the asymmetric response. Another interesting effect is the absence of significant backflow even though there are periods when both valves are clearly open, which results from the dynamics of the fluid motions and their phase relations with the valves. Some backflow is visible at the bottom of plot (d) when the valves are closed, and is due to the modeled leakage.

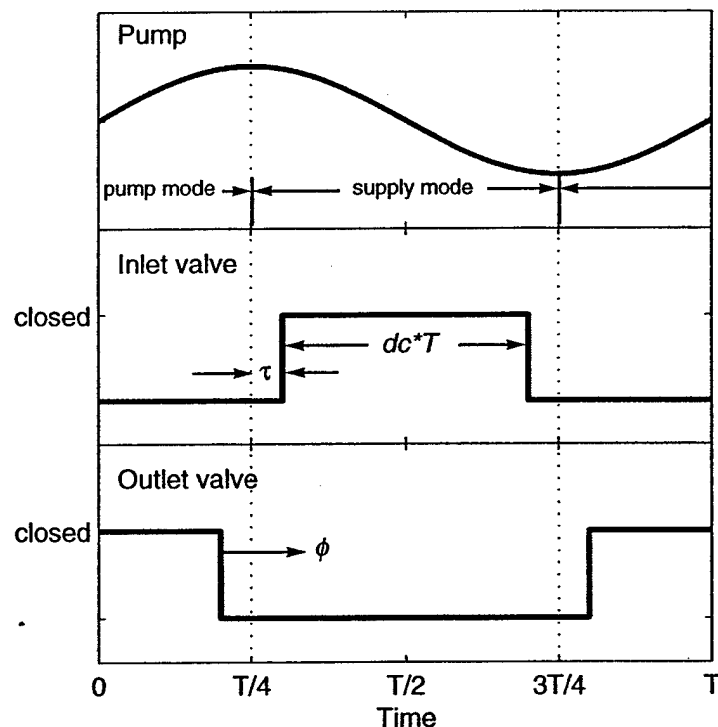


Figure 5.1 System timing. The pump drive signal may be any periodic function (sinusoidal shown for simplicity).

Application of the energy tracking equations given in Chapter 4 provides an explanation for the efficiency of the system. Figure 5.3 shows the destinations of the electrical energy supplied to the pump over the steady-state cycles of interest. Since the system is operating at 21% efficiency, 79% of the supplied energy is being dissipated internally. As the graphs show, the viscous flow resistances of the valves themselves, $R_v(x)$, account for most of the losses. This is a consequence of the valve strokes which are relatively small compared to the dimensions of the flow channels. It can also be seen that a small but not insignificant fraction of the losses occur in sections I of the flow channels, resulting primarily from their long lengths, while the much shorter sections II contribute virtually no losses. Also visible is that the system outlet (valves and channels) is responsible for greater energy loss than the inlet. The reason for this is linked to the different forcing that the valves experience, and the proximity of the driving frequency to the valve resonance. As will be seen and discussed in subsequent sections, primarily in Study 11, because the pump excitation frequency is within one decade of the valve resonance dynamic effects occur in the valve response. One manifestation of these effects is an overshoot in the valve position resulting primarily from the valve actuation step, but also from the simultaneous fluidic and pressure forces. The aforementioned differences in the forces seen by the valves, coupled with the cubic dependence of flow resistance on valve displacement, means that the average flow resistances of the valves over several cycles can vary greatly. The result is that small differences in the respective valve responses are sometimes amplified into large flow dissimilarities. Lastly, the graphs show that the structural damping of the drive contributes little to the total system losses.

The strong dependence of system performance on the valve dynamics suggests that the results of independent parameter variations might be difficult to interpret. For this reason, prior to commencement of the parameter study, the baseline configuration was modified by making the valves artificially fast such that their response time was fast and their dynamics became decoupled from the problem. The change was implemented by reducing m_v by a factor of 100, thereby increasing the bandwidth by 10 and resulting in quasistatic behavior from the valves for the same driving frequency. The simulation results for this

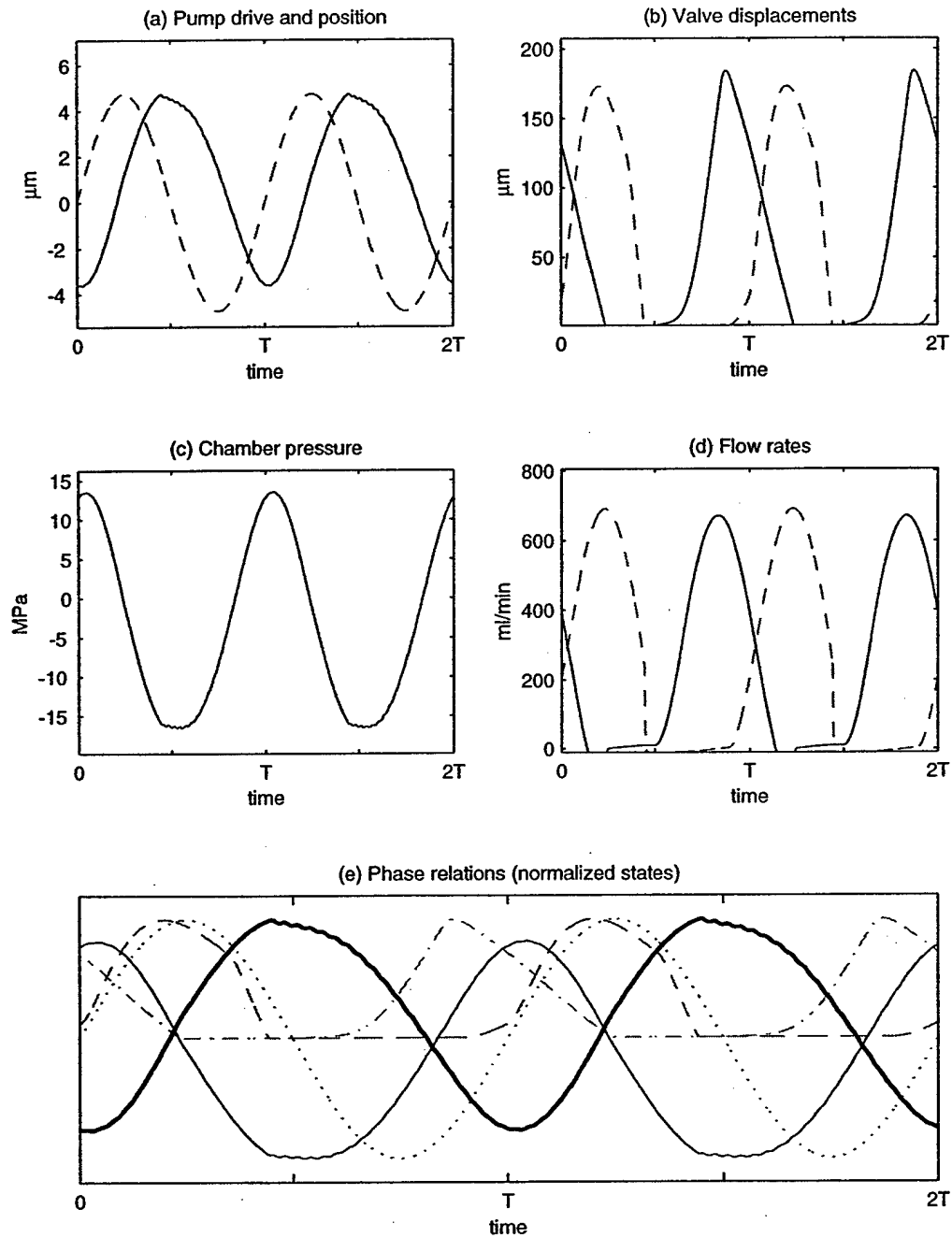


Figure 5.2 Simulation of actuator configuration A: $f = 1.11f_n$, $f_n = 6.69$ kHz, $f_v = 23.4$ kHz. Plot (a) overlays the pump displacement (solid) with the normalized drive signal (dashed). Plots (b) and (d) show the displacements and flows of the inlet (solid) and outlet (dashed) valves. Plot (e) indicates the phase relations between the normalized pump position (heavy solid), chamber pressure (solid), drive signal (dotted), inlet valve displacement (dot-dashed), and outlet valve displacement (dashed).

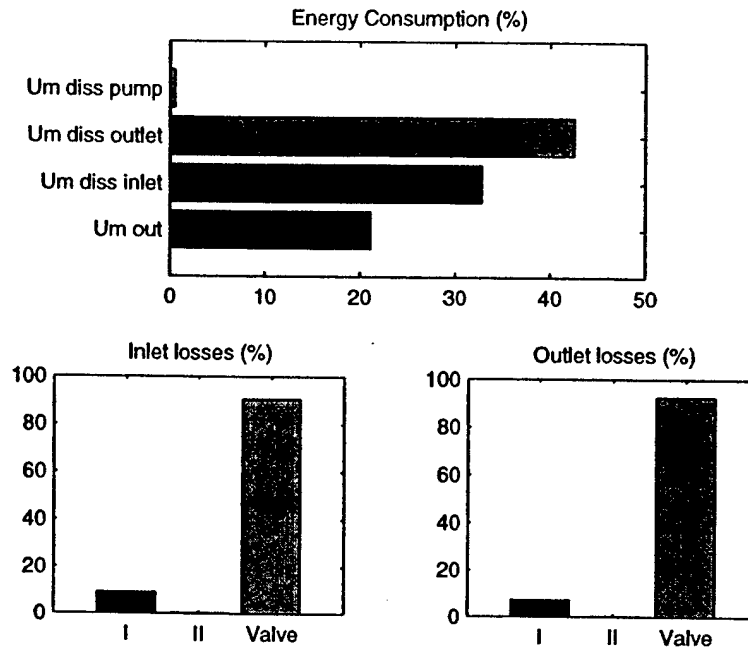


Figure 5.3 Actuator configuration A: energy tracking. The top shows the energy dissipated in the pump, inlet, and outlet, as well as the useful (fluidic) energy output, as a percentage of the electrical energy supplied to the system. The bottom plots show the losses in channel section I, channel section II, and the valve gap, as percentages of the total inlet and outlet losses.

new system, *configuration B*, are shown in Figure 5.4. Although the valves are now faster the performance of the system drops to $PD = 188 \text{ W/kg}$; $\eta = 18\%$; $Q = 34.6 \text{ ml/min}$. Comparison of the simulations of configurations A and B shows that when the valves are not dynamically forced their displacements are smaller (80% less for the inlet, 15% less for the outlet). The outlet valve now achieves a larger excursion than the inlet because it sees a higher pseudostatic pressure. As previously mentioned, the strong dependence of flow resistance on valve displacement explains the dramatic differences between the volumetric fluid flow and associated power output of the two configurations. It also highlights the sensitivity of the model to these effects. The true nature of the phenomenon must be determined experimentally.

Also visible in plot (c) are high frequency oscillations in the chamber pressure, a result of the excitation of the system's higher "drive" mode, that stems from changes in the valve states which occur rapidly with respect to the drive frequency. For example, consider the

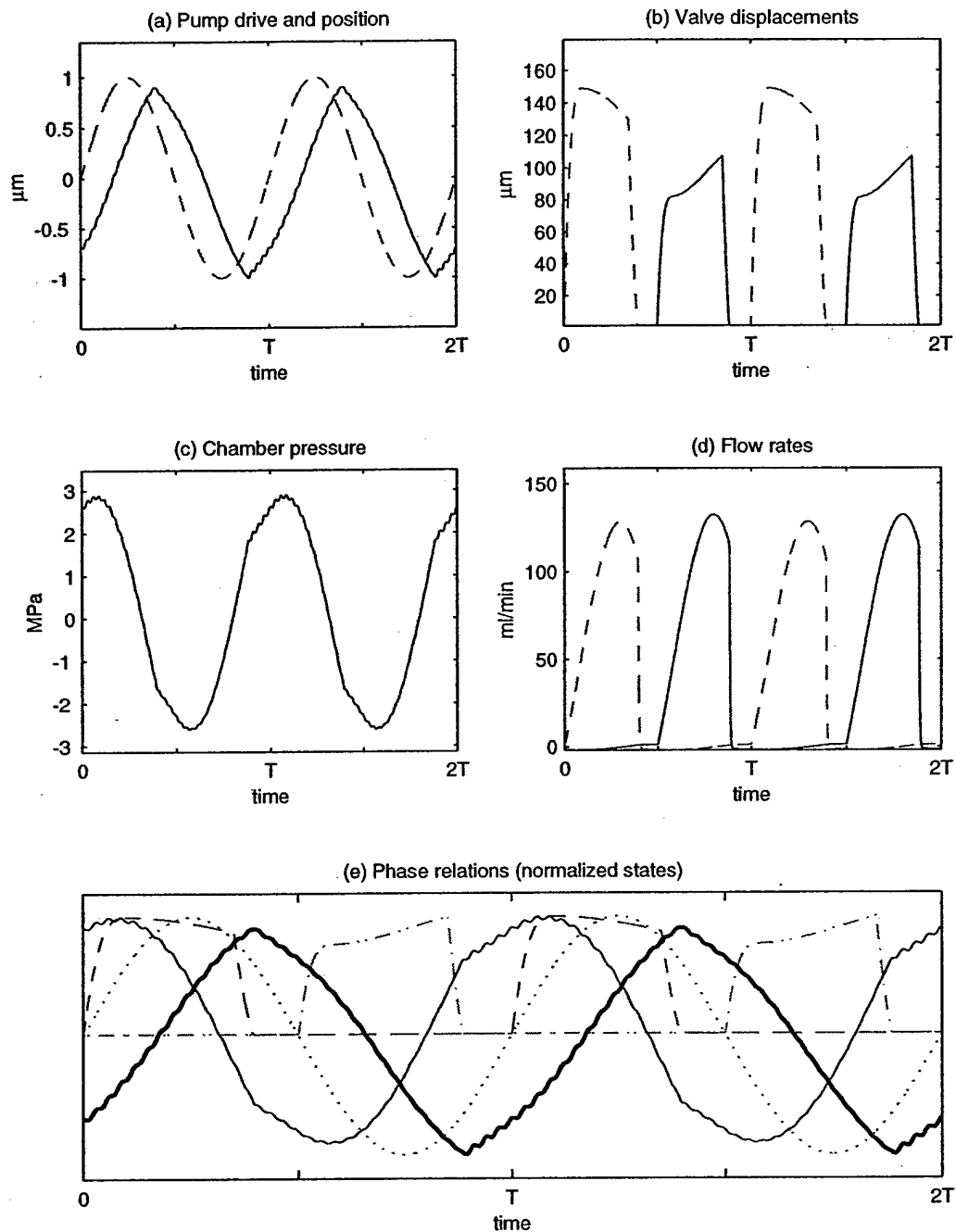


Figure 5.4 Simulation of actuator configuration B: $f = 1.11f_n$, $f_n = 6.69$ kHz, $f_v = 234$ kHz. Plot (a) overlays the pump displacement (solid) with the normalized drive signal (dashed). Plots (b) and (d) show the displacements and flows of the inlet (solid) and outlet (dashed) valves. Plot (e) indicates the phase relations between the normalized pump position (heavy solid), chamber pressure (solid), drive signal (dotted), inlet valve displacement (dot-dashed), and outlet valve displacement (dashed).

case where the pump is in the supply mode, drawing fluid into the chamber. Throughout this phase the drive sees a certain equivalent stiffness. Sudden closure of the valve, however, causes the drive to experience a much higher stiffness as no fluid is allowed into the chamber. The result is a parametric excitation of the high frequency drive mode.

Figure 5.5 shows the results of the energy tracking analysis, where the consequences of attenuated valve excursions are apparent - nearly all of the viscous losses occur in the valve gaps. It is also notable that, as an additional result, the inlet valve is responsible for most of the losses in this configuration, which was not true for configuration A. All other aspects of the power flow are similar to configuration A.

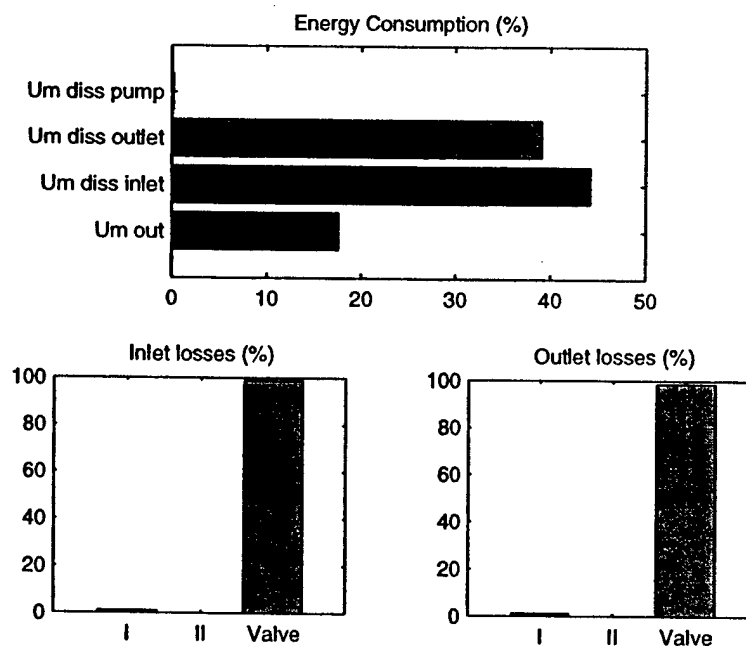


Figure 5.5 Actuator configuration B: energy tracking. The top shows the energy dissipated in the pump, inlet, and outlet, as well as the useful (fluidic) energy output, as a percentage of the electrical energy supplied to the system. The bottom plots show the losses in channel section I, channel section II, and the valve gap, as percentages of the total inlet and outlet losses.

5.3 Parameter Studies

The study was executed by targeting a parameter suspected to strongly influence system behavior and then performing a sweep through some range of values by running multiple simulations. The parameters involved and the results observed are summarized in Table 5.2. Separate simulations were performed using the parameters found to yield optimal or anomalous results in order to understand the mechanism(s) responsible. The time histories of those simulations believed to shed insight into system behavior are included in Appendix C.

The selection of the subject parameters requires some explanation. The parameters chosen can best be classified into two groups: those describing the electrical drive signal, and those describing geometric or other mechanical characteristics of the design. They are summarized below:

Electrical excitation

1. Input waveform
2. Drive frequency versus system frequency
3. Valve phasing (with respect to the pump signal)

Mechanical geometry and loading

4. Chamber capacitance
5. Pressure load
6. Valve leak parameter
7. Mercury as the working fluid
8. Carbon tetrachloride as the working fluid
9. Valve disc diameter
10. System scale
11. Drive frequency versus valve frequency

Due to the previously seen sensitivity of system performance to the dynamics and phase relations present, the nature of the electrical excitation is very important. Initial simulation

TABLE 5.2 Summary of parameter study.

| Study | Config. | Parameter | Best Results |
|-------|---------|--|--|
| 1 | B | waveform | square: PD = 239 W/kg; η = 27%; Q = 44.0 ml/min triangular: PD = 139 W/kg; η = 21%; Q = 25.6 ml/min |
| 2 | B | $f = f_n/10$ to $10f_n$ | major peak: PD = 338 W/kg; η = 22%; Q = 62.3 ml/min minor peak: PD = 55 W/kg; η = 39%; Q = 10.1 ml/min chaotic behavior at when driven at resonance nonfunctional when driven quasistatically |
| 3 | B | $\phi = 0^\circ$ to 350° | $\phi = 80^\circ$: PD = 145 W/kg; η = 45%; Q = 26.7 ml/min |
| 4 | C | $C_c = 10^{15}$ to 10^{21} Pa/m ³ | Improving performance with increasing C_c |
| 5 | B C | PL ^a = 0 to 1 | PL = 0.8: PD = 2170 W/kg; η = 50%; Q = 150.0 ml/min PL = 0.7: PD = 16 W/kg; η = 38%; Q = 22.0 ml/min |
| 6 | B | $\gamma = 10^{-2}$ to 10^1 μ m | Performance rolls off for $\gamma > 3$ μ m |
| 7 | B D | fluid = Hg | $f = 2.01$ kHz: PD = 48 W/kg; η = 18%; Q = 8.9 ml/min $f = 7.43$ kHz: PD = 168 W/kg; η = 18%; Q = 30.9 ml/min |
| 8 | B E | fluid = CCl ₄ | $f = 5.88$ kHz: PD = 146 W/kg; η = 17%; Q = 26.9 ml/min $f = 7.43$ kHz: PD = 281 W/kg; η = 18%; Q = 51.6 ml/min |
| 9 | F | $d_{disc} = 0.2$ to 1 mm | $d_{disc} = 0.75$ mm: PD = 361 W/kg; η = 21%; Q = 66.4 ml/min |
| 10 | G | $\lambda = 10^{-4}$ to 10^0 | $\lambda = 10^{-2}$: PD = 8210 W/kg; η = 18%; Q = $1.5e-3$ ml/min Performance ceases to increase when $\lambda < 10^{-2}$ |
| 11 | A | $f/f_v = 0.1$ to 0.9 | $f/f_v = 0.3$: PD = 1280 W/kg; η = 21%; Q = 236 ml/min |

a. Pressure load (PL) = p_{hpr}/p_{max}

results indicated that the predicted system performance could be swept through its full range of values simply by changing the characteristics of the drive signal. Therefore, all of these characteristics - waveform, frequency, and phase - were selected for investigation. The choice of mechanical parameters was based on a combination of Chapter 4 analyses, intuition, and preliminary simulation results. The chamber capacitance, C_c , was targeted because of its expected impact on system performance as illustrated by the analysis of the canonical hydraulic coupler in Chapter 4. Similarly, knowledge of the impedance matching condition between the pump and the pressure load prompted an investigation to determine the location of the match (i.e. the pressure that would yield the greatest power output). The valve leak parameter, γ , was also chosen. Since no experimental data exists for this parameter, it is useful to determine what value will impact system performance. A judgement can then be made with respect to its affect on system feasibility. Water was selected as the system's working fluid for reasons which are discussed later. However, fac-

tors such as cavitation and thermal considerations that are potentially important for physical implementation demand that the feasibility of using other fluids in the system be investigated. The diameter of the valve disc, d_{disc} , was selected primarily because of its somewhat arbitrary initial size. The reasons for studying the effects of scale on system performance were discussed in detail in preceeding chapters. Finally, the proximity of the system resonance (and related drive frequency) to the valve frequency is explored to determine how fast the pump can be driven, and therefore how much power can be output, before the valve bandwidth limits performance.

Electrical Excitation

Study 1: Input waveform

All of the initial model simulations leading to the baseline design were performed using a sinusoidal drive signal with the intent of exciting the system resonance. The signal, however, can be any periodic function. The valves were always driven with a square wave operating with a 35% duty cycle. It was initially unknown how the system would respond to different waveforms. Two other possibilities were investigated: a first order square wave (Simulation 1a) and a triangular wave (Simulation 1b). A pure (zeroth order) square wave was not used because it strongly excited the system dynamics. The results were that the square wave generated $PD = 239 \text{ W/kg}$; $\eta = 27\%$; $Q = 44.0 \text{ ml/min}$ while the triangular wave provide $PD = 139 \text{ W/kg}$; $\eta = 21\%$; $Q = 25.6 \text{ ml/min}$. Both excited a sinusoidal pressure signal. Although the square wave seemingly provides better performance, the high frequency oscillations incurred would in most cases make it unsuitable for driving the system. Simulations were performed with this waveform using configuration A (i.e. realistic valves) and it was observed that the pressure fluxuations completely disrupted flow rectification. The conclusion for this study is that a sine wave is the best drive signal for the MHST.

Study 2: Drive frequency versus system frequency

System performance is highly dependent on the excitation frequency, f , of the pump. As previously mentioned, it is necessary to drive the system near resonance to obtain reasonable performance. The reason for this can be partially understood by investigating the behavior of the system under quasistatic excitation, which was done in Simulation 2d. It can be seen in the state time histories that the system resonance is excited and extreme pressure oscillations occur (even though the pump vibration amplitude is small the nearly incompressible fluid in the chamber amplifies this into high pressures). In fact, the predicted oscillations are so large that the flow is not rectified. However, it must be remembered that the model cannot predict the damping that will occur in this regime (e.g. frequency dependent acoustic damping at the piston-fluid interface) and the accuracy of this simulation is questionable. Intuition suggests that, at some low frequency where enough oscillations occur that they become completely damped, the pump will certainly function. Such low frequency operation, however, would produce very little power and is consequently of little interest. Therefore, for the purpose of MHST feasibility assessment it can be concluded that the pump will not function if operated significantly below the system resonance.

The logical next step is to investigate the frequency response of the system and find the optimal if it exists. The results of this analysis are shown in Figure 5.6, where a clear peak in the output power is visible near the system's natural frequency. The peak is centered at 5.35 kHz, slightly below the system resonance of 6.69 kHz. Also distinctly visible is a minor peak at 1.60 kHz, or 1/4 of the resonance. It is clear that excitation at frequencies significantly higher than f_n result in poor power output. The efficiency plot is approximately the inverse of the PD plot because the same high flow rates that provide the hydraulic power also result in greater viscous losses through the valves and channels. As expected, efficiency peaks when the power level is minimal. An anomaly was identified during the frequency sweep when $f = f_n$; it is not included in the plot, but is studied below. Three cases were identified for further investigation: (1) operation at the major peak, (2) operation at resonance (3) and operation at the minor peak.

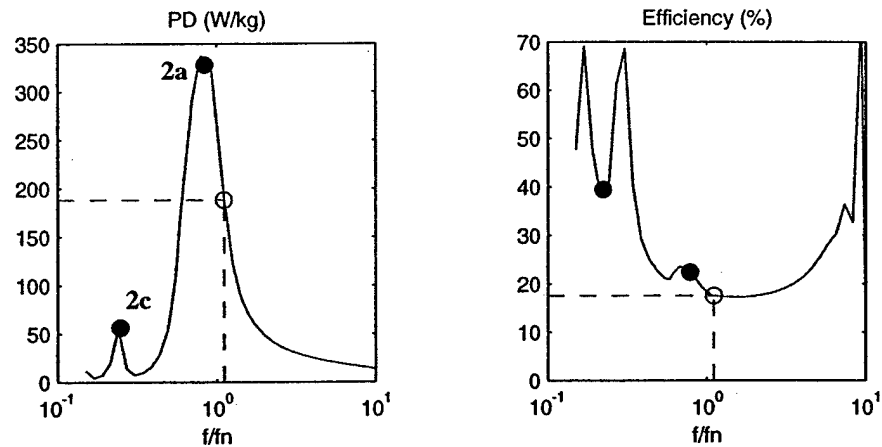


Figure 5.6 Parameter study 2: performance of configuration B versus drive frequency, f . The frequency of the baseline $f = 1.11f_n$ is indicated. The anomaly at $f = f_n$ is not shown. The dots correspond to simulations included in Appendix C.

The first case considered, Simulation 2a, was operation at the major peak, $f = 0.8f_n = 5.35$ kHz. It can be seen that the dynamics of the system are such that the chamber pressure experiences a fluctuation near its peak that causes a rapid oscillation in the outlet flow. The performance is significantly higher than the baseline but successful implementation would almost certainly require avoidance of the pressure jump.

Operation of the system at resonance was considered next. Given that the best performance is obtained by exciting the system's natural frequency, it is logical to suspect the $f = f_n = 6.69$ kHz will yield the optimal results. Indeed, this was true for several designs considered in preliminary simulations. However, configuration B exhibits an interesting phenomenon when driven at resonance. The time histories of the states over 30 cycles are shown in Simulation 2b. Although no detail is visible, it is evident that the system experiences chaotic behavior near the 24th cycle, where a phase inversion occurs between the chamber pressure and the pump, resulting in flow reversal. It is unclear whether this behavior would manifest itself in a physical system.

The last case considered was operation at the minor peak, $f = 0.25f_n = 1.60$ kHz. Inspection of Figure 5.6 suggests that the peak represents a harmonic of the system. Simulation 2c was performed to characterize the system's behavior at this frequency. The perfor-

mance predicted is $PD = 55 \text{ W/kg}$; $\eta = 39\%$; $Q = 10.1 \text{ ml/min}$. Since the driving frequency is $1/4$ of the resonance there are exactly 4 fluid oscillation periods for every pump cycle, but because the system timing is such that exactly 1.5 periods occur when each valve is open, roughly twice as much fluid flows forward as backward, resulting in a positive net flow rate and a peak in the system's power output. A study of possible system harmonics was conducted by sweeping through a series of drive frequencies and taking the power spectral density (PSD) of the ensuing state responses. The magnitude of the outlet flow, Q_{out} , is of particular interest because it is the best indicator of the power output. The results are shown in Figure 5.7 where the presence of superharmonics can be clearly seen. In addition to the predicted system resonance, a significant peak is visible on the 4th harmonic line corresponding to Simulation 2c. Two things were concluded from this study: (1) that the best performance is obtained by operating near (but not necessarily at) the system resonance, and (2) that the system possesses significant harmonics.

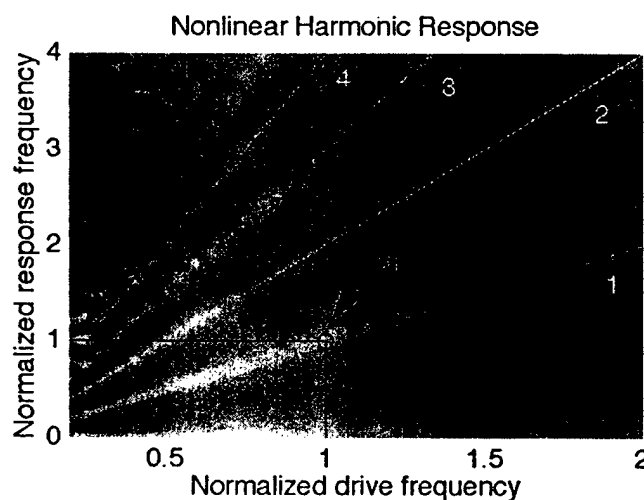


Figure 5.7 Harmonic analysis showing the relation between the input electrical signal and the output, Q_{out} . The x-axis is the drive frequency normalized to f_n ; the y-axis is the response frequency normalized to f_n . The brightness reflects the magnitude of the response calculated on a log scale. The first radial line shows a 1:1 correspondence between the input and output frequencies, while the remaining lines indicate the presence of 2nd, 3rd, and 4th superharmonics. The spotted regions at left are an artifact of the plot resolution. The arrows correspond to simulations included in Appendix C.

Study 3: Valve phasing

System behavior is extremely sensitive to the phasing of the valves with respect to the pump drive signal. Initial simulation results indicated that small variations in the drive signal produced changes in the system dynamics, such as the phase relation between the pump position and pressure, that could completely change the flow pattern. Figure 5.8 shows the power output of the system versus valve phase, where a well defined optimum exists at $\phi \sim 80^\circ$. Simulation 3a was performed using this value with the following results: $PD = 145 \text{ W/kg}$; $\eta = 45\%$; $Q = 26.7 \text{ ml/min}$. Very clean signals with symmetric spacing are visible. Figure 5.9 illustrates the greatly improved efficiency realized by this change in phase. Virtually no energy is dissipated in the drive because the higher dynamics are not being excited, and the lower maximum flow velocities dissipate less energy. The price is a lower power density. It is evident that the performance drops suddenly if a critical phase of approximately 100° is reached, which results in backflow. The conclusion from this study is that, although the optimal valve phase value of 80° is conditional on the design parameters and cannot be generalized to other configurations, changes in valve phasing for any given design can result in drastic changes in system performance and may, in some cases, allow for tailoring of the performance numbers.

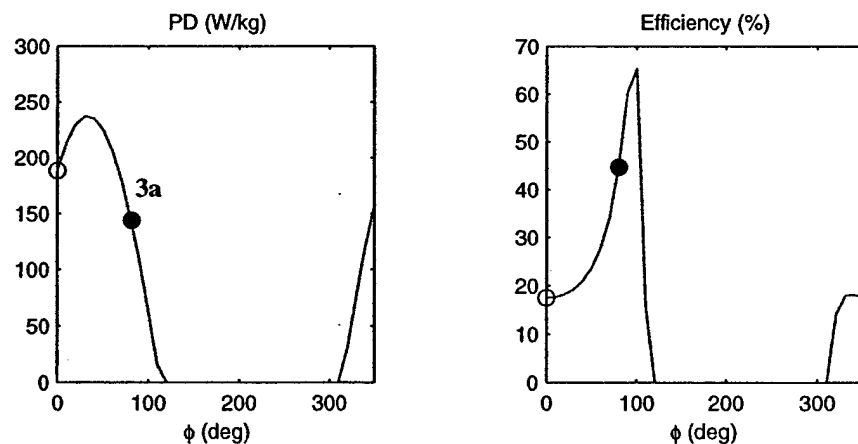


Figure 5.8 Parameter study 3: performance of configuration B versus valve phase, ϕ . The nominal value of 0° is indicated. The dot corresponds to a simulation included in Appendix C.

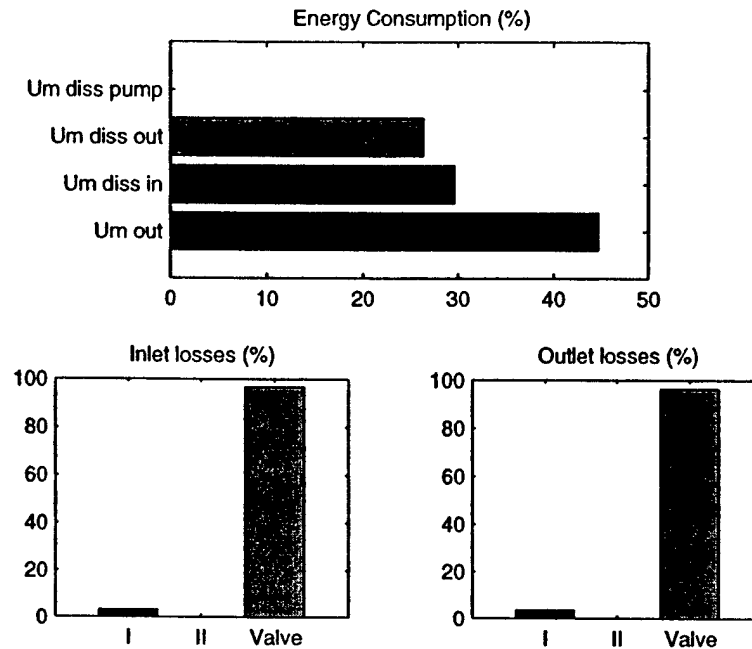


Figure 5.9 Simulation 3a energy tracking. The top shows the energy dissipated in the pump, inlet, and outlet, as well as the useful (fluidic) energy output, as a percentage of the electrical energy supplied to the system. The bottom plots show the losses in channel section I, channel section II, and the valve gap, as percentages of the total inlet and outlet losses.

Mechanical Geometry and Loading

Study 4: Chamber capacitance

The analyses presented in Chapter 4 suggest that the stiffness of the pump chamber greatly impacts the power levels of the system. In this section, the importance of the parameter was characterized by running a series of simulations with different values for C_c . The results are shown in Figure 5.10. In the limiting case of a very compliant chamber (small C_c) the power level approaches zero. It is apparent that the present design, while not ideal, is within 20% of the asymptotic value corresponding to an infinitely stiff chamber (for the given pressure load). When considering different designs for the baseline, it was realized that an alternative to the "long-channel" solution existed: the system frequency could also be lowered by decreasing the chamber capacitance, for instance, by adding flexible membranes to the chamber ceiling structure. When C_c is reduced by a factor of 175 and short channels are used ($L_f = 1$ mm) the system frequency becomes the same as the nominal, $f =$

6.69 kHz. This system is designated *configuration C*. Simulation 4a shows the states of the device when driven at $f = 1.11f_n$. The performance is predicted to be $PD = 11 \text{ W/kg}$; $\eta = 18\%$; $Q = 33.7 \text{ ml/min}$, significantly below the values of configuration B. Most noticeable in the time histories of the states is the close following between the drive signal and the pump position. The low power output is the result of the much lower pressures being generated in the chamber due to the increased flexibility of the chamber. It must be noted, however, that such a system will have a different optimal pressure load than a stiffer system, an effect that is explored in the subsequent study. The conclusion reached in this study is that a reduction in the chamber stiffness greatly reduces the performance of the system, and the benefits derived by such a modification (e.g. tuning of the system resonance) are probably not worth the penalty incurred. It is further concluded that the system efficiency is very insensitive to C_c .

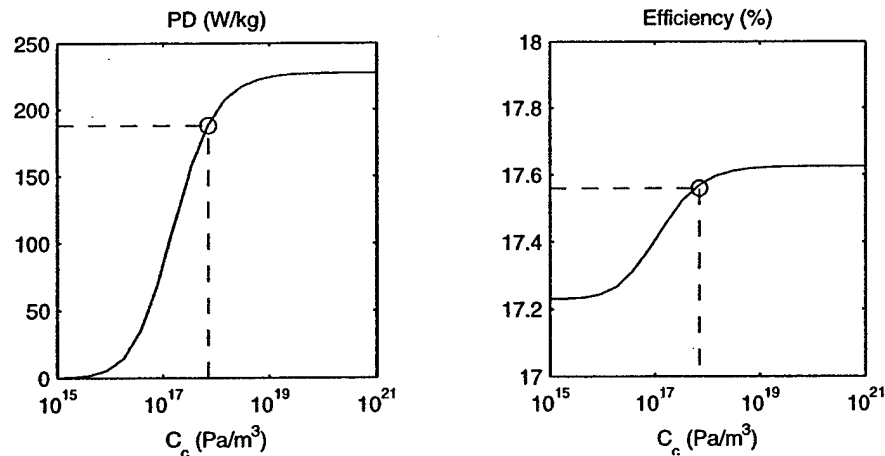


Figure 5.10 Parameter study 4: performance of configuration B versus chamber compliance, C_c . The nominal value of $7.09 \times 10^{17} \text{ Pa/m}^3$ is indicated.

Study 5: Pressure load

The power output of any hydraulic pump depends greatly on the pressure load it is acting against. Therefore, to maximize the performance of the MHST it necessary to find the optimal load. In quasistatic operation the optimal load is nominally one-half of p_{max} . However, other effects make the issue more complicated. This is illustrated below in Figure 5.11, where the PD curve is not the smooth parabola centered at 0.5 that was expected. Two effects explain its shape. First, partly because the valves in configuration B are inefficient, and partly because of the flow dynamics, the greatest power output is seen when the pressure is high and the flow rate (which determines the losses) is low, and the net effect is a shift of the parabola to the right. Second, the high pressures act on the upper valve surfaces and tend to force them open, reducing the flow resistance and boosting performance. The result is a vertical distortion of the curve in the high pressure regions and extremely high power outputs. It is believed that the large valve deflections caused by these pressures would, in fact, fracture the valve diaphragms. Therefore, the performance benefits due to this effect must be acknowledged as a limitation of the model and should not be considered as a viable design option.

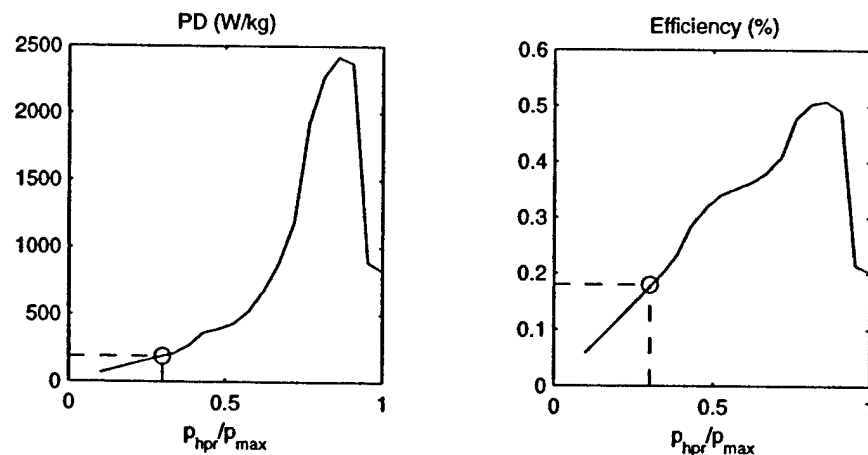


Figure 5.11 Parameter study 5: performance of configuration B versus the normalized pressure load, p_{hpr}/p_{max} . The nominal value of 0.3 is indicated.

For comparison, the analysis was repeated using configuration C, defined above, as the subject system. The results are shown in Figure 5.12. Due to the large pressure reductions caused by the compliant chamber, the effects mentioned in the preceding paragraph are absent and the expected curve is obtained. It can be seen that the maximum achievable PD is 15 W/kg. Noticeable in both Figure 5.11 and Figure 5.12 is that the power output is positive even when $p_{hpr}/p_{max} = 1$. This is due to the definition of p_{max} given in Chapter 3, which represents the pressure generated in a closed chamber when the pump is actuated from its rest position, and does not account for the additional stored elastic energy present as a result of the pump reaching its maximum negative deflection during operation. The conclusion reached in this study is that an optimal pressure load exists where the power density of the system is maximized, and that care should be taken when evaluating what represents a realistic design.

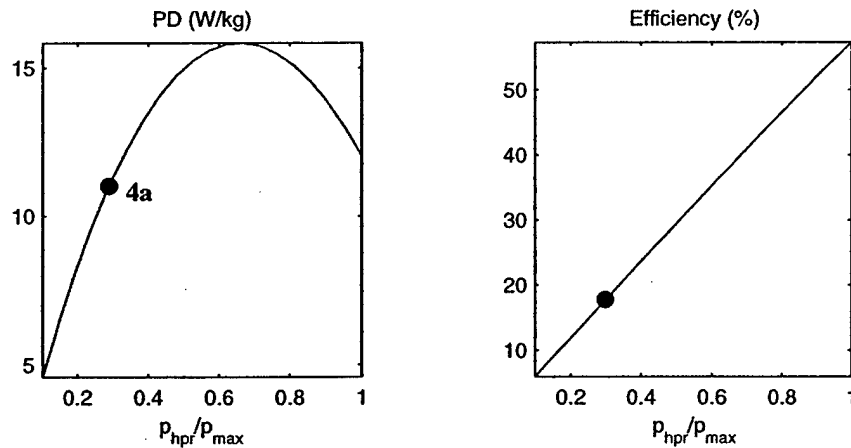


Figure 5.12 Parameter study 5: performance of configuration C versus the normalized pressure load, p_{hpr}/p_{max} . The nominal value of 0.3 is indicated. The dot corresponds to a simulation included in Appendix C.

Study 6: Valve leak parameter

The valve leak parameter, modeled as a minimum valve displacement above the valve seat, γ , is a term that is easily correlatable to experimental data but difficult to predict *a priori*. An investigation into the impact of this parameter on system behavior was therefore performed. As expected, power and efficiency are constant below some critical value (in this case $3\text{ }\mu\text{m}$) corresponding to an adequate valve seal. For $\gamma > \gamma_{crit}$, performance rolls off rapidly as the valves permit greater leakage. The small peak seen in the left plot is a purely a dynamic effect. The numerical value of γ_{crit} for a MHST configuration depends on several factors, most importantly the contact area between the valve and valve seat. It is therefore highly dependant on the ratio of the valve disc diameters to the diameter of sections II of the flow channels. The conclusion reached in this study is that, as expected, performance remains constant for γ below some value that represents adequate valve sealing, but rolls off rapidly once a gap size is reached where the valve begins to leak. For this particular design, that value is $3\text{ }\mu\text{m}$.

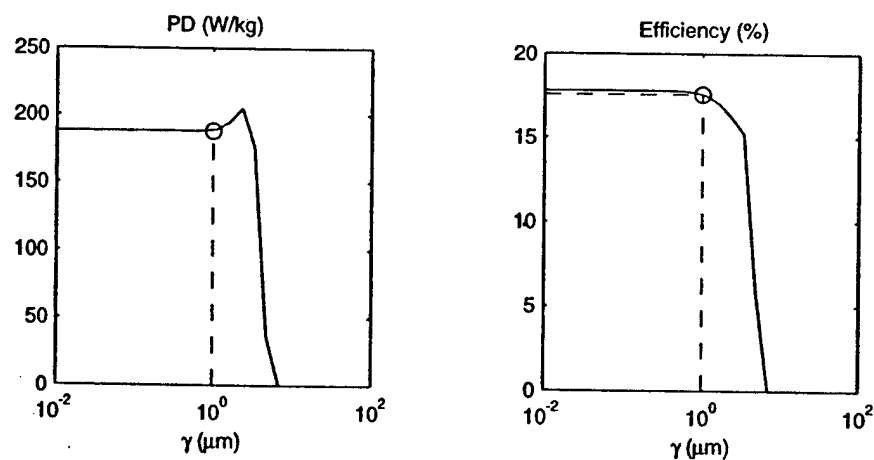


Figure 5.13 Parameter study 6: performance of configuration B versus the valve leak parameter, γ . The nominal value of $1\text{ }\mu\text{m}$ is indicated.

Study 7: Mercury as the working fluid

Mercury offers several key advantages over water as the working fluid in MHSTs: it has a much higher bulk modulus, 25 versus 2.24 GPa for water, and has no vapor pressure at room temperature, possibly aiding the avoidance of cavitation. Its disadvantages are a viscosity that is 50% greater than that of water, much higher density, and toxicity. Additionally, the surface tension of mercury is very high and would almost certainly exacerbate the problem of pump priming. Several simulations were completed to assess the relative merits of using mercury in the design. Since the increase in inductance due to the high density is greater than the stiffness increase provided by the higher bulk modulus, the natural frequency of a system using mercury is significantly lower than that of a water system. The resonance of configuration B, for example, drops to 1.81 kHz. Simulation 7a shows the predicted behavior of this system when excited at $f = 1.11f_n$. The results are $PD = 48 \text{ W/kg}$; $\eta = 18\%$; $Q = 8.9 \text{ ml/min}$, but are not comparable with the previous water system because of the lower frequency operation. Therefore, *configuration D* was defined as a baseline system with short channels ($L_I = 2 \text{ mm}$) in order to boost the frequency to the nominal $f_n = 6.69 \text{ kHz}$. Simulation of this system (Simulation 7b) predicted the following performance: $PD = 168 \text{ W/kg}$; $\eta = 18\%$; $Q = 30.9 \text{ ml/min}$. Inspection of the system behavior, though, shows that the higher fluid density leads to unexpected dynamics in the valve motions. The conclusion reached in this study is that mercury is a viable liquid, but does not provide performance levels as good as those given when water is used.

Study 8: Carbon tetrachloride as the working fluid

Carbon tetrachloride, a nonflammable liquid commonly used as a solvent for oils, greases, and waxes [Avallone and Baumeister, 1987], possess physical properties very similar to water. Although it has no obvious advantages, its use in MHST is explored here primarily to assess its usefulness as an alternative fluid. As with mercury, the density of the fluid, being different than water, leads to a different system frequency. Simulation 8a shows the behavior of configuration B using the fluid ($f_n = 5.30 \text{ kHz}$), while Simulation 8b predicts the response of a system with 60 mm flow channels (*configuration E*) and $f_n = 6.69 \text{ kHz}$. The performance of configuration E is $PD = 281 \text{ W/kg}$; $\eta = 18\%$; $Q = 51.6 \text{ ml/min}$. This

performance is significantly greater than that seen in the water system. Since almost all liquid micropumps use water as the working fluid, it is believed that, in the initial stages of prototype fabrication and testing, the use of water will permit the use of experimental data from the literature, and therefore offers advantages beyond the performance predictions presented here. However, the primary conclusion reached in this section is that carbon tetrachloride may provide performance enhancement that would warrant its experimental investigation as a working fluid.

Study 9: Valve disc diameter

The diameter of the valve disc was initially determined according to the pressure-balancing requirement stipulated in Chapter 2. However, some of the other valve parameters leading to this value were arbitrarily chosen. Therefore, an investigation into the effects that perturbations in this parameter have on the system performance is warranted. Three constraints must be established before investigating the effects of changing the diameter of the valve disc, d_{disc} . Firstly, it will be assumed that the ratio of the valve disc diameter to the channel section II diameter (i.e. the orifice within the valve seat) will remain constant throughout the study. This, however, has implications in that changes in the channel diameter affect the fluid inductance and therefore the system frequency. It must therefore be further stipulated that the system will always be excited at $f = 1.11f_n$. Secondly, increasing d_{disc} alone violates the pressure balanced condition stipulated in Chapter 2. To decouple these effects, the resulting pressure force is neglected throughout the study. Finally, increasing d_{disc} lowers the frequency of the valve. Since the parameter perturbations are to be small, and the disc accounts for a relatively small fraction of the valve's modal mass, these frequency changes will likewise be neglected.

The parameter was swept from $d_{disc} = 0.1$ to 1 mm; the results are shown in Figure 5.14. It can be seen that the performance increase is significant as d_{disc} becomes larger. The reason for this, however, is not obvious. Since the ratio of valve-to-channel diameter was constrained as constant, the viscous flow resistance of the valve is likewise constant (see Chapter 3). The reason for the performance increase is that, due to the larger disc areas,

the pressure force acting on them is larger and they therefore tend to open more. This reduces the flow resistance and boosts the power output. The sudden drop off visible as d_{disc} approaches 1 mm is because the pressure force reaches a point where it overwhelms the actuation force, and the valve can no longer close. The reason for the power increase is essentially the same as for study 5, and similar conclusions must be drawn: in the physical system, the increasing valve deflections caused by the higher pressure forces might result in valve fracture before any significant performance increase was seen. Increasing the valve disc diameter is therefore not considered to be a viable design option.

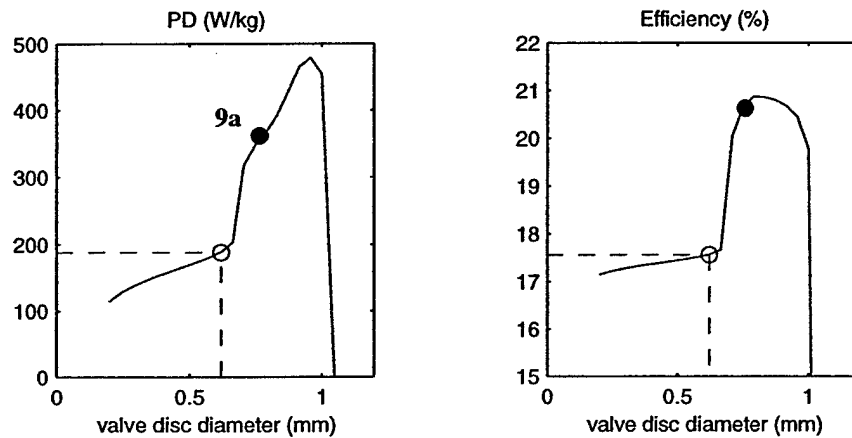


Figure 5.14 Parameter study 9: performance of configuration B versus the valve disc diameter, d_{disc} . The nominal value of 0.62 mm is indicated. The dot corresponds to a simulation included in Appendix C.

Study 10: System scale

Perhaps the most important parameter study in this work is that of system performance versus scale, λ . Investigations into how MHST behavior changes with geometric scaling will help determine if and where an optimum scale exists. As discussed in Chapter 1, it was suspected that system PD would increase linearly with decreasing system scale until, at some level, viscous effects would dominate behavior and eliminate the motivation for further miniaturization. In the forthcoming discussion, $\lambda = 1$ corresponds to the mesoscale systems described above.

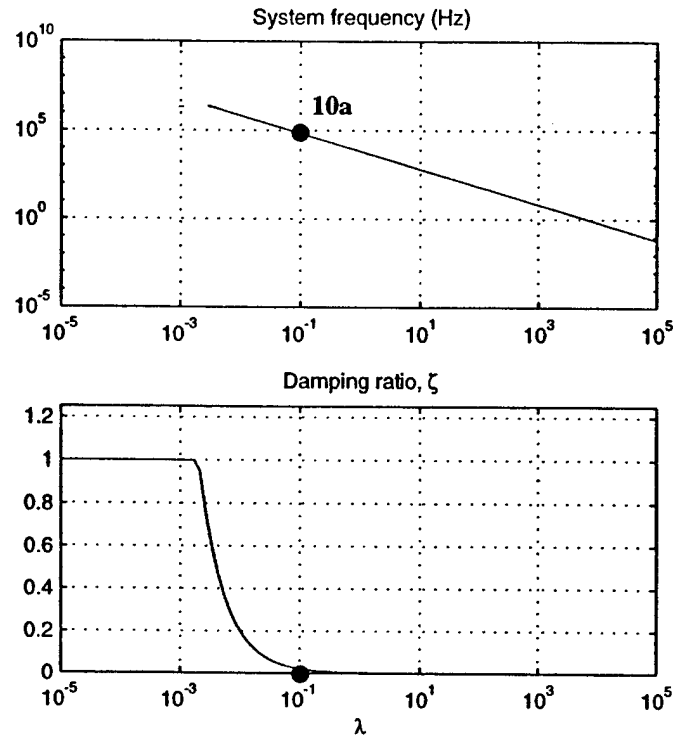


Figure 5.15 System frequency, f_n , and damping ratio, ζ , of configuration B versus system scale, λ . The scale factor is shown with respect to the mesoscale baseline such that $\lambda = 1$ corresponds to the given dimensions for configuration B. Frequency becomes real for $\lambda < 10^{-3}$ where the system is critically damped. The dot corresponds to a simulation included in Appendix C.

An appropriate way to begin the study is to examine how the natural frequency of the system depends on λ by making use of the state-space linear system approximation presented in Chapter 4. The results are shown in Figure 5.15 where it can be seen that the frequency increases as expected until $\lambda_{crit} = 10^{-3}$, where increasingly dominant viscous effects critically damp the system. The system frequency is therefore undefined for $\lambda < \lambda_{crit}$. It is logical to assume that performance trends will experience a transition near this region as well.

Multiple simulations were executed while sweeping through values of λ . As expected, power output begins to level off near $\lambda = 10^{-2}$ and is flat by 10^{-3} . These trends are encouraging and suggest that, subject to microfabrication limitations, performance increases from 10 to 100 can be expected by miniaturizing MHSTs to the MEMS scale. Of immedi-

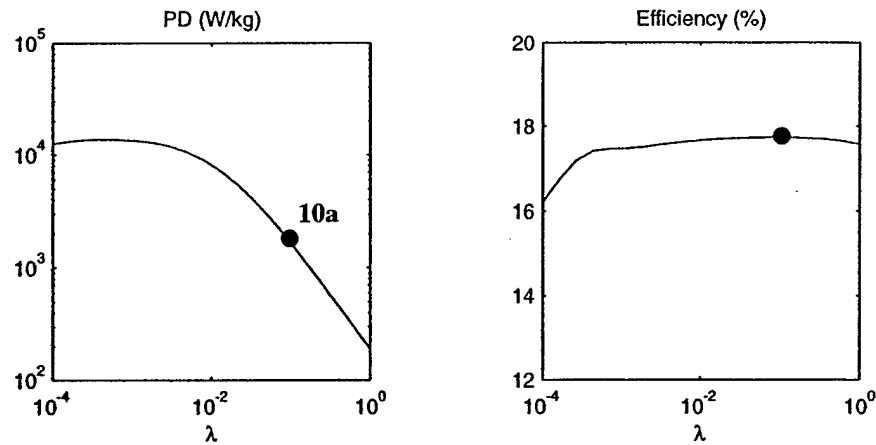


Figure 5.16 Performance of configuration B versus system scale, λ . The scale factor is shown with respect to the mesoscale baseline such that $\lambda = 1$ corresponds to the given dimensions for configuration B. The dot corresponds to a simulation included in Appendix C.

ate interest is the performance of the 1/10th scale system, *configuration G*, which is believed to be within the bounds of current micromachining technology. The behavior of configuration G was computed in Simulation 10a with the following performance results: PD = 1660 W/kg; $\eta = 18\%$; $Q = 0.3$ ml/min. Note that this system is a scaled down version of configuration B, which was capable of PD = 188 W/kg; $\eta = 18\%$; $Q = 34.6$ ml/min. In this case, the 1/10th scale reduction led to a PD increase of 8.8, while the efficiency remained roughly constant.

Study 11: Drive frequency versus valve frequency

The power output of the system is limited by the bandwidth of the valves. As previously seen, the natural frequency of the system can be significantly higher than that of the valves, as was the case for the original baseline design, configuration A. Since the power output is directly dependant on the frequency of operation, it is logical to assume that the mechanism should be operated at the highest frequency possible, which is to say the frequency near which the valve response rolls off. Figure 5.17 below plots the PD of the system for different driving frequencies, f , with respect to the fixed valve frequency, f_v . The system was always driven at $f = 1.11f_n$; the natural frequency was tuned by varying the length of channel section I, L_I . Looking at the left plot it is apparant that, although the

power begins to increase as expected, it then rises upward. This is because the valve is being dynamically excited by the pump. Since the drive frequency is within a decade of the valve resonance, the fluidic and pressure forces acting on the valve cause some overshoot in its position during opening. Although this overshoot is not large, the sensitivity of the valve's flow resistance to its deflection results in a significant reduction in that resistance and a concomitant boost in performance. This is the same phenomenon primarily responsible for the large differences in performance between configurations A and B.

It is also apparent that drive frequencies greater than $0.4f_v$ generate poor performance because the valve response time is not fast enough to keep up with the pump. The result is that, as the frequency is increased, more and more backflow occurs because the pump begins the second half of its cycle before the valve that was open during the first half of the cycle has time to close.

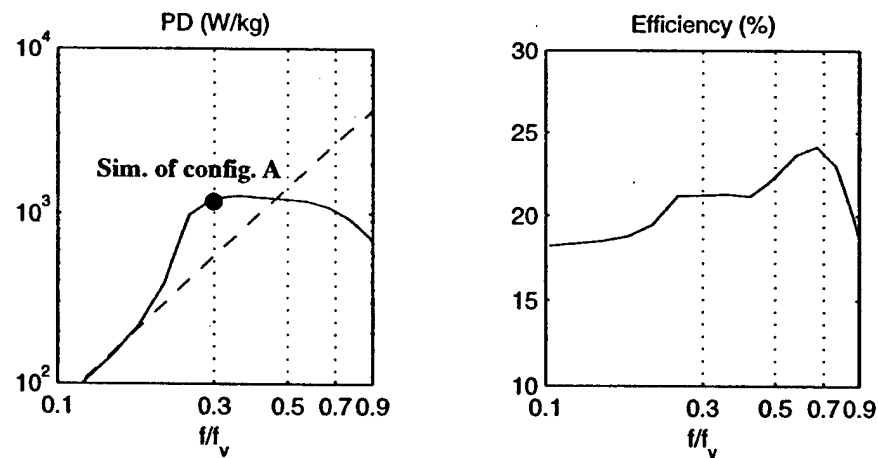


Figure 5.17 Parameter study 11: performance of configuration A versus the valve frequency, f_v . The x-axis is the drive frequency, f , normalized to the valve frequency. The straight line in the left plot projects the expected increase in power density if valve dynamics are neglected. The system was always driven at $f = 1.11f_n$; the natural frequency was varied by tuning L_f , where the minimum and maximum ratios of 0.1 and 0.9 correspond to lengths of 1000 and 9 mm respectively.

5.4 Final Design

Actuator

The knowledge gained from the analyses, computer simulations, and parameter studies was employed to arrive at a final design that, it is believed, represents the potential performance levels of MHSTs. The results obtained that the final design, implemented on a microscale (1/10th the size of the mesoscale device), indicate that the mechanism is capable of a power density that is one to two orders of magnitude greater than conventional electromechanical transducers.

The greatest difference between the final design and baseline configuration A is the length of the flow channels, L_I . As previously discussed, the bandwidth limitation of the valve necessitates the reduction of the system frequency. This can be accomplished either by decreasing the chamber stiffness or increasing the fluid inductance. The option chosen for the parameter study was to increase the fluid inductance by lengthening the flow channels, leading to configuration B. Unfortunately, the lengths necessary (10 cm) do not represent a feasible design, as the rest of the system is only 1 cm in diameter. However, inspection of equation (3.10) shows that the fluid inductance may also be increased by reducing the cross-sectional area of the flow channel. This was the solution adopted for the final design.

Although it was originally thought that the channels should possess the largest cross-sectional areas possible (which is still true if the valves are fast enough) it is shown here that this is not always the case. For the final design, section I was modified as follows: L_I was reduced to 3 mm (using configuration B as the reference), the width was reduced to 0.5 mm from 6 mm (the channel was originally the width of the chamber), and the height was increased from roughly 0.1 mm to 0.4 mm. These numbers were arrived at through many iterations where the frequency benefits resulting from reduced channel areas were weighed against the concomitant viscous flow resistance increases. Table 5.3 summarizes the mechanical characteristics of the final design.

TABLE 5.3 MHST final design characteristics (mesoscale).

| Drive | | Valve | | Valve Seat | |
|---------------------|---------------------------|------------------|----------------------|---------------------------|-----------------------------|
| m_p | 2e-3 g | m_v | 1.26e-4 g | k_{seat} | 2.73e9 N/m |
| m_{piston} | 0.06 g | k_v | 2727 N/m | γ | 1 μ m |
| k_p | 9.22e7 N/m | f_n | 23.39 kHz | Valve stroke ^a | 0.25 |
| C_s | 7.09e17 Pa/m ³ | k_v/k_{cp} | 8 | Channel Section I | |
| k_p/k_c | 0.20 | A_{eff} | 0.25 mm ³ | height | 0.4 mm |
| f_{drive}^b | 161.59 kHz | Field | 0.8 kV/mm | width | 0.5 mm |
| f_{drive}^c | 151.74 kHz | F_b | 0.21 N | length, L_I | 3 mm |
| y_{fr} | 1.4 μ m | x_{fr} | 77 μ m | R | 3.13e9 Pa/m ³ /s |
| Field | 1 kV/mm | p_b | 696.79 kPa | I_f | 1.57e4 m ⁻¹ |
| p_{max} | 926.13 kPa | p_{fr} | 232.69 kPa | Channel Section II | |
| p_{max}/p_{ideal} | 44% | η_{mech} | 10.6% | diameter | 0.59 mm |
| V_d | 0.09 μ l | ED | 23 mJ/kg | length, L_{II} | 0.5 mm |
| System | | | | R | 1.70e8 Pa/m ³ /s |
| $f_1 = f_n^d$ | 9.66 kHz | Materials | | I_f | 1.50e4 m ⁻¹ |
| f_2^e | 249.76 kHz | piezoelectric | PZN:PT | Materials | |
| M_{sys} | ~ 1.0 g | structure | Si, Pyrex | fluid | water |
| p_{hpr}/p_{max} | 0.5 | | | | |

- a. Stroke = allowed deflection / free deflection
b. Frequency of the drive with no fluid in the chamber
c. Frequency of the drive with closed, fluid filled chamber
d. First mode of the coupled structural-fluid system
e. Second mode of the coupled structural-fluid system

The predicted performance numbers for the mesoscale device, as well as the 1/10th scale system, are summarized in Table 5.5. It is evident that the expected performance of the microscale system is one to two orders of magnitude better than the average electromechanical transducers discussed in Chapter 1. The simulation results for the mesoscale design are shown in Figure 5.18. The results of the microsystem simulations are identical except for numerical values.

TABLE 5.4 MHST final design characteristics (microscale).

| Drive | | Valve | | Valve Seat | |
|---------------------|---------------------------|------------------|------------------------|---------------------------|------------------------------|
| m_p | 2e-6 g | m_v | 1.26e-4 g | k_{seat} | 2.73e8 N/m |
| m_{piston} | 6e-5 g | k_v | 272.7 N/m | γ | 1 μ m |
| k_p | 9.22e6 N/m | f_n | 233.9 kHz | Valve stroke ^a | 0.25 |
| C_s | 7.09e20 Pa/m ³ | k_v/k_{cp} | 8 | Channel Section I | |
| k_p/k_c | 0.20 | A_{eff} | 2.5e-3 mm ³ | | |
| f_{drive}^b | 1615.9 kHz | Field | 0.8 kV/mm | | |
| f_{drive}^c | 1517.4 kHz | F_b | 2.1e-3 N | | |
| y_{fr} | 0.14 μ m | x_{fr} | 7.7 μ m | height | 0.04 mm |
| Field | 1 kV/mm | p_b | 6967.9 kPa | width | 0.05 mm |
| p_{max} | 926.13 kPa | p_{fr} | 2326.9 kPa | length, L_I | 0.3 mm |
| p_{max}/p_{ideal} | 44% | η_{mech} | 10.6% | R | 3.13e12 Pa/m ³ /s |
| V_d | 9e-5 μ l | ED | 23 mJ/kg | I_f | 1.57e5 m ⁻¹ |
| System | | | | Channel Section II | |
| | | | | diameter | 0.06 mm |
| | | | | length, L_{II} | 0.05 mm |
| | | | | R | 1.70e11 Pa/m ³ /s |
| | | | | I_f | 1.50e5 m ⁻¹ |
| $f_1 = f_n^d$ | 96.6 kHz | Materials | | | |
| f_2^e | 2497.6 kHz | | | | |
| M_{sys} | ~ 1e-3 g | | | | |
| p_{hpr}/p_{max} | 0.5 | | | | |
| | | | | piezoelectric | PZN:PT |
| | | | | structure | Si, Pyrex |
| | | | | fluid | water |

a. Stroke = allowed deflection / free deflection

b. Frequency of the drive with no fluid in the chamber

c. Frequency of the drive with closed, fluid filled chamber

d. First mode of the coupled structural-fluid system

e. Second mode of the coupled structural-fluid system

The capabilities of the final design are the product of several factors. The best performance was obtained by driving the system precisely at resonance. It is believed that the added viscous resistance of the thinner channels leads to a system that is more robust with respect to the chaotic behavior observed in Simulation 2b. The electrical signal was a sinusoidal waveform with the valves driven by a square wave operating at a relative phase of 310° and a duty cycle of 35%. Part of the reason for improved performance in the final

design is that the system is able to be driven at 41% of the valve resonance, or $ff_v = 0.41$, without loss of flow rectification, which immediately leads to a 10% increase in performance over the baseline system simply because more fluid is being pumped. The redesign of section I of the flow channel, specifically, the increase in its height, also contributes to the boost in power output. The pressure load was reoptimized and a final value of $p_{hpr}/p_{max} = 0.5$ was used. These factors are primarily responsible for the increased performance.

TABLE 5.5 Performance of the final MHST design

| System scale (λ) | PD (W/kg) | η (%) | Q (ml/min) |
|----------------------------|-----------|------------|--------------|
| Mesoscale (1) | 960 | 63 | 106 |
| Microscale (0.1) | 9600 | 51 | 1.1 |

It can be seen in Table 5.5 that a 12% decrease in efficiency is incurred when the system is miniaturized to the microscale. Due to the smaller cross-sectional areas of the flow channels, it is to be expected that viscous effects will hinder system performance at a scale that is larger than the λ_{crit} identified in Study 10. An investigation of the effects of system scale on the performance of the final design was therefore undertaken to ascertain the new optimal scale. Figure 5.19 shows the results of the study, where it can be seen that power density begins to roll off for $10^{-2} < \lambda < 10^{-1}$. It is therefore concluded that the optimal system for the final design is $\lambda = 10^{-1}$, corresponding to the 1/10th microscale system described above. Noticeable in this plot is the prominent decrease in efficiency as scale is reduced to the microscale, where no decrease was seen in configuration B. This is due to the fact that the channels in the final design are much narrower, and significant viscous effects appear at larger scales.

Power Harvester

Although optimization of the performance of the corresponding power harvester is beyond the scope of this report, sample results of initial model simulations are included for illustrative purposes. The final design discussed above was implemented as a power harvester

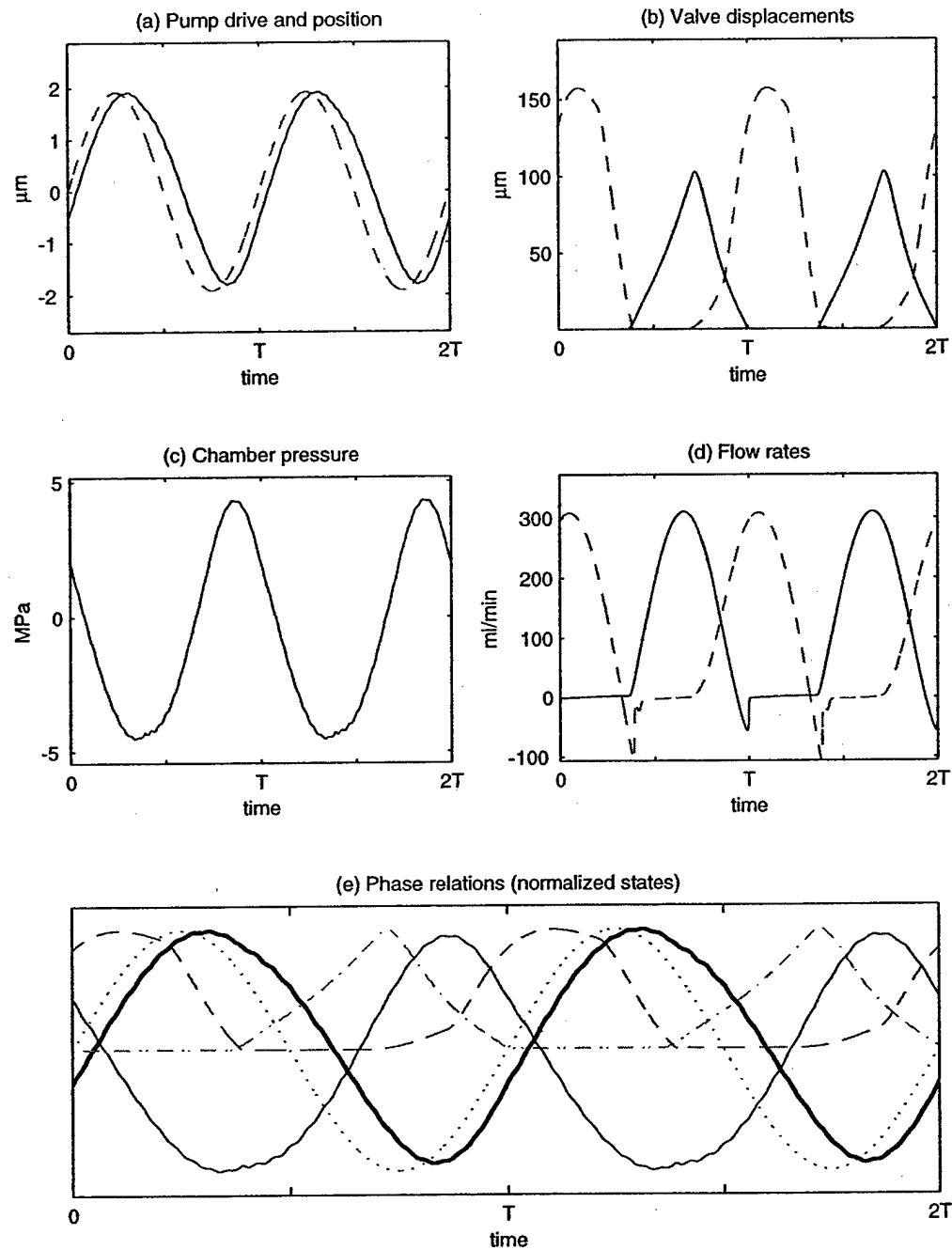


Figure 5.18 Simulation of final (mesoscale) design: $f = f_n = 9.66$ kHz, $f_v = 23.4$ kHz. Plot (a) overlays the pump displacement (solid) with the normalized drive signal (dashed). Plots (b) and (d) show the displacements and flows of the inlet (solid) and outlet (dashed) valves. Plot (e) indicates the phase relations between the normalized pump position (heavy solid), chamber pressure (solid), drive signal (dotted), inlet valve displacement (dot-dashed), and outlet valve displacement (dashed).

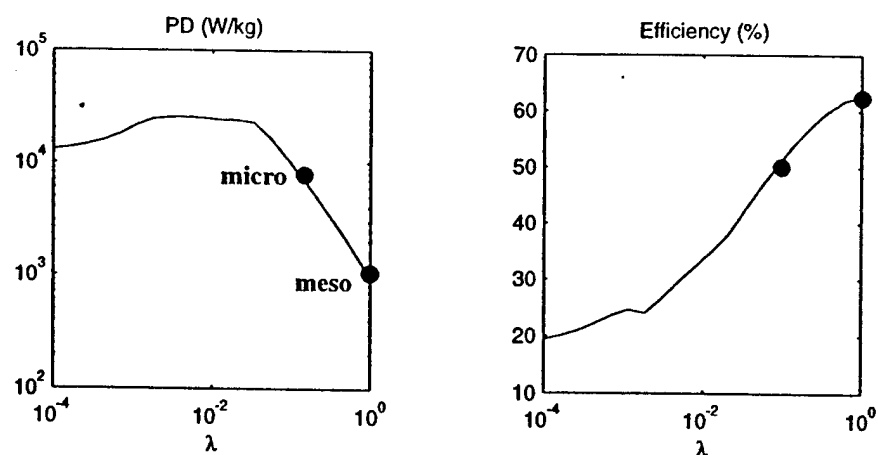


Figure 5.19 Performance of the final design versus system scale, λ . The scale factor is shown with respect to the mesoscale device.

by coupling the rectifying circuit equation (see Chapter 3) and then applying a static high pressure source. During operation the valves were toggled at the natural frequency of the system and the electrical energy extracted was stored in a battery maintained at one-half the peak open-circuit excursion voltage of the piezoelectric element. The time history of the system is included in Appendix C as Simulation 11. Figure 5.20 below shows the electrical power flows in the mechanism corresponding to these plots. As discussed in Chapter 3, when the induced voltage across the piezoelectric element is greater than the battery voltage, the diode bridge conducts and the voltage is clipped. During these periods, charge is transferred from the piezoelectric to the battery as current flows through the diodes.

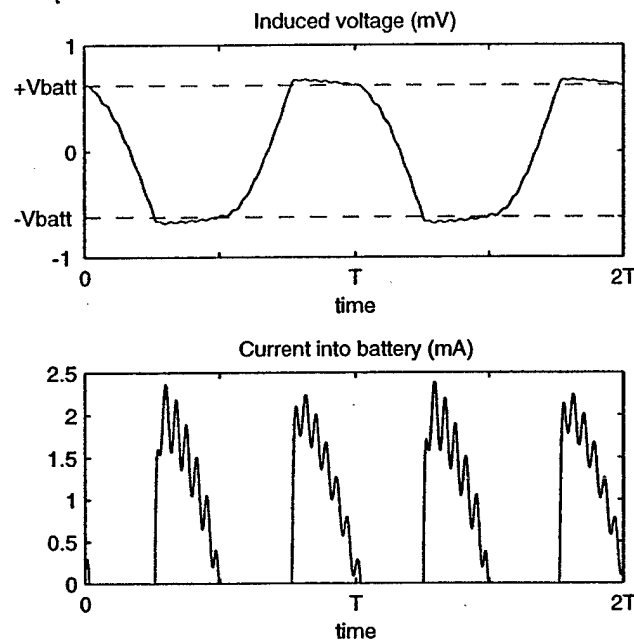


Figure 5.20 Electrical power flow in the power harvester. The top plot shows the induced voltage across the active element being clipped at \pm the battery voltage. The bottom plot shows the current to the battery.

5.5 Summary

This chapter identified a baseline design that exhibited the characteristic behavior of MHST systems, discussed the results of computer simulations of this system and explained the observed dynamics, presented the results of a parameter study focusing on the influential design variables, and defined a final design that represents the achievable performance levels of MHSTs. In the first part of the chapter the definition of the baseline system was discussed, with particular attention given to the tuning of the system by increasing the fluid inductance. This was necessary in order to lower the system resonance below limitations set by the valves. It was shown that effective system performance could only be gained by driving the pump near the fundamental frequency of the system. The simulation results were analyzed by inspecting the time histories of the states and examining the energy tracking in the system. The middle section of the chapter dealt with identifying those parameters to be investigated, then presenting the results of perturbations of those parameters. The final section of the chapter used the information gained in the previ-

ous analyses to define a final mechanism design that would represent the potential performance levels of MHST systems and serve as the focus of the feasibility assessment. Finally, the simulation of the power harvester was discussed.

Chapter 6

CONCLUSIONS AND RECOMMENDATIONS

6.1 Summary

The aim of this thesis was to assess the feasibility of the Micro Hydraulic Solid-State Transducer concept. Two important classes of electromechanical transducers are *actuators*, mechanisms that convert electrical input energy into mechanical forces to perform work on an interfacing structure (or other mechanical load) to alter its state, and *power harvesters*, mechanisms that extract potential mechanical energy from an interfacing system and convert it into electrical energy that can be consumed or stored. An effective metric for comparing transducers for applications with weight and size constraints is the rate of energy conversion normalized by the transducer mass, or *power density*. *Efficiency*, defined in this work to be the ratio of output to input energy, is also a powerful comparison tool as it indicates the effectiveness of the transduction.

The motivation for this thesis was the unexploited power density capabilities of solid-state transduction materials, specifically, the recently emergent single-crystal piezoelectrics. These materials are able to generate extremely high stresses and, because of their high bulk moduli, have very large bandwidths; these two properties engender them with high power densities. However, since the material's optimal power output is the product of its single stroke energy and its bandwidth, it is necessary to operate the device at its maximum frequency to realize this power. Unfortunately, most applications require much slower actuation speeds and, as a result, do not utilize the full potential of the material.

Additionally, compared to more conventional transducers such as electric motors and hydraulic pistons, piezoelectrics are only capable of very small strains which limits their usefulness in many applications.

The major goal of this work was to assess the feasibility of a new transducer comprised of a microhydraulic drive, valves, and pressure reservoirs that is capable of efficiently exploiting the power densities of single-crystal piezoelectrics. The realization of this goal depended on several subsidiary tasks, which formed the objectives of the thesis. The objectives were:

1. Development of a prototype design
2. Derivation of an analytical system model
3. Identification of the key issues and trade-offs in the design process
4. Investigation of the effects of scale on performance
5. Investigation of the effects of parameter changes on system performance

The MHST concept was first introduced in Chapter 1, followed by a discussion of the prototype design and its principle of operation, both as an actuator and a power harvester. In Chapter 2 the rationale behind the design was discussed. The strategy used in the design process was presented as well as the existing goals and constraints. A description of the system components was begun by explaining the function and geometry of the hydraulic amplifier mechanism. The design of the drive, valves, reservoirs, gas chamber, and flow channels was then addressed. The considerations and results of the materials selection process were then set forth, followed by a discussion of the function and integration of the system electronics. Finally, manufacturability of the system was addressed by considering the current state of micromachining technology as well as information gained from the fabrication of prototype drive pistons. Chapter 4 addressed the optimization of the component designs using finite element analysis and static performance metrics after the mathematical tools necessary had been presented in Chapter 3.

The analytical system model was derived in Chapter 3 and consisted of a theoretical model that was used for numerical simulation of the integrated system, and finite element models

of the separate components. The first part of the chapter discussed the requirements of the model and the issues involved, especially the dependence of fluid behavior on system scale. The relevant assumptions were then set forth, from which canonical fluidic component models were derived which highlighted the relations of important design parameters such as chamber compliance, fluid inertia, flow resistance, and so forth. The canonical models were then applied to the design to arrive at a set of equations that fully describe the dynamic behavior of the MHST. Finally, the use of the finite element model to augment the theoretical model by providing numerical values for parameters such as chamber compliance was discussed.

The third objective, identification of the key issues and design trade-offs, was ongoing throughout the thesis. The primary issues requiring attention in the design process are:

- Strong coupling between structure and fluid dynamics
- Viscous energy dissipation in valves and flow channels
- Impact of chamber compliance and fluid compressibility on performance
- Potential for cavitation during operation
- Geometric constraints imposed by microfabrication limitations
- Manufacturing process issues such as fluid encapsulation, piezoelectric element integration, and alignment and bonding

The identification of design trade-offs was discussed primarily in Chapter 4. The most prominent ones were found to be:

Static

- Valve stroke \leftrightarrow valve bandwidth (compliance versus stiffness)
- Large \leftrightarrow small valves (larger valves provide greater strokes and permit larger flow channel diameters but have lower bandwidths and increase system mass)
- Large \leftrightarrow small flexible diaphragm diameter (a diameter that is too small reduces deflection by causing the diaphragm to be clamped, while a diameter that is too large does the same by reducing the hydraulic amplification ratio)

Dynamic

- Large \leftrightarrow small chamber capacitance (a stiff chamber leads to greater power output but causes the system frequency to exceed the valve bandwidth).
- Large \leftrightarrow small valve stroke (small strokes give the valve a greater holding force but constrict flow and lead to viscous losses)
- Power \leftrightarrow efficiency (it is possible to design an arbitrarily efficient system by reducing fluid flow)

The study of performance versus scale began in Chapter 1, where the motivation for miniaturization (i.e. increased power density) was introduced. The general scaling laws for some mechanical phenomena were also presented. Chapter 3 then addressed the modeling issues related to scale, particularly with respect to fluid behavior. Finally, system simulations provided numerical results. The investigation yielded the expected answer: system performance increases linearly with decreasing system scale until a critical size is reached where viscous effects dominate; there is no motivation for miniaturization past this point. For the final design presented in this report the critical size was found to be $\lambda_{crit} \sim 10^{-2}$, with decreasing performance visible past $\lambda \sim 10^{-1}$. These scale factors are in reference to the mesoscale system, with an overall size of roughly 1 cm, suggesting that the optimal system scale is a mechanism with an outer dimension of 0.1-1 mm.

The final objective, investigation of the effects of parameter changes on system performance, was executed in Chapter 5. Although perturbations to a specific system were studied, the trends obtained are, to some extent, generalizable to other microhydraulic systems, and illustrate the impact certain parameters such as chamber capacitance, electrical drive signal characteristics, and pressure load have on system behavior. The information gained from this study was used to arrive at the final MHST design.

6.2 Conclusions

Feasibility

The predicted performance of MHST actuators clearly indicates their potential as an effective transducer technology. Simulations suggest that a microscale device is capable of a power density on the order of 10^4 W/kg, which is one to two orders of magnitude greater than conventional electromechanical transducers. Successful implementation of this mechanism would have a tremendous impact on a wide array of transducer applications.

The feasibility of these devices is contingent on the following issues, which may be grouped into *behavior* and *fabrication* related. The behavior issues are phenomena that must be determined experimentally, while the fabrication issues, already discussed in Chapter 2, relate primarily to the success of future microfabrication research.

Behavior

- *Cavitation*: The presence of acoustic cavitation in MHST systems could impose severe bounds on their success. The phenomenon cannot be predicted by the model and must be experimentally investigated. Additionally, measures must be taken to ensure the uniform pressure in the chamber does not fall below the vapor pressure of the working fluid. In the final design simulation, a minimum gage pressure of -4 MPa (-3.9 MPa atmospheric) was observed. Since the vapor pressure of water is 2339 Pa, it is clear that the average operating pressure of the chamber must be biased to a higher level, and/or another liquid must be used (see discussion on mercury as the working fluid in Chapter 2).
- *Component stress and fatigue*: the stress analysis performed in this work was necessarily simplified due to limited knowledge of the geometric details of the microfabricated structure (e.g. fillet radii at the diaphragm tether points). MHST success relies on the ability to accurately predict and control stresses in the elastic structures. Furthermore, although single-crystal Si has excellent fatigue properties, the high frequencies of MHSTs result in an extremely large number of deformation cycles. Fatigue in these systems is therefore an unknown factor.

Fabrication

- Integration of the piezoelectric material
- Fluid encapsulation
- Alignment and bonding

Valve limited performance

The valve is the primary limiting factor in the current MHST design. It was found that the system was capable of operating at very high frequencies but was limited by the bandwidth of the valves. The present valve design is based on a compromise between a very compliant structure (permitting a large valve stroke) and a very rigid structure (required for high bandwidth). An improved valve would benefit the system in two ways. First, a faster mechanism would permit the design of a pump system with a very high natural frequency, increasing the power output perhaps by a factor of 3-5. Secondly, it was found that, for a given valve design, the efficiency of the system was largely invariant with respect to the other design parameters. Therefore, implementation of a valve with reduced flow resistance (e.g. a larger stroke) may be the only way to significantly boost the performance of MHSTs.

Structural-fluidic dynamic coupling

Due to the strong interactions between the structural capacitance and fluid inductance in microhydraulic systems it is necessary to operate MHSTs at or near their resonant frequencies. Driving frequencies below this level result in pressure and flow oscillations that can lead to a loss of flow rectification, while drive frequencies exceeding it result in very little fluid flow. This requirement can impose severe restrictions on the MHST design. For instance, although it was found that rigid pump chambers allow high pressures to be generated and result in improved power output, they can also cause the system to have a natural frequency that exceeds the limitation imposed by the valve, preventing resonant operation. The result is a fundamental design constraint consisting primarily of a relation between chamber compliance, the fluid inductance, and the valve bandwidth.

Optimal system scale

The optimal system scale for the final design considered in this work was found to be $\lambda \sim 10^{-1}$, or 1/10th the size of the mesoscale system, corresponding to an overall outer diameter of 1 mm. Improved performance was evident with further miniaturization to $\lambda \sim 10^{-2}$, but at a reduced rate due to increasing viscous effects. Although it is believed that a 1/10th scale reduction of the mesoscale MHST is possible, pending successful elimination of the microfabrication obstacles listed in Chapter 2, further miniaturization would be difficult without modification of the design.

Parameter sensitivity

The predicted performance of MHSTs is very sensitive to some of the design parameters, especially the characteristics of the electrical power signal. It was shown that the phase relations between the valve and pump, the shape of the input waveform, and the proximity of the drive frequency to the valve resonance had dramatic effects on system behavior. It is believed that this same sensitivity would be seen in the physical system. In some cases, such as the improved performance obtained by the excitation of the valve dynamics, and the observed chaotic behavior when driven at the system resonance, it is possible that the effects stem from model sensitivity and is unclear whether they would be observed in the physical system.

6.3 Recommendations for Future Work

Prototype fabrication and testing

The logical next step in the development of MHSTs is the fabrication, instrumentation, and testing of a mesoscale system for the purposes expounded in Chapter 2. The data obtained from these experiments will serve to validate/update the model and provide valuable insight into the feasibility of further miniaturization.

Stress and fatigue analysis

One specific area of investigation not addressed in this work is the identification of the failure modes of the mechanism. Much research is required in the areas of stress analysis and control in the Si microstructures, especially fracture mechanics and fatigue characterization. Consideration must also be given to the effects of various bonding techniques on stress. Extensive studies must be made of the fillet radii and surface finish resulting from the chosen manufacturing process(es). Detailed FEM analyses, augmented by experimental fracture data, can then be used to verify or modify the design.

Thermal analysis

Another area requiring investigation is a detailed analysis of thermal effects in the systems. The low efficiencies seen in most of the simulations suggest that a significant percentage of the energy input to the system will be converted to thermal energy via forced viscous flow. It is possible that temperature levels could reach critical levels that vaporize the fluid, plastically deform the structures, or otherwise hinder performance. Measurements should therefore be made to determine the quantity of heat that is generated in the prototype.

Fundamental microfabrication studies

Further research into microfabrication techniques is required if successful MHST are to be realized. The immediate goals of this research were stipulated at the end of Chapter 3. The viability of a 1/10th scale reduction of the mesoscale design must also be studied. Since the diaphragm thicknesses used in the mesoscale system are near the limits of those that are commercially available, it will be necessary to either develop techniques to create finer membranes or modify the design.

Coupled flow analysis

The dynamics of MHSTs are such that the model presented in this report can only approximate the behavior of the flow. To fully understand the fluid phenomena in the system, numerical flow studies with coupled fluid-structure interaction must be implemented. As

mentioned in Chapter 3, this can either be done by using an analysis package capable of such analyses, or by linking a structural finite element model with a CFD package and performing iterative solutions. The results can then be compared with the experimental data to fully characterize the fluid behavior.

REFERENCES

- [Ashby, 1992] Ashby, M. F., *Materials selection in mechanical design*, Pergaman Press, Oxford.
- [Avallone and Baumeister, 1987] Avallone, E.A., and Baumeister, T. III, *Mark's standard handbook for mechanical engineers*, 9th edition, McGraw-Hill, New York.
- [Bent, 1997] Bent, A.A., "Active fiber composites for structural actuation," MIT Ph.D. Thesis.
- [Bass et al., 1994] Bass, V., van der Schoot, B.H., Jeanneret, S., and de Rooij, N.F., "Integrated flow-regulated silicon micropump," *Sensors and Actuators A*, Vol. 43, pp. 335-338.
- [Beuller and Wiley, 1965] Beuller, W.J., and Wiley, R.C., "Nickel - Base Alloys," U.S. Patent 3174851.
- [Bloor et al., 1994] Bloor, D., Flemings, M., Brook, R., Subhash, M., and Cahn, R., editors, *The Encyclopedia of Advanced Materials, Volume 4*, Cambridge, Cambridge University Press.
- [Bosch et al., 1992] Bisch, D., Heimhofer, B., Muck, G., Seidel, H., Thumser, U., and Welser, W., "A silicon microvalve with combined electromagnetic/electrostatic actuation," *Sensors and Actuators*, A37-A38, pp. 684-692.
- [Bourouina and Grandchamp, 1996] Bourouina, T., and Grandchamp, J.-P., "Modeling micropumps with electrical equivalent networks," *Journal of Micromechanics and Microengineering*, Vol. 6, pp. 398-404.
- [Bryzek et al., 1994] Bryzek, J., Peterson, K.E., McCulley, W., "Micromachines on the match," *IEEE Spectrum*, May.
- [Burgess et al., 1997] Burgess, S.C., Moore, D.F., Newland, D.E., and Klaubert, H.L., "A study of mechanical configuration optimisation in micro-systems," *Research in Engineering Design*, Vol. 9, pp. 46-60 .
- [Chan and Hagood, 1994] Chan, K.H., and Hagood, N.W., "Modeling of non-linear piezoceramics for structural actuation," *Proceedings SPIE Smart Structure and Intelligent Systems Conference (Orlando, Florida)*, Vol. 2190, pp. 194-205.
- [Crandall et al., 1982] Crandall, S.H., Karnopp, D.C., Kurtz, E.F. Jr., and Pridmore-Brown, D.C., *Dynamics of mechanical and electromechanical systems*, Krieger Publishing Co., Malabar, Florida.

- [DARPA, 1997] Defense Advances Research Projects Agency (DARPA), Broad agency announcement #97-44, Energy Harvesting, Section I.
- [Du Plessis, 1996] Du Plessis, A.J., "Modeling and experimental testing of twist actuated single cell composite beams for helicopter blade control," MIT S.M. Thesis.
- [Esashi et al., 1989] Esashi, M., Shoji, S., and Nakano, A., "Normally closed microvalve and micropump fabricated on a silicon wafer," *Sensors and Actuators*, Vol. 20, pp. 163-169.
- [Esashi, 1990] Esashi, M., "Integrated microflow control systems," *Sensors and Actuators*, A21-A23, pp. 161-167.
- [Fox and McDonald, 1992] Fox, R.W., and McDonald, A.T., *Introduction to Fluid Mechanics*, Fourth edition, John Wiley & Sons, Inc., New York.
- [Gardner, 1994] Gardner, J.W., *Microsensors: principles and applications*, John Wiley, Chichester.
- [Gerlach and Wurmus, 1995] Gerlach, T., and Wurmus, H., "Working principle and performance of the dynamic micropump," *Proceedings IEEE Micro Electro Mechanical Systems (Amsterdam, Netherlands)*, pp. 221-226.
- [Gravesen et al., 1993] Gravesen, P., Branebjerg, J., and Jensen, O.L., "Microfluidics - a review," *Journal of Micromechanics and Microengineering*, Vol. 3, pp. 168-182.
- [Hagood et al., 1990] Hagood, N.W., Chung, W., and von Flotow, A., "Modeling of piezoelectric actuator dynamics for active structural control," *J. Intelligent Materials, Systems, and Structures* 1, pp. 327-354.
- [Hagood, 1997] Hagood, N.W., personal communication, Nov.
- [Ho and Tai, 1996] Ho, C.-M., and Tai, Y.-C., "Review: MEMS and its applications for flow control," *Journal of Fluids Engineering*, Vol. 118, pp. 437-447.
- [Hollerbach et al., 1992] Hollerbach, J.M., Hunter, I.W., and Ballantyne, J., "A comparative analysis of actuator technologies for robotics," *Robotics Review* 2, Eds. Khatib and Oussama, MIT Press, pp. 299-342.
- [Huber et al., 1996] Huber, J.E., Fleck, N.A., and Ashby, M.F., "The selection of mechanical actuators based on performance indices," *Proceedings of the Royal Society of London, Series A*, Vol. 453, No. 1965, p. 2185.
- [Huff et al., 1993] Huff, M.A., Gilbert, J.R., and Schmidt, M.A., "Flow characteristics of a pressure balanced-microvalve," *Technical Digest of Transducers 93*, pp. 89-101.
- [Hurtado et al., 1995] Hurtado, I., Van Humbeeck, J., and Moo, C., "Elastic modulus

- behavior in dual phase Cu-Al-Ni-Ti-(Mn) shape memory alloys," *Proceedings Smart Structures and Materials Conference (San Diego, California)*, Vol. 2441, pp. 131-138.
- [Isacsson et al., 1994] Isacsson, C., Krus, P., and Palmberg, J-O., "A method for measuring dynamic valve characteristics," *7th International Fluid Power Workshop*, pp. 279-294.
- [Jaffe et al., 1971] Jaffe, B., Cook, W.R., and Jaffe, H., *Piezoelectric Ceramics*, Academic Press, New York.
- [Jerman, 1990] Jerman, H., "Electrically-activated, micromachined diaphragm valves technical digest," *IEEE Sensors & Actuators Workshop*, pp. 65-69.
- [Kelly, 1973] Kelly, A., *Strong Solids*, Clarendon Press, Oxford.
- [Koch et al., 1996] Koch, M., Evans, A.G.R., and Brunnschweiler, A., "Coupled FEM simulation for the characterization of the fluid flow within a cantilever valve," *Proceedings MME96 (Micro Mechanics Europe) (Copenhagen, Denmark)*, pp. 160-163.
- [Lide, 1995] Lide, D.R., editor, *CRC Handbook of Chemistry and Physics*.
- [Mattiati, O.E., 1971] Mattiat, O.E., editor, *Ultrasonic Transducer Materials*, Plenum Press, New York, pp. 101-107
- [Mehregany and Huff, 1995] Mehregany, M., and Huff, M.A., "Microelectromechanical systems," *Proceedings IEEE Cornell conference on advanced concepts in high speed semiconductor devices and circuits (Ithaca, New York)*, pp. 9-18.
- [Miyazaki et al., 1991] Miyazaki, S., Kawai, T., and Araragi, M., "A piezo-electric pump driven by a flexural progressive wave," *Proceedings IEEE Micro Electro Mechanical Systems (Nara, Japan)*, pp. 283-288.
- [Nakagawa et al., 1990] Nakagawa, S., Shoji, S., and Esashi, M., "A micro chemical analyzing system integrated on a silicon wafer," *Proceedings IEEE MEMS Workshop*, pp. 89-94.
- [Nelli Silva et al., 1997] Nelli Silva, E.C., Ono Fonseca, J.S., and Kikuchi, N., "Optimal design of piezoelectric microstructures," *Computational Fluid Mechanics*, Vol. 19, p. 397.
- [Ohnstein et al., 1990] Ohnstein, T., Fukiura, T., Ridley, J., and Bonne, U., "Micromachines silicon microvalve," *Proceedings IEEE MEMS Workshop*, pp. 95-98.
- [Olsson et al., 1996] Olsson, A., Enoksson, P., Stemme, G., and Stemme, E., "An improved valve-less pump fabricated using deep reactive ion etching," *IEEE*

- Annual International Workshop on Micro Electro Mechanical Systems (San Diego, California)*, pp. 479-484.
- [Piché et al., 1995] Piché, R., Ellman, A., and Vilenius, M., "Integration of numerically stiff fluid power circuit models using an L-stable Runge-Kutta method," *7th International Fluid Power Workshop (Bath, England), Fluid Power Series*, Vol. 7, pp. 89-100.
- [Polla et al., 1994] Polla, D.L., Robbins, W.P., Glumac, D.E., Francis, L.F., and Erdman, A.G., "An undergraduate instructional course on microelectromechanical systems fabrication," *IEEE Frontiers in Education Conference (San Jose, California)*, pp. 297-301.
- [Peterson, 1982] Peterson, K.E., "Silicon as a mechanical material", *IEEE Proceedings*, Vol. 70, No. 5, pp. 420-457.
- [Precht and Hall, 1997] Precht, E.F., and Hall, S.R., "Design of a high efficiency discrete servo-flap actuator for helicopter rotor control," *Proceedings SPIE Smart Structures and Integrated Systems Conference (San Diego, California)*, pp. 158-182.
- [Schneider, 1992] Schneider, S.J., Jr., Volume Chairman, *Engineered Materials Handbook*, Vol.4, Ceramics and Glasses, US.
- [Shoji and Esashi, 1988] Shoji, S., and Esashi, M. "Micromachining for chemical sensors," *Chem. Sensor Techn.*, Vol. 1, pp. 179-193.
- [Shoji et al., 1988] Shoji, S., Esashi, M., and Matsuo, M., "Prototype miniature blood gas analyzer fabricated on a silicon wafer," *Sensors and Actuators*, Vol. 14, pp. 101-107.
- [Shoji and Esashi, 1994] Shoji, S., and Esashi, M., "Microflow devices and systems," *Journal of Micromechanics and Microengineering*, Vol. 4, pp. 157-171.
- [Smits, 1990] Smits, J.G., "Piezoelectric micropump with three valves working peristaltically," *Sensors and Actuators*, A21-A23, pp. 203-206.
- [Spearing and Chen, 1997] Spearing, S. M., and Chen, K.S., "Micro-gas turbine engine materials and structures," *Ceramic Engineering and Science Proceedings*, Vol. 18, No. 4.
- [Stehr et al., 1996] Stehr, M., Messner, S., Sandmaier, R., and Zengerle, R., "A new micropump with bidirectional fluid transport and selfblocking effect," *IEEE Annual International Workshop on Micro Electro Mechanical Systems (San Diego, California)*, pp. 485-490.

- [Sze, 1988] Sze, S.M., *VLSI Technology*, Second edition, McGraw-Hill, New York.
- [Tai and Muller, 1989] Tai, Y.C., and Muller, R.S., "IC-Processed electrostatically synchronous micromotors," *Sensors and Actuators*, Vol. 20, pp. 49-55.
- [Trimmer and Jebens, 1989] Trimmer, W., and Jebens, R., "Actuators for micro robots," *Proceedings IEEE International Conference on Robotics and Automation* (Scottsdale, Arizona), Vol. 3, pp. 1547-1552.
- [Ulrich et al., 1995] Ulrich, J., Fuller, H., and Zengerle, R., "Static and dynamic flow simulation of a KOH-etched micro-valve," *Transducers '95, Eurosensors IX* (Stockholm, Sweden), pp. 17-20.
- [van de Pol, 1989] van de Pol, E.C.M., "A pump based on micro-engineering techniques," Thesis, University of Twente, Netherlands.
- [van Lintel et al., 1988] van Lintel, H.T.G., van de Pol, F.C.M., and Bouwstra, S., "A piezoelectric micropump based on micromachining of silicon," *Sensors and Actuators*, Vol. 15, pp. 153-167.
- [Wang et al., 1994] Wang, K.W., Kim, Y.S., and Shea, D.B., "Structural vibration control via electrorheological-fluid-based actuators with adaptive viscous and frictional damping," *Journal of Sound and Vibration*, Vol. 177, No. 2, pp. 227-237.
- [Warkentin and Hagood, 1997] Warkentin, D.J., and Hagood, N.W., "Nonlinear piezoelectric shunting for structural damping," *Proceedings SPIE Smart Structures and Integrated Systems Conference* (San Diego, California), pp. 747-757.
- [Yaws, 1994] Yaws, C.L., *Handbook of Vapor Pressure, Volume 1*, Gulf Publishing Co., Houston.
- [Zengerle et al., 1992] Zengerle, R., Richter, A., and Sandmaier, H., "A micro membrane pump with electrostatic actuation," *Micro Electro Mechanical Systems '92* (Travemunde, Germany), pp. 19-24.
- [Zdeblick and Angell, 1987] Zdeblick, M.J., and Angell, J.B., "A microminiature electric-to-fluidic valve," *Technical Digest of Transducers.87*, pp. 827-829.
- [Zengerle and Richter, 1994] Zengerle, R., and Richter, M., "Simulation of microfluid systems," *Journal of Micromechanics and Microengineering*, Vol. 4, pp. 192-204.

Appendix A

PIEZOELECTRIC ACTUATOR DYNAMICS

The electromechanical equations of motion for the transducer presented in Chapter 3 were obtained using the methods presented in Hagood et al., 1990, "Modelling of Piezoelectric Actuator Dynamics for Structural Control," wherein the coupled sensor and actuator equations for an electroelastic body were derived from Hamilton's principle using a Ritz formulation. This appendix summarizes the technique using the original notation. For further details the reader is referred to the referenced publication.

Ritz Formulation of Electroelasticity:

[taken from Hagood et al., 1990]

The derivation begins by establishing the variational expression for the combined electroelastic body. The generalized form of Hamilton's principle for coupled electromechanical systems is:

$$\int_{t_1}^{t_2} [\delta(T - U + W_e - W_m) + \delta W] dt = 0 \quad (\text{A.1})$$

for piezoceramics the magnetic terms, W_m , are negligible and the others can be defined:

$$T = \int_{V_s} \frac{1}{2} \rho_s \dot{\mathbf{u}}^T \dot{\mathbf{u}} + \int_{V_p} \frac{1}{2} \rho_p \dot{\mathbf{u}}^T \dot{\mathbf{u}} \quad (\text{A.2})$$

$$U = \int_{v_s} \frac{1}{2} S^T T + \int_{v_p} \frac{1}{2} S^T T \quad (\text{A.3})$$

$$W_e = \int_{v_s} \frac{1}{2} E^T D \quad (\text{A.4})$$

where the subscripts s and p refer to the structure and piezoelectric, respectively. Contributions to the electrical energy, W_e , due to fringing field in the structure and free space are neglected. Considering only discrete applied external point forces at locations x_i and applied charges at a discrete set of piezoelectric electrodes:

$$\delta W = \sum_{i=1}^{nf} \delta u(x_i) \cdot f(x_i) - \sum_{j=1}^{nq} \delta \phi_j \cdot q_j \quad (\text{A.5})$$

where $D(x)$ is a vector of electrical displacements (charge/area), $E(x)$ is the vector of electric field in the material (volts/meter), $S(x)$ is the vector of material strains, $T(x)$ is the vector of material stresses (force/area), $\phi(x)$ is the scalar electrical potential, $u(x_i)$ is the vector of mechanical displacements, $f(x_i)$ is the vector of applied force at location x_i , and q_j is the charge applied at electrode j .

The fundamental assumption of the Rayleigh-Ritz formulation is introduced by expressing the displacement and potential functions in terms of generalized coordinates:

$$u(x, t) = \Psi_r(x)r(t) = \begin{bmatrix} \psi_{r_1}(x) & \cdots & \psi_{r_n}(x) \end{bmatrix} \begin{bmatrix} r_1(t) \\ \vdots \\ r_n(t) \end{bmatrix} \quad (\text{A.6})$$

and for the electrical potential

$$\phi(x, t) = \Psi_v(x)v(t) = \begin{bmatrix} \psi_{v_1}(x) & \cdots & \psi_{v_m}(x) \end{bmatrix} \begin{bmatrix} v_1(t) \\ \vdots \\ v_m(t) \end{bmatrix} \quad (\text{A.7})$$

where r_i is the generalized mechanical coordinate and v_i is the generalized electrical coordinate. It is sometimes convenient to let the v_i represent physical voltages at the piezoelectric electrodes, particularly when these are driven by a voltage amplifier.

The only limitation on the assumed displacement distributions, Ψ_{ri} , is that they obey the geometric boundary conditions while the only constraint on the assumed potential distributions, Ψ_{vi} , is that they be consistent with the prescribed voltage boundary conditions (e.g. at ground the potential = 0) and are equipotential conductors. Future equations will be simplified if we use strain and field basis functions:

$$S(x, t) = N_r(x)r(t) \text{ and } E(x, t) = N_v(x)v(t) \quad (\text{A.8})$$

where

$$N_r(x) = L_u \Psi_r(x) \text{ and } N_v(x) = L_\phi \Psi_v(x) \quad (\text{A.9})$$

Here L_u is the linear differential operator for the particular elasticity problem and L_ϕ is the gradient operator.

Allowing arbitrary variations of r and v , two matrix equations in the generalized coordinates are obtained. These will be called the actuator and sensor equations of the electro-elastic system.

$$(M_s + M_p)\ddot{r} + (K_s + K_p)r + \Theta v = B_f F \quad \text{Actuator Equation} \quad (\text{A.10})$$

$$\Theta^T r + C_p v = B_q q \quad \text{Sensor Equation} \quad (\text{A.11})$$

where the mass matrices are defined

$$M_s = \int_{V_s} \Psi_r^T(x) \rho_s \Psi_r(x) \quad M_p = \int_{V_p} \Psi_r^T(x) \rho_p \Psi_r(x) \quad (\text{A.12})$$

and the stiffness matrices are defined (dropping the integrand's explicit spatial dependence)

$$K_s = \int_{v_s} N_r^T c_s N_r \quad K_p = \int_{v_p} N_r^T R_s^T c^E R_s N_r \quad (\text{A.13})$$

the piezoelectric capacitance matrix, C_p , and the electromechanical coupling matrix, Θ , are defined:

$$C_p = \int_{v_p} N_v^T R_E^T \epsilon^s R_E N_v \quad \Theta = \int_{v_p} N_r^T R_s^T e_t R_E N_v \quad (\text{A.14})$$

and finally the forcing matrices are defined

$$B_f = \begin{bmatrix} \Psi_{r1}^T(x_{f_1}) & \dots & \Psi_{r1}^T(x_{f_{nf}}) \\ \vdots & & \vdots \\ \Psi_{rn}^T(x_{f_1}) & \dots & \Psi_{rn}^T(x_{f_{nf}}) \end{bmatrix} \quad (\text{A.15})$$

$$B_q = \begin{bmatrix} \Psi_{v_1}(x_{q_1}) & \dots & \Psi_{v_1}(x_{q_{nq}}) \\ \vdots & & \vdots \\ \Psi_{v_m}(x_{q_1}) & \dots & \Psi_{v_m}(x_{q_{nq}}) \end{bmatrix}$$

where there are n mechanical DOFs and m electrical DOFs as well as nf forces and nq applied charges.

Appendix B

SYSTEM BLOCK DIAGRAMS

This appendix contains the Simulink block diagrams that were used to implement the system model of the *Actuator*. The power harvester diagrams have been omitted because they are identical to those of the actuator, the only differences being sign conventions for flows, pressure gradients, and so forth. An exception is implementation of the dynamics of the drive component, where only the actuator equation exists for the actuator model, but both the actuator and sensor equations exist for the power harvester model. For this reason both drive models are included in this appendix. The sensor equation used is the diode bridge rectifier circuit discussed in Chapter 3. An organizational chart illustrating the structure of the block diagrams appears in Figure B.1.

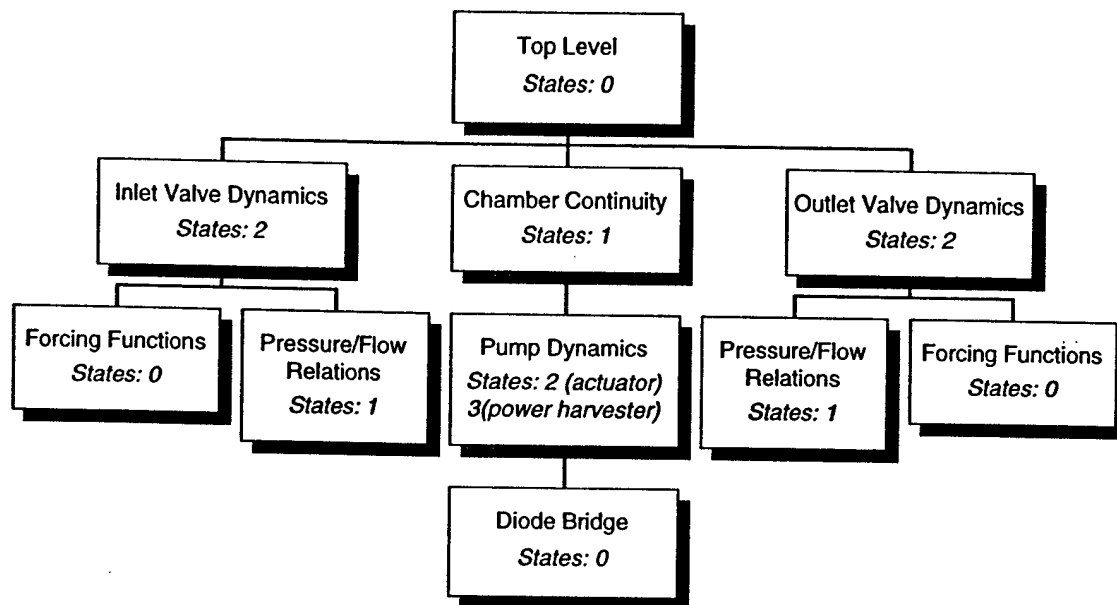


Figure B.1 Organizational chart for the Simulink block diagrams.

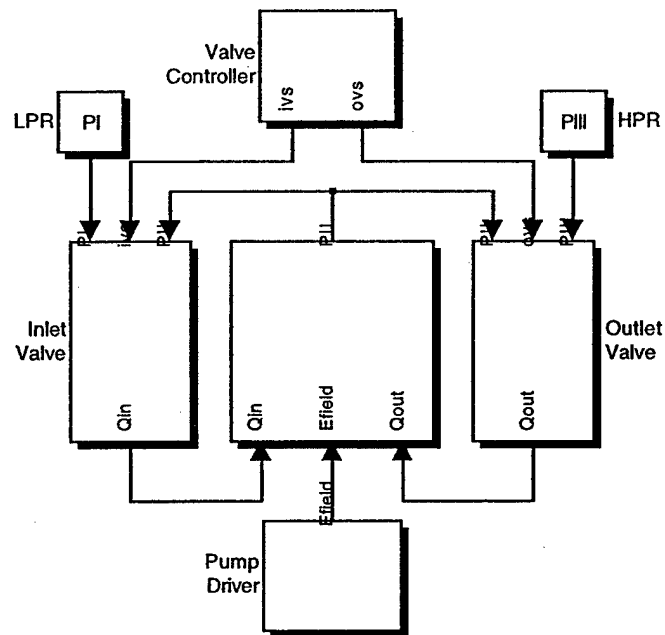


Figure B.2 Top level

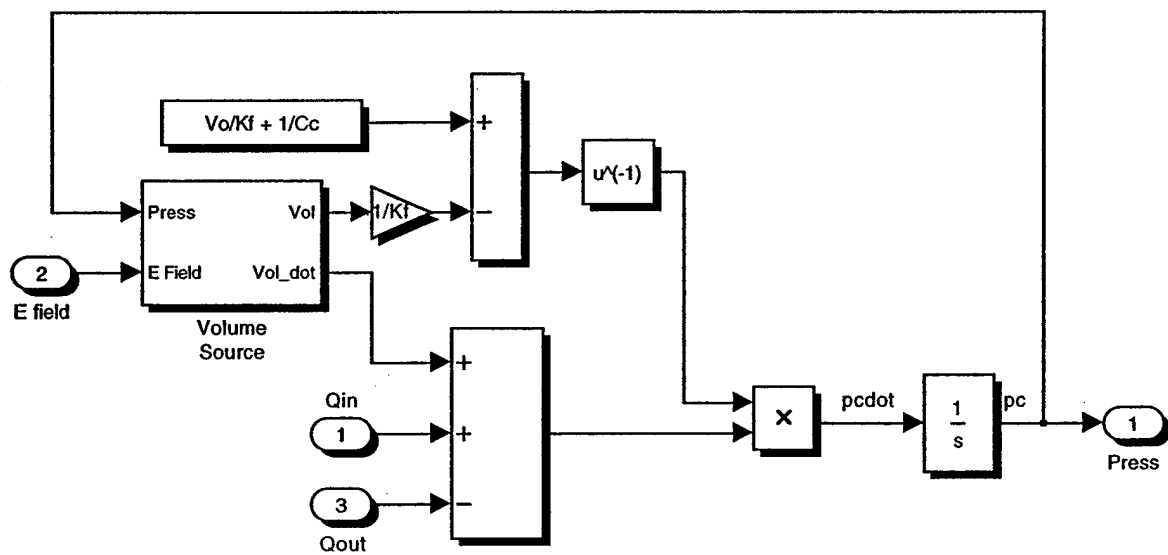


Figure B.3 Chamber continuity

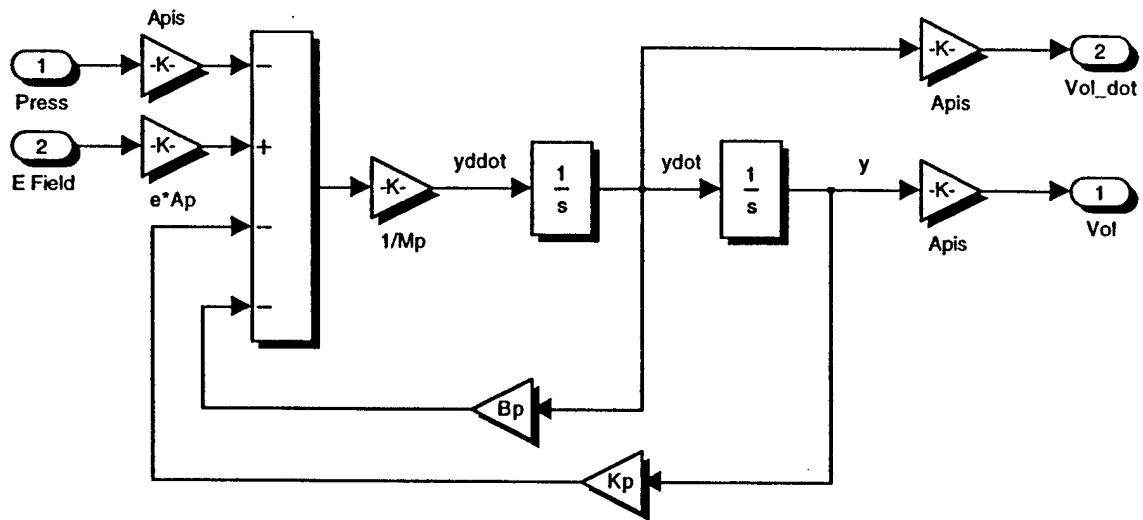


Figure B.4 Drive dynamics for the actuator

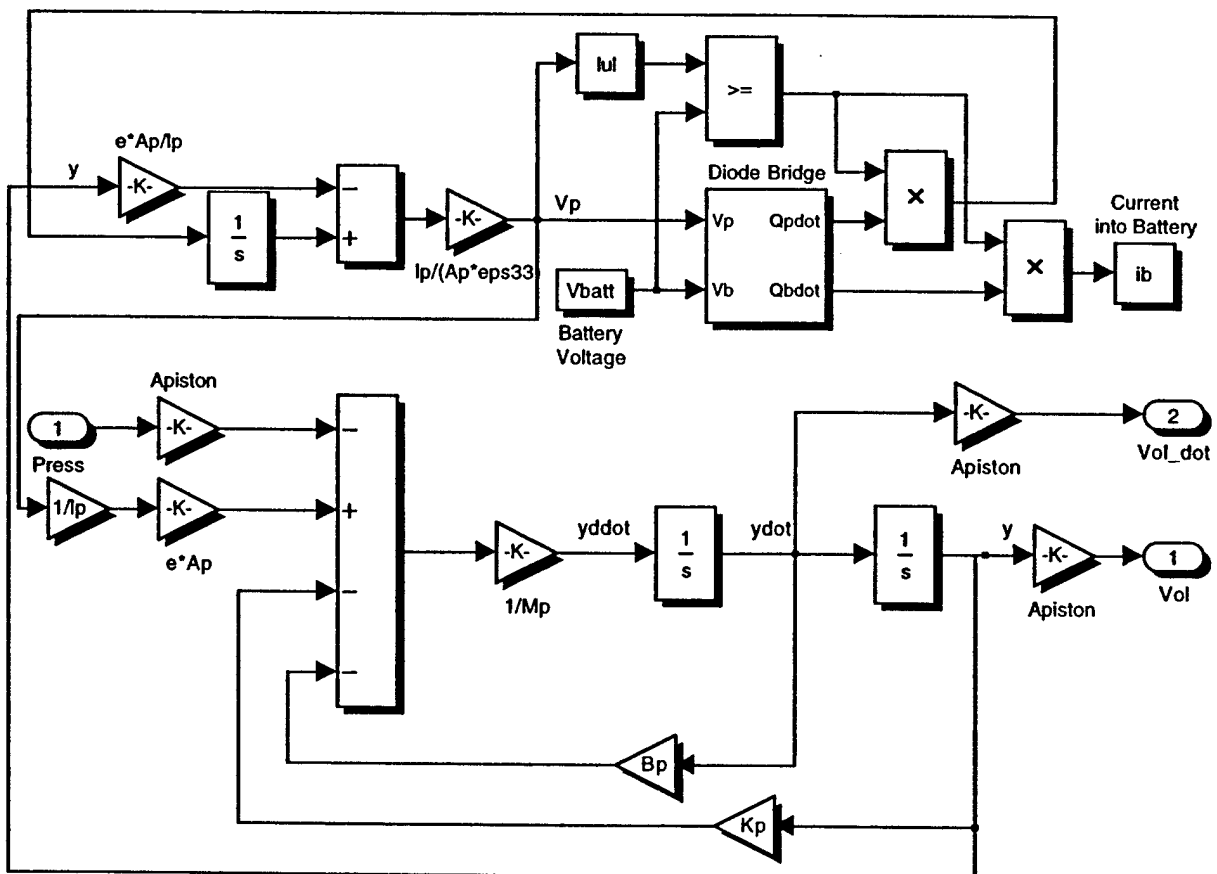


Figure B.5 Drive dynamics for the power harvester. The top portion represents power harvesting circuit.

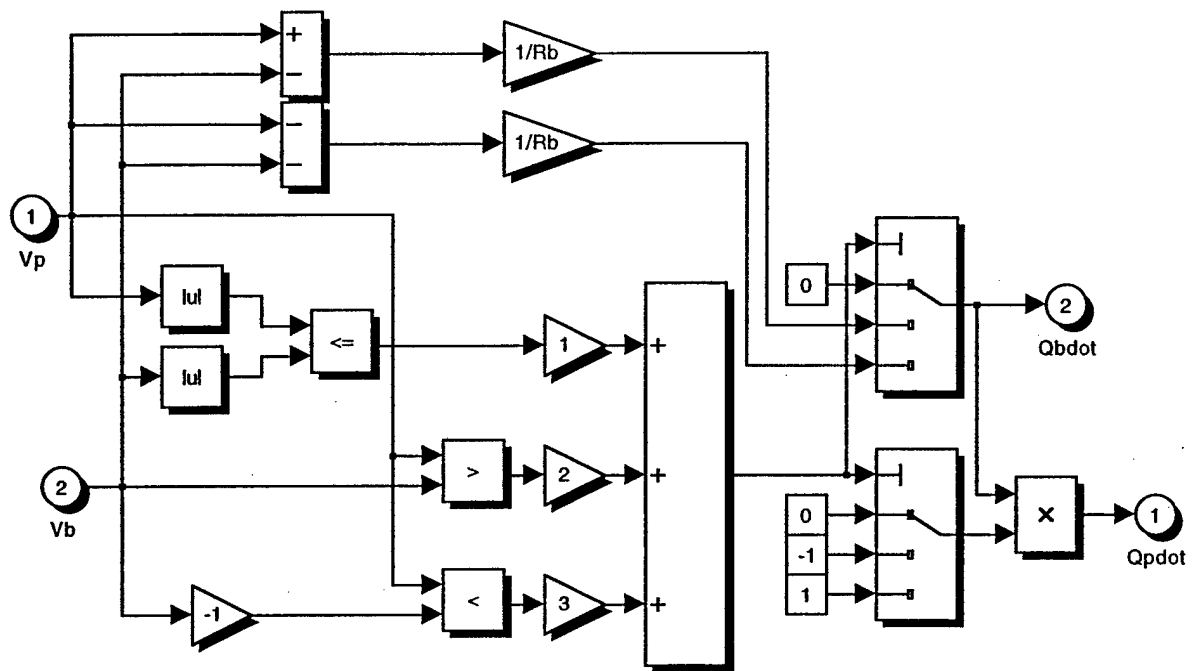


Figure B.6 Diode bridge for the power harvester

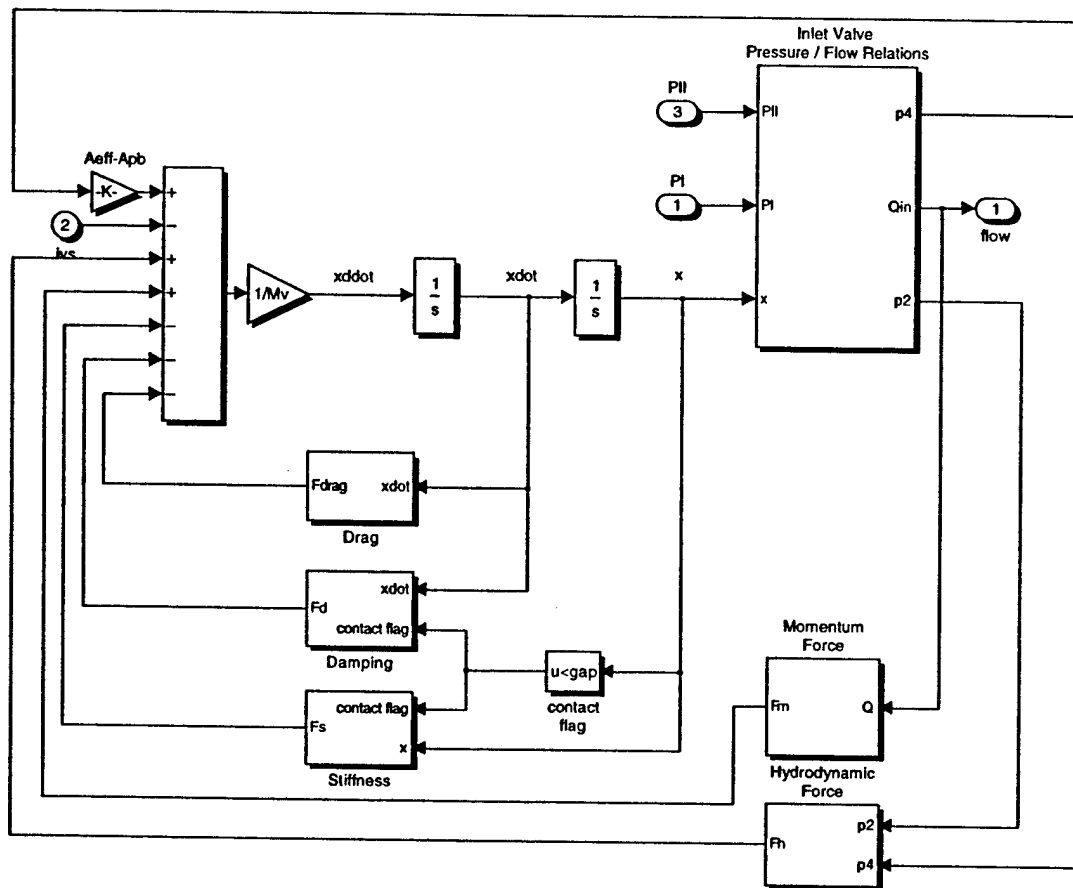


Figure B.7 Inlet valve dynamics

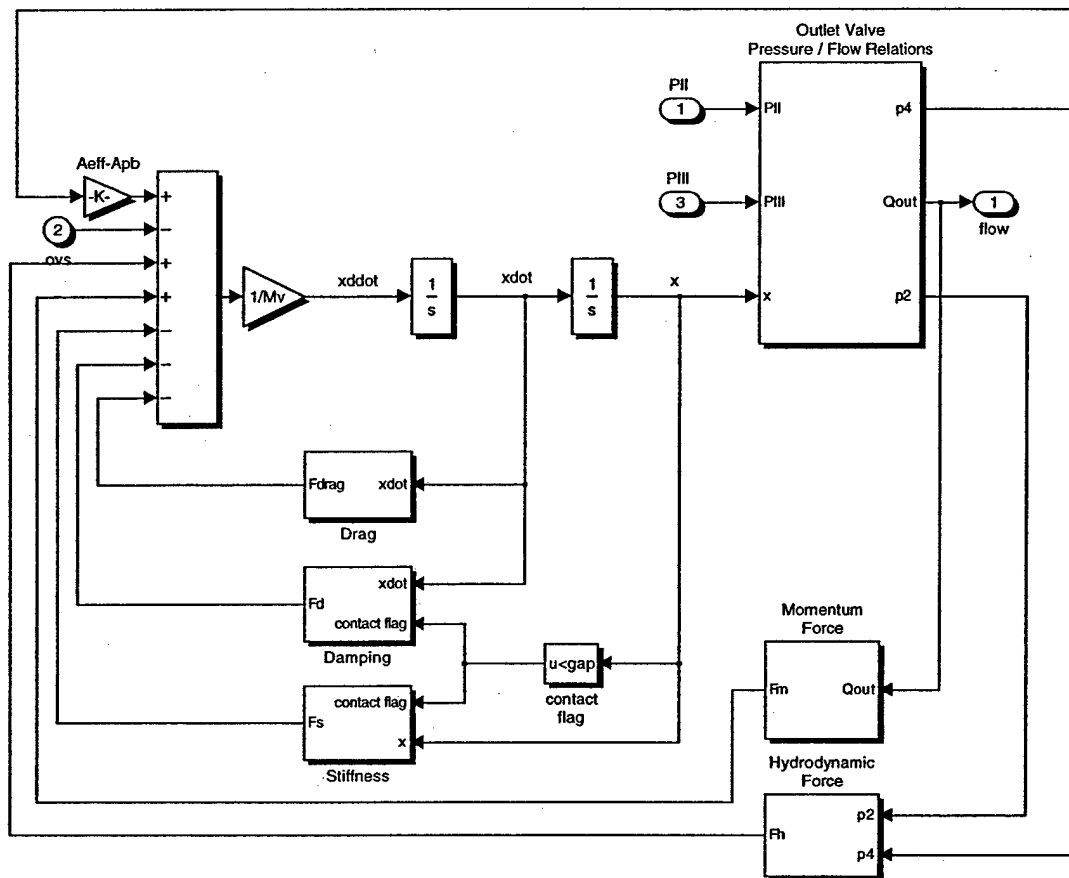
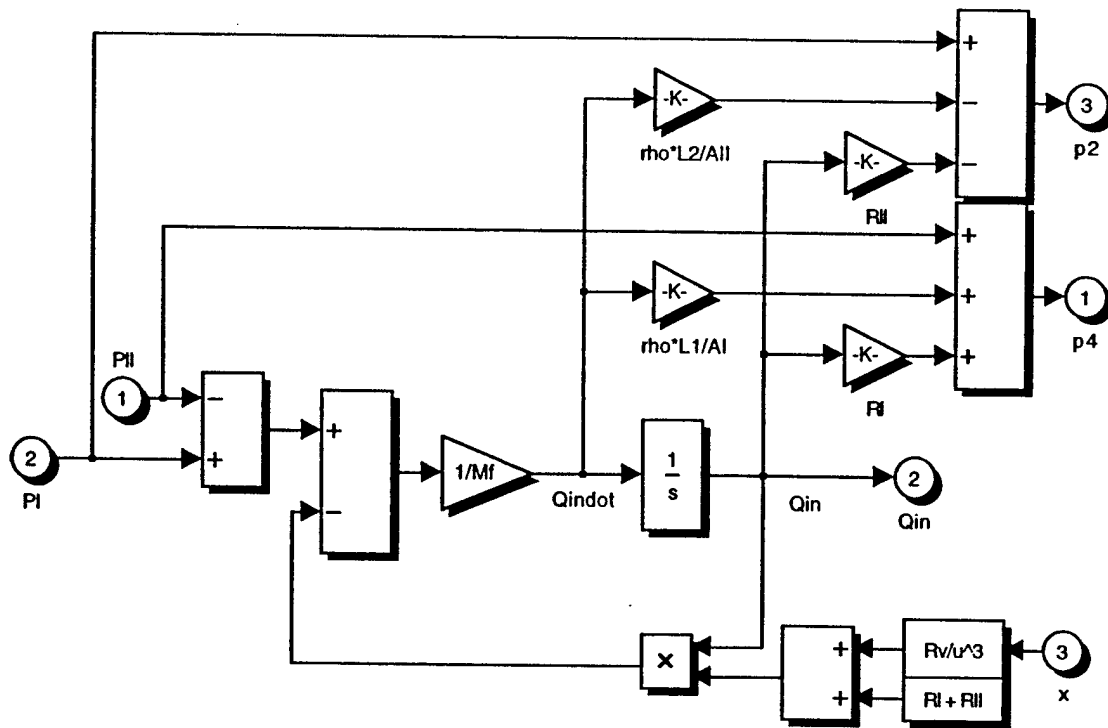
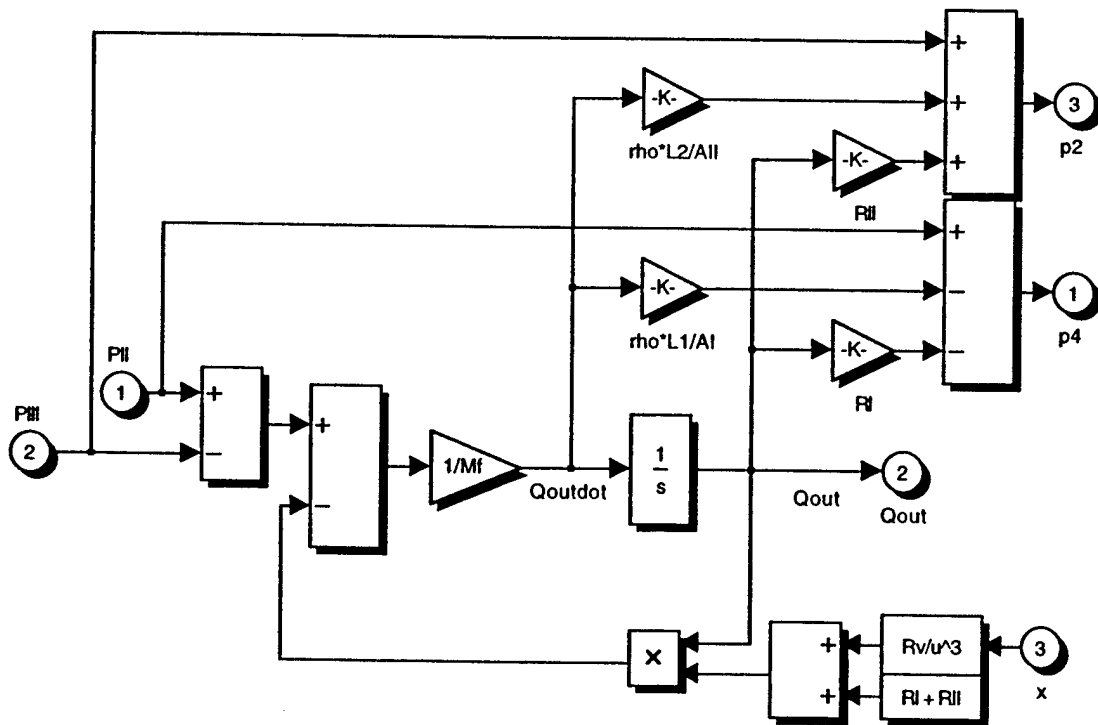


Figure B.8 Outlet valve dynamics



(a)



(b)

Figure B.9 Pressure/flow relations for the (a) inlet and (b) outlet valves

Appendix C

SIMULATIONS

TABLE C.1 Summary of simulation performance.

| Study | Sim. | Config. | PD (W/kg) | η (%) | Q (ml/min) |
|-------|------|---------|-----------|------------|--------------|
| 1 | a | B | 239 | 27 | 44.0 |
| | b | B | 139 | 21 | 25.6 |
| 2 | a | B | 338 | 22 | 62.3 |
| | b | B | - | - | - |
| | c | B | 55 | 39 | 10.1 |
| | d | B | - | - | - |
| 3 | a | B | 145 | 45 | 26.7 |
| 4 | a | C | 11 | 18 | 33.7 |
| 7 | a | B | 48 | 18 | 8.9 |
| | b | D | 168 | 18 | 30.9 |
| 8 | a | B | 146 | 17 | 26.9 |
| | b | E | 281 | 18 | 51.6 |
| 9 | a | F | 361 | 21 | 66.4 |
| 10 | a | G | 1660 | 18 | 0.3 |

TABLE C.2 Summary of electrical input characteristics used in simulations.

| Study | Sim. | Config. | f (kHz) | ϕ (deg) | Shape | Field (kV/mm) |
|-------|------|---------|-----------|--------------|----------|---------------|
| 1 | a | B | 7.43 | 0 | square | 1 |
| | b | B | 7.43 | 0 | triangle | 1 |
| 2 | a | B | 5.35 | 0 | sine | 1 |
| | b | B | 6.69 | 0 | sine | 1 |
| | c | B | 1.60 | 0 | sine | 1 |
| | d | B | 0.1 | 0 | sine | 1 |
| 3 | a | B | 7.43 | 80 | sine | 1 |
| 4 | a | C | 7.43 | 0 | sine | 1 |
| 7 | a | B | 2.01 | 0 | sine | 1 |
| | b | D | 7.43 | 0 | sine | 1 |
| 8 | a | B | 5.88 | 0 | sine | 1 |
| | b | E | 7.43 | 0 | sine | 1 |
| 9 | a | F | 7.43 | 0 | sine | 1 |
| 10 | a | G | 74.3 | 0 | sine | 1 |

TABLE C.3 Summary of mechanical characteristics used in simulations.

| Study | Sim. | Config. | Primary | | | | | Secondary | | |
|-------|------|---------|-----------|------------------|------------|-------------------|-----------------|-------------|-------------|----------------------------|
| | | | λ | Fluid | L_I (mm) | Load ^a | d_{disc} (mm) | f_n (kHz) | f_v (kHz) | C_s (Pa/m ³) |
| 1 | a | B | 1 | H ₂ O | 100 | 0.3 | 0.62 | 6.69 | 23.4 | 7.09e17 |
| | b | B | 1 | H ₂ O | 100 | 0.3 | 0.62 | 6.69 | 234 | 7.09e17 |
| 2 | a | B | 1 | H ₂ O | 100 | 0.3 | 0.62 | 6.69 | 234 | 7.09e17 |
| | b | B | 1 | H ₂ O | 100 | 0.3 | 0.62 | 6.69 | 234 | 7.09e17 |
| | c | B | 1 | H ₂ O | 100 | 0.3 | 0.62 | 6.69 | 234 | 7.09e17 |
| | d | B | 1 | H ₂ O | 100 | 0.3 | 0.62 | 6.69 | 234 | 7.09e17 |
| 3 | a | B | 1 | H ₂ O | 100 | 0.3 | 0.62 | 6.69 | 234 | 7.09e17 |
| 4 | a | C | 1 | H ₂ O | 1 | 0.3 | 0.62 | 6.69 | 234 | 4.05e15 |
| 7 | a | B | 1 | Hg | 100 | 0.3 | 0.62 | 1.81 | 234 | 7.09e17 |
| | b | D | 1 | Hg | 2 | 0.3 | 0.62 | 6.69 | 234 | 7.09e17 |
| 8 | a | B | 1 | CCl ₄ | 100 | 0.3 | 0.62 | 5.30 | 234 | 7.09e17 |
| | b | E | 1 | CCl ₄ | 60 | 0.3 | 0.62 | 6.69 | 234 | 7.09e17 |
| 9 | a | F | 1 | H ₂ O | 100 | 0.3 | 0.75 | 6.74 | 234 | 7.09e17 |
| 10 | a | G | 0.1 | H ₂ O | 10 | 0.3 | 0.62 | 6.69 | 234 | 7.09e17 |

a. Load = p_{hpr}/p_{max}

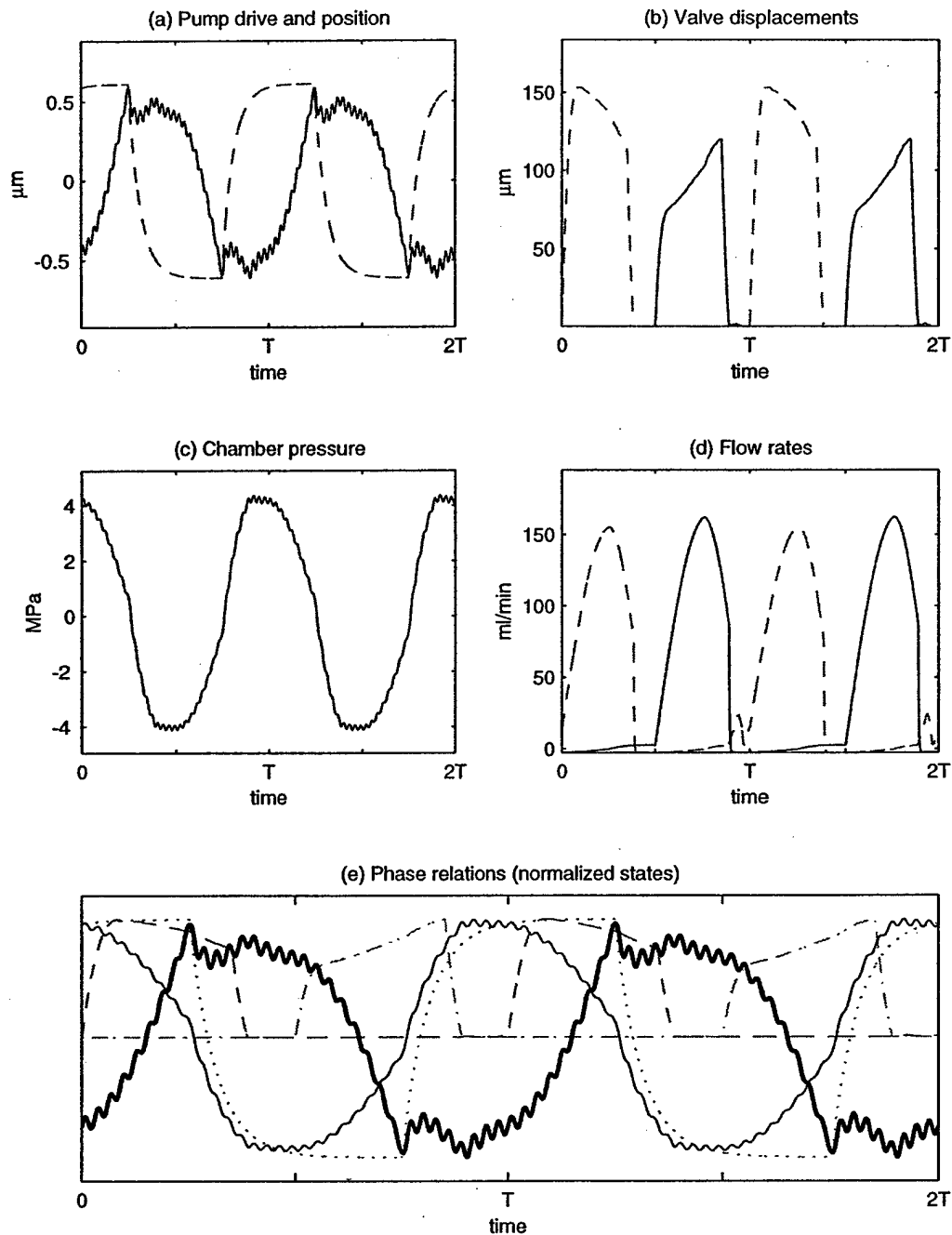


Figure C.1 Simulation 1a: actuator configuration B, operation at $f = 1.11f_n$ using a first order square wave input. Plots (b) and (d) show the displacements and flows of the inlet (solid) and outlet (dashed) valves. Plot (e) indicates the phase relations between the normalized pump position (heavy solid), chamber pressure (solid), drive signal (dotted), inlet valve displacement (dot-dashed), and outlet valve displacement (dashed).

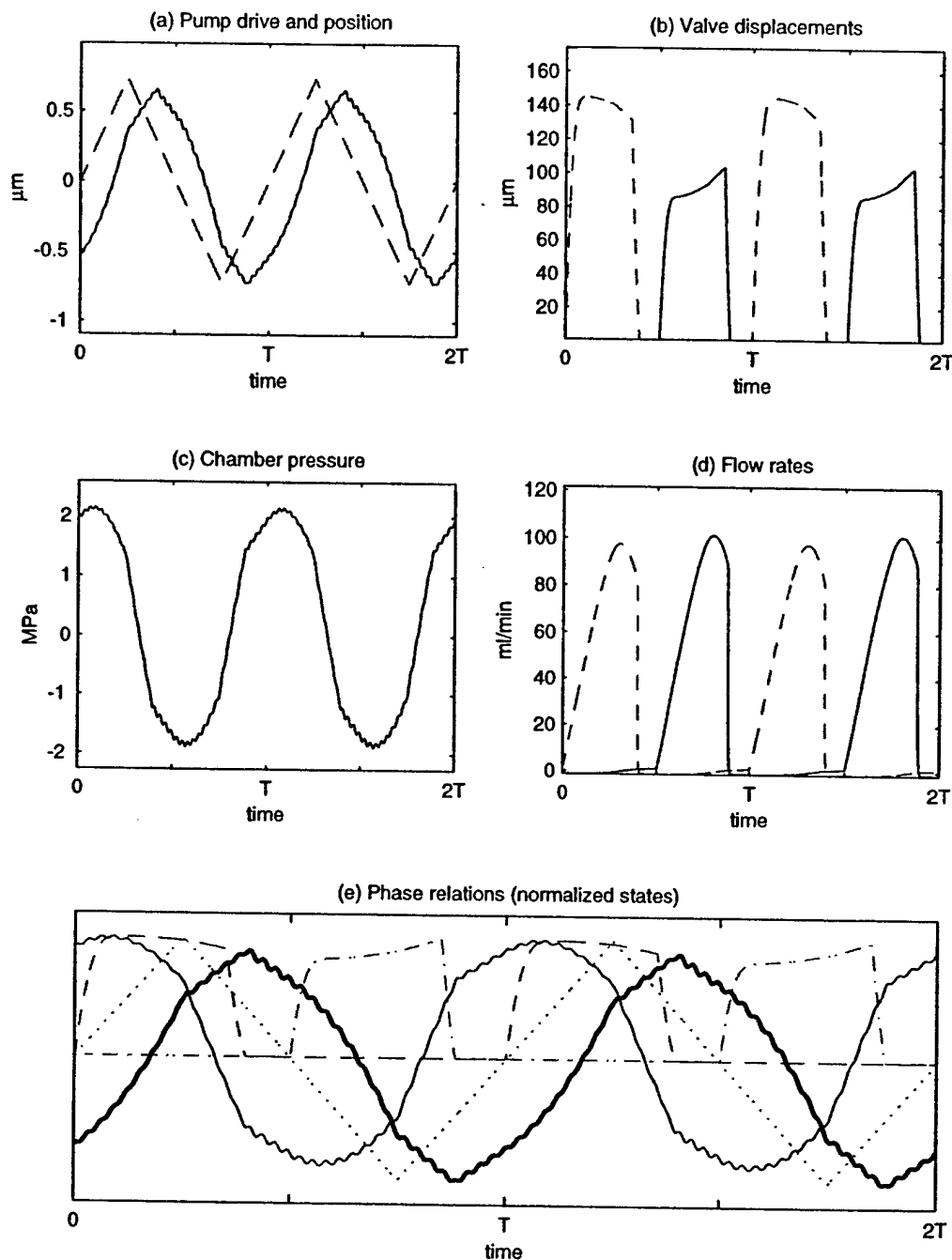


Figure C.2 Simulation 1b: actuator configuration B, operation at $f = 1.11f_n$ using a triangle wave input. Plots (b) and (d) show the displacements and flows of the inlet (solid) and outlet (dashed) valves. Plot (e) indicates the phase relations between the normalized pump position (heavy solid), chamber pressure (solid), drive signal (dotted), inlet valve displacement (dot-dashed), and outlet valve displacement (dashed).

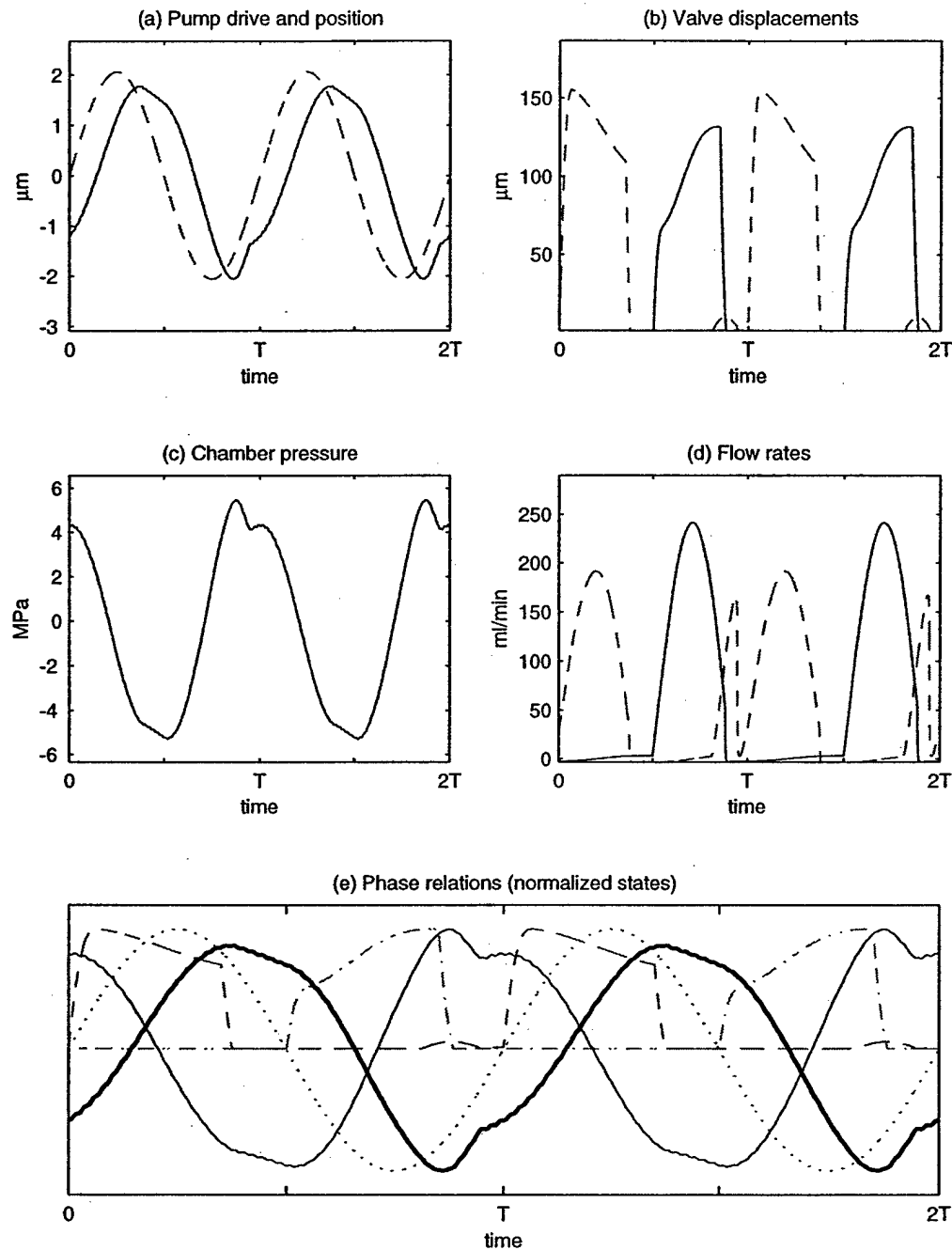


Figure C.3 Simulation 2a: actuator configuration B, operation at the major peak, $f = 0.8f_n$. Plots (b) and (d) show the displacements and flows of the inlet (solid) and outlet (dashed) valves. Plot (e) indicates the phase relations between the normalized pump position (heavy solid), chamber pressure (solid), drive signal (dotted), inlet valve displacement (dot-dashed), and outlet valve displacement (dashed).

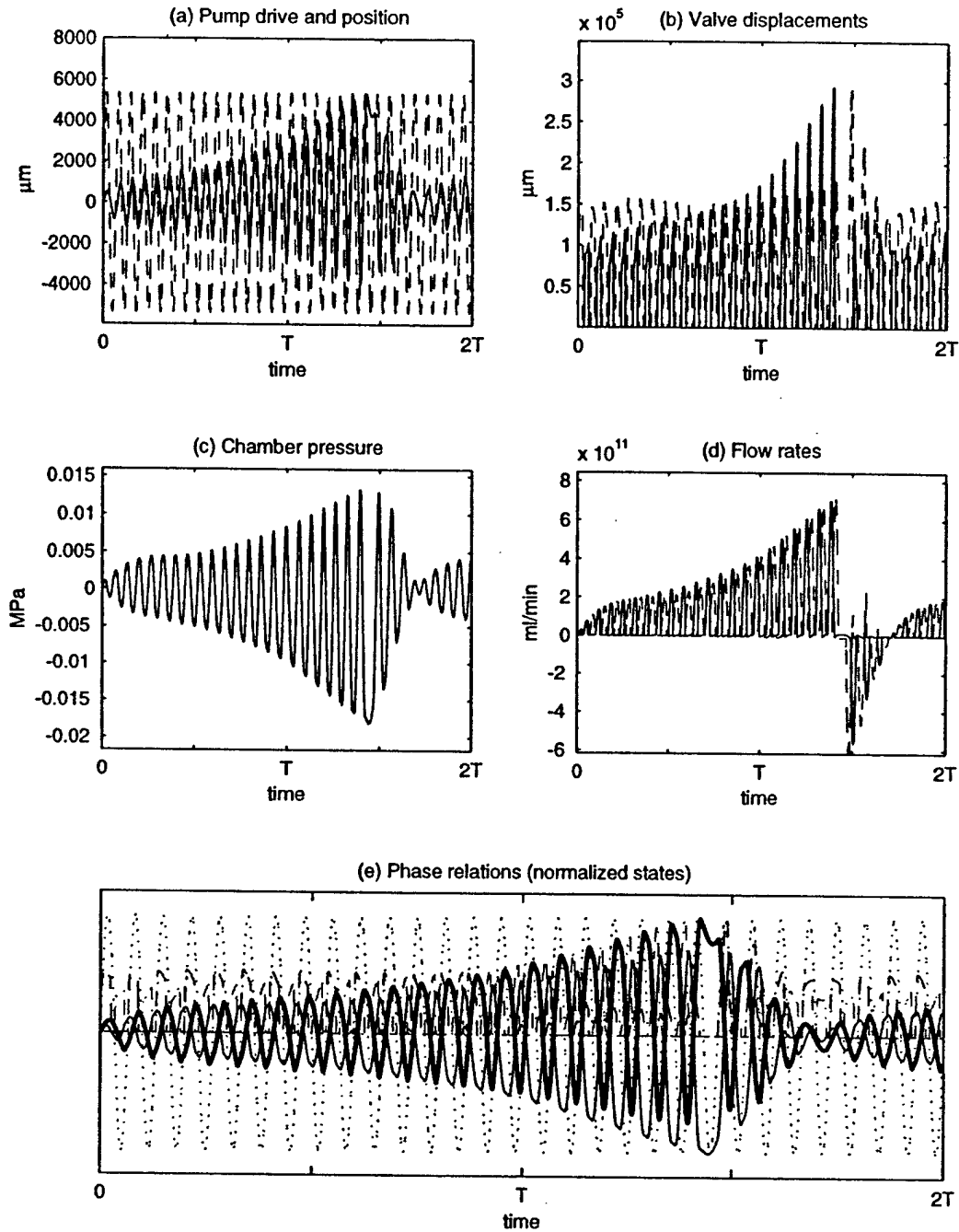


Figure C.4 Simulation 2b: actuator configuration B, operation at resonance, $f = f_n$. Plots (b) and (d) show the displacements and flows of the inlet (solid) and outlet (dashed) valves. Plot (e) indicates the phase relations between the normalized pump position (heavy solid), chamber pressure (solid), drive signal (dotted), inlet valve displacement (dot-dashed), and outlet valve displacement (dashed).

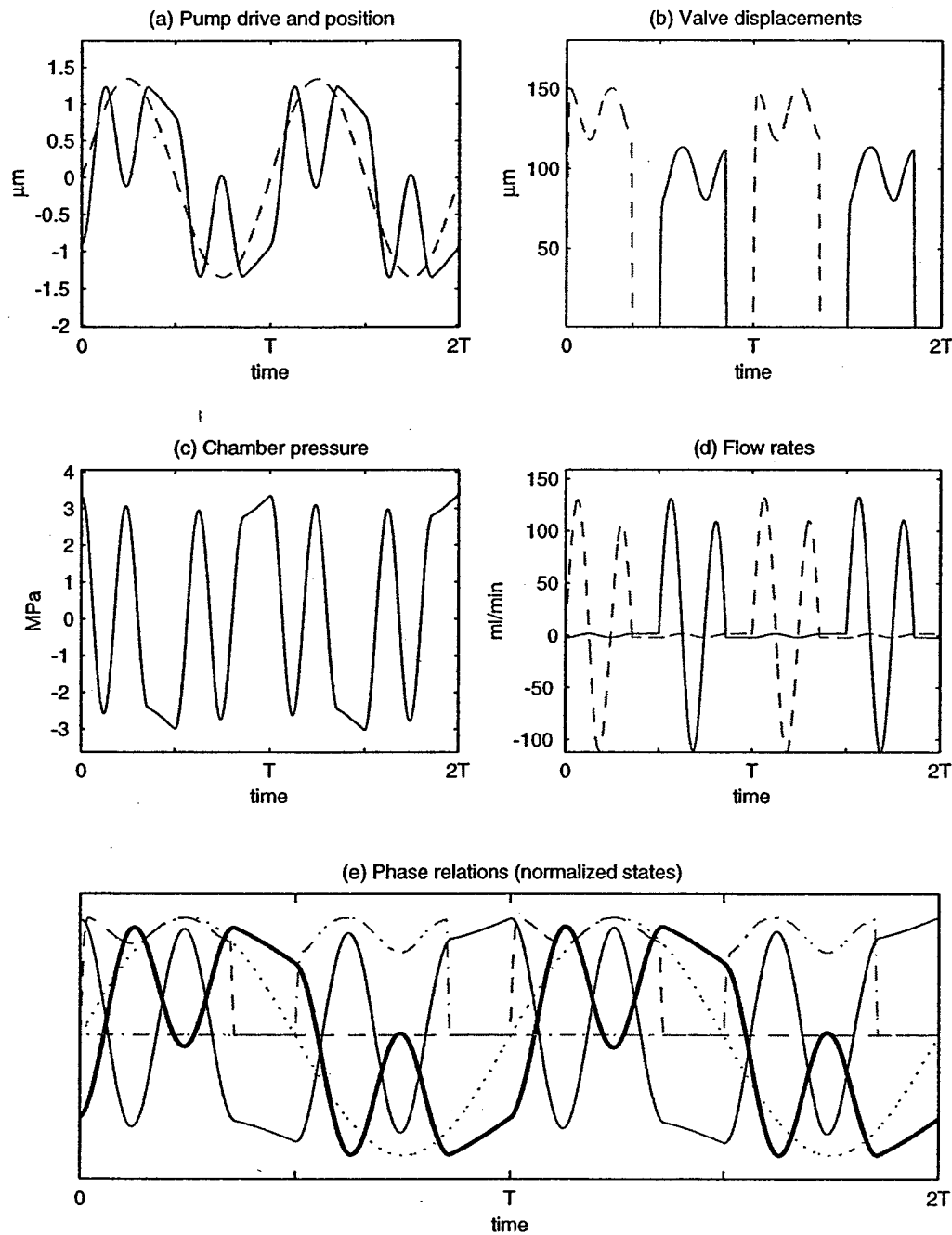


Figure C.5 Simulation 2c: actuator configuration B, operation at the minor peak, $f = 0.25f_n$. Plots (b) and (d) show the displacements and flows of the inlet (solid) and outlet (dashed) valves. Plot (e) indicates the phase relations between the normalized pump position (heavy solid), chamber pressure (solid), drive signal (dotted), inlet valve displacement (dot-dashed), and outlet valve displacement (dashed).

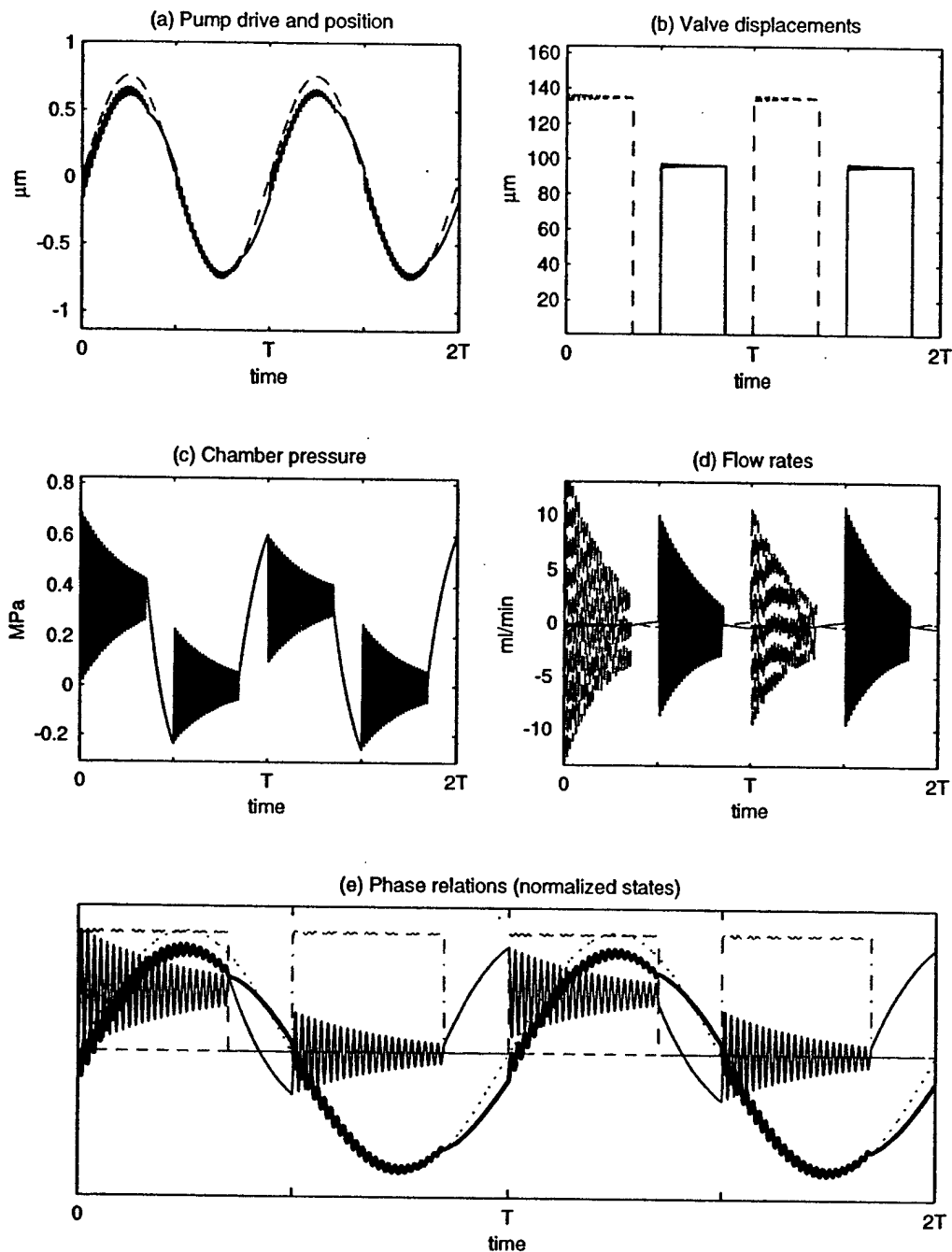


Figure C.6 Simulation 2d: actuator configuration B, quasistatic operation, $f = 100$ Hz. Plots (b) and (d) show the displacements and flows of the inlet (solid) and outlet (dashed) valves. Plot (e) indicates the phase relations between the normalized pump position (heavy solid), chamber pressure (solid), drive signal (dotted), inlet valve displacement (dot-dashed), and outlet valve displacement (dashed).

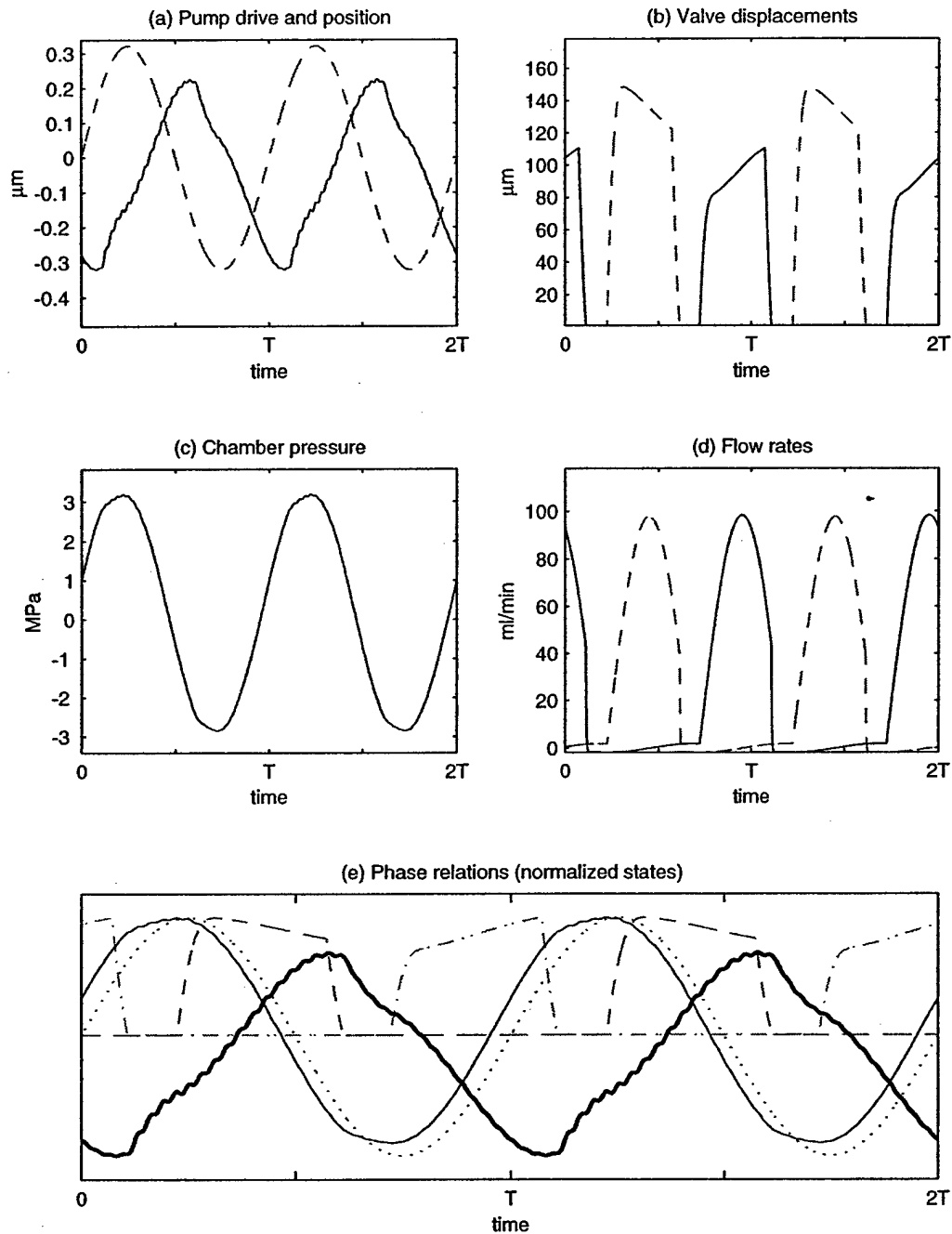


Figure C.7 Simulation 3a: actuator configuration B, $\phi = 80^\circ$, $f = 1.11f_n$. Plots (b) and (d) show the displacements and flows of the inlet (solid) and outlet (dashed) valves. Plot (e) indicates the phase relations between the normalized pump position (heavy solid), chamber pressure (solid), drive signal (dotted), inlet valve displacement (dot-dashed), and outlet valve displacement (dashed).

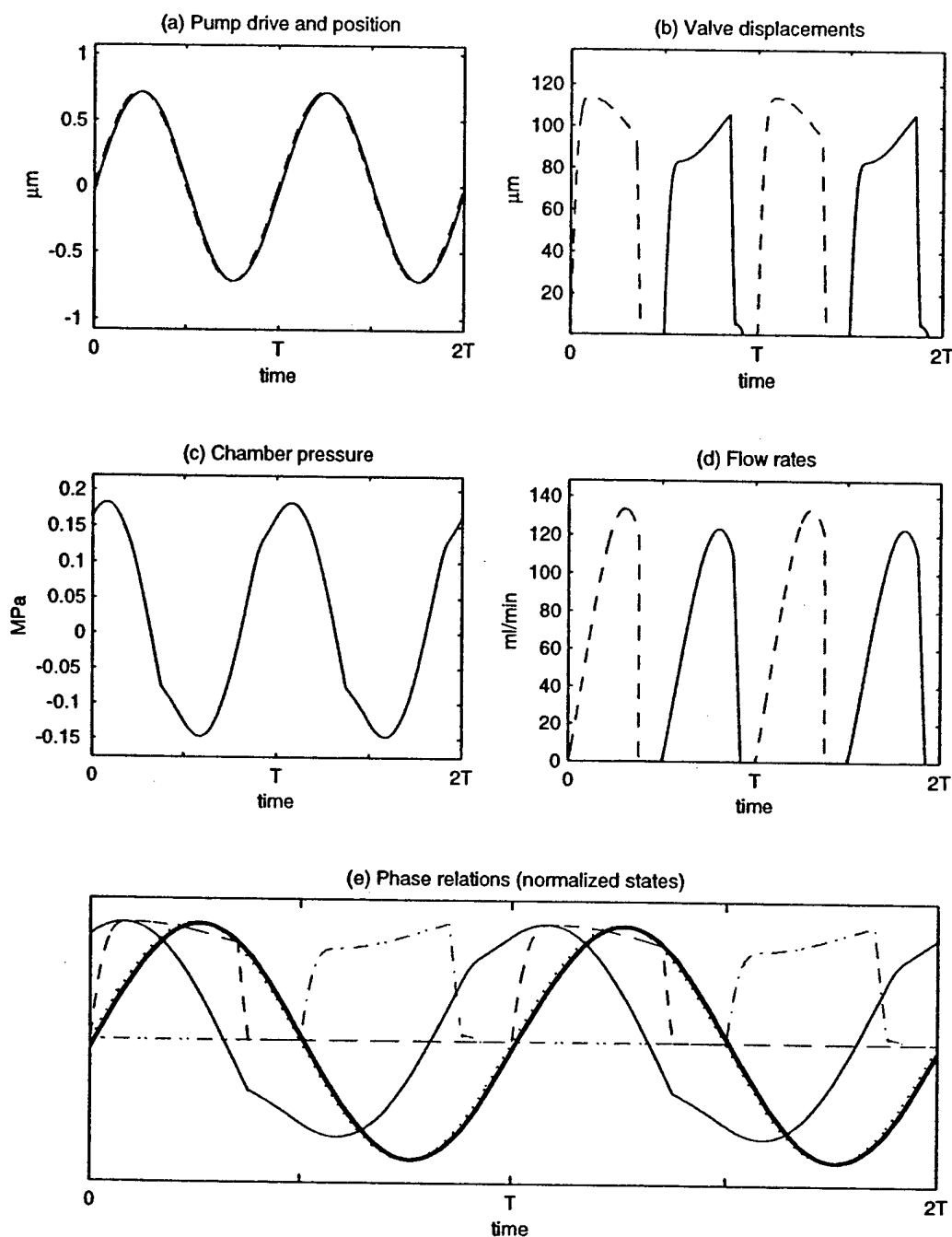


Figure C.8 Simulation 4a: actuator configuration C, $f = 1.11f_n$. Plots (b) and (d) show the displacements and flows of the inlet (solid) and outlet (dashed) valves. Plot (e) indicates the phase relations between the normalized pump position (heavy solid), chamber pressure (solid), drive signal (dotted), inlet valve displacement (dot-dashed), and outlet valve displacement (dashed).

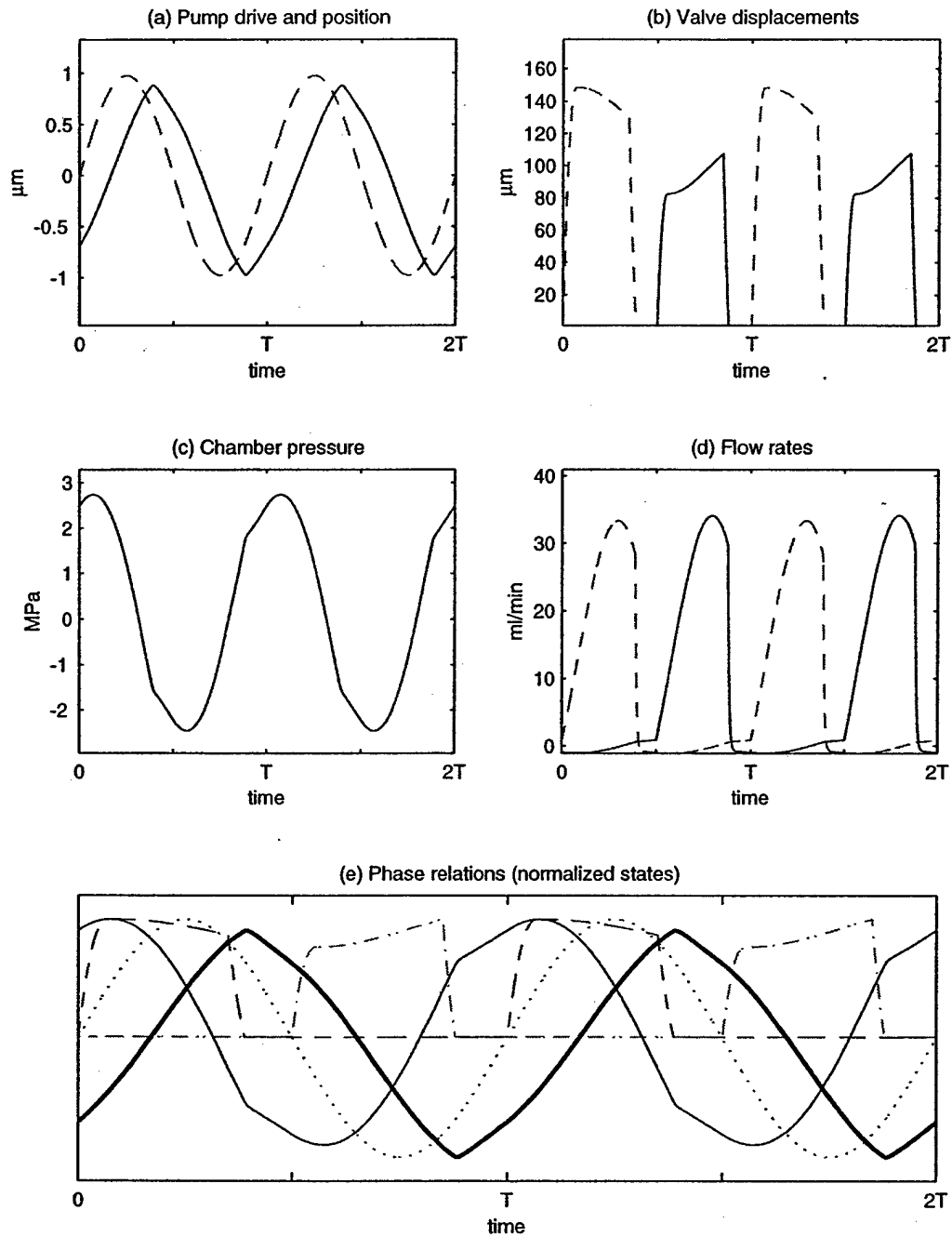


Figure C.9 Simulation 7a: actuator configuration B using Mercury, $f = 1.11f_n$, $f_n = 2.23$ kHz. Plots (b) and (d) show the displacements and flows of the inlet (solid) and outlet (dashed) valves. Plot (e) indicates the phase relations between the normalized pump position (heavy solid), chamber pressure (solid), drive signal (dotted), inlet valve displacement (dot-dashed), and outlet valve displacement (dashed).

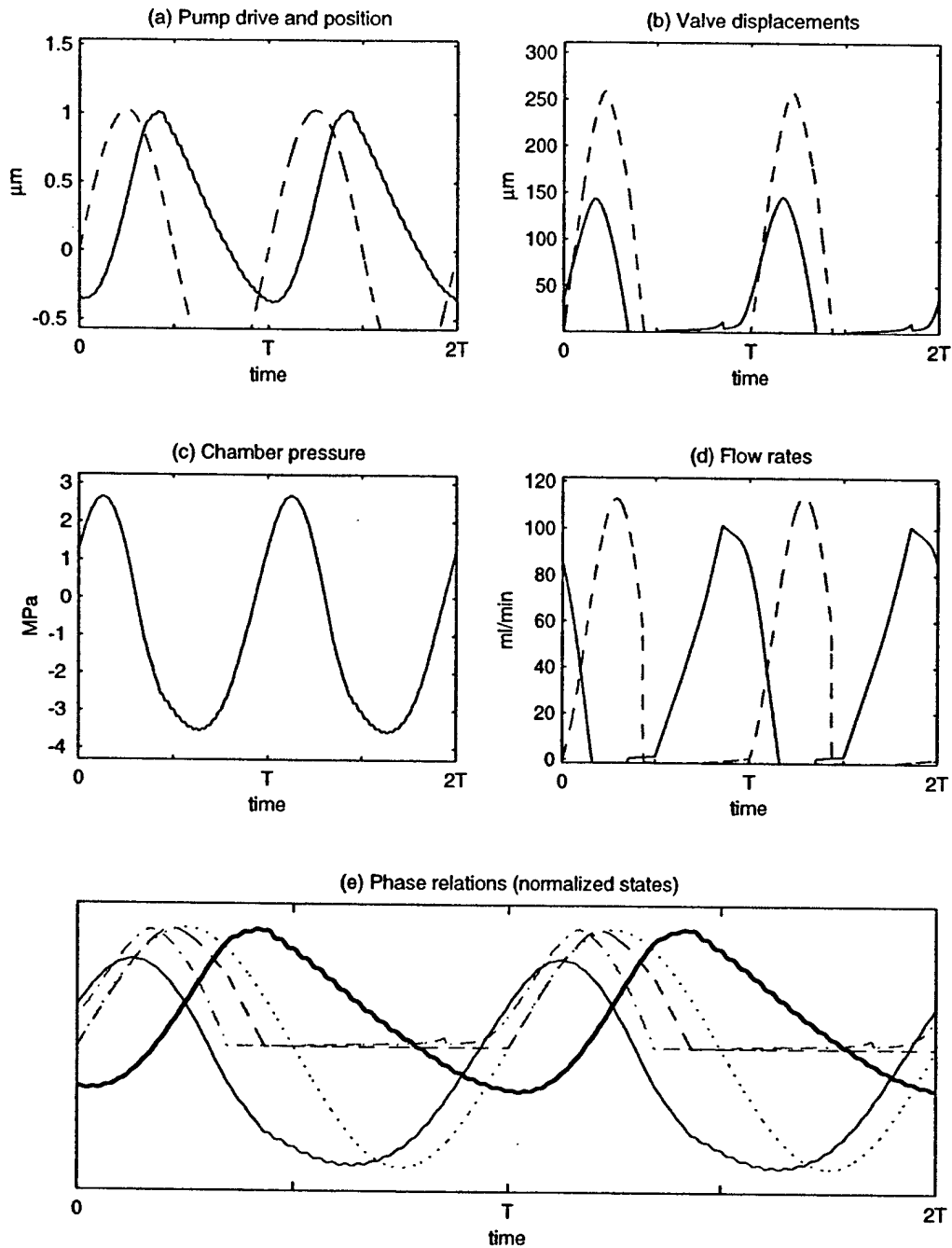


Figure C.10 Simulation 7b: actuator configuration D using Mercury, $f = 1.11f_n$, $f_n = 6.69$ kHz. Plots (b) and (d) show the displacements and flows of the inlet (solid) and outlet (dashed) valves. Plot (e) indicates the phase relations between the normalized pump position (heavy solid), chamber pressure (solid), drive signal (dotted), inlet valve displacement (dot-dashed), and outlet valve displacement (dashed).

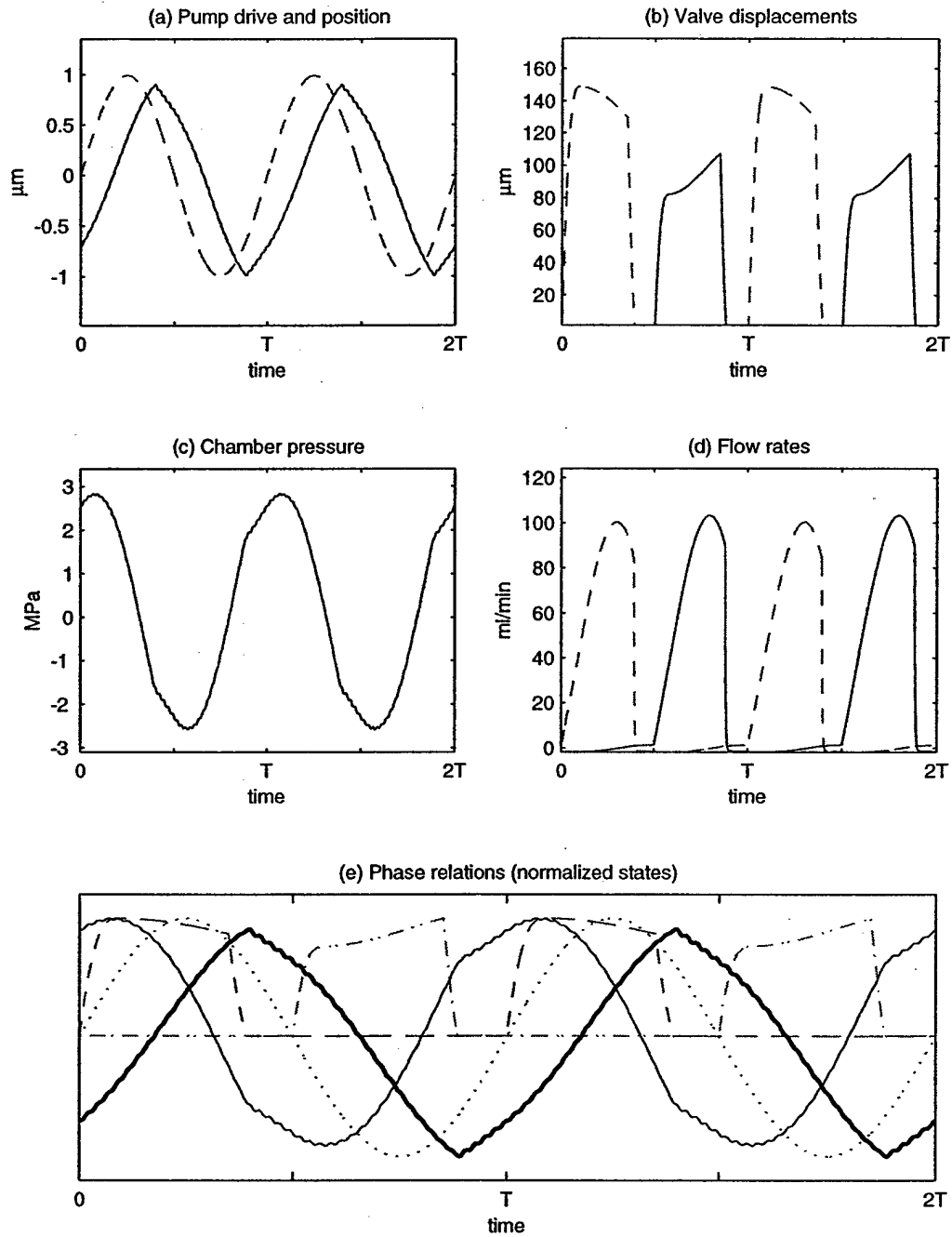


Figure C.11 Simulation 8a: actuator configuration B using Carbon tetrachloride, $f = 1.11f_n$, $f_n = 5.88$ kHz. Plots (b) and (d) show the displacements and flows of the inlet (solid) and outlet (dashed) valves. Plot (e) indicates the phase relations between the normalized pump position (heavy solid), chamber pressure (solid), drive signal (dotted), inlet valve displacement (dot-dashed), and outlet valve displacement (dashed).

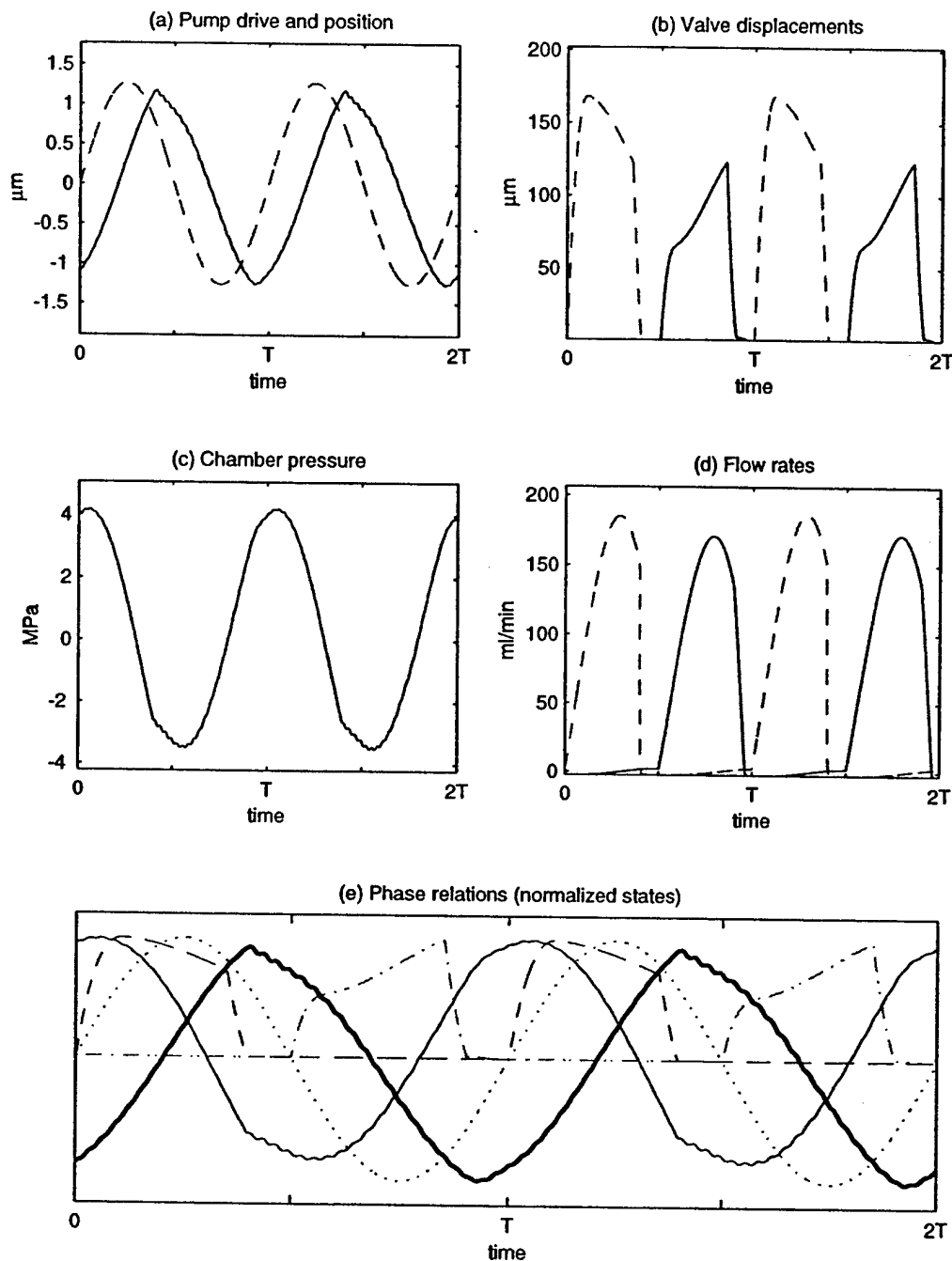


Figure C.12 Simulation 8b: actuator configuration E using Carbon tetrachloride, $f = 1.11f_n$, $f_n = 5.88$ kHz. Plots (b) and (d) show the displacements and flows of the inlet (solid) and outlet (dashed) valves. Plot (e) indicates the phase relations between the normalized pump position (heavy solid), chamber pressure (solid), drive signal (dotted), inlet valve displacement (dot-dashed), and outlet valve displacement (dashed).

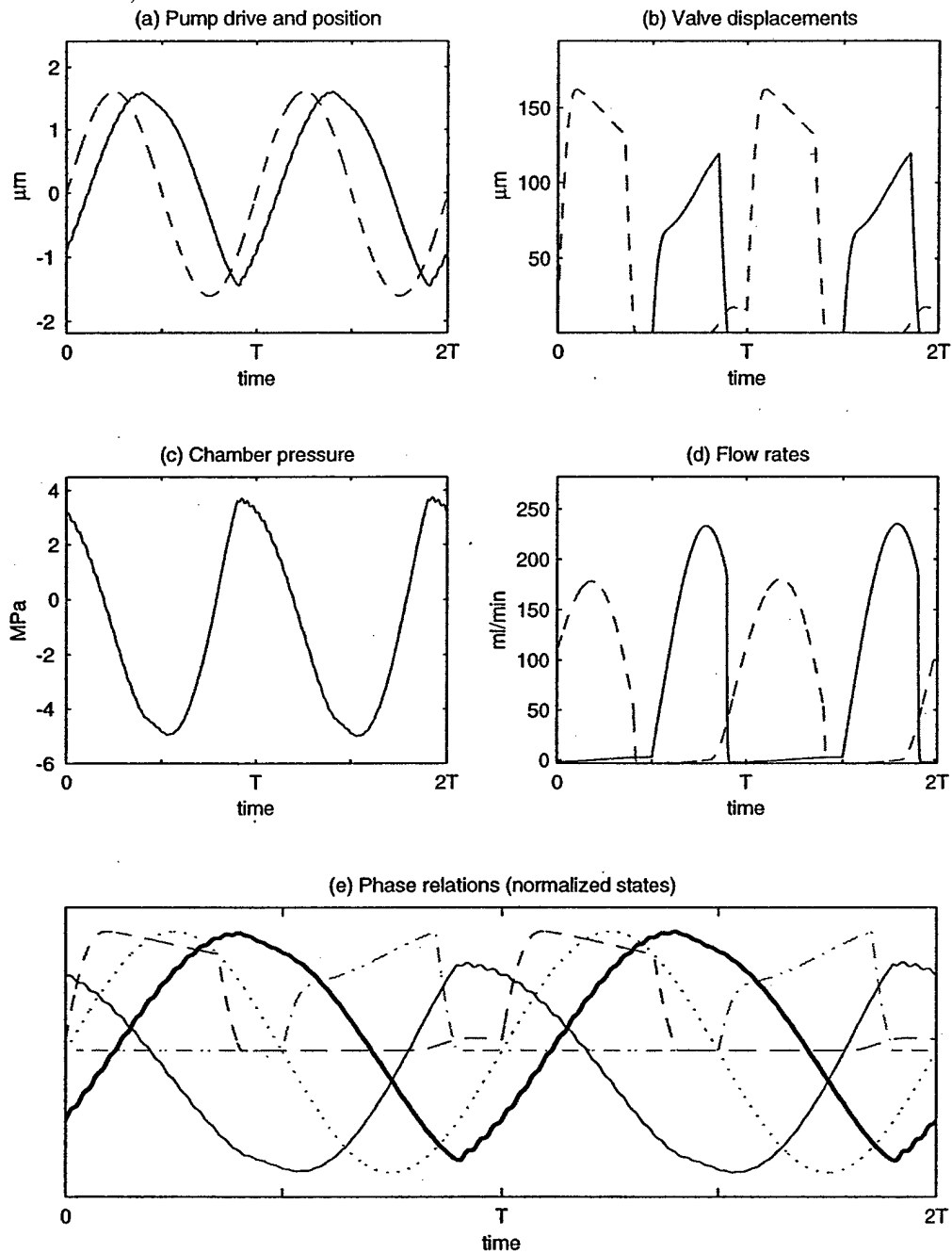


Figure C.13 Simulation 9a: actuator configuration F, $f = 1.11f_n$, $f_n = 6.74$ kHz. Plots (b) and (d) show the displacements and flows of the inlet (solid) and outlet (dashed) valves. Plot (e) indicates the phase relations between the normalized pump position (heavy solid), chamber pressure (solid), drive signal (dotted), inlet valve displacement (dot-dashed), and outlet valve displacement (dashed).

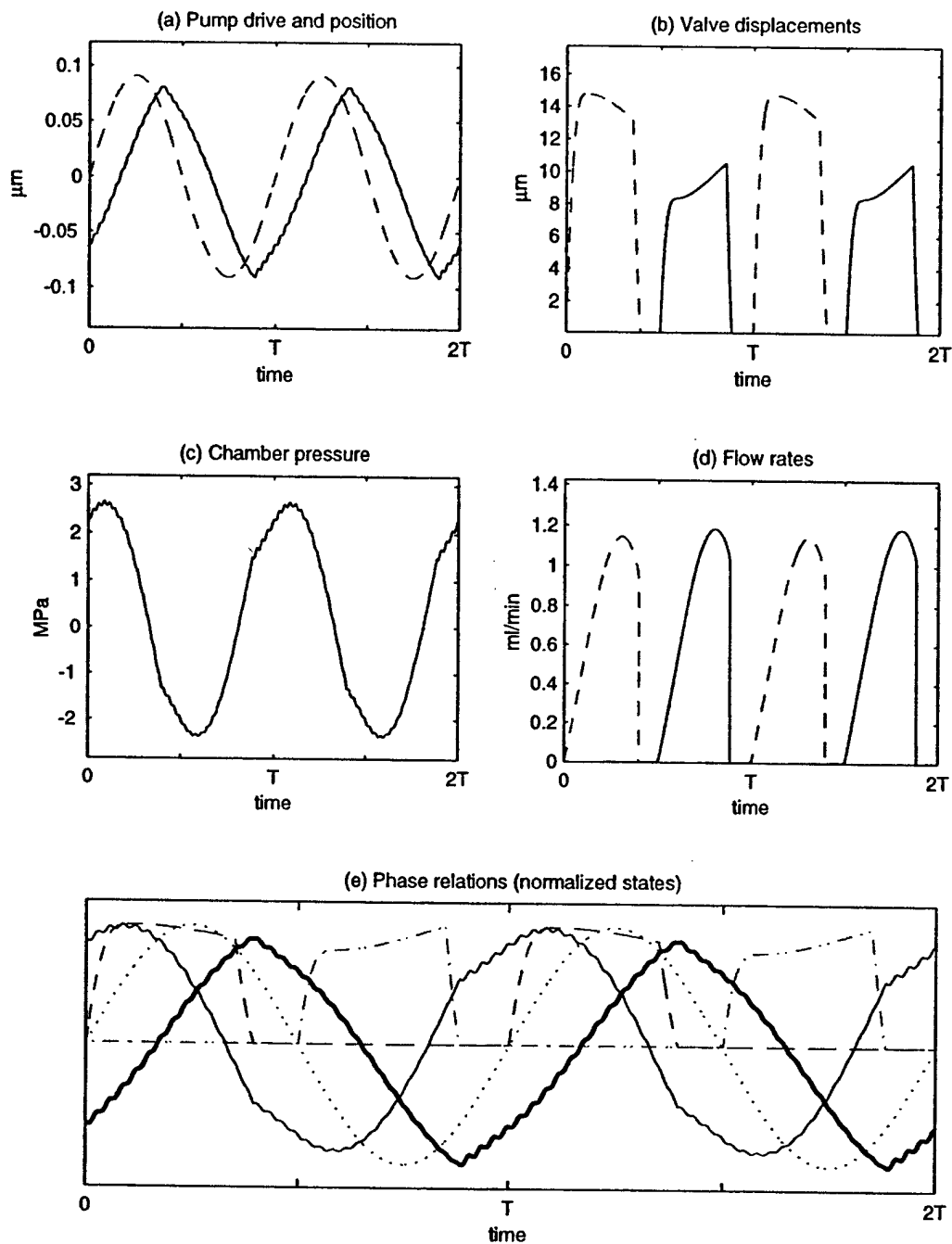


Figure C.14 Simulation 10a: actuator configuration G, $f = 1.11f_n$, $f_n = 66.9$ kHz. Plots (b) and (d) show the displacements and flows of the inlet (solid) and outlet (dashed) valves. Plot (e) indicates the phase relations between the normalized pump position (heavy solid), chamber pressure (solid), drive signal (dotted), inlet valve displacement (dot-dashed), and outlet valve displacement (dashed).

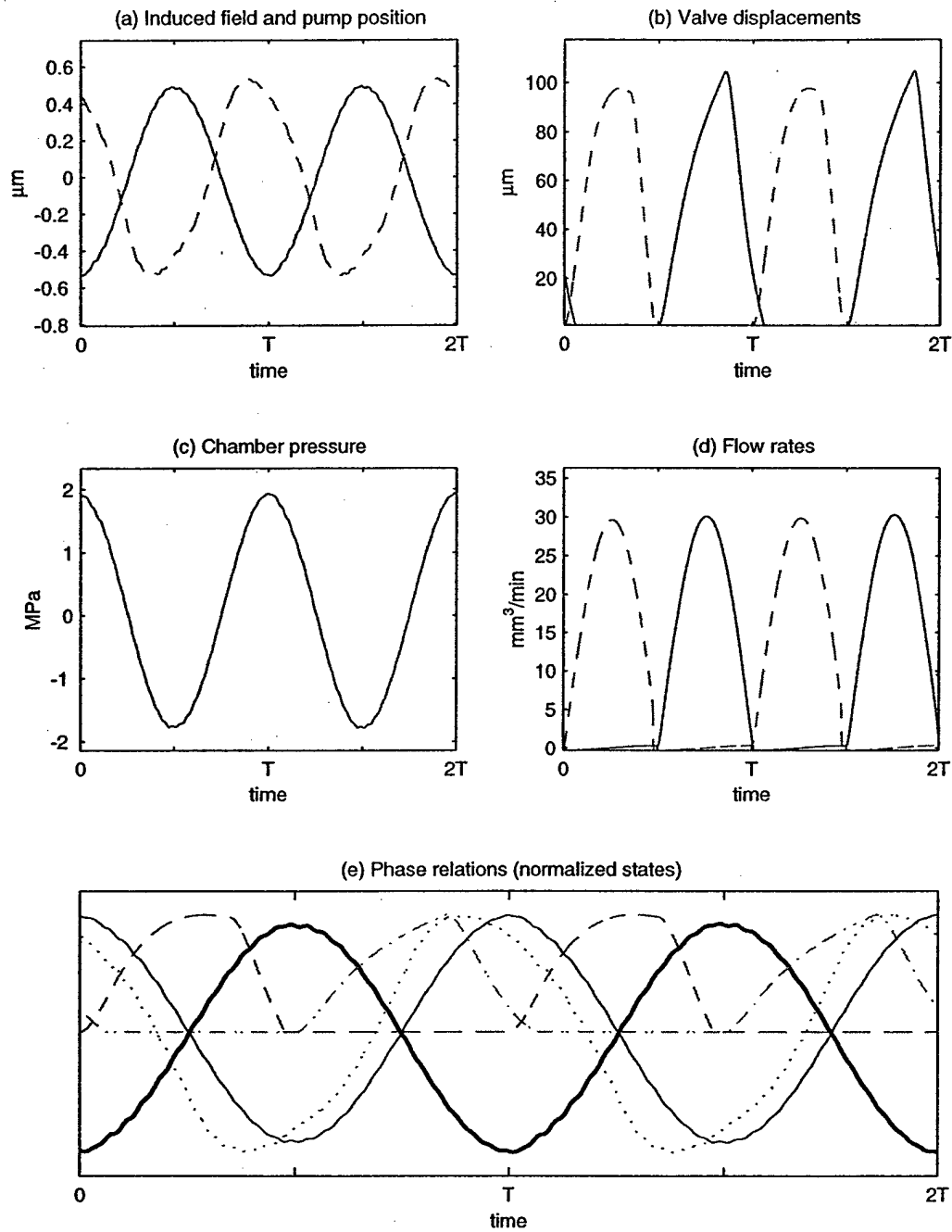


Figure C.15 Simulation 11: power harvester, $f = f_n$, $f_n = 66.9$ kHz. Plots (b) and (d) show the displacements and flows of the inlet (solid) and outlet (dashed) valves. Plot (e) indicates the phase relations between the normalized pump position (heavy solid), chamber pressure (solid), drive signal (dotted), inlet valve displacement (dot-dashed), and outlet valve displacement (dashed).

Appendix D

ANSYS FINITE ELEMENT CODE

VALVE GEOMETRY FILE

```
/BATCH,LIST                                ! Optional Command (to run in batch mode)
/COM, COUPLED-FIELD ACOUSTIC FLUID MODEL
/COM, *** BUILD THE MODEL ***
/FILNAM, valve
/TITLE, valve
/UNITS, SI                                ! Select SI units
/SHOW,                                    ! Specify graphics driver for interactive run
/PREP7

/COM, *** ELEMENT TYPES ***
ET,1,PLANE13                              ! piezo element
ET,2,PLANE42                              ! 4 node solid element
ET,3,FLUID29                              ! 2D acoustic fluid element: with structural interaction
ET,4,FLUID29                              ! 2D acoustic fluid element: no structural interaction
ET,5,SHELL51                              ! axisymmetric shell element

KEYOPT,1,1,7                             ! select all structural and volt dofs for piezo element
KEYOPT,1,3,1                             ! select axisymmetry for piezo element
KEYOPT,2,3,1                             ! select axisymmetric for 8 node solid element
KEYOPT,2,5,2                             ! request nodal stress solution
KEYOPT,3,3,1                             ! select axisymmetric for fluid element
KEYOPT,4,2,1                             ! select 'no structure present' option for element

/COM, *** MATERIALS ***
*ULIB, materials, txt
*USE, TRS-A-Y, 1
*USE, SILICON, 2
*USE, WATER, 3
*USE, PYREX, 4

x = 1                                     ! scale
```

/COM, *** STRUCTURAL GEOMETRY ***

| | | | |
|-------|---|-----------|--|
| tp | = | 600e-6*x | ! thickness of top plate |
| dd | = | 8e-3*x | ! outside diameter of pump |
| db | = | 5.7e-3*x | ! diameter of the button |
| hb | = | 1100e-6*x | ! thickness of the button |
| tb | = | 500e-6*x | ! thickness of base plate |
| lp | = | 1e-3*x | ! length of the piezo element |
| dp | = | 1e-3*x | ! diameter of the piezo element |
| td | = | 10e-6*x | ! thickness of the pump membrane |
| dc | = | 6e-3*x | ! diameter of the chamber |
| hc | = | 500e-6*x | ! height of the chamber |
| tv | = | 5e-6*x | ! thickness of the valve membrane |
| dv | = | 1e-3*x | ! diameter of the valve membrane |
| ch | = | 70e-6*x | ! thickness of the valve cap |
| cd | = | .25e-3*x | ! diameter of valve cap |
| ddisc | = | .62e-3*x | ! diameter of pressure balancing disc |
| hdisc | = | 70e-6*x | ! thickness of pressure balancing disc |
| tol | = | 1e-6 | ! tolerance for selecting nodes |

/COM, *** COMMON COORDINATES ***

| | | |
|---|---|-------------------------|
| a | = | dp/4 |
| b | = | cd/2 |
| c | = | dp/2 |
| d | = | dv/2 |
| e | = | db/2 |
| f | = | dc/2 |
| g | = | dd/2 |
| h | = | tb |
| i | = | tb+lp |
| j | = | tb+lp+hb |
| k | = | tb+lp+hb+hc |
| l | = | tb+lp+hb+hc+tp |
| m | = | tb+lp+hb+hc+tp+ch |
| n | = | tb+lp+hb+hc+tp+ch+hdisc |
| o | = | ddisc/2 |

| | |
|--------|----------------------------|
| R,1,0 | ! fluid reference pressure |
| R,2,td | ! pump membrane thickness |
| R,3,tv | ! valve membrane thickness |

/COM, *** KEYPOINTS ***

K,1,0,h
 K,2,a,h
 K,3,a,i
 K,4,0,i
 K,5,c,h
 K,6,c,i
 K,7,0,0
 K,8,a,0
 K,9,c,0
 K,10,f,0

K,11,g,0
 K,12,g,h
 K,13,f,h
 K,14,g,i
 K,15,f,i
 K,16,e,i
 K,17,e,j
 K,18,c,j
 K,19,a,j
 K,20,0,j
 K,21,f,j
 K,22,g,j
 K,23,g,k
 K,24,f,k
 K,25,e,k
 K,26,d,k
 K,27,b,k
 K,28,0,k
 K,29,g,l
 K,30,f,l
 K,31,e,l
 K,32,d,l
 K,33,b,l
 K,34,0,l
 K,35,b,m
 K,36,0,m
 K,37,0,n
 K,38,b,n
 K,39,o,n
 K,40,o,m

/COM, *** AREAS ***

/PNUM,AREA,1

| | |
|---------------|-----------------------|
| A,1,2,3,4 | ! 1: piezo areas |
| A,2,5,6,3 | ! 2 |
| A,7,8,2,1 | ! 3: structural areas |
| A,8,9,5,2 | ! 4 |
| A,9,10,13,5 | ! 5 |
| A,10,11,12,13 | ! 6 |
| A,13,12,14,15 | ! 7 |
| A,15,14,22,21 | ! 8 |
| A,21,22,23,24 | ! 9 |
| A,24,23,29,30 | ! 10 |
| A,25,24,30,31 | ! 11 |
| A,26,25,31,32 | ! 12 |
| A,6,16,17,18 | ! 13 |
| A,3,6,18,19 | ! 14 |
| A,4,3,19,20 | ! 15 |
| A,28,27,33,34 | ! 16: fluid areas |
| A,27,26,32,33 | ! 17 |
| A,20,19,27,28 | ! 18 |

```

A,19,18,26,27      ! 19
A,18,17,25,26      ! 20
A,17,21,24,25      ! 21
A,16,15,21,17      ! 22
A,34,33,35,36      ! 23: valve cap
A,36,35,38,37      ! 24
A,35,40,39,38      ! 25

/COM, *** ASSIGN AREA ATTRIBUTES ***
LSEL,S,LOC,Y,i-tol,i+tol      ! Select the pump membrane
CM,pumpmem,LINE
LATT,2,2,5

LSEL,S,LOC,Y,l-tol,l+tol      ! Select the valve membrane
CM,valvemem,LINE
LATT,2,3,5

ASEL,S,AREA,,1,2      ! Select the piezo
CM,piezo,AREA
AATT,1,,1      ! Use piezo elements
ASEL,S,AREA,,3,15      ! Select the structural silicon
CM,silicon,AREA
AATT,2,,2      ! Use 4 node solid elements

ASEL,S,AREA,,7      ! Select the pyrex
ASEL,A,AREA,,9
CM,pyrex,AREA
AATT,4,,2      ! Use 4 node solid elements

ASEL,S,AREA,,16,22      ! Select fluid
CM,fluid,AREA
AATT,3,1,3      ! Use fluid elements

ASEL,S,AREA,,23,25      ! Select valve cap
CM,cap,AREA
AATT,2,,2      ! Use 8 node solid elements

/COM, *** MESHING ***
ALLSEL,ALL
vmemsize = 25e-6*x      ! shell element length on valve membrane
pmemsize = 25e-6*x      ! shell element length of pump membrane

! Common number of division groups
nd1      =      3
nd2      =      7
nd3      =      6
nd4      =      2
nd5      =      4
nd6      =      7
nd7      =      5
nd8      =      5

```

| | | |
|------|---|----|
| nd9 | = | 17 |
| nd10 | = | 3 |
| nd11 | = | 3 |
| nd12 | = | 2 |
| nd13 | = | 6 |

LESIZE,1,,,nd11
LESIZE,2,,,nd2
LESIZE,3,,,nd11
LESIZE,4,,,nd2
LESIZE,5,,,nd10
LESIZE,6,,,nd2
LESIZE,7,,,nd10
LESIZE,8,,,nd11
LESIZE,9,,,nd1
LESIZE,10,,,nd1
LESIZE,11,,,nd10
LESIZE,12,,,nd1
LESIZE,13,,,nd8
LESIZE,14,,,nd1
LESIZE,15,,,nd8
LESIZE,16,,,nd7
LESIZE,17,,,nd1
LESIZE,18,,,nd7
LESIZE,19,,,nd2
LESIZE,20,,,nd7
LESIZE,21,,,nd2
LESIZE,22,,,nd3
LESIZE,23,,,nd7
LESIZE,24,,,nd3
LESIZE,25,,,nd5
LESIZE,26,,,nd7
LESIZE,27,,,nd5
LESIZE,28,,,nd6
LESIZE,29,,,nd7
LESIZE,30,,,nd6
LESIZE,31,,,nd4
LESIZE,32,,,nd4
LESIZE,33,,,nd6
LESIZE,34,,,nd9
LESIZE,35,,,nd9
LESIZE,36,,,nd6
LESIZE,37,,,nd9
LESIZE,38,,,nd3
LESIZE,39,,,nd9
LESIZE,40,,,nd3
LESIZE,41,,,nd10
LESIZE,42,,,nd3
LESIZE,43,,,nd11
LESIZE,44,,,nd3
LESIZE,45,,,nd11

```

LESIZE,46,,,nd6
LESIZE,47,,,nd11
LESIZE,48,,,nd6
!LESIZE,49,vmemsize*2
LESIZE,49,,,nd10
LESIZE,50,vmemsize
LESIZE,51,,,nd5
LESIZE,52,,,nd5
LESIZE,53,,,nd5
LESIZE,54,,,nd5
!LESIZE,55,pmemsize*2
LESIZE,55,,,nd4
LESIZE,56,pmemsize
LESIZE,57,,,nd12
LESIZE,58,,,nd11
LESIZE,59,,,nd12
LESIZE,60,,,nd12
LESIZE,61,,,nd11
LESIZE,62,,,nd12
LESIZE,63,,,nd13
LESIZE,64,,,nd12
LESIZE,65,,,nd13

elsize20 = (g-f)/nd7
elsize35 = (e-d)/nd9
elsize36 = tp/nd6
elsize37 = (e-c)/nd9
elsize38 = hb/nd3
elsize47 = b/nd11

! Compute required element sizes

LMESH, valvemem
LMESH, pumpmem
AMESH, ALL

! Mesh valve membrane
! Mesh pump membrane

/COM, *** NODE SETS ***
NSEL,S,LOC,Y,0
CM,bottom,NODE

! Select bottom nodes

NSEL,S,LOC,X,0
CM,center,NODE

! Select center nodes

NSEL,S,LOC,Y,tb+lp
NSEL,R,LOC,X,0,dp/2
CM,top_elec,NODE

! Select the nodes for the top electrode

NSEL,S,LOC,Y,tb
NSEL,R,LOC,X,0,dp/2
CM,bot_elec,NODE

! Select the nodes for the bottom electrode

NSEL,S,LOC,X,0-tol,0+tol
NSEL,R,LOC,Y,n-tol,n+tol

! Select the node in the center of the valve cap

```

CM,vnode,NODE

NSEL,S,LOC,X,0-tol,0+tol
NSEL,R,LOC,Y,i-tol,i+tol
CM,piezn,NODE

! Select the node in the center top of the piezo

NSEL,S,LOC,Y,n-tol,n+tol
CM,capnodes,NODE

! Select the nodes on top of the valve cap

NSEL,S,LOC,Y,l-elsize36
NSEL,R,LOC,X,d
CM,n1,NODE

! Define key nodes

NSEL,S,LOC,Y,l-elsize36
NSEL,R,LOC,X,d+elsize35
CM,n2,NODE

NSEL,S,LOC,Y,l
NSEL,R,LOC,X,d+elsize35
CM,n3,NODE

NSEL,S,LOC,Y,i
NSEL,R,LOC,X,e-elsize37
CM,n4,NODE

NSEL,S,LOC,Y,i+elsize38
NSEL,R,LOC,X,e-elsize37
CM,n5,NODE

NSEL,S,LOC,Y,i+elsize38
NSEL,R,LOC,X,e
CM,n6,NODE

NSEL,S,LOC,Y,l
NSEL,R,LOC,X,b,d
CM,vmnodes,NODE

! Define nodes comprising the valve membrane

NSEL,S,LOC,Y,i
NSEL,R,LOC,X,e,f
CM,pmnodes,NODE
CMGRP,keynodes,n1,n2,n3,n4,n5,n6

! Define nodes comprising pump membrane

/COM, *** CONSTRAINTS ***

CMSEL,S,bottom
D,bottom,UX,0,,,UY

! Constrain bottom

CMSEL,S,center
dsym,symm

! Enforce symmetry

NSEL,S,LOC,Y,l-tol,l+tol
NSEL,R,LOC,X,d+elsize35

! Couple rotational dofs for cantilever

CP,1,ROTZ,ALL

NSEL,S,LOC,Y,l-tol,l+tol
NSEL,R,LOC,X,b-elsize47,b
CP,2,ROTZ,ALL

NSEL,S,LOC,Y,i-tol,i+tol
NSEL,R,LOC,X,e-elsize37,e
CP,3,ROTZ,ALL

NSEL,S,LOC,Y,i-tol,i+tol
NSEL,R,LOC,X,f,f+elsize20
CP,4,ROTZ,ALL

/COM, *** STRUCTURE-FLUID INTERACTION ***

ALLSEL,ALL

ESEL,S,TYPE,,3

NSEL,S,LOC,Y,i

NSEL,A,LOC,Y,j

NSEL,A,LOC,Y,k

NSEL,A,LOC,Y,l

CM,vertcham,NODE ! Define the nodes comprising the floor and ceiling of the chamber

NSEL,S,LOC,X,d

NSEL,A,LOC,X,e

NSEL,A,LOC,X,f

CM,horzcham,NODE ! Define the nodes comprising the vertical wall of the chamber

! Define group of all the nodes defining the chamber outline

CMGRP,chamwall,vertcham,horzcham

CMSEL,S,chamwall

SF,ALL,FSI

! Enforce fluid-structure interaction

/COM, *** AESTHETICS ***

ALLSEL,ALL

/COLOR,NUM,GCYA,1

/COLOR,NUM,DGRA,2

/COLOR,NUM,BLUE,3

/COLOR,NUM,LGRA,5

/NUM,1

/PNUM,MAT,1

NSEL,ALL

/PBC,ALL,,1

/PSF,FSI,2

EPLOT

SAVE

FINISH

STATIC ANALYSIS FILE

```

!**** STATIC ANALYSIS ***
/SOLU
ANTYPE,HARMIC                                ! performe a harmonic analysis
/COM, *** SOLUTION OPTIONS ***
HROPT,FULL                                    ! full solution method
HARFRQ,0,1                                   ! pseudostatic analysis
NSUBST,1                                     ! use 1 substep
ALLSEL,ALL
EPLOT
/COM, *** APPLY LOADS ***
emax      =      8e5
v          =      emax*lp

CMSEL,S,bot_elec
D,bot_elec,VOLT,0

CMSEL,S,top_elec
D,top_elec,VOLT,v

! CMSEL,S,capnodes                            ! To simulate blocked actuator
! D,all,UY,0

! CMSEL,S,capnodes                            ! To determine effective actuator stiffness
! SF,ALL,PRES,1e6

NSEL,ALL
SOLVE
FINISH
/POST1
SET,1,1                                       ! read results file for step 1, substep 1

ALLSEL,ALL
ESEL,ALL                                     ! select all non-fluid elements
ESEL,U,TYPE,,3
ESEL,U,TYPE,,4
PLDISP,0                                     ! display the deformed structure

/COM, *** COMPUTE VOLUMES AND MASSES ***
rhopiezo = 8000
rhosi = 2300
rhofluid = 998
rhopyxex = 2520
ALLSEL,ALL
vinit = 3.141592654/4*(hc*dc**2+hb*(dc**2-db**2))
ETABLE,vols,VOLU
ESEL,S,MAT,,1
SSUM
*GET,vpiezo,ssum,0,item,vols

```

```

ESEL,S,MAT,,2
SSUM
*GET,vsi,ssum,0,item,vols
ESEL,S,MAT,,3
SSUM
*GET,vfluid,ssum,0,item,vols
ESEL,S,MAT,,4
SSUM
*GET,vpyrex,ssum,0,item,vols
mpiezo = rhopiezo*vpiezo
msi = rhosi*vsi
mfluid = rhofluid*vfluid
mpyrex = rhopyrex*vpyrex
mtotal = mpiezo+msi+mfluid+mpyrex
vtotal = vpiezo + vsi + vfluid + vpyrex

CMSEL,S,n1
CMSEL,A,n2
CMSEL,A,n3
CMSEL,A,n4
CMSEL,A,n5
CMSEL,A,n6
PRNSOLN,U,COMP

/COM, *** DESIGN OPTMIZATION PARAMETERS ***
ALLSEL,ALL
CMSEL,S,vnode
*GET,temp1,NODE,,NUM,MIN
vdisp = UY(temp1)
!goal = 1e-3/vdisp
! valve displacement (center)
! function to minimize (i.e. maximize deflection)

ALLSEL,ALL
CMSEL,S,piezn
*GET,temp2,NODE,,NUM,MIN
pdisp = UY(temp2)

ALLSEL,ALL
ESEL,S,TYPE,,3
NSEL,S,EXT
*GET,temp2,NODE,,NUM,MIN
press = PRES(temp2)
! get static pressure in pump chamber (arbitrary fluid
node chosen)

ALLSEL,ALL
CMSEL,S,capnodes
NFORCE
*GET,vforce,FSUM,0,ITEM,FY
! get total vertical force acting on valve
goal2 = 1/vforce

SAVE
FINISH

```

PUMP DIAPHRAGM SUBSTRUCTURE GEOMETRY AND ANALYSIS FILE

```

/BATCH,LIST                                ! Optional Command (to run in batch mode)
/COM, STRUCTURAL MODEL
/COM, *** BUILD THE MODEL ***
/FILNAM,pump_diaphragm
/TITLE,pump_diaphragm
/UNITS,SI                                  ! Select SI units
/SHOW,                                     ! Specify graphics driver for interactive run
/PREP7

/COM, *** ELEMENT TYPES ***
ET,1,PLANE82                              ! 8 node solid element
ET,2,SHELL51                              ! shell elements to enforce linear interpolation
KEYOPT,1,3,1                             ! select axisymmetric for 8 node solid element
KEYOPT,1,5,2                             ! request nodal stress solution

/COM, *** MATERIALS ***
*ULIB,materials.txt
*USE,SILICON,1
*USE,PYREX,2
*USE,STIFFnLIGHT,3

/COM, *** STRUCTURAL GEOMETRY ***
db      =      5.7e-3                      ! diameter of the button
td      =      10e-6                      ! thickness of the diaphragm
dc      =      6e-3                      ! diameter of the chamber
tol     =      1e-6                      ! selection tolerance
elsize37 =      1.38e-4                  ! input length of element 37
elsize38 =      2.2e-4                  ! input length of element 38

R,1,td

/COM, *** KEYPOINTS ***
K,1,db/2+(dc-db)/2,0
K,2,db/2+(dc-db)/2+elsize38,0
K,3,db/2+(dc-db)/2+elsize38,elsize38-td
K,4,db/2+(dc-db)/2,elsize38-td
K,5,db/2+(dc-db)/2+elsize38,elsize38
K,6,db/2+(dc-db)/2,elsize38
K,7,db/2+(dc-db)/2+elsize38,2*elsize38-td
K,8,db/2+(dc-db)/2,2*elsize38-td
K,9,db/2,elsize38-td
K,10,db/2,elsize38
K,11,db/2-elsize37,elsize38-td
K,12,db/2-elsize37,elsize38
K,13,db/2,2*elsize38-td
K,14,db/2-elsize37,2*elsize38-td

/COM, *** AREAS ***

```

```

/PNUM,AREA,1
A,1,2,3,4
A,4,3,5,6
A,6,5,7,8
A,9,4,6,10
A,11,9,10,12
A,12,10,13,14

/COM, *** ASSIGN AREA ATTRIBUTES ***
ASEL,ALL                                ! Select all areas
AATT,1,,1                              ! Use 8 node solid elements

ASEL,S,AREA,,1                          ! Select the pyrex
AATT,2,,1

LSEL,S,LINE,,16
LSEL,A,LINE,,18,19
LATT,3,1,2

/COM, *** MESHING ***
ALLSEL,ALL
ESIZE,2*td                              ! Global element size
te = td/4                               ! Number of elements through diaphragm thickness

LESIZE,5,te                             ! Elements through thickness of diaphragm
LESIZE,7,te
LESIZE,13,te
LESIZE,16,te
n = 2                                   ! Request an aspect ratio of 2 for the interior beam ele-
ments
LESIZE,11,te*2
LESIZE,12,te*2

KSEL,S,KP,,4,6,2                         ! Request finer mesh at the corners
KSEL,A,KP,,9,10
KESIZE,ALL,te

ESHAPE,3                                ! Use mapped meshing
ASEL,S,AREA,,2
ASEL,A,AREA,,4,5
AMESH,ALL

ESHAPE,4                                ! Use free meshing
ASEL,INVE
AMESH,ALL

LMESH,16
LMESH,18,19

/COM, *** NODE SETS ***
NSSEL,S,LOC,Y,0-tol,0+tol              ! Select bottommost nodes

```

CM,bottom,NODE

NSEL,S,LOC,Y,(2*elsize38-td)-tol,(2*elsize38-td)+tol ! Select the upper right nodes

NSEL,R,LOC,X,db/2+(dc-db)/2,db/2+(dc-db)/2+elsize38

CM,topright,NODE

NSEL,S,LOC,X,(db/2+(dc-db)/2+elsize38)-tol,(db/2+(dc-db)/2+elsize38)+tol! Select rightmost nodes

CM,right,NODE

NSEL,S,LOC,X,0-tol,0+tol

! Select center nodes

CM,center,NODE

NSEL,S,LOC,X,db/2,db/2+(dc-db)/2

! Select the nodes exposed to pressure

NSEL,R,LOC,Y,elsize38,2*elsize38-td

CM,wet,NODE

/COM, *** CONSTRAINTS ***

n4x = -.22e-7

n4y = .11e-5

n5x = -.15e-7

n5y = .11e-5

n6x = -.15e-7

n6y = .11e-5

CMSEL,S,bottom

! Fix nodes

CMSEL,A,right

CMSEL,A,topright

D,ALL,UX,0,,,UY

NSEL,S,LOC,Y,elsize38-td

NSEL,R,LOC,X,db/2-elsize37

D,ALL,UX,n4x

D,ALL,UY,n4y

NSEL,S,LOC,Y,2*elsize38-td

NSEL,R,LOC,X,db/2-elsize37

D,ALL,UX,n5x

D,ALL,UY,n5y

NSEL,S,LOC,Y,2*elsize38-td

NSEL,R,LOC,X,db/2

D,ALL,UX,n6x

D,ALL,UY,n6y

NSEL,S,LOC,Y,2*elsize38-td

! couple rotational dofs

NSEL,R,LOC,X,db/2-elsize37,db/2

CP,NEXT,ROTZ,ALL

NSEL,S,LOC,X,db/2-elsize37

NSEL,U,LOC,Y,2*elsize38-td

! remove repeated node

CP,NEXT,ROTZ,ALL

```
NSEL,ALL
/PBC,ALL,,1
EPlot
SAVE
FINISH
```

```
/COM, ***STATIC ANALYSIS ***
```

```
/SOLU
```

```
ANTYPE,STATIC
```

```
p = 232690
```

! externally applied pump chamber pressure

```
ALLSEL,ALL
```

```
EPlot
```

```
SF,wet,PRES,p
```

! apply pressure load to membrane

```
SOLVE
```

```
FINISH
```

```
/POST1
```

```
PLDISP,0
```

VALVE DIAPHRAGM SUBSTRUCTURE GEOMETRY AND ANALYSIS FILE

```

/BATCH,LIST                                ! Optional Command (to run in batch mode)
/COM, STRUCTURAL MODEL
/COM, *** BUILD THE MODEL ***
/FILNAM, valve_diaphragm
/TITLE, valve_diaphragm
/UNITS, SI                                ! Select SI units
/SHOW,                                     ! Specify graphics driver for interactive run
/PREP7

/COM, *** ELEMENT TYPES ***
ET,1, PLANE82                             ! 8 node solid element
ET,2, SHELL51                             ! shell elements to enforce linear interpolation
KEYOPT,1,3,1                             ! select axisymmetric for 8 node solid element
KEYOPT,1,5,2                             ! request nodal stress solution

/COM, *** MATERIALS ***
*ULIB, materials.txt
*USE, SILICON, 1
*USE, STIFFnLIGHT, 2

/COM, *** STRUCTURAL GEOMETRY ***
tv      =      5e-6                       ! thickness of the valve diaphragm
dv      =      1e-3                       ! diameter of the valve diaphragm
ch      =      70e-6                      ! thickness of the valve cap
cd      =      .25e-3                     ! diameter of valve cap
elsize35 =      1.38e-4                   ! input length of element 35
elsize36 =      6.67e-5                   ! input length of element 36

R,1,tv

/COM, *** KEYPOINTS ***
K,1,dv/2,0
K,2,dv/2+elsize35,0
K,3,dv/2+elsize35,elsize36-tv
K,4,dv/2,elsize36-tv
K,5,dv/2+elsize35,elsize36
K,6,dv/2,elsize36
K,7,cd/2,elsize36-tv
K,8,cd/2,elsize36
K,9,0,elsize36-tv
K,10,0,elsize36
K,11,cd/2,elsize36+ch
K,12,0,elsize36+ch

/COM, *** AREAS ***
/PNUM, AREA, 1
A,1,2,3,4
A,4,3,5,6
A,7,4,6,8

```

A,9,7,8,10
A,10,8,11,12

/COM, *** ASSIGN AREA ATTRIBUTES ***

ASEL,ALL

! Select all areas

AATT,1,,1

! Use 8 node solid elements

LSEL,S,LINE,,1,2

LSEL,A,LINE,,5

LATT,2,1,2

/COM, *** MESHING ***

ALLSEL,ALL

ESIZE,5*tv

! Global element size

te = tv/4

! Number of elements through diaphragm thickness

LESIZE,5,te

! Elements through thickness of diaphragm

LESIZE,7,te

LESIZE,10,te

LESIZE,13,te

n = 2

! Request an aspect ratio of 2 for the interior beam elements

ments

LESIZE,8,te*2

LESIZE,9,te*2

KSEL,S,KP,,4,6,2

! Request finer mesh at the corners

KSEL,A,KP,,7,8

KESIZE,ALL,te

ESHAPE,3

! Use mapped meshing

ASEL,S,AREA,,2,4

AMESH,ALL

ESHAPE,4

! Use free meshing

ASEL,INVE

AMESH,ALL

LMESH,1,2

LMESH,5

/COM, *** NODE SETS ***

NSEL,S,LOC,Y,0

! Select bottommost nodes

CM,bottom,NODE

NSEL,S,LOC,X,dv/2+elsize35

! Select rightmost nodes

CM,right,NODE

NSEL,S,LOC,X,LOC,0

! Select center nodes

CM,center,NODE

NSEL,S,LOC,Y,elsize36-tv

! Select the nodes exposed to the pressure

NSEL,R,LOC,X,0,dv/2


```
NSEL,A,LOC,X,dv/2
NSEL,R,LOC,Y,0,elsize36-tv
CM,wet,NODE
```

```
NSEL,S,LOC,X,0
NSEL,R,LOC,Y,elsize36+ch
CM,vnode,NODE
```

! Select the node in the center of the valve diaphragm

```
/COM, *** CONSTRAINTS ***
```

```
n1x = .43e-7
n1y = .55e-6
n2x = .41e-7
n2y = .53e-6
n3x = .55e-7
n3y = .53e-6
```

```
CMSEL,S,center
dsym,symm
```

! Enforce symmetry

```
NSEL,S,LOC,Y,0
NSEL,R,LOC,X,dv/2
D,ALL,UX,n1x
D,ALL,UY,n1y
```

```
NSEL,S,LOC,Y,0
NSEL,R,LOC,X,dv/2+elsize35
D,ALL,UX,n2x
D,ALL,UY,n2y
```

```
NSEL,S,LOC,Y,elsize36
NSEL,R,LOC,X,dv/2+elsize35
D,ALL,UX,n3x
D,ALL,UY,n3y
```

```
NSEL,S,LOC,Y,0
CP,NEXT,ROTZ,ALL
NSEL,S,LOC,X,dv/2+elsize35
NSEL,U,LOC,Y,0
CP,NEXT,ROTZ,ALL
```

! couple rotational dofs together

! unselect the repeated node

```
NSEL,ALL
/PBC,ALL,,1
EPlot
SAVE
FINISH
```

```
/COM, ***STATIC ANALYSIS ***
```

```
/SOLU
ANTYPE,STATIC
```

```
p = 232690
```

! externally applied pump chamber pressure (Pa)

ALLSEL,ALL
EPLOT
SF,wet,PRES,p
SOLVE
FINISH
/POST1
PLDISP,0

! apply pressure load to membrane

6810-64

Design, Modeling, Fabrication, and Testing of a Piezoelectric Microvalve for High Pressure, High Frequency Hydraulic Applications

by

David C. Roberts

S.B., Mechanical Engineering
Massachusetts Institute of Technology, 1995

S.M., Mechanical Engineering
Massachusetts Institute of Technology, 1998

SUBMITTED TO THE DEPARTMENT OF MECHANICAL ENGINEERING
IN PARTIAL FULFILLMENT OF THE DEGREE OF

DOCTORATE OF PHILOSOPHY

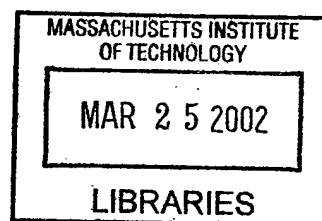
at the

MASSACHUSETTS INSTITUTE OF TECHNOLOGY

February 2002

© 2002 Massachusetts Institute of Technology
All rights reserved

BARKER



David C. Roberts

Signature of Author

Department of Mechanical Engineering

January 10, 2002

Certified by Doctoral Committee

Nesbitt W. Hagood

Nesbitt W. Hagood (Co-Chair), Associate
Professor of Aeronautics and Astronautics

David L. Trumper

David L. Trumper (Co-Chair), Associate
Professor of Mechanical Engineering

Martin A. Schmidt 1/14/02

Martin A. Schmidt
Professor of Electrical Engineering

S. Mark Spearing

S. Mark Spearing, Associate
Professor of Aeronautics and Astronautics

Accepted by

Ain Sonin

Professor Ain Sonin
Chairman, Department Graduate Committee

Design, Modeling, Fabrication, and Testing of a Piezoelectric Microvalve for High Pressure, High Frequency Hydraulic Applications

by

David C. Roberts

Submitted to the Department of Mechanical Engineering on January 10, 2002, in partial fulfillment of the requirements for the Degree of Doctor of Philosophy in Mechanical Engineering.

Abstract

A piezoelectrically-driven hydraulic amplification microvalve for use in high specific power hydraulic pumping applications was designed, fabricated, and experimentally characterized. High frequency, high force actuation capabilities were enabled through the incorporation of one or more bulk piezoelectric material elements beneath a micromachined annular tethered-piston structure. An hydraulic amplification mechanism was employed to amplify the limited stroke of this piezoelectrically-driven piston structure to a significantly larger motion (40-50x) of a micromachined valve membrane with attached valve cap. This valve cap was actuated through its stroke to open and close against a fluid orifice. These design features enabled the valve device to simultaneously meet a set of high frequency (1-10kHz), high pressure (0.1-1MPa), and large stroke (15-40 μ m) requirements that had not previously been satisfied by other microvalves presented in the literature.

This research was carried out through a series of modeling, design, fabrication, assembly, and experimental testing tasks. Linear and non-linear modeling tools characterizing the structural deformations of the active valve sub-systems were developed. These tools enabled accurate prediction of real-time stresses along the micromachined valve membrane structure during deflection into its non-linear large-deflection regime. A systematic design procedure was developed to generate an active valve geometry to satisfy membrane stress limitations and valve power consumption requirements set forth by external hydraulic system performance goals. Fabrication challenges, such as deep-reactive ion etching (DRIE) of the drive element and valve membrane structures, wafer-level silicon-to-silicon fusion bonding and silicon-to-glass anodic bonding operations, preparation and integration of piezoelectric material elements within the micromachined tethered piston structure, die-level assembly and bonding of silicon and glass dies, and filling of degassed fluid within the hydraulic amplification chamber were overcome.

The active valve structural behavior and flow regulation capabilities were evaluated over a range of applied piezoelectric voltages, actuation frequencies, and differential pressures across the valve. For applied piezoelectric voltages up to 500Vpp at 1kHz, the valve devices demonstrated amplification ratios of drive element deflection to valve cap deflection of 40-50x. These amplification ratios correlated within 5 – 10% of the model expectations. Flow regulation experiments proved that a peak average flow rate through the device of 0.21mL/s under a 1kHz sinusoidal drive voltage of 500Vpp, with valve opening of 17 μ m, against a differential pressure of 260kPa could be obtained. Tests revealed that fluid-structural interactions between the valve cap and membrane components and flow instabilities (due to transition between the laminar and turbulent flow regimes through the valve orifice) limited the valve performance capabilities.

Thesis Supervisor: Dr. Nesbitt W. Hagood

Title: Associate Professor of Aeronautics and Astronautics

Acknowledgements

This research work was sponsored by DARPA under Grant #DAAG55-98-1-0361
and by ONR under Grant #N00014-97-1-0880.

The research presented in this thesis could not have been accomplished without the generous support and hard work of a large group of individuals. First and foremost, I would like to thank my advisor, Dr. Nesbitt Hagood, for providing the programmatic resources and support for this research, as well as the numerous opportunities to present this work within the MIT community and at academic conferences. Additionally, his ability to always be one step ahead of the game kept me sharp and forced me to defend and clearly justify all of the decisions made along the path of my PhD work. I would also like to acknowledge my doctoral committee members, Dr. Martin Schmidt, Dr. Mark Spearing, and Dr. David Trumper, for their advice and direction during this work. These interactions have helped me to mature, both intellectually and personally. Additionally, I would like to acknowledge Dr. Kenneth Breuer, at Brown University, for his very helpful guidance on microscale fluid related issues.

I owe a great deal of thanks to Dr. Richard Mlcak, at Boston Microsystems, Inc, for his introduction to the world of MEMS, through initial piezoelectric material integration studies at the onset of the MHT research program four years ago and his continued support in the area of microscale fluid filling and sealing. Additionally, instrumental to the accomplishments embodied within this work were Dr. Laxman Saggere, for his advice on modeling assumptions within my active valve optimization code; Kevin Turner, for his contributions in the area of eutectic bonding; Blair Connelly, for her hard work in the development of testing apparatus for use with the laser vibrometer system used in this work; David Robertson, for his lab organization and debugging activities; Tim Glenn, for his generous support in providing exceptional renderings of MEMS devices for the MHT program; and Seward (Chip) Pulitzer, for his initial system modeling work at the beginning of the program.

Jorge Carretero and Onnik Yaglioglu have been sources of continual support in the development of fluid flow models and full system-level simulations for this active valve device and for MHT systems, in general. Dr. Yu-Hsuan Su was essential to the development of the finite-difference numerical modeling scheme, which serves as the backbone of the non-linear large deflection valve membrane code presented in Chapter 2 of this thesis. Dr. Hanqing Li deserves an unbelievable amount of recognition for his dedication in and out of the cleanroom, providing the MHT program with repeatable and robust fabrication processes for the creation of etched silicon wafers and silicon-glass bonded stacks. Lastly, from the programmatic side of things, I have to give a great deal of thanks to Lodewyk Steyn, who throughout his time on the MHT program, has performed duties above and beyond what were required of him in an effort to unselfishly move the program forward. Without his dedication, especially on the experimental testing side of the program, the validation of fluid-filled active valve devices would not have been accomplished in such an aggressive time frame.

Finally, I would like to thank my family. None of this work could have been accomplished without the positive support from my Mom, Dad, and brother Will. Most importantly, I have to thank my wife, Heather, for her unbelievable support and patience through four and half years of sometimes frustrating, sometimes exhilarating, and all the time stressful research work.

Contents

| | | |
|----------|--|-----------|
| 1 | Introduction | 25 |
| 1.1 | Motivation | 25 |
| 1.2 | Overview of Previous Microvalve Technology | 28 |
| 1.3 | Concept | 33 |
| 1.4 | Challenges | 35 |
| 1.4.1 | Modeling and Design Challenges | 36 |
| 1.4.2 | Device Fabrication, Assembly, and Testing Challenges | 37 |
| 1.5 | Objectives | 39 |
| 1.6 | Approach | 39 |
| 1.7 | Thesis Executive Summary | 41 |
| 2 | Active Valve Linear Model | 47 |
| 2.1 | Valve Geometry and Modeling Procedure | 47 |
| 2.2 | Overview of Linear Plate Theory | 48 |
| 2.2.1 | Deflections Due to Bending | 49 |
| 2.2.2 | Deflections Due to Shearing | 50 |
| 2.2.3 | Combined Deflection Due to Bending and Shearing | 51 |
| 2.2.4 | Comparison of Bending/Shearing Deflections | 51 |
| 2.3 | Detailed Structural Modeling | 52 |
| 2.3.1 | Piezoelectric Material Behavior | 52 |
| 2.3.2 | Drive Element Piston and Tether Behavior | 53 |
| 2.3.3 | Bottom Structural Compliance | 57 |
| 2.3.4 | Fluid Compressibility | 58 |
| 2.3.5 | Top Structural Compliance | 58 |
| 2.3.6 | Valve Cap and Membrane Behavior | 59 |
| 2.4 | Full Active Valve Linear Model | 61 |
| 2.5 | Impact of Multiple Piezoelectric Cylinders | 62 |
| 2.5.1 | Finite-Element Analysis of Piston | 62 |

| | | |
|----------|--|-----------|
| 2.5.2 | Finite-Element Analysis of Bottom Plate | 65 |
| 2.6 | Further Modeling Issues | 66 |
| 2.7 | Conclusions | 67 |
| 3 | Non-Linear Deformation of the Valve Cap and Membrane | 69 |
| 3.1 | Introduction | 69 |
| 3.2 | Plate Geometry | 70 |
| 3.3 | Theory | 70 |
| 3.3.1 | Assumptions | 70 |
| 3.3.2 | Equilibrium Equations | 71 |
| 3.3.3 | Geometric Compatibilities | 72 |
| 3.3.4 | Constitutive Laws | 73 |
| 3.3.5 | Governing Equations | 73 |
| 3.3.6 | In-Plane Prestress | 74 |
| 3.3.7 | Non-Dimensionalized Governing Equations | 76 |
| 3.3.8 | Finite-Difference Implementation | 78 |
| 3.3.9 | Post-Processing Calculations | 81 |
| 3.4 | Results of Numerical Code | 83 |
| 3.4.1 | Loading: $P_1 = P_2 = 0$, $P_3 = 100kPa$, $N_o = 0$ | 84 |
| 3.4.2 | Loading: $P_1 = 2.90MPa$, $P_2 = 0$, $P_3 = 1.30MPa$, $N_o = 0$ | 84 |
| 3.4.3 | Loading: $P_1 = P_2 = 0$, Varying P_3 , $N_o = 0$ | 85 |
| 3.4.4 | Loading: $P_1 = P_2 = 0$, $P_{HAC} = 100kPa$, Varying N_o | 86 |
| 3.5 | Matlab Non-Linear Tools | 87 |
| 3.6 | Conclusions | 89 |
| 4 | Active Valve Non-Linear Model and Simulation | 91 |
| 4.1 | Quasi-Static Active Valve Model | 91 |
| 4.2 | Accuracy of Quasi-Static Model | 93 |
| 4.2.1 | Assumptions in Model | 93 |
| 4.2.2 | FEM Model Geometries and Correlation Procedure | 94 |
| 4.2.3 | Model Correlation Procedure | 95 |
| 4.2.4 | Valve Geometry | 96 |
| 4.2.5 | Model Correlation | 97 |
| 4.3 | Finite-Element Resonant Behavior | 101 |
| 4.4 | Dynamic Active Valve Simulation | 102 |
| 4.4.1 | Linear Matrix Relations | 102 |
| 4.4.2 | Non-Linear Look-Up Tables | 103 |
| 4.4.3 | Piston and Valve Cap Dynamics | 104 |

| | | |
|----------|---|------------|
| 4.5 | Conclusions | 106 |
| 5 | Active Valve Design Procedure | 109 |
| 5.1 | Valve Requirements in Generic MHT System | 110 |
| 5.2 | Modeling of External Hydraulic System | 111 |
| 5.2.1 | MHT Chamber Stiffness | 112 |
| 5.2.2 | Valve Channel Inertial Effects | 113 |
| 5.2.3 | Valve Orifice Flow Relations | 113 |
| 5.2.4 | Chamber Filling Simulation Tool | 116 |
| 5.3 | Systematic Design Procedure | 118 |
| 5.3.1 | Overview | 118 |
| 5.3.2 | System Requirements | 119 |
| 5.3.3 | Step 1: Design of Valve Cap | 119 |
| 5.3.4 | Step 2: Design of Valve Membrane | 121 |
| 5.3.5 | Step 3: Design of Piezoelectric Drive Element | 122 |
| 5.4 | Design Freedoms Within Procedure | 125 |
| 5.4.1 | Design Freedom: $Z_{vc,stroke}$ | 125 |
| 5.4.2 | Design Freedom: t_{vm} | 126 |
| 5.5 | Power Consumption in Active Valve | 134 |
| 5.5.1 | Overview of Energy/Power Consumption | 134 |
| 5.5.2 | Benefit of Multiple Valve Heads | 135 |
| 5.6 | Results of Systematic Design Procedure | 138 |
| 5.7 | Correlation With Dynamic Simulation | 142 |
| 5.8 | Conclusions | 145 |
| 6 | Device Fabrication and Preparation for Testing | 147 |
| 6.1 | Introduction | 147 |
| 6.2 | Fabrication Challenges and Procedures | 148 |
| 6.2.1 | Etching of Tethered Drive Element and Valve Membranes | 149 |
| 6.2.2 | Wafer-Level Bonding | 151 |
| 6.2.3 | Integration of Bulk Piezoelectric Elements | 152 |
| 6.2.4 | Die-Level Assembly and Bonding | 157 |
| 6.2.5 | Fluid Filling/Sealing of HAC | 161 |
| 6.3 | Sub-Component Testing Plan | 165 |
| 6.3.1 | Piezoelectric Drive Element | 165 |
| 6.3.2 | Valve Cap and Membrane | 166 |
| 6.3.3 | Full Active Valve | 167 |
| 6.4 | Testing Apparatus | 167 |

| | | |
|----------|---|------------|
| 6.4.1 | Laser Vibrometer System | 167 |
| 6.4.2 | Fluids Test-Rig | 168 |
| 6.5 | Conclusions | 168 |
| 7 | Sub-Component Study: Piezoelectric Drive Element | 173 |
| 7.1 | Objectives | 173 |
| 7.2 | Device Test-Plan | 174 |
| 7.2.1 | 1st Generation Devices | 174 |
| 7.2.2 | 2nd Generation Device | 176 |
| 7.3 | Device Assembly | 177 |
| 7.4 | Testing Procedure | 180 |
| 7.5 | Experimental Results | 180 |
| 7.5.1 | 1st Generation Devices | 180 |
| 7.5.2 | 2nd Generation Device | 196 |
| 7.6 | Conclusions | 200 |
| 8 | Sub-Component Study: Valve Cap and Membrane | 203 |
| 8.1 | Objectives | 203 |
| 8.2 | Device Test-Plan | 204 |
| 8.2.1 | Geometry | 204 |
| 8.2.2 | Device Assembly | 205 |
| 8.2.3 | Testing Procedure | 205 |
| 8.3 | Theoretical Predictions | 206 |
| 8.3.1 | 1st Modeling Procedure: Numerical Non-linear Deflection Code | 206 |
| 8.3.2 | 2nd Modeling Procedure: Finite-element Code | 207 |
| 8.4 | Experimental Results | 213 |
| 8.4.1 | Fillet Radius Inspection | 213 |
| 8.4.2 | Pressure-Deflection Results | 213 |
| 8.5 | Conclusions | 214 |
| 9 | Active Valve Testing | 217 |
| 9.1 | Objectives | 217 |
| 9.2 | Device Test-Plan | 218 |
| 9.2.1 | Geometry | 218 |
| 9.2.2 | Plan of Study | 218 |
| 9.3 | Experimental Testing Section 1: Active Valve Structural Performance | 220 |
| 9.3.1 | Testing Section 1: Active Valve Structural Performance | 220 |
| 9.3.2 | Testing Section 2: Active Valve Fluid Flow Regulation | 252 |

| | | |
|-----------|---|------------|
| 9.4 | Conclusions | 276 |
| 10 | Conclusions and Recommendations | 279 |
| 10.1 | Summary and Conclusions | 279 |
| 10.1.1 | Thesis Summary | 279 |
| 10.1.2 | Thesis Contributions | 284 |
| 10.2 | Recommended Further Work and the Future of MHTs | 285 |
| 10.2.1 | Redesign for Enhanced Operational Frequency | 286 |
| 10.2.2 | Understanding of Flow Induced Structural Instabilities | 287 |
| 10.2.3 | Materials Characterization | 290 |
| 10.2.4 | Microfabrication Issues | 291 |
| 10.2.5 | Future of MHTs | 292 |
| A | Support Documentation for Active Valve Linear Model | 295 |
| A.1 | ChapterExample.mws | 296 |
| A.2 | FullActiveValve(LINEAR).mws [see Section 2.4] | 299 |
| B | Support Documentation for Non-Linear Valve Cap/Membrane | 313 |
| B.1 | NLValveCapMembrane-CaseA.m [see Section 3.5] | 314 |
| B.2 | NLValveCapMembrane-CaseB.m [see Section 3.5] | 318 |
| B.3 | NLValveCapMembrane-CaseC.m [see Section 3.5] | 322 |
| C | Support Documentation for Full Non-Linear Active Valve Model | 327 |
| C.1 | FullActiveValve(Non-Linear).mws [Section 4.1] | 328 |
| C.2 | NLActiveValveMatlab.m [Section 4.1] | 334 |

List of Figures

| | | |
|------|--|----|
| 1.1 | Upper bound on specific work vs. frequency for various actuation media | 27 |
| 1.2 | Generic block diagrams of Micro-Hydraulic Transducer systems | 28 |
| 1.3 | Selected thermal, electrostatic, and electromagnetic microvalves previously reported in the literature | 29 |
| 1.4 | Selected piezoelectrically-driven microvalves previously reported in the literature | 31 |
| 1.5 | 3-D schematic of the piezoelectrically driven hydraulic amplification microvalve . | 34 |
| 1.6 | Schematic of the fabricated multi-layer active valve structure | 36 |
| 1.7 | Schematic of fabricated multi-layer MHT actuator device | 37 |
| 1.8 | Active valve sub-component fabrication and testing plan | 41 |
| 1.9 | Photograph of a 9-layer piezoelectrically-driven hydraulic amplification microvalve. | 42 |
| 2.1 | 2-D schematic of the piezoelectrically-driven hydraulic amplification microvalve. . | 48 |
| 2.2 | Linear plate theory for a generic circular plate. | 49 |
| 2.3 | Bending and shearing contributions to plate deformation | 52 |
| 2.4 | Modeling of the piezoelectric material element | 53 |
| 2.5 | Modeling of the drive element tethered piston structure | 54 |
| 2.6 | Modeling of the bottom structural plate | 58 |
| 2.7 | Modeling of the top structural plate | 59 |
| 2.8 | Linear modeling of the valve cap and membrane structure | 59 |
| 2.9 | Simplified schematic of the valve membrane structure | 60 |
| 2.10 | Blow-up view of the modeled components in the microvalve | 61 |
| 2.11 | Finite-element schematics of the drive element piston | 63 |
| 2.12 | Compliance coefficients for the drive element piston with multiple piezoelectric cylinders | 64 |
| 2.13 | Finite-element schematics of the bottom plate structure | 65 |
| 2.14 | Compliance coefficients of the bottom plate structure with multiple piezoelectric cylinders | 66 |
| 3.1 | Simplified schematic of the valve membrane structure | 70 |

| | | |
|------|---|-----|
| 3.2 | Force and moment diagrams for a plate section | 71 |
| 3.3 | Schematic of a pretensioned annular plate | 75 |
| 3.4 | Coordinate transformation used within numerical code | 79 |
| 3.5 | Pressure loading terminology on an annular plate | 83 |
| 3.6 | Deflection of a thin annular plate under loading scenario 1 | 84 |
| 3.7 | Deflection of a thin annular plate under loading scenario 2 | 86 |
| 3.8 | Deflection of a thin annular plate under loading scenario 3 | 87 |
| 3.9 | Deflection of a thin annular plate under loading scenario 4 | 88 |
| 3.10 | Numerical code tools to be used throughout thesis | 89 |
| 4.1 | Quasi-static non-linear active valve model overview | 92 |
| 4.2 | Finite-element model of the active valve without fillet radii | 94 |
| 4.3 | Finite-element model of the active valve with fillet radii | 95 |
| 4.4 | Boundary conditions imposed in the active valve finite-element models | 96 |
| 4.5 | Monitored variables in the active valve models | 97 |
| 4.6 | Finite-element stresses predicted in the active valve device | 100 |
| 4.7 | Finite-element modal behavior of the active valve | 102 |
| 4.8 | Dynamic simulation architecture of the active valve | 103 |
| 4.9 | Look-up tables describing valve membrane large deflection behavior | 104 |
| 4.10 | Piston dynamics included in the simulation | 105 |
| 4.11 | Valve cap dynamics included in the simulation | 105 |
| 5.1 | Schematic of a generic MHT power harvesting device | 110 |
| 5.2 | Filling/evacuation of the harvesting chamber through the valves | 112 |
| 5.3 | Modeling of the valve orifice | 113 |
| 5.4 | Look-up tables for valve orifice coefficients | 115 |
| 5.5 | Simulation architecture for chamber filling through active valve | 117 |
| 5.6 | Simulation architecture for active valve orifice and channel | 117 |
| 5.7 | Flowchart for the quasi-static systematic active valve design procedure | 118 |
| 5.8 | Chamber filling as a function of valve cap radius | 120 |
| 5.9 | Design plots for the valve membrane | 121 |
| 5.10 | Modeling of the active valve structure in an impedance match condition | 123 |
| 5.11 | Drive element behavior design plots | 124 |
| 5.12 | Valve cap size vs. imposed valve cap stroke | 126 |
| 5.13 | Valve membrane size and thickness vs. imposed valve cap stroke: Case 1 | 127 |
| 5.14 | Maximum valve membrane stress vs. membrane radius: Case 1 | 128 |
| 5.15 | Example valve membrane deflection plots: Case 1 | 129 |
| 5.16 | Valve membrane size and thickness vs. imposed valve cap stroke: Case 2 | 130 |

| | | |
|------|---|-----|
| 5.17 | Maximum valve membrane stress vs. membrane radius: Case 2 | 131 |
| 5.18 | Example valve membrane deflection plots: Case 2 | 133 |
| 5.19 | Hysteretic energy loss in active valve | 134 |
| 5.20 | Full quasi-static design procedure results: Part 1 | 139 |
| 5.21 | Full quasi-static design procedure results: Part 2 | 140 |
| 5.22 | Full quasi-static design procedure results: Part 3 | 141 |
| 5.23 | Simulation architecture for the filling/evacuation of the MHT system | 143 |
| 5.24 | System simulation plots using the designed active valve geometry | 144 |
| 6.1 | Schematic cross-section of a multi-layer MHT/active valve structure | 148 |
| 6.2 | DRIE etch characteristics of a drive element piston and tether | 149 |
| 6.3 | SEM etch images of a drive element piston and tether | 150 |
| 6.4 | Wafer-level silicon-silicon fusion and silicon-pyrex anodic bond steps | 151 |
| 6.5 | Piezoelectric material surface roughness scans | 153 |
| 6.6 | Piezoelectric thin-film eutectic alloy composition | 154 |
| 6.7 | Precision micrometer measurement of a piezoelectric element thickness | 155 |
| 6.8 | Piezoelectric element tolerancing within drive element structure | 156 |
| 6.9 | Die-level bonding procedure for active valve device | 158 |
| 6.10 | Die-level alignment and bonding jigs | 160 |
| 6.11 | Electrical contact to an active valve chip for anodic bonding | 160 |
| 6.12 | Fluid filling apparatus to fill active valve devices | 161 |
| 6.13 | Fluid filling schematic of component connections | 162 |
| 6.14 | Schematic of the high resistance fluid channel between the HAC and an external bias pressure | 163 |
| 6.15 | Model of the high resistance fluid channel between the HAC and an external bias pressure | 164 |
| 6.16 | Active valve sub-component fabrication and testing plan | 165 |
| 6.17 | Drive element sub-component test structures | 166 |
| 6.18 | Valve membrane sub-component study and full active valve study | 167 |
| 6.19 | Fluids test-rig for testing of the active valve and its sub-components | 169 |
| 7.1 | 3-D schematic of a piezoelectric drive element device | 174 |
| 7.2 | Overview of the drive element sub-component test plan | 175 |
| 7.3 | Drive element geometries and piezoelectric element layout | 176 |
| 7.4 | Exploded view of drive element structure | 177 |
| 7.5 | Assembly of a piezoelectric drive element device | 178 |
| 7.6 | Photographs of fabricated 1st-generation drive element device | 179 |
| 7.7 | Photograph of an assembled 2nd-generation drive element device | 179 |

| | | |
|------|--|-----|
| 7.8 | Measurement points on drive element piston surface using scanning laser vibrometer | 181 |
| 7.9 | Inspection of fillet radii on 1st-generation devices | 182 |
| 7.10 | Piezoelectric material characterization of representative elements | 183 |
| 7.11 | Device 1 transfer functions of piston velocity versus frequency | 185 |
| 7.12 | Device 1 modal behavior | 186 |
| 7.13 | Vibrometer scan images of Device 1 low-frequency 15kHz displacement profile . . | 186 |
| 7.14 | Device 1 displacement time histories for a sinusoidal drive voltage of 500V±500V at $f = 15kHz$ | 187 |
| 7.15 | Device 1 displacement time histories for a sinusoidal drive voltage of 500V±500V at $f = 7kHz$ | 187 |
| 7.16 | Device 1 piston center displacement versus applied voltage at 100Hz | 187 |
| 7.17 | Device 2 transfer functions of piston velocity versus frequency | 189 |
| 7.18 | Device 2 modal behavior | 190 |
| 7.19 | Vibrometer scan images of Device 2 low-frequency 15kHz displacement profile . . | 190 |
| 7.20 | Device 2 displacement time histories for a sinusoidal drive voltage of 500V±500V at $f = 15kHz$ | 191 |
| 7.21 | Device 2 displacement time histories for a sinusoidal drive voltage of 500V±500V at $f = 7kHz$ | 191 |
| 7.22 | Device 2 piston center displacement versus applied voltage at 100Hz | 191 |
| 7.23 | Device 3 transfer functions of piston velocity versus frequency | 193 |
| 7.24 | Vibrometer scan images of selected Device 4 modal behavior | 194 |
| 7.25 | Device 3 ANSYS finite-element model prediction for 1st mode | 194 |
| 7.26 | Vibrometer scan images of Device 3 low-frequency 15kHz displacement profile . . | 194 |
| 7.27 | Device 3 displacement time histories for a sinusoidal drive voltage of 500V±500V at $f = 15kHz$ | 195 |
| 7.28 | Device 3 displacement time histories for a sinusoidal drive voltage of 500V±500V at $f = 7kHz$ | 195 |
| 7.29 | Device 3 piston center displacement versus applied voltage at 100Hz | 195 |
| 7.30 | Device 4 transfer functions of piston velocity versus frequency | 197 |
| 7.31 | Vibrometer scan images of selected Device 4 modal behavior | 198 |
| 7.32 | Vibrometer scan images of Device 4 low-frequency 15kHz displacement profile . . | 198 |
| 7.33 | Device 4 displacement time histories for a sinusoidal drive voltage 500V±500V at $f = 15kHz$ | 199 |
| 7.34 | Device 4 piston center displacement versus applied voltage at 100Hz | 199 |
| 8.1 | 2-D schematic of a valve cap and membrane structure | 204 |
| 8.2 | Dimensions of the fabricated valve cap and membrane structures | 204 |

| | | |
|------|--|-----|
| 8.3 | Valve cap and membrane sub-component structure | 205 |
| 8.4 | Baseline valve cap and membrane design dimensions | 209 |
| 8.5 | Sensitivity of baseline valve cap and membrane design to variations in valve membrane thickness | 210 |
| 8.6 | Finite-element mesh of valve cap and membrane structure | 211 |
| 8.7 | Finite-element stress contours resulting from applied differential pressure loading | 211 |
| 8.8 | Sensitivity of baseline valve cap and membrane design to variations in fillet radius size | 212 |
| 8.9 | Valve cap and membrane experimental pressure-deflection results | 214 |
| 9.1 | Dimensions of active valve devices AV1 and AV2 | 219 |
| 9.2 | Device AV1 low-voltage valve cap frequency response from 500Hz to 100kHz, with and without oil present above the valve structure. | 223 |
| 9.3 | Device AV1 low-voltage piston and valve cap frequency responses from 500Hz to 100kHz, with oil present above the valve structure. | 224 |
| 9.4 | Device AV1 low-voltage valve cap frequency responses from 500Hz to 100kHz, for varying P_{bias} | 225 |
| 9.5 | Device AV1 low-voltage valve cap frequency responses from 500Hz to 100kHz, for varying differential pressure applied to valve cap and membrane structure. | 226 |
| 9.6 | Device AV1 valve cap frequency responses from 500Hz to 3kHz, for $P_{bias} =$ $500kPa$ and increasing high voltage drive levels. | 227 |
| 9.7 | Device AV1 high-voltage piston and valve cap frequency responses from 500Hz to 3kHz, for $P_{bias} = 500kPa$ | 228 |
| 9.8 | Device AV1 valve cap and piston deflection time histories for 1kHz sinusoidal drive voltage levels. | 230 |
| 9.9 | Device AV1 valve cap peak-peak motion, piston peak-peak motion, and device amplification ratio as a function of 1kHz sinusoidal drive voltage levels. | 231 |
| 9.10 | Device AV1 valve cap peak-peak motion, piston peak-peak motion, and device amplification ratio as a function of 1kHz sinusoidal drive voltage levels, with $P_{vc,vm} = 50kPa$ | 232 |
| 9.11 | Experimental verification of the high-frequency channel in device AV1. | 233 |
| 9.12 | Device AV2 low-voltage valve cap frequency response from 500Hz to 100kHz, with and without oil present above the valve structure. | 236 |
| 9.13 | Device AV2 low-voltage valve cap frequency responses from 500Hz to 100kHz, for varying P_{bias} | 237 |
| 9.14 | Device AV2 valve cap frequency responses from 500Hz to 3kHz, for $P_{bias} =$ $500kPa$ and increasing high voltage drive levels. | 238 |

| | |
|--|-----|
| 9.15 Device AV2 high-voltage piston and valve cap frequency responses from 500Hz to 3kHz, for $P_{bias} = 500kPa$. | 239 |
| 9.16 Device AV2 valve cap and piston deflection time histories for 1kHz sinusoidal drive voltage levels. | 240 |
| 9.17 Device AV2 valve cap peak-peak motion, piston peak-peak motion, and device amplification ratio as a function of 1kHz sinusoidal drive voltage levels. | 241 |
| 9.18 Device AV1 and device AV2 quasi-static 1kHz model correlation for fluid bulk modulus $K_f = 2.0GPa$. | 244 |
| 9.19 Device AV1 and device AV2 quasi-static 1kHz model correlation for varying fluid bulk modulus K_f . | 245 |
| 9.20 Finite-element active valve modal frequency sensitivity studies | 248 |
| 9.21 Finite-element modal frequency sensitivity to valve cap added mass | 251 |
| 9.22 Model correlation to device AV1 quasi-static fluid flow rate versus valve opening behavior for differing imposed differential pressures | 253 |
| 9.23 Schematic of valve cap and membrane orifice structure. | 257 |
| 9.24 Representative displacement signals corresponding to stable and unstable valve cap behavior during quasi-static opening. | 258 |
| 9.25 Representative plots for valve cap behavior, differential pressure, and flow rate during quasi-static opening for $P_1 - P_2 = 80kPa$. | 259 |
| 9.26 Valve cap Instability Values during quasi-static opening for $P_1 - P_2 = 80kPa$, $P_1 - P_2 = 130kPa$, and $P_1 - P_2 = 160kPa$. | 260 |
| 9.27 Valve cap Instability Values during quasi-static opening for $P_1 - P_2 = 200kPa$, $P_1 - P_2 = 230kPa$, and $P_1 - P_2 = 240kPa$. | 261 |
| 9.28 Valve cap Instability Values during quasi-static opening for $P_1 - P_2 = 305kPa$ and $P_1 - P_2 = 360kPa$. | 262 |
| 9.29 Complete grouping of all valve cap Instability Values plotted as $P_1 - P_2$ vs. $Z_{vc,opening}$. | 263 |
| 9.30 Estimated boundaries for smooth, rough, and oscillatory regions plotted as $P_1 - P_2$ vs. $Z_{vc,opening}$. | 264 |
| 9.31 Estimated boundaries for unstable and stable regions plotted as $P_1 - P_2$ vs. $Z_{vc,opening}$. | 265 |
| 9.32 Estimated constant Reynolds number curves plotted as $P_1 - P_2$ vs. $Z_{vc,opening}$. | 266 |
| 9.33 Constant Reynolds number curves (experimental vs. model predictions) plotted as $P_1 - P_2$ vs. $Z_{vc,opening}$. | 267 |
| 9.34 Plot of flow resistance coefficient versus Reynolds number for a generic flow orifice contraction structure. | 268 |

| | |
|--|-----|
| 9.35 Device AV1 estimated laminar, transition, and turbulent flow regimes based on experimental data. | 269 |
| 9.36 Schematic of vorticity formation in contraction and expansion fluid flow sections. | 270 |
| 9.37 Laminar, transition, and turbulent representative flow behavior | 271 |
| 9.38 Device AV1 valve cap time histories under varying duty cycle voltage waveforms to piezoelectric drive element. | 273 |
| 9.39 Device AV1 model correlation to experimental flow rate results for varying duty cycles. | 274 |
| 9.40 Device AV1 dynamic flow regulation model correlation at 1kHz for varying dif- ferential pressures. | 275 |

Nomenclature

| | |
|----------------|---|
| A_c | high frequency channel cross-sectional area |
| A_p | piezoelectric material area |
| A_{pis} | drive element piston area |
| A_{vc} | valve cap area |
| A_{vm} | valve membrane area |
| dP_{HAC} | hydraulic amplification chamber pressurization |
| dV_{EHC} | fluid volume change within external energy harvesting chamber |
| dV_{fluid} | hydraulic amplification chamber fluid volume change |
| dV_{pis} | drive element piston swept volume |
| dV_{te} | drive element tether swept volume |
| dV_{de} | drive element total swept volume |
| dV_{top} | top structural plate volume change |
| dV_{vm} | valve cap and membrane swept volume |
| d_{33} | piezoelectric material coefficient |
| E_p | piezoelectric material Young's modulus |
| E_{si} | silicon Young's modulus |
| E_{pyrex} | Pyrex Young's modulus |
| fR | fillet radius |
| F_{vc} | force on valve cap structure |
| F_{vm} | valve membrane force on top structural plate |
| G_{si} | silicon shear modulus |
| H_{HAC} | hydraulic amplification chamber height |
| K_{EHC} | generalized external energy harvesting chamber stiffness |
| K_f | fluid bulk modulus |
| L_c | high frequency channel length |
| L_p | piezoelectric material length |
| N_{vh} | number of valve heads used in parallel within active valve |
| P_{bias} | hydraulic amplification chamber bias pressure |
| P_{EHC} | external energy harvesting chamber pressure |
| P_{EHC}^* | pressure within inlet valve orifice channel |
| P_{EHC}^{**} | pressure within outlet valve orifice channel |

| | |
|----------------------------|---|
| P_{HAC} | hydraulic amplification chamber pressure |
| P_{HPR} | high pressure reservoir pressure |
| P_{LPR} | low pressure reservoir pressure |
| P_{pis} | applied pressure beneath drive element piston |
| P_1 | generalized pressure above valve cap |
| P_2 | generalized pressure above valve membrane |
| Q_{in} | flow rate through inlet valve |
| Q_{out} | flow rate through outlet valve |
| R_{bot}, D_{bot} | bottom structural plate radius, diameter |
| R_{cp} | piezoelectric material spacing radius from drive element center |
| $R_{orifice}, D_{orifice}$ | valve fluid orifice radius, diameter |
| R_p, D_p | piezoelectric material radius, diameter |
| R_{pis}, D_{pis} | drive element piston radius, diameter |
| R_{te}, D_{te} | drive element tethers outer radius, diameter |
| R_{top}, D_{top} | top structural plate radius, diameter |
| R_{vc}, D_{vc} | valve cap radius, diameter |
| R_{vm}, D_{vm} | valve membrane radius, diameter |
| RE | generalized Reynolds number |
| $RE_{Dorifice}$ | Reynolds number through valve orifice |
| t_{bot} | bottom structural plate thickness |
| t_{pis} | drive element piston thickness |
| t_{tetop} | top drive element tether thickness |
| t_{tebot} | bottom drive element tether thickness |
| t_{top} | top structural plate thickness |
| t_{vc} | valve cap thickness |
| t_{vm} | valve membrane thickness |
| T_p | piezoelectric material stress |
| V_p | piezoelectric material voltage |
| V_{HAC} | hydraulic amplification chamber volume |
| W_{hys} | hysteretic energy consumption of active valve |
| Z_{bot} | bottom structural plate deflection |
| Z_{de} | drive element total deflection |
| Z_p | piezoelectric material deflection |
| Z_{pis} | drive element piston deflection |

| | |
|--|---|
| Z_{te} | top drive element tether deflection |
| Z_{top} | top structural plate deflection |
| Z_{vc} | valve cap deflection (absolute) |
| $Z_{vc,opening}$ | valve cap opening distance from orifice |
| $Z_{vc,stroke}$ | valve cap peak-peak stroke |
| α_{si} | silicon shear correction factor |
| ϵ_p | piezoelectric material strain |
| ν_p | piezoelectric material Poisson ratio |
| ν_{Pyrex} | Pyrex Poisson ratio |
| ν_{si} | silicon Poisson ratio |
| ρ_{fluid} | fluid density |
| σ_{vm} | valve membrane radial stress |
| $\sigma_{vm,max}$ | maximum valve membrane radial stress |
| $\zeta_{orifice}$ | valve orifice loss coefficient |
| $\Xi_{Zpis}^P, \Xi_{Zpis}^T, \Xi_{dVpis}^P, \Xi_{dVpis}^T$ | drive element piston compliance coefficients |
| $\Xi_{Ztetop}^F, \Xi_{Ztetop}^P, \Xi_{dVtetop}^F, \Xi_{dVtetop}^P$ | top drive element tether compliance coefficients |
| $\Xi_{Ztebot}^F, \Xi_{Ztebot}^P$ | bottom drive element tether compliance coefficients |
| Ξ_{Zbot}^T | bottom structural plate compliance coefficient |
| $\Xi_{Ztop}^F, \Xi_{Ztop}^P, \Xi_{dVtop}^F, \Xi_{dVtop}^P$ | top structural plate compliance coefficients |
| $\Xi_{Zvc}^F, \Xi_{Zvc}^P, \Xi_{dVvm}^F, \Xi_{dVvm}^P$ | valve cap and membrane compliance coefficients (linear deformation theory) |

Chapter 1

Introduction

1.1 Motivation

The development of a fluidic microvalve, capable of high frequency control of high pressure liquid fluid flows, is a key task in the realization of high specific power ($\frac{W}{kg}$) micropumping technology. Currently, many research efforts around the world are underway to develop compact liquid micropumping systems, the term “micro” referring to devices which are created with fabrication procedures capable of μm -size tolerances and which produce overall micropump dimensions on the order of a few millimeters to a few centimeters. However, the vast majority of these systems are designed for low pressure and low flow rate applications [1] [2] [3] [4] [5] such as drug dispensing and microdosing [6] [7] [8]. The higher performing of these systems are capable of pumping liquids with flow rates on the order of $1000-3000 \frac{\mu L}{min}$ ($0.017-0.050 \frac{mL}{s}$) against differential pressures of between 10kPa and 50kPa. With a typical device mass on the order of ~ 1 gram, these performance values correlate to device-level specific powers below $2.5 \frac{W}{kg}$.

In an effort to develop high specific power micropumping technology (with specific powers $\sim 100-1000 \frac{W}{kg}$) for both actuation and power generation applications, a novel class of Micro-Hydraulic Transducer (MHT) devices has been introduced [1] [10] [11] [12] [13]. These devices combine bulk piezoelectric materials with stiff micromachined structural elements and are designed to enable high frequency pumping of fluid (10-20kHz) against pressure differentials on the order of $\sim 1-2$ MPa, creating flow rates near or in excess of $1 \frac{mL}{s}$.

Piezoelectric materials are well-suited for transducer applications because of their inherently high peak specific powers. Figure 1.1 provides a comparison of the single stroke specific energy ($\frac{J}{kg}$), bandwidth (kHz), and theoretical peak specific power ($\frac{W}{kg}$) for a variety of transducer materials [14] [15] [16]. The product of a material's single stroke specific energy and its bandwidth provides a value for the material's specific power ($\frac{W}{kg}$). Shape-memory alloy materials (denoted SMA), for example, possess a relatively large single stroke specific work ($\sim 5000 \frac{J}{kg}$) in com-

parison to that of standard polycrystalline piezoelectric materials such as PZT-5H ($\sim 10 \frac{J}{kg}$). The maximum operational frequency, or bandwidth ($\sim 10\text{Hz}$), of SMA materials, however, is significantly less than that of standard piezoelectrics ($\sim 100\text{kHz}$). SMA materials and standard piezoelectrics both possess specific powers near $100 \frac{W}{kg}$, however, their optimal implementation as actuation mechanisms is far different. In an application where low frequency, large stroke actuation is desired (such as an on-off microvalve), the use of an SMA material might be preferred over a standard piezoelectric material. Conversely, for an application whereby high frequency, low stroke actuation is required, a piezoelectric material may be preferred. In fact, for this reason, the vast majority of high frequency micropumping systems use piezoelectric materials as their actuation mechanism in conjunction with fast-acting valves. The recent development of single-crystal ferroelectric materials (e.g. PZN-PT), characterized by specific powers approaching $10 \frac{kW}{kg}$ ($\sim 100\times$ greater than those of standard polycrystalline PZT materials) [17], offers further advantages in strain capability over the standard piezoelectrics. These high performing materials, however, have yet to be integrated within high frequency micropumping systems.

The piezoelectric micropumping devices and systems that have been presented in the literature up until this time typically utilize one of two actuation methods as a means to pump fluid: either (1) a deposited thin-film, thick disk, or bimorph of piezoelectric material [2] [3] [6] in contact with a compliant membrane, or (2) a direct-drive stack actuator in contact with a moveable silicon diaphragm. The thin-film, thick-film, and bimorph structural designs presented are not conducive to both high force and high-frequency operation. The direct-drive stack actuation designs [18] [19] [20] are capable of achieving higher frequency operation than the thin-film, thick-film, and bimorph designs, however the presented micropump devices using these designs are limited in their flow rate, pressurization, and frequency capabilities due to inadequacies of the accompanying one-way passive valves used to regulate the fluid flow. Additionally, these previously presented direct-drive stack designs require a significant length of piezoelectric actuation material to create the deflection and fluid pumping volume required for reasonable fluid flow rates. Due to this significant actuator size, an epoxy bonding agent and a relatively compliant silicon diaphragm are required to tolerance the piezoelectric material within the structures. The key design feature which differentiates Micro-Hydraulic Transducer devices from these previous piezoelectric micropumps is the incorporation of a stiff micromachined structural "piston-like" actuation element not only within the pumping chamber of the device, but also within accompanying flow regulation active valves. The annularly-tethered micromachined "piston" structure, driven by miniature bulk piezoelectric elements (almost an order of magnitude smaller than those used in [18] [19] [20]) attached using a thin-film eutectic alloy bond, can achieve structural frequencies well above 10kHz and can actuate against fluid pressurizations near 1MPa . The implementation of such a stiff structure within fluidic systems can enable significantly higher frequency and pressurization capabilities than the previously

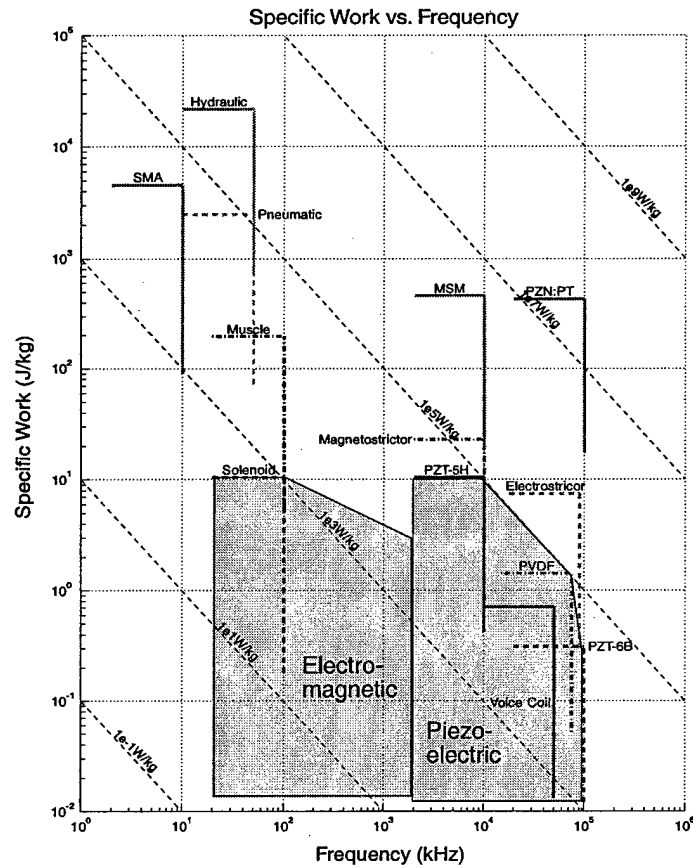


Figure 1.1: Upper bound on specific work vs. frequency for various actuation media. SMA is shape-memory alloy; PZN-PT is single-crystal piezoelectric; MSM is magnetic shape memory materials.

presented piezoelectric micropumps.

As shown in Figure 1.2, a Micro-Hydraulic Transducer system consists of a piezoelectric pump chamber, two actively controlled valves, and a low and high pressure fluid reservoir. In the MHT actuator, electrical energy supplied to the piezoelectric pump chamber results in a pumping of fluid through the valves from the low to high pressure reservoir. In the MHT power harvester, sequenced operation of the valves results in fluid flow from the high to low pressure reservoir, producing a “pinging” of the piezoelectric element within the pump chamber. This cyclic strain on the element induces electrical charge, which can be rectified and stored. The specific power of these transducer devices scales linearly with the frequency of operation and the pressure drop across which the device can operate. Since structural frequencies scale inversely with the geometric size of the device, it is advantageous to build these systems as small as

possible, hence the need for MEMS fabrication and process technologies. The performance of these MHT systems is directly governed by the capabilities of the active valves, which regulate flow into and out of the pump chamber. As a result, to achieve high specific power Micro-Hydraulic Transducer devices, a compact high frequency, high pressure active valve is required. The development of such an active valve is the subject of this thesis.

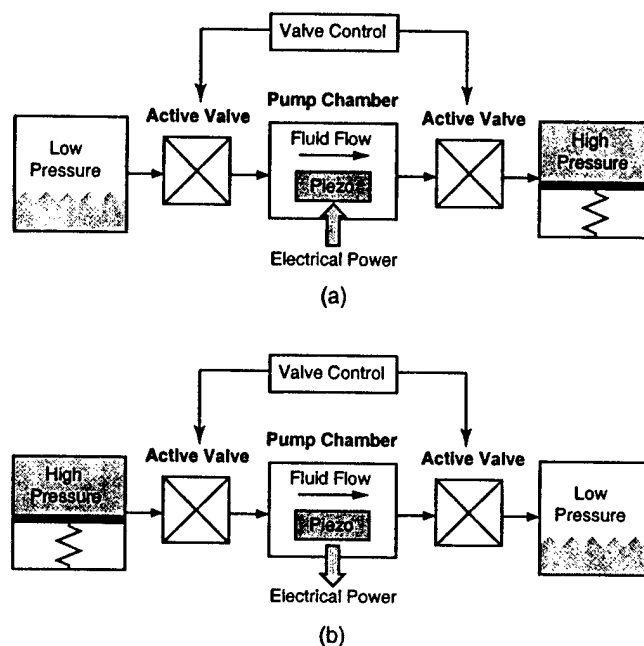


Figure 1.2: Schematics of Micro-Hydraulic Transducer systems: (a) MHT actuator system, (b) MHT power harvesting system. High specific power is achieved through the integration of piezoelectric material with structural stiff small-scale hydraulic systems.

1.2 Overview of Previous Microvalve Technology

Although a significant amount of literature is available describing the development of active valve devices and technology, few if any have been designed for high frequency control of high pressure liquid fluid flows. Novel microvalve designs using thermopneumatic actuation [21] [22], thermal bimetallic actuation [24], SMA actuation [23], electrostatic actuation [25] [26], electromagnetic actuation [27] [28], piezoelectric bender-type actuation (both thin-film and thick film) [29] [30] [31], and piezoelectric stack-type actuation [18] [19] [20] have been presented. A sampling of previously reported microvalves is shown in Figure 1.3 and Figure 1.4.

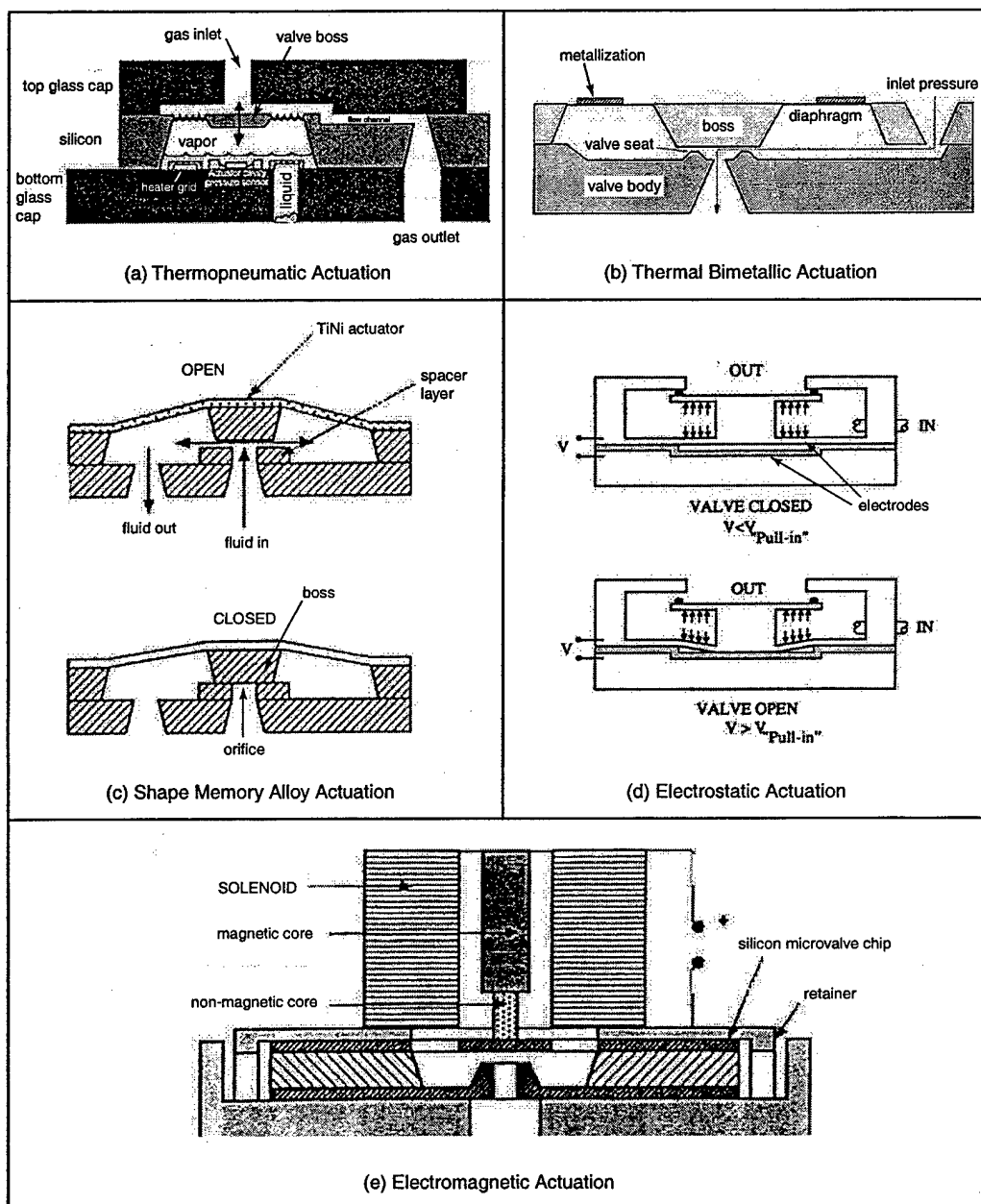


Figure 1.3: Previously reported microvalves: (a) thermopneumatic actuation, Rich [22], (b) thermal bimetallic actuation, Jerman [24], (c) shape memory alloy actuation, Huff [23], (d) electrostatic actuation, Huff [25], and (e) electromagnetic actuation, Pourahmadi [27].

Figure 1.3(a) shows a thermopneumatic microvalve [22] for control of gas flows. A valve central boss is supported by a corrugated silicon membrane. The deflection of the boss is controlled by the vapor pressure of the heated working fluid (parylene) within the contained chamber. A micromachined heater grid exists within the chamber to increase the fluid temperature. For typical operation, a temperature of 80°C (and a corresponding power dissipation of 300mW) is required to move the valve boss through a stroke of 9 μ m in a time of approximately 15 seconds. Maximum pressure rise within the fluid chamber was reported to be 100kPa.

Figure 1.3(b) illustrates a thermal bimetallic valve [24] for use in pneumatic closed-loop pressure or flow control applications. The valve consists of a diaphragm actuator with a central boss which mates to an etched silicon valve body. The actuator includes a circular silicon diaphragm with integrated diffused resistors and an annular region of deposited aluminum. As current is passed through the resistors, the diaphragm increases in temperature. The thermal expansion mismatch between the silicon and aluminum results in a controlled displacement of the central boss. An operational boss deflection of 15 μ m was obtained in response to a temperature increase of 100°C (and a reported corresponding power dissipation of 1W). Regulation of 200kPa differential pressure gas flows in an on-off fashion was demonstrated, resulting in gas flow rates of up to 2mL/s. No actuation response time was reported.

Figure 1.3(c) displays a shape-memory alloy (titanium nickel) actuated microvalve [23] for precise regulation of liquid fluid flow in micro-chemical analysis and drug delivery applications. The shape-memory effect is an athermal phase transformation between the austenitic (high temperature rigid) and martensitic (low temperature ductile) phases. In this valve, a TiNi diaphragm with attached silicon boss is actuated to open and close against a micromachined orifice. The valve was tested in an on-off fashion and it was reported to enable a liquid (DI water) flow rate of 0.1mL/s for an applied differential pressure of 5kPa. Maximum stroke of the valve boss was not reported.

Figure 1.3(d) displays an electrostatic microvalve [25] with a pressure-balancing structural feature that allows it to control fluids at pressures significantly larger than the necessary actuation pressure. The fluid provides a balancing force on the moving part of the structure thereby reducing the force required to open the valve. The moving part of the valve is a plunger which is actuated vertically, and consists of a center-bossed circular base and cap. Electrostatic actuation is enabled through a small gap between the underside of the membrane and the top surface of a bottom support structure. This on-off valve was able to control 220kPa differential gas flows with an actuation voltage of 210V, resulting in a peak flow rate of 2.5mL/s. Due to significant ohmic heating in the device (because of a poor oxide layer), power dissipation was reported to be greater than 10W.

Figure 1.3(e) illustrates an electromagnetic microvalve [27] designed for applications requiring large stroke and large on-off gas flow rates. The microvalve consists of a solenoid housing

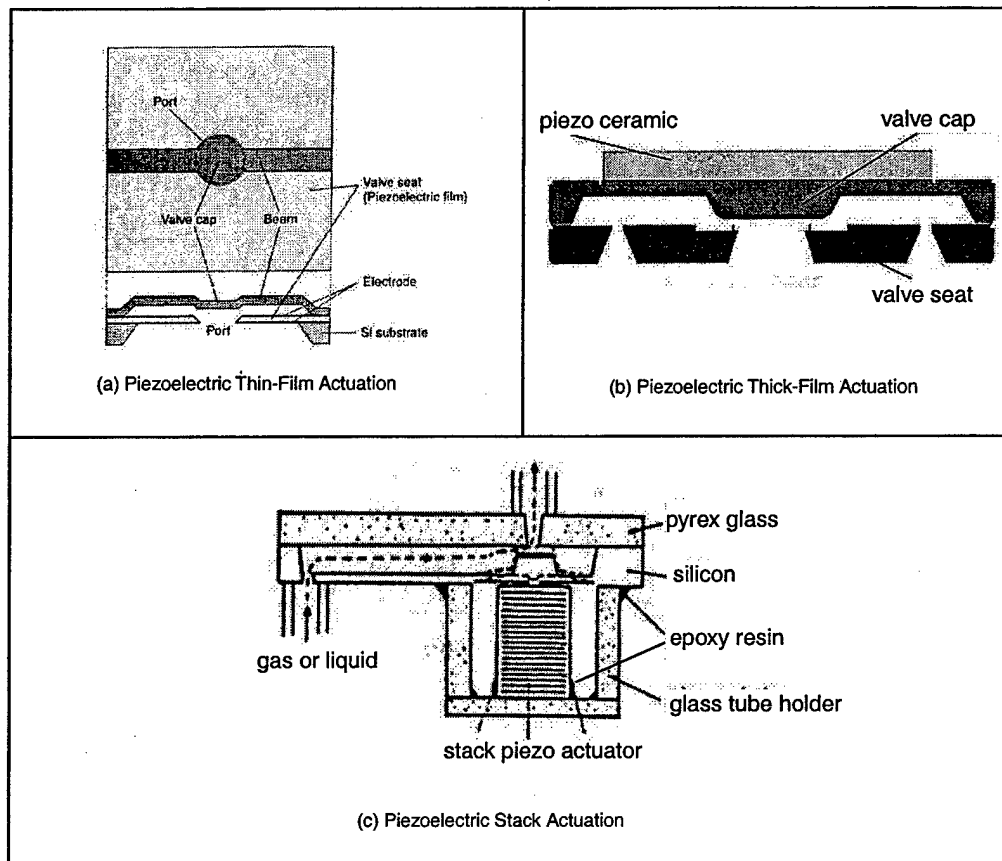


Figure 1.4: Previously reported piezoelectric microvalves: (a) piezoelectric thin-film actuation, Watanabe [30], (b) piezoelectric thick-film actuation, Kluge [31], and (c) piezoelectric stack actuation, Esashi [19].

and a plunger which is rigidly attached to a diaphragm structure. Current applied to the solenoid results in a motion of the plunger against a micromachined orifice. Dimensions of the solenoid attachment are unknown, however the author states that the application for this valve does not require the device to fit within a compact volume. For on-off operation, this direct drive is reported to achieve a maximum valve cap displacement of $100\mu\text{m}$ against a differential pressure of 90kPa , resulting in peak flow rates near 5mL/s . Power dissipation was reported to be greater than 1W .

Figure 1.4(a) displays a portion of a piezoelectrically-driven microvalve matrix [30] for controlling precise levels of gas flow. The valve is constructed of a thin beam with a round valve cap at the center and a valve seat of piezoelectric thin-film bifurcated in the normal direction.

The valve is normally closed due to a residual stress in the beam. For voltage applied to the valve seat, the piezoelectric film shrinks and the inner edge moves radially outward thereby increasing the flow area between the valve cap and this inner edge. The outer diameter of the piezoelectric thin-film is $600\mu\text{m}$ and its thickness is $1\mu\text{m}$. In response to a voltage of 1V, the valve was reported to actuate against a differential pressure of 0.1kPa, resulting in a gas flow rate of 2mL/s.

Figure 1.4(b) illustrates a thick-film piezoelectrically-actuated microvalve [31] for use in high gas flow applications. The valve consists of a micromachined valve cap and membrane structure with an attached (via epoxy) piezoceramic disk to actuate the valve cap against a micromachined valve seat orifice. The valve seat diameter is 2.25mm and the achievable stroke of the valve cap is $30\mu\text{m}$ for an applied voltage of up to 3000V. For on-off operation, the valve was reported to regulate gas flow at 11.6Hz against a differential pressure of 400kPa. The thickness of the piezoceramic disk structure was not detailed.

Figure 1.4(c) displays a piezoelectrically-driven microvalve [19] using a direct drive piezoelectric stack as the actuation mechanism. This valve was designed for use in a liquid micropumping system. The microvalve consists of one silicon and two glass layers anodically bonded together. The silicon contains a inlet through hole, a flow channel, and a moveable diaphragm with a central boss structure. A piezoelectric stack 9mm in length is attached to the underside of the boss using epoxy. In response to a voltage of 90V at a frequency of 30Hz, an estimated liquid pressurization of 8kPa in the pumping chamber of the micropump and a corresponding flow rate of 0.00025mL/s was reported.

The previously described microvalves were selected to illustrate the wide variety of actuation concepts previously reported in the literature. All of these microvalves share a common operational geometry (except for Watanabe [30]) in that a valve boss is affixed to a diaphragm or membrane structure which carries the boss through a predetermined stroke, in response to some form of actuation principle. The majority of these valves were designed for gas flows, and as such estimating their capabilities in handling liquids is difficult to do, although typically flow rates of liquids for a given differential pressure can be expected to be 100-1000x smaller than gas flow rates under the same differential pressures. In general, based on their reported capabilities, it can be concluded that none of these valves is capable of simultaneously satisfying the set of high frequency (1-10kHz), high pressure (0.1-1MPa), and large stroke ($15\text{-}40\mu\text{m}$) requirements needed within full MHT liquid micropumping systems.

The thermal actuation designs (based on thermopneumatic, thermal bimetallic, and shape memory alloy principles) potentially can achieve large stroke and reasonable actuation force. However, these thermally-based devices exhibit excessive power consumption and poor response times on the order of seconds. High-frequency actuation in the kHz range is therefore unachievable. The electrostatic devices are limited in their deflection and pressure generation capabili-

ties, since the electrostatic force generated between two parallel plates scales inversely with their spacing and since electrical breakdown across the gap must be avoided. The electromagnetic concept is impeded by the overall size of external solenoid and housing structures needed to actuate the valve structure. Piezoelectric thin-film and thick-film bender-type designs are limited in their ability to generate both high force and large deflection output. Shoji and Esashi's work aimed at solving this problem through the use of a stack-type piezoelectric actuator material to directly drive the valve membrane. In doing so, however, the piezoelectric stack material was required to be long ($\sim 9\text{mm}$), resulting in a large actuator mass and size. The operational frequency of this device was reported only up to 30Hz.

A promising method for achieving high frequency operation in conjunction with large force and high stroke capability would be to design a microvalve with a means to amplify the stroke of a piezoelectric bulk-type material (for example 1mm in thickness - almost an order of magnitude smaller in length than Shoji and Esashi's stack) into a larger valve membrane stroke. This could be done using a stiff hydraulic fluid within an enclosed chamber to couple the piezoelectric material motion to the valve cap motion using an area ratio amplification concept. This type of structure would thereby achieve high frequency, high pressure, and large valve cap stroke actuation with minimal device power consumption (a further advantage of piezoelectric materials). Numerous macroscale piezoelectric hydraulic amplification mechanisms have been presented in the literature. In an application for active vibration control, a piezoelectric actuator uses the volume change of a piezoelectric ring to create a large deflection of a smaller area contact surface [32]. In an application for vibration control of a rotary dynamic system, the deflection of a stack-type piezoelectric actuator is coupled through a hydraulic line to a smaller size piston, which helps to control the motion of a rotating shaft [33]. These and other [34] piezoelectric hydraulic amplification mechanisms are novel in design, yet do not face the difficult fabrication, assembly, and tolerancing challenges inherent in the development of high frequency MEMS-scale devices.

1.3 Concept

This thesis focuses on the design, modeling, fabrication, and experimental testing of a piezoelectrically driven hydraulic amplification microvalve for high pressure, high frequency applications. The proposed microvalve is shown in Figure 1.5. This device is desired to achieve large valve cap stroke (up to $\sim 40\mu\text{m}$) against high pressure loads ($\sim 0.1\text{--}1\text{MPa}$) through a novel hydraulic amplification mechanism that converts the small displacement ($\sim 1\mu\text{m}$) of a piezoelectric material element into a significantly larger valve cap stroke. The inherent stiffness of the piezoelectric material and the hydraulic fluid chamber enable both high-frequency and high-force actuation capabilities.

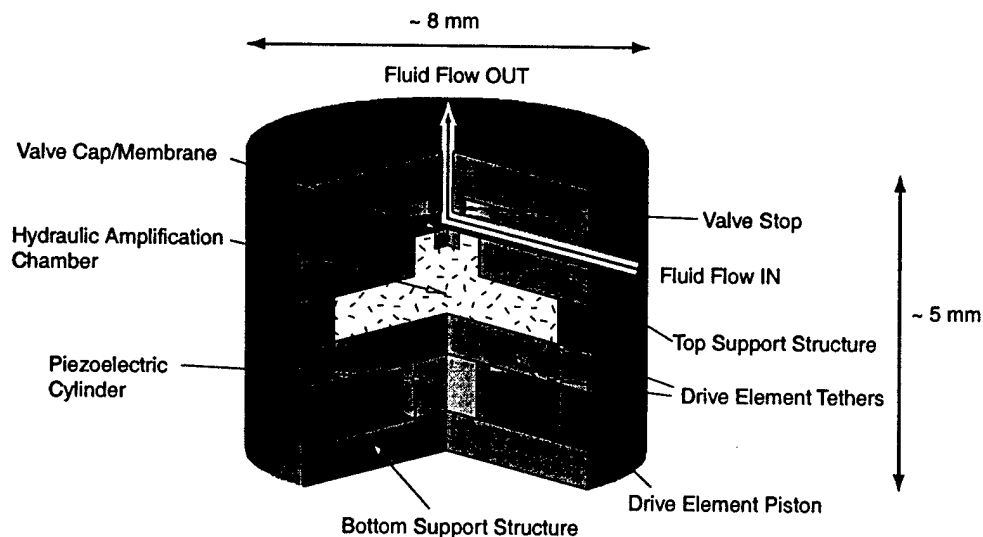


Figure 1.5: Schematic of a piezoelectrically-driven hydraulic amplification microvalve. The primary structural components are designated with arrows. External hydraulic system pressure loading is applied on the top surface of the valve cap and membrane.

The active valve consists of three primary components: a piezoelectric drive element, an enclosed fluid amplification chamber, and a membrane with attached valve cap. The drive element incorporates a circular piston structure supported from beneath by one or more small bulk piezoelectric cylinders and is suspended circumferentially from a surrounding support structure by thin annular micromachined tethers. This novel compact "piston-type" design enables high frequency actuation against a large external pressurization due to the high stiffness of the piston structure and integration of miniature bulk piezoelectric elements beneath the piston using a thin-film bond layer. The lateral dimensions of the tethers are designed to make the tethers compliant enough to allow for rigid piston motion up and down, yet stiff enough to resist bowing under pressurization caused by the hydraulic fluid above the tether during actuation. The tethers provide a seal between the hydraulic fluid above the piston and the piezoelectric chamber below the piston, and also provide a path for electrical contact to the top surface of the piezoelectric cylinders. The fluid chamber resides between the top surface of the drive element piston and the bottom surface of a thin, smaller diameter silicon micromachined valve cap membrane. These design features enable the valve device to simultaneously meet a set of high frequency, high pressure, and large stroke requirements that have not previously been satisfied by other microvalves presented in the literature.

In response to applied piezoelectric voltage, the piezoelectric material strains. The resulting deflection of the drive element piston generates a pressure within the hydraulic amplification chamber which in turn deflects the valve cap and membrane against a fluid orifice, thereby regulating fluid flow through the external hydraulic system. The pressure loadings on the valve cap and membrane during device operation depend on the external microfluidic system application. The piezoelectric material capabilities, the ratio of the piston diameter to the valve membrane diameter, the compliances of the fluid and structural elements in the chamber, the severity to which the valve cap membrane experiences nonlinear behavior, and the nature of the external loading all contribute to the performance of this microvalve device.

The proposed fabrication process for this microvalve involves the assembly of five silicon layers and four glass layers. A 2-D schematic of the microvalve device, illustrating individual silicon and glass layers, is shown in Figure 1.6. The middle glass layer (Layer 3) forms the drive element support structure and the top (Layer 9) and bottom (Layer 1) glass layers provide structural support. The bottom silicon layer (Layer 2) and drive piston silicon layers (Layers 4,5) provide a path for electrical contact to the piezoelectric cylinders. The top four silicon layers (Layers 4,5,7,8) and glass layer (Layer 6) house the hydraulic amplification chamber, valve cap and membrane structure, and fluid inlet and outlet channels. All silicon-silicon wafer interfaces are bonded with high-temperature ($\sim 1300^{\circ}\text{C}$) fusion bonds, and all silicon-glass layer interfaces are bonded using low temperature ($\sim 300^{\circ}\text{C}$) anodic bonds. Attachment of the top and bottom piezoelectric cylinder surfaces to the adjoining silicon is achieved with a low temperature ($\sim 300^{\circ}\text{C}$) AuSn eutectic bond.

Shown in Figure 1.7 is a 3-D schematic of a fabricated silicon and glass multi-layer Micro-Hydraulic Transducer actuator system. This system consists of an inlet and outlet piezoelectrically driven active valve and a centrally-located piezoelectric pump chamber. The pump chamber is comprised essentially of the same drive element structure contained within each active valve component. All of the fabrication and assembly challenges (see Section 1.4.2) inherent in the realization of the active valve component structures are shared by the full MHT device, and as a result the efforts documented within this thesis to successfully fabricate a workable valve device at the same time demonstrate the ability to realize complete MHT systems.

1.4 Challenges

A significant number of challenges had to be overcome to realize a functional piezoelectrically driven hydraulic amplification microvalve. These challenges can be organized into two major groupings: (1) modeling and design challenges and (2) fabrication, assembly, and testing challenges. These challenges are highlighted in the following sections.

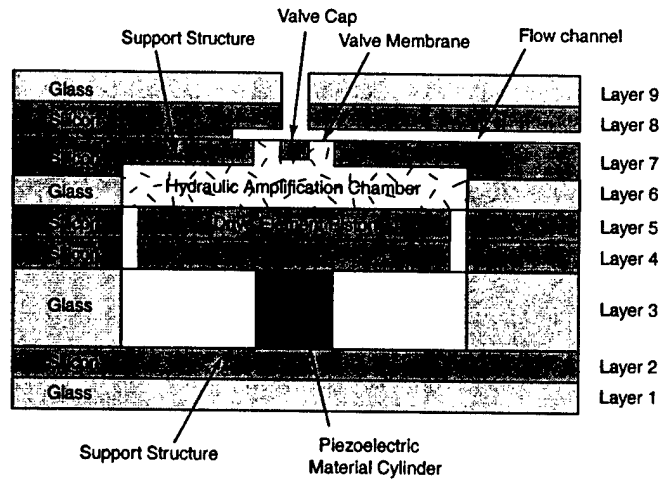


Figure 1.6: 2-D schematic of a microvalve multi-layer silicon and glass structure. Five silicon layers, four glass layers, and one or more piezoelectric material cylinders are joined together to form the microvalve. Enclosed fluid within the hydraulic amplification chamber couples the drive element piston deflection to the valve cap motion.

1.4.1 Modeling and Design Challenges

Structural Modeling of Active Valve

The development of a comprehensive structural model for the active valve requires detailed modeling of the piezoelectric material behavior, the bottom support plate structural compliance, the drive element piston and tether compliances, the hydraulic chamber fluid stiffness, the top support plate structural compliance, and the valve membrane deflection behavior. Stresses within the piezoelectric material, the drive piston tethers, and the valve membrane must be calculated to ensure structural integrity of the device under worst-case system loading conditions. Linear plate deformation theory is adequate for calculating the deflections and stresses associated with the drive piston tether and chamber compliances since these structural deflections are small in comparison to the respective structural thicknesses. However, modeling of the valve membrane requires more advanced non-linear deformation theory.

Non-linear Modeling of Valve Membrane

To achieve a high stroke actuation capability within the active valve device, the valve membrane/plate structure is designed to experience peak deflection magnitudes which exceed the plate structural thickness. This type of large-deflection deformation behavior is characterized by an elongation or stretching of the plate structure and a subsequent generation of a non-zero in-plane tensile stress along the neutral axis. As the plate is deformed significantly into the

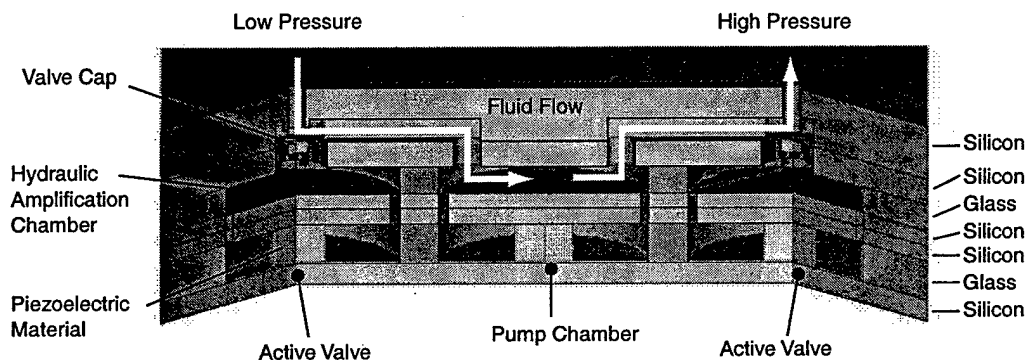


Figure 1.7: 3-D schematic of a Micro-Hydraulic Transducer multi-layer silicon and glass structure. Since a complete MHT system relies on identical fabrication and assembly procedures to those of the component valve, successful testing of the piezoelectrically driven active valve device validates the capability to realize the full MHT system.

large deflection regime, the in-plane tensile stress begins to exceed the bending stresses and the plate stiffness increases. Linear plate theory is inadequate to capture these stiffening effects, and as a result, tools have been developed to accurately model the non-linear large deflection behavior of the valve membrane/plate structure.

Development of Systematic Active Valve Design Procedure

The design and formulation of an active valve geometry which can satisfy performance requirements imposed by an external hydraulic system is an important step in the development of MHT systems. Accurate modeling of the fluid flow behavior through the hydraulic system and interaction of the valve structure with this external system must be developed. Additionally, design parameter variations, such as valve membrane thickness, valve cap stroke, and the number of valve membranes working together in parallel within the active valve device must be properly investigated so as to create an active valve whose membrane structures experience stresses below fracture limits and, as a whole, that consumes as little power as possible during operation.

1.4.2 Device Fabrication, Assembly, and Testing Challenges

Micromachining and Wafer-Bonding

Micromachining of the valve membrane and drive element tether structures within the active valve device is a critical step in the fabrication process. To achieve precise dimensional control of these thin-membrane structures, silicon-on-insulator (SOI) wafers containing a buried oxide

etch-stop layer are used. In performing deep etches in these wafers, the surface roughness of the etch and the tailoring of the fillet radius profiles at the base of the etch must be well-controlled so as to maintain the strength and robustness of the structures. Additionally, upon completing the etching of the various silicon layers, wafer-level silicon-silicon fusion bonding and wafer-level silicon-glass anodic bonding procedures must be carried out to form multi-layer wafer stack structures, in preparation for device assembly.

Piezoelectric Material Integration

Integration of bulk piezoelectric material within the thin-tethered drive element structures is the most critical step in the active valve assembly. Preparation of the material, including polishing, thin-film deposition, and core-drilling, is performed to provide an optimal surface finish of the material in preparation for eutectic bonding to the adjoining silicon layers within the device. Additionally, accurate measurement of the individual piezoelectric element dimensional thicknesses, prior to integration, is required to ensure optimal static and operational deflections of the piston structure which result in minimal stresses in the etched piston tethers. Incorporation of multiple smaller area piezoelectric materials spread out beneath the piston membrane is desired over placement of a single larger area piezoelectric material at the piston center, so as to reduce system compliances and increase actuation efficiency. However, tolerance issues become even more important when dealing with the requirements of multiple bonded elements.

Fluid Filling and Sealing

Encapsulation of a working fluid in the device is a significant challenge at the microscale because surface-to-volume ratios are typically quite large, with surface energies playing a dominant role. Any gas bubbles present in the sealed operational device can create enormous system compliances, potentially rendering the device useless. The elimination of trapped gases during filling of the device and during encapsulation of the fluid port used for filling is critical for high-level performance. The development of a systematic fluid degassing and filling procedure is required for successful realization of a working active valve device.

Device Testing

Experimental testing of a complex microfabricated device can be an extremely challenging activity, due primarily to the lack of physical access to the structures within the device. To thoroughly characterize the performance of the active valve device presented in this thesis, drive element piston and valve cap deflections in response to applied voltages must be measured real-time. Additionally, dynamic pressures (between 0 and 2 MPa) upstream and downstream of the valve orifice and real-time fluid flow rates (as low as $10 \frac{\mu\text{L}}{\text{min}}$ and as high as $1 \frac{\text{mL}}{\text{s}}$) must

be monitored. Development of a test-rig apparatus for carrying out these measurements is a critical task for proper evaluation of the device behavior.

1.5 Objectives

The primary objective of this thesis is to develop a piezoelectrically driven hydraulic amplification microactuator structure, which can be operate as a microvalve for high frequency control of high pressure fluid flows. This research is carried out through a series of modeling, design, fabrication, assembly, and experimental testing tasks. This work will demonstrate the microactuator and valve concepts and evaluate their experimental performance in comparison to behavior predicted by the models developed in the thesis.

A secondary goal of this thesis is to provide a framework of linear and non-linear structural modeling tools and design procedures that can be implemented in the development of high frequency piezoelectric micropumping and microvalving systems. Additionally, a further goal of this thesis is to present a method for small-scale bulk piezoelectric material integration within silicon micromachined thin-tethered structures, a procedure which can enable the realization of compact high-frequency high-stiffness hydraulic actuator structures.

1.6 Approach

The overall scope of this thesis includes each of the challenges presented in Section 1.4, and consequently the thesis is divided into two major parts. The first part (Chapters 2 through 5) focuses on active valve modeling and design. The second part (Chapters 6 through 9) concentrates on active valve fabrication, assembly, and testing. Use of the modeling tools developed in the first part of the thesis enables model-experiment correlation in the later sections.

Chapter 2 introduces the concept of the active valve device and details the procedures used to model the structural valve component compliances. Linear plate theory, with bending and shearing deformation effects included, is implemented. Additionally, the benefits of multiple piezoelectric elements spread out beneath the drive element piston rather than a single centrally-located element are presented through a series of finite-element studies.

Chapter 3 presents the development of a numerical code to model the large deflection behavior of a thin annular plate structure with rigid central cap under pressure loading. This theory has been specifically developed to capture the non-linear stiffening effects present in the valve membrane structure of the active valve, effects which are unaccounted for in the basic linear plate theory presented in Chapter 2. The finite-differencing scheme presented in this chapter is based upon the work of Su [1].

Chapter 4 combines the linear and non-linear modeling tools presented in Chapters 2 and 3 to create a quasi-static structural model of the active valve. In addition, the chapter introduces a dynamic simulation architecture for the valve, which includes inertia and damping associated with the drive element piston and valve cap structural elements. Calculation of the coupled fluid-structure resonant valve frequency, based on finite-element analyses, is also presented.

Chapter 5 uses the modeling tools and simulations developed in the first three chapters to formulate a systematic quasi-static design procedure that can be used to design an active valve geometry based on external hydraulic system performance requirements. This design procedure incorporates the governing fluid flow relations linking the valve cap motion to the external hydraulic system pressures and enables variation of key parameters within the active valve geometry to minimize power consumption. As a check, full system dynamic simulations are run to validate the quality of the valve geometry created using the quasi-static procedure.

Chapter 6 presents an overview of the fabrication challenges encountered and the solutions implemented in the development of the active valve device. A detailed sub-component testing plan for the active valve is presented as well. This systematic plan, as shown in Figure 1.8, breaks the complete active valve structure into manageable sub-component structures according to the primary challenges already detailed. The piezoelectric drive element sub-component study proves the ability to micromachine the tethered piston structure and integrate bulk piezoelectric material beneath the piston. The valve cap and membrane sub-component study validates the non-linear large deflection behavior of the valve membrane structure. Following successful completion of these sub-component studies, a complete active valve device can be fabricated and tested.

Chapter 7 details the piezoelectric drive element sub-component study. Devices are fabricated that incorporate both standard polycrystalline PZT-5H piezoelectric material elements as well as higher-strain single-crystal PZN-PT piezoelectric material. Additionally, devices with three piezoelectric elements spread out beneath the drive piston are compared to single element devices to demonstrate the stiffening benefit of incorporating multiple piezoelectric elements within the drive element structure. These devices are quasi-statically and dynamically characterized to frequencies in excess of 100 kHz.

Chapter 8 details the valve cap and membrane sub-component study. Valve membrane structures are fabricated and inspected to ensure adequate fillet radius control at the base of the etched features. Pressure-deflection experiments are carried out to characterize the degree of non-linearity present in these structures. Experimental results are compared to analytical and finite-element model results in which key parameters have been varied (membrane thickness and fillet radius size) in an effort to determine the sensitivity of the membrane behavior to these parameters.

Schematic Cross-Sections of Test Articles in the Test Plan

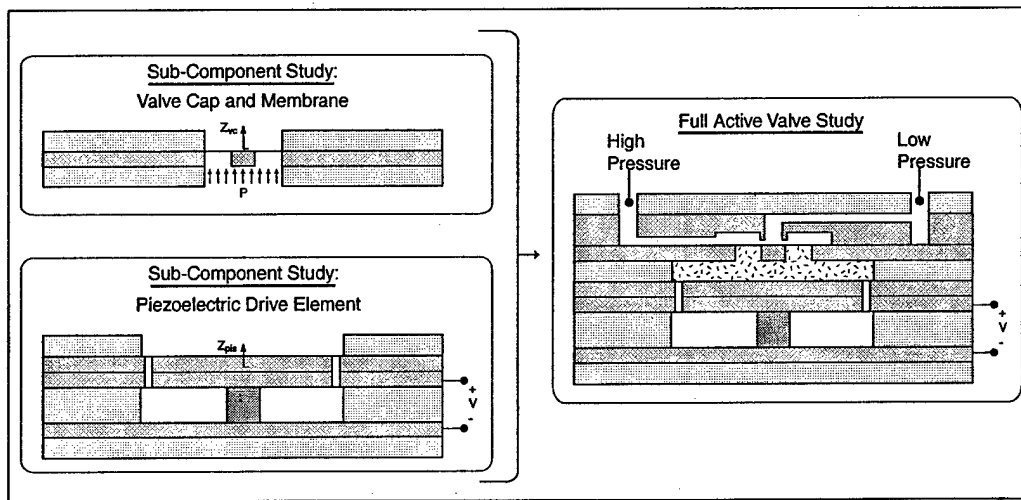


Figure 1.8: Active valve sub-component testing plan. Realization of the full active valve requires performance validation of piezoelectric drive element sub-component, valve cap and membrane sub-component, and hydraulic amplification chamber sub-component.

Chapter 9 presents the experimental testing of the full active valve device, with a focus on voltage-valve cap deformation frequency-dependent behavior, as well as differential pressure-flow characterization of the valve. Correlation to quasi-static and dynamic models is presented.

Lastly, **Chapter 10** concludes the thesis with a summary of accomplishments. Conclusions are drawn and recommendations are made for future work. Appendices are also included, which detail many of the structural models and dynamic simulations presented throughout the thesis.

1.7 Thesis Executive Summary

This thesis demonstrates, through a series of modeling, design, fabrication, assembly, and experimental testing tasks, successful operation of a piezoelectrically-driven hydraulic amplification microvalve for use in Micro-Hydraulic Transducer systems. Linear and non-linear modeling tools characterizing the structural deformations of the active valve sub-systems were developed. These tools enabled accurate prediction of real-time stresses along the micromachined valve membrane structure as it was deflected into its non-linear large-deflection regime. A systematic design procedure was developed to generate an active valve geometry to satisfy membrane stress limitations and valve power consumption requirements set forth by external hydraulic system performance goals. Fabrication challenges, such as deep-reactive ion etching (DRIE) of the drive element and valve membrane structures, wafer-level silicon-to-silicon

fusion bonding and silicon-to-glass anodic bonding operations, preparation and integration of piezoelectric material elements within the micromachined tethered piston structure, die-level assembly and bonding of silicon and glass dies, and filling of degassed fluid within the hydraulic amplification chamber were overcome. A photograph of the completed 9-layer microfabricated valve is shown in Figure 1.9.

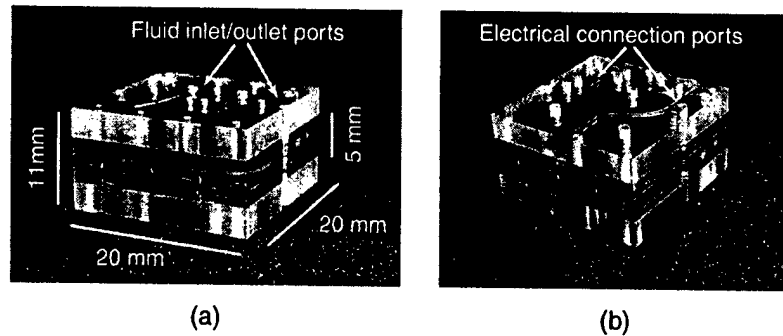


Figure 1.9: Photograph of a 9-layer silicon and glass piezoelectrically-driven hydraulic amplification microvalve, as part of a full MHT system. Dimensions of the valve structure within the full MHT chip are 8mm x 8mm x 5mm.

The active valve structural behavior and flow regulation capabilities were evaluated over a range of applied piezoelectric voltages, actuation frequencies, and differential pressures across the valve. For applied piezoelectric voltages up to 500Vpp at 1kHz, the valve devices demonstrated amplification ratios of drive element deflection to valve cap deflection of 40-50x. These amplification ratios correlate within 5 – 10% of the model expectations. Flow regulation experiments proved that a peak average flow rate through the device of 0.21mL/s under a sinusoidal drive voltage of 500Vpp, with valve opening of 17 μ m, against a differential pressure of 260kPa could be obtained. Tests revealed that fluid-structural interactions between the valve cap and membrane components and flow instabilities (due to transition between the laminar and turbulent flow regimes through the valve orifice) limited the valve performance capabilities.

Bibliography

- [1] H. Van Lintel, F. van de Pol, and A. Bouwstra, "Piezoelectric micropump based on micro-machining of silicon", *Sensors and Actuators*, 15, pp. 153-167, 1988.
- [2] M. Stehr, S. Messner, H. Sandmaier, and R. Zengerle, "The VAMP - a new device for handling liquids or gases," *Sensors and Actuators A*, 57, pp. 153-157, 1996.
- [3] V. Gass, B. van der Schoot, S. Jeanneret, and N. de Rooij, "Integrated flow-regulated silicon micropump," *Sensors and Actuators A*, 43, pp. 335-338, 1994.
- [4] S. Shoji and M. Esashi, "Microflow devices and systems," *Journal of Micromechanics and Microengineering*, 4, pp. 157-171, 1994.
- [5] K. Ikuta, T. Hasewaga, and T. Adachi, "The Optimized SMA Micro Pump Chip Applicable to Liquids and Gases," *Proceedings of the 2001 International Conference on Solid-State Sensors and Actuators (Transducers '01)*, 2001.
- [6] M. Koch, N. Harris, R. Maas, A. Evans, N. White, and A. Brunnschweiler, "Novel micropump design with thick-film piezoelectric actuation," *Measurement Science and Technology*, v.8 n.1, pp. 49-57, Jan 1997.
- [7] P. Watler and M. Sefton, "A Piezoelectric Driven Controlled Release Micropump for Insulin Delivery," *Trans Am Soc Artif Intern Organs*, Vol. XXXVI, pp. 70-77, 1990.
- [8] B. Wagner, H. Quenzer, S. Hoerschelmann, T. Lisec, and M. Jueress, "Micromachined bistable valves for implantable drug delivery systems," *Proceedings of the 18th Annual International Conference of the IEEE Engineering in Medicine and Biology Society*, pp. 254-255, 1997.
- [9] N.W. Hagood, D.C. Roberts, L. Saggere, K.S. Breuer, K.-S. Chen, J.A. Carretero, H.Q. Li, R. Mlcak, S. Pulitzer, M.A. Schmidt, S.M. Spearing, and Y.-H. Su, "Micro Hydraulic Transducer Technology for Actuation and Power Generation," *Proceedings of SPIE: SPIE's 7th Annual International Symposium on Smart Structures and Materials*, Vol. 3985, pp. 680-688, 2000.

- [10] H.Q. Li, D.C. Roberts, J.L. Steyn, K.T. Turner, J.A. Carretero, O. Yaglioglu, Y.-H. Su, L. Saggere, N.W. Hagood, S.M. Spearing, M.A. Schmidt, R. Mlcak, and K.S. Breuer, "A High Frequency High Flow Rate Piezoelectrically Driven MEMS Micropump," Proceedings of the IEEE Solid-State Sensor and Actuator Workshop, Hilton Head, SC. pp. 69-72, 2000.
- [11] D.C. Roberts, J.L. Steyn, H.Q. Li, K.T. Turner, R. Mlcak, L. Saggere, S.M. Spearing, M.A. Schmidt, and N.W. Hagood, "A High-Frequency, High-Stiffness Piezoelectric Micro-Actuator For Hydraulic Applications," Proceedings of the 2001 International Conference on Solid-State Sensors and Actuators (Transducers '01), 2001.
- [12] D.C. Roberts, N.W. Hagood, Y.-H. Su, H.Q. Li, and J.A. Carretero, "Design of a Piezoelectrically-Driven Hydraulic Amplification Microvalve for High Pressure, High Frequency Applications," Proceedings of SPIE's 7th International Symposium on Smart Structures and Materials, Vol. 3985, pp. 616-628, 2000.
- [13] D.C. Roberts, O. Yaglioglu, J. Carretero, Y.-H. Su, L. Saggere, and N.W. Hagood, "Modeling, Design, and Simulation of a Piezoelectric Microvalve for High Pressure, High Frequency Applications," Proceedings of SPIE's 8th International Symposium on Smart Structures and Materials, Vol. 4327, 2001.
- [14] J.M. Hollerbach, I.W. Hunter, J. Ballantyne, "A comparative analysis of actuator technologies for robotics," *Robotics Review* 2, Eds. Khatib and Oussama, MIT Press, pp. 299-342.
- [15] J.E. Huber, N.A. Fleck, and M.F. Ashby, "The selection of mechanical actuators based on performance indices," Proceedings of the Royal Society of London, Series A, Vol. 453, No. 1965, p. 2185.
- [16] S.W. Pulitzer III, "Feasability Assessment and Design of Micro Hydraulic Solid-State Transducers," MIT Master's Thesis. June 1998.
- [17] S. Park and T. Shrout, "Characteristics of Relaxor-Based Piezoelectric Single Crystals for Ultrasonic Transducers," *IEEE Transactions on Ultrasonics, Ferroelectrics, and Frequency Control*, Vol. 44, No. 5, pp. 1140-1147, 1997.
- [18] M. Esashi, S. Shoji, and A. Nakano, "Normally Closed Microvalve and Micropump Fabricated on a Silicon Wafer," *Sensors and Actuators* 20, pp. 163-169, 1989.
- [19] M. Esashi, "Integrated Micro Flow Control Systems," *Sensors and Actuators*, A21-A23, pp. 161-167, 1990.
- [20] S. Shoji, B. Van der Schoot, N. de Rooij, and M. Esashi, "Smallest Dead Volume Microvalves for Integrated Chemical Analyzing Systems," Proceedings of the 1991 Interna-

- tional Conference on Solid-State Sensors and Actuators (Transducers '91), pp. 1052-1055, 1991.
- [21] K. Henning, "Liquid and gas-liquid phase behavior in thermopneumatically actuated microvalves," *Proceedings of SPIE- The International Society for Optical Engineering* v3515, pp. 53-63, 1998.
 - [22] C. Rich and K. Wise, "A Thermopneumatically-Actuated Microvalve With Improved Thermal Efficiency and Integrated State Sensing," *Proceedings of the IEEE Solid-State Sensor and Actuator Workshop*, Hilton Head, SC, pp. 234-237, 2000.
 - [23] M.A. Huff and W.L. Benard, "Thin film titanium-nickel shape memory alloy microfluidic devices," *Proceedings of the Third International Symposium on Microstructures and Microfabricated Systems*, pp. 26-38, 1997.
 - [24] H. Jerman, "Electrically-Activated, Micromachined Diaphragm Valves," *Proceedings of the 1991 International Conference on Solid-State Sensors and Actuators (Transducers '91)*, pp. 1045-1048, 1991.
 - [25] M.A. Huff, "Silicon Micromachined Wafer-Bonded Valves," Ph.D. Thesis, Massachusetts Institute of Technology, 1993.
 - [26] M. Shikida, K. Sato, S. Tanaka, Y. Kawamura, and Y. Fujisaki, "Electrostatically driven gas valve with high conductance," *Journal of Microelectromechanical Systems*, 3(2), pp.76-80, June 1994.
 - [27] F. Pourahmadi, L. Christel, K. Petersen, J. Mallon, and J. Bryzek, "Variable-Flow Micro-Valve Structure Fabricated with Silicon Fusion Bonding," *Proceedings of the IEEE Solid-State Sensor and Actuator Workshop*, Hilton Head, SC, pp. 78-81, 1990.
 - [28] A. Meckes, J. Behrens, and W. Benecke, "Electromagnetically Driven Microvalve Fabricated in Silicon," *Proceedings of the 1997 International Conference on Solid-State Sensors and Actuators (Transducers '97)*, pp. 821-824, 1997.
 - [29] J.G. Smits, "Piezoelectric Micropump with Microvalves", *Proc Eighth Bienn Univ Gov Ind Microelectron Symp. (IEEE n 89CH2769-8)*, Piscataway, NJ, USA. p 92-94
 - [30] T. Watanabe and H. Kuwano, "A microvalve matrix using piezoelectric actuators," *Microsystem Technologies*, pp. 107-111, 1997.
 - [31] S. Kluge, G. Neumayer, U. Schaber, and M. Wackerle, "Pneumatic Silicon Microvalves with Piezoelectric Actuation," *Proceedings of the 2001 International Conference on Solid-State Sensors and Actuators (Transducers '01)*, 2001.

- [32] J. Garcia-Bonito, M.J. Brennan, S.J. Elliot, A. David, and R.J. Pinnington, "A novel high-displacement piezoelectric actuator for active vibration control," *Smart Mater. Struct.* 7, pp. 31-42, 1998.
- [33] P. Tang, A. Palazzolo, A. Kascak, G. Montague, and W. Li, "Combined Piezoelectric-Hydraulic Actuator Based Active Vibration Control for Rotordynamic System," *Journal of Vibration and Acoustics* 117, pp. 285-293, 1995.
- [34] Tsukamoto, "Piezo-Actuator's Displacement Magnifying Mechanism," US Patent 5,233,834. 1993.
- [35] Y.H. Su, K.S. Chen, D.C. Roberts, and S.M. Spearing, "Large Deflection Analysis of a Pre-Stressed Annular Plate With a Rigid Boss Under Axisymmetric Loading", *Journal of Micromech. Microeng.* 11 (2001) pp. 645-653.

Chapter 2

Active Valve Linear Model

This chapter presents the analytical modeling structure of the active valve, focusing on the linear deformation behavior of the various structural components. This chapter begins with an overview of each of the components of the active valve, detailing the corresponding structural geometries and associated assumptions used to model them. This first-level active valve model assumes a single cylindrical piezo material under the drive element piston for ease of modeling. Toward the conclusion of the chapter, the effects of incorporating multiple piezoelectric cylinders are discussed and the corresponding benefits to structural stiffnesses of the piston and the bottom structural plate are presented. The chapter concludes with an identification of the valve components that require further development of non-linear theory.

2.1 Valve Geometry and Modeling Procedure

The proposed piezoelectrically driven hydraulic amplification microvalve is schematically shown in Figure 2.1. The axisymmetric valve is comprised of three primary sub-structures: a piezoelectric drive element, a closed hydraulic amplification chamber, and a membrane with attached valve cap. The drive element sub-structure consists of one or more bulk piezoelectric material cylinders located at the center of the device, each bonded on its top surface to a silicon micromachined piston and on its bottom surface to a silicon support structure. The drive element piston is attached along its outer circumference to a silicon support structure with two thin silicon tethers. The fluid chamber resides between the top surface of the drive element piston and the bottom surface of a smaller diameter silicon micromachined valve cap membrane. In response to an applied piezoelectric voltage, a small deflection of the drive element piston translates into a much larger deflection of the valve cap membrane. The ratio of the piston diameter to the valve membrane diameter, the compliances of the fluid and structural chamber, the severity to which the valve cap membrane experiences nonlinear behavior, and the piezoelectric material performance determine the potential valve stroke for a given applied piezoelectric voltage.

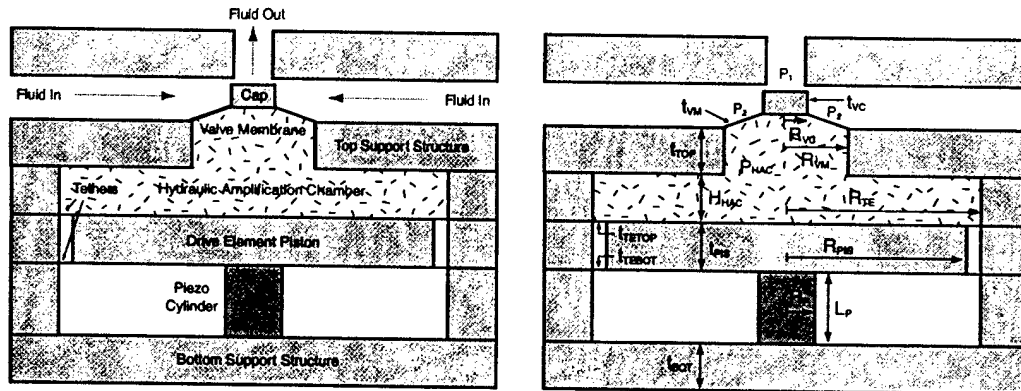


Figure 2.1: 2-D schematic of the piezoelectrically-driven hydraulic amplification microvalve. The nomenclature and key dimensions are detailed.

In developing a comprehensive analytical model for the active valve, the following aspects need to be accurately represented: (1) piezoelectric material behavior, (2) drive element piston and tether deflection behavior, (3) fluid compressibility, (4) hydraulic amplification chamber structural compliance, (5) valve cap and membrane deflection behavior, and (6) bottom structural plate behavior beneath piezoelectric material. The efficiency of the valve drive is a function of how much volume is created due to the various system compliances. The ideal design would call for a very stiff hydraulic fluid and a completely rigid drive element piston and chamber structure. In this case, all of the volume change created by the drive element deflection would exhibit itself in the volume change associated with the valve membrane deflection. Modeling of aspects (2), (4), (5), and (6) require a detailed understanding of linear plate theory. Each of these aspects will be modeled as a plate with applied loading and boundary conditions to determine the deflections and swept volumes due to bending and shearing effects. Non-linear issues such as in-plane stretching will be discussed at the close of the chapter.

2.2 Overview of Linear Plate Theory

In general, a symmetrically loaded circular plate will experience deflections due to bending and shearing. If the plate thickness is small compared to the plate outer radius, the deflection due to bending will be significantly larger than that due to shearing. If the plate thickness is of the same order of magnitude as the plate outer radius, however, the deflection contribution due to shearing effects will no longer be negligible. In these cases, it is advisable to obtain the total deflection as a sum of these two contributing effects. As detailed above, the top chamber structure, the drive element piston, the drive element tethers, the bottom chamber structure, and the valve cap/membrane can be modeled using linear plate theory. The degree to which

each of these structural components may experience non-linear deflection behavior is discussed at the conclusion of this chapter. This section presents the methodology used to model these plate behaviors (in a linear fashion) by way of a simple example. The following sections then detail each of the modeled valve compliances.

An example of a symmetrically loaded circular plate is shown in Figure 2.2. This plate is clamped at its outer radius ($r=a$), guided at its inner radius ($r=b$), and subjected to a pressure loading P over its bottom surface. The plate will experience deflections due to bending and shearing effects.

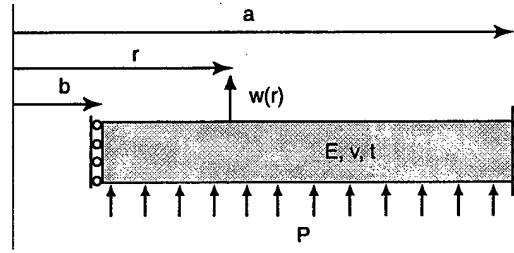


Figure 2.2: Circular plate under axisymmetric pressure loading, with a guided boundary condition at inner radius b and a clamped boundary condition at outer radius a .

2.2.1 Deflections Due to Bending

The governing differential equation for the symmetrical bending of a circular plate can be written as:

$$\frac{d}{dr} \left(\frac{d}{dr} r \left(\frac{d}{dr} w(r) \right) \right) = \frac{Q(r)}{D} \quad (2.1)$$

where $D = \frac{Et^3}{12(1-\nu^2)}$ is the flexural rigidity of the plate and $Q(r)$ is the shear force per unit length as a function of r . $Q(r)$ depends on the nature of the plate loading. In this example case, the shear force is:

$$Q(r) = \frac{P(r^2 - b^2)}{2r} \quad (2.2)$$

The boundary conditions in this example case are:

$$BC1 : w(r = a) = 0 \quad (2.3)$$

$$BC2 : \frac{dw}{dr}(r = a) = 0 \quad (2.4)$$

$$BC3: \frac{dw}{dr}(r=b) = 0 \quad (2.5)$$

By integrating the governing differential equation and applying the imposed boundary conditions, the deflection of the plate $w(r)$ can be determined. In addition, the swept volume associated with the deflection can then be calculated as follows:

$$dV = \int 2\pi r w(r) \partial r. \quad (2.6)$$

For this example plate bending case, the plate deflection at the inner radius ($r=b$) and the swept volume are found to be:

$$w_{bending}(b) = [\Xi_{w_{bending}(b)}^P] P \quad (2.7)$$

$$dV_{bending} = [\Xi_{dV_{bending}}^P] P \quad (2.8)$$

where $\Xi_{w_{bending}(b)}^P$ and $\Xi_{dV_{bending}}^P$ are the plate bending compliances,

$$\Xi_{w_{bending}(b)}^P = \left(\frac{1}{64D(b^2 - a^2)} \right) \left(3b^6 + a^2b^4 \left(-7 + 4 \ln \left[\frac{b}{a} \right] - 16 \ln \left[\frac{b}{a} \right]^2 \right) + a^4b^2 \left(5 - 4 \ln \left[\frac{b}{a} \right] \right) - a^6 \right) \quad (2.9)$$

$$\Xi_{dV_{bending}}^P = \left(\frac{-\pi}{192D(b^2 - a^2)} \right) \left(a^8 - 10a^6b^2 + 24a^4b^4 \left(1 - \ln \left[\frac{b}{a} \right] \right) + a^2b^6 \left(-22 + 24 \ln \left[\frac{b}{a} \right] \right) + 7b^8 \right) \quad (2.10)$$

These compliance coefficients are derived in detail in Appendix A.1.

2.2.2 Deflections Due to Shearing

In cases where the plate thickness is not small compared to the plate outer radius, shearing effects may contribute significantly to the overall deflection. The following analysis structure will allow for estimations of this deflection due to shear.

In general, shearing stresses vary across the thickness of a plate according to the same principle as for beams of narrow rectangular cross-sectional area [3]. The corresponding shearing strain can be written as:

$$\frac{dw}{dr} = \frac{-\alpha Q(r)}{Gt} \quad (2.11)$$

where $G = \frac{E}{2(1-\nu)}$ is the modulus of elasticity in shear of a plate, t is the plate thickness, and $Q(r)$ is, again, the shear force per unit length as a function of r . The coefficient α is the shear correction factor. The boundary condition in this example case is:

$$BC4: w(r = a) = 0 \quad (2.12)$$

By integrating the differential equation and applying the imposed boundary condition, the deflection of the plate $w(r)$ can be determined. The swept volume associated with this deflection can be calculated according to Equation (2.6). For this example plate shearing case, the plate deflection at the inner radius ($r=b$) and the swept volume under the plate are found to be:

$$w_{shear}(b) = \left[\Xi_{w_{shear}(b)}^P \right] P \quad (2.13)$$

$$dV_{shear} = \left[\Xi_{dV_{shear}}^P \right] P \quad (2.14)$$

where $\Xi_{w_{shear}(b)}^P$ and $\Xi_{dV_{shear}}^P$ are the plate shear compliances,

$$\Xi_{w_{shear}(b)}^P = \left(\frac{\alpha}{4Gh} \right) \left(a^2 + b^2 \left(-1 + 2 \ln \left[\frac{b}{a} \right] \right) \right) \quad (2.15)$$

$$\Xi_{dV_{shear}}^P = \left(\frac{\pi\alpha}{8Gh} \right) \left(a^4 - 4a^2b^2 + b^4 \left(3 - 4 \ln \left[\frac{b}{a} \right] \right) \right) \quad (2.16)$$

These compliance coefficients are derived in detail in Appendix A.1.

2.2.3 Combined Deflection Due to Bending and Shearing

The total deflection at ($r=b$) and swept volume of the plate are sums of those contributions due to pure bending effects and shearing effects. In this example case, the plate deflection and swept volume can therefore be written, respectively, as:

$$w(b) = \left[\Xi_{w_{bending}(b)}^P + \Xi_{w_{shear}(b)}^P \right] P = \left[\Xi_{w(b)}^P \right] P \quad (2.17)$$

$$dV = \left[\Xi_{dV_{bending}}^P + \Xi_{dV_{shear}}^P \right] P = \left[\Xi_{dV}^P \right] P \quad (2.18)$$

It is clear from this example that the plate deflection at a desired location and the swept volume can be expressed as linear functions of the loading parameters.

2.2.4 Comparison of Bending/Shearing Deflections

To illustrate the importance of the bending and shearing contributions to the example symmetric annular plate discussed thus far, the overall radial dimensions of the plate and the applied pressure loading are held constant and the plate thickness is varied from a value that is small compared to the plate radial dimensions to a value that is of the same order of magnitude as the radial dimensions. In doing this, one would expect to observe an increasing importance of

the shearing contribution as the plate thickness increases. The following dimensions, material constants, and loading parameters are assigned to the example case, and are typical of those found in the proposed active valve:

$$a = 3\text{mm}, b = 0.5\text{mm}, E = 165\text{GPa}, \nu = 0.22, \alpha = 1.5, P = 1\text{MPa}. \quad (2.19)$$

Deflections (at $r=b$) due to bending and shearing are calculated as the plate thickness is varied from $t = 20\mu\text{m}$ to $t = 2\text{mm}$. The results are shown in Figure 2.3.

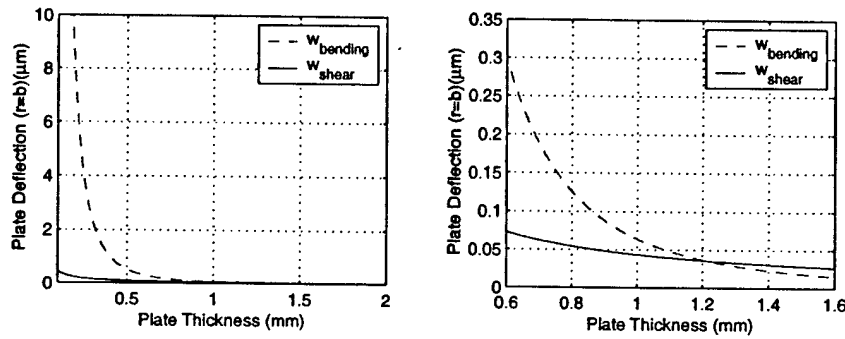


Figure 2.3: Bending and shearing contributions to plate deflection at inner radius ($r=b$). The plot on the right is a close-up view. As the ratio of plate thickness to plate outer radius approaches 1, the deflection due to shearing becomes important. For ratios $\ll 1$, shearing effects are inconsequential compared to bending effects.

These results illustrate the importance of shearing effects as the ratio of plate thickness to plate outer radius approaches 1. For ratios significantly less than 1, deflections due to bending far exceed those due to shearing. In this case, neglecting the shear contributions would have little effect on the calculated deformation. On the other hand, for ratios near and greater than 1, shear contributions are important and therefore, neglecting them would result in overall deformations smaller than those expected in reality. For each of the compliant plate structures within the active valve, except for the valve membrane (where its thickness \ll radial dimensions), both bending and shear effects are included in the deformation analyses.

2.3 Detailed Structural Modeling

2.3.1 Piezoelectric Material Behavior

The piezoelectric material cylinder within the valve drive element strains when a voltage is applied to it. Often, the loading on the material may increase during this actuation step. In the drive element structure, this actuation compressive loading is a combination of the hydraulic

amplification chamber pressure acting over the piston top surface and the tensile drive element tether force acting along the piston outer circumference. In general, for a bulk cylindrical piezoelectric element, as shown in Figure 2.4, subject to an applied voltage V_p and an actuation compressive axial stress ΔT_p , the material axial strain is:

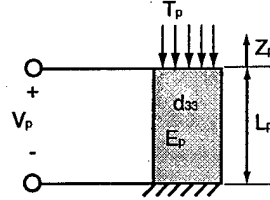


Figure 2.4: Cylindrical piezoelectric element with applied voltage and stress loading.

$$\epsilon_p = \frac{\Delta Z_p}{L_p} = \frac{d_{33} V_p}{L_p} - \frac{\Delta T_p}{E_p} \quad (2.20)$$

The parameter d_{33} is the piezoelectric material coefficient and E_p is the modulus of elasticity. Under the case of zero actuation loading, $\Delta T_p = 0$, the material experiences a maximum strain in response to a voltage V_p . This is termed the free strain condition, $\epsilon_{p,free} = \frac{d_{33} V_p}{L_p}$. At a sufficiently large external load, the material experiences no net strain in response to a voltage. This is termed the blocked force condition, $\Delta T_{p,blocked} = \frac{d_{33} V_p E_p}{L_p}$.

Equation 2.20 assumes perfect 33-direction actuation. In reality, this is not achieved due to transverse clamping of the piezoelectric element at its top and bottom. However, the incorporation of multiple, smaller diameter piezoelectric elements rather than a single large diameter element helps to reduce this clamping effect and supports the assumption. The implementation of multiple, smaller diameter piezoelectric elements is discussed in Section 2.5. For the purposes of the active valve model development in this section, however, a single piezoelectric material cylinder placed at the center of the drive element chamber is assumed.

2.3.2 Drive Element Piston and Tether Behavior

The drive element substructure provides a volume change, which is transferred to the valve cap/membrane through the use of hydraulic fluid. In an ideal case, the drive piston would be a rigid structure and the drive element tethers would be stiff enough to resist significant volume deformation due to the hydraulic amplification chamber pressure, yet compliant enough to allow for adequate piston deflection and to ensure tether stresses below critical levels. The drive element piston and tether structure can be broken into two linked sub-models, as shown in Figure 2.5. The first sub-model captures the behavior of the drive piston and the second sub-model captures the behavior of the drive element tethers.

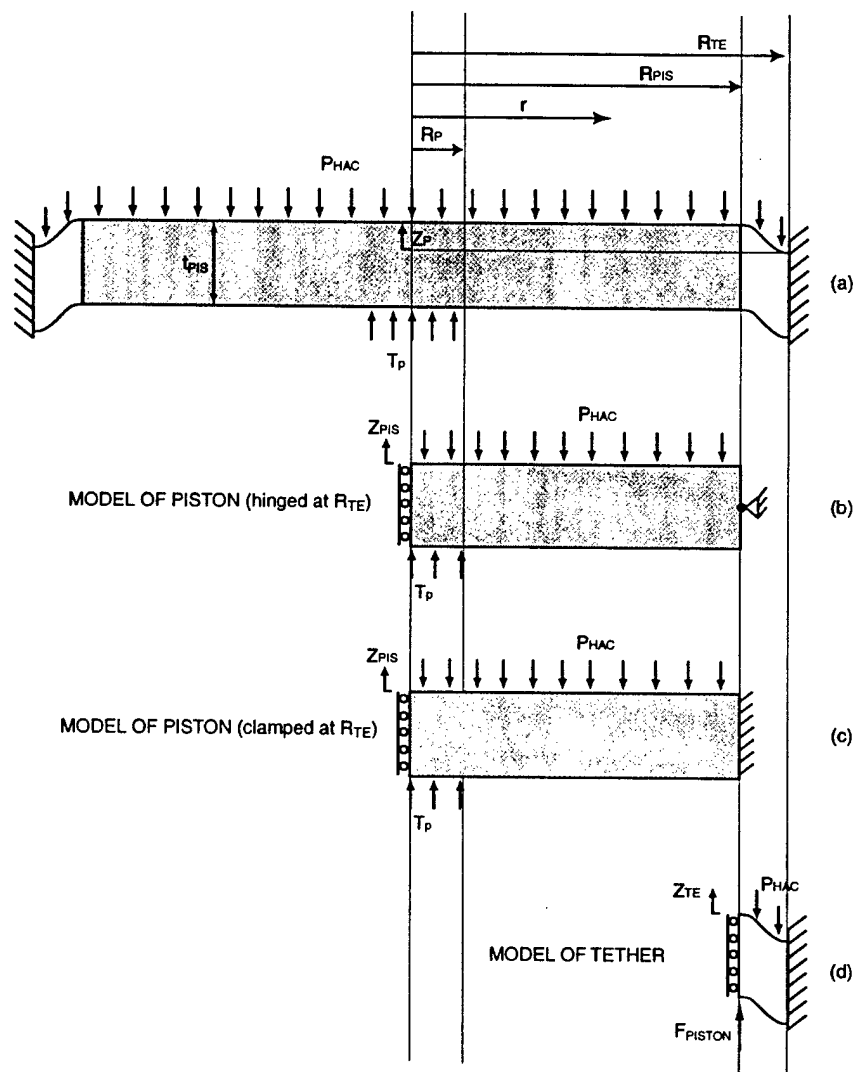


Figure 2.5: Simplification of pressure and stress loading on the drive element piston for use in the linear deflection analysis of the drive element tethers.

Drive Element Piston

Figures 2.5(b) and 2.5(c) present two potential ways to model the deformation of the drive element piston. Both scenarios model the piston as a circular plate with outer radius R_{pis} and thickness t_{pis} and assume the plate to experience a guided boundary condition at its center. Finite-element models have shown this to be a more appropriate (and conservative) boundary condition than enforcing a guided boundary condition at the edge of piezo material, R_p . The piezoelectric material is not infinitely rigid, and therefore does allow for plate bending over the region where the material contacts the piston. The primary difference in the two scenarios is the boundary condition assumptions at the outer piston radius R_{pis} . If the drive element tethers possessed negligible stiffness, one could assume that they exert an insignificant bending moment on the drive piston, resulting in an appropriate hinged boundary condition at R_{pis} , as shown in Figure 2.5(b). On the other hand, if the tethers possessed an infinite stiffness, one could assume them to create a rigid boundary on the piston at this location, as shown in Figure 2.5(c). Finite-element studies have shown that for the typical range of design space for the tethers and piston in this active valve device, the actual structural behavior is approximately halfway between these two limiting scenarios. Therefore, the drive element piston compliances are taken as the average of these limiting scenarios. The hydraulic amplification chamber pressure P_{HAC} acts over the entire top surface of the plate from $r = 0$ to $r = R_{pis}$ and the piezoelectric material stress T_p acts over the bottom surface of the plate from $r = 0$ to $r = R_p$. The piston center deflection Z_{pis} and piston swept volume dV_{pis} (referenced to the hinged outer radius) can therefore be represented by the following relations,

$$Z_{pis} = \left[\Xi_{Z_{pis}}^T \right] T_P - \left[\Xi_{Z_{pis}}^P \right] P_{HAC} \quad (2.21)$$

$$dV_{pis} = \left[\Xi_{dV_{pis}}^T \right] T_P - \left[\Xi_{dV_{pis}}^P \right] P_{HAC} \quad (2.22)$$

where $\Xi_{Z_{pis}}^T$, $\Xi_{Z_{pis}}^P$, $\Xi_{dV_{pis}}^T$, and $\Xi_{dV_{pis}}^P$ are the compliance coefficients defined explicitly in Appendix A.2.

Drive Element Tethers

In Figure 2.5(c), each drive element tether is modeled as a circular plate with inner radius R_{pis} and outer radius R_{ch} . In order to allow for flexibility in design, the top and bottom tethers are defined to have different thicknesses (t_{tetop} or t_{tebot}). Again, assuming that the piston slope at R_{pis} is zero, the boundary condition on each tether at this location is that of a guided interface. At R_{ch} , each plate is rigidly clamped to the valve support structure. The top tether experiences a concentrated force F_{tetop} at $r = R_{pis}$ and a pressure loading P_{HAC} from $r = R_{pis}$ to $r = R_{ch}$.

while the bottom tether experiences only a concentrated force F_{tebot} at $r = R_{pis}$. The deflection (at $r = R_{pis}$) and swept volume of the top tether alone can be written as,

$$Z_{tetop} = [\Xi_{Z_{tetop}}^F] F_{tetop} - [\Xi_{Z_{tetop}}^P] P_{HAC} \quad (2.23)$$

$$dV_{tetop} = [\Xi_{dV_{tetop}}^F] F_{tetop} - [\Xi_{dV_{tetop}}^P] P_{HAC} + A_{pis} Z_{tetop} \quad (2.24)$$

where $\Xi_{Z_{tetop}}^F$, $\Xi_{Z_{tetop}}^P$, $\Xi_{dV_{tetop}}^F$, and $\Xi_{dV_{tetop}}^P$ are coefficients defined explicitly in Appendix A.2.

The deflection (at $r = R_{pis}$) and swept volume of the bottom tether alone can be written as,

$$Z_{tebot} = [\Xi_{Z_{tebot}}^F] F_{tebot} \quad (2.25)$$

$$dV_{tebot} = [\Xi_{dV_{tebot}}^F] F_{tebot} + A_{pis} Z_{tebot} \quad (2.26)$$

where $\Xi_{Z_{tebot}}^F$ and $\Xi_{dV_{tebot}}^F$ are coefficients defined explicitly in Appendix A.2.

Although the equations for the behavior of each tether alone are straightforward, the behavior resulting from both tethers together is more complex. In a two-tether system, both tethers share the same deflection at $r = R_{pis}$; that is, $Z_{te} = Z_{tetop} = Z_{tebot}$. Additionally, the sum of the piston forces on the tethers must be equal to the total force on the piston itself,

$$F_{tetop} + F_{tebot} = F_{piston} = A_p T_p - A_{pis} P_{HAC}. \quad (2.27)$$

The distribution of this force on the tethers is determined by the relative stiffnesses of the tethers, and therefore, the force taken by the top tether can be written as,

$$F_{tetop} = \left[\frac{\Xi_{Z_{tebot}}^F}{\Xi_{Z_{tebot}}^F + \Xi_{Z_{tetop}}^F} \right] F_{piston} \quad (2.28)$$

One can observe from this relation that if the bottom tether has a thickness much less than that of the top tether (ie: $\Xi_{Z_{tebot}}^F \gg \Xi_{Z_{tetop}}^F$), then all of the piston load is taken by the top tether, $F_{tetop} \approx F_{piston}$. Likewise, if the tethers have the same thickness, then each tether carries half of the piston force. Following these arguments, the tether deflection (at $r = R_{pis}$) and the tether swept volume can be expressed as,

$$Z_{te} = Z_{tetop} = \left[\frac{\Xi_{Z_{tetop}}^F \Xi_{Z_{tebot}}^F}{\Xi_{Z_{tebot}}^F + \Xi_{Z_{tetop}}^F} \right] (A_p T_p - A_{pis} P_{HAC}) - \left[\frac{\Xi_{Z_{tetop}}^P \Xi_{Z_{tebot}}^P}{\Xi_{Z_{tebot}}^P + \Xi_{Z_{tetop}}^P} \right] P_{HAC} \quad (2.29)$$

$$dV_{te} = dV_{tetop} = \left[\frac{\Xi_{dV_{tetop}}^F \Xi_{Z_{tebot}}^F}{\Xi_{Z_{tebot}}^F + \Xi_{Z_{tetop}}^F} \right] (A_p T_p - A_{pis} P_{HAC}) - \left[\frac{\Xi_{dV_{tetop}}^P \Xi_{Z_{tebot}}^P}{\Xi_{Z_{tebot}}^P + \Xi_{Z_{tetop}}^P} \right] P_{HAC} + A_{pis} Z_{te} \quad (2.30)$$

In this manner, the deflection of the drive element piston outer radius and the swept volume of the piston and top tether is determined.

Combined Piston and Tether Behavior

Having modeled the piston and tethers individually, it is now possible to express the complete piston/tether deflection and swept volume. The drive element piston center deflection with respect to the active valve structural support is the sum of the piston deflection in the first sub-model and the tether deflection in the second sub-model,

$$Z_{de} = Z_{pis} + Z_{te}. \quad (2.31)$$

Likewise, the total drive element volume change is the sum of the piston swept volume in the first sub-model and the top tether swept volume in the second sub-model,

$$dV_{de} = dV_{pis} + dV_{te}. \quad (2.32)$$

These relations, therefore, fully describe the drive element center deflection and swept volume as a function of the piston and tether stiffness coefficients and the loading, T_p and P_{HAC} .

2.3.3 Bottom Structural Compliance

A rigid valve structure beneath the piezoelectric material cylinder would ensure that all of the piezoelectric strain during actuation goes into the drive element volume change needed for valve cap motion. In reality, this structure is not rigid and as a result this bottom structure deformation serves only to reduce the effective volume change that can be produced by the drive element.

As shown in Figure 2.6, this structure can be modeled as a circular plate with thickness t_{bot} , guided at its center, and clamped at outer radius R_{ch} . Again, as for the drive element piston, the assumption that the piezo in no way helps to stiffen the plate is taken as a conservative estimate. The only loading applied to the plate is the piezoelectric material stress T_p from $r = 0$ to $r = R_p$. The bottom plate center deflection Z_{bot} can therefore be represented by the following relation,

$$Z_{bot} = - \left[\Xi_{Z_{bot}}^T \right] T_p \quad (2.33)$$

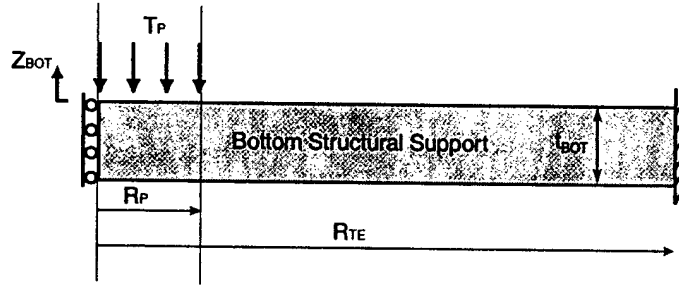


Figure 2.6: Compliance of bottom structure beneath piezoelectric material.

where $\Xi_{Z_{bot}}^T$ is defined explicitly in Appendix A.2.

2.3.4 Fluid Compressibility

During valve actuation, increased pressure within the hydraulic amplification chamber results in compression of the contained fluid. A portion of the drive element volume change will be lost in this undesired volume change of the fluid. The relationship between the fluid volume change dV_{HAC} and the fluid pressure change dP_{HAC} is:

$$dV_{HAC} = - \left(\frac{V_{HAC}}{K_f} \right) dP_{HAC} \quad (2.34)$$

where K_f is the fluid bulk modulus and V_{HAC} is the total fluid volume of the hydraulic amplification chamber.

2.3.5 Top Structural Compliance

For efficient hydraulic amplification within the active valve, the top structural compliance should be small so that minimal drive element actuation volume is lost in this chamber deformation. As shown in Figure 2.7, the top chamber structure can be modeled as an annular plate with inner radius R_{vm} , outer radius R_{ch} , and thickness t_{top} . At R_{vm} , the plate is free and experiences a concentrated force F_{vm} , corresponding to the sum of all the forces acting on the valve cap and membrane,

$$F_{vm} = P_{HAC}A_{vm} - P_1A_{vc} - P_2(A_{vm} - A_{vc}). \quad (2.35)$$

The plate is rigidly clamped at R_{te} . The plate experiences a pressure loading P_{HAC} on its underside.

The top plate inner radius deflection Z_{top} and swept volume dV_{top} can therefore be represented by the following relation,

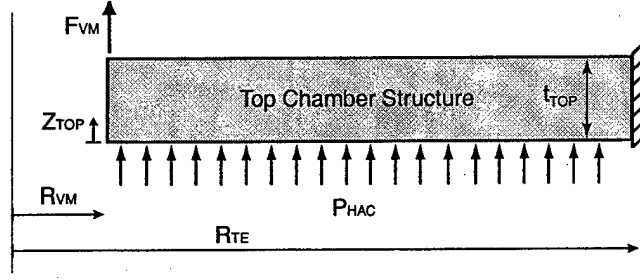


Figure 2.7: Hydraulic amplification chamber structural deformation under P_{HAC} and F_{vm} loading.

$$Z_{top} = [\Xi_{Z_{top}}^P] P_{HAC} + [\Xi_{Z_{top}}^F] F_{vm} \quad (2.36)$$

$$dV_{top} = [\Xi_{dV_{top}}^P] P_{HAC} + [\Xi_{dV_{top}}^F] F_{vm} + A_{vm} Z_{top} \quad (2.37)$$

where $\Xi_{Z_{top}}^P$, $\Xi_{Z_{top}}^F$, $\Xi_{dV_{top}}^P$, and $\Xi_{dV_{top}}^F$ are defined explicitly in Appendix A.2. In reality, the region above the annular chamber structure will not be completely unsupported. As a result, this model provides a worst-case value for the structural chamber volume change.

2.3.6 Valve Cap and Membrane Behavior

For the fluid flow directionality shown in Figure 2.1, a pressure drop occurs as the fluid flows radially inward over the valve membrane, through the contraction over the valve cap, and finally through the expansion into the exit channel. In the structural modeling of the valve cap and membrane, the pressure P_2 is assumed constant over the valve membrane area and the pressure P_1 is assumed constant over the valve cap area (see Chapter 5 for further discussion of these fluid modeling assumptions).

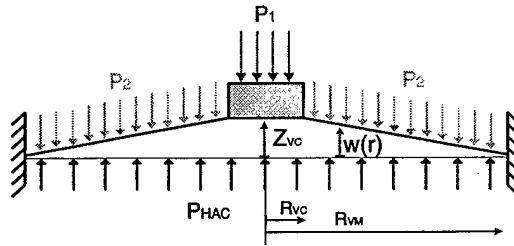


Figure 2.8: Valve membrane and cap, deflected upward from their equilibrium position, under pressure loadings P_{HAC} , P_1 , and P_2 .

As shown in Figure 2.8, the valve membrane experiences a pressure loading P_{HAC} over its entire bottom surface, a pressure loading P_1 over the valve cap top surface, and a pressure loading P_2 over the top surface of the valve membrane. The valve membrane can be modeled as a circular plate with thickness t_{vm} , a guided boundary condition at $r = R_{vc}$, and a clamped boundary condition at $r = R_{vm}$, with a pressure loading $P_{vm} = (P_{HAC} - P_2)$ on the underside of the membrane and a concentrated force $F_{vc} = A_{vc}(P_{HAC} - P_1)$ acting in the upward direction at $r = R_{vc}$ (see Figure 2.9). Bending of the valve cap is neglected in this model. For typical valve cap and membrane dimensions within the active valve structure, finite-element studies have shown that this rigid cap assumption is valid.

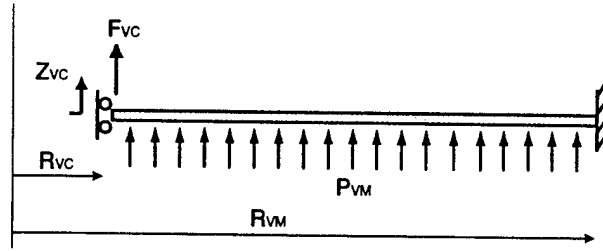


Figure 2.9: Simplified model of the valve cap and membrane with imposed boundary conditions and applied loading.

For linear theory, the inner radius deflection Z_{vc} and the swept volume dV_{vm} can be represented by the following relations,

$$Z_{vc} = \left[\Xi_{Z_{vc}}^P \right] P_{vm} + \left[\Xi_{Z_{vc}}^F \right] F_{vc} \quad (2.38)$$

$$dV_{VM} = \left[\Xi_{dV_{vm}}^P \right] P_{vm} + \left[\Xi_{dV_{vm}}^F \right] F_{vc} + A_{vc} Z_{vc} \quad (2.39)$$

where $\Xi_{Z_{vc}}^P$, $\Xi_{Z_{vc}}^F$, $\Xi_{dV_{vm}}^P$, and $\Xi_{dV_{vm}}^F$ are defined explicitly in Appendix A.2.

2.4 Full Active Valve Linear Model

The complete quasi-static active valve model consists of Equations 6.2, 6.3, 6.4, 2.29, 2.30, 2.33, 2.34, 2.35, 2.36, 2.37, 2.38, and 2.39, combined with the following two equations for displacement matching and volume conservation,

$$Z_p + Z_{bot} = Z_{te} + Z_{pis} \quad (2.40)$$

$$dV_{te} + dV_{pis} + dV_{fluid} - dV_{top} - dV_{vm} = 0. \quad (2.41)$$

Figure 2.10 summarizes the modeling components of the active valve. All equations are represented in a Maple code that solves for T_p and all of the structural component displacements and swept volumes, given the voltage input V_p and the external valve cap and membrane pressure loadings P_1 and P_2 . This model is included in Appendix A.2 for reference.

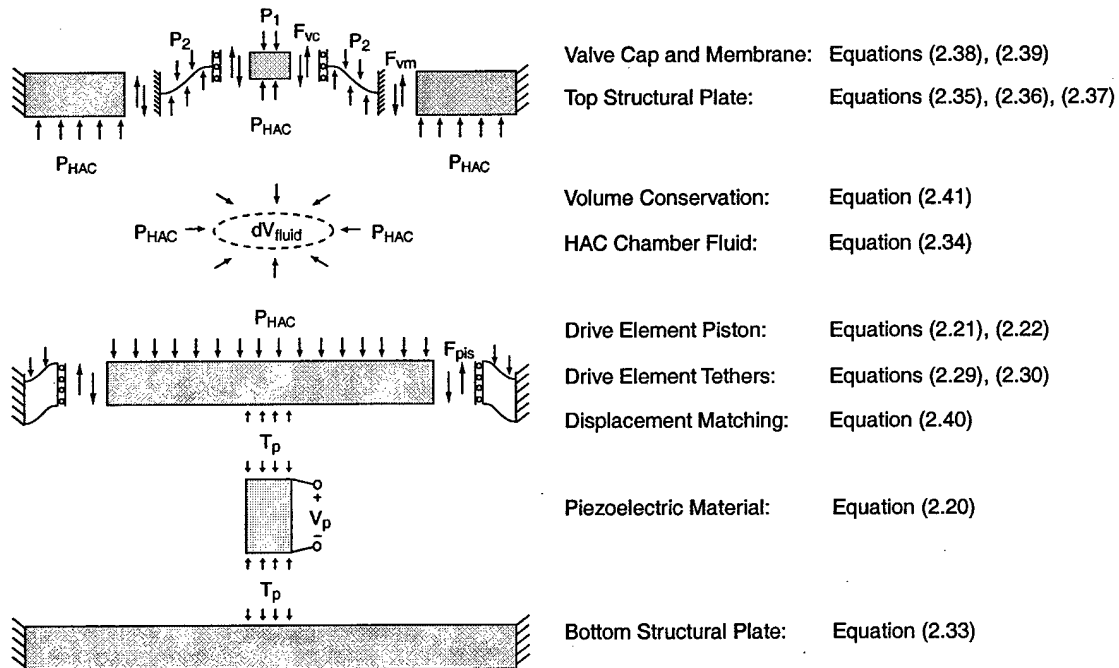


Figure 2.10: Complete linear quasi-static active valve structural model.

2.5 Impact of Multiple Piezoelectric Cylinders

The previous development of analytical theory for the active valve has assumed the piezoelectric actuation material to be a single cylinder located at the center of the drive element piston. To stiffen the drive element actuator structure, it would be desirable to incorporate a matrix of small diameter piezoelectric rods under the piston rather than a single centrally-located large-size cylinder (as long as the rods are sized properly to avoid buckling). Although incorporation of a matrix of rod structures is beyond the scope of this thesis, the use of three smaller diameter piezoelectric cylinders spread out beneath the piston is realizable (Chapter 8 experimentally evaluates this concept). This modeling section investigates the benefits of using three smaller diameter piezoelectric cylinders rather than a single centrally-located one in order to effectively "stiffen" the drive element piston and bottom plate structures.

Since the analytical relations developed thus far have assumed plate theory with boundary conditions corresponding to a single centrally-located piezoelectric cylinder, and since derivation of 3-dimensional plate behavior for multiple cylinder geometries is complex, finite-element models of the structural components are required. This section demonstrates, through example cases, how finite-element models of the drive element piston structure and bottom plate structure can be used to determine the $\Xi_{Z_p}^T$, $\Xi_{Z_p}^P$, $\Xi_{dV_{pis}}^T$, $\Xi_{dV_{pis}}^P$, and $\Xi_{Z_{bot}}^T$ compliance coefficients for three-piezoelectric cylinder geometries. Once determined, these coefficients can simply be substituted into the corresponding structural equations developed for the single-cylinder geometry presented in Sections 2.3.2 and 2.3.3.

2.5.1 Finite-Element Analysis of Piston

As presented in Section 2.3.2, the Ξ compliance coefficients for the piston structure are taken as the average of the hinged and clamped boundary condition scenarios at R_p . For clarity, this section will analyze the effects of three piezoelectric cylinders on a drive piston in the hinged boundary condition scenario. A similar procedure can be carried out for the clamped scenario, but is not documented in the section.

To illustrate the benefits of using three piezoelectric cylinders, a finite-element study comparing a single piezoelectric cylinder piston geometry to geometries with three piezoelectric cylinders is presented. In this study, representative piston geometry and material properties are taken to be: $R_{pis} = 3mm$, $t_{pis} = 800\mu m$, $E_{Si} = 165GPa$, and $\nu_{Si} = 0.22$. For the single piezoelectric cylinder geometry, the cylinder radius is $R_p = 1mm$. For the three piezoelectric cylinder geometry, the radius of each cylinder is sized ($R_p = 0.577mm$) such that the total area of all three is identical to the area of the cylinder in the single piezoelectric cylinder case. The distance R_{cp} of each cylinder from the piston center is varied in this study to illustrate the effect of cylinder placement on the piston compliance. Schematics of the single cylinder and

three cylinder finite-element model geometries are shown in Figure 2.11. The piston structure is guided at its center ($r = 0$) and hinged at its outer radius ($r = R_{pis}$).

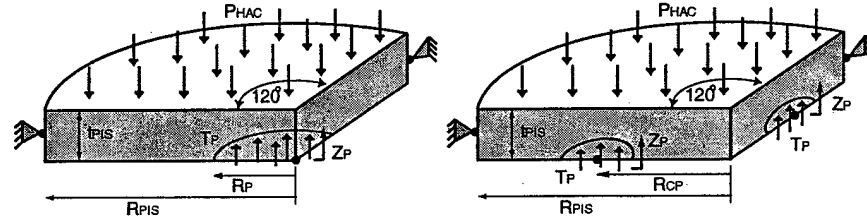


Figure 2.11: Finite-element (ANSYS) models of (a) a single centrally located piezoelectric cylinder beneath the drive element piston, and (b) a three piezoelectric cylinder design with the cylinders spread out beneath the drive element piston.

To determine the compliance coefficients $\Xi_{Z_p}^T$ and $\Xi_{dV_{pis}}^T$ for the drive piston structure, a stress T is applied on the underside of the piston where the cylinder(s) make contact. The resulting displacement at the center of the cylinder(s), Z_p , and the resulting swept volume of the piston structure, dV_{pis} are recorded. Similarly, to determine the compliance coefficients $\Xi_{Z_p}^P$ and $\Xi_{dV_{pis}}^P$, a pressure P is applied on the entire top surface of the piston. The resulting displacement at the center of the cylinder(s), Z_p , and the resulting swept volume of the piston structure, dV_{pis} are recorded. From these responses, the compliance coefficients are calculated.

Single Piezoelectric Cylinder Geometry

In performing finite-element analyses for this single cylinder geometry, the resulting piston compliance coefficients were found to be:

| Loading | Z_p Compliance | dV_{de} Compliance |
|----------|--|---|
| Stress | $\Xi_{Z_p}^T = 2.09e^{-13} \frac{m}{Pa}$ | $\Xi_{dV_{pis}}^T = 2.42e^{-18} \frac{m^3}{Pa}$ |
| Pressure | $\Xi_{Z_p}^P = 8.20e^{-13} \frac{m}{Pa}$ | $\Xi_{dV_{pis}}^P = 1.08e^{-17} \frac{m^3}{Pa}$ |

Three Piezoelectric Cylinder Geometries

Finite-element analyses for the three cylinder geometry were performed, with R_{cp} varying from 1 mm to 2.25 mm. Figure 2.12 plots the compliance coefficients of the three-cylinder geometries as a function of R_{cp} . Taking as an example case, $R_{cp} = 2.25mm$, the compliance coefficients were found to be:

| Loading | Z_p Compliance | dV_{de} Compliance |
|----------|--|---|
| Stress | $\Xi_{Z_p}^T = 0.36e^{-13} \frac{m}{Pa}$ | $\Xi_{dV_{pis}}^T = 0.94e^{-18} \frac{m^3}{Pa}$ |
| Pressure | $\Xi_{Z_p}^P = 3.12e^{-13} \frac{m}{Pa}$ | $\Xi_{dV_{pis}}^P = 1.08e^{-17} \frac{m^3}{Pa}$ |

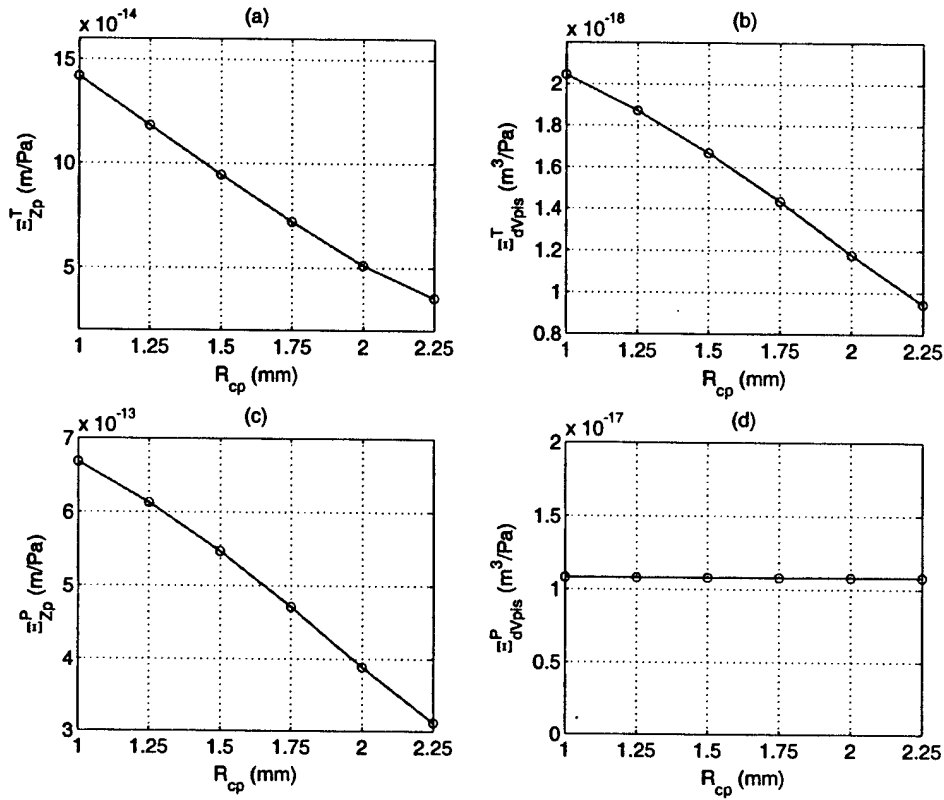


Figure 2.12: Compliance coefficients of the three cylinder piston geometry for varying R_{cp} : (a) Ξ_{Zp}^T , (b) Ξ_{dVpis}^T , (c) Ξ_{Zp}^P , and (d) Ξ_{dVpis}^P .

In comparing these results (for $R_{cp}=2.25$ mm) to those of the single cylinder geometry, it is observed that Ξ_{Zp}^T is reduced by 5.8x, Ξ_{dVpis}^T is reduced by 2.6x, and Ξ_{Zp}^P is reduced by 2.6x. Clearly, the use of three cylinders spread out beneath the piston is beneficial in reducing these coefficients, and therefore stiffening the structure. Ξ_{dVpis}^P , however, remains the same. This is expected since the swept volume of the piston structure (with no cylinders present below) in response to an applied pressure on the piston top surface should be identical for the single and three cylinder geometries. These results demonstrate the stiffening benefits of incorporating three piezoelectric cylinders beneath the drive element piston rather than a single centrally-located one. With these types of finite-element models, one can obtain compliance coefficients for a particular three cylinder drive piston geometry and use these coefficients in the analytical equations developed in Section 2.3.2 to accurately model the valve structural behavior.

2.5.2 Finite-Element Analysis of Bottom Plate

To illustrate the stiffening benefit of using three piezoelectric cylinders above the bottom plate, a finite-element study comparing a single piezoelectric cylinder bottom plate geometry to geometries with three piezoelectric cylinders is presented. In this study, the chamber bottom plate geometry and material properties are assumed to be: $R_{te} = 3.2\text{mm}$, $t_{pis} = 1000\mu\text{m}$, $E_{Si} = 165\text{GPa}$, and $\nu_{Si} = 0.22$. For the single piezoelectric cylinder geometry, the cylinder radius is $R_p = 1\text{mm}$. For the three piezoelectric cylinder geometry, the radius of each cylinder is sized ($R_p = 0.577\text{mm}$) such that the total area of all three is identical to the area of the cylinder in the single piezoelectric cylinder case. Schematics of the single cylinder and three cylinder finite-element model geometries are shown in Figure 2.13. The piston structure is guided at its center ($r = 0$) and clamped at its outer radius ($r = R_{te}$).

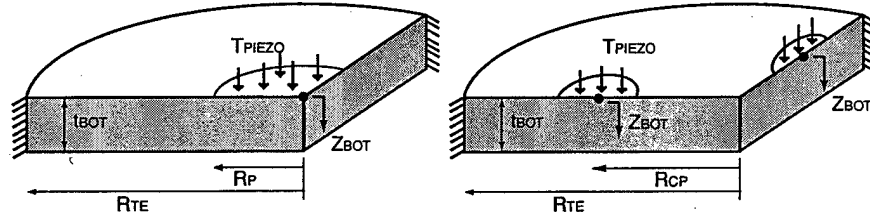


Figure 2.13: Finite-element (ANSYS) models of bottom plate structure with (a) a single centrally located cylinder above the bottom plate, and (b) a three cylinder design, with the cylinders spread out above the bottom plate.

To determine the compliance coefficient for the bottom plate structure $\Xi_{Z_{bot}}^T$, a pressure (stress) T is applied to the top surface of the plate where the cylinder(s) make contact. The resulting displacement at the center of the cylinder(s), Z_{bot} is recorded. From this response, the compliance coefficient is calculated.

Single Piezoelectric Cylinder Geometry

In performing the finite-element analysis for this single cylinder geometry, the resulting piston compliance coefficient was found to be:

| Loading | Z_{bot} Compliance |
|---------|--|
| Stress | $\Xi_{Z_{bot}}^T = 4.79e^{-14} \frac{\text{m}}{\text{Pa}}$ |

Three Piezoelectric Cylinder Geometries

Finite-element analyses for the three cylinder geometry were performed, with R_{cp} varying from 1 mm to 2.25 mm. Figure 2.14 plots the compliance coefficient $\Xi_{Z_{bot}}^T$ of the three-cylinder

geometry as a function of this varying R_{cp} . Taking as an example case, $R_{cp} = 2.25\text{mm}$, the compliance coefficient was found to be:

| Loading | Z_{bot} Compliance |
|---------|--|
| Stress | $\Xi_{Z_{bot}}^T = 0.98e^{-14} \frac{m}{Pa}$ |

In comparing this result (for $R_{cp}=2.25\text{ mm}$) to that of the single cylinder geometry, it is observed that $\Xi_{Z_p}^T$ is reduced by 4.9x. Clearly, the use of three cylinders spread out above the bottom plate is beneficial in reducing the amount by which the centers of the cylinders move downward into the plate. These results demonstrate the stiffening benefits of incorporating three piezoelectric cylinders above the bottom plate structure rather than a single centrally-located one. With this type of finite-element model, one can obtain the compliance coefficient for a particular three cylinder bottom plate geometry and use this coefficient in the analytical equations developed in Section 2.3.3 to accurately model the valve structural behavior.

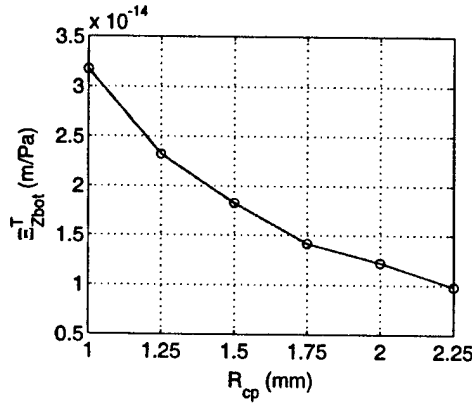


Figure 2.14: Compliance coefficient $\Xi_{Z_{bot}}^T$ of the three cylinder bottom plate geometry for varying R_{cp} .

2.6 Further Modeling Issues

The structural component that requires additional modeling focus is that of the valve cap and membrane. For the typical design space in the proposed active valve, this plate/membrane structure is designed to have a thickness of approximately $10\text{ }\mu\text{m}$, yet experience deflections on this order or larger. In this deflection regime, the plate will begin to stretch, resulting in the generation of in-plane tensile stresses that are unaccounted for in the linear plate theory presented in this chapter. The drive element tethers also possess thicknesses near $10\text{ }\mu\text{m}$, however, because the piston deflection during device operation is expected to be only $1\text{-}2\text{ }\mu\text{m}$, these tethers can be accurately modeled by the linear relations detailed thus far.

2.7 Conclusions

This chapter has developed a linear, quasi-static structural model of the proposed active valve device, including piezoelectric material behavior, deformation of the drive element tethers and the valve cap/membrane structure, and the compliances associated with the drive element piston, bottom structural plate, top structural plate, and hydraulic fluid. In addition, the chapter has demonstrated, through the use of representative finite-element models, the benefits of incorporating multiple piezoelectric cylinders spread out beneath the drive element piston rather than a single centrally-located one. The following chapter will detail the development of numerical non-linear modeling tools for understanding the large deflection deformation behavior of the valve cap and membrane structure.

Bibliography

- [1] S. Timoshenko. *Theory of Plates and Shells*. McGraw-Hill Book Company, Inc., New York and London, 1940.

Chapter 3

Non-Linear Deformation of the Valve Cap and Membrane

This chapter presents the development of a numerical code for the non-linear large-deflection modeling of a thin annular plate structure with rigid central cap under pressure loading. This theory has been specifically developed to model the valve cap and membrane behavior in the proposed active valve device. The chapter begins within an introduction to the valve cap geometry under investigation and the associated nature of the geometric non-linearity. The theory behind this non-linear deformation is then presented, with detailed derivation of the governing equations used in the numerical integration. Representative loading plots for a given valve geometry are then presented to illustrate the numerical code's capability to capture in-plane tensile stresses and boundary layer phenomena. Lastly, three MatlabTM codes are presented that serve as non-linear modeling tools for use in Chapters 4, 5, and 8 of this thesis. The finite-differencing scheme presented in this chapter is based upon the work of Su [1].

3.1 Introduction

In general, the deflection of a structural plate can be represented using linear deformation theory only if the deflection of the plate is less than about half the thickness of the plate. In this small deflection regime, it can be assumed that the plate's neutral axis is unchanged in length as it deforms, ie: it experiences no tensile stress. The only stresses that exist in this plate are the compressive and tensile bending stresses above and below this neutral axis. In a plate experiencing large deflections (that is, deflections greater than half the thickness of the plate), however, the plate begins to stretch and the assumption of zero in-plane tensile stress at the neutral axis is no longer valid. As the plate is deformed more and more into the large deflection regime, the in-plane tensile stress begins to dominate the bending stresses, thereby

increasing the plate stiffness. This marks the onset of membrane behavior, characterized by the inability to withstand bending moments. For plates that experience loads that create this large deflection behavior, it is critical that this in-plane stress be modeled and that the plate stiffening effects be captured.

3.2 Plate Geometry

The plate geometry under consideration in this chapter is shown in Figure 3.1. The plate has outer radius, r_a , inner radius r_b , thickness t , a Young's Modulus E , and a poisson ratio ν . The plate is clamped at its outer radius and guided at its inner radius. The assumption of a guided boundary condition at r_b is a reasonable one since bending of the valve cap is negligible. The plate experiences a pressure loading p underneath the plate from r_b to r_a and a concentrated circumferential force f at r_b .

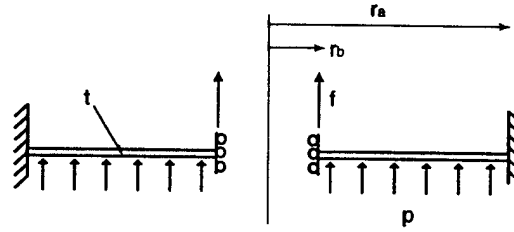


Figure 3.1: Schematic of an annular plate with a rigid central boss under pressure loading.

3.3 Theory

The work presented in this chapter is an extension of Sheplak and Dugundji's work on the large deflection behavior of clamped circular plates (without rigid central caps) [2]. Additionally, the finite-difference implementation contained within this chapter is the result of work done by Su [1].

3.3.1 Assumptions

This chapter follows von Karman plate theory, in which the vertical displacement of the plate w is assumed to be much larger than the lateral displacement u and v and the normals to the undeformed middle surface remain the normals to the deformed middle surface. As a result, the deformed shape of the thin plate can be fully described by the geometry of the neutral surface. In this analysis, only quadratic non-linear terms are retained.

3.3.2 Equilibrium Equations

The forces and moments experienced by a small section of the plate are shown in Figure 3.2, where M_r and M_θ are the radial and tangential moments respectively, N_r is the in-plane tension load per unit circumference, and Q_r is the shear force per unit circumference.

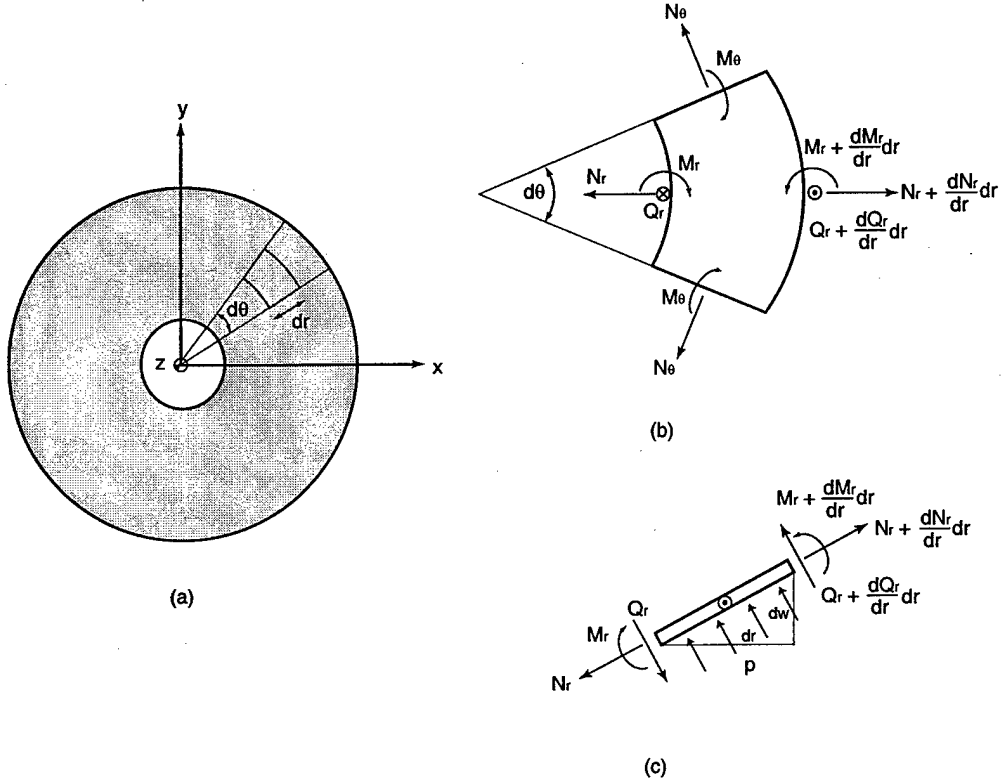


Figure 3.2: Force and moment free-body diagrams for an infinitesimal annular plate section: (a) top view of plate, (b) top view of plate section, (c) side-view of plate section.

To obtain the equilibrium equations for this plate, a radial force balance, a z-direction force balance, and a circumferential moment balance are performed.

The radial force balance produces the following initial relation,

$$\begin{aligned} \sum F_r \rightarrow & (N_r + \frac{dN_r}{dr}dr)(\cos \frac{dw}{dr})(r + dr)d\theta - N_r(\cos \frac{dw}{dr})rd\theta - 2N_\theta(\sin \frac{d\theta}{2})dr - \\ & (Q_r + \frac{dQ_r}{dr}dr)(\sin \frac{dw}{dr})(r + dr)d\theta + Q_r(\sin \frac{dw}{dr})rd\theta - p(\sin \frac{dw}{dr})rdrd\theta = 0. \end{aligned} \quad (3.1)$$

The z-direction force balance produces the following initial relation,

$$\begin{aligned} \sum F_z \rightarrow & (N_r + \frac{dN_r}{dr}dr)(\sin \frac{dw}{dr})(r+dr)d\theta - N_r(\sin \frac{dw}{dr})rd\theta + \\ & (Q_r + \frac{dQ_r}{dr}dr)(\cos \frac{dw}{dr})(r+dr)d\theta - Q_r(\cos \frac{dw}{dr})rd\theta + p(\cos \frac{dw}{dr})rdrd\theta = 0. \end{aligned} \quad (3.2)$$

The circumferential moment balance produces the following initial relation,

$$\sum M_r \rightarrow (M_r + \frac{dM_r}{dr}dr)(r+dr)d\theta - M_rrd\theta + (Q_r + \frac{dQ_r}{dr}dr)(r+dr)(r+dr)d\theta - Q_rr^2d\theta = 0. \quad (3.3)$$

Using the following simplifying relations which hold true for the plate section,

$$\cos \frac{dw}{dr} \sim 1, \quad \sin \frac{dw}{dr} \sim \frac{dw}{dr}, \quad \sin \frac{d\theta}{2} \sim \frac{d\theta}{2}, \quad (dr)^2 \ll dr$$

the force and moment equilibrium balances can be simplified to the following equations respectively,

$$N_r - N_\theta + r \left(\frac{dN_r}{dr} \right) = 0, \quad (3.4)$$

$$\frac{d}{dr} \left(N_rr \frac{dw}{dr} \right) + \frac{d}{dr} (Q_rr) + pr = 0, \quad (3.5)$$

and

$$Q_r + \frac{dM_r}{dr} + \left(\frac{M_r - M_\theta}{r} \right) = 0. \quad (3.6)$$

3.3.3 Geometric Compatibilities

The radial elongation of the neutral axis during deformation can be represented by the following strain displacement relation [3],

$$\epsilon_r = \frac{du}{dr} + \frac{1}{2} \left[\left(\frac{du}{dr} \right)^2 + \left(\frac{dw}{dr} \right)^2 \right]. \quad (3.7)$$

Based on the assumption that $u \ll w$, it follows that the term $(\frac{du}{dr})^2$ is negligible compared to the term $(\frac{dw}{dr})^2$. Therefore, the radial strain displacement relation can be simplified to

$$\epsilon_r = \frac{du}{dr} + \frac{1}{2} \left(\frac{dw}{dr} \right)^2. \quad (3.8)$$

The circumferential strain-displacement relationship is

$$\epsilon_\theta = \frac{u}{r}. \quad (3.9)$$

The first and second principle curvatures for the plate are [3]

$$\kappa_r = -\frac{d^2 w}{dr^2}, \quad \kappa_\theta = -\frac{1}{r} \frac{dw}{dr}. \quad (3.10)$$

3.3.4 Constitutive Laws

Assuming that the plate experiences plane stress, ie: no variations in stress occur through the thickness of the plate, the material Hooke's Law can be written as

$$\epsilon_r = \frac{1}{E} \left(\frac{N_r}{t} - \nu \frac{N_\theta}{t} \right), \quad \epsilon_\theta = \frac{1}{E} \left(\frac{N_\theta}{t} - \nu \frac{N_r}{t} \right) \quad (3.11)$$

where E and ν are the material Young's Modulus and Poisson Ratio respectively. Moment equilibrium in the plate yields

$$M_r = -D(\kappa_r + \nu \kappa_\theta), \quad M_\theta = -D(\kappa_\theta + \nu \kappa_r) \quad (3.12)$$

where D is the plate flexural rigidity, defined by

$$D = \frac{Eh^3}{12(1-\nu^2)}. \quad (3.13)$$

3.3.5 Governing Equations

Beginning with the three equilibrium equations (5.9), (5.10), and (3.6), the governing differential equations for the plate can be derived. Integrating (5.10) with respect to r from r_b to r yields

$$(Q_r r - Q_{r_b} r_b) + \left(N_r \frac{dw}{dr} - N_{r_b} \left(\frac{dw}{dr} \right)_{r_b} \right) + \frac{1}{2} p(r^2 - r_b^2) = 0 \quad (3.14)$$

Since the shear force at r_b is $Q_{r_b} = \frac{-f}{2\pi r_b}$ and since $(\frac{dw}{dr})_{r_b} = 0$, it follows that

$$Q_r + N_r \frac{dw}{dr} + \frac{f}{2\pi r} + \frac{p(r^2 - r_b^2)}{2r} = 0. \quad (3.15)$$

Substituting the moment-curvature relations (3.12) into (3.6) gives

$$Q_r + D \left(\frac{d^3 w}{dr^3} + \frac{1}{r} \frac{d^2 w}{dr^2} - \frac{1}{r^2} \frac{dw}{dr} \right) = 0. \quad (3.16)$$

Combining (3.16) with (3.15) produces

$$\frac{d^3w}{dr^3} + \frac{1}{r} \frac{d^2w}{dr^2} - \frac{1}{r^2} \frac{dw}{dr} - \frac{N_r}{D} \frac{dw}{dr} = \frac{f}{2\pi r D} + \frac{p(r^2 - r_b^2)}{2r D}. \quad (3.17)$$

Rewriting the strain-displacement relations (3.8) and (3.9) in the following manner,

$$r \frac{d\epsilon_r}{dr} + \epsilon_\theta - \epsilon_r + \frac{1}{2} \left(\frac{dw}{dr} \right)^2 = 0, \quad (3.18)$$

and substituting the material Hooke's Law relations (3.11) into (3.18) produces

$$\frac{dN_\theta}{dr} - \left(\frac{N_r - N_\theta}{r} \right) + \frac{Eh}{2r} \left(\frac{dw}{dr} \right)^2 = 0. \quad (3.19)$$

Equations (5.9), (3.17), and (3.19), therefore form a set of three non-linear differential equations in the three unknowns N_r , N_θ , and w . The boundary conditions corresponding to these equations can be written as follows:

$$\text{at } r = r_b : \quad u = r\epsilon_\theta = 0 \rightarrow N_\theta - \nu N_r = 0, \quad \frac{dw}{dr} = 0 \quad (3.20)$$

$$\text{at } r = r_a : \quad u = r\epsilon_\theta = 0 \rightarrow N_\theta - \nu N_r = 0, \quad \frac{dw}{dr} = 0 \quad (3.21)$$

It is interesting to note at this point that these equations are non-linear because of the term $\frac{N_r}{D} \frac{dw}{dr}$ in (3.17). If the plate were deforming only in the linear regime, the term $N_r = 0$, and therefore the three governing differential equations would condense into the following single linear equation,

$$\frac{d^3w}{dr^3} + \frac{1}{r} \frac{d^2w}{dr^2} - \frac{1}{r^2} \frac{dw}{dr} = \frac{f}{2\pi r D} + \frac{p(r^2 - r_b^2)}{2r D} \quad (3.22)$$

which could be integrated three times to obtain a solution for $w(r)$, as was detailed in Chapter 2 of this thesis.

3.3.6 In-Plane Prestress

As often is the case with micromachined thin plate structures, residual tensile stresses in the plate can exist prior to transverse loading. These initial in-plane loads serve to pretension the plate and can significantly affect the resulting deformation behavior. The complete loading parameters, N_r and N_θ , can therefore be decomposed into initial in-plane prestressing components N_{r0} and $N_{\theta0}$, and into components due to the transverse pressure loading \tilde{N}_r and \tilde{N}_θ , as

follows:

$$N_r = N_{r_o} + \tilde{N}_r \quad (3.23)$$

$$N_\theta = N_{\theta_o} + \tilde{N}_\theta. \quad (3.24)$$

These parameters, \tilde{N}_r and \tilde{N}_θ , can be thought of as incremental changes in N_r and N_θ due to the application of the transverse loading on top of the already prestressed plate.

Derivation of N_{r_o} and N_{θ_o}

It is desired to obtain expressions for the in-plane prestress that results from a uniform tension load $N_r = N_o$ applied at $r = r_a$ with zero displacement $u = 0$ at $r = r_b$. Since $p = 0$ and $w(r)$ and its derivatives with respect to r are zero, only (5.9) of the three governing equations remains. The strain-displacement relations (3.8) and (3.9) can be simplified to:

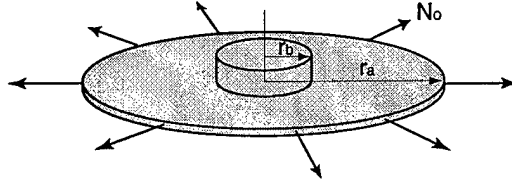


Figure 3.3: Schematic of an annular plate with a rigid central boss under pretension. Loading N_o is applied radially outward at $r = r_a$

$$\epsilon_r = \frac{du}{dr} \quad , \quad \epsilon_\theta = \frac{u}{r}. \quad (3.25)$$

Substituting (3.25) into (3.11) and rearranging for N_r and N_θ produces

$$N_r = \left(\frac{Et}{1-\nu^2} \right) \left(\frac{du}{dr} + \frac{\nu u}{r} \right) \quad , \quad N_\theta = \left(\frac{Et}{1-\nu^2} \right) \left(\nu \frac{du}{dr} + \frac{u}{r} \right). \quad (3.26)$$

Inserting (3.26) into (5.9) results in a solution for $u(r)$:

$$u(r) = \frac{N_o}{\left(\frac{Et}{1-\nu^2} \right) [(1+\nu) + \left(\frac{r_b}{r_a} \right)^2 (1-\nu)]} \left[r - \frac{r_b^2}{r} \right]. \quad (3.27)$$

Inserting this relation for $u(r)$ back into (3.26) yields the following expressions for the initial in-plane tensile loads:

$$N_{ro} = \left(\frac{N_o}{1 + \beta^2} \right) \left[1 + \beta^2 \left(\frac{r_a}{r} \right)^2 \right] \quad (3.28)$$

and

$$N_{\theta o} = \left(\frac{N_o}{1 + \beta^2} \right) \left[1 - \beta^2 \left(\frac{r_a}{r} \right)^2 \right] \quad (3.29)$$

where

$$\beta = \left(\frac{r_b}{r_a} \right) \sqrt{\frac{1 - \nu}{1 + \nu}}. \quad (3.30)$$

It is interesting to observe here that these in-plane tensile loads vary with r , unlike the in-plane tensile loads for a circular plate with no rigid central boss, which do not vary with r ,

$$N_{ro} = N_{\theta o} = \frac{N_o(1 - \nu)^2}{Et}. \quad (3.31)$$

Governing Equations for Complete Loading

Having found expressions for the initial prestressing in-plane loads, (5.2) and (3.29) can be substituted into the three previous governing differential equations (5.9), (3.17), and 3.19) to produce the following three refined governing equations, in terms of \tilde{N}_r , \tilde{N}_θ , and N_o ,

$$\frac{d\tilde{N}_r}{dr} + \frac{\tilde{N}_r - \tilde{N}_\theta}{r} = 0, \quad (3.32)$$

$$\frac{d^3 w}{dr^3} + \frac{1}{r} \frac{d^2 w}{dr^2} - \left(\frac{\beta^2 r_a^2 N_o}{D(1 + \beta^2)} + 1 \right) \frac{dw}{dr} - \left(\frac{\tilde{N}_r}{D} + \frac{N_o}{D(1 + \beta^2)} \right) \frac{dw}{dr} = \frac{f}{2\pi r D} + \frac{p(r^2 - r_b^2)}{2r D}, \quad (3.33)$$

and

$$\frac{d\tilde{N}_r}{dr} - \left(\frac{\tilde{N}_r - \tilde{N}_\theta}{r} \right) + \frac{Et}{2r} \left(\frac{dw}{dr} \right)^2 = 0. \quad (3.34)$$

3.3.7 Non-Dimensionalized Governing Equations

In order to generalize these equations for ease of use, the non-dimensionalization procedure of Sheplak and Dugundji is followed, with the subsequent non-dimensional parameters being defined,

$$\begin{aligned} \xi &= \frac{r}{r_a} & (') &= \frac{d}{d\xi} & W &= \frac{w}{t} & U &= \frac{u}{h} \\ \theta &= \frac{dW}{d\xi} = \frac{r_a}{t} \frac{dw}{dr} & \Psi &= \frac{d\theta}{d\xi} = \frac{r_a^2}{t} \frac{d^2 w}{dr^2} \end{aligned}$$

$$S_r = \frac{\tilde{N}_r r_a^2}{Et^3} \quad S_\theta = \frac{\tilde{N}_\theta r_a^2}{Et^3}. \quad (3.35)$$

The governing equations (3.32), (3.33), and (3.34) can therefore be reexpressed in non-dimensional form as

$$S'_r + \frac{S_r - S_\theta}{\xi} = 0, \quad (3.36)$$

$$\theta'' + \frac{\theta'}{\xi} - \left(k^2 + \frac{s^2 + 1}{\xi^2} \right) \theta - 12(1 - \nu^2) S_r \theta = 6(1 - \nu^2) \left(P\xi - \frac{P}{\xi} \left(\frac{r_b}{r_a} \right)^2 + \frac{F}{\xi} \right), \quad (3.37)$$

and

$$S'_\theta - \left(\frac{S_r - S_\theta}{\xi} \right) = -\frac{1}{2\xi} \theta^2 \quad (3.38)$$

where

$$k = \left(\frac{r_a}{t} \right) \sqrt{\frac{12(1 - \nu^2)N_o}{Et(1 + \beta^2)}}, \quad s = \beta k, \quad P = \frac{pr_a^4}{Et^4}, \quad F = \frac{fr_a^2}{\pi Et^4}. \quad (3.39)$$

The parameters k and s are dimensionless pretension parameters and P is a dimensionless transverse loading parameter. The boundary conditions can be written as

$$\text{at } \xi = \xi_b = \frac{r_b}{r_a}: \quad S_\theta - \nu S_r = 0, \quad \theta = 0 \quad (3.40)$$

$$\text{at } \xi = \xi_a = 1: \quad S_\theta - \nu S_r = 0, \quad \theta = 0. \quad (3.41)$$

For use in the numerical finite-difference code to be discussed in the next section, (3.36), (3.37), and (3.38) can be simplified to two non-dimensional governing equations in the variables S_r and θ by substituting (3.36) into (3.38) to eliminate S_θ . Therefore, the following set of equations is ready for finite-difference implementation:

$$\xi^2 S''_r + 3\xi S'_r = -\frac{\theta^2}{2} \quad (3.42)$$

$$\xi^2 \theta'' + \xi \theta' - [(s^2 + 1) + \xi^2(k^2 + 12(1 - \nu^2)S_r)]\theta = 6(1 - \nu^2) \left(P\xi^3 - P\xi \left(\frac{r_b}{r_a} \right)^2 + F\xi \right) \quad (3.43)$$

where

$$k = \left(\frac{r_a}{t}\right) \sqrt{\frac{12(1-\nu^2)N_o}{Et(1+\beta^2)}} \quad s = \beta k \quad P = \frac{pr_a^4}{Et^4} \quad F = \frac{fr_a^2}{\pi Et^4} \quad (3.44)$$

Boundary Conditions:

$$\text{at } \xi = \xi_b : \quad \xi S'_r + (1-\nu)S_r = 0 \quad , \quad \theta = 0 \quad (3.45)$$

$$\text{at } \xi = \xi_a : \quad \xi S'_r + (1-\nu)S_r = 0 \quad , \quad \theta = 0 \quad (3.46)$$

Post-Equation:

$$S_\theta = \xi S'_r + S_r. \quad (3.47)$$

3.3.8 Finite-Difference Implementation

The non-linear dimensionless governing differential equations (3.42) and (3.43) can not be solved directly due to the presence of the non-linear term $S_r\theta$ in (3.43). As a result, they must be numerically solved. This section details the implementation of a finite-difference scheme to accomplish this goal. Sheplak and Dugundji's work on the non-linear deflection of clamped circular plates highlights the importance of a boundary layer region near the plate's clamped outer radius. For large deflections, it is within this region that a transition from membrane behavior to plate bending behavior occurs. To accurately model this region, Sheplak and Dugundji introduced a coordinate transformation that clusters a higher density of finite-difference grid points in this region than in the central regions of the plate.

In the case of an annular plate with clamped outer radius and guided inner radius (corresponding to a rigid central cap), a similar procedure can be carried out. However, in this situation, it is necessary to introduce a more detailed coordinate transformation that clusters grid points at both $r = r_a$ and $r = r_b$ so that the two corresponding boundary layer regions can be accurately resolved. Letting $\xi_c = \frac{1}{2}(\xi_b + \xi_a)$ and defining η to be a set of equally spaced grid points between 0 and 1, a proposed coordinate transformation is:

$$\text{for } 0 \leq \eta \leq 0.5 : \quad \xi = \xi_b + (\alpha - 1)(\xi_c - \xi_b) \left(\frac{\phi - \phi^{1-2\eta}}{1 + \phi^{1-2\eta}} \right) \quad (3.48)$$

$$\text{for } 0.5 < \eta \leq 1 : \quad \xi = \xi_a + (\alpha - 1)(\xi_c - \xi_a) \left(\frac{\phi - \phi^{2\eta-1}}{1 + \phi^{1-2\eta}} \right) \quad (3.49)$$

where α is a coordinate stretching parameter varying between 1 and ∞ and $\phi = \left[\frac{\alpha+1}{\alpha-1}\right]$.

The closer α is to 1, the higher the mesh density near $r = r_b$ and $r = r_a$ in the coordinate transformation.

An example of this coordinate transformation is illustrated in Figure 3.4, for the case of $\xi_b = 0.1$ and for 20 grid points existing between ξ_b and ξ_a . In Plot 3.4(a), a value of $\alpha = 10$ results in an evenly spaced finite-difference grid mesh between the inner and outer dimensionless boundary of the plate. As α approaches 1 in Plots 3.4(c) and 3.4(d), an increase in the mesh density begins to appear near the boundaries. For the numerical code implemented in this thesis, values of α between 1.01 and 1.05 and number of grid points between 100 and 200 were commonly employed.

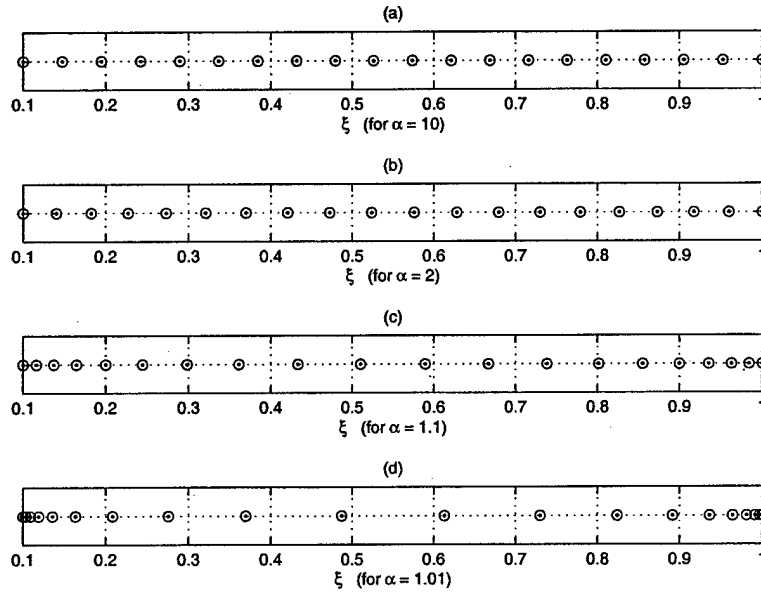


Figure 3.4: Coordinate transformation grid point locations for differing values of α .

Having defined these coordinate transformations, it is required to derive equations for η , $\frac{d\eta}{d\xi}$, and $\frac{d^2\eta}{d\xi^2}$ as functions of ξ for use in the final coordinate transformation governing differential equations to be presented on the following pages. Rearranging (3.48) and (3.49) and taking derivatives with respect to ξ produces the following relations:

For $\xi_b \leq \xi \leq \xi_c$:

$$\eta = \frac{1}{2} \left(1 - \left(\frac{1}{\ln \phi} \right) \ln \left(\frac{m\phi - (\xi - \xi_b)}{m + (\xi - \xi_b)} \right) \right) \quad (3.50)$$

$$\frac{d\eta}{d\xi} = \frac{1}{2 \ln \phi} \left(\frac{m(1 + \phi)}{(m\phi - (\xi - \xi_b))(m + (\xi - \xi_b))} \right) \quad (3.51)$$

$$\frac{d^2\eta}{d\xi^2} = \frac{-1}{2\ln\phi} \left(\frac{m(1+\phi)(n-2\xi)}{[(m\phi - (\xi - \xi_b))(m + (\xi - \xi_b))]^2} \right) \quad (3.52)$$

$$\text{where} \quad m = (\alpha - 1)(\xi_c - \xi_b) \quad (3.53)$$

$$\text{where} \quad n = m\phi - m + 2\xi_b.$$

For $\xi_c \leq \xi \leq \xi_a$:

$$\eta = \frac{1}{2} \left(1 + \left(\frac{1}{\ln\phi} \right) \ln \left(\frac{m\phi - (\xi - \xi_a)}{m + (\xi - \xi_a)} \right) \right) \quad (3.54)$$

$$\frac{d\eta}{d\xi} = \frac{-1}{2\ln\phi} \left(\frac{m(1+\phi)}{(m\phi - (\xi - \xi_a))(m + (\xi - \xi_a))} \right) \quad (3.55)$$

$$\frac{d^2\eta}{d\xi^2} = \frac{1}{2\ln\phi} \left(\frac{m(1+\phi)(n-2\xi)}{[(m\phi - (\xi - \xi_a))(m + (\xi - \xi_a))]^2} \right) \quad (3.56)$$

$$\text{where} \quad m = (\alpha - 1)(\xi_c - \xi_a) \quad (3.57)$$

$$\text{where} \quad n = m\phi - m + 2\xi_a.$$

Incorporating these coordinate transformations into the set of Equations (3.42) - (3.47), the transformed set of equations can be written as

$$\xi^2(\eta) \left(\frac{d\eta}{d\xi} \right)^2 \frac{d^2 S_r(\eta)}{d\eta^2} + \left(\xi^2(\eta) \frac{d^2\eta}{d\xi^2} + 3\xi(\eta) \frac{d\eta}{d\xi} \right) \frac{dS_r(\eta)}{d\eta} = -\frac{\theta^2(\eta)}{2} \quad (3.58)$$

$$\begin{aligned} \xi^2(\eta) \left(\frac{d\eta}{d\xi} \right)^2 \frac{d^2\theta(\eta)}{d\eta^2} + \left(\xi^2(\eta) \frac{d^2\eta}{d\xi^2} + \xi(\eta) \frac{d\eta}{d\xi} \right) \frac{d\theta(\eta)}{d\eta} - [(s^2 + 1) + \xi^2(\eta)(k^2 + 12(1 - \nu^2)S_r(\eta))] \theta(\eta) \\ = 6(1 - \nu^2) \left(P\xi^3(\eta) - P\xi(\eta) \left(\frac{r_b}{r_a} \right)^2 + F\xi(\eta) \right) \end{aligned} \quad (3.59)$$

Boundary Conditions:

$$\text{at } \eta = 0 : \quad \xi \left(\frac{d\eta}{d\xi} \right) \left(\frac{dS_r}{d\eta} \right) + (1 - \nu)S_r(\eta) = 0 \quad , \quad \theta(\eta) = 0 \quad (3.60)$$

$$\text{at } \eta = 1 : \quad \xi \left(\frac{d\eta}{d\xi} \right) \left(\frac{dS_r}{d\eta} \right) + (1 - \nu)S_r(\eta) = 0 \quad , \quad \theta(\eta) = 0 \quad (3.61)$$

Post-Equation:

$$S_\theta(\eta) = \xi(\eta) \left(\frac{d\eta}{d\xi} \right) \frac{dS_r(\eta)}{d\eta} + S_r(\eta). \quad (3.62)$$

These equations are solved using a 2nd-order central finite difference scheme for the interior grid points, a 2nd-order forward difference scheme for the grid point corresponding to the boundary condition at the inner radius, and a 2nd-order backward difference scheme for the grid point corresponding to the boundary condition at the outer radius. These equations are cast into two matrix relations as follows:

$$[A]\theta = C \quad (3.63)$$

$$[B]S_r = -\frac{1}{2}\theta^2. \quad (3.64)$$

An initial guess for θ is taken based on the solution to the linear problem. Based on this θ , S_r is determined and the nonlinear term $12(1 - \nu^2)\xi^2(\eta)S_r$ is calculated. Having incorporated this nonlinear term into $[A]$, the new solution for θ is determined. The error between the previous θ and the newly obtained θ is calculated. If this error is sufficiently small, then the procedure is complete and the solution vector θ has been found. If the error is too large, an under relaxation technique is used to produce a new θ guess and the procedure is repeated. This iteration scheme continues until θ converges to a sufficiently accurate result.

3.3.9 Post-Processing Calculations

Once the non-linear solution procedure has been completed and S_r , S_θ , and θ have been found, it is desired to obtain the deflection w of the plate, the curvature $\frac{d^2w}{dr^2}$ of the plate, and the stresses σ_r and σ_θ within the plate. These calculations are described in the following sections.

Calculation of w

As detailed in (3.35), $\theta = \frac{dW}{d\xi} = \frac{r_a}{t} \frac{dw}{dr}$. To calculate w , finite differences are implemented to express θ in terms of W ,

$$\theta = [W_{matrix}]W. \quad (3.65)$$

Then, since the vector θ is known, this relation is rearranged to solve for W ,

$$W = [W_{matrix}]^{-1}\theta. \quad (3.66)$$

Finally, the dimensional vector w is calculated,

$$w = Wt. \quad (3.67)$$

Calculation of $\frac{d^2 w}{dr^2}$

The non-dimensional plate curvature Ψ is calculated, according to (3.35), using 2nd-order finite difference schemes,

$$\Psi = \frac{d\theta}{d\xi}. \quad (3.68)$$

The dimensional plate curvature is then calculated,

$$\frac{d^2 w}{dr^2} = \Psi \frac{t}{r_a^2}. \quad (3.69)$$

Calculation of σ_r and σ_θ

In general, the dimensional plate stresses can be expressed as

$$\sigma_r = \frac{Et^2}{r_a^2} (S_{ro} + S_r + S_{r,bending}) \quad (3.70)$$

$$\sigma_\theta = \frac{Et^2}{r_a^2} (S_{\theta o} + S_\theta + S_{\theta,bending}) \quad (3.71)$$

where S_{ro} and $S_{\theta o}$ are the dimensionless initial in-plane stresses prior to plate transverse loading, S_r and S_θ are the dimensionless in-plane stresses created during plate deflection, and $S_{r,bending}$ and $S_{\theta,bending}$ are the dimensionless bending stresses created during plate deflection. Each of these contributions is considered as follows.

S_{ro} and $S_{\theta o}$ Combining (5.2), (3.29), and (3.35), the dimensional initial in-plane stresses are found to be

$$S_{ro} = S_{\theta o} = \left(\frac{k^2}{12(1-\nu^2)} \right) \left[1 + \beta^2 \left(\frac{r_a}{r} \right)^2 \right]. \quad (3.72)$$

S_r and S_θ These are the results directly from the numerical code.

$S_{r,bending}$ and $S_{\theta,bending}$ For plate bending, the radial and tangential strains are functions of the distance from the neutral axis [3],

$$\epsilon_{r,bending} = -z \frac{d^2 w}{dr^2}, \quad \epsilon_{\theta,bending} = -\frac{z}{r} \frac{dw}{dr}. \quad (3.73)$$

According to (3.11),

$$\epsilon_r = \frac{1}{E}(\sigma_r - \nu\sigma_\theta) \quad , \quad \epsilon_\theta = \frac{1}{E}(\sigma_\theta - \nu\sigma_r). \quad (3.74)$$

Substituting (3.73) into (3.74) and rearranging in terms of σ_r and σ_θ , then incorporating (3.35) yields,

$$S_{r,bending} = S_{r,bending}(z) = \frac{-z}{(1-\nu^2)t} \left(\Psi + \frac{\nu\theta}{\xi} \right) \quad (3.75)$$

$$S_{\theta,bending} = S_{\theta,bending}(z) = \frac{-z}{(1-\nu^2)t} \left(\frac{\theta}{\xi} + \nu\Psi \right). \quad (3.76)$$

Therefore, the dimensional plate stresses σ_r and σ_θ can be assembled from these three stress contributions.

3.4 Results of Numerical Code

This section presents results to illustrate the capability of the numerical code to capture the non-linear large deflection behavior of a thin annular plate with a rigid central cap. As an example, consider a silicon plate with $r_b = 400\mu m$, $r_a = 800\mu m$, $t_{vm} = 7\mu m$, $E_{si} = 165GPa$, and $\nu = 0.22$. This structure is shown in Figure 3.5. The following subsections use this plate geometry under varying loads to show important non-linear phenomena. Sections 3.4.1 and 3.4.2 highlight the differences between linear and non-linear deflection theory for two distinct loading scenarios. Section 3.4.3 focuses on the presence of thin boundary layer regions near the clamped boundaries and the change in these regions as the plate is deflected more and more into the large deflection regime. And Section 3.4.4 discusses the effect that initial in-plane tension can have on the plate deflection behavior.

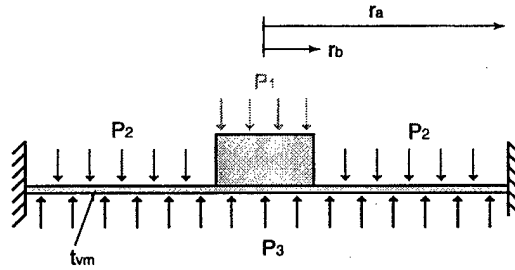


Figure 3.5: Schematic of an annular plate with a rigid central boss under pressure loading P_1 , P_2 , and P_3 .

3.4.1 Loading: $P_1 = P_2 = 0$, $P_3 = 100kPa$, $N_o = 0$

Figure 3.6 displays the linear and non-linear plate behavior for loading of $P_1 = P_2 = 0kPa$ and $P_3 = 100kPa$ and zero initial in-plane tension. From plot(a), it is clear that the deflection ($= 11.5\mu m$) calculated using the numerical code is significantly less than that ($= 31.5\mu m$) predicted by linear theory. Thin plate structures, such as the one under consideration, experience significant in-plane stresses as the deflections grow larger than the plate thickness. It is evident that this non-linear code captures this behavior. Shown in plots (b) and (c) are the dimensional linear and non-linear plate slopes ($\frac{dw}{dr}$) and curvatures ($\frac{d^2w}{dr^2}$). Note the boundary condition enforcement of zero slope at r_b and r_a . Plot (d) illustrates the stress σ_r at the top and bottom plate surfaces predicted by the non-linear code. In this case, the peak tensile stress in the plate is $0.45GPa$ and occurs on the underside of the plate at r_a .

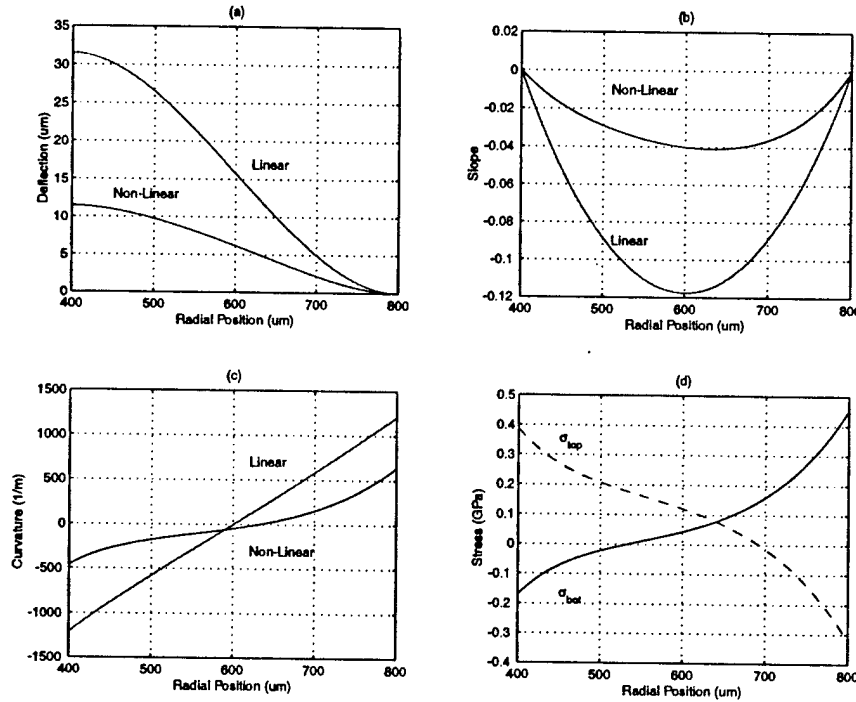


Figure 3.6: Deflection of thin annular plate under loading $P_1 = P_2 = 0$, $P_3 = 100kPa$. Plate dimensions and properties: $r_b = 400\mu m$, $r_a = 800\mu m$, $t = 7\mu m$, $E_{si} = 165GPa$, and $\nu = 0.22$.

3.4.2 Loading: $P_1 = 2.90MPa$, $P_2 = 0$, $P_3 = 1.30MPa$, $N_o = 0$

Figure 3.7 displays the linear and non-linear plate behavior for loading of $P_1 = 2.90MPa$, $P_2 = 0MPa$ and $P_3 = 1.30MPa$, and zero initial in-plane tension loading. These pressure

loadings were chosen to illustrate the difference between linear and non-linear theory even when the valve cap deflection predicted in both cases is identical. From plot(a), it is clear that the inner radius deflection predicted by both the linear and non-linear code is identical ($= 0.7\mu m$). However, the deflection behavior of the interior sections of the plate are quite different, due to the stiffening effect of the plate, which is accurately captured by the non-linear code. Linear theory predicts a peak plate deflection near $18\mu m$ whereas non-linear theory predicts a plate deflection near $9\mu m$. Shown in plots (b) and (c) are the dimensional linear and non-linear plate slopes ($\frac{dw}{dr}$) and curvatures ($\frac{d^2w}{dr^2}$). Again, note the boundary condition enforcement of zero slope at r_b and r_a . Also, note the presence of near constant curvature toward the central portions of the plate for the non-linear theory. This is due to the fact that the structure is behaving more like a membrane than a plate in these sections. At values of r closer to the boundaries at r_b and r_a , the curvature changes significantly. It is in these boundary layer regions that the bending stresses become greater than the in-plane tensile stresses, and the structure transitions back to plate behavior. Plot (d) further illustrates this point. The total stress σ_r at the top and bottom plate surfaces remain almost constant in these central membrane sections, however they increase sharply toward the boundaries. It is here that the bending stresses dominate. In this case, the peak tensile stress in the plate is approximately $1.80GPa$ and occurs on the bottom of the plate at r_b . In this loading situation, although, the inner radius deflection is predicted to be the same by the linear and non-linear code, the deflection of the interior portions of the plate are quite different. When analyzing the active valve behavior, the volume swept under the membrane would be overestimated if linear theory were to be used.

3.4.3 Loading: $P_1 = P_2 = 0$, Varying P_3 , $N_o = 0$

To understand the concept of increasing plate stiffness and the presence of thin boundary layers regions near r_b and r_a as the plate is pushed further into the large deflection regime, the plate is subjected to varying pressure P_3 beneath the membrane and cap and no other loading. Figure 3.8(a) illustrates the cap deflection at $r = r_b$ for increasing applied pressure P_3 from 0 to 10 MPa. A non-linear pressure-deflection curve is evident. As the plate experiences larger deflections, higher pressure increase increments are required to produce the same deflection increments. The plate is becoming stiffer as its deflection increases. Figure 3.8(b) shows a magnification of part of this curve, from 0 to 0.06 MPa applied pressure. Notice that the pressure-deflection curve is linear up to deflections of approximately half the plate thickness, $t_{vm} = 3.5\mu m$. Linear deflection theory is accurate for this small deflection regime.

Figure 3.8(c) displays the normalized plate deflection shapes for P_3 loading of 0.01MPa, 0.1MPa, 1MPa, 10MPa, and 100MPa. When $P_3 = 0.01MPa$, the plate deflection is very small ($2.8\mu m$), and therefore the plate experiences only bending stresses. When $P_3 = 0.1MPa$, the plate deflection is $11\mu m$ and therefore the plate has entered the large deflection regime. From

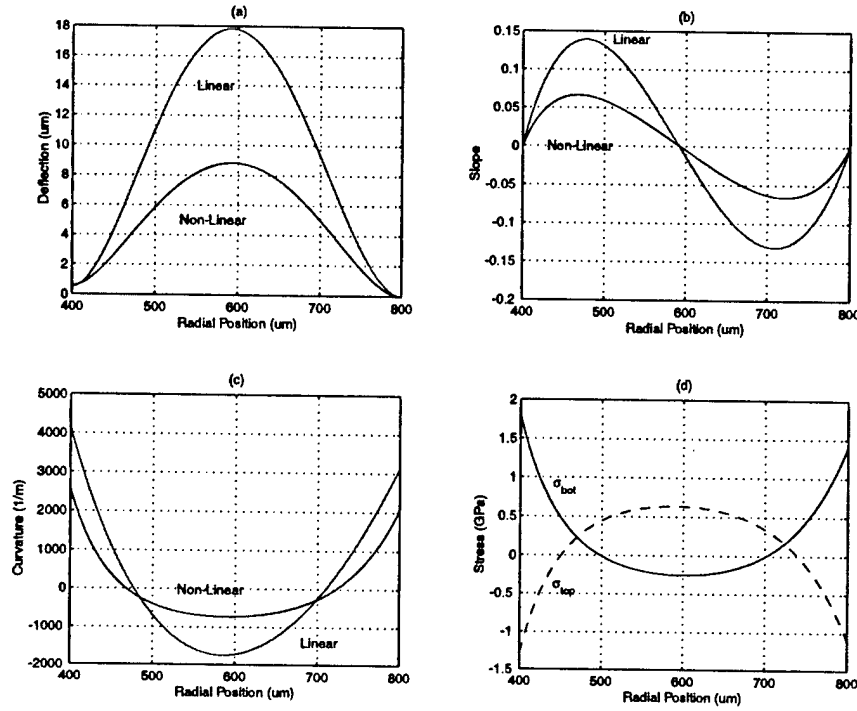


Figure 3.7: Deflection of thin annular plate under loading $P_1 = 2.9 \text{ MPa}$, $P_2 = 0$, $P_3 = 1.3 \text{ MPa}$. Plate dimensions and properties: $r_b = 400 \mu\text{m}$, $r_a = 800 \mu\text{m}$, $t = 7 \mu\text{m}$, $E_{si} = 165 \text{ GPa}$, and $\nu = 0.22$.

Figure 3.8(d), one can observe a slight reduction in the size of boundary layer regions near r_b and r_a . When $P_3 = 10 \text{ MPa}$, the deflection is relatively large ($64 \mu\text{m}$). The boundary layers have been decreased to very thin regions. In the central portions of the plate, the in-plane tensile stresses dominate the bending stresses and therefore the plate curvature is constant. However, near the boundaries, the bending stresses are not negligible and therefore the plate curvature changes significantly. This is the region of transition from membrane to plate behavior.

3.4.4 Loading: $P_1 = P_2 = 0$, $P_{HAC} = 100 \text{ kPa}$, Varying N_o

It is also interesting to note the effect of pretensioning on the plate deflection. Pretensioning the plate in the radial direction has the same effect as forcing the plate to experience large deflections, in that it increases the in-plane tensile stress within the plate. Figure 3.9 illustrates this phenomenon for the plate described above under pressure loading $P_1 = P_2 = 0$ and $P_3 = 100 \text{ kPa}$. As the plate pretension (in units of stress) is increased from zero to 750 MPa , the plate deflection at r_b decreases from $11.5 \mu\text{m}$ to $1.3 \mu\text{m}$. It is therefore critical when micromachining thin plate structure to estimate the magnitude of residual in-plane stresses that could result from

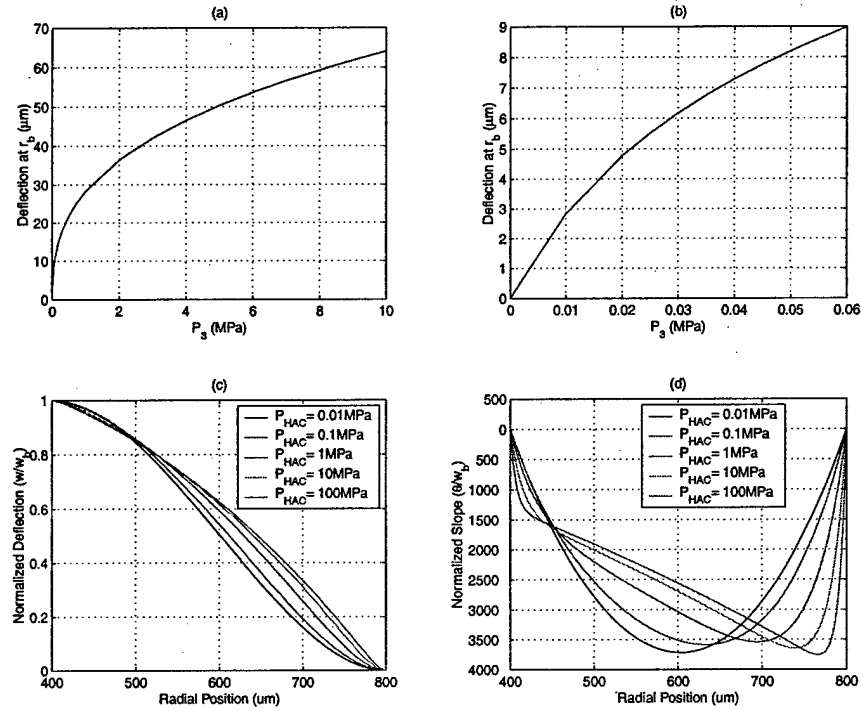


Figure 3.8: Deflection of thin annular plate under varying P_3 loading with $P_1 = P_2 = 0$ and $N_o = 0$. Plate dimensions and properties: $r_b = 400\mu m$, $r_a = 800\mu m$, $t = 7\mu m$, $E_{si} = 165 GPa$, and $\nu = 0.22$.

wafer processing. The presence of any such stresses could substantially alter the performance from that predicted by theory.

3.5 Matlab Non-Linear Tools

The previous results have proven the capability of this numerical code to predict the non-linear deformation behavior of a thin plate structure with a rigid central cap. In the subsequent active valve design, modeling, and optimization chapters of the thesis, this large deflection numerical code is implemented in three distinct ways to allow for a variety of approaches to understanding the non-linear behavior of the valve cap and membrane. Each of these approaches is contained in a separate MatlabTM numerical code, and therefore act as a modeling tool for future use. These approaches are illustrated in Figure 3.10.

The first approach, detailed in Figure 3.10(a), calculates the valve cap deflection and associated plate behavior, given the pressure across the valve membrane P_{vm} and the effective force acting on the valve cap F_{vc} . For the loading terminology in this chapter, the effective

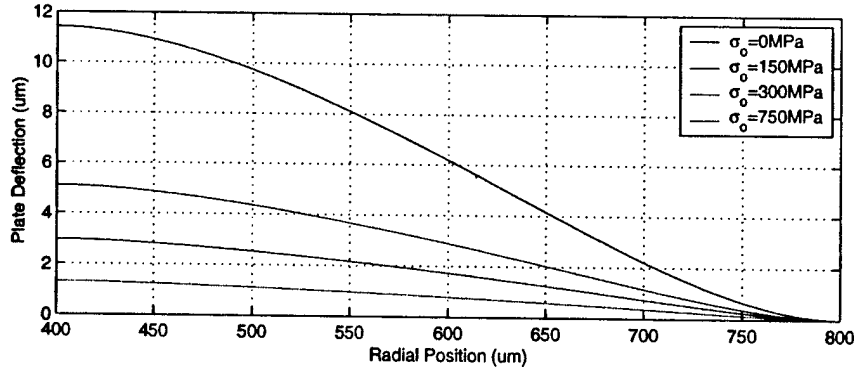


Figure 3.9: Deflection of a thin annular plate under loading $P_1 = P_2 = 0$, $P_{HAC} = 100kPa$, with varying N_o . Plate dimensions and properties: $r_b = 400\mu m$, $r_a = 800\mu m$, $t = 7\mu m$, $E_{si} = 165GPa$, and $\nu = 0.22$.

force on the valve cap would be $F_{vc} = A_{vc}(P_3 - P_1)$. The effective force could be the resultant of only pressures P_3 and P_1 (acting over the valve cap area) if the valve cap is unrestrained, or it could be the resultant of pressures P_3 , P_1 , and a reaction force imposed on the valve cap by an external structure if the cap is closed against a valve stop. This MatlabTM code, labeled NLValveCapMembrane-CaseA.m and included for reference in Appendix B.1, will be used in Chapter 3 as a part of the complete non-linear active valve quasi-static model.

The second approach, detailed in Figure 3.10(b), calculates the pressure across the valve membrane P_{vm} such that the valve deflection attains a certain value Z_{vc} , given a known value of F_{vc} . This MatlabTM code, labeled NLValveCapMembrane-CaseB.m and included for reference in Appendix B.2, will be important in Chapter 5 for determining the necessary $P_{HAC}(t)$ time history within the active valve in order to produce a desired $Z_{vc}(t)$ trajectory when the external loading time histories $P_1(t)$ and $P_2(t)$ are given.

The third approach, detailed in Figure 3.10(c), calculates the force on the valve cap F_{vc} required to produce a particular valve cap deflection Z_{vc} under a known loading P_{vm} . This MatlabTM code, labeled NLValveCapMembrane-CaseC.m and included for reference in Appendix B.3, will be used in Chapter 3 to determine the reaction force exerted by a valve stop structure on the valve cap when given all three pressure loadings P_1 , P_2 , P_3 , and an imposed valve cap deflection (ie: hitting a stop).

All three of these MatlabTM tools share the same non-linear theory and finite-difference implementation as presented in this chapter. They differ only in the organization of the system matrices and the procedure in which the various known and unknown quantities are handled. All are capable of outputting the entire plate spatial deflection vector, as well as the spatial slope and curvature vectors, and the plate top and bottom surface spatial stress vectors. The

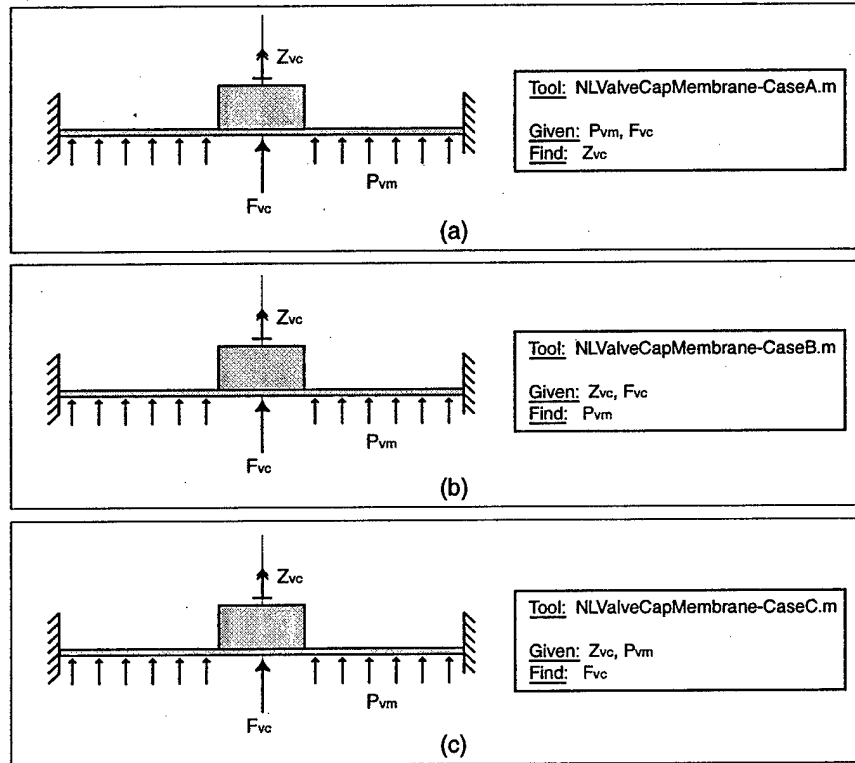


Figure 3.10: Matlab Tools for Use in Subsequent Chapters: (a) NLValveCapMembrane-CaseA.m, (b) NLValveCapMembrane-CaseB.m, and (c) NLValveCapMembrane-CaseC.m.

codes included in Appendix B are written as MatlabTM functions.

3.6 Conclusions

This chapter has presented the theory governing the non-linear deflection of a thin annular plate with a rigid central cap and has detailed the development of a numerical code to capture this behavior. The results of the code have been compared to linear theory and important phenomena such as in-plane pretension effects and plate/membrane boundary layer regions have been discussed. Since this theory is critical for the development of the active valve device proposed in this thesis, three distinct MatlabTM codes/tools have been written for use in the design, modeling, and valve optimization chapters that follow.

Bibliography

- [1] Y.H. Su, K.S. Chen, D.C. Roberts, and S.M. Spearing, "Large Deflection Analysis of a Pre-Stressed Annular Plate With a Rigid Boss Under Axisymmetric Loading", *Journal of Micromech. Microeng.* 11 (2001) pp. 645-653.
- [2] M. Sheplak and J. Dugundji, "Large Deflections of Clamped Circular Plates Under Initial Tension and Transitions to Membrane Behavior", *Journal of Applied Mechanics*, Vol. 65, pp.107-115, March 1998.
- [3] S. Timoshenko. *Theory of Plates and Shells*. McGraw-Hill Book Company, Inc., New York and London, 1940.

Chapter 4

Active Valve Non-Linear Model and Simulation

This chapter combines the linear and non-linear modeling tools presented in Chapters 2 and 3 to create a quasi-static structural model of the full piezoelectrically-driven active valve. In addition, the chapter introduces a dynamic simulation architecture for the valve, which includes the inertia and damping associated with the drive element piston and valve cap structural elements. Calculation of the coupled fluid-structure resonant valve frequency, based on finite-element models, is also presented.

4.1 Quasi-Static Active Valve Model

A quasi-static active valve model, incorporating only linear structural behavior, was presented in Chapter 2. By combining this model with the numerical code developed in Chapter 3 to model the large-deflection behavior of the valve membrane, a complete quasi-static non-linear active valve model can be formulated. This model consists of two primary solving steps, as shown in Figure 4.1. In the first step, a matrix A is generated which captures all linear relationships within the valve structure. In the second step, this matrix is used in combination with one of the previously described non-linear tools, `NLValveCapMembrane-CaseA.m`, to solve iteratively for the complete active valve behavior.

Since the valve membrane is the only structural component of the active valve for which non-linear modeling is required, the linear compliance matrix A can be defined by:

$$Y = [A]U. \quad (4.1)$$

where Y is a vector of active valve variables to be calculated using linear theory, and U is a vector of input variables required to calculate Y . This matrix relation can be rewritten in

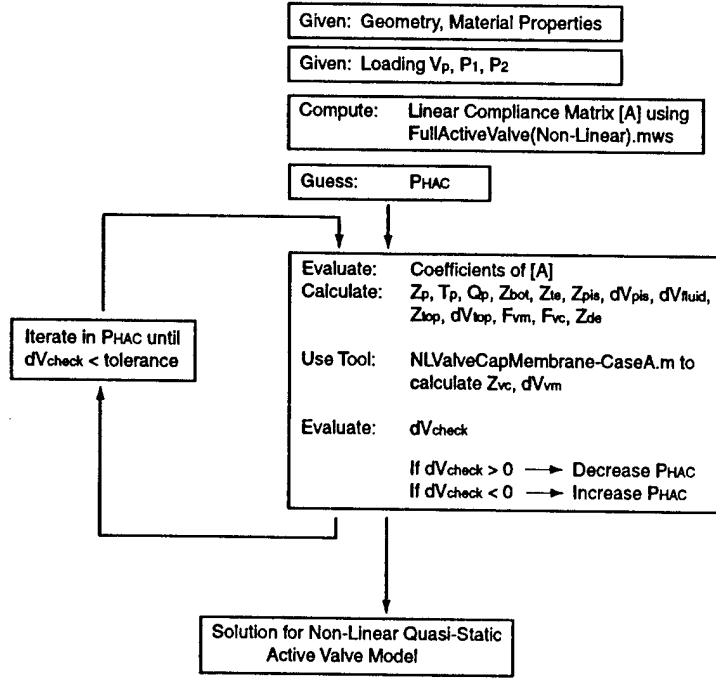


Figure 4.1: Calculation procedure for non-linear quasi-static active valve model.

more detail as:

$$\begin{bmatrix} Z_p \\ T_p \\ Q_p \\ Z_{bot} \\ Z_{te} \\ dV_{te} \\ Z_{pis} \\ dV_{pis} \\ dV_{fluid} \\ Z_{top} \\ dV_{top} \\ F_{vm} \\ F_{vc} \\ Z_{de} \end{bmatrix} = \begin{bmatrix} A_{1,1} & A_{1,2} & A_{1,3} & A_{1,4} \\ A_{2,1} & A_{2,2} & A_{2,3} & A_{2,4} \\ A_{3,1} & A_{3,2} & A_{3,3} & A_{3,4} \\ A_{4,1} & A_{4,2} & A_{4,3} & A_{4,4} \\ A_{5,1} & A_{5,2} & A_{5,3} & A_{5,4} \\ A_{6,1} & A_{6,2} & A_{6,3} & A_{6,4} \\ A_{7,1} & A_{7,2} & A_{7,3} & A_{7,4} \\ A_{8,1} & A_{8,2} & A_{8,3} & A_{8,4} \\ A_{9,1} & A_{9,2} & A_{9,3} & A_{9,4} \\ A_{10,1} & A_{10,2} & A_{10,3} & A_{10,4} \\ A_{11,1} & A_{11,2} & A_{11,3} & A_{11,4} \\ A_{12,1} & A_{12,2} & A_{12,3} & A_{12,4} \\ A_{13,1} & A_{13,2} & A_{13,3} & A_{13,4} \\ A_{14,1} & A_{14,2} & A_{14,3} & A_{14,4} \end{bmatrix} \begin{bmatrix} V_p \\ P_1 \\ P_2 \\ P_{HAC} \end{bmatrix} \quad (4.2)$$

For a given active valve geometry, the coefficients of the linear compliance matrix A are calculated (see MapleTM code FullActiveValve(Non-Linear).mws in Appendix C.1). For a known set of loadings V_p , P_1 , and P_2 , an initial guess for the equilibrium pressure P_{HAC} is assumed,

and the variables contained in Y are calculated. With this value of P_{HAC} , the non-linear tool `NLValveCapMembrane-CaseA.m` is called to calculate Z_{vc} and dV_{vm} . A check is then made of the summation of swept volumes,

$$dV_{check} = dV_{vm} + dV_{top} - dV_{te} - dV_{pis} - dV_{fluid}. \quad (4.3)$$

If $dV_{check} > 0$, the initial guess for P_{HAC} was too large. Conversely, if $dV_{check} < 0$, the initial guess for P_{HAC} was too small. Depending on the result, a modified value of P_{HAC} is attempted. This iteration procedure is carried out until subsequent iteration values of dV_{check} are confined to within a specified tolerance. At this point, an equilibrium solution for the active valve under the specified loading conditions has been achieved.

4.2 Accuracy of Quasi-Static Model

The accuracy of this quasi-static active valve model can be verified by comparing its results under various loading conditions to those of a finite-element model. In making this comparison, the goodness of the assumptions used in this analytical model can be evaluated.

4.2.1 Assumptions in Model

The analytical active valve model uses linear and non-linear plate theory to model the compliances of the structural components. Boundary conditions for each of the components were chosen in an effort to accurately represent the geometries of a real device. However, it would be impossible to achieve 100% perfect correlation between the analytical model and a finite-element model, or a real device. Therefore, prior to comparing the analytical and finite-element models, the following thoughts concerning model correlation are put forth:

1. Both the valve membrane structure and the drive element piston tethers have been modeled with rigid boundary conditions along their respective inner and outer circumferences. In reality, because these interfaces are not in fact rigid, one might expect a "local" softening effect at these locations that would make these plate structures softer than predicted by theory.
2. Bending and shearing effects have been accounted for in the linear analytical equations governing the drive element piston, the top plate structure, and the bottom plate structure. Due to the fact that shearing coefficients are not well understood for these types of plate geometries, some non-correlation between analytical and finite-element results is expected. Additionally, because these plate geometries and associated boundary conditions are somewhat complex (ie: the presence of the piezoelectric cylinder beneath the piston and above the bottom plate), some degree of non-correlation is expected.

It is hoped, however, that even with all of these uncertain issues associated with material properties and geometric boundary conditions, the correlation between the analytical and finite-element model will be within $\sim 10\%$ for a range of loading parameters that covers the design space for the proposed active valve.

4.2.2 FEM Model Geometries and Correlation Procedure

Two finite-element models of the active valve have been developed to estimate the accuracy of the analytical quasi-static active valve model. The first model, illustrated in Figure 4.2, uses 8-node axisymmetric plane elements for all of the component structures, including the fluid. Material properties for silicon and pyrex are assigned appropriately, as are the bulk modulus properties for the contained hydraulic fluid. As shown in Figures 4.2(b) and 4.2(c), the valve membrane and drive element tethers structures do not include fillet radius features. Since the analytical model does not include the effect of fillet radii either, this allows for a level comparison. Estimates of maximum stress in these structures, however, will not be accurate.

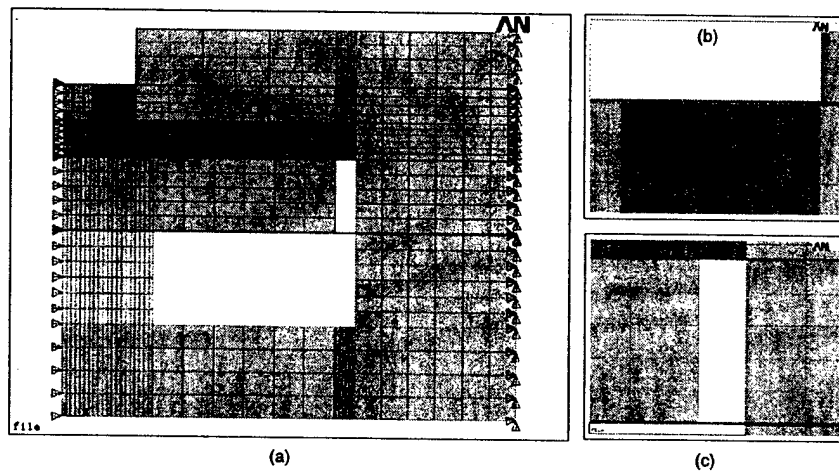


Figure 4.2: An ANSYSTM finite-element model of the full active valve without fillet radius features on the valve membrane and drive element tether structures : (a) entire device, (b) close-up view of valve cap and membrane, and (c) close-up view of drive element tethers.

The second model, illustrated in Figure 4.3, also used 8-node axisymmetric plane elements and the same material definitions. However, this model does include adjustable size fillet radius features on the valve membrane and the drive element tether structures. Figures 4.3(b) and 4.3(c) show close-ups of these regions. This enables a determination of the degree of stiffening that the fillets add to the structures and also allows for accurate estimation of stress concentrations in the structures. Both finite-element models have gone through a convergence

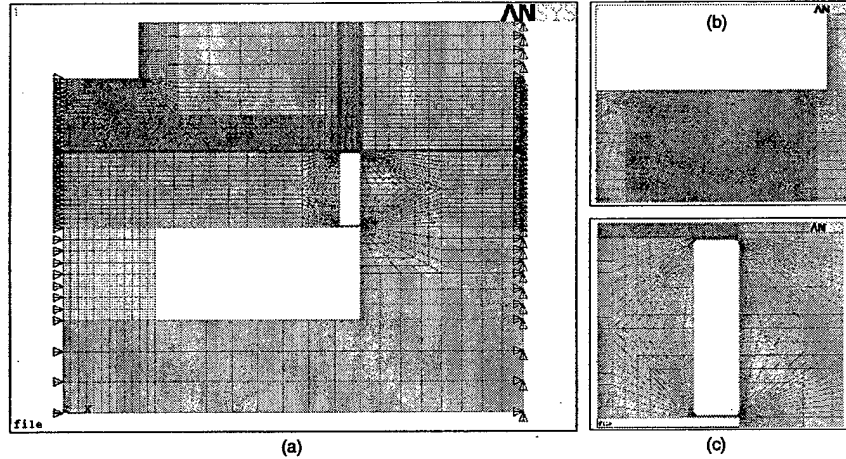


Figure 4.3: ANSYS finite-element model of full active valve with fillet radius features included: (a) entire device, (b) close-up view of valve cap and membrane, and (c) close-up view of drive element tethers.

study to ensure that the element mesh densities are fine enough to produce reliable results.

4.2.3 Model Correlation Procedure

The procedure for comparing the analytical quasi-static active valve model to the finite-element models is documented below. The procedure involves a systematic study of the correlation between these models for varying boundary condition and fillet radius assumptions.

1. To determine the modeling accuracy of the piezoelectric material, valve membrane, drive element tethers, and hydraulic fluid in the analytical model, all other structural components (valve cap, drive piston, top plate, and bottom plate) in the model are made rigid (ie: $\Xi_{Z_{bot}}^T = \Xi_{Z_{pis}}^T = \Xi_{dV_{pis}}^T = \Xi_{Z_{pis}}^P = \Xi_{dV_{pis}}^P = \Xi_{Z_{top}}^P = \Xi_{Z_{top}}^F = 0$). Behavior of the analytical valve is compared to the finite-element model (without fillets) with identical conditions on the component stiffnesses. Figure 4.4(a) illustrates the FEM model. Infinitely stiff regions are shaded dark.
2. To determine the modeling accuracy of the drive piston, top structural plate, and bottom structural plate, the analytical model is run with all compliances in their normal state. Behavior of the analytical model is compared to the finite-element model (without fillets) with infinitely stiff regions as shown in Figure 4.4(b). This comparison will validate the accuracy of the full analytical model with all compliances included.
3. To evaluate the effect of the fillet radius features and additional sidewall material on the

valve behavior, the finite-element model (with fillet radius = $25 \mu m$) with no regions of infinite stiffness is run, as illustrated in Figure 4.4(c). The boundary condition in this model is at the outer radius of the entire structure rather than at the outer radius of the hydraulic amplification chamber. This is a more realistic model of a fabricated valve device. Comparison is made to the full analytical model with all compliances in their normal state.

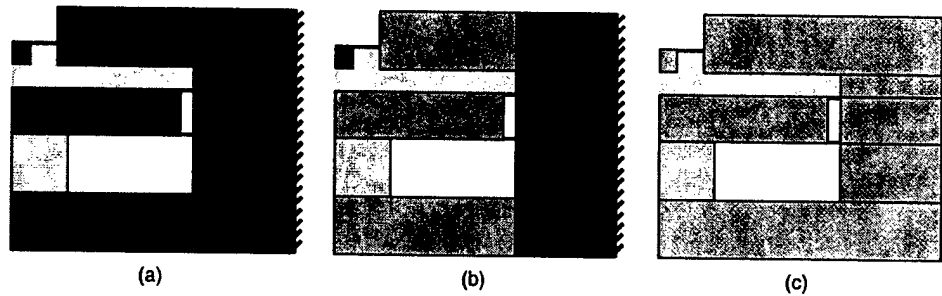


Figure 4.4: ANSYSTM finite-element comparison stages: (a) Top plate, bottom plate, piston, valve cap, and side structures are rigid, (b) Only valve cap and side structures are rigid, and (c) No structures rigid.

To cover the design space for the active valve geometry under consideration, the following three loading scenarios are applied:

1. $V_p=1000 \text{ V}$, $P_1=0$, $P_2 = 0$
2. $V_p=0$, $P_1=1 \text{ MPa}$, $P_2 = 1 \text{ MPa}$
3. $V_p=500 \text{ V}$, $P_1=0.5 \text{ MPa}$, $P_2 = 0$.

These loading scenarios are chosen to capture the valve behavior throughout a complete cycle of deflection. The first loading scenario produces a large positive valve cap deflection, the second loading scenario produces a large negative valve cap deflection, and the third scenario produces a small positive valve cap deflection. The comparison procedure detailed above is carried out for each of the loading scenarios to evaluate the accuracy of the analytical quasi-static active valve model.

4.2.4 Valve Geometry

The active valve geometry used in this comparison study is detailed in the following table. These dimensions are chosen to represent a typical active valve device.

Geometric Dimensions:

| Component | Parameters | | | |
|------------------|-----------------------|-----------------------|-----------------------|-----------------------|
| Valve Cap | $R_{vc} = 310\mu m$ | $R_{vm} = 800\mu m$ | $t_{vm} = 10\mu m$ | $t_{vc} = 400\mu m$ |
| Top/Bottom Plate | $t_{top} = 1000\mu m$ | $t_{bot} = 1000\mu m$ | | |
| HAC Chamber | $R_{te} = 3.225mm$ | $H_{HAC} = 400\mu m$ | | |
| Piston/Tethers | $R_{pis} = 3mm$ | $t_{pis} = 800\mu m$ | $t_{tetop} = 10\mu m$ | $t_{tebot} = 10\mu m$ |
| Piezo | $L_p = 1mm$ | $R_p = 1mm$ | | |

Material Properties:

| Material | Properties | | |
|----------|-----------------------------|-----------------------|----------------------|
| Silicon | $E_{Si} = 165GPa$ | $\nu_{Si} = 0.22$ | $\alpha_{Si} = 1.25$ |
| Pyrex | $E_{pyrex} = 48GPa$ | $\nu_{pyrex} = 0.20$ | |
| Piezo | $d_{33} = 2000\frac{pC}{N}$ | $E_{piezo} = 9.01GPa$ | |
| Fluid | $K_{fluid} = 2.0GPa$ | | |

The critical valve parameters chosen to serve as comparisons between the two models are the valve cap deflection Z_{vc} , the top plate structure deflection Z_{top} , the hydraulic amplification chamber pressure P_{HAC} , the drive piston center deflection Z_{pis} , the top tether deflection Z_{te} , and the bottom plate structure center deflection Z_{bot} . These parameters are reviewed in Figure 4.5. In addition, for the finite-element model with fillet radius features, the maximum membrane stress in the model is also monitored.

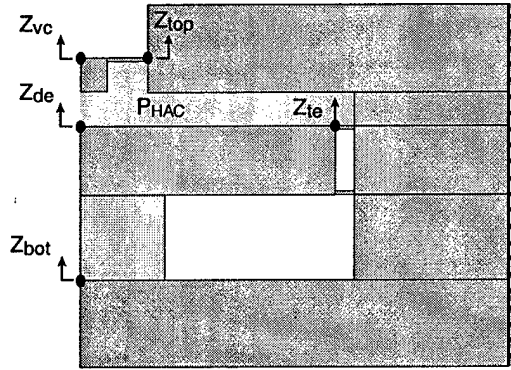


Figure 4.5: Variables monitored in analytic and FEM models.

4.2.5 Model Correlation

Finite-Element Model (without fR), Rigid Compliances

In comparing the analytical model to the finite-element model without fillet radius features for the case where the drive piston, the top structural compliance, the bottom structural compliance, and the valve cap are all designated to be rigid, the results correlate extremely well. Table

4.1 shown below compares these results for the three loading scenarios. For each of the three loading scenarios, the valve cap deflection correlates within 0.4%. All of the other parameters also correlate very well, within 1%. This correlation proves that the valve membrane non-linear relations, the drive element tether relations, the fluid compliance, and the piezoelectric material behavior are all modeled very accurately in the non-linear quasi-static analytical active valve model.

TABLE 4.1: Model Correlation (without fR), Rigid Compliances

| Loading | Model | Variables to Monitor | | | | | | |
|---|----------|-------------------------|-------------------------|-------------------------|--------------------------|--------------------------|--------------------|-------------------------|
| | | Z_{vc} (μm) | Z_{de} (μm) | Z_{te} (μm) | Z_{top} (μm) | Z_{bot} (μm) | P_{HAC} (kPa) | σ_{max} (GPa) |
| Scenario 1 $V_p = 1000V$ $P_1 = 0, P_2 = 0$ | Analytic | 26.269 | 1.136 | 1.136 | 0 | 0 | 781 | 1.45 |
| | FEM | 26.218 | 1.143 | 1.143 | 0 | 0 | 775 | n/a |
| | % Dif | 0.2 % | 0.6 % | 0.6 % | 0 % | 0 % | 0.8 % | n/a |
| | | | | | | | | |
| Scenario 2 $V_p = 0V$ $P_1 = 1MPa, P_2 = 1MPa$ | Analytic | -20.770 | -0.597 | -0.597 | 0 | 0 | 567 | 0.96 |
| | FEM | -20.858 | -0.591 | -0.591 | 0 | 0 | 562 | n/a |
| | % Dif | 0.4 % | 1.0 % | 1.0 % | 0 % | 0 % | 0.9 % | n/a |
| | | | | | | | | |
| Scenario 3 $V_p = 500V$ $P_1 = 0.5MPa, P_2 = 0$ | Analytic | 14.207 | 0.612 | 0.612 | 0 | 0 | 349 | 0.66 |
| | FEM | 14.175 | 0.614 | 0.614 | 0 | 0 | 347 | n/a |
| | % Dif | 0.2 % | 0.3 % | 0.3 % | 0 % | 0 % | 0.6 % | n/a |
| | | | | | | | | |

Finite-Element Model (without fR), Normal Compliances

In comparing the analytical model to the finite-element model without fillet radius features for the case where the drive piston, the top structural compliance, and the bottom structural compliance are returned to their normal values, the results correlate fairly well. The valve cap deflection for the first loading scenario correlates within 3.7%, for the second loading scenario within 0.4%, and for the third loading scenario within 7.5%. This larger value of 7.5% is not that bad since the valve cap deflection is relatively small. As loading is applied that forces the valve cap near zero deflection, one would expect the % error to increase even though the absolute difference between the model deflections is much smaller than $1\mu m$.

TABLE 4.2: Model Correlation (without fR), Normal Compliances

| Loading | Model | Variables to Monitor | | | | | | |
|---|----------|-------------------------|-------------------------|-------------------------|--------------------------|--------------------------|--------------------|-------------------------|
| | | Z_{vc} (μm) | Z_{de} (μm) | Z_{te} (μm) | Z_{top} (μm) | Z_{bot} (μm) | P_{HAC} (kPa) | σ_{maz} (GPa) |
| Scenario 1 $V_p = 1000V$ $P_1 = 0, P_2 = 0$ | Analytic | 21.787 | 1.213 | 0.792 | 0.087 | -0.251 | 482 | 1.03 |
| | FEM | 22.629 | 1.267 | 0.837 | 0.094 | -0.249 | 510 | n/a |
| | % Dif | 3.7 % | 4.3 % | 5.4 % | 7.5 % | 0.8 % | 5.5 % | n/a |
| Scenario 2 $V_p = 0V$ $P_1 = 1MPa, P_2 = 1MPa$ | Analytic | -24.107 | -0.560 | -0.846 | 0.031 | -0.179 | 371 | 1.25 |
| | FEM | -24.009 | -0.532 | 0.834 | 0.039 | -0.180 | 396 | n/a |
| | % Dif | 0.4 % | 5.0 % | 1.4 % | 20.5 % | 0.6 % | 6.3 % | n/a |
| Scenario 3 $V_p = 500V$ $P_1 = 0.5MPa, P_2 = 0$ | Analytic | 9.654 | 0.595 | 0.378 | 0.042 | -0.129 | 249 | 0.45 |
| | FEM | 10.436 | 0.628 | 0.409 | 0.044 | -0.126 | 259 | n/a |
| | % Dif | 7.5 % | 5.3 % | 7.6 % | 4.5 % | 2.3 % | 3.9 % | n/a |

In looking at the other monitored variables, one notices that they all correlate within 7.5%, except for Z_{top} in Loading Scenario 1. Again, though, this deflection is extremely small, and therefore such a significant error has negligible effect on the rest of the system performance. In fact, from Loading Scenario 1, the following swept volumes are obtained from the analytical model: $dV_{pis} = 4.03e^{-12}m^3$, $dV_{te} = 2.38e^{-11}m^3$, $dV_{top} = 1.11e^{-12}m^3$, $dV_{fluid} = -3.32e^{-12}m^3$, and $dV_{vm} = 2.34e^{-11}m^3$. From these, it is calculated that the volume of fluid lost in the top structural plate compliance is approximately 4% of the swept volume of piston and tether together (the actuation swept volume). Overall, this 4% loss is important, but 20.5% of this 4% is not. In conclusion, the analytical valve model predicts the valve cap deflection very well.

Finite-Element Model (with fR), Normal Compliances

In order to evaluate the accuracy of the analytical valve model with respect to a finite-element model that is more characteristic of the real device, no rigidities are assumed in the finite-element model and fillet radius features are taken into consideration. The finite-element results for Loading Scenario 1 are illustrated graphically in Figure 4.6.

A major realistic effect that is considered in this model is the presence of the rigid boundary condition at the outer radius of the device rather than at R_{te} . This condition serves to soften the top and bottom plate compliances. From Table 4.3 below, it is clear that in all three loading scenarios, Z_{top} and Z_{bot} show very large correlation errors near 50%. This is a result of this softening. It is interesting, however, that even with these large deviations in Z_{top} and Z_{bot} , the overall valve cap deflection correlation is excellent (less than 4% for all loading scenarios). The principal reason for this, again, that the absolute swept volumes associated with these deflections are not very large.

TABLE 4.3: Model Correlation (with fR), Rigid Compliances

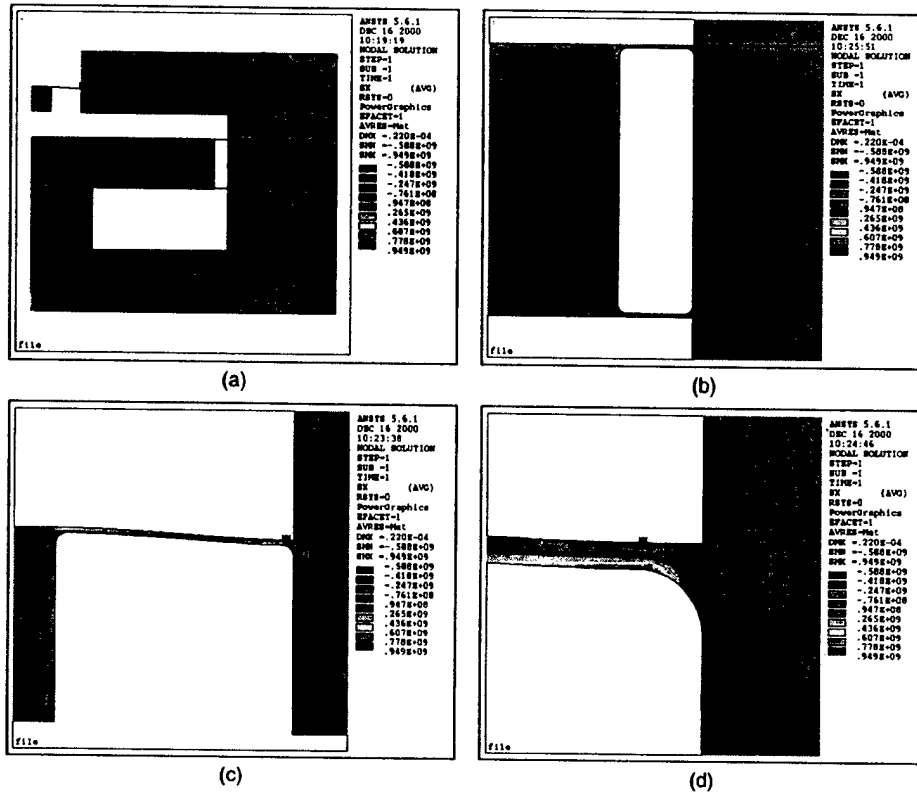


Figure 4.6: ANSYSTM FEM stress contour plots for Loading Scenario 1 on fillet radius model.

| Loading | Model | Variables to Monitor | | | | | | |
|---|----------|-------------------------|-------------------------|-------------------------|--------------------------|--------------------------|--------------------|-------------------------|
| | | Z_{vc} (μm) | Z_{de} (μm) | Z_{te} (μm) | Z_{top} (μm) | Z_{bot} (μm) | P_{HAC} (kPa) | σ_{max} (GPa) |
| Scenario 1 $V_p = 1000V$ $P_1 = 0, P_2 = 0$ | Analytic | 21.787 | 1.213 | 0.792 | 0.087 | -0.251 | 482 | 1.03 |
| | FEM | 22.002 | 1.225 | 0.809 | 0.157 | -0.333 | 464 | 0.95 |
| | % Dif | 1.0 % | 1.0 % | 2.1 % | 44.6 % | 24.6 % | 3.7 % | 7.8 % |
| Scenario 2 $V_p = 0V$ $P_1 = 1MPa, P_2 = 1MPa$ | Analytic | -24.107 | -0.560 | -0.846 | 0.031 | -0.179 | 371 | 1.25 |
| | FEM | -24.269 | -0.552 | -0.826 | 0.071 | -0.237 | 365 | 1.05 |
| | % Dif | 0.7 % | 1.4 % | 2.4 % | 56.3 % | 24.5 % | 1.6 % | 16.0 % |
| Scenario 3 $V_p = 500V$ $P_1 = 0.5MPa, P_2 = 0$ | Analytic | 9.654 | 0.595 | 0.378 | 0.042 | -0.129 | 249 | 0.45 |
| | FEM | 9.283 | 0.590 | 0.371 | 0.078 | -0.176 | 246 | 0.41 |
| | % Dif | 3.8 % | 0.8 % | 1.9 % | 46.2 % | 26.7 % | 1.2 % | 8.9 % |

Another reason, though, has to do with the behavior of the valve cap membrane. Thinking about the valve cap and membrane structure, because the valve cap is no longer rigid, the local behavior at the interface between the membrane and the cap may result in a softer structure. This appears to be the case since a 3.7% less P_{HAC} pressure deflects the valve cap 1.0% more

in the realistic finite-element model than in the analytical model. A counter-effect which most likely helps to minimize this softening of the valve cap and membrane is the presence of the fillet radii. Each fillet radius provides significantly more material at this interface and hence stiffens the structure.

To conclude this section on the analytical quasi-static active valve model, the comparisons between the analytical model and finite-element models have proven that the analytical model very accurately predicts the quasi-static active valve behavior of finite-element models with boundary conditions similar to those expected in fabricated devices. These quasi-static modeling techniques will now serve as the basis for dynamic models which will be able to capture higher-order dynamic effects within the active valve structure.

4.3 Finite-Element Resonant Behavior

To gain a rough idea of the frequency capabilities of this valve structure, a 2-D finite-element model without fillet radius features was evaluated using modal analyses in ANSYSTM. By definition, modal analyses are only valid for purely linear systems. Consequently, the resulting resonant frequencies are good predictions of active valve behavior only if the valve is operated such that valve cap and membrane deflections are within the small-deflection regime (ie: small applied voltage to the piezoelectric material). This model incorporates four-node plane elements for the silicon and glass structural parts of the valve and 4-node acoustic fluid elements for the liquid contained within the hydraulic amplification chamber. These acoustic elements enable fluid-structure interaction between the fluid and the surrounding structure of the HAC chamber. For the active valve geometry used in this chapter, the modal analysis results indicate a first modal frequency at $f_1 = 25.6kHz$ and a second modal frequency at $f_2 = 102.7kHz$, as shown in Figure 4.7.

Since, during real valve operation, the valve cap and membrane structure are required to experience deflections well into the non-linear regime, this first modal frequency can be taken as a lower limit to the actual resonant excitation. As a note to the reader, the active valve geometry considered in this chapter is slightly different from the valve devices built and tested in later parts of this thesis. The valve membrane is slightly thicker ($t_{vm} = 10\mu m$) than in the experimental devices ($t_{vm} = 6\mu m$) and the HAC chamber is slightly reduced in size ($R_{te} = 3.225mm$) than in the experimental devices ($R_{te} = 3.613mm$), differences which serve to make the experimental devices softer than the geometry evaluated in this chapter. As a result, a slightly reduced modal frequency can be expected in the experimental valve device, as detailed in Chapter 9. The modal finite-element models used through this thesis, however, are identical to the one presented in this chapter.

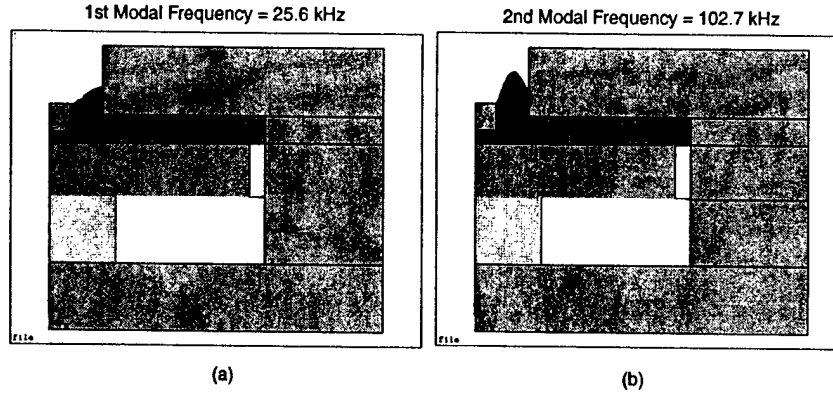


Figure 4.7: ANSYSTM FEM mode shapes: (a) 1st modal frequency = 25.601 kHz, (b) 2nd modal frequency = 102.67 kHz.

4.4 Dynamic Active Valve Simulation

To properly capture the non-linear effects of the valve membrane deformation at high frequency, and to include important dynamic effects, such as the drive element piston inertia and the valve cap inertia and damping, a SimulinkTM simulation architecture is presented in this section. The structural compliances within the active valve simulation are based exactly upon the linear and non-linear modeling tools presented in Chapters 2 and 3 of this thesis. The simulation architecture can be broken down into four major subsystems, as illustrated in Figure 4.8: a matrix of linear coefficients describing the bulk of the active valve behavior, a series of non-linear look-up tables that captures the large-deflection valve membrane deformation and stress, a valve cap dynamics block, and a drive piston dynamics block.

4.4.1 Linear Matrix Relations

As discussed in Chapter 2, all of the structural elements except the valve membrane operate in linear deformation regimes. Within the simulation, therefore, a matrix of compliance and parameter coefficients are included for these linear relations:

$$\begin{bmatrix} T_p \\ F_{te} \\ P_{HAC} \\ Z_{top} \\ Charge \end{bmatrix} = \begin{bmatrix} A_{1,1} & A_{1,2} & A_{1,3} & A_{1,4} & A_{1,5} \\ A_{2,1} & A_{2,2} & A_{2,3} & A_{2,4} & A_{2,5} \\ A_{3,1} & A_{3,2} & A_{3,3} & A_{3,4} & A_{3,5} \\ A_{4,1} & A_{4,2} & A_{4,3} & A_{4,4} & A_{4,5} \\ A_{5,1} & A_{5,2} & A_{5,3} & A_{5,4} & A_{5,5} \end{bmatrix} \begin{bmatrix} Z_{te} \\ F_{vc} \\ dV_{vm} \\ P_{HPR} \\ V_p \end{bmatrix} \quad (4.4)$$

Inputs to this matrix are the Z_p and Z_{vc} variables fed back from the piston and valve cap dynamic blocks respectively, dV_{vm} fed back from the non-linear valve membrane look-up table,

variables F_{vc} , dV_{vm} , and σ_{vm} . The size of the look-up tables is governed by the number of calculation points between the upper and lower limits of the inputs Z_{vc} and P_{vm} . For example, the look-up tables used in the simulations in this section take as inputs a Z_{vc} vector 100 elements in length, covering a range from $Z_{vc} = -50\mu m$ to $Z_{vc} = +50\mu m$, and a P_{vm} vector 100 elements in length, covering a range from $P_{vm} = -1.5MPa$ to $P_{vm} = +1.5MPa$. Convergence studies were performed to validate that these vector resolutions were fine enough for accurate results. The MatlabTM file, NLValveCapMembrane-CaseC.m, detailed at the conclusion of Chapter 3 and included in Appendix B.3, is used to create these look-up tables.

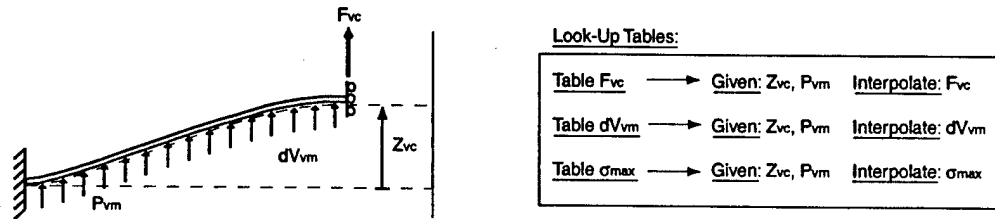


Figure 4.9: Numerical modeling tools are used to generate look-up tables for the non-linear large deflection behavior of the valve cap and membrane. Given a prescribed valve cap displacement Z_{vc} and pressure loading across the membrane P_{vm} , a look-up table for each of F_{vc} , dV_{vm} , and σ_{vm} is created.

4.4.3 Piston and Valve Cap Dynamics

The dynamic behavior of the drive piston structure is governed by the following relation:

$$M_{pis}\ddot{Z}_{pis} + C_{pis}\dot{Z}_{pis} = A_p T_p - A_{pis} P_{HAC} - F_{te} \quad (4.5)$$

The damping coefficient C_{pis} is a lumped parameter that is meant to include the effects of structural damping in the tethers and damping due to fluid interaction. Figure 4.10 displays a schematic of the valve cap mass and the corresponding Simulink block architecture included within the full active valve simulation.

In a similar fashion, the dynamic behavior of the valve cap is represented by the following relation:

$$M_{vc}\ddot{Z}_{vc} + C_{vc}\dot{Z}_{vc} = A_{vc}(P_{HAC} - P_1) - F_{vc} \quad (4.6)$$

The damping coefficient C_{vc} is a lumped parameter that includes the effects of structural damping in the membrane, squeeze film damping due to the valve cap motion when closing the valve, and damping due to fluid-structure interaction. Figure 4.11 displays a schematic of

the valve cap mass and the corresponding Simulink block architecture included within the full active valve simulation.

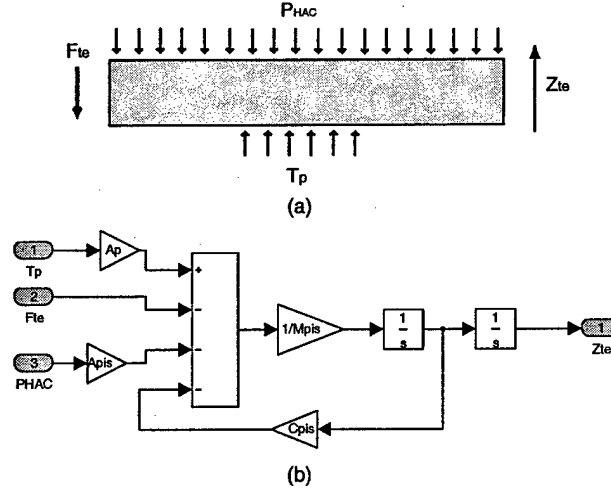


Figure 4.10: Piston Dynamics: (a) free-body diagram of piston structure, and (b) Simulink block architecture.

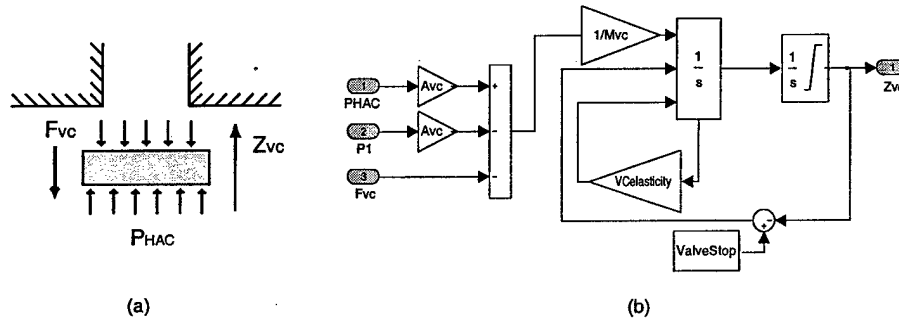


Figure 4.11: Valve cap dynamics: (a) free-body diagram of valve cap structure, and (b) Simulink block architecture.

Exact values of C_{pis} and C_{vc} are difficult to estimate accurately. Values are therefore chosen that result in dynamic responses that are relatively free of high-order oscillations (see results in Figure 5.24), yet still exhibit inertia and phase lag effects. Estimates for the damping ratios of the piston and valve cap (ζ_{pis} and ζ_{vc}) are calculated from these C_{pis} and C_{vc} values by observing the resonant frequency ω_n of each component in small deflection linear regimes, according to the relations $\zeta_{pis} = \frac{C_{pis}}{2\omega_{pis}}$ and $\zeta_{vc} = \frac{C_{vc}}{2\omega_{vc}}$ respectively.

The Simulink block which captures this valve cap dynamic behavior also includes the effect

of the valve cap as it comes into contact with valve stops, either above and/or below the valve cap. This hitting behavior is modeled as an inelastic collision between the cap and the stop. The assumption here is that if the cap impacts the stop with a velocity V_1 , it will bounce back with a lesser velocity V_2 , according to the relation $V_2 = \sqrt{r}V_1$, where $r < 1$ is called the coefficient of restitution. The above formulation for the hitting can be implemented in Simulink by setting V_2 as the initial condition for the valve velocity at the subsequent time step immediately following impact. For further details on active valve and full MHT system simulation results, see Yaglioglu's MIT Master's thesis [8].

4.5 Conclusions

This chapter has presented a complete quasi-static analytical active valve model and a full dynamic active valve simulation architecture for use in predicting structural behavior of a given active valve geometry to a variety of loading conditions. Both models integrate the linear and non-linear tools presented in Chapters 2 and 3, respectively. Overall, the quasi-static analytical active valve model correlates very well with representative finite-element models, thereby justifying many of the boundary condition assumptions in the analytical model. The dynamic simulation architecture enables further investigation of higher-order dynamic effects in the drive element piston and valve cap structures.

Bibliography

- [1] O. Yaglioglu. Master's Thesis, Massachusetts Institute of Technology, 2002.

Chapter 5

Active Valve Design Procedure

So far, this thesis has presented detailed linear and non-linear structural modeling tools that can be used to predict the performance of a given active valve geometry, in response to an applied voltage on the piezoelectric material elements and against known external pressure loadings on the valve cap and membrane structure. Although it is quite important to be able to predict the performance of a predetermined active valve geometry, it is also critical to be able to design a structural geometry that can meet the specifications of and therefore be used within a complete MHT system. In order to accomplish this, relations governing the fluid flow behavior through the MHT system and the interaction of the valve structure with this external hydraulic system must be developed. The goals of this chapter, therefore, are (1) to present modeling tools that capture the interaction between the valve structure and the external hydraulic system, (2) to develop a systematic design procedure that can be used to formulate of an active valve geometry which will satisfy the pressure-flow requirements set by an overall MHT system, and (3) to present higher-order design benefits of incorporating multiple valve cap and membrane structures within the active valve so as to minimize power consumption of the valve.

Section 5.1 revisits a generic MHT system and discusses the performance requirements that this system demands from its active valves. Section 5.2 presents the tools for modeling the pressure-flow relationships in the hydraulic system external to the active valve and develops a related simulation tool for use in the the subsequent design procedure. Section 5.3 details the systematic procedure used to design a single valve cap and membrane active valve geometry. This procedure demonstrates the fundamental steps involved in the design of the active valve, but does not include design options for multiple valve heads. Section 5.4 highlights some important issues associated with free design variables within the procedure. Section 5.5 presents the theory behind valve power consumption and the benefit of incorporating multiple valve caps and membranes within the active valve structure. Section 5.6 presents results of the updated systematic design procedure, which allows for inclusion of multiple valve caps and membranes in the design process. Finally, Section 5.7 validates the capability of the quasi-static design

procedure by comparing the performance of a generated active valve geometry to that of a full dynamic simulation.

5.1 Valve Requirements in Generic MHT System

A schematic of an MHT power harvesting device is shown in Figure 5.1. Out of phase operation of two active valves results in a pulsing flow of fluid from a high pressure reservoir (P_{HPR}) to a low pressure reservoir (P_{LPR}) through a central piezoelectric harvesting chamber [1]. With each cycle of device operation, the increasing and decreasing fluid pressure P_{EHC} in the harvesting chamber (as the chamber fills and evacuates) results in a stressing of the piezoelectric material element(s) and a subsequent generation of charge. For a given harvesting chamber geometry, the system operational frequency f_{sys} and peak-peak pressure P_{EHC} fluctuation in the chamber directly determine the achievable power generation levels. The required cyclic flow rates into and out of the chamber, Q_{in} and Q_{out} , are functions of this pressure fluctuation and the structural chamber volumetric stiffness. Therefore, assuming that a harvesting chamber structural geometry is known, and that f_{sys} , P_{HPR} , P_{LPR} , and a desired P_{EHC} pressure fluctuation are also required, then an inlet and outlet active valve can be designed to permit this overall MHT system performance.

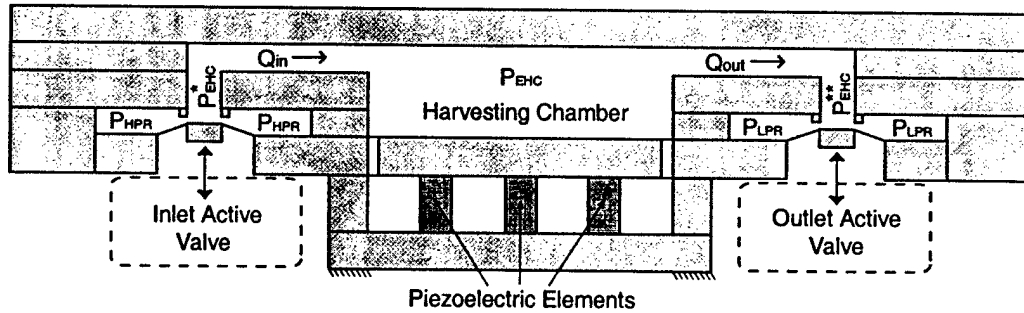


Figure 5.1: Schematic of an MHT power harvesting device. Two active valves regulate flow at high frequency from a high pressure P_{HPR} to a low pressure P_{LPR} . Cyclic pressure change in the harvesting chamber P_{EHC} creates a stressing of the piezoelectric material and a subsequent generation of charge.

In the example MHT power harvesting system shown in Figure 5.1, the top surface of the inlet valve membrane is in contact with the high pressure reservoir and therefore experiences a constant P_{HPR} . The valve cap, on the other hand, sees a changing pressure P_{EHC}^* as the chamber fills and evacuates. Likewise, the top surface of the outlet valve membrane is in contact with the low pressure reservoir and therefore experiences a constant P_{LPR} while the valve cap

sees a changing pressure P_{EHC}^{**} as the chamber fills and evacuates. The assumptions for the areas over which these system pressures act is further detailed in Section 5.2.3. The amounts by which P_{EHC}^* and P_{EHC}^{**} differ from P_{EHC} are functions of the fluid inertial effects in the inlet and outlet flow channels (see Section 5.2.2). With the ability to model these pressure-flow relations through the MHT system, a design procedure can be developed and implemented to design the active valve geometries for the system.

The systematic active valve design procedure that is developed in this chapter is based on quasi-static valve structural behavior. In other words, dynamic effects within the active valve such as those associated with the valve cap mass, the drive element piston mass, and any damping effects are not included. In this way, the basic process of the design procedure can be well understood and estimates for valve geometries to satisfy the MHT system requirements can be generated. Once an active valve geometry is designed in this way, full dynamic simulations of the structure can be run in order to evaluate the goodness of the quasi-static valve design and to enable tweaking of the valve geometries to achieve higher performance. Although this quasi-static design procedure is generic to both the MHT actuator and power harvesting applications, for purposes of clarity, the discussions in this thesis will center on the design of active valves to be used in the previously described MHT power harvesting system. Furthermore, without any loss of generality, the focus of this chapter will be solely on the design of the inlet active valve for the harvesting system.

To regulate flow into the MHT harvesting chamber so as to meet the overall system requirements, the inlet valve membrane and cap structure must be sized properly to ensure adequate stroke of the valve cap and to allow sufficient fluid flow through the orifice to fill the chamber in the allotted time. In addition, under these external pressure loadings, stresses within the valve cap and membrane structure must be kept below the fracture strength of the membrane material. The piezoelectric drive portion of the valve must be designed so as to minimize the overall volume of the device, yet still provide adequate actuation for pressurizing and producing volume change to the hydraulic amplification chamber. Further design issues, such as valve power consumption and the incorporation of multiple valve heads within a single active valve structure, will be covered in detail in this chapter.

5.2 Modeling of External Hydraulic System

Before presenting the quasi-static active valve design procedure, the modeling of the fluid-flow relations in the MHT system external to the active valve structure must be discussed. The inlet active valve within the example MHT power harvesting device regulates flow from the high pressure reservoir to the harvesting chamber. As fluid passes over the valve membrane and cap, it exerts pressures on these structures. These pressures and flow rates are a function

of the opening and closing action of the valve cap against its stop, the geometry of the fluid channel that carries fluid from the valve to the chamber, and the effective hydraulic stiffness of the harvesting chamber being filled. This section details the techniques used to model the pressure-flow relations for each of these system features. In the following discussions, it is assumed that that inlet and outlet valves operate each with a 50% duty cycle, ie: the inlet valve is open exactly for the first half of the MHT system period $T_{sys} = \frac{2\pi}{f_{sys}}$ while the outlet valve is open for exactly the second half of the system period.

5.2.1 MHT Chamber Stiffness

During the first half of a complete device cycle, the inlet valve is open and the outlet valve is closed. As fluid passes through the valve into the harvesting chamber, the chamber pressure increases. The relationship between the amount of fluid entering the chamber and the pressure rise within the chamber is determined by the effective hydraulic chamber stiffness, K_{EHC} . Figure 5.2(a) shows a simplified schematic of this filling process.

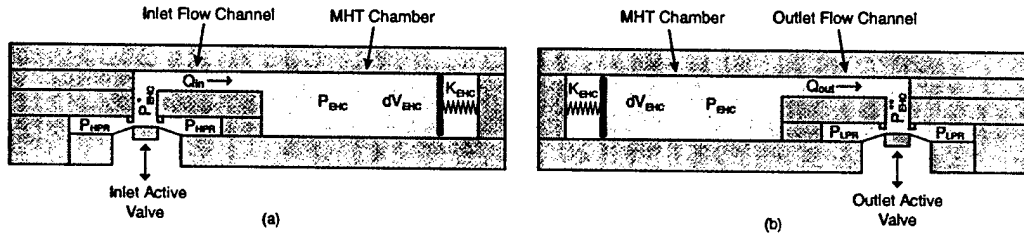


Figure 5.2: Filling and evacuation models for an MHT system: (a) During inlet valve opening and closing, fluid fills the harvesting chamber. (b) During outlet valve opening and closing, fluid evacuates the harvesting chamber. The associated chamber pressure time history $P_{EHC}(t)$ during filling and evacuation is a function of the amount of fluid entering/evacuating the chamber and the chamber volumetric stiffness K_{EHC} .

K_{EHC} is a function of the chamber geometry, material properties, and fluid initial volume. A large K_{EHC} means that a small amount of fluid $dV_{EHC} = \int Q_{in}(t)dt$ flowing into the chamber will result in a large increase in chamber pressure P_{EHC} , whereas a small K_{EHC} means that even a large amount of fluid flow into the chamber will result in only a small chamber pressure increase. The chamber pressure increase as a function of time can be written as

$$\frac{dP_{EHC}}{dt} = K_{EHC}Q_{in}(t). \quad (5.1)$$

A similar model can be used to evaluate the evacuation of fluid through the outlet valve, resulting in a chamber pressure decrease as fluid flows to a low pressure P_{LPR} (see Figure

5.2(b)). For the purposes of this thesis, however, only the inlet valve and corresponding filling of the harvesting chamber are considered.

5.2.2 Valve Channel Inertial Effects

Fluid inertial effects within the flow channel connecting the valve to the harvesting chamber can play a significant role in determining the difference between $P_{EHC}^*(t)$ and $P_{EHC}(t)$ during device operation. This pressure-flow relation can be written as

$$P_{EHC}^*(t) - P_{EHC}(t) = \left(\frac{\rho L_c}{A_c} \right) \dot{Q}_{in} \quad (5.2)$$

where ρ is the fluid density, L_c is the channel length, and A_c is the channel area. For a long channel with small cross-section area, one can expect fluid inertial effects to play a significant role as the pressure P_{EHC}^* builds up to accelerate the fluid slug into the chamber. Conversely, for short channels with large areas, the inertial effects are negligible and the pressure $P_{EHC}^*(t)$ and $P_{EHC}(t)$ will not differ at all. It is important to be aware of these inertial effects when designing and modeling any sort of hydraulic system that contains small channels.

5.2.3 Valve Orifice Flow Relations

Work by previous researchers [3] [4] [5] has shown that for small openings, poppet valves (such as the valve cap in this proposed active valve device) behave as long orifices in which the effects of flow separation and subsequent reattachment dominate the valve flow dynamics.

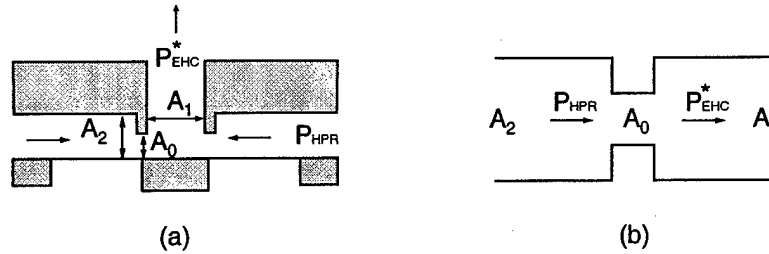


Figure 5.3: Valve orifice representation: (a) valve cap geometry and fluid flow areas, (b) representation of flow through valve as a flow contraction followed by a flow expansion.

Qualitatively, the valve flow can be approximated by a simplified order-of-magnitude valve model. The valve orifice may be characterized as a flow contraction followed by a flow expansion as shown in Figure 5.3(a) and (b). An integral analysis gives a relationship for the combined effect of the flow expansion and contraction. The loss coefficient $\zeta_{orifice}$ is defined as the total

pressure drop $\Delta P = P_{HPR} - P_{EHC}^*$ over the dynamic pressure based on the orifice local mean velocity ($\bar{u} = \frac{Q}{A_0}$)

$$\zeta_{orifice} = \frac{\Delta P}{\frac{1}{2}\rho\bar{u}^2} = \left[\frac{1}{2} \left(1 - \frac{A_0}{A_1} \right)^{\frac{3}{4}} + \left(1 - \frac{A_0}{A_2} \right)^2 \right] \quad (5.3)$$

where the upstream flow area can be approximated as $A_2 = 2\pi R_{vc} H_{upstream}$, the throat area can be approximated by $A_0 = 2\pi R_{vc} Z_{stroke}$, and the downstream flow area can be approximated as $A_1 = \pi R_{vc}^2$. $H_{upstream}$ is the height of the radial flow channel above the valve membrane to the cap and Z_{stroke} is the valve cap opening distance from the valve stop structure.

This approximation, however, is independent of the Reynolds number and therefore holds only for $Re > 10,000$, where fully turbulent flow regimes exist. In microfluidic systems, such as the MHT power harvesting device, Reynolds numbers are expected to fluctuate between approximately 10 and 20,000 as the valve opens and closes [2]. For this reason, correction factors (obtained from experimental results) need to be employed to obtain better estimates of the loss coefficients for these low turbulence and laminar flow regimes [2]. A loss coefficient for each of the contraction and expansion geometries ($\zeta_{contraction}$ and $\zeta_{expansion}$, respectively) is used to approximate the total loss coefficient through the valve, as detailed in the following relation

$$\zeta_{orifice}^* = \zeta_{contraction}(Re, \frac{A_0}{A_2}) + \zeta_{expansion}(Re, \frac{A_0}{A_1}) \quad (5.4)$$

where the Reynolds number is defined as

$$Re = \frac{1}{\pi} \frac{Q}{R_{vc}\nu}. \quad (5.5)$$

Figure 5.4(a) plots $\zeta_{contraction}$ as a function of Re and the contraction area ratio $\frac{A_0}{A_2}$ and Figure 5.4(b) plots $\zeta_{expansion}$ as a function of Re and the expansion area ratio $\frac{A_0}{A_1}$. As a result, the pressure-flow relation for the full valve orifice geometry can be written as

$$\Delta P = P_{HPR} - P_{EHC}^* = \frac{1}{2} \rho \zeta_{orifice}^* \left(\frac{Q^2}{A_0^2} \right). \quad (5.6)$$

All subsequent fluid models discussed in this thesis incorporate these higher-order correction factors to obtain an accurate estimation of the flow behavior. These flow models are based on steady flow phenomenon and do not capture frequency dependent losses. The following assumptions are made to define the valve cap and membrane areas over which the upstream pressure P_{HPR} and the downstream pressure P_{EHC}^* act. Since the valve cap stroke during

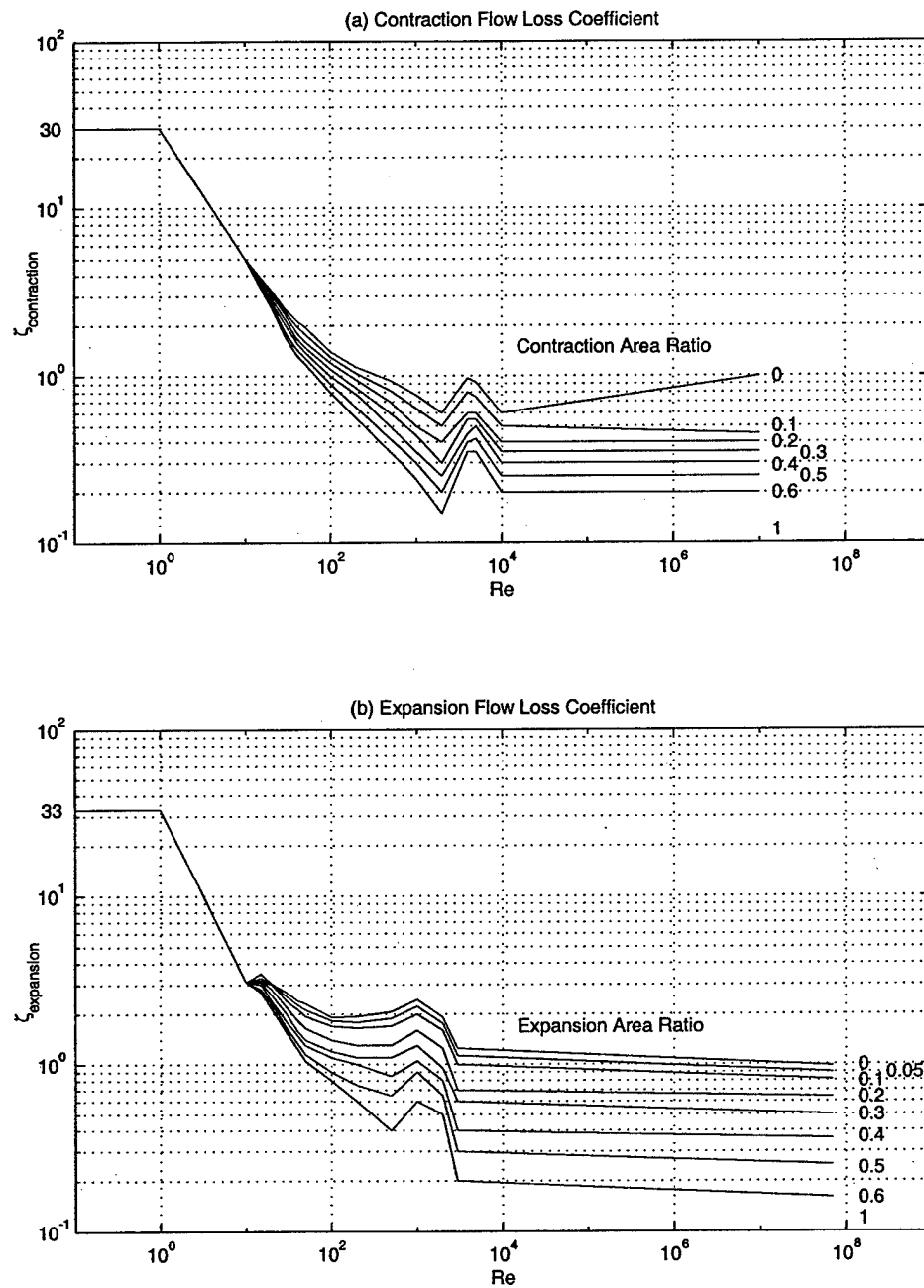


Figure 5.4: Look-Up Tables for flow loss contraction and expansion coefficients. For further details, see [2].

operation is significantly less than $H_{upstream}$, R_{vm} , and R_{vc} , the majority of pressure drop through the valve structures occurs across the contraction and expansion at the valve cap circumference. As a result, at any given instant of time, the pressure acting over the valve membrane area can be approximated as the reservoir pressure P_{HPR} and the pressure acting over the valve cap area can be approximated as P_{EHC}^* . For a specific value of valve cap opening at a given time during the cycle, a relationship therefore exists for the instantaneous fluid flow through the valve as a function of the pressure drop across the valve.

5.2.4 Chamber Filling Simulation Tool

The previously described pressure-flow relations for the harvesting chamber stiffness, valve orifice, and flow channel connecting the valve and chamber can be recast in SimulinkTM to create a simulation tool for fluid filling of the harvesting chamber. For known dimensions of the valve cap, the surrounding structure forming the upstream and downstream flow areas, the valve channel dimensions, the harvesting chamber dimensions and material properties, P_{HPR} , and the desired minimum pressure in the harvesting chamber $P_{EHC,min}$ (the pressure immediately when the outlet valve has closed), and for an assumed valve cap opening profile $Z_{vc,opening}$, the filling behavior of the system through the inlet valve orifice can be simulated. Figure 5.5 illustrates the high-level SimulinkTM model, and Figure 5.6 shows the fluid orifice and valve channel block diagram structure.

A major assumption underlying this simulation is that the accompanying outlet valve of the MHT system has been designed properly to ensure that the harvesting chamber pressure P_{EHC} has decreased to a value of $P_{EHC,min}$ at the instant the outlet valve fully closes. Furthermore, the variable $Z_{vc,opening}$ is the distance between the valve stop and the surface of the valve cap. For example, if the valve being modeled is forced to experience a sinusoidal absolute deflection history from $Z_{vc} = -20\mu m$ (fully open) to $Z_{vc} = +20\mu m$ (fully closed), the corresponding $Z_{vc,opening}$ values are $Z_{vc,opening} = +40\mu m$ (fully open) to $Z_{vc,opening} = 0\mu m$ (fully closed).

This filling simulation will be an important part of the systematic active valve design procedure detailed in the following sections. It will allow for the determination of a valve cap size and imposed valve opening so as to achieve the required P_{EHC} pressure excursion during MHT system filling.

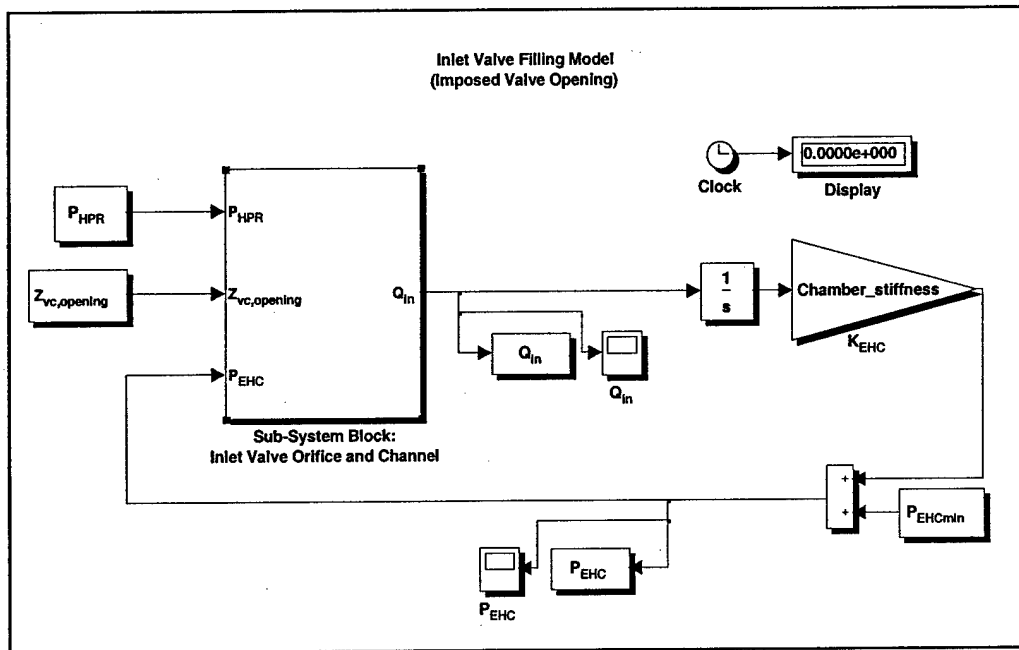


Figure 5.5: SimulinkTM high-level simulation overview for filling of the MHT system through the inlet active valve.

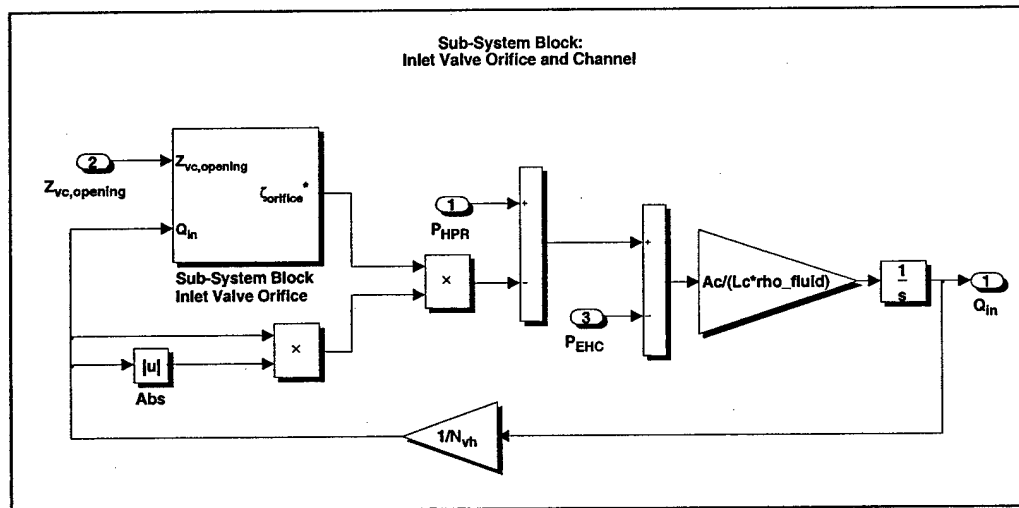


Figure 5.6: SimulinkTM valve orifice and channel sub-system block for filling of the MHT system through the inlet active valve.

5.3 Systematic Design Procedure

This section introduces a systematic design procedure that can be implemented to calculate dimensions of the valve cap, valve membrane, hydraulic amplification chamber, and drive element portion of the inlet active valve to satisfy requirements set forth by the external hydraulic system. This design procedure is based upon quasi-static valve piston and valve cap behavior (ie: $\ddot{Z}_{vc} = \dot{Z}_{vc} = \ddot{Z}_{pis} = \dot{Z}_{pis} = 0$). Depending upon the frequency of operation, this assumption may or may not be a valid one, since system dynamic effects could come into play. It is therefore the purpose of this quasi-static design procedure to generate a valve design, from which a full dynamic simulation can be run to evaluate the goodness of the design and be used as a tool for fine-tuning the valve geometry.

5.3.1 Overview

Figure 5.7 presents a generalized flowchart for this quasi-static design process. Given external system requirements, such as the chamber stiffness K_{EHC} , the P_{EHC} pressure fluctuation from a $P_{EHC,min}$ to a $P_{EHC,max}$ during filling, the reservoir pressure P_{HPR} , and the overall desired system frequency f_{sys} , the following steps are carried out:

1. The valve cap radius R_{vc} (for a chosen valve stroke Z_{stroke}) is calculated to allow for adequate filling of the harvesting chamber.
2. The valve membrane outer radius R_{vm} and required $P_{HAC}(t)$ time history (for a given membrane thickness t_{vm}) are calculated to allow for motion of the cap along its desired trajectory against the known external loads while at the same time ensuring membrane stresses below critical levels.
3. The drive element piston area A_{pis} and piezo area A_p are calculated to provide a stiffness match between the drive piston structure and the load that it encounters and to ensure adequate actuation capabilities.

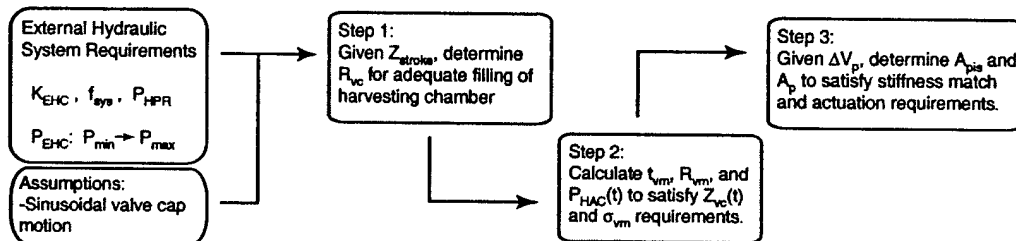


Figure 5.7: Flowchart illustrating the design procedure for the inlet active valve.

The full active valve design procedure, which will be discussed in Section 5.6, includes the ability to consider single valve cap and membrane designs as well as multiple valve cap and membrane designs (from now on N_{vh} is designated as the number of valve heads in the design), varying valve cap strokes $Z_{vc,stroke}$, and varying valve membrane thicknesses t_{vm} . There are important and interesting design issues associated with each of these design freedoms. Sections 5.4.1, 5.4.2, and 5.5 detail these issues. However, in this section, in order to present clearly the physical intuition behind the main steps in the design procedure, the following assumptions are made. First, this section focuses on generation of a single valve cap and membrane valve design. Second, in Step 1 when calculating the valve cap radius for adequate filling of the harvesting chamber, a value for $Z_{vc,stroke}$ is assumed. Third, in Step 2, the valve membrane radius R_{vm} and required $P_{HAC}(t)$ are calculated for an assumed valve membrane thickness t_{vm} .

5.3.2 System Requirements

To facilitate the understanding of the basic steps in the design procedure detailed in the following subsections, numerical system requirements characteristic of a typical MHT are presented here. For $P_{HPR} = 1.2MPa$, the inlet valve opens in a sinusoidal manner to fill a harvesting chamber with $K_{EHC} = 1.5e^{16} \frac{Pa}{m^3}$. The system frequency is chosen to be $f_{sys} = 10kHz$ and it is desired that during this filling process, P_{EHC} should rise from a minimum pressure $P_{min} = 0.2MPa$ to a maximum pressure $P_{max} = 1.0MPa$. It is assumed that the outlet valve is designed properly to allow evacuation from $P_{max} = 1.0MPa$ to $P_{min} = 0.2MPa$ during the time that the inlet valve is closed. In addition, for this example system, the channel dimensions L_c and A_c are chosen to ensure that fluid inertial effects in the channel are negligible (ie: $P_{EHC} = P_{EHC}^*$ at all times).

5.3.3 Step 1: Design of Valve Cap

In the first step of the design procedure, the valve cap radius R_{vc} is calculated so as to allow for exact filling of the harvesting chamber. With the imposed valve cap motion $Z_{vc}(t)$ and the external hydraulic system modeling tools described in Section 5.2, R_{vc} is determined such that the pressure rise in the harvesting chamber increases from its initial minimum of P_{min} to the desired maximum pressure P_{max} at the time the valve completely closes again. In this example procedure, the valve cap stroke is taken to be $Z_{stroke} = 40\mu m$. Equations 5.1, 5.2, 5.3, 5.6 are solved in the previously described Simulink simulation for this purpose. Insufficient filling will result if R_{vc} is not large enough. Conversely, if R_{vc} is too large, the chamber will be filled in excess. Figure 5.8 illustrates adequate and inadequate filling scenarios.

For the example MHT system, a value of $R_{vc} = 241\mu m$ is determined, through iteration, that results in a harvesting chamber pressure rise from $P_{EHC} = 0.2MPa$ to $P_{EHC} = 1.0MPa$

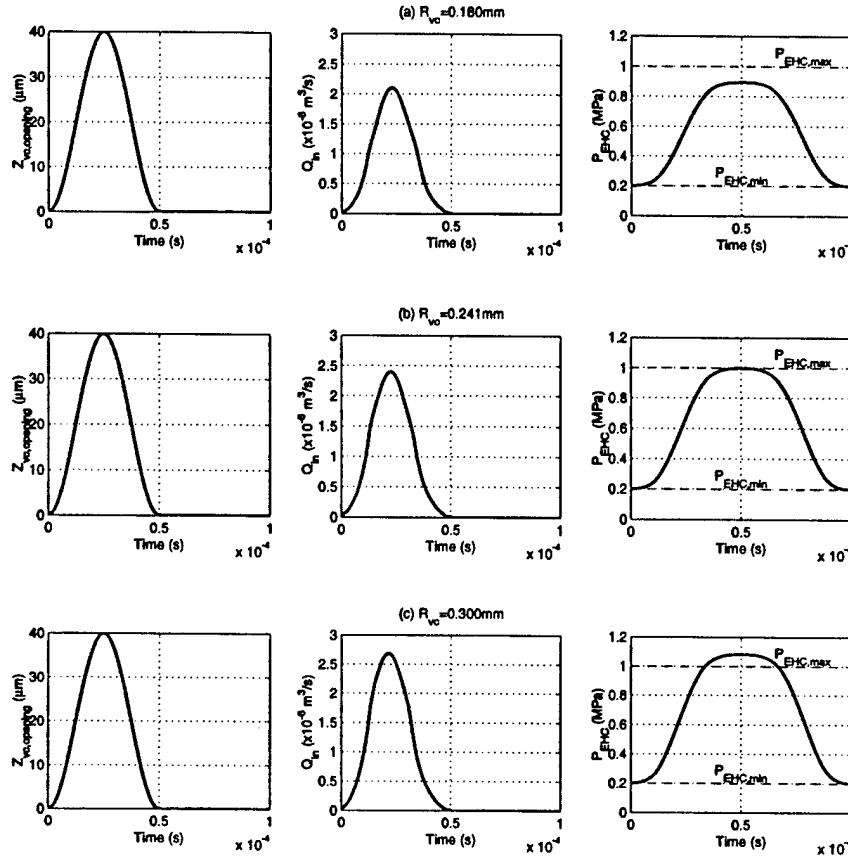


Figure 5.8: Chamber filling plots corresponding to $Z_{stroke} = 40\mu\text{m}$ and differing values of R_{vc} : (a) if $R_{vc} = 180\mu\text{m}$, the chamber can not fill adequately, (b) if $R_{vc} = 241\mu\text{m}$, the chamber fills the desired amount, and (c) if $R_{vc} = 300\mu\text{m}$, the chamber fills in excess of the desired amount.

during the time that the inlet valve is open. Figure 5.8(b) displays the imposed valve cap deflection, the corresponding flow rate Q_{in} through the valve, and the resulting $P_{EHC}(t)$ time history for this case. The valve is completely closed when $Z_{vc,opening} = 0\mu\text{m}$ and is fully open when $Z_{vc,opening} = +40\mu\text{m}$. Note that the chamber fills properly since the pressure at the instant of valve closing is 1.0 MPa . Since a complete $P_{EHC}(t)$ time history is needed for further steps in the design procedure, it is assumed that an outlet valve for the system has been sufficiently designed to evacuate the fluid during the second half of the device cycle. Figure 5.8(a) shows the corresponding results for the case where the valve cap radius is too small, $R_{vc} = 180\mu\text{m}$. Here, the chamber pressure is only able to rise to $P_{EHC} = 0.9 \text{ MPa}$ at the instant the inlet valve closes. Figure 5.8(c) shows the corresponding results for the case where the valve cap radius is too large, $R_{vc} = 300\mu\text{m}$. Here, the chamber pressure rises in excess of

the desired value to $P_{EHC} = 1.08 \text{ MPa}$ at the instant the inlet valve closes.

5.3.4 Step 2: Design of Valve Membrane

In the second step of the design procedure, for a given valve membrane thickness t_{vm} , the outer membrane radius R_{vm} and required $P_{HAC}(t)$ time history are calculated such that the valve cap properly follows its imposed trajectory $Z_{vc}(t)$ and experiences a maximum tensile membrane stress during this motion of $\sigma_{vm} = \sigma_{limit}$. The code calculates the entire stress field along the membrane, however it records only the maximum tensile value for each time instant during the cycle and calls it σ_{vm} . A limiting value for $\sigma_{limit} = 1.0 \text{ GPa}$ is taken from [6] [5]. Since a small value of t_{vm} is desired to minimize actuation requirements, an initial value of $t_{vm} = 7 \mu\text{m}$ is employed. For the given value of t_{vm} , a guess for R_{vm} is taken. Under the constant P_{HPR} loading on the valve membrane and the time-varying loading $P_{EHC}^*(t)$ on the valve cap calculated in Step 1, the required $P_{HAC}(t)$ time history is calculated to force the valve membrane and cap to follow its imposed trajectory $Z_{vc}(t)$. During this time cycle, σ_{vm} is monitored. This procedure becomes an iterative process in R_{vm} until a value of R_{vm} is determined such that at some time during the complete cycle, a peak tensile stress of σ_{limit} is reached. As will be discussed in Section 5.4.2, it might be the case that it is impossible to arrive at a membrane design for this particular value of t_{vm} due to high stresses in the membrane, at which point it will be necessary to increase the membrane thickness. However, this issue is held off until Section 5.4.2.

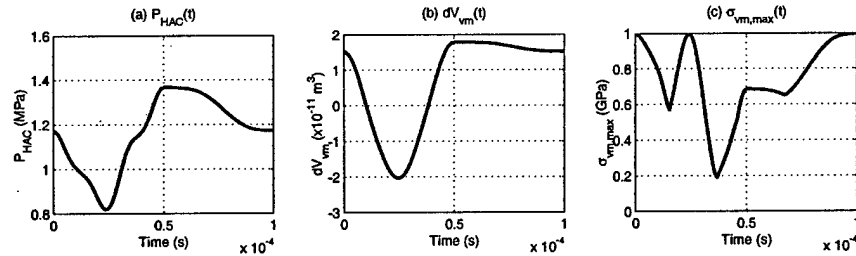


Figure 5.9: Valve membrane behavior corresponding to $Z_{stroke} = 40 \mu\text{m}$, $R_{vc} = 241 \mu\text{m}$, $t_{vm} = 7 \mu\text{m}$, and $R_{vm} = 757 \mu\text{m}$: (a) required hydraulic amplification chamber $P_{HAC}(t)$, (b) corresponding valve cap and membrane swept volume $dV_{vm}(t)$, and (c) peak stress in valve membrane $\sigma_{vm}(t)$.

For the example MHT system, a value of $R_{vm} = 757 \mu\text{m}$ is determined for $t_{vm} = 7 \mu\text{m}$. The required $P_{HAC}(t)$ time history, swept volume time history under the membrane and cap $dV_{vm}(t)$, and the associated membrane stress time history $\sigma_{vm}(t)$ are shown in Figures 5.9(a), (b), and (c) respectively. In Figure 5.9(c), notice that the maximum stress in the membrane during the cycle occurs when the cap is deflected to its minimum value of $Z_{vc} = -20 \mu\text{m}$. The

membrane again experiences a stress of $1.0GPa$ when the cap is at its maximum deflection of $Z_{vc} = +20\mu m$. This reconfirms the design choice to force the membrane into symmetric upward and downward motion so as to maximize total valve cap stroke when restricted to limited membrane stress levels.

5.3.5 Step 3: Design of Piezoelectric Drive Element

In the third step of the design procedure, the piezoelectric material area and drive element piston area are determined so as to create a quasi-static stiffness match with the loading seen by this structure. The goal in doing this is to maximize the energy transfer from the piezoelectric material to the load. As shown in Figure 5.10, the valve cap/membrane and external hydraulic system appear to the drive structure as a stiffness K_{vm} in series with a fluid stiffness K_{HAC} of the hydraulic amplification chamber. A linearization of the actuation curve associated with the motion of the valve cap (described by the time histories $P_{HAC}(t)$ and $dV_{vm}(t)$ calculated in Step 2 of the design procedure and plotted against one another in Figure 5.10(a)) provides an approximation for this K_{vm} stiffness. Combining K_{vm} and K_{HAC} together produces an overall load K_{load} seen by the piezoelectric element. This model neglects the stiffness of the drive piston tethers. Studies have shown that the stiffnesses of these tethers in relation to the K_{vm} and K_{HAC} are small for typical active valve designs. The requirement of a stiffness match between K_{piezo} and K_{load} therefore results in the following equality,

$$K_{piezo} = K_{load} \quad \rightarrow \quad \frac{E_p A_p}{L_p} = \frac{A_{pis}^2}{\left(\frac{\Delta V_{vm}}{\Delta P_{HAC}}\right) + \left(\frac{A_{pis} H_{HAC}}{K_{fluid}}\right)}. \quad (5.7)$$

Substituting this requirement into the following piezoelectric material actuator equation, one obtains a relationship between Z_p and V_p ,

$$Z_p = d_{33} V_p - \frac{F_p}{K_p} = d_{33} V_p - \left(\frac{K_{load}}{K_{piezo}}\right) Z_p \quad \rightarrow \quad Z_p = \frac{1}{2} d_{33} V_p. \quad (5.8)$$

In addition to this impedance match requirement on Z_p , Z_p must also satisfy the volume conservation relation within the active valve structure,

$$Z_p = \frac{\Delta V_{dc}}{A_{pis}} = \frac{\Delta V_{vm} + \Delta V_{fluid}}{A_{pis}} = \left(\frac{1}{A_{pis}}\right) \left[\Delta V_{vm} + \left(\frac{A_{pis} H_{HAC}}{K_{fluid}}\right) \Delta P_{HAC}\right]. \quad (5.9)$$

Eliminating Z_p in Equations 5.8 and 5.9 results in the following equality,

$$\frac{1}{2} d_{33} V_p = \left(\frac{1}{A_{pis}}\right) \left[\Delta V_{vm} + \left(\frac{A_{pis} H_{HAC}}{K_{fluid}}\right) \Delta P_{HAC}\right]. \quad (5.10)$$

Therefore, equations 5.7 and 5.10 form a set of two equations with three unknowns A_{pis} , A_p , and V_p . Equation 5.7 sets the relationship between A_{pis} and A_p for a stiffness match between piezo and load to be achieved while equation 5.10 defines the condition under which valve performance is met, relating the input piezo voltage V_p to the A_{pis} . In observing these equations, it is clear that the smaller the voltage V_p , the larger the values of A_{pis} and A_p need to be. Since one of the goals in the design of this active valve is make its total volume as small as possible, this implies that the valve should work at as large a voltage as possible. In real devices, a limitation of electrical breakdown across the air gap between drive element piston and the bottom structural plate exists, and therefore a maximum allowable V_p for the given piezo length L_p is set. As a result, in the design of this valve, voltage now becomes an imposed quantity. The set of two equations can be solved for the two remaining geometric free design variables A_{pis} and A_p to create a quasi-static stiffness match condition between the piezo and load and to ensure adequate valve performance to satisfy the actuation requirements passed down from the membrane and cap design steps.

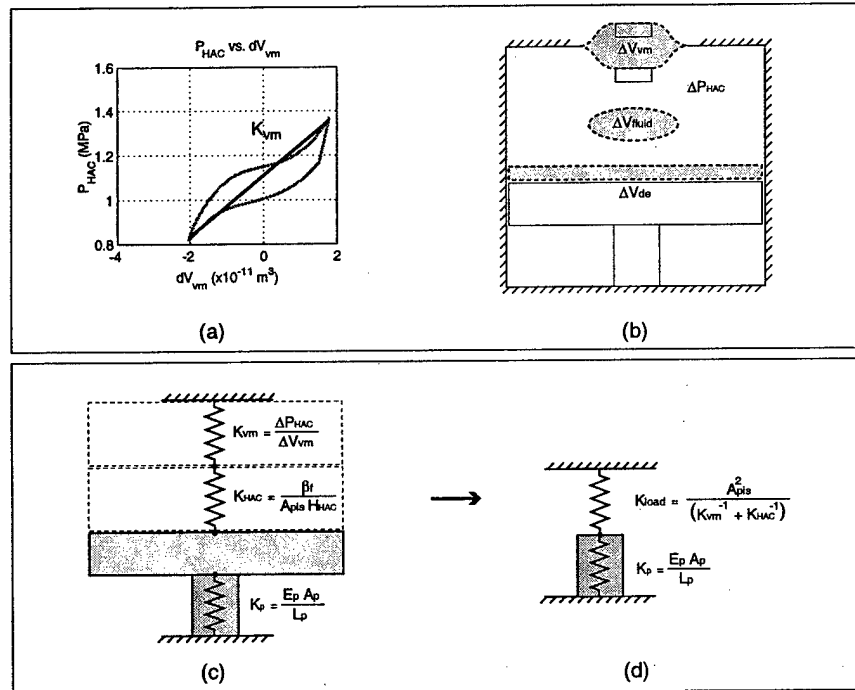


Figure 5.10: Simplification of the active valve device in a quasi-static stiffness match analogy: (a) determination of linearized K_{vm} stiffness load, (b) important actuation volume change and pressure variables, (c) valve membrane volumetric stiffness in series with fluid hydraulic stiffness acting through piston area against piezo displacement stiffness, and (d) lumped linear load spring acting against piezo material.

For the example MHT system, the piezoelectric material thickness is assumed to be $L_p = 1mm$ and the applied peak-peak voltage is assumed to be $V_p = 1000V$. Under these assumptions, a drive piston area and piezo area are calculated to correspond to $R_{pis} = 3.59mm$ and $R_p = 0.88mm$. Figures 5.11(a), (b), and (c) show the required piezoelectric voltage time history V_p to force the valve cap to follow the desired trajectory $Z_{vc}(t)$, the drive element P_{HAC} vs. dV_{de} actuation curve, and the resulting piezoelectric material stress time history T_p , respectively. In comparing Figure 5.11(b) to Figure 5.10(a), notice the increased volume change between dV_{de} and dV_{vm} . This difference is exactly equal to the fluid compressibility volume change dV_{HAC} under the pressure loading $P_{HAC}(t)$. At this point, a design for the active valve has been achieved.

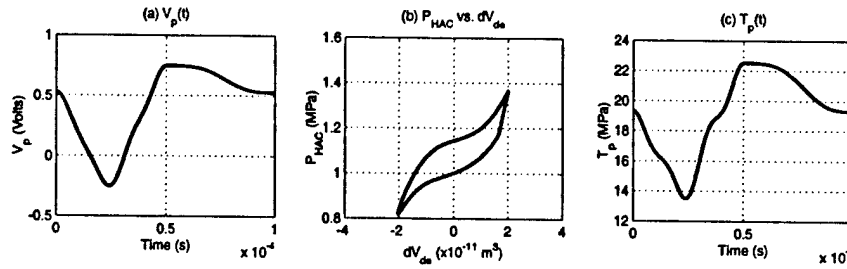


Figure 5.11: Drive element behavior corresponding to $R_{pis} = 3.59mm$ and $R_p = 0.88mm$: (a) required piezoelectric voltage $V_p(t)$, (b) corresponding drive element actuation curve, and (c) stress on piezoelectric material $T_p(t)$.

5.4 Design Freedoms Within Procedure

The basic design procedure for the active valve discussed in Section 5.3 was simplified in three ways in order to ease the explanation of the main steps. First, the valve design was carried out for a valve geometry with only a single valve cap and membrane above the hydraulic amplification chamber ($N_{vh} = 1$). Second, the design assumed a predetermined stroke $Z_{vc,stroke}$ of the valve cap. Third, the design assumed that a value of t_{vm} could be chosen that would result in the successful calculation of the valve membrane outer radius R_{vm} to guarantee stresses below a limiting value. In reality, when designing the active valve structure, one would like to relax all three of these design restrictions so that the design process creates an optimal valve geometry. It might therefore be the case that the optimal active valve design uses five valve caps and membranes in parallel above the hydraulic amplification chamber rather than a single valve cap and membrane, or that the stroke(s) of the valve cap(s) should be $20\mu m$ rather than $40\mu m$, or that $8\mu m$ is the minimal valve membrane thickness that can be used to create a strong enough valve membrane structure. This section will discuss two of these three design freedoms, $Z_{vc,stroke}$ and t_{vm} . The third design freedom, N_{vh} , will be discussed in Section 5.5. All three design freedoms will then be included in the final systematic design procedure presented in Section 5.6.

5.4.1 Design Freedom: $Z_{vc,stroke}$

In the example active valve design procedure presented in Section 5.3, the required valve cap size R_{vc} was calculated that would allow for adequate filling of the harvesting chamber, given that the valve cap was allowed to move through a stroke of $Z_{vc,stroke} = 40\mu m$. It would have also been possible to determine a value for R_{vc} if $Z_{vc,stroke} = 20\mu m$. To maintain fluid flow resistance through the valve structure, it makes sense that as the valve cap stroke is decreased, the radius of the valve cap itself must be increased. Figure 5.12 displays the calculated valve cap radius R_{vc} for a series of different valve cap strokes $Z_{vc,stroke}$ for the example MHT system described in the previous section. For an imposed $Z_{vc,stroke} = 40\mu m$, the design code simulation requires a value of $R_{vc} = 241\mu m$ to ensure proper filling of the harvesting chamber. Alternatively, for an imposed $Z_{vc,stroke} = 20\mu m$, the design code simulation requires a value of $R_{vc} = 688\mu m$ to ensure proper filling of the harvesting chamber. Therefore, different combinations of $Z_{vc,stroke}$ and R_{vc} can effectively fill the chamber, but as the full design procedure in Section 5.6 will illustrate, one combination may be better than others in designing the remaining structures of the valve.

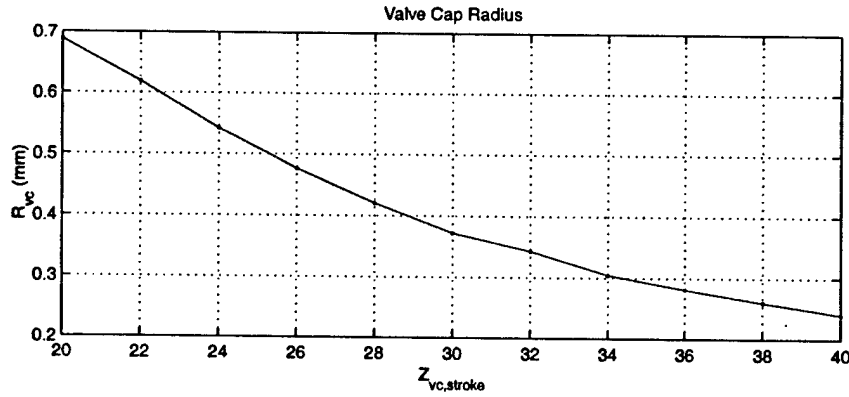


Figure 5.12: Design of valve cap, for $P_{HPR} = 1.2MPa$, $f_{sys} = 10kHz$, $P_{EHC,min} = 0.2MPa$, $P_{EHC,max} = 1.0MPa$, and varying $Z_{vc,stroke}$.

5.4.2 Design Freedom: t_{vm}

For a given size valve cap (value of R_{vc}), the next step in the design procedure is to design a membrane structure which can carry this valve cap through the imposed opening time history against the external pressure loadings, P_{HPR} and $P_{EHC}(t)$. During filling of the chamber, as was discussed in previous sections, P_{HPR} is constant with time over the valve membrane, however, P_{EHC} varies from a minimum to a maximum. The valve membrane radius R_{vm} and thickness t_{vm} must be determined to achieve the desired behavior.

Two example studies will be included in this section to illustrate some important issues concerning the design of the valve membrane structure. The first study will look at the design of the valve membranes for each of the valve cap sizes arrived at in Section 5.4.1, assuming that $P_{HPR} = P_{EHC} = 1.2MPa$ for all time during the opening and closing of the valve cap and membrane. This situation, where the pressures above the cap and membrane structure are constant with time, would never occur in reality. However, the purpose of this study is to illustrate an important point associated with the structural design of the membrane. The second study will then focus on the real case, where $P_{HPR} = 1.2MPa$ during opening and closing, but P_{EHC} does vary as calculated in the design code simulation. The overall conclusion from these comparative studies will be that this changing P_{EHC} pressure with time in certain circumstances does not allow for a valve design of a particular membrane thickness to be calculated that can satisfy the membrane stress limitations. In such cases, it will be necessary to iterate to larger membrane thicknesses to achieve a reasonable design.

Example Study: $P_{HPR} = 1.2MPa$ and $P_{EHC}(t) = 1.2MPa$

In this example study, for each of the valve cap designs presented in Figure 5.12, the design code calculates the valve membrane radius so that for the imposed valve cap displacements and under the constant external loading $P_{HPR} = P_{EHC} = 1.2MPa$, the membrane experiences a peak stress of $\sigma_{vm} = 1GPa$ during its opening/closing cycle. The valve membrane thickness is assumed to be $t_{vm} = 7\mu m$ for these calculations. This is really a lower limit for membrane thickness based on fabrication restrictions.

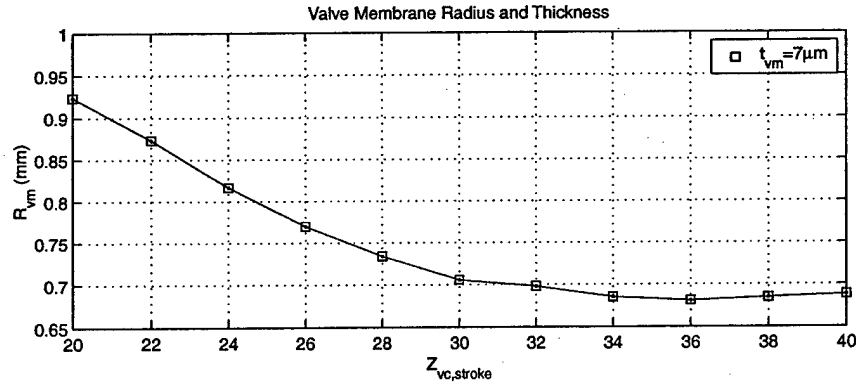


Figure 5.13: Design of valve membrane for the case where the external pressure loading on the valve cap and membrane are held constant during the time that the cap opens and closes, $P_{HPR} = P_{EHC} = 1.2MPa$ constant with time.

Figure 5.13 displays the calculated R_{vm} values for each of the imposed $Z_{vc,stroke}$ and previously calculated R_{vc} values. For an imposed $Z_{vc} = 40\mu m$ and therefore for the previously calculated $R_{vc} = 241\mu m$, the design code procedure calculates a membrane radius of $R_{vm} = 688\mu m$ to ensure stresses below the limit. For an imposed $Z_{vc} = 20\mu m$ and therefore for the previously calculated $R_{vc} = 688\mu m$, the design code procedure calculates a membrane radius of $R_{vm} = 924\mu m$ to ensure stresses below the limit. In all cases for the imposed valve cap stroke between $20\mu m$ and $40\mu m$, the membrane is able to designed with $t_{vm} = 7\mu m$.

To illustrate how the code determines R_{vm} , take the point design for an imposed $Z_{vc,stroke} = 20\mu m$. The valve cap radius has been previously calculated to be $R_{vc} = 688\mu m$. The code begins by guessing a value of R_{vm} , and then determines the required P_{HAC} pressure underneath the cap and membrane at each instant of time to satisfy the required cap displacement against the external pressure loadings. The membrane stress is recorded for all time instants during the complete opening/closing cycle of the valve cap. The code then iterates in R_{vm} until a value is determined that results in the desired peak stress occurring during the valve cap opening/closing cycle.

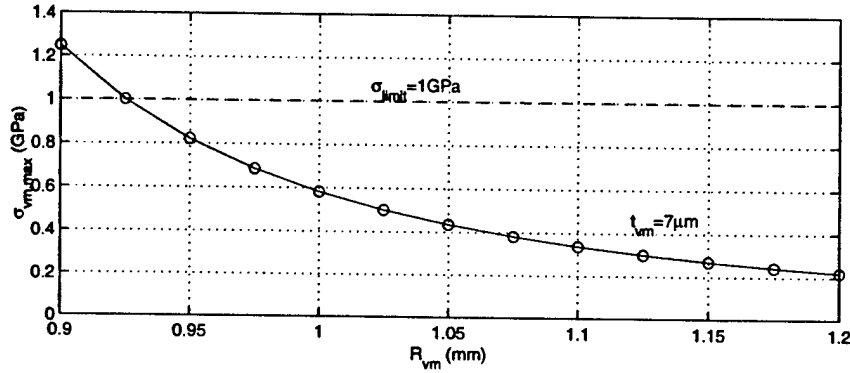


Figure 5.14: For $Z_{vc,stroke} = 20\mu m$, $R_{vc} = 688\mu m$, $P_{HPR} = P_{EHC} = 1.2MPa$ constant with time, and $t_{vm} = 7\mu m$, the membrane peak stress $\sigma_{vm,peak}$ during valve cap motion decreases as R_{vm} is decreased. An R_{vm} to meet the desired $\sigma_{vm,peak} = 1GPa$ can be determined.

Figure 5.14 plots the peak membrane stress during a complete valve membrane cycle for guesses of R_{vm} . Notice that the value of R_{vm} for which $\sigma_{vm,max} = 1.0$ is $924\mu m$. For a small value of $R_{vm} = 900\mu m$, the membrane stress reaches a peak stress of $\sigma_{vm} = 1.24GPa$ during the cycle, whereas for a large value of $R_{vm} = 1200\mu m$, the membrane stress reaches a peak stress of only $\sigma_{vm} = 0.22GPa$ during the cycle. For a value of $R_{vm} = 1010\mu m$ (chosen for demonstration purposes), a peak stress of $\sigma_{vm} = 0.52GPa$ during the cycle is determined. For all of these membrane designs, the peak stress occurs at the time during the cycle when the valve membrane is at peak positive displacement. Figure 5.15 illustrates the spatial displacement and stress distributions of the membrane for these three membrane designs. Notice in Figure 5.15(a), for $R_{vm} = 1200\mu m$, that the stress is low because of the minimal curvature in the membrane at the inner and outer boundaries. Also, there is only a slight shift in the mean stress on the top and bottom membrane surfaces (ie: the membrane is experiencing non-linear stretching of the neutral axis, but only slightly). In Figure 5.15(c), for $R_{vm} = 900\mu m$, the stress is high because of the significant curvature in the membrane at the inner and outer boundaries. In this case, there is a significant shift in the mean stress ($\sim 0.25GPa$) on the top and bottom membrane surfaces as the membrane experiences quite a bit of non-linear stretching. And in Figure 5.15(b), for $R_{vm} = 1010\mu m$, the membrane behavior is between the previous two cases.

The important conclusion from this example study with a constant P_{EHC} above the valve cap during the design of the valve membrane structure is that for the variety of valve cap strokes imposed, a valve membrane with thickness t_{vm} is able to be determined to satisfy the stress limitations. As will be shown in the following example study, as P_{EHC} is allowed to vary, as it would in a real system, different membrane thicknesses will have to be considered.

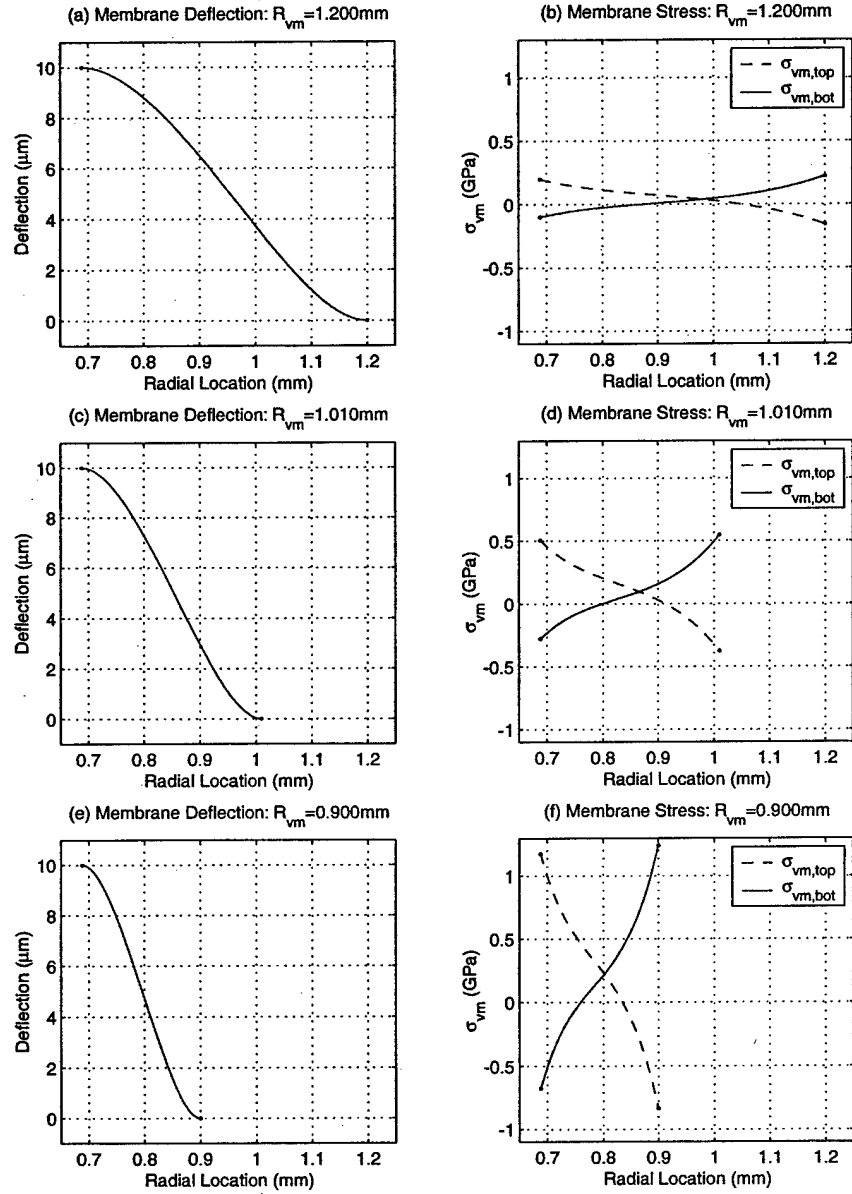


Figure 5.15: Example valve membrane deflection and stress plots for $Z_{vc,stroke} = 20\mu\text{m}$, $R_{vc} = 688\mu\text{m}$, $P_{HPR} = P_{EHC} = 1.2\text{MPa}$ constant with time, and $t_{vm} = 7\mu\text{m}$: (a) $R_{vm} = 1200\mu\text{m}$, (b) $R_{vm} = 1010\mu\text{m}$, and $R_{vm} = 900\mu\text{m}$.

Example Study: $P_{HPR} = 1.2MPa$ and $P_{EHC}(t) = \text{varying}$

In this example study, for each of the valve cap designs presented in Figure 5.12, the design code calculates the valve membrane radius so that for the imposed valve cap displacements and under the external loading $P_{HPR} = 1.2MPa$ and $P_{EHC} = 0.2MPa \rightarrow 1.0MPa$, the membrane experiences a peak stress of $\sigma_{vm} = 1GPa$ during its opening/closing cycle. The valve membrane thickness is desired to be $t_{vm} = 7\mu m$ for these calculations, however, if a membrane design at a certain thickness can not be found, then the thickness is increased. Figure 5.16 displays the calculated R_{vm} values for each of the imposed $Z_{vc,stroke}$ and previously calculated R_{vc} values.

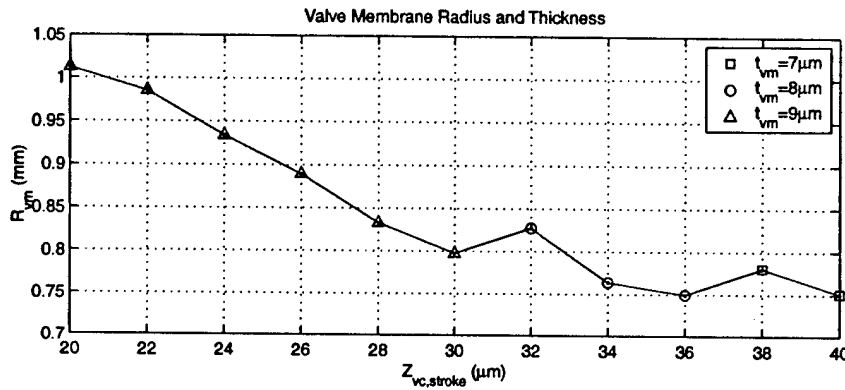


Figure 5.16: Design of the valve membrane for the case where $P_{HPR} = 1.2MPa$ and the external pressure loading on the valve cap P_{EHC} is allowed to vary with time, as it would in a real hydraulic system.

In comparison to the previous example study where a valve membrane with $t_{vm} = 7\mu m$ could be designed for each of the valve cap strokes, in this example study, as $Z_{vc,stroke}$ is reduced from $40\mu m$ to $20\mu m$, t_{vm} must be increased from $7\mu m$ so as to determine R_{vm} values that satisfy the stress requirements. This is a result of the changing P_{EHC} pressure over the valve cap as the cap moves through its cycle. For an imposed $Z_{vc,stroke} = 40\mu m$ and therefore for the previously calculated $R_{vc} = 241\mu m$, the design code procedure is able to determine a membrane radius of $R_{vm} = 751\mu m$ for $t_{vm} = 7\mu m$ to ensure stresses below the limit. For an imposed $Z_{vc,stroke} = 20\mu m$ and therefore for the previously calculated $R_{vc} = 688\mu m$, however, the design code procedure is not able to determine a satisfactory R_{vm} for either $t_{vm} = 7\mu m$ or $t_{vm} = 8\mu m$. Rather, it must increase the membrane thickness to $t_{vm} = 9\mu m$ in order to find a satisfactory membrane radius of $R_{vm} = 1010\mu m$ that ensures stresses below the limit.

Figure 5.17 plots the peak membrane stress during a complete valve membrane cycle for the case of imposed $Z_{vc,stroke} = 20\mu m$ for guesses of R_{vm} at the three thicknesses $t_{vm} = 7\mu m$, $t_{vm} = 8\mu m$, and $t_{vm} = 9\mu m$. For $t_{vm} = 7\mu m$, no value of R_{vm} can be chosen to bring

the stress below the critical limit of $\sigma_{limit} = 1\text{GPa}$. At this thickness, small values of R_{vm} and large values of R_{vm} both result in large stresses due to high membrane curvature at the membrane boundaries. In the case of small R_{vm} , the high curvature is a result of the membrane being so short in width, whereas for the case of large R_{vm} , the high curvature is a result of bowing of the membrane under the large negative pressure differential across the membrane (see later discussion). For $t_{vm} = 8\mu\text{m}$, again no value of R_{vm} can be determined, although the minimum of the curve is approaching σ_{limit} . Finally, for $t_{vm} = 9\mu\text{m}$, a valve membrane radius is achievable. In fact, there are two potential solutions, one at $R_{vm} = 1130\mu\text{m}$ and the other at $R_{vm} = 1015\mu\text{m}$. During the design procedure, the code picks the smaller of the two values, so as to minimize the valve size.

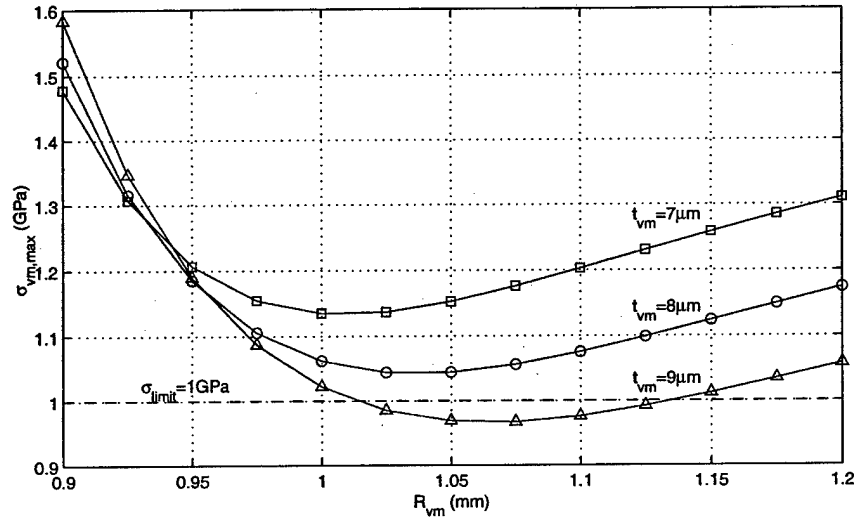


Figure 5.17: For $Z_{vc,stroke} = 20\mu\text{m}$, $R_{vc} = 688\mu\text{m}$, $P_{HPR} = 1.2\text{MPa}$, P_{EHC} varying with time, and for different t_{vm} , the membrane peak stress $\sigma_{vm,peak}$ during valve cap motion reaches a minimum at a particular R_{vm} . A satisfactory R_{vm} for $t_{vm} = 7\mu\text{m}$ and for $t_{vm} = 8\mu\text{m}$ can not be found, however an R_{vm} for $t_{vm} = 9\mu\text{m}$ can be determined to meet the desired $\sigma_{vm,peak} = 1\text{GPa}$.

Figure 5.15 illustrates the spatial displacement and stress distributions of the membrane for three values of membrane radius $R_{vm} = 1200\mu\text{m}$, $R_{vm} = 1010\mu\text{m}$, and $R_{vm} = 900\mu\text{m}$, all for $t_{vm} = 9\mu\text{m}$. Notice in Figure 5.18(a), for $R_{vm} = 1200\mu\text{m}$, that the stress is large because of the significant curvature in the membrane at the inner boundary due to the negative bowing of the membrane. This bowing develops because at the instant when the valve cap is at its maximum deflection upward, the pressure acting on the top surface of the valve cap is at its minimum $P_{EHC} = 0.2\text{MPa}$. Therefore, the required P_{HAC} within the valve hydraulic

amplification chamber at this time instant is low, resulting in a significant negative pressure across the valve membrane. In Figure 5.18(c), for $R_{vm} = 900\mu m$, the stress is high because of the significant curvature in the membrane at the inner and outer boundaries, due to the minimal width of the membrane. And in Figure 5.18(b), for $R_{vm} = 1010\mu m$, the peak membrane stress is $\sigma_{vm,peak} = 1.0GPa$ and occurs at the inner membrane boundary.

This study has shown that in designing to valve membranes to work under varying pressure time histories, depending on the magnitude of the external pressures and their behavior with time, it is sometimes impossible to determine a valve membrane radius for a given membrane thickness to achieve stresses below the critical limits. As a result of this, the final systematic active valve design procedure presented in Section 5.6 is capable of recognizing these restrictions and iterating on the membrane thickness until a satisfactory membrane design is achieved.

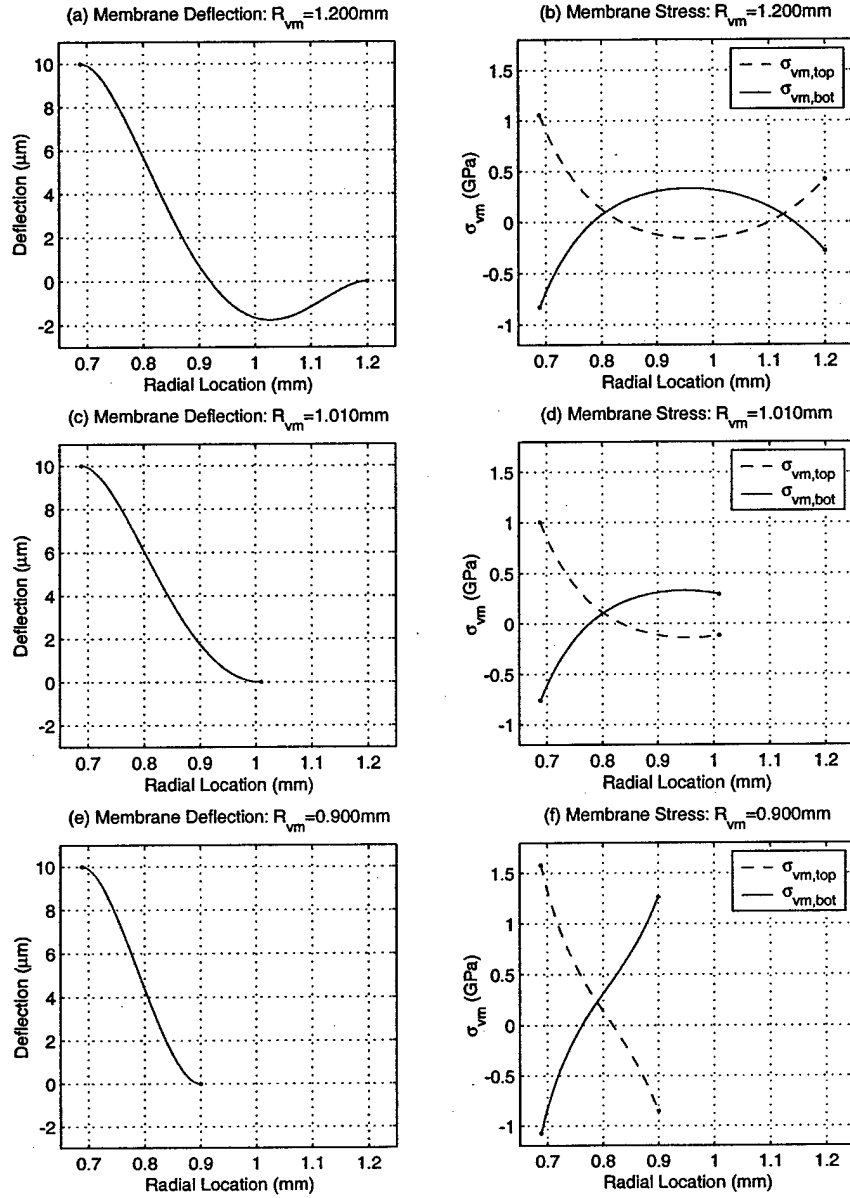


Figure 5.18: Example valve membrane deflection and stress plots for $Z_{vc,stroke} = 20\mu\text{m}$, $R_{vc} = 688\mu\text{m}$, $P_{HPR} = 1.2\text{MPa}$, P_{EHC} varying with time, and $t_{vm} = 9\mu\text{m}$: (a) $R_{vm} = 1200\mu\text{m}$, (b) $R_{vm} = 1010\mu\text{m}$, and (c) $R_{vm} = 900\mu\text{m}$.

5.5 Power Consumption in Active Valve

During each cycle of operation of the active valve, electrical energy flows into and out of the piezoelectric material. The amount of energy required is dependent on the strain of the material and the load that it actuates against. To create a simple method for evaluating these energies in a given active valve geometry, the drive element portion of the valve will be focused on. In the final step of the design procedure, the piezoelectric material diameter and drive element piston diameter were calculated to create a stiffness match condition with the loading that the drive element experienced (see details in Section 5.3.5). Figure 5.11(b) illustrated the drive element actuation curve for the example design in Section 5.3.2. This type of curve will be the basis for evaluating cyclic energy flow in the valve.

5.5.1 Overview of Energy/Power Consumption

Figure 5.19 displays representative drive element actuation plots for a typical active valve design. In Figure 5.19(a), as the piezoelectric material expands and creates a positive drive element volume change dV_{de} , the pressure within the hydraulic amplification chamber P_{HAC} increases, due to the stiffness of the valve membrane and the external pressure loading time histories P_{HPR} and $P_{EHC}(t)$. The piezoelectric material therefore does work W_1 on its environment. In Figure 5.19(b), the piezoelectric material deflection is decreasing, and the corresponding work done by the environment on the piezoelectric material (the drive element) is W_2 . Throughout a full cycle of the valve, a total hysteretic valve energy loss of $W_{hys} = W_1 - W_2$ results. This is due to the fact that during drive element motion upward, the average P_{HAC} pressure that the piston moves against is larger than that which exists to help move the piston downward in the second portion of the valve cycle. This hysteretic energy loss per valve cycle is being put into the external hydraulic system.

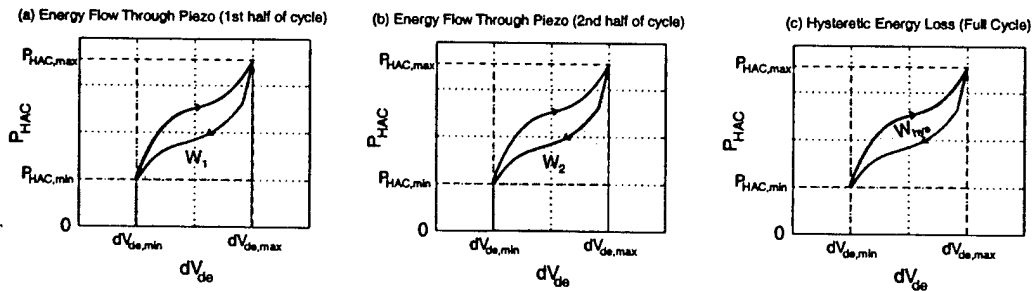


Figure 5.19: Schematic representation of energy flows and losses in active valve, based on drive element actuation behavior: (a) work done by piezo material on load during first half of valve cycle, (b) work done by load on piezo material during second half of valve cycle, and (c) hysteretic energy loss during a full valve cycle.

This hysteretic energy loss can be written in integral form as

$$W_{hys} = W_1 + W_2 = \int_1 P_{HAC} d(V_{de}) + \int_2 P_{HAC} d(V_{de}). \quad (5.11)$$

Note here that W_2 is a negative quantity since work is done by the environment on the drive element. If the piezoelectric material and attached circuitry were 100% efficient, then no other energy loss mechanisms would exist within the valve system. In reality, though, the piezoelectric material and the attached circuitry are not perfectly efficient. Assuming a lumped parameter γ_{loss} as the fraction of energy flowing through the piezoelectric material during a full valve cycle that is lost due to material and circuitry inefficiencies, the total amount of cyclic energy lost in these mechanisms is therefore

$$W_{loss} = \gamma_{loss} (W_1 + |W_2|). \quad (5.12)$$

In order to calculate the power consumption of the valve design, the frequency of operation of the valve f_{sys} is incorporated into the previous relations. The total valve power consumption is thus the product of the valve frequency of operation and the total energy lost by the valve during a single cycle of operation,

$$P_{consumption} = f_{sys} [W_{hys} + W_{loss}]. \quad (5.13)$$

These power consumption quantities P_{hys} , P_{loss} , and $P_{consumption}$ will be monitored in carrying out the full valve systematic design code in order to evaluate the benefits of a particular valve design over another one.

5.5.2 Benefit of Multiple Valve Heads

The incorporation of multiple smaller-sized valve heads (which are designed to achieve the same external system flow performance as a single larger valve head) has the potential to reduce hysteretic energy loss of the active valve device. This phenomenon will be presented from the point of view of the valve cap and membrane acting against the external pressure loadings, since this is the actual structural interface between the active valve and the rest of the MHT system. The hysteretic energy loss of the active valve per cycle is the same whether it is looked at from the point of view of the drive element or the point of view of the valve cap and membrane. This is true because no energy loss mechanisms exist within the valve between the drive piston and the valve cap and membrane. Certainly, structural compliances do exist, but these are energy storage elements, not loss mechanisms. Therefore, it is possible to calculate

the hysteretic energy loss by focusing on just the motion of the valve cap and membrane against the external pressure loadings encountered. Furthermore, since the valve membrane experiences a constant pressure P_{HPR} during the complete actuation cycle, no cyclic work is being done through the valve membrane interface. Therefore, the estimation of valve hysteretic energy loss can be made simply by looking at the valve cap itself, its motion against the time-varying external pressure loading $P_{EHC}(t)$ during a full actuation cycle.

This method of estimating valve hysteretic energy consumption will be used to explain the fundamental benefit of incorporating multiple valve heads within the active valve device rather than just a single valve head. For a given valve cap radius R_{vc} , imposed motion $Z_{vc}(t)$, and known external loading $P_{EHC}(t)$ on the valve cap, the hysteretic energy consumption of the valve during a full actuation cycle can be written as

$$W_{hys} = \int P_{EHC}(t) d(V_{vc}) = \int P_{EHC}(t) \pi(R_{vc})^2 dZ_{vc}. \quad (5.14)$$

where $dV_{vc}(t)$ is the swept volume of the valve cap. For simplicity in the following arguments, this relation can be simplified to the following proportionality,

$$W_{hys} \propto \Delta P_{EHC}^* \pi(R_{vc})^2 Z_{vc,stroke} \quad (5.15)$$

where ΔP_{EHC}^* is the difference between the average encountered pressure as the valve moves upward and the average encountered external pressure as the valve moves downward. Also for the given values of R_{vc} and $Z_{vc,stroke}$, the peak area through which fluid can flow during an actuation cycle is

$$A_{flow} = 2\pi R_{vc} Z_{vc,stroke}. \quad (5.16)$$

Therefore, for a given valve cap size, imposed stroke, and known external pressure loading time history on the valve cap, the hysteretic energy loss per cycle and the peak fluid flow area can be related by

$$\frac{W_{hys}}{A_{flow}} \propto R_{vc}. \quad (5.17)$$

This relation basically states that the ratio of the valve cap structural area (which is proportional to W_{hys}) to the valve cap circumference (which is proportional to fluid flow area) can be decreased by reducing the size of the valve cap radius R_{vc} . To reduce hysteretic energy consumption in the active valve, therefore, the goal should be to reduce this $\frac{W_{hys}}{A_{flow}}$ as much as

possible, while keeping A_{flow} constant. This can be achieved by making individual valve caps smaller and placing many in parallel with multiple valve orifices connecting the high pressure reservoir to the harvesting chamber. Updating Equations 5.15 and 5.16 above to include the freedom to choose a particular number of valve heads N_{vh} within the design leads to

$$W_{hys,N_{vh}} \propto N_{vh} \Delta P_{EHC}^* \pi R_{vc,N_{vh}}^2 Z_{vc,stroke,N_{vh}} \quad (5.18)$$

and

$$A_{flow,N_{vh}} = N_{vh} 2\pi R_{vc,N_{vh}} Z_{vc,stroke,N_{vh}}. \quad (5.19)$$

If the goal is to design a valve with $N_{vh} > 1$ that has the same total flow area as a valve with a single valve head, the following proportionality must be maintained (calculated by equating Equations 5.16 and 5.19),

$$\frac{R_{vc,N_{vh}}}{R_{vc}} \propto \frac{1}{N_{vh}} \frac{Z_{vc,stroke}}{Z_{vc,stroke,N_{vh}}}. \quad (5.20)$$

Inserting this proportionality into Equation 5.18 results in a relation for the hysteretic energy consumption as a function of the number of valve heads employed and the imposed valve cap stroke for the case of multiple valve heads versus the case of just a single valve head,

$$\frac{W_{hys,N_{vh}}}{W_{hys}} \propto \frac{1}{N_{vh}} \frac{Z_{vc,stroke}}{Z_{vc,stroke,N_{vh}}}. \quad (5.21)$$

Therefore, the potential exists to reduce significantly the hysteretic energy consumption in the active valve by incorporating multiple valve heads above the hydraulic amplification chamber rather than a single valve head. For example, by letting $N_{vh} = 10$ and requiring that each of the ten valve heads move through one-half the stroke of a single valve head design, the hysteretic energy consumption of the 10-valve design will be 20% of that of the single valve design. The updated systematic design code detailed in the following section, includes this ability to compare and contrast valve designs with varying N_{vh} and different imposed valve cap strokes $Z_{vc,stroke}$. An additional benefit of incorporating multiple valve heads (that each move a smaller stroke than a single large valve head) is that it becomes easier to structurally design the valve membranes (in that small valve membrane thicknesses are achievable) to support these valve caps within the required stress limitations. This will be illustrated in Section 5.6.

5.6 Results of Systematic Design Procedure

This section presents results of the full systematic active valve design procedure for the example valve requirements defined in Section 5.3.2. As detailed in previous sections, this quasi-static procedure will now incorporate the three design freedoms that were not included in the basic design procedure detailed in Section 5.3, namely the ability to design a valve structure for multiple valve heads ($N_{vh} > 1$), with varying valve cap strokes, and for differing valve membrane thicknesses. Specifically, the results presented in this section focus on a variety of chosen number of valve heads ($N_{vh} = 1, 2, 3, 5$), imposed valve cap strokes between $Z_{vc,stroke} = 8\mu m$ and $Z_{vc,stroke} = 40\mu m$, and available valve membrane thicknesses from $t_{vm} = 7\mu m$ and upward in increments of $1\mu m$. The results clearly demonstrate the potential benefits of multiple valve head geometries for reducing total valve power consumption.

Figure 5.20 plots the calculated valve cap radius, valve membrane thickness and radius, and drive element piston diameter for the variety of N_{vh} and $Z_{vc,stroke}$ values under question. Note that in Figure 5.20(b), for $N_{vh} \geq 2$, valve membranes with $t_{vm} = 7\mu m$ are achievable for all the imposed $Z_{vc,stroke}$ values. As more valve heads are allowed in parallel, each valve membrane gets smaller in size, resulting in reduced “bowing” of the membrane under the pressure loadings. This is the identical phenomenon to that discussed in Section 5.4.2. Also, notice in Figure 5.20(c) that as more valve heads are employed in the design, smaller drive piston dimensions are achieved, due to the fact that less swept volume is required by the valve membranes during actuation.

Figure 5.21 plots the calculated effective piezoelectric material diameter and the maximum compressive stress on the piezoelectric material during a full valve actuation cycle. Notice in Figure 5.21(a) that the required piezoelectric material diameter is generally increasing with increasing N_{vh} . This is due to the fact that the $P_{HAC}(t)$ actuation requirements are increased because of the increased stiffness of the valve membranes. It is important also to monitor the compressive stress seen by the piezoelectric material to ensure that it is below the compressive depolarization limits.

Figure 5.22 plots the estimated hysteretic power consumption, material and circuitry power loss, and total valve power consumption. As seen in Figure 5.22(a), the hysteretic power consumption can be significantly reduced by incorporating multiple valve heads working with moderate valve strokes. In addition, as shown in Figure 5.22(b) material and circuitry losses can also be reduced, since total energy flowing through the piezoelectric material is lessened. Finally, Figure 5.22(c) plots the combined power consumption for the various active valve designs. As indicated in this plot, the valve design that results in the minimum power consumption uses ten valve heads $N_{vh} = 5$, each traveling through a stroke of $Z_{vc,stroke} = 22\mu m$. These results demonstrate the capabilities of this systematic active valve design procedure in evaluating single

and multiple valve head designs under loading conditions put forth by a typical MHT system.

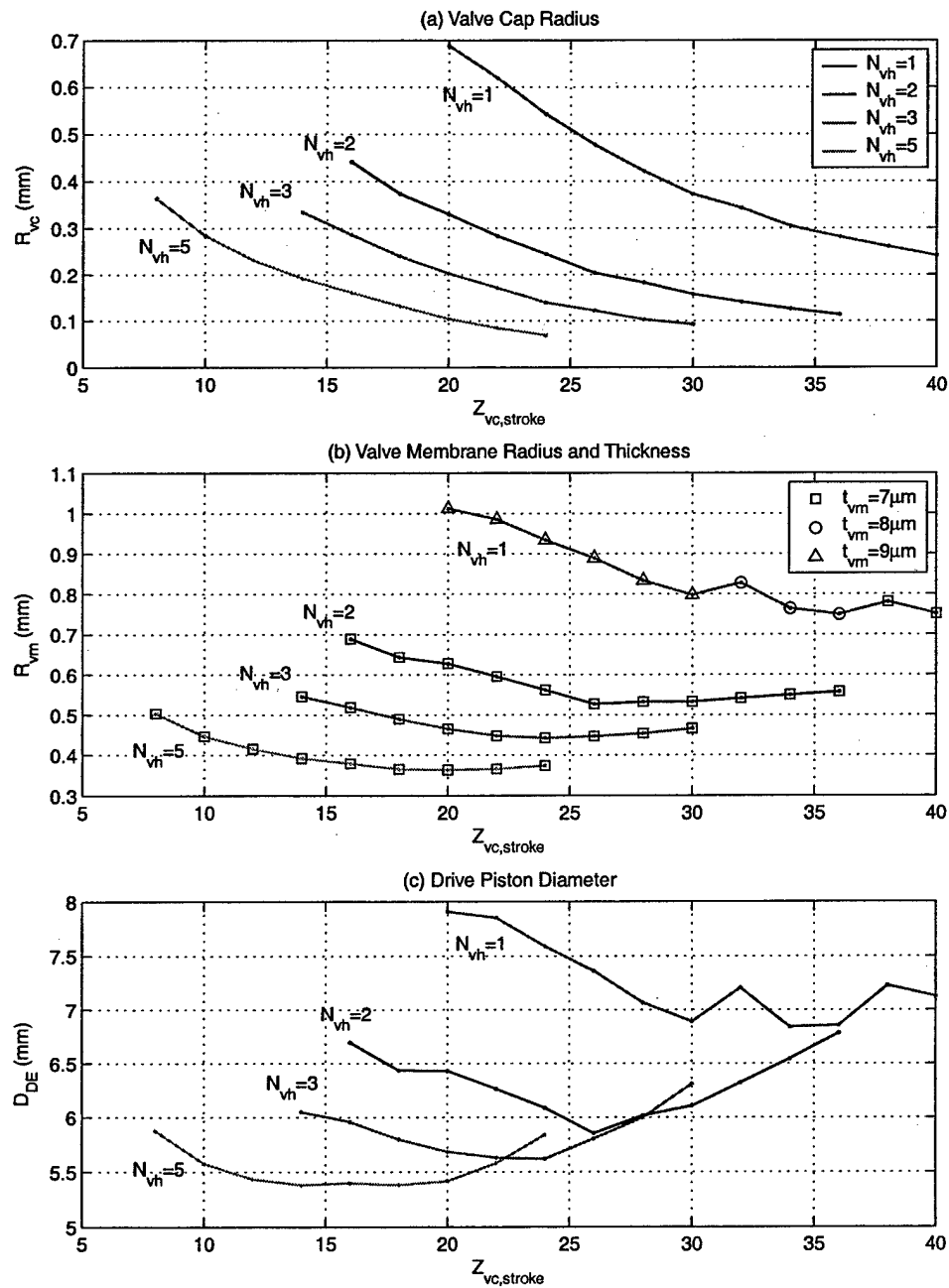


Figure 5.20: Multiple valve head comparison Plot 1

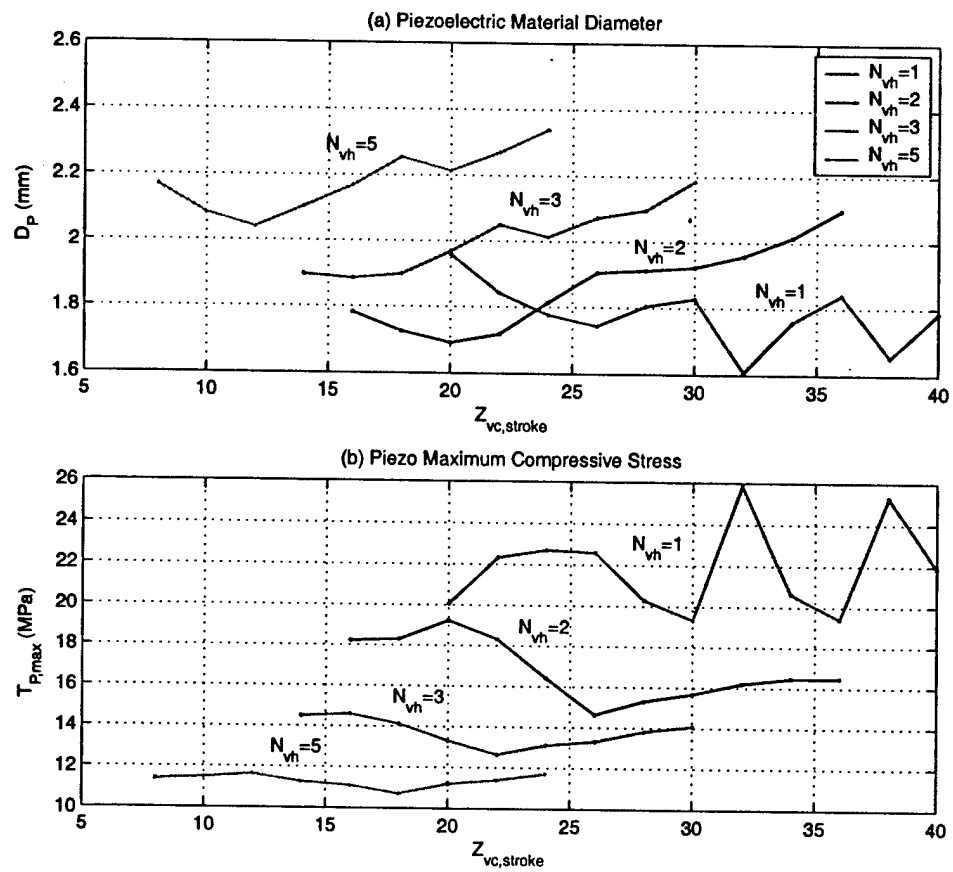


Figure 5.21: Multiple valve head comparison Plot 2

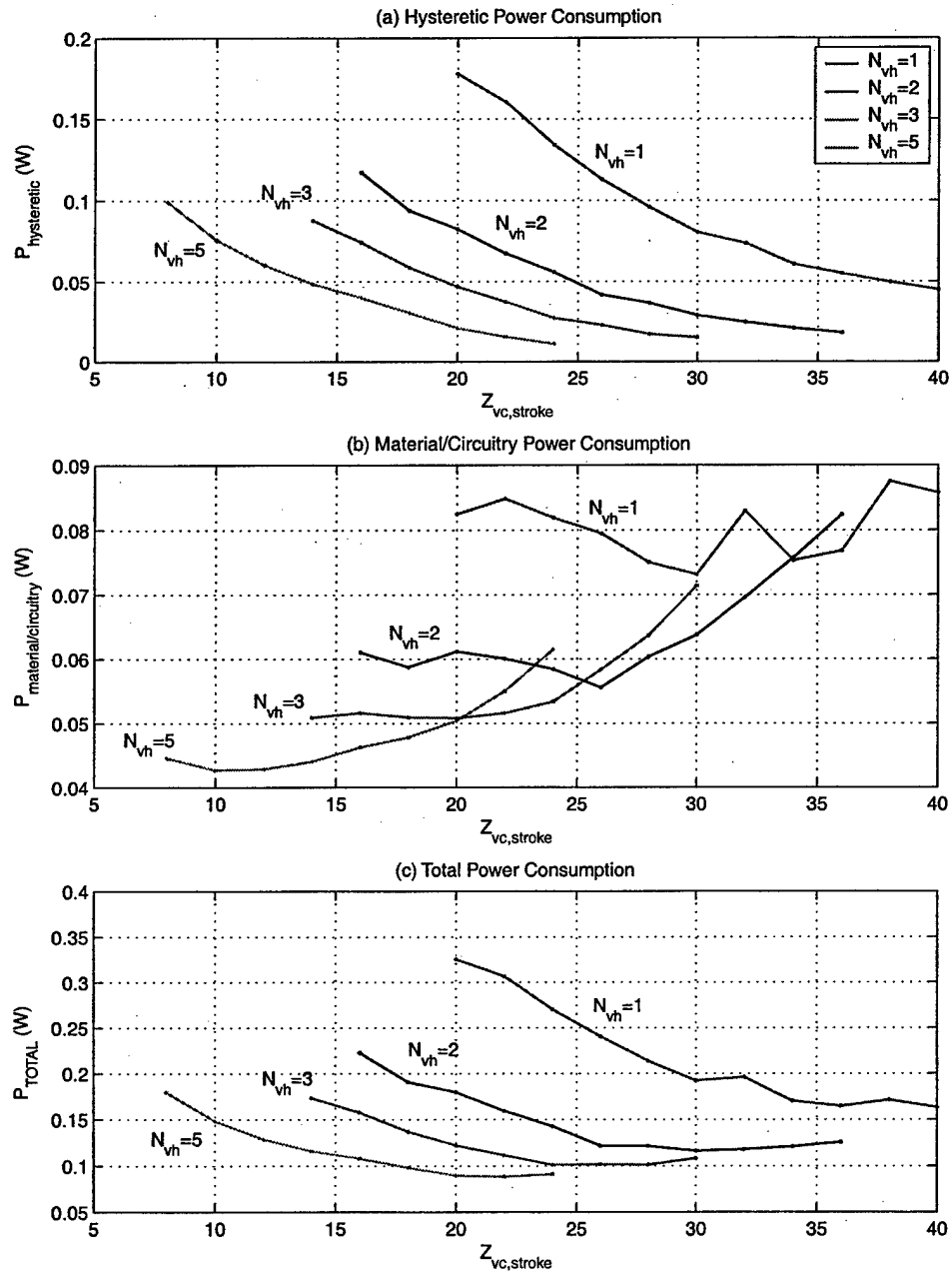


Figure 5.22: Multiple valve head comparison Plot 3

5.7 Correlation With Dynamic Simulation

The systematic design procedure presented in this chapter has been based on quasi-static structural behavior. In reality, dynamic effects within the active valve may result in performance of the valve that differs from quasi-static behavior. This section will take one of the active valve geometries formulated using the systematic design procedure in Section 5.6 and perform a full-scale dynamic simulation of this structure. The results will indicate that, indeed, the design formulated through the quasi-static procedure performs very close to expectations, thereby validating the use of the quasi-static procedure as a powerful tool for designing an active valve structure within a full hydraulic system.

The valve structure that was chosen for simulation is that corresponding to $N_{vh} = 1$ and $Z_{stroke} = 40\mu m$. Revisiting Figures 5.20, 5.21, and 5.22 in Section 5.6, the valve geometry is as follows: $R_{vc} = 241\mu m$, $t_{vm} = 7\mu m$, $R_{vm} = 757\mu m$, $R_{pis} = 3.59mm$, and $R_p = 0.88mm$. The peak-peak voltage applied to the piezoelectric material is 1000V at a frequency of $f = 10kHz$. Referring to Figures 5.8(b), 5.9, and 5.11, this active valve geometry is able to quasi-statically achieve the performance requirements set by the external hydraulic system, namely a pressure fluctuation in the harvesting chamber (with $K_{EHC} = 1.5e^{16} \frac{Pa}{m^3}$) from 0.2MPa to 1.0MPa, given reservoir pressures of $P_{HPR} = 1.2MPa$ and $P_{LPR} = 0$.

In order to evaluate this active valve geometry in a full dynamic simulation, a complete simulation architecture is implemented that includes the active valve simulation (presented in Chapter 4) and the external hydraulic system relations detailed in Section 5.2. Figure 5.23 shows this full simulation architecture. The additional external hydraulic system architecture (including the effects of the fluid orifice pressure-flow relations, the valve channel inertia, and the chamber stiffness) is coupled to this active valve system to simulate full filling and evacuation. In order to create full system pumping behavior, a chamber with both an inlet and outlet active valve is included in the simulation. In addition, critical valve variables, such as $\sigma_{vm}(t)$, $Z_{vc}(t)$, and $P_{HAC}(t)$ are monitored. In this simulation, a positive valve stop at a location of $Z_{vc} = 20\mu m$ is implemented. The results of this simulation for two different values of valve cap damping are shown in Figure 5.24. For further details on full MHT system simulations, refer to [8].

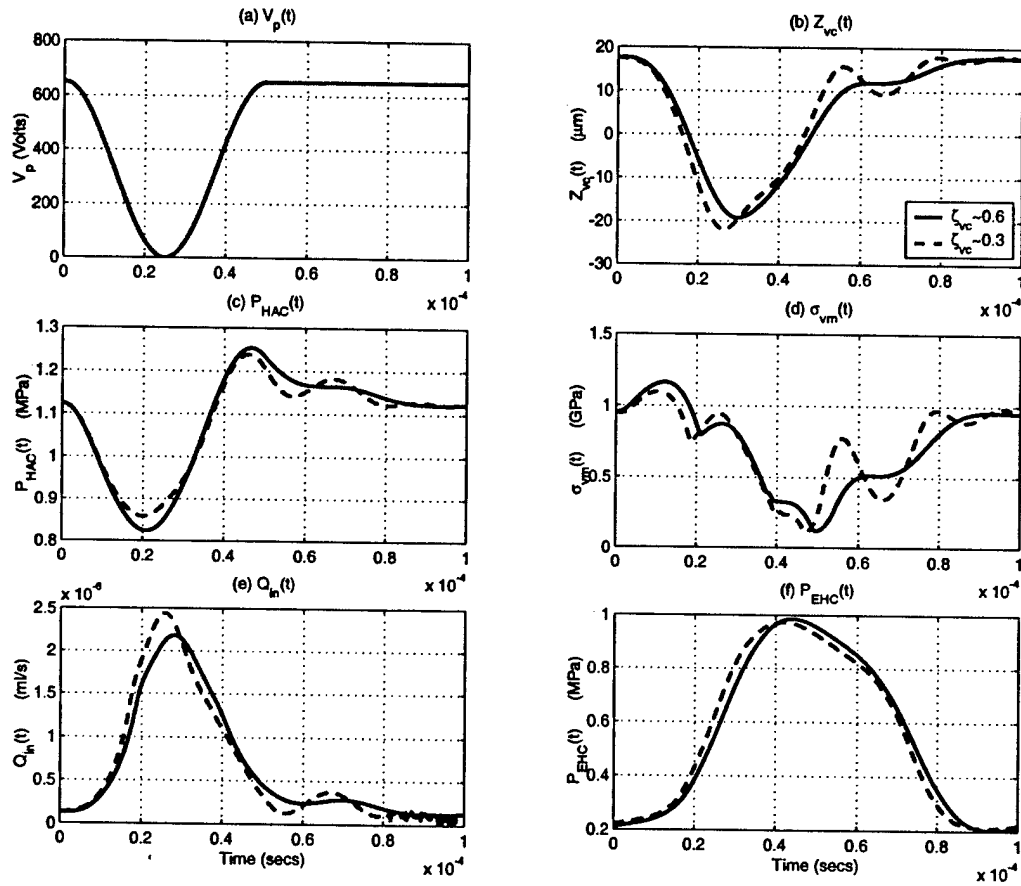


Figure 5.24: Full system simulations: (a) solid line represents case in which $\zeta_{pis} = 0.7$, $\zeta_{vc} = 0.6$, (b) dashed line represents case in which $\zeta_{pis} = 0.7$, $\zeta_{vc} = 0.3$. Note that in these cases, the valve cap does not hit the stop. In these plots, V_p is the applied piezoelectric voltage, $Z_{vc}(t)$ is the position of the valve cap, $P_{HAC}(t)$ is the hydraulic amplification chamber pressure, $\sigma_{vm}(t)$ is the maximum valve membrane stress, $Q_{in}(t)$ is the flow rate through the valve, and $P_{EHC}(t)$ is the external chamber pressure.

Due to dynamic effects in the active valve system, an applied peak-peak voltage of only 650V (compared to the quasi-static value of 1000V) is required to actuate the valve and to produce the proper filling behavior of the harvesting chamber. Notice that the valve cap $Z_{vc}(t)$, HAC pressure $P_{HAC}(t)$, inlet flow rate $Q_{in}(t)$, and resulting harvesting chamber pressure $P_{EHC}(t)$ time histories all correlate very closely to those predicted by the systematic quasi-static design procedure. One interesting note is that the valve membrane stress σ_{vm} time history differs slightly from the quasi-static prediction in the region when the valve cap is just beginning to open. Rather than immediately decreasing, as is predicted in the quasi-static procedure, σ_{vm} actually begins to increase to a peak value of $1.15GPa$ (for $\zeta_{vc} = 0.6$) and to a peak value of $1.05GPa$ (for $\zeta_{vc} = 0.3$) just after opening. This phenomenon is due to the dynamic effects on the valve membrane. Essentially, the P_{HAC} pressure below the membrane decreases substantially before the valve cap is able to move downward (due to the cap's inertia and the effect of damping), resulting in an enhanced membrane curvature at R_{vc} and therefore an increase in σ_{vm} .

These important observations on the membrane stress can be fed back to the quasi-static design procedure. Using a smaller value of limiting stress σ_{limit} , a slightly modified valve geometry can be generated so that dynamic membrane stresses do not exceed the desired bound. Overall, the dynamic performance of the active valve geometry formulated using the systematic quasi-static design procedure detailed in this chapter matches fairly well to desired requirements. This design procedure, therefore, can be very useful in developing valve geometries for use in full hydraulic systems.

5.8 Conclusions

This chapter has introduced the physical equations governing the fluid flow behavior within a generic MHT system, external to the valve cap and membrane structure of the active valve. With these relations, a comprehensive and systematic quasi-static design procedure has been presented that enables a designer to formulate an active valve geometry for use within an MHT system to satisfy certain pressure-flow requirements. This procedure formulates designs and evaluates valve power consumption for geometries with one or more valve heads acting in parallel above the hydraulic amplification chamber and for differing valve cap strokes. Additionally, valve membrane structures are designed to guarantee peak stress levels below a critical value during complete valve time histories. Active valve geometries produced by this design procedure have been analyzed using full dynamic system simulations, and results indicate that dynamic effects do not significantly affect the ability to meet the performance requirements. Overall, this design procedure enables the generation of active valve geometries for a potentially wide variety of hydraulic systems.

Bibliography

- [1] N.W. Hagood, D.C. Roberts, L. Saggere, K.S. Breuer, K-S. Chen, J.A. Carretero, H.Q. Li, R. Mlcak, S. Pulitzer, M.A. Schmidt, S.M. Spearing, and Y-H. Su, "Micro Hydraulic Transducer Technology for Actuation and Power Generation", Proceedings of SPIE, Vol. 3985 (2000), Newport Beach, CA, March 5-9, 2000, pp.680-688.
- [2] J. Carretero and K.S. Breuer, "Measurement and Modeling of the Flow Characteristics of Micro Disk Valves," Proceedings of the 1994 International Mechanical Engineering Conference and Exposition: Microfluidics Symposium, Orlando, FL, Nov. 2000.
- [3] E. Schrenk, "Disc valves, flow patterns, resistance and loading," BHRA T, 1957 (547). Translation from German.
- [4] A. Lichtarowicz, "Flow and Force Characteristics of Flapper Valves," Third International Symposium on Fluid Power, Turin, 1973, pp. B1-1.
- [5] D.N. Johnston, K.A. Edge, and N.D. Vaughan, "Experimental investigation of flow and force characteristics of hydraulic poppet and disc valves," Proceedings of the Institution of Mechanical Engineers, Part A: Power & Process Engineering, 1991 Vol 205, No 3, pp. 161-171.
- [6] S.M. Spearing and K.S. Chen, "Micro-gas turbine engine materials and structures," *Ceramic Engineering & Science Proceedings v.18n 4B*, p. 11-18, 1997.
- [7] K.T. Turner, An Evaluation of Critical Issues for Microhydraulic Transducers: Silicon Wafer Bonding, Strength of Silicon on Insulator Membranes and Gold-Tin Solder Bonding, Massachusetts Institute of Technology, Master's Thesis, 2001.
- [8] O. Yaglioglu. Master's Thesis, Massachusetts Institute of Technology, 2002.

Chapter 6

Device Fabrication and Preparation for Testing

6.1 Introduction

The proposed piezoelectrically-driven hydraulic-amplification microvalve is fabricated using a combination of microscale (silicon patterning and etching) and macroscale (piezoelectric material integration) procedures. As detailed in previous chapters of this thesis, the valve consists of multiple layers of silicon and glass (Pyrex 7740) with integrated piezoelectric elements, all bonded together to form the important structural features of the device. These features are the tethered-piston piezoelectric drive element, the enclosed hydraulic amplification chamber, the valve membrane and orifice structure, and the fluid channels to and from the valve. A cross-section of a full MHT system, with embedded multi-layered active valve structure, is shown in Figure 6.1. Successful fabrication and assembly of a complete MHT system involves overcoming the identical challenges associated with realizing a working active valve device, since the valve structure and full MHT system span the same layers. As a result, the fabrication and assembly processes presented in this chapter are not unique to the active valve, but rather provide a platform of procedures that can be implemented to create a wide variety of micro-hydraulic systems. For the purposes of this thesis, however, only the geometry of the active valve is referred to in the fabrication and assembly discussions.

Layers 1, 3, 6, and 9 of the active valve structure (shown in Figure 6.1) are each borosilicate glass (Pyrex 7740), the features of which are formed through wafer-level ultrasonic machining. Layers 2 and 8 are formed from standard silicon wafers and are etched using deep-reactive ion etching procedures. Layers 4, 5, and 7 are created from silicon-on-insulator (SOI) wafers. The drive element tethers supporting the piston structure in Layers 4 and 5 and the valve membrane and cap structure in Layer 7 are produced using deep-reactive etching, with the buried oxide

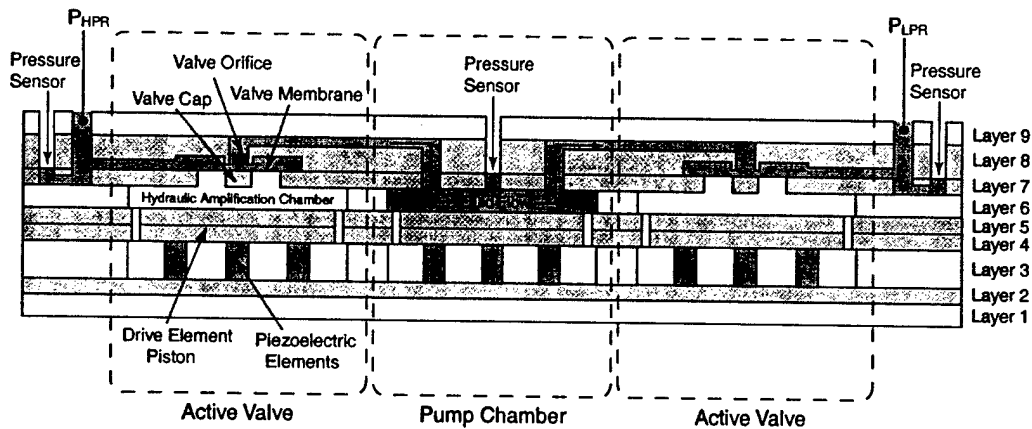


Figure 6.1: Cross-section schematic of a nine-layer multiple wafer MHT system with two embedded active valve structures. Realization of this active valve requires robust bonding of silicon-to-silicon and silicon-to-glass at the wafer-level and integration and bonding of piezoelectric material elements with silicon at the die-level, as will be discussed later in this chapter.

acting as an etch stop for precise control of tether and membrane thicknesses. Three primary bonding mechanisms are used to realize a complete valve device: silicon-silicon fusion bonding, silicon-glass anodic bonding, and silicon-piezoelectric material eutectic bonding.

This chapter first details the critical challenges associated with the fabrication and assembly of this multi-layer active valve device, namely (1) etching of the high-aspect ratio features in silicon-on-insulator wafers to form the tethered drive element piston and valve membrane structures, (2) wafer-level silicon-silicon fusion bonding and wafer-level silicon-glass anodic bonding, (3) preparation, integration, and bonding of the bulk piezoelectric material elements within the drive element structure, (4) die-level assembly of multiple silicon and glass layers, and (5) fluid filling and sealing of the hydraulic amplification chamber. Having laid out the details of these fabrication issues and the procedures used to overcome these obstacles, the chapter then presents a systematic fabrication and testing plan of important active valve sub-components, as a means to prove out the fabrication challenges. Details of each of the sub-component studies leading up to the full active valve are then documented in subsequent chapters of this thesis.

6.2 Fabrication Challenges and Procedures

This section attempts to follow the fabrication and assembly process in order of the steps and challenges involved. The first two challenges focus on the activities relating to wafer-level processing: etching of the drive element tether and valve membrane structures and silicon-silicon and silicon-glass wafer bonding procedures. The second two challenges are concerned

with die-level processing: preparation and integration of the piezoelectric elements within the device and the process flow associated with the die-level silicon-glass anodic bonding. The final challenge focuses on filling and sealing of fluid in the device once the active valve device has been successfully fabricated and assembled at the die-level.

6.2.1 Etching of Tethered Drive Element and Valve Membranes

The drive element tethers and valve membranes within the active valve device are designed to be quite thin (on the order of $7 - 10\mu m$). To achieve precise dimensional control of these features, SOI wafers containing a buried oxide layer a preset distance from one side of the wafer are used. In performing deep etches into the silicon wafer down to the buried oxide layer, it is critical that the surface roughness of the etch and the tailoring of fillet radii profiles at the base of the etched profiles be well-controlled so as to maintain strength and robustness of the thin-membrane structures. Figure 6.2 illustrates etch profiles at the SOI interface of a typical drive element piston that can result, depending on the process chosen and care given to performing the etch. Ideally, one would like to create a fillet radius between the thin tether and the much thicker ($\sim 400\mu m$) central piston structure to minimize stress concentrations, as shown in Figure 6.2(c). It is essential to avoid etch profiles such as the sharp corner shown in Figure 6.2(b) and the "footing" or "notching" profile shown in Figure 6.2(d). These serve to magnify stresses at these interface regions, thereby compromising the overall strength of the structure.

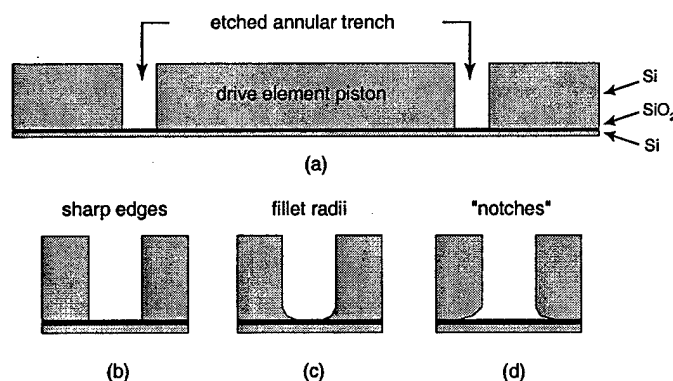


Figure 6.2: Etching of a typical drive element piston structure: (a) cross-section view of drive piston, (b) sharp corner etch features, (c) fillet radius features, and (d) "notching" or "footing" features.

Considerable research work has been done in developing and optimizing deep etching processes for single-crystal silicon materials [1] [2]. The Deep-Reactive Ion Etching (DRIE) process

used to create the structures and devices in this thesis is known as the Bosch Process [1]. This method involves repetitive cycles of plasma etching and passivation to create high aspect ratio deep trenches in silicon. Using photoresist as a masking agent, a timed plasma etch using SF_6 is carried out. Following this timed etch, a passivating film using C_4F_8 is deposited over all exposed surfaces of the wafer, including the etched trench bottom and sidewalls. During the next timed plasma etch, this passivating film is preferentially removed from the bottom of the trenches through ion bombardment, while the film on the sidewalls remains intact. This cyclic process is repeated until the buried-oxide etch stop layer is reached. At this juncture, carefully monitoring of the etch process is performed to ensure that fillet radii of a desired size (based on modeling specifications) are created. Figure 6.3 shows views of a successfully etched drive element piston structure with properly tailored fillet radii.

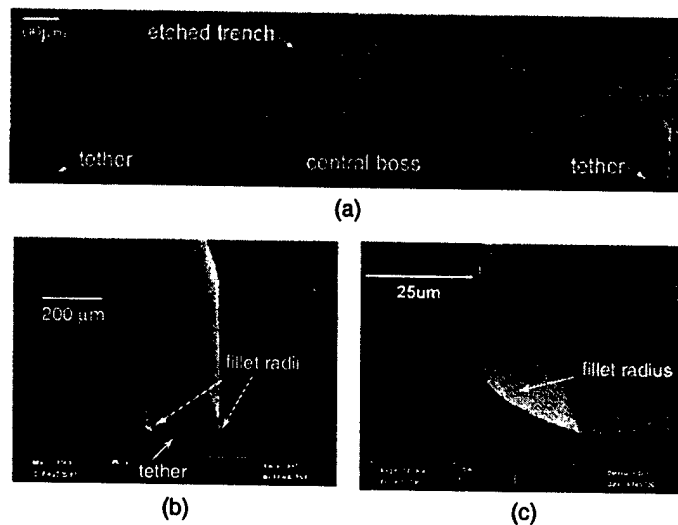


Figure 6.3: SEM images of an etched drive element piston: (a) cross-section view of SOI piston structure, (b) close-up of etched trench, and (c) further close-up of fillet radius feature. In this structure, a 20 – 25 μm fillet radius was achieved. Debris in background was generated during die-saw procedures.

This final “fillet tailoring” step is tedious and difficult because once the silicon has been etched away such that portions of the oxide are visible, very little time is required for lateral etching of the remaining silicon above the oxide layer to be completely etched away, resulting in potential “footing” profiles at the interface. The rapid lateral etching has been studied and investigated by numerous individuals, and it is believed to result from plasma charging effects at the silicon/oxide interface [3] [4] [5]. Consistently controlling these fillet profiles is extremely hard to achieve, as etch parameters such as etch time, passivation time, SF_6 flow rate, electrode power during etching, electrode power during passivation, and C_4F_8 flow rate must be tuned

and optimized. The details of these DRIE process parameters are beyond the scope of this thesis. The purpose of this section, rather, has been to present the significant challenges and obstacles faced in the etching of thin-membrane structures with desired fillet radii profiles. A designer may specify a particular fillet size, but the cleanroom process of achieving that profile is often a time-consuming one.

6.2.2 Wafer-Level Bonding

For the multi-layer active valve structure presented in this thesis, various silicon-silicon and silicon-glass wafer-level bonds are performed. A silicon-silicon wafer-level fusion bonding process is used to bond Layers 4 and 5 together to form Stack 4-5 and Layers 7 and 8 together to form Stack 7-8. A silicon-glass wafer-level anodic bonding process is used to bond Layers 1 and 2 together to form Stack 1-2, Stack 4-5 and Layer 6 together to form Stack 4-5-6, and Stack 7-8 and Layer 9 together to form Stack 7-8-9. Following these wafer-level bonding steps, the stacks are die-sawed into individual dies and cleaned in preparation for die-level bonding and piezoelectric material integration. Further discussion of why certain bond steps are performed at the wafer-level and others at the die-level is covered in Section 6.2.4. Figure 6.4 illustrates the various wafer-level silicon-silicon and silicon-glass bonding steps.

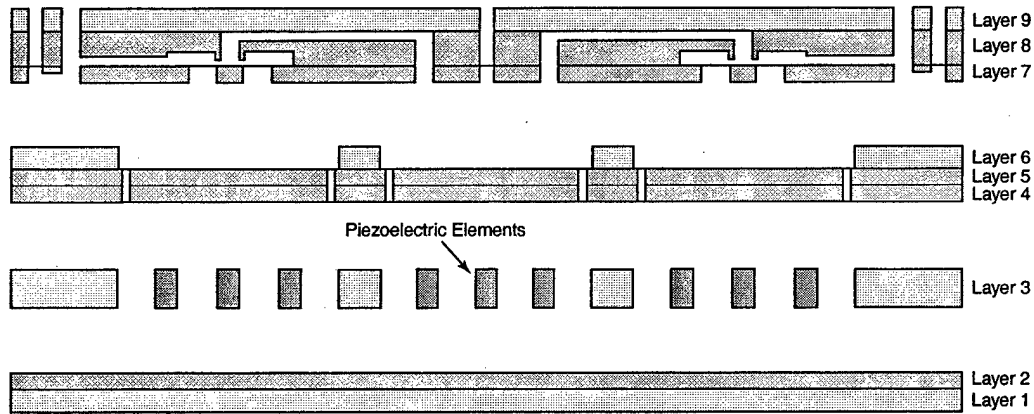


Figure 6.4: Wafer-level silicon-silicon fusion and silicon-glass anodic bonding steps are carried out prior to piezoelectric material integration.

The silicon-silicon fusion bonding process used to create wafer-level stacks for the active valve device is a well developed process and consists of three primary steps [6]: (1) preparation and treatment of the silicon wafer surface to produce a hydrophilic surface, (2) alignment and adhesion of two wafers together (weak van der Waals or hydrogen bonds maintain wafer-wafer adhesion) in a clean room-temperature environment, either in air, inert atmosphere, or vacuum, and (3) high temperature annealing of the wafer stack at 1000°C to promote strong covalent

bonding. The strength of this fusion bond is dependent on the annealing temperature and time [2]. Paramount in the bonding process is the cleanliness of the silicon wafers prior to bonding and of the alignment and bonding apparatus itself. Particulate matter present between the silicon wafers during adhesion can result in significant defect regions characterized by little or no bonding.

The silicon-glass anodic bonding process used to create wafer-level stacks also is a well-developed process. This process involves three primary steps: (1) preparation and cleaning of the silicon and glass surfaces using a piranha soak and an oxygen ashing step, (2) alignment and clamping of the two wafers together, and (3) application of a voltage (1000V) across the wafer interface at elevated temperature (300°). The negative electrode is applied to glass wafer surface not being bonded with the silicon wafer held at ground potential. As for the fusion bonding process, cleanliness of the wafers and the bonding apparatus is paramount for achieving high-quality and low-defect wafer-level bonds.

6.2.3 Integration of Bulk Piezoelectric Elements

Integration of the piezoelectric elements within the device constitutes a critical task in the assembly of the active valve device. This section discusses the important issues related to preparing and tolerancing of the piezoelectric material elements with respect to other features in the device. Details of the actual die-level assembly procedure will be provided in Section 6.2.4.

The top and bottom surfaces of the piezoelectric elements are covered with a thin-film gold-tin (Au-Sn) eutectic alloy for bonding to the adjoining silicon layers at an elevated temperature. In order to achieve good bonding over the complete interface area, the piezoelectric material must possess smooth top and bottom surfaces. A rough surface of the piezoelectric material (and therefore of the metallized layer), would result in only pinpoint contacts between the piezoelectric material and the silicon and therefore a weak bond. Prior to bonding, sizing of the piezoelectric elements with respect to the surrounding Layer 3 glass and etching of seats in the Layer 2 silicon to compensate for thickness mismatch between the piezoelectric material and glass is critical for ensuring a deflection of the drive element piston below levels of fracture stress in the tethers. Each of these piezoelectric material integration issues is covered in detail in the following sub-sections.

Piezoelectric Material Preparation

Virgin piezoelectric materials are obtained from vendors in the form of thin plates, each with a thickness of $\sim 1.1\text{mm}$ and diameter between 1 cm and 5 cm. As received, these plates possess a surface roughness as large as $5\mu\text{m}$. In order to achieve adequate eutectic bonding during

device assembly, a surface roughness near $0.5\mu\text{m}$ is required prior to metallization. To achieve this, the piezoelectric material plates are polished using coarse and fine grain diamond slurry polishing procedures. Figure 6.5 displays typical profilometer scans before and after material polishing for the two primary types of piezoelectric materials used in the valve, PZT-5H and PZN-PT.

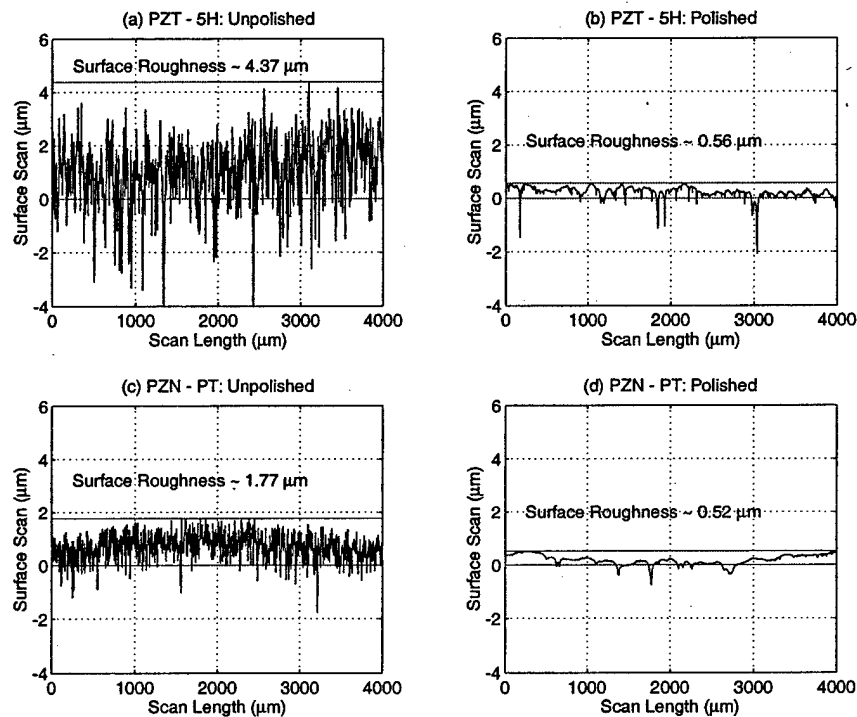


Figure 6.5: Profilometer surface roughness scans of PZT-5H and PZN-PT piezoelectric material plates before and after polishing steps: (a) unpolished PZT-5H material, (b) polished PZT-5H material, (c) unpolished PZN-PT material, (d) polished PZN-PT material. Note that thin deep trenches are not counted within the roughness estimate. However, thin tall “mountains” must be accounted for since these would serve to separate an adjoining layer of material.

During polishing, each plate is sized to yield a thickness of $1\text{mm} \pm 10\mu\text{m}$ with thickness variation across the plate of $\sim 2\mu\text{m}$. Prior to metallization, the material plates are solvent cleaned with a series of acetone, methanol, and isopropanol steps. Additionally, a further cleaning soak in a 20:1 water:nitric acid solution is carried out for 1 minute to remove particulate matter. At this point, the piezoelectric material plates are ready for metallization.

AuSn Eutectic Bonding

To bond mechanically and to connect electrically the piezoelectric material cylinders to the adjoining silicon layers in the active valve device, a reliable bonding mechanism must be employed. This bonding mechanism must allow for tight dimensional control over the bond layer thickness and allow for a bonding temperature and environment that is compatible with the rest of the die-level assembly process. Numerous bonding methods that could potentially work in this device, ranging from polyimides and epoxies to brazing and soldering to gold-based eutectic alloys, have been presented in the literature. A detailed discussion of these research efforts, with application toward the development of MHT technology, is found in [2]. The resulting conclusion of initial work by Mlcak [8] and the subsequent work by Turner [2] was to employ a thin-film AuSn eutectic alloy (composition: 80 wt. % Au and 20 wt. % Sn) as the bonding mechanism within MHT devices in general, and specifically within the active valve device presented in this thesis.

A four layer film structure on the piezoelectric material and a three layer film structure on each of the adjoining silicon layers is deposited in preparation for bonding, as shown in Figure 6.6. The four layer structure on the piezoelectric material consists of 50 nm Ti, 250 nm Pt, 4000 nm AuSn, and 50 nm Au. The Ti serves as an adhesion layer, the Pt as a diffusion barrier, and the final Au as a capping layer to prevent oxidation of Sn in the AuSn alloy. The AuSn layer, chosen to be thick enough ($4\text{ }\mu\text{m}$) to compensate for the piezoelectric material surface roughness ($\sim 0.5\text{ }\mu\text{m}$), is sputtered from an alloy target with 80 wt. % Au and 20 wt. % Sn composition. Sputtering is chosen over evaporation because sputtering allows the stoichiometry of the target to be maintained in the deposited film [9]. The three layer Ti-Pt-Au structure on each of the adjoining silicon pieces enables the eutectic alloy to wet the silicon and is deposited on the die-level using e-beam evaporation procedures.

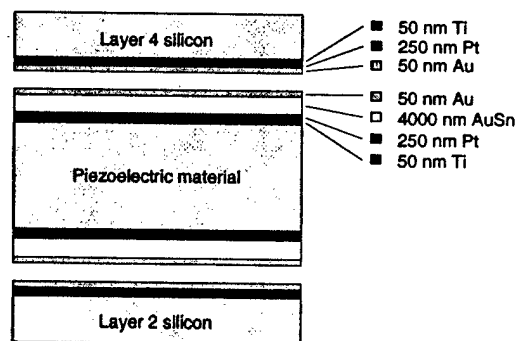


Figure 6.6: Eutectic alloy deposition on the piezoelectric material and adjoining silicon layers. The piezoelectric material contains a 4 layer film structure and each of the silicon layers contains a 3 layer film structure.

Dicing/Core-Drilling of Piezoelectric Elements

Following deposition of the eutectic alloy, the metallized piezoelectric material plates are core-drilled or diced to produce either cylindrical or square piezoelectric elements. As detailed in subsequent chapters of this thesis, devices integrating both cylindrical and square elements have been successfully fabricated and tested. The advantage of using square piezoelectric elements over cylindrical ones is that the process of dicing a piezoelectric material plate in a grid pattern results in the production of 2-3 times the number of elements than can be produced from core-drilling from a identical size plate. By sheer numbers and by the fact that closely located elements will possess almost identical thicknesses (relatively insensitive to variations in thickness across the material plates), the use of square elements increases the odds of being able to select multiple elements of identical thickness to insert into drive element structures. Once the material plate has been either core-drilled or diced, the resulting piezoelectric elements are individually measured for thickness using a hand-held precision micrometer, as shown in Figure 6.7. By calibrating the micrometer before each measurement with a precise thickness gauge block ($1\text{mm} \pm 0.01\ \mu\text{m}$) and averaging repeated series of measurements of the same elements, these thickness measurements are estimated to be accurate within $\sim 0.5\ \mu\text{m}$. The elements are then organized and sorted according to the thickness.

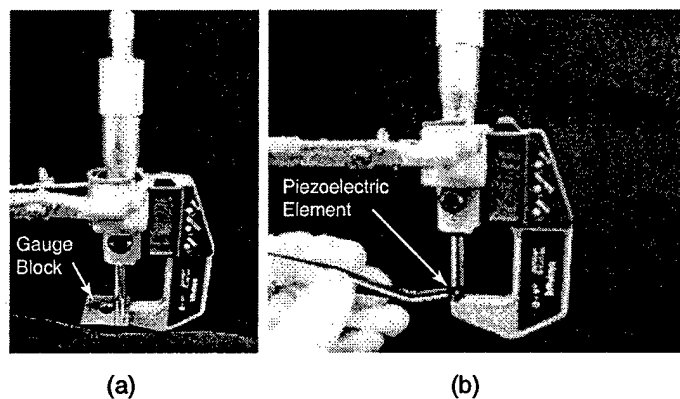


Figure 6.7: Precision micrometer used for thickness measurement of the piezoelectric elements and Layer 3 glass dies prior to device assembly: (a) calibration of micrometer with respect to a 1 mm gauge block, and (b) measurement of an individual piezoelectric element.

Etching of Piezoelectric Element Seats

One of the critical issues during integration of the piezoelectric material elements is guaranteeing an upward deflection of the drive element piston large enough to ensure a preload on the eutectic

alloy interface during bonding, yet small enough to ensure stresses in the piston tethers below the critical value of 1 GPa. Typically, in the drive element structures designed, fabricated, and tested in this thesis, the piston tethers will reach a tensile stress of 1 GPa for displacements near $\sim 9\mu\text{m}$. Therefore, at any time during the bonding, poling, and operation of a device, it is desired to maintain piston displacements no greater than a safe value of $\sim 6\mu\text{m}$. In terms of preload on the eutectic interface, it is desired to ensure a "piston push-up" of $\sim 2\mu\text{m}$. These requirements therefore dictate that at the instant of eutectic bonding, the piezoelectric element(s) beneath the drive element piston must be forcing the piston upward by $\sim 2\mu\text{m}$ and that for all time after that the piston must not be forced to displacements greater than $\sim 6\mu\text{m}$. Considering that this $4\mu\text{m}$ range is 0.4% of the total piezoelectric element thickness, this task represents quite a challenge.

In preparation for piezoelectric element integration, the Layer 3 glass wafer is diced into individual dies, and each of these dies is measured using the hand-held micrometer. As received from the vendor, each of the ultrasonically-machined Layer 3 glass wafers possesses a thickness between $967\mu\text{m}$ and $974\mu\text{m}$, with thickness variation across a given wafer less than $1\mu\text{m}$. At the time of integration, since the piezoelectric elements (with deposited eutectic alloy films) have thicknesses near $1000\mu\text{m}$ and the Layer 3 glass dies have thickness near $970\mu\text{m}$, it is necessary to have the capability to remove this thickness difference of $\sim 30\mu\text{m}$ between the piezoelectric material and the surrounding glass. Ideally, once integrated into the device, the piezoelectric elements' top surfaces should be slightly above level with the Layer 3 glass top surface so as to produce predictable upward displacement of the drive element piston from its equilibrium position ("push-up").

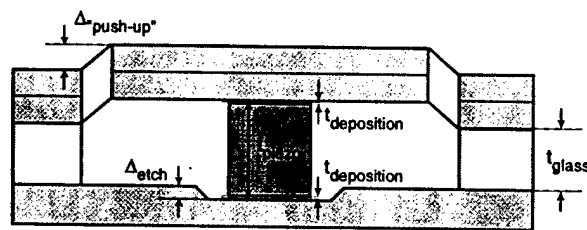


Figure 6.8: Compensation of the piezoelectric element - Layer 3 glass thickness mismatch by plasma etching shallow seats in the Layer 2 bottom silicon die. Precise control of the etch depth is necessary to achieve the desired "push-up" of the drive element piston.

This thickness matching is achieved by plasma etching shallow seats for all of the piezoelectric elements in the Layer 2 bottom silicon wafer, as shown in Figure 6.8. An iterative process of carefully timed etches followed by depth measurements using a scanning profilometer can result in etch depth control to within $\sim 0.5\mu\text{m}$. With this capability to compensate for thickness mismatch between the piezoelectric elements and the surrounding Layer 3 glass, proper

“push-up” of the drive element piston can be achieved during assembly and bonding. On the die-level, each Layer 2 silicon die is matched with a pre-measured (t_{piezo}) grouping of one or three piezoelectric elements (depending on whether a single or multiple piezoelectric valve is being fabricated) and with a pre-measured (t_{glass}) Layer 3 glass die. With knowledge of the three-layer film thickness $t_{deposition}$ (see Section 6.2.3) that will subsequently be deposited on the underside of the drive element piston in Layer 4 and on the top surface of the “to be etched” seats in Layer 2, and with the value of $\Delta_{“push-up”}$ desired after device assembly, the required etch depth (Δ_{etch}) in Layer 2 is determined, according to 6.1.

$$\Delta_{etch} = t_{piezo} + 2t_{deposition} - t_{glass} - \Delta_{“push-up”} \quad (6.1)$$

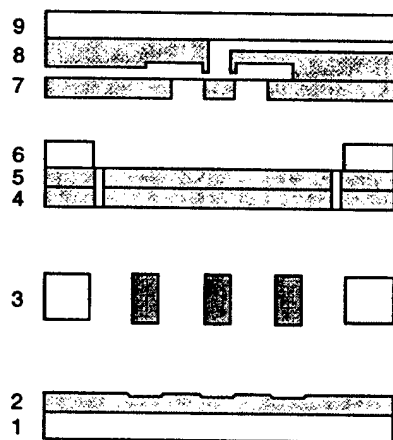
Following etching of the seats, the Layer 1-2 silicon dies are cleaned and combined with Stack 4-5-6 silicon dies for deposition of the three-layer Ti-Pt-Au film structure required for eutectic bonding. This deposition is performed using e-beam evaporation through specially-machined shadow masks to allow for selective coating of the dies. For the Stack 4-5-6 dies, the underside of the drive element piston is coated, and for Layer 2 dies the inside of each of the etch seats is coated.

6.2.4 Die-Level Assembly and Bonding

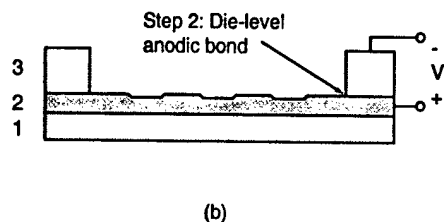
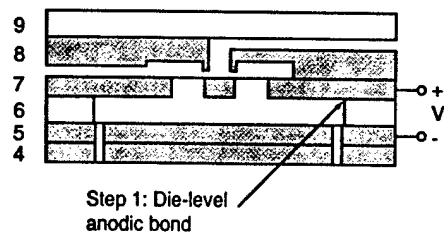
Assembly and Bonding Procedure

Final assembly of the active valve device is performed at the die-level. As shown in Figure 6.9(a), wafer-level etching and bonding procedures, followed by dicing of the stacks into individual dies have resulted in the creation of a Stack 7-8-9 die, a Stack 4-5-6 die, a Stack 1-2 die, and a Layer 3 die. Additionally, piezoelectric material preparations have created individual piezoelectric elements ready for insertion. It is desirable to perform these bonding steps at the die-level, rather than the wafer-level, so as to allow for individual measurements of the Layer 3 glass die thickness and to enable individual control of the seat etching in Layer 2. Additionally, die-level bonding significantly reduces the risk of losing an entire multi-layer wafer structure during wafer-level processing. The die-level assembly process consists of four main steps, as shown in Figure 6.9(b), (c), (d).

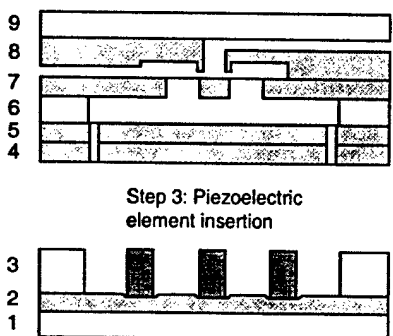
1. Die-level anodic bonding of Stack 4-5-6 to Stack 7-8-9 at a temperature of 300°C and an applied voltage of 1000V across the Layer 6 - Layer 7 interface. This bond is performed at atmospheric pressure. Time of bond = 20 minutes.
2. Die-level anodic bonding of Stack 1-2 to Layer 3 at a temperature of 300°C and an applied voltage of 1000V across the Layer 2 - Layer 3 interface. This bond is performed at atmospheric pressure. Time of bond = 45 minutes.



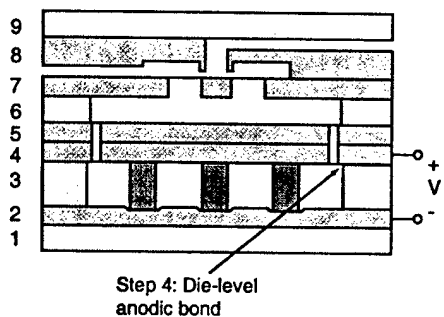
(a)



(b)



(c)



(d)

Figure 6.9: Die-level bonding procedure for active valve device: (a) beginning dies ready for assembly, (b) Step 1: anodic bonding of Stack 4-5-6 to Stack 7-8-9 ; Step 2: anodic bonding of Stack 1-2 to Layer 3, (c) Step 3: insertion of piezoelectric element(s), and (d) Step 4: anodic bonding of Stack 1-2-3 to Stack 4-5-6-7-8-9.

3. Alignment and placement of one or more piezoelectric material elements within the Stack 1-2-3 die.
4. Simultaneous die-level anodic bonding of Stack 1-2-3 to Stack 4-5-6-7-8-9 and eutectic bonding of piezoelectric element(s) to Layer 2 and Layer 4 silicon. This bond is performed in a reducing atmosphere of $Ar - 5\%H_2$ gas at pressure 10^{-2} torr and temperature $300^\circ C$. Additionally, a voltage of 1000V is applied across the Layer 3 - Layer 4 interface. Time of bond = 60 minutes.

A reducing atmosphere is chosen for the final simultaneous anodic/eutectic bond to ensure no oxidation of the Sn within the AuSn alloy and to achieve a void-free eutectic bond [2]. Additionally, following this bond, the device is cooled under vacuum to ensure removal of all trapped gases within the bond. Completion of these four die-level bonding steps produces an active valve structure that is ready for filling of the hydraulic amplification chamber.

Assembly Jigs

The die-level anodic bonding discussed above is performed using the specially machined alignment and bonding jigs shown in Figure 6.10. The 1st-generation jig, shown in Figure 6.10(a), provides a large central contact surface onto which a die can be placed and the bottom surface held at either positive or negative voltage. An outer ring with attached spring clamps for clamping of one die onto another is held at ground potential. Once inserted into an oven, electrical contact is made through attached feet on the underside of the jig. Alignment, placement, and clamping of a dies and insertion of piezoelectric elements is facilitated by a vacuum chuck with 3-axis motion capability and a range in each of these directions of 1 cm. The 2nd-generation jig, shown in Figure 6.10(b), is more compact than the 1st-generation jig. It likewise provides electrical contact through thin wire clamps, but additionally allows for edge alignment of dies to a central area with ceramic insulating locator pins. Figure 6.11 illustrates an active valve device in the final bonding step using the 2nd-generation anodic bonding jig.

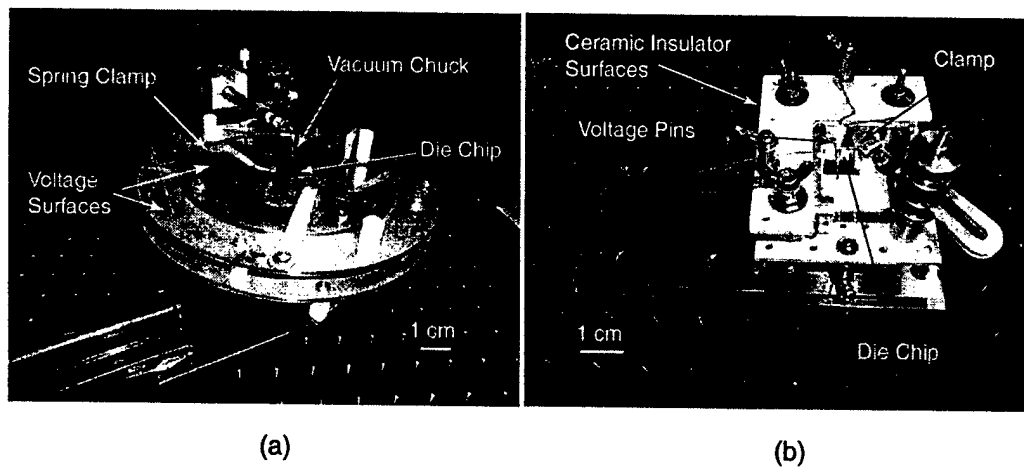


Figure 6.10: Die-level alignment and bonding jigs: (a) 1st-generation jig, (b) 2nd-generation jig.



Figure 6.11: Electrical contact to an active valve chip for anodic bonding: (a) side view of chip in jig and (b) top view of chip in jig. Electrical cantilever pins contact various layers of the device for bonding procedures.

6.2.5 Fluid Filling/Sealing of HAC

Introducing fluid into the hydraulic amplification chamber of the active valve is a critical step in preparing the device for operation. Any bubbles or trapped residual gas within the amplification chamber will significantly increase its compliance, thereby eliminating efficient coupling between the drive element and valve membrane structure. This section briefly details the fluid filling procedure and issues associated with sealing.

Procedure for Filling

A fluid-filling apparatus and procedure developed by Richard Mlcak (Boston Microsystems, Inc) and updated by Lodewyk Steyn (MIT) was used to fill the active valve devices developed in this thesis. The apparatus, shown in Figure 6.12, consists of a filling chamber, a fluid reservoir chamber, a vacuum pump, and a series of valves connecting these components together. A schematic of the component connections is shown in Figure 6.13. A detailed explanation of the filling procedure and issues associated with the development of this procedure can be found in [10] and [11]. The major steps in the filling process are as follows:

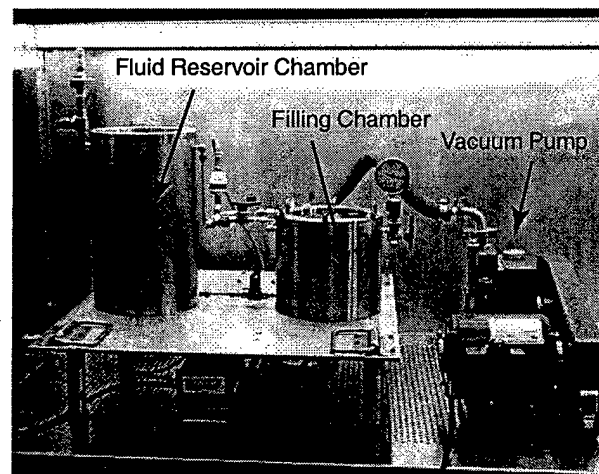


Figure 6.12: Fluid filling apparatus to fill active valve devices. System consists of a fluid reservoir chamber, a filling chamber, a vacuum pump, and series a valves connecting all components together.

1. The assembled, bonded, and poled active valve device is inserted into the filling chamber. The chamber is then closed, with no fluid present in this chamber. Valve 1, Valve 3, and Valve 5 are closed.

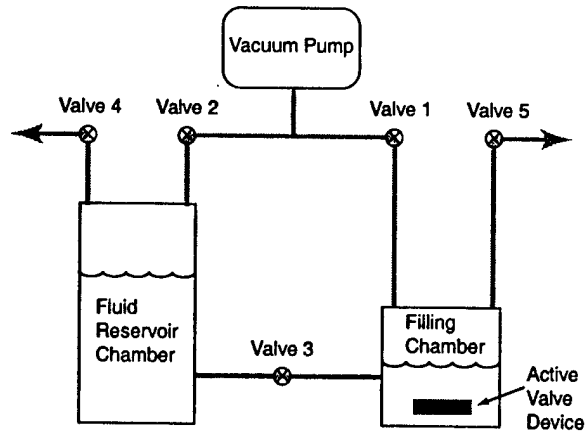


Figure 6.13: Fluid filling schematic of component connections.

2. With the fluid reservoir chamber full of fluid, Valve 4 is closed and Valve 2 is opened. The vacuum pump is initiated to outgas the fluid in the reservoir chamber. After a period of 1 hour, Valve 2 is closed. Valve 4 is then opened to bring the reservoir pressure back to atmospheric pressure.
3. Valve 3 is opened to introduce a small amount of fluid into the filling chamber from the reservoir chamber. Valve 3 is then closed. Valve 1 is then opened and the filling chamber is evacuated to approximately 1 torr. This evacuation acts to boil off the fluid introduced into the filling chamber. The hydraulic amplification chamber and other fluidic channels in the device are thereby filled with silicon oil vapor, which easily wets the walls of these structures. After 10 minutes, Valve 1 is closed.
4. Valve 3 is opened for a sufficient time to deliver to the filling chamber a volume of fluid that submerges the valve device and the jig within which it rests. Valve 3 is then closed.
5. Valve 5 is opened to pressurize the filling chamber to atmospheric pressure. This step, which lasts for approximately 1 hour, serves to "push" the fluid into the hydraulic amplification chamber. The device is then removed from the filling chamber and is ready for testing.

During this filling procedure, the active valve device is securely clamped within a test-jig apparatus. Prior to removal from the filling chamber, a valve located on the test jig that leads to the HAC chamber is closed. Once hooked up to the experimental testing apparatus, this valve is opened to an external pressure regulator (see next section).

Sealing Issues

In order to maintain a compressive stress on the piezoelectric elements at all times and to eliminate the potential for cavitation within the hydraulic amplification chamber during actuation, the fluid within the chamber is required to be held at a positive bias pressure (typically 0.5-2MPa). The value of this bias pressure P_{bias} is determined based on the P_{HAC} pressure fluctuations expected during active valve operation (determined using numerical simulation). P_{bias} should be chosen to ensure that P_{HAC} never passes below zero during actuation. Sealing of the HAC chamber at a desired bias pressure was not an option in this thesis because such a procedure had not been developed. Further discussion of sealing and encapsulation studies for these types of devices can be found in [11]. For the purposes of the active valve described in this thesis, therefore, it was required to develop a means to bias the P_{HAC} after the fluid filling operation was complete and without completely sealing the chamber.

To accomplish this objective, a small cross-sectional area fluid channel was etched into the underside of Layer 7 so to provide a connecting path between the hydraulic amplification chamber and an external pressure regulator. Figure 6.14 illustrates this concept. By incorporating a high resistance fluid channel in this location, static bias pressures dictated by the external regulator can be imposed on the chamber, however, high frequency pressure fluctuations created during actuation remain confined to the chamber. In essence, this channel acts as a low pass filter for transmission of pressure fluctuations into and out of the chamber. The channel length, width, and height were designed to be 1mm, $10\mu m$, and $10\mu m$ respectively. The channel was desired to be long and thin so as to create a large flow resistance during actuation. However, the channel width and height were designed large enough so as to be able to initially fill the device with fluid using the procedure detailed above in a reasonable amount of time (on the order of 20 minutes).

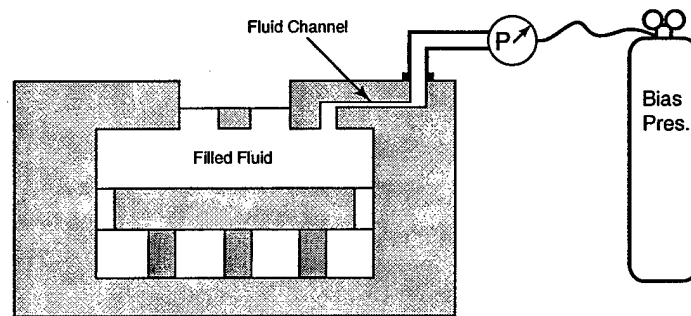


Figure 6.14: Schematic of the high resistance fluid channel between the HAC and an external bias pressure regulator. This channel was etched into the underside of Layer 7.

To design properly this high resistance flow channel for use in the active valve geometry

detailed in this thesis, a model was developed to capture the inertia and flow resistance associated with a fluid slug within the channel (see Figure 6.15). The assumptions in this model are: (1) the fluid slug occupies the entire length of the channel, (2) the fluid slug interacts with the volumetric stiffness of the hydraulic amplification chamber (designated as K_{HAC}), and (3) the fluid slug flow behavior is governed by Hagen-Poiseuille flow relations. The variable ΔV_{slug} is defined as the volume of fluid pushed into/pulled out of the HAC chamber during an actuation cycle of the active valve. The variable ΔP_{slug} is defined as the differential pressure seen across the fluid slug during this actuation cycle due to pressure fluctuations within the HAC chamber.

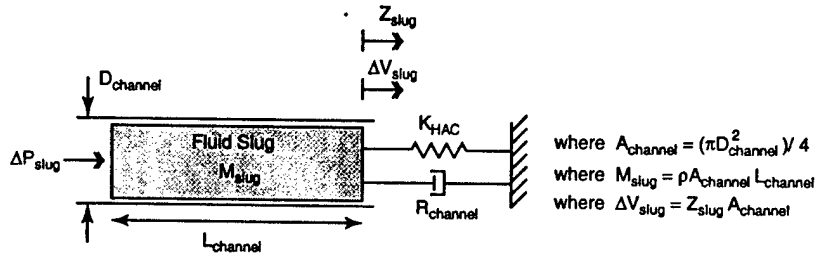


Figure 6.15: Model of the high resistance fluid channel between the HAC and an external bias pressure regulator. A fluid slug within the channel is modeled. This slug is acted upon by an external stiffness associated with the HAC chamber stiffness. Additionally, the flow resistance of this slug through the channel is modeled using laminar Hagen-Poiseuille flow relations.

Based on the model schematic in Figure 6.15, a differential equation for the slug behavior can be written,

$$\left(\frac{M_{slug}}{A_{channel}^2} \right) \Delta \ddot{V}_{slug} + R_{channel} \Delta \dot{V}_{slug} + K_{HAC} \Delta V_{slug} = \Delta P_{slug} \quad (6.2)$$

where $R_{channel} = \left(\frac{128\mu L_{channel}}{\pi D_{channel}^4} \right)$ is based on Hagen-Poiseuille flow in a circular channel [8]. In this relation, μ is the viscosity of the fluid. Inserting this flow relation into Equation 6.2 and rearranging in the frequency domain, a transfer function relating ΔV_{slug} to ΔP_{slug} is obtained

$$\frac{\Delta V_{slug}}{\Delta P_{slug}} = \frac{\left(\frac{\pi D_{channel}^2}{4\rho L_{channel}} \right)}{s^2 + \left(\frac{32\mu}{\rho D_{channel}^2} \right) s + \left(\frac{K_{HAC} \pi D_{channel}^2}{4\rho L_{channel}} \right)} \quad (6.3)$$

where ρ is the density of the fluid in the channel. The natural frequency (known as the Helmholtz frequency) of this fluid-structure interaction event can be written as

$$f_{Helmholtz} = \frac{1}{2\pi} \sqrt{\frac{K_{HAC} \pi D_{channel}^2}{4\rho L_{channel}}} \quad (6.4)$$

In designing the channel dimensions, the following parameter values (which correlate with the active valve geometry fabricated in this thesis) were assumed: $L_{channel} = 1mm$, $D_{channel} = 11.3\mu m$, $K_{HAC} = 1.0e^{17} \frac{Pa}{m^3}$, $\rho = 760 \frac{kg}{m^3}$, and $\mu = 6.5e^{-4} \frac{kg}{ms}$. These values result in a frequency of 48Hz for which ΔV_{slug} is 1% of the drive element volume change. Additionally, a Helmholtz frequency of $f_{Helmholtz} = 578Hz$ results. However, Helmholtz resonant behavior of this slug is non-existent due to the dominant fluid viscous losses in the channel. Additionally, with these channel dimensions, it is estimated that during initial fluid filling, the HAC chamber should fill in approximately 5-10 minutes under atmospheric pressurization in Step 5 of the above fluid filling procedure. Chapter 9 includes experimental verification of the performance of this high fluid resistance channel within working high frequency active valve devices.

6.3 Sub-Component Testing Plan

To solve and to overcome the previously described fabrication challenges, a fabrication and experimental test plan was developed. This plan divides the full piezoelectrically-driven active valve device into simpler decoupled sub-components structures, which can be independently fabricated, assembled, and tested. The sub-component structures are the piezoelectric drive element and the valve cap and membrane structure. Figure 6.16 outlines this plan. This section provides a general overview of the sub-component geometries and the important questions that need to be answered in each of the sub-component studies. Subsequent chapters of this thesis go on to provide complete and detailed experimental validation of each of the sub-components.

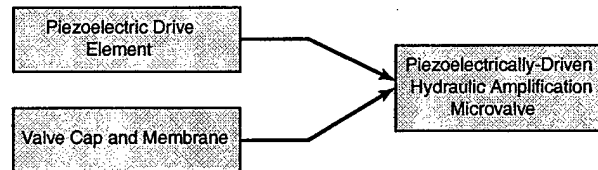


Figure 6.16: Sub-component fabrication and testing plan. Realization of a full piezoelectrically-driven hydraulic amplification microvalve depends on successful validation of the piezoelectric drive element and the valve cap and membrane deformation behavior. Fluid filling success is evaluated with the full active valve device.

6.3.1 Piezoelectric Drive Element

The piezoelectric drive element provides actuation volume change and pressurization to the hydraulic amplification chamber and therefore the valve cap and membrane as it opens and closes against a fluid orifice. This sub-component study proves that etching of the high-aspect ratio tethered piston structures and control of fillet radii at the base of these etches can be

performed in a repeatable fashion. Additionally, wafer-level silicon-silicon fusion bonding were validated to form Stack 4-5. As shown in Figure 6.17, devices were constructed with single-layer pistons as well as double-layer pistons for stiffness comparison. Piezoelectric material, both PZT-5H and PZN-PT, were processed to create individual piezoelectric elements for insertion into drive element structures. Sub-component devices with a single element placed centrally beneath the drive piston as well as devices with three piezoelectric elements spaced out uniformly beneath the drive piston were fabricated to validate enhanced stiffening benefits of drive element actuators with multiple piezoelectric elements (again see Figure 6.17). The drive element sub-component devices were experimentally tested to evaluate both quasi-static deformation behavior (frequencies ≤ 15 kHz) and dynamic modal behavior (up to 200 kHz) under a wide range of applied voltages. Completion of this sub-component study enables incorporation of the drive element actuator structure within complete active valve structures.

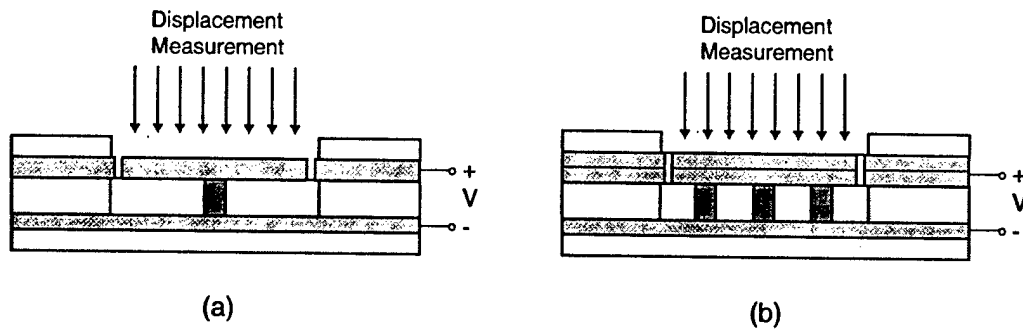


Figure 6.17: Drive element sub-component study: (a) devices with a single piezoelectric element centrally-located beneath the piston as well as devices with single-layer pistons will be fabricated, (b) devices with three piezoelectric elements positioned beneath the piston and devices with double-layer pistons will also be fabricated.

6.3.2 Valve Cap and Membrane

The valve cap and membrane structure reacts to differential pressures to open and close against a fluid orifice. This sub-component study validates the etching of the membrane and control of fillet radii at the oxide etch stop. Valve membrane structures were tested to verify non-linear pressure-deflection behavior, and results were compared to the non-linear numerical models presented in Chapter 3 of this thesis. The sub-component structure used for these tests is shown in Figure ??(a). Gas pressure was introduced into the amplification chamber to directly force the valve cap and membrane structure upward. Additionally, gas pressure was introduced above the membrane as well to deform the structure in the downward direction. Deflection of the valve cap was measured using a laser vibrometry system. Completion of this sub-component

study provides an understanding of the valve membrane stiffness in response to applied pressures and therefore enables subsequent fluid filling and testing of full active valve devices.

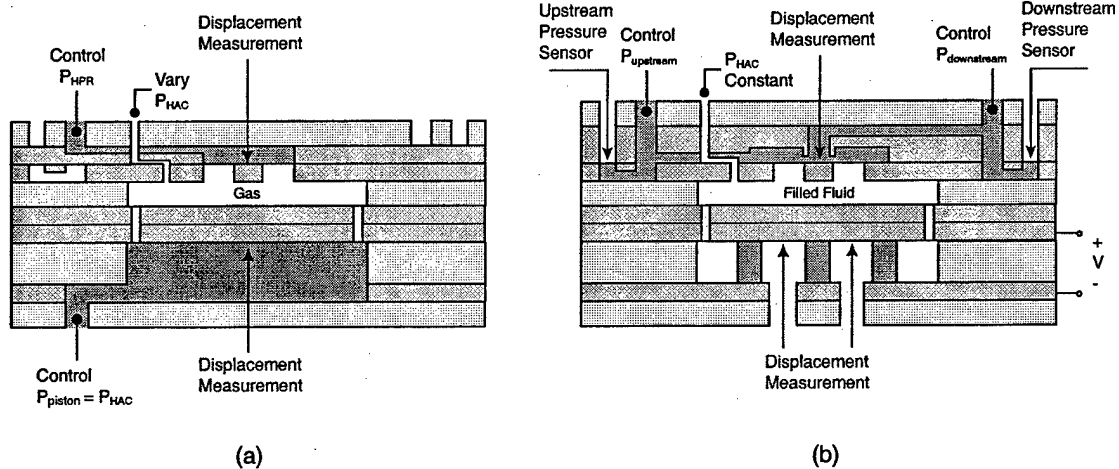


Figure 6.18: Valve membrane sub-component study and full active valve study: (a) valve cap and membrane within assembled chamber were deformed with gas pressure to determine structural stiffness, (b) the active valve device was fully characterized for pressure-flow behavior and limitations in dynamic performance. Note that the high resistance flow channel and the external fluid flow path above valve cap overlap in this schematic. In reality, these channels are offset spatially from one another.

6.3.3 Full Active Valve

Having successfully completed the two sub-component studies, a full active valve device was tested. The structure of this device is shown in Figure 6.18. Displacements of the valve cap in response to applied piezoelectric voltage were determined. In addition to evaluating the opening and closing capability of the valve in response to voltage, differential pressure - flow relations were established across the flow channel. Dynamic transfer functions of the full valve device were obtained and limitations in device performance were established.

6.4 Testing Apparatus

6.4.1 Laser Vibrometer System

A laser vibrometer system was used to measure the structural vibrations of the drive element piston and valve cap during the experimental testing of the full active valve and its sub-component structures. This system uses a technique known as laser doppler vibrometry to detect the ve-

locity of a moving surface. The wave used for this purpose is a laser, typically HeNe or of similar wavelength. When this wave strikes a moving surface and reflects back, a frequency shift is introduced. If the reflected wave is compared with the incident wave, the frequency shift results in a beating phenomenon, where the beat frequency is proportional to the velocity of the moving surface. Measuring this beat frequency therefore gives the velocity of the surface being measured.

During testing of the active valve and its sub-components, some of the measurements were taken through a medium of air in contact with the moving surface and some were taken through a medium of silicon oil in contact with the moving surface. As described in [13], the Doppler frequency shift, and hence the beat frequency, is proportional to the target velocity and also proportional to the refractive index of the medium in contact with the target. The silicon oil used in the valve (Dow Corning DC200 0.65 centistoke oil) has a refractive index of 1.375. Therefore, in taking measurements using this laser vibrometer system, any measurement values taken with this oil in contact with the moving surface were divided by 1.375 to obtain the proper values. All results incorporating oil in contact with the valve cap in subsequent chapters have been properly scaled by this value.

6.4.2 Fluids Test-Rig

The fluids testing rig used in the active valve and sub-component studies documented in this thesis was designed, built, and constructed by Lodewyk Steyn. Figure 6.19 illustrates a portion of this set-up. The explicit details of this test-rig are contained in [11]. In summary, this set-up enables the control of a wide range of pressure loadings on the drive element piston, within the HAC chamber, and on the valve cap and membrane upstream and downstream of the valve orifice flow channel for the active and sub-component studies. Fluid reservoirs contain degassed silicon oil for the purposes of creating fluid flow in testing the active valve device. A series of absolute and differential pressure sensors are located throughout the set-up to enable real-time measurements of the static and dynamic pressures at critical locations within the valve device. Further discussions of which pressures were measured for which experiments are included in the subsequent experimental chapters of this thesis.

6.5 Conclusions

This chapter has presented the fabrication and assembly challenges faced in realizing a working piezoelectrically driven hydraulic amplification microvalve. The wafer-level fabrication process, piezoelectric material preparation and integration issues, and die-level assembly and bonding procedures were discussed. Additionally, an overview of the active valve sub-component test plan was presented. The details of these sub-component studies are covered in subsequent

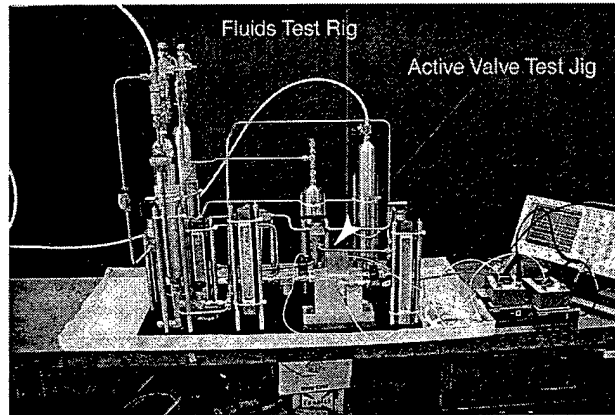


Figure 6.19: Fluids test-rig for testing of the active valve and its sub-components. This set-up contains fluid reservoirs, static and dynamic pressure sensors, flow sensors, and absolute and differential pressure sensors for evaluating device performance during testing.

chapters.

Bibliography

- [1] A.A. Ayon, K-S. Chen, K.A. Lohner, S.M. Spearing, H.H. Sawin, and M.A. Schmidt, "Deep Reactive Ion Etching of Silicon," *Materials Research Society Symposium Proceedings*. v. 546, pp.51-61, 1999.
- [2] K-S. Chen, A. Ayon, and S.M. Spearing, "Controlling and Testing the Fracture Strength of Silicon on the Mesoscale," *Journal of the American Ceramic Society*, 83 [6], pp.1476-84, 2000.
- [3] J.C. Arnold and H.H. Sawin, "Charging of pattern features during plasma etching," *J. Appl. Phys.*, vol. 70, no. 10, pp.5314-5317, 1991.
- [4] T. Kinoshita, M. Hane, and J.P. McVittie, "Notching as an example of charging in uniform high-density plasmas," *J. Vac. Sci. Technol. B, Microelectron. Process. Phenom.*, vol. B14, no. 1, pp.560-565, 1996.
- [5] T. Nowaza, T. Kinoshita, T. Nishizawa, A. Narai, T. Inoue, and A. Nakae, "The electron charging effects of plasma on notch profile defects," *Jpn. J. Appl. Phys.*, vol. 34, pt. 1, no. 4B, pp.2107-2113, 1995.
- [6] U. Gosele and Q.-Y. Tong. Semiconductor wafer bonding. *Annual Review of Materials Science*, 28, pp. 215-241, 1998.
- [7] K.T. Turner, An Evaluation of Critical Issues for Microhydraulic Transducers: Silicon Wafer Bonding, Strength of Silicon on Insulator Membranes and Gold-Tin Solder Bonding. MIT Master's Thesis. June 2001.
- [8] R. Mlcak, Numerous presentations at MIT on the development of a bonding technology between piezoelectric material and silicon for use in MHT technology, 1997-2000.
- [9] M. Ohring. *The Materials Science of Thin Films*. Academic Press, New York, 1992.
- [10] R. Mlcak. *Wafer-scale Fluid Filling System: Standard Operating Procedure and Manual*. Document was provided to MIT from Boston Microsystems, Inc. in October 2000.

- [11] J.L. Steyn, Master's Thesis, Massachusetts Institute of Technology, 2002.
- [12] F.M. White, *Fluid Mechanics*, 2nd ed. McGraw-Hill Inc, 1986.
- [13] H.D. Young, *University Physics*, 8th ed. Addison Wesley, 1992.

Chapter 7

Sub-Component Study: Piezoelectric Drive Element

7.1 Objectives

The purpose of this sub-component study was to evaluate the fabrication and assembly process flow of the piezoelectric drive element structure, shown in Figure 7.1, and to obtain quasi-static and high-frequency experimental data on completed devices. Specifically, the three primary objectives of this study were:

1. To determine whether both single-layer and double-layer piston structures could be fabricated and assembled in drive element devices. As compared to single-layer pistons, the double-layer design enhances the structural stiffness of the micro-actuator device.
2. To determine whether standard polycrystalline PZT-5H and higher-performing single-crystal PZN-PT materials [4] could be processed and integrated within tethered-piston drive element structures. Although the final active valve devices (detailed in Chapter 9) incorporated solely PZN-PT material, the high cost of this material forced initial studies to work with less costly PZT-5H material.
3. To determine whether both single and multiple piezoelectric elements could be successfully integrated beneath the drive element piston. Multiple elements spread out beneath the piston serve to stiffen the micro-actuator structure. However, tolerancing and bonding of multiple elements within the device is more challenging.

Successful integration of these types of piezoelectric materials with properly etched and bonded tethered piston structures demonstrates the potential for high-frequency, high-stiffness actuation within full active valve devices.

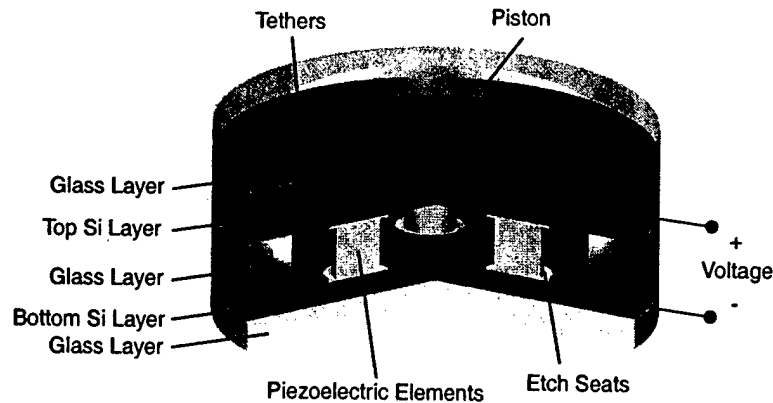


Figure 7.1: 3-D schematic of a piezoelectric drive element device. Three piezoelectric cylinders are sandwiched between a lower support silicon layer and an upper double silicon layer tethered-piston structure. Voltage is carried along the upper and lower silicon layers.

7.2 Device Test-Plan

The overall piezoelectric drive element sub-component study was divided into two parts. In the first part, "1st-generation" drive element devices were fabricated and tested. In the second part, "2nd-generation" drive element devices, slightly different in geometry than the "1st-generation" devices, were fabricated and tested. Ideally, a consistent geometry would have been preferred throughout the full study. Unfortunately, due to research program scheduling and resource limitations, the use of different geometries was unavoidable. The experimental results of the two sub-studies combined together, however, do provide overwhelming evidence that integration of piezoelectric elements within micromachined silicon thin-tethered piston structures is achievable. The overall device test plan is illustrated in Figure 7.2. The three major design variations contained within this sub-component study were: (1) use of a single-layer silicon drive piston structure versus use of a double-layer piston structure, (2) integration of PZT-5H material versus integration of PZN-PT material, and (3) incorporation of a single piezoelectric element beneath the piston versus integration of three elements spread out beneath the piston.

7.2.1 1st Generation Devices

As shown in Figure 7.2, the 1st-generation study included the fabrication and testing of three unique drive element devices, all incorporating a single-layer silicon drive piston. Device 1 incorporates a single PZT-5H cylindrical piezoelectric element centrally located beneath the tethered piston. Device 2 incorporates a single PZN-PT cylindrical piezoelectric element also

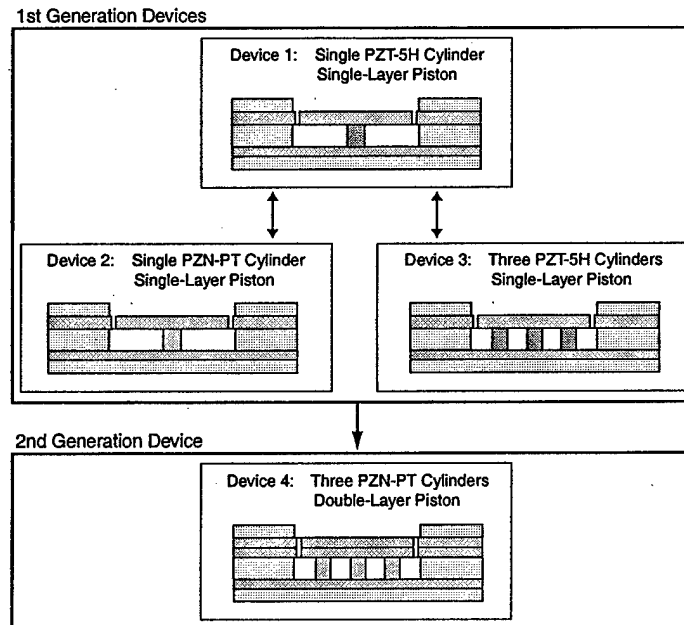


Figure 7.2: Overview of the drive element sub-component test plan. Within the 1st generation study, devices incorporating single and three piezoelectric cylinders (both PZT-5H and PZN-PT) beneath single-layer drive pistons were fabricated and tested. Within the 2nd generation study, devices with three PZN-PT square piezoelectric elements beneath double-layer drive pistons were fabricated and tested.

centrally located beneath the piston structure. Device 3 incorporates three PZT-5H cylindrical elements spread out uniformly beneath the piston. In all three devices, the piezoelectric cylinder thicknesses are $\sim 1\text{mm}$, while the drive piston has a thickness of $390\mu\text{m}$ and the tether has a thickness of $9\mu\text{m}$. Figures 7.3(a) and (b) illustrate the top-view layout and dimensions of these single-cylinder and three-cylinder 1st-generation drive element devices, respectively. Experimental comparison of Device 2 with Device 1 demonstrates the benefits and drawbacks of incorporating the higher-strain capability, yet lower stiffness PZN-PT material versus PZT-5H material. Experimental comparison of Device 3 with Device 1 demonstrates the enhanced stiffening effects of incorporating multiple piezoelectric elements rather than a single centrally-located one within the drive element structure. Additionally, this comparison uncovers any potential difficulties involved in obtaining adequate eutectic bonding between all three cylinders and the adjacent silicon surfaces.

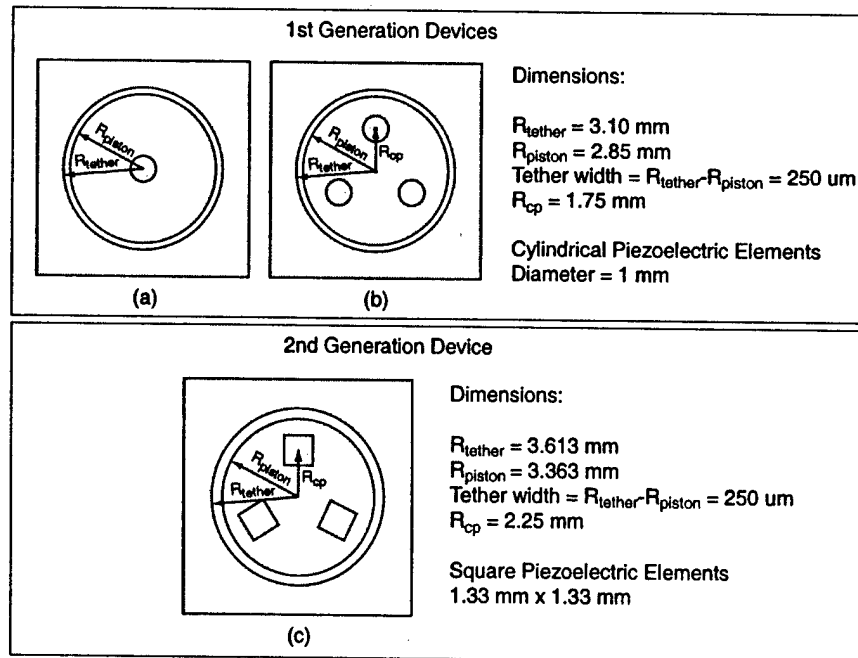


Figure 7.3: Drive element geometries and piezoelectric material layout for 1st and 2nd-generation devices: (a) 1st-generation device with a single piezoelectric cylinder, (b) 1st-generation device with three piezoelectric cylinders, and (c) 2nd-generation device with three piezoelectric square elements.

7.2.2 2nd Generation Device

As shown in Figure 7.2, the 2nd-generation study focused on the integration of three PZN-PT material elements beneath a double-layer drive element piston structure. This double-layer structure, as contained in the final design of the microvalve presented in Chapter 9, is critical for reducing compliance effects within the active valve during piezoelectric actuation. As for the 1st-generation devices, the piezoelectric element thicknesses are $\sim 1 \text{ mm}$. Since the piston is comprised of two layers, its total thickness is $780 \text{ }\mu\text{m}$ with each tether having a thickness of $8 \text{ }\mu\text{m}$. Figure 7.3(c) illustrates the top-view layout and dimensions of this 2nd-generation drive element device, Device 4. In order to maximize use of PZN-PT material, square elements rather than cylindrical elements were incorporated in this structure (significantly more piezoelectric elements can be created by dicing a given size plate into squares rather than core-drilling cylinders from this plate). Successful fabrication and experimental evaluation of this final drive element device proves that such a micro-actuator structure can be implemented in the full active valve.

7.3 Device Assembly

As shown in Figure 7.4, the drive element structures consist of five primary layers, two of which are silicon and three of which are glass. The bottom silicon layer contains etched seats for thickness compensation of the piezoelectric elements with respect to the surrounding glass and also contains gold pads for electrical contact. The top silicon layer contains the etched tethered-piston structure. For 1st-generation devices, this layer is formed from a single silicon wafer, whereas for 2nd-generation devices, this layer is formed through wafer-level bonding of two etched silicon wafers. The top and bottom glass layers provide support for clamping during device testing.

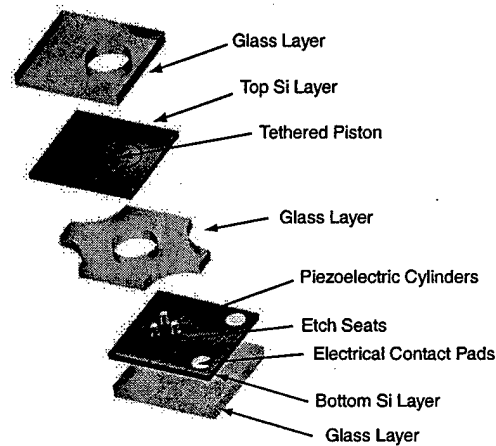


Figure 7.4: Exploded view of a 1st-generation piezoelectric drive element structure. One or more piezoelectric cylinders are arranged within a circular glass chamber, supported beneath by a silicon layer with etched seats and bonded above to a micromachined piston.

As shown in Figure 7.5 and detailed in Chapter 6, a series of wafer-level/die-level anodic bonding steps and a final simultaneous anodic-eutectic bonding step were carried out to complete each of the drive element devices. Following this assembly, wires were soldered to the contact pads on the top and bottom silicon layers to provide electrical contact to the piezoelectric material. Poling of the device was performed by heating the device to approximately half the piezoelectric material Curie temperature ($T_{curie} = 190^{\circ}C$ for PZT-5H and $T_{curie} = 150^{\circ}C$ for PZN-PT) and applying a voltage of 1000V. Photographs of a 1st-generation drive element device prior to and following electrical lead attachment are shown in Figure 7.6(a) and (b) respectively. Photographs of a 2nd-generation drive element are shown in Figure 7.7.

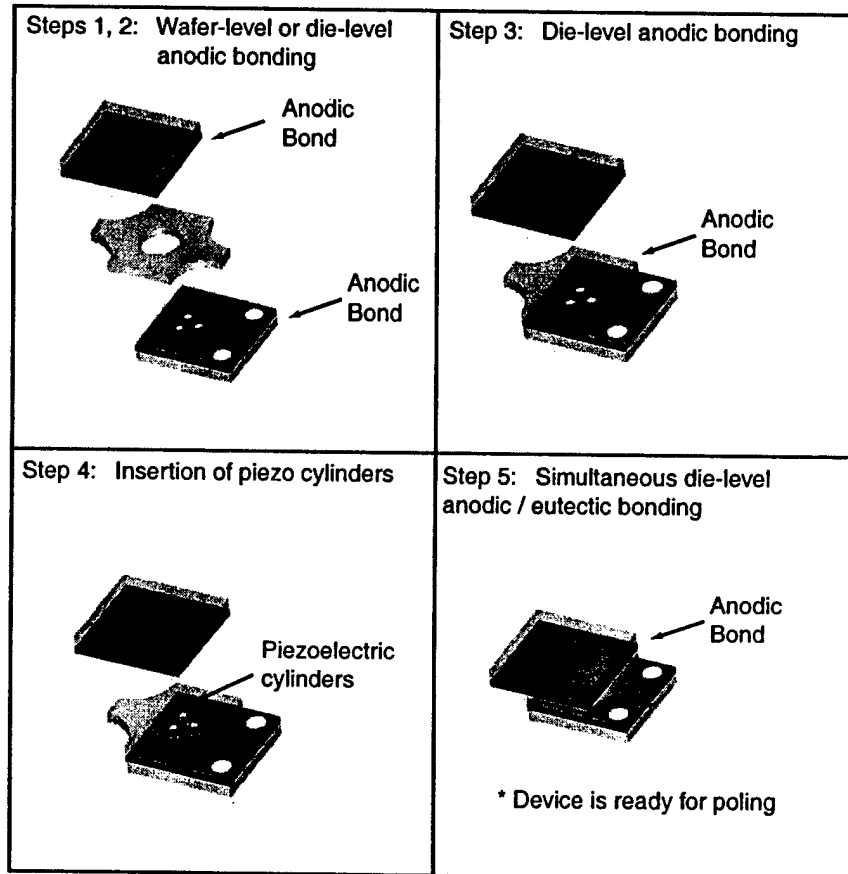


Figure 7.5: Assembly of a piezoelectric drive element device. Die-level anodic bonding procedures at $T=300^{\circ}$ and 1000V were carried out to bond five layers together. The final anodic bonding step also serves to melt the eutectic alloy, forming the bond between the piezoelectric cylinders and the top and bottom silicon layers.

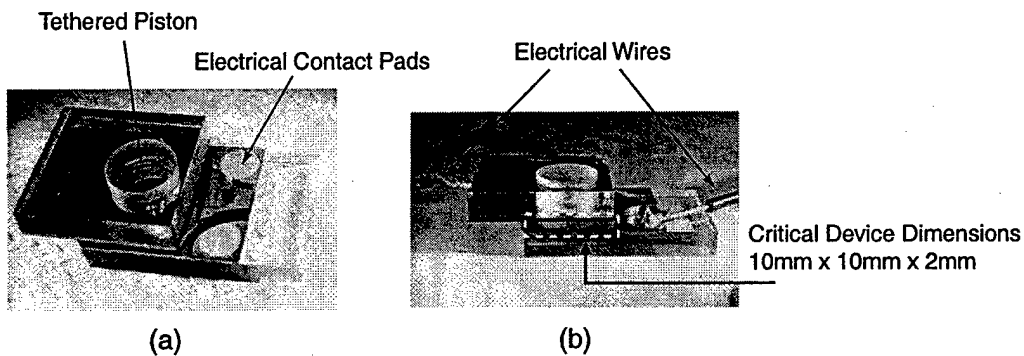


Figure 7.6: Photographs of an assembled 1st-generation piezoelectric drive element device: (a) a packaged device ready for attachment of electrical wires, prior to device poling, (b) a device ready for experimental testing. The critical device dimensions are 10mm x 10mm x 2mm. Thick glass packaging layers were used for clamping purposes during testing.

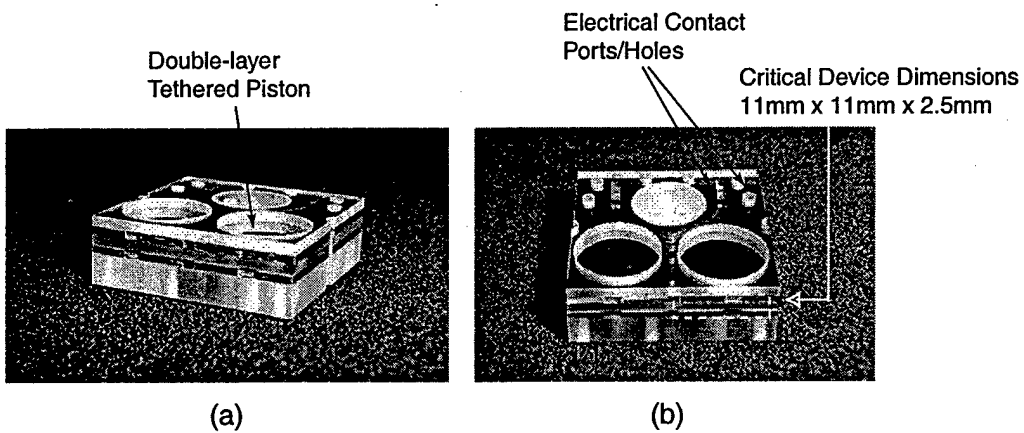


Figure 7.7: Photograph of an assembled 2nd-generation piezoelectric drive element device: thick glass packaging layers were used for clamping purposes during testing.

7.4 Testing Procedure

The process of experimentally testing a given drive element device consisted of three major steps. The first step involved careful microscopic inspection of the device to evaluate the fillet radius profile along the etched drive element tether. For 1st-generation devices, where single-layer pistons were used, measurements were taken following device assembly. However, for 2nd-generation devices, where a bonded double-layer piston prevented viewing of the piston etch, measurements were taken on each of the drive element tethers prior to wafer-level bonding. Knowledge of the fillet radius sizes was important for later evaluation of device performance.

The second step involved characterization of stand-alone piezoelectric material elements that came from the same batch (plate) of material that yielded the elements that were integrated within the device. This was a critical procedure so that comparison of drive element device voltage-deflection behavior could be compared to that of representative piezoelectric material elements.

The third step involved rigorous experimental testing of the device. Each device was rigidly clamped to a test-jig surface and experimentally evaluated using a scanning laser vibrometer system. As shown in Figure 7.8, scan points were defined over the top surface of the tethered piston and along the circumferential boundary supporting the piston. Three measurement procedures were used to characterize device performance. In the first procedure, a low-voltage ($0V \pm 25V$) sweep signal was applied to each device over a frequency range of 10kHz to 200kHz to determine the onset of dynamic modal characteristics. A transfer function of velocity (averaged over all scan points) versus frequency was recorded. Close-up frequency sweeps around dominant modal frequencies were then carried out to obtain high-resolution mode shape behavior. In the second procedure, a sinusoidal voltage of $500V \pm 500V$ was applied to each device at selected frequencies of 15kHz and 7kHz to evaluate device behavior below the modal frequencies. At each of these low-frequencies, displacement time histories at the piston center and at an outer edge of the piston were recorded. In the third procedure, voltage-deflection curves (of the piston center) for varying levels of applied voltage were obtained at a frequency of 100Hz to determine the true quasi-static voltage dependent performance of the device.

7.5 Experimental Results

7.5.1 1st Generation Devices

Measurement of Fillet Radius Profiles

Following assembly of each 1st-generation drive element device, careful inspection of the drive element piston tether was performed to characterize the uniformity of the fillet radii along the tether circumference. As shown in Figure 7.9(a), measurements were taken at eight equally

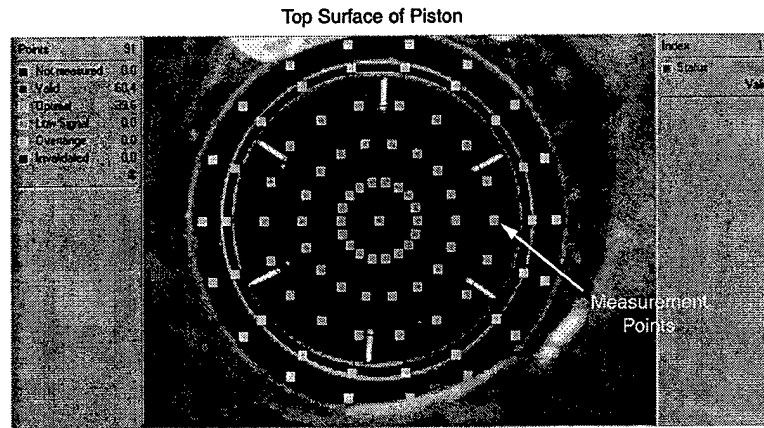


Figure 7.8: A scanning laser vibrometer system was used to characterize modal and quasi-static performance of each device. Measurement points are defined on the top surface of the piston.

spaced locations along the circumference. The first measurement point is located at 12 o'clock and numbering proceeds in the clockwise direction. The measurement terminology is illustrated in Figure 7.9(b). Using a microscope eyepiece with calibrated graduations, the tether width from the base of one fillet radius to the base of the opposite fillet radius was recorded. Additionally, the total trench width was measured. From these measurements, an average value for the fillet radius on each side of the trench was determined. Figure 7.9(c), (d), and (e) present the tether width and fillet radius measurements as a function of location along the tether circumference for Devices 1, 2, and 3, respectively. For Device 1, the tether width varies between $138\mu\text{m}$ and $163\mu\text{m}$ in a single sinusoidal cycle along the circumference (ie: the fillet radii vary from $43\mu\text{m}$ to $56\mu\text{m}$). Likewise, the tether width of Device 2 also varies sinusoidally, but with slightly larger variation, between $165\mu\text{m}$ and $200\mu\text{m}$. For these two devices, due to this tether variation, the overall piston/tether stiffness is non-uniform around the circumference. For Device 3, tether width variation is also observed, however, in a more random fashion between $178\mu\text{m}$ and $195\mu\text{m}$.

Characterization of Piezoelectric Material

In order provide a basis for voltage-deflection comparison when testing completed drive element devices, representative PZT-5H and PZN-PT material cylinders were individually characterized (sufficiently long after poling, four days, to ensure adequate relaxation of the material). Figure 7.10 plots the results for three cylinders of each material at 10Hz for a driving voltage of $500V \pm 500V$. A very low frequency was chosen to guarantee true quasi-static behavior. The three PZT-5H cylinders exhibited peak deflections at 1000V between $0.75\mu\text{m}$ and $0.82\mu\text{m}$. The three PZN-PT cylinders exhibited peak deflections at 1000V between $1.35\mu\text{m}$ and $1.55\mu\text{m}$.

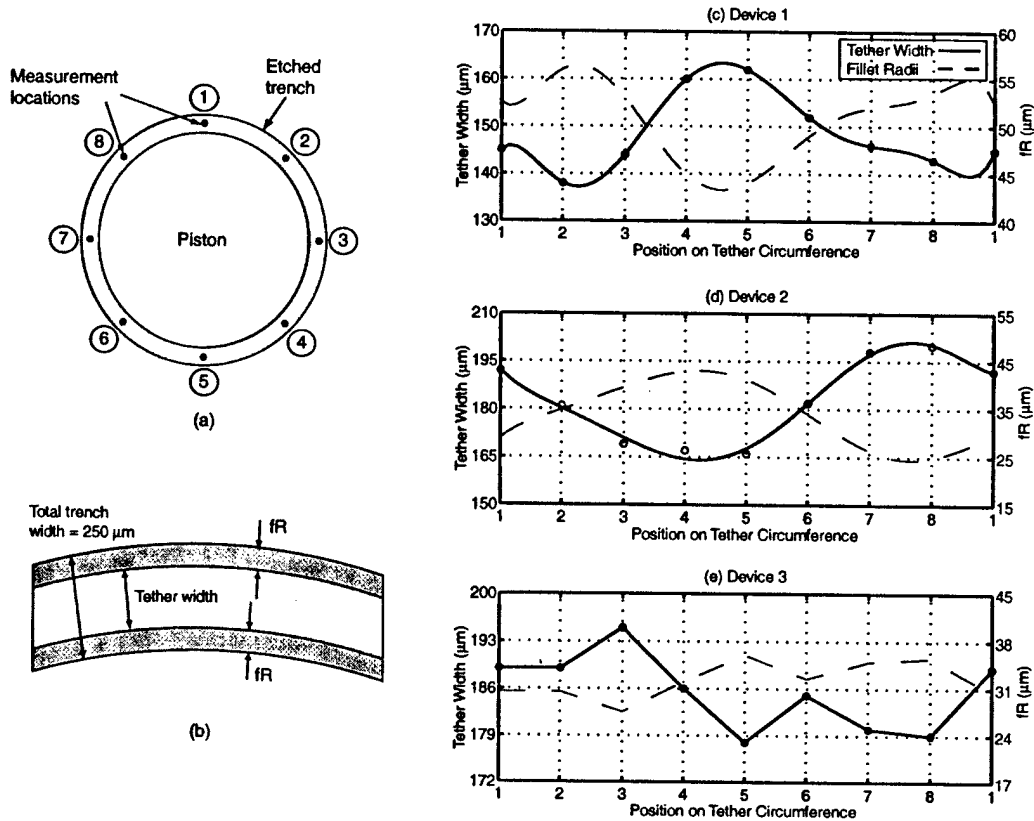


Figure 7.9: Inspection of tether width and fillet radii on Device 1, 2, and 3 tethered pistons: (a) definition of measurement locations around trench circumference, (b) average $fR = \frac{1}{2}(\text{total trench width} - \text{measured tether width})$, (c) Device 1 measurements, (d) Device 2 measurements, and (e) Device 3 measurements.

Finite-element models of drive element devices have indicated that the stiffness of the tether is insignificant compared to that of the piezoelectric materials, and therefore it does little to restrict the free-strain deflection of the piezoelectric material. As a result, these stand-alone piezoelectric element results provide an accurate expectation for quasi-static drive element device voltage-deflection performance.

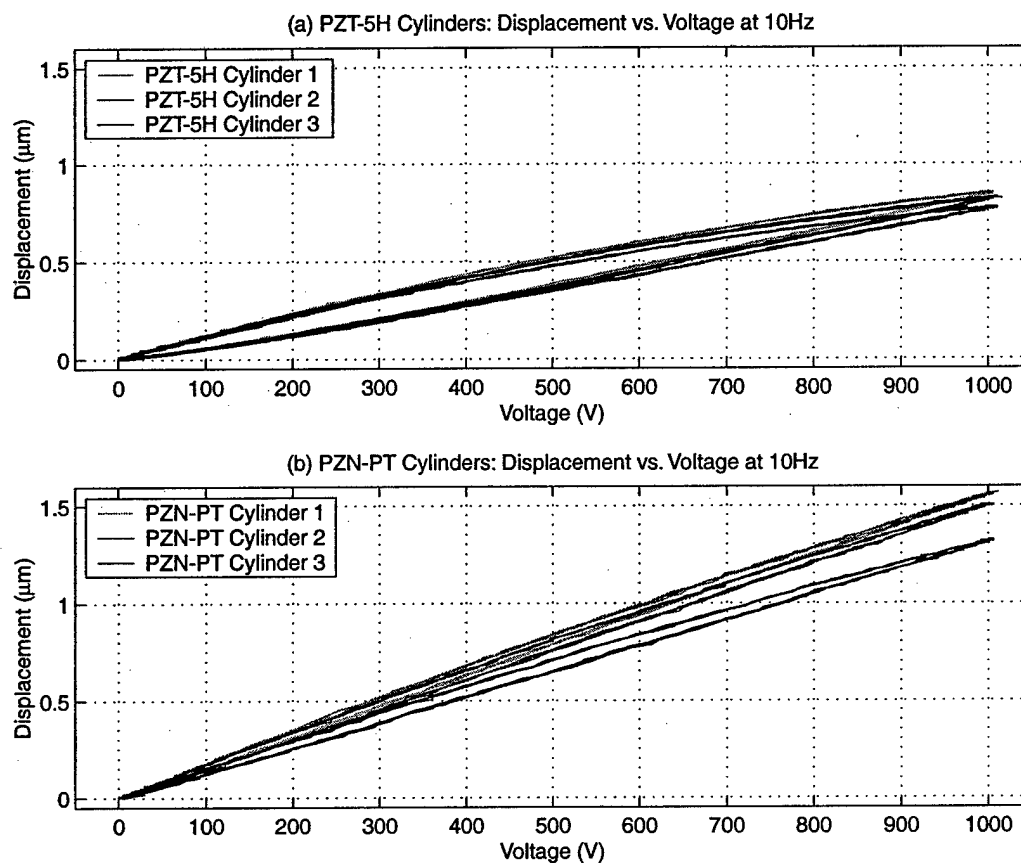


Figure 7.10: Piezoelectric material characterization on representative stand-alone PZT-5H and PZN-PT cylinders: (a) voltage-deflection responses at 10Hz for three different PZT-5H cylinders for $V = 500V \pm 500V$ (these cylinders were taken from the identical PZT-5H material plate that yielded the cylinders used in Devices 1 and 3), (b) voltage-deflection responses at 10Hz for three different PZN-PT cylinders for $V = 500V \pm 500V$ (these cylinders were taken from the identical PZN-PT material plate that yielded the cylinder used in Device 2).

Experimental Testing of Device 1

Figure 7.11(a) plots the transfer function of averaged velocity over the scanned piston surface versus frequency for Device 1. Figure 7.11(b) plots these transfer functions for specific locations on the piston surface, at the center and at an outer edge. Figure 7.12(a) presents experimental mode shapes of the device at selected modal frequencies. The device experiences a “1 – Θ ” tilt mode at $f = 31kHz$, followed by a “plunge” mode at $f = 80kHz$, and a “2 – Θ ” mode at $f = 131kHz$. As shown in Figure 7.12, these modal frequencies correlate well with finite-element models of the device. The frequency difference in the “1 – Θ ” mode between finite-element model and experiment could be attributed to imperfect placement of the cylinder beneath the piston or non-uniform fillet radii around the piston tether. In looking at Figure 7.11(b), notice that the velocity amplitudes are significantly more pronounced at the piston edge compared to the piston center. This is especially true for the “1 – Θ ” tilt mode and the “plunge” mode.

Figure 7.13 illustrates the displacement profile of the device at 15kHz with an applied sinusoidal voltage of $500V \pm 500V$. Slight tilting of the piston surface is observed, and is again likely influenced by imperfect piezoelectric cylinder placement or non-uniformity in fillet radius etching. Figure 7.14 displays the corresponding displacement profiles at the piston center and piston edge. Higher-order dynamic oscillations of $f = 80kHz$ are observed within the lower 15kHz drive frequency. These higher-order oscillations are more pronounced at the piston edge than at the piston center, which could be attributed to non-linearities inherent in the piezoelectric material or in the tether structure. The overall measured peak-peak deflection at the piston center, $\delta_{p-p} = 0.69\mu m$, is slightly lower than the expected range of $\delta_{p-p} = 0.75 - 0.82\mu m$. Most likely, this is a result of material inconsistency among the piezoelectric cylinders.

Figure 7.15 displays the displacement profiles at the piston center and piston edge at a driving frequency of 7kHz. Higher-order dynamic oscillations of $f = 80kHz$ are again observed in the piston edge displacement signal, but with a lower magnitude. As for the piston center response at 15kHz, the overall measured peak-peak deflection at the piston center at 7kHz, $\delta_{p-p} = 0.70\mu m$, is slightly lower than the expected range of $\delta_{p-p} = 0.75 - 0.82\mu m$. Figure 7.16 plots the voltage-deflection curves for the piston center at 100Hz as a function of varying applied voltage levels, from $100V \pm 100V$ to $500V \pm 500V$. Hysteresis in the PZT-5H material is clearly evident from the wide sweeping shapes of the curves. Overall, however, the peak displacement is close to linear with applied voltage.

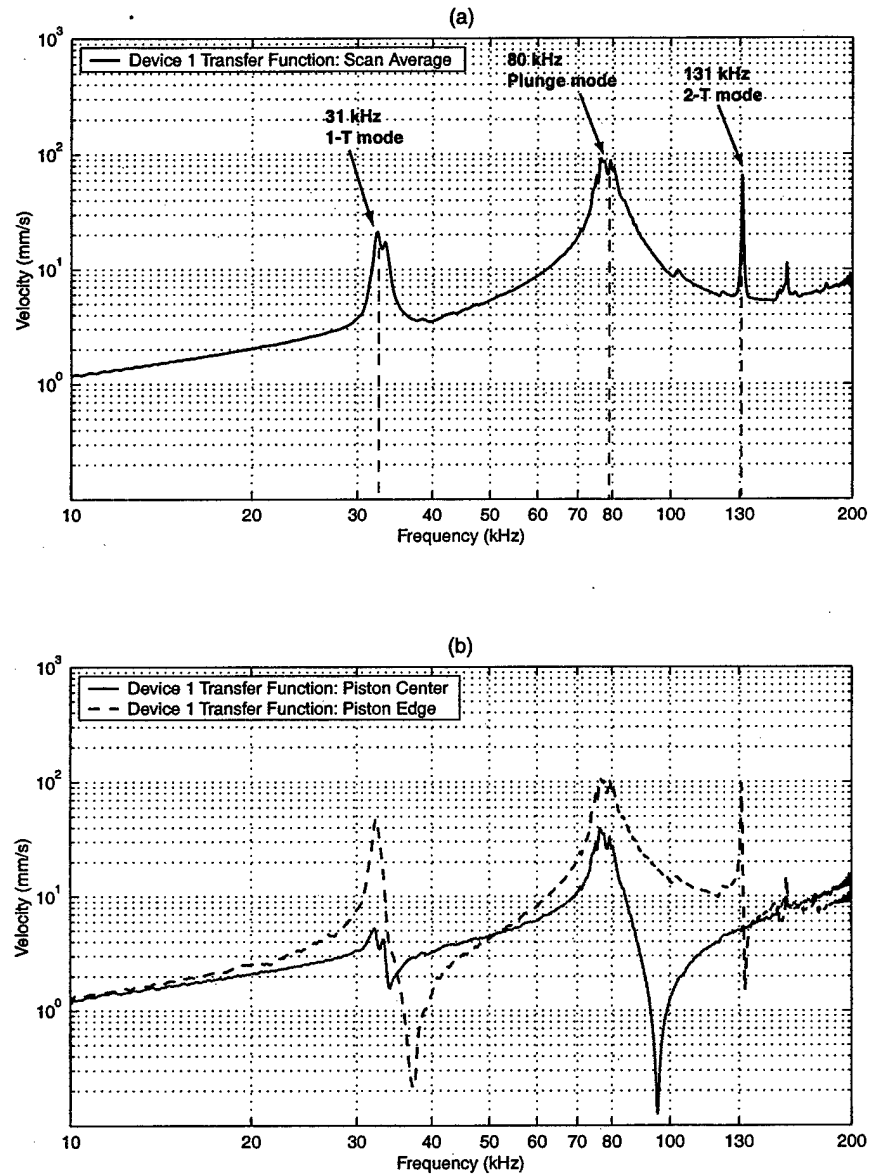


Figure 7.11: Device 1 transfer functions of piston velocity versus frequency for a sweep input from 10kHz to 200kHz and small signal drive voltage $0V \pm 25V$: (a) averaged velocity over piston surface, and (b) velocity at center and edge locations on piston surface. Modal behavior is present at 31kHz, 80kHz, and 131kHz. Phase information was not recorded for this device.

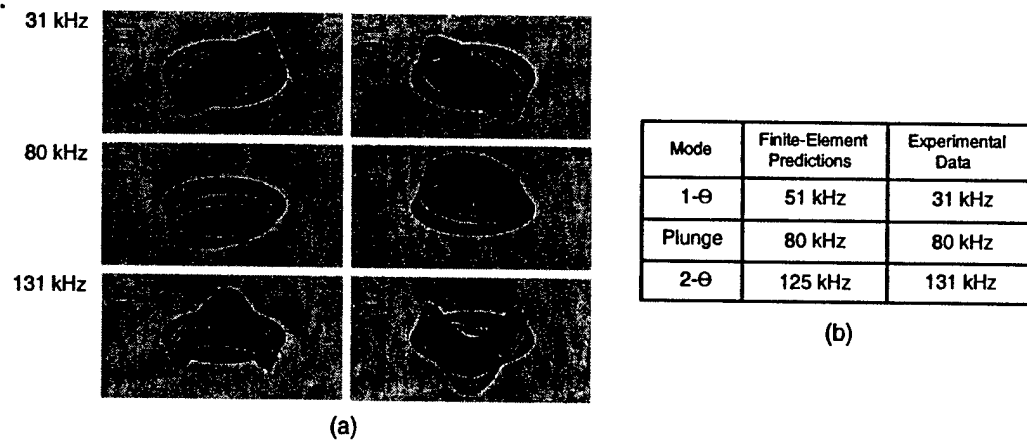


Figure 7.12: Device 1 modal behavior: (a) vibrometer scans of device: “1 – Θ ” tilt mode at $f = 31\text{kHz}$, “plunge” mode at $f = 80\text{kHz}$, and “2 – Θ ” mode at $f = 131\text{kHz}$, (b) comparison to results from the ANSYS finite-element model.

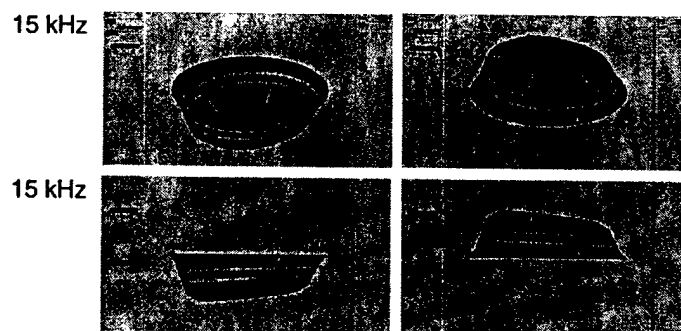


Figure 7.13: Vibrometer scan images of Device 1 low-frequency 15kHz displacement profile. The tilting of the piston surface is likely due to an uncentered piezoelectric cylinder or a non-uniform fillet radius in etched piston trench.

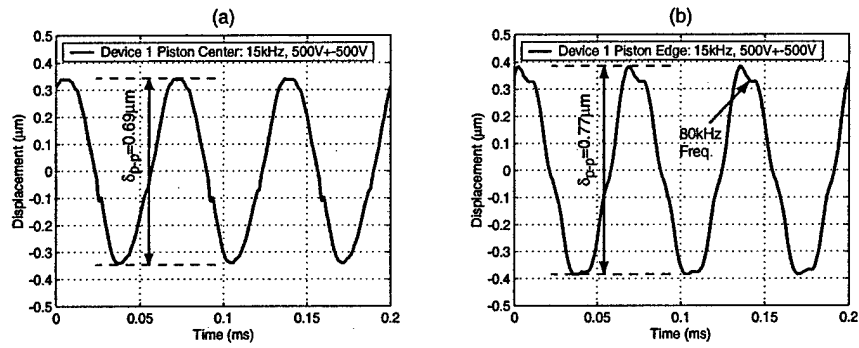


Figure 7.14: Device 1 displacement time histories for a sinusoidal drive voltage of $500V \pm 500V$ at $f = 15kHz$: (a) piston center displacement and (b) piston edge displacement. Note the presence of 80kHz oscillations in the edge displacement time history.

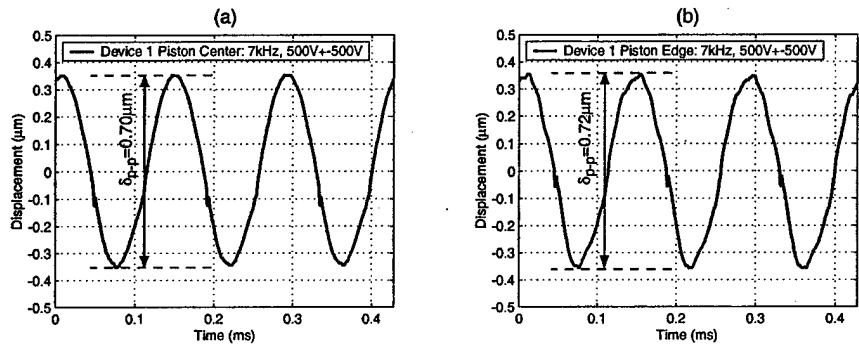


Figure 7.15: Device 1 displacement time histories for a sinusoidal drive voltage of $500V \pm 500V$ at $f = 7kHz$: (a) piston center displacement and (b) piston edge displacement.

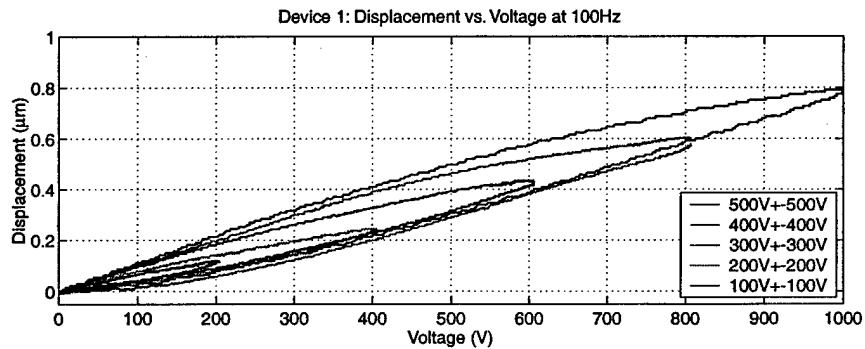


Figure 7.16: Device 1 piston center displacement behavior versus applied voltage at 100Hz.

Experimental Testing of Device 2

Figure 7.17(a) plots the transfer function of averaged velocity over the scanned piston surface versus frequency for Device 2. Figure 7.17(b) plots these transfer functions for specific locations on the piston surface, at the center and at an outer edge. Figure 7.18(a) presents experimental mode shapes of the device at selected modal frequencies. In comparing this dynamic response to that of Device 1, the overall modal shapes are similar, however, the frequencies at which they occur are shifted downward. The "1 - Θ " tilt mode occurs at $f = 30kHz$, the "plunge" mode at $f = 61kHz$, and the "2 - Θ " mode at $f = 112kHz$. This frequency shift is expected since PZN-PT is a softer material than PZT-5H. As shown in Figure 7.18(b), these modal frequencies correlate well with finite-element models of the device. In looking at Figure 7.17(b), notice that the velocity amplitudes are significantly more pronounced at the piston edge compared to the piston center. This is especially true for the "1 - Θ " tilt mode and the "plunge" mode.

The displacement profile of Device 2 at 15kHz with an applied sinusoidal voltage of $500V \pm 500V$ exhibits a non-uniform tilt (see Figure 7.19) in much the same manner as Device 1. The displacement time history at the piston edge exhibits components of the device "plunge" mode (see Figure 7.20). However, in comparison with Device 1 the magnitude of the piston center displacement in Device 2 is significantly increased to $\delta_{p-p} = 1.42\mu m$. This value correlates well with the expected peak-peak displacement range of $\delta_{p-p} = 1.35 - 1.55\mu m$.

Figure 7.21 displays the displacement profiles at the piston center and piston edge at a driving frequency of 7kHz. Dynamic oscillations of $f = 61kHz$ are again observed in the piston edge displacement signal, and this signal has a decreased overall amplitude from the 15kHz response. As for the piston center response at 15kHz, the overall measured peak-peak deflection of the piston center at 7kHz, $\delta_{p-p} = 1.39\mu m$, correlates well to the expected range of $\delta_{p-p} = 1.35 - 1.55\mu m$. Figure 7.22 plots the voltage-deflection curves for the piston center at 100Hz as a function of varying applied voltage levels, from $100V \pm 100V$ to $500V \pm 500V$. Comparing these curves to those of Device 1, it is clear that the PZN-PT material exhibits significantly reduced hysteretic behavior than the PZT-5H material. Additionally, the peak displacement is seen to be linear with applied voltage.

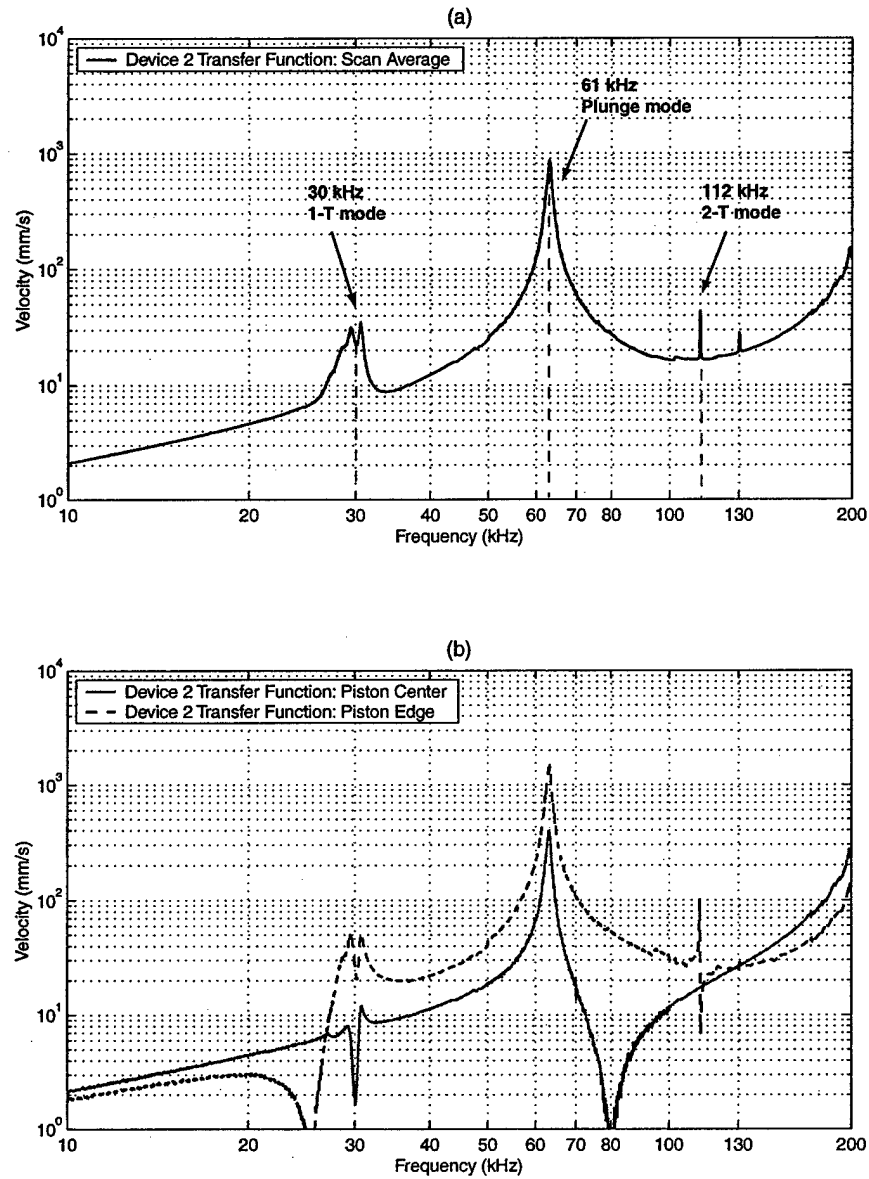


Figure 7.17: Device 2 transfer functions of piston velocity versus frequency for a sweep input from 10kHz to 200kHz and small signal drive voltage $0V \pm 25V$: (a) averaged velocity over piston surface, and (b) velocity at center and edge locations on piston surface. Modal behavior is present at 30kHz, 61kHz, and 112kHz. Phase information was not recorded for this device.

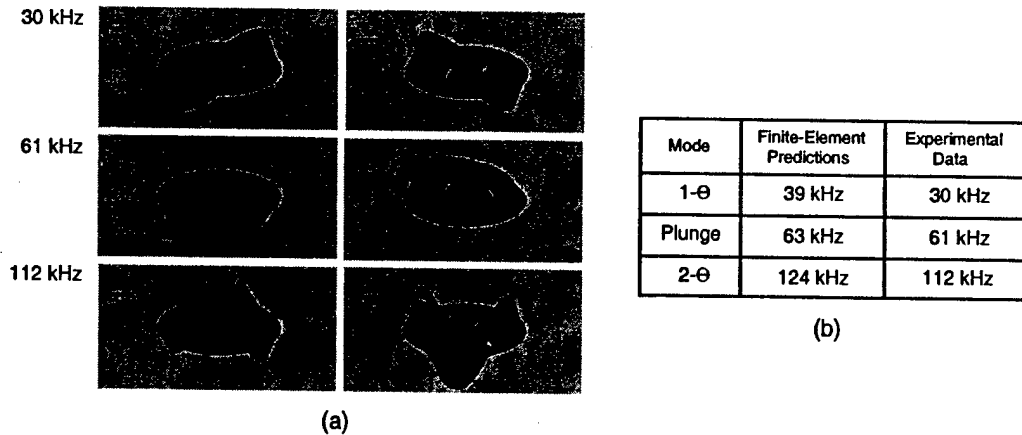


Figure 7.18: Device 2 modal behavior: (a) vibrometer scan images of device behavior: “1 – Θ ” tilt mode at $f = 30kHz$, “plunge” mode at $f = 61kHz$, and “2 – Θ ” mode at $f = 112kHz$, (b) comparison to results from the ANSYS finite-element model.

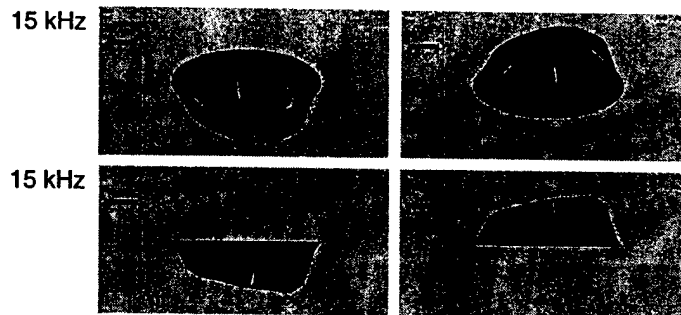


Figure 7.19: Vibrometer scan images of Device 2 low-frequency 15kHz displacement profile. The tilting of the piston surface is likely due to an uncentered piezoelectric cylinder or non-uniform fillet radius in etch piston trench.

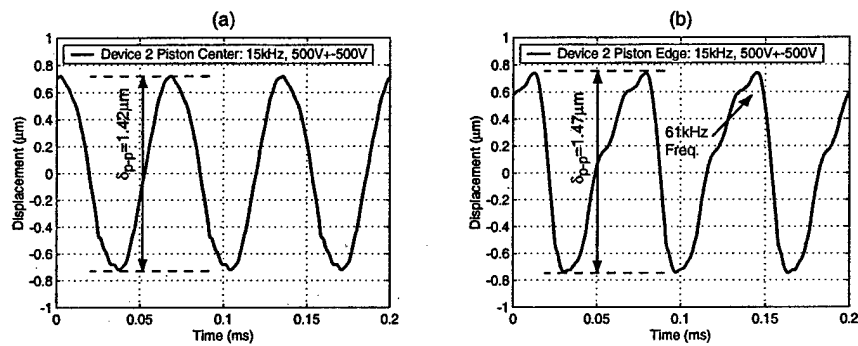


Figure 7.20: Device 2 displacement time histories for a sinusoidal drive voltage of $500V \pm 500V$ at $f = 15kHz$: (a) piston center displacement and (b) piston edge displacement. Note the presence of 61kHz oscillations in the edge displacement time history.

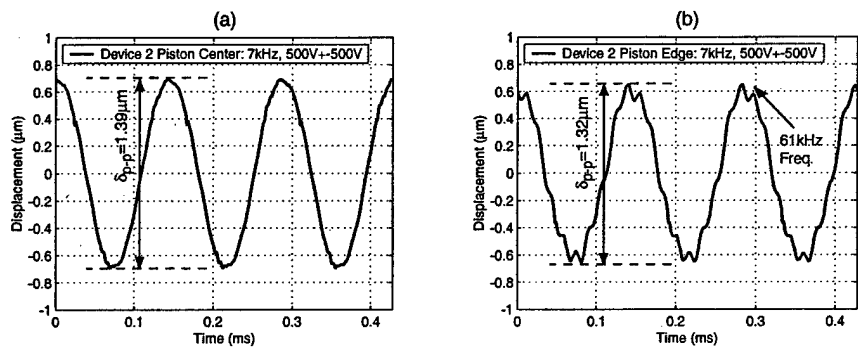


Figure 7.21: Device 2 displacement time histories for a sinusoidal drive voltage of $500V \pm 500V$ at $f = 7kHz$: (a) piston center displacement and (b) piston edge displacement.

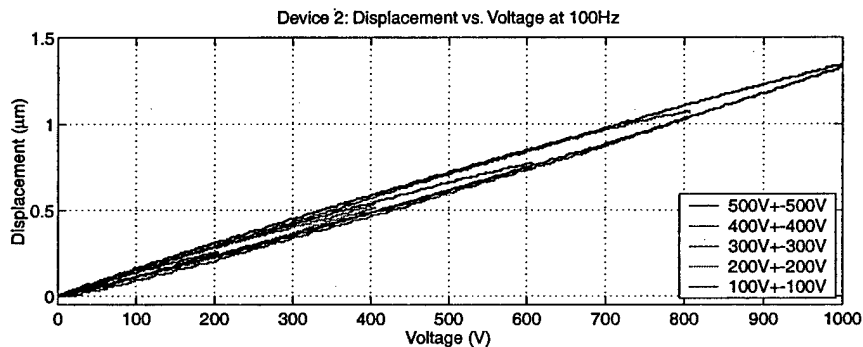


Figure 7.22: Device 2 piston center displacement versus applied voltage at 100Hz.

Experimental Testing of Device 3

Figure 7.23(a) plots the transfer function of averaged velocity over the scanned piston surface versus frequency for Device 3. Figure 7.23(b) plots these transfer functions for specific locations on the piston surface, at the center and at an outer edge. In comparing this dynamic response to that of Device 1, modal behavior is not observed until frequencies near $f = 80\text{kHz}$. The placement of multiple cylinders beneath the piston eliminates tilting behavior at frequencies in the 30kHz to 80kHz range. As shown in Figure 7.24, initial modal behavior is characterized by non-symmetric motion of the piston surface, most likely due to unsymmetric placement of the piezoelectric elements beneath the piston, differences in material properties among the elements, or a non-uniform fillet radius profile along the tether circumference. A perfectly symmetric finite-element model of this device predicts 1st modal behavior at 225kHz (see Figure 7.25).

For low-frequency actuation, the multiple piezoelectric cylinder stiffening effect is observed in Figure 7.26 as the displacement profile at 15kHz experiences minimal tilting during actuation. In addition, as shown in Figure 7.27, the displacement time histories at the piston center and piston edge are relatively free from higher order oscillations. A small contribution with frequency $f \sim 90\text{kHz}$ is evident in the piston edge displacement time history. As for Device 1, the magnitude of the piston center displacement in Device 3, $\delta_{p-p} = 0.72\mu\text{m}$, is slightly lower than the expected range of $\delta_{p-p} = 0.75 - 0.82\mu\text{m}$.

Figure 7.28 displays the displacement profiles at the piston center and piston edge at a driving frequency of 7kHz. Again, almost perfect displacement behavior free from higher-order oscillations is observed. The overall measured peak-peak deflection at the piston center at 7kHz, $\delta_{p-p} = 0.76\mu\text{m}$, is within the expected range of $\delta_{p-p} = 0.75 - 0.82\mu\text{m}$. As was the case for Device 1, the deflection behavior under quasi-static driving conditions (see Figure 7.29) is linear with the applied voltage. Overall, these results indicate that the incorporation of multiple piezoelectric cylinders spread out beneath the tethered piston is achievable.

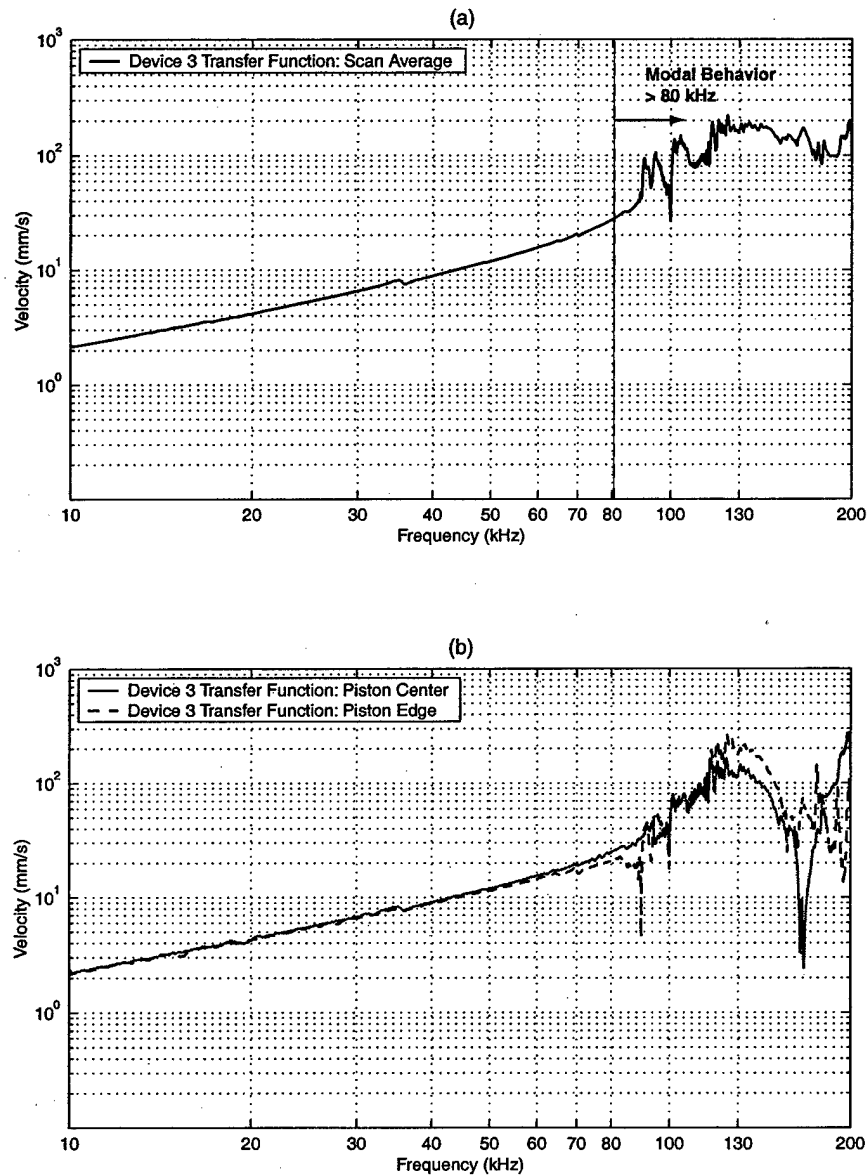


Figure 7.23: Device 3 transfer functions of piston velocity versus frequency for a sweep input from 10kHz to 200kHz and small signal drive voltage $0V \pm 25V$: (a) averaged velocity over piston surface, and (b) velocity at center and edge locations on piston surface. Modal behavior is not present below 80kHz. Phase information was not recorded for this device.

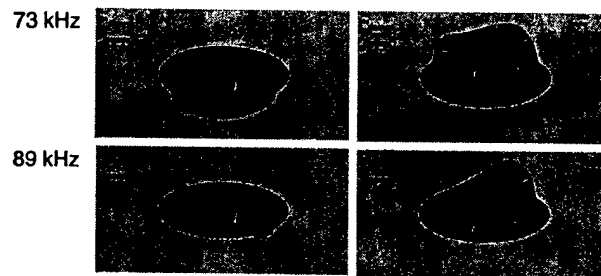


Figure 7.24: Vibrometer scan images of selected Device 3 modal behavior above 70kHz: behavior at 73kHz and 89kHz.

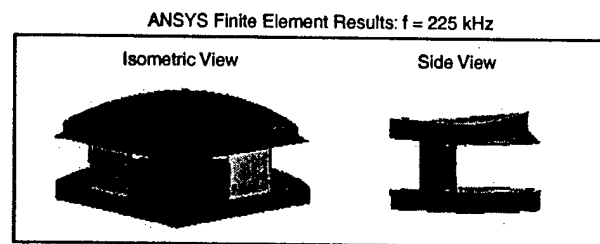


Figure 7.25: Device 3 ANSYS finite-element model prediction for 1st mode shape at 225 kHz.

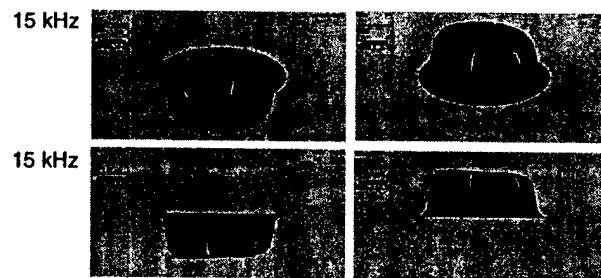


Figure 7.26: Vibrometer scan images of Device 3 low-frequency 15kHz displacement profile. Presence of multiple piezoelectric cylinders beneath piston serves to stiffen actuator structure and reduce tilting behavior.

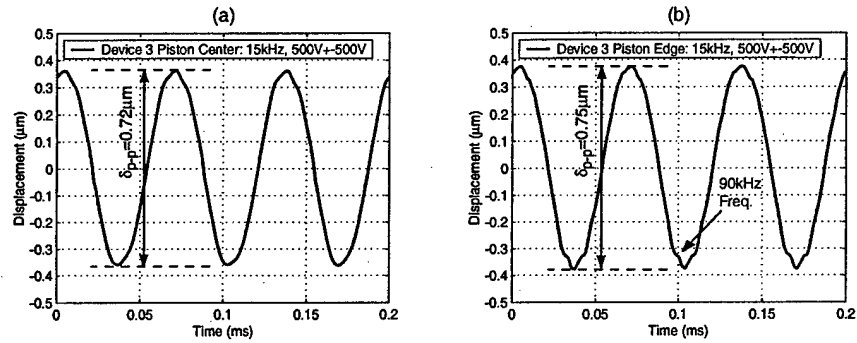


Figure 7.27: Device 3 displacement time histories for a sinusoidal drive voltage of $500\text{V} \pm 500\text{V}$ at $f = 15\text{kHz}$: (a) piston center displacement and (b) piston edge displacement. Note the slight presence of a 90kHz oscillation in the edge displacement time history.

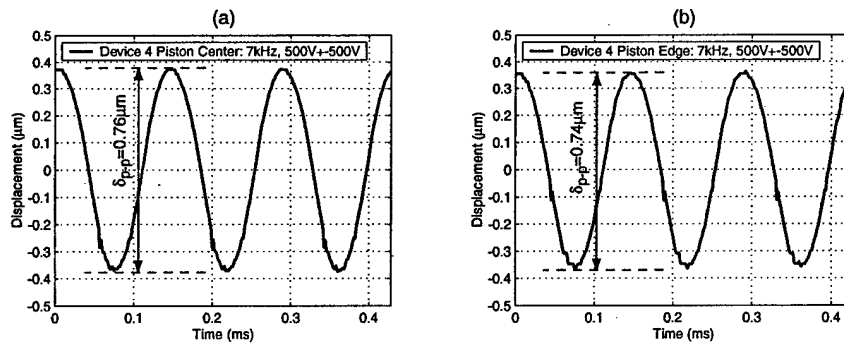


Figure 7.28: Device 3 displacement time histories for a sinusoidal drive voltage of $500\text{V} \pm 500\text{V}$ at $f = 7\text{kHz}$: (a) piston center displacement and (b) piston edge displacement.

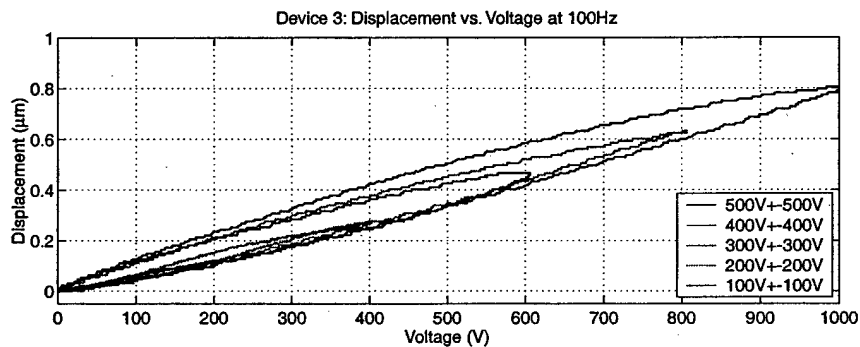


Figure 7.29: Device 3 piston center displacement versus applied voltage at 100Hz.

7.5.2 2nd Generation Device

Measurement of Fillet Radius Profiles

As was performed for the 1st-generation drive element devices, careful inspection of the drive element tethers in Device 4 was also carried out. Since this device incorporates a double-layer piston structure, these inspections were performed prior to wafer-level Si-Si fusion bonding of the piston structure. For the lower piston tethers and upper piston tethers, fillet radii between 25-35 μm (ie: tether widths between 180-200 μm) were measured with no observable defects along the tethers, indicating excellent uniformity during the previous DRIE etching procedures.

Characterization of Piezoelectric Material

PZN-PT material similar to that in the 1st-generation drive element devices was used in Device 4. As a result, the PZN-PT material squares were expected to produce voltage-deflection behavior in the same range as shown in Figure 7.10 (ie: peak deflections at 1000V between 1.35 μm and 1.55 μm).

Experimental Testing of Device 4

Figure 7.30(a) plots the transfer function of averaged velocity over the scanned piston surface versus frequency for Device 4. Figure 7.30(b) plots these transfer functions for specific locations on the piston surface, at the center and at an outer edge. As shown in Figure 7.31, modal behavior begins near 50kHz and is characterized by non-symmetric tilting motion of the piston surface, most likely due to unsymmetric placement of the piezoelectric elements beneath the piston or differences in material properties among the elements. A perfectly symmetric finite-element model of this device predicts 1st modal behavior (piston plunge) at 155kHz and 2nd modal behavior (1- Θ piston tilting) at 288kHz.

For low-frequency actuation at 15kHz and at a voltage of 1000V peak-peak, the drive element piston experiences minimal tilting (as shown in Figure 7.32), indicating a well-built and toleranced drive element device. The degree of piston tilting is illustrated more clearly in Figure 7.33. The displacement time history at the piston center (Figure 7.33(a)) is very smooth with no higher order oscillations. Likewise, the displacement time histories at the piston edge locations with maximum peak-peak motions (Figure 7.33(b)) are also completely free from higher order oscillations. In comparing the peak-peak deflections of these opposite piston edges, the magnitude of tilt is estimated to be $\sim 4\%$ of the piston center deflection. The piston center displacement ($\delta_{p-p} = 1.41\mu\text{m}$) correlates well with the expected range of $\delta_{p-p} = 1.35 - 1.55\mu\text{m}$. As was the case for the first generation drive element devices, the deflection behavior under quasi-static driving conditions is linear with the applied voltage. Figure 7.34 illustrates this voltage dependent behavior at 100Hz.

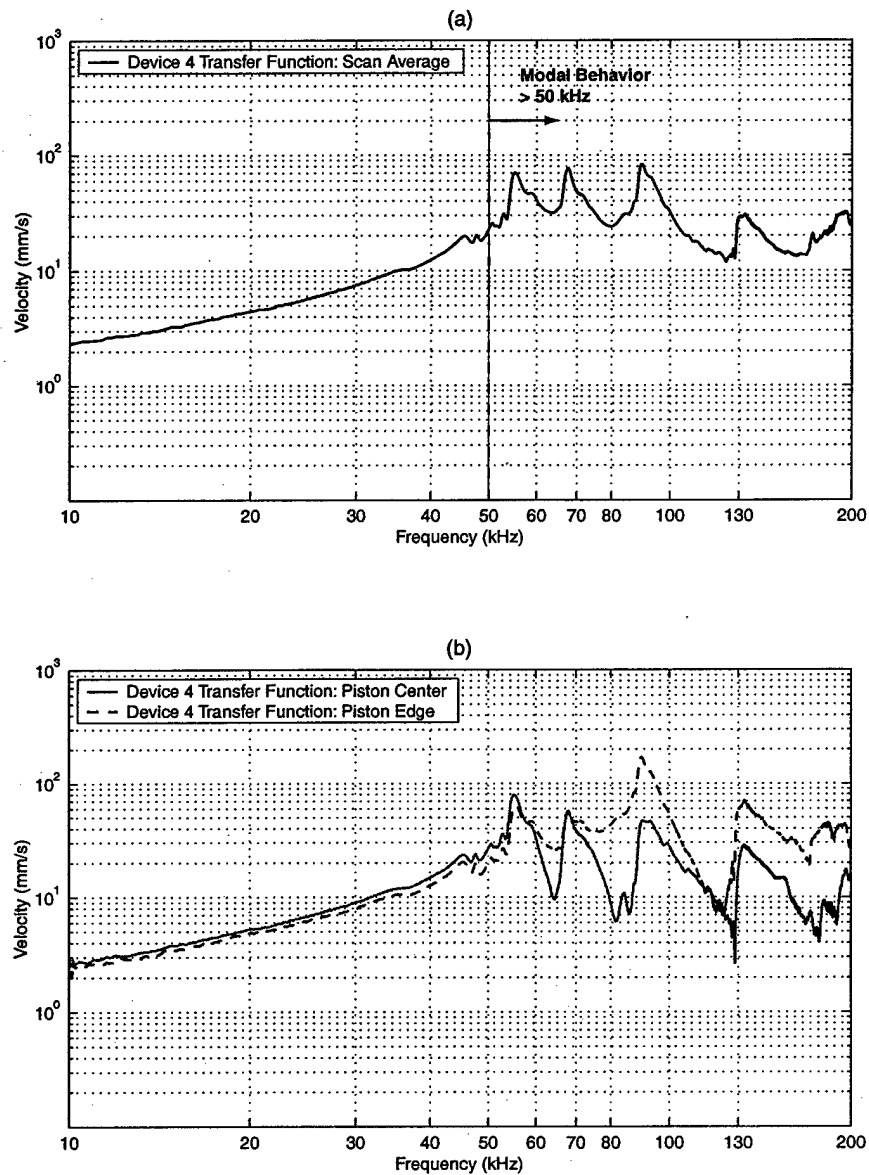


Figure 7.30: Device 4 transfer functions of piston velocity versus frequency for a sweep input from 10kHz to 200kHz and small signal drive voltage $0V \pm 25V$: (a) averaged velocity over piston surface, and (b) velocity at center and edge locations on piston surface. Modal behavior is present near 50kHz. Phase information was not recorded for this device.

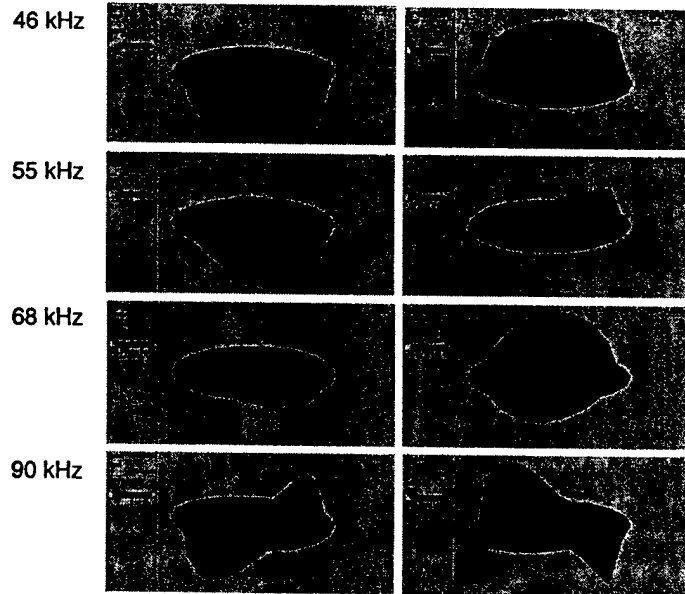


Figure 7.31: Vibrometer scan images of selected Device 4 modal behavior between 45kHz and 90kHz.

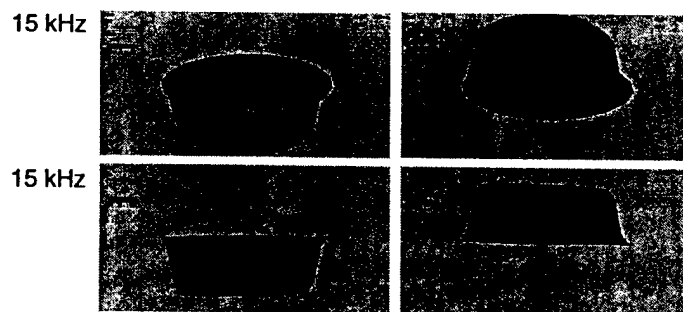


Figure 7.32: Vibrometer scan images of Device 4 low-frequency 15kHz displacement profile. This multiple piezoelectric cylinder device exhibits minimal tilting behavior at 15kHz.

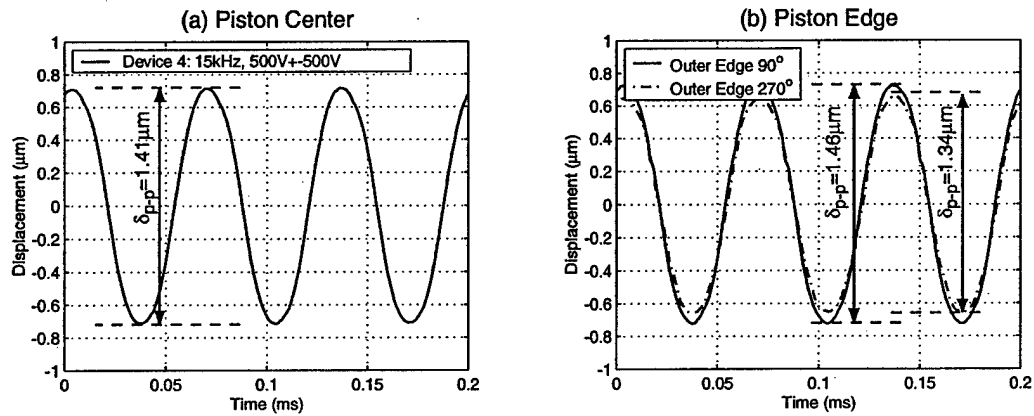


Figure 7.33: Device 4 displacement time histories for sinusoidal drive voltage of $500\text{V} \pm 500\text{V}$ at $f = 15\text{kHz}$: (a) piston center displacement and (b) piston edge displacements. These results indicate a rigid well-toleranced device.

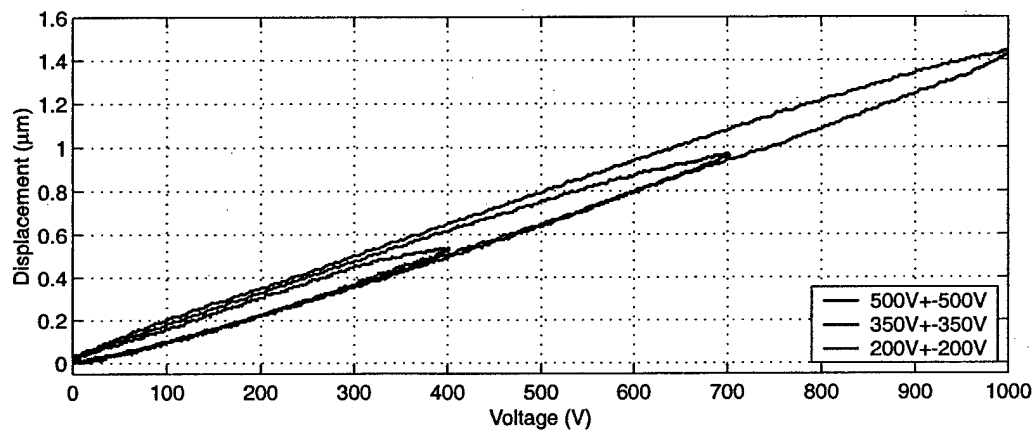


Figure 7.34: Device 4 piston center displacement versus applied voltage at 100Hz.

7.6 Conclusions

This chapter has presented the development and testing of a variety of piezoelectric drive element devices. The results indicate that the incorporation of a single centrally-located piezoelectric element and the incorporation of multiple elements spread out symmetrically beneath single-layer and double-layer tethered piston structures can be performed in a repeatable and predictable fashion. Additionally, processing, tolerancing, and drilling/dicing procedures of high performing PZN-PT elements, in addition to standard polycrystalline PZT-5H elements, have been proven. This drive element manufacturing capability serves now as a foundation for the development and assembly of the full active valve devices presented in the following chapters.

Bibliography

- [1] S.E. Park and T.R. Shrout, "Characteristics of Relaxor-Based Piezoelectric Single Crystals for Ultrasonic Transducers," *IEEE Trans. Ultrasonics, Ferroelectrics, and Frequency Control*, Vol.44, No.5, Sept. 1997, pp. 1140-1147.
- [2] D.C. Roberts, J.L. Steyn, H.Q. Li, K.T. Turner, R. Mlcak, L. Saggere, S.M. Spearing, M.A. Schmidt, and N.W. Hagood, "A High-Frequency, High-Stiffness Piezoelectric Micro-Actuator For Hydraulic Applications," *Proceedings of the 11th International Conference on Solid-State Sensors and Actuators, Munich, Germany, June 10-14, 2001*.

Chapter 8

Sub-Component Study: Valve Cap and Membrane

8.1 Objectives

The purpose of this study was to evaluate the fabrication process flow of the valve cap and membrane sub-component structure, shown in Figure 8.1, and to experimentally characterize the deflection behavior of a series of these membrane structures to differential pressure loadings. Specifically, the three primary objectives of this study were:

1. To demonstrate the capability to etch valve cap and membrane structures from silicon-on-insulator wafers, with accurate control over the fillet radii at the base of the etch.
2. To experimentally characterize the pressure-deflection behavior of the valve cap and membrane structures, and correlate these results to predictions from the structural models presented in Chapter 3 of this thesis. These structures are pressurized to significant levels at which non-linear large deformation behavior is expected.
3. To provide sensitivity analyses on key geometric parameters such as membrane thickness and fillet radius size to provide an understanding of fabrication process variability on structural pressure-deflection behavior.

Successful fabrication and experimental evaluation of these valve cap and membrane structures enables the further assembly and testing of full active valve devices.

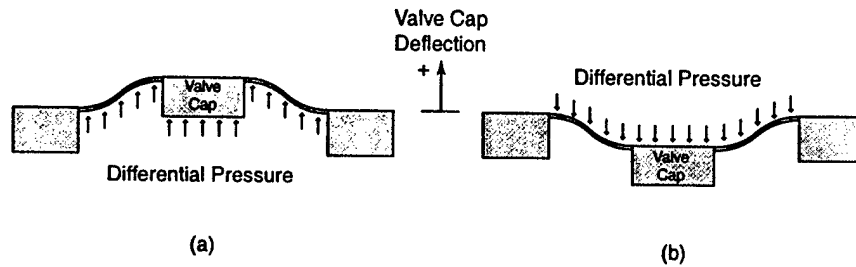


Figure 8.1: 2-D schematic of a valve cap and membrane structure: (a) deformation in response to a positive differential pressure, and (b) deformation in response to negative differential pressure.

8.2 Device Test-Plan

8.2.1 Geometry

The valve cap and membrane structures fabricated for this study had the dimensions illustrated in Figure 8.2. No valve stop exists above the valve cap in the positive direction (unlike in the full active valve device where the fluid orifice is present) in order to facilitate measurement of the valve cap and membrane deflections from above. However, a valve stop in the negative direction, situated $15\mu\text{m}$ below the underside of the valve cap, does exist. In response to positive differential pressures across the structure (creating positive valve cap deflections), the membrane is therefore unrestrained. In response to negative differential pressures, however, the valve cap deflection is limited to $-15\mu\text{m}$.

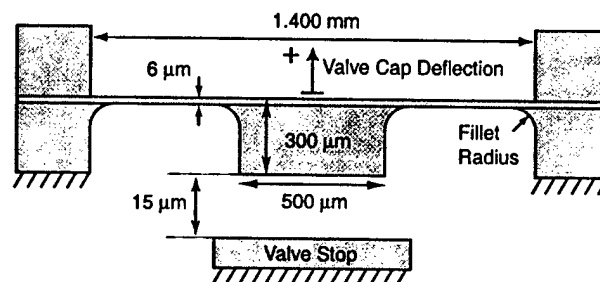


Figure 8.2: Dimensions of the fabricated valve cap and membrane structures: valve cap thickness = $300\mu\text{m}$, membrane thickness = $6\mu\text{m}$, valve cap diameter = $500\mu\text{m}$, and valve membrane outer diameter = 1.4 mm . Fillet radii are shown in schematic.

8.2.2 Device Assembly

As presented in Chapter 7, testing of the valve cap and membrane structure is enabled through fabrication and assembly of the test device illustrated in Figure 8.3. This device consists of Layers N1, N2, N3, 4, 5, 6, N7, N8, and N9. Layers 4, 5, and 6 are identical to those layers used in a full active valve device, however the remaining layers are substituted for the final active valve layers to provide measurement access to the various components. Valve membrane deflection measurements are performed for applied gas pressure to the inside of the HAC chamber and to the top surface of the valve cap and membrane.

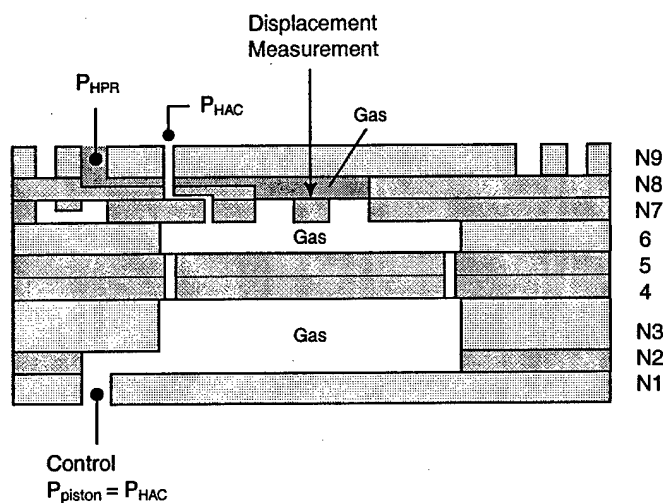


Figure 8.3: Valve cap and membrane sub-component structure. Gas pressure is used above and below the valve structure to obtain pressure-deflection measurements.

8.2.3 Testing Procedure

The valve membrane sub-component device was inserted into the fluids test-rig discussed in Chapter 7 for experimental testing. Gas pressure was independently regulated inside of the hydraulic amplification chamber (P_{HAC}) and above the valve cap and membrane surface (P_{HPR}) so as to provide either a positive or negative differential pressure across the valve cap and membrane structure. The pressure below the unrestrained drive element piston (P_{piston}) was maintained at the same value as P_{HAC} to ensure zero deflection of this structure, thereby minimizing its potential for breaking. Through glass Layer 9, the deflection of the valve cap was monitored using a laser vibrometer system. Differential pressures from -0.40 MPa to 0.40 MPa were imposed on the valve cap and membrane structures and resulting deflection measurements were obtained.

8.3 Theoretical Predictions

In order to accurately predict the response of these valve membrane test structures to various pressure loadings, detailed modeling of the non-linear deflection behavior is required. In addition, sensitivity analyses on the membrane thickness and the fillet radius size are necessary to understand potential differences between predicted and experimental behavior. To accomplish these objectives, two parallel modeling procedures were implemented. The first procedure uses the numerical non-linear deflection code presented in Chapter 3 of this thesis to understand the effects of varying membrane thickness on the deflection behavior of the structure. Because this code is based on simplified plate theory, it does not include fillet radii geometries. As a result, a second procedure is implemented to develop finite-element models of the valve cap and membrane structures, which incorporate fillet radius features. Through the use of both modeling procedures, thorough understanding of the experimental results can be obtained.

8.3.1 1st Modeling Procedure: Numerical Non-linear Deflection Code

The MatlabTM codes, DAVE80200NLValveCaseA.m and DAVE80200NLValveCaseC.m (previously discussed in Chapter 3 and included for reference in Appendix B), are combined to capture the behavior of the valve cap and membrane structure for positive and negative differential pressure loadings. The results are discussed in the following sub-sections.

Baseline Design Pressure-Deflection Behavior

Figure 8.4 plots the valve cap deflection and maximum membrane tensile stress as a function of applied differential pressure from -0.40 MPa to 0.40 MPa. Results for linear and non-linear theory are shown. In comparing these curves, it is clear that non-linear deformation theory is required for accurate prediction of the valve membrane structural behavior. For the peak positive differential pressure of 0.40 MPa, a valve cap deflection of 22.6 μm and corresponding maximum membrane stress of 1.06 GPa are predicted. Due to the presence of a valve stop in the negative direction, a valve cap deflection of -15 μm and a corresponding maximum membrane stress of 1.00 GPa are predicted for an applied differential pressure of -0.40 MPa.

Sensitivity to Valve Membrane Thickness

Although the valve cap and membrane structures tested in this study have measured membrane thicknesses between 6 μm and 7 μm , these measurements are only accurate to within $\pm 1\mu\text{m}$. As a result, it is important to predict the structural behavior over a range of membrane thickness. Figure 8.5 plots the valve cap deflection and maximum membrane tensile stress as a function of applied differential pressure from -0.40 MPa to 0.40 MPa for membrane thicknesses of 6 μm , 7 μm , and 8 μm . In comparison to predictions for the 6 μm membrane (valve cap deflection=22.6

μm), the 7 μm membrane is predicted to deflect 20.8 μm (8 % difference), and the 8 μm membrane is predicted to deflect 19.6 μm (13 % difference) for an applied differential pressure of 0.40 MPa. The corresponding stresses also differ by similar percentages. Based on these predictions, variations in membrane thickness should not drastically effect structural behavior, although it is an important fabrication uncertainty to keep in mind.

Sensitivity to Membrane In-Plane Prestress

During fabrication procedures of the valve cap and membrane structures, the oxide above the membrane is stripped. Ideally, this procedure should eliminate any residual stress contained within the membrane structure. However, other procedures, such as anodic bonding of device layers, could potentially create residual stresses along the valve membrane due to thermal expansion mismatch between the silicon and pyrex layers. Calculations have indicated that these valve membrane structures will experience at most a residual tensile stress of 5 MPa for an anodic bonding temperature of up to 330C (50C above the ideal matched anodic bonding temperature of 280C) [1], a stress which has negligible effect on the stiffness of the valve membranes structures in response to pressure loading. As a result, since the anodic bonding procedures in this thesis are always carried out at 300C, these valve membranes should be free of residual tensile stress.

8.3.2 2nd Modeling Procedure: Finite-element Code

Finite-element models have been developed that incorporate fillet radius features along the inner and outer circumference of the valve membrane. Figure 8.6 displays a mesh of the valve cap and membrane geometry, with detailed focus on the meshing grid around the fillet radius features. In this figure, the fillet radius has size 30 μm . Figure 8.7 shows a representative stress contour plot of the structure when subjected to a positive differential pressure of 0.30MPa.

Sensitivity to Fillet Radius Size

Using these finite-element models, valve cap deflection and maximum membrane stress plots as a function of varying fillet radius are acquired, as shown in Figure 8.8. The fillet radius at the inner and outer valve membrane circumference is varied to be 15 μm , 30 μm , 45 μm , and 60 μm . As evidenced in the plots, an increase in the fillet size serves to stiffen the overall membrane structure, resulting in reduced valve cap deflections. For example, for an applied differential pressure of 0.40 MPa, the valve cap with fR=15 μm experiences a deflection of almost 23 μm whereas the valve cap with fR=60 μm experiences a deflection of approximately 20 μm . The maximum membrane stress curves follow a similar pattern. In the valve cap and membrane

experiments discussed later in this chapter, careful inspection of the membrane fillet radii is performed prior to testing to enable understanding of the structural behavior.

Note on Theoretical Predictions

The presence of a fillet radius along the valve membrane inner and outer membrane surfaces clearly has an effect on the structural stiffness, as evidenced in comparing Figures 8.5 and 8.8. For very small fillet radius sizes, these features act as stress concentrations. As such, the finite-element models with small fillet radii predict stresses significantly larger than those predicted by the numerical code (which includes no effect of fillet radii). Conversely, the finite-element models with large fillet radii predict smaller stresses than those predicted by the numerical code, mainly because the fillet structure actually results in a stiffening of the membrane and a subsequent reduction in the deflection magnitude of the valve cap. The fillet radii features present on the fabricated valve membrane structures discussed in the following experimental section were able to be controlled to within $35 - 50\mu m$, a range which is characterized by reasonably good correlation between finite-element and numerical pressure-deflection predictions. As such, when comparing experimental pressure-deflection behavior with theory in the following section of this chapter, the numerical predictions will be used.

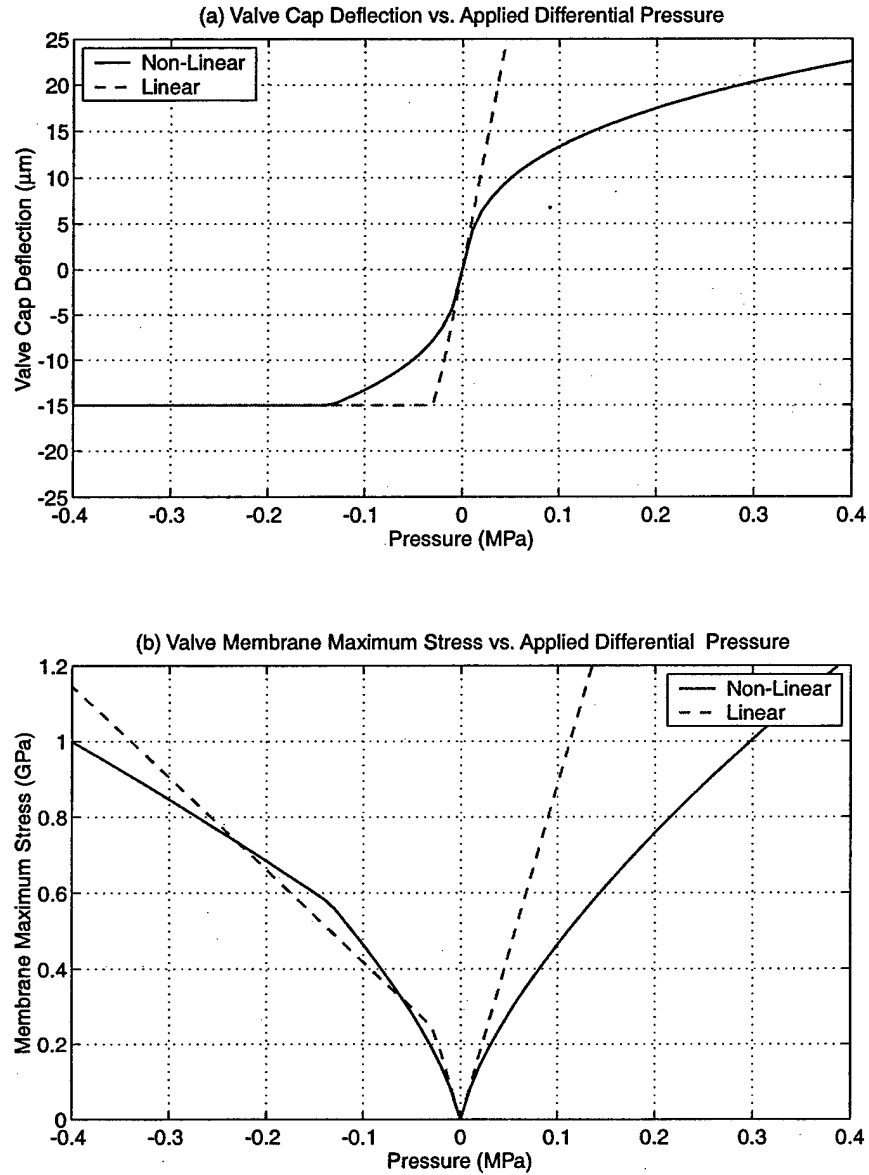


Figure 8.4: Baseline valve cap and membrane design $\rightarrow r_{vc} = 250\mu\text{m}$, $r_{vm} = 700\mu\text{m}$, $t_{vm} = 6\mu\text{m}$: (a) valve cap deflection vs. applied differential pressure, and (b) maximum stress in valve membrane vs. applied differential pressure. Note: valve stop present at $-15\mu\text{m}$.

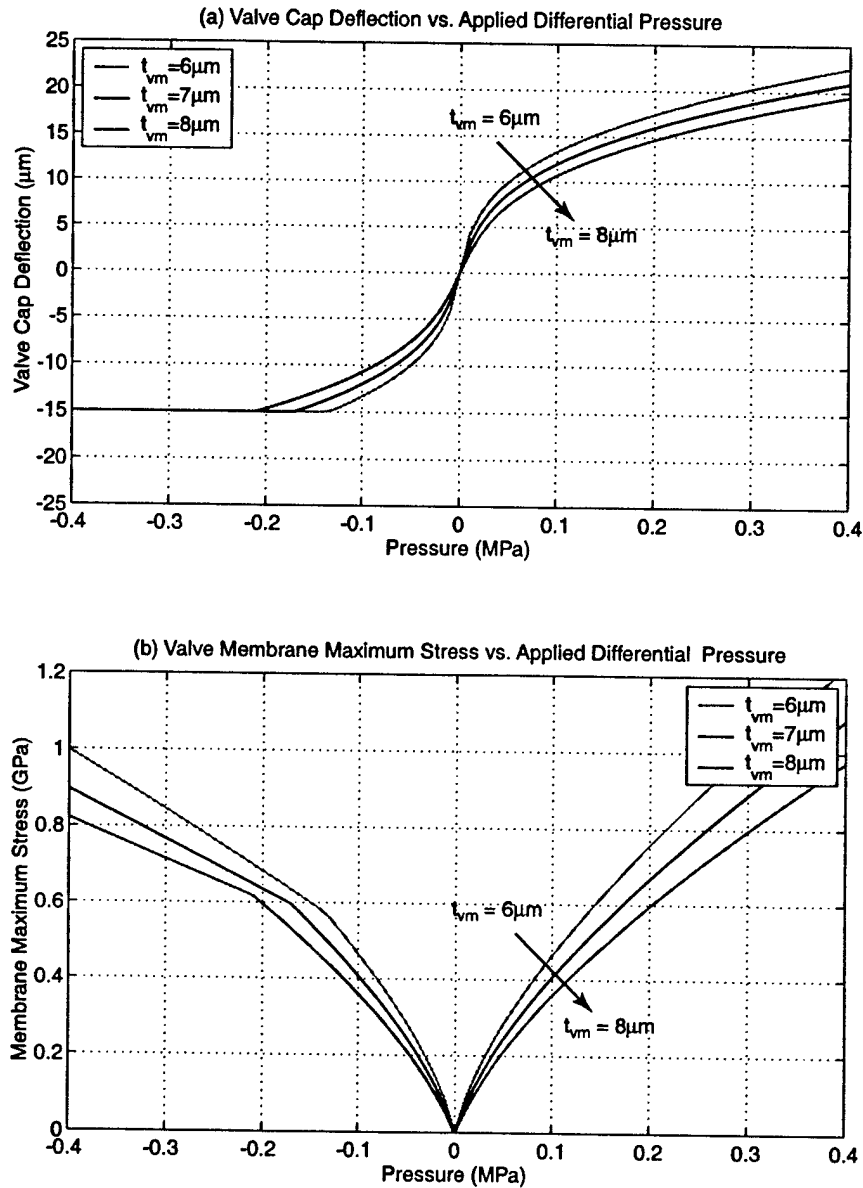


Figure 8.5: Sensitivity of baseline valve cap and membrane design to variations in valve membrane thickness $\rightarrow r_{vc} = 250\mu m$, $r_{vm} = 700\mu m$, $t_{vm} = [6\mu m, 7\mu m, 8\mu m]$: (a) valve cap deflection vs. applied differential pressure, and (b) maximum stress in valve membrane vs. applied differential pressure. Note: valve stop present at $-15\mu m$.

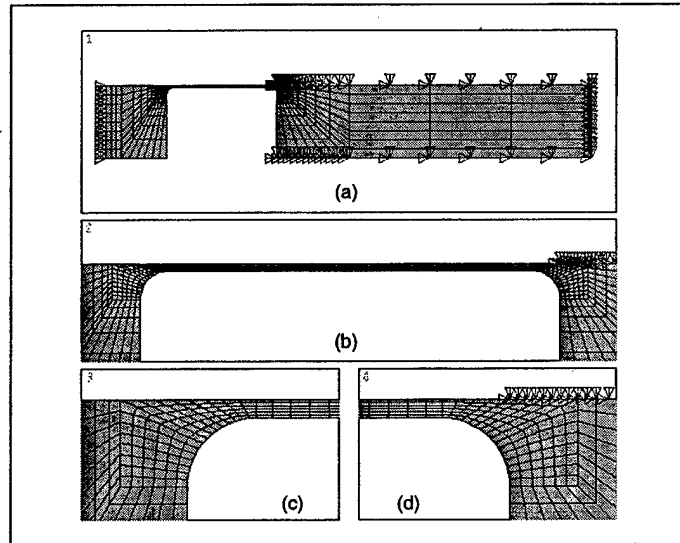


Figure 8.6: Finite-element mesh (ANSYSTM) of valve cap and membrane structure: (a) full view of 2-D axisymmetric model, (b) close-up view of membrane, (c) close-up view of inner fillet radius, and (d) close-up view of outer fillet radius.

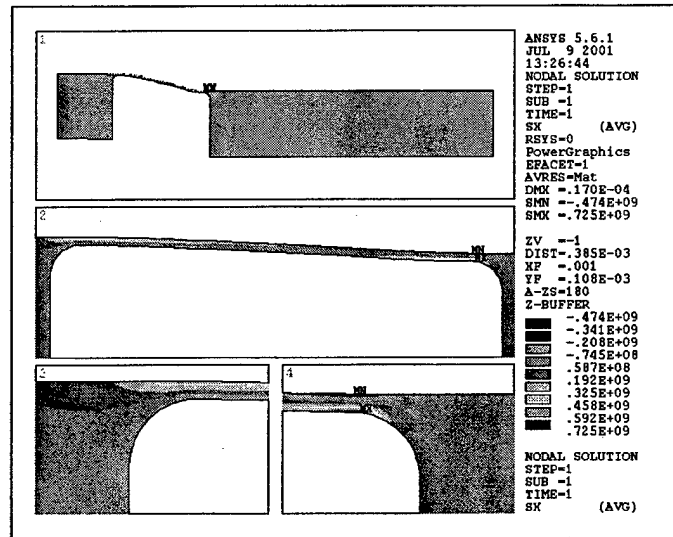


Figure 8.7: Finite-element stress contours resulting from applied differential pressure loading of 0.30 MPa. Fillet radii in model are $fR = 30\mu m$. Peak tensile stress (0.868 MPa) occurs at base of fillet radius along outer membrane circumference.

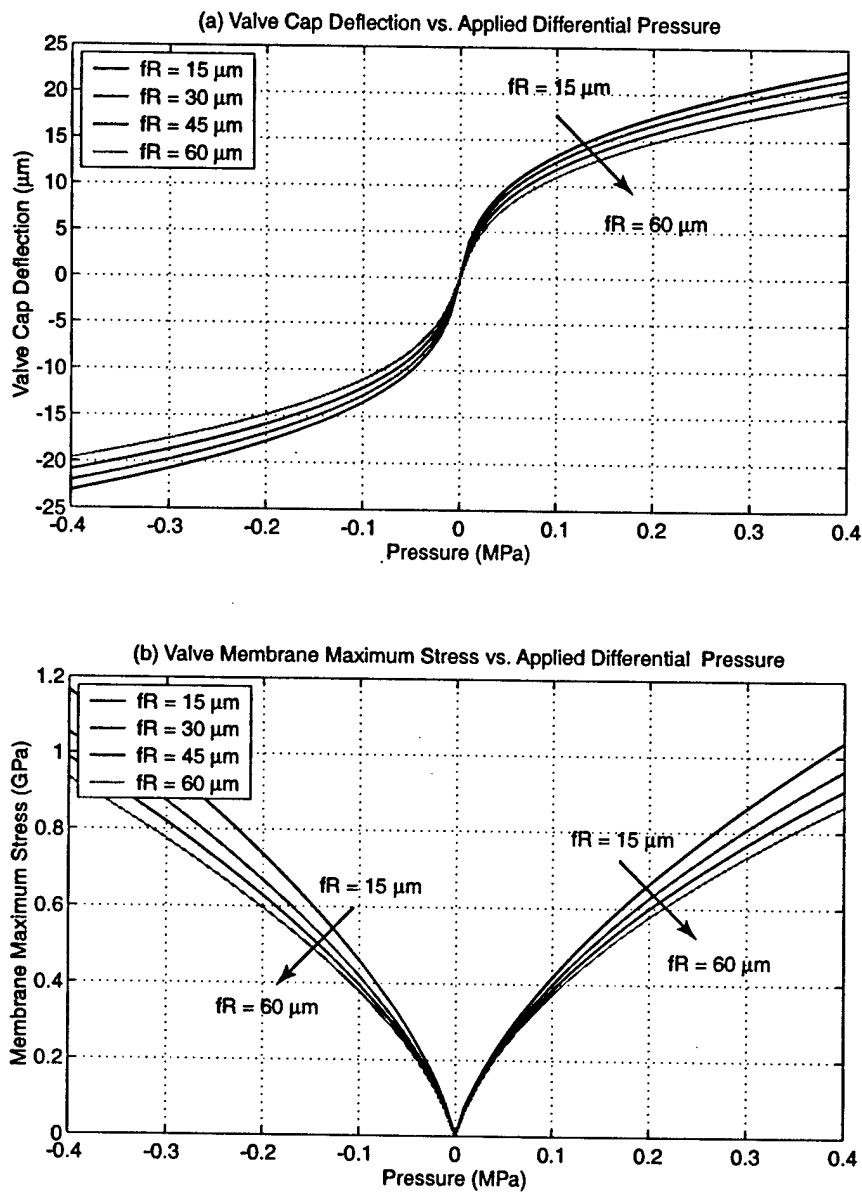


Figure 8.8: Sensitivity of baseline valve cap and membrane design to variations in fillet radius size $\rightarrow r_{vc} = 250\mu\text{m}$, $r_{vm} = 700\mu\text{m}$, $t_{vm} = 6\mu\text{m}$, $fR = [15\mu\text{m}, 30\mu\text{m}, 45\mu\text{m}, 60\mu\text{m}]$: (a) valve cap deflection vs. applied differential pressure, and (b) maximum stress in valve membrane vs. applied differential pressure. Note: valve stop at $-15\mu\text{m}$ not implemented in this finite-element model.

8.4 Experimental Results

Three representative valve cap and membrane sub-component structures (referred to as Valve Membrane 1, Valve Membrane 2, and Valve Membrane 3 in subsequent discussions) were experimentally tested to validate structural behavior. Prior to testing and before die-level bonding of Stack 4-5-6 to Stack N7-N8-N9, inspection of the valve membrane fillet radii in Layer N7 was performed. This section details these inspections, as well as the experimental pressure-deflection results for each of these membrane structures.

8.4.1 Fillet Radius Inspection

Each of the three representative valve membrane structures was inspected for the presence of defects along the etched membrane and for consistency in fillet radius size. Valve Membrane 1 possessed a consistent fillet radius size of 45-50 μm and no defects along the membrane. Valve Membrane 2 possessed a consistent fillet radius size of 40-50 μm and no defects along the membrane. And similarly, Valve Membrane 3 possessed a fillet radius size of 35-40 μm and no defects along the membrane. Overall, these three valve membrane structures well represent the majority of etched valve membrane structures in their fillet radius consistency and lack of defects.

8.4.2 Pressure-Deflection Results

In order to determine the pressure-deflection behavior of these valve membrane structures, a pressure time history was imposed on the structure using a valve and pressure sensor set-up and the valve cap deflection was measured using a laser vibrometer system. Figure ?? overlays the pressure-deflection results for Valve Membranes 1, 2, and 3 with the structural predictions for $t_{vm} = 6\mu m$ and $t_{vm} = 7\mu m$ presented previously. Overall, all three membrane structures correlate well with each other and with predictions. Note that the valve membrane stops vary between -15 and -16 μm due to non-uniform etch depths during fabrication.

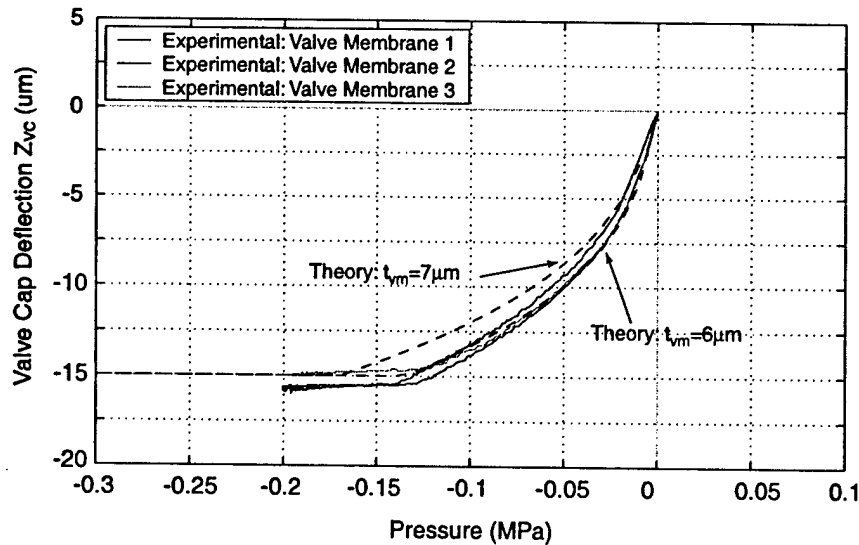


Figure 8.9: Valve cap and membrane experimental pressure-deflection results compared to theoretical expectations. The three representative valve cap and membrane structures correlate well with each other and with predicted behavior. Note that valve stops vary between -15 and -16 μm due to non-uniformity in etching these features.

8.5 Conclusions

This chapter has presented successful correlation between valve membrane structural behavior and modeling predictions. Representative valve membranes that possessed consistent fillet radius profiles around the membrane and the absence of any significant etch defects were experimentally characterized. Pressure-deflection results correlate extremely well with predicted behavior obtained using finite-element models and the non-linear deformation code presented in Chapter 3. Overall, this chapter has verified that these valve membrane structures can be consistently fabricated for use in full active valve devices, and that these structures exhibit expected pressure-deflection behavior.

Bibliography

- [1] Corning web information on the thermal expansion behavior of Pyrex 7740 and its use with Silicon for anodic bonding. (<http://www.corning.com/lightingmaterials/waferglass.html>)

Chapter 9

Active Valve Testing

9.1 Objectives

The purpose of this testing study was to evaluate the quasi-static and dynamic structural performance of the complete active valve device and to determine its limitations in regulating the flow of fluid against imposed differential pressures. Specifically, the four primary objectives of this study are:

1. To understand the dynamic behavior of the active valve device and to determine the range of driving frequency for which the valve behaves in a quasi-static manner. In essence, this goal focuses on locating the resonant frequencies of the structure. The effect of having or not having fluid present in the flow channel above the valve cap and membrane on the onset of valve resonant behavior is determined.
2. To evaluate the amplification ratio of the active valve structure under a variety of voltage levels and internal and external bias pressures for a driving frequency below resonance to ensure quasi-static operation. This is accomplished by measuring the drive piston and valve cap deflections under conditions that force the valve cap through its full stroke of operation, including interaction with the valve stops above and below the valve cap.
3. To characterize the differential pressure-flow rate curves for the valve cap and orifice geometry of the active valve device. This is accomplished by measuring an average fluid flow rate through the valve orifice as a function of valve cap opening downward from the upper valve stop. Motion of the valve cap through its stroke is controlled at a very slow rate to achieve quasi-static measurements of flow rate at given valve openings.
4. To characterize the dynamic capability of the active valve structure in regulating fluid flow against a preset differential pressure across the valve at a driving frequency below resonance to ensure quasi-static operation. Successful operation of the valve structure in

this manner proves its capabilities as a flow regulation device. A further goal is to identify the limiting differential pressures against which the active valve can function.

9.2 Device Test-Plan

9.2.1 Geometry

A schematic of the fabricated active valve device is illustrated in Figure 9.1. The device incorporates three PZN-PT piezoelectric square elements (each with cross-sectional area $1.06\text{mm} \times 1.06\text{mm}$) beneath a double-layer tethered piston structure. The top and bottom tethers of the piston are each $250\mu\text{m}$ in width and each have a thickness of $8\mu\text{m}$. A valve cap and membrane structure is positioned above the hydraulic amplification chamber, with a structural stop (formed by the glass Layer 6 within the HAC chamber) $\sim 16.5\mu\text{m}$ below the equilibrium position of the valve cap. Glass Layer 6 contains a series of "HAC through-holes" and "HAC radial channels" to carry the fluid from the lower to upper portion of the HAC chamber. The valve cap has a diameter of $500\mu\text{m}$ and the valve membrane has an outer diameter of $1400\mu\text{m}$. A valve orifice is located $\sim 16.5\mu\text{m}$ above the valve cap equilibrium position. The orifice has an inner diameter of $450\mu\text{m}$. The drive element piston structure is consistent with the 2nd-generation drive element devices (except for the use of slightly reduced-area square piezoelectric elements) fabricated and tested as part of the drive element sub-component study detailed in Chapter 7. In addition, the valve cap and membrane structure is consistent with the valve structures fabricated and tested as part of the valve cap and membrane sub-component study detailed in Chapter 8.

9.2.2 Plan of Study

As detailed in the introduction to this chapter, the characterization of each active valve device was carried out through a series of four experimental testing studies. The first two studies focus on the dynamic and quasi-static behavior of the active valve structure, while the second two studies focus on the fluid flow regulation capability of the structure. In evaluating these objectives, numerous active valve devices were built. Two of these devices are covered in detail in this chapter (and thesis). The first active valve device (subsequently referred to as device AV1) successfully made it through the majority of all four testing studies. It failed during an experiment to determine its limitations in regulating high pressure flows. The second device (subsequently referred to as device AV2) broke during completion of the first two studies, and as a result, no flow regulation data was taken for this device. A discussion of this failure is described in the chapter. This chapter is organized into two primary sections, in accordance with these experimental testing studies. The first section details the results of the dynamic and

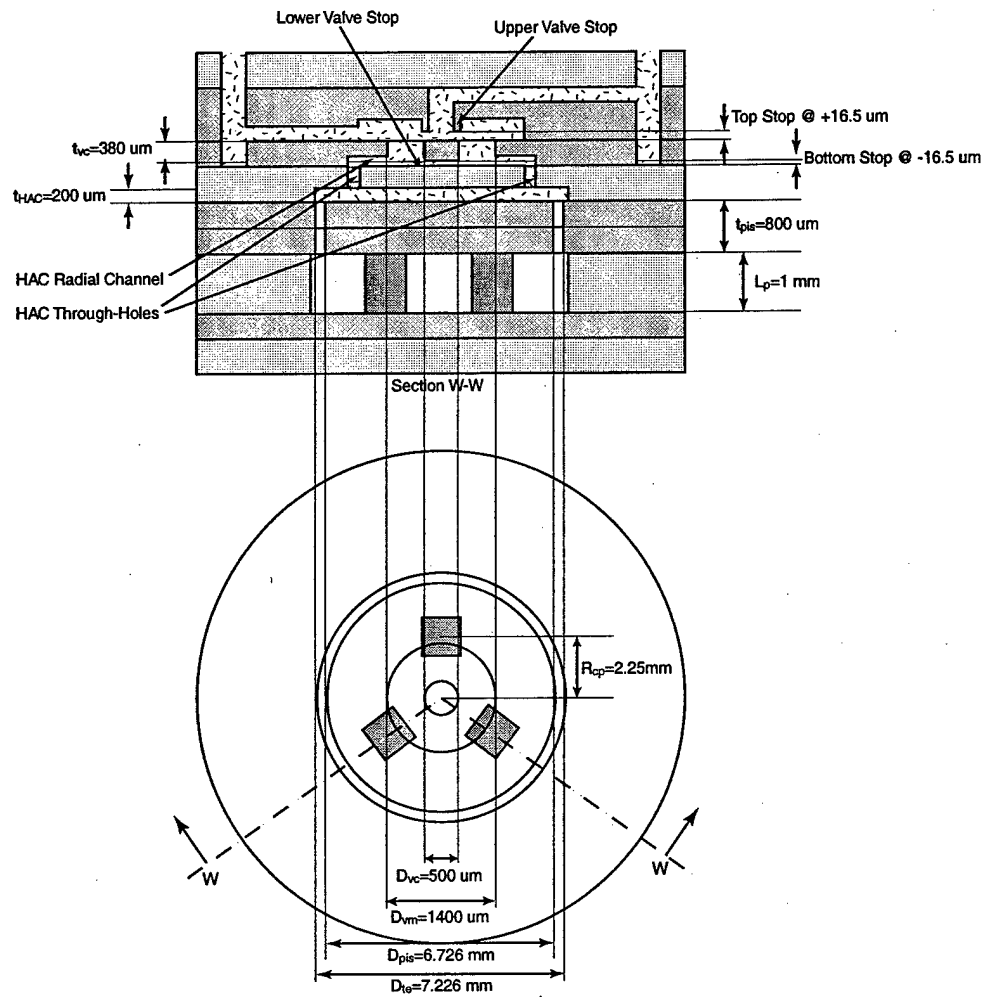


Figure 9.1: Dimensions of active valve devices AV1 and AV2. Three square PZN-PT elements are incorporated beneath a double-layer tethered piston. A valve cap and membrane structure interacts with the fluid orifice structure at $Z_{vc} = +16.5\mu m$ and with the glass Layer 6 structure within the HAC chamber at $Z_{vc} = -16.5\mu m$. In the lower figure, only geometries beneath the valve cap structure (ie: beneath Layer 7) are detailed.

quasi-static active valve testing studies (for both device AV1 and device AV2), and the second section covers the valve flow regulation studies (for device AV1).

9.3 Experimental Testing Section 1: Active Valve Structural Performance

9.3.1 Testing Section 1: Active Valve Structural Performance

To characterize the frequency dependant behavior of each active valve device, the following tests were performed. A low-voltage ($0V \pm 5V$) sweep signal from 500Hz to 100kHz was applied to the piezoelectric drive element structure. The corresponding valve cap and piston displacements were measured using a laser scanning vibrometer system. The effect of bias pressure (ie: $P_{bias} = P_{HAC} = P_1 = P_2$, where $P_{bias} \geq 0$), up to 500 kPa, on the frequency response of the active valve device was evaluated. Additionally, higher-voltage (up to 600V_{pp}) sweep signals were applied over a lower range of frequency from 500Hz to 3kHz to evaluate the valve cap and piston behavior in a range of quasi-static frequencies below resonance.

To characterize the quasi-static behavior of each active valve device, a series of tests was run at a chosen frequency of operation (ie: 1kHz for these tests) sufficiently below the resonant frequency to ensure quasi-static structural behavior. The effects of increasing voltage and increasing bias pressure on the device amplification ratio were determined. Additionally, the capability of the device to open and close the valve cap against the fluid orifice was evaluated.

Active Valve Device AV1

Figures 9.2 through 9.7 display the structural testing results for active valve device AV1. Figure 9.2 plots the valve cap frequency response from 500Hz to 100kHz for an applied low-voltage sweep signal of $0V \pm 5V$ under the condition that silicon oil is not present above the valve cap and membrane structure and under the condition that silicon oil is present above the valve cap and membrane structure. These tests were performed with $P_{bias} = 500kPa$ to ensure that cavitation of the fluid within the HAC did not occur. Without oil, the resonant frequency of the structure is 10kHz. With oil, this frequency drops to slightly less than 5kHz. This reduction is due to the added mass of the fluid on the top surface of the valve cap and membrane. It is interesting to notice the presence of numerous resonant peaks (at 6.5kHz and 8kHz), in addition to the primary resonant peak at 5kHz, for the response with oil. Without oil, no additional resonant behavior is observed beyond the primary 10kHz resonance until approximately 40kHz. The additional peaks in the response with oil present are most likely a result of fluid-structure interactions between the oil and the experimental test-jig flow tubes external to the device or between the oil and the flow channels internal to the device. Pressure waves could be interacting within these channels and affecting the valve behavior. Additionally, the primary resonant peak of the response (at 5kHz) with oil above the structure is not as sharp as that without oil, due to the increased damping introduced by the fluid within the system. Based on the experimental

resonant peak amplitude, in comparison to expected behavior determined from the active valve model described in Chapter 5, the damping ratio of this structure is estimated to be 0.16.

Figure 9.3 overlays the frequency response of the drive element piston with that of the valve cap, for the case in which oil is present above the valve structure at the same operating conditions as previously described. The piston response exhibits the same resonant peak behavior as the valve cap response. The increase in piston displacement amplitude at frequencies below 1kHz is due to measurement limitations in the vibrometer system (essentially the magnitude of the measured velocities and displacements are of the same order as the noise floor of the system). The results indicate that the amplification ratio of the valve device is steady (between 40x-50x) over the range of frequencies below resonance.

Figure 9.4 plots the low-voltage valve cap frequency response from 500Hz to 100kHz for a varying bias pressure from $P_{bias} = 100kPa$ to $P_{bias} = 500kPa$. For the PZN-PT material integrated within these valve devices, material testing results by Lin [1] indicate that the piezoelectric material strain capability degrades near a compressive stress of 10MPa. For the geometry of these active valve devices tested, a bias pressure of $P_{bias} = 500kPa$ correlates to a compressive stress on the piezoelectric square elements beneath the piston of approximately 6.1MPa. These bias pressure tests therefore evaluate whether degradation occurs up to 6.1MPa. Higher bias pressure tests were to be performed following the completion of all four major testing sections. Clearly from the results, a variation in P_{bias} from 100kPa to 500kPa has no noticeable effect on the frequency response of the structure. Again, the upper limit to P_{bias} was not evaluated until all other experimental tests on the active valve device were completed, for safety reasons, to minimize potential breakage of the device.

Each of the previous frequency sweeps was carried out with the valve cap and membrane structure at its equilibrium position (zero deflection upward or downward) by ensuring that the pressures above the valve cap and membrane structure (P_1 and P_2) were identical to the pressure within the hydraulic amplification chamber (P_{HAC}). Under these conditions, in order to close the valve cap against the valve orifice (+16.5 μm above this equilibrium position) during quasi-static sinusoidal operation, a large voltage on the piezoelectric drive element could be required. Another potential way of operating the active valve device to ensure that the valve cap can close against the valve orifice for lower operating voltages is to impose a differential pressure (referred to as $\Delta P_{vc,vm} = P_{HAC} - P_1$, where $P_1 = P_2$ for example) across the valve cap and membrane structure to create a positive offset deflection of the valve cap about which oscillation can then occur. This method reduces the overall stroke of the valve cap (due to the non-linearity of the valve membrane - see next paragraph), but ensures valve closure against the orifice. To evaluate this alternative operation concept on the resonant behavior of active valve device, additional low-voltage frequency sweeps were carried out with $\Delta P_{vc,vm} = 20kPa$ and $\Delta P_{vc,vm} = 50kPa$, which produce offset valve cap displacements of $Z_{vc} \sim +6\mu m$ and $Z_{vc} \sim +10\mu m$ respectively.

Figure 9.5 compares the results.

With increasing offset displacement of the valve cap above its equilibrium position, the effective stiffness of the valve membrane structure for low-voltage (and therefore low amplitude) oscillations should increase since the membrane moves into its large-deflection regime. As a result, one would expect the resonant peak to shift to a increased frequency (due to the higher stiffness) and the magnitude of this peak to be reduced (also due to the higher stiffness). As shown in Figure 9.5(a), both of these results are clearly observed. As $\Delta P_{vc,vm}$ is increased from 0kPa to 20kPa to 50kPa, the resonant peak increases from $\sim 5kHz$ to $\sim 6kHz$ to $\sim 6.5kHz$, respectively. Additionally, the valve cap oscillation amplitude decreases from $\sim 4\mu m$ to $\sim 1.6\mu m$ to $\sim 0.8\mu m$ for this increase in $\Delta P_{vc,vm}$. This amplitude reduction is most clearly seen in Figure 9.5(b), which plots the amplitude on a linear scale. High-voltage quasi-static active valve operation under these differential pressure conditions is discussed further in the later half of Testing Section 1.

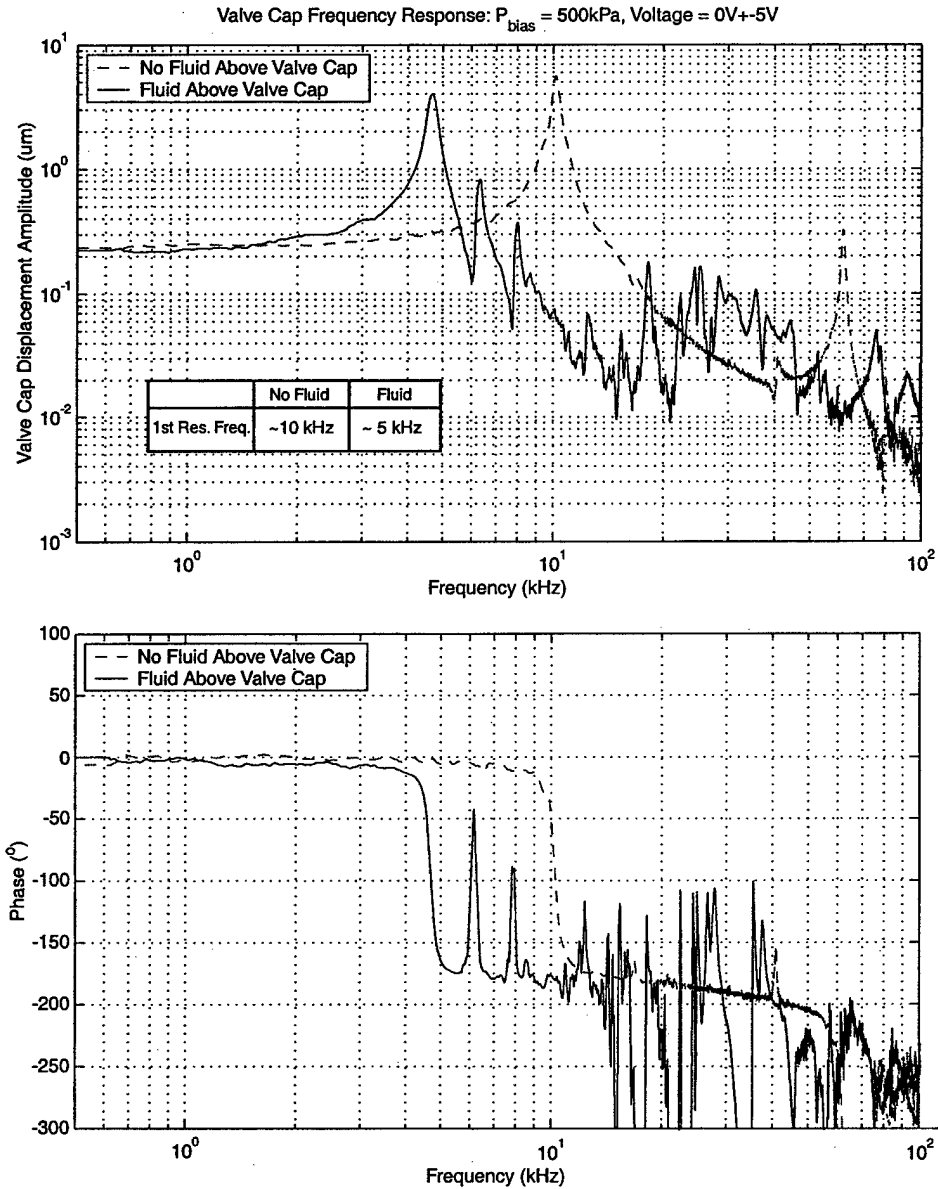


Figure 9.2: Device AV1 low-voltage ($0V \pm 5V$) valve cap frequency response from 500Hz to 100kHz, with and without oil present above the valve structure. The bias pressure in these tests was maintained at $P_{bias} = 500\text{kPa}$. The presence of oil in the flow channel above the valve cap creates an added mass that reduces the resonant frequency from 10kHz to 5kHz.

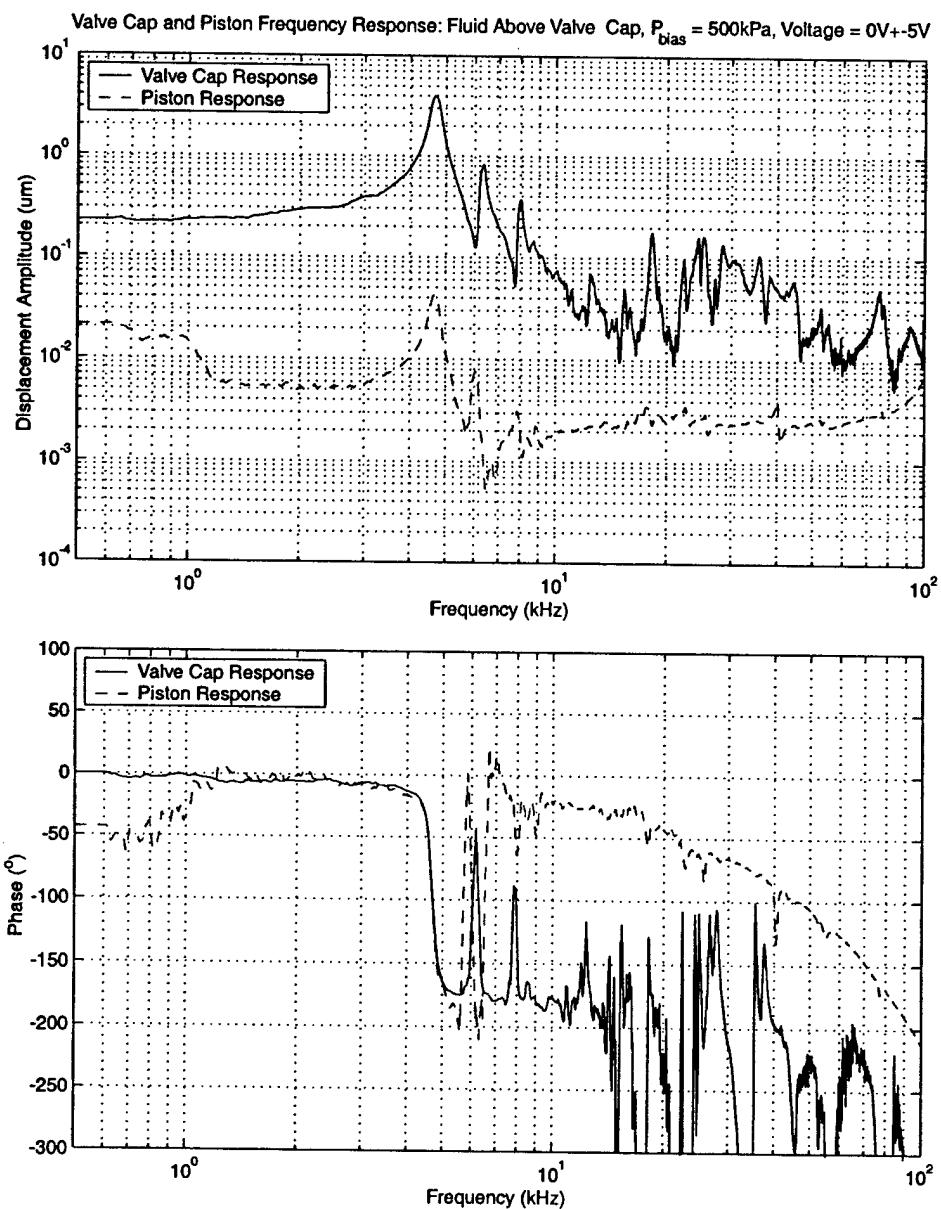


Figure 9.3: Device AV1 low-voltage ($0V \pm 5V$) piston and valve cap frequency responses from 500Hz to 100kHz, with oil present above the valve structure. The bias pressure in these tests was maintained at $P_{bias} = 500\text{kPa}$. An amplification ratio between 40x-50x is observed for frequencies below resonance.

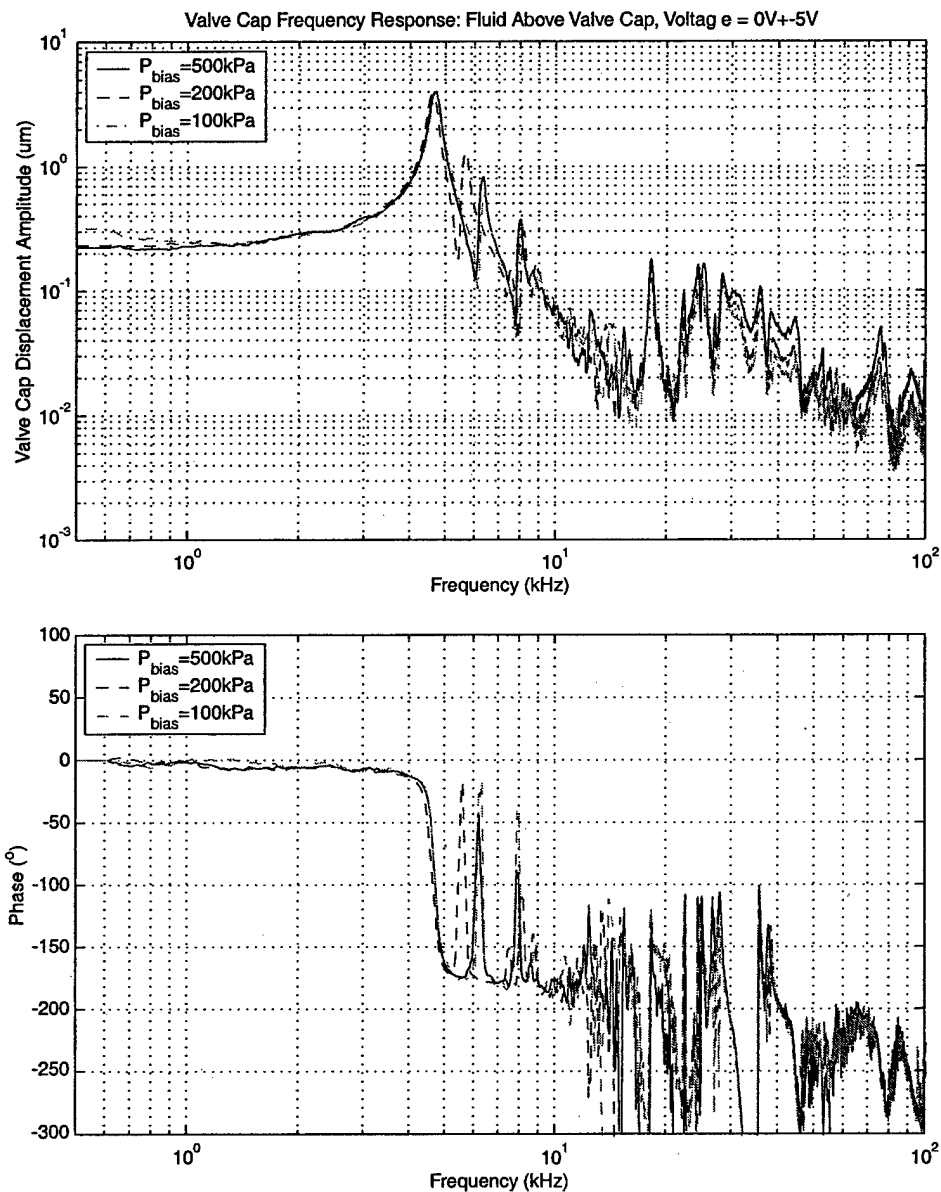


Figure 9.4: Device AV1 low-voltage valve cap frequency responses from 500Hz to 100kHz, for varying P_{bias} . Results indicate that frequency behavior is not affected by an increase in bias pressure from $P_{\text{bias}} = 100\text{kPa}$ to $P_{\text{bias}} = 500\text{kPa}$.

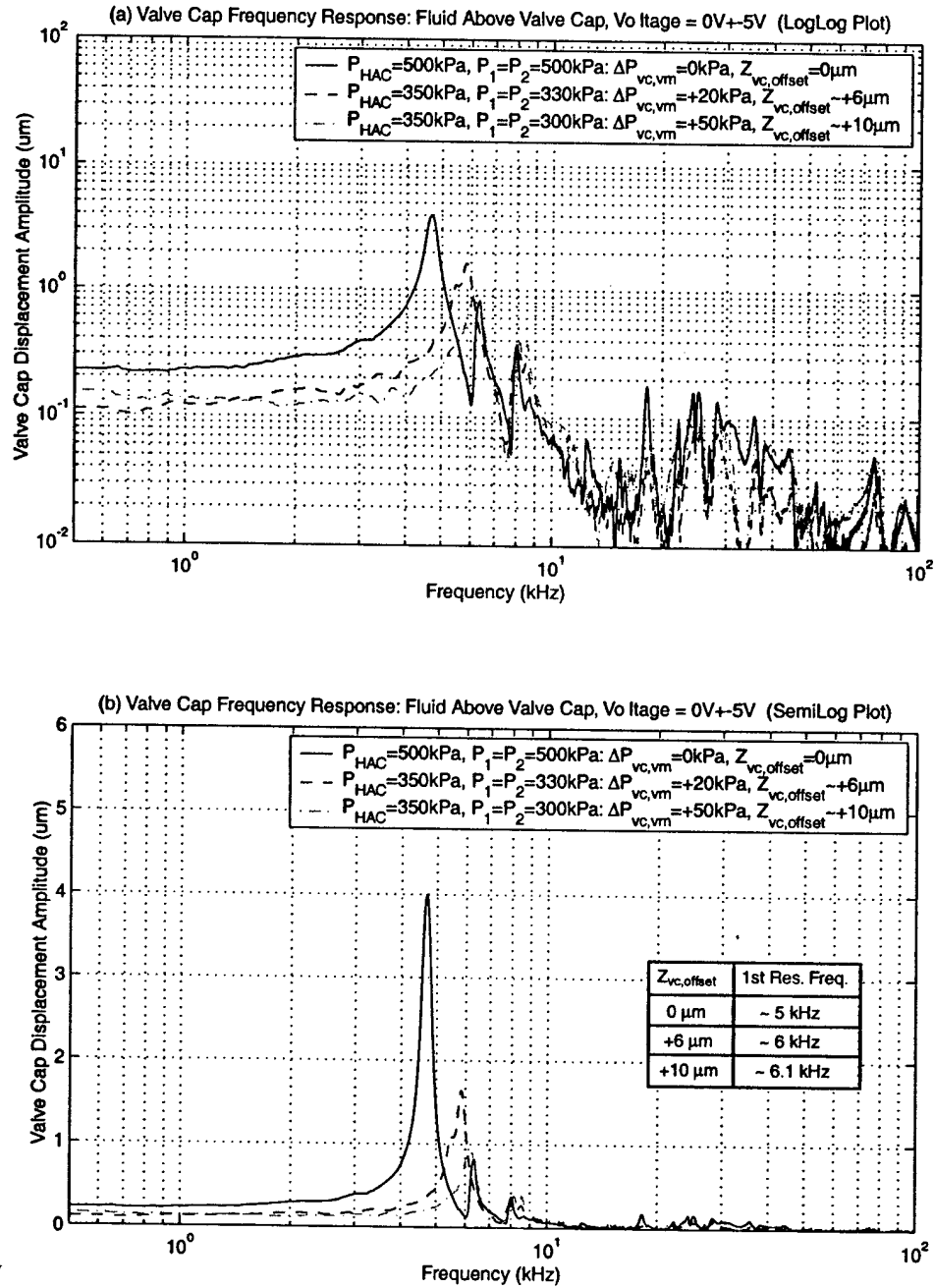


Figure 9.5: Device AV1 low-voltage valve cap frequency responses from 500Hz to 100kHz, for varying differential pressure applied to valve cap and membrane structure. For increasing differential pressure $\Delta P_{vc,vm}$ across valve cap and membrane, the resonant peak shifts upward and the valve cap vibration amplitude decrease. These phenomena are due to the membrane stiffening as it is forced higher into its large-deflection regime.

A series of tests was also run on active valve device AV1 to characterize the high-voltage frequency response of the structure for a range of frequencies below resonance. Since the resonant peak of this device is present at 5kHz, a range was chosen to include 500Hz to 3kHz. Figure 9.6 plots the valve cap frequency response from 500Hz to 3kHz for a series of increasing drive voltage levels from 50Vpp to 600Vpp, all with $P_{bias} = 500kPa$. At the lower voltage drive levels, the valve cap deflection amplitude is essentially constant over these frequencies. As the voltage is increased, regions of increased valve cap deflection appear near 1.7-1.9kHz. This frequency value is approximately $\frac{1}{3}$ of the low-voltage resonant frequency of the active valve device. This region, therefore, is a result of sub-harmonic excitation of the device. Figure 9.7 plots the valve cap versus piston deflection amplitude over this frequency range for an applied voltage of 600Vpp. In comparing these frequency responses, the amplification capabilities of the active valve device is evident. Figure 9.7(a) plots these curves on a logarithmic amplitude scale, and Figure 9.7(b) plots the curves on a linear amplitude scale. Over this range of frequencies, the amplification ratio is between 40x-50x.

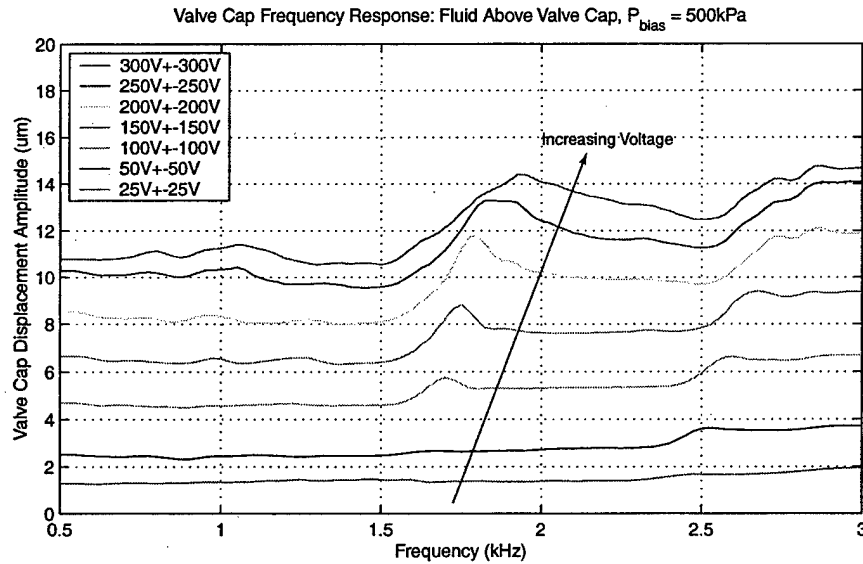


Figure 9.6: Device AV1 valve cap frequency responses from 500Hz to 3kHz, for $P_{bias} = 500kPa$ and increasing high voltage drive levels. Harmonic excitation behavior near $\sim 1.7 - 1.9kHz$ becomes evident as voltage levels are increased (ie: as valve membrane structure moves further into its non-linear large-deflection regime).

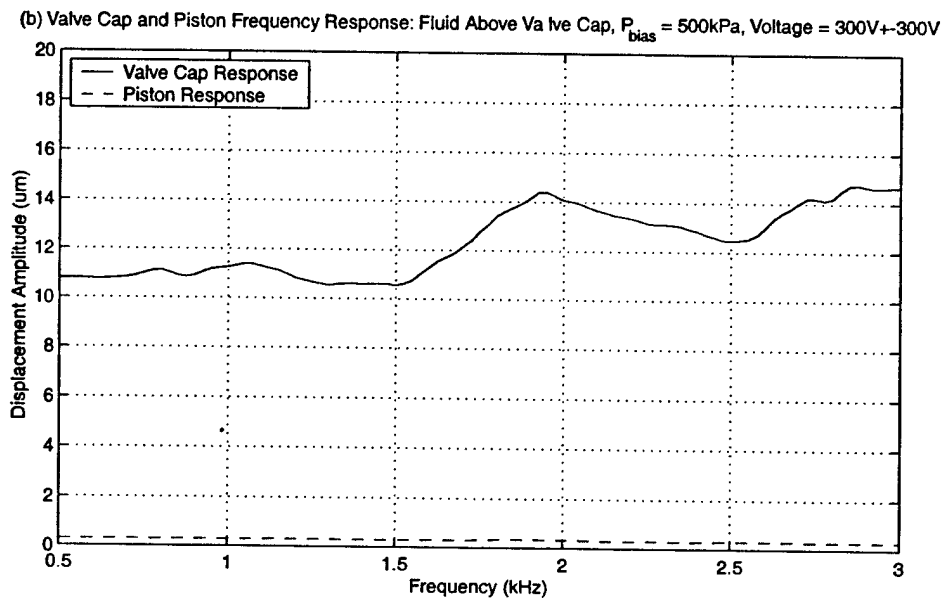
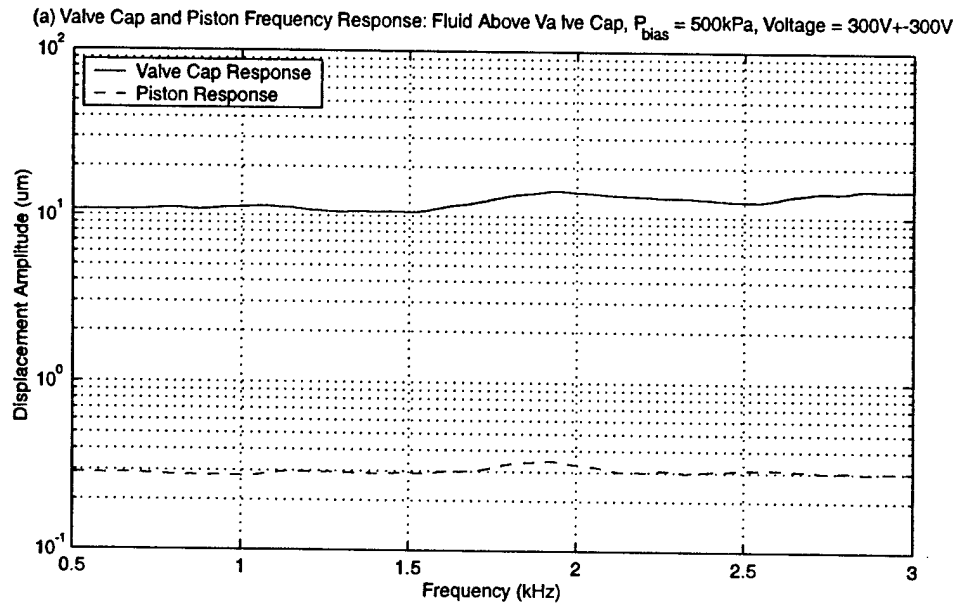


Figure 9.7: Device AV1 high-voltage piston and valve cap frequency responses from 500Hz to 3kHz, for $P_{bias} = 500\text{kPa}$. Amplification of active valve device is consistent between 40x-50x over this range of frequency.

The previous frequency sweep experimental tests found the resonant frequency of device AV1 to be $\sim 5kHz$. In order to evaluate the quasi-static performance of the structure under the larger drive voltage levels at which the valve was designed to operate, a frequency of operation of $1kHz$ was chosen. All subsequent structural testing was performed at this frequency. Figure 9.8 plots the valve cap and piston displacement time histories, respectively, over a range of applied voltages from $50V_{pp}$ to $600V_{pp}$. In Figure 9.8(a), the dotted lines at $+16.5\mu m$ and $-16.5\mu m$ indicate the position of the upper and lower valve stops, respectively. For an applied voltage of $50V_{pp}$, the response of the valve cap is purely sinusoidal. As the voltage is increased to $600V_{pp}$, the resulting valve cap displacement time history contains small amplitude higher frequency ($\sim 5kHz$) oscillations due to the non-linear nature of the valve membrane structure. These oscillations become more pronounced as the voltage is increased. In Figure 9.8(b), the drive element deflection time histories are somewhat rough in nature due to the noise level of the measurement system. As the deflections increase in amplitude, the effect of this noise floor diminishes.

Figure 9.9 takes these deflection time histories (at $P_{bias} = 500kPa$), and plots the valve cap peak-peak displacement, piston peak-peak displacement, and corresponding device amplification ratio as a function of applied voltage to the piezoelectric drive element. The amplification ratio is observed to decrease from 49 to 41 with increasing voltage. This decrease is a result of increased pressurization within the HAC chamber due to the increase in the valve membrane stiffness, and therefore increased deformation of the structure and fluid within the chamber, for increased voltage. In essence, as the voltage is increased, a smaller percentage of the drive element swept volume is transferred to the valve membrane since more volume is lost in chamber compliances. Overall, as will be detailed in the model correlation part of Testing Section 1, this range of amplification ratio correlates extremely well with the expected range based on the models developed in the first half of this thesis. These tests were also performed under decreased bias pressures, and these results are additionally presented in Figure 9.9. For decreased P_{bias} , the valve cap and piston deflections slightly increase, most likely due to better performance of the piezoelectric material under lower loading. As expected, however, the amplification ratio is not affected by the reduced bias pressure.

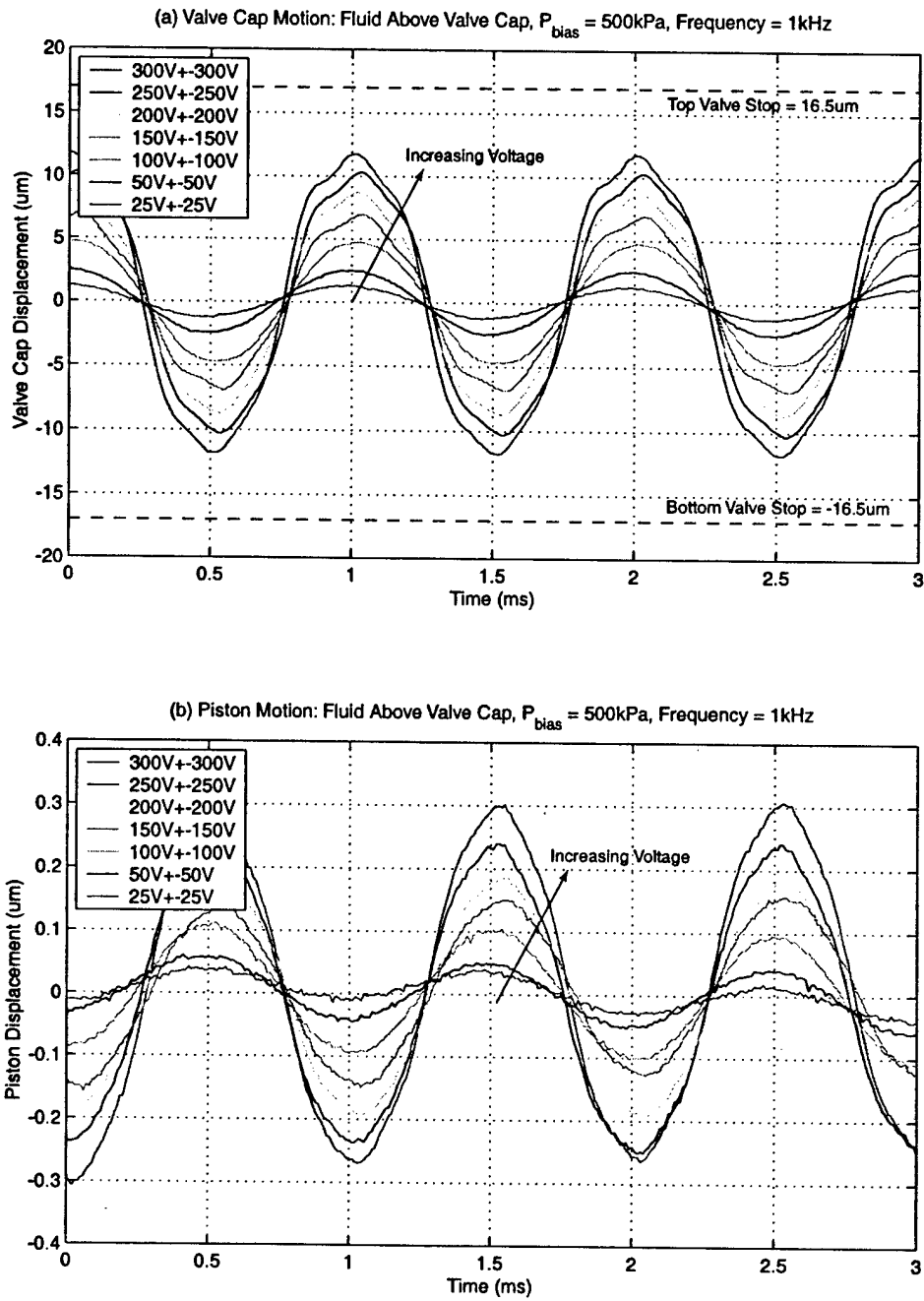


Figure 9.8: Device AV1 valve cap and piston deflection time histories for 1kHz sinusoidal drive voltage levels. As voltage is increased, small amplitude 5kHz oscillations appear in deflection responses. A voltage of 600Vpp is not sufficient to close valve cap against the valve orifice.

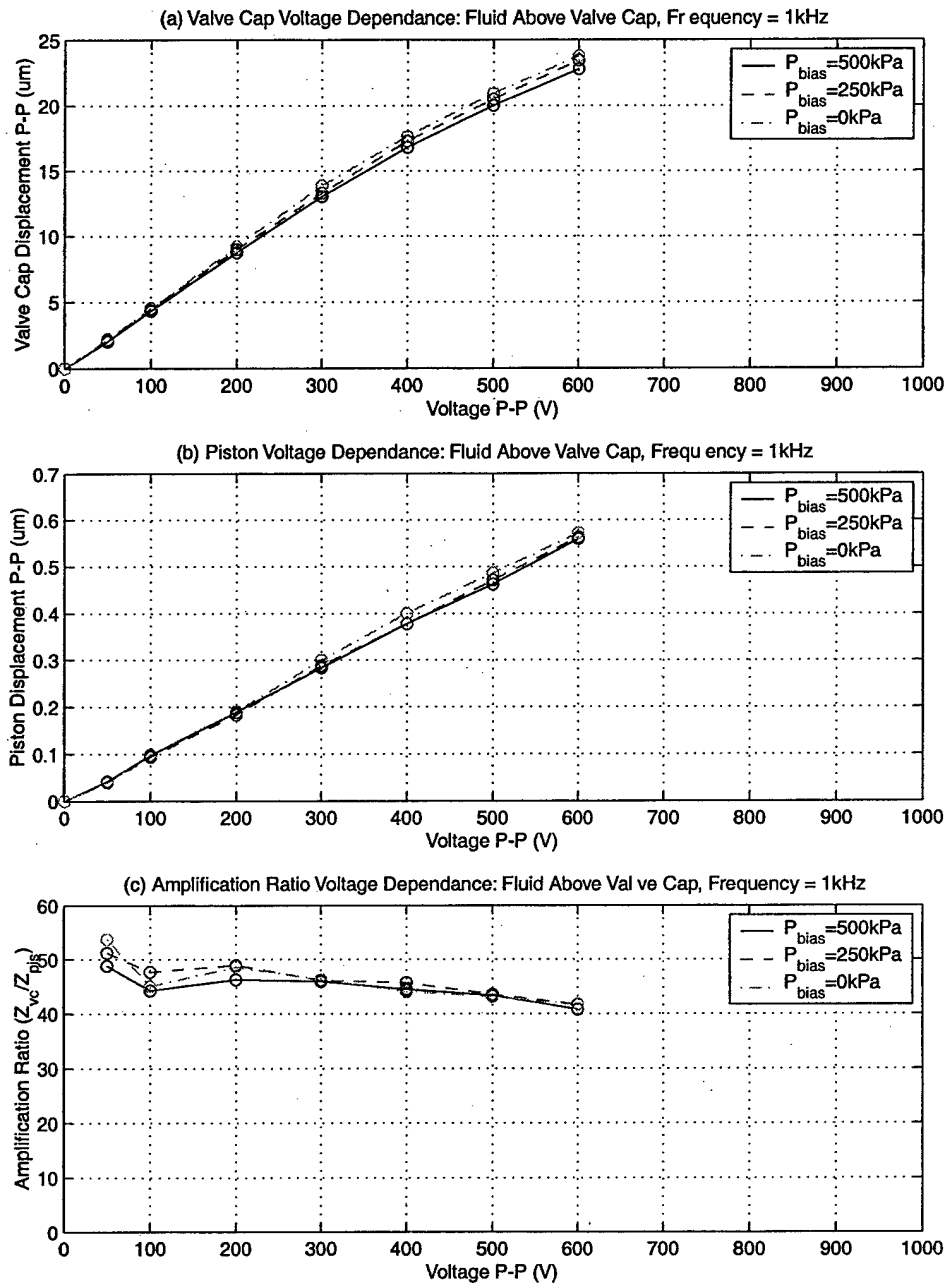


Figure 9.9: Device AV1 valve cap peak-peak motion, piston peak-peak motion, and device amplification ratio as a function of 1kHz sinusoidal drive voltage levels. Due to non-linear stiffness of the valve membrane structure, the amplification ratio decreases from $\sim 50x$ to $\sim 40x$ as the drive voltage is increased to 600Vpp.

In the previous tests at 1kHz, applied voltages were limited to 600Vpp to minimize the potential for device failure (due to stresses in drive element tethers - see the AV2 testing part of Testing Section 1 for an explanation). As a result, the valve cap never was able to close against the valve orifice. In order to observe valve closing and verify that the valve membrane is able to withstand these deflection magnitudes during dynamic operation, a series of tests was performed whereby a differential pressure of $P_{vc,vm} = 50kPa$ was applied across the valve cap and membrane to deflect it to an offset position of $\sim +10\mu m$. Voltages from 50Vpp to 600Vpp were then applied to evaluate closing behavior. Figure 9.10 plots the resulting valve cap deflection time histories. Notice that applied voltages of 500Vpp and 600Vpp successfully force the valve cap closed. Since the valve membrane is offset into its large deflection regime, the higher voltage deflection time histories become non-symmetric about this offset deflection. Additionally, the rounded nature of these curves as the cap hits the upper valve stop (valve orifice) indicates that squeeze-film damping may be playing a positive role in damping out potential vibrations due to high velocity impact of the valve cap on the valve stop.

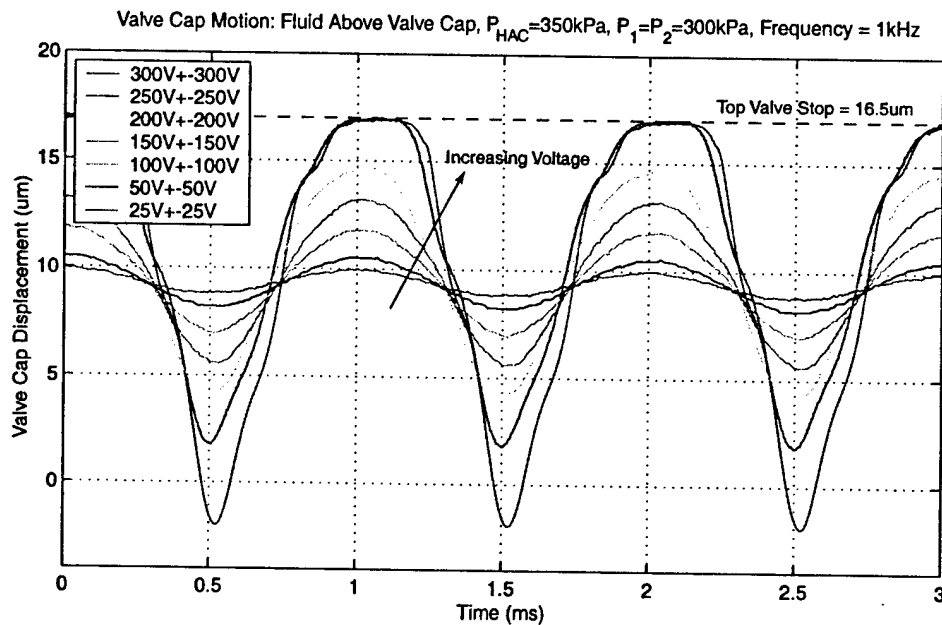


Figure 9.10: Device AV1 valve cap peak-peak motion, piston peak-peak motion, and device amplification ratio as a function of 1kHz sinusoidal drive voltage levels, with $P_{vc,vm} = 50kPa$. As the valve cap impacts the orifice stop, squeeze film damping may be aiding to damp undesired structural vibrations.

Overall, these series of low-voltage frequency sweep tests and higher-voltage quasi-static 1kHz tests have proven that active valve device AV1 successfully operates as a piezoelectrically-

driven hydraulic amplification microactuator structure. The series of tests detailed in Testing Section 2 will evaluate its capability to regulate fluid flow at high-frequency.

Evaluation of Device AV1 High-Frequency Channel The experimental data for device AV1 described in the previous sections was taken using the micromachined high-frequency channel (detailed in Chapter 6) as a means to control the static pressure P_{HAC} within the hydraulic amplification chamber, yet also to allow dynamic pressure fluctuations within the chamber created by piezoelectric actuation of the drive element. This channel, located between the HAC chamber and the external pressure port in the device, was designed to have a length of 1mm, a width of $10\mu m$, and a height of $10\mu m$. Although the previous set of data clearly indicates that this high-frequency channel must be satisfying its objective, the specific limitations of the channel are not clear. In an effort to evaluate the lower-limit frequency at which fluid begins to leak out of this channel during the positive stroke of the drive element actuation cycle, a series of tests for varying applied voltage to the piezoelectric elements were carried out.

In each test, the valve cap displacement amplitude was measured for an applied piezoelectric sinusoidal voltage (100Vpp, 200Vpp, and 400Vpp) over a frequency range from 1kHz to 0.1Hz. Figure 9.11 plots the valve cap displacement amplitude as function of frequency for these different applied voltage levels. Overall, the results indicate that this high-frequency channel behaves as a low pass filter with $\sim 1\%$ reduction in performance at a frequency of $\sim 1 - 2Hz$. These experimental results correlate quite well to the conservative channel design procedure (detailed in Chapter 6) in which a 1% reduction in performance was estimated to occur at a frequency of 48Hz. As a result, during actuation of the active valve at the desired frequencies in excess of 500Hz, the channel allows negligible fluid volume to move into and out of the hydraulic amplification chamber.

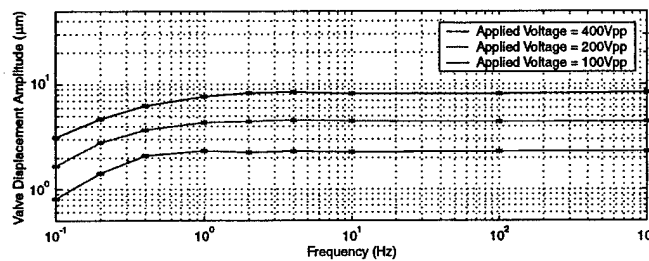


Figure 9.11: Experimental verification of the high-frequency channel in device AV1. The channel, with a length of 1mm, a width of $10\mu m$, and a height of $10\mu m$, successfully restricts fluid flow from the chamber during cyclic actuation down to a cutoff frequency near 1Hz.

Active Valve Device AV2

This section documents the frequency response characteristics and quasi-static operational capabilities of active valve device AV2. The tests performed were identical to those carried out for device AV1. As such, only selected plots are included in this section. The overall objective of this section is to demonstrate that both devices behave in the same manner. As a result, a conclusion can be made that repeatability in fabricating and assembling these devices is excellent.

Figure 9.12 plots the valve cap frequency response from 500Hz to 100kHz for an applied low-voltage sweep signal of $0V \pm 5V$ under the condition that silicon oil is not present above the valve cap and membrane structure and under the condition that silicon oil is present above the valve cap and membrane structure. As for device AV1, these tests were performed with $P_{bias} = 500kPa$ to ensure that cavitation of the fluid within the HAC did not occur. Without oil, the resonant frequency of the structure is evident at 10.5kHz. With oil, this frequency drops to slightly less than 5kHz. These results are essentially the same as those found for device AV1.

Figure 9.13 plots the valve cap frequency responses under these voltage sweep signal inputs for a varying bias pressure. Clearly from the results, a variation in P_{bias} from 100kPa to 500kPa has no noticeable effect on the frequency response of the structure.

Figure 9.14 plots a series of valve cap frequency responses from 500Hz to 3kHz for increasing drive voltage levels from 50Vpp to 500Vpp, all with $P_{bias} = 500kPa$. As was observed for device AV1, as the voltage is increased, regions of increased valve cap deflection appear near 1.7-1.9kHz. This frequency value is approximately $\frac{1}{3}$ of the low-voltage resonant frequency of the active valve device. This region, therefore, is a result of sub-harmonic oscillations of the device. Figure 9.15 plots the valve cap versus piston deflection amplitude over this frequency range for an applied voltage of 500Vpp. In comparing these frequency responses, the amplification capability of the active valve device is evident. Figure 9.15(a) plots these curves on a logarithmic amplitude scale, and Figure 9.15(b) plots them on a linear amplitude scale. Over this range of frequencies, the amplification ratio is in the range of 40x-50x, an identical result as for the amplification ratio found for device AV1.

In order to evaluate the quasi-static performance of device AV2, a frequency of operation of 1kHz was chosen. Figure 9.16(a) and (b) plot the valve cap and piston displacement time histories, respectively, over a range of applied voltages from 50Vpp to 900Vpp. In Figure 9.16(a), the dotted lines at $+16.5\mu m$ and $-16.5\mu m$ indicate the position of the upper and lower valve stops, respectively. For an applied voltage of 50Vpp, the response of the valve cap is purely sinusoidal. As the voltage is increased to 900Vpp, the resulting valve cap displacement time history contains significant higher frequency ($\sim 5kHz$) oscillations due to the non-linear nature of the valve membrane structure. These oscillations become more pronounced as the voltage is increased. In the chronology of the testing procedure for devices AV1 and AV2,

device AV2 was tested before device AV1 was tested. During testing of device AV2, voltage was increased to 1000Vpp. At this voltage level, the drive element piston tethers broke and silicon oil leaked out of the HAC chamber. Data was therefore only able to be taken on the valve cap behavior up to 900Vpp and on the piston behavior up to 800Vpp. This is the reason that device AV1 was tested only up to 600Vpp (see previous section).

Figure 9.17 takes these deflection time histories (at $P_{bias} = 500kPa$), and plots the valve cap peak-peak displacement, piston peak-peak displacement, and corresponding device amplification ratio as a function of applied voltage to the piezoelectric drive element. The amplification ratio is observed to vary from 40x to 50x, mainly decreasing with increasing voltage. As for device AV1, this decrease is a result of increased pressurization within the HAC chamber, and therefore increased deformation of the structure and fluid within the chamber, for increased voltage. In essence, as the voltage is increased, a smaller percentage of the drive element swept volume is transferred to the valve membrane since more volume is lost in chamber compliances. Overall, however, this range of amplification ratio correlates well with the expected range based on the models developed in the first half of this thesis (see Model Correlation part of Testing Section 1).

Piston failure in device AV2 is attributed to the fact that, although the drive element tethers were designed to have a thickness of $8\mu m$, their measured thickness was closer to $6\mu m$. As a result, under the calculated pressure loading of $\sim 700kPa$ (corresponding to drive voltage of 1000V and $P_{bias} = 500kPa$), the drive element tethers were expected to experience a stress approaching 1GPa, a value which is taken as a limit for the structural integrity of the silicon membrane structures [2]. Future drive element piston structures incorporate tethers which have a thickness of $8\mu m$. Although the complete series of tests that were performed on device AV1 were not able to be carried out on device AV2, the test results documented in this section indicate that this valve device also successfully operated as a piezoelectrically-driven hydraulic amplification microactuator structure.

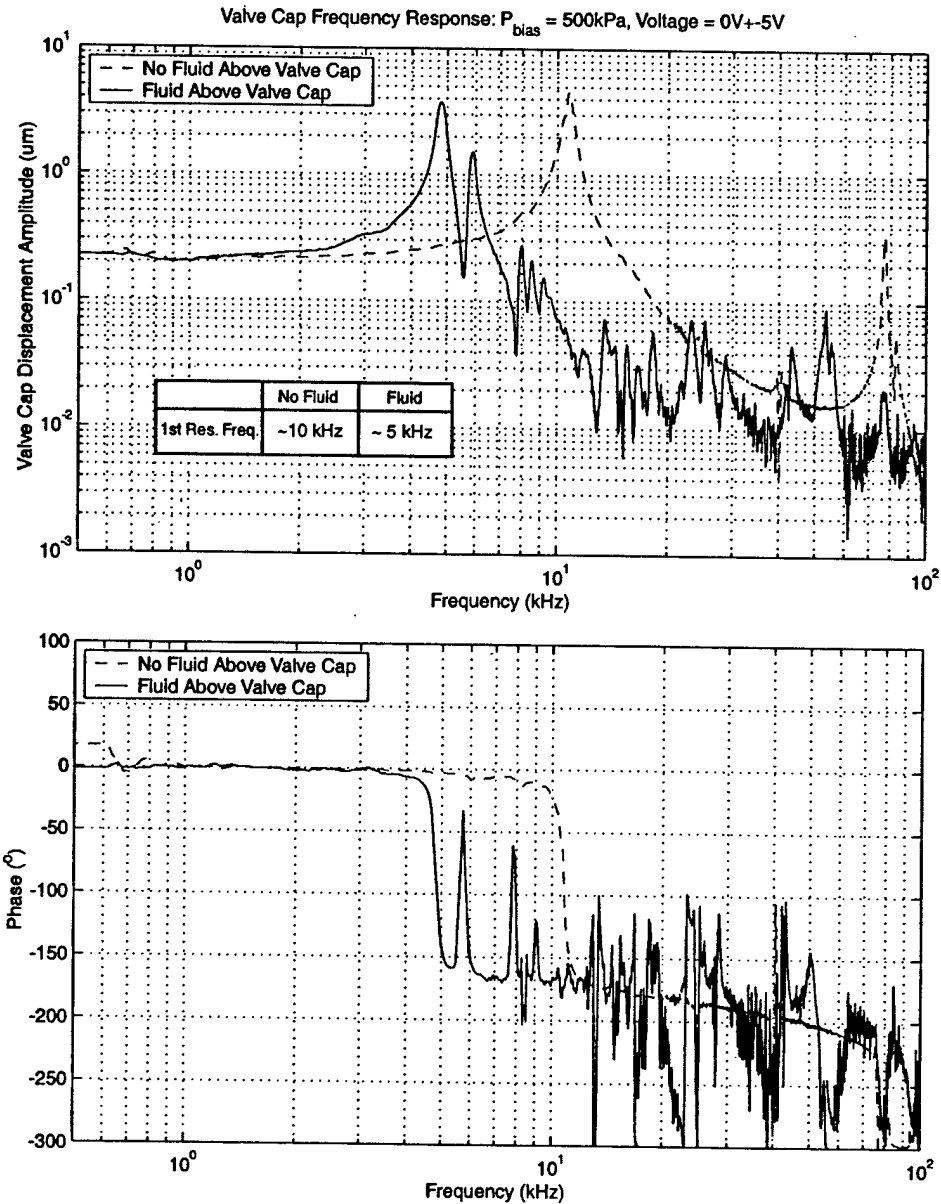


Figure 9.12: Device AV2 low-voltage ($0V \pm 5V$) valve cap frequency response from 500Hz to 100kHz, with and without oil present above the valve structure. The bias pressure in these tests was maintained at $P_{bias} = 500\text{kPa}$. The presence of oil in the flow channel above the valve cap creates an added mass that reduces the resonant frequency from 10.5kHz to 5kHz.

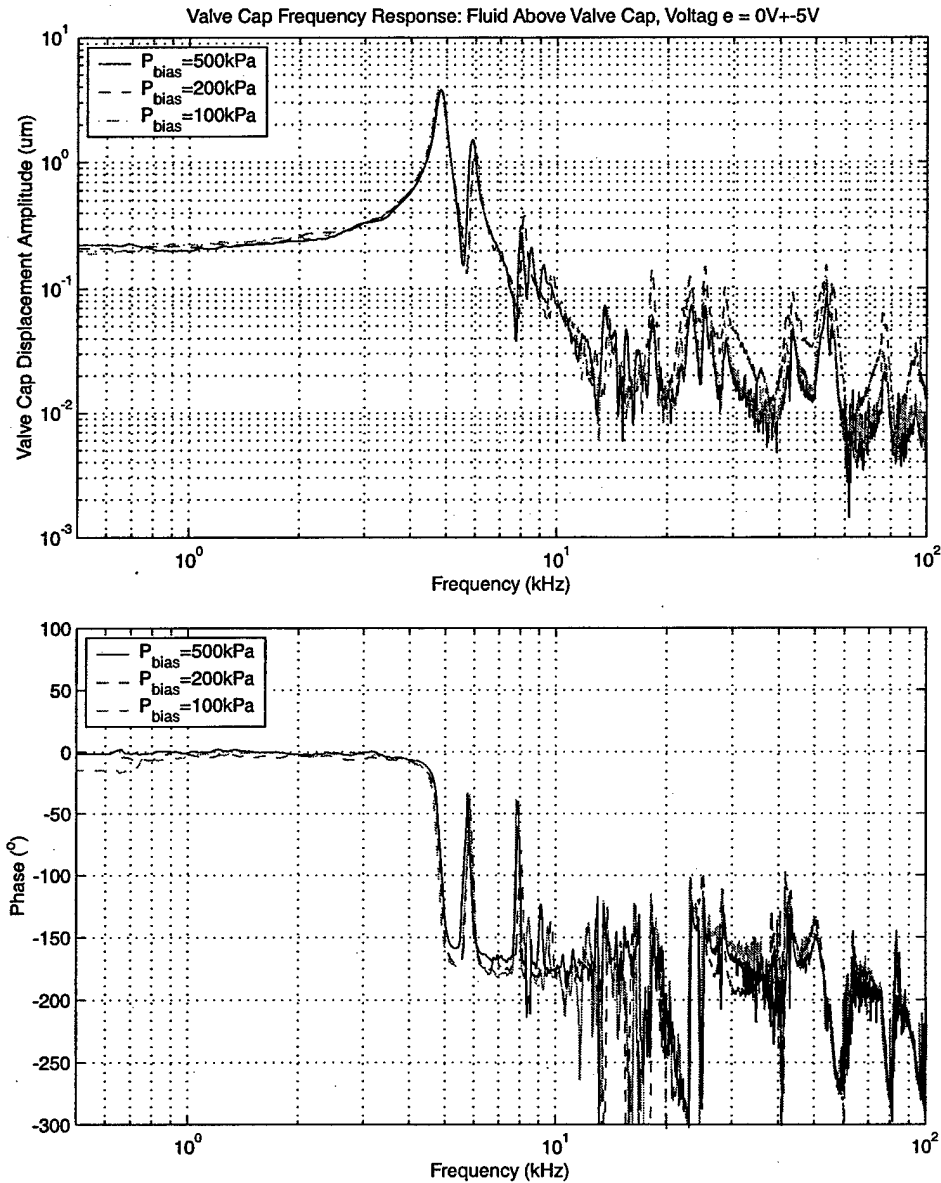


Figure 9.13: Device AV2 low-voltage valve cap frequency responses from 500Hz to 100kHz, for varying P_{bias} . Results indicate that frequency behavior is not affected by an increase in bias pressure from $P_{bias} = 100\text{kPa}$ to $P_{bias} = 500\text{kPa}$.

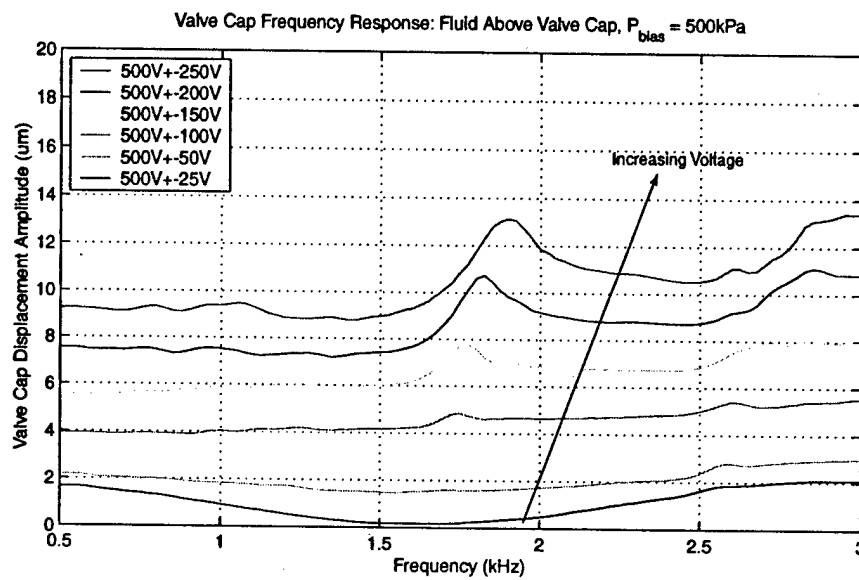


Figure 9.14: Device AV2 valve cap frequency responses from 500Hz to 3kHz, for $P_{bias} = 500kPa$ and increasing high voltage drive levels. Harmonic excitation behavior near $\sim 1.7 - 1.9kHz$ becomes evident as voltage levels are increased (ie: as valve membrane structure moves further into its non-linear large-deflection regime). It is unknown why the valve cap displacement dips downward between 500Hz and 2.5kHz for the voltage drive levels of 50Vpp and 100Vpp.

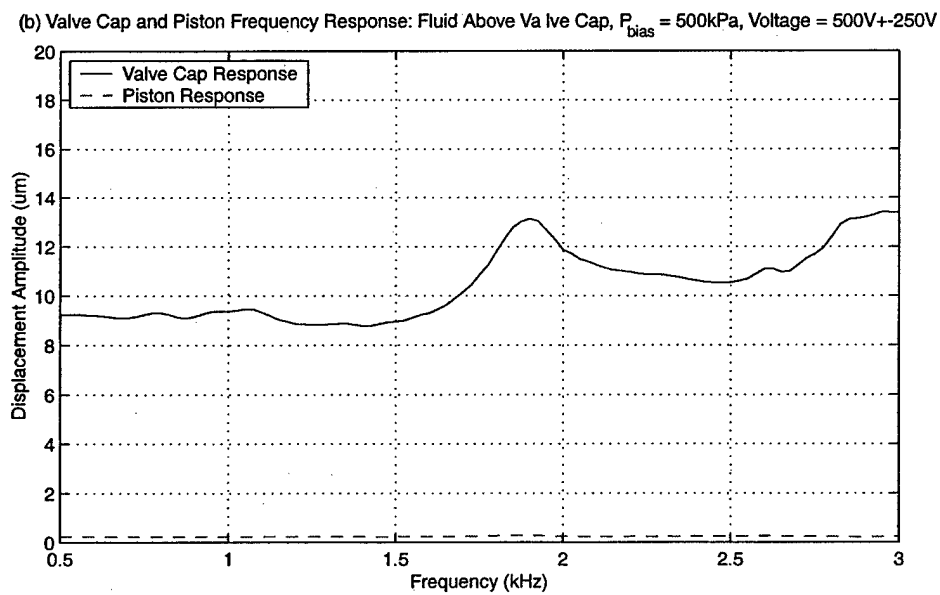
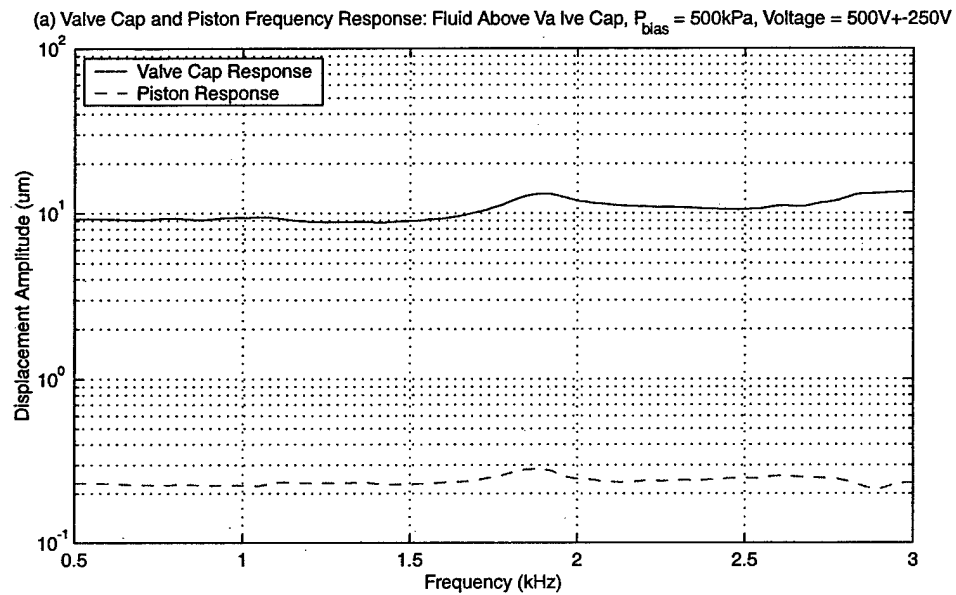


Figure 9.15: Device AV2 high-voltage piston and valve cap frequency responses from 500Hz to 3kHz, for $P_{bias} = 500\text{kPa}$. Amplification of active valve device is consistent between 40x-50x over this range of frequency.

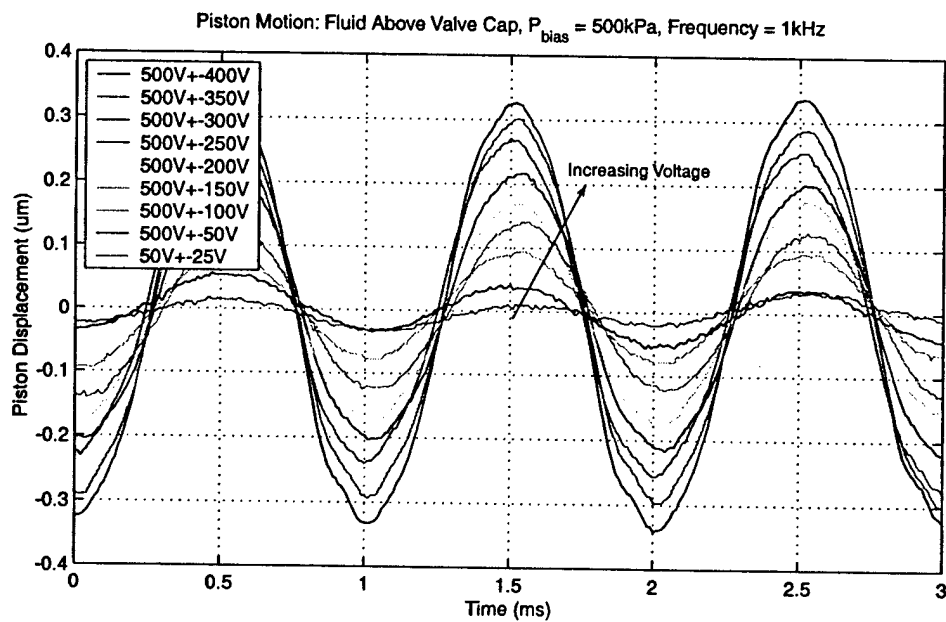
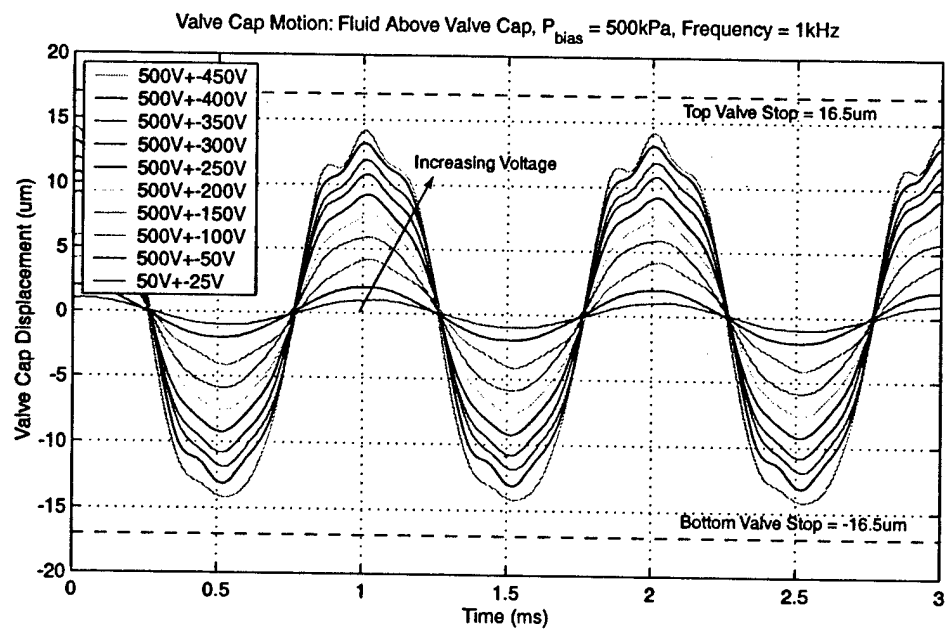


Figure 9.16: Device AV2 valve cap and piston deflection time histories for 1kHz sinusoidal drive voltage levels. As voltage is increased, small amplitude 5kHz oscillations appear in deflection responses. A voltage of 900Vpp is not sufficient to close the valve cap against the valve orifice.

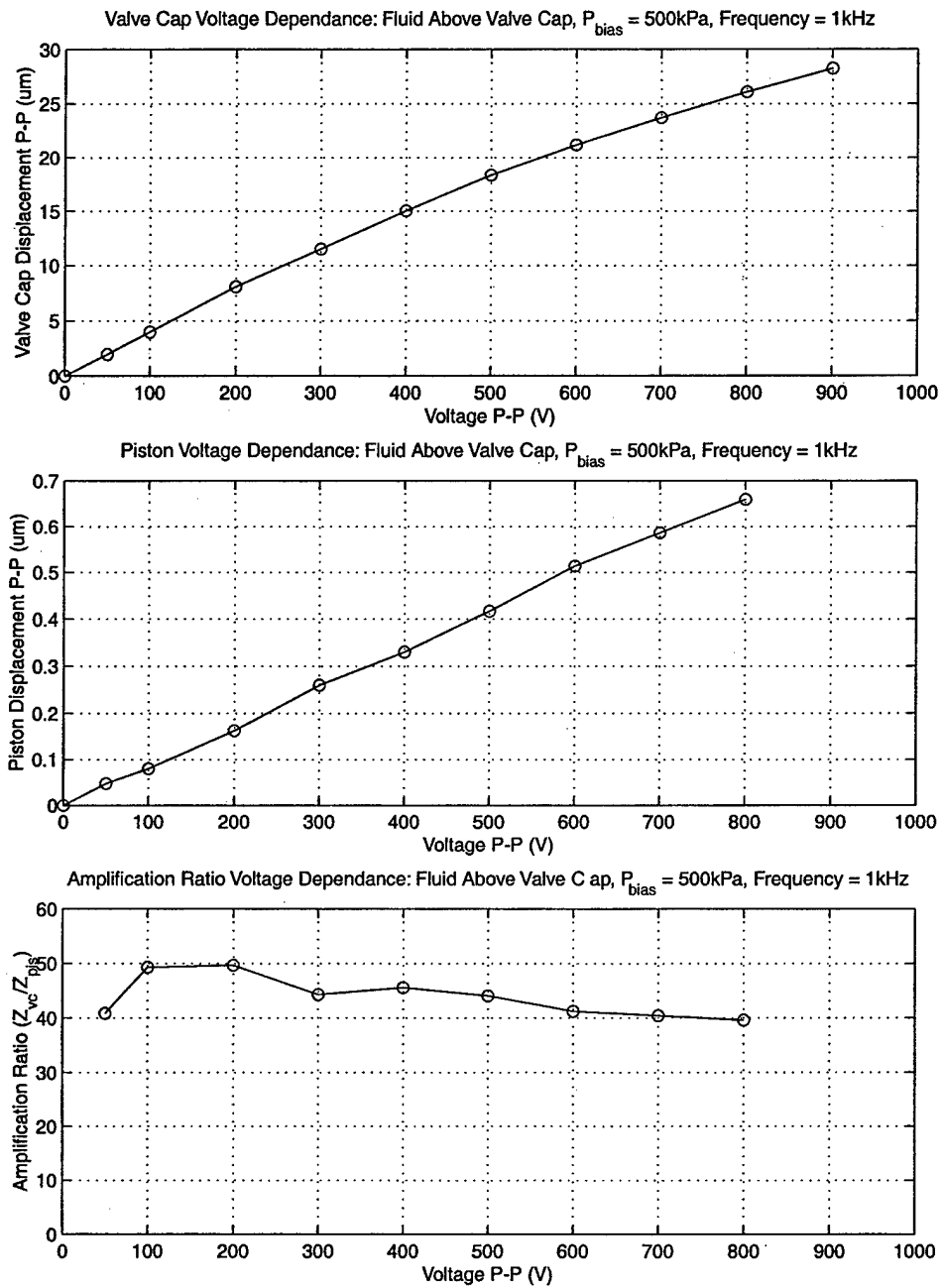


Figure 9.17: Device AV2 valve cap peak-peak motion, piston peak-peak motion, and device amplification ratio as a function of 1kHz sinusoidal drive voltage levels. Due to the non-linear stiffness of the valve membrane structure, the amplification ratio decreases from $\sim 50x$ to $\sim 40x$ as the drive voltage is increased to 900Vpp.

Model Correlation

With the data presented in the previous section, model correlation efforts were pursued to compare these results to the expected results from the analytical and finite-element models documented in the first series of chapters in this thesis. In this section, the high-voltage quasi-static performance at 1kHz is correlated to model expectation using the full non-linear analytical active valve model presented in Chapter 4. Following this, the low-voltage frequency response performance is correlated to the predictions from the active valve finite-element model presented in Chapter 4, as well.

1kHz Quasi-Static Correlation Prior to comparing results for the 1kHz operating conditions, a static pressurization test was performed on the drive element structure within device AV1 to determine the mechanical stiffness of the piezoelectric material elements. In this test, the pressure within the hydraulic amplification chamber was increased from $P_{HAC} = 0kPa$ to $P_{HAC} = 500kPa$ over a time span of 90 seconds, and the displacement of the drive element piston was measured in real-time using the laser vibrometer system. In response to this 500kPa pressurization, the piston moved through a displacement of $0.90\mu m$. With this result and with the geometry of the structure presented in Figure 9.1, the Young's Modulus of the PZN-PT material was determined to be $E_p = 6.76GPa$. This value is 74% of the nominal modulus ($E_p = 9.01GPa$) given by the manufacturer [3] and assumed for active valve design optimization throughout the earlier chapters of this thesis. It should be stated that the manufacturer's material data sheet [3] quoted the modulus within only $\pm 20\%$, and as a result, this experimentally determined reduced modulus from nominal was not completely unexpected. In the model correlation studies that follow, the effect of piezoelectric material Young's Modulus variation is evaluated. Additionally, as presented in Chapter 1, the piezoelectric coefficient assumed in the active valve design procedures was $d_{33} = 2000pC/N$. As shown in Chapter 7, in evaluating performance of the drive element devices, the actual coefficient for high-voltage behavior of this material was found to be in the range of $d_{33} = 1300 - 1500pC/N$. In the model correlation studies that follow, the effect of piezoelectric d_{33} variation is also evaluated.

Figure 9.18 plots the experimental 1kHz sinusoidal voltage drive data for devices AV1 and AV2 against theoretical plots obtained from the full valve analytical model. The operational conditions for these tests and simulations are: a bias pressure $P_{bias} = 500kPa$, a frequency 1kHz, and a varying applied voltage to the piezoelectric material. Shown on this plot are a series of model curves that span the range of d_{33} and E_p coefficients. For example, Model Case 1 assumes an ideal $d_{33} = 2000pC/N$ and an $E_p = 9.01GPa$. At a peak-peak voltage of $V_{p,PP} = 600V$, for example, the model deflection is $Z_{vc,PP} = 32.7\mu m$, as compared to the experimental deflection for device AV1 of $Z_{vc,PP} = 23.1$ and for device AV2 of $Z_{vc,PP} = 21.6$. Reducing the piezoelectric coefficient to $d_{33} = 1500pC/N$ and maintaining $E_p = 9.01GPa$

produces the curve for Model Case 2. A sharp reduction in valve cap deflection is observed. At $V_{p,PP} = 600V$, the model deflection is $Z_{vc,PP} = 27.5\mu m$. Now, reducing the modulus to $E_p = 6.76GPa$ for the expected range of piezoelectric coefficient $d_{33} = 1300 - 1500pC/N$ produces Model Case 3 and Model Case 4, respectively. These are the curves within which the experimental data should lie, since the d_{33} and E_p coefficients are taken from previous experimental studies. For Model Case 3, the model deflection is $Z_{vc,PP} = 25.9\mu m$, and for Model Case 4 the model deflection is $Z_{vc,PP} = 23.7\mu m$.

In observing 9.18(b), the piston deflection experimental data points do fall within these bounds. The experimental valve cap deflection data points, however, lie slightly below the lower bound. These two observations indicate that the drive element structure is well characterized by the values of $d_{33} = 1300 - 1500pC/N$ and $E_p = 6.76GPa$. The lower than expected valve cap deflection experimental data, in comparison to the models, must therefore be a result of additional compliance within the hydraulic coupler mechanism itself. Since Chapter 7 validated that the valve membrane structures correlate extremely well with the non-linear model code, this compliance must be associated with either the fluid itself or a structural compliance of the hydraulic amplification chamber walls. This theory is supported by the amplification ratio data shown in Figure 9.18(c), where the amplification ratio as a function of applied voltage is slightly less than model predictions. However, all amplification ratio data indicate very good correlation within 5 – 10% of model predictions.

In order to further evaluate the issue of a lower than modeled fluid bulk modulus, two further model correlation cases were carried out. In all design chapters of this thesis, the fluid bulk modulus of the silicon oil was assumed to be $K_f = 2.0GPa$ [4]. The previous plots just discussed assumed this value. Depending on how well the fluid is degassed and free of bubbles, this value could be substantially lower. To evaluate the effect of a reduced fluid bulk modulus, Model Case 4 was repeated (with $d_{33} = 1300pC/N$ and $E_p = 6.76GPa$) for $K_f = 1.0GPa$ and $K_f = 0.5GPa$. These cases are labeled Model Case 5 and Model Case 6, respectively. As shown in Figure 9.19, a change in fluid bulk modulus does indeed result in expectations closer to the experimental data. Even for a reduction in fluid stiffness of 4 times, however, the amplification mechanism still performs well. This is a result of the fact that, in general, the fluid is stiff enough that its volume reduction during pressurization is significantly smaller than the actuation volume change produced by the drive element during operation.

These model correlation studies indicate that for the experimentally determined piezoelectric material properties $d_{33} = 1300 - 1500pC/N$ and $E_p = 6.76GPa$, active devices AV1 and AV2 perform very close to model predictions for quasi-static operation at 1kHz. Slight discrepancies in performance can most likely be attributed to a smaller than expected fluid bulk modulus or equivalent structural compliance within the hydraulic amplification chamber.

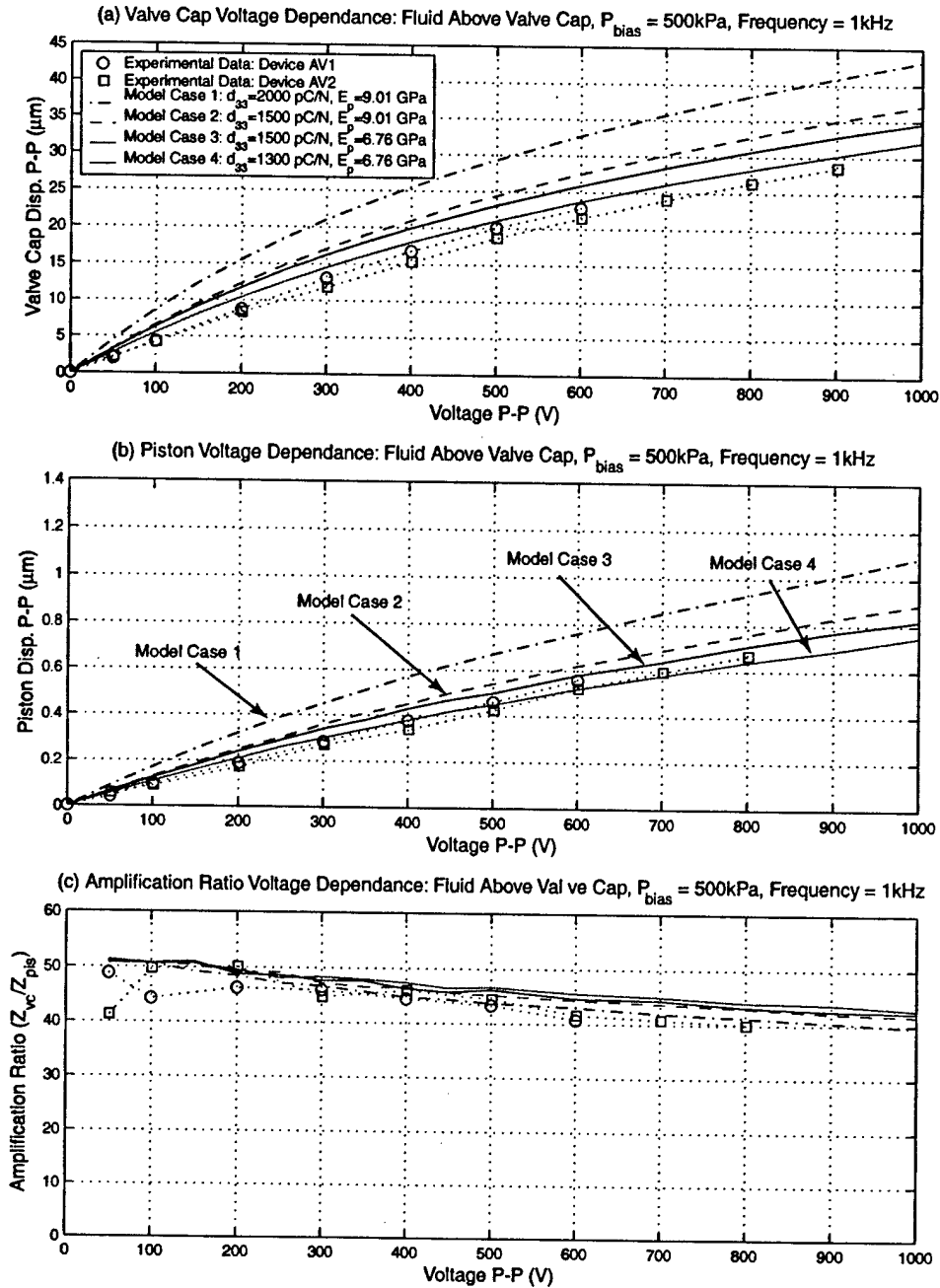


Figure 9.18: Device AV1 and device AV2 quasi-static 1kHz model correlation for fluid bulk modulus $K_f = 2.0\text{GPa}$. Results indicate the piston deflection is very close to the expected theoretical bounds for $d_{33} = 1300 - 1500\text{pC/N}$ and $E_p = 6.76\text{GPa}$. Due to the fact that the valve cap deflection is further from the theoretical bounds, it is believed that fluid compliance or HAC structural compliance is creating a loss mechanism.

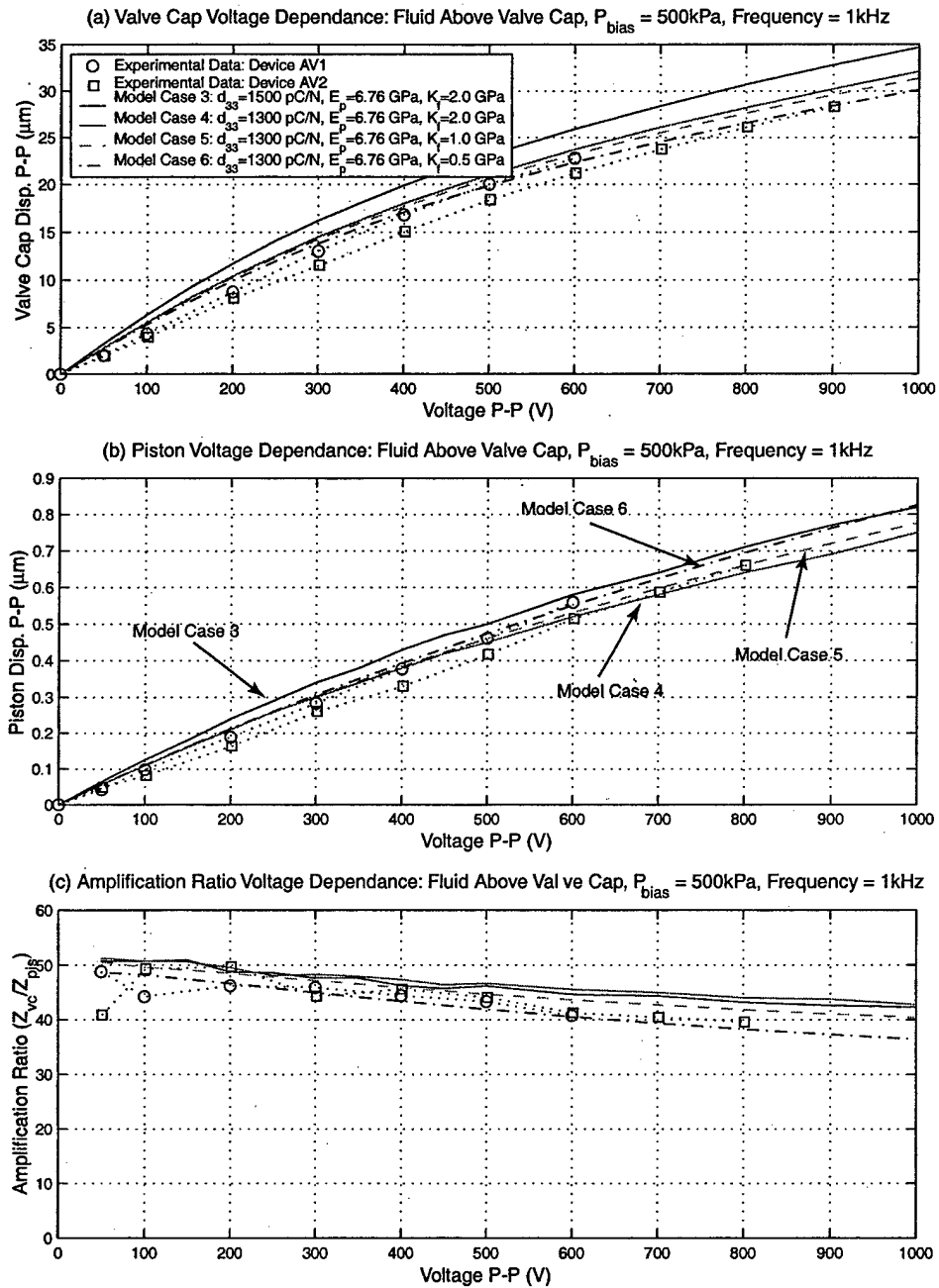


Figure 9.19: Device AV1 and device AV2 quasi-static 1kHz model correlation for varying fluid bulk modulus K_f . Results indicate a 75% reduction in the fluid bulk modulus would enable good correlation between experimental and theoretical results.

Low-Voltage Frequency Response Having correlated the quasi-static 1kHz high-voltage structural behavior of the microvalve to expected results based on the analytic models presented in this thesis, an effort is now made to understand the resonant frequency behavior at low-voltage. The 1st set of tests on device AV1 and device AV2 determined the onset of resonance for a low-voltage ($0V \pm 5V$) sweep signal over a frequency range from 500Hz to 100kHz. These voltage levels were used to ensure that non-linear stretching of the valve membrane structure did not occur. Non-linearities in the structure would create a stiffer operational regime and, therefore, a corresponding increase in the frequency at which "resonance" occurs. As a result, low-voltage excitation produces a conservative estimate for resonant behavior, which can then be used to determine a desirable quasi-static frequency of operation for the valve. Without fluid above the valve cap and membrane structure, devices AV1 and AV2 were found to exhibit resonance at $\sim 10kHz$. With fluid present above the valve cap and membrane structure, resonance was observed at $\sim 5kHz$. In this model correlation section, an effort is made to correlate the active valve resonant behavior without the presence of external fluid to theoretical expectations based on the finite-element model described in Chapter 4. Furthermore, an effort is made to estimate the effect of the external fluid added mass on the active valve resonant frequency and to correlate this effect to the experimental downward shift in resonant frequency from $\sim 10kHz$ to $\sim 5kHz$.

Without Fluid Above Valve Cap and Membrane An axisymmetric 2-D finite-element model was built for this correlation study with no fluid present above the valve cap and membrane. This model incorporates four-node plane elements for the silicon and glass structural parts of the valve and 4-node acoustic fluid elements for the liquid contained within the hydraulic amplification chamber. These acoustic elements enable fluid-structure interaction between the fluid and the surrounding structure of the HAC chamber. Sensitivity analyses were carried out to evaluate the first resonant frequencies of the coupled system, as a function of variations in important structural parameters and material properties. The parameters investigated were (1) the HAC fluid bulk modulus K_f , (2) the valve membrane thickness t_{vm} , (3) the piezoelectric material stiffness E_p , (4) the HAC fluid chamber height t_{HAC} , (5) the bottom support plate thickness t_{bot} , and (6) the top structural plate thickness t_{top} . The results of these sensitivity analyses are shown in Figure 9.20. In each analysis, the experimental baseline design for the active valve is specified. This baseline design includes the following values for the parameters under investigation: $K_f = 2GPa$, $t_{vm} = 6\mu m$, $E_p = 6.76GPa$, $t_{bot} = 1000\mu m$, $t_{top} = 1000\mu m$, and $t_{HAC} = 200\mu m$. With these baseline parameter values, a first modal frequency of 14.1kHz was determined. This theoretical value is significantly larger than the experimentally determined 1st modal frequency of 10kHz, and as a result, the sensitivity analyses that follow are meant to determine why this is.

Figure 9.20(a) shows the effect of reduced bulk modulus on the valve first modal frequency. The active valve was designed assuming a fluid bulk modulus value of $K_f = 2GPa$. The previous quasi-static model correlation section concluded that a reduction in bulk modulus down to $K_f = 0.5GPa$ could explain the voltage-valve cap deflection performance reduction seen experimentally at 1kHz. From this modal analysis, however, it is clear that this reduction in modulus to $K_f = 0.5GPa$ has minimal effect on the 1st modal frequency, dropping it only to 13.7kHz. In fact, a reduction to $K_f = 0.02GPa$ is required to bring the 1st modal frequency down to 10kHz. It is therefore concluded that the expected fluid bulk modulus value of $K_f = 0.5GPa$ is not the prime reason for the lower-than expected 1st modal frequency.

Figure 9.20(b) shows the effect of valve membrane thickness on the valve first modal frequency. Based on the valve membrane pressure-deflection results detailed in Chapter 8 (for which there was excellent correlation between theoretical and experimental results for $t_{vm} = 6\mu m$), it is quite certain that the valve membrane thickness is very near to $t_{vm} = 6\mu m$. Figure 9.20(b) (solid line) shows that even if the thickness were to deviate anywhere within $t_{vm} = 5 - 7\mu m$, the effect on the first modal frequency would be quite small. It is therefore concluded that a slight deviation in valve membrane thickness from the experimentally verified value of $t_{vm} = 6\mu m$ would not be sufficient to reduce the first modal frequency from 14.1kHz to 10kHz. Additionally, the dotted line in this plot illustrates the first modal frequency of the stand-alone valve cap and membrane structure (with no fluid in contact with its bottom surface) as a function of valve membrane thickness. One observes, in this case, that the modal frequency is very sensitive to valve membrane thickness. The important observation here is that the presence of the fluid in the HAC chamber serves to reduce the modal frequency (from 32.9kHz for the stand-alone valve membrane to 19.6kHz for the active valve coupled system) for a large thickness valve membrane (added mass effect to be discussed shortly) whereas for a small thickness valve membrane the presence of fluid in the HAC serves to increase the modal frequency (from 8.7kHz for the stand-alone valve membrane to 12.6kHz for the active valve coupled system). This illustrates the importance of performing full fluid-structural interaction analyses to predict the full valve modal frequency rather than estimating this modal frequency based on just one of the stand-alone structural components of the full valve.

Figure 9.20(c) shows the effect of piezoelectric material modulus E_p on the valve first modal frequency. In Chapter 9, this E_p value was experimentally determined to be 6.76GPa. It is clear from this plot that the valve modal frequency is insensitive to slight variations (between $E_p = 6 - 8GPa$) in this value. It is therefore concluded that the reduction in the first modal frequency from 14.1kHz to 10kHz can not be attributed to an unexpected value of E_p .

Figures 9.20(d) and 9.20(e) illustrate the effect of the top and bottom structural plate thicknesses on the valve first modal frequency. It makes sense that if the bottom structural plate were to be significantly reduced in thickness, then the drive element portion of the valve

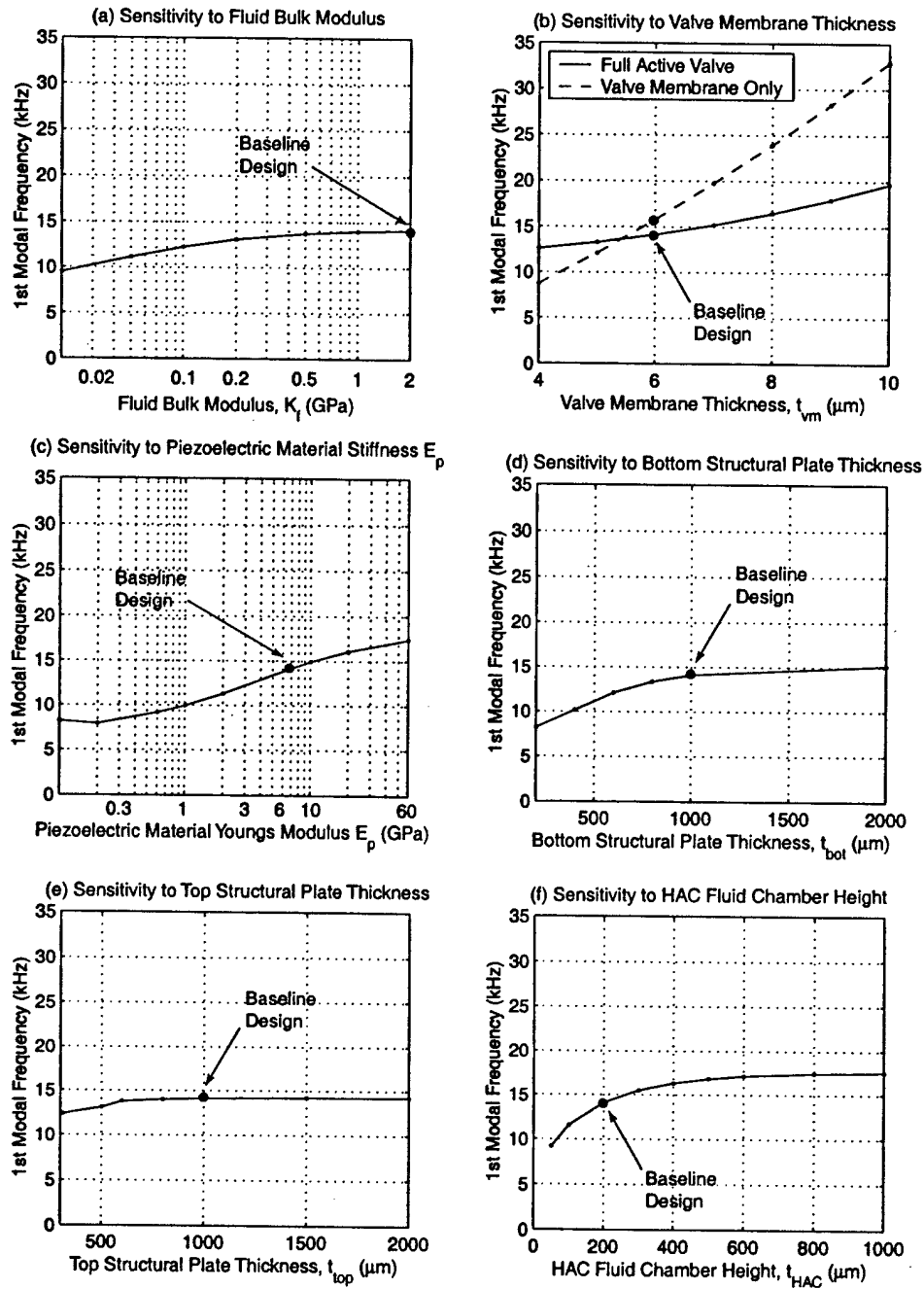


Figure 9.20: Finite-element active valve modal frequency sensitivity studies for (a) the HAC fluid bulk modulus K_f , (b) the valve membrane thickness t_{vm} , (c) the piezoelectric material stiffness E_p , (d) the HAC fluid chamber height t_{HAC} , (e) the bottom support plate thickness t_{bot} , and (f) the top structural plate thickness t_{top} .

would become much softer than in the baseline design, and the full valve modal frequency could be expected to drop. This phenomenon is observed in Figure 9.20(d). Likewise, if the top structural plate were to be significantly reduced in thickness, the HAC structural chamber would become much softer than in the baseline design, and the full valve modal frequency could be expected to drop. This phenomenon is observed in Figure 9.20(e). In the active valve devices experimentally tested in this thesis, however, the thicknesses of these two plates are well-characterized to each have a thickness of at least $1000\mu m$. Therefore, it is concluded that the top and bottom plate thicknesses do not contribute to the reduction in the active valve first modal frequency from 14.1kHz to 10kHz.

Figure 9.20(f) shows the effect of the HAC fluid chamber height t_{HAC} on the the valve first modal frequency. The plot illustrates that the modal frequency is extremely sensitive to a reduction in this chamber height from the baseline design value of $t_{HAC} = 200\mu m$ (where the first modal frequency is 14.1kHz) to a smaller value of $t_{HAC} = 50\mu m$ (where the 1st modal frequency is 9.2kHz). The reason for this significant frequency reduction as the chamber height is reduced is the presence of inertial coupling between the moving drive element piston and the adjacent glass surfaces that form the top of the HAC chamber. A comprehensive discussion of inertia coupling is found in Blevins [5]. The following excerpt is taken from [5]:

As a cross section accelerates in a fluid, pressure gradients will be generated in the surrounding fluid. These pressure gradients can exert fluid forces on adjacent structures. If the adjacent structures are not rigid, they will in turn deflect and generate forces on the accelerating cross section. This interaction between adjacent elastic structures is called inertial coupling. Inertial coupling increases as the distance between structures decreases. Inertial coupling can significantly affect the natural frequencies and mode shapes of [closely-packed structures] if the density of the surrounding fluid is comparable to or larger than the average density of the [structures]. *Blevins, p.403*

Prior to assembly of devices AV1 and AV2, the chamber height t_{HAC} of these devices was measured to be $\sim 200\mu m$. However, the geometry of the glass layer that forms this chamber is significantly more complex (see valve structure shown in Figure 9.1) than just having a volume of fluid $200\mu m$ in height above the drive element piston and beneath the valve cap and membrane. In reality, a series of fluid channels exists (termed "HAC Through Holes" and "HAC Radial Channels" in Figure 9.1) through this glass layer to allow fluid to couple the piston motion to the valve membrane motion. During the design stages of the active valve device, a bottom structural stop beneath the valve cap (at $Z_{vc} = -16.5\mu m$) was set as a requirement. These channels were therefore implemented to satisfy this requirement. The heights of the "HAC Radial Channel" features in Layer 7 are no more than $100\mu m$, and as a

result, acceleration of fluid in these channels could be a significant inertial coupling effect. Based on these arguments, it is concluded that the small-size fluid pathways through the complex glass Layer 6 HAC chamber are the most probable reason for the reduction in active valve modal frequency from the baseline design FEM expectation of 14.1kHz to the experimentally-determined frequency of 10kHz . Future valve design iterations should include larger t_{HAC} chamber heights (ie: $t_{HAC} = 500\mu\text{m}$) with no complex fluid routing pathways. Eliminating the presence of the valve cap bottom structural stop might be a necessary consequence.

With Fluid Above Valve Cap and Membrane The previous model correlation section determined that inertial coupling effects between the accelerating fluid and the piston structure within the HAC chamber were the most likely reason for the lower-than expected active valve first modal frequency, when no fluid was present above the valve cap and membrane structure of the valve. Experimentally, without this fluid above the valve cap and membrane, the first modal frequency was found to be $\sim 10\text{kHz}$. With this fluid above the valve cap and membrane, the modal frequency was found to be $\sim 5\text{kHz}$. The following section attempts to explain this downward shift in valve modal frequency.

The conclusion of this section will be that the presence of fluid above the valve cap and membrane structure serves to increase the effective mass of the valve cap and membrane, thereby reducing the overall modal frequency. This statement is consistent with a discussion found in Blevins [5] concerning the effect of surrounding fluid on a circular plate in vibration. The following excerpt is taken from [5]:

As an elastic plate vibrates in a fluid, the fluid immediately surrounding the plate is set into motion and the plate will radiate sound waves into the far field... In general, the fluid will impose both added mass and damping forces on the plate. The added mass will lower the natural frequency of the plate from that which would be measured in a vacuum, and the damping of the plate will be increased. *Blevins, p.413*

Taking as an example a circular disk with radius r_a exposed on one side to an inviscid compressible fluid of density ρ_{fluid} (Blevins, p.414), the added mass of the disk for acceleration perpendicular to the plane of the disk can be estimated as $M_{added} = \frac{8}{3}\rho_{fluid}r_a^3$. For a back-of-the-envelope calculation on the valve cap and membrane in the active valve, let $r_a = R_{vm}$. The corresponding added mass is therefore $M_{added} = \frac{8}{3}(777\frac{\text{kg}}{\text{m}^3})(700\mu\text{m})^3 = 7.11\text{e-}^7\text{kg}$. The baseline mass of the valve cap structure is $M_{vc} = \rho_{Si}\pi R_{vc}^2 t_{vc} = (2200\frac{\text{kg}}{\text{m}^3})\pi(250\mu\text{m})^2(300\mu\text{m}) = 1.30\text{e-}^7\text{kg}$.

To therefore estimate the reduction in active valve first modal frequency due to the presence of fluid above the valve cap and membrane, the finite-element model from the previous section

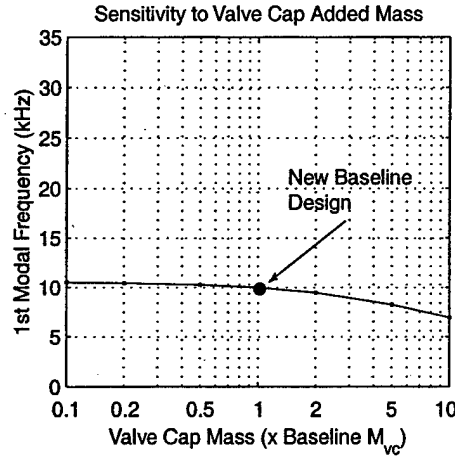


Figure 9.21: Finite-element modal frequency sensitivity to valve cap added mass. The presence of fluid above the valve cap and membrane structure creates an effective added mass to the coupled structure which serves to reduce the first modal frequency of the active valve device.

was run with a modified density of the valve cap material such that its mass was equal to $M_{vc,modified} = M_{vc} + M_{added} = 8.42e^{-7}kg$ (an increase from the original valve cap mass of 6.5 times). In this comparison study, a new baseline valve design was chosen to include a fluid bulk modulus value of $K_f = 0.5GPa$ and an HAC chamber height of $t_{HAC} = 66\mu m$ so that the first modal frequency of the valve without the added mass was exactly 10.0kHz. This baseline FEM model therefore matched the experimental result without fluid above the valve cap and membrane. Now, with the addition of the added mass (x6.5), the first modal frequency of the valve was determined to be 7.8kHz (a 22% decrease from the new baseline design modal frequency of 10.0kHz). Figure 9.21 illustrates the theoretical effect of added mass (from x0.1 to x10) on the first modal frequency of the active valve structure. Over this range of added mass, the first modal frequency is affected, but not substantially.

For the active valve devices tested experimentally, there is a 50% reduction in the first modal frequency (from $\sim 10kHz$ to $\sim 5kHz$) due to the presence of fluid above the valve cap and membrane. The above study on the new baseline design (in which a 22% reduction was calculated) provides for an added mass argument that also applies to the experimental results, however, this value of added mass only partially reduces the first modal frequency to correlate with the experimental results. Since this added mass calculation was for a circular plate in an infinite fluid medium, and since in the real active valve structure, there exist structural surfaces within 50-100 μm of the top surface of the valve cap and membrane, it is likely that the same sort of inertial coupling effects as discussed in the previous section are coming into play. These unmodeled effects could potentially cause a further reduction in first modal frequency.

It is therefore concluded that the fluid mass (acceleration and inertia effects) above the valve cap and membrane and the presence of the flow channel structure near to this valve cap and membrane provide an additional mass seen by the active valve structure as it vibrates, thereby reducing the valve first modal frequency from the case when no fluid exists above the valve cap and membrane. Future active valve design iterations should more thoroughly evaluate this added mass effect on valve dynamic performance. The recommendation section of Chapter 10 further discusses these recommended future analyses.

9.3.2 Testing Section 2: Active Valve Fluid Flow Regulation

To characterize the flow regulation capability of the active valve devices documented in this thesis, a series of tests was performed. The first test focused on experimentally determining the quasi-static flow rate versus valve cap opening curves for varying applied differential pressures $P_1 - P_2$ across the valve orifice. These results were then compared to predictions based on the flow models developed in Chapter 5 of this thesis and based on [2]. The second test evaluated the flow regulation capability of the active valve by varying the duty cycle of valve opening at a prescribed differential pressure $P_1 - P_2$ and measuring the average flow rate through the valve orifice. The third test evaluated the flow regulation capability of the active valve at a prescribed operating frequency of 1kHz for increasing differential pressures across the valve orifice. Limitations in valve performance could therefore be determined as this differential pressure was increased. For each of these tests, an estimate of the measurement error is included in the experimental results plots detailed in this section.

Static Flow Tests

To determine the quasi-static flow rate versus valve opening curves for a series of imposed differential pressures across the valve orifice, the fluids test-rig (described in Chapter 6) was used. In these tests, no voltage was applied to the piezoelectric material. Rather, the valve cap position was controlled by regulating the pressure P_{HAC} to the hydraulic amplification chamber. For a given test run at a desired differential pressure $P_1 - P_2$, P_{HAC} was first increased to move the valve cap upward against the fluid orifice (with $P_1 = P_2 = 0$). P_1 and P_2 were then independently increased to set the desired differential pressure across the orifice. In order to maintain the valve cap against the orifice, P_{HAC} was varied real-time in conjunction with the increases in P_1 and P_2 . With the proper differential pressure set, a data acquisition system was started, into which the valve cap displacement, pressure measurement of P_{HAC} , pressure measurement of P_1 , pressure measurement of P_2 , and flow sensor measurement Q_{avg} were input. As detailed in Chapter 6, the flow rate measurements were taken using a calibrated flow orifice system.

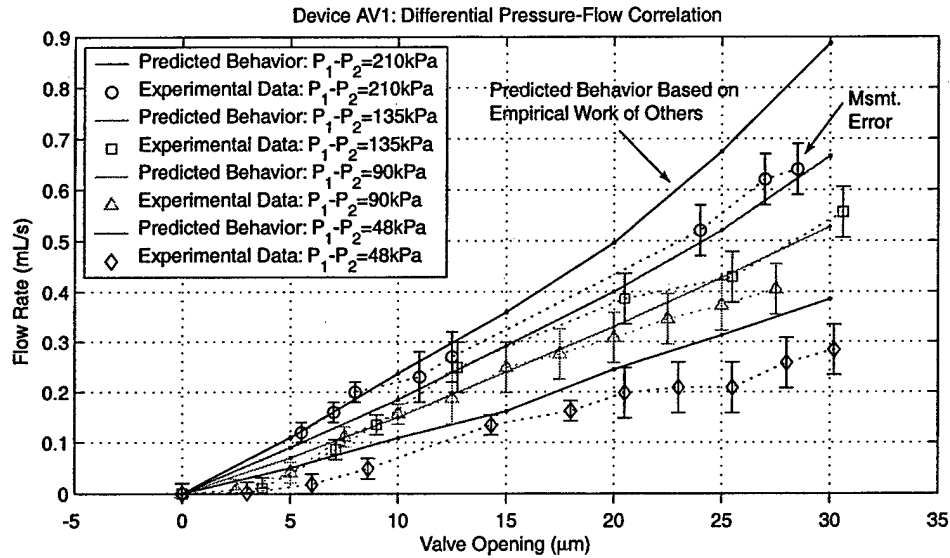


Figure 9.22: Model correlation to device AV1 quasi-static fluid flow rate versus valve opening behavior for differing imposed differential pressures. The experimental flow rates fall approximately 10 – 30% short of predictions based on the empirical work of others. Error bars on the data indicate estimates of measurement error. Two flow sensors of different ranges were used in these experiments, resulting in different levels of measurement error for lower and higher flow rates. These measurement errors were estimated based on the flow sensor calibration errors, the accuracy of the applied differential pressure, and human error associated with controlling the quasi-static nature of the experiments.

In order to obtain quasi-static flow measurements for a given valve cap opening, P_{HAC} was decreased slowly over a period of approximately 10 minutes. The valve cap was allowed to move through its full stroke of 30–33 μm . The time constant of the flow orifice sensor was on the order of a few seconds, and therefore this measurement procedure enabled quasi-static measurements. Tests were performed for differential pressures of $P_1 - P_2 = 48\text{kPa}$, 90kPa, 135kPa, and 210kPa. For each test run, selected points were chosen to plot. Figure 9.22 overlays these experimental results with the predicted behavior based on the flow models used in Chapter 5 of this thesis. Since the Chapter 5 flow models are based on a compilation of empirical work from other researchers, the line of predicted behavior in Figure 9.22 is understood to be of only “limited accuracy”, in other words, it is not based on exact theory. In general, this comparison shows that the predicted behavior based on the empirical work of others overpredicts the flow rate behavior by approximately 10 – 30%. This is most likely due to differing geometric features between the orifice structures contained within the empirical results and the valve orifice structure in this thesis. Specifically, since the empirical results are based on macroscale orifice structures

with rounded and filleted features, one would expect better flow rate capabilities for given applied differential pressure and valve opening than in the microscale valve orifice structure detailed in this thesis, which possesses comparatively sharp corners. Furthermore, at small valve openings, the flow rate appears to be choked. Only when the valve cap reaches an opening of $\sim 4\mu\text{m}$ does the fluid really begin to flow. Based on this data, active valve device AV1 can be characterized as a flow control device. These differential-pressure flow experiments were performed for differential pressures up to $P_1 - P_2 = 210\text{kPa}$. When tested to differential pressures greater than this value, interesting oscillatory behavior of the valve cap structure occurred. These observations and the corresponding efforts to determine the cause of these phenomena are detailed in the following section.

Self-Oscillatory Behavior of Valve Cap During Static Flow Tests

The original objective of the static flow tests described above was to evaluate the differential pressure-flow behavior through the valve orifice for $P_1 - P_2$ up to 800kPa , since this was the designed-for maximum differential pressure to be experienced in a complete MHT micropumping system. However, in testing the valve beyond $P_1 - P_2 = 210\text{kPa}$, self-oscillatory behavior of the valve cap at its resonant frequency of 5kHz was observed and measured (remember, in these tests, there is no actuation of the piezoelectric drive elements – all pressures are controlled via external regulators). It is believed that this oscillatory behavior may be induced by vortices and unsteady flow phenomena as the flow transitions from the laminar to the turbulent flow regime. In an effort to evaluate this hypothesis, the following experiments were carried out.

For each of a series of differential pressures ($P_1 - P_2 = 80\text{kPa}$, 130kPa , 160kPa , 200kPa , 230kPa , 240kPa , 305kPa , and 360kPa), the valve cap was controlled to slowly open from its closed position using the same procedure as for the static flow tests. During this process, the valve opening $Z_{vc,opening}$, the quasi-static flow rate Q_{avg} , and the imposed differential pressure $P_1 - P_2$ were measured real-time. The valve orifice geometry is shown in Figure 9.23. Numerous data points were selected and post-processing operations were performed to calculate the Reynolds number of the flow through the valve orifice, according to the relation $RE_{Dorifice} = \frac{Q_{avg}}{D_{orifice}\nu}$. Additionally, an "Instability Value" was determined for each data point corresponding to the behavior of the valve cap as it opened. The three types of valve cap behaviors observed (using the laser vibrometer system) during these tests were (1) smooth steady motion of the valve cap, (2) slightly rough motion of the valve cap (but always with negligible amplitude), and (3) oscillatory motion of the valve cap at a frequency of 5kHz and with peak-peak displacement of $3 - 4\mu\text{m}$. Figure 9.24 displays typical displacement signals over a time period of 10 ms for each of these types of behaviors. At each data point, an Instability Value of 1, 2, or 3 was assigned for each of the respective measured behaviors. Since the valve cap structure essentially reacts as a sensor to any pressure fluctuations in the flow channel above

it, these assigned Instability Values can provide some insight into the behavior of the fluid as it flows through the orifice.

Figure 9.25 displays an example test run for the case of $P_1 - P_2 = 80kPa$. Plots of the Instability Value versus $Z_{vc,opening}$, $P_1 - P_2$ versus $Z_{vc,opening}$, Q_{avg} versus $Z_{vc,opening}$, and $RE_{Dorifice}$ versus $Z_{vc,opening}$ are included. Notice that since the Reynolds number is proportional to the average flow rate, the Q_{avg} and $RE_{Dorifice}$ curves in Figure 9.25(c) are identical, only the axes are scaled differently. Additionally, notice that $P_1 - P_2$ is not constant over the length of the run. During the testing, it was very difficult to maintain the differential pressure at a constant value. For this test case of $P_1 - P_2 = 80kPa$, the valve cap smoothly moves through an opening trajectory, up to approximately $Z_{vc,opening} = 19\mu m$. At these conditions, the valve cap displacement begins to exhibit a slight roughness in its measured displacement (with roughness amplitude less than $0.4\mu m$), but continues to open with no effect on valve cap position. At $Z_{vc,opening} = 28\mu m$, the valve cap displacement returns to smooth behavior. The corresponding Reynolds numbers for these transition points are $RE_{Dorifice} = 788$ and $RE_{Dorifice} = 928$, respectively. In Figure 9.25(a), an Instability Value of 1 represents the smooth motion of the valve cap. An Instability Value of 2 represents slightly rough motion.

In order to obtain some understanding of the relationship between the valve cap behavior and the corresponding $RE_{Dorifice}$, test runs were carried out for the 8 differential pressure settings detailed above. Figure 9.26 plots the Instability Value versus $Z_{vc,opening}$ curve for $P_1 - P_2 = 80kPa$, $P_1 - P_2 = 130kPa$, and $P_1 - P_2 = 160kPa$ respectively. Figure 9.27 plots the Instability Value versus $Z_{vc,opening}$ curve for $P_1 - P_2 = 200kPa$, $P_1 - P_2 = 2300kPa$, and $P_1 - P_2 = 240kPa$ respectively. Figure 9.28 plots the Instability Value versus $Z_{vc,opening}$ curve for $P_1 - P_2 = 305kPa$ and $P_1 - P_2 = 360kPa$ respectively. In observing these plots, it is clear that oscillatory behavior does not occur until the case of $P_1 - P_2 = 200kPa$. Under this differential pressure, at a value of $Z_{vc,opening} = 8\mu m$, the valve cap experiences a transition from smooth motion to oscillatory behavior with a frequency of 5kHz and a peak-peak displacement of $6 - 8\mu m$. The corresponding Reynolds number for this transition is $RE_{Dorifice} = 615$. At a deflection of $Z_{vc,opening} = 19\mu m$, the valve cap stops oscillating and exhibits only slightly rough behavior. The corresponding Reynolds number for this transition is $RE_{Dorifice} = 969$. And finally, when the valve cap approaches the lower valve stop, its motion once again becomes smooth, most likely caused by interaction with the solid surface below it. The corresponding Reynolds number for this transition is $RE_{Dorifice} = 2000$. Similar behavior is observed for larger imposed differential pressures as well. For the case of $P_1 - P_2 = 360kPa$, multiple transitions between smooth, oscillatory, and rough are observed. It appears as though upon separation from the upper valve orifice stop, the valve cap immediately begins to oscillate. It then transitions back to smooth behavior at $Z_{vc,opening} = 4.5\mu m$, back to oscillatory motion at $Z_{vc,opening} = 7.5\mu m$, back to smooth motion at $Z_{vc,opening} = 13\mu m$, and then to rough behavior

at $Z_{vc,opening} = 20\mu m$.

To better understand the relationship between these transition behaviors and the Reynolds number at which they occur, all 8 plots are combined in Figure 9.29. Regions of smooth, rough, and oscillatory behavior are clearly evident. Figure 9.30 is produced by estimating the boundaries between these regions and labeling the corresponding $RE_{Dorifice}$ values at these boundary data points. In this plot, the distinct regions are detailed. Notice that a transition to rough valve cap motion occurs for Reynolds numbers between $RE_{Dorifice} = 800 - 1100$. Additionally, for large differential pressures, oscillatory valve cap behavior begins typically at $RE_{Dorifice} = 500 - 600$. Since rough valve cap behavior is characterized by only a tiny roughness in the displacement response (typically peak-peak displacement of less than $0.4\mu m$), the valve cap itself remains in a stable operating condition. It is only when large amplitude oscillatory response occurs that the valve cap becomes unstable. Figure 9.31 plots this stable versus unstable representation. In essence, smooth and rough valve cap behavior have been grouped together to form the stable regions. Figure 9.32 plots experimental lines of constant Reynolds number over the data points for all 8 test cases and Figure 9.33 compares these lines of constant Reynolds number to the expected lines obtained from model simulations presented in Chapter 4. Notice that all of the experimentally determined lines of constant $RE_{Dorifice}$ are very close to the theoretical predictions for low to moderate values of imposed differential pressure (ie: up to $P_1 - P_2 = 150kPa$). Once the differential pressure is increased further, experimental correlation to theory is still good for low valve openings (lines of constant $RE_{Dorifice} = 400, 500, 800$), however the experimental lines of larger constant $RE_{Dorifice} = 1000, 1500, 2200$ begin to bend more sharply upward from the theoretical predictions. This bending is directly in relation to the region of oscillatory behavior, which is bounded by a value of $RE_{Dorifice} \sim 1000 - 1100$ for the larger differential pressures. If one were to conclude that the measurements of smooth valve cap motion correspond to a laminar flow regime and that the slightly rough valve cap motion corresponds to a turbulent flow regime, it could therefore be argued that the oscillatory behavior of the valve cap structure occurs in a transition regime (characterized by $RE_{Dorifice}$ between ~ 500 and ~ 1100).

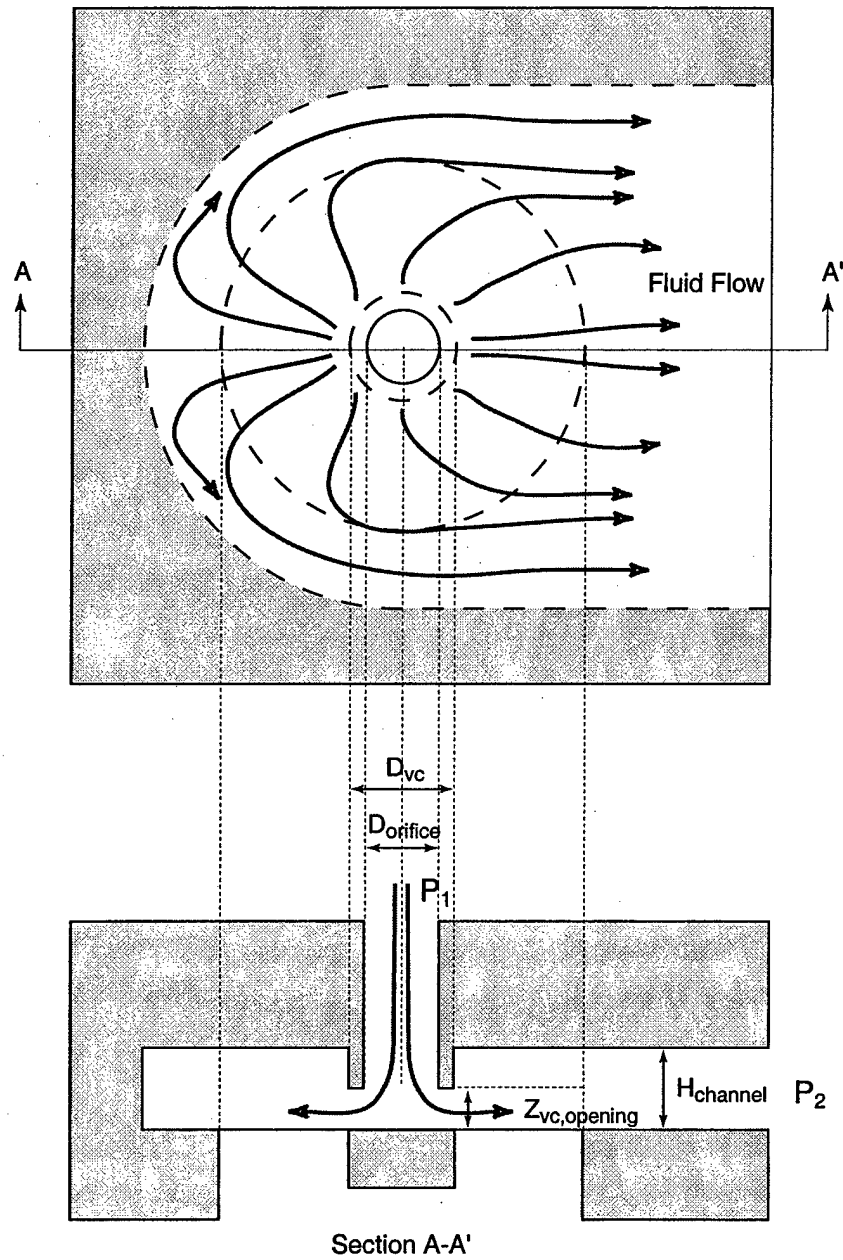


Figure 9.23: Schematic of valve cap and membrane orifice structure. For the active valve geometry tested in this thesis, $D_{orifice} = 500\mu m$, $Z_{vc,opening} = 0-30\mu m$, and $H_{channel} \sim 100\mu m$. Notice that the fluid flows radially outward over valve membrane, primarily to one side of the structure. The other side is blocked.

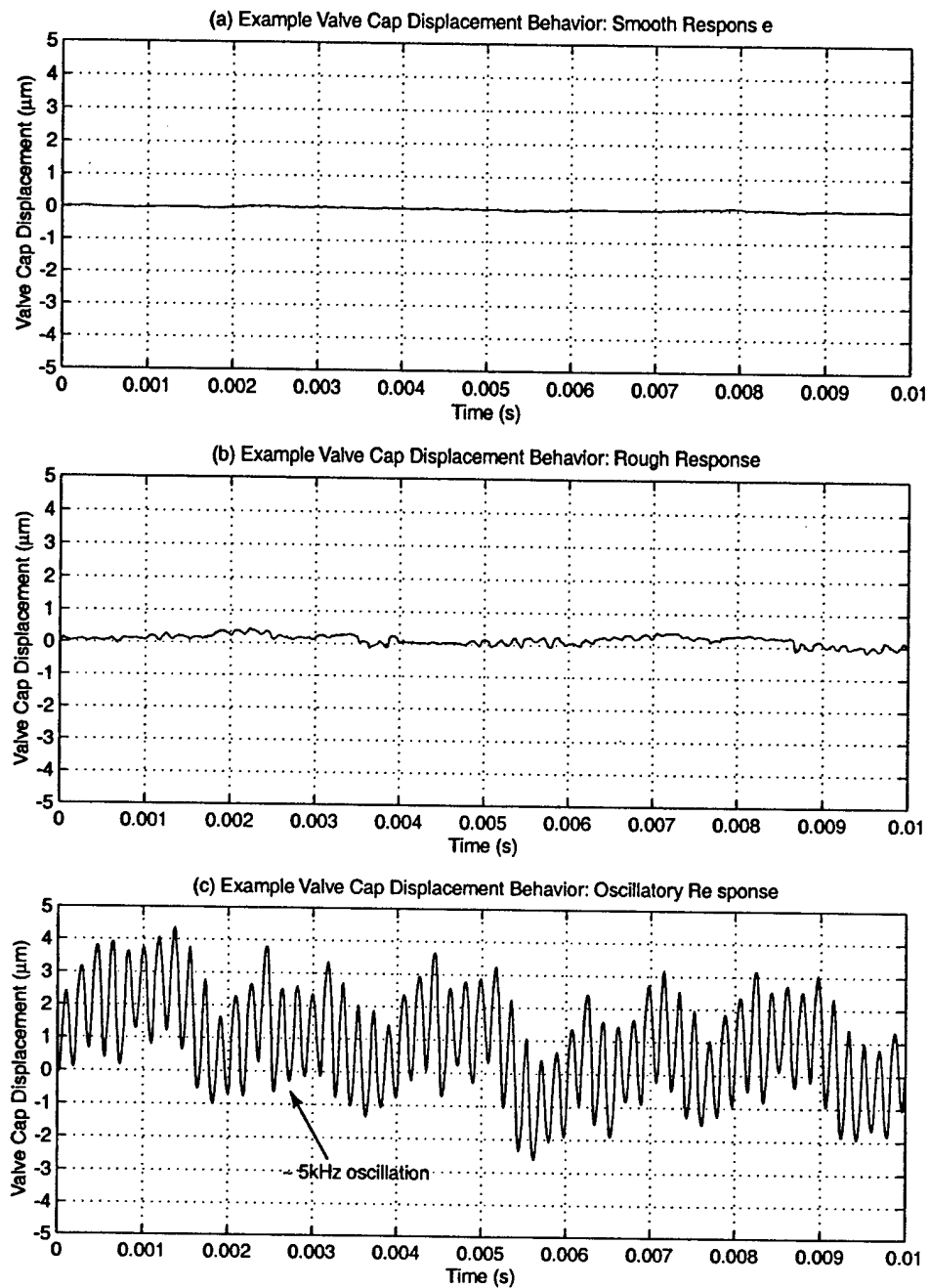


Figure 9.24: Representative displacement signals corresponding to stable and unstable valve cap behavior during quasi-static opening: (a) smooth displacement response (Instability Value=1), (b) slightly rough displacement response (Instability Value=2), characterized by random peak-peak motion less than $0.4\mu\text{m}$, and (c) oscillatory response characterized by $3 - 4\mu\text{m}$ peak-peak oscillations at 5kHz (Instability Value=3).

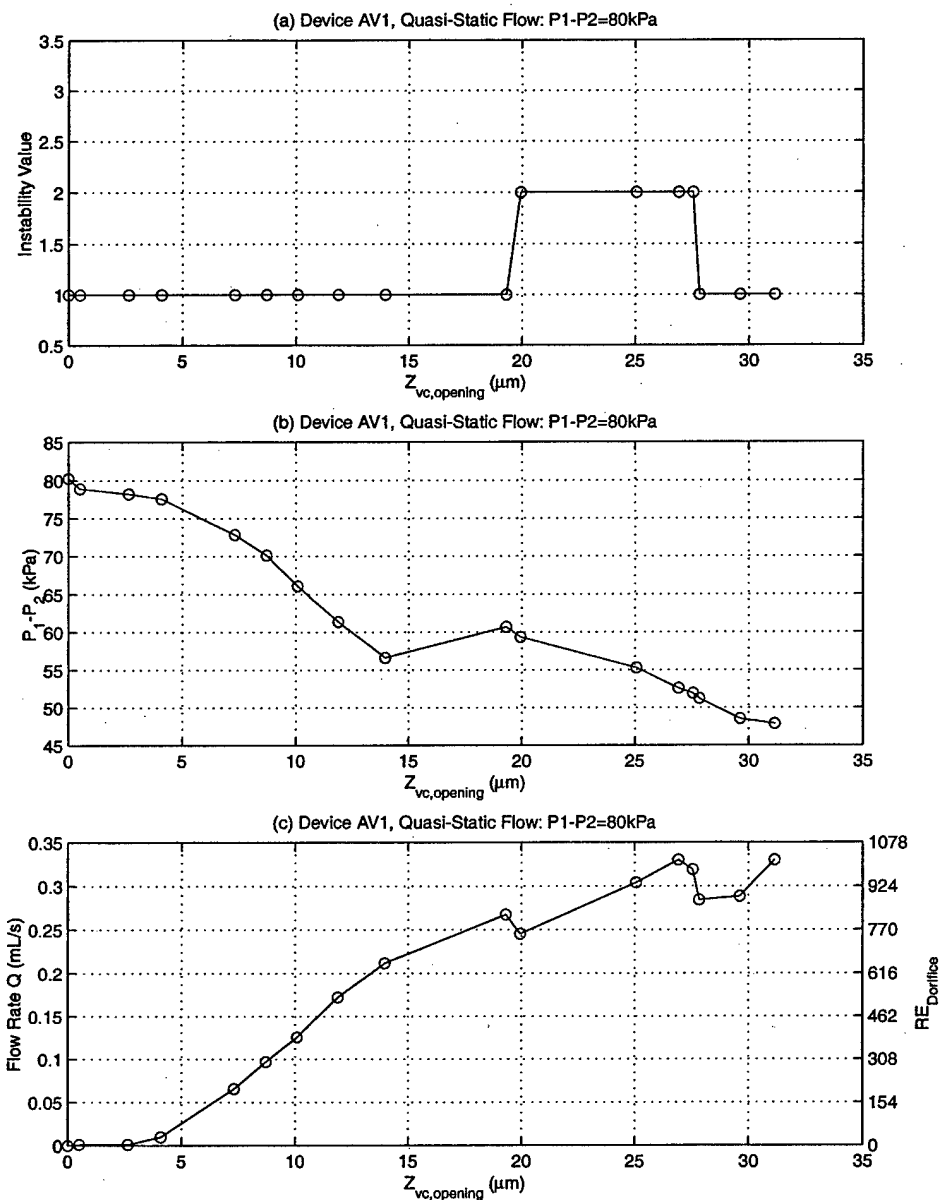


Figure 9.25: Representative plots for valve cap behavior, differential pressure, and flow rate during quasi-static opening for $P_1 - P_2 = 80 \text{ kPa}$. The valve cap opening motion transitions from smooth behavior to rough behavior at a deflection of $Z_{vc, opening} = 19 \mu\text{m}$ and transitions back to smooth behavior at a deflection of $Z_{vc, opening} = 28 \mu\text{m}$.

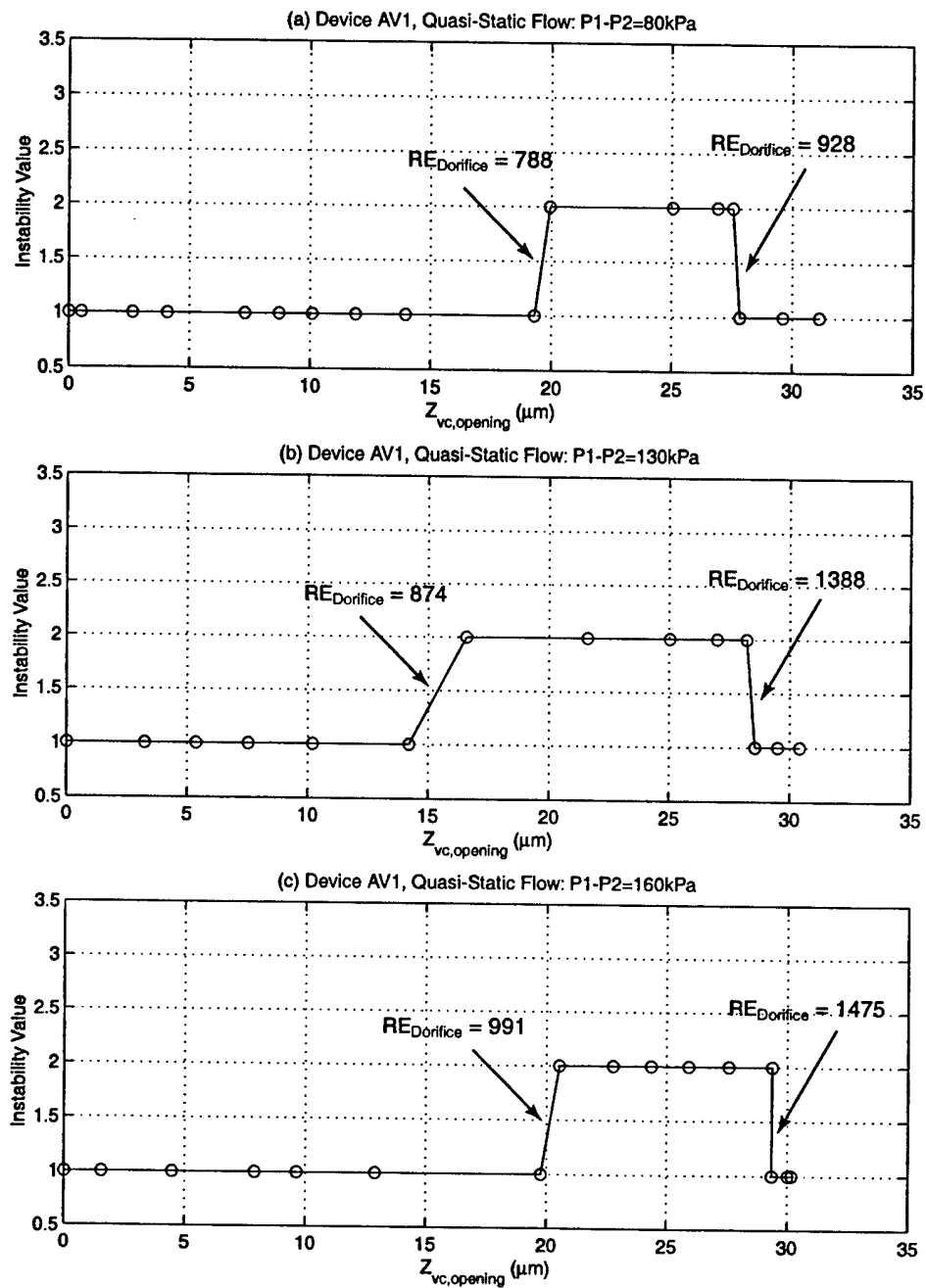


Figure 9.26: Valve cap Instability Values during quasi-static opening for $P_1 - P_2 = 80 \text{ kPa}$, $P_1 - P_2 = 130 \text{ kPa}$, and $P_1 - P_2 = 160 \text{ kPa}$. Corresponding Reynolds numbers are labeled at the transition locations.

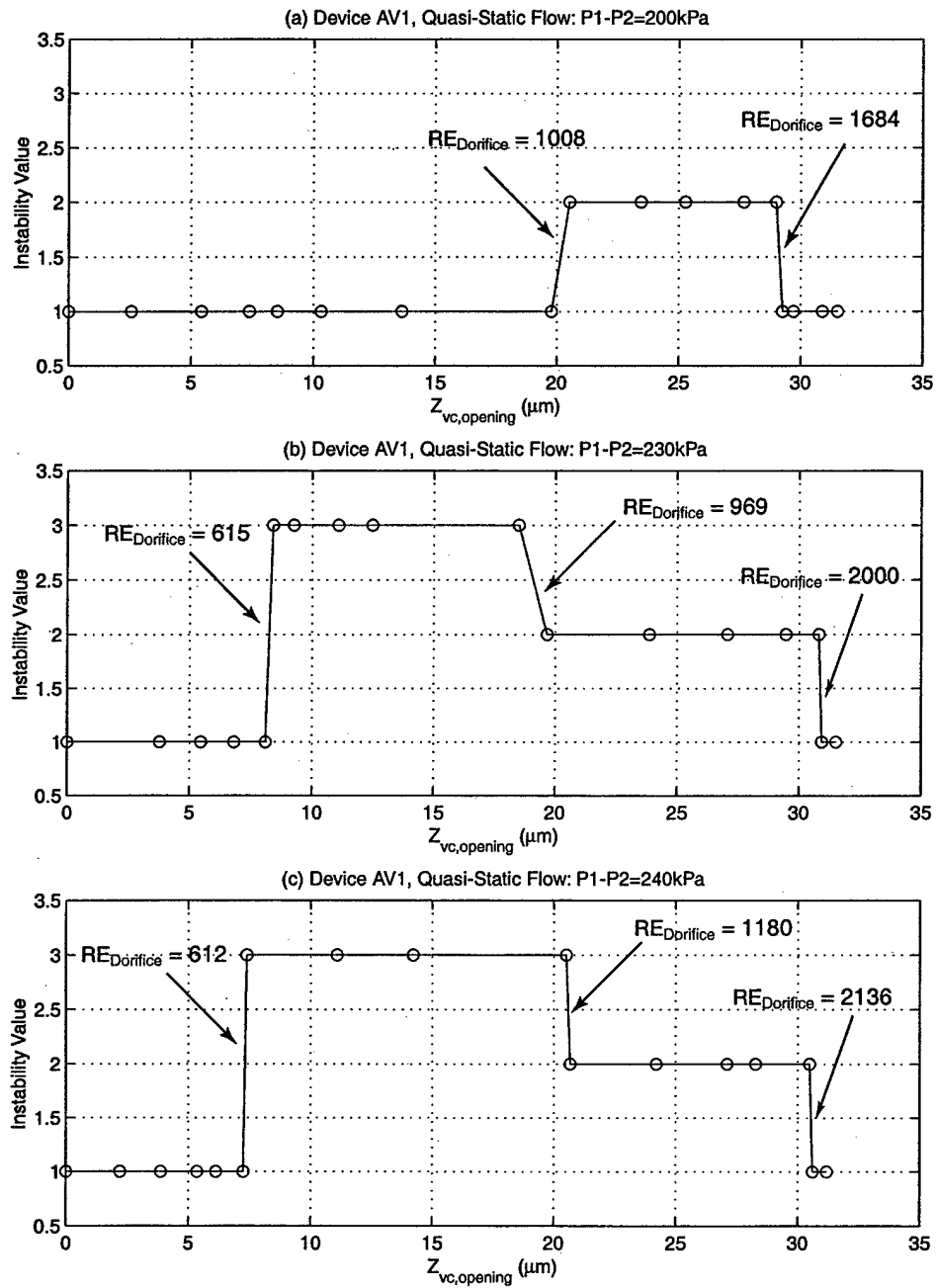


Figure 9.27: Valve cap Instability Values during quasi-static opening for $P_1 - P_2 = 200 \text{ kPa}$, $P_1 - P_2 = 230 \text{ kPa}$, and $P_1 - P_2 = 240 \text{ kPa}$. Corresponding Reynolds numbers are labeled at the transition locations.

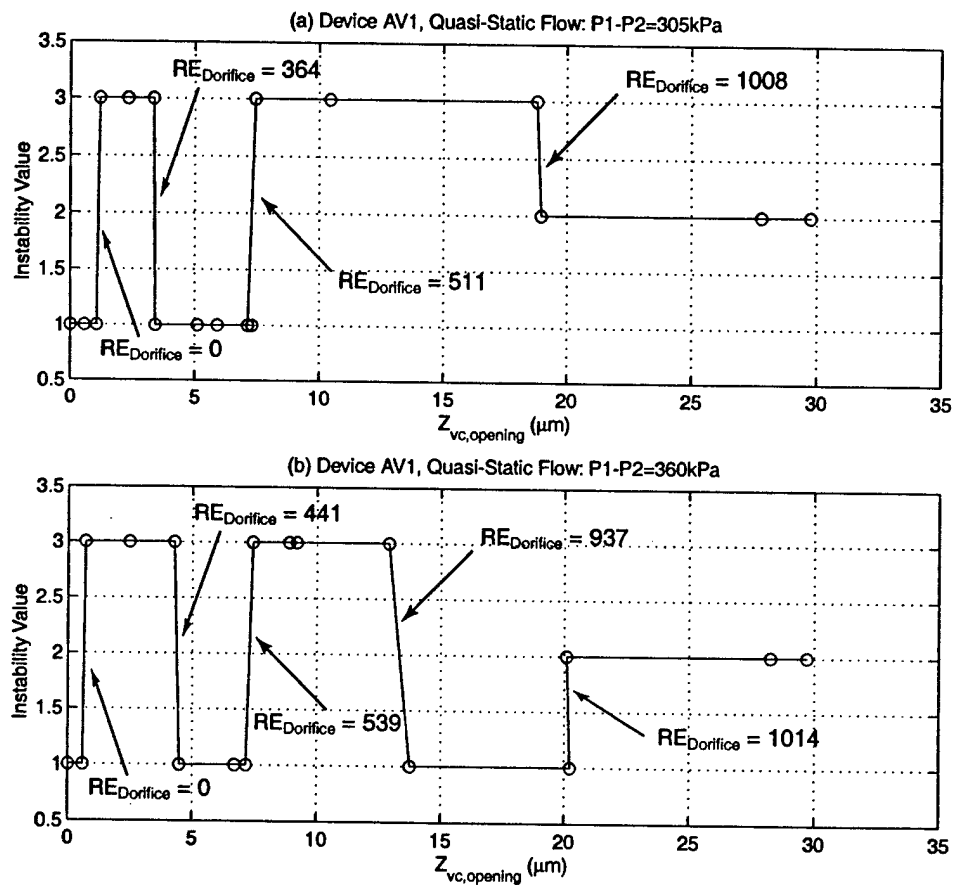


Figure 9.28: Valve cap Instability Values during quasi-static opening for $P_1 - P_2 = 305 \text{ kPa}$ and $P_1 - P_2 = 360 \text{ kPa}$. Corresponding Reynolds numbers are labeled at the transition locations.

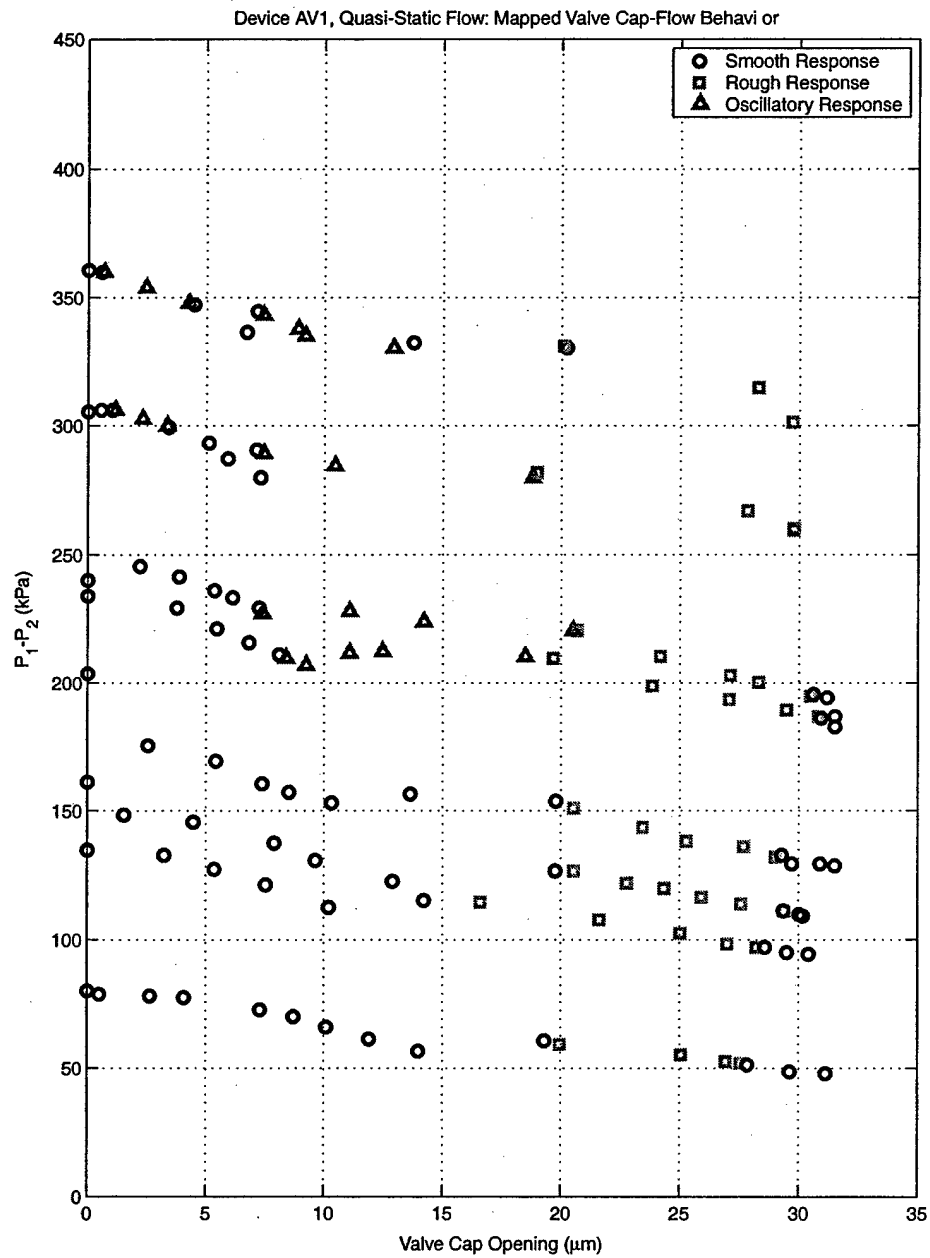


Figure 9.29: Complete grouping of all valve cap Instability Values plotted as $P_1 - P_2$ vs. $Z_{vc,opening}$. Region of valve cap oscillation defined by triangular data points.

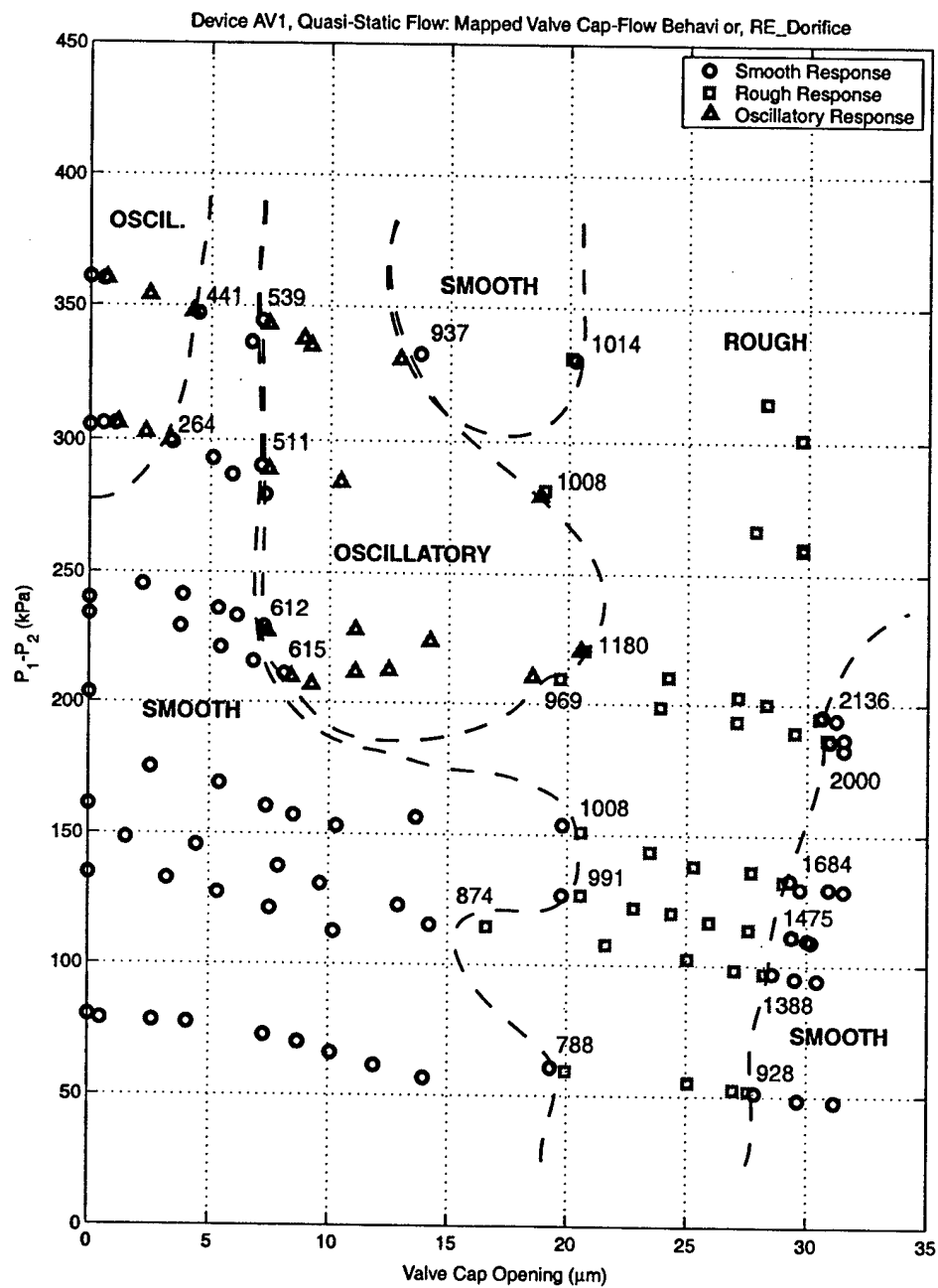


Figure 9.30: Estimated boundaries for smooth, rough, and oscillatory regions plotted as $P_1 - P_2$ vs. $Z_{vc, opening}$. Corresponding transition Reynolds numbers are displayed along these boundary lines.

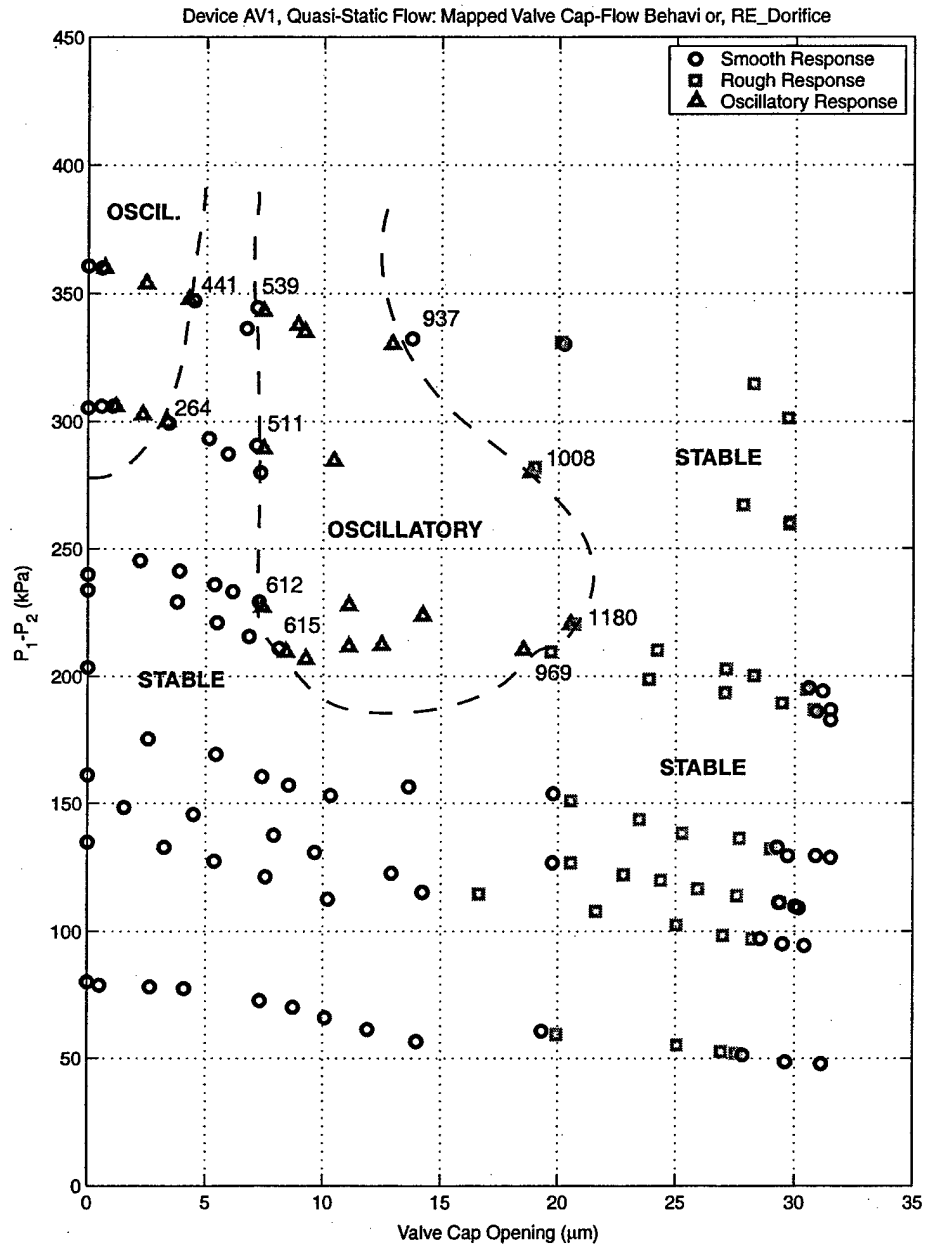


Figure 9.31: Estimated boundaries for unstable and stable regions plotted as $P_1 - P_2$ vs. $Z_{vc, opening}$. Corresponding transition Reynolds numbers are displayed along these boundary lines.

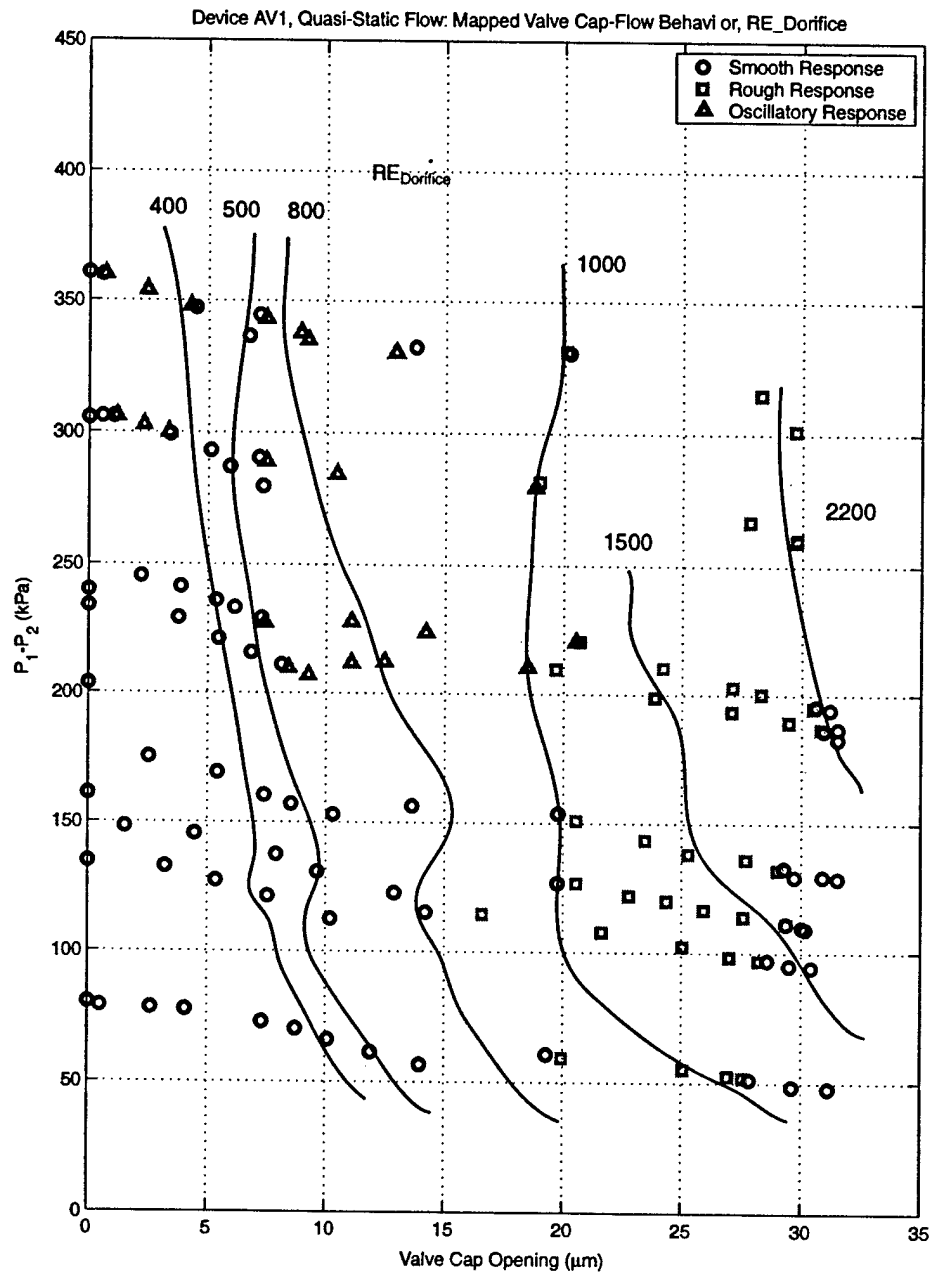


Figure 9.32: Estimated constant Reynolds number curves plotted as $P_1 - P_2$ vs. $Z_{vc,opening}$. Lines are estimated by interpolating between adjacent data points.

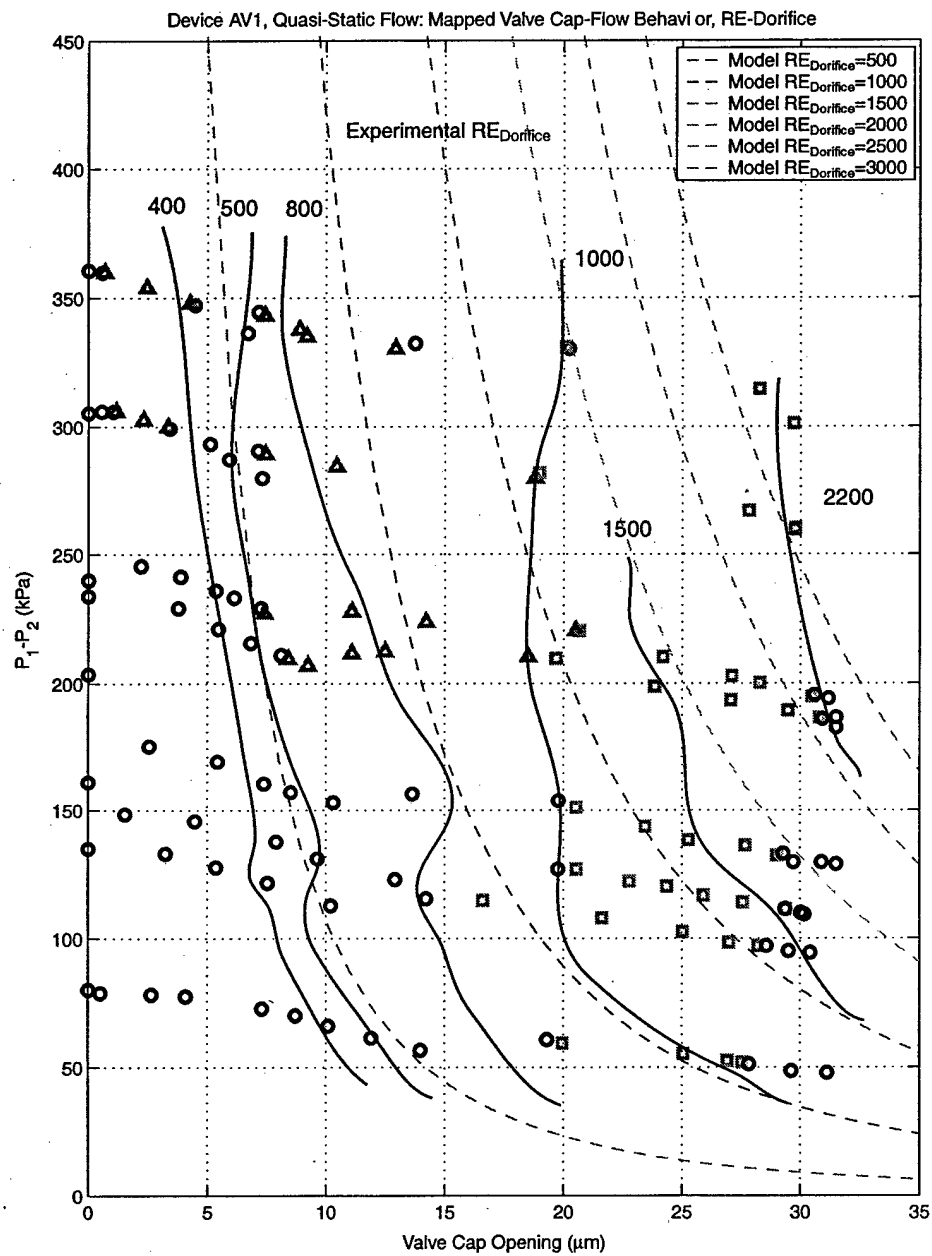


Figure 9.33: Constant Reynolds number curves (experimental vs. model predictions) plotted as $P_1 - P_2$ vs. $Z_{vc,opening}$. Experimental lines are estimated by interpolating between adjacent data points.

The presence of a transition regime between laminar and turbulent flow for the experimental data can be further illustrated by plotting the data in a different way. Typically, in characterizing the physical sections of a fluid system (ie: a constant area pipe, a bend, an orifice, etc), a fluid resistance coefficient for each of the sections can be defined. This resistant coefficient ζ is defined as the total pressure lost through the flow section divided by the dynamic pressure within the flow section [7], written in equation form as

$$\zeta = \frac{\Delta P}{\frac{1}{2} \rho_{fluid} u_{local}^2}, \quad (9.1)$$

where ΔP is the pressure drop through the flow section (in the case of the valve orifice $\Delta P = P_1 - P_2$) and u_{local} is the fluid velocity through the section (in the case of the valve orifice $u_{local} = \frac{Q_{avg}}{A_{orifice}} = \frac{4Q_{avg}}{\pi D_{orifice}^2}$). A universal method for observing the transition between laminar and turbulent flow in a physical section of a flow system is to plot this flow resistance coefficient ζ versus the Reynolds number in that section (in the case of the valve orifice $RE_{D_{orifice}}$). Figure 9.34, taken from [7], shows an example of this type of plot for a generic fluid orifice contraction section of a fluid system, where the quantity $\frac{F_2}{F_1}$ defines the geometric contraction ratio. Notice that for low Reynolds number, ζ is inversely proportional to RE (laminar flow regime) whereas for large RE, ζ is independent of RE (turbulent flow regime). In between these two regions is defined the transition regime where the flow transitions from laminar to turbulent.

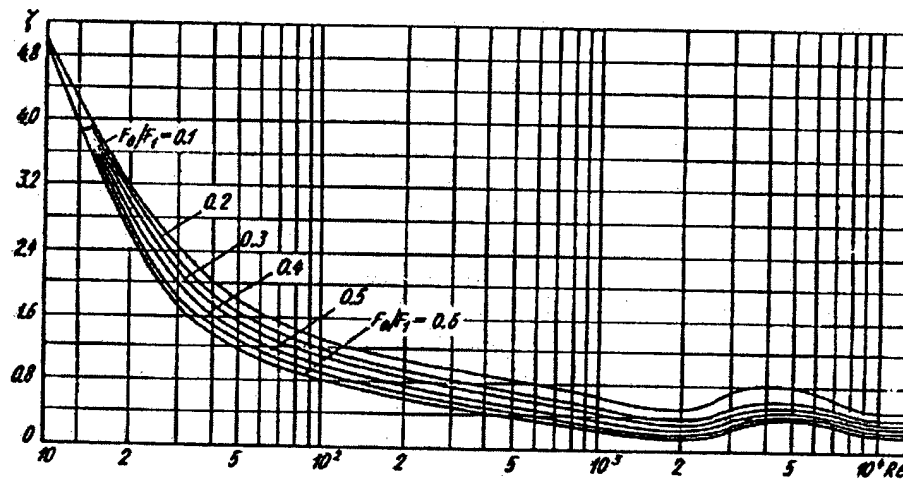


Figure 9.34: Plot of flow resistance coefficient ζ versus Reynolds number for a generic flow orifice contraction structure [7]. The laminar flow regime is characterized by an inversely proportional relationship between ζ and Reynolds number whereas the turbulent flow regime is characterized by no relation between ζ and RE. Transition occurs between these two regimes.

For laminar fluid flow through an orifice, the flow rate is proportional to the applied differential pressure ($Q_{avg} \propto \Delta P$) [2] [7], whereas for turbulent flow the flow rate is quadratically related to the differential pressure ($Q_{avg} \propto \sqrt{\Delta P}$) [2] [7]. Substituting these pressure-flow relations into 9.1, it can be determined that in the laminar flow regime ζ is inversely proportional to the Reynolds number, and that in the turbulent flow regime ζ is independent of the Reynolds number. This is consistent with Figure 9.34. Therefore, for the experimental data in this thesis, a plot similar to Figure 9.34 should be able to be created, where the slope of the ζ curve transitions from a negative value to a value of zero as $RE_{Dorifice}$ increases. In doing this, a determination as to whether the oscillatory valve cap behavior correlates to the transition between the laminar and turbulent flow regimes can be obtained. To evaluate this hypothesis, the experimental data is replotted as $\zeta_{orifice}$ versus $RE_{Dorifice}$ in Figure 9.35.

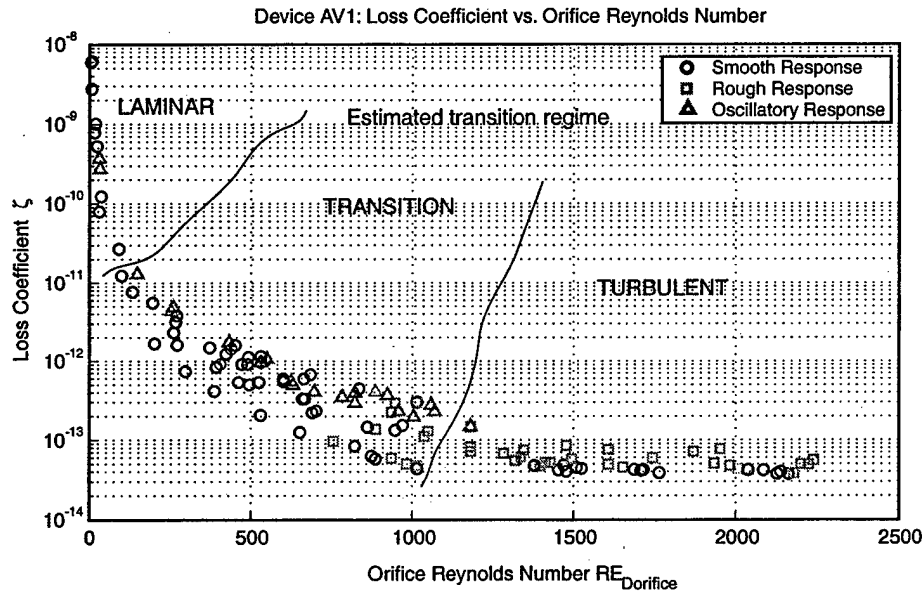


Figure 9.35: Device AV1 estimated laminar, transition, and turbulent flow regimes as a function of $RE_{Dorifice}$ based on experimental data. Laminar regime is characterized by $\zeta \propto \frac{1}{RE_{Dorifice}}$ and turbulent regime is characterized by ζ being independent of $RE_{Dorifice}$. The majority of oscillatory data points occur within estimated boundaries of this transition regime.

Notice that, indeed, for increasing $RE_{Dorifice}$ from 0 to 500, ζ monotonically decreases, and for increasing $RE_{Dorifice}$ from 1100 to 2500, ζ remains constant. One may notice that the points above $RE_{Dorifice} = 1100$ contain both smooth and rough valve cap behavior. Due to the fact that the differentiation between smooth and rough was a difficult task, it could be that in reality the smooth data points were mistaken for rough behavior. However, the important data

points of oscillatory behavior were clearly differentiable from both smooth and rough behavior and therefore there is no question as to their validity. These observations indicate the presence of reasonably well-defined laminar and turbulent flow regimes within the experimental results. Furthermore, the vast majority of the oscillatory data points lie within the region between $RE_{Dorifice} = 500$ and $RE_{Dorifice} = 1100$. Based on these results, it can be argued that the oscillatory behavior of the valve cap is directly related to the presence of transition between laminar and turbulent flow in the valve orifice.

The following question must now be addressed: Does this conclusion that valve cap oscillatory behavior is related to the transition between laminar and turbulent fluid flow make sense? This question is answered through a discussion of laminar, turbulent, and transitional flow regimes based on literature contained within the fluids mechanics community.

As detailed in the fluid modeling portion of Chapter 5, the valve cap and orifice structure consists of two physical flow sections in series: a contraction section followed by an expansion section. Both of these types of flow sections result in the formation of vortices, the severity of which increases as the Reynolds number grows larger. Figure 9.36 (a) and (b) illustrate schematics of a typical fluid expansion section and a fluid contraction section, respectively, and the corresponding regions where vortices are present [7]. In general as fluid passes through these sections, the fluid boundary layers present upstream of the section are not able to remain intact in passing through the section. Shear layers form where the boundary layers separate from the original structural surfaces, and these shear layers tend to roll up in swirling vortices, which create unsteady forces on any surrounding structure [5] (such as the valve cap and membrane in the active valve).

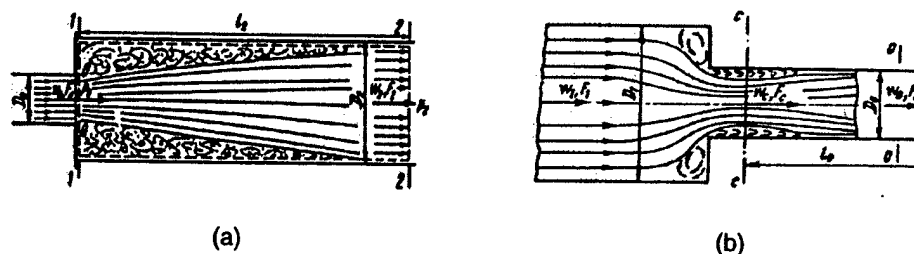


Figure 9.36: Schematic of vorticity formation in contraction and expansion fluid flow sections [7]: (a) expansion section, (b) contraction section.

This unsteady forcing is further enhanced if the flow is experiencing transition between laminar and turbulent behavior. In general, laminar viscous flow is characterized by smooth and steady fluid motion, whereas turbulent flow is characterized by continuous and almost random fluctuation in the velocities of the fluid particles. Both regimes have been studied for

a wide variety of flow geometries. Laminar flow theory is mathematically understood for many of these geometries. Turbulent flow behavior, however, is primarily an experimentally observed fact, which can be analyzed only through statistical understanding [8]. The transition between these two regimes is understood hardly at all. The transition regime is defined as the change (over space, time, and a certain Reynolds number range) of a laminar flow into a turbulent flow. Figure 9.37 illustrates a time history comparison of these three flow regime behaviors.

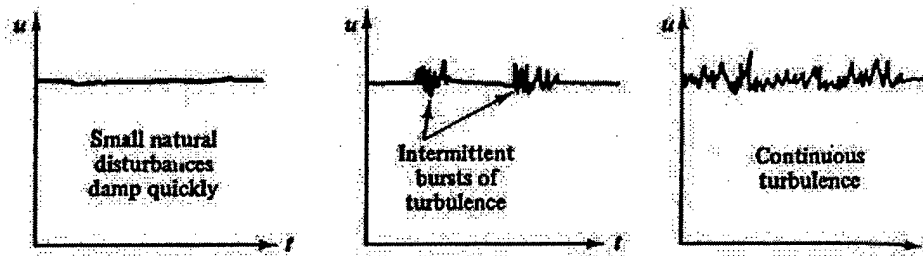


Figure 9.37: Laminar, transition, and turbulent representative flow behavior [8]: (a) laminar flow, (b) transition flow characterized by intermittent bursts of turbulent flow, and (c) turbulent flow.

In laminar flow, there may be occasional natural disturbances in the flow, however, they damp out very quickly. In fully turbulent flow, continuous rapid and random fluctuations are present. In transition, there exist sharp bursts of turbulent fluctuation as the increasing Reynolds number causes a breakdown or instability of laminar motion. Transition through the valve orifice in this thesis, therefore, could very well be characterized by intermittent increases and decreases in the intensity level of the vorticity formation through the orifice, thereby resulting in a significant oscillation of the forcing on the valve cap and the compliant valve membrane structure. It is this vortex-induced structural interaction between the fluid flow and the elastic valve structure that could be setting the valve cap oscillations into motion.

The experimental results presented in this section have provided insight into the approximate value of Reynolds number for which the valve cap structure begins to experience unstable oscillatory behavior. In the valve flow regulation experiments that follow, results will first be obtained for relatively low differential pressure situations to avoid the potential for valve failure due to these oscillations. Once flow regulation has been proved at low differential pressures, tests will then be performed at higher differential pressures to test the limits of the active valve device under these unknown flow regime conditions.

Duty Cycle Flow Regulation Tests

To evaluate the capability of the active valve to regulate flow for applied voltage to the piezo-electric elements, a series of varying duty cycle test runs were carried out for an imposed differential pressure across the valve orifice of $P_1 - P_2 = 35kPa$. This low differential pressure was chosen to ensure flow regimes that do not excite valve cap oscillatory behavior. For each duty cycle run, the valve cap motion was controlled between a minimum valve cap absolute displacement (from its equilibrium position) of $Z_{vc} = 4.0\mu m$ to a maximum valve cap absolute displacement of $Z_{vc} = 11.5\mu m$. Since the valve orifice is located a distance of $16.5\mu m$ above the equilibrium position of the valve cap, it can be stated equivalently that the valve cap opening was controlled between a minimum opening of $Z_{vc,opening} = 5\mu m$ to a maximum opening of $Z_{vc,opening} = 12.5\mu m$. Duty cycle voltage waveforms from zero to 100 were applied to the active valve such that the resulting valve cap motions shown in Figure 9.38 were obtained. A duty cycle of zero means that the valve cap was maintained constantly at its minimum opening of $Z_{vc,opening} = 5\mu m$ and a duty cycle of 100 means that the valve cap was maintained constantly at its maximum opening of $Z_{vc,opening} = 12.5\mu m$. A duty cycle of 30, for example, means that the valve cap was effectively held at its minimum opening for 70% of the cycle and at its maximum opening for 30% of the cycle.

The results of these tests are shown in Figure 9.39. As the duty cycle is increased from zero to 100, the average flow rate through the valve orifice increases monotonically, thereby proving that the valve device is capable of regulating flow. Using the simulation tools detailed in Chapter 5 of this thesis, predicted results for the flow rates were calculated. These are overlayed with the experimental results in Figure 9.39. The comparison indicates that for reasonable valve openings, the measured flow rate correlates quite well with the model predictions. However, for small valve openings near $Z_{vc,opening} = 5\mu m$, the measured flow rate is significantly less than predicted. In essence, the flow appears to be choked more than expected at small valve openings. This observation agrees with the results at small valve openings of the quasi-static flow rate versus valve opening curves discussed previously. As discussed in the previous static flow test section, since the Chapter 5 flow models are based on a compilation of empirical work from other researchers, the lines of predicted behavior in Figure 9.39 are understood to be of only "limited accuracy", in other words, they are not based on exact theory. In addition to modeling the case of a controlled valve opening of $Z_{vc,opening} = 5 - 12.5\mu m$, model predictions for a controlled valve opening of $Z_{vc,opening} = 7 - 14.5\mu m$ and a controlled valve opening of $Z_{vc,opening} = 8.5 - 16.5\mu m$ were also determined. These results are also shown in Figure 9.39 to convey the sensitivity of the offset valve opening on flow rate through the orifice. Shifts of a just a few μm s in the opening direction within the flow models result in significantly increased flow rate values.

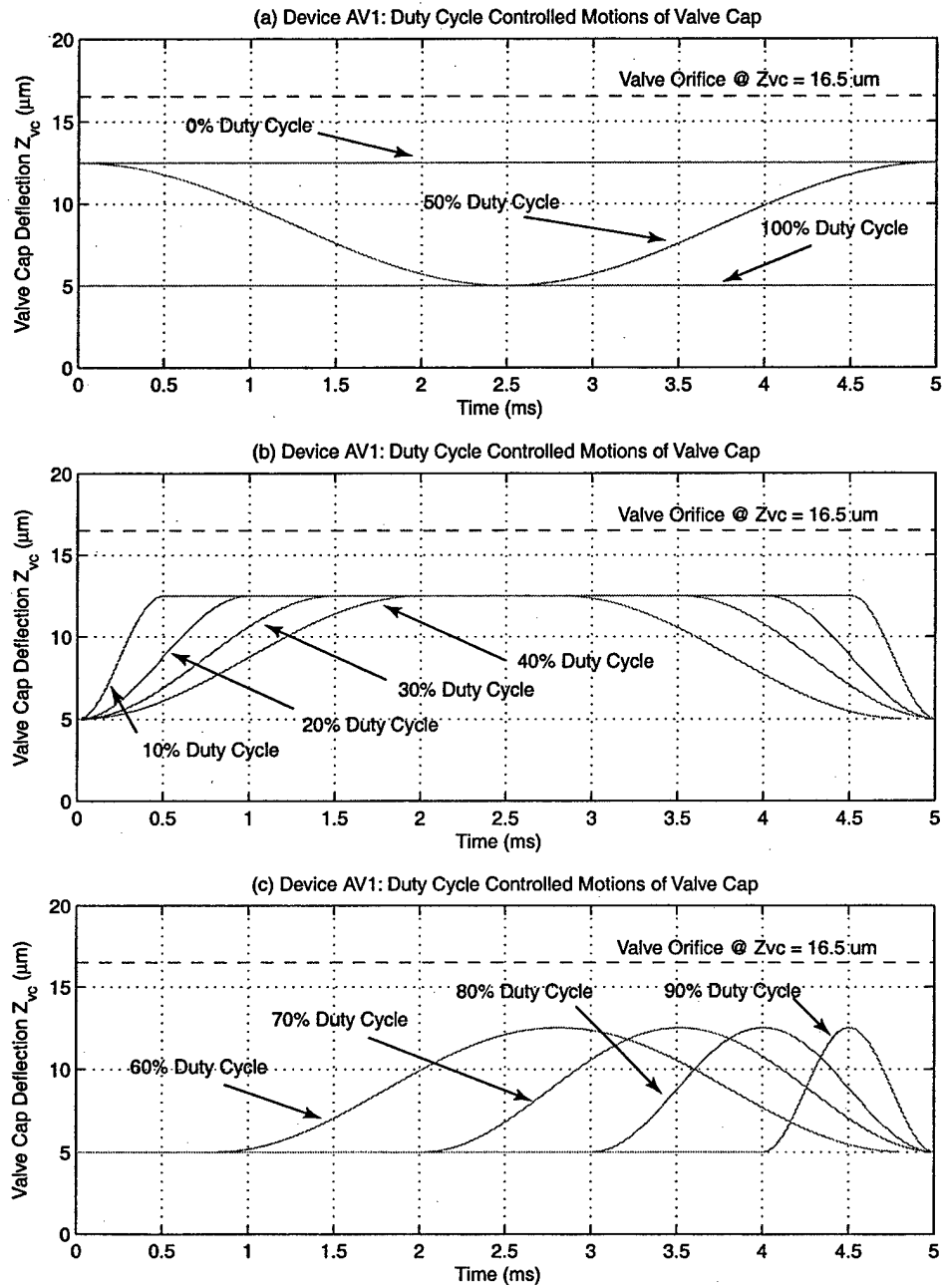


Figure 9.38: Device AV1 valve cap time histories under different duty cycle voltage waveforms to piezoelectric drive element. The valve cap is controlled to reach a maximum valve cap displacement of $Z_{vc} = 12.5 \mu\text{m}$ and to reach a minimum valve cap displacement of $Z_{vc} = 4 \mu\text{m}$.

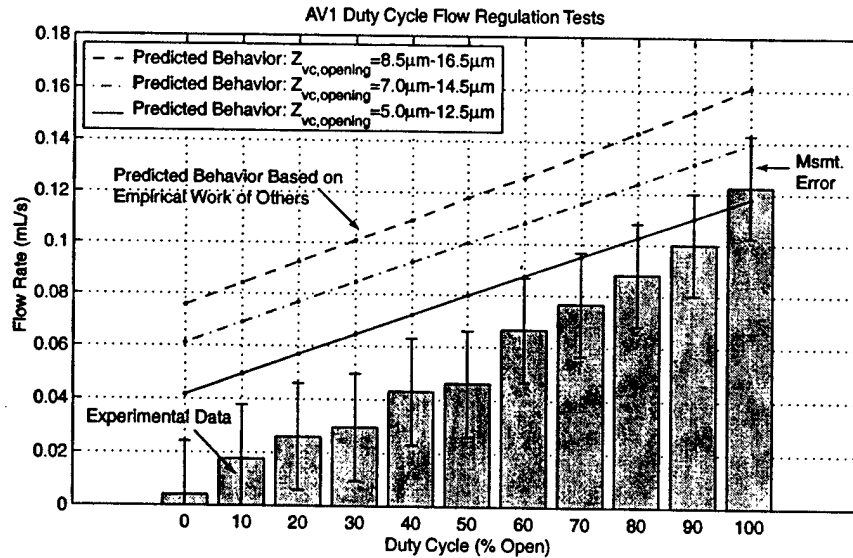


Figure 9.39: Device AV1 model correlation to experimental flow rate results for varying duty cycle inputs. Comparison illustrates good correlation for larger valve openings. For small opening, the flow appears choked. Error bars on the data indicate the measurement error, which was estimated based on the flow sensor calibration error and the accuracy of the applied differential pressure.

1kHz Flow Regulation Tests at Increasing Differential Pressure

To evaluate the capability of the active valve device to regulate flow at 1kHz, a series of tests was carried out for increasing differential pressures across the valve orifice. In addition to proving flow regulation at 1kHz, a further purpose of this study was to determine the maximum differential pressure across which the valve could operate. Since the magnitude of the unstable oscillatory behavior observed for the static flow tests at differential pressures greater than $P_1 - P_2 = 210kPa$ was no more than $3 - 4\mu m$ peak-peak, it was hoped that by operating the active valve device dynamically at 1kHz with total valve cap stroke of $15 - 20\mu m$, the effect of the 5kHz oscillations might not affect the overall flow regulation capability of the valve. As such, tests were performed for differential pressures in excess of $P_1 - P_2 = 210kPa$.

Flow regulation tests at 1kHz were performed for differential pressures $P_1 - P_2 = 24kPa$, $95kPa$, $145kPa$, $200kPa$, $260kPa$, and $340kPa$. By controlling P_{HAC} with respect to the magnitude of P_1 and P_2 , the valve cap was displaced statically upward to a deflection of $Z_{vc} = 11\mu m$. A sinusoidal voltage of $500V_{pp}$ was then applied to the piezoelectric drive element at 1kHz to actuate the valve cap upward against the valve orifice and downward toward the original equilibrium position of the valve cap. In all test runs, it was desired to just barely close the valve cap against the orifice at its maximum displacement, and to maintain $Z_{vc} = 0$ at its

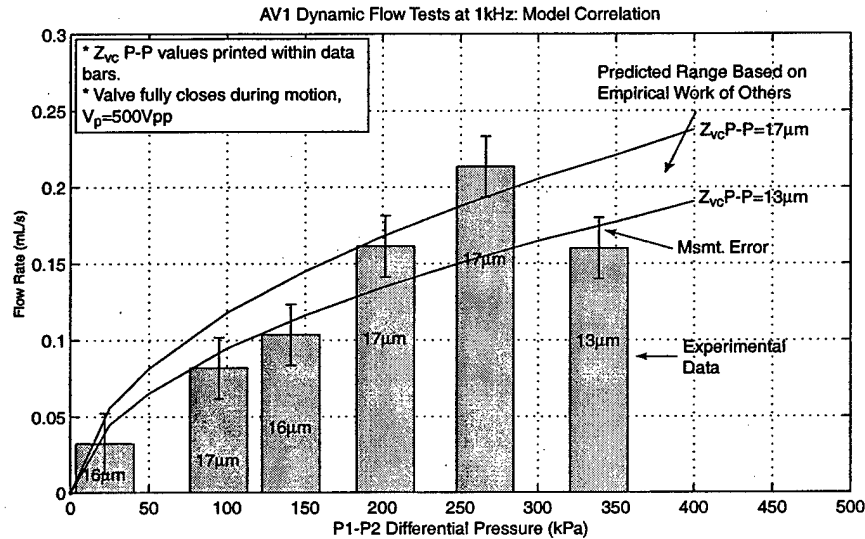


Figure 9.40: Device AV1 dynamic flow regulation model correlation at 1kHz for varying differential pressures. Correlation is good over range of differential pressures. Error bars on the data indicate the measurement error, which was estimated based on the flow sensor calibration error and the accuracy of the applied differential pressure.

minimum displacement. In others words, it was desired to always ensure a valve opening stroke of $16.5\mu m$. Figure 9.40 plots the experimentally measured flow rates for each of the differential pressure test cases. Because of the difficulty in achieving a valve cap stroke during actuation of $Z_{vc,opening} = 16.5\mu m$, the actual measured stroke of the valve cap during actuation is printed inside of each data bar. An applied voltage of 500Vpp was held constant for all of these test runs. It was noticed that for the differential pressure case of $P_1 - P_2 = 340kPa$, a valve cap stroke of $13\mu m$ resulted, rather than the typical $16 - 17\mu m$ of the previous test cases. It was believed in this case that the piezoelectric material capability may have been affected by the high pressure excursions (estimated maximum to be $P_{HAC} \sim 600kPa$) within the HAC chamber.

Figure 9.40 also plots the experimental results versus the model expectations obtained using the active valve simulation tools developed in Chapter 5. Model predictions for the limiting cases of $Z_{vc,opening} = 13\mu m$ and $Z_{vc,opening} = 17\mu m$ are shown. The model correlation indicates that the active valve regulates flow in excellent correlation with the model predictions. As discussed in the previous flow testing sections, since the Chapter 5 flow models are based on a compilation of empirical work from other researchers, the line of predicted behavior in Figure 9.40 is understood to be of only "limited accuracy", in other words, it is not based on exact theory. Upon carrying out a subsequent test run at $P_1 - P_2 = 450kPa$, as the differential pressure was being set across the valve orifice, the valve cap was observed to begin oscillating (with no

applied piezoelectric drive element voltage at this point). Very quickly afterward (fractions of a second, the valve cap lodged itself permanently against the bottom orifice. Subsequent efforts to move the valve cap upward by pressurizing and depressurizing the HAC chamber resulted in a $1\mu\text{m}$ amplitude tilting of the valve cap. Based on this response, it is believed that the valve membrane fractured in response to the oscillatory valve cap motion caused by unstable transitional flow through the valve orifice. Because this device failed in this manner, experimental testing of active valve device AV1 was concluded.

9.4 Conclusions

This chapter has summarized the experimental tests performed on active valve devices AV1 and AV2. Both devices were proven to successfully operate as piezoelectrically-driven hydraulic amplification micro-actuator structures. For applied piezoelectric voltages up to 600V_{pp} at 1kHz , these devices demonstrated amplification ratios of drive element deflection to valve cap deflection of $40\times$ - $50\times$. These amplification ratios correlate within $5 - 10\%$ of the model expectations. Although valve cap peak-peak deflections for the applied voltage levels were measured to be $20 - 30\%$ lower than model expectations for the idealized E_p and d_{33} piezoelectric material coefficients used in the design optimization chapters of this thesis, correlation to model results that incorporate modified piezoelectric material properties based on proper experimental characterization of the material is within $5 - 10\%$.

Flow regulation experiments on active valve device AV1 proved that this valve structure can successfully regulate fluid flow at a frequency of 1kHz for valve cap peak-peak displacements of $17\mu\text{m}$ up to differential pressures of 260kPa . For this condition, a peak average flow rate through the device of 0.21mL/s was obtained under a sinusoidal drive voltage of 500V_{pp} . Additionally, quasi-static differential pressure-flow rate curves were measured up to a differential pressure of 210kPa for the full range of valve cap stroke up to $33\mu\text{m}$. The measured flow rates were $10 - 30\%$ lower than the expected flow rates based on the models presented in Chapter 4. Self-oscillatory motion of the valve membrane was observed for various combinations of valve cap opening and differential pressures in excess of 210kPa . The nature of the flow behavior (based on Reynolds number) was studied for a variety of valve opening situations. The results indicate that these self-excited valve cap oscillations were most probably a result of transitional flow (between laminar and turbulence) through the valve orifice structure, a regime which limited the valve operation to relatively low differential pressures below 350kPa . Overall, this piezoelectrically-driven hydraulic amplification microvalve was successfully proven to regulate fluid flow through microscale channels at high frequency.

Bibliography

- [1] C.Y. Lin, Ph.D. Thesis. MIT. 2002.
- [2] K.T. Turner, An Evaluation of Critical Issues for Microhydraulic Transducers: Silicon Wafer Bonding, Strength of Silicon on Insulator Membranes and Gold-Tin Solder Bonding. MIT Master's Thesis. June 2001.
- [3] TRS Ceramics Data Sheet for PZN-PT.
- [4] Dow-Corning data sheet on silicon oil.
- [5] R.D. Blevins, Formulas for Natural Frequency and Mode Shape, R.E. Krieger, Malabar, FL, 1984.
- [6] J. Carretero and K.S. Breuer, "Measurement and Modeling of the Flow Characteristics of Micro Disk Valves," Proceedings of the 1994 International Mechanical Engineering Conference and Exposition: Microfluidics Symposium, Orlando, FL, Nov. 2000.
- [7] I.E. Idelchik, "Handbook of Fluid Resistance," CRC Press, Boca Raton, FL, 1994.
- [8] F.M. White, "Viscous Fluid Flow," McGraw-Hill, New York, NY, 1991.

Chapter 10

Conclusions and Recommendations

This chapter summarizes the modeling, design, fabrication, and testing research presented in this thesis. The thesis objectives and the thesis contributions are reviewed. Conclusions are drawn based on the results presented and recommendations for future work are detailed. Additionally, it is the purpose of this chapter to evaluate the impact of these thesis results on the performance capabilities and overall future of Micro-Hydraulic Transducer systems.

10.1 Summary and Conclusions

10.1.1 Thesis Summary

The primary objective of this thesis was to develop, from the initial concept stage to the experimental testing of a fabricated device, a piezoelectrically driven hydraulic amplification microvalve for high frequency control of high pressure fluid flow. This research was carried out through a series of modeling, design, fabrication, assembly, and experimental testing tasks. This work demonstrated the valve concept and evaluated the valve performance in comparison to behavior predicted by the models developed in the thesis.

A secondary goal of this thesis was to provide a framework of linear and non-linear structural modeling tools and design procedures that can be implemented in the development of high frequency piezoelectric micropumping and microvalving systems. Additionally, a further goal of this thesis was to present a method for small-scale bulk piezoelectric material integration within silicon micromachined thin-tethered structures, a procedure which can enable the realization of compact high-frequency high-stiffness hydraulic actuator structures.

These objectives were divided into two major sections of the thesis. The first section, consisting of Chapters 1 through 5, focused on the conceptual design of the active valve structure, the development of structural modeling tools to predict the important linear and non-linear structural behaviors of the device component structures, the implementation of these modeling

tools within an active valve simulation architecture, and the development of a systematic design procedure that can be used to generate an active valve geometry based on external hydraulic system performance requirements. The second section, consisting of Chapters 6 through 9, highlighted the fabrication challenges inherent in building this active valve device and defined the fabrication process flow for the assembly of the device, including piezoelectric material integration. Additionally, comprehensive experiments were carried out to experimentally evaluate the piezoelectric drive element sub-component structure, the valve cap and membrane sub-component structure, and the full piezoelectrically-driven hydraulic amplification microvalve device. Each of the chapters is summarized below.

Chapter 1 introduced the concept of the piezoelectrically-driven hydraulic amplification microvalve for use in high specific power hydraulic pumping applications. High frequency, high force actuation capability in the valve is enabled through the incorporation of solid-state bulk piezoelectric material elements beneath a compact and stiff structural piston mechanism. High stroke valve motion is achieved through the incorporation of a hydraulic amplification chamber between the moveable piston structure and a micromachined valve membrane. This enclosed fluid chamber, connecting the large cross-sectional area piston structure to a smaller cross-sectional area valve membrane structure, enables an amplification (40 – 50x) of the limited piezoelectric material stroke into a significantly increased valve membrane and valve cap deflection. These design features enable the valve device to simultaneously meet a set of high frequency, high pressure, and large stroke requirements that have not previously been satisfied by other microvalves presented in the literature.

Chapter 2 introduced the geometry of the active valve device and detailed the important structural elements within the device that needed to be accurately modeled. The structural deformations of the piezoelectric material elements, the drive element piston, the bottom support structure, the hydraulic amplification chamber, the top support structure, and the valve cap and membrane structure were modeled using linear plate theory, with bending and shearing deformation effects included. Additionally, theoretical studies were performed to demonstrate the benefits, by stiffening the drive element piston actuation structure, of integrating multiple piezoelectric material elements spread out beneath the drive element piston rather than integrating just a single centrally-located material element beneath the piston. These studies provided the optimal dimensional spacing of the three piezoelectric elements beneath the drive element piston in the fabricated and experimentally characterized active valve devices presented in Chapter 9.

Chapter 3 presented the development of a numerical code to model the large deflection behavior of a thin annular plate structure with rigid central cap under pressure loading. The work presented in this chapter was based on a finite-difference scheme developed by Su [1]. This numerical code served as a modeling tool for use in the full active valve non-linear model and

system simulation presented in Chapter 4. The theory was specifically developed to capture the non-linear stiffening effects present in the valve membrane structure of the active valve. The linear plate theory representation that was presented in Chapter 2 is not able to capture these stiffening effects. A series of valve cap and membrane geometries and pressure loading scenarios, characteristic of those found and experienced in the final active valve device, was presented to demonstrate the capabilities of this modeling tool to capture the large deflection behavior of the structure.

Chapter 4 presented a complete quasi-static structural model of the active valve. This model was comprised of the linear and non-linear modeling tools presented in Chapters 2 and 3, respectively. An evaluation of the assumptions within the structural model was performed through a series of comparison studies to a finite-element model of the active valve structure for a variety of loading scenarios. In addition, the chapter introduced a dynamic simulation architecture for the valve, which included inertia and damping associated with the drive element piston and valve cap structural elements. Calculation of the coupled fluid-structure resonant valve frequency, based on finite-element analyses, was also presented. The predicted resonance was based on a finite-element model that did not include the added mass of the fluid above the valve cap and membrane structure. As a result, this model overpredicted the valve resonant frequency in comparison to experimental results on the fabricated valve devices detailed in Chapter 9.

Chapter 5 formulated a systematic quasi-static design procedure that can be used to generate an active valve geometry based on external hydraulic system performance requirements. This design procedure was based on the modeling tools and simulations developed in Chapters 2, 3, and 4 of the thesis. Additionally, the procedure incorporated the governing fluid flow relations linking the valve cap motion to the external hydraulic system pressures and enabled variation of key parameters within the active valve geometry (such as valve membrane thickness and the number of valve membranes used in parallel) to satisfy predetermined valve membrane stress limitations. A powerful characteristic of the systematic design procedure is the ability to monitor the stress at all positions along the valve membrane for any and all potential pressure loading scenarios experienced by the structure. This enables the designer to very accurately predict the maximum stress that the valve membrane will experience during its full actuation cycle as it opens and closes against the fluid orifice. As a check, full system dynamic simulations were run to validate the goodness of the valve geometry created using the quasi-static design procedure.

Chapter 6 presented an overview of the fabrication challenges encountered and the solutions implemented in the development of the active valve device. These challenges included the wafer-level etching of the drive element and valve membrane structures, the wafer-level silicon-to-silicon and silicon-to-glass bonding operations, preparation and integration of the piezoelec-

tric material elements with the device, die-level assembly and bonding procedures, and the filling of degassed fluid within the hydraulic amplification chamber following device assembly. Additionally, the modeling and design of a micromachined high-resistance fluid channel was documented that enabled a static bias pressure to be imposed on the hydraulic amplification chamber without affecting the high-frequency actuation behavior of the active valve device.

Chapter 6 also presented a detailed sub-component testing plan for the active valve structure. This systematic plan separated the complete active valve structure into manageable sub-component devices according to the primary challenges previously detailed. The piezoelectric drive element sub-component study, whose purpose it was to prove the ability to micromachine the tethered piston structure and integrate bulk piezoelectric material beneath the piston, and the valve cap and membrane sub-component study, whose objective it was to validate the non-linear large deflection behavior of the valve membrane structures, were outlined. Additionally, the full active valve testing plan was outlined.

Chapter 7 presented the experimental results for the piezoelectric drive element sub-component study. A series of drive element devices was fabricated in an effort to demonstrate that both standard polycrystalline PZT-5H piezoelectric material as well as higher-strain single-crystal PZN-PT piezoelectric material could be incorporated beneath micromachined piston structures. An additional goal was to demonstrate that devices with three piezoelectric elements spread out beneath the drive piston could be manufactured in a reliable manner. Quasi-static high-voltage experimental tests were performed on these devices at a frequency of 15kHz and dynamic low-voltage frequency tests were carried out between frequencies of 10kHz and 200kHz to identify modal characteristics.

The results indicated that the procedure formulated in Chapter 6 for integrating piezoelectric material elements, both PZT-5H and PZN-PT, within these micromachined structures is repeatable. All devices fabricated experienced a tolerance match between the piezoelectric elements and the surrounding supporting structures within $\sim 1\mu m$, thereby ensuring predictable "push-up" of the piston structure during assembly. Drive element devices incorporating a single piezoelectric material beneath the piston experienced modal "1- Θ " tilting behavior at frequencies as low as 30kHz. Additionally, quasi-static actuation of the devices at 15kHz and 1000Vpp resulted in a slight tilting of the piston structures as they moved up and down through their actuation cycles. These tilting effects were attributed to imperfect placement of the piezoelectric element beneath the center of the piston and to non-uniform fillet radius etch profiles, characterized through microscope measurements, around the etched tether of the piston. Drive element devices incorporating three piezoelectric material elements experienced negligible tilting behavior during actuation at 15kHz and 1000Vpp due to the enhanced support of the piston from below. For these devices, modal behavior was not observed until frequencies in excess of 50kHz. This sub-component study successfully demonstrated the capability to fabricate and

assemble these component structures for use in full active valve devices.

Chapter 8 presented the experimental results for the valve cap and membrane sub-component study. A series of valve membrane structures was fabricated and inspected to ensure adequate fillet radius control at the base of the etched features. Pressure-deflection experiments were carried out for differential pressures across the structure of up to 200kPa in an effort to characterize its non-linear large deflection behavior. Theoretical studies, using the non-linear numerical tools presented in Chapter 3, were carried out to determine deformation and membrane stress sensitivities to valve membrane thickness and fillet radius size. The experimental valve cap deflections, in response to pressure loading, were found to correlate within $\sim 5\%$ of theoretical expectations. The valve membranes were deflected sufficiently to impact the valve stop in glass Layer 6, a condition which results in a predicted membrane stress of 0.65GPa. In these tests, no membranes fractured. This sub-component study successfully demonstrated the capability to fabricate the valve cap and membrane structure required in the full active valve device and verified that this structure behaves as predicted in its non-linear large deflection regime.

Chapter 9 presented the experimental results of the full active valve testing study. The goals of these experiments were to evaluate the quasi-static and dynamic structural performance of the active valve device and determine some initial limitations in its ability to regulate fluid flow against imposed differential pressures. For the purposes of this study, two active valve devices were built and experimentally characterized. Both devices were proven to successfully operate as piezoelectrically-driven hydraulic amplification microactuator structures. For applied piezoelectric voltages up to 600Vpp at 1kHz, these devices demonstrated amplification ratios of drive element deflection to valve cap deflection of 40x-50x. These amplification ratios correlate within 5 – 10% of the model expectations. Although valve cap peak-peak deflections for the applied voltage levels were measured to be 20 – 30% lower than model expectations for the idealized E_p and d_{33} piezoelectric material coefficients used in the design optimization chapters of this thesis, correlation to model results that incorporate modified piezoelectric material properties based on proper experimental characterization of the material is within 5 – 10%.

Flow regulation experiments proved that this valve structure can successfully regulate fluid flow at a frequency of 1kHz for valve cap peak-peak displacements of $17\mu m$ up to differential pressures of 260kPa. For this condition, a peak average flow rate through the device of 0.21mL/s was obtained under a sinusoidal drive voltage of 500Vpp. Additionally, quasi-static differential pressure-flow rate curves were measured up to a differential pressure of 210kPa for the full range of valve cap stroke up to $33\mu m$. The measured flow rates are 10 – 30% lower than those expected based on the models presented in Chapter 4. The onset of transition and turbulent flow regimes, which depending on the valve cap opening and the differential pressure could set the valve cap into self-excited oscillatory motion, was identified for differential pressures in excess of 210kPa. The nature of the flow behavior (based on Reynolds number) was studied

for a variety of valve opening situations. The results indicate that these self-excited valve cap oscillations were most likely a result of a transition flow regime between laminar and turbulence through the valve orifice structure, a regime which limits the valve operation to relatively low differential pressures below 350kPa. Overall, though, this piezoelectrically-driven hydraulic amplification microvalve has been successfully proven to regulate fluid flow through microscale channels at high frequency.

10.1.2 Thesis Contributions

The results presented in this thesis support the following conclusions, which address the primary objectives of this research:

1. A piezoelectrically-driven hydraulic amplification microvalve is a viable concept for the regulation of high differential pressure ($> 300kPa$) fluid flows at high frequency ($\geq 1kHz$), resulting in significant fluid flow capability.
2. Integration of miniaturized bulk piezoelectric materials (with dimensions less than 1mm x 1mm x 1mm) within micromachined thin-tethered piston structures is a viable method for achieving compact high frequency, high force actuation capability in microhydraulic systems.
3. Linear and non-linear modeling tools for the design of active valve devices, such as this one which incorporate thin-membrane valve structures, have been developed. These modeling tools enable accurate monitoring of real-time membrane stress levels at all locations along the membrane for all potential pressure loading scenarios experienced by the structure.

Although performing short of the original frequency and differential pressure design specifications set forth at the beginning of this thesis, the demonstrated valve capabilities place this device superior to any other microvalve presented in the literature (see Chapter 1) for simultaneously meeting a set of high frequency (1-10kHz), high pressure(0.1-1MPa), and large stroke (15-40 μm) requirements for regulating liquid fluid flows in micro hydraulic systems. It is the belief of this author that future design iterations could be successful in creating a microvalve structure that could operate at a frequency of 10-15kHz against differential pressures approaching 1MPa. The following section details further work that could enable this design goal and addresses the question "What do the results of this thesis mean to the overall future of high-specific power Micro-Hydraulic Transducer systems?".

10.2 Recommended Further Work and the Future of MHTs

The results presented in this thesis have identified a number of issues and areas which require further development and investigation. In this section, these issues will first be organized into those that are deemed fundamentally critical for the development of the next generation piezoelectrically-driven hydraulic amplification active valve to meet the high frequency ($>10\text{kHz}$) and large differential pressure ($\sim 1\text{MPa}$) requirements set forth at the beginning of this thesis, and those that are worth investigating as a means to make modest improvements in device performance and to ease manufacturability concerns. Once this overall list has been defined, each of the issues will then be discussed in detail.

Based on the results of this thesis, it is clear that a piezoelectrically-driven hydraulic amplification microvalve can be designed, built, and successfully operated to regulate liquid fluid flows. The valve design experimentally characterized in this thesis, however, fell short of its operational goals in two primary ways. The first of these shortcomings was the valve's low 1st modal structural frequency (5kHz), which limited valve quasi-static operation frequency to $1\text{-}2\text{kHz}$. Since the original design goal was to operate this valve within an MHT system at a frequency of at least 10kHz , it can be stated that the valve severely underperformed. This is a shortcoming that this author believes can be overcome in future design iterations with more attention given to the important fluid-structural coupling and added mass phenomena that directly affect the valve's dynamic behavior. The second of these shortcomings was the unexpected interaction between the valve structure and the fluid flow at differential pressures in excess of 210kPa . Chapter 9 included a thorough analysis of the related experimental data, resulting in the conclusion that the unstable self-oscillatory valve cap behavior was most probably caused by instabilities within the flow regime (such as vortices) as a transition from laminar to turbulence occurs. Whereas the first shortcoming can be overcome fairly easily within a redesign effort, this flow-induced instability issue is likely to require significantly more effort in the future (both in modeling and in detailed experimentation) to better characterize the fluid flow regimes that occur through these sorts of microvalve orifices and to more accurately capture interactions between these flow phenomena and adjacent compliant structures (such as the valve cap and membrane in this active valve design).

The two issues previously discussed are the critical ones which have most severely limited this active valve to lower than desired performance levels. On the positive side, however, it can be confidently stated that all of the structural models developed in this thesis for predicting quasi-static valve performance (Chapters 1-5) were in extremely good correlation with the 1kHz experimental data presented in Chapter 9. The experimentally characterized valve cap deflections and valve amplification ratios for the full range of operating voltages were within $5\text{-}10\%$ of model expectations, a result which confirms these documented models as important

tools within future valve design iterations. The additional areas of recommended future work (in addition to the two major issues discussed above), therefore, fall not within the realm of active valve structural modeling, but rather within the area of material characterization and microfabrication. Under the heading of material characterization is, first, the need for better understanding of single-crystal PZN-PT piezoelectric materials and, second, the need for better understanding of the stress limitations within etched single-crystal silicon material (especially SOI wafers). Under the heading of microfabrication are a variety of issues relating to the manufacturability of this highly-complex, multilayer valve structure.

In summary, the recommended future work is divided into the following sections: (1) a valve structural redesign phase to enable quasi-static operational frequencies at or above 10kHz, (2) a major program to characterize the flow regimes through microvalve orifices and to understand the potential impact that this flow behavior has in interacting with adjacent compliant structures (flow induced structural instabilities), (3) further characterization of the actuation capabilities of single-crystal piezoelectric materials and the stress limitations of SOI etched structures, and (4) the re-evaluation of user-intensive microfabrication steps and the development of a less complex active valve structure. These sections of recommended future work are discussed in detail in the following sections.

10.2.1 Redesign for Enhanced Operational Frequency

The modal frequency model correlation studies performed in Chapter 9 identified the hydraulic amplification chamber geometry as a key contributor to the reduction in frequency of the valve 1st modal frequency. Additionally, it was determined that the added mass of the external fluid above the valve cap and membrane structure had an important effect in limiting this frequency as well. A redesign effort should be performed on this active valve to increase its first modal frequency to within the range of 10-15kHz. The active valve geometry tested in this thesis incorporated a Layer 6 HAC chamber geometry characterized by a chamber height of $t_{HAC} = 200\mu m$ and a series of small dimensioned through-holes and flow channels (with dimensions as small as $100\mu m$) connecting the lower half of the HAC chamber to the upper half of the chamber. This intricate geometry was required in order to guarantee the presence of a rigid motion stop $\sim 16.5\mu m$ below the underside of the valve cap. In such closely-packed structures, inertial coupling between the structural elements and the accelerating fluid can significantly reduce modal frequencies of the system, as discussed in Chapter 9. The next generation active valve should incorporate an HAC chamber with reasonable height (ie: $t_{HAC} = 500\mu m$) and without any complex arrangement of holes and channels. The chamber should be a single simple cylindrical volume defined on its bottom surface by the tethered piston and on its top surface by the valve cap membrane and top support structure. In this re-design, no bottom stop would be present, a necessary consequence. Based on experimental

testing in this thesis, the valve should still operate successfully without this stop present. The simplification of this chamber geometry will, therefore, minimize the effect of inertia coupling and allow for a higher 1st modal frequency. One may argue that a larger volume fluid chamber will increase the compliance of this coupling mechanism between the piston and the valve membrane, an argument which is true. However, the degree to which performance would be reduced is negligible compared to the benefit of a higher operating frequency. Additionally, by incorporating the external fluid above the valve cap and membrane within future finite-element models, the influence if this added mass can be taken into account in designing a valve to meet a quasi-static frequency greater than 10kHz.

The modal frequency model correlation study performed in Chapter 9 also presented the effect of valve membrane thickness on the overall 1st valve modal frequency. It was shown that an increase in valve membrane thickness from $t_{vm} = 6\mu m$ to $t_{vm} = 10\mu m$ would increase the 1st modal frequency of the active valve from 14kHz to 20kHz (without fluid above valve cap and membrane). This is based on the fact that, in general, the stiffness of a plate scales with the cube of its thickness. This stiffening would help to increase the modal frequency, however, it would require more actuation authority from the drive element portion of the valve. Based on the tradeoffs documented in Chapter 5 of this thesis, such a tradeoff in frequency for a slightly larger piezoelectric material volume beneath the piston is worthy of investigation in the next generation design. Careful attention to the potential deflections and predicted stress levels seen in this larger thickness membrane during actuation would be required to maintain structural integrity. In essence, this redesign effort should use the exact modeling tools documented in Chapter 5 of this thesis, but include a more rigorous modal frequency evaluation during the process. An additional benefit of a thicker valve membrane would be the potential for reducing the magnitude of the flow-induced instability (to be discussed in the following section) caused by the interaction of the fluid flow through the orifice with the adjacent compliant valve membrane. A significantly stiffer membrane structure might eliminate the severity of this interaction all together.

10.2.2 Understanding of Flow Induced Structural Instabilities

For the active valve devices experimentally characterized in this thesis, flow-induced structural vibrations of the valve cap and membrane limited the differential pressure across which the active valve could regulate flow. Although significant analysis work was performed on the experimental data containing this instability behavior and although a plausible explanation for the said behavior was put forth in the conclusions of this thesis, it is believed by the author that a vast number of fluid flow issues and questions must be further investigated and answered before the observed phenomena can be understood fully and before the impact on full MHT systems can be estimated. These issues focus on two major tasks: (1) the characterization

of the flow behavior through microvalve orifices and (2) the understanding of the interaction between this flow through microvalve orifices and any adjacent compliant structures. These tasks are detailed in the following sections.

Flow Characterization Through Microvalve Orifices

The majority of experimental testing on valves for use within microsystems has been done on macroscale valves. The fluid models used throughout this thesis, in fact, were based on this method of testing, with the results being accepted at the microscale [2]. In order to fully understand the flow behavior as the Reynolds number passes from zero to in excess of 10,000 during valve opening and closing, and in particular, to understand the critical nature of the transition regime between laminar and turbulent flow, microscale valve experiments must be carried out. These experiments must utilize rigid valve cap structures that are in no way affected by the fluid flow, and conversely, that do not themselves influence the flow behavior. In this way, an understanding of vortex formation and flow instabilities can be obtained independent of adjacent compliant structures. Tests could be performed using many of the microfabricated layers used for the active valve in this thesis. However, one would need to incorporate a precisely controlled solenoid or long piezoelectric stack actuator bonded to a rigid valve cap (without an adjacent compliant membrane) which could be moved upward and downward against the fluid orifice. It is critical that no compliant structures exist in the region of the orifice flow so that the resulting flow behavior is solely a function of the orifice geometry and applied operating conditions. The following experimental tests could be carried out:

1. Slow static valve opening tests, identical to those performed in the instability section of Chapter 9, whereby the valve cap is lowered from its fully closed position against the valve orifice over a sufficiently long period of time (~ 10 minutes) to ensure flow behavior for a static valve opening. The valve cap deflection, flow rate, and dynamic pressure directly upstream and downstream of the valve cap should be measured and recorded real-time. Without a compliant structure (ie: the valve membrane) present during this test, an understanding of the relationships between differential pressure, flow rate, and dynamic pressure can be obtained and an estimation of the laminar, transition, and turbulent flow regimes could be carried out.
2. In conjunction with the test described above, flow velocimetry measurement techniques should be implemented to visualize the flow as it passes through the microvalve orifice. Vortex shedding and unsteady flow phenomena could be identified in an effort to evaluate the regions of laminar, transition, and turbulent flow as a function of Reynolds number. These velocimetry techniques are designed to illuminate and measure particle and surface motions using infrared wavelengths, taking advantage of the fact that silicon is largely

transmissive to light with wavelengths greater than $1\mu m$. Such a system could allow observation of particles within the flow stream inside of the silicon-based valve orifice microdevice [3]. By analyzing images using both time-of-flight and phase-locked techniques, quantitative measurements about the motion of the fluid could be taken.

3. Using both of the above testing methods, valve orifices with varying types of orifice "sharpness" could be evaluated. The creation of vortices in these microstructures is most likely enhanced by the sharp expansion that occurs as fluid flows radially outward across the membrane. Current MEMS fabrication processes limit the degree of "chamfering" that can be done on corners. It is possible, though, that future microfabrication processes will be developed to enable smoothing of these types of orifice structures.

With the experiments described above, a thorough characterization of the flow behavior through microvalve orifices could be obtained, independent from its interaction with adjacent compliant structures.

Flow-Induced Instabilities of Adjacent Valve Membrane Structure

With a detailed understanding of the flow regimes through microvalve orifice geometries, experiments could be run to evaluate the impact of these flow regimes on the stability of adjacent compliant valve cap membrane structures. The structures tested could be similar to the full valves tested in this thesis. The following experimental tests could be carried out:

1. During the slow valve opening tests discussed previously, it would be very useful to capture instantaneous snapshots (with period $\sim 10ms$) repeatedly during the full 10 minute long experimental test. This would require a more sophisticated A/D measurement system than was used in this thesis, in which low data sampling rates (ie: 10 data points per second) could be used for the extended period test and much higher sampling rates (ie: 1,000,000 data points per second) could be used for the snapshots. In this manner, during valve opening, as the valve cap transitions from stable to unstable oscillatory behavior, these snapshots could capture the nature of this transition behavior.
2. Additionally, during these tests, rather than measuring just the center point of the valve cap using the laser vibrometer system, it would be informative to scan over the entire surface of the valve cap. In this manner, tilting motion of the valve cap could be analyzed as a cause of any unstable flow behavior. Since the valve cap stiffness is minimal for tilting motions (no net volume change beneath the valve cap occurs), these motions could easily be caused by unstable flow regions around the valve cap or, conversely, unstable flow behavior (vortices) could be a result of valve cap tilting. Therefore, measurement of the valve cap tilting could be informative. The spot size of the laser vibrometer system

used in this thesis, however, is too large for such a spatial measurement procedure. Micro laser vibrometer systems could be attempted, however, these systems are typically housed within microscope stage set-ups, which would limit the ability to incorporate the active valve test-rig and jig under the lens. Further brainstorming ideas are needed for outfitting such a small spot size measurement technique.

3. In addition to measuring the whole valve cap motion during this testing, it would also be beneficial to spatially measure the deformation of the valve cap membrane. In this manner, the onset of structural oscillations could be matched with estimated flow regime phenomena. Unfortunately, in the current system, the valve membrane is not in the line of sight of the vibrometer laser beam, due to the presence of silicon layers above and below. Velocimetry (to measure the motion of a moving surface) could be a potential solution, as discussed earlier. Or other sensing methods could be used to measure the dynamic behavior of the membrane, such as incorporation of piezoresistive material in the membrane. This method, however, would require significant fabrication complexity and the need for electrical lead-ins and lead-outs to the membrane, which would only further increase the complexity of the device assembly and bonding procedures.
4. A further interesting experiment which could be performed on the existing active valve design would be to reverse the flow direction through the valve orifice and determine if the same flow-induced vibrations occur. Since in either flow direction the orifice is comprised of a contraction and an expansion of similar magnitude area ratio, the flow is expected to behave consistently. The one main difference, however, is that over the compliant membrane itself, the flow will be experiencing a contraction rather than an expansion, a difference which might result in less severe formation of vortices. The instability discussion in Chapter 9, however, did include schematics from the fluid mechanics literature that indicated similar vorticity fields for both expansion and contraction flow geometries.

A further recommended task would be to develop a theoretical model for the fluid-structural interaction between this flow behavior and the compliant valve structure, using FEM and CFD analyses. The major problem with this, however, is that these modeling procedures require user input for governing flow relations. Since transition regimes between laminar and turbulent flow are not understood theoretically, there would be no way to instruct these programs on how to behave. As a result, the models would be only as accurate as the user's understanding of the flow behavior, which unfortunately is severely limited.

10.2.3 Materials Characterization

In the development of this active valve device, single-crystal ferroelectric material was the desired material for use due to its enhanced strain capabilities in comparison to the polycrys-

talline PZT-5H material. The published [4] PZN-PT material properties ($d_{33} = 2000\text{pC/N}$ and $E_p = 9.01\text{GPa}$) used in the design and optimization chapters of this thesis were found to overpredict the actual capability of the material based on the experiments detailed in Chapters 7 and 9. As a result, overall valve deflection versus voltage was lower than designed for. More detailed characterization studies should be performed on this PZN-PT material to better understand its actuation capabilities under the high voltage and relatively high stress conditions experienced in these active valve devices. Additionally, further development efforts by the manufacturers of this material to improve its performance characteristics (and maintain consistency across different batches of material) would enable more reliable design iterations to take place. In general, this valve design desires a piezoelectric material with as large a d_{33} and as large a Young's modulus E_p as possible.

Additionally from a materials standpoint, the reliability of the active valve device and its capabilities for operating against large pressures and with significant valve cap stroke are directly affected by the yield stress levels of the etched silicon membranes that form the valve and the drive piston tethers. Given a value for yield stress (ie: in the design and optimization section of this thesis a value of 1 GPa was used [5]), the systematic design procedure presented in Chapter 5 is able to generate an active valve geometry that guarantees a maximum stress during theoretical operation below this value of yield stress. This assumed limit, therefore, directly influences the resulting size and dimensions of the active valve device. Further work to better characterize this yield stress limit (based on defects in the etched structures) or further work to enhance the strength of these filleted features with possible post DRIE smoothing procedures would enable more compact valve designs that work at higher stress levels.

10.2.4 Microfabrication Issues

From a fabrication and assembly standpoint, this active valve device is far from a cost-effective manufacturable entity, primarily due to the extremely intensive Silicon-on-Insulator wafer DRIE etching steps for Layers 4, 5, and 7. Currently these etch procedures require tight control of fillet radii dimensions at the base of 300 – 400 μm deep etches, a requirement which necessitates numerous human inspection and handling steps. If etch procedures could be developed that minimize the depth of this etch so as to improve fillet radius uniformity across a given valve membrane structure or piston tether, the processing time and human intervention requirements could be drastically reduced. Additionally, the reliabilities of wafer-level silicon-to-silicon fusion bonding and silicon-glass anodic bonding are far from optimal at present. Although improvements in yields on a given wafer have occurred over the course of this MHT program at MIT, further optimization and processing studies could only help to improve wafer yields.

Finally, this active valve device is a 9-layer silicon and glass structure with integrated piezoelectric material elements. A general philosophy is “the fewer number of layers, the better”, as

long as each of the reduced layers is not substantially increased in complexity. Efforts should be pursued to redesign this active valve structure to still maintain the required structural elements, yet do so in such a way that eliminates as many layers as possible. A further improvement to the device would be to find a way to create a micro-seal between the hydraulic amplification chamber and the piezoelectric material chamber without the need for solid annular tethered structures. Limitations exist now in the ability to create very deep, thin and smooth gap etches in silicon. If such a thin trench could be micromachined and if a relatively compliant polymer material of some sort could be made to fill that thin gap, then the drive element piston would be capable of moving up and down in response to the piezoelectric material voltage without the need for these micromachined annular tethers. Of course, new problems such as electrical contact to the top surface of the piezoelectric materials and the release of a free-standing piston structure present themselves. Fabrication brainstorming ideas such as these should be continued in an effort to progress to next-generation valve devices.

10.2.5 Future of MHTs

This chapter has reviewed the performance of the active valve and has outlined a series of future activities that could be pursued in an effort to improve its performance. In general, the piezoelectrically-driven hydraulic amplification microvalve documented in this thesis successfully outperforms all liquid-regulation active valves previously presented in the literature (see Chapter 1), in terms of simultaneously satisfying a set of high frequency ($\sim 1kHz$), high pressure ($\sim 300kPa$), and large stroke ($\sim 40\mu m$) requirements. In this sense, the development of the device has been a success. However, the performance limitations observed through device experimentation indicate that, in order for this valve technology to be successful in the designed-for high specific power ($\sim 1000 \frac{W}{kg}$) micropumping applications (MHTs) introduced in Chapter 1, significant further research and redesign is required. Even with the current limited active valve capabilities observed in this thesis, however, full MHT micropumping systems incorporating these valves are estimated to operate with specific powers between $25-30 \frac{W}{kg}$, at least an order of magnitude larger than the best micropumping systems ($2.5 \frac{W}{kg}$) presented in the literature and detailed in Chapter 1. With this future work, it may be possible to realize an active valve device capable of operating at the desired quasi-static operational frequency ($> 10kHz$) and high differential pressure ($> 1MPa$), enabling it to successfully regulate liquid flow within the higher specific power MHT systems.

As detailed in this chapter, a structural redesign effort should be pursued, incorporating updated finite-element models with inertia coupling and external fluid added mass effects, to achieve a valve design with quasi-static frequency in excess of $10kHz$. It is the belief of this author that, by simplifying the hydraulic amplification chamber geometry, increasing the valve membrane thickness, and increasing the piezoelectric material volume beneath the drive element

piston, this frequency enhancement could be readily achieved while maintaining similar stroke capability. However, this guarantees only that the structure can successfully operate as a high-frequency microactuator against a constant external loading. It is the differential pressure applied to the device, and the resulting fluid flow through the valve orifice structure that will most likely limit the flow regulation capability of the structure, as observed in this thesis. The future work to more comprehensively understand the fluid flow regimes through these small scale orifice structures and, more importantly, the interaction of this flow with the adjacent compliant valve membrane structure is, therefore, of vital importance to the success of higher-performing valve devices for use in MHT systems. It is quite possible that by increasing the valve membrane thickness, as discussed in this chapter, the valve flow-induced structural oscillations could be significantly reduced. However, this hypothesis can only be proven through the detailed fluid-structural coupling models and experimental procedures recommended in this chapter. It is, therefore, the belief of this author that this microvalve device can be successfully redesigned to meet the structural high frequency requirements for use in high specific power MHT systems. What is unknown in this stage of the research, however, is the expected nature of fluid-structural interaction and corresponding flow-induced vibrations of the valve cap and membrane at these higher drive frequency levels and higher differential pressures. Future research must address these issues.

Bibliography

- [1] Y.H. Su, K.S. Chen, D.C. Roberts, and S.M. Spearing, "Large Deflection Analysis of a Pre-Stressed Annular Plate With a Rigid Boss Under Axisymmetric Loading," *Journal of Micromech. Microeng.* 11 (2001) pp. 645-653.
- [2] J. Carretero and K.S. Breuer, "Measurement and Modeling of the Flow Characteristics of Micro Disk Valves," Proceedings of the 1994 International Mechanical Engineering Conference and Exposition: Microfluidics Symposium, Orlando, FL, Nov. 2000.
- [3] K.S. Breuer, J.C. Bird, G. Han, and K.J.A. Westin, "Infrared Diagnostics for the measurement of fluid and solid motion in micromachined Devices," Proceedings, ASME IMECE, New York, NY. November 2001.
- [4] S.E. Park and T.R. Shrout, "Characteristics of Relaxor-Based Piezoelectric Single Crystals for Ultrasonic Transducers," *IEEE Trans. Ultrasonics, Ferroelectrics, and Frequency Control*, Vol.44, No.5, Sept. 1997, pp. 1140-1147.
- [5] K.T. Turner, An Evaluation of Critical Issues for Microhydraulic Transducers: Silicon Wafer Bonding, Strength of Silicon on Insulator Membranes and Gold-Tin Solder Bonding. MIT Master's Thesis. June 2001.

Appendix A

Support Documentation for Active Valve Linear Model

A.1 ChapterExample.mws

```

File: ChapterExample.mws
David C. Roberts
This file calculates the linear deflection and swept volume of an annular plate with outer
radius a and inner radius b. There is an applied pressure P from inner radius b to
outer radius a. The plate is guided at r=b and clamped at r=a. This problem is included
in the modeling chapter as a demonstration example of how this linear theory is carried
out. The pressure P serves to deflect the plate in the positive direction. These calculations
include deflections due to bending and shearing effects, since the plate thickness is not
necessarily << than the plate outer radius.
[ > restart;
[ > Digits:=40;

Digits:=40

[ Calculate Deflection, Swept Volume Due to BENDING

[ Define Governing Plate Bending Equation and Shear Force
[ > eqn:='diff(1/r*diff(x*diff(w(x),x),x),x)=Q(x)/D';

$$\frac{\partial}{\partial r} \left( \frac{\partial}{\partial r} \left( \frac{w(r)}{r} \right) \right) = \frac{Q(r)}{D}$$

[ Shear force in terms of P:
[ > Q(x):= P*P1*(x^2-b^2)/(2*P1*x);

$$Q(r) := \frac{1}{2} \frac{P(r^2 - b^2)}{r}$$

[ Integrate the Governing Plate Bending Equation
[ Calculate the deflection, w_bending(r), due to bending:
[ > Q1(x):=(int(Q(x)/D,x)+C1)*x;
[ > Q2(x):=(int(Q1(x),x)+C2)/x;
[ > w_bending(x):=(int(Q2(x),x)+C3);

$$Q1(r) := \left( \frac{1}{4} \frac{P r^2}{D} - \frac{1}{2} \frac{P b^2 \ln(r)}{D} + C1 \right) r$$


$$Q2(r) := \frac{\frac{1}{16} \frac{P r^4}{D} - \frac{1}{4} \frac{P b^2 r^2 \ln(r)}{D} + \frac{1}{8} \frac{P b^2 r^2}{D} + \frac{1}{2} C1 r^2 + C2}{r}$$


$$w\_bending(r) := \frac{1}{64} \frac{P r^4}{D} - \frac{1}{8} \frac{P b^2 r^2 \ln(r)}{D} + \frac{1}{8} \frac{P b^2 r^2}{D} + \frac{1}{4} C1 r^2 + C2 \ln(r) + C3$$

[ Apply BCs and Solve for W_bending(r)
[ > BC1:=subs({r=a},w_bending(x))=0;

$$BC1 := \frac{1}{64} \frac{P a^4}{D} - \frac{1}{8} \frac{P b^2 a^2 \ln(a)}{D} + \frac{1}{8} \frac{P b^2 a^2}{D} + \frac{1}{4} C1 a^2 + C2 \ln(a) + C3 = 0$$

[ > BC2:=subs({r=a},diff(w_bending(x),x))=0;

$$BC2 := \frac{1}{16} \frac{P a^2}{D} - \frac{1}{4} \frac{P b^2 \ln(a)}{D} + \frac{1}{8} \frac{P b^2 a}{D} + \frac{1}{2} C1 a + \frac{C2}{a} = 0$$

[ > BC3:=subs({r=b},diff(w_bending(x),x))=0;

$$BC3 := \frac{3}{16} \frac{P b^3}{D} - \frac{1}{4} \frac{P b^3 \ln(b)}{D} + \frac{1}{2} C1 b + \frac{C2}{b} = 0$$

[ > Set1:=solve({BC1,BC2,BC3},{C1,C2,C3});
[ Determine the general expression for plate deflection, W_bending(r):
[ > W_bending(x):=collect(subs(Set1,w_bending(x)),{D,P});

```

Page 1

```

W_bending(r) := 
$$\left( \frac{1}{64} r^4 - \frac{1}{8} b^2 r^2 \ln(r) + \frac{1}{8} b^2 r^2 - \frac{1}{32} \frac{(-a^4 + 4 b^2 a^2 \ln(a) - 2 b^2 a^2 + 3 b^4 - 4 b^4 \ln(b)) r^2}{-a^2 + b^2} - \frac{1}{16} \frac{b^2 a^2 \left( a^2 - b^2 + 4 b^2 \ln\left(\frac{b}{a}\right) \right) \ln(r)}{-a^2 + b^2} - \frac{1}{64} \frac{a^2 (a^4 - 4 b^2 a^2 \ln(a) - 3 b^2 a^2 + 2 b^4 + 8 b^4 \ln(b) + 16 b^4 \ln(a)^2 - 4 b^4 \ln(a) - 16 b^4 \ln(a) \ln(b))}{-a^2 + b^2} \right) P / D$$

[ Determine the plate deflection at r=b. This is denoted Wb_bending.
> Wb_bending:=collect(simplify(subs({r=b},W_bending(x))),{D,P});
Wb_bending := 
$$-\frac{1}{64} \left( 7 b^4 a^2 - 3 b^4 - 4 b^4 \ln(b) a^2 - 5 b^2 a^4 + 4 b^4 a^2 \ln(a) + 4 b^2 a^4 \ln(b) + 16 b^4 a^2 \ln(b) \ln\left(\frac{b}{a}\right) + a^6 - 4 a^4 b^2 \ln(a) + 16 a^2 b^4 \ln(a)^2 - 16 a^2 b^4 \ln(a) \ln(b) \right) P / (D (-a^2 + b^2))$$


[ Calculate Swept Volume, dV_bending, Due to Bending
[ This is the swept volume under only the plate. The swept volume from r=0 to r=b must also be considered.
> dV_bending:=collect(simplify(int(2*Pi*r*W_bending(x),x=b..a)),{P1,D,P});
dV_bending := 
$$\frac{1}{192} P \pi \left( -a^8 + 10 a^6 b^2 - 24 a^4 b^4 - 48 a^4 b^4 \ln\left(\frac{b}{a}\right) \ln(a) + 24 a^4 b^4 \ln\left(\frac{b}{a}\right) - 48 a^4 b^4 \ln(a)^2 + 48 a^4 b^4 \ln(a) \ln(b) + 22 b^6 a^2 - 7 b^8 + 48 b^6 a^2 \ln(b) \ln\left(\frac{b}{a}\right) - 24 b^6 a^2 \ln\left(\frac{b}{a}\right) + 48 b^6 a^2 \ln(a)^2 - 48 b^6 a^2 \ln(a) \ln(b) \right) / (D (-a^2 + b^2))$$


[ Calculate Deflection, Swept Volume Due to SHEARING
[ Define Governing Plate Shearing Equation and Integrate
> eqn2:=diff(w(x),x)=-alpha*Q(x)/G/h';
eqn2 := 
$$\frac{\partial}{\partial x} w(x) = -\frac{\alpha Q(x)}{G h}$$

[ Calculate the deflection, W_shearing, due to shear effects (shear coefficient, alpha=1.5);
> w_shearing(x):=int(-alpha*Q(x)/G/h,x)+C4;
w_shearing(r) := 
$$-\frac{1}{4} \frac{\alpha P r^2}{G h} + \frac{1}{2} \frac{\alpha P b^2 \ln(r)}{G h} + C4$$

[ Apply BC and Solve for W_shearing(r)
> BC4:=subs({r=a},w_shearing(x))=0;
BC4 := 
$$-\frac{1}{4} \frac{\alpha P a^2}{G h} + \frac{1}{2} \frac{\alpha P b^2 \ln(a)}{G h} + C4 = 0$$

[ Set2:=solve({BC4},{C4});
> W_shearing(x):=subs(Set2,w_shearing(x));
W_shearing(r) := 
$$-\frac{1}{4} \frac{\alpha P r^2}{G h} + \frac{1}{2} \frac{\alpha P b^2 \ln(r)}{G h} - \frac{1}{4} \frac{\alpha P (-a^2 + 2 b^2 \ln(a))}{G h}$$

[ Determine the plate deflection at r=b. This is denoted Wb_shearing.
> Wb_shearing:=collect(simplify(subs({r=b},W_shearing(x))),{P1});
Wb_shearing := 
$$-\frac{1}{4} \frac{\alpha P (b^2 - 2 b^2 \ln(b) - a^2 + 2 b^2 \ln(a))}{G h}$$


```

Page 2

Calculate Swept Volume Due to Shearing, dV_shearing

```
> dV_shearing:=collect(simplify(int(2*Pi*r*W_shearing(r),r=b..a)),{P});
```

$$dV_{shearing} := \frac{1}{8} \frac{\pi \alpha P (a^4 - 4 b^3 a^2 + 3 b^4 - 4 b^4 \ln(b) + 4 b^4 \ln(a))}{G h}$$

Total Deflection and Swept Volume

Sum the deflections due to bending and shear into the total plate deflection at $r=b$, W_b :

```
> Wb:=collect(Wb_bending + Wb_shearing, {P});
```

$$W_b := \left(-\frac{1}{64} \left(7 b^4 a^2 - 3 b^4 - 4 b^4 \ln(b) a^2 - 5 b^3 a^4 + 4 b^4 a^2 \ln(a) + 4 b^3 a^4 \ln(b) + 16 b^4 a^2 \ln(b) \ln\left(\frac{b}{a}\right) + a^6 \right. \right. \\ \left. \left. - 4 a^4 b^2 \ln(a) + 16 a^2 b^4 \ln(a)^2 - 16 a^2 b^4 \ln(a) \ln(b) \right) / (D (-a^2 + b^2)) - \frac{1}{4} \frac{\alpha (b^3 - 2 b^3 \ln(b) - a^2 + 2 b^2 \ln(a))}{G h} \right) P$$

Sum the displaced volumes due to bending and shear into the total displaced volume, dV:

```
> dV:=collect(dV_bending+dV_shearing, {P});
```

$$dV := \left(\frac{1}{192} \pi \left(-a^4 + 10 a^4 b^2 - 24 a^4 b^4 - 48 a^4 b^4 \ln\left(\frac{b}{a}\right) \ln(a) + 24 a^4 b^4 \ln\left(\frac{b}{a}\right) - 48 a^4 b^4 \ln(a)^2 + 48 a^4 b^4 \ln(a) \ln(b) \right. \right. \\ \left. \left. + 22 b^6 a^2 - 7 b^6 + 48 b^6 a^2 \ln(b) \ln\left(\frac{b}{a}\right) - 24 b^6 a^2 \ln\left(\frac{b}{a}\right) + 48 b^6 a^2 \ln(a)^2 - 48 b^6 a^2 \ln(a) \ln(b) \right) / (D (-a^2 + b^2)) \right. \\ \left. + \frac{1}{8} \frac{\pi \alpha (a^4 - 4 b^3 a^2 + 3 b^4 - 4 b^4 \ln(b) + 4 b^4 \ln(a))}{G h} \right) P$$

Substitution of Example Values

```
> Wb_EXAMPLE:=evalf(subs({alpha=1.5,a=3.15e-3,b=0.80e-3,E=165e9,nu=0.22,h=1000e-6},subs(
P=1e6,D=E*h^3/(12*(1-nu^2)),G=E/2/(1+nu),Wb)));
Wb_EXAMPLE := .986574732573098211629339004226204575890 10^-7
> dV_EXAMPLE:=evalf(subs({alpha=1.5,a=3.15e-3,b=0.80e-3,E=165e9,nu=0.22,h=1000e-6},subs(P
=1e6,D=E*h^3/(12*(1-nu^2)),G=E/2/(1+nu),dV)));
dV_EXAMPLE := .1320442285992528857571432424955844654522 10^-11
>
```

A.2 FullActiveValve(LINEAR).mws [see Section 2.4]

```

File: FullActiveValve(LINEAR).mws
David C. Roberts
This file solves the linear valve analytical model described in Chapter 2 of thesis. The inputs are P1, P2, and Vp.
The valve behavior is calculated.
> restart;
> Digits:=40;

Digits := 40

Step 1: Define Linear Quasi-Static Relations

Piezoelectric Material
[ This relation assumes perfect d33 actuation (no effect of transverse clamping).
> EQN1 := X[p] = d[33]*V[p] - (L[p]/E[p])*T[p];

EQN1 := X_p = d_33 V_p - \frac{L_p T_p}{E_p}

[ This relation determines the piezo charge.
> EQN2 := Q[p] = (eT[33]*A[p]/L[p])*V[p] + (d[33]*A[p])*T[p];

EQN2 := Q_p = \frac{eT_{33} A_p V_p}{L_p} + d_{33} A_p T_p

Bottom Structural Compliance
[ Circular plate with stress imposed over central region.
> EQN3 := X[bot] = (Xl[Zbot,T]) * T[p];

EQN3 := X_bot = X_{Zbot, T} T_p

Drive Element Tethers
> EQN4 := Z[te] =
(Xl[Ztstop,F]*Xl[Ztbot,F]) / (Xl[Ztstop,F]+Xl[Ztbot,F]) * (A[p]*T[p]-A[pis]*P[HAC]) -
(Xl[Ztstop,P]*Xl[Ztbot,P]) / (Xl[Ztstop,P]+Xl[Ztbot,P]) * P[HAC];

EQN4 := Z_{te} = \frac{X_{Ztstop, F} X_{Ztbot, F} (A_p T_p - A_{pis} P_{HAC})}{X_{Ztstop, F} + X_{Ztbot, F}} - \frac{X_{Ztstop, P} X_{Ztbot, P} P_{HAC}}{X_{Ztstop, P} + X_{Ztbot, P}}

> EQN5 := dV[te] =
(Xl[dVtstop,F]*Xl[Ztbot,F]) / (Xl[Ztstop,F]+Xl[Ztbot,F]) * (A[p]*T[p]-A[pis]*P[HAC]) -
(Xl[dVtstop,P]*Xl[Ztbot,P]) / (Xl[Ztstop,P]+Xl[Ztbot,P]) * P[HAC] + A[pis]*Z[te];

EQN5 := dV_{te} = \frac{X_{dVtstop, F} X_{Ztbot, F} (A_p T_p - A_{pis} P_{HAC})}{X_{Ztstop, F} + X_{Ztbot, F}} - \frac{X_{dVtstop, P} X_{Ztbot, P} P_{HAC}}{X_{Ztstop, P} + X_{Ztbot, P}} + A_{pis} Z_{te}

Drive Element Piston
> EQN6 := X[pis] = Xl[Zpis,T]*T[p] - Xl[Xpis,P]*P[HAC];

EQN6 := X_{pis} = X_{Zpis, T} T_p - X_{Xpis, P} P_{HAC}
> EQN7 := dV[pis] = Xl[dVpis,T]*T[p] - Xl[dVpis,P]*P[HAC];

EQN7 := dV_{pis} = X_{dVpis, T} T_p - X_{dVpis, P} P_{HAC}

Fluid Compressibility
> EQN8 := dV[fluid] = -(V[HAC]/K[Z])*P[HAC];

```

Page 1

$$EQN8 := dV_{fluid} = - \frac{V_{MAC} P_{MAC}}{K_f}$$

Top Structural Compliance

[> EQN9 := $Z[top] = X1[Z[top], P] * P[MAC] + X1[Z[top], F] * F[vm];$

$EQN9 := Z_{top} = \Sigma_{Z_{top}, P} P_{MAC} + \Sigma_{Z_{top}, F} F_{vm}$

[> EQN10 := $dV[top] = X1[dV[top], P] * P[MAC] + X1[dV[top], F] * F[vm] + A[vm] * Z[top];$

$EQN10 := dV_{top} = \Sigma_{dV_{top}, P} P_{MAC} + \Sigma_{dV_{top}, F} F_{vm} + A_{vm} Z_{top}$

[> EQN11 := $F[vm] = (A[vm] - A[vc]) * (P[MAC] - P[2]) + A[vc] * (P[MAC] - P[1]);$

$EQN11 := F_{vm} = (A_{vm} - A_{vc}) (P_{MAC} - P_2) + A_{vc} (P_{MAC} - P_1)$

Valve Cap/Membrane

[Note: I have included the contribution to valve cap deflection due to top chamber deflection. The corresponding volume contribution is already included in the Top Structural Compliance section.

[> EQN12 := $Z[vc] = X1[Z[vc], P] * (P[MAC] - P[2]) + X1[Z[vc], F] * F[vc] + Z[top];$

$EQN12 := Z_{vc} = \Sigma_{Z_{vc}, P} (P_{MAC} - P_2) + \Sigma_{Z_{vc}, F} F_{vc} + Z_{top}$

[> EQN13 := $dV[vm] = X1[dV[vm], P] * (P[MAC] - P[2]) + X1[dV[vm], F] * F[vc] + A[vc] * Z[vc];$

$EQN13 := dV_{vm} = \Sigma_{dV_{vm}, P} (P_{MAC} - P_2) + \Sigma_{dV_{vm}, F} F_{vc} + A_{vc} Z_{vc}$

[> EQN14 := $F[vc] = (P[MAC] - P[1]) * A[vc];$

$EQN14 := F_{vc} = A_{vc} (P_{MAC} - P_1)$

Deflection, Swept Volume Conservation

[All structural deflections and swept volumes are defined to be positive in the upward direction.

[> EQN15 := $Z[p] + Z[bot] = Z[ta] + Z[pis];$

$EQN15 := Z_p + Z_{bot} = Z_{ta} + Z_{pis}$

[> EQN16 := $0 = dV[ta] + dV[pis] + dV[fluid] - dV[top] - dV[vm];$

$EQN16 := 0 = dV_{ta} + dV_{pis} + dV_{fluid} - dV_{top} - dV_{vm}$

Other Relations

[Variables as functions of other variables.

[> EQN17 := $Z[de] = Z[ta] + Z[pis];$

$EQN17 := Z_{de} = Z_{ta} + Z_{pis}$

Step 2: Define Geometric/Material Parameters

[Geometric Parameters:

[> R[vc] := 0.31e-3; R[vm] := 0.80e-3; t[vm] := 10e-6; A[vc] := $\pi * R[vc]^2$; A[vm] := $\pi * R[vm]^2$;

$t[vc] := 400e-6$;

[> Z[p] := 1e-3; R[p] := 1e-3; A[p] := $\pi * R[p]^2$;

[> R[pis] := 3e-3; R[ch] := 3.225e-3; t[pis] := 800e-6; t[topte] := 10e-6; t[botte] := 10e-6;

$A[pis] := \pi * R[pis]^2$;

[> t[bot] := 1000e-6;

[> R[MAC] := 400e-6; V[MAC] := $\pi * R[ch]^2 * R[MAC] + \pi * (R[vm]^2 - R[vc]^2) * t[vc]$;

[> t[top] := 1000e-6;

[Material Parameters:

```
> d[33]:=2000e-12: sD[33]:=16.4e-12: sE[33]:=111e-12: E[p]:=1/sE[33]:
eT[33]:=d[33]^2/(sE[33]-sD[33]): E[s1]:=165e9: nu[s1]:=0.22: K[x]:=2e9: alpha[s1]:=1.25:
```

Step 3: Calculate Linear Plate Coefficients

Bottom Structural Compliance

```
Circular plate clamped at outer radius (r=a) with stress imposed over central region (r=0 to r=b).
Positive deflection is upward, whereas positive stress acts downward. This relation includes
bending and shearing effects, see BottomChamberPlate(WORST).mws.
> eqn:='diff(1/x*diff(x*diff(Z(x),x),x),x)=Q(x)/D':
> Q_0b(x):=-Tp*Pi*x^2/(2*Pi*x):
> Q1(x):=(int(Q_0b(x)/D,x)+C1)*x:
Q2(x):=(int(Q1(x),x))/x:
Xbot_0b_bending(x):=int(Q2(x),x)+C3:
> BC1:=subs({x=b},Xbot_0b_bending(x))=Xb_bending:
> BC2:=subs({x=b},diff(Xbot_0b_bending(x),x))=dXb_bending:
> BC3:=subs({x=b},diff(diff(Xbot_0b_bending(x),x),x)+
nu/x*diff(Xbot_0b_bending(x),x))=d2Xb_bending:
> eqn:='diff(1/x*diff(x*diff(Z(x),x),x),x)=Q(x)/D':
> Q_ba(x):=-Tp*Pi*b^2/(2*Pi*x):
> Q1(x):=(int(Q_ba(x)/D,x)+C4)*x:
Q2(x):=(int(Q1(x),x)+C5)/x:
Xbot_ba_bending(x):=int(Q2(x),x)+C6:
> BC4:=subs({x=a},Xbot_ba_bending(x))=0:
> BC5:=subs({x=a},diff(Xbot_ba_bending(x),x))=0:
> BC6:=subs({x=b},Xbot_ba_bending(x))=Xb_bending:
> BC7:=subs({x=b},diff(Xbot_ba_bending(x),x))=dXb_bending:
> BC8:=subs({x=b},diff(diff(Xbot_ba_bending(x),x),x)+
nu/x*diff(Xbot_ba_bending(x),x))=d2Xb_bending:
> Set1:=solve({BC1,BC2,BC3,BC4,BC5,BC6,BC7,BC8},{C1,C3,C4,C5,C6,Xb_bending,d2Xb_bending}):
> Xbot_0b_BENDING(x):=collect(subs(Set1,Xbot_0b_bending(x)),{D,Tp}):
> Xbot_ba_BENDING(x):=collect(subs(Set1,Xbot_ba_bending(x)),{D,Tp}):
> dVbot_0b_BENDING:=collect(simplify(int(2*Pi*x*Xbot_0b_BENDING(x),x=0..b)),{Tp}):
> dVbot_ba_BENDING:=collect(simplify(int(2*Pi*x*Xbot_ba_BENDING(x),x=b..a)),{Tp}):
> eqn4:='diff(Z(x),x)=-alpha*Q(x)/G/h':
> Xbot_0b_shearing(x):=int(-alpha*Q_0b(x)/G/h,x)+C7:
> BC9:=subs({x=b},Xbot_0b_shearing(x))=Xb_shearing:
> eqn4:='diff(Z(x),x)=-alpha*Q(x)/G/h':
> Xbot_ba_shearing(x):=int(-alpha*Q_ba(x)/G/h,x)+C8:
> BC10:=subs({x=a},Xbot_ba_shearing(x))=0:
> BC11:=subs({x=b},Xbot_ba_shearing(x))=Xb_shearing:
> Set2:=solve({BC9,BC10,BC11},{C7,C8,Xb_shearing}):
> Xbot_0b_SHEARING(x):=collect(subs(Set2,Xbot_0b_shearing(x)),{D,Tp}):
> Xbot_ba_SHEARING(x):=collect(subs(Set2,Xbot_ba_shearing(x)),{D,Tp}):
```

Page 3

Drive Element Tethers

Page 4


```

+  $\pi a^6 - 4 \pi a^4 b^2 \ln(a) + 16 \pi a^2 \ln(a)^2 b^4 - 16 \pi a^2 \ln(a) b^4 \ln(b)$   $\Bigg) / (\pi (a^2 - b^2) D)$ 
 $\Xi_{dVttop, P} := .7246716855091782654098385470407258607940 \cdot 10^{-11}$ 
> X1[dVttop, F] := subs({PHAC=0, F[topa]=1}, dVtether1_BENDING);
X1[dVttop, F] := evalf(subs({a=R[ch], b=R[pis], h=t[topa], D=E[si]*t[topa]^3/(12*(1-mu[si]^2))}, X1[dVttop, F]));
 $\Xi_{dVttop, P} := -\frac{1}{192} \left( -12 b^4 \ln(b) a^2 + 24 b^4 a^2 \ln\left(\frac{b}{a}\right) - 3 a^6 + 12 a^4 b^2 \ln(b) - 12 a^4 b^2 \ln(a) - 24 a^4 b^2 \ln\left(\frac{b}{a}\right) \right.$ 
 $\left. + 48 a^4 \ln(a)^2 b^2 + 48 a^4 b^2 \ln\left(\frac{b}{a}\right) \ln(a) - 48 a^4 \ln(a) b^2 \ln(b) + 15 a^4 b^2 + 48 a^2 \ln(a) b^4 \ln(b) - 48 b^4 a^2 \ln\left(\frac{b}{a}\right) \ln(b) \right.$ 
 $\left. - 48 a^2 \ln(a)^2 b^4 - 21 b^4 a^2 + 12 b^4 a^2 \ln(a) + 9 b^6 \right) / ((a^2 - b^2) D)$ 
 $\Xi_{dVttop, P} := .7246716855091782654098385470406784 \cdot 10^{-11}$ 
> X1[dVttop, F] := -subs({PHAC=1, F[topa]=0}, dVtether1_BENDING);
X1[dVttop, F] := evalf(subs({a=R[ch], b=R[pis], h=t[topa], D=E[si]*t[topa]^3/(12*(1-mu[si]^2))}, X1[dVttop, F]));
 $\Xi_{dVttop, P} := \frac{1}{192} \left( \left( 24 b^4 a^2 \ln\left(\frac{b}{a}\right) + a^6 - 48 a^4 \ln(a) b^4 \ln(b) + 48 a^4 b^4 \ln\left(\frac{b}{a}\right) \ln(a) + 48 a^4 \ln(a)^2 b^4 - 24 a^4 b^4 \ln\left(\frac{b}{a}\right) \right. \right.$ 
 $\left. + 24 a^4 b^4 - 10 a^4 b^2 - 48 b^4 a^2 \ln\left(\frac{b}{a}\right) \ln(b) - 48 a^2 \ln(a)^2 b^4 + 48 a^2 \ln(a) b^4 \ln(b) + 7 b^6 - 22 b^4 a^2 \right) \pi / ((a^2 - b^2) D)$ 
 $\Xi_{dVttop, P} := .1672014327695025501669898411677512555127 \cdot 10^{-16}$ 

```

BOTTOM TETHER
Annular plate clamped at outer radius (r=a) and guided at inner radius (r=b) with concentrated force applied upward at inner radius (r=b) and pressure over annulus. These relations include bending effects only, see TetherBottom3.mws.

```

> eqn:=diff(1/x*diff(x*diff(E(x),x),x),x)=Q(x)/D';
> Q(x):=F[botte]/(2*Pi*x) - PHAC*Pi*(x^2-b^2)/(2*Pi*x);
> Q1(x):=(int(Q(x)/D,x)+C1)*x;
Q2(x):=(int(Q1(x),x)+C2)/x;
Xtether2_bending(x):=expand(int(Q2(x),x)+C3);
> BC1:=subs({x=a}, Xtether2_bending(x))=0;
> BC2:=subs({x=a}, diff(Xtether2_bending(x),x))=0;
> BC3:=subs({x=b}, diff(Xtether2_bending(x),x))=0;
> Set1:=solve({BC1,BC2,BC3},{C1,C2,C3});
> Xtether2_BENDING(x):=collect(subs(Set1,Xtether2_bending(x)),{F[botte],D,PHAC});
> Xtether2:=collect(simplify(subs({x=b}, Xtether2_BENDING(x))),{F[botte],D,PHAC});
> dVtether2_BENDING:=collect(simplify(int(2*Pi*x*Xtether2_BENDING(x),x=b..a)),{Pi,F[botte],D,PHAC});
> X1[Xtbot, F] := subs({PHAC=0, F[botte]=1}, Xtether2);
X1[Xtbot, F] := evalf(subs({a=R[ch], b=R[pis], h=t[botte], D=E[si]*t[botte]^3/(12*(1-mu[si]^2))}, X1[Xtbot, F]));

```

Page 5

```


$$\Xi_{\text{Stabot},P} := -\frac{1}{64} \frac{8b^3a^2 - 4b^4 + 16b^3a^2 \ln\left(\frac{b}{a}\right) \ln(b) - 4a^4 + 16a^3 \ln(a)^3 b^2 - 16a^2 \ln(a) b^3 \ln(b)}{\pi(a^2 - b^2)D}$$


$$\Xi_{\text{Stabot},P} := .3358560090822692575226480248142747504821 \cdot 10^{-9}$$

> Xi[Stabot,P] := -subs({PRAC=1, V[botte]=0}, Stathex2);
Xi[Stabot,P] := evalf(subs({a=R[ch], b=R[pis], h=t[botte], D=E[s1]*t[botte]^3/(12*(1-mu[s1]^2))}, Xi[Stabot,P]));

$$\Xi_{\text{Stabot},P} := \frac{1}{64} \left( 7\pi b^4 a^2 - 3\pi b^4 - 5\pi a^4 b^2 + 4\pi b^4 a^2 \ln(a) - 4\pi b^4 \ln(b) a^2 + 4\pi b^3 a^4 \ln(b) + 16\pi b^4 a^2 \ln(b) \ln\left(\frac{b}{a}\right) + \pi a^4 - 4\pi a^4 b^2 \ln(a) + 16\pi a^2 \ln(a)^3 b^4 - 16\pi a^2 \ln(a) b^4 \ln(b) \right) / (\pi(a^2 - b^2)D)$$


$$\Xi_{\text{Stabot},P} := .7246716855091782654098385470407258607940 \cdot 10^{-11}$$

> Xi[dVtabot,P] := subs({PRAC=0, V[botte]=1}, dVtathex2_BENDING);
Xi[dVtabot,P] := evalf(subs({a=R[ch], b=R[pis], h=t[botte], D=E[s1]*t[botte]^3/(12*(1-mu[s1]^2))}, Xi[dVtabot,P]));

$$\Xi_{\text{dVtabot},P} := -\frac{1}{192} \left( -12b^4 \ln(b) a^2 + 24b^4 a^2 \ln\left(\frac{b}{a}\right) - 3a^4 + 12a^4 b^2 \ln(b) - 12a^4 b^2 \ln(a) - 24a^4 b^2 \ln\left(\frac{b}{a}\right) + 48a^4 \ln(a)^3 b^2 + 48a^4 b^2 \ln\left(\frac{b}{a}\right) \ln(a) - 48a^4 \ln(a) b^2 \ln(b) + 15a^4 b^2 + 48a^2 \ln(a) b^4 \ln(b) - 48b^4 a^3 \ln\left(\frac{b}{a}\right) \ln(b) - 48a^3 \ln(a)^3 b^4 - 21b^4 a^2 + 12b^4 a^2 \ln(a) + 9b^4 \right) / ((a^2 - b^2)D)$$


$$\Xi_{\text{dVtabot},P} := .7246716855091782654098385470406784 \cdot 10^{-11}$$

> Xi[dVtabot,P] := -subs({PRAC=1, V[botte]=0}, dVtathex2_BENDING);
Xi[dVtabot,P] := evalf(subs({a=R[ch], b=R[pis], h=t[botte], D=E[s1]*t[botte]^3/(12*(1-mu[s1]^2))}, Xi[dVtabot,P]));

$$\Xi_{\text{dVtabot},P} := \frac{1}{192} \left( 24b^4 a^2 \ln\left(\frac{b}{a}\right) + a^4 - 48a^4 \ln(a) b^4 \ln(b) + 48a^4 b^4 \ln\left(\frac{b}{a}\right) \ln(a) + 48a^4 \ln(a)^3 b^4 - 24a^4 b^4 \ln\left(\frac{b}{a}\right) + 24a^4 b^4 - 10a^4 b^3 - 48b^4 a^3 \ln\left(\frac{b}{a}\right) \ln(b) - 48a^3 \ln(a)^3 b^4 + 48a^2 \ln(a) b^4 \ln(b) + 7b^4 - 22b^4 a^2 \right) / ((a^2 - b^2)D)$$


$$\Xi_{\text{dVtabot},P} := .1672014327695025501669898411677512555127 \cdot 10^{-16}$$


```

Drive Element Piston (More Compliant: Hinged Outer Circumference)

Circular plate hinged at outer radius (r=a) with pressure acting downward over entire plate (from r=0 to r=a) and stress acting upward in central region (from r=0 to r=b). Positive plate deflection is defined in the upward direction. These relations include bending and shearing effects, see Piston(WORST).mws.

```

> eqn := 'diff(1/r*diff(x*diff(z(x),x),x),x) = Q(x)/D';
> Q_0b(x) := (Tp-PRAC)*P1*x^2/(2*pi*x);
> Q1(x) := (int(Q_0b(x)/D,x)+C1)*x;
> Q2(x) := (int(Q1(x),x))/x;
> Epi_0b_bending(x) := int(Q2(x),x)+C3;
> BC1 := subs({r=b}, Epi_0b_bending(x)) = Xb_bending;
> BC2 := subs({r=b}, diff(Epi_0b_bending(x),x)) = dXb_bending;
> BC3 := subs({r=b}, diff(diff(Epi_0b_bending(x),x),x) +

```

Page 6

```

[ nu/r*diff(Epis_Ob_bending(x),x)=d2Zb_bending:
[ > eqn:=diff(1/r*diff(r*diff(Z(x),x),x),x)=Q(x)/D':
[ > Q_ba(x):=Tp*Pi*b^2/(2*Pi*r) - PHAC*Pi*r^2/(2*Pi*r):
[ > Q1(x):=(int(Q_ba(x)/D,x)+C4)*x:
[ Q2(x):=(int(Q1(x),x)+C5)/x:
[ Epis_ba_bending(x):=int(Q2(x),x)+C6:
[ > BC4:=subs({x=a},Epis_ba_bending(x))=0:
[ > BC5:=subs({x=a},diff(diff(Epis_ba_bending(x),x),x) +
[ nu/r*diff(Epis_ba_bending(x),x))=0:
[ > BC6:=subs({x=b},Epis_ba_bending(x))=Zb_bending:
[ > BC7:=subs({x=b},diff(Epis_ba_bending(x),x))=dZb_bending:
[ > BC8:=subs({x=b},diff(diff(Epis_ba_bending(x),x),x) +
[ nu/r*diff(Epis_ba_bending(x),x))=d2Zb_bending:
[ > Set1:=solve({BC1,BC2,BC3,BC4,BC5,BC6,BC7,BC8},{C1,C3,C4,C5,C6,Zb_bending,dZb_bending,d
[ 2Zb_bending}):
[ > Epis_Ob_BENDING(x):=collect(subs(Set1,Epis_Ob_bending(x)),{D,Tp,PHAC}):
[ > Epis_ba_BENDING(x):=collect(subs(Set1,Epis_ba_bending(x)),{D,Tp,PHAC}):
[ > dVpis_Ob_BENDING:=collect(simplify(int(2*Pi*r*Epis_Ob_BENDING(x),x=0..b)),{Tp,PHAC}):
[ > dVpis_ba_BENDING:=collect(simplify(int(2*Pi*r*Epis_ba_BENDING(x),x=b..a)),{Tp,PHAC}):
[ > eqn4:=diff(Z(x),x)=-alpha*Q(x)/G/h':
[ > Epis_Ob_shearing(x):=int(-alpha*Q_Ob(x)/G/h,x)+C7:
[ > BC9:=subs({x=b},Epis_Ob_shearing(x))=Zb_shearing:
[ > eqn4:=diff(Z(x),x)=-alpha*Q(x)/G/h':
[ > Epis_ba_shearing(x):=int(-alpha*Q_ba(x)/G/h,x)+C8:
[ > BC10:=subs({x=a},Epis_ba_shearing(x))=0:
[ > BC11:=subs({x=b},Epis_ba_shearing(x))=Zb_shearing:
[ > Set2:=solve({BC9,BC10,BC11},{C7,C8,Zb_shearing}):
[ > Epis_Ob_SHEARING(x):=collect(subs(Set2,Epis_Ob_shearing(x)),{D,Tp,PHAC}):
[ > Epis_ba_SHEARING(x):=collect(subs(Set2,Epis_ba_shearing(x)),{D,Tp,PHAC}):
[ > dVpis_Ob_SHEARING:=collect(simplify(int(2*Pi*r*Epis_Ob_SHEARING(x),x=0..b)),{Tp,PHAC}):
[ > dVpis_ba_SHEARING:=collect(simplify(int(2*Pi*r*Epis_ba_SHEARING(x),x=b..a)),{Tp,PHAC}):
[ > Epis_Ob(x):=collect(Epis_Ob_BENDING(x) + Epis_Ob_SHEARING(x),{Tp,PHAC}):
[ > Epis_ba(x):=collect(Epis_ba_BENDING(x) + Epis_ba_SHEARING(x),{Tp,PHAC}):
[ > Epis_0:=subs({x=0},collect(Epis_Ob_BENDING(x) + Epis_Ob_SHEARING(x),{Tp,PHAC})):
[ > dVpis:=collect(simplify(dVpis_Ob_BENDING + dVpis_ba_BENDING + dVpis_Ob_SHEARING +
[ dVpis_ba_SHEARING),{Tp,PHAC}):
[ > X11[Epis,T] := subs({PHAC=0,Tp=1},Epis_0);
[ X11[Epis,T]:=evalf(subs({a=R[pis],b=R[p],nu=nu[ai],alpha=alpha[ai],h=t[pis],D=E[ai]*t[
[ pis]^3/(12*(1-nu[ai]^2)),G=E[ai]/(2*(1+nu[ai]))},X11[Epis,T]));

$$\Xi_{1,2\mu,r} = \frac{1}{64} \frac{-7b^4 + 12b^2a^2 + 4vb^2a^2 - 3vb^4 + 4\ln\left(\frac{b}{a}\right)b^4 + 4\ln\left(\frac{b}{a}\right)vb^4}{(1+\nu)D} - \frac{1}{4} \frac{\alpha(-b^2 + 2b^2\ln(b) - 2\ln(a)b^2)}{Gh}$$


```

Page 7


```

> BC5:=subs({x=a},diff(Epis_ba_bending(x),x))=0:
> BC6:=subs({x=b},Epis_ba_bending(x))=Zb_bending:
> BC7:=subs({x=b},diff(Epis_ba_bending(x),x))=dEb_bending:
> BC8:=subs({x=b},diff(diff(Epis_ba_bending(x),x),x) +
nu/x*diff(Epis_ba_bending(x),x))=d2Eb_bending:
> Set1:=solve({BC1,BC2,BC3,BC4,BC5,BC6,BC7,BC8},{C1,C3,C4,C5,C6,Zb_bending,dEb_bending,
2Eb_bending}):
> Epis_Ob_BENDING(x):=collect(subs(Set1,Epis_Ob_bending(x)),(D,Tp,PHAC)):
> Epis_ba_BENDING(x):=collect(subs(Set1,Epis_ba_bending(x)),(D,Tp,PHAC)):
> dVpis_Ob_BENDING:=collect(simplify(int(2*Pi*x*Epis_Ob_BENDING(x),x=0..b)),(Tp,PHAC)):
> dVpis_ba_BENDING:=collect(simplify(int(2*Pi*x*Epis_ba_BENDING(x),x=b..a)),(Tp,PHAC)):
> eqn4:='diff(Z(x),x)=-alpha*Q(x)/G/h':
> Epis_Ob_shearing(x):=int(-alpha*Q_Ob(x)/G/h,x)+C7:
> BC9:=subs({x=b},Epis_Ob_shearing(x))=Eb_shearing:
> eqn4:='diff(Z(x),x)=-alpha*Q(x)/G/h':
> Epis_ba_shearing(x):=int(-alpha*Q_ba(x)/G/h,x)+C8:
> BC10:=subs({x=a},Epis_ba_shearing(x))=0:
> BC11:=subs({x=b},Epis_ba_shearing(x))=Zb_shearing:
> Set2:=solve({BC9,BC10,BC11},{C7,C8,Zb_shearing}):
> Epis_Ob_SHEARING(x):=collect(subs(Set2,Epis_Ob_shearing(x)),(D,Tp,PHAC)):
> Epis_ba_SHEARING(x):=collect(subs(Set2,Epis_ba_shearing(x)),(D,Tp,PHAC)):
> dVpis_Ob_SHEARING:=collect(simplify(int(2*Pi*x*Epis_Ob_SHEARING(x),x=0..b)),(Tp,PHAC)):
> dVpis_ba_SHEARING:=collect(simplify(int(2*Pi*x*Epis_ba_SHEARING(x),x=b..a)),(Tp,PHAC)):
> Epis_Ob(x):=collect(Epis_Ob_BENDING(x) + Epis_Ob_SHEARING(x),(Tp,PHAC)):
> Epis_ba(x):=collect(Epis_ba_BENDING(x) + Epis_ba_SHEARING(x),(Tp,PHAC)):
> Epis_0:=subs({x=0},collect(Epis_Ob_BENDING(x) + Epis_Ob_SHEARING(x),(Tp,PHAC))):
> dVpist:=collect(simplify(dVpis_Ob_BENDING + dVpis_ba_BENDING + dVpis_Ob_SHEARING +
dVpis_ba_SHEARING),(Tp,PHAC)):
> X12[Epis,T] := subs({PHAC=0,Tp=1},Epis_0);
X12[Epis,T]:=evalf(subs({a=R[pis],b=R[p],nu=nu[si],alpha=alpha[si],h=t[pis],D=E[si]*t[
pis]^3/(12*(1-nu[si]^2)),G=E[si]/(2*(1+nu[si]))},X12[Epis,T]));

$$\Xi_{2_{\text{qu},T}} := \frac{-\frac{3}{64}b^4 + \frac{1}{16}b^2a^2 + \frac{1}{16}\ln\left(\frac{b}{a}\right)b^4}{D} - \frac{1}{4} \frac{\alpha(-b^3 + 2b^2\ln(b) - 2\ln(a)b^3)}{Gh}$$


$$\Xi_{2_{\text{qu},T}} := .78884836686998640767250030356035147167 \cdot 10^{11}$$

> X12[Epis,P] := -subs({PHAC=1,Tp=0},Epis_0);
X12[Epis,P]:=evalf(subs({a=R[pis],b=R[p],nu=nu[si],alpha=alpha[si],h=t[pis],D=E[si]*t[
pis]^3/(12*(1-nu[si]^2)),G=E[si]/(2*(1+nu[si]))},X12[Epis,P]));

$$\Xi_{2_{\text{qu},P}} := \frac{1}{64} \frac{a^4}{D} + \frac{1}{4} \frac{\alpha a^2}{Gh}$$


$$\Xi_{2_{\text{qu},P}} := .223063742897727272727272727272727272727272727272727273 \cdot 10^{12}$$

> X12[dVpis,T] := subs({PHAC=0,Tp=1},dVpist);

```

Page 9

```

X12[dVpis,T] := evalf(subs({a=R[pis],b=R[p],nu=nu[s1],alpha=alpha[s1],hwt[pis],D=E[s1]*t
[pis]^3/(12*(1-nu[s1]^2)),G=E[s1]/(2*(1+nu[s1]))},X12[dVpis,T]));

E2_dVpis_r := 1/192
pi(48*a^3*b^3*D-24*a*b^4*D-3*b^4*G*h*a^3+24*b^4*G*h*(b/a)+3*b^3*G*h*a^4-24*b^4*G*h*ln(b)+24*b^4*G*h*ln(a)+b^4*G*h)
/(D*G*h)

E2_dVpis_r := .6341969310342016231443513844306627385162 10^-18

> X12[dVpis,P] := -subs({FRAC=1,Type=0},dVpis,t);
X12[dVpis,P] := evalf(subs({a=R[pis],b=R[p],nu=nu[s1],alpha=alpha[s1],hwt[pis],D=E[s1]*t
[pis]^3/(12*(1-nu[s1]^2)),G=E[s1]/(2*(1+nu[s1]))},X12[dVpis,P]));

E2_dVpis_r := 1/192 * pi(-a^4*G*h-24*a^4*D)
D*G*h

E2_dVpis_r := .2347316925014454026966632223282621962794 10^-17

Drive Element Piston (Averaged Compliance)

This section averages the compliances effects from the previous two sections on the piston.
In reality, the tethers are compliant enough that they don't provide a rigid boundary condition
at r=a, however they are not soft enough to provide a hinge there either. Therefore, the compliance
is assumed as the average of the two. This effect has been shown with FEM.

> DERatio:=0.5;

DERatio := .5

> X1[Epis,T] := (1-DERatio)*X11[Epis,T] + (DERatio)*X12[Epis,T];

E_dEpi_r := .1377449219142713680403997730308330787445 10^-12

> X1[Epis,P] := (1-DERatio)*X11[Epis,P] + (DERatio)*X12[Epis,P];

E_dEpi_r := .50351473721590909090909090909090909092 10^-12

> X1[dVpis,T] := (1-DERatio)*X11[dVpis,T] + (DERatio)*X12[dVpis,T];

E_dVpis_r := .1466311782062712642937790352294156777490 10^-17

> X1[dVpis,P] := (1-DERatio)*X11[dVpis,P] + (DERatio)*X12[dVpis,P];

E_dVpis_r := .6312099450503241827158900246632211207317 10^-17

Top Structural Compliance

Angular plate clamped at outer radius (r=a) and free at inner radius (r=b) with a pressure applied
underneath plate from r=b to r=a and a concentrated force applied upward at r=b. Positive plate
deflection is defined in the upward direction. These relations include bending and shearing effects,
see TopChamberPlate.mws.

> eqn := 'diff(1/r*diff(r*diff(z(x),x),x),x)=Q(x)/D':
> Q(x) := Pvm/(2*pi*x) + FRAC*P1*(x^2-b^2)/(2*pi*x):
> Q1(x) := (Int(Q(x)/D,x)+C1)*x:

```

Page 10

```

Q2(x):=(int(Q1(x),x)+C2)/x:
Stop_bending(x):=int(Q2(x),x)+C3:
[ > BC1:=subs({x=a},Stop_bending(x))=0:
[ > BC2:=subs({x=a},diff(Stop_bending(x),x))=0:
[ > BC3:=subs({x=b},diff(Stop_bending(x),x)+nu/x*diff(Stop_bending(x),x))=0:
[ > Set1:=solve({BC1,BC2,BC3},{C1,C2,C3}):
[ > Stop_bending(x):=collect(subs(Set1,Stop_bending(x)),{Fvm,D,PHAC}):
[ > Stop_bend:=collect(simplify(subs({x=b},Stop_bending(x))),{Fvm,D,PHAC}):
[ > dVtop_BENDING:=collect(simplify(int(2*Pi*x*Stop_bending(x),x=b..a)),{Pi,Fvm,D,PHAC}):
[ > eqn2:='diff(Z(x),x)=-alpha*Q(x)/G/h':
[ > Stop_shearing(x):=int(-alpha*Q(x)/G/h,x)+C4:
[ > BC4:=subs({x=a},Stop_shearing(x))=0:
[ > Set2:=solve({BC4},{C4}):
[ > Stop_shearing(x):=subs(Set2,Stop_shearing(x)):
[ > Stop_shear:=collect(simplify(subs({x=b},Stop_shearing(x))),{Fvm,PHAC}):
[ > dVtop_SHEARING:=collect(simplify(int(2*Pi*x*Stop_shearing(x),x=b..a)),{Fvm,PHAC}):
[ > Stop1:=collect(Stop_bend + Stop_shear,{Fvm,PHAC}):
[ > dVtop1:=collect(dVtop_BENDING+dVtop_SHEARING,{Fvm,PHAC}):
[ > X1[Stop,P] := subs({PHAC=1,Fvm=0},Stop1):
X1[Stop,P]:=evalf(subs({a=R[ch],b=R[vm],nu=nu[s1],alpha=alpha[s1],h=t[top],D=E[s1]*t[top]^3/(12*(1-nu[s1]^2)),G=E[s1]/(2*(1+nu[s1]))},X1[Stop,P])):
Xi_top:= -1/64*(3*pi*b^6*v - pi*b^4*a^2 - 16*pi*b^4*a^2*ln(b)*ln(b/a) - 16*pi*b^4*a^2*ln(b)*ln(b/a) + 4*pi*a^4*v*b^2*ln(a)
+ 16*pi*a^2*ln(a)*b^4*ln(b) - 16*pi*a^2*ln(a)^3*b^4*v - 4*pi*b^6*a^2*v*ln(a) + 7*pi*b^6 + 4*pi*b^4*ln(b)*a^2*v - pi*a^6*v - 4*pi*b^2*a^4*ln(b)*v
+ 16*pi*a^2*ln(a)*v*b^4*ln(b) + pi*a^4 - 7*pi*a^4*b^2 - 16*pi*a^2*ln(a)^3*b^4 + 4*pi*a^4*b^2*ln(a) - 7*pi*b^4*a^2*v + 5*pi*b^2*v*a^4
+ 20*pi*b^4*a^2*ln(a) - 4*pi*b^2*a^2*ln(b) - 20*pi*b^4*ln(b)*a^2)/(pi*(-a^2+a^2*v-b^2-v*b^2)*D)
+ 1/4*(-b^2*pi+2*b^2*ln(b)*pi+a^2*pi-2*b^2*ln(a)*pi)/G*h*pi
Xi_top:= .1442510763604847433456380046056248573029 10^12
[ > X1[Stop,P] := subs({PHAC=0,Fvm=1},Stop1):
X1[Stop,P]:=evalf(subs({a=R[ch],b=R[vm],nu=nu[s1],alpha=alpha[s1],h=t[top],D=E[s1]*t[top]^3/(12*(1-nu[s1]^2)),G=E[s1]/(2*(1+nu[s1]))},X1[Stop,P])):
Xi_top:= -1/64*(8*v*b^5*a^2 + 16*a^2*ln(a)^3*b^3 + 32*b^5*ln(b)*a^2 - 32*a^2*ln(a)*b^2 - 4*v*a^4 - 4*v*b^4 + 4*a^4
+ 16*b^5*a^2*ln(b)*ln(b/a) + 16*b^3*a^2*ln(b/a)*ln(b) - 16*a^2*ln(a)*v*b^3*ln(b) - 16*a^2*ln(a)*b^3*ln(b) + 16*a^2*ln(a)^3*v*b^3
+ 8*b^5*a^2 - 12*b^4)/(pi*(-a^2+a^2*v-b^2-v*b^2)*D) + 1/4*(-2*ln(b)+2*ln(a))/G*h*pi
Xi_top:= .1775479105428133086725272014729944768799 10^7
[ > X1[dVtop,P] := subs({PHAC=1,Fvm=0},dVtop1):
X1[dVtop,P]:=evalf(subs({a=R[ch],b=R[vm],nu=nu[s1],alpha=alpha[s1],h=t[top],D=E[s1]*t[top]^3/(12*(1-nu[s1]^2)),G=E[s1]/(2*(1+nu[s1]))},X1[dVtop,P])):

```

Page 11

$$\begin{aligned} E_{\text{top},F} = & -\frac{1}{192} \left((-2a^6b^2 - 13b^6 + a^6 + 12a^4b^4 + 2b^4a^2 - 48a^2\ln(a)v b^4\ln(b) + 22a^2v b^6 + 10a^6v b^2 \right. \\ & - 24a^4v b^4 - a^6v - 7v b^6 - 48a^4b^4\ln\left(\frac{b}{a}\right)v\ln(a) + 48a^2b^4\ln\left(\frac{b}{a}\right)v\ln(b) + 48a^4\ln(a)v b^4\ln(b) - 24b^6a^2\ln\left(\frac{b}{a}\right) \\ & - 48a^4\ln(a)^2b^4 + 24a^4b^4\ln\left(\frac{b}{a}\right) + 48a^2\ln(a)^2b^4 + 48a^2\ln(a)^2b^4v + 48a^4\ln(a)b^4\ln(b) - 48a^4b^4\ln\left(\frac{b}{a}\right)\ln(a) \\ & + 48b^6a^2\ln\left(\frac{b}{a}\right)\ln(b) - 48a^2\ln(a)b^4\ln(b) - 48a^4\ln(a)^2b^4v - 24a^2b^6\ln\left(\frac{b}{a}\right)v + 24a^4b^4\ln\left(\frac{b}{a}\right)v - 48b^6\ln(a)a^2 \\ & \left. + 48b^6\ln(b)a^2\right) \pi \Big/ ((-a^2 + a^2v - b^2 - vb^2)D) - \frac{1}{8} \frac{\alpha(4b^2a^2\pi - a^6\pi - 3b^6\pi + 4b^4\ln(b)\pi - 4b^4\ln(a)\pi)}{Gh} \\ E_{\text{top},F} = & -1618097346275169420654979054561191650143 \cdot 10^{-17} \\ > \text{X1}[dVtop,F] := \text{subs}(\{PMA=0, Pvm=1\}, dVtop1); \\ \text{X1}[dVtop,F] := & \text{evalf}(\text{subs}(\{a=R[ch], b=R[wm], nu=nu[s1], alpha=alpha[s1], h=t[top], D=E[s1]*t[\\ & \text{top}]^3/(12*(1-nu[s1]^2)), Q=E[s1]/(2*(1+nu[s1]))\}, \text{X1}[dVtop,F])); \\ E_{\text{top},F} = & -\frac{1}{192} \left((-21a^6b^2 - 84b^6\ln(b)a^2 + 84b^4a^2\ln(a) - 3b^6a^2 + 3a^6 + 9vb^6 + 21b^6 - 48a^2\ln(a)^2vb^4 \right. \\ & - 24a^4b^2\ln\left(\frac{b}{a}\right)v + 48a^4\ln(a)^2vb^2 + 48a^4b^2\ln\left(\frac{b}{a}\right)v\ln(a) + 12a^2v\ln(a)b^4 - 12a^2vb^4\ln(b) \\ & + 48a^2v\ln(a)b^4\ln(b) - 48b^6a^2\ln\left(\frac{b}{a}\right)v\ln(b) - 48a^4\ln(a)v b^2\ln(b) - 3a^4v + 24b^6a^2\ln\left(\frac{b}{a}\right)v + 15a^4vb^2 \\ & - 12a^4\ln(a)v b^2 + 12a^4vb^2\ln(b) - 21a^2vb^6 + 48a^4b^2\ln\left(\frac{b}{a}\right)\ln(a) - 48a^4\ln(a)b^2\ln(b) + 48a^2\ln(a)b^4\ln(b) \\ & - 48b^6a^2\ln\left(\frac{b}{a}\right)\ln(b) + 24b^6a^2\ln\left(\frac{b}{a}\right) + 12a^2b^2\ln(b) - 12a^4b^2\ln(a) - 24a^4b^2\ln\left(\frac{b}{a}\right) + 48a^4\ln(a)^2b^2 \\ & \left. - 48a^2\ln(a)^2b^2\right) \Big/ ((-a^2 + a^2v - b^2 - vb^2)D) - \frac{1}{8} \frac{\alpha(-2a^2 + 2b^2 - 4b^2\ln(b) + 4\ln(a)b^2)}{Gh} \\ E_{\text{top},F} = & -1442510763604847433456380046056248573035 \cdot 10^{-17} \end{aligned}$$



Valve Cap/Membrane

Annular plate clamped at outer radius ($r=a$) and guided at inner radius ($r=b$) with differential pressure applied underneath plate from $r=b$ to $r=a$ and concentrated force applied upward at $r=b$. Positive plate deflection is defined in the upward direction. These relations only include bending effects, see ValveCapMembrane.mws.

```
[ > eqn := 'diff(1/r*diff(r*diff(w(x),x),x),x) = Q(x)/D';
[ > Q(x) := Fvc/(2*pi*x) + Pvm*pi*(x^2-b^2)/(2*pi*x);
[ > Q1(x) := (int(Q(x)/D,x)+C1)*x;
[ > Q2(x) := (int(Q1(x),x)+C2)/x;
[ > Evm_bending(x) := expand(int(Q2(x),x)+C3);
[ > BC1 := subs({r=a}, Evm_bending(x))=0;
[ > BC2 := subs({r=a}, diff(Evm_bending(x),x))=0;
[ > BC3 := subs({r=b}, diff(Evm_bending(x),x))=0;
[ > Set1 := solve({BC1,BC2,BC3},{C1,C2,C3});
[ > Evm_BENDING(x) := collect(subs(Set1,Evm_bending(x)),{Fvc,D,Pvm});
[ > Evcl := collect(simplify(subs({r=b}, Evm_BENDING(x))),{Fvc,D,Pvm});
[ > dVvm_BENDING := collect(simplify(int(2*pi*r*Evm_BENDING(x),r=b..a)),{P1,Fvc,D,Pvm});
```



```

> Xi[Zvc,P] := subs({Fvc=0,Pvm=1},Zvc1);
Xi[Zvc,P] := evalf(subs({a=R[vm],b=R[vc],h=t[vm],D=E[s1]*t[vm]^3/(12*(1-mu[s1]^2))},Xi[Zvc,P]));
Xi[Zvc,P] := 1/64 * (7*pi*b^4*a^3 - 3*pi*b^4 - 5*pi*a^4*b^2 + 4*pi*b^4*a^2*ln(a) - 4*pi*b^4*ln(b)*a^2 + 4*pi*b^4*a^2*ln(b) + 16*pi*b^4*a^2*ln(b)*ln(b/a) + pi*a^4 - 4*pi*a^4*b^2*ln(a) + 16*pi*a^2*ln(a)^2*b^4 - 16*pi*a^2*ln(a)*b^4*ln(b)) / (pi*(a^2-b^2)*D)
Xi[Zvc,P] := .1236306944873668358747037186342053319349 10^9

> Xi[dVvm,P] := subs({Fvc=1,Pvm=0},Zvc1);
Xi[dVvm,P] := evalf(subs({a=R[vm],b=R[vc],h=t[vm],D=E[s1]*t[vm]^3/(12*(1-mu[s1]^2))},Xi[dVvm,P]));
Xi[dVvm,P] := 1/64 * (4*a^4 - 16*a^2*ln(a)^3*b^2 + 4*b^4 - 8*b^4*a^2 - 16*b^2*a^2*ln(b/a)*ln(b) + 16*a^3*ln(a)*b^2*ln(b)) / (pi*(a^2-b^2)*D)
Xi[dVvm,P] := .0001891300225883061570524241081849325118186

> Xi[dVvm,P] := subs({Fvc=0,Pvm=1},dVvm_BENDING);
Xi[dVvm,P] := evalf(subs({a=R[vm],b=R[vc],h=t[vm],D=E[s1]*t[vm]^3/(12*(1-mu[s1]^2))},Xi[dVvm,P]));
Xi[dVvm,P] := 1/192 * ((24*b^4*a^2*ln(b/a) + a^4 - 48*a^4*ln(a)*b^2*ln(b) + 48*a^4*b^4*ln(b/a)*ln(a) + 48*a^4*ln(a)^3*b^4 - 24*a^4*b^4*ln(b/a) + 24*a^4*b^4 - 10*a^4*b^2 - 48*b^4*a^2*ln(b/a)*ln(b) - 48*a^2*ln(a)^2*b^4 + 48*a^2*ln(a)*b^4*ln(b) + 7*b^4 - 22*b^4*a^2) * pi) / ((a^2-b^2)*D)
Xi[dVvm,P] := .9031509650514488184176314920963760635496 10^16

> Xi[dVvm,P] := subs({Fvc=1,Pvm=0},dVvm_BENDING);
Xi[dVvm,P] := evalf(subs({a=R[vm],b=R[vc],h=t[vm],D=E[s1]*t[vm]^3/(12*(1-mu[s1]^2))},Xi[dVvm,P]));
Xi[dVvm,P] := 1/192 * (-15*a^4*b^2 - 9*b^4 - 48*a^2*ln(a)*b^4*ln(b) + 48*b^4*a^2*ln(b/a)*ln(b) + 21*b^4*a^2 + 48*a^2*ln(a)^2*b^4 + 12*b^4*ln(b)*a^2 - 12*b^4*a^2*ln(a) - 24*b^4*a^2*ln(b/a) + 3*a^4 - 48*a^4*b^2*ln(b/a)*ln(a) + 48*a^4*ln(a)*b^2*ln(b) - 48*a^4*ln(a)^2*b^2 - 12*a^4*b^2*ln(b) + 24*a^4*b^2*ln(b/a) + 12*a^4*b^2*ln(a)) / ((a^2-b^2)*D)
Xi[dVvm,P] := .123630694487366835874703718634205331944 10^9

```

Step 4: Solve Equations

```

> Solutions:=solve({EQN1,EQN2,EQN3,EQN4,EQN5,EQN6,EQN7,EQN8,EQN9,EQN10,EQN11,EQN12,EQN13,EQ
N14,EQN15,EQN16,EQN17},{Z[p],T[p],Z[bot],Z[te],P[HAC],dV[te],Z[pie],dV[pie],dV[fluid],Z[t
op],dV[top],V[vm],Z[vc],dV[vm],V[vc],Q[p],Z[de]});
> SolutionsValues:=evalf(subs({P[1]=0.5e6,P[2]=0e6,V[p]=500},Solutions));
SolutionsValues := { T_p = .2231936350709793062278122870357821015647 10^7,
Z_bot = -.1163329724718546223813989792182145983230 10^4, Z_p = .7522550650712129700871283613902818672634 10^4,
dV_bot = .1872711788601659056212980592568417325255 10^11, F_vm = .2949951827261501434908943661858065648750,

```


Appendix B

Support Documentation for Non-Linear Valve Cap/Membrane

B.1 NLValveCapMembrane-CaseA.m [see Section 3.5]

```
function [y,r,Vtotal,psi,W,theta,xi,thetaND,psiND,sigma_r_top,sigma_r_bot,yvc,maxstress] =
NLValveCapMembrane_CaseA(Pvm,Fvc,rb,ra,tvm,E,nu,flagNL,No)

%NLValveCapMembrane_CaseA.m

%David C. Roberts
%This Matlab code solves for the non-linear deflection behavior of the valve cap
%membrane under loading Pvm and Fvc. The deflection, slope,
%curvature, swept volume, and membrane stress are calculated. Case A refers to the
%fact that we are applying both loading inputs Pvm and Fvc and determining the
%structural response. Prior to calling of this code, the user must define Pvm and
%Fvc as functions of P1, P2, and PHAC. The loadings are defined as follows:
%Pvm = pressure differential across valve membrane = PHAC-P2
%Fvc = force seen by valve cap = Avc*(PHAC-P1)
%The plate/membrane is characterized by inner radius rb, outer radius ra, thickness
%tvm, and material properties E and nu. If flagNL=0, only linear theory will be
%considered. If flagNL=1, non-linear theory will be considered. No is the value of
%the in-plane pretension. In this file yvc is the valve cap deflection (Zvc).

format long;

%%%%%%%%%%%%%%%%%%%%%%%%%%%%%%%%%%%%%%%%%%%%%%%%%%%%%%%%%%%%%%%%%%%%%%%%
%Convert Inputs to Dimensionless Quantities
P = (Pvm*ra^4)/(E*tvm^4); %Dimensionless loading of pressure difference across
cap/membrane
F = (Fvc*ra^2)/(pi*E*tvm^4); %Dimensionless loading due to additional force on cap
%%%%%%%%%%%%%%%%%%%%%%%%%%%%%%%%%%%%%%%%%%%%%%%%%%%%%%%%%%%%%%%%%%%%%%%%

beta = sqrt((1-nu)/(1+nu))*(rb/ra);
k = (ra/tvm)*sqrt((12*(1-nu^2)*No)/(E*tvm*(1-beta^2)));
a = beta*k;

%%%%%%%%%%%%%%%%%%%%%%%%%%%%%%%%%%%%%%%%%%%%%%%%%%%%%%%%%%%%%%%%%%%%%%%%
%%Section 2: Define grid spacing and coordinate transformation parameters
%%for finite-difference method
%%%%%%%%%%%%%%%%%%%%%%%%%%%%%%%%%%%%%%%%%%%%%%%%%%%%%%%%%%%%%%%%%%%%%%%%
Npoints=200; %The total # of grid points to use (MUST KEEP IT EVEN)
alpha=1.01; %Grid density parameter
phi=(alpha+1)/(alpha-1); %Grid density ratio
hr = 1/(Npoints-1); %Size of grid spacing
eta = 0:hr:1; %Vector of evenly spaced points between 0 and 1

xi_b = rb/ra; %Non-dimensional position of inner radius
xi_c = (rb+ra)/(2*ra); %Non-dimensional position of midpoint along membrane
xi_a = ra/ra; %Non-dimensional position of outer radius

%For the grid points from xi_b to xi_c, define the derivatives of eta with respect to xi
for i=1:Npoints/2,
xi(i) = xi_b + (alpha-1)*(xi_c-xi_b)*(phi-phi^(1-2*eta(i)))/(1+phi^(1-2*eta(i)));
m = (alpha-1)*(xi_c-xi_b);
m2 = m*phi - m + 2*xi(i)*B;
deta(i) = (0.5/log(phi))*(m*(1+phi))/((m*phi-(xi(i)-xi_b))*(m*(xi(i)-xi_b)));
d2eta(i) = -(0.5/log(phi))*(m*(1+phi)*(m2-2*xi(i)))/((m*phi-(xi(i)-xi_b))*(m*(xi(i)-
xi_b)))^2;
end

%For the grid points from xi_c to xi_a
for i=Npoints/2+1:Npoints,
xi(i) = xi_b + (alpha-1)*(xi_c-xi_b)*(phi-phi^(1-2*eta(i)))/(1+phi^(1-2*eta(i)));
m = (alpha-1)*(xi_c-xi_b);
m2 = m*phi - m + 2*xi(i)*B;
deta(i) = (0.5/log(phi))*(m*(1+phi))/((m*phi-(xi(i)-xi_b))*(m*(xi(i)-xi_b)));
d2eta(i) = -(0.5/log(phi))*(m*(1+phi)*(m2-2*xi(i)))/((m*phi-(xi(i)-xi_b))*(m*(xi(i)-
xi_b)))^2;
end
```

```

#####
***Section 3: Finite-Difference Implementation
#####

%Governing equations at internal points (from 2 to Npoints-1)
for i=2:Npoints-1,
    A(i,i-1) = (xi(i)^2*deta(i)^2)/(hr^2) - (xi(i)^2*d2deta(i) + xi(i)*deta(i))/(2*hr);
    A(i,i) = -( (2*xi(i)^2*deta(i)^2)/(hr^2) + (s^2+1) + xi(i)^2*k^2 );
    A(i,i+1) = (xi(i)^2*deta(i)^2)/(hr^2) + (xi(i)^2*d2deta(i) + xi(i)*deta(i))/(2*hr);

    B(i,i-1) = (xi(i)^2*deta(i)^2)/(hr^2) - (xi(i)^2*d2deta(i) + 3*xi(i)*deta(i))/(2*hr);
    B(i,i) = -(2*xi(i)^2*deta(i)^2)/(hr^2);
    B(i,i+1) = (xi(i)^2*deta(i)^2)/(hr^2) + (xi(i)^2*d2deta(i) + 3*xi(i)*deta(i))/(2*hr);

    C(i) = 6*(1-nu^2)*P*(xi(i)^3 - xi(i)*(rb/ra)^2) + 6*(1-nu^2)*P*xi(i);
end

%Boundary condition equations at xi_b (grid point #1)
A(1,1) = 1;
B(1,1) = -3*xi(1)*deta(1)/(2*hr) + (1-nu);
B(1,2) = 4*xi(1)*deta(1)/(2*hr);
B(1,3) = -xi(1)*deta(1)/(2*hr);
C(1) = 0;

%Boundary condition equations at xi_a (grid point #Npoints)
A(Npoints,Npoints) = 1;
B(Npoints,Npoints-2) = xi(Npoints)*deta(Npoints)/(2*hr);
B(Npoints,Npoints-1) = -4*xi(Npoints)*deta(Npoints)/(2*hr);
B(Npoints,Npoints) = 3*xi(Npoints)*deta(Npoints)/(2*hr) + (1-nu);
C(Npoints) = 0;

#####
***Section 4: Provide an initial guess for the theta vector (plate slope), to be
***used in the finite-difference iteration procedure.
#####

if k==0,
    %theta = (-0.75*(1-nu^2)*P*xi.*(1-xi.^2))'; %Linear result
    theta=xi';
else
    theta=xi';
end

#####
***Section 5: Matrix Manipulation Procedure
#####

Niterations=500; %Perform up to 500 iterations
tolerance1=1e-8;
tolerance2=1e-8;
omega=0.45; %Under-relaxation parameter
if flagNL==1 %This variable is passed into file.
    NLoption=1; %0 = Linear solution; 1 = NonLinear solution
else
    NLoption=0;
end

for i=1:Niterations,
    i;
    for j=2:Npoints-1 %Define D vector for each iteration
        D(j) = -0.5*theta(j).^2;
    end
    D(1)=0;
    D(Npoints)=0;

    Sr = inv(B)*D'*NLoption; %Solve for Sr

```

```

v_Sr = 12*(1-nu^2)*xi'.^2.*Sr;      %Calculate non-linear correction term v_Sr
A2 = A - diag(v_Sr,0);              %Subtract non-linear correction term from A
theta_new = inv(A2)*C';              %Calculate new theta vector

inner_product = (theta_new'*theta)/sqrt(theta_new'*theta_new)/sqrt(theta'*theta);
length_ratio = sqrt(theta_new'*theta_new)/sqrt(theta'*theta);

if (1-inner_product) >= tolerance1 | (1-length_ratio) >= tolerance2
    theta = (1-omega)*theta + omega*theta_new;
else
    break;
end
end

%%%%%%%%%%%%%%%%%%%%%%%%%%%%%%%%%%%%%%%%%%%%%%%%%%%%%%%%%%%%%%%%%%%%%%%%%%%%%%
%%Section 6: Calculate Deflection, Curvature, Stress, and Swept Volume in this
%%post-processing section.
%%%%%%%%%%%%%%%%%%%%%%%%%%%%%%%%%%%%%%%%%%%%%%%%%%%%%%%%%%%%%%%%%%%%%%%%%%%%%%

%PLATE DEFLECTION: Calculate plate deflection vector from the final theta vector,
%using 2nd-order forward, backward, and central difference methods to express
%theta in terms of W. Then, using matrix inversion to obtain the vector W.
i=1; %BC at rb
Wmatrix(i,1) = deta(i)*(-3/(2*hr));
Wmatrix(i,i+1) = deta(i)*(2/hr);
Wmatrix(i,i+2) = deta(i)*(-1/(2*hr));

for i=2:Npoints-1 %Inner grid points
    Wmatrix(i,i-1) = deta(i)*(-1/(2*hr));
    Wmatrix(i,i+1) = deta(i)*(1/(2*hr));
end

%BC at ra --> Do not do for the outer boundary condition. We already know that
%the deflection at ra is equal to zero.

W = inv(Wmatrix(1:Npoints-1,1:Npoints-1))*theta(1:Npoints-1);
W=[W;0];
%Done

%PLATE CURVATURE: Calculate plate curvature vector from the final theta vector,
%using 2nd-order forward, backward, and central difference methods.
i=1; %BC at rb
psi(i) = deta(i)*(1/(2*hr))*(-3*theta(i) + 4*theta(i+1) - theta(i+2));

for i=2:Npoints-1 %Inner grid points
    psi(i) = deta(i)*(1/(2*hr))*(theta(i+1) - theta(i-1));
end

i=Npoints; %BC at ra
psi(i) = deta(i)*(1/(2*hr))*(3*theta(i) - 4*theta(i-1) + theta(i-2));
%Done

%PLATE STRESS: Calculate the stress vectors in the plate.

for i=1:Npoints
    Sro(i) = (k^2/(12*(1-nu^2)))*(1 + beta^2/(xi(i)^2));
    sigma_r_top(i) = (E*ttvm^2/ra^2)*(Sro(i) + Sr(i) - (1/(2*(1-nu^2)))*(psi(i) +
    (nu*theta(i))./xi(i)));
    sigma_r_bot(i) = (E*ttvm^2/ra^2)*(Sro(i) + Sr(i) + (1/(2*(1-nu^2)))*(psi(i) +
    (nu*theta(i))./xi(i)));
end
if max(sigma_r_top) > max(sigma_r_bot)
    maxstress = abs(max(sigma_r_top));
else
    maxstress = abs(max(sigma_r_bot));
end

```

```

end
%Done

%CONVERSION TO NON_DIMENSIONAL PARAMETERS
r=xi*ra;
y=W*tvm;
thetaND=theta*tvm/ra; %This non-dimensional theta is dw/dr
psiND=psi*tvm/(ra^2); %This non-dimensional psi is d2w/dr2

%PLATE SWEEP VOLUME: Calculate total swept volume under cap and membrane.
V=0;
for i=1:Npoints-1
    dv(i) = pi*(r(i+1)^2-r(i)^2)*0.5*(y(i+1)+y(i));
    V = V + dv(i);
end
yvc = y(1);
Vcap = yvc*pi*rb^2;
Vtotal = Vcap + V;
%Done

```

B.2 NLValveCapMembrane-CaseB.m [see Section 3.5]

```
function
[y,r,Vtotal,psi,W,theta,xi,thetaND,psiND,sigma_r_top,sigma_r_bot,yvc,Pvm,maxstress] =
NLValveCapMembrane_CaseB(Fvcstar,yvc_imposed,rb,ra,tv,E,nu,flagNL,No)

%NLValveCapMembrane_CaseB.m

%David C. Roberts
%This Matlab code solves for the non-linear deflection behavior of the valve cap/
%membrane under loading Fvcstar and a desired valve cap deflection at r=rb. The
%required Pvm to produce this deflection and the resulting deflection, slope,
%curvature, swept volume, and membrane stress are calculated. Case B refers to the
%fact that we are applying a known cap force (in addition to that due to Pvm) and
%imposing a cap deflection, and then solving for the required Pvm and the resulting
%structural response. Prior to calling of this code, the user must define Fvcstar
%as a function of P1 and P2. This Fvcstar loading is defined as follows:
% Fvcstar = Avc*(P2-P1)
%After running this code, the user can then back out PHAC using the following relation:
% PHAC = Pvm+P2
%The plate/membrane is characterized by inner radius rb, outer radius ra, thickness
%tvm, and material properties E and nu. If flagNL=0, only linear theory will be
%considered. If flagNL=1, non-linear theory will be considered. No is the value of
%the in-plane pretension. In this file, yvc is the valve cap deflection (Zvc).

format long;

%%%%%%%%%%%%%%%%%%%%%%%%%%%%%%%%%%%%%%%%%%%%%%%%%%%%%%%%%%%%%%%%%%%%%%%%
%Convert Inputs to Dimensionless Quantities
Wb=yvc_imposed/tvm;
F = (Fvcstar*ra^2)/(pi*E*tvm^4); %Dimensionless loading due to additional force on cap
%%%%%%%%%%%%%%%%%%%%%%%%%%%%%%%%%%%%%%%%%%%%%%%%%%%%%%%%%%%%%%%%%%%%%%%%

beta = sqrt((1-nu)/(1+nu))*(rb/ra);
k = (ra/tvm)*sqrt((12*(1-nu^2)*No)/(E*tvm*(1-beta^2)));
s = beta*k;

%%%%%%%%%%%%%%%%%%%%%%%%%%%%%%%%%%%%%%%%%%%%%%%%%%%%%%%%%%%%%%%%%%%%%%%%
%%Section 2: Define grid spacing and coordinate transformation parameters
%%for finite-difference method
%%%%%%%%%%%%%%%%%%%%%%%%%%%%%%%%%%%%%%%%%%%%%%%%%%%%%%%%%%%%%%%%%%%%%%%%
Npoints=200; %The total # of grid points to use (MUST KEEP IT EVEN)
alpha=1.01; %Grid density parameter
phi=(alpha+1)/(alpha-1); %Grid density ratio
hr = 1/(Npoints-1); %Size of grid spacing
eta = 0:hr:1; %Vector of evenly spaced points between 0 and 1

xi_b = rb/ra; %Non-dimensional position of inner radius
xi_c = (rb+ra)/(2*ra); %Non-dimensional position of midpoint along membrane
xi_a = ra/ra; %Non-dimensional position of outer radius

%For the grid points from xi_b to xi_c, define the derivatives of eta with respect to xi
for i=1:Npoints/2,
xi(i) = xi_b + (alpha-1)*(xi_c-xi_b)*(phi-phi^(1-2*eta(i)))/(1+phi^(1-2*eta(i)));
m = (alpha-1)*(xi_c-xi_b);
m2 = m*phi - m + 2*xi_b;
deta(i) = (0.5/log(phi))*(m*(1+phi))/((m*phi-(xi(i)-xi_b))*(m+(xi(i)-xi_b)));
d2eta(i) = -(0.5/log(phi))*(m*(1+phi)*(m2-2*xi(i)))/((m*phi-(xi(i)-xi_b))*(m+(xi(i)-xi_b)))^2;
end

%For the grid points from xi_c to xi_a
for i=Npoints/2+1:Npoints,
xi(i) = xi_b + (alpha-1)*(xi_c-xi_b)*(phi-phi^(1-2*eta(i)))/(1+phi^(1-2*eta(i)));
m = (alpha-1)*(xi_c-xi_b);
m2 = m*phi - m + 2*xi_b;
deta(i) = (0.5/log(phi))*(m*(1+phi))/((m*phi-(xi(i)-xi_b))*(m+(xi(i)-xi_b)));
d2eta(i) = -(0.5/log(phi))*(m*(1+phi)*(m2-2*xi(i)))/((m*phi-(xi(i)-xi_b))*(m+(xi(i)-xi_b)))^2;
end
```



```

end

%%%%%%%%%%%%%%%%%%%%%%%%%%%%%%%%%%%%%%%%%%%%%%%%%%%%%%%%%%%%%%%%%%%%%%%%%%%%%%
***Section 3: Finite-Difference Implementation
%%%%%%%%%%%%%%%%%%%%%%%%%%%%%%%%%%%%%%%%%%%%%%%%%%%%%%%%%%%%%%%%%%%%%%%%%%%%%%

%Governing equations at internal points (from 2 to Npoints-1)
for i=2:Npoints-1,
    A(i,i-1) = (xi(i)^2*deta(i)^2)/(hr^2) - (xi(i)^2*d2deta(i) + xi(i)*deta(i))/(2*hr);
    A(i,i) = -(2*xi(i)^2*deta(i)^2)/(hr^2) + (n^2+1) + xi(i)^2*k^2;
    A(i,i+1) = (xi(i)^2*deta(i)^2)/(hr^2) + (xi(i)^2*d2deta(i) + xi(i)*deta(i))/(2*hr);

    B(i,i-1) = (xi(i)^2*deta(i)^2)/(hr^2) - (xi(i)^2*d2deta(i) + 3*xi(i)*deta(i))/(2*hr);
    B(i,i) = -(2*xi(i)^2*deta(i)^2)/(hr^2);
    B(i,i+1) = (xi(i)^2*deta(i)^2)/(hr^2) + (xi(i)^2*d2deta(i) + 3*xi(i)*deta(i))/(2*hr);

    C(i) = 6*(1-nu^2)*F*xi(i);
end

%Boundary condition equations at xi_b (grid point #1)
A(1,1) = 1;
B(1,1) = -3*xi(1)*deta(1)/(2*hr) + (1-nu);
B(1,2) = 4*xi(1)*deta(1)/(2*hr);
B(1,3) = -xi(1)*deta(1)/(2*hr);
C(1) = 0;

%Boundary condition equations at xi_a (grid point Npoints)
A(Npoints,Npoints) = 1;
B(Npoints,Npoints-2) = xi(Npoints)*deta(Npoints)/(2*hr);
B(Npoints,Npoints-1) = -4*xi(Npoints)*deta(Npoints)/(2*hr);
B(Npoints,Npoints) = 3*xi(Npoints)*deta(Npoints)/(2*hr) + (1-nu);
C(Npoints) = 0;

%IMPORTANT: Since P is an unknown, an extra column and row are added to A to solve for P
%and therefore the added entry to C is the non-dimensional deflection Wb.

%Define entries in additional column of A
A(1,Npoints+1) = 0; %BC at r=rb
for i=2:Npoints-1
    A(i,Npoints+1) = -6*(1-nu^2)*(xi(i)^3); %central points
end
A(Npoints,Npoints+1) = 0; %BC at r=ra
A(Npoints+1,Npoints+1) = 0; %This is a meaningless entry so it must be zero.

%Define entries in additional row of A
A(Npoints+1,1) = -(hr/2)/deta(1);
for i=2:Npoints-1
    A(Npoints+1,i) = -(hr)/deta(i);
end
A(Npoints+1,Npoints) = -(hr/2)/deta(Npoints);

%Define additional entry in C
C(Npoints+1) = Wb;

%%%%%%%%%%%%%%%%%%%%%%%%%%%%%%%%%%%%%%%%%%%%%%%%%%%%%%%%%%%%%%%%%%%%%%%%%%%%%%
***Section 4: Provide an initial guess for the theta vector (plate slope), to be
***used in the finite-difference iteration procedure.
%%%%%%%%%%%%%%%%%%%%%%%%%%%%%%%%%%%%%%%%%%%%%%%%%%%%%%%%%%%%%%%%%%%%%%%%%%%%%%

if k==0,
    %theta = (-0.75*(1-nu^2)*F*xi.*(1-xi.^2)); %Linear result
    theta=xi';
else
    theta=whoops;
end

```

```

#####
***Section 5: Matrix Manipulation Procedure
#####

NIterations=500;          %Perform up to 500 iterations
tolerance1=1e-8;
tolerance2=1e-8;
omega=0.45;              %Under-relaxation parameter
if flagNL==1              %This variable is passed into file.
    NLoption=1;           %0 = Linear solution; 1 = NonLinear solution
else
    NLoption=0;
end

for i=1:NIterations,
    1;
    for j=2:Npoints-1      %Define D vector for each iteration
        D(j) = -0.5*theta(j).^2;
    end
    D(1)=0;
    D(Npoints)=0;

    Sr = inv(B)*D'*NLoption; %Solve for Sr
    v_Sr = 12*(1-nu^2)*xi'.^2.*Sr; %Calculate non-linear correction term v_Sr
    v_Sr(Npoints+1) = 0; %Make v_Sr the proper length
    A2 = A - diag(v_Sr,0); %Subtract non-linear correction term from A
    theta_new = inv(A2)*C'; %Calculate new theta vector
    P_result = theta_new(Npoints+1); %Record the calculated value of P
    theta_new = theta_new(1:Npoints); %Remove the P entry from the theta vector

    inner_product = (theta_new'*theta)/sqrt(theta_new'*theta_new)/sqrt(theta'*theta);
    length_ratio = sqrt(theta_new'*theta_new)/sqrt(theta'*theta);

    if (1-inner_product) >= tolerance1 | (1-length_ratio) >= tolerance2
        theta = (1-omega)*theta + omega*theta_new;
    else
        break;
    end
end

#####
***Section 6: Calculate Deflection, Curvature, Stress, and Swept Volume in this
***post-processing section.
#####

%PRESSURE Pvm: Calculate the differential pressure across the membrane.
Pvm = P_result*E*twm^4/ra^4;
%Done

%PLATE DEFLECTION: Calculate plate deflection vector from the final theta vector,
%using 2nd-order forward, backward, and central difference methods to express
%theta in terms of W. Then, using matrix inversion to obtain the vector W.
i=1; %BC at rb
Wmatrix(i,1) = deta(i)*(-3/(2*hr));
Wmatrix(i,i+1) = deta(i)*(2/hr);
Wmatrix(i,i+2) = deta(i)*(-1/(2*hr));

for i=2:Npoints-1 %Inner grid points
    Wmatrix(i,i-1) = deta(i)*(-1/(2*hr));
    Wmatrix(i,i+1) = deta(i)*(1/(2*hr));
end

%BC at ra --> Do not do for the outer boundary condition. We already know that
%the deflection at ra is equal to zero.

W = inv(Wmatrix(1:Npoints-1,1:Npoints-1))*theta(1:Npoints-1);

```

```

W=[W;0];
%Done

%PLATE CURVATURE: Calculate plate curvature vector from the final theta vector,
%using 2nd-order forward, backward, and central difference methods.
i=1; %BC at rb
psi(i) = deta(i)*(1/(2*hr))*(-3*theta(i) + 4*theta(i+1) - theta(i+2));

for i=2:Npoints-1 %Inner grid points
    psi(i) = deta(i)*(1/(2*hr))*(theta(i+1) - theta(i-1));
end

i=Npoints; %BC at ra
psi(i) = deta(i)*(1/(2*hr))*(3*theta(i) - 4*theta(i-1) + theta(i-2));
%Done

%PLATE STRESS: Calculate the stress vectors in the plate.
for i=1:Npoints
    Sro(i) = (k^2/(12*(1-nu^2)))*(1 + beta^2/(xi(i)^2));
    sigma_r_top(i) = (E*tvm^2/ra^2)*(Sro(i) + Sr(i) - (1/(2*(1-nu^2)))*(psi(i) +
    (nu*theta(i))./xi(i)));
    sigma_r_bot(i) = (E*tvm^2/ra^2)*(Sro(i) + Sr(i) + (1/(2*(1-nu^2)))*(psi(i) +
    (nu*theta(i))./xi(i)));
end
if max(sigma_r_top) > max(sigma_r_bot)
    maxstress = abs(max(sigma_r_top));
else
    maxstress = abs(max(sigma_r_bot));
end
%Done

%CONVERSION TO NON_DIMENSIONAL PARAMETERS
r=xi*ra;
y=W*tvm;
thetaND=theta*tvm/ra; %This non-dimensional theta is dw/dr
psiND=psi*tvm/(ra^2); %This non-dimensional psi is d2w/dr2

%PLATE SWEEP VOLUME: Calculate total swept volume under cap and membrane.
V=0;
for i=1:Npoints-1
    dV(i) = pi*(r(i+1)^2-r(i)^2)*0.5*(y(i+1)+y(i));
    V = V + dV(i);
end
yvc = y(1);
Vcap = yvc*pi*rb^2;
Vtotal = Vcap + V;
%Done

```

B.3 NLValveCapMembrane-CaseC.m [see Section 3.5]

```
function
[y,r,Vtotal,psi,W,theta,xi,thetaND,psiND,sigma_r_top,sigma_r_bot,yvc,Fvc,maxstress] =
NLValveCapMembrane_CaseC(Pvm,yvc_imposed,rb,ra,tvm,E,nu,flagNL,No)

%NLValveCapMembrane_CaseC.m

%David C. Roberts
%This Matlab code solves for the non-linear deflection behavior of the valve cap/
%membrane under loading Pvm and a desired valve cap deflection at r=rb. The required
%Fvc to produce this deflection and the resulting deflection, slope, curvature,
%seep volume, and membrane stress are calculated. Case C refers to the fact that
%we are applying Pvm and imposing a cap deflection, and then solving for the Fvc
%and the resulting structural response. Prior to calling this code, the user must
%define Pvm as a function of PHAC and P2. This Pvm loading is defined as follows:
% Pvm = PHAC-P2
%
%
%The plate/membrane is characterized by inner radius rb, outer radius ra, thickness
%tvm, and material properties E and nu. If flagNL=0, only linear theory will be
%considered. If flagNL=1, non-linear theory will be considered. No is the value of
%the in-plane pretension. In this file, yvc is the valve cap deflection (Zvc).

format long;

%%%%%%%%%%%%%%%%%%%%%%%%%%%%%%%%%%%%%%%%%%%%%%%%%%%%%%%%%%%%%%%%%%%%%%%%
%Convert Inputs to Dimensionless Quantities
Wb=yvc_imposed/tvm;
P = (Pvm*ra^4)/(E*tvm^4); %Dimensionless loading of pressure across cap/membrane

%%%%%%%%%%%%%%%%%%%%%%%%%%%%%%%%%%%%%%%%%%%%%%%%%%%%%%%%%%%%%%%%%%%%%%%%
beta = sqrt((1-nu)/(1+nu))*(rb/ra);
k = (ra/tvm)*sqrt((12*(1-nu^2)*No)/(E*tvm*(1-beta^2)));
s = beta*k;

%%%%%%%%%%%%%%%%%%%%%%%%%%%%%%%%%%%%%%%%%%%%%%%%%%%%%%%%%%%%%%%%%%%%%%%%
%%Section 2: Define grid spacing and coordinate transformation parameters
%%for finite-difference method
%%%%%%%%%%%%%%%%%%%%%%%%%%%%%%%%%%%%%%%%%%%%%%%%%%%%%%%%%%%%%%%%%%%%%%%%
Npoints=200; %The total # of grid points to use (MUST KEEP IT EVEN)
alpha=1.01; %Grid density parameter
phi=(alpha+1)/(alpha-1); %Grid density ratio
hr = 1/(Npoints-1); %Size of grid spacing
eta = 0:hr:1; %Vector of evenly spaced points between 0 and 1

xi_b = rb/ra; %Non-dimensional position of inner radius
xi_c = (rb+ra)/(2*ra); %Non-dimensional position of midpoint along membrane
xi_a = ra/ra; %Non-dimensional position of outer radius

%For the grid points from xi_b to xi_c, define the derivatives of eta with respect to xi
for i=1:Npoints/2,
xi(i) = xi_b + (alpha-1)*(xi_c-xi_b)*(phi-phi^(1-2*eta(i)))/(1+phi^(1-2*eta(i)));
m = (alpha-1)*(xi_c-xi_b);
m2 = m*phi - m + 2*xi_b;
deta(i) = (0.5/log(phi))*(m*(1+phi))/((m*phi-(xi(i)-xi_b))*(m*(xi(i)-xi_b)));
d2eta(i) = -(0.5/log(phi))*(m*(1+phi)*(m2-2*xi(i)))/((m*phi-(xi(i)-xi_b))*(m*(xi(i)-xi_b)))^2;
end

%For the grid points from xi_c to xi_a
for i=Npoints/2+1:Npoints,
xi(i) = xi_b + (alpha-1)*(xi_c-xi_b)*(phi-phi^(1-2*eta(i)))/(1+phi^(1-2*eta(i)));
m = (alpha-1)*(xi_c-xi_b);
m2 = m*phi - m + 2*xi_b;
deta(i) = (0.5/log(phi))*(m*(1+phi))/((m*phi-(xi(i)-xi_b))*(m*(xi(i)-xi_b)));
d2eta(i) = -(0.5/log(phi))*(m*(1+phi)*(m2-2*xi(i)))/((m*phi-(xi(i)-xi_b))*(m*(xi(i)-xi_b)))^2;
```

```

end

%%%%%%%%%%%%%%%%%%%%%%%%%%%%%%%%%%%%%%%%%%%%%%%%%%%%%%%%%%%%%%%%%%%%%%%%%%%%%%
%%Section 3: Finite-Difference Implementation
%%%%%%%%%%%%%%%%%%%%%%%%%%%%%%%%%%%%%%%%%%%%%%%%%%%%%%%%%%%%%%%%%%%%%%%%%%%%%%

%Governing equations at internal points (from 2 to Npoints-1)
for i=2:Npoints-1,
    A(i,i-1) = (xi(i)^2*deta(i)^2)/(hr^2) - (xi(i)^2*d2deta(i) + xi(i)*deta(i))/(2*hr);
    A(i,i) = -(2*xi(i)^2*deta(i)^2)/(hr^2) + (s^2+1) + xi(i)^2*k^2;
    A(i,i+1) = (xi(i)^2*deta(i)^2)/(hr^2) + (xi(i)^2*d2deta(i) + xi(i)*deta(i))/(2*hr);

    B(i,i-1) = (xi(i)^2*deta(i)^2)/(hr^2) - (xi(i)^2*d2deta(i) + 3*xi(i)*deta(i))/(2*hr);
    B(i,i) = -(2*xi(i)^2*deta(i)^2)/(hr^2);
    B(i,i+1) = (xi(i)^2*deta(i)^2)/(hr^2) + (xi(i)^2*d2deta(i) + 3*xi(i)*deta(i))/(2*hr);

    C(i) = 6*(1-nu^2)*P*(xi(i)^3 - xi(i)*(rb/ra)^2);
end

%Boundary condition equations at xi_b (grid point #1)
A(1,1) = 1;
B(1,1) = -3*xi(1)*deta(1)/(2*hr) + (1-nu);
B(1,2) = 4*xi(1)*deta(1)/(2*hr);
B(1,3) = -xi(1)*deta(1)/(2*hr);
C(1) = 0;

%Boundary condition equations at xi_a (grid point #Npoints)
A(Npoints,Npoints) = 1;
B(Npoints,Npoints-2) = xi(Npoints)*deta(Npoints)/(2*hr);
B(Npoints,Npoints-1) = -4*xi(Npoints)*deta(Npoints)/(2*hr);
B(Npoints,Npoints) = 3*xi(Npoints)*deta(Npoints)/(2*hr) + (1-nu);
C(Npoints) = 0;

%IMPORTANT: Since F is an unknown, an extra column and row are added to A to solve for F
%and therefore the added entry to C is the non-dimensional deflection Wb.

%Define entries in additional column of A
A(1,Npoints+1) = 0; %BC at r=rb
for i=2:Npoints-1
    A(i,Npoints+1) = -6*(1-nu^2)*xi(i); %central points
end
A(Npoints,Npoints+1) = 0; %BC at r=ra
A(Npoints+1,Npoints+1) = 0; %This is a meaningless entry so it must be zero.

%Define entries in additional row of A
A(Npoints+1,1) = -(hr/2)/deta(1);
for i=2:Npoints-1
    A(Npoints+1,i) = -(hr)/deta(i);
end
A(Npoints+1,Npoints) = -(hr/2)/deta(Npoints);

%Define additional entry in C
C(Npoints+1) = Wb;

%%%%%%%%%%%%%%%%%%%%%%%%%%%%%%%%%%%%%%%%%%%%%%%%%%%%%%%%%%%%%%%%%%%%%%%%%%%%%%
%%Section 4: Provide an initial guess for the theta vector (plate slope), to be
%%used in the finite-difference iteration procedure.
%%%%%%%%%%%%%%%%%%%%%%%%%%%%%%%%%%%%%%%%%%%%%%%%%%%%%%%%%%%%%%%%%%%%%%%%%%%%%%

if k==0,
    %theta = (-0.75*(1-nu^2)*P*xi.*(1-xi.^2))'; %Linear result
    theta=xi';
else
    theta=xi';
end

```

```

#####
***Section 5: Matrix Manipulation Procedure
#####

Niterations=500;          %Perform up to 500 iterations
tolerance1=1e-8;
tolerance2=1e-8;
omega=0.45;              %Under-relaxation parameter
if flagNL==1              %this variable is passed into file.
    Nloption=1;           %0 = Linear solution; 1 = NonLinear solution
else
    Nloption=0;
end

for i=1:Niterations,
    1;
    for j=2:Npoints-1      %Define D vector for each iteration
        D(j) = -0.5*theta(j).^2;
    end
    D(1)=0;
    D(Npoints)=0;

    Sr = inv(B)*D'*Nloption; %Solve for Sr
    v_Sr = 12*(1-nu^2)*xi'.^2.*Sr; %Calculate non-linear correction term v_Sr
    v_Sr(Npoints+1) = 0; %Make v_Sr the proper length
    A2 = A - diag(v_Sr,0); %Subtract non-linear correction term from A
    theta_new = inv(A2)*C'; %Calculate new theta vector
    F_result = theta_new(Npoints+1); %Record the calculated value of F
    theta_new = theta_new(1:Npoints); %Remove the F entry from the theta vector

    inner_product = (theta_new'*theta)/sqrt(theta_new'*theta_new)/sqrt(theta'*theta);
    length_ratio = sqrt(theta_new'*theta_new)/sqrt(theta'*theta);

    if (1-inner_product) >= tolerance1 | (1-length_ratio) >= tolerance2
        theta = (1-omega)*theta + omega*theta_new;
    else
        break;
    end
end

#####
***Section 6: Calculate Deflection, Curvature, Stress, and Swept Volume in this
***post-processing section.
#####

%CALCULATE Fvcstar
Fvc = F_result*(pi*E*tvm^4)/(ra^2); %Dimensionalize the additional cap force
%Done

%PLATE DEFLECTION: Calculate plate deflection vector from the final theta vector,
%using 2nd-order forward, backward, and central difference methods to express
%theta in terms of W. Then, using matrix inversion to obtain the vector W.
i=1; %BC at xb
Wmatrix(i,i) = deta(i)*(-3/(2*hr));
Wmatrix(i,i+1) = deta(i)*(2/hr);
Wmatrix(i,i+2) = deta(i)*(-1/(2*hr));

for i=2:Npoints-1 %Inner grid points
    Wmatrix(i,i-1) = deta(i)*(-1/(2*hr));
    Wmatrix(i,i+1) = deta(i)*(1/(2*hr));
end

%BC at ra --> Do not do for the outer boundary condition. We already know that
%the deflection at ra is equal to zero.

W = inv(Wmatrix(1:Npoints-1,1:Npoints-1))*theta(1:Npoints-1);
W=[W;0];

```

```

%Done

%PLATE CURVATURE: Calculate plate curvature vector from the final theta vector,
%using 2nd-order forward, backward, and central difference methods.
i=1; %BC at rb
psi(i) = deta(i)*(1/(2*hr))*(-3*theta(i) + 4*theta(i+1) - theta(i+2));

for i=2:Npoints-1 %Inner grid points
    psi(i) = deta(i)*(1/(2*hr))*(theta(i+1) - theta(i-1));
end

i=Npoints; %BC at ra
psi(i) = deta(i)*(1/(2*hr))*(3*theta(i) - 4*theta(i-1) + theta(i-2));
%Done

%PLATE STRESS: Calculate the stress vectors in the plate.

for i=1:Npoints
    Sro(i) = (k^2/(12*(1-nu^2)))*(1 + beta^2/(xi(i)^2));
    sigma_r_top(i) = (E*tvm^2/ra^2)*(Sro(i) + Sr(i) - (1/(2*(1-nu^2)))*(psi(i) +
    (nu*theta(i))./xi(i)));
    sigma_r_bot(i) = (E*tvm^2/ra^2)*(Sro(i) + Sr(i) + (1/(2*(1-nu^2)))*(psi(i) +
    (nu*theta(i))./xi(i)));
end
if max(sigma_r_top) > max(sigma_r_bot)
    maxstress = abs(max(sigma_r_top));
else
    maxstress = abs(max(sigma_r_bot));
end
%Done

%CONVERSION TO NON_DIMENSIONAL PARAMETERS
r=xi*ra;
y=W*tvm;
thetaND=theta*tvm/ra; %This non-dimensional theta is dw/dr
psiND=psi*tvm/(ra^2); %This non-dimensional psi is d2w/dr2

%PLATE SWEEP VOLUME: Calculate total swept volume under cap and membrane.
V=0;
for i=1:Npoints-1
    dV(i) = pi*(r(i+1)^2-r(i)^2)*0.5*(y(i+1)+y(i));
    V = V + dV(i);
end
yvc = y(1);
Vcap = yvc*pi*rb^2;
Vtotal = Vcap + V;
%Done

```


Appendix C

Support Documentation for Full Non-Linear Active Valve Model

C.1 FullActiveValve(Non-Linear).mws [Section 4.1]

File: FullActiveValve(NON-LINEAR).mws
 David C. Roberts
 This file creates the active valve matrix used in the full non-linear active valve Matlab model developed by Dave Roberts.
 This file defines all the active valve relations (except for the non-linear membrane relations which are solved for in the
 Matlab code: NLAActiveValveMatlab.m) and solves for the coefficients of the valve matrix A.
 > restart;
 > Digits:=40;

Digits := 40

Step 1: Define Linear Quasi-Static Relations

Piezoelectric Material
 [This relation assumes perfect d33 actuation (no effect of transverse clamping).
 > EQN1 := X[p] = d[33]*V[p] - (L[p]/E[p])*T[p];

$$EQN1 := Z_p = d_{33} V_p - \frac{L_p T_p}{E_p}$$
 [This relation determines the piezo charge.
 > EQN2 := Q[p] = (eT[33]*A[p]/L[p])*V[p] + (d[33]*A[p])*T[p];

$$EQN2 := Q_p = \frac{eT_{33} A_p V_p}{L_p} + d_{33} A_p T_p$$

Bottom Structural Compliance
 [Circular plate with stress imposed over central region.
 > EQN3 := X[bot] = (X1[Xbot,T]) * T[p];

$$EQN3 := Z_{bot} = \Xi_{Zbot, T} T_p$$

Drive Element Tethers
 > EQN4 := Z[te] =
 (X1[Xtstop,V]*X1[Xtbot,V]) / (X1[Xtstop,V]+X1[Xtbot,V]) * (A[p]*T[p]-A[pis]*P[HAC]) -
 (X1[Xtstop,V]*X1[Xtbot,P]) / (X1[Xtstop,V]+X1[Xtbot,V]) * P[HAC];

$$EQN4 := Z_p = \frac{\Xi_{Ztstop, P} \Xi_{Ztbot, P} (A_p T_p - A_{pis} P_{HAC})}{\Xi_{Ztstop, P} + \Xi_{Ztbot, P}} - \frac{\Xi_{Ztstop, P} \Xi_{Ztbot, P} P_{HAC}}{\Xi_{Ztstop, P} + \Xi_{Ztbot, P}}$$
 > EQN5 := dV[te] =
 (X1[dVtstop,V]*X1[Xtbot,V]) / (X1[Xtstop,V]+X1[Xtbot,V]) * (A[p]*T[p]-A[pis]*P[HAC]) -
 (X1[dVtstop,P]*X1[Xtbot,P]) / (X1[Xtstop,V]+X1[Xtbot,V]) * P[HAC] + A[pis]*X[te];

$$EQN5 := dV_p = \frac{\Xi_{dVtstop, P} \Xi_{Ztbot, P} (A_p T_p - A_{pis} P_{HAC})}{\Xi_{Ztstop, P} + \Xi_{Ztbot, P}} - \frac{\Xi_{dVtstop, P} \Xi_{Ztbot, P} P_{HAC}}{\Xi_{Ztstop, P} + \Xi_{Ztbot, P}} + A_{pis} Z_p$$

Drive Element Piston
 > EQN6 := X[pis] = X1[Xpis,T]*T[p] - X1[Xpis,P]*P[HAC];

$$EQN6 := Z_{pis} = \Xi_{Xpis, T} T_p - \Xi_{Xpis, P} P_{HAC}$$
 > EQN7 := dV[pis] = X1[dVpis,T]*T[p] - X1[dVpis,P]*P[HAC];

$$EQN7 := dV_{pis} = \Xi_{dVpis, T} T_p - \Xi_{dVpis, P} P_{HAC}$$

Fluid Compressibility
 > EQN8 := dV[fluid] = -(V[HAC]/E[d])*P[HAC];

Page 1

$$EQN3 := dV_{fluid} = -\frac{V_{HAC} P_{HAC}}{K_f}$$

Top Structural Compliance

- > EQN9 := Z[top] = X1[Ztop, F]*P[HAC] + X1[Ztop, F]*F[vm];
- $EQN9 := Z_{top} = \Xi_{Ztop, F} P_{HAC} + \Xi_{Ztop, F} F_{vm}$
- > EQN10 := dV[top] = X1[dVtop, F]*P[HAC] + X1[dVtop, F]*F[vm] + A[vm]*Z[top];
- $EQN10 := dV_{top} = \Xi_{dVtop, F} P_{HAC} + \Xi_{dVtop, F} F_{vm} + A_{vm} Z_{top}$
- > EQN11 := F[vm] = (A[vm]-A[vc])*(P[HAC]-P[1]) + A[vc]*(P[HAC]-P[1]);
- $EQN11 := F_{vm} = (A_{vm} - A_{vc})(P_{HAC} - P_1) + A_{vc}(P_{HAC} - P_1)$

Valve Cap/Membrane

- [The only valve/cap membrane relation defined here is the sum of the forces on the valve cap.
- > EQN12 := F[vc] = (P[HAC]-P[1])*A[vc];
- $EQN12 := F_{vc} = A_{vc}(P_{HAC} - P_1)$

Deflection, Swept Volume Conservation

- [All structural deflections and swept volumes are defined to be positive in the upward direction.
- > EQN13 := Z[p] + Z[bot] = Z[ta] + Z[pia];
- $EQN13 := Z_p + Z_{bot} = Z_u + Z_{pu}$

Other Relations

- [Variables as functions of other variables.
- > EQN14 := Z[da] = Z[ta] + Z[pia];
- $EQN14 := Z_{da} = Z_u + Z_{pu}$

Step 2: Define Geometric/Material Parameters

- [Geometric Parameters:
- > R[vc]:=0.31e-3; R[vm]:=0.80e-3; t[vm]:=10e-6; A[vc]:=Pi*R[vc]^2; A[vm]:=Pi*R[vm]^2;
- t[vc]:=400e-6;
- > L[p]:=1e-3; R[p]:=1e-3; A[p]:=Pi*R[p]^2;
- > R[pia]:=3e-3; R[ch]:=3.225e-3; t[pia]:=800e-6; t[toptta]:=10e-6; t[botta]:=10e-6;
- A[pia]:=Pi*R[pia]^2;
- > t[bot]:=1000e-6;
- > H[HAC]:=400e-6; V[HAC]:=Pi*R[ch]^2*H[HAC] + Pi*(R[vm]^2-R[vc]^2)*t[vc];
- > t[top]:=1000e-6;
- [Material Parameters:
- > d[33]:=2000e-12; sD[33]:=16.4e-12; sE[33]:=111e-12; E[p]:=1/sE[33];
- eT[33]:=d[33]^2/(sE[33]-sD[33]); E[s1]:=165e9; nu[s1]:=0.22; K[L]:=2e9; alpha[s1]:=1.25;

Step 3: Calculate Linear Plate Coefficients

- Bottom Structural Compliance [Identical to FullActiveValve(LINEAR).mws]**
- Drive Element Tethers [Identical to FullActiveValve(LINEAR).mws]**
- Drive Element Piston (More Compliant: Hinged Outer Circumference) [Identical to**

Page 2

FullActiveValve(LINEAR).mws]

 Drive Element Piston (Less Compliant: Rigid Outer Circumference) [Identical to FullActiveValve(LINEAR).mws]

 Drive Element Piston (Averaged Compliance) [Identical to FullActiveValve(LINEAR).mws]

 Top Structural Compliance [Identical to FullActiveValve(LINEAR).mws]

Step 4: Solve Equations

The variables [Zp, Tp, Qp, Zbot, Zic, dVie, Zpis, dVpis, dVfluid, Ztop, dVtop, Fvm, Fvc, and Zde] are solved for in terms of the other variables [Vp, P1, P2, and PHAC]. Once solved for, each of the coefficients is assigned to the proper location in matrix A, which are then passed to NLAActiveValveMatlab.m.

```
> Solutions:=solve([EQN1, EQN2, EQN3, EQN4, EQN5, EQN6, EQN7, EQN8, EQN9, EQN10, EQN11, EQN12, EQN13, EQN14], [E[p], T[p], Q[p], Z[bot], Z[te], dV[te], E[ps], dV[ps], dV[fluid], Z[top], dV[top], F[vm], F[vc], Z[de]]):  
[  
  > A11:=evalf(subs({V[p]=1, P[1]=0, P[2]=0, P[PHAC]=0}, subs(Solutions, E[p]))):  
  > A12:=evalf(subs({V[p]=0, P[1]=1, P[2]=0, P[PHAC]=0}, subs(Solutions, E[p]))):  
  > A13:=evalf(subs({V[p]=0, P[1]=0, P[2]=1, P[PHAC]=0}, subs(Solutions, E[p]))):  
  > A14:=evalf(subs({V[p]=0, P[1]=0, P[2]=0, P[PHAC]=1}, subs(Solutions, E[p]))):  
  >  
  > A21:=evalf(subs({V[p]=1, P[1]=0, P[2]=0, P[PHAC]=0}, subs(Solutions, T[p]))):  
  > A22:=evalf(subs({V[p]=0, P[1]=1, P[2]=0, P[PHAC]=0}, subs(Solutions, T[p]))):  
  > A23:=evalf(subs({V[p]=0, P[1]=0, P[2]=1, P[PHAC]=0}, subs(Solutions, T[p]))):  
  > A24:=evalf(subs({V[p]=0, P[1]=0, P[2]=0, P[PHAC]=1}, subs(Solutions, T[p]))):  
  >  
  > A31:=evalf(subs({V[p]=1, P[1]=0, P[2]=0, P[PHAC]=0}, subs(Solutions, Q[p]))):  
  > A32:=evalf(subs({V[p]=0, P[1]=1, P[2]=0, P[PHAC]=0}, subs(Solutions, Q[p]))):  
  > A33:=evalf(subs({V[p]=0, P[1]=0, P[2]=1, P[PHAC]=0}, subs(Solutions, Q[p]))):  
  > A34:=evalf(subs({V[p]=0, P[1]=0, P[2]=0, P[PHAC]=1}, subs(Solutions, Q[p]))):  
  >  
  > A41:=evalf(subs({V[p]=1, P[1]=0, P[2]=0, P[PHAC]=0}, subs(Solutions, Z[bot]))):  
  > A42:=evalf(subs({V[p]=0, P[1]=1, P[2]=0, P[PHAC]=0}, subs(Solutions, Z[bot]))):  
  > A43:=evalf(subs({V[p]=0, P[1]=0, P[2]=1, P[PHAC]=0}, subs(Solutions, Z[bot]))):  
  > A44:=evalf(subs({V[p]=0, P[1]=0, P[2]=0, P[PHAC]=1}, subs(Solutions, Z[bot]))):  
  >  
  > A51:=evalf(subs({V[p]=1, P[1]=0, P[2]=0, P[PHAC]=0}, subs(Solutions, Z[te]))):  
  > A52:=evalf(subs({V[p]=0, P[1]=1, P[2]=0, P[PHAC]=0}, subs(Solutions, Z[te]))):  
  > A53:=evalf(subs({V[p]=0, P[1]=0, P[2]=1, P[PHAC]=0}, subs(Solutions, Z[te]))):  
  > A54:=evalf(subs({V[p]=0, P[1]=0, P[2]=0, P[PHAC]=1}, subs(Solutions, Z[te]))):  
  >  
  > A61:=evalf(subs({V[p]=1, P[1]=0, P[2]=0, P[PHAC]=0}, subs(Solutions, dV[te]))):  
  > A62:=evalf(subs({V[p]=0, P[1]=1, P[2]=0, P[PHAC]=0}, subs(Solutions, dV[te]))):  
  > A63:=evalf(subs({V[p]=0, P[1]=0, P[2]=1, P[PHAC]=0}, subs(Solutions, dV[te]))):
```

```

[> A64:=evalf(subs({V[p]=0,P[1]=0,P[2]=0,P[HAC]=1},subs(Solutions,dV[te]))):
[>
[> A71:=evalf(subs({V[p]=1,P[1]=0,P[2]=0,P[HAC]=0},subs(Solutions,Z[pi]))):
[> A72:=evalf(subs({V[p]=0,P[1]=1,P[2]=0,P[HAC]=0},subs(Solutions,Z[pi]))):
[> A73:=evalf(subs({V[p]=0,P[1]=0,P[2]=1,P[HAC]=0},subs(Solutions,Z[pi]))):
[> A74:=evalf(subs({V[p]=0,P[1]=0,P[2]=0,P[HAC]=1},subs(Solutions,Z[pi]))):
[>
[> A81:=evalf(subs({V[p]=1,P[1]=0,P[2]=0,P[HAC]=0},subs(Solutions,dV[pi]))):
[> A82:=evalf(subs({V[p]=0,P[1]=1,P[2]=0,P[HAC]=0},subs(Solutions,dV[pi]))):
[> A83:=evalf(subs({V[p]=0,P[1]=0,P[2]=1,P[HAC]=0},subs(Solutions,dV[pi]))):
[> A84:=evalf(subs({V[p]=0,P[1]=0,P[2]=0,P[HAC]=1},subs(Solutions,dV[pi]))):
[>
[> A91:=evalf(subs({V[p]=1,P[1]=0,P[2]=0,P[HAC]=0},subs(Solutions,dV[fluid]))):
[> A92:=evalf(subs({V[p]=0,P[1]=1,P[2]=0,P[HAC]=0},subs(Solutions,dV[fluid]))):
[> A93:=evalf(subs({V[p]=0,P[1]=0,P[2]=1,P[HAC]=0},subs(Solutions,dV[fluid]))):
[> A94:=evalf(subs({V[p]=0,P[1]=0,P[2]=0,P[HAC]=1},subs(Solutions,dV[fluid]))):
[>
[> A101:=evalf(subs({V[p]=1,P[1]=0,P[2]=0,P[HAC]=0},subs(Solutions,Z[top]))):
[> A102:=evalf(subs({V[p]=0,P[1]=1,P[2]=0,P[HAC]=0},subs(Solutions,Z[top]))):
[> A103:=evalf(subs({V[p]=0,P[1]=0,P[2]=1,P[HAC]=0},subs(Solutions,Z[top]))):
[> A104:=evalf(subs({V[p]=0,P[1]=0,P[2]=0,P[HAC]=1},subs(Solutions,Z[top]))):
[>
[> A111:=evalf(subs({V[p]=1,P[1]=0,P[2]=0,P[HAC]=0},subs(Solutions,dV[top]))):
[> A112:=evalf(subs({V[p]=0,P[1]=1,P[2]=0,P[HAC]=0},subs(Solutions,dV[top]))):
[> A113:=evalf(subs({V[p]=0,P[1]=0,P[2]=1,P[HAC]=0},subs(Solutions,dV[top]))):
[> A114:=evalf(subs({V[p]=0,P[1]=0,P[2]=0,P[HAC]=1},subs(Solutions,dV[top]))):
[>
[> A121:=evalf(subs({V[p]=1,P[1]=0,P[2]=0,P[HAC]=0},subs(Solutions,F[vm]))):
[> A122:=evalf(subs({V[p]=0,P[1]=1,P[2]=0,P[HAC]=0},subs(Solutions,F[vm]))):
[> A123:=evalf(subs({V[p]=0,P[1]=0,P[2]=1,P[HAC]=0},subs(Solutions,F[vm]))):
[> A124:=evalf(subs({V[p]=0,P[1]=0,P[2]=0,P[HAC]=1},subs(Solutions,F[vm]))):
[>
[> A131:=evalf(subs({V[p]=1,P[1]=0,P[2]=0,P[HAC]=0},subs(Solutions,F[vc]))):
[> A132:=evalf(subs({V[p]=0,P[1]=1,P[2]=0,P[HAC]=0},subs(Solutions,F[vc]))):
[> A133:=evalf(subs({V[p]=0,P[1]=0,P[2]=1,P[HAC]=0},subs(Solutions,F[vc]))):
[> A134:=evalf(subs({V[p]=0,P[1]=0,P[2]=0,P[HAC]=1},subs(Solutions,F[vc]))):
[>
[> A141:=evalf(subs({V[p]=1,P[1]=0,P[2]=0,P[HAC]=0},subs(Solutions,Z[de]))):
[> A142:=evalf(subs({V[p]=0,P[1]=1,P[2]=0,P[HAC]=0},subs(Solutions,Z[de]))):
[> A143:=evalf(subs({V[p]=0,P[1]=0,P[2]=1,P[HAC]=0},subs(Solutions,Z[de]))):
[> A144:=evalf(subs({V[p]=0,P[1]=0,P[2]=0,P[HAC]=1},subs(Solutions,Z[de]))):
[>

```

 Step 5: Output Matrix to Matlab File

Page 4

```

Now that all the matrix coefficients have been solved for, it is necessary to output these values to a file which Matlab can read.
Also,
output the important valve geometry parameters (rb, ra, tvn, E, nu) for use in the non-linear Matlab code.
[ > interface(cho=0);
[ > write('FullActiveValveMatrix.m');
[ > printf('A(1,1) = %+2.08e;',A11);
[ > printf('A(1,2) = %+2.08e;',A12);
[ > printf('A(1,3) = %+2.08e;',A13);
[ > printf('A(1,4) = %+2.08e;',A14);
[ > printf('A(2,1) = %+2.08e;',A21);
[ > printf('A(2,2) = %+2.08e;',A22);
[ > printf('A(2,3) = %+2.08e;',A23);
[ > printf('A(2,4) = %+2.08e;',A24);
[ > printf('A(3,1) = %+2.08e;',A31);
[ > printf('A(3,2) = %+2.08e;',A32);
[ > printf('A(3,3) = %+2.08e;',A33);
[ > printf('A(3,4) = %+2.08e;',A34);
[ > printf('A(4,1) = %+2.08e;',A41);
[ > printf('A(4,2) = %+2.08e;',A42);
[ > printf('A(4,3) = %+2.08e;',A43);
[ > printf('A(4,4) = %+2.08e;',A44);
[ > printf('A(5,1) = %+2.08e;',A51);
[ > printf('A(5,2) = %+2.08e;',A52);
[ > printf('A(5,3) = %+2.08e;',A53);
[ > printf('A(5,4) = %+2.08e;',A54);
[ > printf('A(6,1) = %+2.08e;',A61);
[ > printf('A(6,2) = %+2.08e;',A62);
[ > printf('A(6,3) = %+2.08e;',A63);
[ > printf('A(6,4) = %+2.08e;',A64);
[ > printf('A(7,1) = %+2.08e;',A71);
[ > printf('A(7,2) = %+2.08e;',A72);
[ > printf('A(7,3) = %+2.08e;',A73);
[ > printf('A(7,4) = %+2.08e;',A74);
[ > printf('A(8,1) = %+2.08e;',A81);
[ > printf('A(8,2) = %+2.08e;',A82);
[ > printf('A(8,3) = %+2.08e;',A83);
[ > printf('A(8,4) = %+2.08e;',A84);
[ > printf('A(9,1) = %+2.08e;',A91);
[ > printf('A(9,2) = %+2.08e;',A92);
[ > printf('A(9,3) = %+2.08e;',A93);
[ > printf('A(9,4) = %+2.08e;',A94);
[ > printf('A(10,1) = %+2.08e;',A101);
[ > printf('A(10,2) = %+2.08e;',A102);
[ > printf('A(10,3) = %+2.08e;',A103);

```

Page 5

```
[ > printf('A(10,4) = %2.08e;',A104);
[ > printf('A(11,1) = %2.08e;',A111);
[ > printf('A(11,2) = %2.08e;',A112);
[ > printf('A(11,3) = %2.08e;',A113);
[ > printf('A(11,4) = %2.08e;',A114);
[ > printf('A(12,1) = %2.08e;',A121);
[ > printf('A(12,2) = %2.08e;',A122);
[ > printf('A(12,3) = %2.08e;',A123);
[ > printf('A(12,4) = %2.08e;',A124);
[ > printf('A(13,1) = %2.08e;',A131);
[ > printf('A(13,2) = %2.08e;',A132);
[ > printf('A(13,3) = %2.08e;',A133);
[ > printf('A(13,4) = %2.08e;',A134);
[ > printf('A(14,1) = %2.08e;',A141);
[ > printf('A(14,2) = %2.08e;',A142);
[ > printf('A(14,3) = %2.08e;',A143);
[ > printf('A(14,4) = %2.08e;',A144);
[ > printf('xvc = %2.08e;',R[vc]);
[ > printf('xvm = %2.08e;',R[vm]);
[ > printf('xvm = %2.08e;',t[vm]);
[ > printf('xsi = %2.08e;',E[s1]);
[ > printf('mus1 = %2.08e;',mu[s1]);
[ > writeto('terminal');
[ >
```

Page 6

C.2 NActiveValveMatlab.m [Section 4.1]

```

%[NActiveValveMatlab.m]    DAVID C. ROBERTS
%
% This file calculates the behavior of the active valve, with non-linear valve/cap
% membrane deformation included. First, the Maple file FullActiveValve(Non-Linear).mws
% is run in order to generate the matrix of linear valve relation coefficients. That matrix
% is then used in this file.

clear;
close all;
format long;
NActiveValveMatrix;    %Read in the linear matrix coefficients and the valve geometry
                        %from this file, which was generated by running
                        %NActiveValveMaple.mws. The matrix values go from A11,A12,A13,
                        %A14, A21, ..., A141,A142,A143,A144 and the valve geometry
                        %variables read in are rvc, rvm, tvn, Esl, nusi.

#####DEFINE INPUT PARAMETERS#####
Vp=500;    %Piezo Voltage
P1=0.5e6;    %Pressure on top of valve cap
P2=0e6;    %Pressure on top of valve membrane
flagNL=1;    %Include non-linearity if flagNL=1
No=0;    %Initial in-plane prestress

#####PROVIDE INITIAL GUESS FOR PHAC#####
PHACguess=0.0013e6;
PHAC1=PHACguess;
PHAC2=PHACguess;
check0=1;
check1=1;
i=0;
j=0

%Determine Volume discrepancy for initial PHAC guess
U=[Vp P1 P2 PHAC1];    %Vector of input parameters to compliance matrix
S=A*U';    %S is the vector of all linear responses
Fvc=S(13); Pvm=PHAC1-P2;    %Define these loadings for use in NActiveValve_MembraneCaseA.m
[y,r,Vtotal,psi,W,theta,xi,thetaND,psiND,sigma_r_top,sigma_r_bot,yvc,maxstress] =
NActiveValve_MembraneCaseA(Pvm,Fvc,rvc,rvm,tnv,Esl,nusi,flagNL,No);
dVvm=Vtotal; dVte=S(6); dVpis=S(8); dVfluid=S(9); dVtop=S(11);
check1 = (dVvm + dVtop - dVte - dVpis - dVfluid);
check0=check1;
%Done

%Determine range of PHAC (between PHAC0 and PHAC1) within which the real PHAC lies
while check0*check1/(abs(check0*check1))> 0
    i=0;
    j=j+1;

    PHAC0 = PHAC1;
    PHAC1 = PHAC2;
    check0 = check1

    U=[Vp P1 P2 PHAC1];    %Vector of input parameters to compliance matrix
    S=A*U';    %S is the vector of all linear responses
    Fvc=S(13); Pvm=PHAC1-P2;    %Define these loadings for use in
NActiveValve_MembraneCaseA.m
[y,r,Vtotal,psi,W,theta,xi,thetaND,psiND,sigma_r_top,sigma_r_bot,yvc,maxstress] =
NActiveValve_MembraneCaseA(Pvm,Fvc,rvc,rvm,tnv,Esl,nusi,flagNL,No);
dVvm=Vtotal; dVte=S(6); dVpis=S(8); dVfluid=S(9); dVtop=S(11);
    check1 = (dVvm + dVtop - dVte - dVpis - dVfluid);

    if check1 < 0
        PHAC2 = 10*PHAC1;
    end
end

```



```

elseif check1 > 0
    PHAC2 = 0.1*PHAC1;
else
    break;
end
end
if PHAC1<PHAC0          %rearrange PHAC0 to be less than PHAC1
    PHACmax=PHAC0;
    PHACmin=PHAC1;
    PHAC1=PHACmax
    PHAC0=PHACmin
else
    %DONE,it has been determined that PHAC lies between PHAC0 and PHAC1

j=0;

%Determine solution for Pvc
PHACm=0.5*(PHAC0+PHAC1);
firsthalf=0;

while abs((PHAC1-PHAC0)/PHAC0) > 0.0001

    i=1
    j=j+1

    if firsthalf==1

        U=[P1 P2 PHACm];          %Vector of input parameters to compliance matrix
        S=A*U';                  %S is the vector of all linear responses
        Fvc=S(13); Pvm=PHACm-P2; %Define these loadings for use in
        NlActiveValve_MembraneCaseA.m
        [y,r,VtTotal,psi,W,theta,xi,thetaND,psiND,sigma_r_top,sigma_r_bot,yvc,maxstress] =
        NlActiveValve_MembraneCaseA(Pvm,Fvc,rvc,rvm,tvm,Esi,nusi,flagNL,No);
        dVvm=VtTotal; dVte=S(6); dVpis=S(8); dVfluid=S(9); dVtop=S(11);
        checkm = (dVvm + dVtop - dVte - dVpis - dVfluid);

    else

        U=[P1 P2 PHAC0];          %Vector of input parameters to compliance matrix
        S=A*U';                  %S is the vector of all linear responses
        Fvc=S(13); Pvm=PHAC0-P2; %Define these loadings for use in
        NlActiveValve_MembraneCaseA.m
        [y,r,VtTotal,psi,W,theta,xi,thetaND,psiND,sigma_r_top,sigma_r_bot,yvc,maxstress] =
        NlActiveValve_MembraneCaseA(Pvm,Fvc,rvc,rvm,tvm,Esi,nusi,flagNL,No);
        dVvm=VtTotal; dVte=S(6); dVpis=S(8); dVfluid=S(9); dVtop=S(11);
        check0 = (dVvm + dVtop - dVte - dVpis - dVfluid);

        U=[P1 P2 PHACm];          %Vector of input parameters to compliance matrix
        S=A*U';                  %S is the vector of all linear responses
        Fvc=S(13); Pvm=PHACm-P2; %Define these loadings for use in
        NlActiveValve_MembraneCaseA.m
        [y,r,VtTotal,psi,W,theta,xi,thetaND,psiND,sigma_r_top,sigma_r_bot,yvc,maxstress] =
        NlActiveValve_MembraneCaseA(Pvm,Fvc,rvc,rvm,tvm,Esi,nusi,flagNL,No);
        dVvm=VtTotal; dVte=S(6); dVpis=S(8); dVfluid=S(9); dVtop=S(11);
        checkm = (dVvm + dVtop - dVte - dVpis - dVfluid);

    end

    if check0*checkm <= 0
        PHAC1=PHACm;
        firsthalf=1;
    else
        PHAC0=PHACm;
        firsthalf=0;
    end
end

```

```

    PHACm=0.5*(PHAC0+PHAC1)
end
PHAC=PHACm;
%DONE, PHAC solution has been determined

%Evaluate all parameters for last value of PHACm
U=[Vp P1 P2 PHACm]; %Vector of input parameters to compliance matrix
S=A*U'; %S is the vector of all linear responses
Fvc=S(13); Pvm=PHACm-P2; %Define these loadings for use in NLAActiveValve_MembraneCaseA.m
[y,x,Vtotal,psi,W,theta,xi,thetaND,psiND,sigma_r_top,sigma_r_bot,yvc,maxstress] =
NLAActiveValve_MembraneCaseA(Pvm,Fvc,rvc,rvm,tvm,Esl,nusi,flagNL,No);

Zp=S(1) %Print to screen all results
Tp=S(2)
Qp=S(3)
Zbot=S(4)
Zte=S(5)
dVte=S(6)
Zpis=S(7)
dVpis=S(8)
dVfluid=S(9)
Ztop=S(10)
dVtop=S(11)
Fvm=S(12)
Fvc=S(13)
Zde=S(14)
Zvc=yvc+Ztop
dVvm=Vtotal
maxstress
%DONE

```

Hydraulic Amplification for Actuation in MicroElectroMechanical Systems

by

J. Lodewyk Steyn

B.Eng.(Mechanical), 1998
University of Pretoria, South Africa

Submitted to the Department of Aeronautical and Astronautical Engineering
in partial fulfillment of the requirements for the degree of

Master of Science

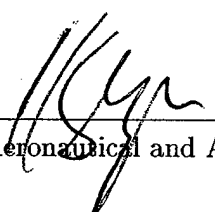
at the

MASSACHUSETTS INSTITUTE OF TECHNOLOGY

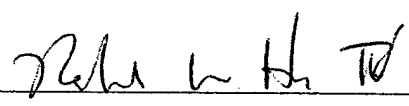
February 2002

© Massachusetts Institute of Technology, MMII. All rights reserved.


Author

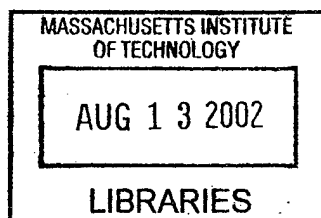

Department of Aeronautical and Astronautical Engineering
1 February 2002

Certified by


Nesbitt W. Hagood IV
Associate Professor of Aeronautics and Astronautics
Thesis Supervisor

Accepted by


Wallace E. VanderVelde
Professor of Aeronautics and Astronautics
Chairman, Committee on Graduate Students



AERO 1

Hydraulic Amplification for Actuation in MicroElectroMechanical Systems

by
J. Lodewyk Steyn

Submitted to the Department of Aeronautical and Astronautical Engineering
on 1 February 2002, in partial fulfillment of the
requirements for the degree of
Master of Science

Abstract

In this work the concept of hydraulic amplification as a means of stroke amplification is explored for applications in MicroElectroMechanical Systems (MEMS). Building on the batch fabrication technologies of the semiconductor industry, MEMS technology could enable the simultaneous fabrication of multiple microhydraulic systems of which hydraulic amplifiers would form part. Precision lithography would furthermore make dense arrays of microhydraulic systems possible, with the eventual goal being to create high power density microscale actuation and power generation systems.

This document provides an overview of the design considerations required for a successful microfabricated hydraulic amplifier, and proceeds to discuss the techniques developed to successfully fabricate, assemble and test such a device. Deep Reactive Ion Etching (DRIE) techniques were developed for creating strong tethered membrane structures using Silicon On Insulator (SOI) technology. Bonding techniques included silicon-silicon fusion bonding of fragile wafers and silicon-glass anodic bonding and alignment on the wafer and die level to produce multi-layered structures. Liquid filling of micromachined dead volumes through micron-size channels was performed. Static sealing techniques for leak-free sealing of micromachined, filled dead volumes with minimal seal compression and dynamic sealing techniques when quasi-static actuation is not a prerequisite were successfully developed.

Using these techniques, several hydraulic amplification devices have been produced. Testing of these devices revealed good correlation with theoretical predictions. Stroke amplification ratios as high as 48 : 1 have been observed. In addition, natural frequencies of up to 10kHz were measured. In conclusion, this work verifies the viability of hydraulic amplification for applications in microscale actuation systems.

Thesis Supervisor: Nesbitt W. Hagood IV

Title: Associate Professor of Aeronautics and Astronautics

Acknowledgments

This work was not an individual effort, and the author would like to thank the following persons for their contributions:

Professor Nesbitt Hagood, for his advice and guidance. Furthermore, Professors Kenny Breuer, Mark Spearing and Marty Schmidt for their advice.

Hanqing Li, for his constant advice and guidance and, most of all, for teaching me the art of microfabrication. It has been a truly eye-opening experience, which I will cherish for the rest of my career. The reader will also notice Hanqing's contributions throughout this work, with respect to mask design and process development.

Dave Roberts whose inputs in the whole development of this device were invaluable. In addition, for generating most of the model results for the hydraulic amplifier, for providing me with his code to use for the model-experiment correlation, and for his contributions to this document.

Developing MHT devices with Dave and Hanqing has been nothing but enjoyable, and it was a privilege to work with people of such caliber.

Jorge Carretero, for his words of wisdom and for his initial work on the fluid test bench.

Kevin Turner, for his feedback during our fillet radius process development.

Rick Mlcak, for his contributions in terms of fluid filling and the initial fabrication process development, on which these devices rely.

Onnik Yaglioglu, for the MHT device modeling.

Dave Robertson, AMSL lab manager, for his assistance and friendliness in the lab.

The following undergraduate students made significant contributions to this work under the MIT UROP program: Blair Connelly, for teaching us how to use the vibrometer, for making our chip trays, and other assistance in the lab. Geeta Gupta, for being my draftsman. Erik Stockham, for the LabView coding and his flowmeter, not mentioned in this document, but certainly very useful for the valves and the pumps and harvesters.

The author would further like to thank the MIT Microsystems Technology Laboratories for the use of their facilities. The following staff members were particularly helpful during the fabrication process: Bernard Alamariu, Kurt Broderick, Vicky Diadiuk, Paul McGrath and Paul Tierney.

The author expresses his gratitude to Professor Liou from the University of Nebraska for

the high-quality gold-tin thin film deposition performed on the piezoelectric materials used in the piezoelectrically driven hydraulic amplifiers.

In addition, I would like to thank my father, Professor Jasper Steyn, of the Department of Mechanical Engineering of the University of Pretoria, for his advice, guidance, and support and also for proofreading this document.

And then, in any such project, there are the people, family and friends, around oneself, not directly involved with the work, but still part of one's life, and thus indirectly involved and contributing and... always... supporting. To those people in my life I would like to extend this brief, personal, sincerest, "thank you".

This research was performed under ONR grants N00014-01-1-0857 and N00014-97-1-0880 and DARPA grant DAAG55-98-1-0361.

Contents

| | | |
|----------|--|-----------|
| 1 | Introduction | 19 |
| 1.1 | Objective | 19 |
| 1.2 | Survey of previous work | 20 |
| 1.2.1 | Macroscale hydraulic amplification | 20 |
| 1.2.2 | Microscale stroke amplification | 22 |
| 1.2.3 | Microfluidic and microhydraulic systems | 23 |
| 1.3 | Motivation | 24 |
| 1.4 | Method of investigation | 25 |
| | | |
| 2 | Design considerations | 29 |
| 2.1 | The ideal hydraulic amplifier | 29 |
| 2.2 | The practical hydraulic amplifier | 30 |
| 2.3 | The hydraulic amplifier evaluated in this work | 30 |
| 2.3.1 | Design considerations | 32 |
| 2.3.2 | Critical dimensions of the devices built | 33 |
| 2.4 | Stiffness matrix | 33 |
| 2.4.1 | A simple spring-based analogy | 35 |
| 2.4.2 | An hydraulic amplifier with sliding seals | 36 |
| 2.4.3 | An hydraulic amplifier with flexural seals | 38 |
| 2.5 | The nonlinear case | 39 |
| 2.5.1 | Nonlinear modeling and design of the hydraulic amplifier | 40 |
| 2.5.2 | Nonlinear simulation results | 42 |
| 2.6 | Summary | 42 |
| | | |
| 3 | Fabrication and device assembly | 49 |

8 Contents

| | | |
|----------|---|-----------|
| 3.1 | Fabrication overview | 49 |
| 3.2 | Process flow for creating silicon membrane structures | 50 |
| 3.2.1 | Membrane fillet radius control | 52 |
| 3.3 | Silicon fusion bonding techniques | 54 |
| 3.4 | Anodic bonding techniques and die-level assembly | 55 |
| 3.4.1 | Wafer-scale anodic bonding | 55 |
| 3.4.2 | Die-level assembly | 58 |
| 3.5 | Summary | 61 |
| 4 | Filling and sealing techniques | 63 |
| 4.1 | Filling techniques | 63 |
| 4.1.1 | Fluid requirements | 63 |
| 4.1.2 | Filling process | 64 |
| 4.1.3 | Initial tests | 67 |
| 4.2 | Sealing concepts | 68 |
| 4.2.1 | Static sealing | 68 |
| 4.2.2 | Dynamic sealing | 69 |
| 4.3 | Summary | 72 |
| 5 | Experimental techniques | 73 |
| 5.1 | Test rig requirements | 73 |
| 5.2 | System overview | 73 |
| 5.3 | Device test jigs | 74 |
| 5.4 | The fluid test bench | 75 |
| 5.4.1 | Gas pressure regulating module | 75 |
| 5.4.2 | Gas-liquid pressurization module | 76 |
| 5.4.3 | Pressure measurement and control module | 80 |
| 5.4.4 | Vacuum module | 80 |
| 5.5 | Displacement measurement | 83 |
| 5.6 | Data acquisition | 83 |

| | | |
|----------|--|------------|
| 5.7 | Testing protocols | 83 |
| 5.7.1 | Testing of static hydraulic amplifiers | 86 |
| 5.7.2 | Testing of dynamic hydraulic amplifiers | 87 |
| 6 | Experimental results | 89 |
| 6.1 | Overview | 89 |
| 6.2 | Pressure Deflection results | 91 |
| 6.2.1 | Pressure-deflection characteristics of the large piston | 91 |
| 6.2.2 | Pressure-deflection characteristics of the small piston structures | 92 |
| 6.2.3 | Summary: Pressure deflection results | 94 |
| 6.3 | Static hydraulic amplification tests | 95 |
| 6.3.1 | Testing: HAC Device 3 | 95 |
| 6.3.2 | Amplification ratios: HAC Device 3 | 97 |
| 6.3.3 | Stiffness matrix: HAC Device 3 | 99 |
| 6.3.4 | Testing: HAC Device 4 | 105 |
| 6.3.5 | Amplification ratios: HAC Device 3 | 105 |
| 6.3.6 | Stiffness matrix: HAC Device 4 | 109 |
| 6.3.7 | Static hydraulic amplification as a two-variable function | 112 |
| 6.4 | Dynamic hydraulic amplification tests | 112 |
| 6.5 | Summary of the test results | 116 |
| 7 | Conclusions and recommendations | 117 |
| 7.1 | Conclusions | 117 |
| 7.2 | Recommendations | 118 |
| 7.3 | Final remarks | 119 |
| A | Material properties | 125 |
| B | Equipment list | 127 |
| C | Detail designs | 131 |

10 Contents

| | |
|---|------------|
| C.1 Die-level anodic bonding jig | 131 |
| C.2 Test jig for the hydraulic amplifier | 145 |
| D Computer code | 157 |
| D.1 Matlab codes used for modeling of the HAC | 157 |
| D.1.1 Bisection method iteration code for modeling of the HAC | 157 |
| D.1.2 Nonlinear annular plate code | 161 |
| D.2 Matlab code used for data analysis and computation | 166 |
| E Masks | 209 |

List of figures

| | | |
|------|--|----|
| 1.1 | MHT 3D section view | 20 |
| 1.2 | MHT modes of operation: Pump vs. Generator | 21 |
| 1.3 | MHT 3D layers | 25 |
| 1.4 | MHT cross section | 26 |
| 1.5 | The hydraulic amplifier | 27 |
| 1.6 | Tethered piston | 27 |
| 2.1 | The ideal hydraulic amplifier. | 30 |
| 2.2 | Hydraulic amplification device types | 31 |
| 2.3 | Piston nomenclature | 33 |
| 2.4 | A simple three-spring analogy | 36 |
| 2.5 | An hydraulic amplifier with sliding seals | 36 |
| 2.6 | HAC: Simplified schematic | 40 |
| 2.7 | Large piston simulation results - 1 small piston | 43 |
| 2.8 | Small piston simulation results - 1 small piston | 43 |
| 2.9 | P_{HAC} simulation results - 1 small piston | 44 |
| 2.10 | Simulation results: Stress - 1 small piston | 45 |
| 2.11 | Large piston simulation results - 10 small pistons | 45 |
| 2.12 | Small piston simulation results - 10 small pistons | 46 |
| 2.13 | P_{HAC} simulation results - 10 small pistons | 47 |
| 2.14 | Simulation results: Stress - 10 small pistons | 48 |
| 2.15 | Simulation results in 3D | 48 |
| 3.1 | Silicon membrane fabrication | 50 |
| 3.2 | Large piston SEM | 51 |
| 3.3 | SEM's of typical channel structures | 52 |

12 List of figures

| | | |
|------|---|----|
| 3.4 | Fillet feature detail | 53 |
| 3.5 | Fillet SEM's | 53 |
| 3.6 | Layer 4 etch mask | 56 |
| 3.7 | The basic principle of anodic bonding. | 57 |
| 3.8 | Anodic bonding jig. | 58 |
| 3.9 | Three-point alignment | 59 |
| 3.10 | Anodic bonding jig with chip | 60 |
| 3.11 | Assembled hydraulic amplifier photograph | 60 |
| 4.1 | Bulk modulus vs. fluid pressure | 64 |
| 4.2 | Vapor lines for a selection of linear siloxanes | 65 |
| 4.3 | Filling system schematic | 65 |
| 4.4 | Filling system photograph | 66 |
| 4.5 | Filling test chip | 68 |
| 4.6 | Static sealing concepts | 69 |
| 4.7 | Schematic of the dynamic seal | 70 |
| 4.8 | Model of the dynamic seal | 71 |
| 4.9 | Dynamic seal results | 71 |
| 5.1 | Test jig | 75 |
| 5.2 | Top clamp | 76 |
| 5.3 | Fluid system schematic | 77 |
| 5.4 | The gas pressure regulating module. | 78 |
| 5.5 | The gas-liquid pressurization module. | 79 |
| 5.6 | Pressure measurement and control module. | 81 |
| 5.7 | Vacuum module. | 82 |
| 5.8 | Regulator bank | 84 |
| 5.9 | The test rig | 85 |
| 5.10 | The test rig - side view | 86 |
| 6.1 | Static hydraulic amplifier | 91 |
| 6.2 | Pressure deflection results | 93 |

| | | |
|------|--|-----|
| 6.3 | Pressure deflection results | 93 |
| 6.4 | Pressure deflection results | 94 |
| 6.5 | Typical test run data | 96 |
| 6.6 | HAC Large piston data | 97 |
| 6.7 | HAC Small piston data | 98 |
| 6.8 | HAC Large piston model correlation | 98 |
| 6.9 | HAC Small piston model correlation | 99 |
| 6.10 | Amplification ratio | 100 |
| 6.11 | Amplification sensitivity | 100 |
| 6.12 | Deflection results for Device 3 | 101 |
| 6.13 | HAC Large piston model correlation | 103 |
| 6.14 | HAC Small piston model correlation | 104 |
| 6.15 | HAC Large piston data | 106 |
| 6.16 | HAC Small piston data | 106 |
| 6.17 | HAC Large piston model correlation | 107 |
| 6.18 | HAC Small piston model correlation | 107 |
| 6.19 | Amplification ratio | 108 |
| 6.20 | Amplification sensitivity | 108 |
| 6.21 | HAC Large piston model correlation | 110 |
| 6.22 | HAC Small piston model correlation | 111 |
| 6.23 | Results in 3D | 112 |
| 6.24 | Dynamic hydraulic amplifier | 113 |
| 6.25 | Frequency response | 114 |
| 6.26 | Time history | 114 |
| 6.27 | Deflection versus drive voltage | 115 |
| 6.28 | Amplification ratio | 115 |
| C.1 | Assembly jig main part | 132 |
| C.2 | Assembly jig lower ceramic plate | 133 |
| C.3 | Assembly jig upper ceramic plate | 134 |
| C.4 | Assembly jig chip rest (ceramic) | 135 |

14 List of figures

| | |
|--|-----|
| C.5 Assembly jig ceramic bushing | 136 |
| C.6 Assembly jig stainless steel bushing | 137 |
| C.7 Assembly jig ceramic alignment pin | 138 |
| C.8 Assembly jig ceramic clamping pin | 139 |
| C.9 Assembly jig wire clamp lower part | 140 |
| C.10 Assembly jig wire clamp lower part | 141 |
| C.11 Assembly jig leaf spring | 142 |
| C.12 Assembly jig lower contact plate | 143 |
| C.13 Assembly jig upper contact plate | 144 |
| C.14 Test jig 3D view 1 | 146 |
| C.15 Test jig 3D view 2 | 147 |
| C.16 Test jig front view 1 | 148 |
| C.17 Test jig front view 2 | 149 |
| C.18 Test jig front section 1 | 150 |
| C.19 Test jig front detail 1 | 151 |
| C.20 Test jig front detail 2 | 152 |
| C.21 Test jig front detail 3 | 153 |
| C.22 Test jig side detail 1 | 154 |
| C.23 Test jig rear view 1 | 155 |
| C.24 Test jig mount | 156 |
| | |
| E.1 Glass layers | 211 |
| E.2 Layer 3 glass patterns | 212 |
| E.3 Layer 4 masks | 213 |
| E.4 Layer 5 masks | 214 |
| E.5 Layer 7 masks | 215 |
| E.6 Layer 8 masks | 216 |
| E.7 Wafer scale masks of Layer 7 | 217 |
| E.8 Plan view | 218 |

List of tables

| | | |
|-----|--|-----|
| 2.1 | Large piston dimensions for all hydraulic amplifiers built | 34 |
| 2.2 | Small piston dimensions for hydraulic amplifiers with a single small piston . | 34 |
| 2.3 | Small piston dimensions for hydraulic amplifiers with ten small pistons . . . | 34 |
| 2.4 | Other dimensions and values | 34 |
| 6.1 | Outline of the hydraulic amplification devices assembled and tested | 90 |
| 6.2 | Large piston inverse compressibility | 92 |
| 6.3 | Small piston inverse compressibility for devices with a single small piston. . | 94 |
| 6.4 | Small piston inverse compressibility for devices with 10 small pistons. . . . | 95 |
| 6.5 | Inverse compressibilities for the pistons of HAC Device 3. | 101 |
| 6.6 | Inverse compressibilities for the pistons of HAC Device 4. | 109 |

Nomenclature

Variables and constants

| Name | Units | Description |
|----------|----------|--------------------------------|
| A | m^2 | Area |
| AR | | Amplification ratio |
| AS | | Amplification sensitivity |
| C | m/Pa | Compressibility matrix |
| D | Pa/m | Inverse compressibility matrix |
| F | N | Force |
| h | m | Height |
| k | N/m | Stiffness |
| P | Pa | Pressure |
| r | m | Radius |
| t | m | Thickness |
| V | m^3 | Volume |
| V | V | Voltage |
| w | m | Width |
| z | m | Vertical displacement |
| β | Pa | Bulk modulus |
| γ | m^{-1} | Geometric ratio (Area/Volume) |
| ψ | Pa/m | Inverse compressibility |

Subscripts

| | |
|-------|--|
| HAC | Hydraulic Amplification Chamber property |
| c | Lumped chamber property |
| 1 | Large piston property |
| 2 | Small piston property |
| f | Chamber fluid property |
| eff | Effective |
| m | Membrane |
| t | Trench |

18 NOMENCLATURE

| | |
|--------------|---------------------------------|
| <i>SOI</i> | Silicon On Insulator |
| <i>r</i> | Fillet radius feature |
| <i>w</i> | Wafer |
| <i>a</i> | Outer radius of tethered piston |
| <i>b</i> | Inner radius of tethered piston |
| <i>p - p</i> | Peak-to-peak |

Acronymns

| | |
|------|---------------------------------|
| AV | Active Valve |
| BOE | Buffered Oxide Etch |
| DRIE | Deep Reactive Ion Etching |
| HAC | Hydraulic Amplification Chamber |
| MEMS | MicroElectroMechanical Systems |
| MHT | MicroHydraulic Transducer |
| RIE | Reactive Ion Etching |
| SOI | Silicon On Insulator |

Hydraulic diagram naming conventions

| | |
|-----|-----------------------------|
| APR | Absolute Pressure Regulator |
| BEV | BEllows Valve |
| BV | Ball Valve |
| CT | Cold Trap |
| FT | Filter |
| LN | Liquid Nitrogen |
| NV | Needle Valve |
| RV | Relief Valve |
| SPS | Static Pressure Sensor |
| SV | Solenoid Valve |
| TK | Tank |
| V | Valve |
| VG | Vacuum Gauge |
| VP | Vacuum Pump |

Chapter 1

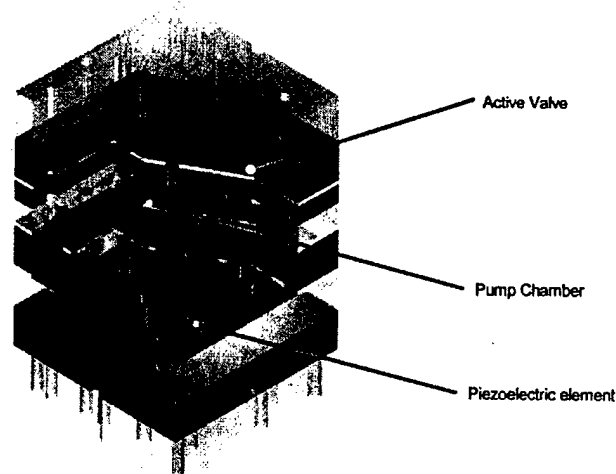
Introduction

At a time when the mere existence of the air around us was a debatable topic, the French mathematician and scientist Blaise Pascal (1623-1662) presented a remarkable series of scientific studies on the behavior of fluids [1]. In 1653, his studies led to the formulation of what is now known as Pascal's law, which can be stated as: "Pressure applied to an enclosed fluid is transmitted undiminished to every portion of the fluid and the walls of the containing vessel" [2]. It is from this simple principle that the concept of hydraulic force amplification or stroke amplification can be derived. Hydraulic amplification is a conceptually elegant means of mechanical amplification, with few moving parts and no mechanisms.

1.1 Objective

The objective of the work presented here is to explore the feasibility of hydraulic coupling as a means of stroke amplification for actuation in a microscale hydraulic system. For the purposes of this discussion, the term "microscale" will refer to any device that is fabricated by means of microfabrication technology.

The microscale hydraulic system, in this case, is a piezoelectrically driven microfluidic prime mover with a piezoelectric piston and two piezoelectrically driven active valves. Thanks to its active valves, this device, also called a MicroHydraulic Transducer (MHT), pictured in Figure 1.1 can be operated as either a pump or a generator. The pump/generator modes of operation are shown in Figure 1.2. Due to the requirement of both large stroke and high frequency actuation of the active valves, direct actuation by piezoelectric elements is not feasible, and hydraulic amplification provides an attractive means for amplifying the stroke of the piezoelectric valve actuators. For background on this device, and the general concept of a MicroHydraulic Transducer, the reader is referred to [3],[4]. In this work, we will introduce the concept of hydraulic amplification for actuation in MicroElectroMechanical Systems (MEMS) by evaluating the performance of the hydraulic amplifiers of the



3D Modeling by H.Q. Li. Rendering by J.L. Steyn

Figure 1.1: 3D Section view of a MicroHydraulic Transducer Device.

MicroHydraulic Transducer shown in Figure 1.1.

1.2 Survey of previous work

Although hydraulic amplification has not been investigated for microfabricated devices, numerous macroscopic systems using hydraulic amplification have been reported. This section provides a brief overview of some previous work, and also some general work in microhydraulic and microfluidic systems.

1.2.1 Macroscale hydraulic amplification

Hydraulic *force* amplification forms an integral part of modern industry, where servo-hydraulic systems can be found in applications ranging from earthmoving equipment to aerospace applications. Hydraulic *stroke* amplification, however, is less common.

Tang presented an hydraulic stroke amplifier, employing very viscous, stiff fluids, so-called

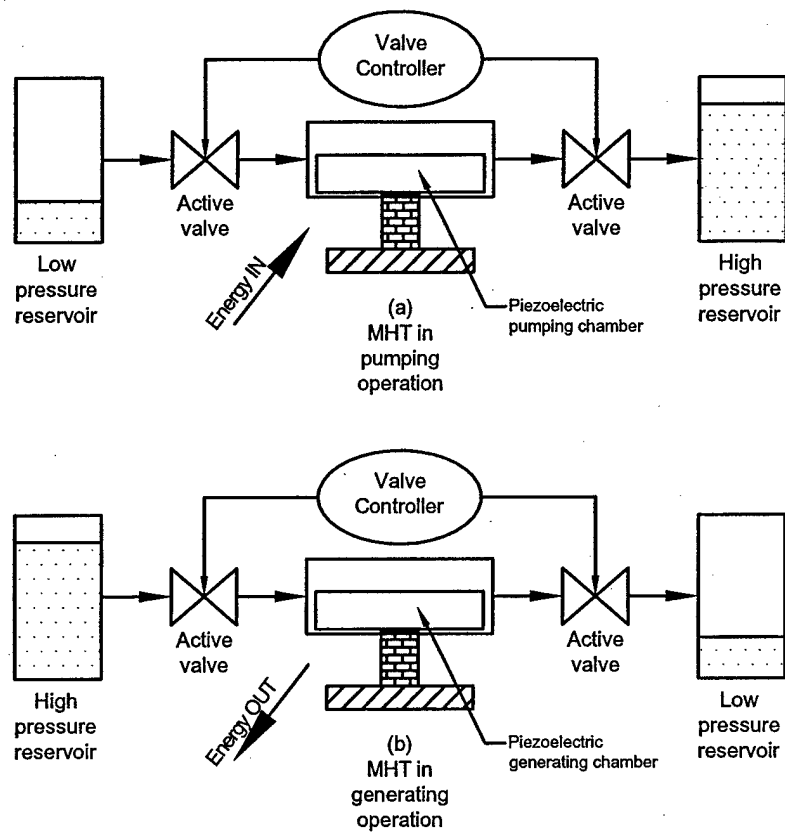


Figure 1.2: The two modes of operation for an active valve MHT device: (a) Pumping/Actuation and (b) Power generation.

liquid plastic PVC, for active vibration control of rotorblades. [5] Using ultrasonic techniques, bulk modulus measurements of the fluids are reported, and range from 1.9GPa to 2GPa, compared to a measured bulk modulus of 2.2GPa for water.

In [6] another application for active vibration control prompted the need for hydraulic amplification of piezoelectric actuation. Using ethylene glycol as the hydraulic fluid, a novel ring-type actuator was produced.

1.2.2 Microscale stroke amplification

Although hydraulic amplification of force and stroke has not been applied in the field of MEMS until now, other means of mechanical stroke amplification techniques have been explored. Where piezoelectric actuation is desired, bimorph beam structures have been fabricated to convert the in-plane strain of the piezoelectric element into an out-of-plane motion. The piezoelectric material takes the form of a thin film, either zinc oxide (*ZnO*) or ceramic lead zirconate titanate (*PZT*). These beam structures were claimed to have potential applications in, amongst others, mass sensing [7], sound generation [8] and thin film characterization [9].

In work by Rogers [10] a number of compliant flexure systems for stroke amplification is mentioned, with amplification ratios of 5 to 50 and efficiencies of greater than 80%, where the efficiency is defined, in this case, as¹:

$$\eta_{mech} = \frac{(Force\ out) \times (Displacement\ out)}{(Force\ in) \times (Displacement\ in)} \quad (1.1)$$

These flexural linkage systems are visually quite impressive. A theoretical treatment on multi-stage cascaded flexural linkage systems is presented in [12]. Amplification ratios as high as 148:1 are reported. In general, the literature provides limited information on the actual stiffnesses of these mechanisms. However, it is apparent from the size of the devices discussed, as well as the method of fabrication - surface micromachining - that these flexural amplification devices are mostly suited for light-duty applications. In the work presented here we will strive to develop a stroke amplifier that will provide substantial (large force) actuation authority on the microscale.

¹For a more comprehensive treatment on actuation efficiencies, based on macroscale stroke amplification devices, the attention of the reader is also drawn to the work of Precht and Hall [11].

1.2.3 Microfluidic and microhydraulic systems

Numerous microfluidic devices for various applications have been reported. Of these devices, micropumps and microvalves, in particular, could be used to construct microhydraulic systems. In any such system, the proposed microscale hydraulic amplification concept can be an enabling technology to accomplish such tasks as large stroke valve operation and general force or stroke amplified mechanical actuation. For completeness we present here an overview of some of the highlights in the development of micropumps and microvalves for potential use in small-scale hydraulic systems.

Often, hydraulic systems will require a prime mover that can take the form of a pump or a generator. In 1988 Van Lintel [13] reported a piezoelectrically driven micromachined silicon pump with a maximum flow rate of approximately $0.6\mu\text{l}/\text{min}$ and a maximum pressure head of approximately $2.5mH_2O$. A year later Esashi [14] reported a piezoelectric micropump with a maximum flow and ΔP of $20\mu\text{l}/\text{min}$ and $0.78mH_2O$ respectively. Recently, in the same project of which this study forms part, using features of the MHT technology described earlier [4], a seven layer silicon-glass piezoelectric micropump capable of delivering up to $3000\mu\text{l}/\text{min}$, or setting up differential pressures as high as $450kPa$ was developed [15]. With functional dimensions of approximately $8 \times 8 \times 10mm$, this device demonstrated that small-scale high power density prime movers can become a reality. The performance of this pump is matched and, in some cases, even exceeded by elektrokinetic pumps as described, for example, in [16]. Elektrokinetic pumps are mechanically very simple and robust, but suffer from a finite lifetime due to the electrochemical reaction that drives the flow.

A large number of microvalves for various applications have been developed and reported in the literature, and a detailed discussion of previous microvalves is not presented. Indeed, microvalves have seen development to the stage where they have already found commercial applications such as mass flow control and pilot valves. See, for example, [17]. It should be noted that valves developed specifically for liquid applications are less common than those for gas applications. This fact is also reflected in the review by Gravesen [18]. The reader is referred to this review for a more complete overview of the earlier microvalves. A newer, high-frequency, high-pressure, high-flowrate microvalve that was enabled by the hydraulic amplification technology discussed in this document is presented by Roberts [19], and the reader is encouraged to review his work in conjunction with the work presented here.

A brief remark has to be made on devices that are sometimes referred to as "fluidic amplifiers". Reported by Zdeblick [20] and later Vollmer [21] and also called "wall attachment

amplifiers", these devices operate on flow streams to either amplify the flow rate or the pressure. These devices can also find useful applications in microhydraulic systems, but we want to emphasize that the device that we will refer to as an *hydraulic amplifier* in this work is completely different from devices previously developed and subsequently named *fluidic amplifiers*.

1.3 Motivation

Recent developments in MEMS have brought quite a number of devices that can be classified as "Power-MEMS" devices, with the purpose of performing meaningful mechanical work rather than simple sensing or chemical analysis. See for example, [22]. MHT technology, as discussed previously, also falls in this category by attempting to exploit the benefits of piezoelectric materials on the microscale.

As is shown in [3], piezoelectric materials can be made to operate efficiently as electromechanical transducers, even at high mechanical loads. Like most so-called "smart" materials, piezoelectric materials have the drawback of being able to provide only minimal actuation stroke. They can, however, operate at very high frequencies, usually with a minimal reduction in their actuation authority. Since the mechanical power output of a transducer will be proportional to $Work/cycle \times frequency$, it is clear that high frequency operation is desirable for high power output.

For high frequency operation of the piezoelectric material, the structure that is driven by this material should ideally have a high natural frequency. MEMS provides a means of producing small, stiff structures with high natural frequencies. MHT technology then uses hydraulic fluid as a rectifying medium. The energy is transferred from the piezoelectric element to the fluid, which can then be used to drive, say, an hydraulic actuator at a slightly lower frequency to provide actuation for "real-world" mechanical applications, where the desired frequency of operation might be in the $1 - 100Hz$ range, compared to the $10kHz$ operation desired for the piezoelectric actuation element.

Even on the microscale, however, the stroke provided by the piezoelectric material may not be sufficient to operate, for example, a microvalve in an MHT system. Therefore, for microscale applications of piezoelectric materials, there exists a definite need for stiff, compact stroke amplification mechanisms or devices.

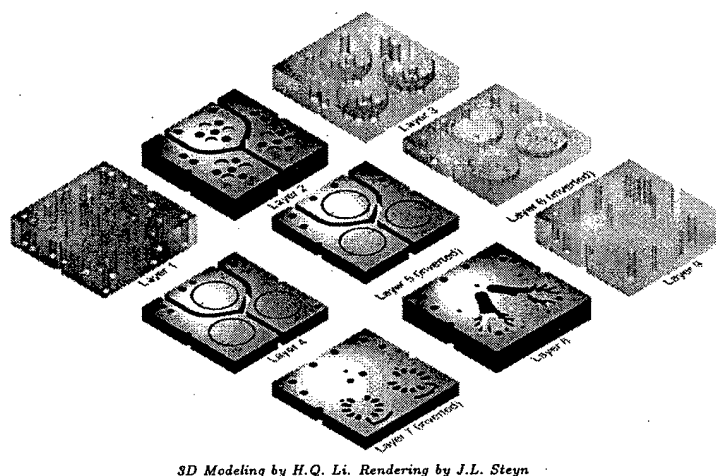


Figure 1.3: 3D View of the layers of the MHT Device.

The *primary motivation* for the development of a microscale hydraulic amplifier is this need for a "power-MEMS" type stroke amplifier for microscale piezoelectric applications, in contrast to previous stroke amplification devices, discussed in Section 1.2.2, and geared solely towards light-duty sensing and positioning applications. A *secondary motivation* for this research is the complete void in the field of MEMS in terms of either hydraulic force or stroke amplification, and the need to gain some insight into the requirements with respect to the design and operation of such devices.

1.4 Method of investigation

Using the MHT device mentioned previously as a test bed, this work demonstrates that hydraulic amplification is a viable and an elegant means for stroke amplification. Figures 1.3 and 1.4 show the major components of this device in more detail. As a full experimental microhydraulic transducer, this device has the following design features:

- Dimensions of $20 \times 20 \times 10\text{mm}$
- Five silicon and four glass layers, making a nine layer device

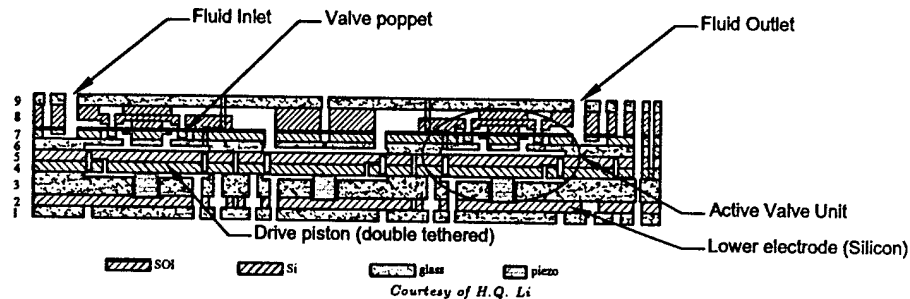
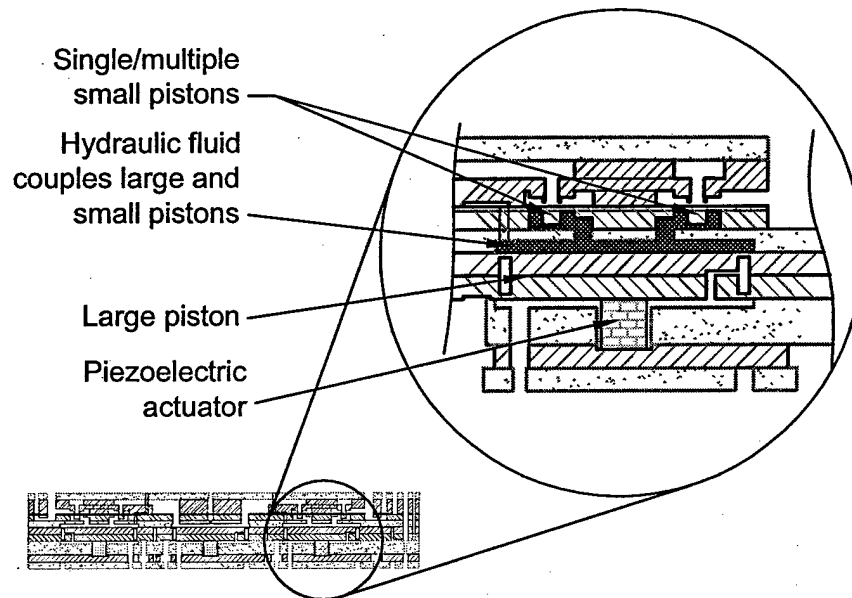


Figure 1.4: Expanded cross section view of the MHT Device.

- Three groups of three piezoelectric elements for three piezoelectrically driven microactuator structures
- Two hydraulically amplified active valves.
- One pumping (or energy generating) chamber

In this work, the hydraulic amplifier under consideration, as a subcomponent of the full MHT device, is shown in Figure 1.5. The MHT system, and therefore also the hydraulic amplifier as one of its subcomponents, rely heavily on the use of tethered piston structures to create moving pistons on the microscale. These tethered pistons with flexural seals and rigid center bosses are compatible with conventional micromachining techniques, as we will discuss in Chapter 3. The operation of a basic tethered piston is shown in Figure 1.6.

In the chapters that follow, the issues that had to be addressed with respect to the design, fabrication, fluid filling, sealing and eventual testing and evaluation of a successful MEMS hydraulic amplifier will be discussed. Finally experimental results with good agreement to theoretical predictions are presented.



Courtesy of H.Q. Li

Figure 1.5: The hydraulic amplifier as part of the MHT device.

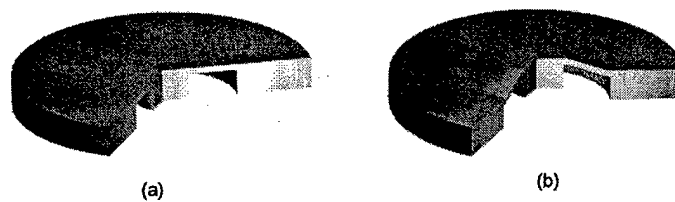


Figure 1.6: The operation of a tethered piston. All moving components rely on this mechanism. (a) Shows an undeflected tethered membrane, and (b) one that has been deflected, either by a load at the center (e.g. piezoelectric actuation) or by a pressure differential applied over the structure.

Chapter 2

Design considerations

In order to produce a successful hydraulic amplification device, whether be it on the microscale or the macroscale, certain aspects of its design require careful thought to ensure that the functional requirements established be met. This chapter provides a brief overview of the issues that were addressed in the design of the particular hydraulic amplification device mentioned in Chapter 1. For a more detailed treatment of some the material presented here, the reader is referred to [19].

2.1 The ideal hydraulic amplifier

When considering the design of a closed hydraulic system which, to first order, obeys Pascal's law, it is always beneficial to keep in mind the ideal hydraulic amplifier ¹. In the ideal hydraulic amplifier it is assumed that all structural components have infinite stiffness and that the coupling fluid is fully incompressible (i.e. infinite bulk modulus). Furthermore, it is assumed that the mass of all components are negligible, and that the device will have infinite bandwidth of operating frequency. It goes without saying that the device should be completely lossless. Figure 2.1 depicts a conceptually ideal hydraulic amplifier.

In this case, due to conservation of mass, the amplification is given by the area ratio:

$$\frac{z_1}{z_2} = \frac{A_2}{A_1} \quad (2.1)$$

¹The electrical analogy to this would be the ideal transformer. See, for example [23]

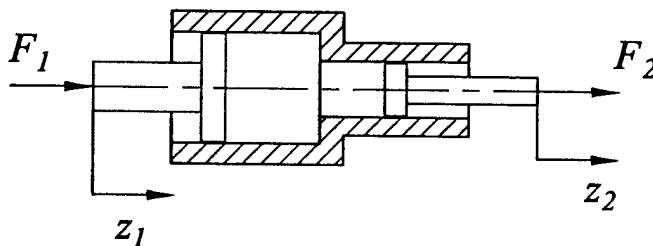


Figure 2.1: The ideal hydraulic amplifier.

2.2 The practical hydraulic amplifier

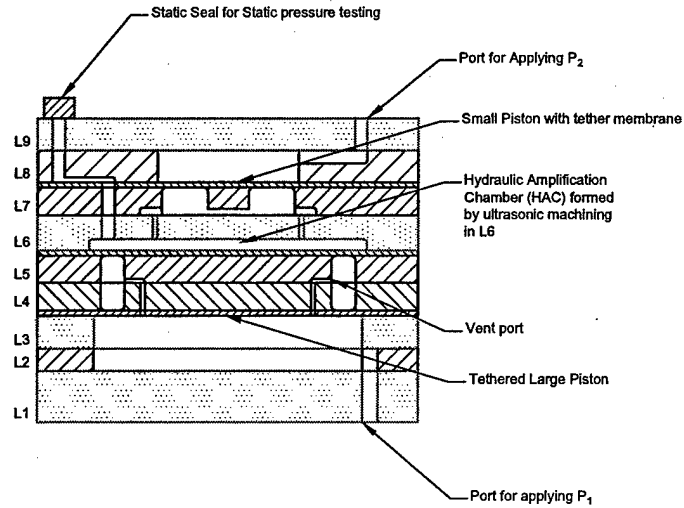
By changing the following assumptions, the ideal hydraulic amplifier is transformed into a practical hydraulic amplifier:

- The coupling fluid has a finite bulk modulus.
- The structural components have nonzero compliance.
- The structural components have mass.
- The fluid itself also has inertia.
- Provision should be made for losses. An example is viscous losses due to squeeze film damping, depending on the geometry of the device under consideration

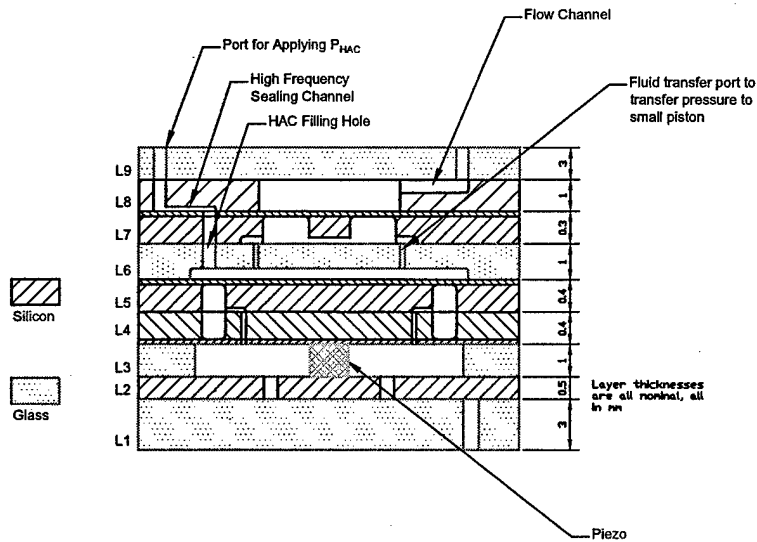
It will be obvious to the reader that, in particular, the added compliance (both fluidic and structural) of the practical hydraulic amplifier will be a dominant limiting factor in the static performance of such a device. In this work we will be concerned mostly with the static behavior of hydraulic amplifiers as actuation couplers.

2.3 The hydraulic amplifier evaluated in this work

The hydraulic amplification devices that were evaluated in this work are schematically shown in Figure 2.2. These devices are constructed using microfabrication techniques. They feature two tethered-membrane piston-type elements.



(a)



(b)

Figure 2.2: Hydraulic amplification devices evaluated in this work: a) Static pressure actuated and b) Dynamic piezoelectrically driven.

These devices have the following design features and associated aspects that need to be addressed in analysis, fabrication and testing:

- A nine layer device, with five silicon and four glass layers.
- A tethered large piston structure, with the annular tether thickness defined by the thickness of the Silicon-On-Insulator (SOI) layers of Layers 4 and 5 in Figure 2.2. All pressures and deflections relating to the large piston will have subscript 1. Note that this piston is a double-tethered piston, designed to increase the natural frequency of the structure [19].
- A tethered small piston structure with the annular tether thickness defined by the SOI layer of Layer 7 in Figure 2.2. All pressures and deflections relating to the small piston will have subscript 2. If needed, more than one small piston can be driven from a single large piston. This work investigates the behaviour of *two* small piston configurations, namely a device with a *single* small piston, and also one with an array of *ten* small pistons.
- An hydraulic amplification chamber formed by ultrasonic machining into glass Layer 6 in Figure 2.2.

In addition, the device can either be pressure actuated, as shown in Figure 2.2a, or it can be piezoelectrically driven, as shown in Figure 2.2b.

2.3.1 Design considerations

The design of the devices mentioned in Section 2.3 was accomplished through use of the following techniques ²:

- Baseline design of the final MHT device as a starting point for the design process [4].
- System-level design of the final MHT device to determine the required pressures and deflections. These were used as the structural inputs for the design steps that followed [24], [19].

²The author gratefully acknowledges the work done by D.C. Roberts, O. Yaglioglu, Y.-H. Su and J.A. Carretero in terms of the structural and fluidic modeling of this device

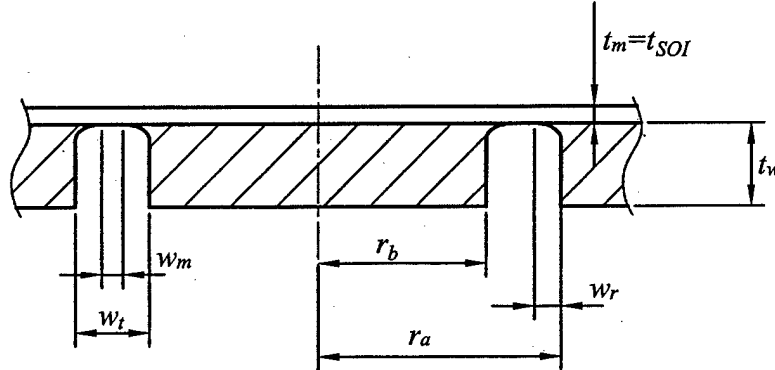


Figure 2.3: Nomenclature for a piston with microfabricated membrane tethers

- Preliminary design of the tethered membrane structures through use of a nonlinear annular plate code [25], [19]. This also included a coupled modeling of the HAC using a nonlinear plate code for the tether-membrane structures and a linear plate equation for the bending of the large piston to produce an iterative nonlinear model of the HAC.
- Verification of proper chamber height to minimize squeeze film damping effects [26].
- Verification of the initial design through finite element simulation [19].

2.3.2 Critical dimensions of the devices built

Figure 2.3 outlines the relevant dimensions that are important when designing a tethered piston structure. Tables 2.1, 2.2, 2.3 and 2.4 provide the dimensions obtained for two types of hydraulic amplifier, designed using the procedures described in 2.3.1. (See [19] and [24]) The associated material properties are given in Appendix A for reference.

2.4 The stiffness matrix of a flexural seal based hydraulic amplifier

To evaluate the stiffness of an hydraulic amplification device, it is sometimes useful to define a stiffness matrix to enable one to evaluate the performance of the device as a mechanical

| | | |
|-----------------|-------------|-----------------|
| r_a | $3613\mu m$ | Outer radius |
| r_b | $3388\mu m$ | Inner radius |
| w_r | $20\mu m$ | Fillet width |
| t_w | $400\mu m$ | Wafer thickness |
| $t_m = t_{SOI}$ | $10\mu m$ | SOI thickness |

Table 2.1: Large piston dimensions for all hydraulic amplifiers built

| | | |
|-----------------|------------|-----------------|
| r_a | $696\mu m$ | Outer radius |
| r_b | $254\mu m$ | Inner radius |
| w_r | $20\mu m$ | Fillet width |
| t_w | $300\mu m$ | Wafer thickness |
| $t_m = t_{SOI}$ | $7\mu m$ | SOI thickness |

Table 2.2: Small piston dimensions for hydraulic amplifiers with a single small piston

| | | |
|-----------------|------------|-----------------|
| r_a | $368\mu m$ | Outer radius |
| r_b | $97\mu m$ | Inner radius |
| w_r | $20\mu m$ | Fillet width |
| t_w | $300\mu m$ | Wafer thickness |
| $t_m = t_{SOI}$ | $7\mu m$ | SOI thickness |

Table 2.3: Small piston dimensions for hydraulic amplifiers with ten small pistons

| | | |
|-------|------------|----------------|
| V_c | $8.3nl$ | Chamber volume |
| h_c | $200\mu m$ | Chamber height |

Table 2.4: Other dimensions and values

transducer or coupler. This also aids in visualizing the effect of various compliances in the system, and assists in debugging, should fabricated devices not perform to expectations.

In such a device, various compliances of different orders of magnitude can be present. For example, the working fluid might be a very stiff part of the hydraulic amplifier, especially when dealing with flexure-sealed structures, as is the case for the devices considered in this work. In this scenario, the membranes themselves will typically be the most compliant elements and the effect of this compliance can readily be incorporated in the models used to design the hydraulic amplifiers [19]. However, the introduction of a bubble into the fluid might affect the effective bulk modulus of the chamber by orders of magnitude, hence making the fluid a compliance that needs to be considered as well.

We will introduce the concept of a stiffness matrix by considering a much simplified case, using, instead of fluid, pistons and pressures, a simple spring system. Thereafter, we will consider a fictitious hydraulic amplification device with perfect sliding seals, to introduce the concept of amplification into the stiffness matrix. Thereafter, we will consider the more complex case of a tethered structure where the fluid pressure is now acting not only on the pistons but on the membrane tethers themselves. In all the arguments presented, we will deal with a linear coupler. Introducing nonlinearity will invalidate the simple concept of a stiffness matrix and will require, rather, a *stiffness function* to be considered, as is mentioned in Section 2.5. In addition, we only consider a static, pressure actuated hydraulic amplification device in this argument.

2.4.1 A simple spring-based analogy

In this case, as shown in in Figure 2.4, we can write down the following stiffness matrix for the system:

$$\begin{Bmatrix} F_1 \\ F_2 \end{Bmatrix} = \begin{bmatrix} k_c + k_1 & -k_c \\ -k_c & k_c + k_2 \end{bmatrix} \begin{Bmatrix} z_1 \\ z_2 \end{Bmatrix} \quad (2.2)$$

The inverse of this matrix will be the *compliance matrix*. In Equation 2.2 the springs k_1 and k_2 are equivalent to the membrane tether stiffnesses in the hydraulic amplifier depicted in Figure 2.2, and the spring k_c is related to the *lumped* stiffness of the chamber itself, including the bulk modulus of the fluid as well as the compliance of the tether seals. Note that if

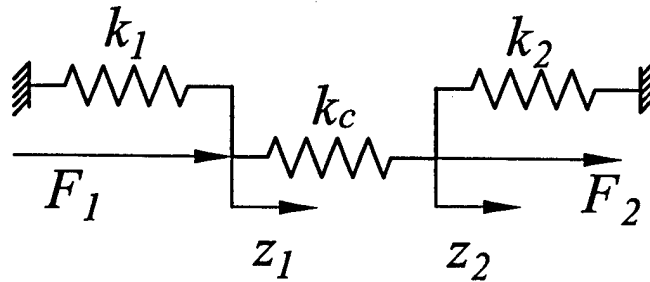


Figure 2.4: A simple three-spring coupler analogy

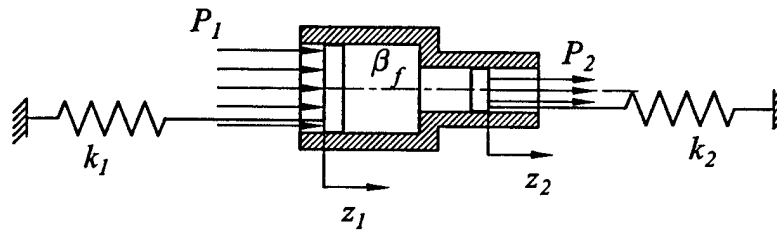


Figure 2.5: An hydraulic amplifier with sliding seals

$k_1 = k_2 = 0$, the matrix will be singular. In general, soft springs are desirable for k_1 and k_2 , and a hard spring is desirable for k_c . This implies that, in general, the stiffness matrix will be *almost* singular. In the discussions that follow, both in this chapter, and also in Chapter 6, reference will be made to this fact. However simple it may be, this three-spring analogy proves to be the most useful in understanding and conveying the basic compliance effects that need to be considered when designing and testing an hydraulic amplifier. The paragraphs that follow will look at particular cases in more detail.

2.4.2 An hydraulic amplifier with sliding seals

Here an ideal hydraulic amplifier with return springs and a finite fluid bulk modulus is considered, as shown in Figure 2.5. In this case we can say the following about the pressure acting on the large piston:

$$\begin{aligned}
P_1 &= \frac{k_1}{A_1} z_1 + \frac{\beta_f \Delta V_1}{V_c} - \frac{\beta_f \Delta V_2}{V_c} \\
&= \frac{k_1}{A_1} z_1 + \frac{\beta_f A_1 z_1}{V_c} - \frac{\beta_f A_2 z_2}{V_c}
\end{aligned} \tag{2.3}$$

Note that, in this case, the chamber compliance only depends on β_f , the bulk modulus of the fluid. At this point it makes sense to introduce the concept of what can be defined as the *inverse compressibility matrix*, given in Equation 2.4, which gives as result a vector of pressures rather than a vector of forces when it operates on a displacement vector. It can therefore also be called a displacement-pressure operator. In the SI system it has units of Pa/m .

$$\begin{Bmatrix} P_1 \\ P_2 \end{Bmatrix} = \begin{bmatrix} \frac{\beta_f A_1}{V_c} + \frac{k_1}{A_1} & -\frac{\beta_f A_2}{V_c} \\ -\frac{\beta_f A_1}{V_c} & \frac{\beta_f A_2}{V_c} + \frac{k_2}{A_2} \end{bmatrix} \begin{Bmatrix} z_1 \\ z_2 \end{Bmatrix} \tag{2.4}$$

Note that the inverse compressibility matrix, as shown in Equation 2.4 is, in general, not symmetric. We can proceed to define the stiffness matrix as follows: In Equation 2.5, the effective force on the large piston can be defined.

$$F_{eff,1} = P_1 A_1 = k_1 z_1 + \frac{\beta_f A_1^2}{V_c} z_1 - \frac{\beta_f A_1 A_2}{V_c} z_2 \tag{2.5}$$

Similarly, we can also write the expression for the effective force on the small piston:

$$F_{eff,2} = P_2 A_2 = k_2 z_2 + \frac{\beta_f A_2^2}{V_c} z_2 - \frac{\beta_f A_1 A_2}{V_c} z_1 \tag{2.6}$$

This enables us to define the stiffness matrix for an hydraulic amplifier with sliding seals:

$$\begin{Bmatrix} F_1 \\ F_2 \end{Bmatrix} = \begin{bmatrix} \frac{\beta_f A_1^2}{V_c} + k_1 & -\frac{\beta_f A_1 A_2}{V_c} \\ -\frac{\beta_f A_1 A_2}{V_c} & \frac{\beta_f A_2^2}{V_c} + k_2 \end{bmatrix} \begin{Bmatrix} z_1 \\ z_2 \end{Bmatrix} \tag{2.7}$$

This stiffness matrix is symmetric. Furthermore, it is almost singular, just like the previous

matrices in Equations 2.2 and 2.4.

2.4.3 An hydraulic amplifier with flexural seals

We are now ready to consider an hydraulic amplifier of the type investigated in this work. A simplified schematic view is shown in Figure 2.6. In this case the flexural seals contribute to the compliance of the HAC, and it is necessary to revert to the *effective* chamber bulk modulus (β_c) first introduced in Equation 2.2 to account for this additional compliance. In addition, the flexural seals, or tethers, also act as part of their respective pistons. It therefore becomes necessary to define an *effective* area for the pistons that includes a portion of the tether area. Introducing the changes into Equations 2.4 and 2.7, we obtain the following expressions:

$$\begin{Bmatrix} P_1 \\ P_2 \end{Bmatrix} = \begin{bmatrix} \frac{\beta_c A_{1,eff}}{V_c} + \frac{k_1}{A_{1,eff}} & -\frac{\beta_c A_{2,eff}}{V_c} \\ -\frac{\beta_c A_{1,eff}}{V_c} & \frac{\beta_c A_{2,eff}}{V_c} + \frac{k_2}{A_{2,eff}} \end{bmatrix} \begin{Bmatrix} z_1 \\ z_2 \end{Bmatrix} \quad (2.8)$$

$$\begin{Bmatrix} F_1 \\ F_2 \end{Bmatrix} = \begin{bmatrix} \frac{\beta_c A_{1,eff}^2}{V_c} + k_1 & -\frac{\beta_c A_{2,eff} A_{1,eff}}{V_c} \\ -\frac{\beta_c A_{1,eff} A_{2,eff}}{V_c} & \frac{\beta_c A_{2,eff}^2}{V_c} + k_2 \end{bmatrix} \begin{Bmatrix} z_1 \\ z_2 \end{Bmatrix} \quad (2.9)$$

The use of effective areas in the equations mentioned above brings with it the complication of correctly defining these areas. To correctly define the effective area, one needs to find the equivalent diameter of a rigid sliding piston, as discussed in Section 2.4.2 that will, for a given deflection, z , produce the same volume change, ΔV as a piston with annular flexural seals. In the case where the deflections are small, this approximation is feasible. For large deformations, one will find that the effective area will change throughout the stroke of the piston.

Because all experimental work presented in Chapter 6 was done by means of applying pressure loadings and measuring resultant displacements, we will use the following version of Equation 2.8 from now on:

$$\begin{Bmatrix} P_1 \\ P_2 \end{Bmatrix} = \begin{bmatrix} \beta_c \gamma_1 + \psi_1 & -\beta_c \gamma_2 \\ -\beta_c \gamma_1 & \beta_c \gamma_2 + \psi_2 \end{bmatrix} \begin{Bmatrix} z_1 \\ z_2 \end{Bmatrix} \quad (2.10)$$

Or, in vector-matrix notation:

$$\mathbf{P} = \mathbf{D}\mathbf{z} \quad (2.11)$$

Where, in this inverse compressibility matrix, we note that, for small deflections of either the large piston or the small piston, when they are tested *individually*, and not as part of the coupler, we can write:

$$\begin{aligned} P_1 &= \psi_1 z_1 \\ P_2 &= \psi_2 z_2 \end{aligned} \quad (2.12)$$

And, furthermore:

$$\begin{aligned} \gamma_1 &= \frac{A_{1,eff}}{V_c} \\ \gamma_2 &= \frac{A_{2,eff}}{V_c} \end{aligned}$$

The inverse of this matrix, the compressibility matrix, will then have the form:

$$\begin{aligned} \begin{Bmatrix} z_1 \\ z_2 \end{Bmatrix} &= \frac{1}{\Delta} \begin{bmatrix} \beta_c \gamma_2 + \psi_2 & \beta_c \gamma_2 \\ \beta_c \gamma_1 & \beta_c \gamma_1 + \psi_1 \end{bmatrix} \begin{Bmatrix} P_1 \\ P_2 \end{Bmatrix} \\ \Delta &= \beta_c \gamma_1 \psi_2 + \beta_c \gamma_2 \psi_1 + \psi_1 \psi_2 \end{aligned} \quad (2.13)$$

Or:

$$\mathbf{z} = \mathbf{C}\mathbf{P} \quad (2.14)$$

2.5 The nonlinear case

When dealing with large displacements³, there no longer exists a stiffness matrix for the hydraulic coupler, but rather, a stiffness function. Or, in the case of pressures and displacements, an inverse compressibility function, as shown in 2.15 and a compressibility function

³In the case of plate structures, including the tethered piston shown in Figure 1.6, a "large displacement" is typically assumed to be approximately $> 1/3$ of the plate thickness, in this case t_{SOI} .

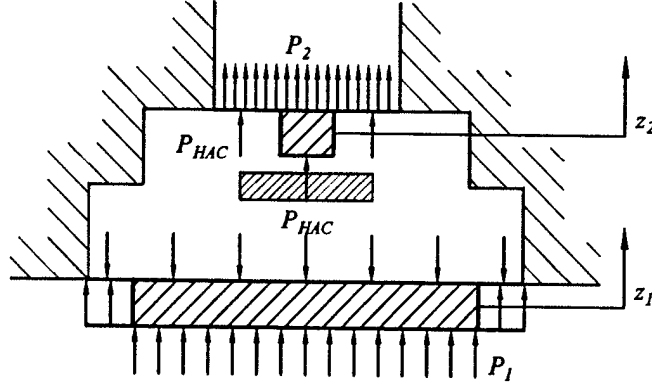


Figure 2.6: A simplified schematic of the static hydraulic amplifier

as in 2.16:

$$P_1 = f(z_1, z_2) \quad (2.15)$$

$$P_2 = g(z_1, z_2)$$

$$z_1 = \tilde{f}(P_1, P_2) \quad (2.16)$$

$$z_2 = \tilde{g}(P_1, P_2)$$

2.5.1 Nonlinear modeling and design of the hydraulic amplifier

Expressing the functions f, g, \tilde{f} and \tilde{g} shown in (2.15) and in (2.16) in analytical form is not trivial. Indeed, in this work, no closed-form expressions were ever derived for f, g, \tilde{f} or \tilde{g} . Using numerical modeling one can, however, evaluate these functions numerically.

Under numerical modeling, we also imply the numerical solution of the large deformation equations for an annular plate with a rigid center boss, as described in detail by Su and Roberts [25],[19]. With the theory described in these references, one can proceed to set up the nonlinear quasi-static model of the hydraulic amplifier in the following manner:

- Model the two tether structures, that is, the small piston tether and the large piston tether, using the nonlinear annular plate theory described in [25] and [19]. Note that the large piston deflections (z_1) were small in this work, and a linear plate theory would also have sufficed for the large piston.
- Add additional compliance due to bending and shear of the large piston. Here, a linear thick plate theory, including shear deformation, can be used. The classical reference is Timoshenko [27]. The small piston center boss is assumed to be rigid. This assumption was valid for the geometry used.
- Model the fluid as a closed hydraulic volume with a constant bulk modulus.

We then have a coupled system. The inputs, or "loading" of the system are the two pressures, P_1 and P_2 . The unknown pressure is P_{HAC} . We know the following:

$$z_1 = f_1(P_1, P_{HAC}) \quad (2.17)$$

$$z_2 = f_2(P_2, P_{HAC}) \quad (2.18)$$

$$P_{HAC} = f_3(\Delta V_f) = \beta_f \frac{\Delta V_f}{V_c} \quad (2.19)$$

We further know that the volume change caused by the large piston, the volume change caused by the small piston and the volume change due to fluid compression must add up to zero⁴:

$$\Delta V_1 + \Delta V_2 = \Delta V_f \quad (2.20)$$

Furthermore, the volume changes can be described by :

$$\Delta V_1 = g_1(z_1) = g_1(f_1(P_1, P_{HAC})) \quad (2.21)$$

$$\Delta V_2 = g_2(z_2) = g_2(f_2(P_2, P_{HAC})) \quad (2.22)$$

$$\Delta V_f = \frac{V_c P_{HAC}}{\beta_f} \quad (2.23)$$

Where we note that ΔV_1 and ΔV_2 in (2.21) and (2.22) are now nonlinear functions of the inputs, P_1 and P_2 . The method for obtaining these functions is described in detail in the work by Roberts and Su.

The system in (2.21)-(2.23) can be solved iteratively in a cascaded iteration procedure. Iteration is performed to determine ΔV_1 and ΔV_2 , based on the nonlinear plate theory,

⁴Where everything that causes a volume reduction of the HAC is considered negative, and everything that causes an increase is positive in this relation.

using an assumed P_{HAC} as an initial guess. Then, by using Equation 2.20 with a suitable convergence criterium, the final coupled solution can be obtained. The functions for ΔV_1 and ΔV_2 , although nonlinear, are well-behaved, and most numerical techniques should work. In this work, a simple bisection method was used⁵. (See, for example [28].)

2.5.2 Nonlinear simulation results

Using the techniques described in Section 2.5.1, the two configurations (one or ten small pistons) of hydraulic amplifiers were modeled⁶. Figures 2.7 to 2.10 are the results of simulations on an hydraulic amplifier with one small piston, and Figures 2.11 to 2.14 show the expected behavior of a device with 10 small pistons. *Note:* The results shown here were computed for $t_{SOI} = 8\mu m$ for the large piston and $t_{SOI} = 6\mu m$ for the small piston. These values are closer to the measured and expected thicknesses of the actual devices that will be discussed in Chapter 6. It was therefore decided to show results that agree with the model predictions in Chapter 6, rather than results based on the design values mentioned in Section 2.3.2.

By performing suitable interpolation, the functions \tilde{f} and \tilde{g} , introduced in (2.16), can be plotted as 2-variable functions in three dimensions. The results are shown in Figure 2.15. These functions will receive some further attention in Chapter 6.

2.6 Summary

This chapter briefly addressed the relevant aspects that need to be considered in order to design a flexural seal based hydraulic amplifier. For a more detailed treatment of the design considerations the reader is referred to the works mentioned in Section 2.3.1. In addition, the concept of the hydraulic amplifier as a two-port coupler was introduced. In the linear case, a 2×2 stiffness matrix can be defined for this coupler. In the nonlinear case, it becomes two coupled nonlinear functions. Designing a working hydraulic amplifier implies that careful consideration should also be given to the method by which it is going to be fabricated. The next chapter addresses the issues relating to the fabrication and assembly of the MEMS-based hydraulic amplifiers evaluated in this work.

⁵The relevant computer codes can be found in Appendix D

⁶D.C. Roberts kindly contributed the results presented in this section.

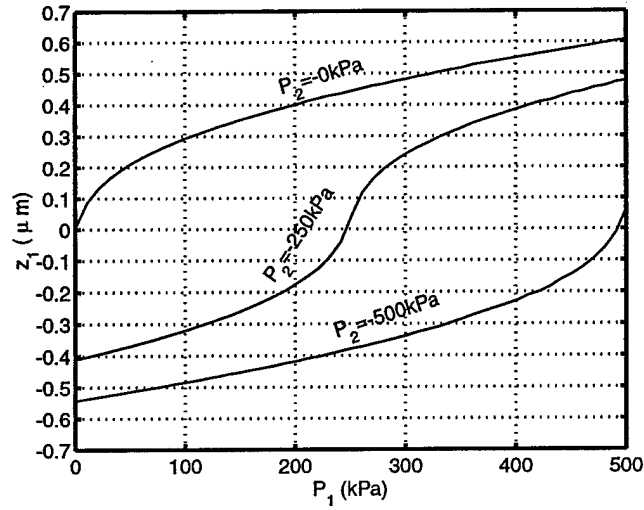


Figure 2.7: Large piston simulation results for an hydraulic amplifier with one small piston. $t_{SOI,1} = 8\mu m$, $t_{SOI,2} = 6\mu m$.

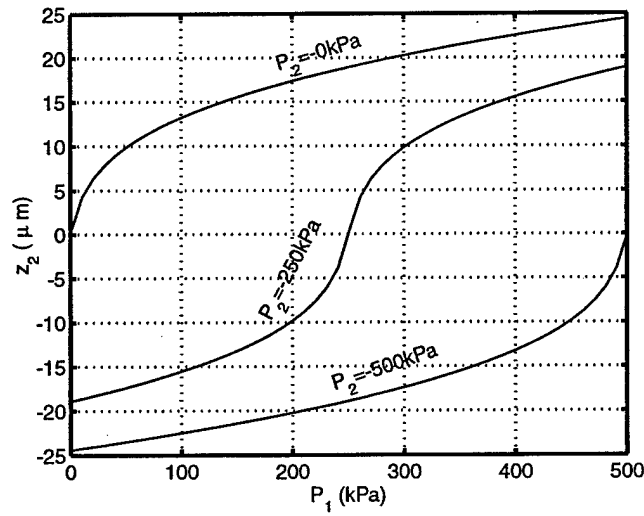


Figure 2.8: Small piston simulation results for an hydraulic amplifier with one small piston. $t_{SOI,1} = 8\mu m$, $t_{SOI,2} = 6\mu m$.

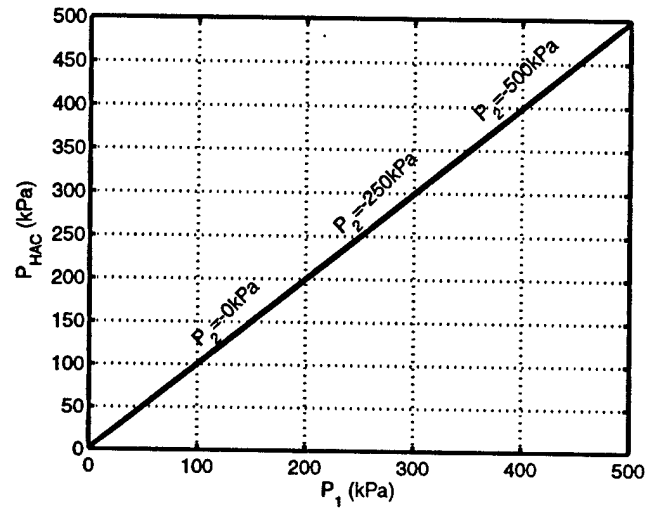


Figure 2.9: P_{HAC} as a function of P_1 for an hydraulic amplifier with one small piston. Note that the slope of all three lines is approximately equal to 1, indicating that $P_1 \approx P_{HAC}$, which proves that the large piston essentially acts as a pressure transfer element for the geometries designed. $t_{SOI,1} = 8\mu m$, $t_{SOI,2} = 6\mu m$.

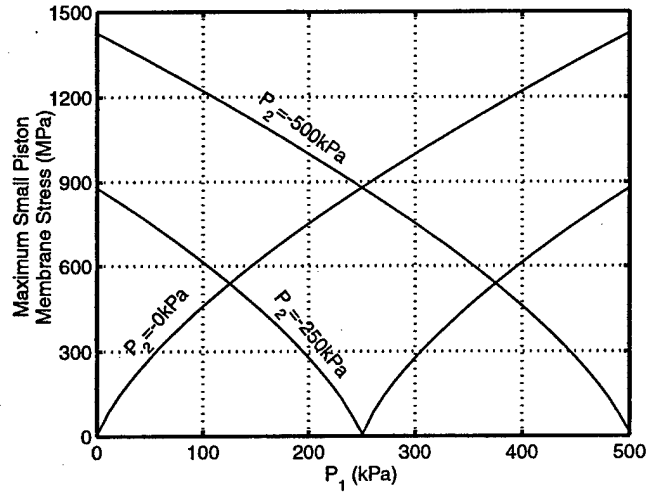


Figure 2.10: Maximum stress in the small piston membrane tether for an hydraulic amplifier with one small piston. $t_{SOI,1} = 8\mu m$, $t_{SOI,2} = 6\mu m$.

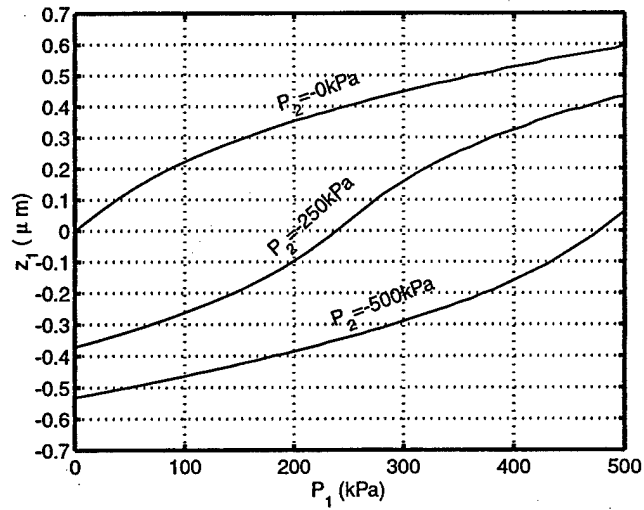


Figure 2.11: Large piston simulation results for an hydraulic amplifier with 10 small pistons. $t_{SOI,1} = 8\mu m$, $t_{SOI,2} = 6\mu m$.

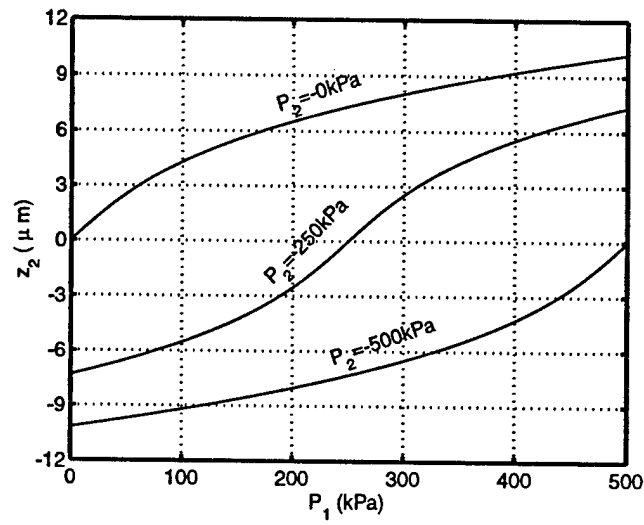


Figure 2.12: Small piston simulation results for an hydraulic amplifier with 10 small pistons.
 $t_{SOI,1} = 8\mu\text{m}$, $t_{SOI,2} = 6\mu\text{m}$.

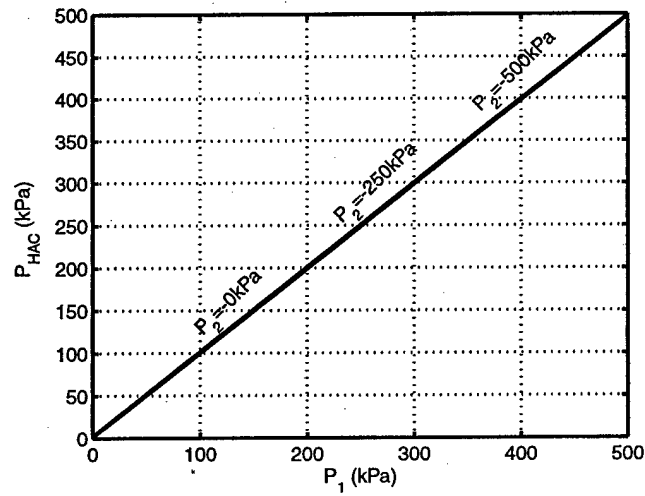


Figure 2.13: P_{HAC} as a function of P_1 for an hydraulic amplifier with 10 small pistons. Note again that the slope of all three lines is approximately equal to 1, indicating that $P_1 \approx P_{HAC}$, which proves that the large piston essentially acts as a pressure transfer element for the geometries designed. $t_{SOI,1} = 8\mu m$, $t_{SOI,2} = 6\mu m$.

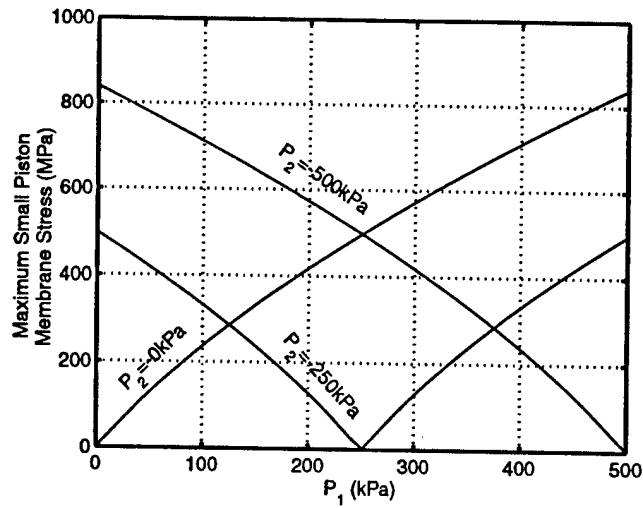


Figure 2.14: Maximum stress in the small piston membrane tether for an hydraulic amplifier with 10 small pistons. $t_{SOI,1} = 8\mu\text{m}$, $t_{SOI,2} = 6\mu\text{m}$.

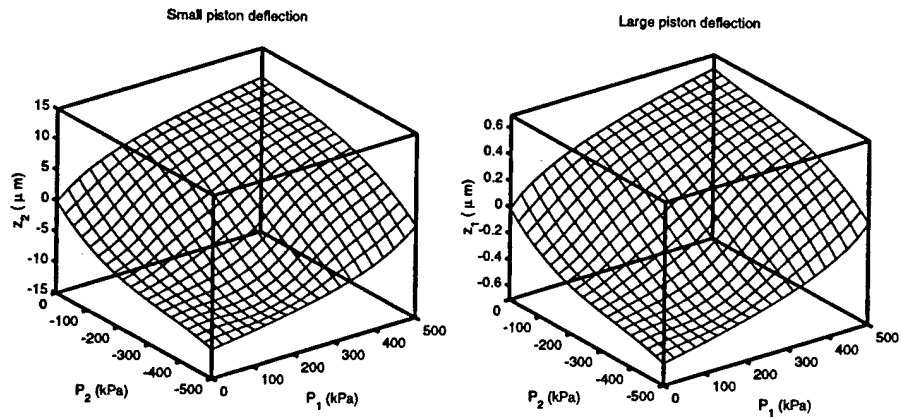


Figure 2.15: Small and large piston deflections as functions of both P_1 and P_2 for a device with 10 small pistons. These two graphs can be seen as numerical representations of \tilde{g} and \tilde{f} of Equation 2.16.

Fabrication and device assembly

Effective fabrication of a fluidic-based power MEMS device is often a complex task. In many cases, where conventional micromachining technology is used, through-wafer etching is required. In addition, multiple layers are usually needed to create the desired three-dimensional structures that would make up a device consisting of moving parts, flow channels, inlet and outlet ports and electrical connections. In [22] an interesting example of such a multi-faceted process is presented. This chapter will address the fabrication techniques that were used to produce the hydraulic amplification devices evaluated in this work.

3.1 Fabrication overview

In Chapter 2 the two types of devices investigated in this document were introduced. For both devices shown in Figure 2.2, the fabrication process required to produce a device can be divided into the following major subtasks:

- Silicon tethered membrane fabrication, using Silicon-On-Insulator (SOI) wafers.
- Structural silicon layer fabrication. Double-side polished wafers are used for this purpose.
- Glass layer fabrication by ultrasonic machining. The glass used was *Pyrex*TM7740 by Corning.
- Wafer scale fusion bonding of silicon-silicon wafer pairs and anodic bonding of silicon-glass wafer pairs.
- Die-level alignment and anodic bonding to complete the assembly.

In the case of the piezoelectrically driven device, a piezoelectric element has to be integrated during the final bond step. For more information, the reader is referred to [19] and to [29].

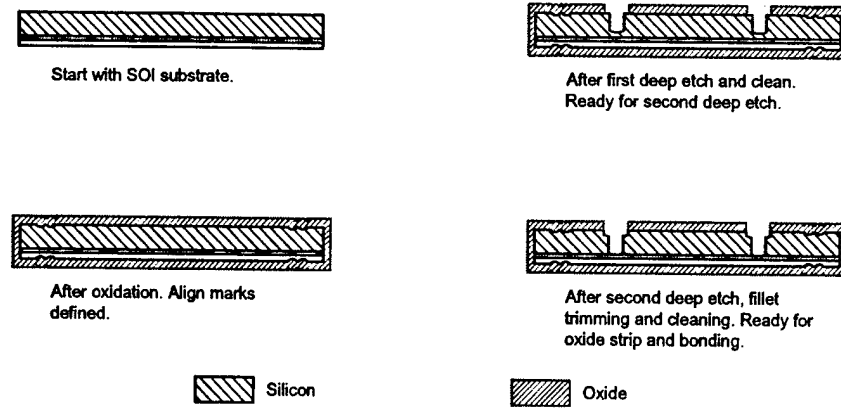


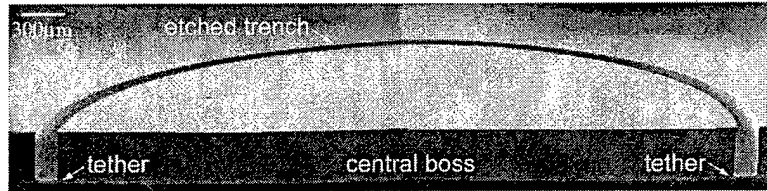
Figure 3.1: Selected steps of the process required to produce a tethered silicon membrane structure.

3.2 Process flow for creating silicon membrane structures

Figure 3.1 depicts the process used to produce the silicon membrane structures used in the devices characterized in this work¹. A scanning electron micrograph of such a structure is shown in Figure 3.2. The process flow for creating a structure like this from an SOI substrate can be summarized in the following steps [30]:

1. Start with a Silicon on Insulator (SOI) wafer, double side polished. Device layer thicknesses of $7\mu\text{m}$ to $10\mu\text{m}$ were used. The wafer thicknesses ranged from 300 to $400\mu\text{m}$.
2. Grow first layer of protective thermal oxide at 1100°C , $0.6\mu\text{m}$ thick.
3. Pattern align marks on both sides, using OCG825 standard thin photoresist. Etch in 7:1 Buffered Oxide Etch (BOE).
4. Etch align marks in Silicon using reactive ion etching (RIE)..
5. Grow second layer of protective thermal oxide at 1100°C , to a total thickness of $1.7\mu\text{m}$.
6. Pattern oxide using BOE, to define the nested mask

¹For corresponding mask sets, the reader is referred to Appendix E



Courtesy of K.T. Turner. Created from two separate images.

Figure 3.2: Scanning Electron Micrograph (SEM) of a prototype large piston. This piston was cut in half for illustrative purposes. Also note that this piston was fabricated using a single deep etch. No stepped features are visible on the sidewalls.

7. Recoat with photoresist, using Clariant AZ4620 thick photoresist. A thickness of approximately $10\mu\text{m}$ after baking is desired. Define the first Deep Reactive Ion Etching (DRIE) etch mask. Mount the wafer on a handle substrate using AZ4620 photoresist.
8. Perform the first deep etch using an STS ICP DRIE tool ² to approximately $20\mu\text{m}$ away from the buried oxide. Dismount wafer in acetone and strip photoresist using a process consisting of burning the organic materials in an oxygen plasma ("ashing") and performing a chemical cleaning step, using a mixture of 3 parts H_2SO_4 added to 1 part of H_2O_2 ("Piranha cleaning").
9. Remount wafer on handle substrate and perform the final etch.
10. Dismount in acetone, and clean using again ashing and piranha. Just prior to fusion bonding, the oxide would be stripped with BOE and an RCA cleaning step would be performed.

The procedure described above will allow the fabrication of a basic tethered silicon membrane structure. It has been found that some amount of exposed silicon outside of the etched membrane features, as provided by the nested mask process, tends to simplify the fillet radius control procedure somewhat. This procedure is described in Section 3.2.1.

Additional features, e.g. flow channels, can be defined in the nested mask and the nested mask etch depth can be tailored (within the bounds of the wafer's structure) to suit the requirements of the features needed. Figure 3.3 shows two examples of what can be achieved

²Please refer to Appendix B for non-standard fabrication tools used.

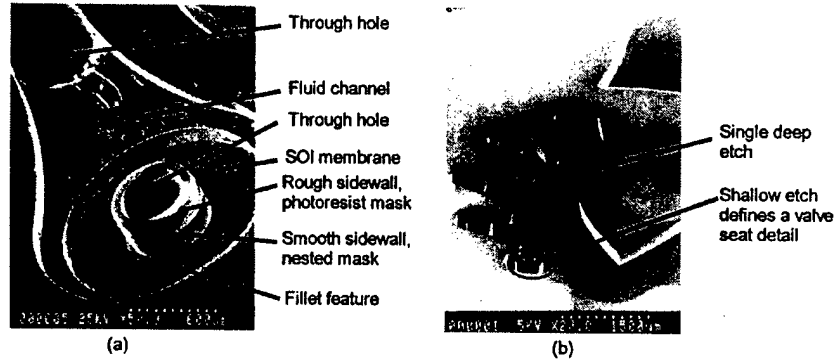


Figure 3.3: SEM images of typical channel structures that can be realized with a nested mask process. (a) depicts a checkvalve, as was used in the pump described in [15]. (b) shows a ten-valve manifold of the MHT device shown in Figure 1.1. This manifold has undergone its first deep etch, and is ready for the nested mask etch. Numerous shallow etches can be used, as is shown here, to define additional shallow features.

using the nested mask process. Note that in addition to the two deep etches allowed by the nested mask process, additional shallow features can be added. The depth of these shallow features is limited by the lithographic process. In this work it has been found that features deeper than approximately $20\mu\text{m}$ (and of in-plane dimensions greater than $\sim 500\mu\text{m}$) will not be well suited to an additional lithography step involving the spin-casting of photoresist and subsequent exposure. Another interesting observation is that the nested mask, a hard SiO_2 mask, will generally provide a smoother sidewall than the initial photoresist mask. This can be attributed to a phenomenon sometimes referred to as "micromasking", where photoresist is removed from the top of the substrate by the DRIE process, and subsequently redeposited on the trench walls, leading to sidewall roughness.

3.2.1 Membrane fillet radius control

An aspect not addressed until now has been the nature of the fillet feature (See Figures 3.4 and 3.5) at the bottom of the etched trench after the final DRIE etch described above. It has been shown [29] that a proper fillet feature is critical when high strength membrane tethers are desired, as is the case for the MHT device. Attaining a good fillet feature can be a daunting task, primarily due to a combination of the following two effects:

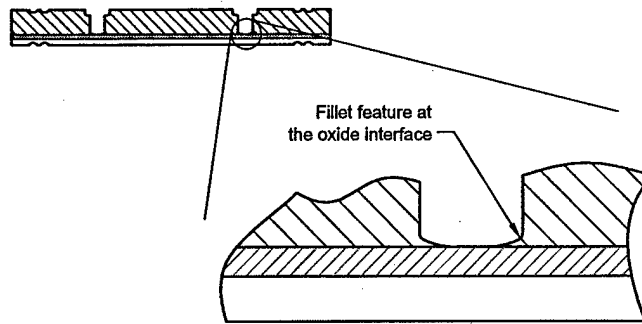
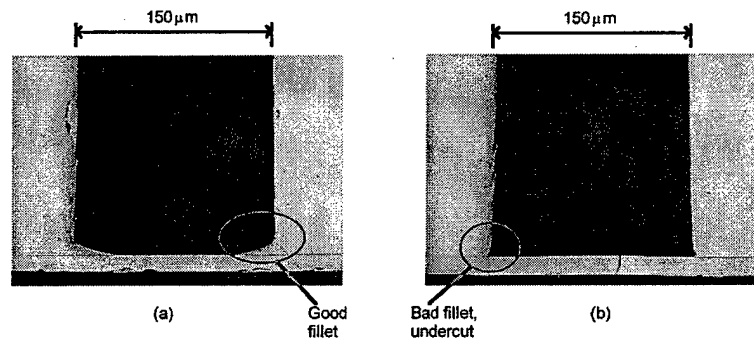


Figure 3.4: Idealized fillet feature at the bottom of the etched trench.



Courtesy of K.T. Turner.

Figure 3.5: Two possible outcomes after etching an SOI membrane using DRIE: (a) Good fillet feature obtained by proper timing of the deep etch and (b) an undercut fillet feature. Undercut will cause a stress concentration, significantly reducing the strength of the structure.

- Nonuniformity in the DRIE etching using current DRIE technologies.
- The natural tendency of the DRIE process to undercut and produce a "footing" feature, rather than the desired fillet feature, when the buried oxide etch stop is reached as is shown in Figure 3.5. (For an explanation of this phenomenon, see, for example, [31].)

In this work, the membranes were fabricated using an iterative process involving multiple etching and inspection steps for the width of these membranes. The membrane widths were estimated during processing using a microscope with a calibrated reticle. Membrane width was found to be the preferred parameter for fillet radius quality control, rather than the fillet width itself, due to difficulties associated with properly estimating the endpoint of the fillet.

Should, upon inspection, it be found that a particular membrane was properly etched, this membrane would then be covered with OCG825 photoresist using a bent wire to deposit a droplet of photoresist on the feature. The photoresist would then be baked for approximately 5 minutes, after which a second coating of photoresist would be applied, and another baking step for approximately 10 minutes would follow. Afterwards, the wafer would be returned to the DRIE tool for further etching.

This procedure would be repeated until all the membranes have been fully etched. After this step, the wafer would be prepared for fusion bonding.

It has also been shown that surface roughness can have a significant effect on the effective fracture strength of silicon, due to the fact that it is a brittle material with no plastic deformation at room temperature [32]. On the large piston tether membranes, the decision was made to switch to an isotropic etch recipe in the DRIE process in an attempt to further improve the surface finish of the fillet features. Tolerance constraints did not allow this procedure to be performed on the small piston membrane tethers.

3.3 Silicon fusion bonding techniques

Silicon fusion bonding is the process by which two silicon substrates having surfaces with roughness no greater than 10\AA and minimal bow are brought into intimate contact. Van der Waals forces keep the wafers in contact. Subsequent annealing at temperatures above

1000°C will result in a bond strength approaching that of single crystal silicon [33]. For successful fusion bonding, substrate surface finish and cleanliness is of the utmost importance.

The devices evaluated in this work required two separate wafer-scale silicon-silicon fusion bonding steps to be performed:

- Bond Layers 4 and 5 to form a double-tethered piston structure. (For the layer numbers, see Figure 2.2)
- Bond Layer 7, the membrane layer, to Layer 8, the fluid channel layer that provides a pressurization path to the top of the membranes, and also forms a proper "clamped" boundary condition for the membrane tether.

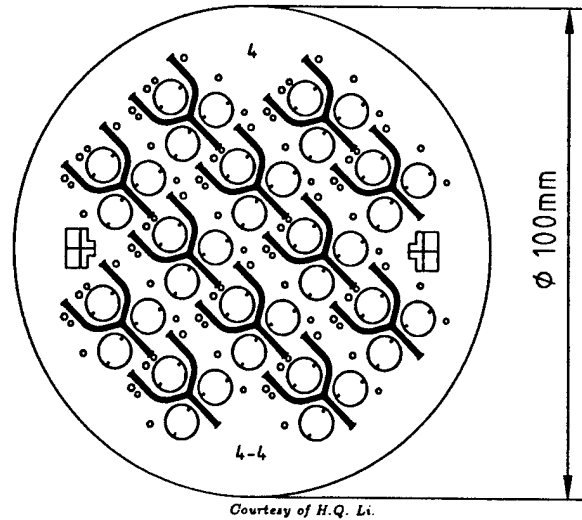
The bond between Layers 4 and 5 proved to be challenging, due to the very compliant nature of the wafers being bonded. Figure 3.6 illustrates the large amount of material removed from these wafers during processing. To prevent these wafers from becoming stuck during alignment prior to bonding, it was necessary to increase the separation of the wafers from the 75 μ m normally used to approximately 150 μ m. All silicon fusion bonds were performed using an Electronic Visions EV450 aligner and AB1-PV bonder.

3.4 Anodic bonding techniques and die-level assembly

3.4.1 Wafer-scale anodic bonding

Due to electrical constraints in the full MHT device, it was required that the three large pistons of this device, as well as their lower electrodes, be fully electrically insulated from each other. The insulation was accomplished by etching a Y-shaped trench in each die. This enabled the three pistons to be insulated after die-sawing [30]. See Figure 3.6 and also Figure 1.3.

This feature required that Layers 4 and 5 in Figure 2.2 be anodically bonded to Layer 6 on the wafer scale prior to dicing. For the same reason, Layers 1 and 2 had to be bonded on the wafer scale for the piezoelectrically driven devices. In this particular case, it was crucial to ensure a proper surface finish on the glass after bonding to allow subsequent bonds to be performed in order to create a multi-layered sandwich structure.



Courtesy of H.Q. Li.

Figure 3.6: Deep etch mask for Layer 4. Note the Y-shaped trenches on each die. Removing large amounts of material may result in excessive wafer bow and problems with pre-alignment stiction.

Figure 3.7 illustrates the basic principle of anodic bonding. An anodic bond between silicon and a suitable glass (for example, *Pyrex*TM 7740) is formed by placing a smooth silicon surface in contact with a smooth glass surface. Thereafter, this silicon-glass stack is heated to mobilize the ions in the glass. An electric field is then applied across the glass by contacting the silicon and glass layers. This field acts to draw sodium ions away from the bond interface, leaving behind oxygen ions which then bond to the silicon, forming SiO_2 [33]. The applied field also has the effect of causing an electrostatic attraction between the silicon and glass layers, ensuring intimate contact. Note that this field effectively acts only across the depletion zone shown in Figure 3.7, and the attraction is therefore quite strong.

From Figure 3.7 it should be clear to the reader that the sodium ions migrating away from the bond interface will eventually manifest themselves as a sodium compound (NaOH) on the glass surface [34]. This accumulation of sodium is generally associated with surface damage. To minimize this damage, it was found to be necessary to create a uniform smooth and flat graphite electrode as a contact to the glass layer. It was found that any surface irregularities in the electrode would exacerbate the accumulation of sodium compounds in the regions of those irregularities.

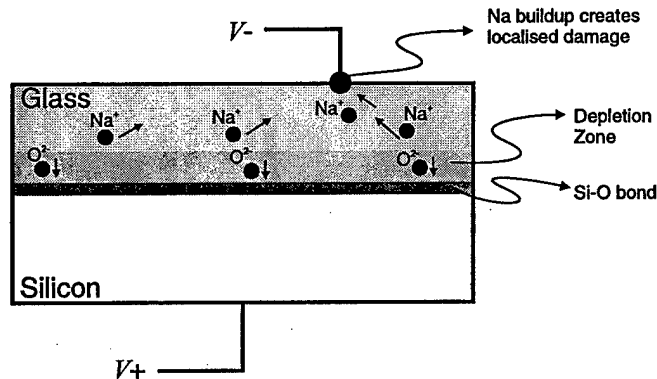


Figure 3.7: The basic principle of anodic bonding.

When assembling multi-layer Si-glass sandwich structures, it is also important to bear in mind that the bond time should be long enough to ensure a complete bond, but no longer. Any additional time after the bond is complete will once again only tend to exacerbate the accumulation of unwanted sodium on the electrode side of the glass. In addition, when performing the second anodic bond, it is possible to use the first bonded silicon layer as the glass contact for this bond. In this case, particular care should be taken not to overbond, as one will run the risk of forming precipitates in the glass, observed as brown speckles. A further discussion of this phenomenon is found in [35]. With all anodic bonding performed for the hydraulic amplification devices, it was found to be very useful to monitor the bond current during the bond. Usually, the bond was assumed to be complete when the current had fallen to approximately $1/8$ of its initial value.

In all anodic bonding performed, both on the wafer level and the die level, a voltage of $1000V$ was used, at a temperature of $300^\circ C$. The bond time depended on the thickness of the glass layer which ultimately determined both the field strength and the amount of sodium that had to be transported. In all cases, the $1/8$ value criterium was used. All bonds were performed at atmospheric pressure, except for the final die-level bond on the piezoelectrically driven devices. This bond had to be performed in a reducing atmosphere [29].

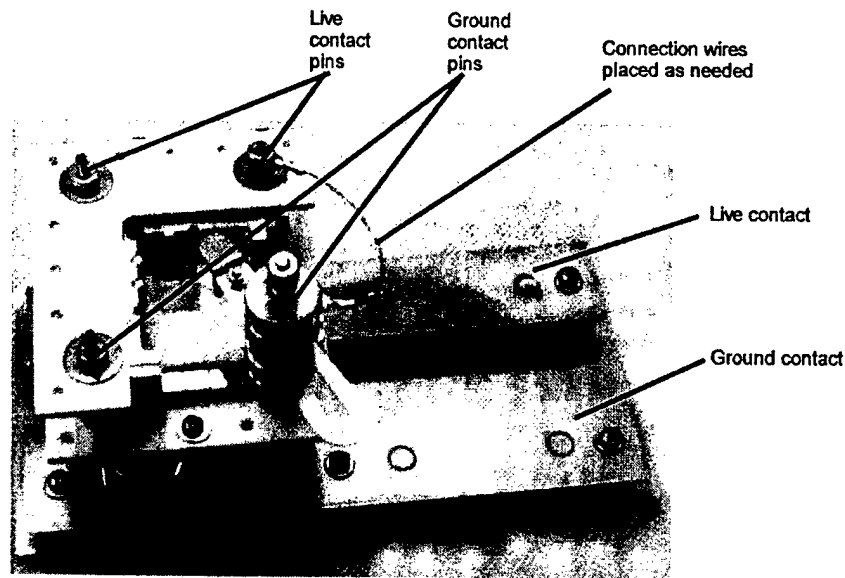


Figure 3.8: Anodic bonding jig.

3.4.2 Die-level assembly

To complete the assembly of an hydraulic amplification device, it was required to anodically bond, on the die level, the following sets of layers (See, again, Figure 2.2):

- Layers 1 and 2, wafer scale bonded anodically.
- Layer 3 - a separate glass layer.
- Layers 4, 5 and 6, fusion bonded and anodically bonded on the wafer scale.
- Layers 7 and 8, fusion bonded on the wafer scale.
- Layer 9 - another separate glass layer.

To facilitate alignment on the die-level, an alignment jig, shown in Figure 3.8 was built. (See Appendix C for the detail design of this jig.) This jig relies on 2D kinematic alignment of dies, and requires that all dies be the same size. This feat is accomplished by ensuring

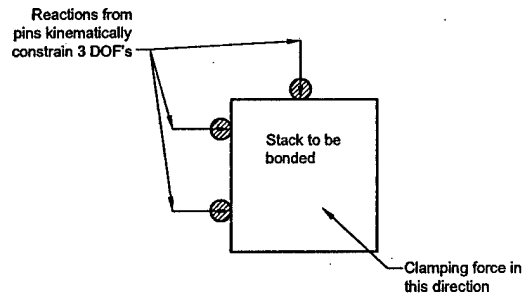


Figure 3.9: Three-point alignment as used in the anodic bonding jig. The three pins were made from glass-mica machineable ceramic.

that all dies are cut with the same blade during the dicing operation. The jig has three pins that allow the dies to be pushed into an alignment corner, as shown in Figure 3.9. This ensures that the three degrees of freedom are constrained. Figure 3.10 shows the jig with a device that is being bonded. The clamping, contacts and alignment pins are all visible.

The following bond sequence was used in the assembly:

1. Bond the Layer 1-2 pair to Layer 3.
2. Bond Layer 9 to the layer 7-8 pair.
3. Bond the stack of Layers 4-5-6 to Layers 7-8-9
4. Finally, bond the lower part of the device, Layers 1-2-3, to the upper part, Layers 4-5-6-7-8-9.

In the case of the piezoelectrically driven hydraulic amplifiers, the final anodic bond was performed together with a solder bond to attach the piezoelectric element to the large piston of the hydraulic amplifier. This procedure is described in detail in [19] and [29].

Figure 3.11 shows a fully assembled hydraulic amplifier.

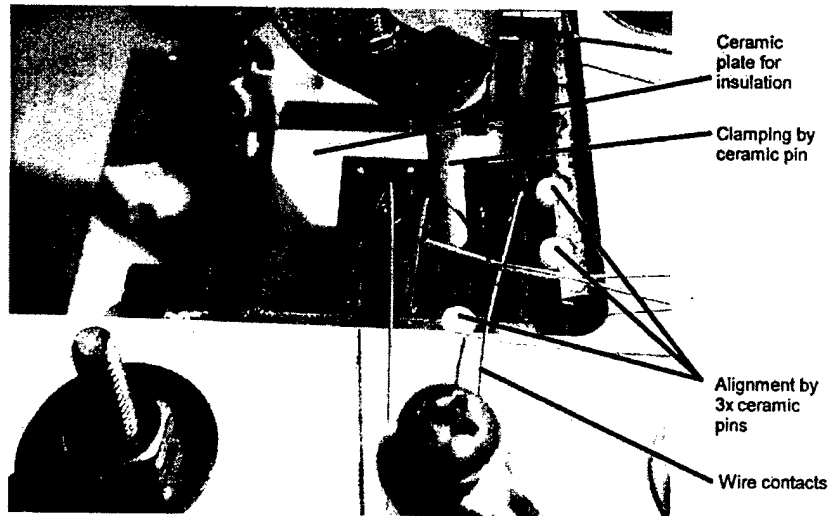


Figure 3.10: Close-up of the anodic bonding jig, with a device being bonded. Note the alignment by alignment pins, the wire contacts, the clamping method and the insulation.

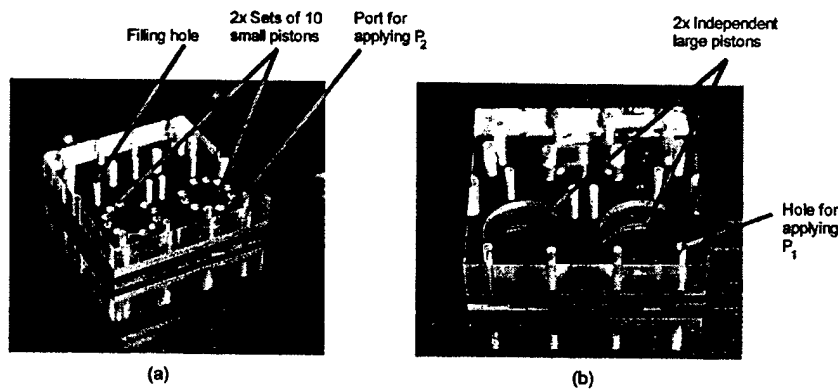


Figure 3.11: Assembled static hydraulic amplification device with ten small pistons and one large one. Each such stack contains two independent hydraulic amplification devices. (a) Shows a top view, with the two sets of ten small pistons, and (b) a bottom view, with the two large pistons. Note the third piston, which is not used for this device, but only for the full MHT device mentioned in Chapter 1.

3.5 Summary

In this chapter we looked at a typical process flow for producing a multi-layered silicon-glass bulk micromachined hydraulic amplification device. To build a device such as shown in Figure 3.11, it was necessary to develop, in addition to what can be considered a "conventional" DRIE-based process flow, techniques for:

- Controlling the fillet radii of deep etched trenches in SOI wafers and
- Wafer-level and die-level aligned anodic bonding to create silicon-glass sandwich structures.

After assembly, the hydraulic amplification device is still in a particulate-free condition. The next step, before operating the device, involves filling and sealing of hydraulic amplification chamber. These procedures are described in Chapter 4.

Chapter 4

Filling and sealing techniques

In Chapter 2 it was shown that, for effective hydraulic amplification, compliance of the system needs to be minimized. Hence, reliable filling and sealing techniques were required to ensure the stiffest hydraulic amplification chamber possible. This chapter describes filling techniques initially developed by Boston MicroSystems [36], and further refined for the particular devices tested here. It also addresses the sealing techniques that were developed to properly seal the hydraulic amplification chambers for either static or dynamic sealing purposes.

4.1 Filling techniques

4.1.1 Fluid requirements

For the full MHT device, the working fluid had to satisfy the following requirements [36]:

- Low viscosity, for minimal viscous losses.
- High bulk modulus, for minimal compliance.
- Should wet silicon surfaces well, to ease filling of small cavities.
- Should be dielectric, due to the high voltage operation of the device.

Based on these requirements a volatile silicone oil, Hexamethyldisiloxane (Produced by Dow Corning under the trade name DC200 0.65cst), was chosen as the system fluid. This was also the fluid used in all hydraulic amplifiers tested in this document. This is based on the assumption that the filling procedure used to fill the HAC's would also be used to fill the device itself at the same time, requiring that the fluid in the HAC be the same as the fluid

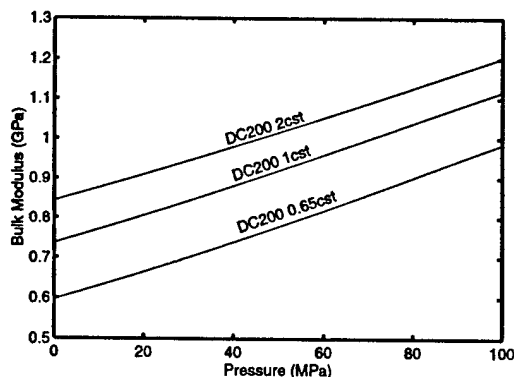


Figure 4.1: Bulk modulus vs. fluid pressure for a selection of volatile silicone oils, adapted from data as supplied by Dow Corning [37]. Note that the amount of outgassing performed on these fluids is unknown.

in the device. In other applications, or using different filling techniques, this requirement of using one type of oil for the whole MHT system could probably be relaxed.

The properties of various silicone oils indicate that there is a tradeoff between viscosity and bulk modulus. This is also shown in Figure 4.1. In the case where it is possible to use a different fluid in the HAC, it might pay off to investigate slightly more viscous fluids with higher bulk moduli. Note, however, that filling of the HAC, as described in the previous section, relies on the working fluid also possessing a high vapor pressure. This requirement eliminates most of the high viscosity oils. (See Figure 4.2)

4.1.2 Filling process

To ensure bubble-free filling of the HAC, a filling system and associated filling process was developed. Figure 4.3 shows a schematic of the apparatus and Figure 4.4 is a photograph of the same apparatus.

To fill and seal an HAC, the following process was developed:

1. Set the initial condition of the system: All valves closed.
2. Open Tank B, and place the device test jig (Discussed in Chapter 5), as well as the

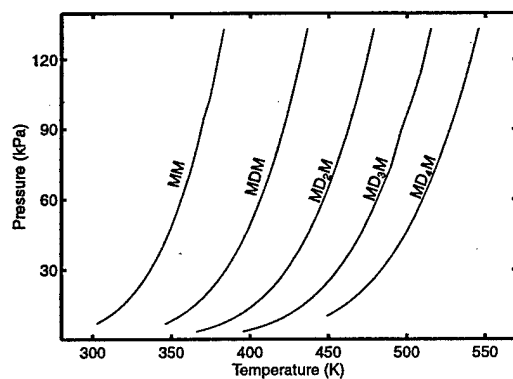


Figure 4.2: Vapor lines for a selection of linear siloxanes, adapted from [38]. The graphs show the vapor lines for Hexamethyldisiloxane (MM), Octamethyltrisiloxane (MDM), Decamethyltetrasiloxane (MD_2M), Dodecamethylpentasiloxane (MD_3M) and Tetradecamethylhexasiloxane (MD_4M). Dow Corning DC200 0.65cst consists of MM and trace impurities. The other viscosities may contain blends of the compounds mentioned above.

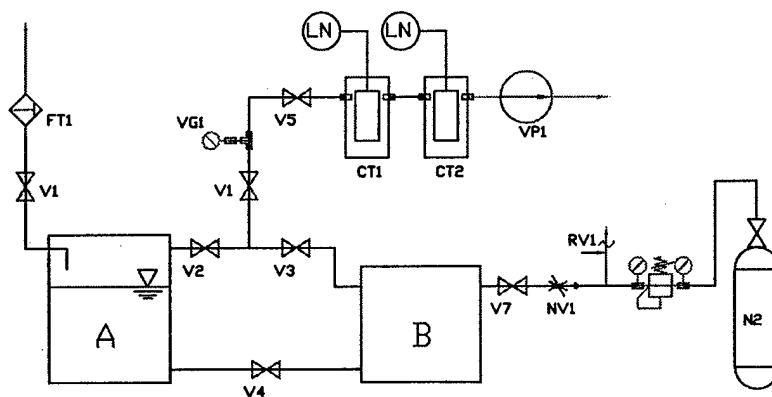


Figure 4.3: Schematic representation of the filling system

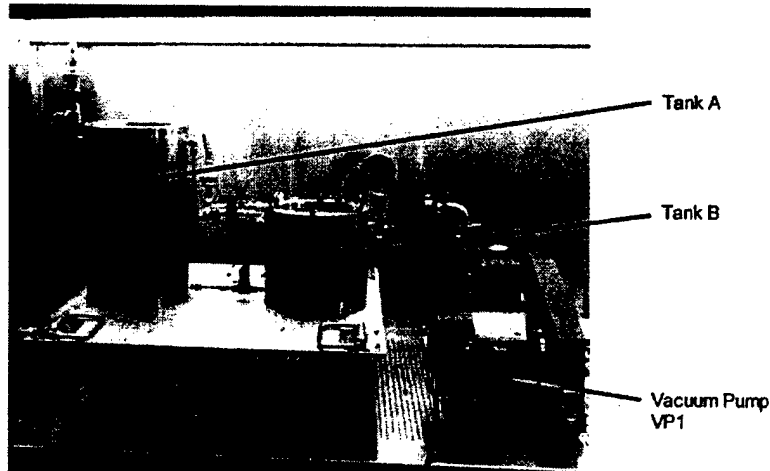


Figure 4.4: The fluid filling system. The cold traps are not shown in this photograph.

device, inside. Do not mount the device in the jig yet. This will be done after filling. Also do not install any o-rings in the jig. They are installed after filling. Close Tank B.

3. Start vacuum pump VP1.
4. When sufficient vacuum has been attained in the cold traps, CT1 and CT2, fill CT1 and CT2 with liquid nitrogen. Open ball valves V5 and V1.
5. *Substep if Tank A is not already filled with silicone oil:* Connect silicone oil reservoir (not shown) to Tank A via V6. FT1 will filter the inlet stream. Open V6 and V2. This will draw the silicone oil into Tank A, and simultaneously outgas the oil. Dissolved gases tend to reduce the effective bulk modulus of the oil, an undesired effect. After Tank A is filled, Close V6 and V2. Disconnect silicone oil reservoir and vent Tank A to atmosphere through V6.
6. Open V3. Evacuate Tank B to 5mmHg or less.
7. *Vapor purging step:* Slowly open V4 and allow a small amount of silicone oil to flow into Tank B. In this case, a fluid level of approximately 10mm was used in Tank B. Close V4.
8. Continue pumping on Tank B for approximately 90 minutes. All of the oil in Tank B

should have evaporated, and would have been caught in CT1. Ensure that Tank B is at a pressure of 5mmHg or less.

9. *Filling:* Close V3. Slowly open V4 and allow the fluid to submerge the jig and the device. Close V4 when the contents of Tank B are submerged.
10. *Pressurising:* Open V7 and needle valve NV1. Adjust the regulator, APR1, to provide an absolute pressure of 1.5atm . This will ensure that the pressure in the HAC asymptotes to a slightly higher pressure than atmosphere.
11. Reduce the pressure in Tank B to 1atm absolute pressure, and open Tank B.
12. With the device and the jig still submerged, insert the o-ring seals into the jig, mount the device and clamp to seal.

4.1.3 Initial tests

In this work it was necessary to fill a dead volume of approximately 8.3nl through a channel of dimensions $10\mu\text{m} \times 10\mu\text{m} \times 1\text{mm}$. The motivation for this channel will be discussed in Section 4.2.2. The nature of the design of the hydraulic amplification devices prevented any visual inspection of the HAC for bubbles after filling. It was therefore essential to verify the filling procedure described in Section 4.1.2, and to ensure that it was very robust. To this end, a set of experimental devices was fabricated in such a manner that the filling procedure could be seen through a suitable glass window. A device consisting of a glass-silicon-glass sandwich structure was fabricated using DRIE and a simple two step lithography process. A completed filling test chip is shown in Figure 4.5. Assembly was performed on the die level, using simultaneous anodic bonding of the top and bottom glass layers. In this case, conventional machining, using diamond tools, was used to drill holes in the top glass layer.

Using the procedure as described above, and visually monitoring the filling of each chamber using a microscope, it was verified that bubble-free filling could be obtained. The filling time after initiating the pressurization step was found to be approximately 7 minutes. After this time, no visible bubbles were detected. Two of these devices were assembled, giving a total of four chambers to be filled. Both chips were filled successfully on the first attempts to fill them. These results provided the needed confidence to fill and test the full hydraulic amplification devices.

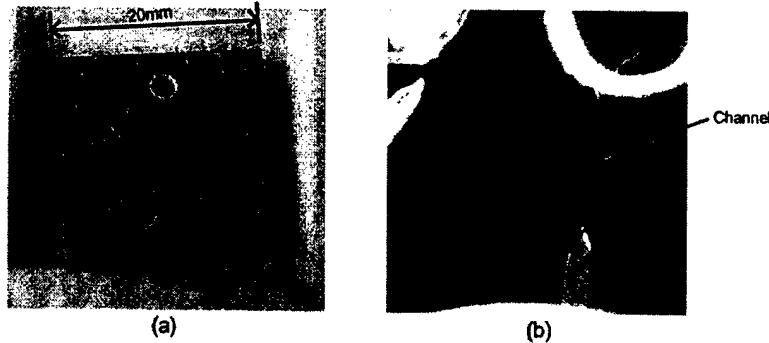


Figure 4.5: (a) Experimental filling test chip with two $10\mu\text{m} \times 10\mu\text{m} \times 1\text{mm}$ channels and matching dead volumes. (b) Detail of the filling channel. The dead volume had to be evacuated through this channel prior to filling.

4.2 Sealing concepts

Sealing of an hydraulic amplifier can be challenging. As discussed in Chapter 2, one would like to maximize the stiffness of the hydraulic coupler. This also means that any imposed volume change, as might be introduced by a seal pressing against an opening and subsequently bulging could introduce a large pressure increase in the hydraulic amplification chamber. (See Figure 4.6a). This led to the development of two sealing strategies for the two different types of tests performed on the hydraulic amplifiers evaluated in this work. The first type is a traditional static seal, as described above, and the second type, for high frequency hydraulic amplifiers, is a dynamic seal relying on a flow restriction.

4.2.1 Static sealing

For static sealing of the hydraulic amplifiers a seal consisting of a teflon sheet, $125\mu\text{m}$ thick, backed by a brass plate and preloaded with an o-ring was used, as illustrated in Figure 4.6b. This method enabled reliable sealing of the hydraulic amplifiers while giving minimal seal compression and volume change in the HAC, even with a sealing hole diameter in the glass layer of $800\mu\text{m}$. Should seal compression be of greater concern, the sealing hole diameter can be further reduced by micromachining the inlet port to the HAC [30].

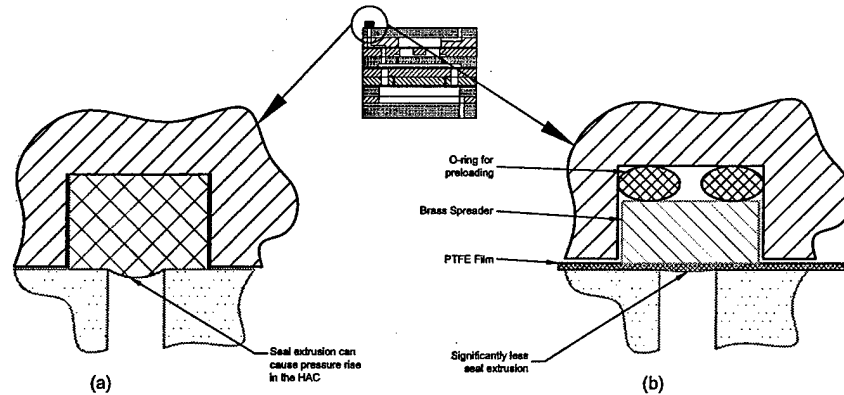
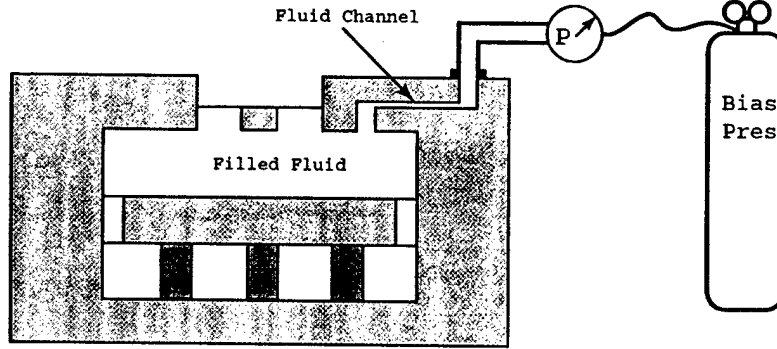


Figure 4.6: Static sealing of the hydraulic amplifier: a) The basic concept of a elastomeric or plastic seal. Seal compression could introduce large pressure changes in the HAC. b) Using a PTFE film for sealing, with a load spreader and a preloading element.

4.2.2 Dynamic sealing

If the hydraulic amplifier is to be operated only at high frequencies, another sealing technique can be used. By providing a suitable flow restriction on the inlet port to the HAC, it can be shown that high frequency pressure fluctuations generated by the large piston inside the HAC will not be transmitted to the outside. This restriction will have the effect of a low pass filter, allowing low frequency pressure variations to enter and leave the HAC. Using this sealing technique, the concerns related to seal compression are eliminated and it becomes easier to control the static pressure in the HAC. These benefits come at the cost of an external pressurization system that must be added to the device. For experimental purposes, this was not a concern. Figure 4.7 illustrates the basic principle. In addition, the external pressurization system provides the benefit of setting a constant pressure bias in the HAC. This in turn allows for balancing of the steady-state pressure on the small piston, and can also be used to control the static position of the small piston, should an offset be desired as, for example, in the case of a valve [19]. Furthermore, placing a bias pressure on the HAC reduces the likelihood of cavitation that could be induced by high frequency operation of the large piston.

A simple way to design this type of seal is to assume it to be a channel of suitable dimensions, containing a fluid slug. (See Figure 4.8.) By selecting the appropriate boundary conditions



Courtesy of D.C. Roberts

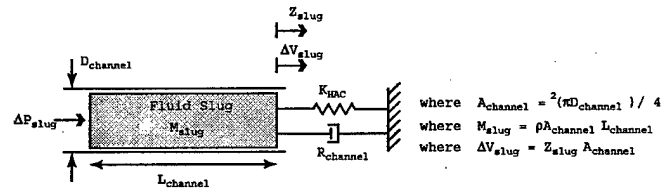
Figure 4.7: Schematic of the high resistance fluid channel between the HAC and an external bias pressure regulator. This channel was etched into the underside of Layer 7.

for the fluid slug in the channel, and by estimating the losses in the channel using Hagen-Poiseuille flow, one can predict the cutoff frequency of such a channel. As discussed in [19], such a channel was designed using the following equation of motion, as given by Roberts, as a starting point:

$$\left(\frac{M_{slug}}{A_{channel}^2} \right) \Delta \ddot{V}_{slug} + R_{channel} \Delta \dot{V}_{slug} + K_{HAC} \Delta V_{slug} = \Delta P_{slug} \quad (4.1)$$

A channel of dimensions $10\mu m \times 10\mu m \times 1mm$ was designed. Letting $L_{channel} = 1mm$, $D_{channel} = 11.3\mu m$, $K_{HAC} = 1.0e^{17} Pa/m^3$, $\rho_{fluid} = 760kg/m^3$, and $\mu_{fluid} = 6.5e^{-4} kg/(ms)$ gives a frequency of $48Hz$ for which ΔV_{slug} is 1% of the large piston volume change. For a further treatment of this subject, the reader is referred to [19].

Test results, as shown in Figure 4.9 clearly indicate the effectiveness of this channel. A lower cutoff frequency of approximately $0.1Hz$ was observed. This frequency is even less than the design cutoff frequency. It is also significantly less than the design frequency for the hydraulic amplifier, of between 1 and $15kHz$. This ensures that the full pressure swing created by the piezoelectric actuators acting on the large piston is transferred to the smaller piston. The results shown in Figure 4.9 were obtained with AV Device 1 that is discussed in Chapter 6. For information on the experimental equipment required to obtain the results in Figure 4.9, the reader is referred to Chapter 5.



Courtesy of D.C. Roberts.

Figure 4.8: Model of the high resistance fluid channel between the HAC and an external bias pressure regulator. A fluid slug within the channel is modeled. This slug is acted upon by an external stiffness associated with the HAC chamber stiffness. Additionally, the flow resistance of this slug through the channel is modeled using laminar Hagen-Poiseuille flow relations.

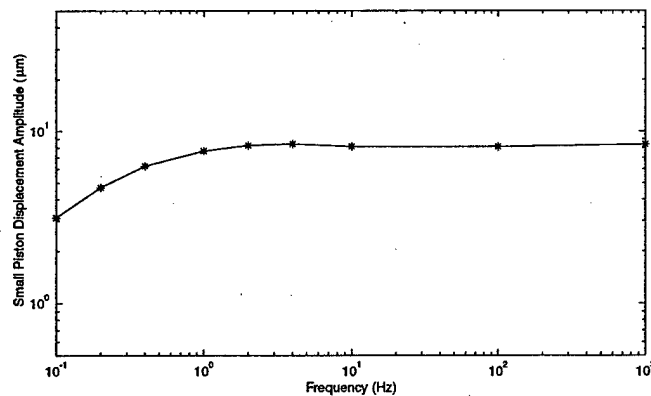


Figure 4.9: Experimental results of tests performed on a flow restriction-type dynamic seal. This test was performed by applying a sinusoidal excitation of $200V_{p-p}$ to the piezoelectric element of the large piston, and measuring the displacement of the small piston for the frequencies shown. Note the good quasi-static performance down to 1Hz.

4.3 Summary

The bubble-free filling and successful sealing of the HAC can be seen as the two most critical steps in the process of producing an hydraulic amplifier. An improperly filled and sealed hydraulic amplifier cannot be expected to function as desired, regardless of its design or the fabrication techniques used. The procedures that were developed in this work have been proven to yield reliable filling and sealing results, as will be shown in Chapter 6. Before presenting the results, however, Chapter 5 will discuss the macroscale systems and test jigs required to enable the instrumentation and testing of the hydraulic amplifiers evaluated in this work.

Experimental techniques

5.1 Requirements of the experimental setup

To enable experimental evaluation of the hydraulic amplification devices that had been built, an appropriate test bench had to be developed to enable the measuring of all important parameters. To evaluate the performance of an hydraulic amplification unit, such a test bench had to satisfy the following requirements:

- Enable fluid pressure to be applied to either one of both sides of the device. Also, to accurately measure the relevant pressures.
- Enable electrical connection to the device, in the case of a piezoelectrically driven device.
- Provide a means for measuring out of plane displacement of the tethered piston structures.
- Provide, in addition, a means for evacuating the device and refilling the device with fluid.¹

5.2 System overview

To address all the requirements mentioned previously, a system containing the following five subsystems was built:

¹This excludes the hydraulic amplification chamber itself. The filling and sealing of this chamber was dealt with in the previous chapter.

1. Device testing section, including the device test jig and the pressure measurement and control module, for measuring steady pressures.
2. Gas pressure regulating module.
3. Gas-liquid pressurization module, to enable pressurization of the working fluid.
4. Vacuum module, to enable evacuation and filling of the system.

It was found useful to construct the system in this modular fashion. The functioning of the various modules will be described in the sections that follow. For all equipment used, the reader is referred to Appendix B.

5.3 Device test jigs

The purpose of a test jig is to provide an interface between the microfabricated device, in this case an hydraulic amplifier, and the macroscale environment with which it has to interact. Although the test jig could also be called the "packaging" for the device, as described at length in [39] and [31], a distinction is made here between a component to be used for testing the MEMS device, and a component used to package the device for use in commercial applications.

Figures 5.1 and 5.2 show the test jig designed for the static hydraulic amplifiers. The detail design of this jig is given in Appendix C. In the design of this test jig the following aspects were considered:

- Provide reliable sealing of all fluid connections to the device. Accomplished by o-rings.
- Provide sufficient, but not excessive, clamping force. Accomplished by using springs for preload.
- Expose as much of the device area as possible for ease of laser displacement measurement. This was done. In addition, the jig was manufactured from aluminum and anodized black, to minimize reflection.
- Ensure proper electrical insulation. The device was insulated from the jig with an acetel-type plastic insert.

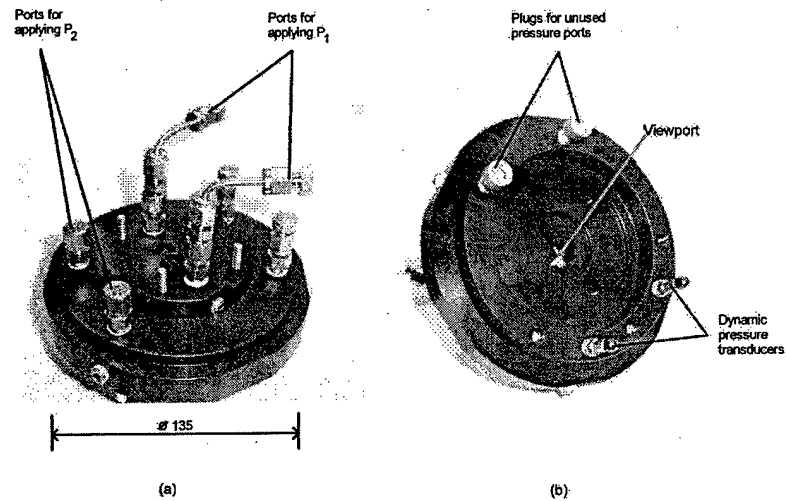


Figure 5.1: Two views of the test jig: Top view (a) and bottom view (b). Note the viewport for laser displacement measurement.

- Allow for measuring of dynamic pressure fluctuations near the device. Provision was made for the installation of PCB model 112A22 dynamic pressure transducers on the jig.
- Had to fit in the fluid filling system discussed in Chapter 4.

5.4 The fluid test bench

The remaining four modules mentioned in Section 5.2 will now be given attention. Figure 5.3 is a schematic drawing of all the modules, each of which will be discussed in detail.

5.4.1 Gas pressure regulating module

Figure 5.4 illustrates the layout of the pressure regulating module. This module supplies regulated pressure to the test bench, and relies on double regulation, using Concoa Series

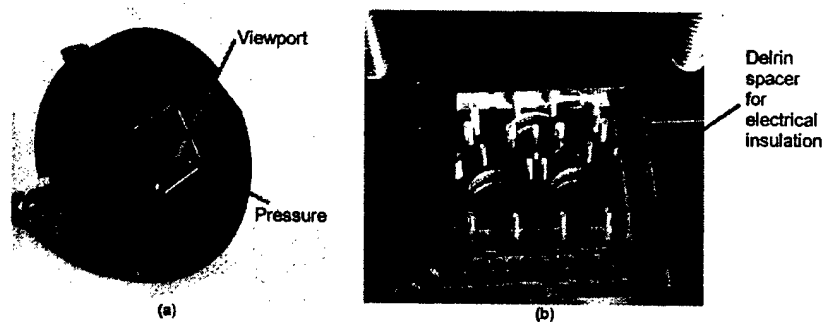


Figure 5.2: The top clamp (a) shows a recess for the device, two optical viewports and also two fluid pressurization ports. The device is inserted into the main jig (b) and then clamped with the top clamp.

402 regulators. Even with double regulation, a certain amount of leak-through and drift can still occur when using process-grade regulators. Therefore, a continuous bleed-off system, using two sets of two Swagelok SS-2SS needle valves, *NV1*, *NV2*, *NV4* and *NV5*, was utilized whenever exact pressure control was needed.

5.4.2 Gas-liquid pressurization module

To provide the capability of pressurizing the hydraulic amplifier with a liquid instead of a gas, a gas-liquid pressurization module was added to the test bench. This is schematically shown in Figure 5.5. This module consists of a stainless steel tank, *TK2* - a Swagelok part number 304L - *HDF4* - 500 500cm³ sample cylinder - pressurized from the top by nitrogen, and filled through a filling tube with DC200 0.65cst silicone oil. The oil is drawn into the vessel by vacuum, outgassing the liquid in the same process. A clear nylon tube, rated at 625psi working pressure, was added on the side of this vessel for level visualization. Stainless steel bellows valves (*BEV1*, *BEV3*), Swagelok part number SS-4H, were used for gas-liquid shutoff, and stainless steel ball valves (*BV1*, *BV3*, *BV5*) - Swagelok SS-42S4 - were used for all other shutoff purposes. For the most part, 1/4" seamless 304L stainless steel tubing was used in the construction of this module.

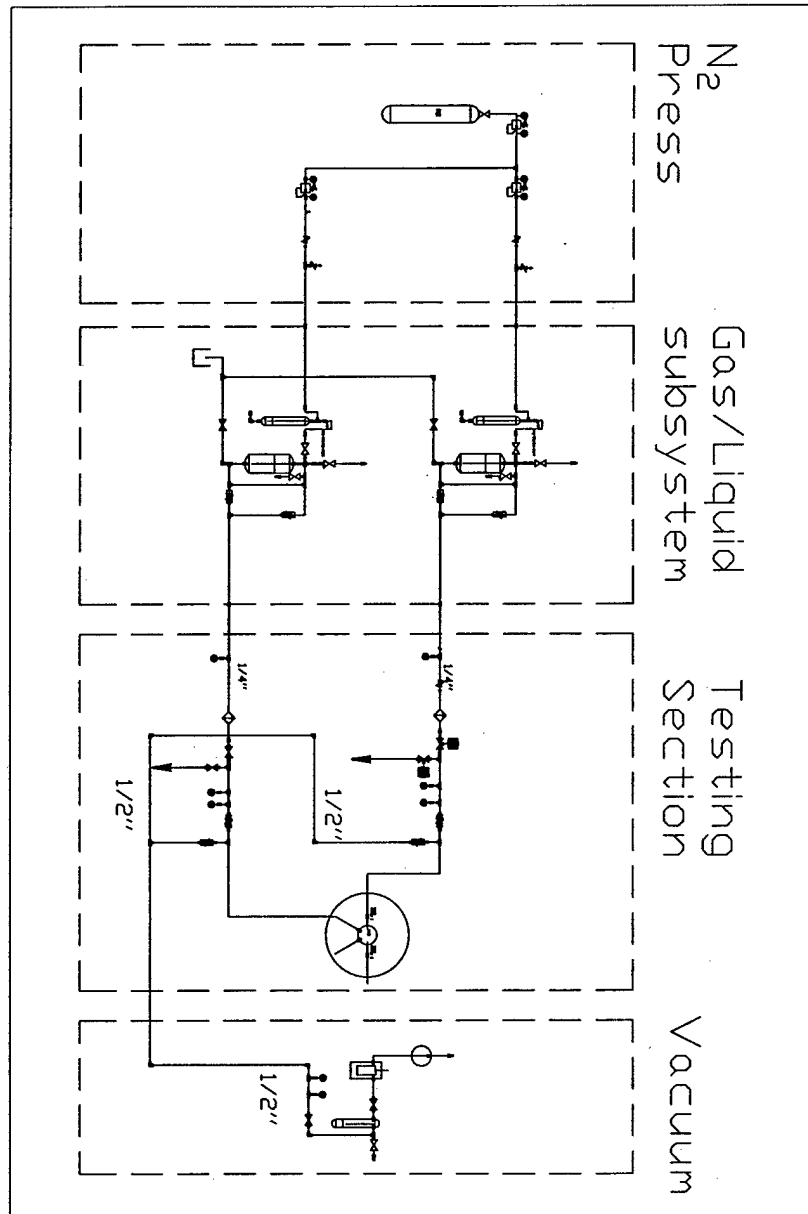


Figure 5.3: Schematic representation of the full fluidic testing system used for performing experiments on the Hydraulic Amplification Devices.

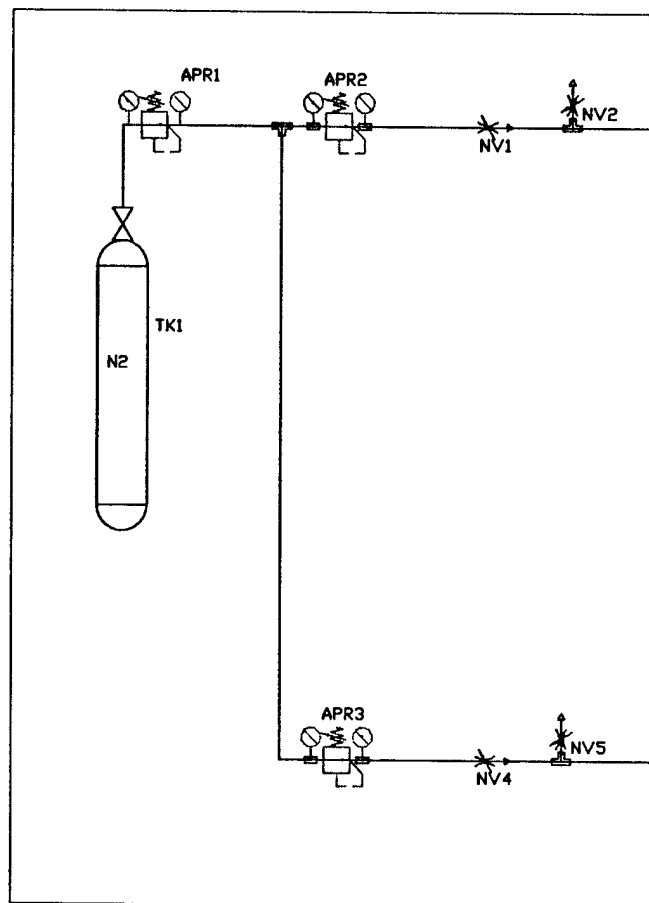


Figure 5.4: The gas pressure regulating module.

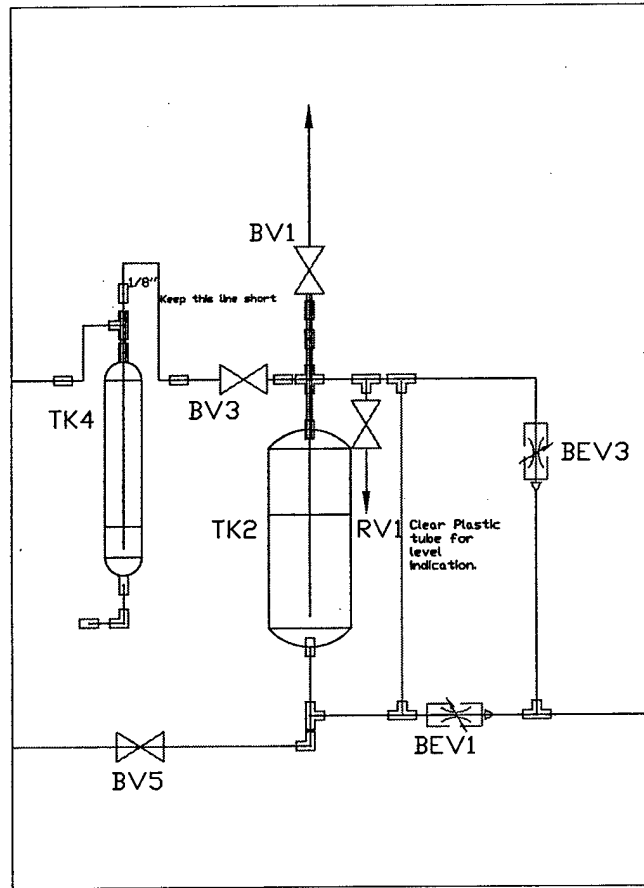


Figure 5.5: The gas-liquid pressurization module.

5.4.3 Pressure measurement and control module

The essence of the fluidic test bench for the hydraulic amplifier is contained within the pressure measurement and control module. In Figure 5.6 the following components are of importance:

- Two static gauge pressure transducers per pressurization line. Sensotec FP2000 type sensors (500 $psig$, 0 – 5 VDC , 0.1% accuracy) (*SPS2*, *SPS4*) were used for high pressure measurements, and for low pressure measurements the same type of sensors, but with the following specifications: (100 $psig$, 0 – 5 VDC , 0.1% accuracy) (*SPS7*, *SPS8*).
- Two Parker Series 9 fast acting high pressure solenoid valves (*SV1*, *SV2*) on one of the pressurization lines, to allow for rapid pressurization and venting of the device being tested. Controlled by a signal from the data acquisition system, these valves enabled, to a large extent, automation of the testing procedure. (See Figure 6.5)
- Two Swagelok SS-42S4 ball valves on the other pressurization line (*BV10*, *BV11*). These valves perform the same function as *SV1* and *SV2*, but in a manual fashion. Using solenoid valves worked so well that it is recommended that two sets of solenoid valves be used instead, should similar experiments ever be attempted.
- Swagelok SS-4TF-05 0.5 μm filters on both supply lines leading to the device.
- As in the case shown in Figure 5.5, stainless steel bellows valves (*BEV5* – *BEV8*) were used for gas-liquid shutoff.

5.4.4 Vacuum module

The vacuum module, depicted schematically in Figure 5.7 encompasses the vacuum pump (*VP1*), cold trap (*CT1*) and a thermocouple vacuum gauge and meter (*SPS6*). All vacuum connections were made using 1/2" tube, either in stainless steel or polypropylene. The vacuum module was used to evacuate flow systems prior to filling with silicone oil. A pressure of approximately 5 $mmHg$ was found to be sufficient for bubble free filling of flow channels.

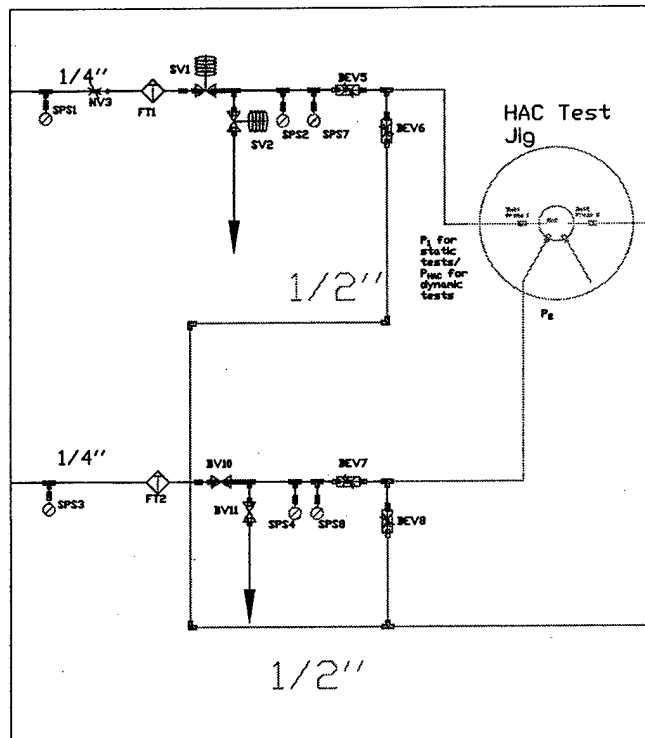


Figure 5.6: Pressure measurement and control module.

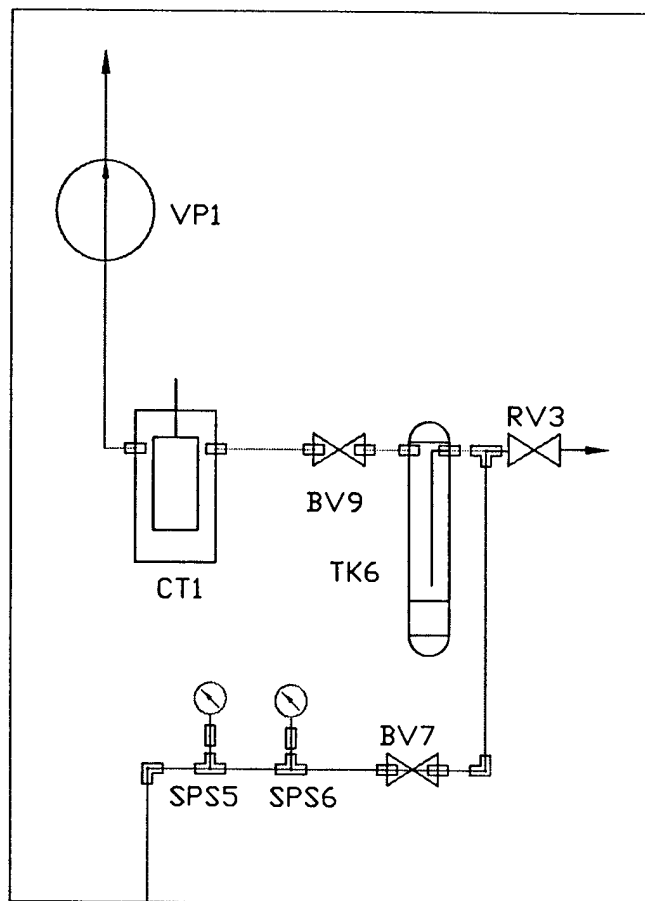


Figure 5.7: Vacuum module.

5.5 Displacement measurement

All displacement measurements were performed with a Polytec PI PSV-300 Scanning Laser Vibrometry system. Using doppler principles, this system measures the velocity of a moving target. By integration, displacement is obtained. The system was outfitted with a precision displacement measuring board with a rated resolution of $2nm$. Testing has shown that the actual resolution is dependent on the amount of ambient noise present, and also on the nature of the surface being measured. The best actual resolution obtained for near-zero frequency displacement measurements was found to be between 10 and $50nm$, depending on the noise present when the measurements were performed.

All of the instrumentation and hardware used to test the hydraulic amplification devices have now been discussed. Figures 5.8, 5.9 and 5.10 are photographs of the testing system that has, up until now, only been described schematically.

5.6 Data acquisition

All data acquisition was performed using two National Instruments PCI-6110 boards installed in a desktop computer with an Intel Pentium III $700MHz$ processor and $128MB$ RAM. The data acquisition system allowed the simultaneous, synchronized, measurement of up to eight input channels, at sampling rates of up to $4MHz$. In addition, it also allowed for simultaneous synchronized generation of four arbitrary waveform outputs at frequencies up to $25kHz$, using data acquisition software as developed by [40] using the National Instruments LabView language.

5.7 Testing protocols

Prior to testing the device, either a static or dynamic hydraulic amplifier, it is filled using the procedures described in Chapter 4 and subsequently clamped in the test jig described in Section 5.3. For testing the devices, two different testing procedures were followed for the static and dynamic devices, and these will be discussed briefly.

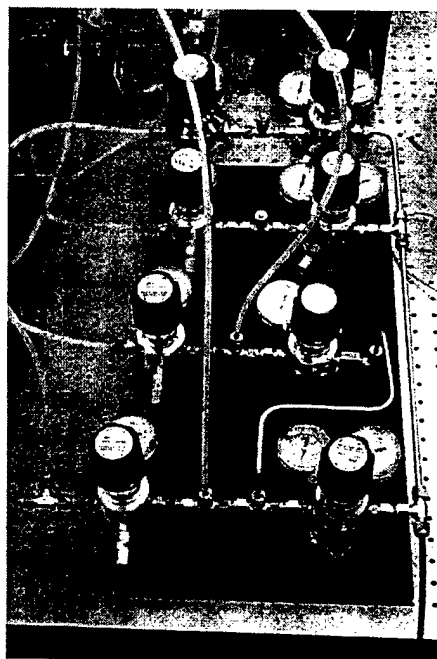


Figure 5.8: Regulator bank. Note that this is the regulator bank for the full MHT device. Only two sets of the four displayed are used. Note the double regulation from a regulated tank output.

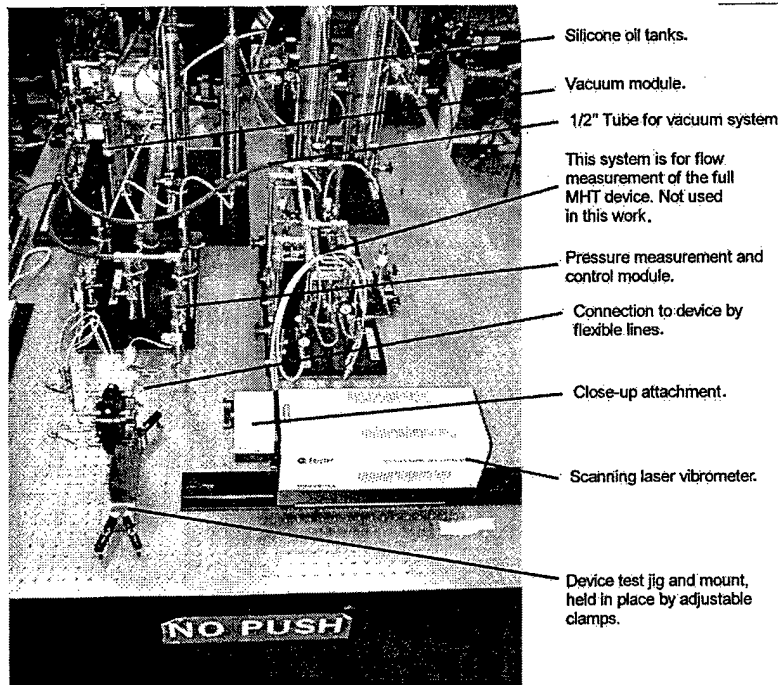


Figure 5.9: Photograph of the entire test rig. All tests were performed on an optical vibration isolation table.

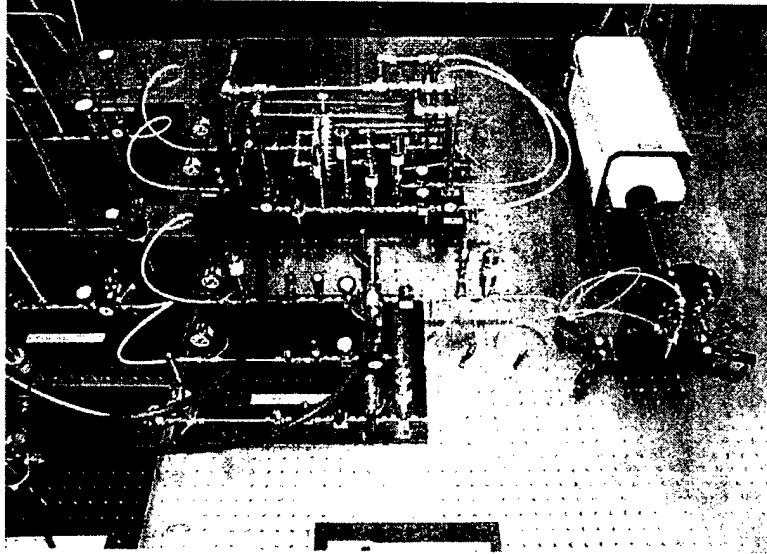


Figure 5.10: Side angle photograph of the test rig, with more detail on the pressure measurement and control module.

5.7.1 Testing of static hydraulic amplifiers

The following aspects, not necessarily in the order mentioned, should be considered during the testing of a static hydraulic amplifier:

- Decide whether the device is going to be tested in a full liquid system, a gas system, or a gas-liquid system. For static devices, for optical clarity, it was found desirable to test in a gas-liquid system.² In this configuration, *TK2* in Figure 5.5 is bypassed using *BEV3*.³ Note that the device and the test jig were filled with liquid, but the pressurization lines were operated using nitrogen. Concerns about water hammer from operating *SV1*, *SV2* (Shown in Figure 5.6) were the motivation for not using a full liquid system in this case. The displacement measurement obtained from the

²Meaning measuring through silicone oil instead of gas. During the filling process, the device is filled with oil. If this oil is subsequently removed from the device, a residue often is left behind, which hinders measurements.

³The equivalents of *TK2* and *BEV3* are also used in this manner. These are not shown explicitly, but can be found in Figure 5.3

laser vibrometer had to be corrected for the different index of refraction of the fluid in all cases where the measurements were performed on an interface with silicone oil rather than air. It can be shown that dividing by the index of refraction gives the desired correction.

- Set the pressures P_1 and P_2 on *APR2* and *APR3*.
- Set the appropriate acquisition rate in the data acquisition system, and ready the system for testing.
- Start by switching *SV1* and *SV2* to provide a pulsing pressure for P_1 . (See, again, Figure 6.5).
- Use *BV10* and *BV11* to vary P_2 .
- In all these tests, *BEV5* and *BEV7* are fully open, and *BEV6* and *BEV8* are fully closed.

5.7.2 Testing of dynamic hydraulic amplifiers

- Once again, decide whether to use liquid, gas or gas-liquid. In this case, tests were generally performed using either a full gas system, or a full liquid system.
- In these tests, P_1 and P_{HAC} are applied. They are not varied or pulsed as in the static case. Therefore, it is advisable to remove *SV1* and *SV2* from the system for these tests. *SV1* and *SV2* are normally closed valves, and although it is possible to apply a voltage to keep *SV1* open continuously, it is not desirable and may damage the valve coil.
- Set P_1 and P_{HAC} on *APR2* and *APR3*. In all tests presented in this work $P_1 = P_{HAC}$. Therefore, in this case, P_1 and P_{HAC} were controlled from the same regulator, using an appropriate tube to connect the two ports.
- Prepare the data acquisition system for testing.
- Apply the drive voltage to the piezoelectric element. This potential is named V_1 , and is applied on Layers 2 and 4 of Figure 2.2. Tests were performed using either frequency sweeps or sinusoidal excitation.

With these testing protocols, it was possible to perform the experiments that will be described in Chapter 6.

Experimental Evaluation of Hydraulic Amplification Devices

Having discussed all issues relevant to the successful design, fabrication and testing of an experimental hydraulic amplification device, this chapter deals with the subsequent tests performed on a selection of devices based on the MIT EH4 energy harvesting device discussed in the introduction.

6.1 Overview of the experimental work

In brief, the devices were characterized in the following manner:

- Pressure-deflection characteristics of the tethered piston structures.
- Static performance measurements on two hydraulic amplifiers: One with ten small pistons and one large one as well as a device with a single small piston. Gas pressurization techniques were used.
- Demonstration of dynamic performance of a device with one small piston and a piezo-electrically driven large piston.

In total, four hydraulic amplification devices were built and tested. Table 6.1 summarizes the devices built, and the tests performed on them.

| Device number | Device type | Tests performed | Comments |
|---------------|---|--|---|
| HAC Device 1 | Single small piston static hydraulic amplifier, no piezoelectric elements | Static Characterization of small and large pistons | Device cracked during initial testing due to excessive clamping force in test jig |
| HAC Device 2 | Single small piston static hydraulic amplifier, no piezoelectric elements | Static Characterization of small and large pistons | Device cracked after filling due to excessive clamping force in test jig |
| HAC Device 3 | Ten small piston static hydraulic amplifier, no piezoelectric elements | Static Characterization of small and large pistons, Characterization of hydraulic amplification capabilities | Device was subjected to full range of characterization tests without failure. |
| HAC Device 4 | Single small piston static hydraulic amplifier, no piezoelectric elements | Characterization of hydraulic amplification capabilities | Device was subjected to full range of characterization tests without failure. |
| AV Device 1 | Single small piston active valve device. Piezoelectrically driven | Dynamic testing of the hydraulic amplification concept, evaluation of the performance of the high-frequency sealing channel. | Device was subjected to full range of dynamic tests without failure. |

Table 6.1: Outline of the hydraulic amplification devices assembled and tested

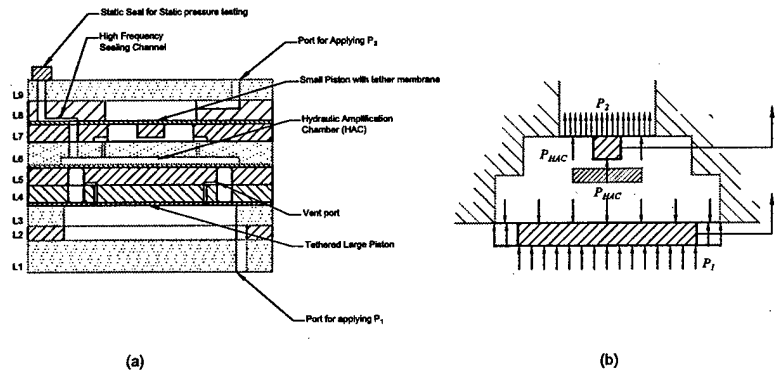


Figure 6.1: Two representations of the static hydraulic amplification device: (a) A detailed cross section schematic view, and (b) A simplified functional schematic, with nomenclature to be used.

6.2 Pressure Deflection results

The purpose of performing simple pressure deflection tests of the tethered structures is to determine the stiffnesses of the individual components of the hydraulic amplification device. These will later be used in correlating the experimental results of the full hydraulic amplification devices with the theoretical predictions. For each device, the pressure-deflection characteristics of both the large piston and the small piston were evaluated. Figure 6.1 illustrates the geometry under consideration and also the nomenclature that will be used. Note that, in this case, $P_{HAC} = 0$, and we only apply P_1 for the large piston and P_2 for the small piston. All results presented in this section reflect the aggregate of all tests performed on a given type of membrane structure, rather than discussing the testing of each individual membrane. This will maintain the focus of our discussion and will also give the reader a sense for the amount of variation from specimen to specimen that can be expected when using the fabrication techniques described in Chapter 3.

6.2.1 Pressure-deflection characteristics of the large piston

All of the devices listed in Table 6.1 had the exact same design geometry for the large pistons. However, due to variations in the fabrication process, all of the large pistons were slightly different. Figure 6.2 displays the pressure-deflection results obtained for a selection

| | |
|--------------------------|------|
| $\psi_{1,exp}$ | 11.3 |
| $\psi_{1,theo(8\mu m)}$ | 8.9 |
| $\psi_{1,theo(9\mu m)}$ | 12.7 |
| $\psi_{1,theo(10\mu m)}$ | 17.4 |

Note: All units are in $kPa/\mu m$.

Table 6.2: Large piston inverse compressibility

of these pistons, along with a prediction from the nonlinear model developed in [25].

We can further proceed, based on the information shown, to compute the linearized inverse compressibility coefficients for the experimental results and also for the theoretical predictions, as defined in Equation 2.13. The results are shown in Table 6.2. Referring back to Table 2.1 and also to Chapter 3, we recall that the design required a $10\mu m$ thick SOI layer. The starting substrate for these pistons had a device layer thickness of, nominally, $11\mu m$ with a variation of $\pm 1\mu m$. After the oxidation process, approximately $0.7\mu m$ is removed, therefore reducing the SOI thickness to $10.3 \pm 1\mu m$. Measurements performed after processing on pieces from the wafer edge, using a KLA-Tencor P10 surface profilometer, indicate that the final thickness of the device layer at the edge location was $8 \pm 0.5\mu m$ on various positions of the wafer edge. Therefore, for small deflections, the model agreement appears to be very good and within the bounds of measurement errors and fabrication tolerances.

6.2.2 Pressure-deflection characteristics of the small piston structures

As mentioned in Section 2.3, two types of small piston configurations were used. Figure 6.3 shows the pressure-deflection characteristics of a device with a single small piston, and Figure 6.4 shows the same for a device with ten smaller pistons.

For these two cases one can proceed and again compute the small-deflection inverse compressibility coefficients, as was done for the large pistons. Table 6.3 gives these coefficients for the devices having a single small piston, and Table 6.4 gives the coefficients for HAC Device 3. In both of these cases, the starting wafer had a device layer thickness of $8 \pm 1\mu m$. After processing, this thickness would be reduced to approximately $7.3 \pm 1\mu m$, based on the fabrication process. Post-fabrication measurements on the wafer edge gave a thickness of $6 \pm 0.5\mu m$ on various positions of the wafer edge. Once again, the agreement with model predictions is good, and within the bounds of fabrication capabilities and measurement

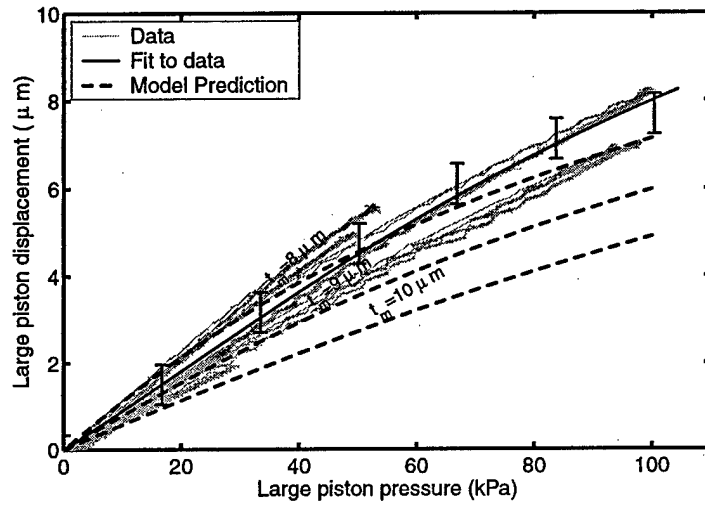


Figure 6.2: Results from pressure-deflection tests on the large pistons, obtained from HAC devices 1,2 and 3

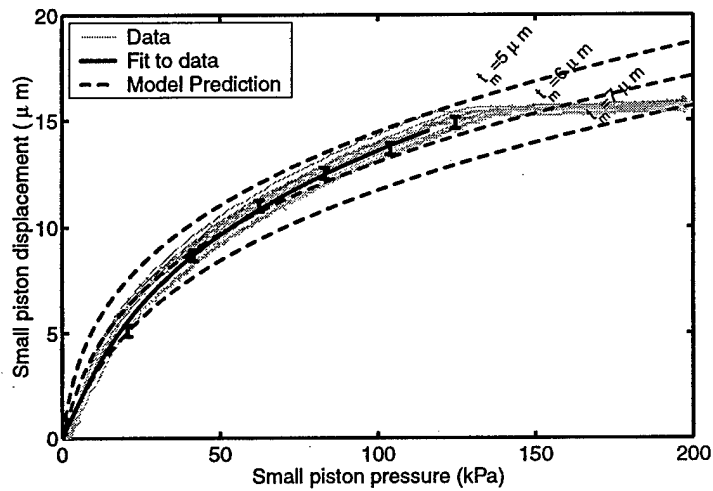


Figure 6.3: Results from pressure-deflection tests on a selection of small pistons from HAC Devices 1 and 2, both having one small piston per hydraulic amplifier.

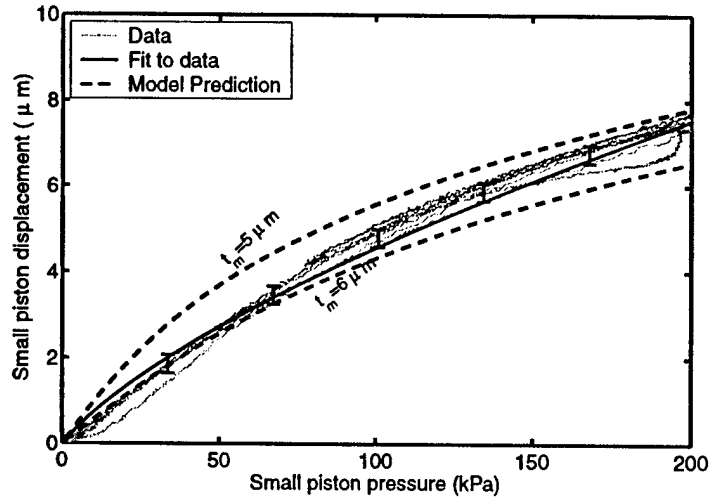


Figure 6.4: Results from pressure-deflection tests on a selection of small pistons from HAC Device 3, a device with ten small pistons per hydraulic amplifier.

| | |
|-------------------------|-----|
| $\psi_{2,exp}$ | 3.1 |
| $\psi_{2,theo(5\mu m)}$ | 1.0 |
| $\psi_{2,theo(6\mu m)}$ | 1.8 |
| $\psi_{2,theo(7\mu m)}$ | 3.0 |

Note: All units are in kPa/ μ m.

Table 6.3: Small piston inverse compressibility for devices with a single small piston.

tolerances.

6.2.3 Summary: Pressure deflection results

This section presented pressure deflection data on the small and large piston geometries employed in the hydraulic amplifiers that were tested. In all results it appears that the pistons were slightly more compliant than predictions based on design values. After post-fabrication metrology and model corrections, it was shown that the values obtained were still within the bounds of tolerances quoted by the wafer suppliers, as well as tolerances in the subsequent fabrication processes. After performing these tests, the models were

| | |
|-------------------------|------|
| $\psi_{2,exp}$ | 13.0 |
| $\psi_{2,theo(5\mu m)}$ | 10.1 |
| $\psi_{2,theo(6\mu m)}$ | 17.5 |

Note: All units are in $kPa/\mu m$.

Table 6.4: Small piston inverse compressibility for devices with 10 small pistons.

appropriately adjusted before continuing to the next section, which involves the testing of a filled hydraulic amplifier.

6.3 Static hydraulic amplification tests

Two devices mentioned in Table 6.1 underwent static hydraulic amplification tests: HAC Device 3 was a device with 10 small pistons and HAC Device 4 was a device with a single small piston. The static behavior of both devices was evaluated by pressurizing both the small piston(s) and the large piston, and measuring the displacement of both. Due to constraints in the measurement system, simultaneous measurements were not possible. However, by accurately controlling the respective pressures, reliable results were obtained. In all static tests performed, P_1 was switched by the solenoid valves discussed in Section 5.4.3. P_2 was switched manually using ball valves. Figure 6.5 shows representative time-histories obtained for a typical hydraulic amplification test run.

6.3.1 Tests performed, and correlation with nonlinear models: HAC Device 3

Figures 6.6 and 6.7 show the deflections of the large piston and one of the small pistons for P_1 varying from 0 to $500kPa$ and for P_2 having values 0, 92, 298 and $500kPa$. Keeping in mind the pressure-deflection results from Section 6.2.1 it should be clear to the reader that the large piston acts as a pressure transfer element with very little pressure differential across this piston for the deflections observed in Figure 6.6. The small piston in turn responds to the pressure transferred by the large piston. In both figures the data is displayed along with cubic fits to the data. In all subsequent analyses the *fitted* data will be used instead of the raw data. Note that the fits are cubic, and were performed on the *inverse* of the data shown. The reader should bear in mind that, to first order, the tethered membrane piston structure can be seen to be analogous to a Duffing-type spring, as described, for example,

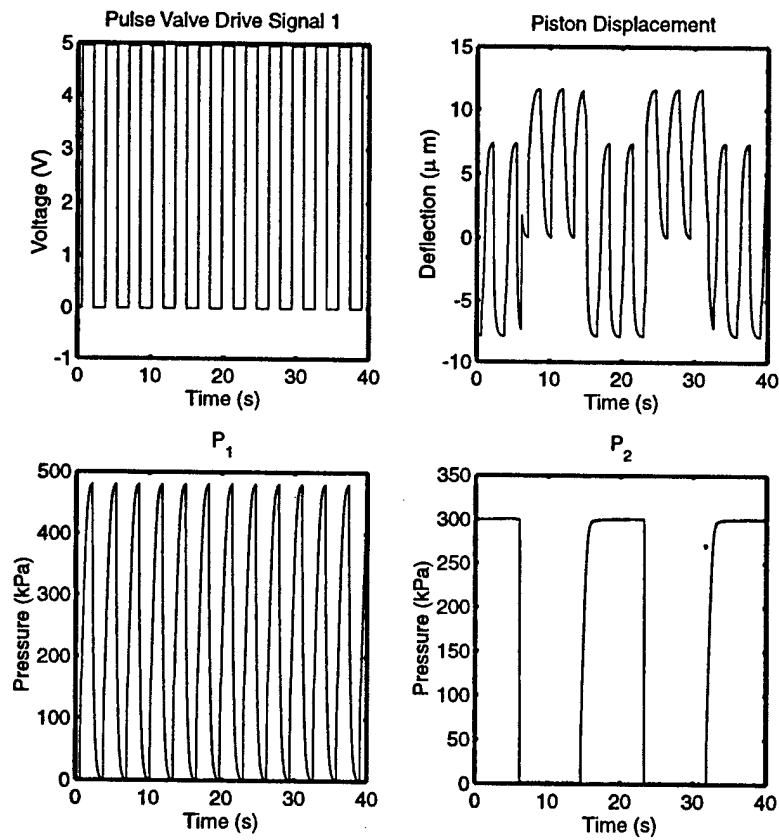


Figure 6.5: Typical data obtained from an hydraulic amplification test run. By accurately controlling P_2 during each small piston - large piston measurement pair, it was possible to obtain good data without resorting to two-sided displacement measurement.

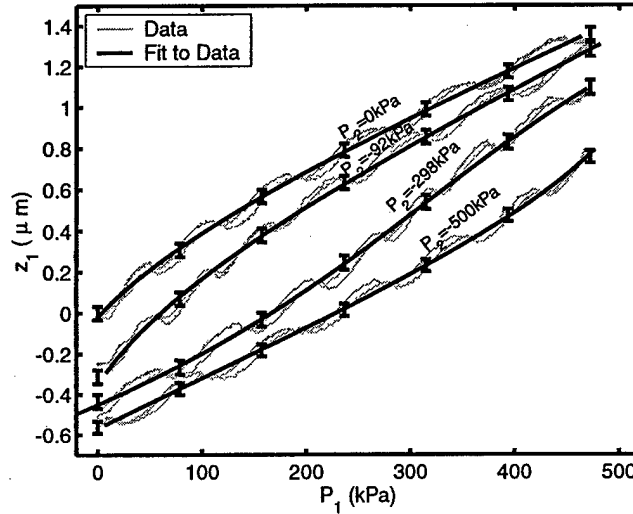


Figure 6.6: Hydraulic amplification data for the large piston of HAC Device 3. For all subsequent analysis, the fitted data will be used.

in [41]. In the case of a Duffing spring, the spring force is a cubic polynomial function of the deflection. The inverse - that the deflection is a cubic polynomial function of the spring force - does not hold. It is the same for the membrane structures, with the exception that a pressure takes the place of the force, as discussed in Chapter 2.

Figures 6.8 and 6.9 now show the model results plotted over the experimental results. Note that the large piston deflects significantly more than model predictions, indicating a reduced stiffness of the HAC.

6.3.2 Amplification ratio and amplification sensitivity: HAC Device 3

A suitable figure of merit in evaluating the performance of an hydraulic amplifier would be an amplification ratio or an amplification factor. This ratio can be computed using two different methods. The first method, which we will define as the amplification ratio, is defined as:

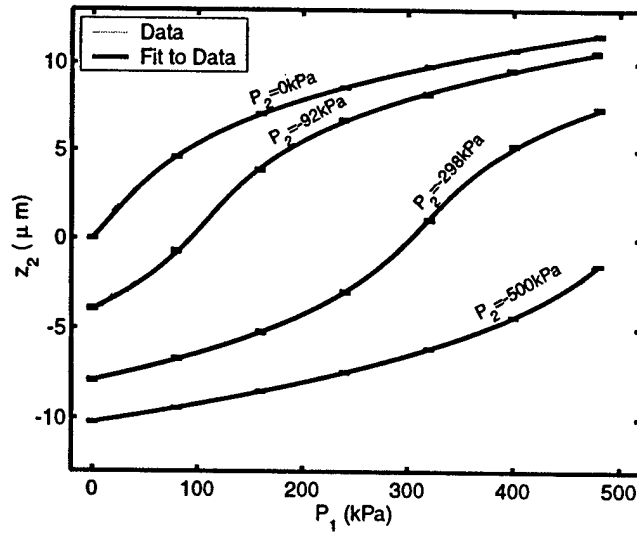


Figure 6.7: Hydraulic amplification data for the small piston of HAC Device 3. Note that the scatter in data for the small piston is very small, due to good measurement resolution and large amplitude motions.

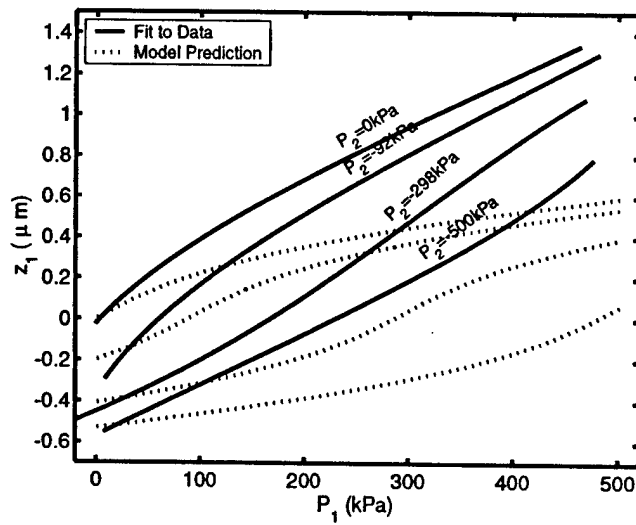


Figure 6.8: Adding model data to Figure 6.6. HAC Device 3.

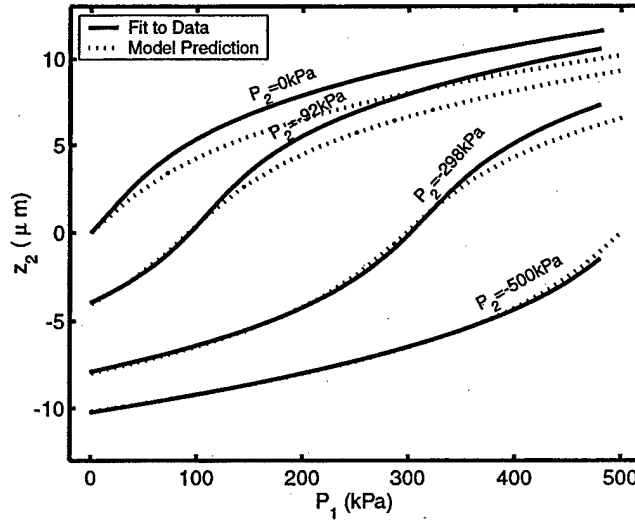


Figure 6.9: Adding model data to Figure 6.7. HAC Device 3.

$$AR = \left(\frac{z_2(P_1) - z_2(0)}{z_1(P_1) - z_1(0)} \right)_{P_2=const} \quad (6.1)$$

Figure 6.10 shows this amplification ratio. Note that the amplification ratio is always a maximum near the "linear region" of the operating regime. The second method, shown in Figure 6.11 uses the incremental displacement amplification which allows us to write an expression for the amplification sensitivity:

$$AS = \left(\frac{\partial z_2}{\partial z_1} \right)_{P_1, P_2=const} \quad (6.2)$$

6.3.3 Small deflection stiffness matrix comparisons: HAC Device 3

One can proceed and compute the small-deflection inverse compressibility matrix of the coupler, as described in Section 2.4. In Section 6.2 the results of the tests on all tethered piston structures are given. Figure 6.12 gives the results obtained for the large piston

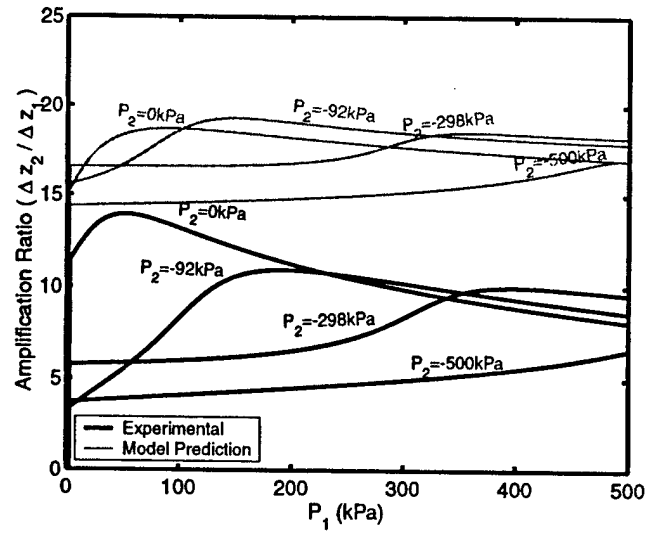


Figure 6.10: Amplification ratios for the tests performed. HAC Device 3.

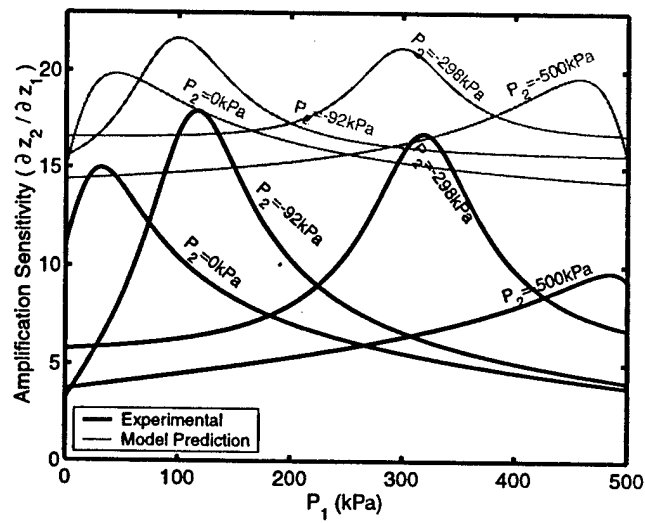


Figure 6.11: Amplification sensitivities for the tests performed. HAC Device 3.

| | |
|----------------|------|
| $\psi_{1,exp}$ | 15.2 |
| $\psi_{2,exp}$ | 15.4 |

Note: All units are in kPa/ μm .

Table 6.5: Inverse compressibilities for the pistons of HAC Device 3.

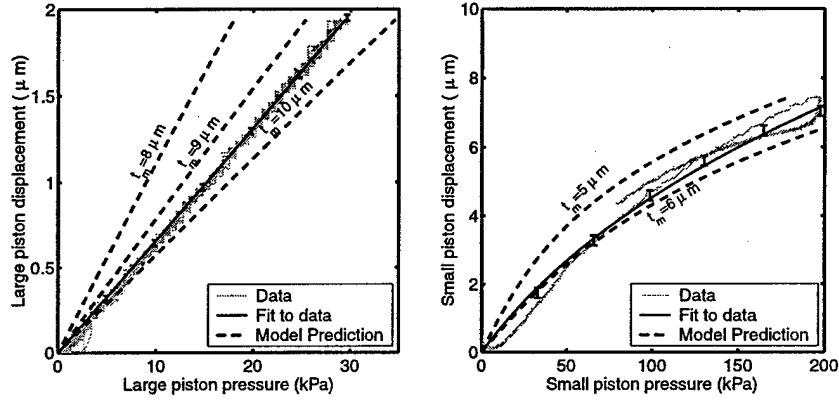


Figure 6.12: Pressure-deflection results for the large and small pistons of HAC Device 3.

and small piston tested in this section. For these individual tethered piston structures, the scatter in the data is significantly less, due to the elimination of variations in the fabrication process and variations in SOI device layer thickness as elements of uncertainty. For these particular structures, the inverse compressibilities, ψ_1 and ψ_2 , are given in Table 6.5.

We now proceed to compute the inverse compressibility matrix for this coupler. By taking two values of z_2 at two values of P_2 and a matching P_1 , and then finding the corresponding values for z_1 at those values of P_2 and P_1 , we can set up a system of linear equations, and solve for the four coefficients, as shown in Equation 6.3.

$$\begin{pmatrix} P_{1a} \\ P_{2a} \\ P_{1b} \\ P_{2b} \end{pmatrix} = \begin{bmatrix} z_{1a} & z_{2a} & 0 & 0 \\ 0 & 0 & z_{1a} & z_{2a} \\ z_{1b} & z_{2b} & 0 & 0 \\ 0 & 0 & z_{1b} & z_{2b} \end{bmatrix} \begin{pmatrix} D_{11} \\ D_{12} \\ D_{21} \\ D_{22} \end{pmatrix} \quad (6.3)$$

where:

$$\mathbf{D} = \begin{bmatrix} D_{11} & D_{12} \\ D_{21} & D_{22} \end{bmatrix} \quad (6.4)$$

and, recalling from Equation 2.11 that:

$$\mathbf{P} = \mathbf{D}\mathbf{z} \quad (6.5)$$

For $z_{2a} = 1\mu m$, $P_{2a} = -92kPa$ and $z_{2b} = -1\mu m$, $P_{2b} = -298kPa$, and finding the matching values for P_1 and z_1 in both the experimental and theoretical cases, the following \mathbf{D} -matrices were computed:

$$\mathbf{D}_{theo} = \begin{bmatrix} 7.38 \times 10^3 & -3.49 \times 10^2 \\ -7.38 \times 10^3 & 3.67 \times 10^2 \end{bmatrix} kPa/\mu m \quad (6.6)$$

$$\mathbf{D}_{exp} = \begin{bmatrix} 6.34 \times 10^2 & -1.90 \times 10^1 \\ -6.32 \times 10^2 & 3.46 \times 10^1 \end{bmatrix} kPa/\mu m \quad (6.7)$$

Dividing (6.6) element-wise by (6.7), we find the following ratios:

$$\begin{bmatrix} 11.6 & 18.4 \\ 11.7 & 10.6 \end{bmatrix} \quad (6.8)$$

In a similar fashion, we can compute theoretical and experimental \mathbf{C} -matrices, as described in Equation 2.14, and we find, for the same values as used for the \mathbf{D} -matrices:

$$\mathbf{C}_{theo} = \begin{bmatrix} 2.75 \times 10^{-3} & 2.61 \times 10^{-3} \\ 5.53 \times 10^{-2} & 5.53 \times 10^{-2} \end{bmatrix} \mu m/kPa \quad (6.9)$$

$$\mathbf{C}_{exp} = \begin{bmatrix} 3.48 \times 10^{-3} & 1.91 \times 10^{-3} \\ 6.37 \times 10^{-2} & 6.39 \times 10^{-2} \end{bmatrix} \mu m/kPa \quad (6.10)$$

And, dividing (6.9) element-wise by (6.10):

$$\begin{bmatrix} 0.8 & 1.4 \\ 0.9 & 0.9 \end{bmatrix} \quad (6.11)$$

Note that, due to the almost-singular nature of the matrices, as discussed in Section 2.4, the apparent factor 10 discrepancy in (6.8) is not reflected as a factor 0.1 in (6.11). It should be pointed out that the tests performed were tests aimed at measuring *compressibility*, and not *inverse compressibility* - i.e. a load was applied, and a deflection was measured. For

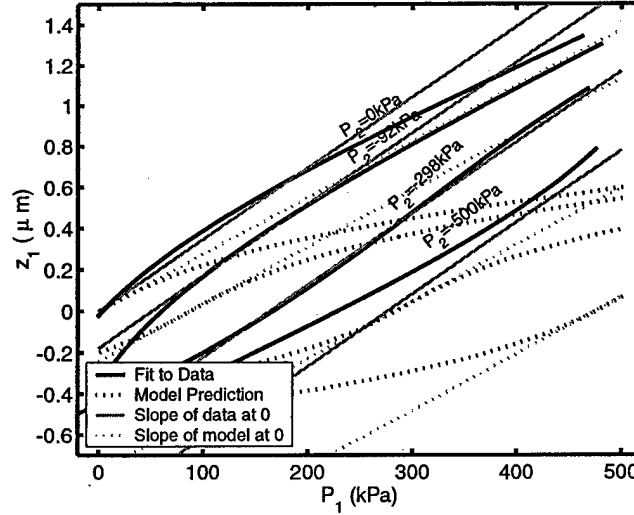


Figure 6.13: Large piston results with the linearization about 0 added. HAC Device 3.

measuring the inverse compressibility, or, in the case of a simple spring, the stiffness, we would have had to impose a displacement, and measure the resulting load.

Therefore, in Figures 6.8 and 6.9 we see no sign of a factor 10 discrepancy. Figures 6.13 and 6.14 are repeats of Figures 6.8 and 6.9, but with the linearizations given by (6.9) and (6.10) added to them.

A discrepancy that is apparent in both the theoretical and experimental data is that $|D_{11}|$ is not significantly greater than $|D_{21}|$ in (6.6) and (6.7). Recall from Equation 2.10 that:

$$D_{11} = \beta_c \gamma_1 + \psi_1$$

$$D_{21} = -\beta_c \gamma_1$$

The discrepancy in the *theoretical* case is readily explained by the fact that a chosen value of $z_2 = \pm 1 \mu m$ already adds some nonlinearity to the system, combined with the fact that, in the theoretical case, $D_{11} = O(10^3)$, whereas $\psi_1 = O(10)$. The effect of ψ_1 is almost negligible and easily masked by numerical artefacts. It has been verified that, for smaller values of z_2 , the condition of $|D_{11}| > |D_{21}|$ is obtained. In (6.7), we do have that $|D_{11}| > |D_{21}|$, but the difference, approximately $2 kPa/\mu m$, is less than the measured value of $\psi_1 = 15.2 kPa/\mu m$.

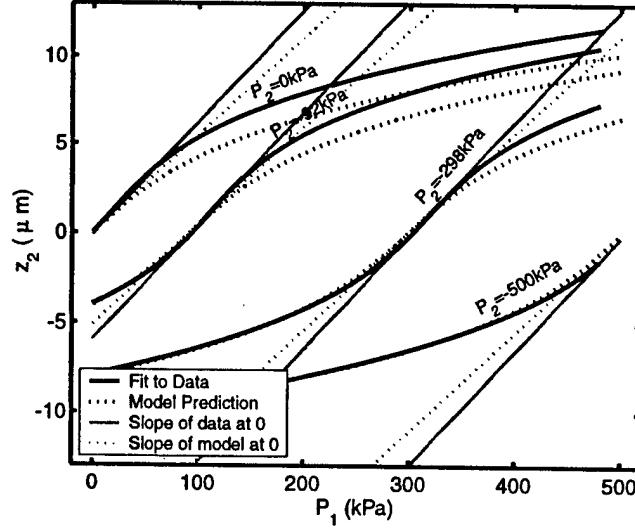


Figure 6.14: Small piston results with the linearization about 0 added. HAC Device 3.

This discrepancy can probably be attributed to an error in the measurements taken.

One more calculation remains to evaluate the quality of the data presented in this section. We can subtract the appropriate values for ψ_1 and ψ_2 from the theoretical and experimental \mathbf{D} -matrices, to get a matrix of the form:

$$\tilde{\mathbf{D}} = \begin{bmatrix} \beta_c \gamma_1 & -\beta_c \gamma_2 \\ -\beta_c \gamma_1 & \beta_c \gamma_2 \end{bmatrix} \quad (6.12)$$

In the theoretical and experimental cases we then obtain:

$$\tilde{\mathbf{D}}_{theo} = \begin{bmatrix} 7.37 \times 10^3 & -3.49 \times 10^2 \\ -7.38 \times 10^3 & 3.49 \times 10^2 \end{bmatrix} \quad (6.13)$$

$$\tilde{\mathbf{D}}_{exp} = \begin{bmatrix} 6.19 \times 10^2 & -1.90 \times 10^1 \\ -6.32 \times 10^2 & 1.92 \times 10^1 \end{bmatrix} \quad (6.14)$$

Element-wise division yields:

$$\begin{bmatrix} 11.9 & 18.4 \\ 11.7 & 18.2 \end{bmatrix} \quad (6.15)$$

We note that, in reality, (6.15) should have all entries be identical. We recall that in Equation 6.12:

$$\gamma_1 = \frac{A_{1,eff}}{V_c}$$

$$\gamma_2 = \frac{A_{2,eff}}{V_c}$$

Therefore, γ_1 and γ_2 depend solely on geometry, which should be very similar from model to experiment. Therefore, one should expect to see all four entries in (6.15) reflect the ratio of:

$$\frac{\beta_{c,theo}}{\beta_{c,exp}}$$

The discrepancy in (6.15) is attributed to measurement errors. Any other variation would not violate the physics of the system.

6.3.4 Tests performed, and correlation with nonlinear models: HAC Device 4

Both hydraulic amplifiers in HAC Device 4 were tested. The results of the two devices match closely, and only one set is discussed here. Figures 6.15 and 6.16 show the deflections of the large piston and the small piston for P_1 varying from 0 to 200kPa and for P_2 having values 0, 53, 105, 153, 206 and 253kPa. Again, the data is displayed along with cubic fits to the data.

Figures 6.17 and 6.18 now show the model results plotted over the experimental results. As was the case for HAC Device 3, the large piston deflects significantly more than model predictions, indicating a reduced stiffness of the HAC.

6.3.5 Amplification ratio and amplification sensitivity: HAC Device 4

Using Equations 6.1 and 6.2, we proceed to compute the amplification ratio and amplification sensitivity for HAC Device 4. The results are shown in Figures 6.19 and 6.20. The amplification ratio is higher than predicted for $P_2 = 0kPa$. This could probably attributed to a measurement irregularity. Also, in this case, the amplification sensitivity is higher for the experimental case. This is due to a smaller incremental change in z_1 for the measured values.

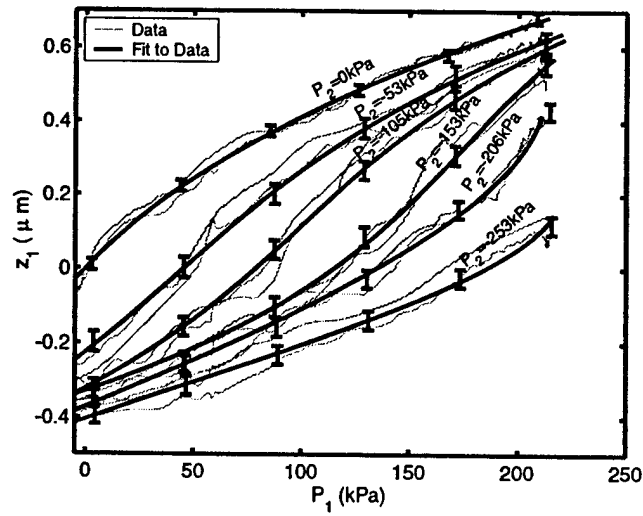


Figure 6.15: Hydraulic amplification data for the large piston of HAC Device 4.

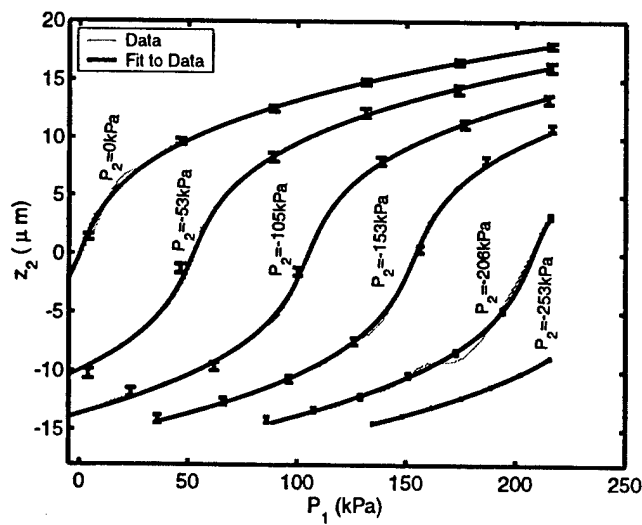


Figure 6.16: Hydraulic amplification data for the small piston of HAC Device 4.

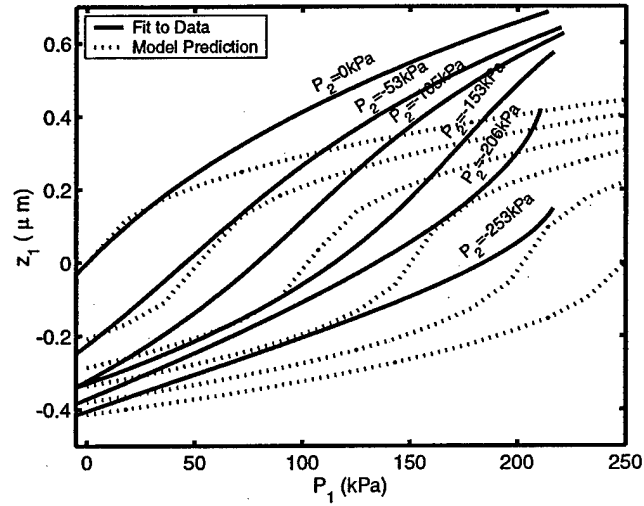


Figure 6.17: Adding model data to Figure 6.15. HAC Device 4.

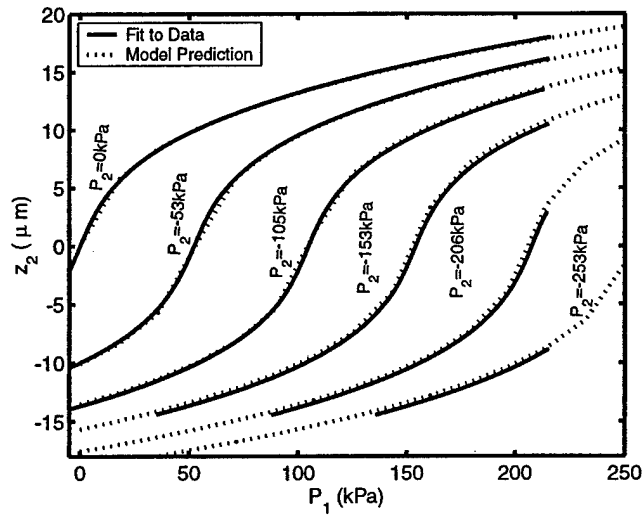


Figure 6.18: Adding model data to Figure 6.16. HAC Device 4. The good correlation is attributed to the fact that the large piston sees a very small ΔP .

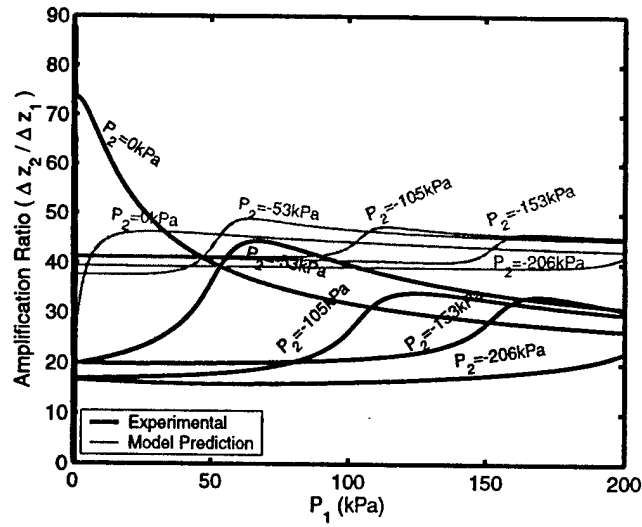


Figure 6.19: Amplification ratios for the tests performed. HAC Device 4.

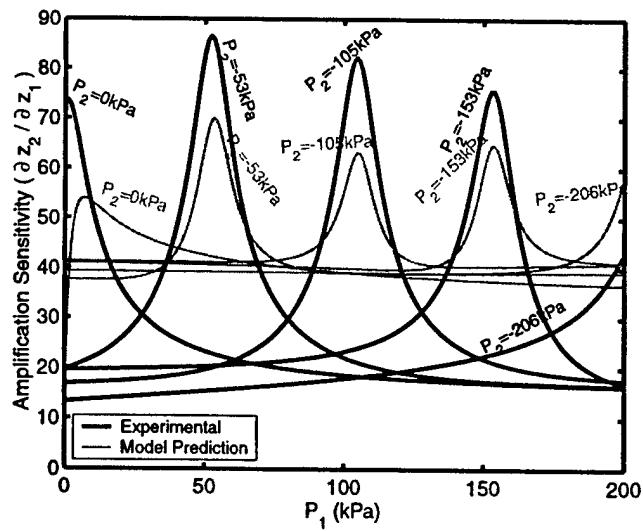


Figure 6.20: Amplification sensitivities for the tests performed. HAC Device 4.

| | |
|----------------|------|
| $\psi_{1,exp}$ | 11.3 |
| $\psi_{2,exp}$ | 3.1 |

Note: All units are in $kPa/\mu m$.

Table 6.6: Inverse compressibilities for the pistons of HAC Device 4.

6.3.6 Small deflection stiffness matrix comparisons: HAC Device 4

This section is a repeat of Section 6.3.3 for the hydraulic amplifier with a single small piston. No individual membrane characterizations were performed on this device. The results from HAC Devices 1 and 2 were used instead. The inverse compressibilities that were used, ψ_1 and ψ_2 , are given again in Table 6.6.

As was done in Section 6.3.3, we compute the inverse compressibility matrix. For $z_{2a} = 1\mu m$, $P_{2a} = 0kPa$ and $z_{2b} = -1\mu m$, $P_{2b} = -153kPa$, and finding the matching values for P_1 and z_1 in both the experimental and theoretical cases, the following \mathbf{D} -matrices were computed:

$$\mathbf{D}_{theo} = \begin{bmatrix} 4.18 \times 10^3 & -1.12 \times 10^2 \\ -4.18 \times 10^3 & 1.14 \times 10^2 \end{bmatrix} kPa/\mu m \quad (6.16)$$

$$\mathbf{D}_{exp} = \begin{bmatrix} 7.67 \times 10^2 & -8.20 \\ -7.71 \times 10^2 & 9.40 \end{bmatrix} kPa/\mu m \quad (6.17)$$

Dividing (6.16) element-wise by (6.17), we find:

$$\begin{bmatrix} 5.4 & 13.6 \\ 5.4 & 12.1 \end{bmatrix} \quad (6.18)$$

We note that there seems to be slightly better correlation between the predicted and measured inverse compressibilities when (6.18) is compared to (6.8). This could be due to an HAC that was better filled. In a similar fashion, we compute theoretical and experimental \mathbf{C} -matrices:

$$\mathbf{C}_{theo} = \begin{bmatrix} 1.47 \times 10^{-2} & 1.45 \times 10^{-2} \\ 5.41 \times 10^{-1} & 5.41 \times 10^{-1} \end{bmatrix} \mu m/kPa \quad (6.19)$$

$$\mathbf{C}_{exp} = \begin{bmatrix} 1.06 \times 10^{-2} & 9.23 \times 10^{-3} \\ 8.68 \times 10^{-1} & 8.63 \times 10^{-1} \end{bmatrix} \mu m/kPa \quad (6.20)$$

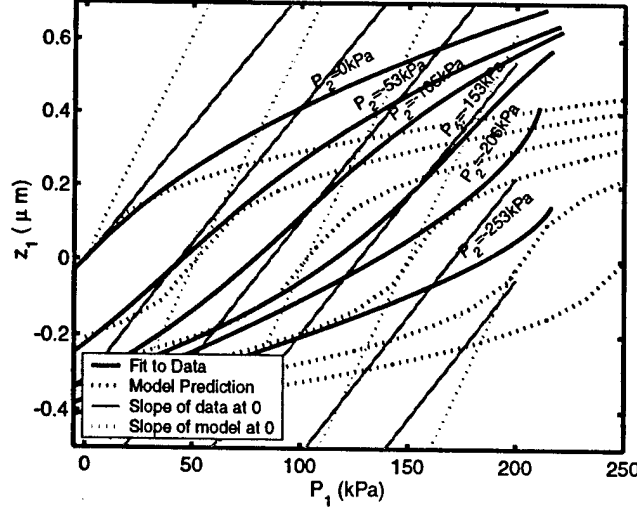


Figure 6.21: Large piston results with the linearization about 0 added. HAC Device 4.

And, dividing (6.19) element-wise by (6.20):

$$\begin{bmatrix} 1.4 & 1.6 \\ 0.6 & 0.6 \end{bmatrix} \quad (6.21)$$

Once again, the ratios seen in (6.21) are not the inverse of those seen in (6.18). Figures 6.21 and 6.22 are repeats of Figures 6.17 and 6.18 with the linearizations given by (6.19) and (6.20) added to them.

The discrepancy between $|D_{11}|$ and $|D_{21}|$ as discussed previously can once again be seen in (6.16) and (6.17). In (6.17), we now have that $|D_{11}| < |D_{21}|$. Measurement errors could cause such a discrepancy.

Subtracting the appropriate values for ψ_1 and ψ_2 from the theoretical and experimental D-matrices, we obtain:

$$\tilde{\mathbf{D}}_{theo} = \begin{bmatrix} 4.17 \times 10^3 & -1.12 \times 10^2 \\ -4.18 \times 10^3 & 1.12 \times 10^2 \end{bmatrix} \quad (6.22)$$

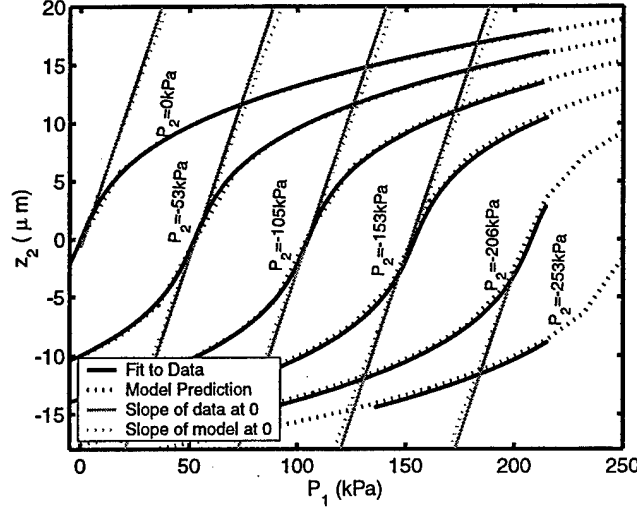


Figure 6.22: Small piston results with the linearization about 0 added. HAC Device 4.

$$\tilde{D}_{exp} = \begin{bmatrix} 7.56 \times 10^2 & -8.20 \times 10^1 \\ -7.71 \times 10^2 & 6.30 \times 10^1 \end{bmatrix} \quad (6.23)$$

And element-wise division yields:

$$\begin{bmatrix} 5.5 & 13.6 \\ 5.4 & 17.8 \end{bmatrix} \quad (6.24)$$

Once again, as was the case in (6.15), the fact that all entries in (6.24) are not equal is attributed to measurement errors. Note that $|D_{11,theo}| < |D_{21,theo}|$ because z_2 was chosen to be relatively large. Choosing a smaller z_2 will yield the correct result. For these experiments however, it was decided not to use a z_2 that is too small, causing the analyses to be overly sensitive to possible measurement errors.

In summary, two static hydraulic amplifiers with different theoretical amplification ratios have been tested. The same trends have been seen in the tests of both HAC Device 3 and HAC Device 4, with the latter device, HAC Device 4, appearing to be the one that was better filled and sealed. Amplification ratios of up to 40:1 were observed, when ignoring the $P_2 = 0 \text{ kPa}$ result for HAC Device 4. In addition, amplification sensitivities of approximately 80:1 were obtained.

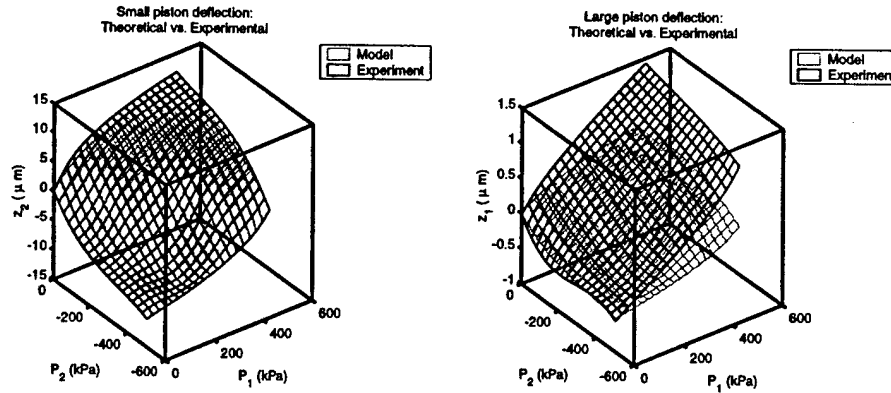


Figure 6.23: Small and large piston deflections as functions of both P_1 and P_2 . HAC Device 3.

6.3.7 Static hydraulic amplification as a two-variable function

For completeness, the attention of the reader is drawn to the fact that, as described in the section on the nonlinear case (Section 2.5), the deflections can be written as nonlinear functions of the two pressures, and vice-versa. Graphs from experimental and theoretical results can be constructed and, by using suitable interpolation, the theoretical and experimental responses can be visualized in a three-dimensional manner, as shown in Figure 6.23.

6.4 Dynamic hydraulic amplification tests

This section attempts to briefly demonstrate the dynamic capabilities of the hydraulic amplifiers developed in this work. The dynamic tests discussed here were performed on the HAC of a piezoelectrically driven active valve, as described in [19]¹. In these tests the large piston was actuated by three radially equispaced PZN-PT single crystal piezoelectric elements, instead of the pressure that was previously used. Furthermore, the HAC was not statically sealed, but rather dynamically using the technique described in Section 4.2.2. The dynamic hydraulic amplifier is depicted schematically in Figure 6.24.

¹In Table 6.1 this device is referred to as AV Device 1

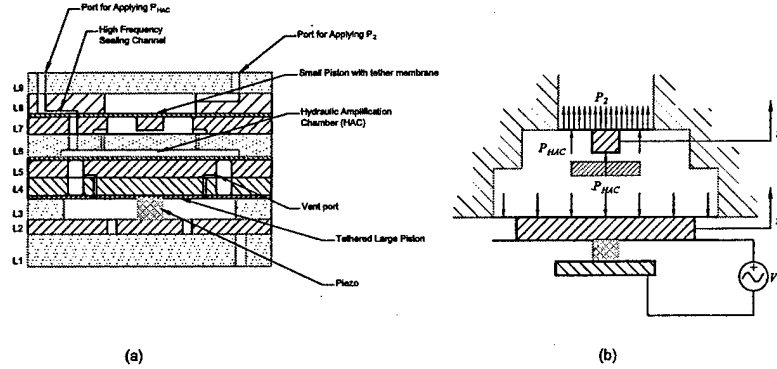


Figure 6.24: Two representations of the dynamic hydraulic amplification device: (a) A detailed cross section schematic view, and (b) A simplified functional schematic, with nomenclature to be used.

The device tested was one with a single small piston. The first test performed was a low amplitude frequency sweep to determine the bandwidth of the hydraulic amplifier. Figure 6.25 shows the results of this test. When no silicone oil is present on top of the small piston, the first resonance occurs at approximately $10kHz$. Adding oil introduces additional inertia, with a corresponding reduction in natural frequency to approximately $5kHz$. For a further discussion of this phenomenon, the reader is referred to [19].

In addition, quasi-static tests were performed at various voltage levels, at a frequency of $1kHz$. Figure 6.26 shows a typical time history of the small and large pistons for the case where $V_1 = 400V \pm 400V$, $P_{HAC} = P_2 = 500kPa$. Figure 6.27 shows the deflection versus different values for V_1 . The corresponding amplification ratio as a function of V_1 is depicted in Figure 6.28. In this case, the amplification ratio is defined as:

$$AR = \frac{z_{2,p-p}}{z_{1,p-p}} \quad (6.25)$$

Note the equivalence of Figure 6.27 with Figures 6.6 and 6.7, where a voltage takes the place of pressure actuation for the dynamic tests. Varying P_2 to obtain the same sets of curves as seen for the static case was not feasible, due to the fact that the dynamic seal used in the piezoelectric hydraulic amplifier would not allow for a quasi-steady pressure differential to be applied between P_{HAC} and P_2 without changing the equilibrium position of the small piston. Changing P_2 at sufficiently high frequency was not possible with the experimental equipment used.

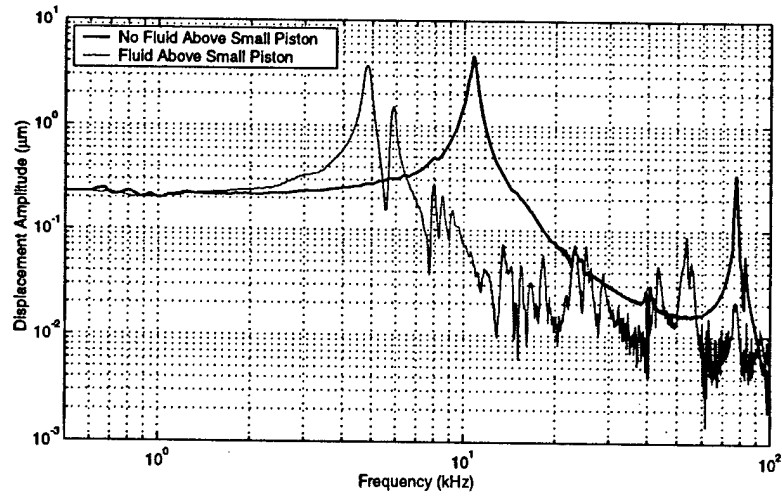


Figure 6.25: Frequency response of AV Device 1 with and without silicone oil on top of the small piston. $V_1 = 0V \pm 5V$, $P_{HAC} = P_2 = 500kPa$

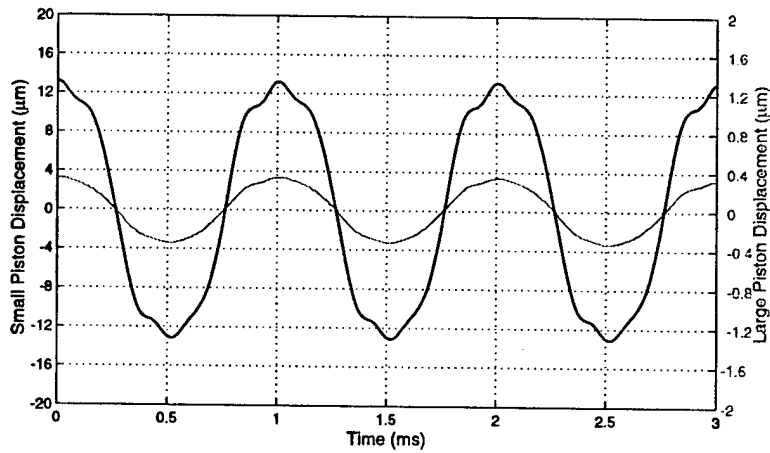
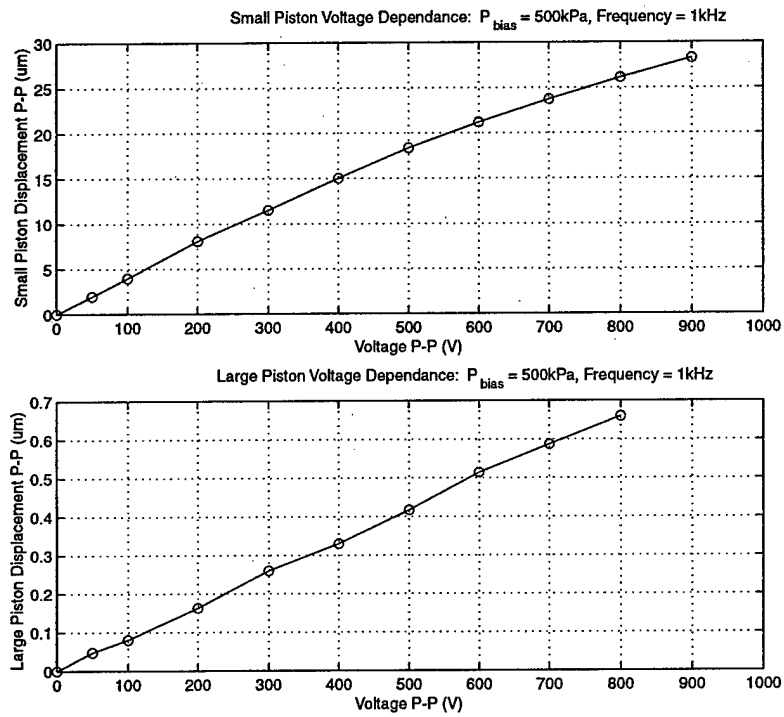
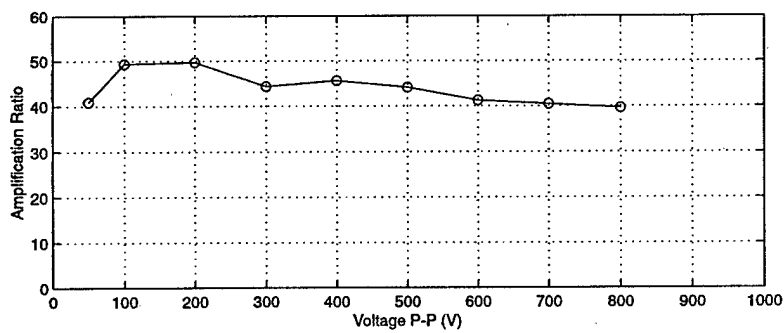


Figure 6.26: Time history of AV Device 1 with silicone oil on top of the small piston.

Figure 6.27: Deflection of the small and large pistons as a function of V_1 .Figure 6.28: Amplification ratio as a function of V_1 .

For a detailed discussion of these results, the reader is again referred to [19]. For the purposes of the argument presented in this document, it can be concluded that these dynamic tests indicate that the HAC has sufficient bandwidth for high frequency operation of microvalves and other micromanipulators. The added mass effect of the silicone oil on the natural frequency of the device shows that the effect of the system being driven by the hydraulic amplifier should be accounted for when designing a microscale hydraulic amplifier, as is the case for any actuator-load pair.

6.5 Summary of the test results

In this chapter we presented the following results:

- Pressure-deflection results for the three different types of tethered-membrane structures. It was shown that the measured results compared well with model predictions, when considering measurement errors and fabrication tolerances.
- Static hydraulic amplification results for two types of hydraulic amplifiers. The compressibility matrix coefficients, equivalent to a compliance matrix, were found to be close to those predicted by analytical models. See (6.11),(6.21). Further data analysis on the inverse compressibility matrices revealed possible measurement errors. Despite these errors, however, the data clearly indicates that a stiff hydraulic amplifier was produced.
- Dynamic hydraulic amplification results for a piezoelectrically driven hydraulic amplifier. These tests were performed to show that the hydraulic amplifier has sufficient bandwidth. A first natural frequency of approximately $10kHz$ was achieved, reducing to $5kHz$ when silicone oil was added on top of the small piston.

In conclusion these first test results on microfabricated hydraulic amplifiers prove that hydraulic amplification is a viable means of stroke enhancement for MEMS applications.

Conclusions and recommendations

7.1 Conclusions

In this work, a number of significant accomplishments have been made, and these are summarized as follows:

- Fabrication techniques for fabricating high-quality tethered membrane structures have been developed [30].
- Reliable die-level alignment anodic bonding techniques have been developed and employed with success in the assembly of not only hydraulic amplification devices, but also complete MHT devices, significantly reducing the risks associated with full-wafer processing of fragile experimental wafers.
- Reliable filling procedures have been developed for the bubble-free filling of hydraulic dead volumes through channels of cross-section $10\mu \times 10\mu m$ and $1000\mu m$ in length.
- Static sealing techniques for experimental devices have been developed and proven to be reliable in sealing HAC's with minimal seal extrusion and HAC pressure rise.
- Dynamic sealing techniques, based on labyrinth seal technology, were conceived and proven to be a valid means of sealing an HAC that will operate at frequencies higher than the cutoff frequency of the dynamic seal.
- A fluid testing system was developed to enable the successful testing of HAC devices.
- A reliable test jig for the device was developed as a subsystem of the fluid testing system.
- Building on all items mentioned above, hydraulic amplification devices were successfully designed, fabricated and tested to prove the concept of hydraulic amplification for MEMS. The devices have been shown to have amplification ratios and stiffnesses that

agree well with theoretical predictions. In addition, it was shown that a microscale hydraulic amplifier, properly designed, will have sufficient bandwidth for high-frequency micromechanical actuation.

7.2 Recommendations

It is recommended that the following issues be addressed in further studies in hydraulic amplification devices.

- The fillet radius control techniques for fabricating the SOI membrane structures need substantial improvement. A process with minimal human intervention is required.
- This work dealt primarily with stroke amplification. The reverse application, namely force amplification, could be useful for increasing the force generated by, e.g. electrostatic actuation techniques. An investigation into this matter may prove fruitful.
- In addition to piezoelectric actuation, hydraulic amplifiers lend themselves to be driven by other types of actuation. The usefulness of hydraulic amplification in an electrostatic or electromagnetic system is worth investigating.
- The effect of various aspects of the device geometry on the natural frequency of the devices needs to be investigated in more detail. This study would also include the effect of geometry on the fluidic behavior of the device.
- The filling and sealing procedures, although robust, are tedious. Additional work to further improve and understand the filling process, as well as better sealing techniques for commercial applications, are recommended.
- It is probably wise to state that the per unit cost of devices, influenced by the aforementioned items in this list, as well as some others, needs to be reduced significantly to make hydraulic amplification commercially viable for MEMS. This is said with the understanding that the devices presented in this work were fabricated solely for research purposes, with cost not being a concern.

7.3 Final remarks

In conclusion it can be stated that hydraulic amplification for use in MEMS can now be considered feasible. Although this work has addressed the investigation from a mostly experimental point of view on a select few devices, it is safe to assume that the techniques developed and knowledge gained here, especially with reference to membrane fabrication and fluid filling and sealing, will enable future hydraulic amplification devices to rely on these building blocks for their success.

References

- [1] B. Pascal. *Récit de Grande Expérience de l'Équilibre des Liquers*. A. Asher and Co., Berlin, 1893, reprinted from correspondence dated 1648.
- [2] H.D. Young. *University Physics - Extended Version with Modern Physics*. Addison Wesley Publishing Company, Reading, Massachusetts, USA, 8th edition, 1992.
- [3] N.W. Hagood *et al.* Development of micro-hydraulic transducer technology. *Proceedings ICAST '99*, October 11-13, 1999.
- [4] S. Pulitzer. Feasibility assessment and design of micro hydraulic solid-state transducers. Master's thesis, MIT, 1998.
- [5] P. Tang *et al.* Combined piezoelectric-hydraulic actuator based active vibration control for rotordynamic system. *Transactions of the ASME - Journal of Vibration and Acoustics*, 117:285-293, 1995.
- [6] J. Garcia-Bonito *et al.* A novel high-displacement piezoelectric actuator for active vibration control. *Smart Materials and Structures*, 7:31-42, 1998.
- [7] V. Ferrari *et al.* Development and application of mass sensors based on flexural resonances in alumina beams. *IEEE Trans. on Ultrasonics, Ferroelectrics and Frequency Control*, 43(4):601-608, 1996.
- [8] S.S. Lee and R. M. White. Self-excited piezoelectric cantilever oscillators. *Proc. of the 8th International Conference on Solid-State Sensors and Actuators, and Eurosensors IX, Stockholm, Sweden*, pages 417-420, 1995.
- [9] Luginbuhl *et al.* Piezoelectric cantilever beams actuated by pzt sol-gel thin film. *Proc. of the 8th International Conference on Solid-State Sensors and Actuators, and Eurosensors IX, Stockholm, Sweden*, pages 413-416, 1995.
- [10] M.S. Rogers *et al.* A new class of high-force, low voltage, compliant actuation systems. *Proceedings of the 2000 Solid State Sensor and Actuator Workshop, Hilton Head*, pages 210-213, 2000.
- [11] E.F. Prechtel and S.R. Hall. Design of a high efficiency, large stroke, electromechanical actuator. *Smart materials and structures*, 8(1):13-30, 1999.
- [12] X.-P.S. Su and H.S. Yang. Design of compliant microleverage mechanisms. *Sensors and Actuators A*, 87:146-156, 2001.

- [13] H.T.G. Van Lintel *et al.* A piezoelectric micropump based on micromachining of silicon. *Sensors and Actuators*, 15:153–167, 1988.
- [14] M. Esashi *et al.* Normally closed microvalve and micropump fabricated on a silicon wafer. *Sensors and Actuators*, 20:163–169, 1989.
- [15] H.Q. Li *et al.* A high frequency high flow rate piezoelectrically driven MEMS micropump. *Proceedings of the 2000 Solid State Sensor and Actuator Workshop, Hilton Head*, pages 69–72, 2000.
- [16] S. Zeng *et al.* Fabrication and characterization of electrokinetic micropumps. *Proceedings of the 2000 Inter Society Conference on Thermal Phenomena, IEEE*, pages 31–36, 2000.
- [17] J.S. Fitch *et al.* Pressure-based mass-flow control using thermopneumatically-actuated microvalves. *Proceedings of the 1998 Solid State Sensor and Actuator Workshop, Hilton Head*, pages 162–165, 1998.
- [18] P. Gravesen *et al.* Microfluidics - a review. *Journal of Micromechanics and Microengineering*, 3(4):168–182, 1993.
- [19] D.C. Roberts. *Design, modeling, fabrication and testing of a piezoelectric microvalve for high pressure, high frequency hydraulic applications*. PhD thesis, MIT, 2002.
- [20] M.J. Zdeblick *et al.* A microminiature fluidic amplifier. *Sensors and Actuators*, 15:427–433, 1988.
- [21] J. Vollmer *et al.* Bistable fluidic elements in LIGA technique for flow control in fluidic microactuators. *Sensors and Actuators A*, 43:330–334, 1994.
- [22] C.-C. Lin *et al.* Fabrication and characterization of a micro turbine/bearing rig. *Proceedings MEMS '99, IEEE*, pages 529–533, 1999.
- [23] P.C. Sen. *Principles of electric machines and power electronics*. John Wiley and Sons, New York, 2nd edition, 1997.
- [24] O. Yaglioglu. Modeling and design considerations for a microhydraulic piezoelectric power generator. Master's thesis, MIT, 2002.
- [25] Y.-H. Su *et al.* Large deflection analysis of a pre-stressed annular plate with a rigid boss under axisymmetric loading. *Journal of Micromechanics and Microengineering*, 11:645–653, 2001.
- [26] J.A. Carretero. Personal communication, 1999–2001.
- [27] S. Timoshenko and S. Woinowski-Krieger. *Theory of plates and shells*. McGraw-Hill, New York, 2nd edition, 1959.
- [28] R.L. Burden and J.D. Faires. *Numerical Analysis*. Brooks/Cole, Pacific Grove, California, USA, 6th edition, 1997.

-
- [29] K.T. Turner. An evaluation of critical issues for microhydraulic transducers: Silicon wafer bonding, strength of silicon on insulator membranes and gold-tin solder bonding. Master's thesis, MIT, 2001.
- [30] H.Q. Li. Personal communication, 1999-2001.
- [31] N. Maluf. *An Introduction to Microelectromechanical Systems Engineering*. Artech House, Boston, 1st edition, 2000.
- [32] K.-S. Chen, A.A. Ayon, and S.M. Spearing. Controlling and testing the fracture strength of silicon on the mesoscale. *J. Am. Ceram. Soc.*, 83(6):1476-84, 2000.
- [33] M.A. Schmidt. Wafer-to-wafer bonding for microstructure formation. *Proc. of the IEEE*, 86(8):1575-1585, 1998.
- [34] M. Despont *et al.* Fabrication of a silicon-pyrex-silicon stack by a.c. anodic bonding. *Sensors and Actuators A*, 55:219-224, 1996.
- [35] M.M. Visser. Chemical analysis of bonded and debonded silicon-glass interfaces. *J. Micromech. Microeng.*, 11(5):N1-N6, 2001. Technical Note.
- [36] R. Mlcak. Boston MicroSystems, Woburn, MA, Personal communication, 1999-2001.
- [37] Dow Corning. *Compressibility at High Pressures of Various Dow Corning Silicone Fluids, as adapted from BridgeMan, P.W., Proc. Acad. Arts Sci., Vol. 77, No. 4, pp115-146, February 1949*. Midland, Michigan, U.S.A, March 1962.
- [38] Dow Corning. *Data provided as published in Journal of Chemical and Engineering Data, Vol31, No.3 1986*. Midland, Michigan, U.S.A, 1986.
- [39] S.D. Senturia. *Microsystem Design*. Kluwer Academic Publishers, Boston, 1st edition, 2001.
- [40] E.S. Stockham. Personal communication, 2000-2001.
- [41] A.H. Nayfeh and D.T. Mook. *Nonlinear Oscillations*. John Wiley and Sons, Inc., New York, USA, 1st edition, 1979.
- [42] Swagelok. *General catalog*. Solon, Ohio, U.S.A, 2000.
- [43] Concoa. *Regulators catalog*. Virginia Beach, Virginia, U.S.A, 2001.
- [44] Parker Hannifin Corporation, General Valve Division. <http://www.pneutronics.com/gv/>. <http://www.parker.com/>.

Appendix A

Material properties

The following material properties were used for performing calculations:

Silicon, single crystal, (100)

| Property name | Units | Quantity |
|-----------------------------|-------------------------|----------|
| Young's modulus (Effective) | <i>GPa</i> | 165 |
| Poisson's ratio (Effective) | | 0.22 |
| Density | <i>kg/m³</i> | 2330 |
| Tensile strength | <i>GPa</i> | 1.0 |

Glass (*PyrexTM7740*)

| Property name | Units | Quantity |
|-----------------------------|-------------------------|----------|
| Young's modulus (Effective) | <i>GPa</i> | 62.8 |
| Poisson's ratio (Effective) | | 0.20 |
| Density | <i>kg/m³</i> | 2230 |
| Tensile strength | <i>MPa</i> | 7 |

Silicone oil - Hexamethyldisiloxane (*Dow Corning DC200 0.65cst*)

| Property name | Units | Quantity |
|-----------------------|------------|----------|
| Bulk Modulus | <i>GPa</i> | 0.6 |
| Specific gravity | | 0.760 |
| Viscosity | <i>cst</i> | 0.65 |
| Vapor pressure @ 25°C | <i>kPa</i> | 6.7 |

126 A Material properties

| | | |
|----------------------|----------|--------|
| Boiling point @ 1atm | <i>K</i> | 373.15 |
|----------------------|----------|--------|

Piezoelectric material - Single crystal PZT-PT (*TRS Ceramics*)

| Property name | Units | Quantity |
|-------------------------------------|-------------------------|----------|
| Young's modulus (Effective) | <i>GPa</i> | 6.76 |
| Piezoelectric constant (d_{33}) | <i>pC/N</i> | 1300 |
| Density | <i>kg/m³</i> | 8315 |

Appendix B

Equipment list

- (2×) Acopian Model 15EB100 15V AC-DC power supplies
- (1×) Bertan Associates Inc. Series 230 High Voltage Power Supply, 0-3kV, 0-5mA
- (1×) Branson Model 3510R-DTH ultrasonic cleaner
- (2×) Clear Air Products Model CAP412-5959A-1 Laminar flow workstations
- (3×) Concoa Model 4025301-580 regulators
- (2×) Concoa Model 4052001-000 regulators
- (1×) Dell XPS700r Desktop computer, Intel PentiumIII 700MHz Processor, 128MB RAM, SCSI HDD
- (1×) Dremel Model 395 Multipro tool
- (1×) Electronic Visions EV450 Aligner and AB1-Pv Bonder.
- (1×) GW Model GPS-3030D Lab Power Supply
- (1×) Hewlett Packard Model 33120A Function generator
- (2×) Industrial Test Equipment Model 112722-1 DC HV Power Supply
- (2×) Industrial Test Equipment Model 250A RF Amplifier
- (1×) MDC NW16 LN Foreline trap, KDFT-4075-2LN, P/N 434002
- (1×) MDC NW63 LN Foreline trap, LDFT-8250-2LN, P/N 434020
- (1×) Mitutoyo Digital Micrometer, Model 293-721-30, S/N 8084339
- (1×) MTI Model MTI-2000 Fotonic Sensor with fiber optic probes
- (2×) National Instruments BNC-2090 Connection units

- (2×) National Instruments PCI-6110 A/D in, D/A out Data acquisition boards
- (1×) Nikon Optiphot 88 microscope
- (1×) Olympus SZ60 Stereo microscope
- (1×) Omega Inc. Omegaette HH306 Thermometer
- (1×) Panasonic Model PV-7400 VCR unit
- (2×) Parker Hannifin Model 009-225-900 24VDC Fast acting solenoid valves
- (2×) PCB Piezotronics Model 112A22 dynamic pressure transducers
- (1×) PCB Piezotronics Series 481 signal conditioner
- (1×) Polytec PI OFV056 Scanning Head
- (1×) Polytec PI OFV056C Close-up attachment
- (1×) Polytec PI OFV3001 Vibrometer controller with 2nm resolution board
- (1×) Polytec PI OFV310 Focus controller
- (1×) Polytec PI PSV-Z-040-F Junction Box
- (7×) Red Bulls
- (1×) Sensotec FDD1BR.2D5A6A 0-5V 100psid pressure transducer, 0.1%
- (1×) Sensotec FDW1CJ.2D5A6A 0-5V 150psid pressure transducer, 0.1%
- (1×) Sensotec FPG1BR.2D5A6A 0-5V 100psig pressure transducer, 0.1%
- (2×) Sensotec FPG1CR.2D5A6A 0-5V 500psig pressure transducer, 0.1%
- (1×) Sony Model PVM-1350 Monitor
- (1×) Surface Technology Systems (STS) ICP Deep Reactive Ion Etch tool
- (15×) Swagelok SS-42S4 Ball valves
- (8×) Swagelok SS-4H Bellows valves
- (2×) Tektronix TDS210 Two-channel oscilloscopes
- (1×) T-M Vacuum Products Inc. Model SS806NS-14 Vacuum Oven

- (1×) Varian Convectorr vacuum gauge with Panelvac meter
- (1×) Welch vacuum pump Model 1392B-01 with Emerson Model S55NXMPF-6788
Electric motor

130 B Equipment list

Appendix C

Detail designs

C.1 Die-level anodic bonding jig

The detail design for the die-level anodic bonding jig, as shown in Figure 3.8, is given here. All parts not shown are standard off-the-shelf components. Some of the standard knurled thumbwheels required minor modifications for this application. The four posts on the corners of the jig are standard 6-32 threaded rod. The bushings shown in Figures C.5 and C.6 require a piece of seamless 304L stainless steel tubing to be cut to protect the ceramic parts against abrasion from the threaded rods.

The complexity of this design comes from the requirements of being able to make contact to multiple layers in a silicon-glass sandwich structure, from both the top and bottom of the stack. In addition, this jig has to withstand temperatures as high as 500°C , eliminating most, if not all, polymers for use as insulators. In addition, care had to be taken to allow for thermal expansion. Therefore, the main stainless steel part is "floating", both mechanically and electrically, between the four posts, but the potential of this part is effectively set by the threaded rod contact that is connected to the post attached to Spacer2, shown in Figure C.6. This post was chosen to be at ground potential and the main part is pressed against it by springs acting on the opposite ceramic bushes. The use of a positive-negative switchable power supply made device stacking and pre-bonding assembly easy. After assembly, the power supply simply had to be set to ensure that the glass is at a negative potential with respect to the silicon.

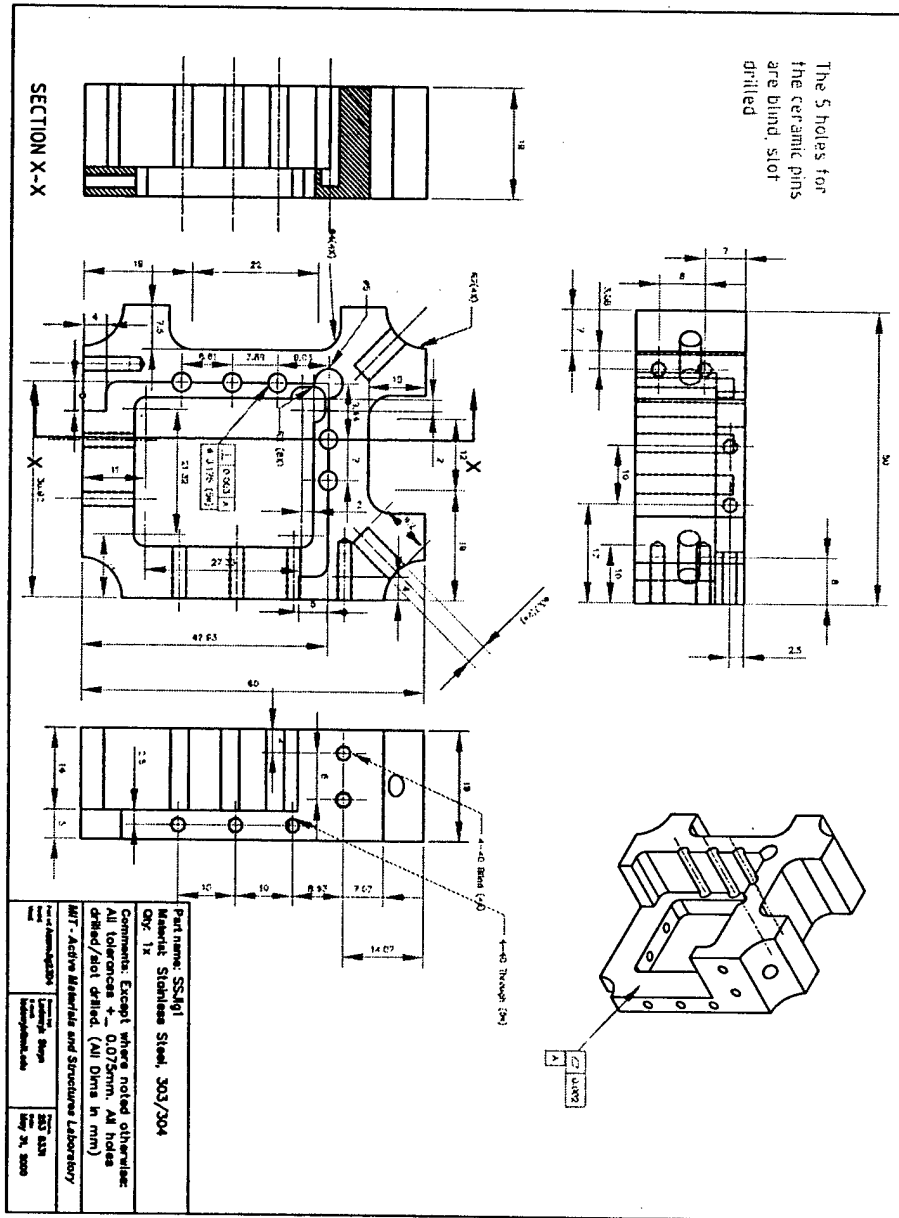


Figure C.1: Main stainless steel part

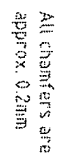


Figure C.2: Lower ceramic plate

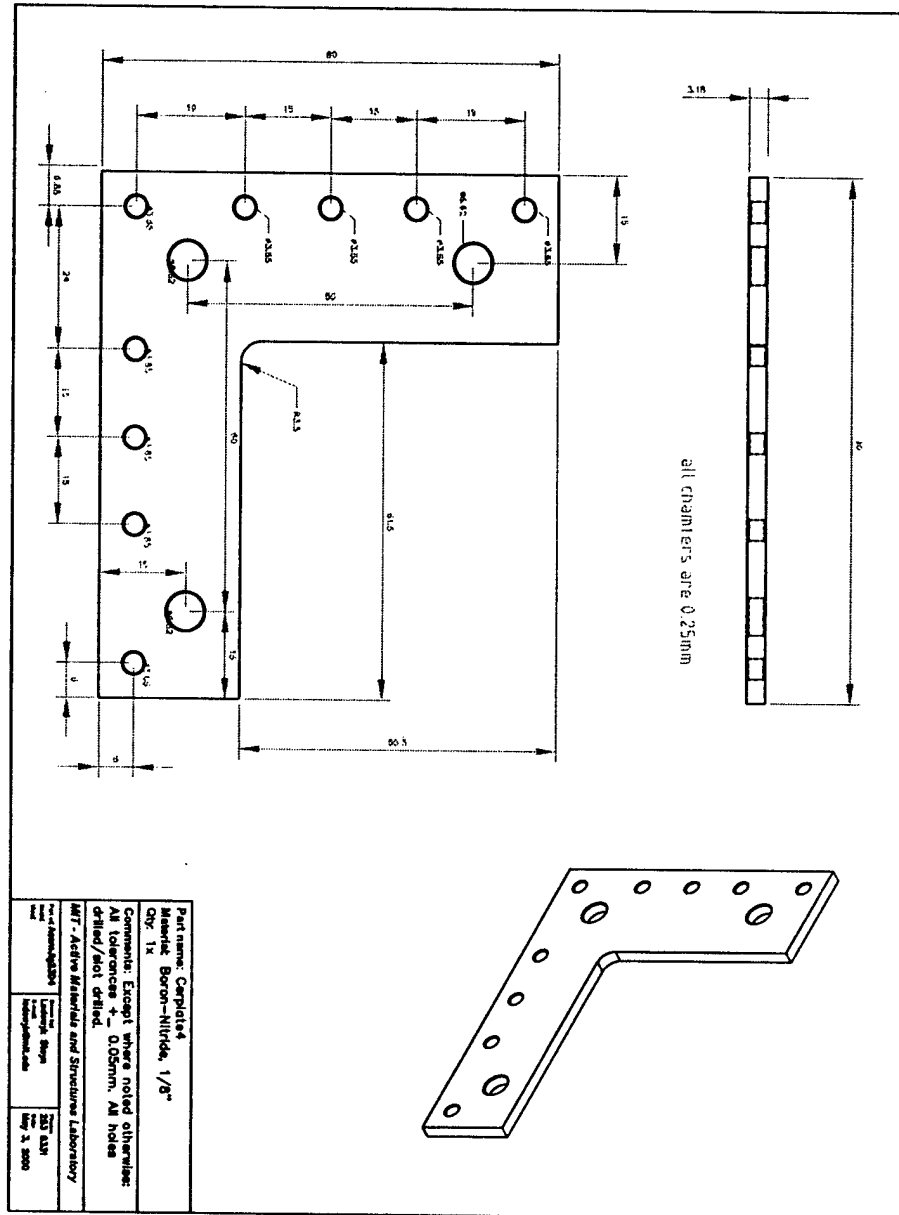


Figure C.3: Upper ceramic plate

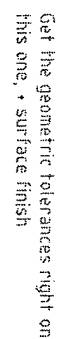


Figure C.4: Chip rest (ceramic)

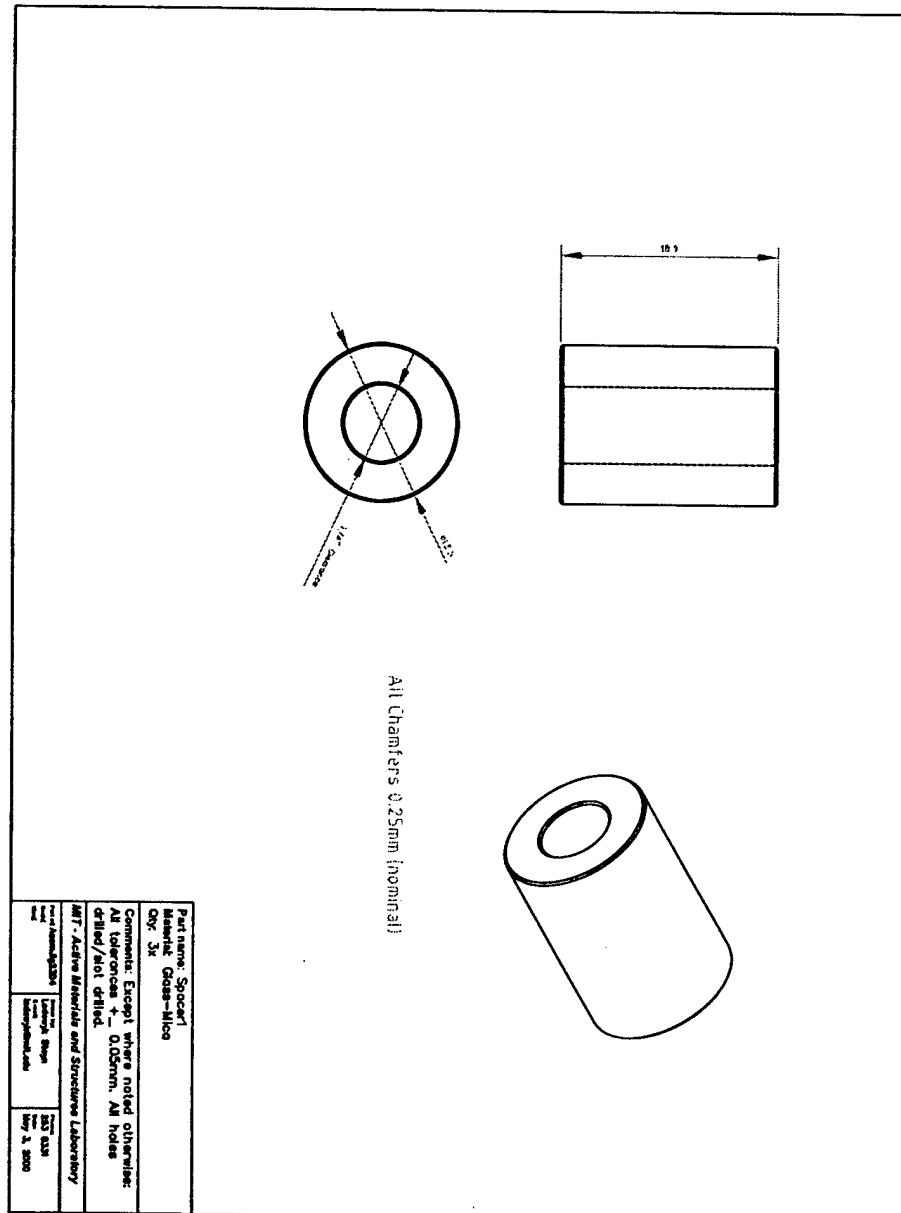


Figure C.5: Ceramic bushing

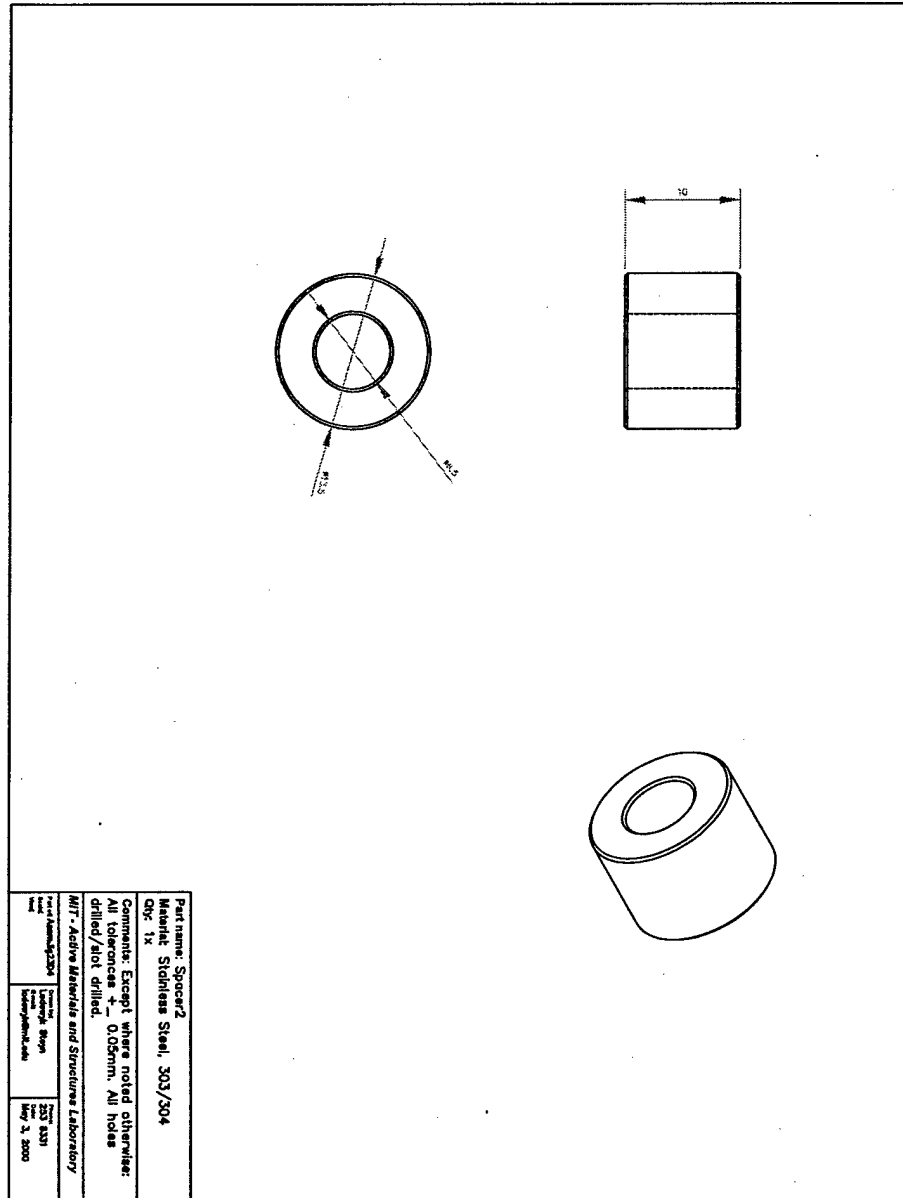


Figure C.6: Stainless steel bushing

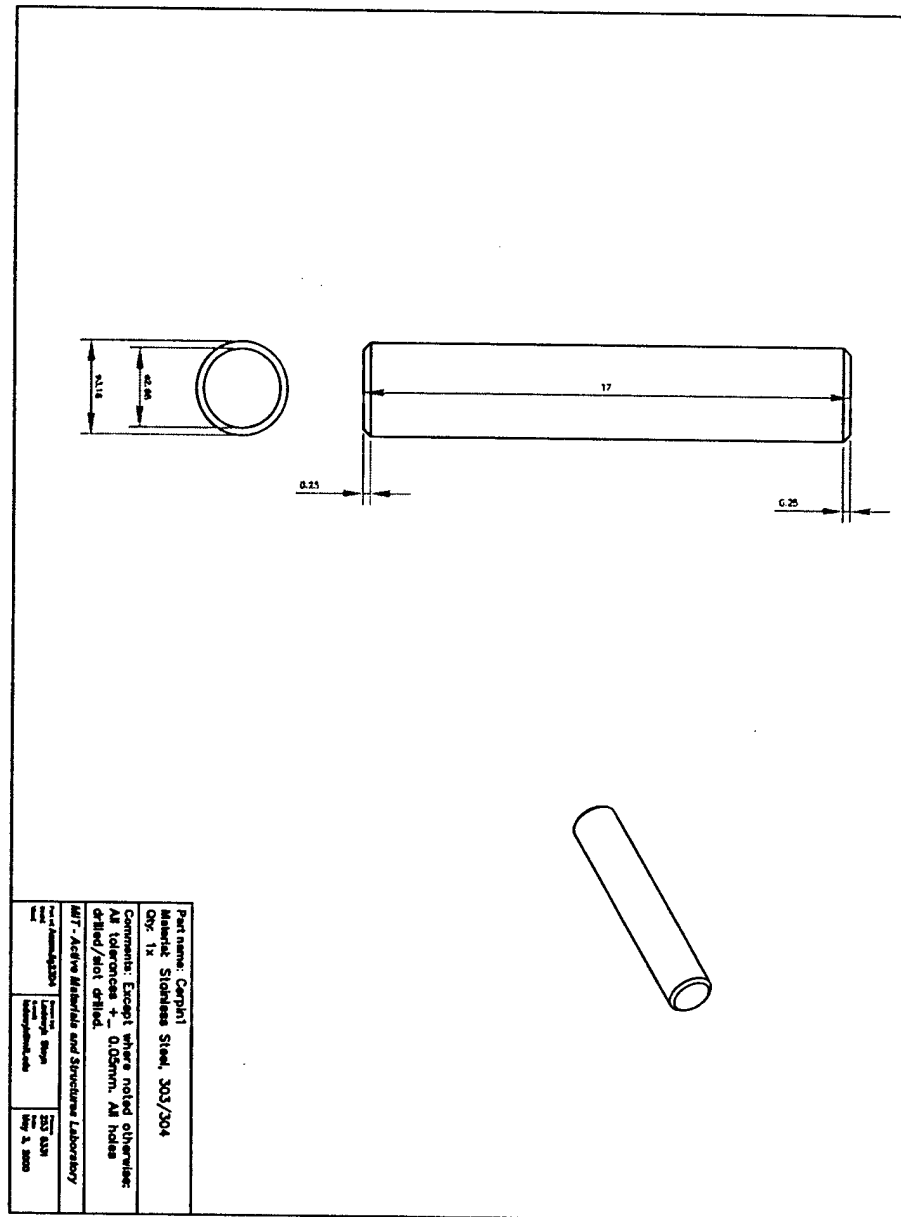


Figure C.7: Ceramic alignment pin

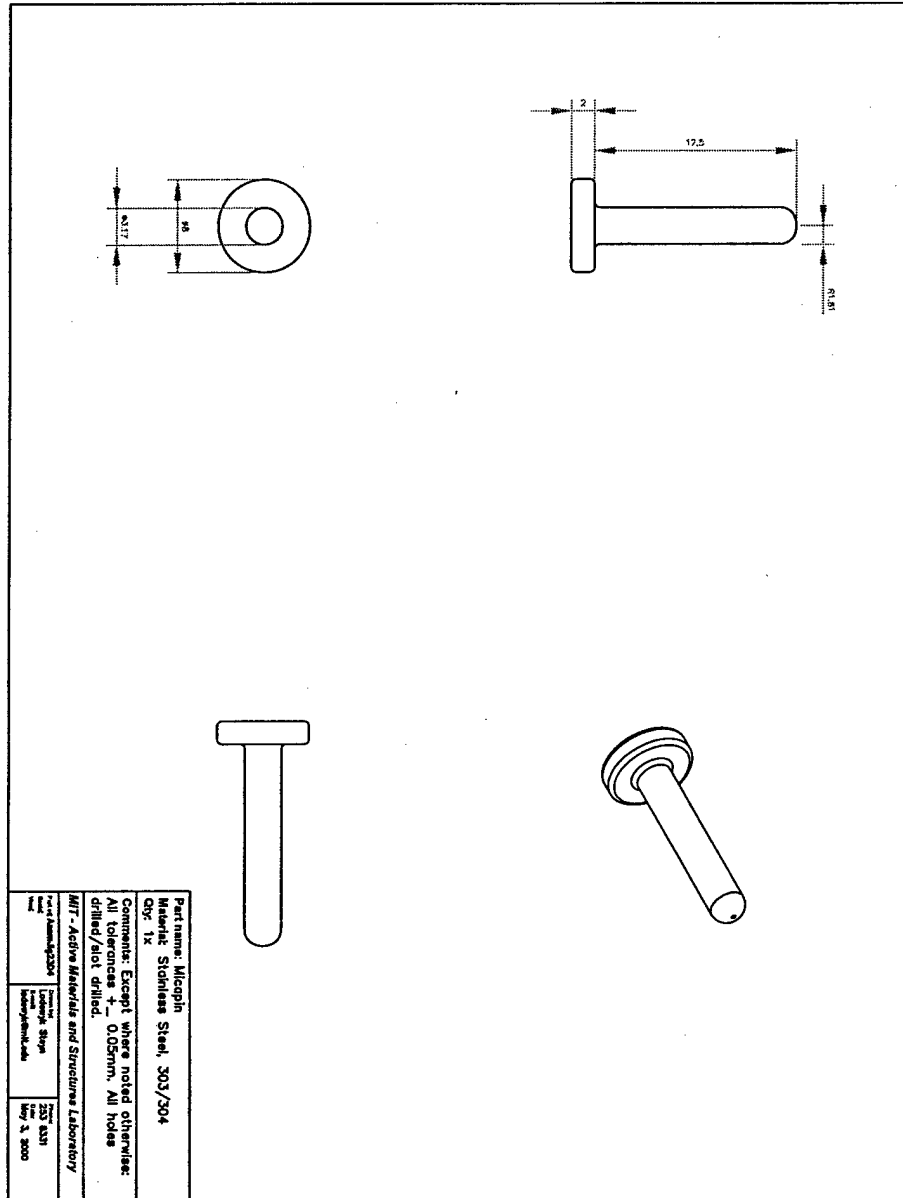


Figure C.8: Ceramic clamping pin

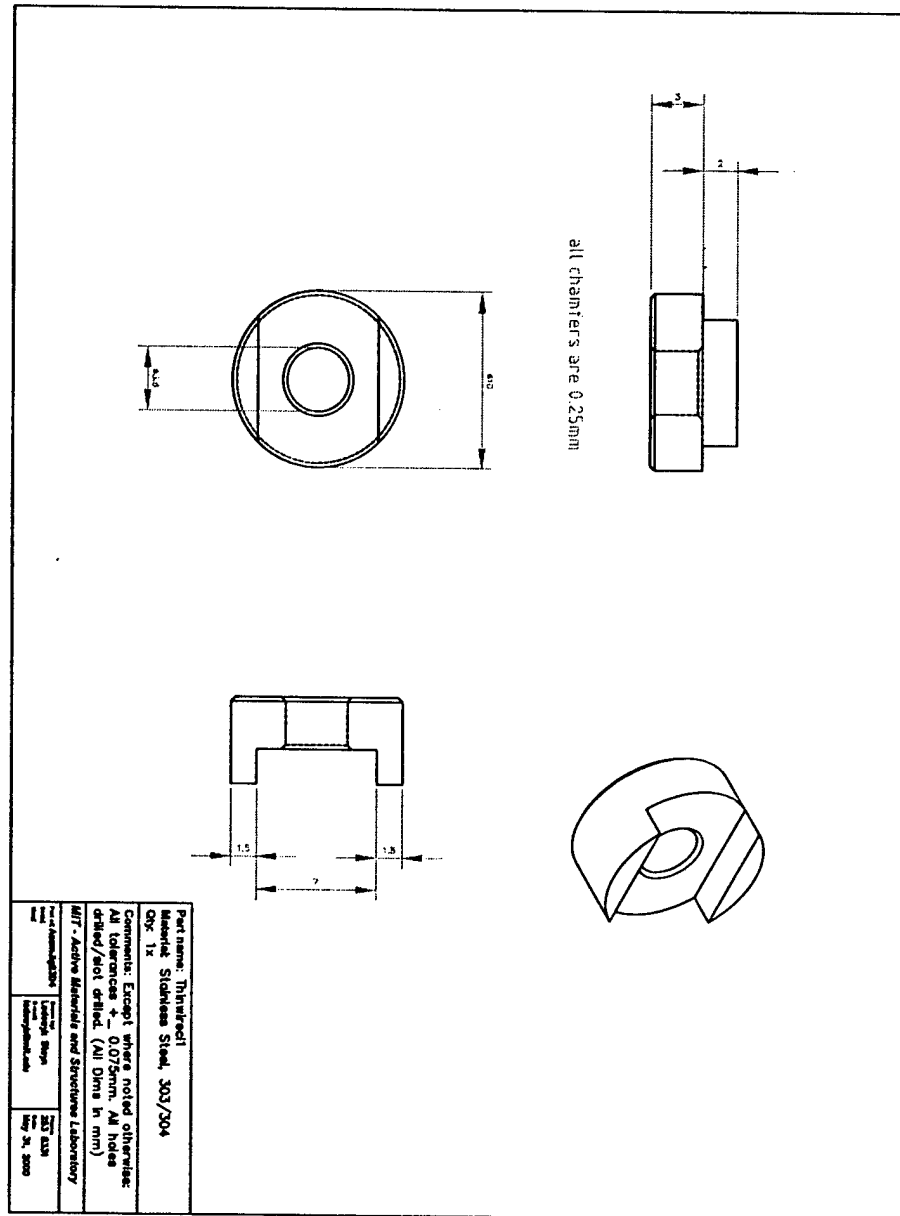


Figure C.9: Wire clamp lower part

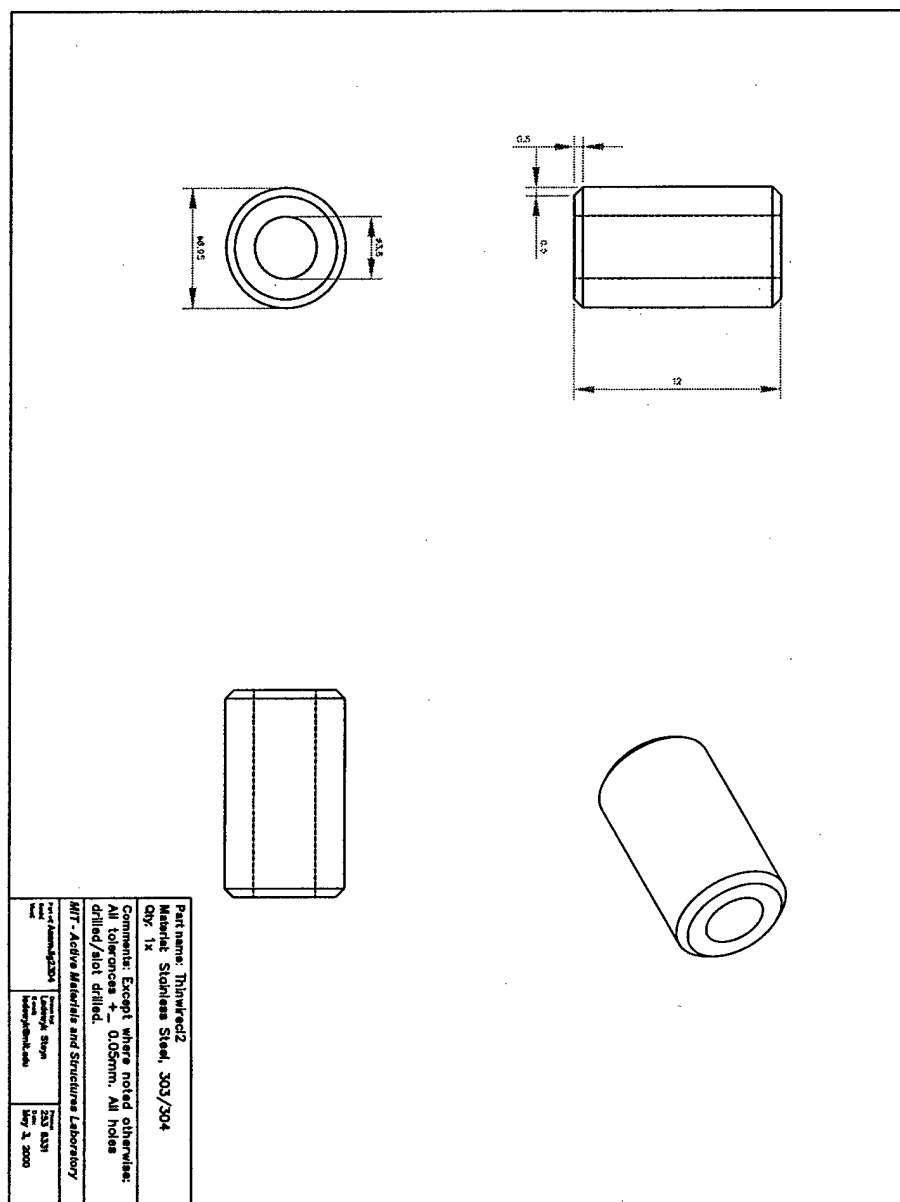


Figure C.10: Wire clamp upper part

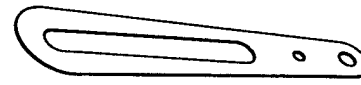


Figure C.11: Leaf spring

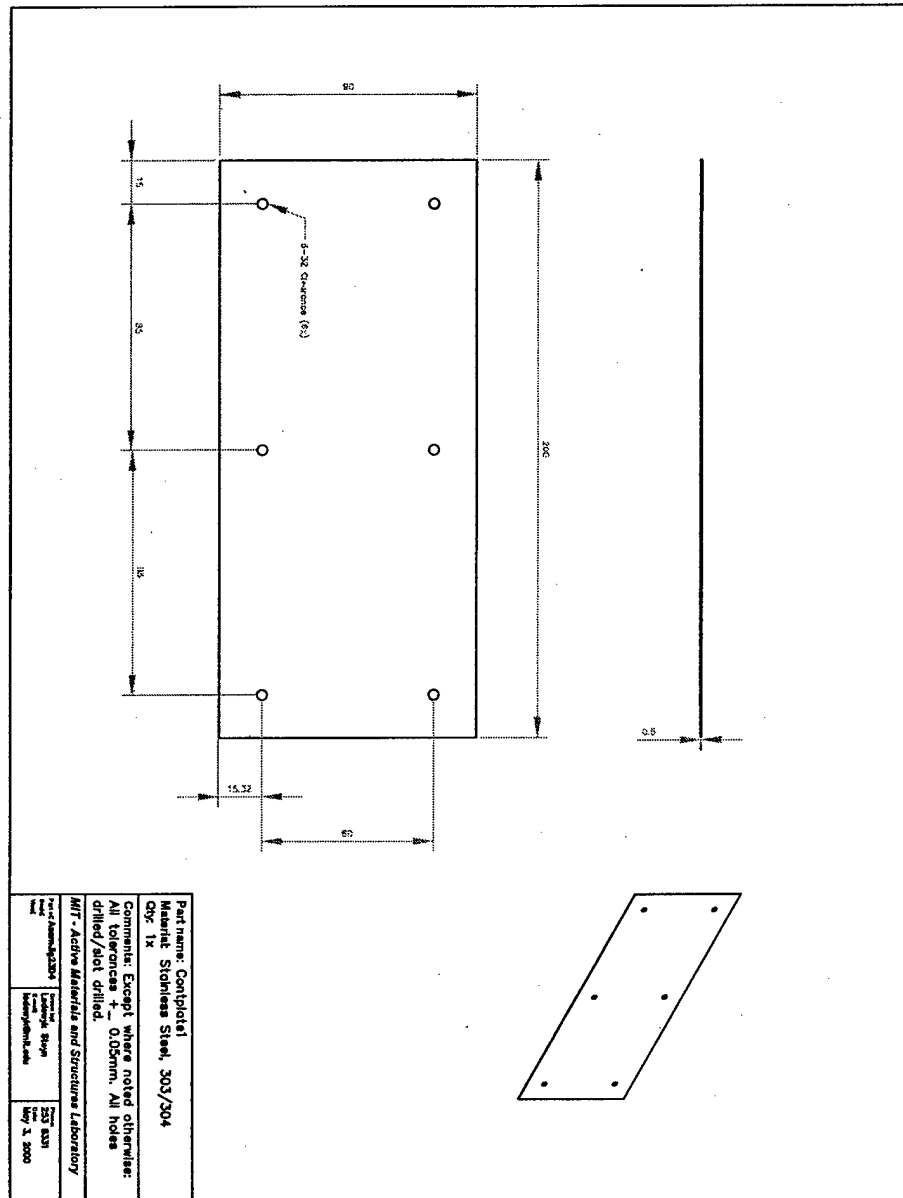


Figure C.12: Lower contact plate

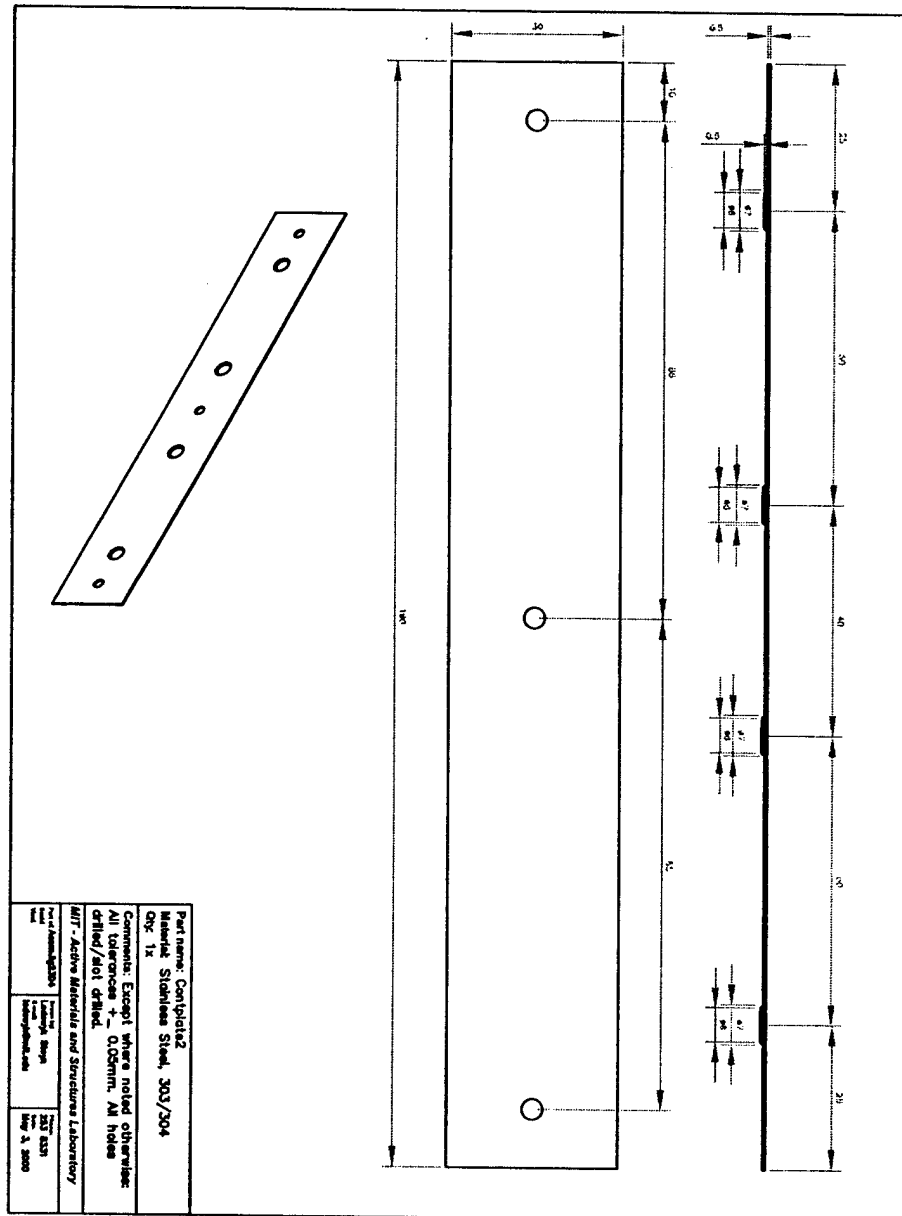


Figure C.13: Upper contact plate

C.2 Test jig for the hydraulic amplifier

This section includes the detail drawings of the test jig that was used to test the hydraulic amplifier. The material used was 6061 – T6 aluminum, and the jig was anodized black to prevent glare while performing optical measurements.

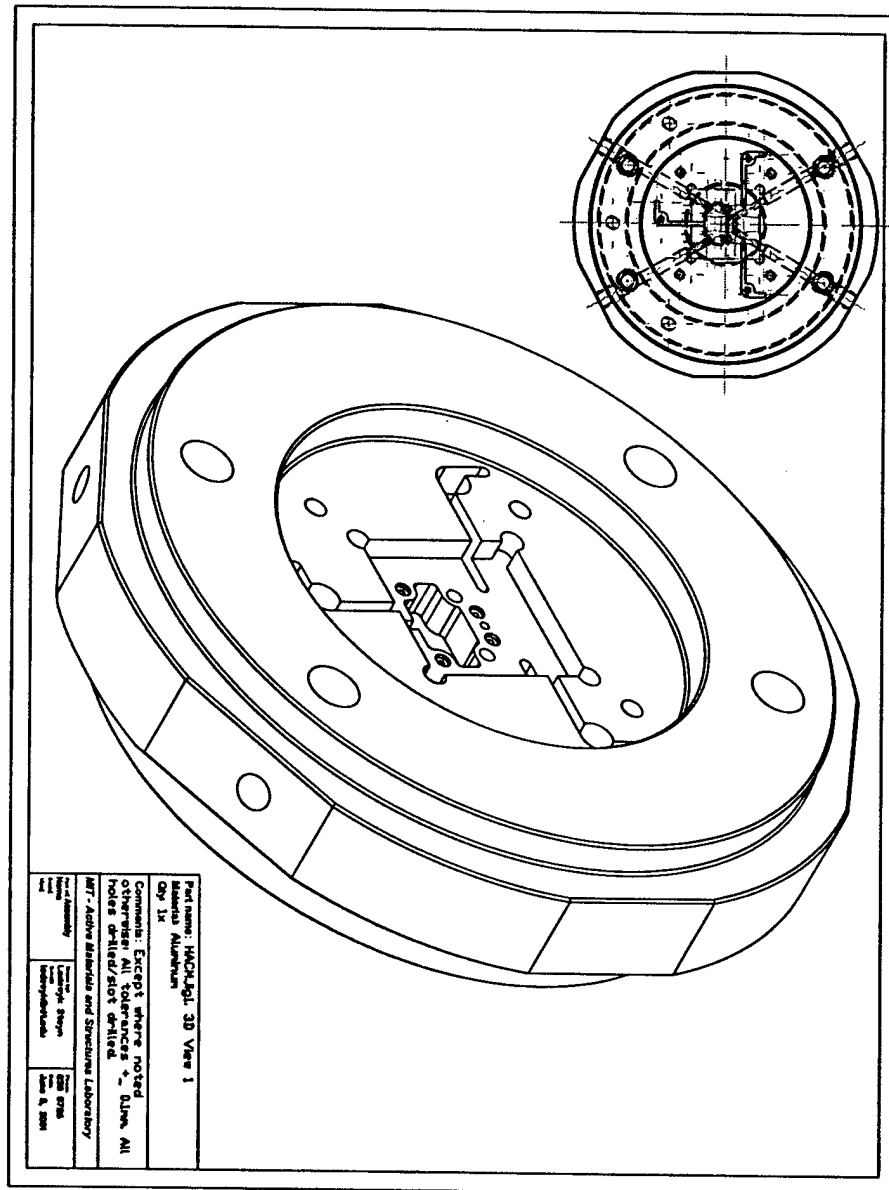


Figure C.14: 3D view 1

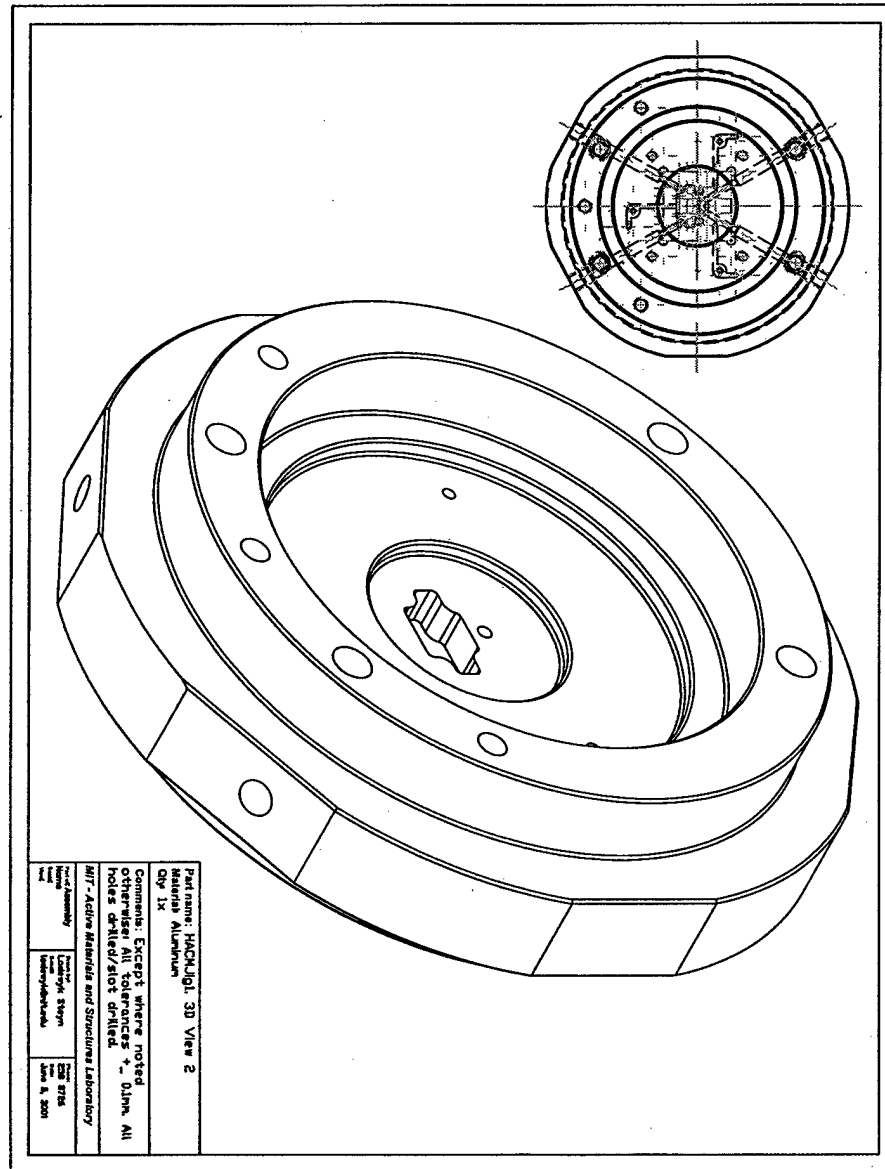


Figure C.15: 3D view 2

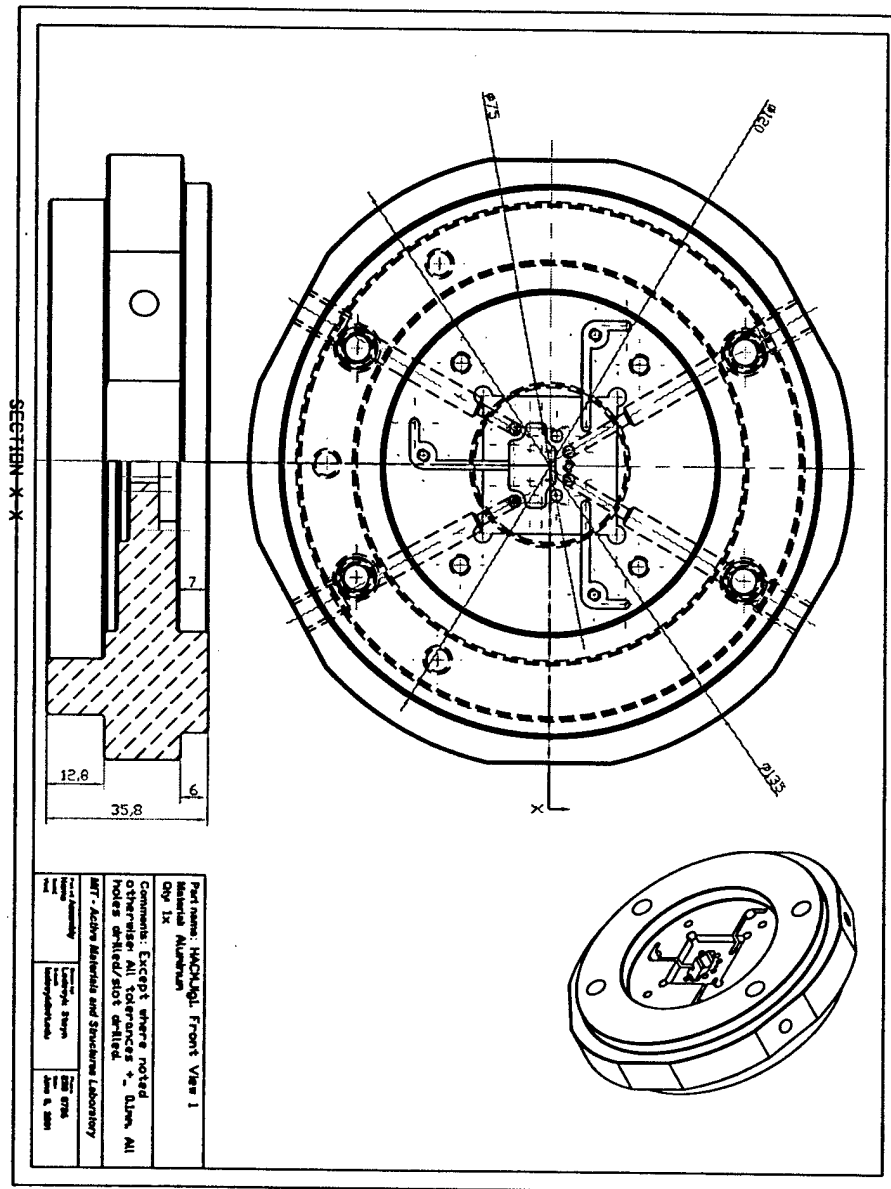


Figure C.16: Front view 1

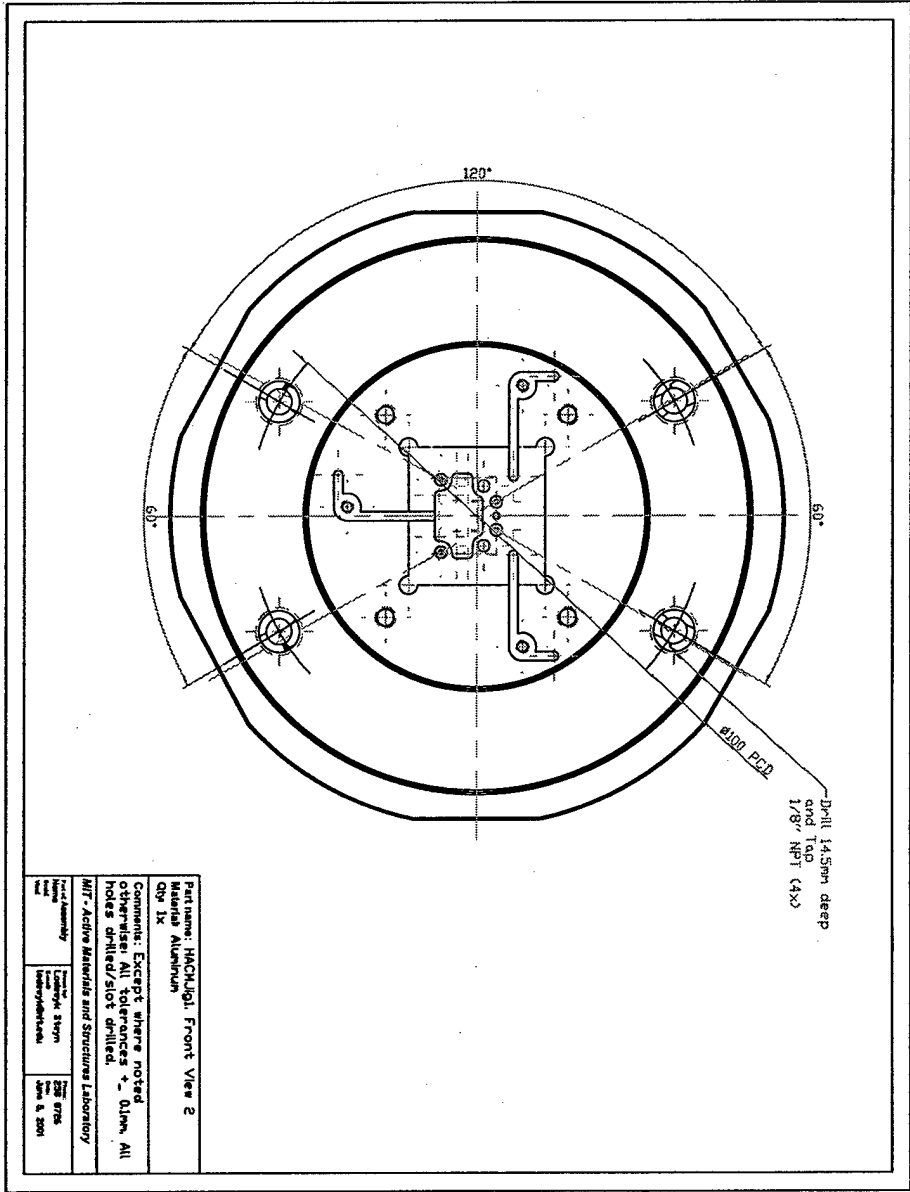


Figure C.17: Front view 2

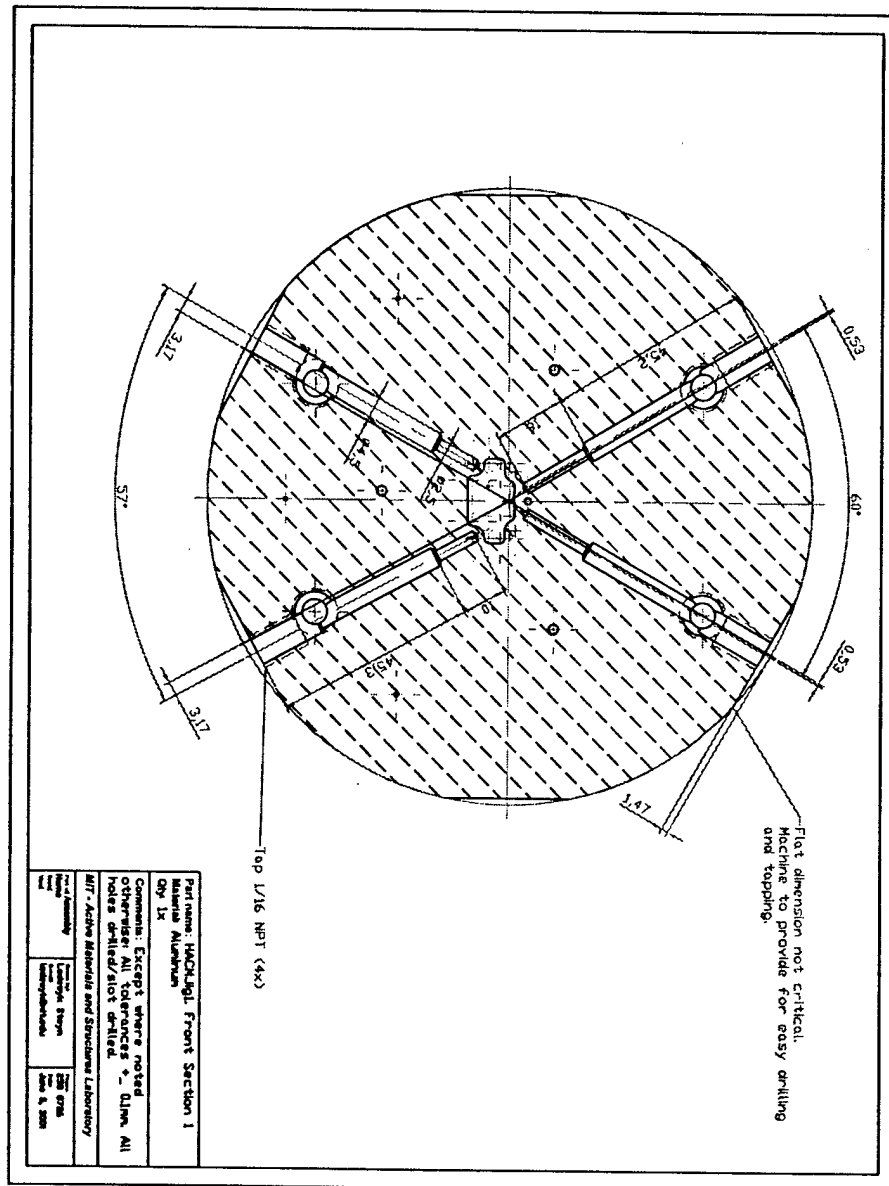


Figure C.18: Front section 1

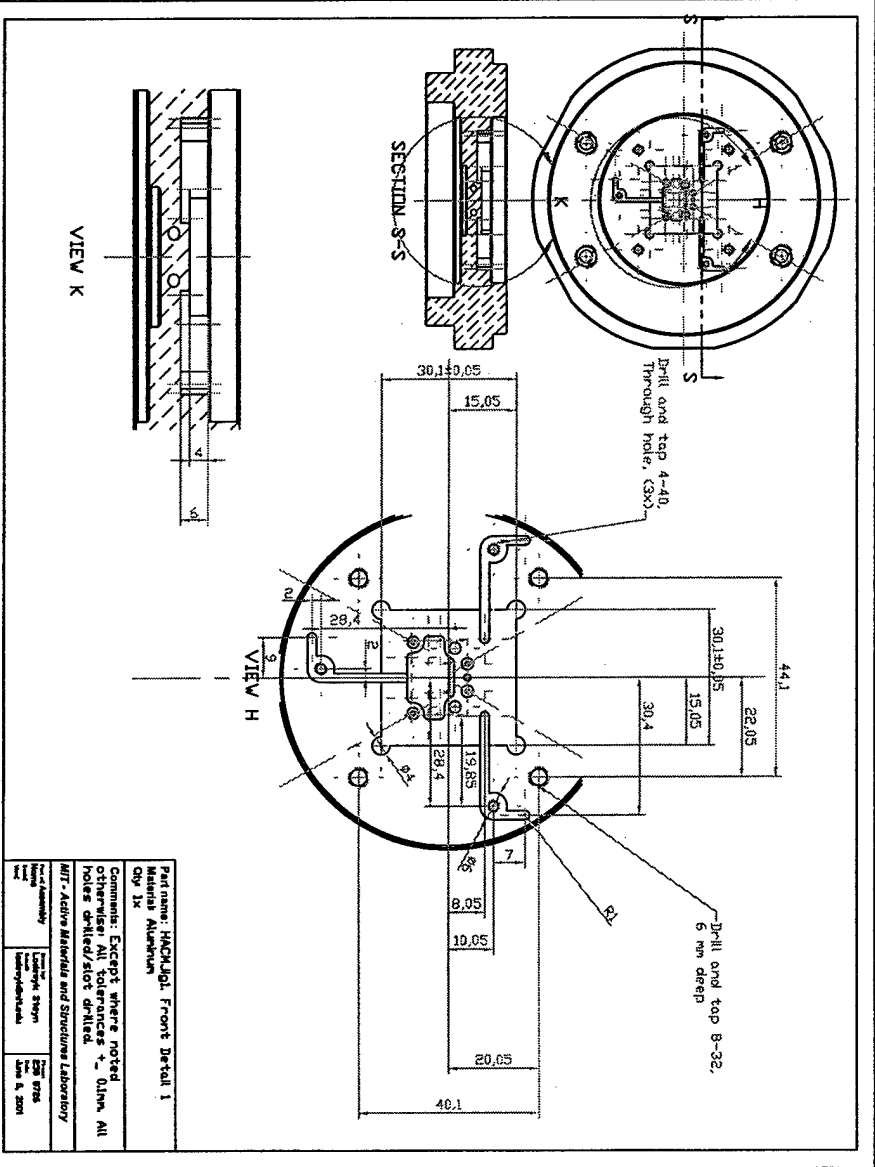


Figure C.19: Front detail 1

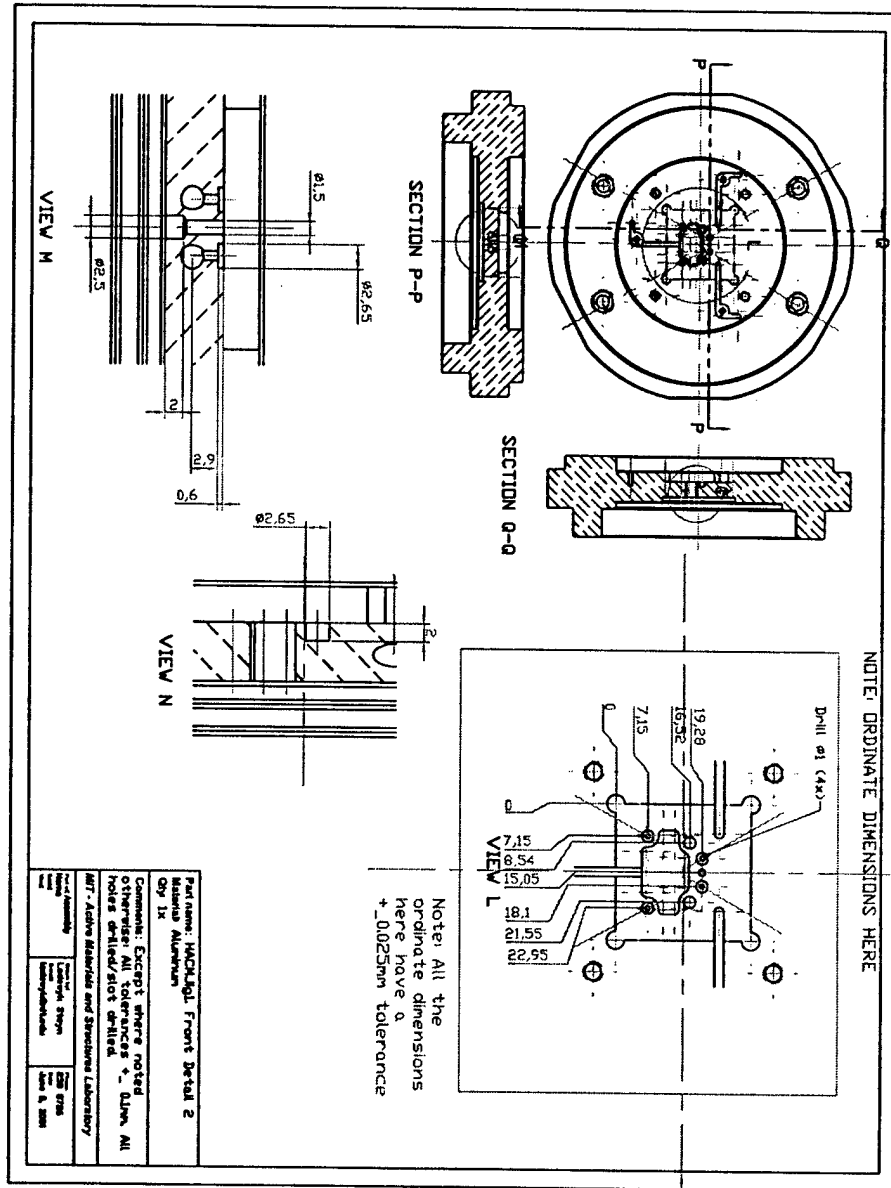


Figure C.20: Front detail 2

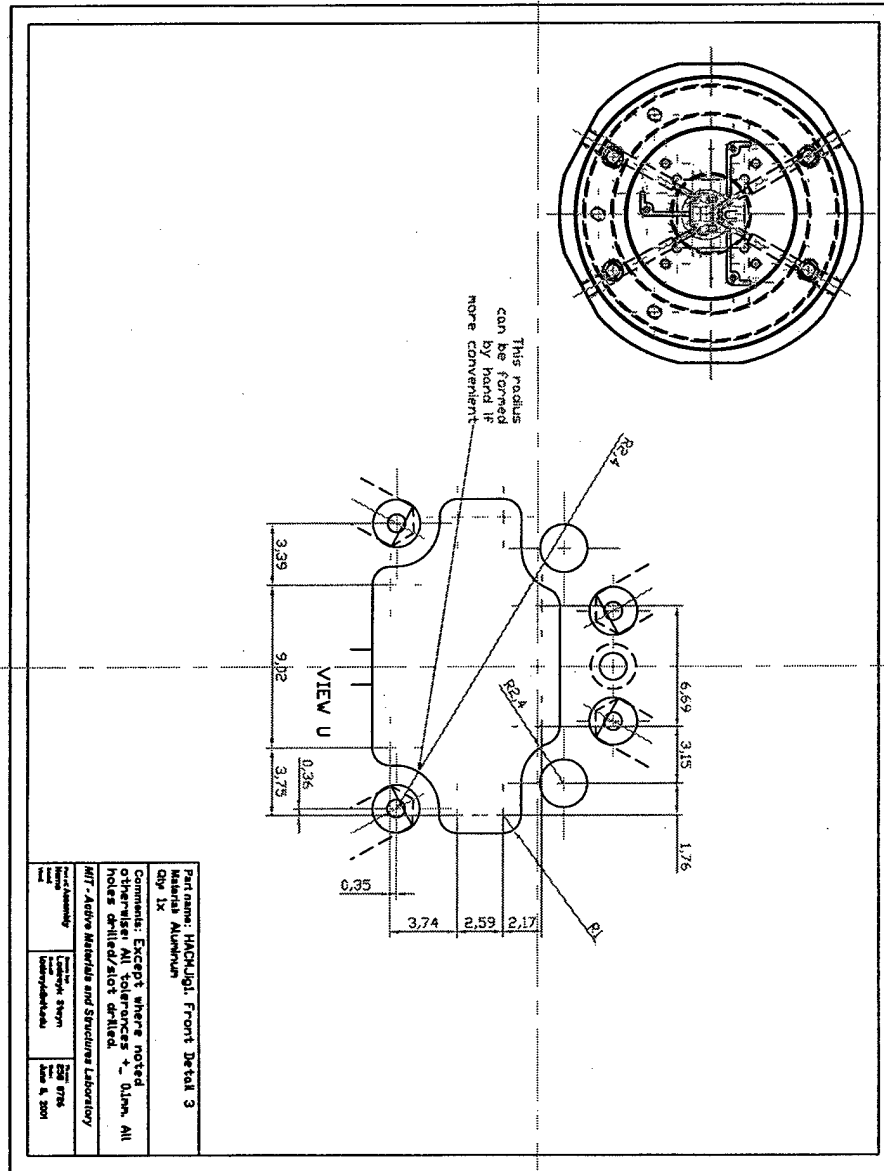


Figure C.21: Front detail 3

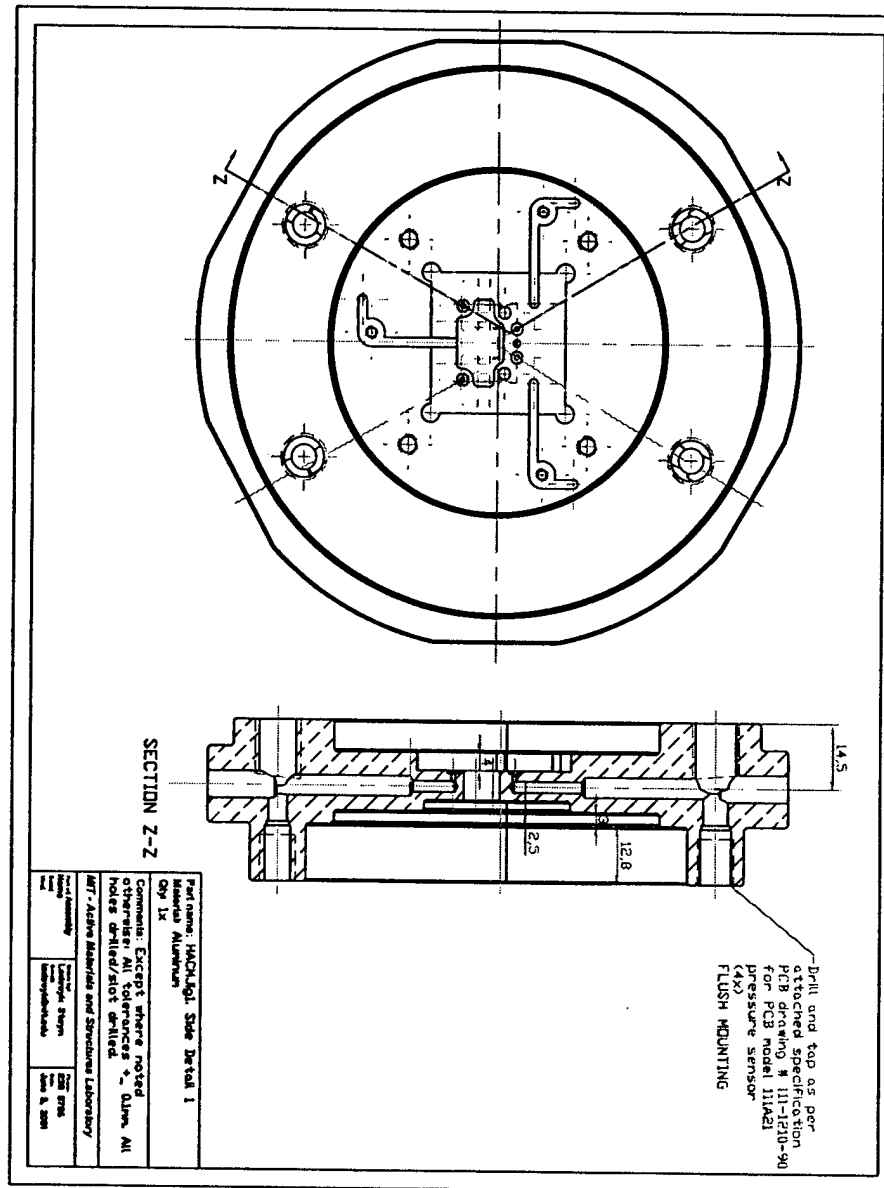


Figure C.22: Side detail 1

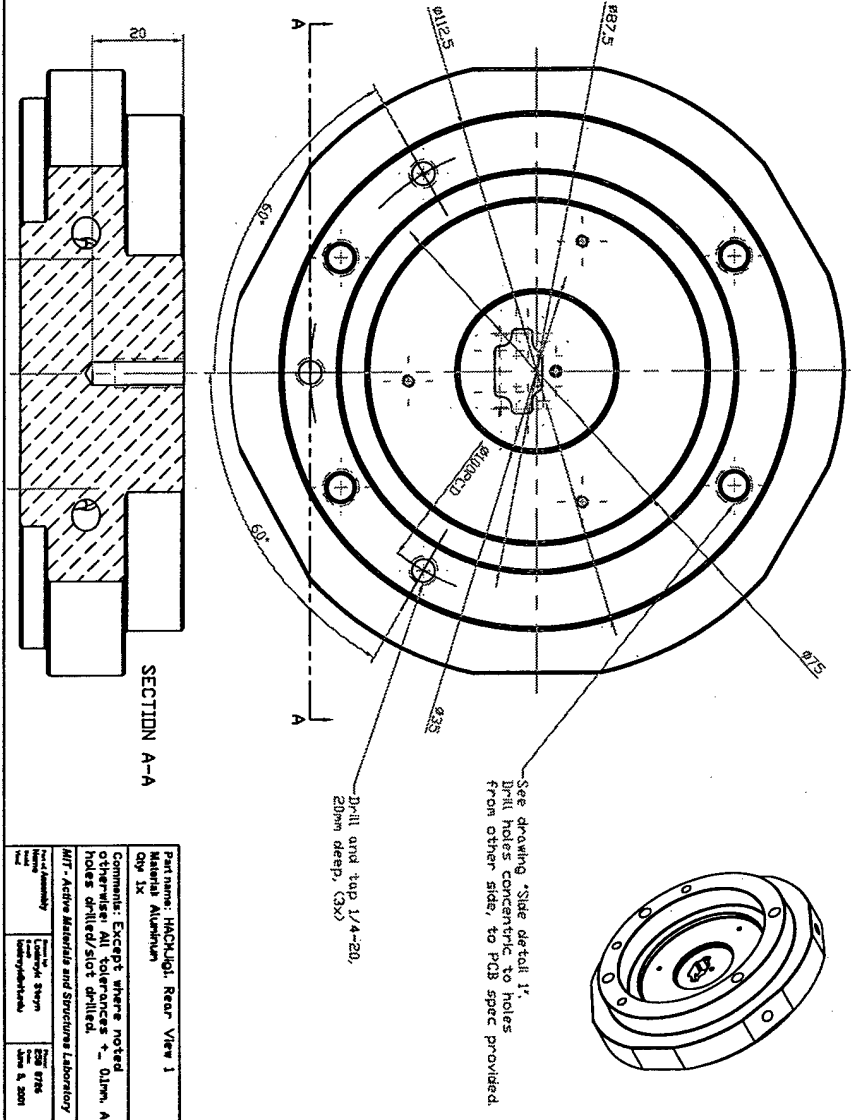


Figure C.23: Rear view 1

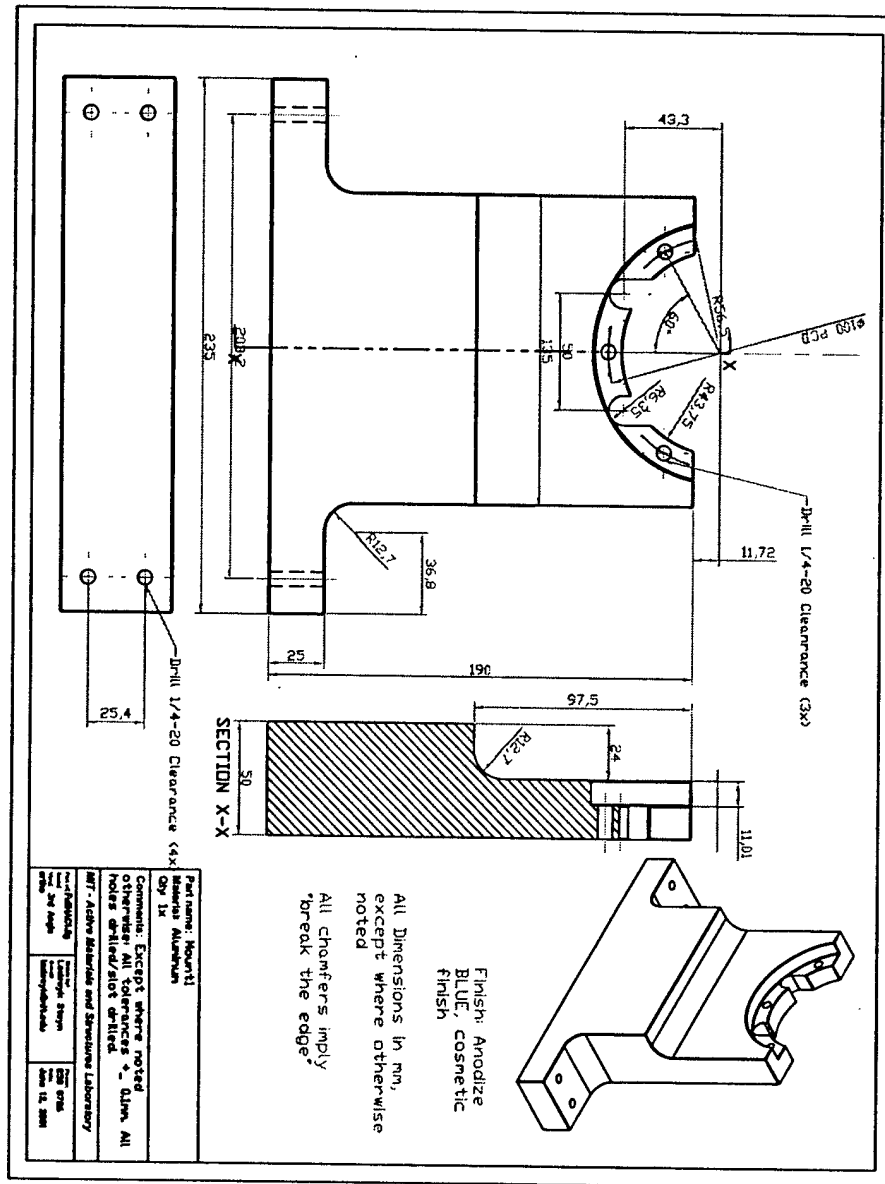


Figure C.24: Mount

Appendix D

Computer code

D.1 Matlab codes used for modeling of the HAC

These codes were contributed by D.C. Roberts, and are included here for completeness.

D.1.1 Bisection method iteration code for modeling of the HAC

This code calls the nonlinear plate code and uses bisection to solve for z_1 and z_2 , using the following equation as a convergence criterium (See (2.20)):

$$\Delta V_1 + \Delta V_2 = \Delta V_f \quad (D.1)$$

```
function [Zte, dVte, dVfluid, Ztop, dVtop, Fvm, Zde, dVvm, Maxstress, Zvc, PHAC]...
    =HAC1ValveMatlabIterateSubCode(Ppis,PHPR)

%9-16-01 DAVID C. ROBERTS
%
% This file iterates in PHAC to determine the equilibrium solution
% for the HAC device behavior (1-Valve devices).

%Read in compliance coefficients from Maple generated .m file
HAC1ValveMatlabIterateMatrix; %Read in compliance coefficients

%%%%%%%%%%%%%%%%%%%%%%%%%%%%%%%%%%%%%%%%%%%%%%%%%%%%%%%%%%%%%%%%%%%%%%%%%%%%%%
%DEFINE IMPORTANT PARAMETERS%%%%%%%%%%%%%%%%%%%%%%%%%%%%%%%%%%%%%%%%%%%%%%%%%%%%%%%%
flagNL=1; %Include non-linearity if flagNL=1
No=0; %Initial in-plane prestress

%%%%%%%%%%%%%%%%%%%%%%%%%%%%%%%%%%%%%%%%%%%%%%%%%%%%%%%%%%%%%%%%%%%%%%%%%%%%%%
%PROVIDE INITIAL GUESS FOR PHAC%%%%%%%%%%%%%%%%%%%%%%%%%%%%%%%%%%%%%%%%%%%%%%%%%%%%%%%%
PHACguess=0.0013e6;
PHAC1=PHACguess;
PHAC2=PHACguess;
check0=1;
check1=1;
```

158 D Computer code

```

i=0
j=0

%Determine Volume discrepancy for initial PHAC guess
U=[Ppis PHPR PHAC1]; %Vector of input parameters to compliance matrix
S=A*U'; %S is the vector of all linear responses
Fvc=Av*(PHAC1-PHPR); Pvm=PHAC1-PHPR; %Define these loadings for use in
%NLActiveValve_MembraneCaseA.m
[y,r,Vtotal,psi,W,theta,xi,thetaND,psiND,sigma_r_top,sigma_r_bot,yvc,maxstress]...
    = NLActiveValve_MembraneCaseA(Pvm,Fvc,rvc,rvm,tvm,Esi,nusi,flagNL,No);
dVvm=Vtotal; dVte=S(2); dVfluid=S(3); dVtop=S(5);
check1 = (dVvm + dVtop - dVte - dVfluid);
check0=check1;
%Done

%Determine range of PHAC (between PHAC0 and PHAC1) within which
%the real PHAC lies
while check0*check1/(abs(check0*check1))>> 0
i=0
    j=j+1

    PHAC0 = PHAC1;
    PHAC1 = PHAC2
    check0 = check1

    U=[Ppis PHPR PHAC1]; %Vector of input parameters to
    %compliance matrix
    S=A*U'; %S is the vector of all
    %linear responses
    Fvc=Av*(PHAC1-PHPR); Pvm=PHAC1-PHPR; %Define these
    %loadings for use in NLActiveValve_MembraneCaseA.m
    [y,r,Vtotal,psi,W,theta,xi,thetaND,psiND,sigma_r_top,sigma_r_bot,yvc,...
        maxstress] = NLActiveValve_MembraneCaseA(Pvm,Fvc,rvc,rvm,tvm,Esi,nusi,flagNL,No);
    dVvm=Vtotal; dVte=S(2); dVfluid=S(3); dVtop=S(5);
    check1 = (dVvm + dVtop - dVte - dVfluid);

    if check1 < 0
        PHAC2 = 10*PHAC1;
    elseif check1 > 0
        PHAC2 = 0.1*PHAC1;
    else
        break;
    end
end

if PHAC1<PHAC0 %rearrange PHAC0 to be less than PHAC1
PHACmax=PHAC0;
    PHACmin=PHAC1;
    PHAC1=PHACmax
    PHAC0=PHACmin
else
end

```



```

%DONE,it has been determined that PHAC lies between PHACO and PHAC1

j=0;

%Determine solution for PHAC
PHACm=0.5*(PHACO+PHAC1);
firsthalf=0;

while abs((PHAC1-PHACO)/PHACO) > 0.0001

    i=1
    j=j+1

    if firsthalf==1

        U=[Ppis PHPR PHACm]; %Vector of input parameters to %
        %compliance matrix
        S=A*U'; %S is the vector of all
        %linear responses
        Fvc=AvC*(PHACm-PHPR); Pvm=PHACm-PHPR; %Define these loadings
        %for use in NLAActiveValve_MembraneCaseA.m
        [y,r,Vtotal,psi,W,theta,xi,thetaND,psiND,...
         sigma_r_top,sigma_r_bot,yvc,maxstress] = ...
            NLAActiveValve_MembraneCaseA(Pvm,Fvc,rvC,rvm,tvm,Esi,nusi,flagNL,No);
        dVvm=Vtotal; dVte=S(2); dVfluid=S(3); dVtop=S(5);
        checkm = (dVvm + dVtop - dVte - dVfluid);

    else

        U=[Ppis PHPR PHACO]; %Vector of input parameters to
        %compliance matrix
        S=A*U'; %S is the vector of all
        %linear responses
        Fvc=AvC*(PHACO-PHPR); Pvm=PHACO-PHPR; %Define these loadings
        %for use in NLAActiveValve_MembraneCaseA.m
        [y,r,Vtotal,psi,W,theta,xi,thetaND,psiND,...
         sigma_r_top,sigma_r_bot,yvc,maxstress] = ...
            NLAActiveValve_MembraneCaseA(Pvm,Fvc,rvC,rvm,tvm,Esi,nusi,flagNL,No);
        dVvm=Vtotal; dVte=S(2); dVfluid=S(3); dVtop=S(5);
        check0 = (dVvm + dVtop - dVte - dVfluid);

        U=[Ppis PHPR PHACm]; %Vector of input parameters %
        %to compliance matrix
        S=A*U'; %S is the vector of all %
        %linear responses
        Fvc=AvC*(PHACm-PHPR); Pvm=PHACm-PHPR; %Define these loadings for %
        %use in NLAActiveValve_MembraneCaseA.m
        [y,r,Vtotal,psi,W,theta,xi,thetaND,psiND,...
         sigma_r_top,sigma_r_bot,yvc,maxstress] = ...
            NLAActiveValve_MembraneCaseA(Pvm,Fvc,rvC,rvm,tvm,Esi,nusi,flagNL,No);
        dVvm=Vtotal; dVte=S(2); dVfluid=S(3); dVtop=S(5);

```

160 D Computer code

```

checkm = (dVvm + dVtop - dVte - dVfluid);

end

if check0+checkm <= 0
    PHAC1=PHACm;
    firsthalf=1;
else
    PHAC0=PHACm;
    firsthalf=0;
end

PHACm=0.5*(PHAC0+PHAC1)
end
PHAC=PHACm;
%DONE, PHAC solution has been determined

%Evaluate all parameters for last value of PHACm

U=[Ppis PHPR PHACm]; %Vector of input parameters
%to compliance matrix
S=A*U'; %S is the vector of all linear
%responses
Fvc=Avc*(PHACm-PHPR); Pvm=PHACm-PHPR; %Define these loadings for
%use in NLActiveValve_MembraneCaseA.m
[y,r,Vtotal,psi,W,theta,xi,thetaND,psiND,...
    sigma_r_top,sigma_r_bot,yvc,maxstress] = ...
    NLActiveValve_MembraneCaseA(Pvm,Fvc,rvr,rvm,tvm,Esi,nusi,flagNL,No);

Zte=S(1);
dVte=S(2);
dVfluid=S(3);
Ztop=S(4);
dVtop=S(5);
Fvm=S(6);
Zde=S(7);
dVvm=Vtotal;
Maxstress=maxstress;
Zvc=yvc+Ztop;
PHAC=PHACm;

%DONE

```

D.1.2 Nonlinear annular plate code

```

function [y,r,Vtotal,psi,W,theta,xi,thetaND,psiND,sigma_r_top,sigma_r_bot,yvc,maxstress]...
    = NlActiveValve_MembraneCaseA(Pvm,Fvc,rb,ra,tvm,E,nu,flagNL,No)

%NLValveCapMembrane_CaseA.m

%David C. Roberts, 11-30-2000
%This Matlab code solves for the non-linear deflection behavior of the valve cap
%/membrane under loading Pvm and Fvc. The deflection, slope,
%curvature, swept volume, and membrane stress are calculated. Case A refers to the
%fact that we are applying both loading inputs Pvm and Fvc and determining the
%structural response. Prior to calling of this code, the user must define Pvm and
%Fvc as functions of P1, P2, and PHAC. The loadings are defined as follows:
% Pvm = pressure differential across valve membrane = PHAC-P2
% Fvcstar = force seen by valve cap = Avc*(PHAC-P1)
%The plate/membrane is characterized by inner radius rb, outer radius ra, thickness
%tvm, and material properties E and nu.

format long;

%%%%%%%%%%%%%%%%%%%%%%%%%%%%%%%%%%%%%%%%%%%%%%%%%%%%%%%%%%%%%%%%%%%%%%%%
%Convert Inputs to Dimensionless Quantities
P = (Pvm*ra^4)/(E*tvm^4); %Dimensionless loading of pressure
%difference across cap/membrane
F = (Fvc*ra^2)/(pi*E*tvm^4); %Dimensionless loading due to additional
%force on cap

%%%%%%%%%%%%%%%%%%%%%%%%%%%%%%%%%%%%%%%%%%%%%%%%%%%%%%%%%%%%%%%%%%%%%%%%

beta = sqrt((1-nu)/(1+nu))*(rb/ra);
k = (ra/tvm)*sqrt((12*(1-nu^2)*No)/(E*tvm*(1-beta^2)));
s = beta*k;

%%%%%%%%%%%%%%%%%%%%%%%%%%%%%%%%%%%%%%%%%%%%%%%%%%%%%%%%%%%%%%%%%%%%%%%%
%%Section 2: Define grid spacing and coordinate transformation parameters
%%for finite-difference method
%%%%%%%%%%%%%%%%%%%%%%%%%%%%%%%%%%%%%%%%%%%%%%%%%%%%%%%%%%%%%%%%%%%%%%%%
Npoints=200; %The total # of grid points to use (MUST KEEP IT EVEN)
alpha=1.01; %Grid density parameter
phi=(alpha+1)/(alpha-1); %Grid density ratio
hr = 1/(Npoints-1); %Size of grid spacing
eta = 0:hr:1; %Vector of evenly spaced points between 0 and 1

xi_b = rb/ra; %Non-dimensional position of inner radius
xi_c = (rb+ra)/(2*ra); %Non-dimensional position of midpoint along membrane
xi_a = ra/ra; %Non-dimensional position of outer radius

%For the grid points from xi_b to xi_c, define the derivatives of eta with respect to xi
for i=1:Npoints/2,
xi(i) = xi_b + (alpha-1)*(xi_c-xi_b)*(phi-phi^(1-2*eta(i)))/...
    (1+phi^(1-2*eta(i)));

```

```

m = (alpha-1)*(xi_c-xi_b);
m2 = m*phi - m + 2*xi_b;
deta(i) = (0.5/log(phi))*(m*(1+phi))/((m*phi-(xi(i)-xi_b))*...
(m+(xi(i)-xi_b)));
d2eta(i) = -(0.5/log(phi))*(m*(1+phi)*(m2-2*xi(i)))/...
((m*phi-(xi(i)-xi_b))*(m+(xi(i)-xi_b)))^2;
end

%For the grid points from xi_c to xi_a
for i=Npoints/2+1:Npoints,
xi(i) = xi_b + (alpha-1)*(xi_c-xi_b)*(phi-phi^(1-2*eta(i)))/...
(1+phi^(1-2*eta(i)));
m = (alpha-1)*(xi_c-xi_b);
m2 = m*phi - m + 2*xi_b;
deta(i) = (0.5/log(phi))*(m*(1+phi))/((m*phi-(xi(i)-xi_b))*...
(m+(xi(i)-xi_b)));
d2eta(i) = -(0.5/log(phi))*(m*(1+phi)*(m2-2*xi(i)))/...
((m*phi-(xi(i)-xi_b))*(m+(xi(i)-xi_b)))^2;
end

%%%%%%%%%%%%%%%%%%%%%%%%%%%%%%%%%%%%%%%%%%%%%%%%%%%%%%%%%%%%%%%%%%%%%%%%%%%%%%
%%%%%%%%%%%%%%%%%%%%%%%%%%%%%%%%%%%%%%%%%%%%%%%%%%%%%%%%%%%%%%%%%%%%%%%%%%%%%%
%%Section 3: Finite-Difference Implementation
%(based on Equation 7-7 in Chapter 2, DCR Thesis)
%%%%%%%%%%%%%%%%%%%%%%%%%%%%%%%%%%%%%%%%%%%%%%%%%%%%%%%%%%%%%%%%%%%%%%%%%%%%%%
%%%%%%%%%%%%%%%%%%%%%%%%%%%%%%%%%%%%%%%%%%%%%%%%%%%%%%%%%%%%%%%%%%%%%%%%%%%%%%

%Governing equations at internal points (from 2 to Npoints-1)
for i=2:Npoints-1,
    A(i,i-1) = (xi(i)^2*deta(i)^2)/(hr^2) - (xi(i)^2*d2eta(i)...
    + xi(i)*deta(i))/(2*hr);
    A(i,i) = -( (2*xi(i)^2*deta(i)^2)/(hr^2) + (s^2+1) + ...
    xi(i)^2*k^2 );
    A(i,i+1) = (xi(i)^2*deta(i)^2)/(hr^2) + (xi(i)^2*d2eta(i) + ...
    xi(i)*deta(i))/(2*hr);

    B(i,i-1) = (xi(i)^2*deta(i)^2)/(hr^2) - (xi(i)^2*d2eta(i) + ...
    3*xi(i)*deta(i))/(2*hr);
    B(i,i) = -(2*xi(i)^2*deta(i)^2)/(hr^2);
    B(i,i+1) = (xi(i)^2*deta(i)^2)/(hr^2) + (xi(i)^2*d2eta(i) + ...
    3*xi(i)*deta(i))/(2*hr);

    C(i) = 6*(1-nu^2)*P*(xi(i)^3 - xi(i)*(rb/ra)^2) + 6*(1-nu^2)*F*xi(i);
end

%Boundary condition equations at xi_b (grid point #1)
A(1,1) = 1;
B(1,1) = -3*xi(1)*deta(1)/(2*hr) + (1-nu);
B(1,2) = 4*xi(1)*deta(1)/(2*hr);
B(1,3) = -xi(1)*deta(1)/(2*hr);
C(1) = 0;

```

```

%Boundary condition equations at xi_a (grid point #Npoints)
A(Npoints,Npoints) = 1;
B(Npoints,Npoints-2) = xi(Npoints)*deta(Npoints)/(2*hr);
B(Npoints,Npoints-1) = -4*xi(Npoints)*deta(Npoints)/(2*hr);
B(Npoints,Npoints) = 3*xi(Npoints)*deta(Npoints)/(2*hr) + (1-nu);
C(Npoints) = 0;

%%%%%%%%%%%%%%%%%%%%%%%%%%%%%%%%%%%%%%%%%%%%%%%%%%%%%%%%%%%%%%%%%%%%%%%%
%%%%%%%%%%%%%%%%%%%%%%%%%%%%%%%%%%%%%%%%%%%%%%%%%%%%%%%%%%%%%%%%%%%%%%%%
%%Section 4: Provide an initial guess for the theta vector
%(plate slope), to be
%%used in the finite-difference iteration procedure.
%%%%%%%%%%%%%%%%%%%%%%%%%%%%%%%%%%%%%%%%%%%%%%%%%%%%%%%%%%%%%%%%%%%%%%%%
%%%%%%%%%%%%%%%%%%%%%%%%%%%%%%%%%%%%%%%%%%%%%%%%%%%%%%%%%%%%%%%%%%%%%%%%

if k==0,
    %theta = (-0.75*(1-nu^2)*P*xi.*(1-xi.^2))'; %Linear result
    theta=xi';
else
    theta=xi';
end

%%%%%%%%%%%%%%%%%%%%%%%%%%%%%%%%%%%%%%%%%%%%%%%%%%%%%%%%%%%%%%%%%%%%%%%%
%%%%%%%%%%%%%%%%%%%%%%%%%%%%%%%%%%%%%%%%%%%%%%%%%%%%%%%%%%%%%%%%%%%%%%%%
%%Section 5: Matrix Manipulation Procedure
%%%%%%%%%%%%%%%%%%%%%%%%%%%%%%%%%%%%%%%%%%%%%%%%%%%%%%%%%%%%%%%%%%%%%%%%
%%%%%%%%%%%%%%%%%%%%%%%%%%%%%%%%%%%%%%%%%%%%%%%%%%%%%%%%%%%%%%%%%%%%%%%%

Niterations=500; %Perform up to 500 iterations
tolerance1=1e-8;
tolerance2=1e-8;
omega=0.45; %Under-relaxation parameter
if flagNL==1 %This variable is passed into file.
    NLoption=1; %0 = Linear solution; 1 = NonLinear solution
else
    NLoption=0;
end

for i=1:Niterations,
    i;
    for j=2:Npoints-1 %Define D vector for each iteration
        D(j) = -0.5*theta(j).^2;
    end
    D(1)=0;
    D(Npoints)=0;

    Sr = inv(B)*D'*NLoption; %Solve for Sr
    v_Sr = 12*(1-nu^2)*xi'.^2.*Sr; %Calculate non-linear correction term v_Sr
    A2 = A - diag(v_Sr,0); %Subtract non-linear correction term from A

```

```

theta_new = inv(A2)*C'; %Calculate new theta vector

inner_product = (theta_new'*theta)/sqrt(theta_new'*theta_new)/...
sqrt(theta'*theta);
length_ratio = sqrt(theta_new'*theta_new)/sqrt(theta'*theta);

if (1-inner_product) >= tolerance1 | (1-length_ratio) >= tolerance2
    theta = (1-omega)*theta + omega*theta_new;
else
    break;
end
end

%%%%%%%%%%%%%%%%%%%%%%%%%%%%%%%%%%%%%%%%%%%%%%%%%%%%%%%%%%%%%%%%%%%%%%%%
%%%%%%%%%%%%%%%%%%%%%%%%%%%%%%%%%%%%%%%%%%%%%%%%%%%%%%%%%%%%%%%%%%%%%%%%
%%Section 6: Calculate Deflection, Curvature, Stress, and
%Swept Volume in this
%%post-processing section.
%%%%%%%%%%%%%%%%%%%%%%%%%%%%%%%%%%%%%%%%%%%%%%%%%%%%%%%%%%%%%%%%%%%%%%%%
%%%%%%%%%%%%%%%%%%%%%%%%%%%%%%%%%%%%%%%%%%%%%%%%%%%%%%%%%%%%%%%%%%%%%%%%

%PLATE DEFLECTION: Calculate plate deflection vector from the final theta vector,
%using 2nd-order forward, backward, and central difference methods to express
%theta in terms of W. Then, using matrix inversion to obtain the vector W.
i=1; %BC at rb
Wmatrix(i,1) = deta(i)*(-3/(2*hr));
Wmatrix(i,i+1) = deta(i)*(2/hr);
Wmatrix(i,i+2) = deta(i)*(-1/(2*hr));

for i=2:Npoints-1 %Inner grid points
    Wmatrix(i,i-1) = deta(i)*(-1/(2*hr));
    Wmatrix(i,i+1) = deta(i)*(1/(2*hr));
end

%BC at ra --> Do not do for the outer boundary condition. We already know that
%the deflection at ra is equal to zero.

W = inv(Wmatrix(1:Npoints-1,1:Npoints-1))*theta(1:Npoints-1);
W=[W;0];
%Done

%PLATE CURVATURE: Calculate plate curvature vector from the final theta vector,
%using 2nd-order forward, backward, and central difference methods.
i=1; %BC at rb
psi(i) = deta(i)*(1/(2*hr))*(-3*theta(i) + 4*theta(i+1) - theta(i+2));

for i=2:Npoints-1 %Inner grid points
    psi(i) = deta(i)*(1/(2*hr))*(theta(i+1) - theta(i-1));
end

```

```

i=Npoints; %BC at ra
psi(i) = deta(i)*(1/(2*hr))*(3*theta(i) - 4*theta(i-1) + theta(i-2));
%Done

%PLATE STRESS: Calculate the stress vectors in the plate.

for i=1:Npoints
    Sro(i) = (k^2/(12*(1-nu^2)))*(1 + beta^2/(xi(i)^2));
    sigma_r_top(i) = (E*tvm^2/ra^2)*(Sro(i) + Sr(i) - ...
        (1/(2*(1-nu^2)))*(psi(i) + (nu*theta(i))./xi(i)));
    sigma_r_bot(i) = (E*tvm^2/ra^2)*(Sro(i) + Sr(i) + ...
        (1/(2*(1-nu^2)))*(psi(i) + (nu*theta(i))./xi(i)));
end
if max(sigma_r_top) > max(sigma_r_bot)
    maxstress = abs(max(sigma_r_top));
else
    maxstress = abs(max(sigma_r_bot));
end
%Done

%CONVERSION TO NON_DIMENSIONAL PARAMETERS
r=xi*ra;
y=W*tvm;
thetaND=theta*tvm/ra; %This non-dimensional theta is dw/dr
psiND=psi*tvm/(ra^2); %This non-dimensional psi is d2w/dr2

%PLATE SWEPT VOLUME: Calculate total swept volume under cap and membrane.
V=0;
for i=1:Npoints-1
    dV(i) = pi*(r(i+1)^2-r(i)^2)*0.5*(y(i+1)+y(i));
    V = V + dV(i);
end
yvc = y(1);
Vcap = yvc*pi*rb^2;
Vtotal = Vcap + V;
%Done

```

D.2 Matlab code used for data analysis and computation

```
% Lodewyk Steyn
% Code to postprocess the HAC data taken in October 2001
% Computes the stiffness matrix
% Reads in theoretical data as generated by Dave's code
%

%%Polytec Calibration Factors:
%% for 50kPa tests --> 2um/V
%% for 100kPa tests --> 8um/V
%% for 150kPa tests --> 8um/V
%% for 200kPa tests --> 20um/V

clear all;
close all;

%*****
% USER INPUT

%The psi_1 psi_2 matrix, to be subtracted from the D matrices.
% the units are in kPa/um

psiipsi2E = [15.2 0
             0 15.4]

psiipsi2I = [8.9 0
             0 17.5]

% Plotstage % For the 2D plots
% Set to the following values:
% 1: Just experimental data and curve fits
% 2: Experimental curve fits, no error bars, and theoretical curves added
% 3: Experiment, model, and the linear lines

Plotstage = 3;

% number of plot points to plot for the model values on the curves
nmodcorrpts = 15;

% PHPR Question
% Make all PHPR's negative?

PHPRsgn = -1;

% Readflag
% Set = 1 if you want to read in a new datacell, or to 0 if you want to load the old one.
Readflag = 0
```



```

% Read model data
% Set = 1 if you want to read model data.
ModReadflag = 0

% Mplotflag
% Set to 1 if you want to plot all the time histories
Mplotflag = 0

% To do postprocessing or not
Postprocflag = 1;

% File to save datacell to
wfilename = 'PisBValB_workfile.mat'

wfilename_mod = 'PisBValB_workfile_mod.mat'

% Number of channels in each file
Nchannels = 4;

chan1str = 'Pulse Valve Drive Signal 1';
chan2str = 'Piston Displacement';
chan3str = 'P_1';
chan4str = 'P_2';

%Number of files to read:
nfiles1 = 6;

%Array of model file names to be read

modfilearray = {'HAC10ValveData_Phpr0kPa_8um_6um.mat'
                'HAC10ValveData_Phpr92kPa_8um_6um.mat'
                'HAC10ValveData_Phpr298kPa_8um_6um.mat'
                'HAC10ValveData_Phpr500kPa_8um_6um.mat'}

% Array of the corresponding PHPR's for the model files - NOTE - USE THE POSITIVE VALUES!!
modfileP_HPR_S = [0
                  92
                  298
                  500];

% Change the sign appropriately
modfileP_HPR_S = modfileP_HPR_S*PHPRsgn;

% Caption of the data to be stored in the model cell array
modfilecaption = 'PHAC PPisvary1 Zde1 Zvc1 maxstress1'

% Polytec Settings for each file % Also correct for index of refraction
PolytecFactors = [0.5/1.3745
                  0.5/1.3745
                  0.5/1.3745]

```

168 D Computer code

```

8/1.3745
8/1.3745
8/1.3745];

% Values to shift the Polytec Channels by to get the correct zero values (in um)
% These are for each file, and are obtained after the first run of this code
% Subtract!! these values from the actual data....

PolytecYshifts = [-0.16
-0.25
-0.05
-0.05
-0.025
-0.05]

XXXXXXXXXXXXXXXXXXXX

% Create a matrix with all the drive element XY plots to be done.
% Columns are: Col1: File # Col2: Start time in Secs Col3: End time in Secs
DEplots = [3 24.4 26.9 % 0kPa PHPR
1 32.4 34.8 % 100 kPa
2 16.5 19 % 300
3 16.4 19] % 500

DEsign = -1 % To make Data negative, make it -1, to Make it Pos, make it 1

VCplots = [5 8.5 11.7 % 0kPa
4 13.4 16.6 % 100
5 18.2 21.4 % 300
6 18.2 21.4] % 500

VCsign = 1 % To make Data negative, make it -1, to Make it Pos, make it 1

%!!!! NOTE We compute P as a function of X, and not the other way around !!!!!
% !!!! AND THEN WE PLOT THE INVERSE !!!!!
% Why.... Because if  $P = k_1 \cdot x + k_2 \cdot x^3$ , it
% DOES NOT MEAN THAT  $x = s_1 \cdot P + s_2 \cdot P^3$  !!!

% Define degree of polynomials to fit to the respective data

DEPolydeg = 3;

DEPolydeg_err = 3; % For error bars

VCPolydeg = 3;

VCPolydeg_err = 7; % For error bars

%*****
%*****

```

```

% 2D XY Plot axis limits
%*****
%*****

yde_lims = [-0.7 1.5]

yvc_lims = [-13 13]

xPde_lims = [-20 520]

%*****
% 2D and 3D plot Axis labels
%*****

xPde_labl = 'P_1 (kPa)';
xPde_labl3D = {'P_1 (kPa)'};
yPhpr_labl = 'P_2 (kPa)';
yPhpr_labl3D = {'P_2 (kPa)'};
zde_labl = 'z_1 ( \mu m)';
zvc_labl = 'z_2 ( \mu m)';

curvefract = 0.6 % for placing labels on the curves

%*****

%*****
% 2D Plot figure properties
%*****

% All units here in pixels

Plot1pos = [200 200 700 500]
Plot1axpos = [65 65 570 380]
Plot1units = 'pixels'
Plot1fontsize = 14
Plot1linewidth = 2

% Plot 2 will form part of a 2-plot set, for the drive element and the valve
Plot2pos = [250 250 500 500]
Plot2axpos = [65 65 370 370]
Plot2units = 'pixels'
Plot2fontsize = 14
Plot2linewidth = 2

% Plot r is for the raw data
Plotrpos = [150 100 700 700]
Plotrunits = 'pixels'
Plotrfontsize = 12
Plotrlinewidth = 2

```

```
% Font size for the curve legend:
curvelegfntsiz = 10
```

```
%*****
% Stiffness matrix parameters
%*****
```

```
% First Value of valve cap deflection to use in um
zVCsdef1 = 1;
% Second value of valve cap deflection
zVCsdef2 = -1
```

```
% Indices of the DEplots and VCplots to use for computing the stiffness matrix
% ONLY 2 allowed
Exp_Kidxs = [2
3];
```

```
% Indices of the modfilearray to use for the stiffness matrix
% ONLY 2 Allowed
Theo_Kidxs = [2
3];
```

```
%*****
% End Stiffness matrix parameters
%*****
```

```
%Number of points to plot for each curve fit
ncfitpts = 200;
```

```
FitLwidth = 1.5; % Linewidth of the fitted curves
```

```
% Number of points for error bars
nerrbpts = 7;
```

```
XXXXXXXXXX
```

```
% Static pressure sensor calibration factor
SensPressFact1 = 6.894*100/4.9939; %6.894 Pa/psi ; 4.9939 V/100psi (Sensotec FDDBR,2D5A6A, 769233)
```

```
XXXXXXXXXX
```

```

% Static Sensor 2 calibration factor
SensPressFact2 = 6.894*150/5.0111 % Sensotec FDW 150 psi differential sensor

% Define a color vector with the appropriate colors for the different lines
PColVect = ['r'
            'g'
            'b'
            'c'
            'm'
            'k'];

%*****
% 3D Plotting Parameters
%*****

% Number of points to use for the functions when doing the surface plots
nfcnpts = 200
% Number of points per axis for the surface plots
n3dpts = 20

% PPiston values for surface plots
Ppismmin = 0
Ppismmax = 500

% Note, Phprmin should obey the sign convention - IT WILL NOT BE AUTOMATICALLY CORRECTED
% Phpr values for surface plots
Phprmin = -500
Phprmax = 0

% END: USER INPUT
%*****
%*****
%*****

nmodfiles = size(modfilearray,1);

if Readflag == 1
    %*****
    % Section : Files read
    %*****

    % Open the files to generate the appropriate plots]

    fid_v = zeros(nfiles1,1)

```

```

% File 1:

fid_v(1,1) = fopen('HACDev3Fil3_PisB_PPis500kPa_PHPR100kPa_05umV_Run1.txt','r');
fid_v(2,1) = fopen('HACDev3Fil3_PisB_PPis500kPa_PHPR300kPa_05umV_Run1.txt','r');
fid_v(3,1) = fopen('HACDev3Fil3_PisB_PPis500kPa_PHPR500kPa_05umV_Run1.txt','r');
fid_v(4,1) = fopen('HACDev3Fil3_ValvB_PPis500kPa_PHPR100kPa_8umV_Mem7_Run1.txt','r');
fid_v(5,1) = fopen('HACDev3Fil3_ValvB_PPis500kPa_PHPR300kPa_8umV_Mem7_Run1.txt','r');
fid_v(6,1) = fopen('HACDev3Fil3_ValvB_PPis500kPa_PHPR500kPa_8umV_Mem7_Run1.txt','r');

% Read the sampling rates in Scans per second
% Create a cell array with the same amount of columns as the number of files

DataCell = cell(3,nfiles1);

for i1 = 1:nfiles1
    [DataCell{1,i1} count1]=fscanf(fid_v(i1,1),'%e',[1 1]); % Get the scanrate for each file
end

% Read the data into the cell array

for i1 = 1:nfiles1
    [A count1]=fscanf(fid_v(i1,1),'%e',[Nchannels inf]);
    fclose(fid_v(i1,1));

    DataCell{2,i1} = A'; % Assign the appropriate column in the dataset to the file
    %number read in above
end

%*****
% Files read Cell array assigned
%*****

save(wfilename,'DataCell');

else

    load(wfilename);

end

%*****
% Read Model Files
%*****

if ModReadflag == 1

    %*****
    %*****

```

```

% Import appropriate data from NL code
%*****
%*****

% Create a cell array that will store all the data of all of the
% model files in a single structure

ModelCell = cell(2,nmodfiles);

% Load the appropriate model files

%Your variables are:
%PHAC1      Pvary1      Zdel      Zvc1      maxstress1

for ii = 1:nmodfiles
    load(modfilearray{ii,1}); % Load the model file\
    nptsmod = size(PHAC1,2); % Compute # of points in the file

    A = zeros(nptsmod,5);
    A(:,1) = PHAC1'/1000; % Get the p[ressure in kPa
    A(:,2) = Pvary1'/1000; % Get the pressure in kPa
    A(:,3) = Zdel'*1e6; % Get it in um
    A(:,4) = Zvc1'*1e6; % Get it in um
    A(:,5) = maxstress1'/1e6; % Get the stress in MPa

    ModelCell{1,ii} = modfilecaption;
    ModelCell{2,ii} = A;
end

%*****
% All Model Files Loaded
%*****

save(wfilename_mod,'ModelCell');

else

    load(wfilename_mod);
end

%*****
% Set the time Vectors
%*****

% Define the time interval

```

```
for i1 = 1:nfiles1
    dT1 = 1/DataCell{1,i1}; % Get the scanrate for the file under inspection

    npts = size(DataCell{2,i1},1);

    Time1 = zeros(npts,1);

    for i2=1:npts
        Time1(i2,1)=dT1*i2;
    end

    DataCell{3,i1} = Time1;

end

%*****
% Time Vectors Set
%*****

%*****
% Scale the data appropriately - convert the voltages into Data
%*****

for i1 = 1:nfiles1
    A = DataCell{2,i1};

    A(:,2) = A(:,2)*PolytecFactors(i1,1);
    A(:,3) = A(:,3)*SensPressFact1;
    A(:,4) = A(:,4)*SensPressFact2;

    DataCell{2,i1} = A;
end

%*****
% Data Scaled
%*****

%*****
% Adjust DC offsets on the Sensotec pressure transducers and also the Polytec
%*****

for i1 = 1:nfiles1
    A = DataCell{2,i1};
```



```

A(:,2) = A(:,2) - PolytecYshifts(ii,1);
A(:,3) = A(:,3) - min(A(:,3));
A(:,4) = A(:,4) - min(A(:,4));

DataCell{2,ii} = A;
end

%*****
% DC Offsets Adjusted
%*****

%*****
% Plot results for each file
%*****
if Mplotflag == 1

    % Set up the figure handles for these plots;

    hmplots = zeros(nfiles1,1);
    hmsubplots = zeros(nfiles1,4);
    hmsubhandls = zeros(nfiles1,4);
    xlabh = zeros(nfiles1,4);
    ylabh = zeros(nfiles1,4);
    tith = zeros(nfiles1,4);

    for ii = 1:nfiles1

        A = DataCell{2,ii};
        Time1 = DataCell{3,ii};

        hmplots(ii,1) = figure('color','w','position',Plotrpos);

        hmsubplots(ii,1) = subplot(2,2,1);

        hmsubhandls(ii,1) = plot(Time1,A(:,1));
        %grid
        xlabh(ii,1) = xlabel('Time (s)')
        ylabh(ii,1) = ylabel('Voltage (V)')
        tith(ii,1) = title(chan1str)

        hmsubplots(ii,2) = subplot(2,2,2);
        hmsubhandls(ii,2) = plot(Time1,A(:,2));
        %grid
        xlabh(ii,2) = xlabel('Time (s)')
        ylabh(ii,2) = ylabel('Deflection (\mu m)')
        tith(ii,2) = title(chan2str)
    end
end

```

```

hmsubplots(i1,3) = subplot(2,2,3);
hmsubhandles(i1,3) = plot(Time1,A(:,3));
%grid
xlabelh(i1,3) = xlabel('Time (s)')
ylabelh(i1,3) = ylabel('Pressure (kPa)')
tith(i1,3) = title(chan3str)

hmsubplots(i1,4) = subplot(2,2,4);
hmsubhandles(i1,4) = plot(Time1,A(:,4));
%grid
xlabelh(i1,4) = xlabel('Time (s)')
ylabelh(i1,4) = ylabel('Pressure (kPa)')
tith(i1,4) = title(chan4str)
end

% Make the plots pretty:
set(hmsubplots,'fontsize',Plotrfontsize,'linewidth',Plotrlinewidth)
set(hmsubhandles,'color','k');

set(xlabelh,'fontsize',Plotrfontsize);
set(ylabelh,'fontsize',Plotrfontsize);
set(tith,'fontsize',Plotrfontsize);

end
%*****
% Plots Completed
%*****

if Postprocflag == 1

%*****
% Make the two X-Y plots
%*****

% Determine the length of the plot color vector

ncolors = size(PColVect,1);

%*****
% DE plots
%*****

% Create a cell array with all the XY data for the respective plots

nDEplt = size(DEplots,1);
DE_XYCell = cell(2,nDEplt);

```

```

h11 = figure('color','w');
h11a = axes('box','on');

DElinehand1 = zeros(nDEplt,1);

for i1 = 1:nDEplt

    dat_idx = DEplots(i1,1);

    % Load the appropriate time data
    A = DataCell{2,dat_idx};
    Time1 = DataCell{3,dat_idx};

    npts = size(Time1,1);

    t1 = DEplots(i1,2);
    t2 = DEplots(i1,3);

    tmax = Time1(npts,1);

    % Approximate the data indices
    dat_idx_1 = floor(t1/tmax*npts);
    dat_idx_2 = floor(t2/tmax*npts);

    P_Save = A(dat_idx_1:dat_idx_2,3);
    Delta_Save = DEsign*A(dat_idx_1:dat_idx_2,2);

    A_Save = [P_Save Delta_Save];

    PHPR_Save = mean(A(dat_idx_1:dat_idx_2,4)); % Define the average value of PHPR

    DE_XYCell{1,i1} = PHPR_Save*PHPRsgn; % Sign Change
    DE_XYCell{2,i1} = A_Save;

    % Get a color index for this plot
    col_idx = ceil(((i1/ncolors) - floor(i1/ncolors))*ncolors);

    axes(h11a);

    DElinehand1(i1,1) = line(P_Save,Delta_Save,'color',PColVect(col_idx,1))

end

xlabel('Pressure (kPa)');
ylabel('Deflection (um)');

```

```

%*****
% VC plots
%*****

% Create a cell array with all the XY data for the respective plots

nVCplt = size(VCplots,1);
VC_XYCell = cell(2,nVCplt);

h22 = figure('color','w');
h22a = axes('box','on');

VClinehandl = zeros(nVCplt,1);

for i1 = 1:nVCplt

    dat_idx = VCplots(i1,1);

    % Load the appropriate time data
    A = DataCell{2,dat_idx};
    Time1 = DataCell{3,dat_idx};

    npts = size(Time1,1);

    t1 = VCplots(i1,2);
    t2 = VCplots(i1,3);

    tmax = Time1(npts,1);

    % Approximate the data indices
    dat_idx_1 = floor(t1/tmax*npts);
    dat_idx_2 = floor(t2/tmax*npts);

    P_Save = A(dat_idx_1:dat_idx_2,3);
    Delta_Save = VCsign*A(dat_idx_1:dat_idx_2,2);

    A_Save = [P_Save Delta_Save];

    PHPR_Save = mean(A(dat_idx_1:dat_idx_2,4)); % Define the average value of PHPR

    VC_XYCell{1,i1} = PHPR_Save*PHPRsgn; % Sign change
    VC_XYCell{2,i1} = A_Save;

    % Get a color index for this plot
    col_idx = ceil(((i1/ncolors) - floor(i1/ncolors))*ncolors);

    axes(h22a);

```

```

Vclinehandl(ii,1) = line(P_Save,Delta_Save,'color',PColVect(col_idx,1))

end

xlabel('Pressure (kPa)');
ylabel('Deflection (um)');

%*****
% XY PLOTS COMPLETED
%*****

% Now we have the data for the XY plots

%*****
% Perform Curve fits on all the XY-plots
% We perform 2 types of curve fits
% One PROPER one, to be used for further computation
% And one inverse (incorrect) one, to be used for
% making errorbars
%*****

% Drive elements

% Create a cell array with two rows: One for the polynomial coefficients and one
% for the regression correlation structure
DE_PolyCell = cell(4,nDEplt);
DE_PolyCell_wrong = cell(2,nDEplt);

DEfithandl = zeros(nDEplt,1);
DEebarhandl = zeros(2,nDEplt); % Error bars have 2 handles, one for the bars, and one %
for the line

DElabhdl = zeros(nDEplt,1);

for ii = 1:nDEplt

    % Load the XY data
    A = DE_XYCell{2,ii};

    % Fit a curve to it
    %!!!! NOTE We compute P as a function of X, and not the other way around !!!!!
    % !!!! AND THEN WE PLOT THE INVERSE !!!!!
    % Why.... Because if  $F = k_1x + k_2x^3$ , it DOES NOT MEAN THAT  $x = s_1F + s_2F^3$  !!!
    [P,S] = polyfit(A(:,2),A(:,1),DEPolydeg); % Linear fit for this data

    %Store this data into the new cell array

    DE_PolyCell{1,ii} = P;

```

```
DE_PolyCell{2,i1} = S;

% Also fit the inverse curve, but this is not so nice.
[P,S] = polyfit(A(:,1),A(:,2),DEPolydeg_err);

%Store this data into the new cell array
DE_PolyCell_wrong{1,i1} = P;
DE_PolyCell_wrong{2,i1} = S;

% Determine the x-limits for this plot
xmin = min(A(:,2));
xmax = max(A(:,2));

% Create an x-vector with the appropriate number of points
Xvect = linspace(xmin,xmax,ncfitpts);

% Create y -vector with the correct curve fit
[Yvect,delta] = polyval(DE_PolyCell{1,i1},Xvect,DE_PolyCell{2,i1});

% Perform plot on the previous axes
col_idx = ceil(((i1/ncolors) - floor(i1/ncolors))*ncolors);

axes(h11a);
hold on;
% Plot the fit on the axes
DEfithandl(i1,1) = line(Yvect,Xvect,'color',PColVect(col_idx,1),'linewidth',FitLwidth)

%*****
% Store PHPR and the domain
P_hpr_x = DE_IXCell{1,i1}; % Also extract the corresponding PHPR
DE_PolyCell{3,i1} = P_hpr_x;
DE_PolyCell{4,i1} = [xmin xmax];
```

```

%*****
%*****

%*****
% Place text on the curves for each P2 (PHPR)

ctext1 = strcat('P_2=',strcat(num2str(modfileP_HPR_S(i1,1),'%.0f'),'kPa'));

DElabhdl(i1,1) = curvelabel2(ctext1,h11a,xPde_lims,yde_lims,curvefract,Yvect,Xvect);

%*****

% Create the error bar plot
xemin = min(A(:,1));
xemax = max(A(:,1));

Xv_err = linspace(xemin,xemax,nerrbpts); % Use inverse data for error bars

[Yv_err,Edelta] = polyval(DE_PolyCell_wrong{1,i1},Xv_err,DE_PolyCell_wrong{2,i1});

DEebarhdl(:,i1) = errorbar(Xv_err,Yv_err,Edelta)

set(DEebarhdl(1,i1),'color',PColVect(col_idx,1),'linewidth',FitLwidth);

delete(DEebarhdl(2,i1)); % Delete the lines from the errobar plot

end

% Valve Caps

% Create a cell array with two rows: One for the polynomial coefficients and one
% for the regression correlation structure
VC_PolyCell = cell(4,nVCplt);
VC_PolyCell_wrong = cell(2,nVCplt);

VCfithandl = zeros(nVCplt,1);
VCebarhandl = zeros(2,nVCplt); % Error bars have 2 handles, one for the bars, and one for
%the line

VClabhdl = zeros(nVCplt,1);

for i1 = 1:nVCplt

    % Load the XY data
    A = VC_XYCell{2,i1};

```

```

% Fit a curve to it
%!!!! NOTE We compute P as a function of X, and not the other way around !!!!!
% !!!! AND THEN WE PLOT THE INVERSE !!!!!
% Why.... Because if  $F = k_1x + k_2x^3$ , it DOES NOT MEAN THAT  $x = s_1F + s_2F^3$  !!!
[P,S] = polyfit(A(:,2),A(:,1),VCPolydeg); % Linear fit for this data

%Store this data into the new cell array

VC_PolyCell{1,i1} = P;
VC_PolyCell{2,i1} = S;

% Also fit the inverse curve, but this is not so nice.

[P,S] = polyfit(A(:,1),A(:,2),VCPolydeg_err);

%Store this data into the new cell array

VC_PolyCell_wrong{1,i1} = P;
VC_PolyCell_wrong{2,i1} = S;

% Determine the x-limits for this plot

xmin = min(A(:,2));
xmax = max(A(:,2));

% Create an x-vector with the appropriate number of points
Xvect = linspace(xmin,xmax,ncfitpts);

% Create y -vector with the correct curve fit
[Yvect,delta] = polyval(VC_PolyCell{1,i1},Xvect,VC_PolyCell{2,i1});

% Perform plot on the previous axes
col_idx = ceil(((i1/ncolors) - floor(i1/ncolors))*ncolors);

axes(h22a);
hold on;
% Plot the fit on the axes
VCfithandl(i1,1) = line(Yvect,Xvect,'color',PColVect(col_idx,1),'linewidth',FitLwidth)

%*****
% Store PHPR and the domain

P_hpr_x = VC_XYCell{1,i1}; % Also extract the corresponding PHPR

```



```

VC_PolyCell{3,i1} = P_hpr_x;
VC_PolyCell{4,i1} = [xmin xmax];

%*****
%*****

%*****
% Place text on the curves for each P2 (PHPR)

ctext1 = strcat('P_2=',strcat(num2str(modfileP_HPR_S(i1,1),'%4.0f'),'kPa'));

VClabhdl(i1,1) = curvelabel2(ctext1,h22a,xPde_lims,yvc_lims,curvefract,Yvect,Xvect);

%*****

% Create the error bar plot
xemin = min(A(:,1));
xemax = max(A(:,1));

Xv_err = linspace(xemin,xemax,nerrbpts); % Use inverse data for error bars

[Yv_err,Edelta] = polyval(VC_PolyCell_wrong{1,i1},Xv_err,VC_PolyCell_wrong{2,i1});

VCebarhdl(:,i1) = errorbar(Xv_err,Yv_err,Edelta)

set(VCebarhdl(1,i1),'color',PColVect(col_idx,1),'linewidth',FitLwidth);

delete(VCebarhdl(2,i1)); % Delete the lines from the errorbar plot

end

%*****
%*****
% Overplot the model over the measured data
%*****
%*****

DEmodhdl = zeros(nmodfiles,1);

```

```

VCmodhandl = zeros(nmodfiles,1);

for i1 = 1:nmodfiles

    % Retrieve Data from the cell array:

    A = ModelCell{2,i1};

    % Resample the model data to reduce the number of points, or otherwise
    % the plots will be garbage in B&W

    % get the x-vector;

    Xvecfop = A(:,2);
    Yvec1fop = A(:,3);
    Yvec2fop = A(:,4);

    xfopmin = min(Xvecfop);
    xfopmax = max(Xvecfop);
    Xfopred = (linspace(xfopmin,xfopmax,nmodcorrpts))';

    Yfopired = interp1(Xvecfop,Yvec1fop,Xfopred,'spline');
    Yfop2red = interp1(Xvecfop,Yvec2fop,Xfopred,'spline');

    % Set the DE axes
    axes(h11a);

    DEmodhandl(i1,1) = line(Xfopred,Yfopired,'color','k','linestyle','-','linewidth',0.8...
        , 'marker','p','markersize',5);

    axes(h22a);

    VCmodhandl(i1,1) = line(Xfopred,Yfop2red,'color','k','linestyle','-','linewidth',0.8...
        , 'marker','p','markersize',5);

end

%*****
% Next steps:

% 1. Do curve fits on the theoretical data, and get the appropriate polynomials

% 2. Compute the small deflection stiffness matrices - EASY!!!, because we already have
%     the curve fits, where  $P = f(z)$  - just keep z small!!

%*****
%*****
% Perform curve fits on the theoretical data from Dave's curves

```

```

%*****
%*****

% Create a cell array with two rows: One for the polynomial coefficients and one
% for the regression correlation structure
DE_PolyCell_mod = cell(4,nmodfiles);
%DE_PolyCell_wrong_mod = cell(2,nmodfiles);

VC_PolyCell_mod = cell(4,nmodfiles);
%VC_PolyCell_wrong_mod = cell(2,nmodfiles);

for i1 = 1:nmodfiles

    % Load the appropriate model data
    A = ModelCell{2,i1};

    %Remember: A has the following column structure:
    % PHAC Pvary1 zDE zVc stress

    % Fit a curve to the Drive element, and then the valve cap:
    %!!!! NOTE We compute P as a function of X, and not the other way around !!!!!
    % !!!! AND THEN WE PLOT THE INVERSE !!!!!
    % Why.... Because if  $F = k1*x + k2*x^3$ , it DOES NOT MEAN THAT  $x = s1*F + s2*F^3$  !!!
    [P,S] = polyfit(A(:,3),A(:,2),DEPolydeg); %

    %Store this data into the new cell array

    DE_PolyCell_mod{1,i1} = P;
    DE_PolyCell_mod{2,i1} = S;

    % Now, we have to find the domain for this one

    xmin = min(A(:,3));
    xmax = max(A(:,3));

    %*****
    % Store PHPR and the domain

    P_hpr_x = modfileP_HPR_S(i1,1); % Also extract the corresponding PHPR

    DE_PolyCell_mod{3,i1} = P_hpr_x;
    DE_PolyCell_mod{4,i1} = [xmin xmax];

    %*****
    %*****

```

```

% Also fit the valve:
[P,S] = polyfit(A(:,4),A(:,2),VCPolydeg); % Linear fit for this data

%Store this data into the new cell array

VC_PolyCell_mod{1,i1} = P;
VC_PolyCell_mod{2,i1} = S;

% Now, we have to find the domain for this one

xmin = min(A(:,4));
xmax = max(A(:,4));

%*****
% Store PHPR and the domain

P_hpr_x = modfileP_HPR_S(i1,1); % Also extract the corresponding PHPR

VC_PolyCell_mod{3,i1} = P_hpr_x;
VC_PolyCell_mod{4,i1} = [xmin xmax];

%*****
%*****

end

%*****
%*****

% Now, we have all the fitted curves of P(z).

%*****
%*****

% Note, we will now change the signs to keep everything consistent

%*****
%*****

% Let us compute the pressures corresponding to the valve cap deflection specified
% in the USER INPUT section

Pcoefs = VC_PolyCell{1,Exp_Kidxs(1,1)}

```

```

% Compute the first drive element pressure
PDE1 = polyval(Pcoefs,zVCsdef1)

% Now determine the PHPR, based on the average between the PHPR
% taken for the measurement on the valve, and
% that of the measurement taken on the drive element.

PHPR1 = (DE_XYCell{1,Exp_Kidxs(1,1)} + VC_XYCell{1,Exp_Kidxs(1,1)})/2

% also, determine the zDE corresponding to this zVC

Pcoefs = DE_PolyCell{1,Exp_Kidxs(1,1)}
% subtract PDE1 from the constant term, to find the root.

size_poly = size(Pcoefs,2);

Pcoefs(1,size_poly) = Pcoefs(1,size_poly) - PDE1

zDE_s = roots(Pcoefs)

% Now we have to pick the correct root.

zDEidx = input('Please type in the index of the correct zDE in the matrix above...')

% Now assign zDE
zDEsdef1 = zDE_s(zDEidx,1);

%*****
% Second Experimental pressure condition
%*****

Pcoefs = VC_PolyCell{1,Exp_Kidxs(2,1)}

% Compute the first drive element pressure
PDE2 = polyval(Pcoefs,zVCsdef2)

% Now determine the PHPR, based on the average between the PHPR
% taken for the measurement on the valve, and
% that of the measurement taken on the drive element.

PHPR2 = (DE_XYCell{1,Exp_Kidxs(2,1)} + VC_XYCell{1,Exp_Kidxs(2,1)})/2

% also, determine the zDE corresponding to this zVC

Pcoefs = DE_PolyCell{1,Exp_Kidxs(2,1)}
% subtract PDE1 from the constant term, to find the root.

size_poly = size(Pcoefs,2)

Pcoefs(1,size_poly) = Pcoefs(1,size_poly) - PDE2

```

```

zDE_s = roots(Pcoefs)

% Now we have to pick the correct root.

zDEidx = input('Please type in the index of the correct zDE in the matrix above...')

% Now assign zDE
zDEsdef2 = zDE_s(zDEidx,1);

%*****

XXXXXXXXXXXXXXXXXXXXXXXXXXXXXXXXXXXXXXXXXXXXXXXXXXXXXXXXXXXXXXXXXXXX
% Assign the matrices to solve for BOTH Stiffness AND COMPLIANCE

Press_EXP = [PDE1
              PHPR1
              PDE2
              PHPR2];

Defls_EXP = [zDEsdef1 zVCsdef1 0 0
              0 0 zDEsdef1 zVCsdef1
              zDEsdef2 zVCsdef2 0 0
              0 0 zDEsdef2 zVCsdef2];

Dvect_EXP = [zDEsdef1
              zVCsdef1
              zDEsdef2
              zVCsdef2];

Pmatx_EXP = [PDE1 PHPR1 0 0
              0 0 PDE1 PHPR1
              PDE2 PHPR2 0 0
              0 0 PDE2 PHPR2];

XXXXXXXXXXXXXXXXXXXXXXXXXXXXXXXXXXXXXXXXXXXXXXXXXXXXXXXXXXXXXXXXXXXX

Betas_EXP = inv(Defls_EXP)*Press_EXP
Svect_EXP = inv(Pmatx_EXP)*Dvect_EXP

epsilon_EXP = (zDEsdef1-zDEsdef2)/(zDEsdef2)

delta_EXP = (zVCsdef1-zVCsdef2)/(zVCsdef2)

epsilon2_EXP = (PDE1-PDE2)/PDE1
delta2_EXP = (PHPR1-PHPR2)/PHPR1

%*****
%*****

% DO THE SAME FOR THE THEORETICAL DATA

```

```

%*****

Pcoefs = VC_PolyCell_mod{1,Theo_Kidxs(1,1)}

% Compute the first drive element pressure
PDE1 = polyval(Pcoefs,zVCsdef1)

% Now determine the PHPR, from user input

PHPR1 = modfileP_HPR_S(Theo_Kidxs(1,1),1)

% also, determine the zDE corresponding to this zVC

Pcoefs = DE_PolyCell_mod{1,Theo_Kidxs(1,1)};
% subtract PDE1 from the constant term, to find the root.

size_poly = size(Pcoefs,2);

Pcoefs(1,size_poly) = Pcoefs(1,size_poly) - PDE1;

zDE_s = roots(Pcoefs)

% Now we have to pick the correct root.

zDEidx = input('Please type in the index of the correct zDE in the matrix above...')

% Now assign zDE
zDEsdef1 = zDE_s(zDEidx,1);

%*****
% Second THEORETICAL pressure condition
%*****

Pcoefs = VC_PolyCell_mod{1,Theo_Kidxs(2,1)}

% Compute the first drive element pressure
PDE2 = polyval(Pcoefs,zVCsdef2)

PHPR2 = modfileP_HPR_S(Theo_Kidxs(2,1),1)

% also, determine the zDE corresponding to this zVC

Pcoefs = DE_PolyCell_mod{1,Theo_Kidxs(2,1)};
% subtract PDE1 from the constant term, to find the root.

size_poly = size(Pcoefs,2);

Pcoefs(1,size_poly) = Pcoefs(1,size_poly) - PDE2;

```

```

zDE_s = roots(Pcoefs)

% Now we have to pick the correct root.

zDEidx = input('Please type in the index of the correct zDE in the matrix above...')

% Now assign zDE
zDEsdef2 = zDE_s(zDEidx,1);

%*****

%%%%%%%%%%%%%%%%%%%%%%%%%%%%%%%%%%%%%%%%%%%%%%%%%%%%%%%%%%%%%%%%%%%%%%%%%%%%%%
% Assign the matrices to solve for BOTH Stiffness AND COMPLIANCE
%%%%%%%%%%%%%%%%%%%%%%%%%%%%%%%%%%%%%%%%%%%%%%%%%%%%%%%%%%%%%%%%%%%%%%%%%%%%%%

Press_THEO = [PDE1
              PHPR1
              PDE2
              PHPR2];

Defls_THEO = [zDEsdef1 zVCsdef1 0 0
              0 0 zDEsdef1 zVCsdef1
              zDEsdef2 zVCsdef2 0 0
              0 0 zDEsdef2 zVCsdef2];

Dvect_THEO = [zDEsdef1
              zVCsdef1
              zDEsdef2
              zVCsdef2];

Pmatx_THEO = [PDE1 PHPR1 0 0
              0 0 PDE1 PHPR1
              PDE2 PHPR2 0 0
              0 0 PDE2 PHPR2];

%%%%%%%%%%%%%%%%%%%%%%%%%%%%%%%%%%%%%%%%%%%%%%%%%%%%%%%%%%%%%%%%%%%%%%%%%%%%%%

format short e

Betas_THEO = inv(Defls_THEO)*Press_THEO
Svect_THEO = inv(Pmatx_THEO)*Dvect_THEO

% Output the "delta indicators" for the terms that are different
% in the matrices we are solving.
% If they are < 0.5, we are probably in trouble
epsilon_THEO = (zDEsdef1-zDEsdef2)/(zDEsdef1)
epsilon_EXP

delta_THEO = (zVCsdef1-zVCsdef2)/(zVCsdef1)

epsilon2_THEO = (PDE1-PDE2)/PDE1
delta2_THEO = (PHPR1-PHPR2)/PHPR1

```



```

delta_EXP

epsilon2_EXP
delta2_EXP

Betas_EXP
Svect_EXP

BetaME = [Betas_EXP(1,1) Betas_EXP(2,1)
          Betas_EXP(3,1) Betas_EXP(4,1)]

SmatxME = [Svect_EXP(1,1) Svect_EXP(2,1)
           Svect_EXP(3,1) Svect_EXP(4,1)]

BetaMT = [Betas_THEO(1,1) Betas_THEO(2,1)
          Betas_THEO(3,1) Betas_THEO(4,1)]

SmatxMT = [Svect_THEO(1,1) Svect_THEO(2,1)
           Svect_THEO(3,1) Svect_THEO(4,1)]

format short

%% NEXT STEP - plot the chosen points on the graphs!!!!

% Drive element piston
axes(h11a);

DEsEXPptshand = line([Press_EXP(1,1) Press_EXP(3,1)],...
                    [Defls_EXP(1,1) Defls_EXP(3,1)], 'color', 'r', 'linestyle', 'none', 'marker', '*', ...
                    'MarkerSize', 12);

DEsTHPptshand = line([Press_THEO(1,1) Press_THEO(3,1)],...
                    [Defls_THEO(1,1) Defls_THEO(3,1)], 'color', 'k', 'linestyle', 'none', 'marker', 'x', ...
                    'MarkerSize', 12);

%Valve Piston!!!!
axes(h22a);

VCsEXPptshand = line([Press_EXP(1,1) Press_EXP(3,1)],...
                    [Defls_EXP(1,2) Defls_EXP(3,2)], 'color', 'r', 'linestyle', 'none', 'marker', '*', ...
                    'MarkerSize', 12);

VCsTHPptshand = line([Press_THEO(1,1) Press_THEO(3,1)],...
                    [Defls_THEO(1,2) Defls_THEO(3,2)], 'color', 'k', 'linestyle', 'none', 'marker', 'x', ...
                    'MarkerSize', 12);

```

```

%*****
%*****
%*****
%*****

% Attempt at making 3d plots of the following:

% 1: Experimental data
% 2: Model data
% 3: Experimental stiffness plane
% 4: Theoretical stiffness plane

%*****
%*****
%*****
%*****
%*****

%*****
% Nonlinear plots first - they look cooler

% We will use the following variables:

% VC_PolyCell_mod
% VC_PolyCell
% DE_PolyCell_mod
% DE_PolyCell

% All of the above have the following structure:

% Row1: Polynomial Coefs for polyeval function
% Row2: An S-structure for error estimation
% Row3: The corresponding PPHR at which the fit was done
% Row4: The xmin and xmax values over which the curve fit
% is valid. THIS IS NB, because we hardcode invert the fcns!!!

%*****

[XMATX,YMATX,VCE_ZMATX] = hac3dinterp1(VC_PolyCell,nfcnpts,n3dpts,Ppismmin,Ppismmax,...
    Phprmin,Phprmax);
[XMATX,YMATX,VCT_ZMATX] = hac3dinterp1(VC_PolyCell_mod,nfcnpts,n3dpts,Ppismmin,...
    Ppismmax,Phprmin,Phprmax);
[XMATX,YMATX,DEE_ZMATX] = hac3dinterp1(DE_PolyCell,nfcnpts,n3dpts,Ppismmin,...
    Ppismmax,Phprmin,Phprmax);
[XMATX,YMATX,DET_ZMATX] = hac3dinterp1(DE_PolyCell_mod,nfcnpts,n3dpts,Ppismmin,...
    Ppismmax,Phprmin,Phprmax);

```

```

VCDE3D1handl = figure('color','w','position',[100 180 900 450]);

hold on;

VC3Daxes1 = subplot(1,2,1);
set(VC3Daxes1,'linewidth',2,'box','on');

VC3dmeshh1 = surface(XMATX,YMATX,VCT_ZMATX,'facecolor','none','edgecolor',...
    [0.6 0.6 0.6],'linewidth',0.8)
VC3dmeshh2 = surface(XMATX,YMATX,VCE_ZMATX,'facecolor','none','edgecolor',...
    [0 0 0],'linewidth',1)

% Set view before resize
view(-37.5,30);
% Set position after the plot is complete
set(VC3Daxes1,'units','pixels','position',[60 60 340 310]);

xlabel(xPde_labl3D);
ylabel(yPhpr_labl3D);
zlabel(zvc_labl);
title({'Small piston deflection:','Theoretical vs. Experimental'})
legend('Model','Experiment')

DE3Daxes1 = subplot(1,2,2);

set(DE3Daxes1,'linewidth',2,'box','on');

DE3dmeshh1 = surface(XMATX,YMATX,DET_ZMATX,'facecolor','none','edgecolor',...
    [0.6 0.6 0.6],'linewidth',0.8)
DE3dmeshh2 = surface(XMATX,YMATX,DEE_ZMATX,'facecolor','none','edgecolor',...
    [0 0 0],'linewidth',1)

% Set view before resize
view(-37.5,30);
% Set position after the plot is complete
set(DE3Daxes1,'units','pixels','position',[490 60 340 310]);

xlabel(xPde_labl3D);
ylabel(yPhpr_labl3D);
zlabel(zde_labl);
title({'Large piston deflection:','Theoretical vs. Experimental'})
legend('Model','Experiment')

%*****
%*****
%*****

```

```

% Now we compute xyz data for the linear functions, the stiffness estimates

% We have the following two matrices to use:

%SmatxME - experimental "compliance"

%SmatxMT - theoretical "compliance"

% [ zDE ]   =   [s11  s12] [PPIS]
% [ zVC ]     [s21  s22] [PHPR]

%*****
%*****
%*****

% This is very easy, because we have XMATX and YMATX:

DESE_ZMATX = zeros(n3dpts);
DEST_ZMATX = zeros(n3dpts);
VCSE_ZMATX = zeros(n3dpts);
VCST_ZMATX = zeros(n3dpts);

for i1 = 1:n3dpts %x-index, or the PDE index
    for i2 = 1:n3dpts % y-index or the PHPR index

        Pminivect = [XMATX(i1,i2)
                     YMATX(i1,i2)];

        DESE_ZMATX(i1,i2) = SmatxME(1,:)*Pminivect;

        DEST_ZMATX(i1,i2) = SmatxMT(1,:)*Pminivect;

        VCSE_ZMATX(i1,i2) = SmatxME(2,:)*Pminivect;

        VCST_ZMATX(i1,i2) = SmatxMT(2,:)*Pminivect;

    end
end

VCDE3D2hand1 = figure('color','w','position',[100 180 900 450]);

VC3Daxes2 = subplot(1,2,1)
set(VC3Daxes2,'linewidth',2,'box','on');

VC3dmeshh21 = surface(XMATX,YMATX,VCST_ZMATX,'facecolor','none','edgecolor','b')
VC3dmeshh22 = surface(XMATX,YMATX,VCSE_ZMATX,'facecolor','none','edgecolor','k')

```

```

% Set view before resize
view(-37.5,30);
% Set position after the plot is complete
set(VC3Daxesh2,'units','pixels','position',[60 60 340 310]);

xlabel(xPde_lab13D);
ylabel(yPhpr_lab13D);
zlabel(zvc_lab1);
title({'Small piston linear stiffness:','Theoretical vs. Experimental'})
legend('Model','Experiment')

DE3Daxesh2 = subplot(1,2,2)
set(DE3Daxesh2,'linewidth',2,'box','on');

DE3dmeshh21 = surface(XMATX,YMATX,DEST_ZMATX,'facecolor','none','edgecolor','b')
DE3dmeshh22 = surface(XMATX,YMATX,DESE_ZMATX,'facecolor','none','edgecolor','k')

% Set view before resize
view(-37.5,30);
% Set position after the plot is complete
set(DE3Daxesh2,'units','pixels','position',[490 60 340 310]);

xlabel(xPde_lab13D);
ylabel(yPhpr_lab13D);
zlabel(zde_lab1);
title({'Large piston linear stiffness:','Theoretical vs. Experimental'})
legend('Model','Experiment')

%*****
%*****
%*****

% Overplot the two experimental linear stiffness meshes with their corresponding
%nonlinear buddies.

VC3D3handl = figure('color','w','position',[100 180 900 450]);

VC3Daxesh3 = subplot(1,2,1)
set(VC3Daxesh3,'linewidth',2,'box','on');

```

```

VC3dmeshh31 = surface(XMATX,YMATX,VCE_ZMATX,'facecolor','none','edgecolor','b')

VC3dmeshh32 = surface(XMATX,YMATX,VCSE_ZMATX,'facecolor','none','edgecolor','r')

% Set view before resize
view(-37.5,30);
% Set position after the plot is complete
set(VC3Daxesh3,'units','pixels','position',[60 60 340 310]);

xlabel(xPde_lab13D);
ylabel(yPhpr_lab13D);
zlabel(zvc_lab1);
title({'Small piston Comparison:' ; 'Experimental Nonlinear vs. Linearised about  $z_{\{2\}} = 0\}$ })
legend('Experiment','Linearization')

DE3Daxesh3 = subplot(1,2,2)
set(DE3Daxesh3,'linewidth',2,'box','on');

DE3dmeshh31 = surface(XMATX,YMATX,DEE_ZMATX,'facecolor','none','edgecolor','b')

DE3dmeshh32 = surface(XMATX,YMATX,DESE_ZMATX,'facecolor','none','edgecolor','r')

% Set view before resize
view(-37.5,30);
% Set position after the plot is complete
set(DE3Daxesh3,'units','pixels','position',[490 60 340 310]);

xlabel(xPde_lab13D);
ylabel(yPhpr_lab13D);
zlabel(zde_lab1);
title({'Large piston Comparison:' ; 'Experimental Nonlinear vs. Linearised about  $z_{\{1\}} = 0\}$ })
legend('Experiment','Linearization')

%*****
%*****
%*****

%*****
%*****
% Create line plots to show the equivalence of the stiffness matrices

```

```

% Just overplot them over the original plots
% Both experimental and also theoretical

DEexpSMatH = zeros(nDEplt,1);
VCexpSMatH = zeros(nDEplt,1);

for i1 = 1:nDEplt

    % Displacement vector

    zde_vect_fop = zeros(n3dpts,1);

    % We will use XMATX again - why not?!

    PHPR1 = DE_PolyCell{3,i1};

    for i2 = 1:n3dpts
        Pminivect = [XMATX(i2,1)
                     PHPR1];
        zde_vect_fop(i2,1) = SmatxME(1,:)*Pminivect;
    end

    axes(h11a);
    DEexpSMatH(i1,1) = line(XMATX(:,1),zde_vect_fop);

    zde_vect_fop = zeros(n3dpts,1);

    % We will use XMATX again - why not?!

    PHPR1 = VC_PolyCell{3,i1};

    for i2 = 1:n3dpts
        Pminivect = [XMATX(i2,1)
                     PHPR1];
        zde_vect_fop(i2,1) = SmatxME(2,:)*Pminivect;
    end

    axes(h22a);
    VCexpSMatH(i1,1) = line(XMATX(:,1),zde_vect_fop);

end

% Now the theoretical overplots:

DEthSMatH = zeros(nDEplt,1);
VCthSMatH = zeros(nDEplt,1);

```

[illegible]


```

%*****
%*****

%*****
%*****

set(VCexpSMatH,'linestyle','-','color',[0.5 0.5 0.5],'marker','none','markersize',...
    4,'linewidth',0.5)
set(DEexpSMatH,'linestyle','-','color',[0.5 0.5 0.5],'marker','none','markersize',...
    4,'linewidth',0.5)

set(VCthSMatH,'linestyle','-','color',[0.5 0.5 0.5],'marker','p','markersize',4,...
    'linewidth',0.5)
set(DEthSMatH,'linestyle','-','color',[0.5 0.5 0.5],'marker','p','markersize',4,...
    'linewidth',0.5)

% Set the axes limits, labels and line thicknesses:

set(h11a,'xlim',xPde_lims,'ylim',yde_lims,'linewidth',2,'fontsize',12);
set(h22a,'xlim',xPde_lims,'ylim',yvc_lims,'linewidth',2,'fontsize',12);

axes(h11a)

xlabel(xPde_labl)
ylabel(zde_labl)
%title('Large piston motion vs. Applied pressure');

% Add a legend to the fits
%DElegendhandl = legend(DEfithandl,'P_2=0','P_2=92','P_2=298','P_2=500',2);

axes(h22a)
xlabel(xPde_labl)
ylabel(zvc_labl)
%VClegendhandl = legend(VCfithandl,'P_2=0','P_2=92','P_2=298','P_2=500',2);

set(DEfithandl,'color','k','linewidth',2);
set(VCfithandl,'color','k','linewidth',2);
set(DEebarhandl(1,:), 'color','k','linewidth',2);
set(VCebarhandl(1,:), 'color','k','linewidth',2);

set(DElabhdl,'fontsize',curvelegfntsiz);
set(VClabhdl,'fontsize',curvelegfntsiz);

set(DElinehandl,'linewidth',0.8,'color',[0.75 0.75 0.75])
set(VClinehandl,'linewidth',0.8,'color',[0.75 0.75 0.75])

```

```

% Get the graphs right for the stage of plotting we're in:

legends2d = cell(2,2);

switch Plotstage
case 1
    delete(DEmodhandl);
    delete(VCmodhandl);
    delete(DEexpSMatH);
    delete(VCexpSMatH);
    delete(DEthSMatH);
    delete(VCthSMatH);
    % Legend
    [legends2d{1,1},legends2d{1,2}] = legend(h11a,[DElinehandl(1,1) DEfithandl(1,1)]...
        ,'Data','Fit to Data',2);
    [legends2d{2,1},legends2d{2,2}] = legend(h22a,[VClinehandl(1,1) VCfithandl(1,1)]...
        ,'Data','Fit to Data',2);
case 2
    delete(DElinehandl);
    delete(VClinehandl);
    delete(DEebarhandl(1,:));
    delete(VCebarhandl(1,:));
    delete(DEexpSMatH);
    delete(VCexpSMatH);
    delete(DEthSMatH);
    delete(VCthSMatH);
    % Legend
    [legends2d{1,1},legends2d{1,2}] = legend(h11a,[DEfithandl(1,1) DEmodhandl(1,1)]...
        ,'Fit to Data','Model Prediction',2);
    [legends2d{2,1},legends2d{2,2}] = legend(h22a,[VCfithandl(1,1) VCmodhandl(1,1)]...
        ,'Fit to Data','Model Prediction',2);
case 3
    delete(DEebarhandl(1,:));
    delete(VCebarhandl(1,:));
    delete(DElinehandl);
    delete(VClinehandl);
    % Legend
    [legends2d{1,1},legends2d{1,2}] = legend(h11a,...
        [DEfithandl(1,1) DEmodhandl(1,1) DEexpSMatH(1,1) DEthSMatH(1,1)],...
        'Fit to Data','Model Prediction','Slope of data at 0','Slope of model at 0',2);
    [legends2d{2,1},legends2d{2,2}] = legend(h22a,...
        [VCfithandl(1,1) VCmodhandl(1,1) VCexpSMatH(1,1) VCthSMatH(1,1)],...
        'Fit to Data','Model Prediction','Slope of data at 0','Slope of model at 0',2);

end

set(legends2d{1,2}(1,1),'fontsize',10);
set(legends2d{2,2}(1,1),'fontsize',10);

```

```

%*****
%*****

%*****
%*****

%*****
%*****

%*****
%*****

%*****
%*****
%*****
%*****
%*****
%*****
%*****
%*****
%*****
%*****
%*****
%*****
%*****
%*****
%*****
%*****
%*****

% Plot out the stiffness matrices in a nice readable format:
disp(sprintf('*****'))
disp(sprintf('*****'))
disp(sprintf('***** Output of the stiffness matrix solutions *****'))
disp(sprintf('*****'))
disp(sprintf('*****'))
disp(sprintf('\n\nTheoretical inverse compressibility matrix, where:\n'))
disp(sprintf('{P1} = [b11 b12] {z1}'))
disp(sprintf('{P2} = [b21 b22] {z2}\n\n'))

disp(sprintf('Units are in kPa/um:'))

disp(sprintf('{P1} = [%11.3e %11.3e] {z1}',BetaMT(1,1),BetaMT(1,2)))
disp(sprintf('{P2} = [%11.3e %11.3e] {z2}',BetaMT(2,1),BetaMT(2,2)))

disp(sprintf('\n\nExperimental inverse compressibility matrix in kPa/um:\n'))

disp(sprintf('{P1} = [%11.3e %11.3e] {z1}',BetaME(1,1),BetaME(1,2)))
disp(sprintf('{P2} = [%11.3e %11.3e] {z2}',BetaME(2,1),BetaME(2,2)))

disp(sprintf('\n\nRatio of the elements of the matrices:\n'))

Betaratio = BetaMT./BetaME;

```

202 D Computer code

```

disp(sprintf('%6.1f %6.1f',Betaratio(1,1),Betaratio(1,2)))
disp(sprintf('%6.1f %6.1f',Betaratio(2,1),Betaratio(2,2)))

% Also subtract the measured stiffnesses from the theo and exp data

BetaTildeTHEO = BetaMT - psi1psi2T;
BetaTildeEXP = BetaME - psi1psi2E;

disp(sprintf('\n\nD-Tilde, THEORETICAL in kPa/um:\n'))

disp(sprintf('%11.3e %11.3e',BetaTildeTHEO(1,1),BetaTildeTHEO(1,2)))
disp(sprintf('%11.3e %11.3e',BetaTildeTHEO(2,1),BetaTildeTHEO(2,2)))

disp(sprintf('\n\nD-Tilde, EXPERIMENTAL in kPa/um:\n'))

disp(sprintf('%11.3e %11.3e',BetaTildeEXP(1,1),BetaTildeEXP(1,2)))
disp(sprintf('%11.3e %11.3e',BetaTildeEXP(2,1),BetaTildeEXP(2,2)))

disp(sprintf('\n\nRatio of the elements of the D-Tilde matrices:\n'))

DTilderatio = BetaTildeTHEO./BetaTildeEXP;

disp(sprintf('%6.1f %6.1f',DTilderatio(1,1),DTilderatio(1,2)))
disp(sprintf('%6.1f %6.1f',DTilderatio(2,1),DTilderatio(2,2)))

disp(sprintf('*****'))
disp(sprintf('\n\nTheoretical compressibility matrix, where:\n'))
disp(sprintf('{z1} = [b11 b12] {P1}'))
disp(sprintf('{z2} = [b21 b22] {P2}\n\n'))

disp(sprintf('Units are in kPa/um:'))

disp(sprintf('{z1} = [%11.3e %11.3e] {P1}',SmatxMT(1,1),SmatxMT(1,2)))
disp(sprintf('{z2} = [%11.3e %11.3e] {P2}',SmatxMT(2,1),SmatxMT(2,2)))

disp(sprintf('\n\nExperimental Compressibility matrix in kPa/um:\n'))

disp(sprintf('{z1} = [%11.3e %11.3e] {P1}',SmatxME(1,1),SmatxME(1,2)))
disp(sprintf('{z2} = [%11.3e %11.3e] {P2}',SmatxME(2,1),SmatxME(2,2)))

disp(sprintf('\n\nRatio of the elements of the matrices:\n'))

Sratio = SmatxMT./SmatxME;

disp(sprintf('%6.1f %6.1f',Sratio(1,1),Sratio(1,2)))
disp(sprintf('%6.1f %6.1f',Sratio(2,1),Sratio(2,2)))

disp(sprintf('*****'))
disp(sprintf('*****'))

```

```

%*****
%*****
%*****
%*****
%*****
%*****
%***** COMPUTING AMPLIFICATION RATIOS *****
%*****
%*****
%*****
%*****
%*****
%*****
%*****
%*****
%*****
%*****

% This will make for a cool 3D plot sometime.....

% This subprogram will compute the amplification ratios
% based on fitted theoretical and fitted experimental data
% by differentiating the polynomials and looking at the relative change in AR

hAR = figure('color','w');
hARa = axes('box','on');

ARexphandl = zeros(nDEplt,1);
ARmodhandl = zeros(nmodfiles,1);

ARexplabhdl = zeros(nDEplt,1);
ARmodlabhdl = zeros(nmodfiles,1);

curvefractAR = [0.2
    0.4
    0.6
    0.8];

% First, we look at the experimental data:

for i1 = 1:nDEplt

    A1 = DE_PolyCell{1,i1}; % Extract the Drive element polynomial
    A2 = VC_PolyCell{1,i1}; % Extract the Valve cap polynomial

    PHPRfop = modfileP_HPR_S(i1,1); % extract the estimated PHPR

    % compute the derivatives of the polynomials

```

```
dA1 = polyder(A1); % dP1/dz1
dA2 = polyder(A2); % dP2/dz2

% Find values for these
% at the appropriate values for z1,z2

z1lims = DE_PolyCell{4,i1};
z2lims = VC_PolyCell{4,i1};

z1vect = (linspace(z1lims(1,1),z1lims(1,2),ncfitpts))';
z2vect = (linspace(z2lims(1,1),z2lims(1,2),ncfitpts))';

% Also create a regularly spaced P1 vector, because we will interpolate
% So that we can eventually compare apples with apples

P1reg = (linspace(Ppismmin,Ppismmax,ncfitpts))';

% Now, we evaluate the derivative of the function at each value of z
% ALSO evaluate the function ITSELF at each value of z

P1_fz1_irreg = polyval(A1,z1vect);
P1_gz2_irreg = polyval(A2,z2vect);

% dP1/dz1 = polyval(dA1,z1vect);
% dP2/dz2 = polyval(dA2,z2vect);

% Interpolate to have irregular z vectors for each P1 vector

z1irregP1 = interp1(P1_fz1_irreg,z1vect,P1reg,'spline');
z2irregP1 = interp1(P1_gz2_irreg,z2vect,P1reg,'spline');

% Now, each of the irregular z's has a little friend in P1reg

% For each IRREGULAR z we can compute the corresponding dP/dz

dP1dz1_dfz1 = polyval(dA1,z1irregP1); % Now we have the derivatives
dP1dz2_dgz2 = polyval(dA2,z2irregP1);

% Each of the two functions above also has a matching value in P1reg

% The amplification ratio is dz2/dz1 ===== (dP1/dz1)/(dP1/dz2) - check it

AR_P1reg = dP1dz1_dfz1./dP1dz2_dgz2;

% Plot the amplification ratio on the graph

axes(hARa);

ARexphand1(i1,i) = line(P1reg,AR_P1reg);
```

```

%*****
% Place a legend for PHPR on the plot

ctext1 = strcat('P_2=',strcat(num2str(modfileP_HPR_S(i1,1),'%4.0f'),'kPa'));

ARexplabhd1(i1,1) = curvelabel2(ctext1,hARa,[0 500],[0 22],...
    curvefractAR(i1,1),Pireg,AR_Pireg);

%*****

%*****

end

%Now, the model:

for i1 = 1:nmodfiles

    A1 = DE_PolyCell_mod{1,i1}; % Extract the Drive element polynomial
    A2 = VC_PolyCell_mod{1,i1}; % Extract the Valve cap polynomial

    PHPRfop = modfileP_HPR_S(i1,1); % extract the estimated PHPR

    z1lims = DE_PolyCell_mod{4,i1};
    z2lims = VC_PolyCell_mod{4,i1};

    % compute the derivatives of the polynomials

    dA1 = polyder(A1); % dP1/dz1
    dA2 = polyder(A2); % dP2/dz2

    % Find values for these
    % at the appropriate values for z1,z2

    z1vect = (linspace(z1lims(1,1),z1lims(1,2),ncfitpts))';
    z2vect = (linspace(z2lims(1,1),z2lims(1,2),ncfitpts))';

    % Also create a regularly spaced P1 vector, because we will interpolate
    % So that we can eventually compare apples with apples

    Pireg = linspace(Ppismmin,Ppismmax,ncfitpts);

    % Now, we evaluate the derivative of the function at each value of z
    % ALSO evaluate the function ITSELF at each value of z

```

```

P1_fz1_irreg = polyval(A1,z1vect);
P1_gz2_irreg = polyval(A2,z2vect);

% dP/dz1 = polyval(dA1,z1vect);
% dP/dz2 = polyval(dA2,z2vect);

% Interpolate to have irregular z vectors for each P1 vector

z1irregP1 = interp1(P1_fz1_irreg,z1vect,P1reg,'spline');
z2irregP1 = interp1(P1_gz2_irreg,z2vect,P1reg,'spline');

% Now, each of the irregular z's has a little friend in P1reg

% For each IRREGULAR z we can compute the corresponding dP/dz

dP1dz1_dfz1 = polyval(dA1,z1irregP1); % Now we have the derivatives
dP1dz2_dgz2 = polyval(dA2,z2irregP1);

% Each of the two functions above also has a matching value in P1reg

% The amplification ratio is dz2/dz1 ===== (dP1/dz1)/(dP1/dz2) - check it

AR_P1reg = dP1dz1_dfz1./dP1dz2_dgz2;

% Plot the amplification ratio on the graph

axes(hARa);

ARmodhand1(i1,1) = line(P1reg,AR_P1reg,'color','k');
%*****
% Place a legend for PHPR on the plot
ctext1 = strcat('P_2=',strcat(num2str(modfileP_HPR_S(i1,1),'%4.0f'),'kPa'));

ARmodlabhd1(i1,1) = curvelabel2(ctext1,hARa,[0 500],[0 22],...
    curvefractAR(i1,1),P1reg,AR_P1reg);
%*****

end

% Make the plot pretty

set(hARa,'linewidth',2,'fontsize',12,'xlim',[Ppimin Ppimax],'ylim',[0 23])
xlabel('P_1');
ylabel('Amplification Ratio (z_1/z_2)');

% Set the colors of the plots
set(ARexphand1,'color','k','linewidth',2);
set(ARmodhand1,'color',[0.5 0.5 0.5],'linewidth',1);

set(ARmodlabhd1,'fontsize',10,'color',[0.5 0.5 0.5]);

```



```
end % Postprocflag
```


Appendix E

Masks

This appendix contains a selection of masks from the set that was used to form the devices shown in Figure 2.2. It should give the reader an idea of what is involved in the creation of a multi-layered device with multiple silicon and glass layers. Figure E.1 shows the glass patterns of the full MHT device. All glass layers were ultrasonically machined. Prior to ultrasonic machining, wafer-scale align marks were patterned on the glass wafers using BOE. Care had to be taken during the exposure step, because the substrates were transparent. The ultrasonic machining was then done to the align marks provided. Figure E.2 shows different patterns for Layer 3, to be able to accommodate piezoelectric elements of various sizes. It also shows the pattern that was used for the static, pressure operated hydraulic amplifier (L3 Big Hole).

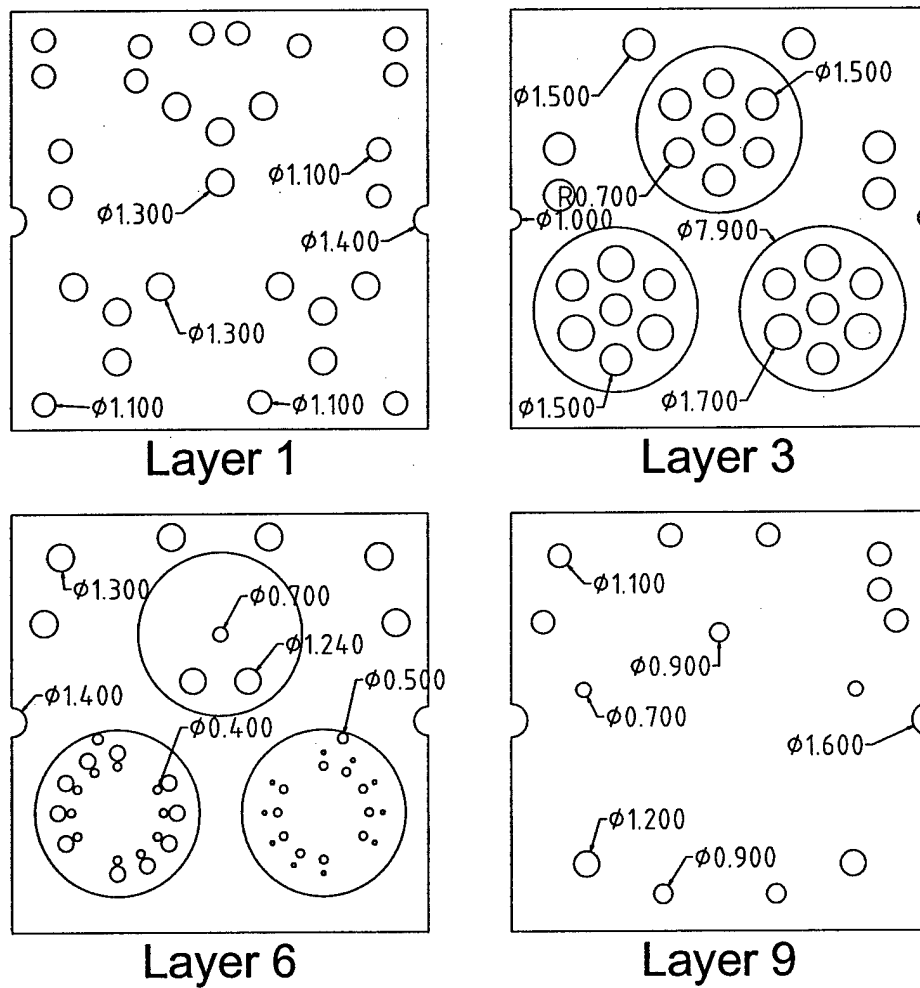
The masks for the large piston (Layers 4 and 5) are shown in Figures E.3 and E.4. Note the nearly identical process for the two layers. The main difference lies in the venting channels in Layer 5, and the venting holes in Layer 4.

Figure E.5 shows the mask flow for Layer 7, the layer containing the small pistons. In this figure, a mask set for a device with a single small piston is shown. Ten small pistons were created using the same mask flow, but with different geometries.

In Figure E.6 the masks for Layer 8 are shown, along with a mask set for an hydraulic amplifier with two small pistons (which was not tested). Note, especially in this figure, the use of so-called "halo" masks to etch through-wafer features. Halo masks are often used for performing uniform DRIE etching when features of various sizes are present on the wafer. Keeping the trench width constant for all through-wafer features helps to maintain a constant etch rate.

Figure E.7 is the wafer scale process flow associated with Figure E.5. Note the steps for creating features such as align marks and cutting lines for the dicing operation.

A plan view for all the layers of the full MHT device is shown in Figure E.8. This figure is an overlay of all the masks needed to fabricate the device.



Courtesy of H.Q. Li

Figure E.1: The glass layers of the full ten valve MHT device.

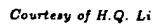
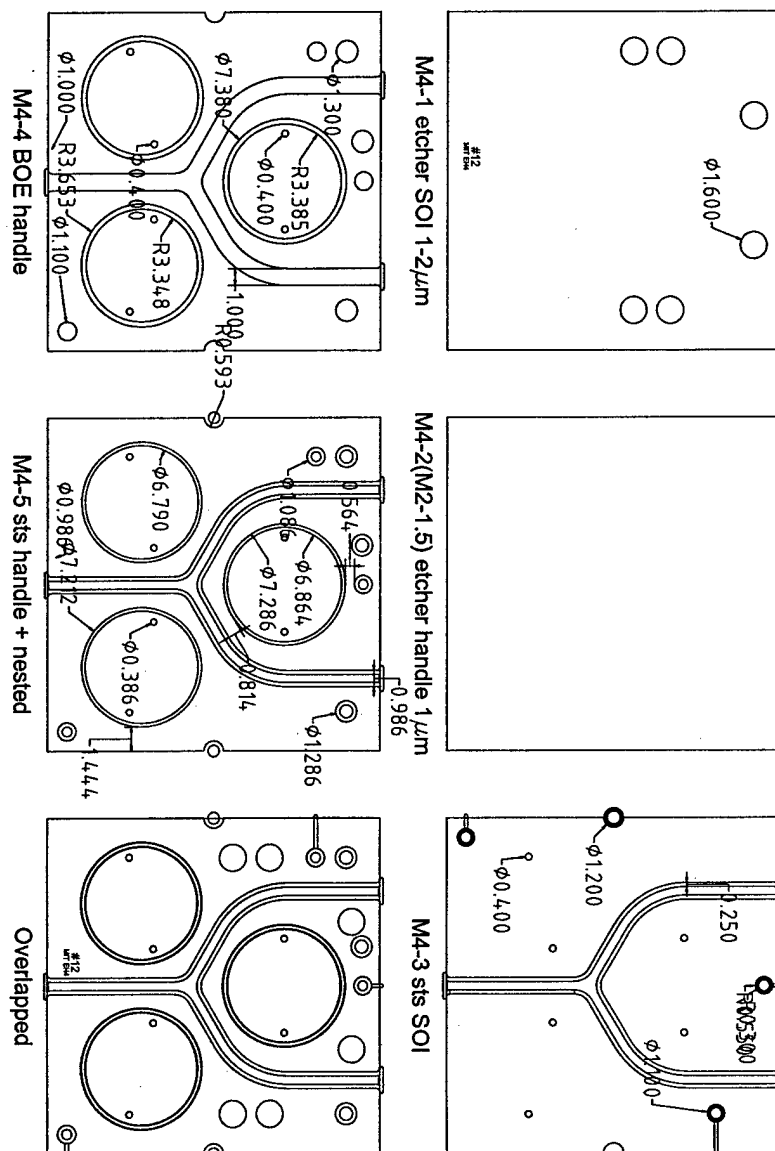
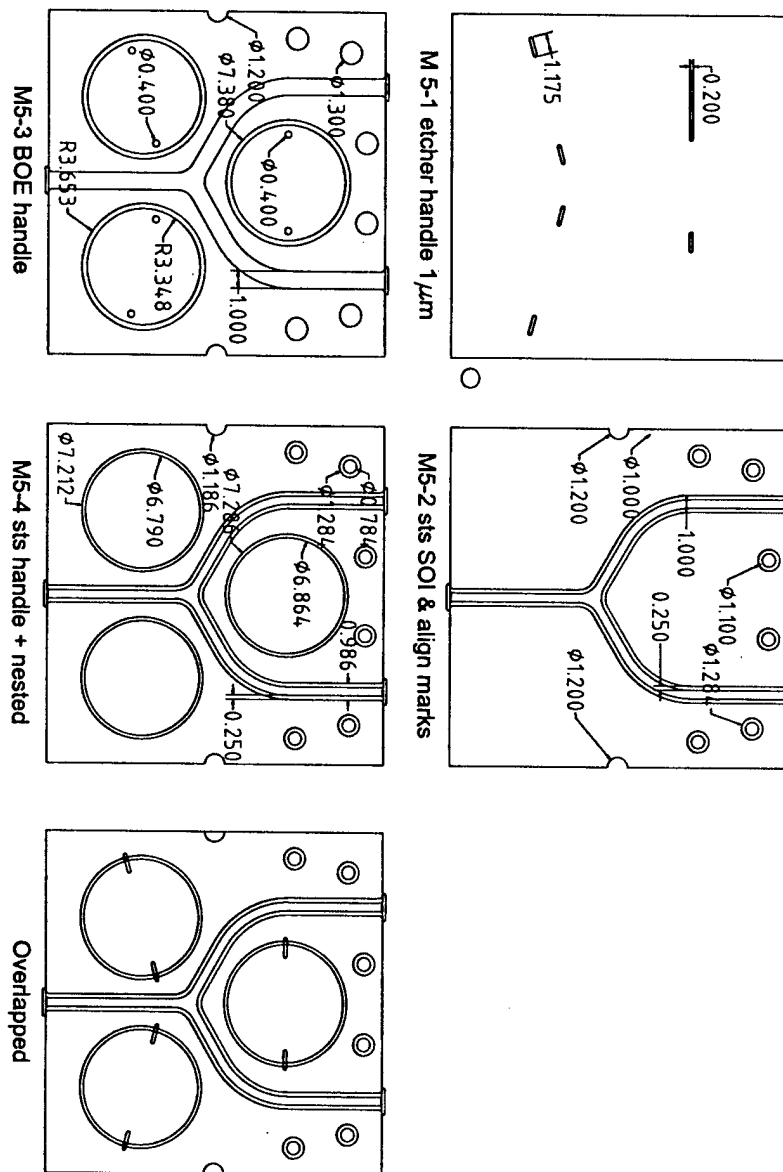


Figure E.2: Different configurations for Layer 3. L3-3 is the standard Layer 3, L3-4 is for accommodating a single large piezoelectric element, L3-5 has additional holes for optical displacement measurement and L3 Big Hole was used for the static hydraulic amplifiers.



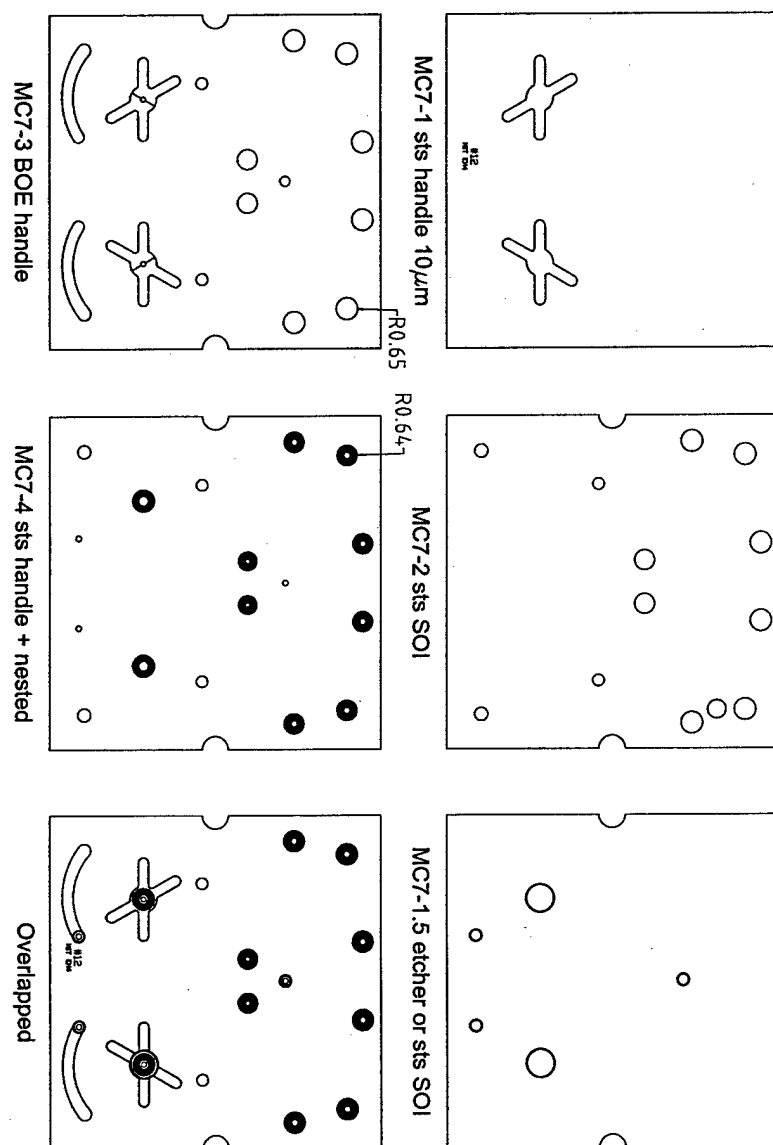
Courtesy of H.Q. Li

Figure E.3: Mask set for Layer 4.



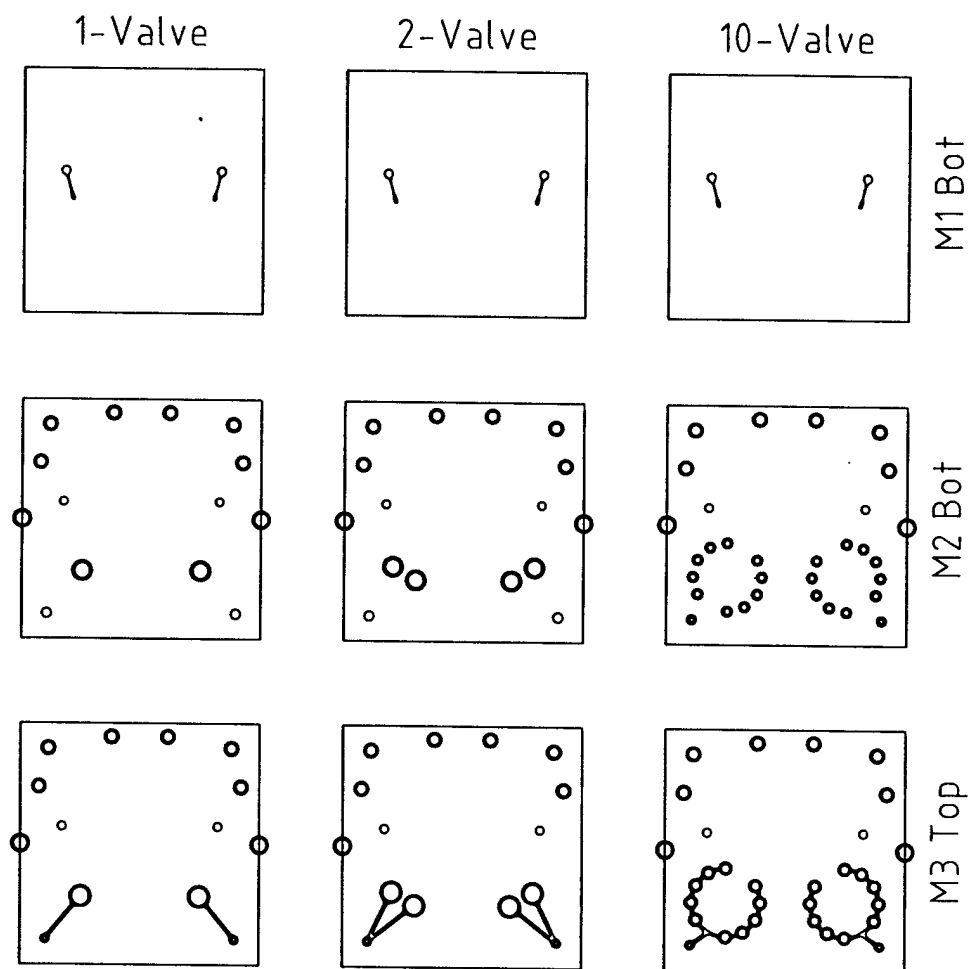
Courtesy of H.Q. Li

Figure E.4: Mask set for Layer 5.



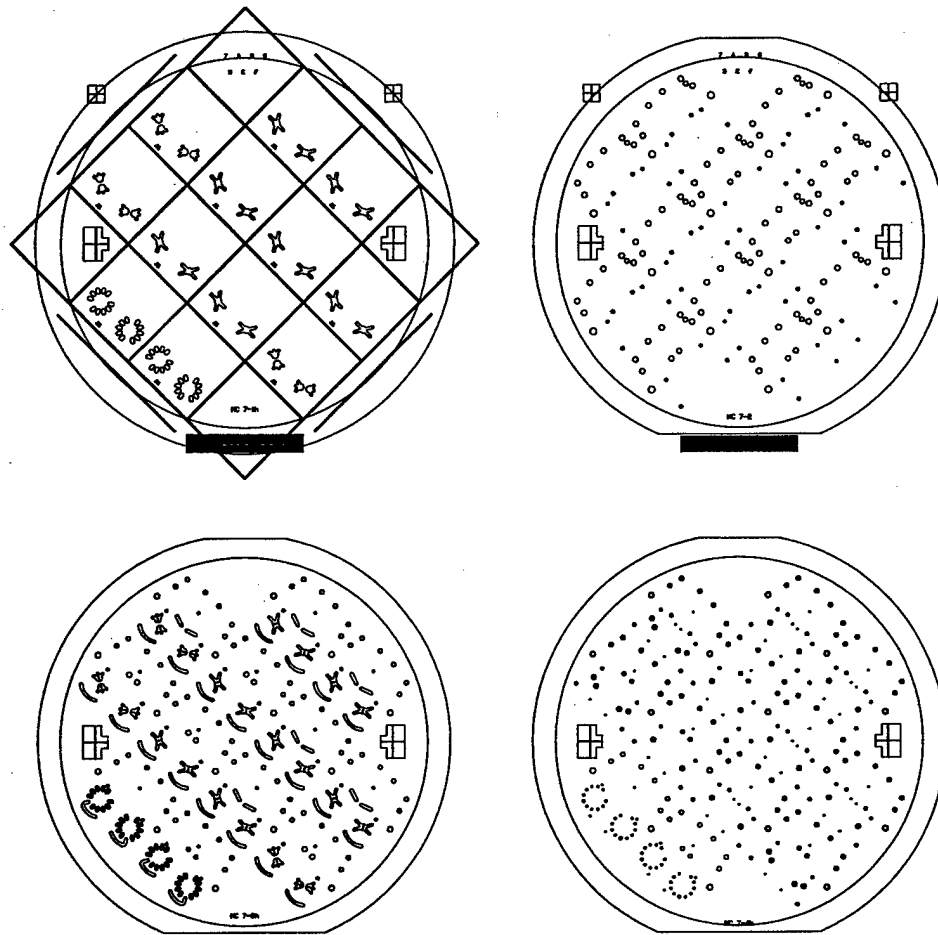
Courtesy of H.Q. Li

Figure E.5: Mask set for Layer 7. This is the mask set for the device with one small piston. The ones with ten small pistons have the same mask flow, but a different geometry.



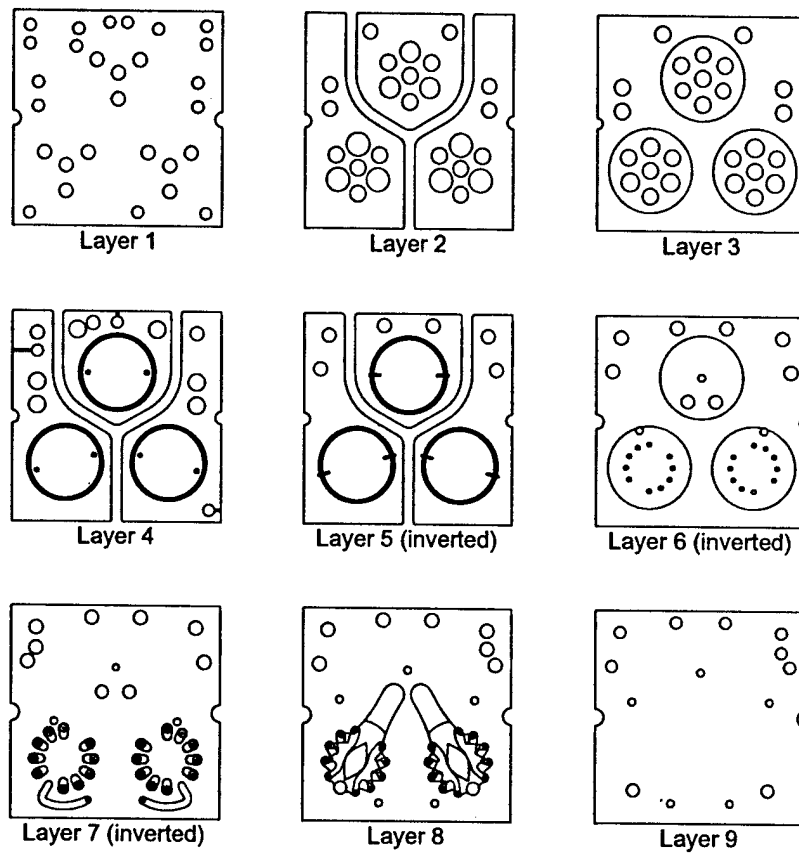
Courtesy of H.Q. Li

Figure E.6: Die-level mask set for Layer 8 of three types of hydraulic amplifiers: One, two and ten small pistons. Although dies with two small pistons were fabricated, as also shown in Figure E.7, none were tested in this work.



Courtesy of H.Q. Li

Figure E.7: Wafer scale masks of Layer 7. The first mask is also used to define align marks, globally aligned to the wafer, as well as cutting lines for the dicing operation.



Courtesy of H.Q. Li

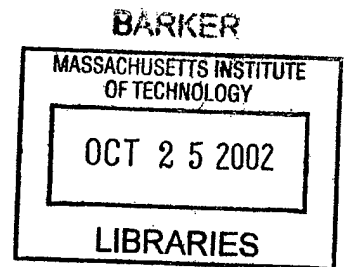
Figure E.8: Plan view of all the layers of the full ten valve MHT device.

Modeling and Design Considerations for a
Micro-Hydraulic Piezoelectric Power Generator

by

Onnik Yaglioglu

B.S. Mechanical Engineering
Bogazici University, 1999



Submitted to the Department of Mechanical Engineering and the
Department of Electrical Engineering and Computer Science
in Partial Fulfillment of the Requirements for the Degrees of

Master of Science in Mechanical Engineering

and

Master of Science in Electrical Engineering and Computer Science

at the

MASSACHUSETTS INSTITUTE OF TECHNOLOGY

February 2002

© 2002 Massachusetts Institute of Technology. All rights reserved.

Signature of Author
Department of Mechanical Engineering
January 15, 2002

Certified by
Nesbitt W. Hagood, IV
Associate Professor of Aeronautics and Astronautics
Thesis Supervisor

Certified by
Alexander H. Slocum
Professor of Mechanical Engineering, MacVicar Faculty Fellow
Departmental Reader

Accepted by
Ain A. Sonin
Chairman, Department Committee on Graduate Students
Department of Mechanical Engineering

Accepted by
Arthur C. Smith
Chairman, Committee on Graduate Students
Department of Electrical Engineering and Computer Science

Modeling and Design Considerations for a Micro-Hydraulic Piezoelectric Power Generator

by
Onnik Yaglioglu

Submitted to the Department of Mechanical Engineering and the
Department of Electrical Engineering and Computer Science
on January 15, 2002, in partial fulfillment of the
requirements for the degrees of
Master of Science in Mechanical Engineering
and
Master of Science in Electrical Engineering and Computer Science

Abstract

Piezoelectric Micro-Hydraulic Transducers are compact high power density transducers, which can function bi-directionally as actuators/micropumps and/or power generators. They are designed to generate 0.5-1W power at frequencies of ~10-20kHz, resulting in high power densities approaching 500W/kg. These devices are comprised of a main chamber, two actively controlled valves, a low-pressure reservoir and a high-pressure reservoir. This thesis reports on modeling and design considerations for Micro-Hydraulic Piezoelectric Power Generators. Since these devices are complex fluid and structural systems, comprehensive simulation tools are needed for effective design. Operation of each subcomponent of the device is highly coupled and every design decision should be made with remaining components in mind. A system level simulation tool has been developed using Matlab/Simulink, by integrating models for different energy domains, namely fluids, structures, piezoelectrics and circuitry. The simulation architecture allows for integration of the elastic equations of structural members into the dynamic simulations as well as monitoring of important parameters such as chamber pressure, flowrate, and various structural component deflections and stresses. Using the simulation, the operation of the system is analyzed and important design considerations are evaluated. Fluidic oscillations within the system are analyzed and an optimization procedure for the membrane structure within the main chamber is presented. Parameter studies are performed for different piezoelectric materials, system compliances, and circuit topologies. Tradeoffs between operation conditions and their effect on the performance are discussed. A design procedure is developed. Results indicate that system efficiency is highly dependent on compliances within the device structure, the type of piezoelectric material used and rectifier circuit topology.

Thesis Supervisor: Nesbitt W. Hagood, IV
Title: Associate Professor of Aeronautics and Astronautics

Departmental Reader: Alexander H. Slocum
Title: Professor of Mechanical Engineering, MacVicar Faculty Fellow

Acknowledgements

Special thanks goes to my family and my girlfriend. Without their support, this thesis could not have been completed. I would like to thank to my family for their continuous support and care. And, many thanks to my girlfriend for her patience and support.

Many thanks to Hagop Hachickian and Hachickian family for their continuous support and help since the very first day I came to Boston.

I would like to thank my colleagues in the MHT group. Yu Hsuan Su, thanks very much for your help and valuable insights you provided me. David Roberts, thanks for your guidance and valuable discussions. And Jorge Carretero, thanks for your support throughout the completion of this thesis.

I also would like to thank to Harry Callahan for his help in circuit modeling. Boston is missing you and your guitar sound! Next time you come, we are definitely going to jam!

Finally, I would like to thank to Boston. It is such a great city to have fun and relax. I don't know what I would do without the R&B and Jazz clubs. And, Cantab Lounge is always going to be my favorite place.

This thesis is dedicated to my family.

This research work was sponsored by DARPA under Grant #DAAG55-98-1-0361 and by ONR under Grant #N00014-97-1-0880.

Nomenclature

| | |
|-----------------|--|
| P_{HPR} | high pressure reservoir pressure |
| P_{LPR} | low pressure reservoir pressure |
| P_{ch} | main chamber pressure |
| ΔP_{ch} | main chamber pressure band |
| P_{int-in} | inlet valve intermediate pressure |
| $P_{int-out}$ | outlet valve intermediate pressure |
| Q_{in} | inlet valve flow rate |
| Q_{out} | outlet valve flow rate |
| vo_{in} | inlet valve opening |
| vo_{out} | outlet valve opening |
| C_s | structural compliance of main chamber |
| C_{eff} | effective compliance of the main chamber |
| V_o | initial fluid volume of the main chamber |
| β_f | bulk modulus of working fluid |
| E | Young modulus of Silicon |
| ν | Poissons ratio of silicon |
| ρ | density of working fluid |
| D_{ch} | chamber diameter |
| D_{pis} | piston diameter |
| R_{vc} | valve cap radius |
| w_t | tether width |
| H_{ch} | chamber height |

| | |
|------------------|--|
| D_p | piezoelectric element diameter |
| L_p | piezoelectric element length |
| t_{top} | top support structure thickness |
| t_{bot} | bottom support structure thickness |
| t_{pis} | piston thickness |
| t_{tetop} | top tether thickness |
| t_{tebot} | bottom tether thickness |
| x_{pis} | piston deflection |
| x_{te} | tether deflection |
| x_b | bottom support structure deflection |
| ΔV_{tp} | volume swept by top support structure |
| ΔV_{pis} | volume swept by deflection of piston |
| ΔV_{pb} | volume swept by bending of piston |
| ΔV_{te} | volume swept by tether bending |
| F_{te} | force between piston and tethers |
| F_p | force on piezoelectric element |
| d_{33} | piezoelectric constant |
| s_{33}^D | open circuit compliance of piezoelectric element |
| s_{33}^E | closed circuit compliance of piezoelectric element |
| k_{33} | coupling coefficient of piezoelectric element |
| k_{eff} | effective coupling factor |
| V_p | voltage on piezoelectric element |
| I_p | current through piezoelectric element |
| V_b | battery voltage |
| I_b | current through battery |
| Q_p | charge on piezoelectric element |
| σ_d | depolarization stress of piezoelectric element |
| f | operation frequency |
| η | system efficiency |
| W | generated power |

Contents

| | | |
|----------|--|-----------|
| 1 | Introduction | 21 |
| 1.1 | Microhydraulic Piezoelectric Transducers | 21 |
| 1.2 | Configuration and Operation | 23 |
| 1.3 | Preliminary Design Considerations | 26 |
| 1.4 | Objective, Scope and Organization of the Thesis | 28 |
| 2 | Piezoelectric Power Generation and Circuitry | 31 |
| 2.1 | Introduction | 31 |
| 2.2 | Previous Work | 32 |
| 2.3 | Theoretical Background | 36 |
| 2.4 | Circuitry Considerations | 40 |
| 2.4.1 | Modeling | 41 |
| 2.4.2 | Simulation and Analysis | 44 |
| 2.5 | Other Circuits | 59 |
| 2.6 | Piezoelectric Material Comparison | 62 |
| 2.7 | Conclusion | 66 |
| 3 | Energy Harvesting Chamber and Preliminary Design Considerations | 67 |
| 3.1 | Configuration and Operation of the Energy Harvesting Chamber | 67 |
| 3.2 | Modeling | 69 |
| 3.2.1 | Piezoelectric Cylinder | 69 |
| 3.2.2 | Chamber Continuity | 70 |
| 3.2.3 | Fluid Model | 72 |

| | | |
|----------|--|------------|
| 3.2.4 | Circuitry | 77 |
| 3.3 | Working Fluid | 77 |
| 3.4 | Simulation and Analysis | 78 |
| 3.4.1 | Energy Harvesting Chamber and Full Bridge Rectifier | 79 |
| 3.4.2 | Energy Harvesting Chamber and Full Bridge Rectifier with Voltage De- tector Circuit | 83 |
| 3.5 | Discussion | 91 |
| 3.6 | Summary and Conclusion | 96 |
| 4 | Detailed Model of the Energy Harvesting Chamber | 99 |
| 4.1 | Analysis of a Simplified Chamber Structure | 99 |
| 4.2 | Detailed Analysis of Structural Components | 102 |
| 4.2.1 | Top Support Structure | 102 |
| 4.2.2 | Bottom Support Structure | 104 |
| 4.2.3 | Piston | 106 |
| 4.2.4 | Piston Tethers | 107 |
| 4.3 | Simulation Architecture | 110 |
| 4.4 | Conclusion | 114 |
| 5 | Further Design Considerations and Design Procedure | 115 |
| 5.1 | Further Design Considerations | 115 |
| 5.1.1 | Fluidic Oscillations | 115 |
| 5.1.2 | Chamber filling and evacuation | 122 |
| 5.1.3 | Tether Structure Optimization | 124 |
| 5.1.4 | Operation Conditions and Trade-offs | 129 |
| 5.1.5 | Bias Pressure | 135 |
| 5.1.6 | Scaling Issues | 138 |
| 5.2 | Design Procedure | 141 |
| 5.2.1 | Preliminary design decisions | 141 |
| 5.2.2 | Parameters imposed by active valve design | 142 |
| 5.2.3 | Parameters imposed by fabrication process | 143 |

| | | |
|----------|--|------------|
| 5.2.4 | Design Procedure | 143 |
| 5.3 | Design Examples | 147 |
| 5.3.1 | Design Example 1 | 147 |
| 5.3.2 | Design Example 2 | 148 |
| 5.4 | Summary | 157 |
| 6 | Conclusions and Recommendations for Future Work | 159 |
| 6.1 | Summary | 159 |
| 6.2 | Recommendations for Future Work | 162 |
| A | Simulink Block Diagrams | 171 |
| B | Matlab Files | 181 |
| C | Maple Files | 187 |

List of Figures

| | | |
|-----|---|----|
| 1-1 | (a) Configuration of power generator (b) Configuration of actuator/ micropump. The actuator/micropump configuration can also be operated with check valves instead of active valves, which are necessary for power generator configuration. . | 22 |
| 1-2 | Device layout for power generator configuration. Top and bottom packaging pyrex layers not shown. | 24 |
| 1-3 | Generic operation duty cycle of the power generator. | 25 |
| 1-4 | (a) 5-layer device for subcomponent testing (b) Complete 9-layer device (c) SEM of micromachined tethered piston structure [7]. | 27 |
| 1-5 | Overall system architecture for the heel strike power generation configuration. . . | 28 |
| 2-1 | Graphic illustration of electromechanical energy conversion and definition of the piezoelectric coupling factor k_{33} given in [18] (a) Conversion of energy from a mechanical source to electrical work (b) Conversion of energy from an electrical source to mechanical work. | 38 |
| 2-2 | Alternative idealized work cycles given in [8]. | 39 |
| 2-3 | Alternative circuits to rectify and store the electrical energy generated by the piezoelectric element. | 41 |
| 2-4 | Simulation architecture used to simulate the piezoelectric element connected to the full bridge rectifier. The force is imposed on the piezoelectric element. . . . | 45 |
| 2-5 | Time histories from the simulation of the piezoelectric element connected to the full bridge rectifier for the case of imposed force. The generated power is $I_b V_b$. . | 47 |
| 2-6 | Force vs. deflection and voltage vs. charge plots of the piezoelectric element compressed under the applied force for the case of full bridge rectifier. | 48 |

| | | |
|------|--|----|
| 2-7 | Effect of battery voltage on power. | 49 |
| 2-8 | Effect of bias force on the workcycle. | 50 |
| 2-9 | General presentation of the work cycle of the piezoelectric element in terms of stress, strain, electric field and charge density for the case of regular diode bridge. | 52 |
| 2-10 | Illustration of the effective coupling factor for the case of regular diode bridge. | 53 |
| 2-11 | Time histories from the simulation of the piezoelectric element connected to the full bridge rectifier and voltage detector circuit. The time intervals between the dashed lines present the intervals where the switch(SCR) is in its "on" state. | 55 |
| 2-12 | Force vs. deflection and voltage vs. charge plots of the piezoelectric element compressed under the applied force for the case of full bridge rectifier and voltage detector circuit. | 56 |
| 2-13 | General presentation of the work cycle of the piezoelectric element in terms of stress, strain, electric field and charge density for the case of the full bridge rectifier and voltage detector circuit. | 57 |
| 2-14 | Illustration of the effective coupling factor for the full bridge rectifier and voltage detection circuit. | 58 |
| 2-15 | Other alternative circuits for piezoelectric power generation. | 59 |
| 2-16 | Simulation results of the piezoelectric element shunted by a resistor for different resistance values. | 60 |
| 2-17 | Comparison of resistive shunting(at optimum resistance) with full bridge rectifier and full bridge rectifier with voltage detector. | 61 |
| 2-18 | Simulation results of the full bridge rectifier connected to a capacitor. | 62 |
| 2-19 | Force vs. deflection plot from the simulation of the full bridge rectifier with additional inductor. | 63 |
| 2-20 | Effective coupling factors of the diode bridge and the diode bridge with voltage detector as a function of the coupling coefficient. | 64 |
| 2-21 | Piezoelectric Material Comparison: (a) Effective coupling factor (b) Energy density. | 65 |
| 3-1 | Energy harvesting chamber configuration. | 68 |
| 3-2 | Duty cycles of generic operation of the energy harvesting chamber. The valve openings have the same duty cycle as the flowrates and are not shown here. | 68 |

| | | |
|------|---|----|
| 3-3 | Device schematics showing pressures at different locations. | 73 |
| 3-4 | Valve orifice representation:(a) Valve cap geometry and fluid flow areas, (b) Representation of flow through the valve as a flow contraction followed by a flow expansion. | 74 |
| 3-5 | Look-Up tables used for flow loss contraction and expansion coefficients. The loss coefficients are obtained from [51]. | 75 |
| 3-6 | Simulation architecture used in Simulink. | 79 |
| 3-7 | Simulation of the energy harvesting chamber attached to the full bridge rectifier circuit. | 80 |
| 3-8 | Force vs. displacement curve of the piezoelectric element from the simulation of the harvesting chamber attached to the full bridge rectifier. | 82 |
| 3-9 | Simulation of the energy harvesting chamber attached to the full bridge rectifier and voltage detector circuit. The time intervals between the dashed lines present the intervals where the switch(SCR) is in its "on" state. | 84 |
| 3-10 | Force vs. displacement curve of the piezoelectric element from the simulation of the energy harvesting chamber attached to the full bridge rectifier and voltage detector circuit. | 85 |
| 3-11 | Time histories of the force and deflection of the piezoelectric element. | 85 |
| 3-12 | Force vs. displacement curve of the piezoelectric element and slopes at different periods of operations. | 87 |
| 3-13 | The effect of effective chamber compliance on force vs. deflection curve and effective coupling factor. | 90 |
| 3-14 | Flowrate and frequency requirement for 0.5 W power requirement. | 92 |
| 3-15 | System efficiency as a function of the effective chamber compliance. | 93 |
| 3-16 | Required flowrates for 0.5 power generation. Comparison of different piezoelectric elements and different circuitry. | 94 |
| 3-17 | Required frequencies for the 0.5W power requirement. Comparison of different piezoelectric materials and circuitry. Note that the required frequency in the case of regular rectifier is independent of the chamber compliance. | 95 |

| | | |
|------|--|-----|
| 3-18 | Comparison of different piezoelectric materials and circuitry in terms of system efficiency. | 96 |
| 3-19 | Maximum system efficiency(which corresponds to the case where the effective compliance of the chamber is zero)as a function of the coupling coefficient. . . . | 98 |
| 4-1 | (a) Simplified chamber structure consisting of a fluid chamber with a compliant wall (b) Deformation of the top plate and swept volume. | 100 |
| 4-2 | Comparison of fluidic and structural compliances for a generic chamber structure at different chamber diameters for fixed chamber height and top plate thickness. | 101 |
| 4-3 | (a) Schematic illustrating the dimensional parameters of the chamber, (b) deformation of structural components and sign conventions, (c) free body diagrams and sign conventions. Deflections are exaggerated. | 103 |
| 4-4 | Model of the bottom support structure: circular plate with a circular hole at its center with guided boundary condition at inner radius b and clamped boundary condition at outer radius a. | 105 |
| 4-5 | Model of the piston: circular plate with a circular hole at its center with guided boundary condition at inner radius b and clamped boundary condition at outer radius a. | 106 |
| 4-6 | Model of the top tether: circular plate with a circular hole at its center with guided boundary condition at inner radius b and clamped boundary condition at outer radius a. | 108 |
| 4-7 | Simulation architecture used to integrate the elastic equations into system level simulation. | 113 |
| 5-1 | Helmholtz Resonator. | 116 |
| 5-2 | Simulation of the chamber with constant overall compliance for different channel geometries. | 118 |
| 5-3 | Comparison of flowrate time histories for different L/A ratios. | 118 |
| 5-4 | Simulation of the chamber attached to circuitry for different channel geometries. | 119 |
| 5-5 | Effect of L/A ratio on pressure band and generated power. | 120 |
| 5-6 | Effect of valve opening on the pressure band in the chamber. | 123 |

| | | |
|------|--|-----|
| 5-7 | Effect of operation frequency on the pressure band in the chamber. | 123 |
| 5-8 | (a) Schematic illustrating the hypothetical chamber (b) good tether design providing large piezoelectric element compression (c) poor tether design, either too thin or large width, resulting in low chamber pressure and small piezoelectric element compression (d) poor tether design, either very thick or small width, resulting in large pressures but small piezoelectric element compression. | 125 |
| 5-9 | (a) Piston deflection for different tether thicknesses and widths,(b).corresponding pressures in the chamber (c) compliance of the chamber. The dashed line corresponds to the hypothetical case where piston diameter is equal to chamber diameter and there is perfect sealing. | 126 |
| 5-10 | (a) Schetch illustrating tether deflection. (b),(c),and (d) show the stress components on the bottom surface and deflected shape of the tether for 3 different cases.(b) good tether design, (c) poor tether design where the tether is too compliant, and (d) poor tether design where the tether is too stiff. | 127 |
| 5-11 | (a) SEM picture of micromachined piston structure [7](b)detailed view of the tether and the fillet. | 128 |
| 5-12 | Comparison of different piezoelectric materials in terms of required operation frequency at different chamber diameters for a power requirement of 0.5W. . . . | 131 |
| 5-13 | Comparison of different piezoelectric materials in terms of required flowrate at different chamber diameters for a power requirement of 0.5W. | 132 |
| 5-14 | Comparison of different piezoelectric elements in terms of system efficiency for different reservoir pressures and chamber diameters. | 134 |
| 5-15 | Required operation frequency and flowrate for different power requirements at different chamber diameters ($P_{HPR} = 2MPa$, piezoelectric material: $PZN-PT$). | 135 |
| 5-16 | Schematic illustrating the effect of bias pressure.(a) not biased case (b) biased case | 136 |
| 5-17 | Effect of bias pressure on required frequency, flowrate and efficiency. | 137 |
| 5-18 | Design procedure. | 144 |
| 5-19 | (a) System layout (b) System level simulation architecture (c) The chamber and piezo block in the overall system architecture which was developed in Chapter 4. | 146 |
| 5-20 | Tether structure design. Piston deflection shown for different tether widths. . . | 148 |

| | |
|--|-----|
| 5-21 Simulation time histories of the design example 1. | 150 |
| 5-22 Simulation time histories of the design example 1. | 151 |
| 5-23 Simulation time histories of the design example 1. | 152 |
| 5-24 Simulation time histories of the design example 2. | 154 |
| 5-25 Simulation time histories of the design example 2. | 155 |
| 5-26 Simulation time histories of the design example 2. | 156 |
| | |
| A-1 Simulink model of the piezoelectric element. | 172 |
| A-2 Simulink model of the diode bridge. | 173 |
| A-3 Simulink model of the diode bridge attached to an inductor, voltage detector and SCR(Silicon Controlled Rectifier). | 174 |
| A-4 Implementation of the voltage detector circuit. | 175 |
| A-5 Simulink model of the full system including the chamber, piezoelectric element, fluid models and circuitry. | 176 |
| A-6 Simulink model of the main chamber and the piezoelectric element. | 177 |
| A-7 Simulink model of the inlet valve and fluid channel. | 178 |
| A-8 Simulink model of the outlet valve and fluid channel. | 179 |
| | |
| B-1 Matlab code used in Chapter 3 to calculate the required frequency, flowrate and efficiency for different circuitry. | 182 |
| B-2 Matlab code used in Chapter 5 to calculate the required frequency, flowrate and efficiency of the system attached to regular diode bridge for different reservoir pressures and chamber diameters. | 183 |
| B-3 Matlab code used for tether optimization. | 184 |
| B-4 Matlab code used for writing system parameters into the workplace to be read by the Simulink model for the system level simulation. | 185 |

List of Tables

| | | |
|-----|--|-----|
| 2.1 | Geometry and operation conditions used in simulation | 45 |
| 2.2 | Comparison of circuitry in terms of energy density and effective coupling factor . | 63 |
| 2.3 | Properties of different piezoelectric materials | 66 |
| 3.1 | Comparison of different working fluids | 78 |
| 3.2 | The geometry and operation conditions used in the simulation | 78 |
| 3.3 | Summary and comparison of circuitry in terms of performance indices | 97 |
| 5.1 | Summary of preliminary design decisions applied to the design examples. | 147 |
| 5.2 | Summary of design and performance parameters of design example 1. | 149 |
| 5.3 | Summary of design and performance parameters of design example 2. | 153 |

Chapter 1

Introduction

This chapter presents the configuration, operation and motivation of microhydraulic-piezoelectric power generators. Preliminary design considerations are discussed. The objective, scope and organization of the thesis are presented.

1.1 Microhydraulic Piezoelectric Transducers

Transducers are devices that convert physical energy from one form to another. Actuators and power generators are examples of transducer devices. The performance and usefulness of a transducer for most applications are highly dependent on two important characteristics: compactness and power density, that is, power output of the transducer per its unit volume. Conventional transducers, generally, not only tend to be heavy and bulky, but are also limited in terms of power transduction capabilities because of their low bandwidths. For instance, conventional hydraulic systems possess high single-stroke work, but their power densities are greatly reduced by their large mass. Recent advances in active materials technology have led to the development of many compact solid-state transducers. However, the power output from these solid-state transducers is fairly limited for most macro applications. Although the single-stroke work output of solid-state materials such as piezoelectric materials is relatively small, such materials possess very high bandwidths, and as such, are capable of high power output. However, since most applications do not require high frequency actuation, the high bandwidth potential of piezoelectric materials is not fully utilized. Since a transducer's power

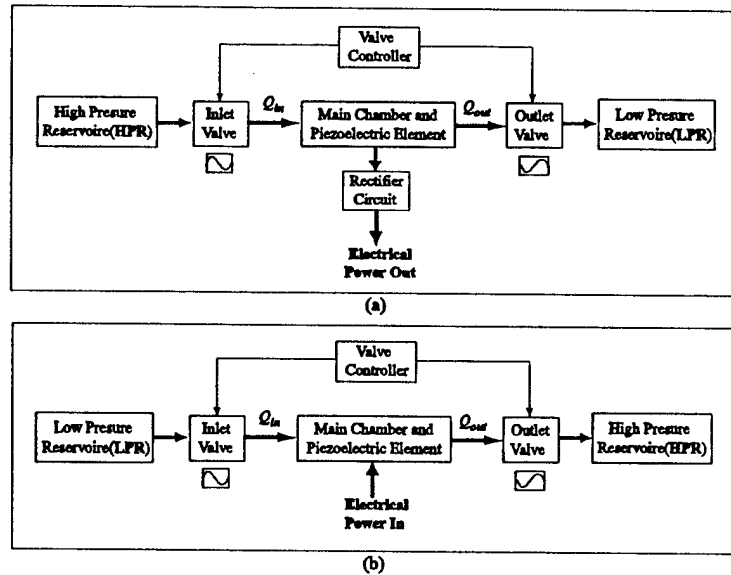


Figure 1-1: (a) Configuration of power generator (b) Configuration of actuator/ micropump. The actuator/micropump configuration can also be operated with check valves instead of active valves, which are necessary for power generator configuration.

output is the product of its single stroke energy and its bandwidth, it is feasible to create high performance transducers by combining high single-stroke force of a hydraulic system and high frequency displacements of a piezoelectric element in a synergistic manner[1]. This concept can be further exploited to create high performance transducers with very high power densities by miniaturizing the transducer systems. The state-of-the-art micromachining (or MEMS) technology has the potential to allow for the implementation of this concept at the micro scale.

Research and development of microfluidic devices has received a significant amount of interest in the past years. The feasibility of micromachining many of the key building blocks (flow channels, pumps, active/passive valves) of a micro-fluidic system including the integration of solid-state materials such as piezoelectric materials to actuate valves has already been demonstrated, and researchers are now striving to create complete microfluidic systems. However, the microfluidic devices developed thus far mostly feature small flow conductance, limited stroke, and low power density, and are mostly geared towards small flow/force applications such as microdosing of fluids. An extensive literature review on microfluidic devices can be found in

[2].

A unique feature of piezoelectric microhydraulic transducers is their ability to operate as both an actuator and a power generator, by merely reversing the direction of their operation. As actuators, these transducers transform electrical energy input into mechanical/hydraulic energy output, and as power generators, the transducers transform mechanical/hydraulic energy input into electrical energy that can be stored in a battery or a capacitor. These high performance transducers can significantly enhance the scope of micromachined transducers technology by enabling many novel applications. When utilized as actuators, they are capable of extending the usefulness of active material based structural actuation beyond small strain applications [1]. These actuators can also be useful in miniature robotics. As power generators, the transducers can extract electrical energy from wasted mechanical energy sources such as vibrations of operating machinery, heel strike of human gait, wind, sound and function as disposable batteries for numerous small electronic devices in both civilian and military applications. A literature survey about piezoelectric power generation will be presented in Chapter 2. Detailed information and comparisons of various transducers can be found in [2] where a feasibility analysis of Micro Hydraulic Transducers has been performed.

1.2 Configuration and Operation

The concept of piezoelectric micro-hydraulic transducer (MHT) is schematically illustrated in Figure 1-1 for actuator and power generator configurations. The transducers are comprised of the following generic components: the main chamber which houses a piezoelectrically driven tethered piston, two actively controlled valves, a low-pressure fluid reservoir (LPR), and a high-pressure fluid reservoir (HPR). The power generator configuration requires rectification circuitry to rectify and store the voltage generated by the piezoelectric element. The two active valves, one operating between the HPR and the main chamber and the other one operating between the main chamber and the LPR regulate the fluid flow into and out of the main chamber. The piezoelectric element within the pump chamber serves as the main energy transducing element. A detailed drawing of the device is shown in Figure 1-2.

When operating as an actuator/pump, the electrical signal applied to the piezoelectric

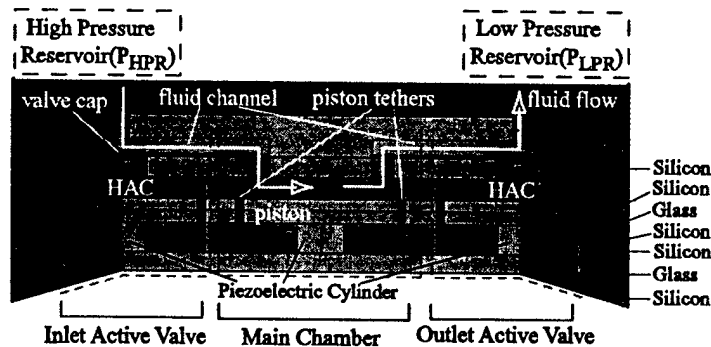


Figure 1-2: Device layout for power generator configuration. Top and bottom packaging pyrex layers not shown.

element results in pressure fluctuations inside the main chamber. When operating as a power generator, pressure fluctuations within the main chamber are converted to an electrical signal, which is rectified and stored in a battery or capacitor. In the actuator configuration, the voltage applied to the piezoelectric element induces a strain in the element resulting in a net volume change in the pump chamber. A controller synchronized with the pump signal cycles the active valves out of phase with each other in a specified duty cycle, transforming the volume oscillations of the chamber into a net fluid flow from the low pressure reservoir to the high pressure reservoir.

In the power generator configuration, the transducer operates in a manner that is reverse of the actuator. The controller toggles the valves with a phasing that allows fluid flow from the high pressure reservoir to the low pressure reservoir, thus transforming the static fluid pressure into high frequency pulses on the piezoelectric element via the piston. Valve actuation at high frequency creates a near sinusoidal cyclic stress on the piezoelectric element, thereby generating electrical charge across the element. Coupled circuitry rectifies this electrical energy and stores it in a battery or capacitor. It should be noted that, for the actuator/micropump configuration, check valves can also be used, instead of active valves, which is demonstrated in [3]. However, for the power generator configuration, active valves are necessary in order to convert the static pressure differential into pressure fluctuations on the piston. Generic operation duty cycle of the power generator configuration is shown in Figure 1-3.

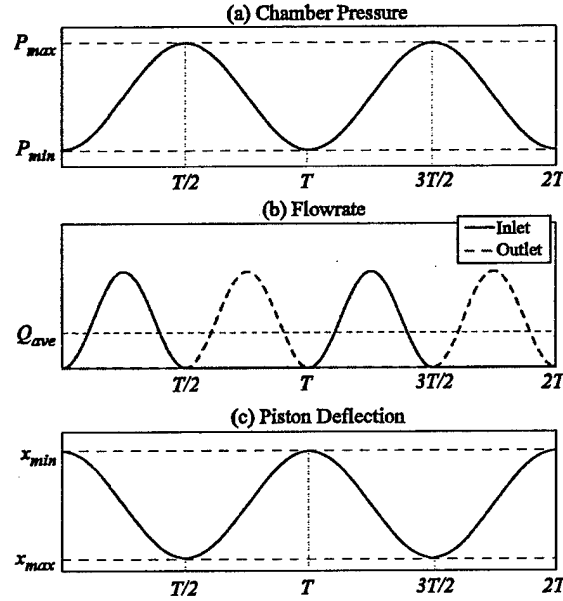


Figure 1-3: Generic operation duty cycle of the power generator.

Active valves are comprised of a similar chamber/piston structure, called hydraulic amplification chamber (HAC), which incorporates a fluid enclosed in the volume between the piston and the valve diaphragm, which effectively serves to amplify the small displacements of the piezoelectric material into significantly larger displacements of the valve cap and effectively transmits the high force actuation capability of the piezoelectric material. As the piston in the active valve is displaced by the piezoelectric element, the pressure of the compressed fluid acts to deform the smaller area valve membrane located at the top of the chamber. Deflection of the rigid cap at the center of the valve membrane blocks fluid flow through the corresponding fluid orifice. The utilization of the hydraulic amplification chamber also leads to minimization of the actuator material, and thus helps in achieving high power densities. The ability to micromachine the device provides the scope to further miniaturize the system to micro scales, leading to higher valve frequencies and therefore enhanced device power densities.

As shown in Figure 1-2, in each chamber, namely inlet HAC, main chamber (energy harvesting chamber) and outlet HAC, a piezoelectric element is sandwiched between the device

structure and a moveable piston plate. The piston plate is sufficiently thick for rigidity and is tethered to the chamber wall through thin flexible diaphragms that extend radially from the outer edges of the cylinder. The structure effectively constitutes a piston that can move vertically up and down when a net force is applied to it.

The prototype MHT device consists of a 9-layer stack of pyrex and silicon micromachined layers, as shown in Figure 1-2 and Figure 1-4. Sealing of the piston in the main chamber is provided by annular tethers which are created through Deep Reactive Ion Etching (DRIE) of a SOI wafer. The tether thickness ($\sim 10\mu\text{m}$) is defined by the SOI device layer, and the buried oxide acts as an etch stop. All glass layers are patterned by conventional diamond core drilling. Piezoelectric cylinders are core drilled from piezoelectric substrate plates, onto which a Ti-Pt-AuSn-Au multilayer film is sputter-deposited for eutectic bonding. The device assembly is accomplished through anodic bonding of the glass layers to the silicon layers at 300°C , a process which also enables the AuSn eutectic alloy to melt. Upon cooling, the alloy solidifies, bonding the piezoelectric cylinders to the silicon layers. Detailed information about the fabrication techniques developed for piezoelectric micro-hydraulic transducers can be found in [3], [6], and [7].

1.3 Preliminary Design Considerations

The proposed MHT devices derive their enhanced performance from several inherent design features. For efficient device operation, the compliances within the system, which result from the deformations of the structural members like piston, tether and support structures, and compression of the working fluid within the chambers should be minimum. This implies that the chambers should have small volumes and the structural members should be as thick as possible. This introduces trade-offs between fabrication limitations and design requirements. The type of piezoelectric element also affects system efficiency since the coupling coefficient of the element determines the electromechanical energy conversion work-cycle. For the power generator configuration the rectifier circuit topology is another factor affecting system efficiency, since it determines the electromechanical energy conversion work-cycle along with the piezoelectric material.

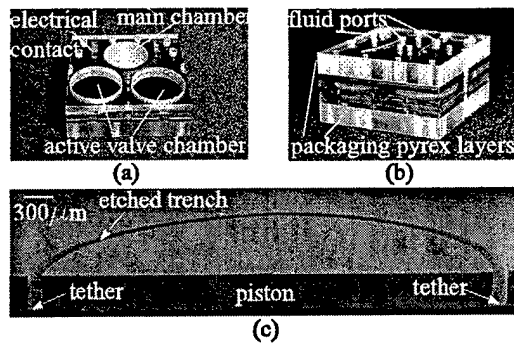


Figure 1-4: (a) 5-layer device for subcomponent testing (b) Complete 9-layer device (c) SEM of micromachined tethered piston structure [7].

Design of the piston tether structure is very crucial for system operation. The tethers should be flexible enough to allow sufficient motion of the piston, yet stiff enough to avoid introduction of excessive compliance into the system. Similar design consideration is also valid for the valve membrane. Achieving high power density critically depends on valves having high bandwidth (frequencies in the tens of kilohertz), sufficient actuation force to overcome large pressures ($\sim 1\text{--}2$ MPa) and large stroke ($\sim 20\text{--}30\mu\text{m}$). The valve membranes should be designed such that they are flexible enough to allow for large valve stroke and stiff enough to operate against high pressures and have high natural frequencies. Large stroke actuation of the valve cap generally results in nonlinear membrane behavior.

Possible fluidic and structural oscillations within the system should be considered. For example the fluid channels and the main chamber constitute a resonating system similar to a Helmholtz resonator. Similarly, piezoelectric element and piston dynamics, which affect the bandwidth of the device, should also be considered.

Important design limitations are maximum allowable stress in the membranes and the depolarization stress of the piezoelectric material. The stress in the tether structures shouldn't exceed 1GPa [7]. Piezoelectric materials also differ in their depolarization stress, which determines the energy density of the material. If during the operation, the stress on the piezoelectric element exceeds the depolarization stress, the element loses its functionality.

The choice of working fluid is also important since different fluids have different bulk moduli,

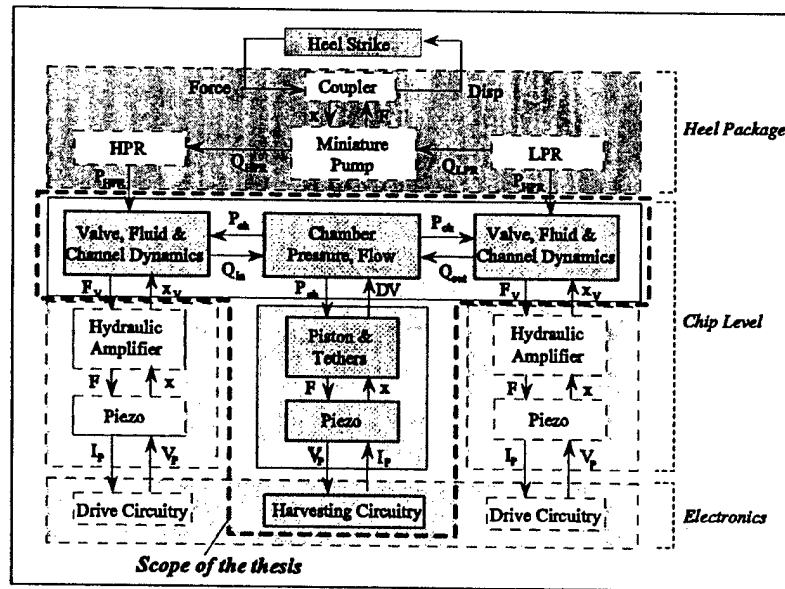


Figure 1-5: Overall system architecture for the heel strike power generation configuration.

densities and viscosities.

1.4 Objective, Scope and Organization of the Thesis

Since these devices are complex, comprehensive simulation tools are needed for effective design. Operation of each subcomponent of the device is highly coupled and every design decision should be made with remaining components in mind. The simulation tool should allow for the monitoring of important parameters such as chamber pressure, flowrate, and various structural component deflections and stresses. A system level simulation tool is needed which should be developed by integration of different energy domains, namely fluids, structures, piezoelectric material and circuitry. The challenges in modeling and simulation are: microscale fluid flow, incorporation of membrane behavior into dynamic simulation, prediction of structural compliances and incorporation of the elastic equations of the structural members into simulation.

The MHT group at MIT Active Material and Structures Laboratory(AMSL) has obtained good experimental correlation for subcomponent models from tests on piezoelectrically driven

piston/tether structure, hydraulic amplification chamber structure and valve membrane [6], flow tests through macro disc valves [4], and micropumps [3].

This thesis focuses on the modeling and design of piezoelectric microhydraulic transducers used as power generators. The system architecture for a possible application, namely heel strike power generation configuration is shown in Figure 1-5. The scope of the thesis is shown with the dashed line in the system architecture. The heel package design will not be discussed. Also design of the active valve structure will not be discussed, which is detailed in [5]. Orifice models developed in [4] are used for fluid flow through the valves.

The objectives of this thesis are:

- To develop a comprehensive system level model and simulation tool to analyze the main chamber and the associated fluid channels and valves,
- To gain insight into system operation and understand the factors affecting the system performance,
- Develop a design procedure, which should be complemented by the design of the active valves.

The organization of the thesis is as follows: Chapter 2 presents an analysis of piezoelectric power generation based on linear electromechanical energy conversion. Effect of circuitry and piezoelectric material on energy density and effective coupling factor is discussed. Chapter 3 presents a simple model of the energy harvesting chamber, simulations with the coupled circuitry and preliminary design considerations. The interaction of the main chamber and the circuitry is discussed. The circuits presented in Chapter 2 and different piezoelectric materials are compared in terms of flowrate and frequency requirements for a given pressure differential and power, and in terms of system efficiency. Chapter 4 presents the detailed modelling of the energy harvesting chamber and investigates the contribution of different structural components on the effective compliance of the chamber. It also presents the simulation architecture used for integrating elastic equations into system level simulation. Chapter 5 discusses further design considerations for choosing chamber geometry with regard to operation conditions like maximum pressure, operation frequency and flowrate. Parameter studies are performed and a design procedure is developed. Chapter 6 summarizes important results and conclusions presented in previous chapters and presents recommendations for future work.

Chapter 2

Piezoelectric Power Generation and Circuitry

This chapter presents an analysis of piezoelectric power generation based on linear electromechanical energy conversion. Effect of circuitry and piezoelectric material on electromechanical energy conversion and energy density is discussed.

2.1 Introduction

Piezoelectric materials are mostly used as sensors and actuators. Since they are capable of electromechanical energy conversion and some have high coupling coefficients, which is an indication of the efficiency of the electromechanical energy conversion, they can be also used as power generators from ambient vibration or impact energy, and as structural vibration dampers. The idea and the governing principles are the same for power generation and structural vibration damping, using piezoelectric elements and passive circuit elements. Damping of structural vibrations with passive electrical circuit elements is discussed in [15] and [14]. This method eliminates the need for viscoelastic materials or mechanical vibration absorbers attached to the structure, or complex amplifiers which are required by the piezoelectric materials for active structural control systems [15]. The coupling between mechanical and electrical domains provided by the piezoelectric effect allows the damping mechanism to be implemented as electrical circuit elements rather than physical masses, springs and dampers. Most of the discussions

which are valid for the structural damping applications with piezoelectric elements are valid for the power generation from ambient vibration or impact energy with piezoelectric elements. In both cases, the purpose is to transfer as much energy from the mechanical to the electrical domain. The transferred energy to the electrical domain can be either dissipated or stored. If a piezoelectric element is shunted with a resistor or with a resistor and inductor network, the converted electrical energy is basically dissipated. However, if the piezoelectric element is connected to a rectifier circuit, a diode bridge for example, with a capacitor or battery, the converted electrical energy can be stored.

2.2 Previous Work

Structural damping with piezoelectric elements shunted with a resistor and a resistor-inductor network is analyzed in [15]. In the resistive shunting the electromechanical energy conversion efficiency depends on the operation frequency, and the optimum frequency depends on the resistance value. In other words, optimum efficiency is obtained when the impedance of the piezoelectric element is equal to the impedance of the resistance. Shunting with a resistor and inductor introduces an electrical resonance, which can be optimally tuned to structural resonances for maximum vibration damping.

Linear shunting components such as resistive elements or resistive-inductive-capacitive circuits produce behavior analogous to that of viscoelastic damping materials and tuned proof-mass dampers. Nonlinear piezoelectric shunting for structural damping using a piezoelectric element attached to a diode bridge and a DC voltage is presented in [14]. The rectified DC shunt performs less well in terms of energy conversion efficiency compared with the resistive shunt at optimum frequency. However, unlike the resistive shunt, the rectified DC shunt is independent of frequency and the transferred energy can be recovered depending on the implementation of the DC voltage source.

Power generation characteristics of piezoelectric elements in response to impact loads are investigated in [9], [10] and [11]. In the first two, a ball is dropped from a certain height onto a piezoelectric plate vibrator. In the first one, the piezoelectric vibrator is shunted with a resistor and the efficiency of transformation from mechanical to electrical energy in terms of initial

height and shunted resistance value is investigated. The efficiency is defined as the ratio of the electrical energy dissipated in the resistor to the initial impact energy. The input mechanical impact energy affects the efficiency due to nonlinearity in the vibrator and as expected there is an optimum resistance value. They conclude that efficiency increases with decreasing input impact energy, increasing mechanical quality factor Q_m , increasing electromechanical coupling coefficient k_{33}^2 and decreasing dielectric loss $\tan \delta$. They obtain a maximum efficiency of 52%.

The same authors of [9] investigate the power generation characteristics of the same system attached to a diode bridge and capacitor instead of a resistor in [10]. In this case the transformation efficiency is defined as the ratio of the impact energy to the energy stored in the capacitor. As the capacitance of the capacitor increases, the electric charge increases because the duration of the oscillation becomes longer and the output voltage decreases. They conclude that there exists an optimum capacitance value in terms of transformation efficiency. They obtain a maximum efficiency of 35%. It should be noted that, if a force were imposed on a piezoelectric element, the voltage on the capacitor would always increase until half of the open circuit voltage which corresponds to the maximum stress on the piezoelectric element, regardless of the capacitance of the capacitor. The value of the capacitance would change the duration in which the maximum voltage is reached and the stored energy in the capacitor would be proportional to its capacitance, since the maximum voltage is constant for a given maximum stress. In the paper discussed above, the force on the piezoelectric element is not imposed, it is determined depending on the impedances of the vibrator and the capacitor. In this case, the impedance matching principle cannot be applied since the system is nonlinear because of the diode bridge. No power density figures are reported in [9] and [10].

Piezoelectric power generation from thermal energy is presented in [20]. This paper discusses an energy conversion system in which thermal energy is converted to high frequency, high voltage electric a.c energy. The conversion system is composed of a thermal-acoustic natural heat engine and a piezoelectric transduction system to convert the acoustic energy to electric energy.

Another system to convert acoustic energy to electric energy is presented in [35]. The device is designed to convert waste acoustic energy, e.g. in automobile or airplane jet engines to electrical energy in a predetermined frequency range. The system consists of a piezoelectric bending element, means for mounting the piezoelectric bending element in an acoustic energy

path and a tuning means mounted on to the piezoelectric bending element to set the resonant frequency of oscillation of the piezoelectric bending element within the predetermined frequency range.

The idea of piezoelectric power generation from the ocean waves is patented in [27]-[32] by Ocean Power Technologies, Inc. The motivation in these studies is to utilize the enormous amount of mechanical energy present in the oceans. [27] relates to the generation of electrical power from waves on the surface of bodies of water, and particularly to the conversion of the mechanical energy of such waves to electrical energy by means of piezoelectric materials. The system consists of piezoelectric elements in the form of one or a laminate of sheets, each sheet having an electrode on opposite surfaces thereof, a support means for maintaining the structure in a preselected position within and below the surface of the water. In certain embodiments, the elements are designed to enter into mechanical resonance in response to the passage of waves thereover, increasing the mechanical coupling efficiency between the waves and the elements. Similar approaches are presented in [28] and [30]. In [28], a float on a body of water is mechanically coupled to a piezoelectric material member for causing alternate straining and de-straining of the member in response to the up and down movement of the member in response to passing waves, thereby causing the member to generate electric energy. The output impedance of the float is matched to the input impedance of the member for increasing the energy transfer from the float to the member. In [30], the system comprises a weighted member supported from a piezoelectric element for applying a preselected strain to the element. In one embodiment, the element is supported by a float floating on the surface of the water. In another embodiment, the element is supported above the surface of the water and the weighted member, of negative buoyancy, is immersed in the water. Means are provided for tuning the natural frequency of the system to cause it to enter into mechanical resonance in response to passing waves. Similar approaches are presented in [29], [31] and [32].

Some circuitry considerations for piezoelectric power generation are presented in [33] and [26]. [33] presents a DC bias scheme for improved efficiency for applications including electrostrictive materials, which have very weak piezoelectric characteristics. However, if a DC bias is applied, the piezoelectric characteristics can be significantly increased. [26] presents an alternative rectifier circuit, which includes an inductor, a SCR(silicon controlled rectifier) and

a voltage detection circuit in the conduction path between the piezoelectric element and the storage element, a capacitor for example. The object is to optimize the transfer of the energy produced by a piezoelectric transducer to a load. Another circuit designed for a wide variety of applications is presented in [36].

Piezoelectric power generation for electronic wristwatch applications is presented in [23]-[25]. [23] presents an electronic wristwatch having a piezoelectric generator in it. The generator converts energy from mechanical to electrical energy to drive the electronic wristwatch. The oscillation of a weight produces mechanical energy as it oscillates. A wheel train transmits the mechanical energy to the generator by applying a torque to the generator. The generated voltage is rectified with a diode bridge. Similar systems are presented in [24] and [25].

Piezoelectric power generation from wind energy is presented in [21] and [22]. The system presented in [22] consists of a piezoelectric transducer mounted on a resilient blade which in turn is mounted on an independently flexible support member. Fluid flow against the blade causes bending stresses in the piezoelectric polymer which produces electric power.

Other piezoelectric power generation systems are presented in [34], [39], [38] and [37]. [34] presents a piezoelectric fluidic-electric generator which consists of a piezoelectric bending element, means for driving the piezoelectric bending element to oscillate with the energy of the fluid stream, and electrodes connected to the piezoelectric element to conduct current generated by the oscillatory motion of the piezoelectric element. [39] presents a system which consists of a piezoelectric array which is mounted on one or more tires of a motor vehicle. As the vehicle drives on the road, the tire is flexed during each revolution to distort the piezoelectric elements and generate electricity.

Piezoelectric materials are also used in power electronics applications such as transformers. Piezoelectric transformers are composite resonators made of two bonded piezoelectric parts. The vibration of one part, excited by an input electric voltage, induces an output voltage across the other part [40]. In other words, a piezoelectric transformer works by using the direct and converse piezoelectric effects to acoustically transform power from one voltage and current level to another [44]. Detailed information about the operational characteristics of piezoelectric transformers can be found in [41] and [42].

Piezoelectric transformers have low-electric noise because they transmit power by mechan-

ical vibration. They can also operate efficiently at high frequencies, whereas conventional electromagnetic transformers are not efficient at high frequencies because of core loss and copper loss. Other advantages over the electromagnetic transformers can be stated as high voltage isolation between primary and secondary, high frequency operation leading to reduction in the filter capacitors and low weight and size [43]. Since piezoelectric transformers have much higher power densities than electromagnetic transducers, they are very promising as power electronic components for miniature and lightweight electrical equipment.

Fundamental limits on energy transfer of piezoelectric transformers are discussed in [44]. The discussion details similar considerations to those of the piezoelectric power generation concept. One has to consider the work cycle of electromechanical energy conversion and associated circuitry. Also the maximum electric field, the maximum surface charge density, the maximum stress and the maximum strain of the piezoelectric element are important criteria to consider when determining the limitations of power transfer in a piezoelectric transformer, as well as in a piezoelectric power generation system.

2.3 Theoretical Background

The linear electromechanical energy conversion process with piezoelectric ceramics is by far the easiest to handle, since the piezoelectric, dielectric and elastic constants can be applied directly [8]. In linear analysis, the coefficients mentioned above are assumed to be constant during the operation. The nonlinearity at high fields and hysteresis effects are ignored, i.e. the losses due to nonlinear effects are not considered. It is also assumed that the operation frequency is well below the lowest resonant frequency of the piezoelectric element, i.e. the operation can be considered as quasi-static. The linear constitutive relationships for a general piezoelectric element are:

$$\begin{bmatrix} D \\ S \end{bmatrix} = \begin{bmatrix} \epsilon^T & d \\ d_t & s^E \end{bmatrix} \begin{bmatrix} E \\ T \end{bmatrix} \quad (2.1)$$

where D is a vector of electric displacements or charge density(charge/area), S is the vector of material engineering strains, E is the vector of electrical field in the material(volts/meter),

T is the vector of material stresses (force/area), ϵ is the matrix of dielectric constants, d is the matrix of piezoelectric constants and s is the matrix of compliance coefficients of the piezoelectric element. The superscripts $()^T$ and $()^E$ signify that the coefficients are measured at constant stress and constant electric field respectively and the subscript $()_t$ denotes the matrix transpose. In this chapter, a specific case will be considered where the piezoelectric element is subjected to compression parallel to the polarization of the element. It is assumed that the lateral dimensions are small compared to the axial dimension, so that only the axial stress T_3 needs to be considered ($T_1 = T_2 \approx 0$). Or, it can be assumed that, the element is free to expand in lateral directions so that T_3 is the only nonzero stress component. Under these conditions, equation 2.1 reduces to

$$\begin{bmatrix} D_3 \\ S_3 \end{bmatrix} = \begin{bmatrix} \epsilon_{33}^T & d_{33} \\ d_{33} & s_{33}^E \end{bmatrix} \begin{bmatrix} E_3 \\ T_3 \end{bmatrix} \quad (2.2)$$

where the first and second subscripts of the piezoelectric, dielectric and elastic constants denote the orientation of the electric field and the stress respectively.

Quasi-static coupling factors, or coefficients, are very common and useful definitions for piezoelectric energy conversion. The coupling coefficients are dimensionless and thus they provide a useful comparison between different piezoelectric materials independent of the specific values of permittivity or compliance. The definition of the coupling coefficient described above is given in [18]. Figure 2-1 illustrates graphically the meaning of the coupling coefficient k_{33} . The cycle shown is as follows: first, the piezoelectric element is compressed under short circuit condition, then the compressive stress is removed under open circuit condition, and then the cycle is completed under constant stress condition by applying an ideal electric load. As work is done on the electric load, the strain returns to its initial state. For the idealized case illustrated in Figure 2-1(a), the coupling coefficient is defined as:

$$(k_{33})^2 = \frac{W_1}{W_1 + W_2} = \frac{s_{33}^E - s_{33}^D}{s_{33}^E} = \frac{d_{33}^2}{s_{33}^E \epsilon_{33}^T} \quad (2.3)$$

where W_1 is the work done on the electric load and W_2 is the part of the energy unavailable to the electric load or the reversible stored elastic energy (strain energy).

Similarly, the coupling coefficient for energy conversion from electrical energy to mechanical

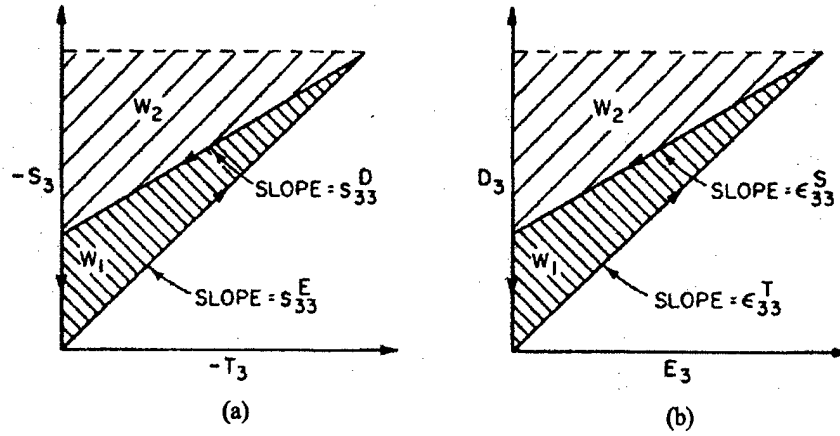


Figure 2-1: Graphic illustration of electromechanical energy conversion and definition of the piezoelectric coupling factor k_{33} given in [18] (a) Conversion of energy from a mechanical source to electrical work (b) Conversion of energy from an electrical source to mechanical work.

energy can be derived using the idealized cycle illustrated in Figure 2-1(b). First, the element is mechanically free when the electric source is connected. Then the element is blocked mechanically parallel to polarization before the electric source is disconnected. Then with $E_3 = 0$ the mechanical block is removed and in its place a finite mechanical load is provided. For this idealized cycle of work illustrated in Figure 2-1(b), the coupling coefficient is defined as:

$$(k_{33})^2 = \frac{W_1}{W_1 + W_2} = \frac{e_{33}^T - e_{33}^{S_3=0}}{\epsilon_{33}^T} = \frac{d_{33}^2}{s_{33}^E \epsilon_{33}^T} \quad (2.4)$$

where W_1 is the work done on the mechanical load and W_2 is the part of the energy unavailable to the mechanical load.

The idealized work cycles illustrated in Figure 2-1 correspond to the standard definition of the piezoelectric coupling coefficient. Berlincourt proposes alternative work cycles of reversible electromechanical energy conversion in [8]. These cycles are shown in Figure 2-2. The first one, which is illustrated in Figure 2-2(a) corresponds to a case where the element is compressed with the electric load not connected, i.e. under open circuit conditions, then the electric load is connected with stress maintained, then the mechanical stress is reduced to zero with the electric load again disconnected and finally the electric load is connected and the element

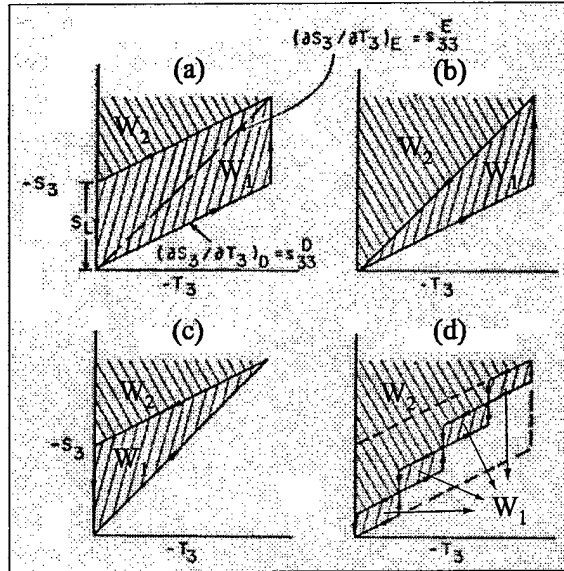


Figure 2-2: Alternative idealized work cycles given in [8].

returns to its initial state under constant stress. In the cycle illustrated in Figure 2-2(b), the element is compressed under open circuit condition, then the electric load is connected with stress maintained and finally the electric load is connected and the stress is reduced under closed circuit condition and the element returns to its initial state. The cycle in Figure 2-2(c) is identical to the cycle used for deriving the coupling coefficient in Figure 2-1. The cycle in Figure 2-2(d) corresponds to a case where the energy conversion occurs at several intermediate levels.

Berlincourt [8] defines an *effective coupling factor*, which is equal to

$$k_{eff}^2 = \frac{W_1}{W_1 + W_2} \quad (2.5)$$

He applies this definition to each of the different work cycles described above. Then he expresses the effective coupling factors for each of the different cycles in terms of the standard coupling coefficient given in Equation 2.3 as follows:

$$k_{eff(a)} = k_{33} \sqrt{2/(1 + k_{33}^2)} \quad (2.6)$$

$$k_{eff(b)} = k_{33} \sqrt{1 + k_{33}^2} \quad (2.7)$$

$$k_{eff(c)} = k_{33} \quad (2.8)$$

$$k_{eff(d)} = k_{33} \sqrt{2/(n + k_{33}^2)} \quad (2.9)$$

where k_{33} is the standard coupling coefficient and n is the number of intermediate levels in Figure 2-2(d). From equation 2.6 it is apparent that the coupling coefficient corresponding to the first case in Figure 2-2 is greater than the standard coupling coefficient defined previously.

It is important to note that, the cycles described so far are idealized or hypothetical cycles. The energy conversion process occurs with the mechanical and electrical energy sources connected and disconnected at will. However, no explanation has been given in terms of how these cycles can be achieved or approximated in a real application. In other words, the mechanical and electrical infrastructures which would allow these cycles to occur are not discussed. In this chapter, conversion from mechanical to electrical energy is considered, with emphasize on the circuitry used which basically determines the work-cycle. In other words, the rectifying circuitry is the electrical infrastructure in the power generation process. In the following sections two different circuit topologies will be analyzed in detail in terms of the effective coupling factor and energy density.

2.4 Circuitry Considerations

Although in the literature different mechanisms for piezoelectric power generation has been presented and some studies performed for piezoelectric material characterization for power generation, no detailed analysis has been presented in terms of effective coupling factor, energy density and piezoelectric material comparison with regard to circuitry. This section analyzes two different circuits for rectifying and storing the electrical energy generated by the piezoelectric element. These circuits constitute examples of nonlinear shunting of piezoelectric elements. The first one is a regular full bridge rectifier with a battery attached to it. The second circuitry is the same circuit proposed in [26] for piezoelectric power generation, which consists of a full bridge

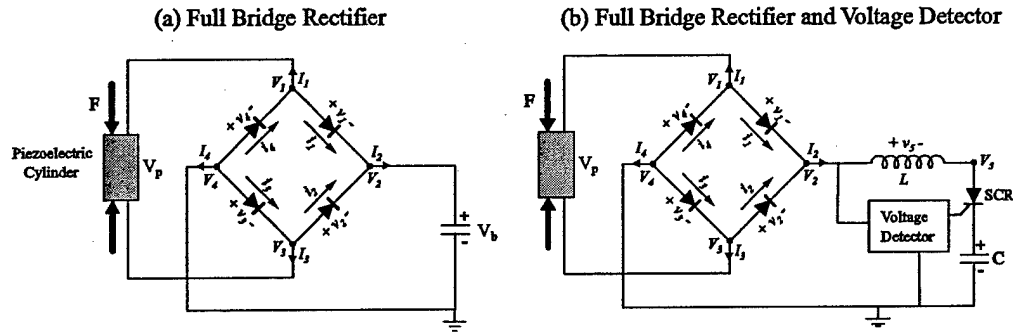


Figure 2-3: Alternative circuits to rectify and store the electrical energy generated by the piezoelectric element.

rectifier, an inductor, a silicon controlled rectifier (SCR), a voltage detector and a capacitor to store the electrical energy. The circuits are shown in Figure 2-3.

2.4.1 Modeling

This section presents the modeling of the piezoelectric element and the circuitry. The models are same for the two circuits under consideration except some small differences.

Piezoelectric Element

Linear piezoelectric constitutive relationships are assumed. The form of the constitutive equations used here is as follows:

$$\begin{bmatrix} S \\ E \end{bmatrix} = \begin{bmatrix} s_{33}^D & \frac{d_{33}}{\varepsilon_{33}^T} \\ \frac{d_{33}}{\varepsilon_{33}^T} & -\frac{1}{\varepsilon_{33}^T} \end{bmatrix} \begin{bmatrix} T \\ D \end{bmatrix} \quad (2.10)$$

where D is the charge field, S is the strain, E is the electric field, and T is the stress. For a cross-sectional area of A_p and length of L_p , the expressions for the deflection of the piezoelectric element and the voltage across it become:

$$x_p = \frac{L_p}{A_p} (s_{33}^D F_p + \frac{d_{33}}{\varepsilon_{33}^T} Q_p) \quad (2.11)$$

$$V_p = \frac{L_p}{A_p} \left(\frac{d_{33}}{\epsilon_{33}^T} F_p - \frac{1}{\epsilon_{33}^T} Q_p \right) \quad (2.12)$$

where x_p is the deflection, Q_p is the charge, F_p is the force applied on the piezoelectric cylinder, and V_p is the voltage across the piezoelectric cylinder. And the current through the piezoelectric element is given by:

$$I_p = \frac{dQ_p}{dt} \quad (2.13)$$

Diode Bridge

The model of the diode bridge rectifier is based on [52]. The governing equations can be derived using Kirchoffs laws and diode equations. The notation in Figure 2-3 is used. Applying Kirchoffs Current Law (*KCL*) in the junctions 1,2,3,and 4, we get:

$$I_1 = i_4 - i_1 \quad (2.14)$$

$$I_2 = i_1 + i_2$$

$$I_3 = i_3 - i_2$$

$$I_4 = -i_3 - i_4$$

The voltages across the diodes are given by:

$$v_1 = V_1 - V_2 \quad (2.15)$$

$$v_2 = V_3 - V_2$$

$$v_3 = V_4 - V_3$$

$$v_4 = V_4 - V_1$$

Applying Kirchoffs Voltage Law (*KVL*) around the loops corresponding to the cases where $V_p > 0$ and $V_p < 0$ we get:

$$\begin{aligned}
-V_p + v_1 + V_b + v_3 &= 0 & \text{for } V_p > 0 \\
V_p + v_2 + V_b + v_4 &= 0 & \text{for } V_p < 0
\end{aligned} \tag{2.16}$$

For the case where $V_p > 0$, the currents flowing through diodes #1 and #3 are the same, and for the case where $V_p < 0$, the currents flowing through diodes #2 and #4 are the same. Since all the diodes have the same constitutive relationship, we can write:

$$\begin{aligned}
V_1 - V_2 &= V_4 - V_3 & \text{for } V_p > 0 \\
V_4 - V_1 &= V_3 - V_2 & \text{for } V_p < 0
\end{aligned} \tag{2.17}$$

Recognizing that $V_p = V_1 - V_3$, $V_2 = V_b$, $V_4 = 0$ (ground) and using equation 2.17 we can write:

$$\begin{aligned}
V_1 &= \frac{V_b + V_p}{2} \\
V_3 &= \frac{V_b - V_p}{2}
\end{aligned} \tag{2.18}$$

The *voltage – current* relationships (constitutive law) of the diodes are:

$$\begin{aligned}
i_n &= I_o \left[\exp \frac{qv_n}{\eta kT} - 1 \right], & v_n &\geq 0 \\
i_n &= 0 & v_n &< 0
\end{aligned} \tag{2.19}$$

where the subscript $()_n$ denotes the diode number, $q = 1.60 \times 10^{-19}(C)$ is the electron charge, $k = 1.38 \times 10^{-23}(J/K)$ is the Boltzman constant and T is the temperature($T = 300K$). I_o and η are diode properties. For CS57-04 diode (Collmer Semiconductor, Inc.), whose values will be used throughout the thesis, they are measured to be: $I_o = 10^{-6}$ and $\eta = 17.25$ [19].

Diode Bridge and Voltage Detection Circuit

For the diode bridge with the voltage detection circuit, the model is similar. The equations 2.14, 2.15, and 2.19 are valid. However because of the implementation of the voltage detection circuit and SCR, the simulation architecture is different [53], which is shown in Appendix A. The voltage detection circuit is not modeled. Only its function is implemented in Simulink. The Kirchoffs Voltage Law can be written for this case using the notation in Figure 2-3 as:

$$\begin{aligned} -V_p + v_1 + v_5 + V_{SCR} + V_c + v_3 &= 0 \quad \text{for } V_p > 0 \\ V_p + v_2 + v_5 + V_{SCR} + V_c + v_4 &= 0 \quad \text{for } V_p < 0 \end{aligned} \quad (2.20)$$

The voltage across the inductor is given by:

$$v_5 = L \frac{d(I_2)}{dt} \quad (2.21)$$

And we can also write

$$V_c = \frac{1}{C} \int I_2 \quad (2.22)$$

2.4.2 Simulation and Analysis

Simulations are performed using Matlab/Simulink. The Simulink blocks and additional details are given in the Appendix A. The Simulink architecture is shown in Figure 2-4. The piezoelectric element block includes the constitutive relationships and the circuit block includes the equations corresponding to the circuitry. The piezoelectric element is excited with an imposed force on it. The geometry and operation conditions chosen for the simulation are shown in Table 2.1.

The imposed force is sinusoidal with an offset, namely it fluctuates between zero and the force corresponding to the maximum applicable stress, which is the depolarization stress of the piezoelectric element. In the case of PZN-4.5%PT, the depolarization stress is measured to be around 10 MPa [19]. For the chosen piezoelectric cylinder diameter, the maximum force is 31.4 N . Detailed comparison of different piezoelectric materials will be presented in section 2.6.

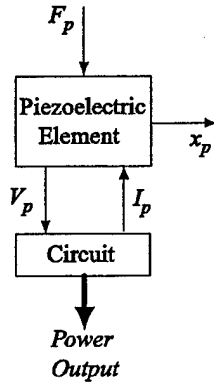


Figure 2-4: Simulation architecture used to simulate the piezoelectric element connected to the full bridge rectifier. The force is imposed on the piezoelectric element.

| | |
|--|-----------------|
| Length of the piezoelectric element, L_p | $1mm$ |
| Diameter of the piezoelectric element, D_p | $2mm$ |
| Operation frequency, f | $20kHz$ |
| Maximum force, F_p | $31.4N$ |
| Optimum battery voltage, V_b | $90V$ |
| Piezoelectric material | $PZN - 4.5\%PT$ |

Table 2.1: Geometry and operation conditions used in simulation

Full Bridge Rectifier

Simulation Simulation time histories are shown in Figure 2-5. The operation at steady state can be summarized as follows: During the compression of the piezoelectric element the voltage on it increases. If it reaches the battery voltage, current starts to flow through the battery and in fact the piezoelectric element voltage is a little bit higher than the battery voltage during this interval which causes the current to flow. The amount which the piezoelectric element voltage exceeds the battery voltage during this interval depends on the diode properties and other resistances in the system. When the force on the piezoelectric element begins decreasing, the voltage decreases too and when it becomes less than the battery voltage current stops flowing through the battery. As the force on the piezoelectric element keeps decreasing, the voltage on the piezoelectric elements keep decreasing until it reaches the negative value of the battery voltage. At this point, current begins to flow through the battery, now, however, from a different branch of the diode bridge, namely through different diodes. Again during this interval the voltage on the piezoelectric element exceeds the battery voltage a little bit (in this case it is lower than the negative value of the battery voltage). When the force begins increasing, the voltage begins increasing too and again no current flows through the battery. Throughout the operation, the voltage on the piezoelectric element fluctuates between the negative and positive values of the battery voltage.

In order to get insight into the energy conversion mechanism and to derive the governing equations in the next section, it is worthwhile to look at the force vs. deflection and voltage vs. charge plots of the piezoelectric element. These are plotted in Figure 2-6. The most important observation is that there are two major regimes during the operation: Operation under open circuit conditions, where the compliance of the piezoelectric element is small, i.e the piezoelectric element is hard; and operation under closed circuit conditions, where the compliance of the piezoelectric element is large, i.e the piezoelectric element is soft. The compliances in these regimes are s_{33}^D and s_{33}^E for open circuit and closed circuit conditions respectively. The shaded region in Figure 2-6 corresponds to the stored electrical energy in one cycle. The generated power is then simply this energy times the operation frequency.

The battery voltage has an important effect on the performance. The simulation results presented in Figure 2-5 and Figure 2-6 correspond to the optimum battery voltage (90V). The

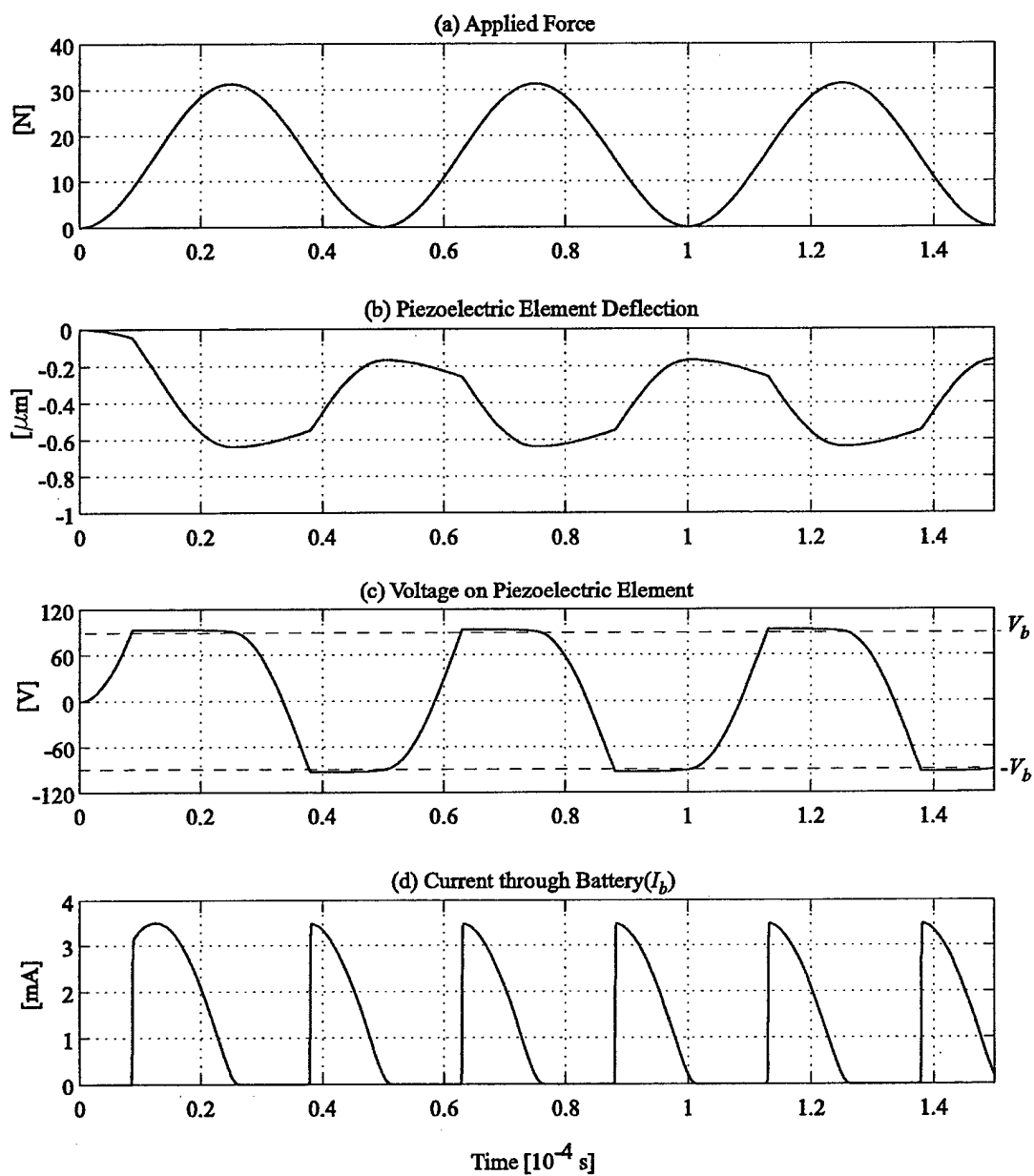


Figure 2-5: Time histories from the simulation of the piezoelectric element connected to the full bridge rectifier for the case of imposed force. The generated power is $I_b V_b$.

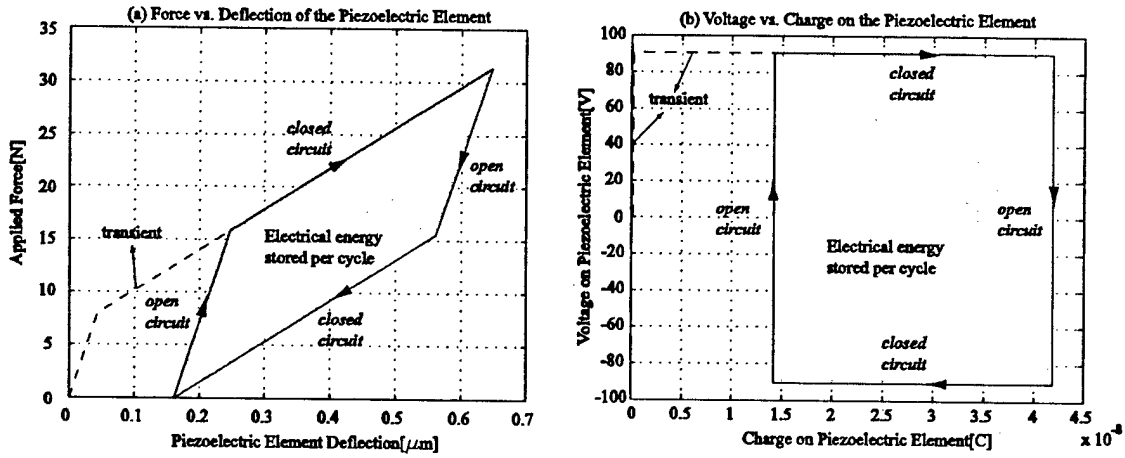


Figure 2-6: Force vs. deflection and voltage vs. charge plots of the piezoelectric element compressed under the applied force for the case of full bridge rectifier.

force vs. deflection of the piezoelectric element for different values of battery voltage is shown in Figure 2-7. It is found that, the maximum power is obtained with an optimum battery voltage of:

$$V_{b(opt)} = \frac{V_{oc}}{4} = \frac{1}{4} \frac{\sigma(s_{33}^E - s_{33}^D)L_p}{d_{33}} \quad (2.23)$$

where V_{oc} is the open circuit voltage of the piezoelectric element, s_{33}^E and s_{33}^D are the closed circuit and open circuit compliances of the piezoelectric element respectively, d_{33} is the piezoelectric coefficient, σ is the maximum stress on the piezoelectric element, and L_p is the length of the piezoelectric element. Open circuit voltage at a given stress is the voltage generated by the piezoelectric element when compressed under open circuit conditions. In fact the optimum battery is the voltage which optimizes the shape of the force vs. displacement curve for maximum enclosed area.

It should be noted that the above analysis is done for a case where the force on the piezoelectric element is varying between zero and a maximum value which corresponds to the depolarization stress of the piezoelectric element. In order to analyze the case where the force is biased, the system is simulated for nonzero positive or negative minimum forces. It has been discovered

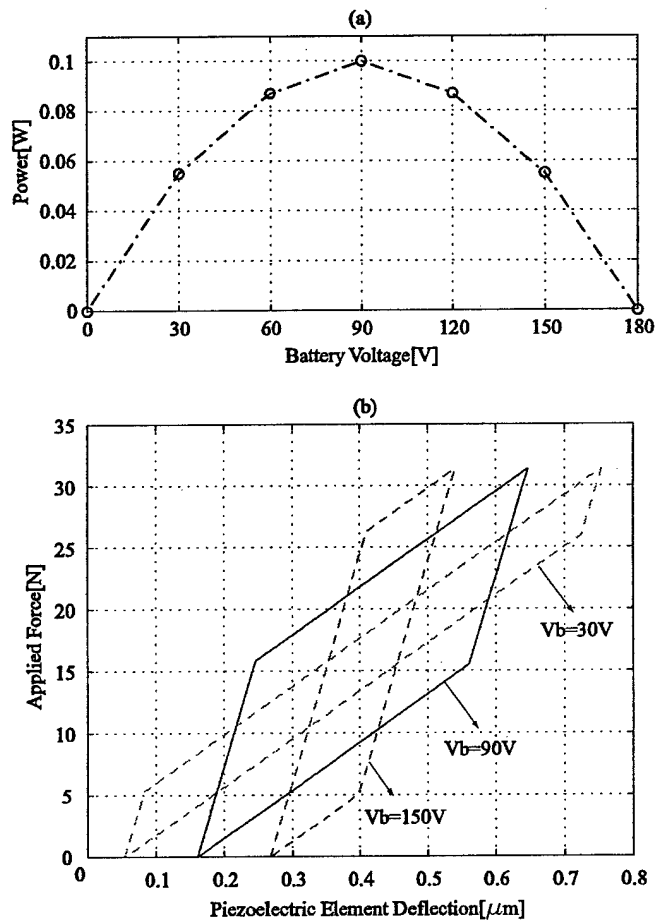


Figure 2-7: Effect of battery voltage on power.

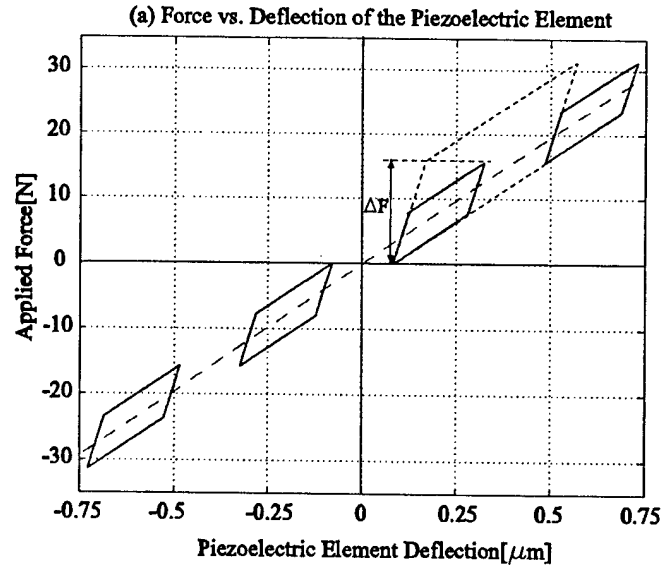


Figure 2-8: Effect of bias force on the workcycle.

that the optimum battery voltage depends only on the stress band on the piezoelectric element, namely on the difference of the maximum and minimum stresses on the piezoelectric element. Figure 2-8 shows the workcycles for different applied forces which have the same peak to peak values but different bias values. For each case the optimum battery voltage is the same since the stress band resulting from each case is the same. Equation 2.23 can be rewritten as:

$$V_{b(opt)} = \frac{1}{4} \frac{\Delta\sigma(s_{33}^E - s_{33}^D)L_p}{d_{33}} \quad (2.24)$$

where $\Delta\sigma$ is the stress band on the piezoelectric element.

Analysis In order to investigate the work cycle of the piezoelectric element, we can analyze the stress vs. strain and electric field vs. charge density plots of the piezoelectric element in detail. Important features of the work cycle is shown in Figure 2-9 which corresponds to the optimum battery voltage case. It is important to not that, the dashed line, which corresponds to the case in which the piezoelectric element would be compressed in closed circuit conditions, passes through the middle of the stress vs. strain curve. We also know the slopes of the curve

in the two different regimes, namely open circuit and closed circuit regimes. Using simple geometry, we can derive the coordinates of the corner points. From the voltage vs. charge plot in Figure 2-6 we see that the voltage of the piezoelectric element fluctuates between the positive and negative values of the battery voltage. Using constitutive relationships to calculate the corresponding charge on the piezoelectric element at different states, we can get the electric field vs. the charge density plot. These are shown in Figure 2-9.

The electrical energy stored (per piezoelectric element volume) in the battery in one cycle for the case of optimum battery voltage, which is equal to the enclosed area by the stress vs. strain or electric field vs charge density curve can obtained using simple geometry from Figure 2-9 as:

$$E = \frac{1}{4}(s_{33}^E - s_{33}^D)\sigma^2 \quad (2.25)$$

where s_{33}^E and s_{33}^D are the closed circuit and open circuit compliances of the piezoelectric element respectively and σ is the maximum stress on the piezoelectric element.

Then, the generated power by the piezoelectric element can be expressed as:

$$W = \frac{1}{4}(s_{33}^E - s_{33}^D)\sigma^2 V_p f \quad (2.26)$$

where V_p is the volume of the piezoelectric element and f is the operation frequency. From the above equation it can be seen that the power depends heavily on the stress on the piezoelectric element. The most important limitation on piezoelectric power generation is the depolarization stress. For stresses larger than this, piezoelectric element coefficients degrade and performance decreases drastically. Each piezoelectric element has a different depolarization stress, which constitute an important factor when determining their feasibility as power generators. Detailed comparison of different piezoelectric elements will be presented in Section 2.6.

Effective coupling factor for an electromechanical energy conversion mechanism, in this case a system which converts mechanical energy into electrical energy is defined as the ratio of the mechanical work done on the system to the electrical energy stored in one cycle. This definition is the same as the one used to derive the coupling coefficient. This is illustrated in Figure 2-10. From the above definition we can write:

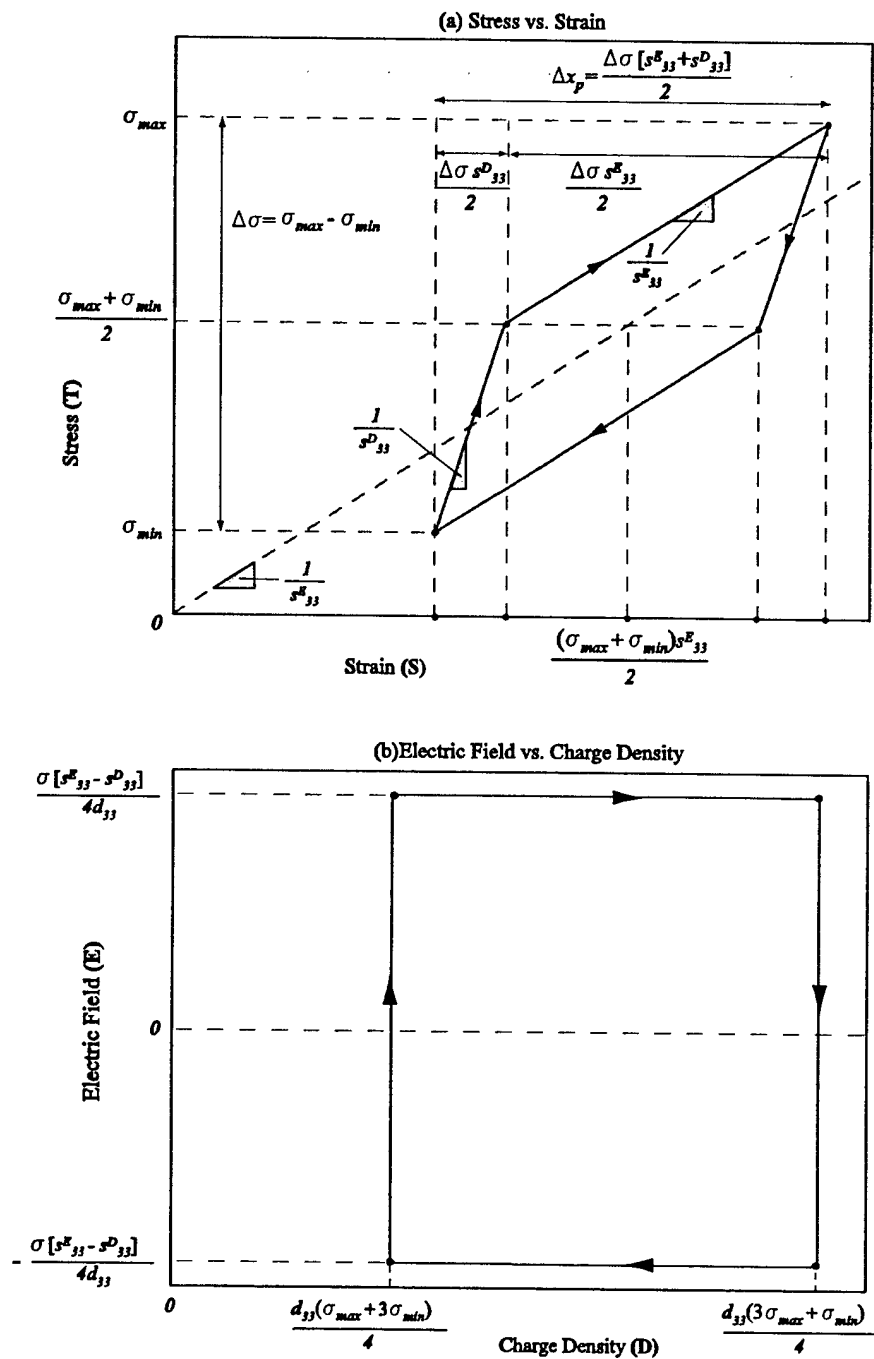


Figure 2-9: General presentation of the work cycle of the piezoelectric element in terms of stress, strain, electric field and charge density for the case of regular diode bridge.

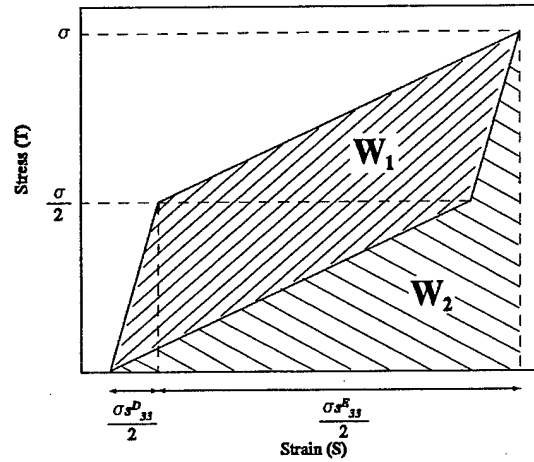


Figure 2-10: Illustration of the effective coupling factor for the case of regular diode bridge.

$$k_{eff}^2 = \frac{W_1}{W_1 + W_2} \quad (2.27)$$

Again using geometry, the effective coupling factor can be derived in terms of the piezoelectric material compliances as:

$$k_{eff}^2 = \frac{2(s_{33}^E - s_{33}^D)}{3s_{33}^E + s_{33}^D} \quad (2.28)$$

The definition of the coupling coefficient of a piezoelectric element was given in section 2.3. Using equations 2.3 and 2.28, the effective coupling factor for the full bridge rectifier case can be expressed in terms of the coupling coefficient as:

$$k_{eff}^2 = \frac{2k_{33}^2}{k_{33}^2 + 2} \quad (2.29)$$

Full Bridge Rectifier and Voltage Detection Circuit

The operation of this circuit is as follows: The voltage detector circuit detects the voltage right after the diode bridge (V_2). Initially, the SCR is in "off" state. If V_2 reaches its maximum and begins decreasing, the voltage detector sends a current signal to SCR which turns it on. If the detected voltage reaches zero, the voltage detector sends another signal to SCR which turns it

off.

Simulation The simulation architecture is the same as in Figure 2-4. The implementation of the switching of the SCR and additional details of the Simulink model are presented in Appendix A. Again, the force is imposed on the piezoelectric element. The geometry, operation frequency and the piezoelectric material are the same as in the previous section. The time histories resulting from the simulation are shown in Figure 2-11.

Again, in order to get insight into the energy conversion mechanism and to derive the governing equations, it is worthwhile to look at the force vs. deflection and voltage vs. charge plots for the piezoelectric element. These are plotted in Figure 2-12. We can see that there are two basic operation regimes. The first one is operation under open circuit conditions, where the compliance of the piezoelectric element is low, i.e the piezoelectric element is hard. The second operation regime is defined with the *almost flat* lines in Figure 2-12. This regime corresponds to the time intervals, where the switch (SCR) is on. In this regime, the piezoelectric material behaves as a very soft material.

Since the SCR is initially closed, the piezoelectric element is first compressed under open circuit conditions, until the applied force reaches its maximum and begins to decrease (period 1-2). In this period, the voltage on the piezoelectric element reaches the open circuit voltage corresponding to the maximum stress applied on the element. Once the force begins to decrease, the detected voltage, which is the rectified piezoelectric element voltage, begins to decrease too, which causes the switch to turn on. After the switch turns on, the voltage decreases very fast and the piezoelectric element is compressed with a very small effective stiffness. The switch turns again off once the voltage reaches zero. During the period when the switch is on (2-3), the piezoelectric element is squeezed until the point, as if it was being squeezed under the same stress and closed circuit conditions. We can verify this by looking to the voltage vs. charge plot. In state 3, the voltage on the piezoelectric element is zero and the force on it is almost the maximum force. Of course, this rapid compression occurs in finite time and during this time interval, the force decreases a little bit, which results in the *almost flat* region in force vs. deflection plot. The shorter the "on" state, the flatter will be the line. It can be concluded that, the performance of the system with this cycle depends highly on the time history of the

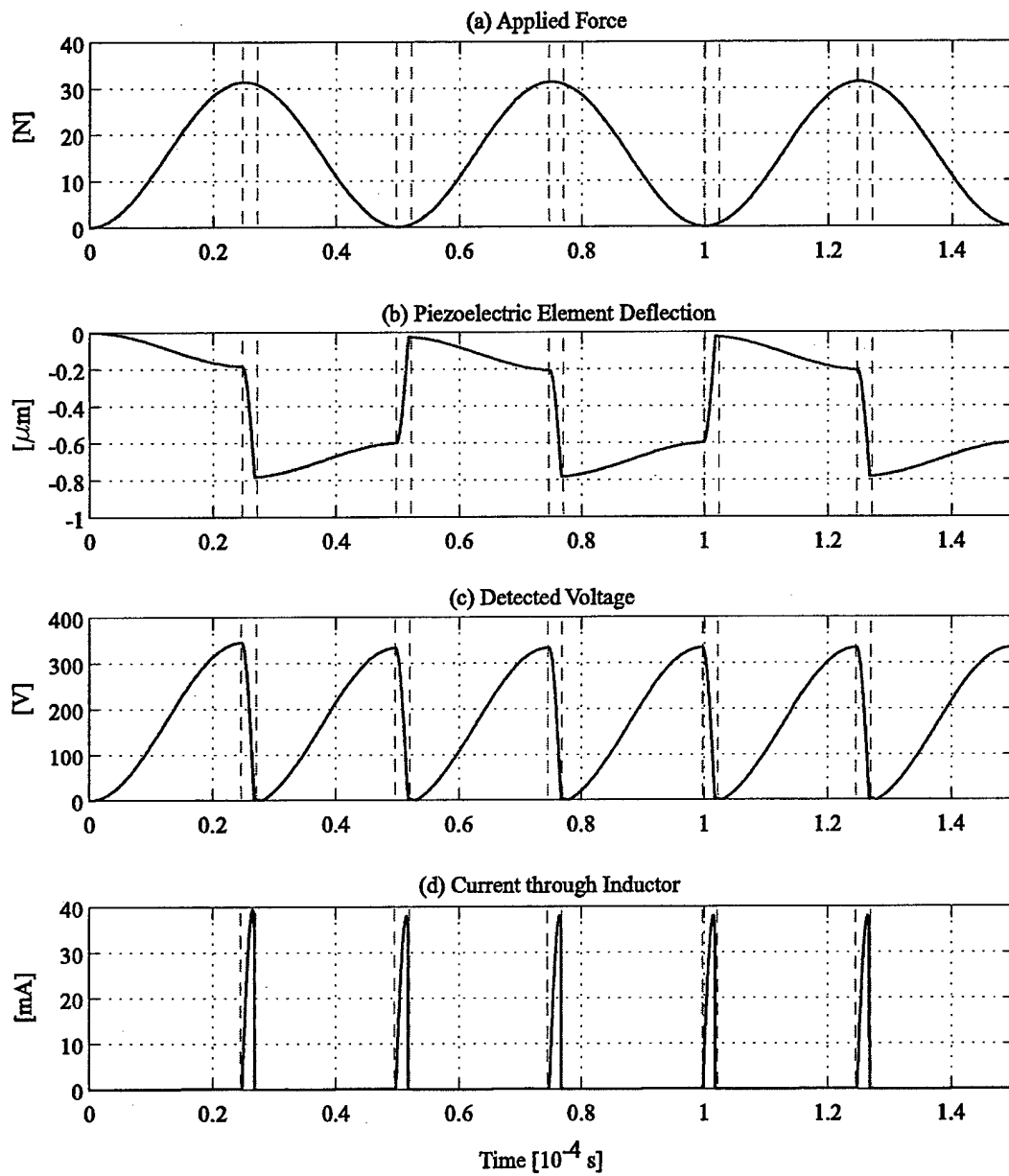


Figure 2-11: Time histories from the simulation of the piezoelectric element connected to the full bridge rectifier and voltage detector circuit. The time intervals between the dashed lines present the intervals where the switch(SCR) is in its "on" state.

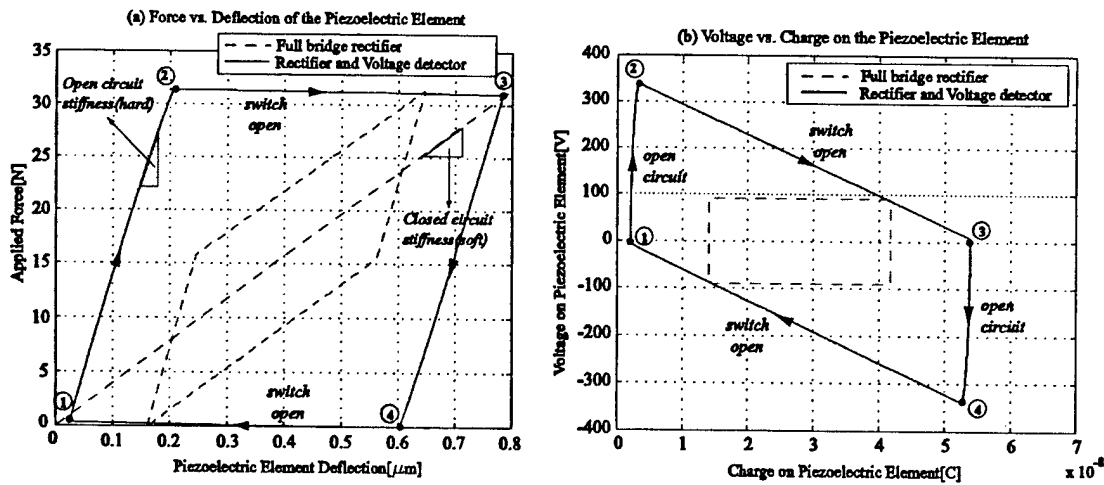


Figure 2-12: Force vs. deflection and voltage vs. charge plots of the piezoelectric element compressed under the applied force for the case of full bridge rectifier and voltage detector circuit.

applied force.

Analysis After the observations done in the previous section, we can derive the equations which determine the maximum strain and charge of the piezoelectric element, the energy stored per cycle and the effective coupling factor. To keep the analysis more general, we again analyze the work cycles in terms of stress vs. strain and electric field vs. charge density plots. Important features of the idealized work cycles are shown in Figure 2-13. As mentioned earlier, there is a finite time associated with the transition between states 2-3 and 4-1, where the force does not remain at its maximum value. This time interval depends highly on the value of the inductor used. In the simulation, an inductor of 20mH is used. It should be also mentioned that, the capacitor has to be large enough to avoid saturation. The simulation results are very close to the idealized cycles, which can be seen comparing Figure 2-12 and Figure 2-13. It should be also mentioned that, the difference between these figures should be counted partly on a simulation artifact. The switch operation and open circuit and closed circuit conditions are simulated using very large and very small resistances respectively. It can be concluded that, the idealized curves in Figure 2-13 are very good approximations to the actual work cycles.

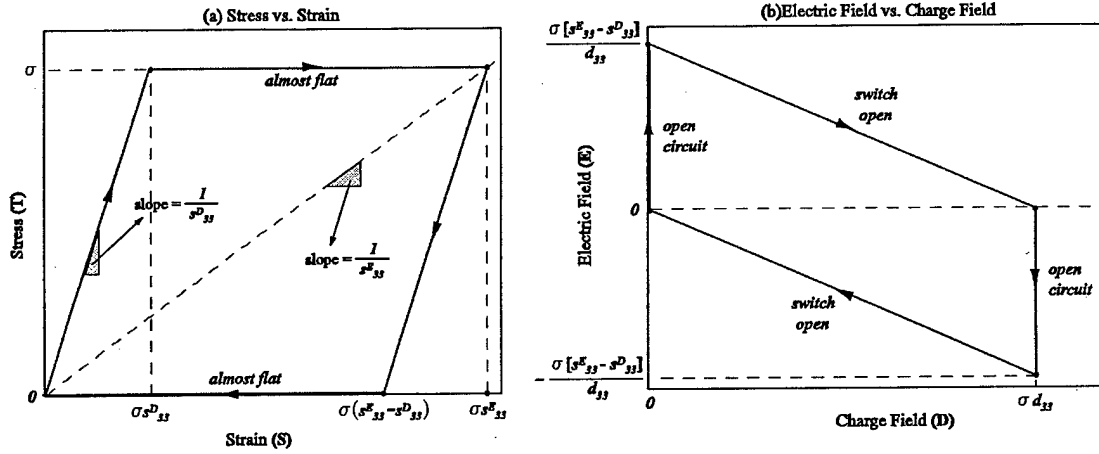


Figure 2-13: General presentation of the work cycle of the piezoelectric element in terms of stress, strain, electric field and charge density for the case of the full bridge rectifier and voltage detector circuit.

The derivation of the coordinates of the points in Figure 2-13 is straightforward. The strain values can be found by using the slopes of the stress vs. strain curve. The maximum charge can be calculated using the constitutive relationships for the condition of zero electric field and maximum stress. The electrical energy stored in the capacitor in one cycle, which is equal to the enclosed area by the stress vs. strain and electric field vs. charge density curve can be obtained easily as:

$$E = (s_{33}^E - s_{33}^D) \sigma^2 \quad (2.30)$$

where s_{33}^E and s_{33}^D are the closed circuit and open circuit compliances of the piezoelectric element respectively and σ is the maximum stress on the piezoelectric element.

Then, the generated power by the piezoelectric element can be expressed as:

$$W = (s_{33}^E - s_{33}^D) \sigma^2 V_p f \quad (2.31)$$

where V_p is the volume of the piezoelectric element and f is the operation frequency. From the above equation it can be seen that the power depends heavily on the stress on the piezo-

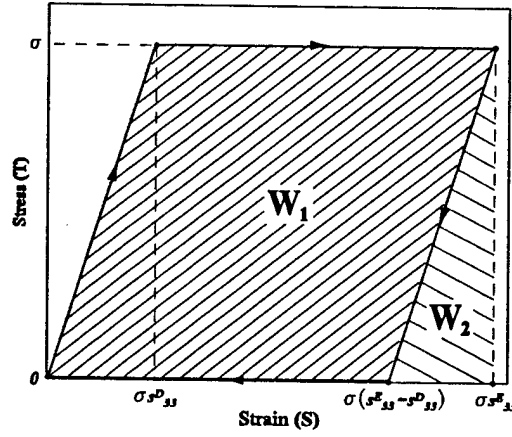


Figure 2-14: Illustration of the effective coupling factor for the full bridge rectifier and voltage detection circuit.

electric element. The power generated with this circuitry is four times bigger than the power generated using the full bridge rectifier under the same conditions, namely same applied force and frequency.

Using the definition in equation 2.27 and from Figure 2-14, the effective coupling factor can be obtained as:

$$k_{eff}^2 = \frac{W_1}{W_1 + W_2} = \frac{2(s_{33}^E - s_{33}^D)}{2s_{33}^E - s_{33}^D} \quad (2.32)$$

Using equations 2.3 and 2.32, we can express the effective coupling factor of the coupling coefficient as:

$$k_{eff}^2 = \frac{2k_{33}^2}{k_{33}^2 + 1} \quad (2.33)$$

It is very interesting to note that the diode bridge and the voltage detection circuit proposed by Smalser in [26] result in the hypothetical electromechanical energy conversion work-cycle proposed by Berlincourt [8]. This cycle is shown in Figure 2-2(a). The expression in equation 2.6 is identical to equation 2.33.

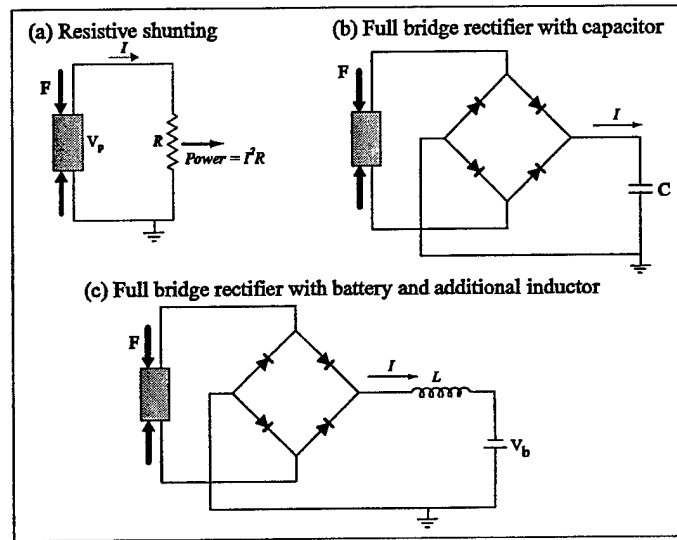


Figure 2-15: Other alternative circuits for piezoelectric power generation.

2.5 Other Circuits

This section discusses some other alternative circuits for piezoelectric power generation, shown in Figure 2-15. The geometry, operation frequency and the piezoelectric material used for the simulations are the same as in the previous section.

A much simpler circuit than the ones presented in previous sections is that involving just a resistor. Resistive shunting of piezoelectric elements for structural damping is discussed in [15]. The resistive shunting exhibits frequency dependent behavior and the converted electrical energy is dissipated, not stored. Figure 2-16 shows the force vs. deflection and voltage vs. charge plots from the simulation of the piezoelectric element shunted by a resistor. It can be seen that, for relatively small resistance values, the piezoelectric element behaves close to the closed circuit condition, whereas for large resistance values, it behaves close to the open circuit condition. It should be noted that the simulations presented in Figure 2-16 are performed at a certain frequency. If one were to keep the resistance constant and change the frequency, similar behavior would be observed. Namely, at very large frequencies the behavior would be close to open circuit behavior, whereas at very low frequencies, the behavior would be close to closed

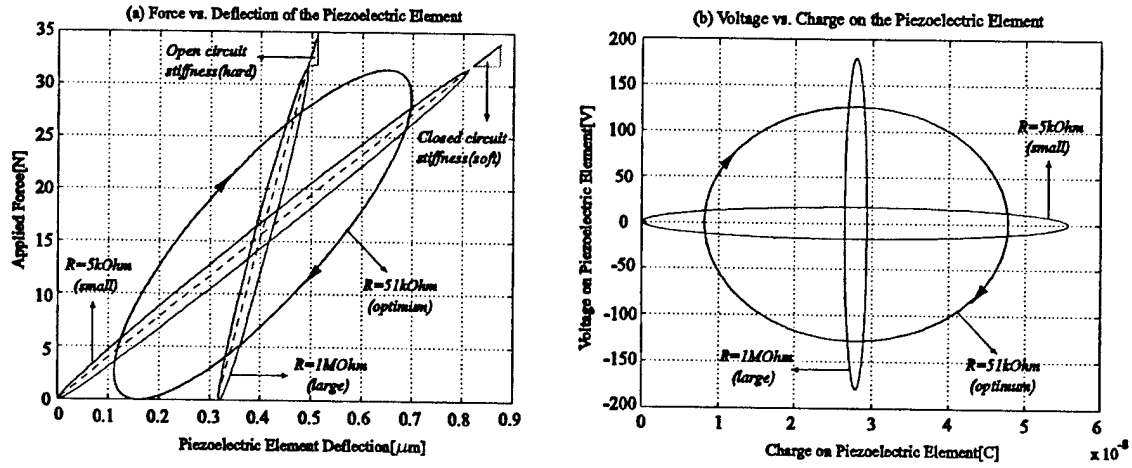


Figure 2-16: Simulation results of the piezoelectric element shunted by a resistor for different resistance values.

circuit behavior. Indeed, the maximum electromechanical energy conversion occurs when the impedance of the load, which is the resistor, is matched to the impedance of the piezoelectric element. In other words, for a given piezoelectric element and geometry, at any given resistance value there exists an optimum frequency, or at any given frequency there exists an optimum resistance value. The optimum resistance value is given as:

$$R_{opt} = \frac{1}{2\pi f C^T} \quad (2.34)$$

where f is the operation frequency and C^T is the capacitance of the piezoelectric element under constant stress, which can be expressed as:

$$C^T = \frac{e_{33}^T A_p}{L_p} \quad (2.35)$$

where e_{33}^T is the dielectric constant and A_p and L_p are the cross-sectional area and the length of the piezoelectric element respectively.

Figure 2-17 compares the resistive shunting (for optimum resistance value) with the circuits presented in previous sections. Resistive shunting performs better compared to the full bridge rectifier in terms of electromechanical energy conversion. However, as mentioned earlier, the

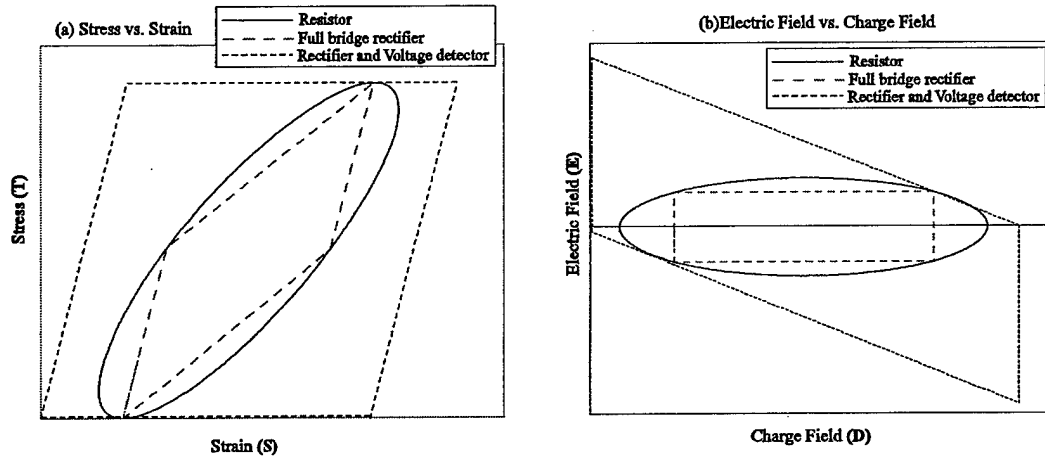


Figure 2-17: Comparison of resistive shunting(at optimum resistance) with full bridge rectifier and full bridge rectifier with voltage detector.

performance depends heavily on operation frequency and the electrical energy is not stored, which make resistive shunting not a suitable option for power generation.

An alternative circuit can be full bridge rectifier and a capacitor connected to it, instead of a battery or a DC voltage source as presented in section 2.4.2. This is actually the same circuit configuration as presented in [10]. The simulation results are shown in Figure 2-18. As can be seen from the plots, the behavior heavily depends on the value of the capacitor. Obviously, energy cannot be transferred to the capacitor after the voltage of the capacitor nearly reaches half of the open circuit voltage of the piezoelectric element, which corresponds to the maximum stress. As expected, the higher the capacitance, the larger is the stored energy, since the final voltage is the same regardless of the capacitance value. This statement contradicts with the conclusion made in [10] because in this simulation the force is imposed on the piezoelectric element. In [10], no force is imposed on the piezoelectric element. The dynamics of the system (falling ball, vibration of the plate etc.) is determined by the circuitry, i.e. the capacitor and there exists an optimum capacitance value for maximum energy transfer.

Another alternative would be to add an inductor to the full bridge rectifier in series with the battery. The simulation results corresponding to the optimum inductor value are shown in Figure 2-19. It can be seen that both the stored energy per cycle and the effective coupling

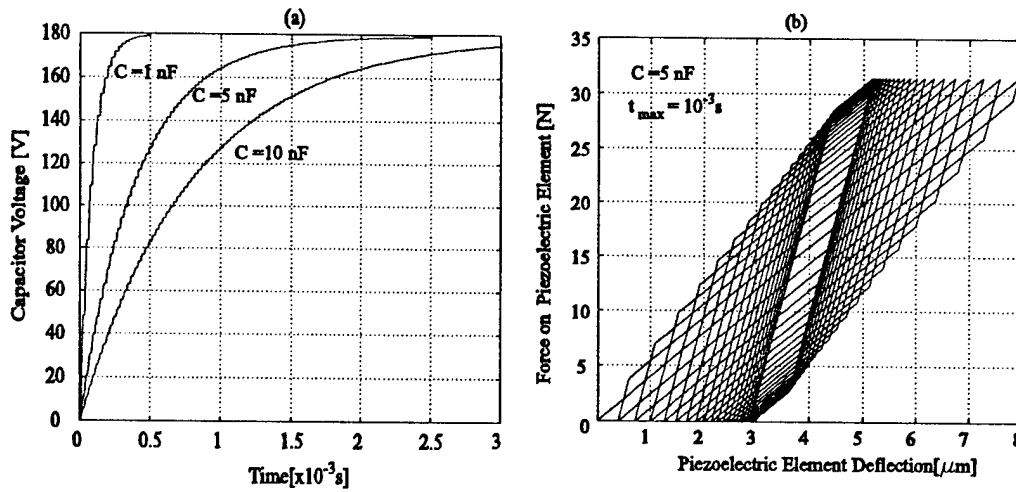


Figure 2-18: Simulation results of the full bridge rectifier connected to a capacitor.

factor increases with the addition of the inductor. However, in order to get this behavior, the value of the inductor should be tuned to the optimum value at a given frequency and for this particular example the required inductance is about 100mH, which is physically very large and not practical.

We can generally conclude that, the circuits discussed in the previous section are better suited for piezoelectric power generation since they can store the electrical energy and the behavior is not frequency dependent.

2.6 Piezoelectric Material Comparison

Section 2.4 presented an analysis of two different circuits and expressions derived for the effective coupling factor and generated power. This section presents a comparison of different piezoelectric materials in terms of energy density and effective coupling factor for different shunting conditions, i.e. with different circuits connected, using the expressions derived in Section 2.4. The important expressions for energy density and effective coupling factor are summarized in Table 2.2. The effective coupling factors for the two circuits presented in Table 2.2 are plotted as a function of the coupling coefficient in Figure 2-20. It can be seen that the effective coupling

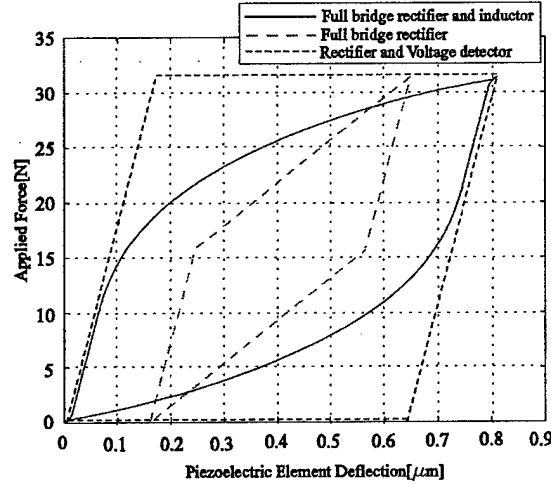


Figure 2-19: Force vs. deflection plot from the simulation of the full bridge rectifier with additional inductor.

| | Rectifier | Rectifier+Voltage Detector |
|---------------------------|---|--|
| Energy Density | $ED = \frac{1}{4}(s_{33}^E - s_{33}^D)\sigma_d^2$ | $ED = (s_{33}^E - s_{33}^D)\sigma_d^2$ |
| Effective coupling factor | $k_{eff}^2 = \frac{2k_{33}^2}{k_{33}^2 + 2}$ | $k_{eff}^2 = \frac{2k_{33}^2}{k_{33}^2 + 1}$ |

Table 2.2: Comparison of circuitry in terms of energy density and effective coupling factor

factor for the case of the diode bridge is always smaller than the coupling coefficient whereas the effective coupling factor for the case of the diode bridge with voltage detector is always larger than the coupling coefficient. This can be also presented with the following inequality:

$$\sqrt{\frac{2k_{33}^2}{k_{33}^2 + 2}} < k_{33} < \sqrt{\frac{2k_{33}^2}{k_{33}^2 + 1}} \quad (2.36)$$

which is valid since $k_{33} < 1$.

The energy density of a piezoelectric material, i.e. the maximum energy which can be extracted from a piezoelectric element in one cycle is mostly limited by the depolarization stress of the piezoelectric element, which means that if a stress higher than the depolarization stress

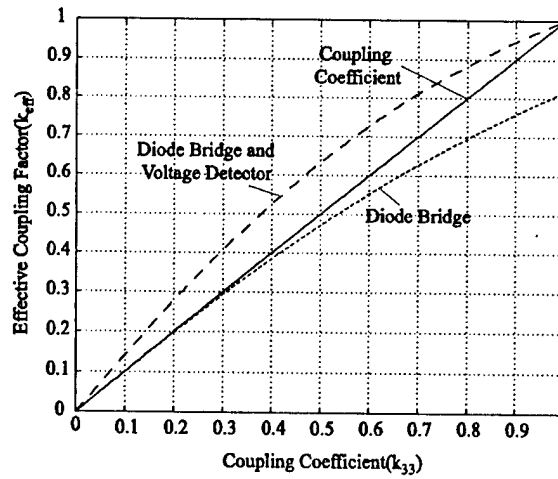


Figure 2-20: Effective coupling factors of the diode bridge and the diode bridge with voltage detector as a function of the coupling coefficient.

is applied, the material begins to dipole and the piezoelectric, dielectric and elastic coefficients begin to degrade. Behavior of different PZT ceramics and PZN-PT single crystal piezoelectric elements under high stress are investigated in [46] and [19] respectively. The assumption for the maximum stress limit, i.e. the assumed values for the depolarization stress are based on the above mentioned references. Other studies about piezoelectric elements under high fields are presented in [45]-[49]. Elastic and piezoelectric properties of different piezoelectric materials along with depolarization stress values are compiled in Table 3.3.

Different piezoelectric materials are compared in terms of their energy densities and effective coupling factors for different circuitry in Figure 2-10. It is interesting to note that, although the single crystal piezoelectric material(PZN-PT) has very high effective coupling factor, it has a very low energy density compared to PZT-8 or PZT-4S because of its small depolarization stress. We can generally say that, the effective coupling factor is a function of the coupling coefficient and the circuitry, whereas the energy density is a function of coupling coefficient, circuitry and the depolarization stress. As mentioned earlier, for a piezoelectric element, the energy density obtained with the diode bridge and voltage detector circuit is four times larger than the energy density obtained with just the diode bridge.

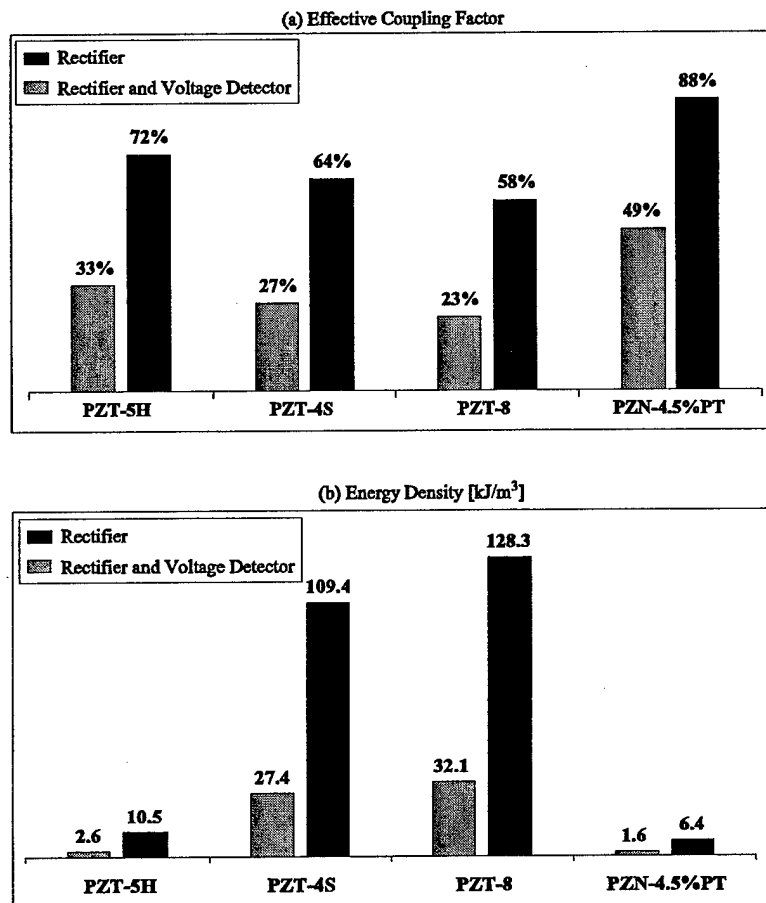


Figure 2-21: Piezoelectric Material Comparison: (a) Effective coupling factor (b) Energy density.

| | PZT-4S | PZT-5H | PZT-8 | PZN-4.5%PT |
|-----------------------------------|--------|--------|-------|------------|
| $s_{33}^E[10^{-12}m^2/N]$ | 15.5 | 20.7 | 13.9 | 81 |
| $s_{33}^D[10^{-12}m^2/N]$ | 7.9 | 9.01 | 8.2 | 17 |
| k_{33} | 0.7 | 0.75 | 0.64 | 0.89 |
| $d_{33}[10^{-12}m/V]$ | 350 | 593 | 250 | 1780 |
| <i>Depolarization Stress[MPa]</i> | 120 | 30 | 150 | 10 |

Table 2.3: Properties of different piezoelectric materials

2.7 Conclusion

This chapter presented an analysis of two different circuitries for piezoelectric power generation. Analytical expressions are derived for the generated power and effective coupling factor for a given piezoelectric material and circuitry. Different piezoelectric materials are compared in terms of their power generation characteristics. Among the materials analyzed, PZT-8 has the highest energy density. Despite its large coupling coefficient, the single crystal material PZN-PT has very low energy density, which is a consequence of its low depolarization stress. However, the coupling coefficient becomes an important criteria if the piezoelectric element is considered along with its surrounding system, for example the infrastructure which provides the force on the element, which is the energy harvesting chamber in the microhydraulic power generation device. It should be remembered that in the analysis presented in this chapter a prescribed force is imposed on the piezoelectric element. This issue will be addressed in the next chapter.

Chapter 3

Energy Harvesting Chamber and Preliminary Design Considerations

This chapter presents a simple model of the energy harvesting chamber, simulations with the coupled circuitry and preliminary design considerations. The interaction of the energy harvesting chamber and the circuitry is discussed. The two circuits presented in Chapter 2 and different piezoelectric materials are compared in terms of the flowrate and frequency requirements for a given pressure differential and power, and in terms of system efficiency.

3.1 Configuration and Operation of the Energy Harvesting Chamber

The Energy Harvesting Chamber consists of a fluid chamber, a piston and a piezoelectric cylinder. The configuration of the energy harvesting chamber and its basic components are shown in Figure 3-1.

The piston converts the pressure in the chamber to a force on the piezoelectric cylinder. The inlet and outlet valves operate 180° out of phase at high frequency and convert the static pressure differential ($P_{HPR} - P_{LPR}$) into pressure fluctuations in the chamber. This results in cyclic compression of the piezoelectric cylinder, which is coupled to the circuitry. The generic operation and typical duty cycles are shown in Figure 3-2.

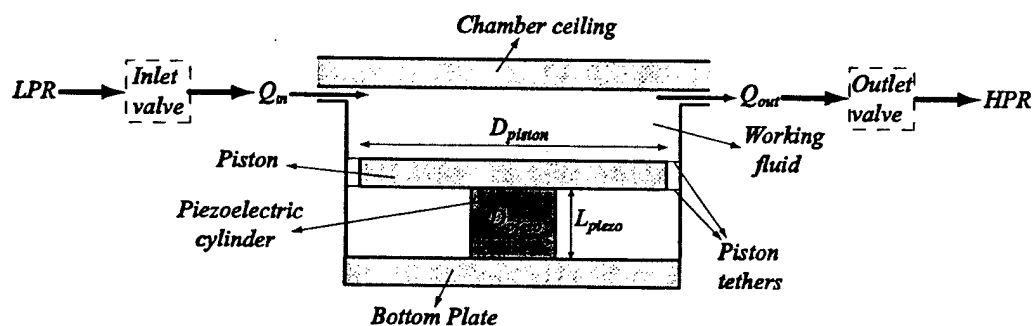


Figure 3-1: Energy harvesting chamber configuration.

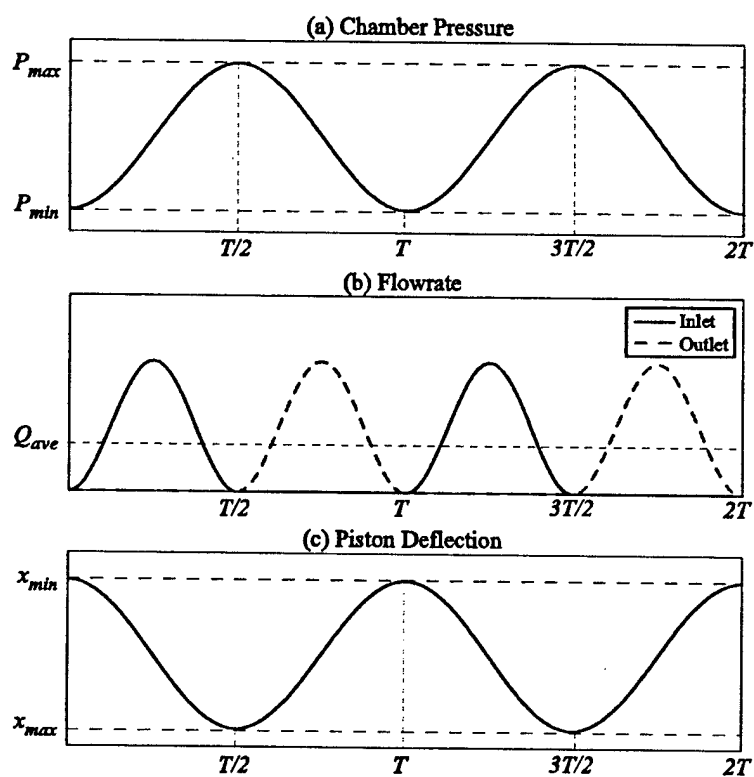


Figure 3-2: Duty cycles of generic operation of the energy harvesting chamber. The valve openings have the same duty cycle as the flowrates and are not shown here.

In the chamber, the hydraulic energy is converted into mechanical energy, which is converted into electrical energy in the piezoelectric element and then the electrical energy is stored in the coupled circuitry. There is a strong coupling between the hydraulic/mechanical system and the circuitry, in other words, the electrical circuit affects the behavior of the system dramatically, an issue which should be analyzed in detail.

3.2 Modeling

In order to understand the interaction between the hydraulic, mechanical and electrical system, a simple model of the energy harvesting chamber will be used to simulate a representative system. The basic assumptions are:

- The effect of piston tethers on the motion of the piston is neglected perfect sealing between the piston and the chamber walls is assumed
- An effective compliance, C_{eff} , is assigned for the chamber, which includes the combined effect of the bending of the piston, chamber ceiling (top plate), bottom plate and piston tethers as well as fluid compression inside the chamber. C_{eff} will be defined in section 3.2.2.
- Piston dynamics is neglected.

The detailed structural modeling and analysis of the compliance contributions of the structural members in the chamber will be presented in Chapter 4.

3.2.1 Piezoelectric Cylinder

The piezoelectric material is modeled using the same constitutive relationship given in Chapter 2, namely:

$$\begin{bmatrix} S \\ E \end{bmatrix} = \begin{bmatrix} s_{33}^D & \frac{d_{33}}{\epsilon_{33}^T} \\ \frac{d_{33}}{\epsilon_{33}^T} & -\frac{1}{\epsilon_{33}^T} \end{bmatrix} \begin{bmatrix} T \\ D \end{bmatrix} \quad (3.1)$$

where D is the charge field, S is the displacement field (strain), E is the electric field, and T is the stress. For a cross-sectional area of A_p and length of L_p , the expressions for the deflection

of the piezoelectric element and the voltage across it become:

$$x_p = \frac{L_p}{A_p} (s_{33}^D F_p + \frac{d_{33}}{\epsilon_{33}^T} Q_p) \quad (3.2)$$

$$V_p = \frac{L_p}{A_p} (\frac{d_{33}}{\epsilon_{33}^T} F_p - \frac{1}{\epsilon_{33}^T} Q_p) \quad (3.3)$$

where x_p is the deflection, Q_p is the charge, F_p is the force applied on the piezoelectric cylinder, and V_p is the voltage across the piezoelectric cylinder. And the current through the piezoelectric element is given by:

$$I_p = \frac{dQ_p}{dt} \quad (3.4)$$

3.2.2 Chamber Continuity

The chamber converts the hydraulic energy into mechanical energy via the piston, which applies a force on the piezoelectric cylinder. In order to derive the expression for the chamber pressure, continuity equation inside the chamber should be considered. Consider an initial fluid volume inside the chamber. The time rate of the pressure change in the chamber is given by:

$$\frac{dP_{ch}}{dt} = \frac{\beta_f}{V_o} \frac{dV}{dt} \quad (3.5)$$

where β_f is the bulk modulus of the fluid, V_o is the initial volume of the fluid inside the chamber and $\frac{dV}{dt}$ is the volume change of the fluid. Sources of the volume change are:

- Net flowrate into the chamber
- Piston Movement
- Additional volume created inside the chamber by the deformation of the structural members due to chamber pressure

Then, the time rate of the total volume change in the chamber can be expressed as:

$$\frac{dV}{dt} = Q_{in} - Q_{out} - \frac{dx_p}{dt} A_{pis} - \frac{dV_s}{dt} \quad (3.6)$$

where x_p is the displacement of the piston, which is equal to the deflection of the piezoelectric cylinder, A_{pis} is the cross-sectional area of the piston, and V_s is the total volume displaced by

the deformation of the structural members inside the chamber. The source of this additional volume might be the deformation of the top and bottom plate of the chamber, deformation of the piston tethers and deformation of the piston itself. The individual sources of the structural compliance of the chamber will be analyzed in detail in Chapter 4.

Combining equations 3.5 and 3.6, we get:

$$\frac{dP_{ch}}{dt} = \frac{\beta_f}{V_o} \left(Q_{in} - Q_{out} - \frac{dx_p}{dt} A_{pis} - \frac{dV_s}{dt} \right) \quad (3.7)$$

We can define the overall structural compliance as:

$$C_s = \frac{dV_s}{dP_{ch}} \quad (3.8)$$

From equations 3.7 and 3.8, we get the expression for the chamber pressure as:

$$\frac{dP_{ch}}{dt} = \left(\frac{V_o}{\beta_f} + C_s \right)^{-1} \left(Q_{in} - Q_{out} - \frac{dx_p}{dt} A_{pis} \right) \quad (3.9)$$

For simplicity, we can define an effective compliance for the chamber, which represents all the compliance sources as:

$$C_{eff} = \left(\frac{V_o}{\beta_f} + C_s \right) \quad (3.10)$$

where the first and the second terms correspond to the fluidic compliance and structural compliance respectively, which act like parallel capacitors in electrical circuit analogy.

We can rewrite 3.9 as follows:

$$\frac{dP_{ch}}{dt} = \frac{1}{C_{eff}} \left(Q_{in} - Q_{out} - \frac{dx_p}{dt} A_{pis} \right) \quad (3.11)$$

It is important to note that, in the above analysis the initial fluid volume inside the chamber, V_o , is assumed to be much larger than the volume displaced by the piston and the volume displaced due to the deformation of the structural members inside the chamber. If the deflection of the piston becomes comparable to the chamber height, the volume displaced by the piston becomes comparable with the initial volume of the chamber, and that effect should be taken into consideration, which will result in nonlinear behavior, i.e nonlinear compliance.

The generic duty cycle of the operation is shown in Figure 3-2. The average flowrate can be calculated using the following relationship:

$$Q_{ave} = \frac{\int_0^{T/2} Q_{in} dt}{T} = \frac{\int_{T/2}^T Q_{out} dt}{T} \quad (3.12)$$

It is also important to note that:

$$\int_{T/2}^T Q_{in} dt = \int_0^{T/2} Q_{out} dt = 0 \quad (3.13)$$

Integrating equation 3.11 from $t = 0$ to $t = \frac{T}{2}$, using equation 3.12 and arranging terms, we get the expression for the average flowrate as:

$$Q_{ave} = A_{pis}(x_{max} - x_{min})f + C_{eff}(P_{max} - P_{min})f \quad (3.14)$$

where A_{pis} is the cross-sectional area of the piston and f is the operation frequency. The same expression can be obtained by integrating equation 3.11 from $t = \frac{T}{2}$ to $t = T$. The first term in equation 3.14 corresponds to the flowrate required to move the piston and squeeze the piezoelectric element. The second term corresponds to the flowrate required due to the compliances in the chamber.

3.2.3 Fluid Model

The schematic of the device with pressures at different locations within the system is shown in Figure 3-3 where P_{int-in} is the intermediate pressure at the exit of the inlet channel, and $P_{int-out}$ is the intermediate pressure at the entrance to the outlet valve. Inlet and outlet channels have the same geometry. Details of the Simulink architecture is given in the Appendix A.

Valve Orifice Flow Relations

Work by previous researches has shown that for small openings, poppet valves, such as the valve cap in the active valves within the MHT systems, behave as long orifices in which the effects of flow separation and subsequent re-attachement dominate the valve flow dynamics[5].

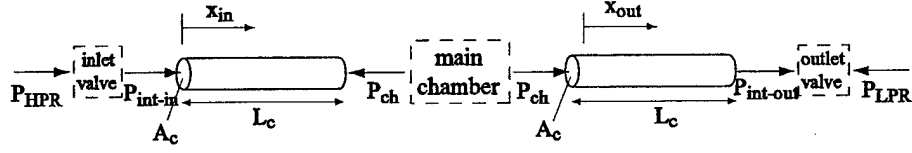


Figure 3-3: Device schematics showing pressures at different locations.

Qualitatively, the valve flow can be approximated by a simplified order-of-magnitude valve model. The valve orifice may be characterized as a flow contraction followed by a flow expansion as shown in Figure 3-4(a) and (b). An integral analysis gives a relationship for the combined effect of the flow expansion and contraction. The loss coefficient $\zeta_{orifice}$ is defined as the total pressure drop $\Delta P = P_{HPR} - P_{int}$ (for the inlet valve) over the dynamic pressure based on the orifice local mean velocity ($\bar{u} = \frac{Q}{A_o}$)

$$\zeta_{orifice} = \frac{\Delta P}{\frac{1}{2}\rho\bar{u}^2} = \left[\frac{1}{2} \left(1 - \frac{A_o}{A_1} \right)^{\frac{3}{4}} + \left(1 - \frac{A_o}{A_2} \right)^2 \right] \quad (3.15)$$

where the upstream, throat and downstream flow areas can be approximated as:

$$A_2 = 2\pi R_{vc} H_c \quad (3.16)$$

$$A_o = 2\pi R_{vc} x_{vc} \quad (3.17)$$

$$A_1 = \pi R_{vc}^2 \quad (3.18)$$

respectively, where H_c is the height of the radial flow channel above the valve membrane, x_{vc} is the valve cap distance from the valve stop structure and R_{vc} is the radius of the valve cap.

This approximation, however, is independent of the Reynolds number and therefore holds only for $Re \geq 10,000$, where the flow is in fully turbulent regime. In the MHT power generator, Reynolds numbers are expected to fluctuate between approximately 10 and 20,000 as the valves

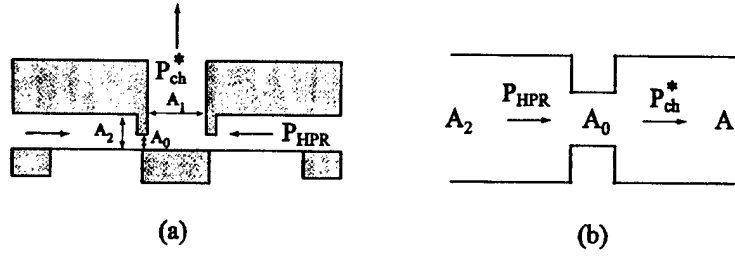


Figure 3-4: Valve orifice representation:(a) Valve cap geometry and fluid flow areas, (b) Representation of flow through the valve as a flow contraction followed by a flow expansion.

open and close. For this reason, correction factors obtained from experimental results need to be employed to obtain better estimates of the loss coefficients for these low turbulence and laminar flow regimes[4]. A loss coefficient for each of the contraction and expansion geometries, $\zeta_{contraction}$ and $\zeta_{expansion}$, respectively, is used to approximate the total loss coefficient through the valve, as detailed in the following relation:

$$\zeta_{orifice}^* = \zeta_{contraction}(Re, \frac{A_o}{A_2}) + \zeta_{expansion}(Re, \frac{A_o}{A_1}) \quad (3.19)$$

where Reynolds number is defined as:

$$Re = \frac{1}{\pi} \frac{Q}{R_{vc} \nu} \quad (3.20)$$

Figure 3-5(a) plots $\zeta_{contraction}$ as a function of Reynolds number and contraction area ratio $\frac{A_o}{A_2}$, and Figure 3-5(b) plots $\zeta_{expansion}$ as a function of Reynolds number and the expansion area ratio $\frac{A_o}{A_1}$. As a result, the pressure-flow relation for the full valve orifice geometry can be written as:

$$\Delta P = \frac{1}{2} \rho \zeta_{orifice}^* \left(\frac{Q^2}{A_o^2} \right) \quad (3.21)$$

All subsequent fluid models discussed in this thesis incorporate these higher-order correction factors to obtain an accurate estimation of the flow behavior. These flow models are based on steady flow phenomenon and do not capture frequency dependent losses. For a specific value of valve cap opening at a given time during the cycle, a relationship therefore exists for the

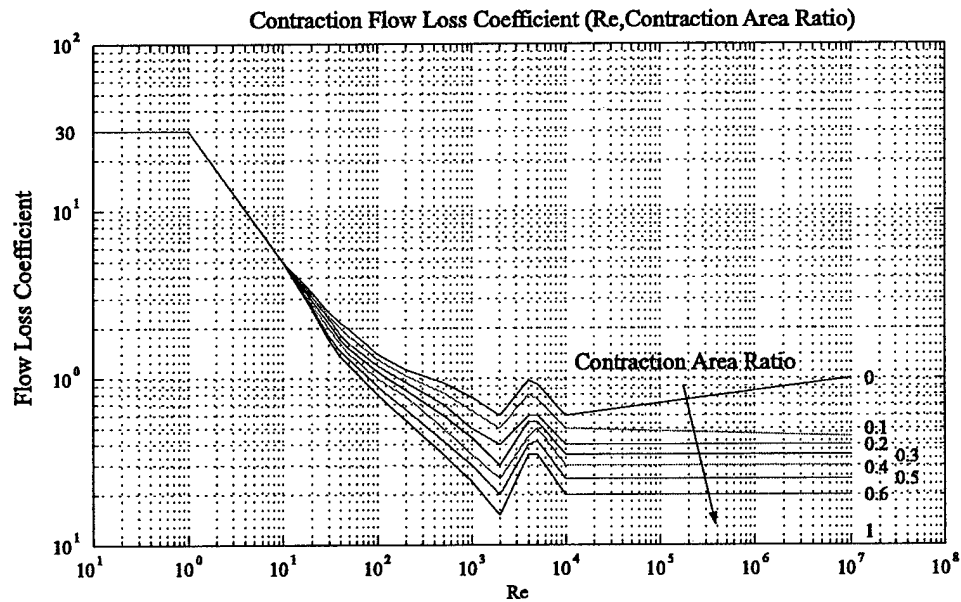
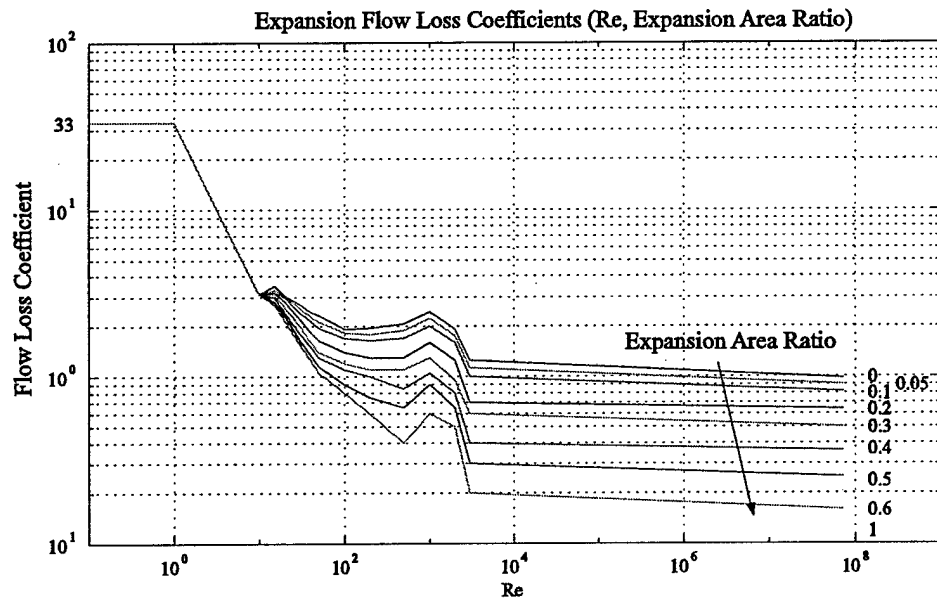


Figure 3-5: Look-Up tables used for flow loss contraction and expansion coefficients. The loss coefficients are obtained from [51].

instantaneous fluid flow through the valve as a function of the pressure drop across the valve.

Equation 3.21 can be rewritten for inlet and outlet valves using the notation in Figure 3-3 as:

$$P_{HPR} - P_{int-in}(t) = R_{in}(Q_{in}, v_{o_{in}})Q_{in}^2 \quad (3.22)$$

$$P_{int-out}(t) - P_{LPR} = R_{out}(Q_{out}, v_{o_{out}})Q_{out}^2 \quad (3.23)$$

where R_{in} and R_{out} represent the flow resistances of the inlet and outlet valves, respectively, which are functions of the flowrate and the corresponding valve opening at a given instant of time.

Flow in the Channels

Due to the high Reynolds numbers, the flow in the channels is expected to be inertia dominated. Furthermore, the compliance in the fluid channels is usually negligible due to the fact that the channels are surrounded by rigid walls and their volume is much smaller than that of the chamber. Under this assumptions the flow inside the channels is modeled as one dimensional inviscid and incompressible flow. The pressure-flowrate relationship in this case is given as:

$$\Delta P = I \frac{dQ}{dt} = \left(\frac{\rho L_c}{A_c} \right) \frac{dQ}{dt} \quad (3.24)$$

where I is defined as the fluid inductance inside the channel, ρ is the fluid density and L_c and A_c are the length and cross-sectional area of the fluid channel respectively. For the case of inlet valve and outlet valve fluid channels, the pressure-flow relations can be written as:

$$P_{int-in}(t) - P_{ch}(t) = \left(\frac{\rho L_c}{A_c} \right) \frac{dQ_{in}}{dt} \quad (3.25)$$

$$P_{ch}(t) - P_{int-out}(t) = \left(\frac{\rho L_c}{A_c} \right) \frac{dQ_{out}}{dt} \quad (3.26)$$

For a long channel with small cross-sectional area, one can expect fluid inertial effects to

play a significant role as the pressure difference builds up to accelerate the fluid slug into the chamber. Conversely, for short channels with large cross-sectional areas, the inertial effects are negligible and the pressure P_{int-in} and P_{ch} or P_{ch} and $P_{int-out}$ will not differ much. It is important to consider inertial effects when designing hydraulic systems containing small channels.

Governing Equations

Combining equations 3.22, 3.23, 3.25, and 3.26 we can obtain the governing equations for the fluid flow in the system, which are integrated into the system level simulation, as:

$$P_{HPR} - P_{ch}(t) = R_{in}(Q_{in}, v_{oin})Q_{in}^2 + \left(\frac{\rho L_c}{A_c}\right) \frac{dQ_{in}}{dt} \quad (3.27)$$

$$P_{ch}(t) - P_{LPR} = R_{out}(Q_{out}, v_{oot})Q_{out}^2 + \left(\frac{\rho L_c}{A_c}\right) \frac{dQ_{out}}{dt} \quad (3.28)$$

Although not explicitly seen, the intermediate pressures can be easily calculated and monitored in the system level simulation, which are important in terms of stresses in the valve membranes and power consumption in the active valves since they are assumed to act on the valve cap, where the reservoir pressures are assumed to act on the membranes[6].

3.2.4 Circuitry

The same circuit models presented in Chapter 2 will be used.

3.3 Working Fluid

Fluid properties which are important in terms of system performance are listed in Table 3.3 for alternative working fluids. The density of a working fluid effects the dynamic behavior of the system because of the fluid inductance in the fluid channels. A low density fluid is desirable since it would increase the bandwidth of the system. The viscosity of a working fluid effects the energy dissipated in the valves. A more viscous fluid would provide the same amount of flowrate with larger valves or valve openings, causing an increase in power consumption in the

| | Density[kg/m ³] | Viscosity[Pa/s] | Bulk Modulus[GPa] |
|--------------|-----------------------------|-----------------|-------------------|
| Water | 1000 | 1.0e-3 | 2.24 |
| Mercury | 13,570 | 1.5e-3 | 25.0 |
| Silicone Oil | 760 | 4.9e-4 | 2.0(degassed) |

Table 3.1: Comparison of different working fluids

| | |
|--|------------------------------|
| <i>Length of the piezoelectric cylinder</i> | 1mm |
| <i>Diameter of the piezoelectric cylinder</i> | 2mm |
| <i>Diameter of the piston</i> | 4.5mm |
| <i>Effective chamber compliance (C_{eff})</i> | $2 \times 10^{-18} [m^3/Pa]$ |
| P_{HPR} | 2MPa |
| P_{LPR} | 0MPa |
| <i>Operation Frequency</i> | 10kHz |
| <i>Fluid channel length</i> | 1mm |
| <i>Fluid channel cross-section</i> | 50 μm x 100 μm |
| <i>Piezoelectric Material</i> | PZN-4.5%PT |

Table 3.2: The geometry and operation conditions used in the simulation

valves. The bulk modulus effects the system compliance. Silicone oil is chosen as the working fluid because of its low density, low viscosity and a bulk modulus comparable to that of water.

3.4 Simulation and Analysis

The equations presented in the previous section will be simulated using Simulink. The coupled equations used to simulate the system are 3.2, 3.3, 3.4, 3.11, 3.27, 3.28 and equations for the circuitry, which were given in Chapter 2.

The simulation architecture is shown in Figure 3-6. For the analysis in this chapter, a representative system will be analyzed, for which the geometry and operation conditions are presented in Table 3.2.

In the following analysis, the valve openings are imposed and reservoir pressures are assumed to be constant. The valve size and opening are adjusted such that the pressure in the energy harvesting chamber attains the high pressure reservoir pressure (P_{HPR}) and low pressure reservoir pressure (P_{LPR}) as its maximum and minimum pressures respectively. In other words, the pressure inside the chamber fluctuates between P_{HPR} and P_{LPR} . The valves operate 180° out of phase.

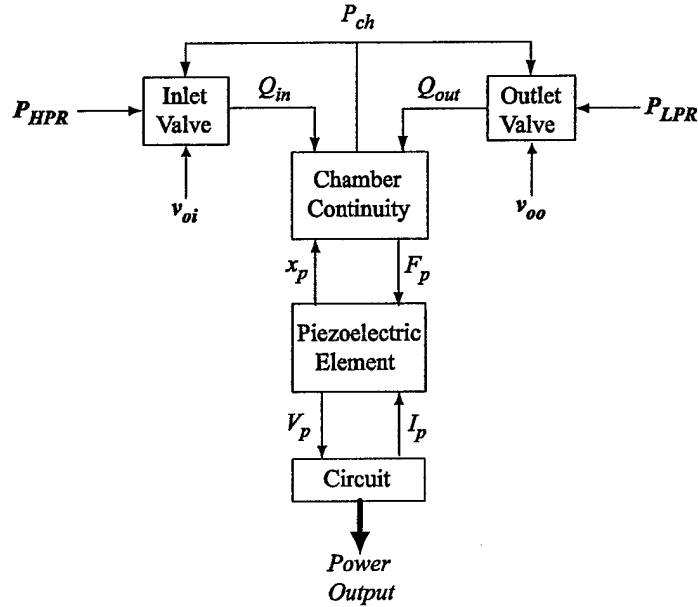


Figure 3-6: Simulation architecture used in Simulink.

3.4.1 Energy Harvesting Chamber and Full Bridge Rectifier

This section presents the simulation and analysis of the energy harvesting chamber attached to the full bridge rectifier using the model presented in the previous section. The time histories of the chamber pressure, flowrate and piston deflection, which is equal to the deflection of the piezoelectric element, are shown in Figure 3-7.

In order to understand the interaction between the hydraulic/mechanical system and the circuitry, and its implications on flowrate and frequency for a given power requirement, it is worthwhile to investigate the plot of force on the piezoelectric element vs displacement of the piezoelectric element. This is shown in Figure 3-8. It is interesting to note that the curve in Figure 3-8 has the exact same shape of the force vs. displacement curve presented in Chapter 2 for the case of the imposed force on a piezoelectric cylinder attached to a diode bridge. From this we can conclude that the force vs. displacement curve of a piezoelectric element attached to the full bridge rectifier does not depend on the time history of the applied force. So, the equations derived in Chapter 2 for the full bridge rectifier will be used here to derive

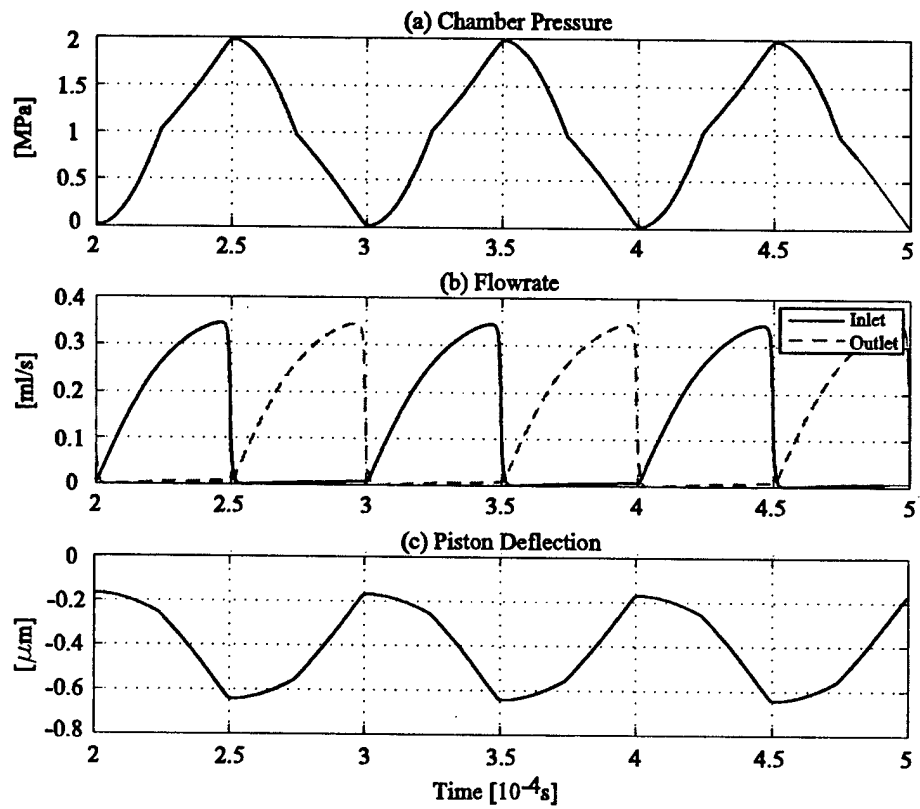


Figure 3-7: Simulation of the energy harvesting chamber attached to the full bridge rectifier circuit.

the governing equations for required frequency, flowrate and system efficiency.

For a given operation frequency and power requirement, the required cross-sectional area of the piezoelectric element can be obtained from equation 2.25 as:

$$A_p = \frac{4W}{(s_{33}^E - s_{33}^D)\sigma^2 L_p f} \quad (3.29)$$

where W is the generated power, L_p is the length of the piezoelectric cylinder and f is the operation frequency. Since the maximum pressure in the chamber is P_{HPR} , the cross-sectional area of the piston should be equal to:

$$A_{pis} = \frac{\sigma_d A_p}{P_{HPR}} \quad (3.30)$$

where σ_d is the depolarization stress of the piezoelectric element. From the results derived in Chapter 2, the total deflection of the piston/piezoelectric cylinder is given by:

$$\Delta x_p = \frac{1}{2}\sigma_d L_p (s_{33}^E + s_{33}^D) \quad (3.31)$$

Using equations 5.31, 3.29, 3.30, and 3.31, the required flowrate for a given power requirement and maximum chamber pressure can be derived as follows:

$$Q = \frac{2(s_{33}^E + s_{33}^D)W}{(s_{33}^E - s_{33}^D)P_{HPR}} + C_{eff}P_{HPR}f \quad (3.32)$$

The first term in equation 3.32 corresponds to the flowrate which is required just to move the piston. The second term corresponds to the additional flowrate required due to the chamber compliance. If we consider the ideal case, where the chamber is not compliant, i.e $C_{eff} = 0$, the minimum required flowrate is given by

$$Q_{\min} = \frac{2(s_{33}^E + s_{33}^D)W}{(s_{33}^E - s_{33}^D)P_{HPR}} \quad (3.33)$$

In order to evaluate the performance of the energy harvesting chamber, we can define the efficiency of the chamber as follows:

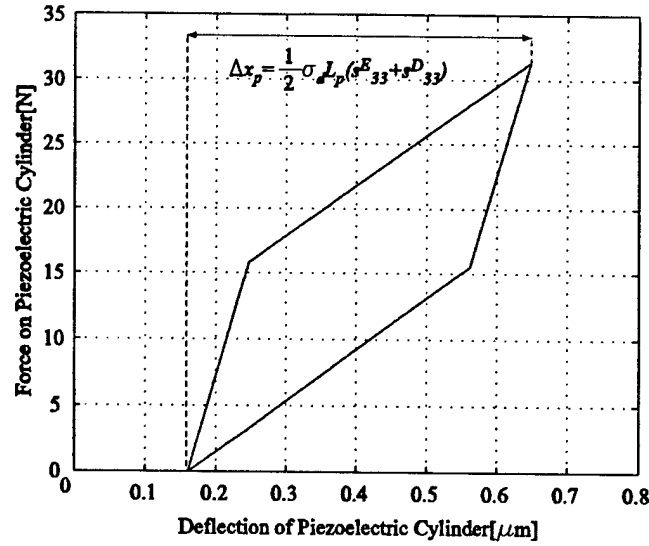


Figure 3-8: Force vs. displacement curve of the piezoelectric element from the simulation of the harvesting chamber attached to the full bridge rectifier.

$$\eta_{ch} = \frac{\text{Electrical Power Out}}{\text{Hydraulic Power In}} = \frac{W}{QP_{HPR}} \quad (3.34)$$

In the extreme case, where the effective chamber compliance is zero, the efficiency has its maximum value, which can be obtained from equations 3.32 and 3.34 as:

$$\eta_{ch \max} = \frac{(s_{33}^E - s_{33}^D)}{2(s_{33}^E + s_{33}^D)} = \frac{k_{33}^2}{4 - 2k_{33}^2} \quad (3.35)$$

It is interesting to note that the maximum efficiency of the chamber depends only on the coupling coefficient of the piezoelectric material. This suggests that, regardless of the geometry and operation conditions, the above expression puts an upper bound on the system efficiency, which is only a function of the piezoelectric element chosen. It is important to note that the above definition of the efficiency corresponds only to the energy harvesting chamber. If the overall system is considered, the electrical power consumption in the active valves should be taken into consideration.

3.4.2 Energy Harvesting Chamber and Full Bridge Rectifier with Voltage Detector Circuit

This section presents the simulation and analysis of the Energy Harvesting Chamber attached to the full bridge rectifier and voltage detector circuit. The geometry and the operation conditions are the same as in the previous section. The time histories of the chamber pressure, flowrate and piston deflection are shown in Figure 3-9.

It is interesting to note that there are sudden pressure drops inside the chamber and the time histories of the chamber pressure and the piston deflection are quite different from the time histories presented in the previous section. The most important observation is that during the periods when the switch is on, the pressure decreases/increases suddenly because the fluid cannot fill/evacuate the chamber immediately due to the fluid inertia of the fluid in the channels. In order to understand the interaction between the hydraulic/mechanical system and the circuit, and its implications on flowrate and frequency requirements for a given power, we can investigate the force vs. displacement plot of the piezoelectric element which is shown in Figure 3-10.

In Figure 3-10, the force vs. displacement curve of the piezoelectric element for this case is compared to the chamber attached to full bridge rectifier and to the case where the force is imposed on the piezoelectric element attached to the regular diode bridge and voltage detector. It is interesting to note that the new curve is much different than the imposed force case. In the latter case, which was discussed in Chapter 2, during the interval when the switch is on, the force is almost constant, and the portion of the curve corresponding to that period is almost flat. However, for the chamber, during the interval when the switch is on, the piezo becomes very soft, and the piston moves up or down very rapidly, which causes sudden pressure drops/rises inside the chamber, as can be seen in Figure 3-9. In order to analyze the behavior of the system, we can divide the time history into four periods, as shown in Figure 3-11.

In the periods 1-2 and 3-4 the piezoelectric element is open circuited, and the deflections at the states 1 and 3 correspond to the deflection as if the material was short circuited and the same force as in 1 and 3 was applied. In other words, F_1, F_3, x_1 , and x_3 should satisfy the following equations.

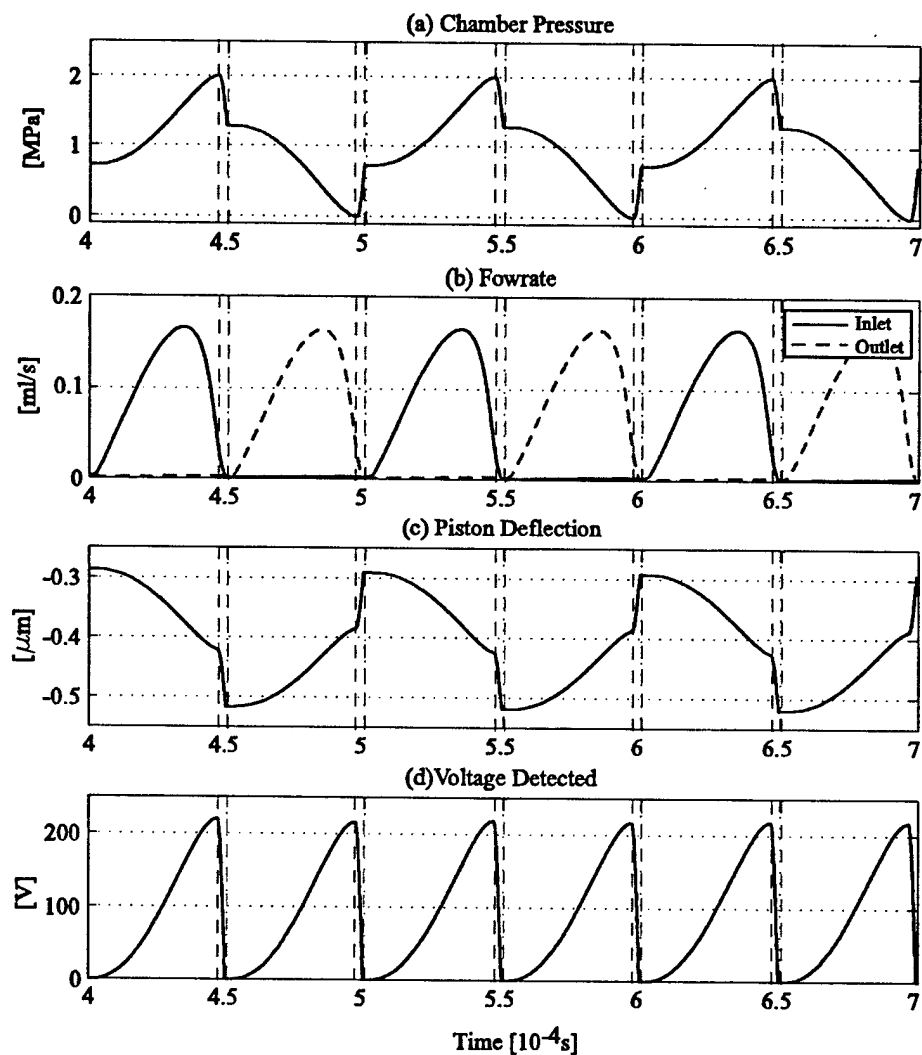


Figure 3-9: Simulation of the energy harvesting chamber attached to the full bridge rectifier and voltage detector circuit. The time intervals between the dashed lines present the intervals where the switch(SCR) is in its "on" state.

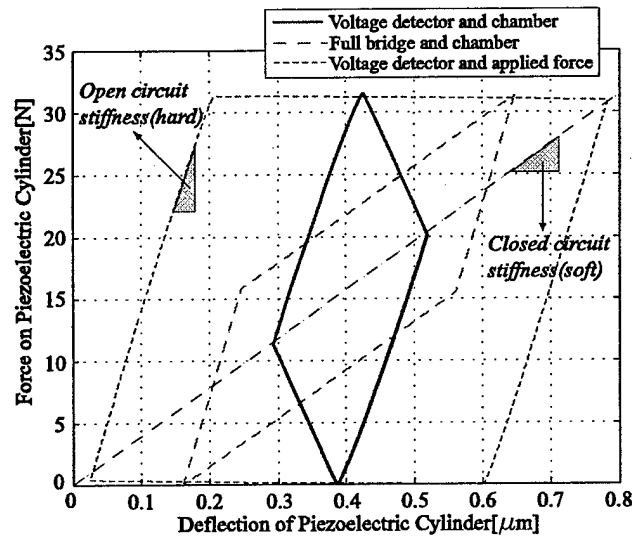


Figure 3-10: Force vs. displacement curve of the piezoelectric element from the simulation of the energy harvesting chamber attached to the full bridge rectifier and voltage detector circuit.

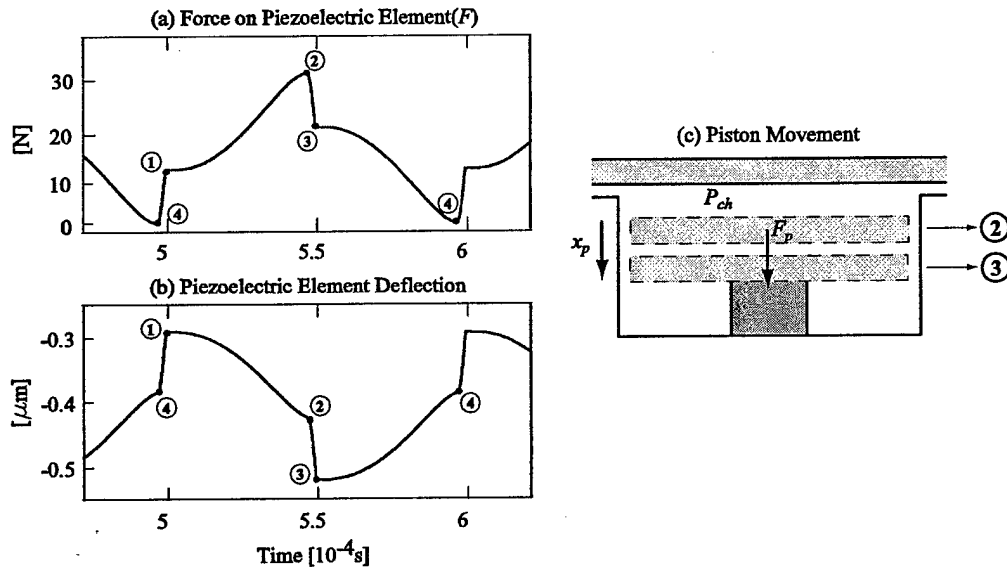


Figure 3-11: Time histories of the force and deflection of the piezoelectric element.

$$x_1 = F_1 \frac{s_{33}^E L_p}{A_p} \quad (3.36)$$

$$x_3 = F_3 \frac{s_{33}^E L_p}{A_p} \quad (3.37)$$

Since in the periods 1-2 and 3-4 the piezoelectric element is open circuited, the slope of the force vs deflection curve in these periods is simply the open circuit stiffness of the piezoelectric element and the following equations should be satisfied.

$$F_2 - F_1 = \frac{A_p}{s_{33}^D L_p} (x_2 - x_1) \quad (3.38)$$

$$F_3 - F_4 = \frac{A_p}{s_{33}^D L_p} (x_3 - x_4) \quad (3.39)$$

In order to understand the behavior in the periods 2-3 and 4-1, let us consider the period 2-3. At state 2, the pressure is maximum and at state 3, the voltage on the piezoelectric element is zero. In the period 2-3, there is almost no flowrate, which suggests that the pressure change in the chamber in this period, which is the sudden pressure drop, is only because of the volume change due to piston movement. In other words, the pressures at states 2 and 3 should satisfy the following equation.

$$P_2 - P_3 = (x_3 - x_2) \frac{A_{pis}}{C_{eff}} \quad (3.40)$$

where

$$P = \frac{F}{A_{pis}} \quad (3.41)$$

From equations 3.40 and 3.41, we can write:

$$F_2 - F_3 = (x_3 - x_2) \frac{(A_{pis})^2}{C_{eff}} \quad (3.42)$$

Similarly for the period 4-1, we can write:

$$F_1 - F_4 = (x_4 - x_1) \frac{(A_{pis})^2}{C_{eff}} \quad (3.43)$$

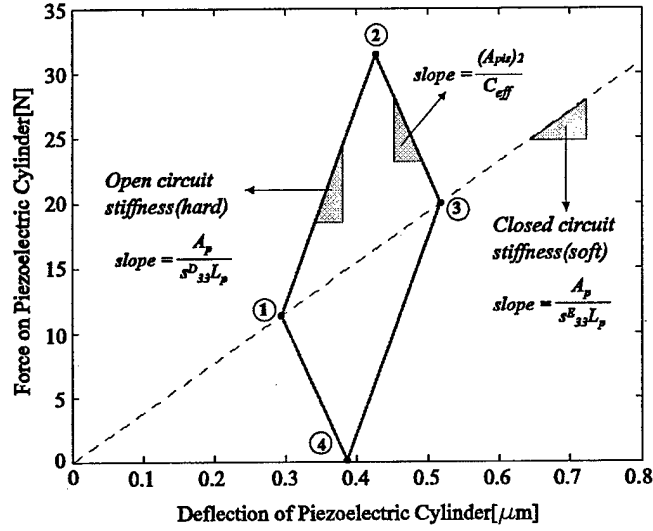


Figure 3-12: Force vs. displacement curve of the piezoelectric element and slopes at different periods of operations.

We also know that:

$$F_2 = \sigma_d A_p \quad \text{and} \quad F_4 = 0 \quad (3.44)$$

where σ_d is the depolarization stress of the piezoelectric element.

By solving equations 3.36, 3.37, 3.38, 3.39, 3.42, 3.43, and 3.44 we can determine the coordinates of the force vs. deflection curve of the piezoelectric element and we can also calculate the electrical energy stored per cycle, which is the area enclosed by the force vs. deflection curve, the effective coupling factor and system efficiency in terms of chamber geometry, piezoelectric cylinder geometry, chamber compliance and maximum pressure inside the chamber. The force vs. displacement curve of the piezoelectric element and the slopes of the curve at different periods are shown in Figure 3-12. It is interesting to note that in this case, the force vs. deflection curve depends on the chamber compliance, whereas in the case of the energy harvesting chamber attached to the full bridge rectifier, the slopes were determined only by the piezoelectric material geometry and properties.

The coordinates of the force vs displacement curve are as follows:

$$(x_1, F_1) = \left(\frac{\sigma_d A_{pis}^2 L_p^2 s_{33}^E (s_{33}^E - s_{33}^D)}{C_{eff} A_p + A_{pis}^2 L_p (2s_{33}^E - s_{33}^D)}, \frac{\sigma_d A_{pis}^2 L_p A_p (s_{33}^E - s_{33}^D)}{C_{eff} A_p + A_{pis}^2 L_p (2s_{33}^E - s_{33}^D)} \right) \quad (3.45)$$

$$(x_2, F_2) = \left(\frac{\sigma_d L_p^2 (s_{33}^E)^2 A_{pis}^2 + \sigma_d C_{eff} L_p A_p s_{33}^D}{C_{eff} A_p + A_{pis}^2 L_p (2s_{33}^E - s_{33}^D)}, \sigma_d A_p \right) \quad (3.46)$$

$$(x_3, F_3) = \left(\frac{\sigma_d L_p^2 (s_{33}^E)^2 A_{pis}^2 + \sigma_d C_{eff} L_p A_p s_{33}^E}{C_{eff} A_p + A_{pis}^2 L_p (2s_{33}^E - s_{33}^D)}, \frac{\sigma_d A_p L_p A_{pis}^2 s_{33}^E + \sigma_d C_{eff} A_p^2}{C_{eff} A_p + A_{pis}^2 L_p (2s_{33}^E - s_{33}^D)} \right) \quad (3.47)$$

$$(x_4, F_4) = \left(\frac{(\sigma_d s_{33}^E A_{pis}^2 L_p^2 + \sigma_d C_{eff} L_p A_p)(s_{33}^E - s_{33}^D)}{C_{eff} A_p + A_{pis}^2 L_p (2s_{33}^E - s_{33}^D)}, 0 \right) \quad (3.48)$$

Using the coordinates of the points given in the above equations, electrical energy stored per cycle can be calculated as:

$$E = \frac{\sigma_d^2 L_p A_p (s_{33}^E - s_{33}^D) (A_p C_{eff} + s_{33}^E A_{pis}^2 L_p) (A_p C_{eff} + s_{33}^D A_{pis}^2 L_p)}{[A_{pis}^2 L_p (2s_{33}^E - s_{33}^D) + C_{eff} A_p]^2} \quad (3.49)$$

From equation 5.31 we can write the expression for the flowrate as:

$$Q_{ave} = A_{pis} (x_3 - x_1) f + C_{eff} P_{HPR} f \quad (3.50)$$

For a given power requirement W , we can determine the required frequency using:

$$f = \frac{W}{E} \quad (3.51)$$

The required flowrate for a given power requirement can be derived from equations 3.45, 3.47, 3.49, 3.50, and 3.51 as:

$$Q_{ave} = \frac{W [s_{33}^E C_{eff} P_{HPR}^2 + \sigma_d^2 L_p A_p s_{33}^E (2s_{33}^E - s_{33}^D)]}{P_{HPR} (C_{eff} P_{HPR}^2 + \sigma_d^2 L_p A_p s_{33}^E) (s_{33}^E - s_{33}^D)} + \frac{W P_{HPR} C_{eff} [C_{eff} P_{HPR}^2 + \sigma_d^2 L_p A_p (2s_{33}^E - s_{33}^D)]^2}{\sigma_d^2 A_p L_p (s_{33}^E - s_{33}^D) (C_{eff} P_{HPR}^2 + \sigma_d^2 L_p A_p s_{33}^E) (C_{eff} P_{HPR}^2 + \sigma_d^2 L_p A_p s_{33}^D)} \quad (3.52)$$

In the extreme case where the effective chamber compliance is zero, namely $C_{eff} = 0$, the

expression for the required flowrate simply reduces to

$$Q_{\min} = \frac{(2s_{33}^E - s_{33}^D)W}{(s_{33}^E - s_{33}^D)P_{HPR}} \quad (3.53)$$

From the above expression we can get the maximum system efficiency using the definition given in equation 3.34 as

$$\eta_{ch \max} = \frac{(s_{33}^E - s_{33}^D)}{(2s_{33}^E - s_{33}^D)} = \frac{k_{33}^2}{1 + k_{33}^2} \quad (3.54)$$

where, as in the previous section, the maximum efficiency depends only on the coupling coefficient of the piezoelectric material.

Figure 3-13 shows the force vs. deflection curve of the piezoelectric element for different values of chamber compliance. It is interesting to note that, as the chamber compliance increases, the curve approaches the curve for the case where the force is imposed. One might think that having large compliance would have a positive effect on system performance, since the area inside the curve, which is the electrical energy stored per cycle, increases with increasing compliance. For a given power requirement lower frequencies and lower flowrates would be required. However, as the compliance increases, the required flowrate increases dramatically due to the second term in equation 3.50. This effect overwhelms the effect of decreased flowrate due to lower frequency requirement and the maximum system efficiency occurs again for the case where the chamber compliance is zero. The two extreme cases, namely $C_{eff} = 0$ and $C_{eff} = \infty$ are shown in Figure 3-13 (b).

The effective coupling factor from mechanical to electrical energy was defined in Chapter 2 and the expressions were derived for different circuits for the imposed force case. For the case of the energy harvesting chamber attached to the full bridge rectifier, the effective coupling factor is the same as the one for the imposed force case since for the full bridge rectifier, the force vs. displacement curve doesn't depend on the time history of the force on the piezoelectric element. However, it was found that, the force vs. displacement curve for full bridge rectifier and voltage detector depends on the time history of the force on the piezoelectric element, and in this case the curve depends on the chamber compliance. The effective coupling factor was defined in Chapter 2. From Figure 3-13 we can write:

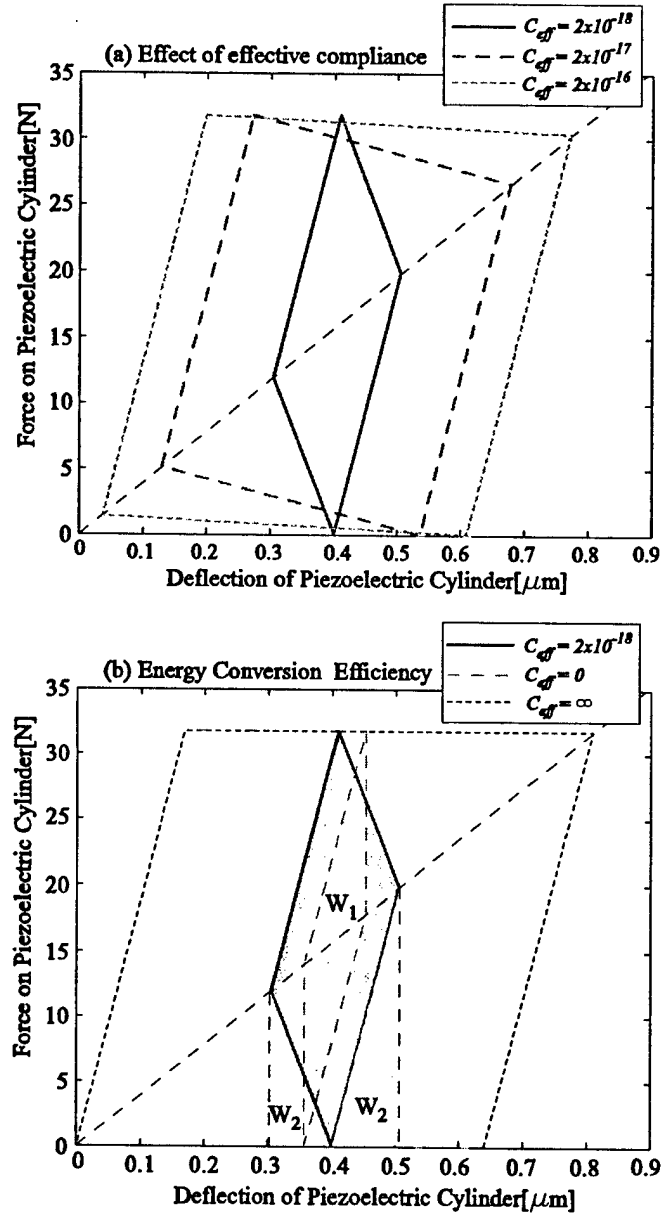


Figure 3-13: The effect of effective chamber compliance on force vs. deflection curve and effective coupling factor.

$$k_{eff}^2 = \frac{W_1}{W_1 + W_2} \quad (3.55)$$

The effective coupling factor can be calculated using the coordinates of the force vs. deflection curve. For the case where the effective chamber compliance is infinity, the effective coupling factor is:

$$C_{eff} = \infty \rightarrow k_{eff}^2 = \frac{2(s_{33}^E - s_{33}^D)}{2s_{33}^E - s_{33}^D} \quad (3.56)$$

for which case the electrical energy stored per cycle is:

$$E_{(C_{eff}=\infty)} = (s_{33}^E - s_{33}^D) \sigma_d^2 A_p L_p \quad (3.57)$$

which is the same amount of energy stored for the case of imposed force on piezoelectric element with the same circuitry.

For the case where the effective chamber compliance is zero, the effective coupling factor becomes:

$$C_{eff} = 0 \rightarrow k_{eff}^2 = \frac{2(s_{33}^E - s_{33}^D)}{3s_{33}^E - 2s_{33}^D} \quad (3.58)$$

for which case the electrical energy stored per cycle is:

$$E_{(C_{eff}=0)} = \frac{\sigma_d^2 A_p L_p (s_{33}^E - s_{33}^D) s_{33}^E s_{33}^D}{(2s_{33}^E - s_{33}^D)^2} \quad (3.59)$$

3.5 Discussion

This section presents a comparison of circuitry and piezoelectric materials in terms of their effect on important performance metrics such as flowrate, frequency and efficiency using the results obtained in previous sections of this chapter. Let us consider the system analyzed in Section 3.4, for which the geometric parameters were given in Table 3.2. Now, however, the effective chamber compliance will be varied and its effect on system performance will be investigated. This could be accomplished, for example, by changing the thicknesses of the structural members or by changing the chamber height. For a power requirement of $0.5W$, the required frequency

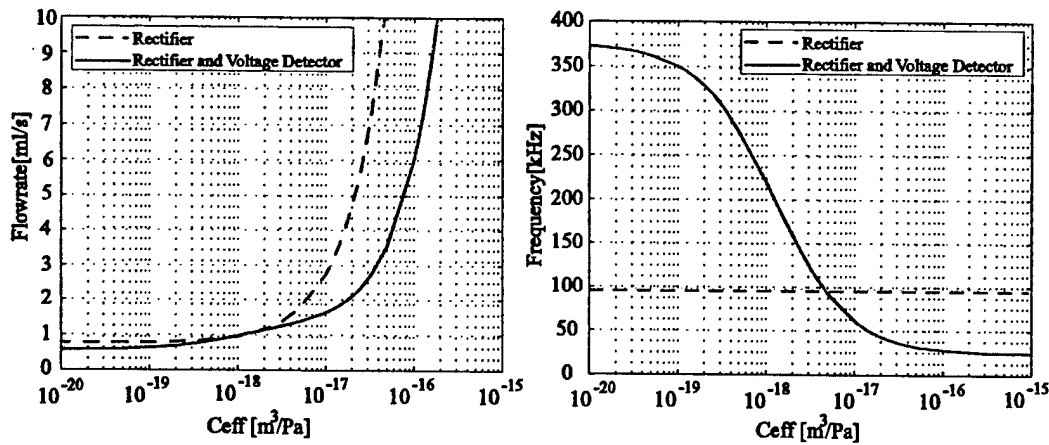


Figure 3-14: Flowrate and frequency requirement for 0.5 W power requirement.

and flowrate is plotted as a function of effective chamber compliance in Figure 3-14. It can be noted from Figure 3-14 that the frequency requirement for the full bridge rectifier case does not depend on effective chamber compliance since the force vs. displacement graph is the same for any chamber compliance and the energy stored per cycle depends only on the maximum stress on the piezoelectric element and piezoelectric material properties. However, since the force vs. displacement curve for the rectifier with voltage detector case depends heavily on the effective chamber compliance, the electrical energy stored per cycle depends on the compliance. So, for a given power requirement, the required frequency depends on the effective compliance as well. In terms of flowrate requirement, it can be easily seen that, as the system gets more compliant, the required flowrate increases dramatically. It should be pointed out that, for a microfluidic device, even flowrates on the order of 1 ml/s can be considered very high, and special high performance microvalves are needed. It is obvious that, prediction of the effective chamber compliance will constitute a crucial part of the modelling and design process. This will be addressed in Chapter 4.

The system efficiency, which was defined in equation 3.34 is plotted as a function of the effective chamber compliance in Figure 3-15. It can be noted that, as the effective chamber compliance gets smaller and smaller, in other words, as the chamber gets less and less compliant, the efficiency values approach their maximum values which were given in equations 3.35 and

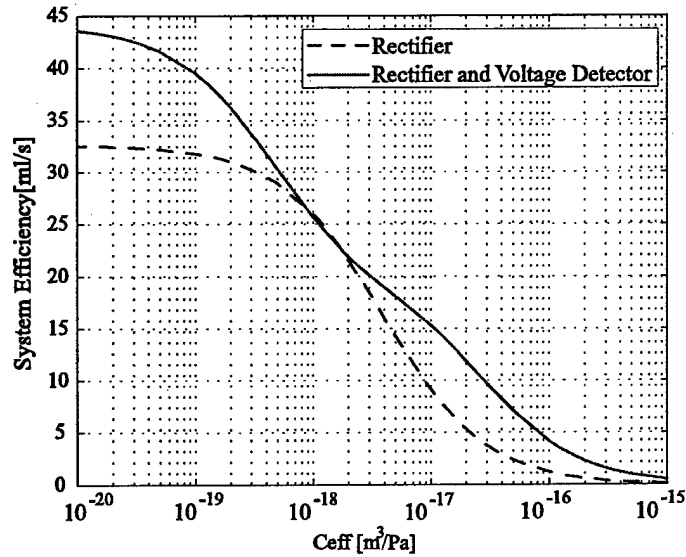


Figure 3-15: System efficiency as a function of the effective chamber compliance.

3.54 for the rectifier and rectifier and voltage detector circuit cases respectively. As mentioned earlier, these maximum efficiency values depend only on the piezoelectric material used.

Using the relations derived in previous sections, we can also compare different piezoelectric materials in terms of flowrate and frequency requirements and system efficiency. Again, let's consider the same system for the $0.5W$ power requirement. Figure 3-16 shows the required flowrates for different piezoelectric materials and different circuitry as a function of effective chamber compliance. It should be noted that for each piezoelectric material, the piezo diameter, D_p , is adjusted such that at the maximum chamber pressure, the stress on the piezoelectric element is equal to its depolarization stress, σ_d . The required flowrates for the rectifier circuit with voltage detector are significantly less than the case with just the rectifier. It can be also observed that PZN-PT requires the least flowrate and PZT-8 requires the most flowrate at low compliance values.

The required frequencies for different piezoelectric materials are shown in Figure 3-17. As mentioned earlier the required operation frequency in the case of rectifier circuit is constant, regardless of the effective chamber compliance. Since the force vs. displacement curve in the

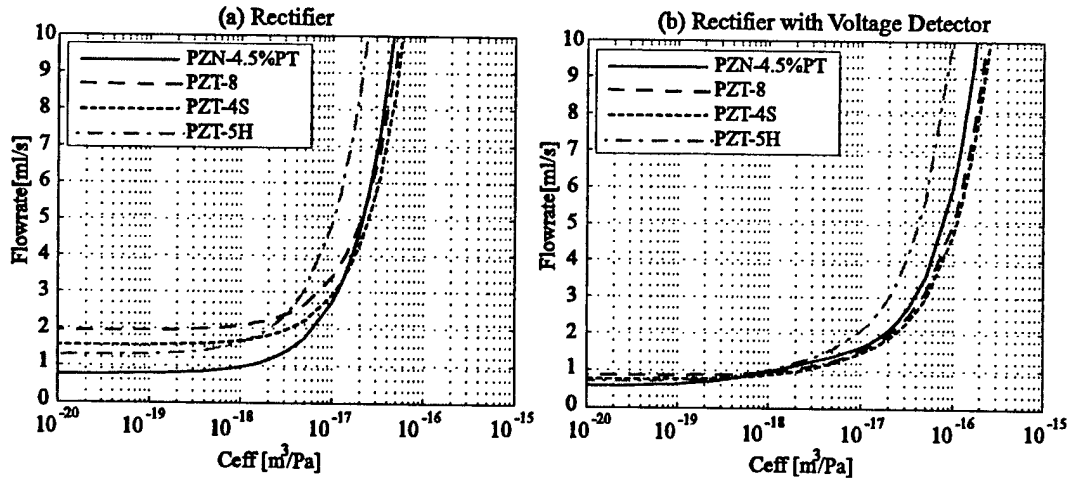


Figure 3-16: Required flowrates for 0.5 power generation. Comparison of different piezoelectric elements and different circuitry.

case of the rectifier and voltage detection circuit depends heavily on the effective chamber compliance, the required frequency for a certain power requirement depends on the effective chamber compliance. Since the materials PZT-8 and PZT-4S have very high depolarization stresses compared to PZT-5H and PZN-PT, the electrical energy stored per cycle for PZT-8 and PZT-4S is much larger, which means reduced frequency requirements for the same power requirement. For example, although PZN-PT has the highest coupling coefficient ($k_{33} = 0.89$) among the piezoelectric materials discussed here, it requires higher operation frequencies due to its low depolarization stress.

Figure 3-18 shows the system efficiency for different piezoelectric materials and circuitry. It can be seen that, the chamber with the rectifier circuit and voltage detector is more efficient than the case with the rectifier. As the effective compliance gets smaller and smaller, the system efficiencies approach their maximum value, which are given by equations 3.35 and 3.54 for rectifier and rectifier with voltage detector cases respectively. As expected, PZN-PT is the most efficient material due to its high coupling coefficient ($k_{33} = 0.89$) and PZT-8 is the least efficient material due to its low coupling coefficient ($k_{33} = 0.64$). Although PZT-8 is the least efficient one, it might be a better suited material since the system with PZN-PT has very high

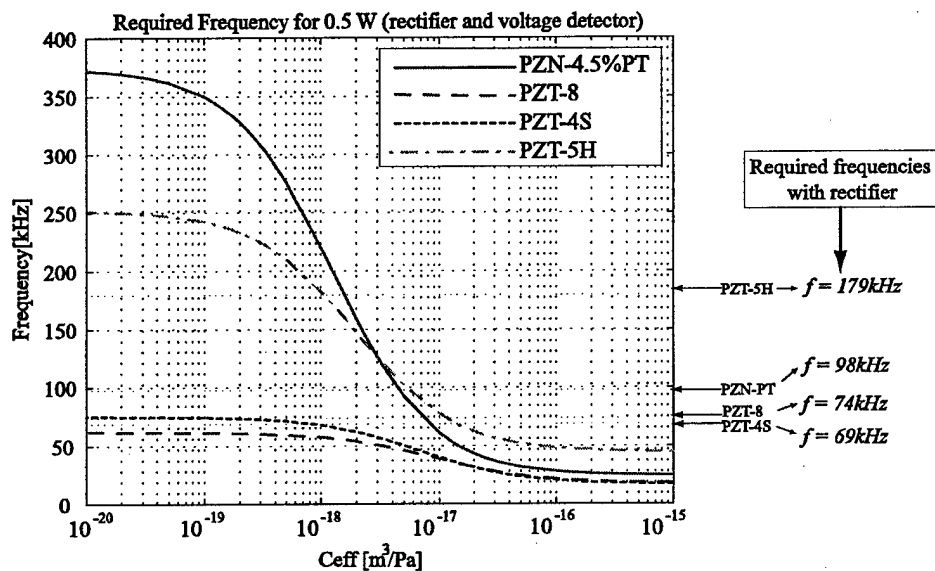


Figure 3-17: Required frequencies for the 0.5W power requirement. Comparison of different piezoelectric materials and circuitry. Note that the required frequency in the case of regular rectifier is independent of the chamber compliance.

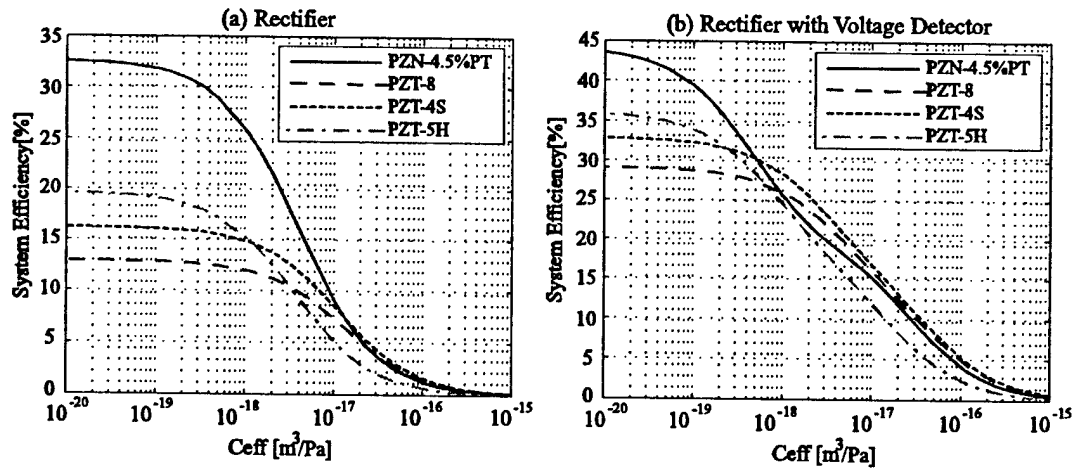


Figure 3-18: Comparison of different piezoelectric materials and circuitry in terms of system efficiency.

frequency requirements. The material selection process should address the design trade-offs and should take the remaining components of the system, for example the active valves, into consideration. One might choose to use PZN-PT which requires very high frequencies, but this frequency can exceed the bandwidth of the active valves. This issue will be addressed in Chapter 5.

One should remember that the analysis of the chamber attached to the rectifier and the voltage detector presented in this chapter assumed that the impedances (inductances) of the fluid channels are large enough such that there are sudden pressure drops inside the chamber and the governing equations are derived assuming that in the time interval where the SCR is in its "on" state, there is no net flowrate into the chamber.

3.6 Summary and Conclusion

This chapter presented a simple analysis of the energy harvesting chamber and a case study using a simulation for a predetermined chamber geometry and operating conditions. The interaction between the chamber and the circuitry has been investigated. Some of the important performance metrics derived in the previous sections are summarized in Table 3.3.

| | Rectifier | Rectifier+Voltage Detector |
|---------------------------|---|--|
| Effective Coupling Factor | $k_{eff}^2 = \frac{2k_{33}^2}{k_{33}^2 + 2}$ | $k_{eff(C_{eff}=0)}^2 = \frac{2k_{33}^2}{2k_{33}^2 + 1}$ |
| Minimum Required Flowrate | $Q_{min} = \frac{(4 - 2k_{33}^2)W}{k_{33}^2 P_{HPR}}$ | $Q_{min} = \frac{(1 + k_{33}^2)W}{k_{33}^2 P_{HPR}}$ |
| Maximum System Efficiency | $\eta = \frac{k_{33}^2}{4 - 2k_{33}^2}$ | $\eta = \frac{k_{33}^2}{1 + k_{33}^2}$ |

Table 3.3: Summary and comparison of circuitry in terms of performance indices

The first row summarizes the expressions obtained for the effective coupling factor for the two circuits analyzed in this chapter. The second expression in the first row represents the effective coupling factor for the rectifier with voltage detection circuit for the case where $C_{eff} = 0$, which corresponds to the most efficient operation condition for the energy harvesting chamber. However, maximum effective coupling factor for this circuit occurs when $C_{eff} = \infty$, which is the same as the effective coupling factor of the same circuit for the applied force case, which was presented in Chapter 2. The effective coupling factor for the full bridge rectifier case is the same regardless of the effective compliance of the energy harvesting chamber. The second row presents the minimum required flowrate for a given power requirement and maximum pressure in the chamber. The third row represent the maximum system efficiency. The second and third rows correspond to the case where $C_{eff} = 0$. As mentioned earlier, the maximum system efficiency of the energy harvesting chamber depends only on the piezoelectric material chosen, namely the coupling coefficient(k_{33}). The expressions are plotted as a function of the coupling coefficient in Figure 3-19. A comparison of different piezoelectric materials is also made on the same plot.

The expressions for the maximum system efficiency in Table 3.3 put an upper limit on the system efficiency. It is interesting to note that, at $k_{33} = 1$ the two curves reach the same point, which is 50% efficiency. This means that, even with a perfect piezoelectric material($k_{33} = 1$) and zero effective compliance, which are not possible, the system efficiency cannot exceed 50%.

The most important conclusion of this chapter is that the performance of the energy harvesting chamber depends on

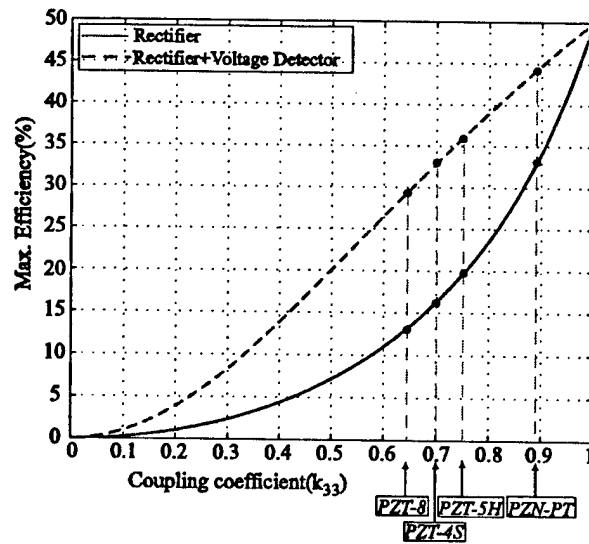


Figure 3-19: Maximum system efficiency(which corresponds to the case where the effective compliance of the chamber is zero)as a function of the coupling coefficient.

- Rectification circuit topology
- Piezoelectric material (k_{33}, σ_d)
- Chamber compliance(C_{eff})

Again it should be emphasized that the efficiency definition in this chapter corresponds only to the energy harvesting chamber. The electrical power consumption in the active valves is not considered.

Chapter 4

Detailed Model of the Energy Harvesting Chamber

This chapter presents the detailed modelling of the energy harvesting chamber. In Chapter 3, an effective chamber compliance (C_{eff}) based on a typical MHT device was assumed to be used in the simulation and the effect of compliance on system performance was analyzed. This chapter investigates the contribution of different structural components on the effective compliance of the chamber. It also presents the simulation architecture used for integrating elastic equations into the system level simulation.

4.1 Analysis of a Simplified Chamber Structure

Consider a simple circular chamber structure consisting of a fluid chamber and rigid walls, except the top portion of the chamber, as shown in Figure 4-1. The compliant portion can be modeled as a clamped circular plate which deforms under the action of uniform pressure underneath. For small deflections, the deformation of the top plate can be assumed to be linear and can be analyzed using linear plate theory [50].

For a uniform pressure distribution P and a radius of a , the deflection of the top plate as a function of the radial distance is given as:

$$w(r) = \frac{P}{64D} (a^2 - r^2)^2 \quad (4.1)$$

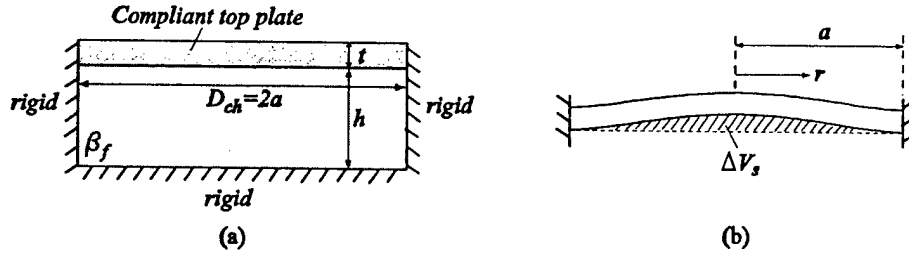


Figure 4-1: (a) Simplified chamber structure consisting of a fluid chamber with a compliant wall (b) Deformation of the top plate and swept volume.

where D is the flexural rigidity of the plate given by:

$$D = \frac{Et^3}{12(1 - \nu^2)} \quad (4.2)$$

where E and ν is the Young Modulus and Poisson ratio of the material respectively, and t is the thickness of the plate. The additional volume created in the chamber due to the deformation of the plate can be calculated by integrating equation 4.1 over the plate:

$$\Delta V_s = \int_0^a w(r) 2\pi r dr = \frac{P\pi a^6(1 - \nu^2)}{16Et^3} \quad (4.3)$$

The structural compliance was defined in Chapter 3 as:

$$C_s = \frac{\Delta V_s}{\Delta P} \quad (4.4)$$

which represents the volume change of the chamber due to structural deformations in response to a change in chamber pressure. In this simple example, the top plate is the only compliant structural member. Using equations 4.4 and 4.3, the structural compliance can be calculated as:

$$C_s = \frac{\pi a^6(1 - \nu^2)}{16Et^3} \quad (4.5)$$

The effective chamber compliance can be obtained as:

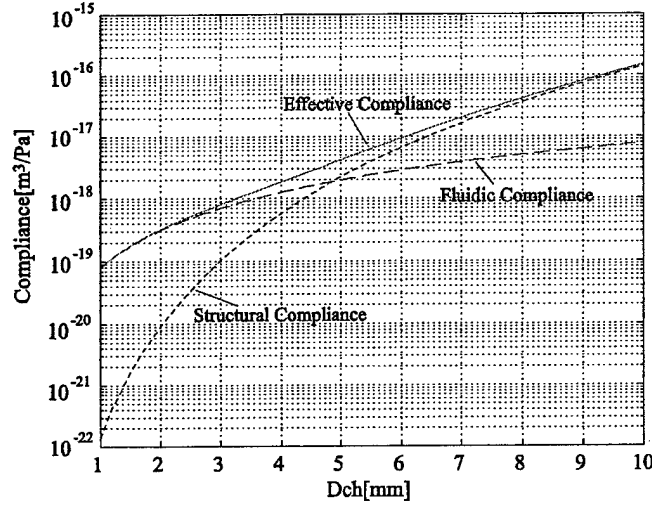


Figure 4-2: Comparison of fluidic and structural compliances for a generic chamber structure at different chamber diameters for fixed chamber height and top plate thickness.

$$C_{eff} = \left(\frac{V_o}{\beta_f} + C_s \right) = \left(\frac{\pi a^2 h}{\beta_f} + \frac{\pi a^6 (1 - \nu^2)}{16 E t^3} \right) \quad (4.6)$$

where V_o is the initial fluid volume inside the chamber, β_f is the bulk modulus of the fluid and h is the height of the chamber.

Consider a chamber with top plate thickness of $500\mu m$ and chamber height of $200\mu m$. Figure 4-2 shows a comparison of fluidic and structural compliances for different chamber diameters. It can be seen that, for small chamber diameters, the compliance of the chamber is dominated by the fluidic compliance, whereas at large chamber diameters the structural compliance dominates. However, it should be noted that, if all the geometric parameters are scaled the same amount, the ratio of the fluidic and structural compliances will remain the same. This issue will be discussed further in Chapter 5.

4.2 Detailed Analysis of Structural Components

A simplified chamber structure consisting of a compliant top plate and a fluidic chamber has been analyzed in the previous section. This section will present detailed analysis of individual structural compliances of the energy harvesting chamber which will include the deformation of the top and bottom support structures, deformation of the piston and bending of the tethers. Figure 4-3 shows geometric parameters of the structural components, corresponding deformations and the free body diagrams which will be used in the formulations of the governing equations.

These deformations inside the energy harvesting chamber can be adequately represented by the linear plate theory [50]. Each component will be modeled as a plate with applied loading and boundary conditions to determine the deflections and swept volumes. In general, a symmetrically loaded circular plate will experience deflections due to bending as well as shearing. If the plate thickness is small compared to the plate outer radius, the deflection due to bending will be significantly larger than that due to shearing. Since the radii of the structural components analyzed are larger than the corresponding thicknesses, deformations only due to bending will be considered.

4.2.1 Top Support Structure

The top support structure is modeled as a clamped circular plate which deforms under the action of a uniform pressure distribution underneath. The governing differential equation for the symmetrical bending of a circular plate is given as:

$$\frac{d}{dr} \left[\frac{1}{r} \frac{d}{dr} \left(r \frac{dw(r)}{dr} \right) \right] = \frac{Q(r)}{D} \quad (4.7)$$

where D is the flexural rigidity given in equation 4.2, $w(r)$ is the deflection of the plate, and $Q(r)$ is the shear force per unit length. For a uniformly loaded circular plate the shear force per unit length is given as:

$$Q(r) = \frac{P_{ch}r}{2} \quad (4.8)$$

where P is the pressure. The boundary conditions are:

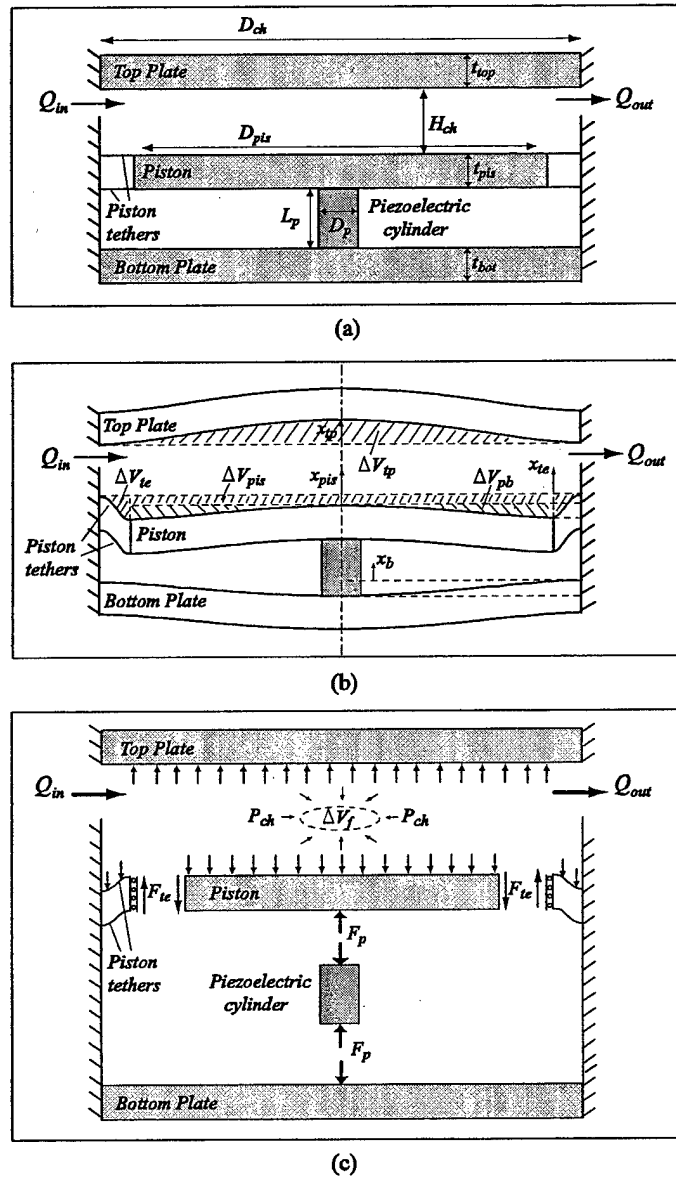


Figure 4-3: (a) Schematic illustrating the dimensional parameters of the chamber, (b) deformation of structural components and sign conventions, (c) free body diagrams and sign conventions. Deflections are exaggerated.

$$w(r = a) = 0 \quad (4.9)$$

$$\frac{dw}{dr}(r = a) = 0 \quad (4.10)$$

$$\frac{dw}{dr}(r = 0) = 0 \quad (4.11)$$

By integrating the governing differential equation and applying the boundary conditions, the deflection of the plate $w(r)$ can be determined as:

$$w(r) = \frac{P_{ch}}{64D} (a^2 - r^2)^2 \quad (4.12)$$

The deflection of the midpoint of the top support structure can be obtained by calculating the deflection of the top plate at $r = 0$:

$$x_{tp} = \frac{3P_{ch}a^4(1 - \nu^2)}{16Et^3} = k_{dtp}P_{ch} \quad (4.13)$$

where k_{dtp} depends only on the chamber diameter and the top plate thickness.

The corresponding swept volume can be calculated by integrating equation 4.12 over the plate as:

$$\Delta V_{tp} = \int_0^a w(r)2\pi r dr = \frac{P_{ch}\pi a^6(1 - \nu^2)}{16Et^3} = k_{tp}P_{ch} \quad (4.14)$$

where k_{tp} depends only on the chamber diameter and the top plate thickness.

Equations 4.12 and 4.14 are the same equations used in the previous section.

4.2.2 Bottom Support Structure

A rigid bottom structure beneath the piezoelectric element would ensure that all of the deflection of the piston goes into the compression of the piezoelectric element. In reality, this structure is not rigid and as a result this bottom structure deformation results in less compression of the piezoelectric element at a given chamber pressure.

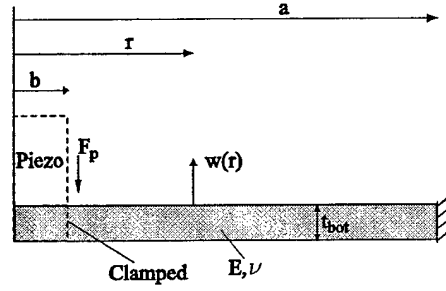


Figure 4-4: Model of the bottom support structure: circular plate with a circular hole at its center with guided boundary condition at inner radius b and clamped boundary condition at outer radius a .

The bottom support structure is modeled as a circular plate with a circular hole at the center which is clamped at its outer radius ($r = a$) and guided at its inner radius ($r = b$), shown in Figure 4-4. In this case the shear force per unit length is given as:

$$Q(r) = \frac{-F_p}{2\pi r} \quad (4.15)$$

where F_p is the force acting on the bottom support structure through the guided support in the inner radius ($r = b$). The boundary conditions are:

$$w(r = a) = 0 \quad (4.16)$$

$$\frac{dw}{dr}(r = a) = 0 \quad (4.17)$$

$$\frac{dw}{dr}(r = b) = 0 \quad (4.18)$$

The deflection of the bottom plate, x_b , can be calculated by integrating equation 4.7 and applying the boundary conditions to obtain:

$$x_b = k_b F_p \quad (4.19)$$

where k_b is the stiffness of the bottom plate which depends on the thickness of the bottom plate, t_{bot} , inner radius ($b = D_p/2$), and outer radius ($a = D_{ch}/2$).

4.2.3 Piston

The piston is modeled as a circular plate with a circular hole at the center which is simply supported at its outer radius ($r = a$) assuming that the tethers exert insignificant bending moments on the piston at its outer radius, and guided at its inner radius ($r = b$), shown in Figure 4-5. In this case the shear force per unit length is given as:

$$Q(r) = \frac{F_p}{2\pi r} - \frac{P_{ch}r}{2} \quad (4.20)$$

where F_p is the force acting on the piston through the guided support in the inner radius ($r = b$).

The boundary conditions are:

$$w(r = a) = 0 \quad (4.21)$$

$$M_r(r = a) = -D \left(\frac{d^2 w(r = a)}{dr^2} + \frac{\nu}{r} \frac{dw(r = a)}{dr} \right) = 0 \quad (4.22)$$

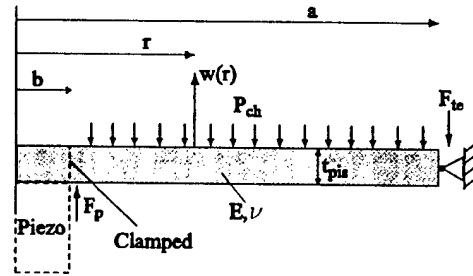


Figure 4-5: Model of the piston: circular plate with a circular hole at its center with guided boundary condition at inner radius b and clamped boundary condition at outer radius a .

$$\frac{dw}{dr}(r = b) = 0 \quad (4.23)$$

where M_r denotes the bending moment per unit length along circumferential sections of the plate. The deflection of the piston and the corresponding swept volume can be calculated by integrating equation 4.7 and applying the boundary conditions to obtain:

$$x_{pb} = x_{pis} - x_{te} = k_{p1}F_p + k_{p2}P_{ch} \quad (4.24)$$

$$\Delta V_{pb} = k_{p3}F_p + k_{p4}P_{ch} \quad (4.25)$$

where k_{p1} , k_{p2} , k_{p3} , and k_{p4} depend on the thickness of the piston, t_{pis} , inner radius ($b = D_p/2$), and outer radius ($a = D_{pis}/2$). The dynamics of the piston can be represented using the free body diagram in Figure 4-3 as:

$$M_{pis} \frac{d^2 x_{pis}}{dt^2} = -A_{pis}P_{ch} + F_p - F_{te} = F_{net} \quad (4.26)$$

4.2.4 Piston Tethers

In this section, tethers corresponding to a double layer piston structure will be analyzed which consist of a top and bottom tether structure. In order to allow for flexibility in design, the top and bottom tethers are defined to have different thicknesses (t_{tetop} , t_{tobot}). The top tether is modeled as a circular plate with a circular hole at the center which is clamped at its outer radius and guided at its inner radius, shown in Figure 4-6. It experiences a concentrated force, F_{tetop} , at its inner radius and a uniform pressure loading, P_{ch} . The shear force per unit length is given as:

$$Q(r) = \frac{F_{tetop}}{2\pi r} - \frac{P_{ch}(r^2 - b^2)}{2r} \quad (4.27)$$

The boundary conditions are:

$$w(r = a) = 0 \quad (4.28)$$

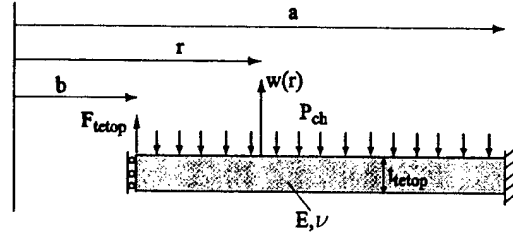


Figure 4-6: Model of the top tether: circular plate with a circular hole at its center with guided boundary condition at inner radius b and clamped boundary condition at outer radius a .

$$\frac{dw}{dr}(r = a) = 0 \quad (4.29)$$

$$\frac{dw}{dr}(r = b) = 0 \quad (4.30)$$

The deflection of the top tether and the corresponding swept volume can be calculated by integrating equation 4.7 and applying the boundary conditions to obtain:

$$x_{te} = k_{tt1}F_{tetop} + k_{tt2}P_{ch} \quad (4.31)$$

$$\Delta V_{te} = k_{tt3}F_{tetop} + k_{tt4}P_{ch} \quad (4.32)$$

where k_{tt1} , k_{tt2} , k_{tt3} , and, k_{tt4} depend on the thickness of the top tether, t_{tetop} , inner radius ($b = D_{pis}/2$), and outer radius ($a = D_{ch}/2$).

Since the tethers are much thinner than the support structures and the piston, it is important to consider the stress in the tethers and make sure that they don't exceed the critical value of $1GPa$ [7]. For a circular plate subject to symmetrical bending, the two stress components can be calculated as:

$$\sigma_r = -\frac{6M_r}{h^2} \quad (4.33)$$

$$\sigma_t = -\frac{6M_t}{h^2} \quad (4.34)$$

where M_r and M_t are the bending moment per unit length along the circumferential sections of the plate and along the diametral section of the plate respectively, and h is the thickness of the plate. The bending moments are obtained as:

$$M_r = -D \left(\frac{d^2 w}{dr^2} + \frac{\nu}{r} \frac{dw}{dr} \right) \quad (4.35)$$

$$M_t = -D \left(\frac{1}{r} \frac{dw}{dr} + \nu \frac{d^2 w}{dr^2} \right) \quad (4.36)$$

where D is the flexural rigidity of the plate. Using the equations 4.33, 4.34, 4.35, 4.36, the stress components can be calculated after the governing plate equation 4.7 is integrated using appropriate boundary conditions and the deflection of the plate, w , is determined. As will be seen later in the next chapter, σ_r is generally bigger than σ_t and the maximum stress occurs at $a = D_{ch}/2$. Then we can write the maximum stress in the top tether as:

$$\sigma_{\max} = \sigma_{tt} = -\frac{6M_r(r = D_{ch}/2)}{t_{ttop}^2} \quad (4.37)$$

which can be alternatively expressed as:

$$\sigma_{tt} = s_{tt1} F_{ttop} + s_{tt2} P_{ch} \quad (4.38)$$

where s_{tt1} and s_{tt2} depend on the thickness of the top tether, t_{ttop} , inner radius ($b = D_{pis}/2$), and outer radius ($a = D_{ch}/2$).

The bottom tether is modeled in the same way as the top tether, except it experiences only a concentrated force, F_{tebot} , at its inner radius and no pressure loading. The shear force per unit length is:

$$Q(r) = \frac{F_{tebot}}{2\pi r} \quad (4.39)$$

The boundary conditions are the same as the boundary conditions for the top tether. The

deflection of the bottom tether, which is equal to the deflection of the top tether can be obtained by integrating equation 4.7 and applying the boundary conditions to obtain:

$$x_{te} = k_{tb} F_{tebot} \quad (4.40)$$

where k_{tb} depends on the thickness of the bottom tether, t_{tebot} , inner radius ($b = D_{pis}/2$), and outer radius ($a = D_{ch}/2$).

Similarly, the stress in the bottom tether can be calculated as:

$$\sigma_{tb} = s_{tb} F_{tebot} \quad (4.41)$$

where s_{tb} depends again on the thickness of the bottom tether, t_{tebot} , inner radius ($b = D_{pis}/2$), and outer radius ($a = D_{ch}/2$)

We can also write:

$$F_{te} = F_{tetop} + F_{tebot} \quad (4.42)$$

which represents the force balance at the connection point of the tethers with the piston.

Detailed derivations of the elastic equations of the structural components are detailed in Appendix C.

4.3 Simulation Architecture

This section will present the simulation architecture used for integrating the elastic equations into the system level simulation.

Chamber Continuity

The continuity equation was derived in the previous chapter. In this section a more detailed equation will be derived considering the volume displaced in the chamber due to deformations of individual structural members. In the previous chapter, all the volume displaced by deformations was analyzed as a bulk value, namely ΔV_s , and was used to define the structural compliance, C_s . Rewriting equation 3.5, we have:

$$\frac{dP_{ch}}{dt} = \frac{\beta_f}{V_o} \frac{dV}{dt} \quad (4.43)$$

where β_f is the bulk modulus of the fluid, V_o is the initial volume of the fluid inside the chamber and $\frac{dV}{dt}$ is the rate of the volume change of the fluid. Sources of the volume change are net flowrate into the chamber, piston movement and additional volume created inside the chamber due to structural deformations. Considering these effects and integrating equation 4.43, we can write:

$$P_{ch} = \frac{\beta_f}{V_o} \left(\int_0^t (Q_{in} - Q_{out}) dt + \Delta V_{pis} + \Delta V_{pb} + \Delta V_{te} - \Delta V_{tp} \right) \quad (4.44)$$

where ΔV_{pis} , ΔV_{pb} , ΔV_{te} , ΔV_{tp} represent the swept volume due to the motion of the piston, deformation of the piston, deformation of the top tether and deformation of the top support structure respectively. The swept volume due to the motion of the piston is simply equal to:

$$\Delta V_{pis} = x_{pis} A_{pis} \quad (4.45)$$

where A_{pis} is the area of the piston. By arranging equation 4.44 we can obtain:

$$P_{ch} = \left(\frac{V_o}{\beta_f} + C_{tp} \right)^{-1} \left(\int_0^t (Q_{in} - Q_{out}) dt + x_{pis} A_{pis} + \Delta V_{pb} + \Delta V_{te} \right) \quad (4.46)$$

where C_{tp} represents the structural compliance corresponding to the deformation of the top support structure, which is given by equation 4.5.

Piezoelectric Cylinder

For a cross-sectional area of A_p and length L_p , the net deflection of the piezoelectric element and the voltage across it can be expressed using linear constitutive relationships as:

$$x_b - x_{pis} = \frac{L_p}{A_p} (s_{33}^D F_p + \frac{d_{33}}{\epsilon_{33}^T} Q_p) \quad (4.47)$$

$$V_p = \frac{L_p}{A_p} \left(\frac{d_{33}}{\epsilon_{33}^T} F_p - \frac{1}{\epsilon_{33}^T} Q_p \right) \quad (4.48)$$

where Q_p is the charge on the piezoelectric element.

Equations 4.13, 4.14, 4.19, 4.24, 4.25, 4.26, 4.31, 4.32, 4.38, 4.40, 4.41, 4.42, 4.44, 4.47, and 4.48 (15eqns) can be solved for the 15 unknowns, namely V_p , x_{tp} , ΔV_{tp} , ΔV_{te} , ΔV_{pb} , x_b , x_{te} , F_{te} , F_{te-top} , F_{te-bot} , σ_{tt} , σ_{tb} , F_p , P_{ch} , and F_{net} in terms of Q_p , x_{pis} , and Q_{net} where

$$Q_{net} = \int_0^t (Q_{in} - Q_{out}) dt \quad (4.49)$$

which represents the net fluid volume change inside the chamber due to the fluid flow into and out of the chamber [52]. The elastic equations along with the chamber continuity equation and piezoelectric element constitutive relationships are solved in Maple and the coefficients (A_{11} , A_{12} ...) of the 15×3 matrix required by the simulation architecture, shown in Figure 4-7, is calculated. The coefficients are then processed in a Matlab code to generate the 15×3 matrix, which is fed to Simulink. The details are presented in Appendix B and Appendix C. The Simulink blocks of the system model are presented in Appendix A.

The matrix equation solved in Simulink is as follows:

$$\begin{bmatrix} V_p \\ x_{tp} \\ \Delta V_{tp} \\ \Delta V_{te} \\ \Delta V_{pb} \\ x_b \\ x_{te} \\ F_{te} \\ F_{te-top} \\ F_{te-bot} \\ \sigma_{tt} \\ \sigma_{tb} \\ F_p \\ P_{ch} \\ F_{net} \end{bmatrix} = \begin{bmatrix} A_{11} & A_{12} & A_{13} \\ A_{21} & A_{22} & A_{23} \\ A_{31} & A_{32} & A_{33} \\ A_{41} & A_{42} & A_{43} \\ A_{51} & A_{52} & A_{53} \\ A_{61} & A_{62} & A_{63} \\ A_{71} & A_{72} & A_{73} \\ A_{81} & A_{82} & A_{83} \\ A_{91} & A_{92} & A_{93} \\ A_{101} & A_{102} & A_{103} \\ A_{111} & A_{112} & A_{113} \\ A_{121} & A_{122} & A_{123} \\ A_{131} & A_{132} & A_{133} \\ A_{141} & A_{142} & A_{143} \\ A_{151} & A_{152} & A_{153} \end{bmatrix} \begin{bmatrix} Q_p \\ x_{pis} \\ Q_{net} \end{bmatrix} \quad (4.50)$$

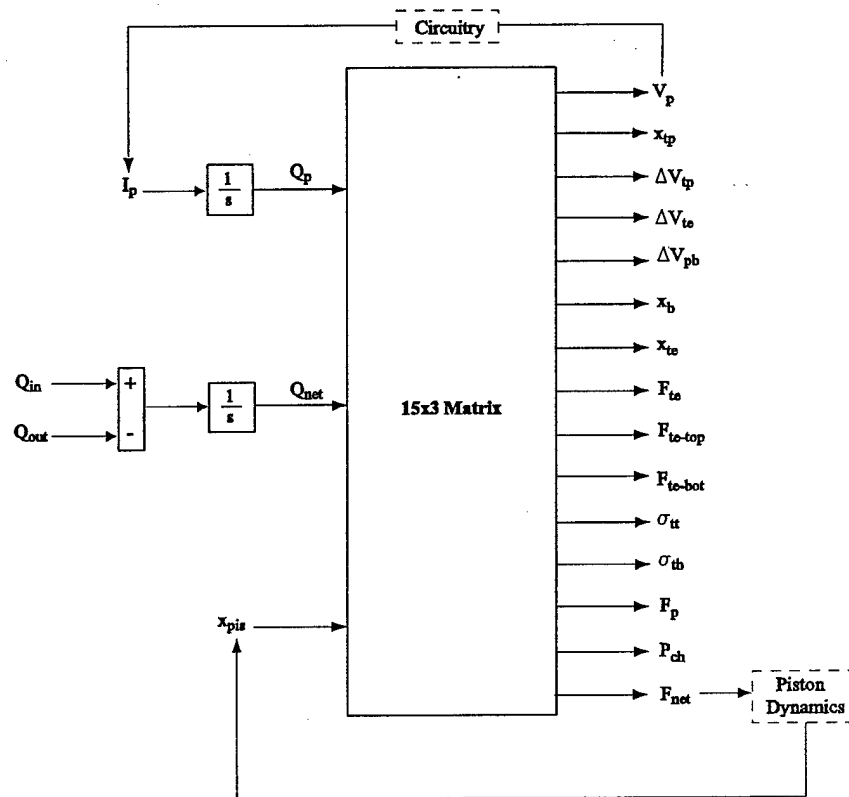


Figure 4-7: Simulation architecture used to integrate the elastic equations into system level simulation.

where the matrix coefficients are calculated using Maple.

The simulation architecture allows for integration of the elastic equations into the dynamic simulations as well as for monitoring important parameters like deflections and swept volumes of the individual structural components and stresses in the tethers.

4.4 Conclusion

This chapter presented detailed analysis of the energy harvesting chamber in terms of the deformations of individual structural components. The deformations are analyzed using linear plate theory. It is assumed that the deflections due to bending are significantly larger than those due to shearing. A simulation architecture is presented to be included in the overall system level simulation, which allows for inclusion of the elastic equations into the dynamic simulation and allows for monitoring important parameters.

Chapter 5

Further Design Considerations and Design Procedure

This chapter presents further design considerations in addition to those issues discussed in Chapter 3. These are fluidic oscillations within the system, chamber filling and evacuation, tether structure optimization and the effect of operation conditions and geometry on system performance. At the end of the chapter, a design procedure along with two design examples and simulation results will be presented. The system is analyzed only for the case where the chamber is attached to the regular bridge.

5.1 Further Design Considerations

5.1.1 Fluidic Oscillations

Inertial effects should be considered when designing hydraulic systems containing small channels. In fact, in the MHT devices, the fluid channels and the main chamber constitute a resonating system similar to a Helmholtz resonator, shown in Figure 5-1, which comprises a fluid channel and a chamber with an effective compliance C . The natural frequency of the Helmholtz resonator can be calculated by considering the free-body diagram of the fluid slug within the channel. The equation of motion of the fluid slug can be written as:

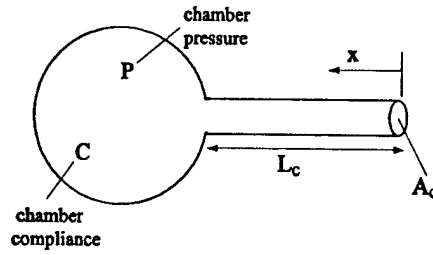


Figure 5-1: Helmholtz Resonator.

$$\rho A_c L_c \frac{d^2 x}{dt^2} + P A_c = 0 \quad (5.1)$$

where P is the pressure inside the chamber which builds up as a result of the additional fluid flow into the chamber, which can be expressed as:

$$P = \frac{A_c x}{C} \quad (5.2)$$

Combining equations 5.1 and 5.2 we can obtain the governing equation for the Helmholtz resonator as:

$$\ddot{x} + \left(\frac{A_c}{\rho C L_c} \right) x = 0 \quad (5.3)$$

The natural frequency of the resonator can be easily obtained from equation 5.3:

$$\omega_n = \sqrt{\frac{A_c}{\rho C L_c}} \quad (5.4)$$

We can conclude that the natural frequency of the oscillations similar to Helmholtz resonator within the system depends on the channel geometry ($\frac{L_c}{A_c}$ ratio), the compliance of the chamber and the density of the working fluid. The chamber compliance here refers to the overall chamber, including the compression of the piezoelectric element. In Chapter 3, an effective chamber compliance, C_{eff} , was defined which took only the structural deformations and fluid compression into account, but not the compression of the piezoelectric element. In the context of this discussion, it is convenient to define an overall chamber compliance, C , which includes

the structural deformations, fluid compression, and the deformation of the piezoelectric element. The overall chamber compliance in this case can be defined as:

$$C = \frac{\Delta V_f}{\Delta P_{ch}} = \frac{\int (Q_{in} - Q_{out}) dt}{\Delta P_{ch}} \quad (5.5)$$

where ΔV_f is the fluid volume change in the chamber due to the fluid flow. In fact, this compliance is not a constant value in the actual power generator since the stiffness of the piezoelectric element changes constantly (the stiffness flips between open-circuit and close-circuit stiffnesses of the piezoelectric element) during the operation, as discussed in Chapter 2 and Chapter 3. In the following two subsections, the fluidic oscillations will be analyzed for two cases. In the first case, a constant overall chamber compliance will be assumed for simplicity and in order to get insight, and in the second case the actual system, i.e. the chamber attached to the rectifier circuit will be analyzed in terms of fluidic oscillations.

Analysis with Constant Overall Chamber Compliance

Consider a chamber with constant overall chamber compliance, $C = 10^{-17} [m^3/Pa]$, as defined in equation 5.5. Figure 5-2 shows the simulation of the system for different chamber geometries, i.e. for different L_c/A_c ratios. In the simulation, the operation conditions, valve size and openings are adjusted such that the chamber pressure fluctuates between P_{HPR} and P_{LPR} for the case where the inertial effects in the channels are negligible. These conditions are: $P_{HPR} = 2MPa$, $P_{LPR} = 0$, $f = 10kHz$, $R_{vc} = 200\mu m$, $vo_{in} = vo_{out} = 20\mu m$, and the working fluid is silicon-oil.

It can be seen that there exists an optimum L_c/A_c value for which the difference between the maximum and minimum pressures, i.e. the pressure band, ΔP_{ch} , is maximum. This value is approximately $25000(1/m)$. The pressure band is not very sensitive to L_c/A_c around the optimum value, i.e. $L_c/A_c = 24000$ or $L_c/A_c = 26000$ results pretty much in the same pressure band. In fact, the optimum value of the L_c/A_c can be approximated using equation 5.4. Figure 5-3 shows the inlet flowrate time histories from the simulation. It can be seen that, the fluid inductance in the channel causes the flow to lag, i.e. the flowrate reaches its maximum at a later time compared to the case where the fluid inductance is negligible.

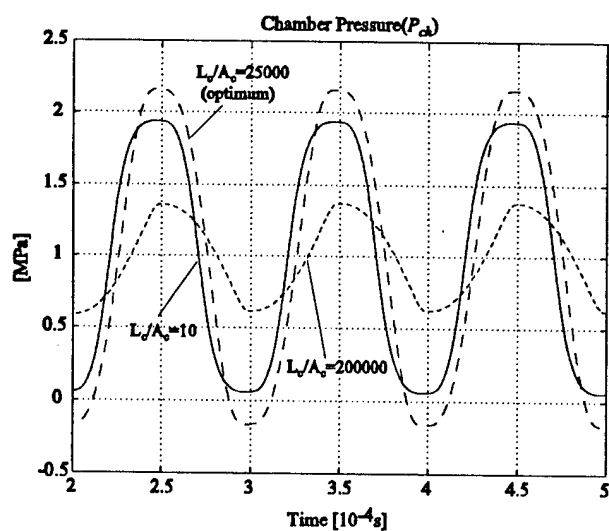


Figure 5-2: Simulation of the chamber with constant overall compliance for different channel geometries.

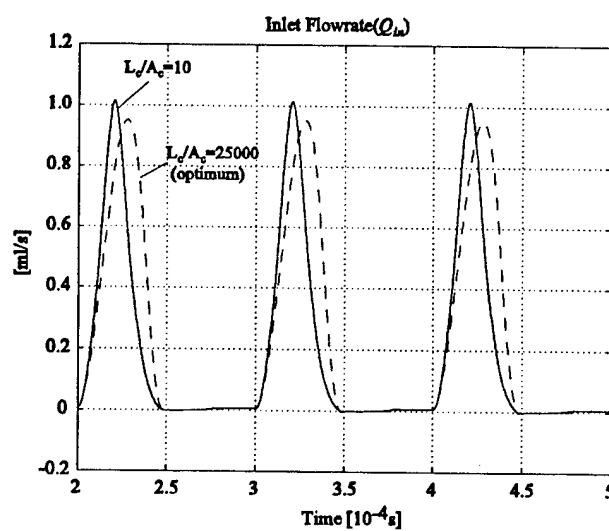


Figure 5-3: Comparison of flowrate time histories for different L/A ratios.

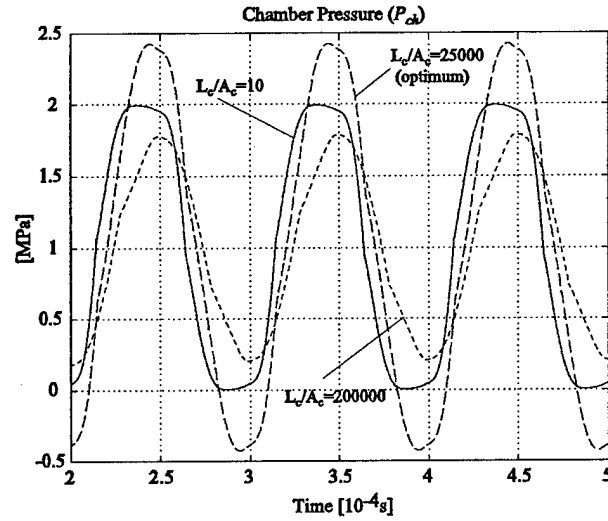


Figure 5-4: Simulation of the chamber attached to circuitry for different channel geometries.

Analysis of the chamber attached to circuitry

Consider the chamber geometry, effective compliance and operation conditions presented in Table 3.2 of Chapter 3. Figure 5-4 shows the simulation of the same geometry for different L_c/A_c ratios. Again, the valve size and opening is adjusted such that the chamber pressure fluctuates between P_{HPR} and P_{LPR} for the case where the inertial effects in the channels are negligible. These conditions are: $P_{HPR} = 2MPa$, $P_{LPR} = 0$, $f = 10kHz$, $R_{vc} = 200\mu m$, $vo_{in} = vo_{out} = 20\mu m$, the working fluid is silicon-oil, and the battery voltage, V_b , is $90V$, which is optimized for a pressure band of $2MPa$. Similar to the case where a constant overall chamber compliance was assumed, there exists an optimum L_c/A_c value for which the difference between the maximum and minimum pressures, i.e. the pressure band, ΔP_{ch} , is maximum.

Figure 5-5 shows the effect of L_c/A_c ratio on pressure band and generated power. Throughout the simulations the battery voltage was not changed. In fact, in a design, the battery voltage should be determined according to the expected pressure band, which determines the stress band on the piezoelectric element. For example, for the optimum L_c/A_c ratio, the pressure band is $2.435MPa$, which suggests a battery voltage of approximately $125V$. If the simulation is repeated with this value, the pressure band is now $2.472MPa$, which is slightly different than

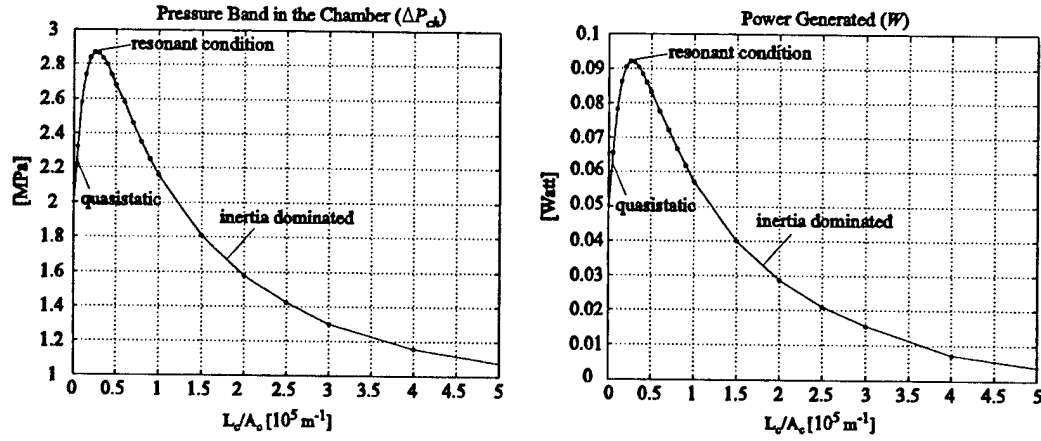


Figure 5-5: Effect of L/A ratio on pressure band and generated power.

the previous value, and the generated power is 0.1068W. The slight change in the pressure band suggests that the change in the battery voltage caused a small change in the overall chamber compliance, because it basically determines the voltage level where the piezoelectric element will change its stiffness, and therefore effects the time intervals in which the piezoelectric element posses the different stiffnesses. The expression for the optimum battery voltage was given in Chapter 2 as:

$$V_b = \frac{1}{4} \frac{\Delta\sigma(s_{33}^E - s_{33}^D)L_p}{d_{33}} \quad (5.6)$$

which can be written in terms of the pressure band in the chamber as:

$$V_b = \frac{1}{4} \frac{\Delta P_{ch} A_{pis}}{A_p} \frac{(s_{33}^E - s_{33}^D)L_p}{d_{33}} \quad (5.7)$$

where A_{pis} and A_p are the piston area and the cross-sectional area of the piezoelectric cylinder respectively, and $\Delta\sigma$ is the stress band on the piezoelectric element. It should be noted that, when writing equation 5.7 the effect of tethers and piston dynamics is neglected. In other words, static force balance between the piston and piezoelectric element is assumed and the force applied by the tethers on the piston is neglected. This issue will be addressed later.

We can conclude that, for a given overall chamber compliance there exists an optimum L_c/A_c ratio at a certain operation frequency, or similarly, there exists an optimum operation

frequency for a certain overall compliance and L_c/A_c ratio. The fluidic oscillations should be considered in any design procedure and the channels should be designed accordingly. This will be addressed later in the discussion of the design procedure.

The overall chamber compliance was defined as the compliance of the chamber including the compliances due to structural deformations and fluidic compliance, which is represented by the effective compliance, C_{eff} , and the compliance due to the deflection of the piezoelectric element. The compliance due to the deflection of the piezoelectric element can be calculated considering the volume displaced by the piston due to the deflection of the element as a response to the pressure change in the chamber:

$$C_p = \frac{\Delta V_{pis}}{\Delta P_{ch}} = \frac{\Delta x_p A_{pis}}{\Delta P_{ch}} = \frac{\left(\frac{\Delta P_{ch} A_{pis}}{k_p} \right) A_{pis}}{\Delta P_{ch}} = \frac{A_{pis}^2}{k_p} \quad (5.8)$$

where k_p is the stiffness of the piezoelectric element, which can be expressed as:

$$k_p = \frac{A_p}{s_{33} L_p} \quad (5.9)$$

where A_p and L_p are the cross-sectional area and the length of the piezoelectric element respectively, and s_{33} is the compliance coefficient of the element. As mentioned earlier, the stiffness of the piezoelectric element changes constantly during the operation between the open circuit and closed circuit stiffnesses, which should be calculated using s_{33}^D and s_{33}^E respectively. Therefore the system is highly nonlinear and it is impossible to express the resonant frequency, or the optimum L_c/A_c ratio analytically. However we can get a first order estimation of the resonant frequency using one of the stiffnesses above. For example using the open circuit compliance coefficient, s_{33}^D , and from equations 5.4, 5.8, and 5.9 we obtain:

$$f_n = \frac{1}{2\pi} \sqrt{\frac{A_c}{L_c \rho (C_{eff} + C_p)}} = \frac{1}{2\pi} \sqrt{\frac{A_c}{L_c \rho \left(\frac{V_o}{\beta_f} + C_s + \frac{s_{33}^D L_p A_{pis}^2}{A_p} \right)}} \quad (5.10)$$

where C_{eff} is the effective chamber compliance.

It is very important to note that in the simulations presented in this and the previous

sections (Figures 5-2 and 5-4), the pressure in the chamber overshoot the reservoir pressures (P_{HPR} and P_{LPR}) in the resonance conditions, which resulted in negative pressures, which should be avoided because of cavitation. In the design procedure, the operation conditions should be adjusted such that there won't be any cavitation. For example the system can be biased, i.e. the reservoir pressures can be increased keeping the difference the same. Or, the valve openings can be adjusted accordingly. The motivation for operating at resonance condition is that the same pressure band can be achieved with smaller valve cap sizes or valve openings compared to the case of negligible or very large fluid inductance in the channels, resulting in reduced power consumption in the active valves.

5.1.2 Chamber filling and evacuation

In order to attain the desired pressure bands inside the chamber, it is important to design the valve sizes, openings and the operation frequency accordingly. Consider the chamber attached to the circuitry discussed in the previous section. Figure 5-6 shows the effect of valve opening on pressure band in the chamber. A valve opening of $20\mu m$ provides perfect filling and subsequent evacuation of the chamber in the required time interval and the chamber pressure fluctuates between the reservoir pressures. A small valve opening of $5\mu m$ results in poor(slow) filling and evacuation, resulting in a reduced pressure band. A large valve opening of $50\mu m$ provides very fast filling and evacuation, which causes the chamber pressure to retain its maximum and minimum values for long time intervals. The latter results in the same power generated, however it also results in more power consumption in the active valves due to the higher stroke. A similar result would be obtained by keeping the valve opening the same, but increasing the valve cap size. Again more power would be consumed in the active valves.

Figure 5-7 shows the effect of operation frequency on the pressure band in the chamber. It can be seen that, for a fixed valve opening, different operation frequencies result in system behaviors similar to the ones in Figure 5-6. At high frequency, there is not enough time for the valve to fill and evacuate the chamber in the required time interval. Similarly, at low frequency, there is more than enough time for the valves to fill and evacuate, which results in similar behavior to the case of large valve opening. This implies that, the valve opening can be reduced for reduced power consumption in the active valve and yet the same power can be

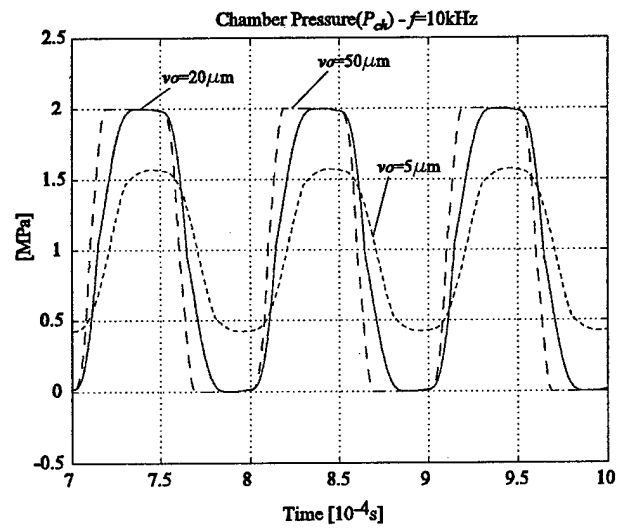


Figure 5-6: Effect of valve opening on the pressure band in the chamber.

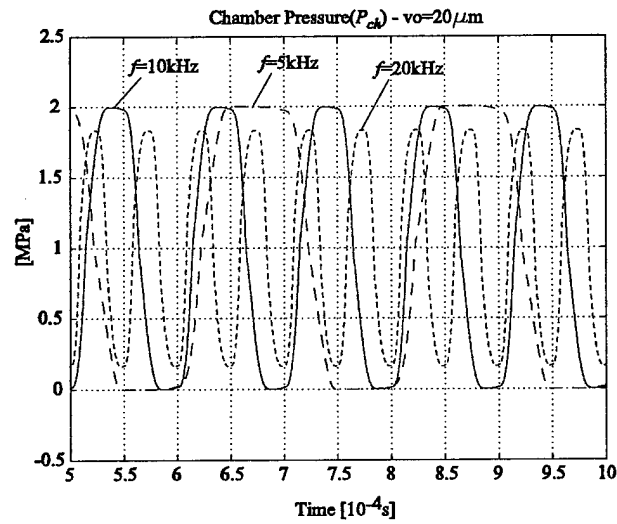


Figure 5-7: Effect of operation frequency on the pressure band in the chamber.

generated as long as the pressure band in the chamber is kept at the desired level.

In the two cases analyzed above, the valve cap size could be analyzed instead of valve opening, which would lead to the same conclusions. The combination of the valve size and the valve opening define the overall valve resistance. We can conclude that, for a designed operation frequency and pressure band, it is important to design the valve size and opening such that they will provide just enough filling and evacuation of the chamber in the required time interval, which is defined by the operation frequency, so that the chamber pressure fluctuates between the reservoir pressures in the most economical way. As will be addressed later, the pressure band is a very important design parameter, since the power generated is proportional to the square of the stress band on the piezoelectric element. Additional design considerations concerning the design of the valve size and opening is not within the scope of this thesis. The design optimization of the active valves is detailed in [5].

5.1.3 Tether Structure Optimization

Design of the piston tether structure is very crucial for system operation. The tethers should be flexible enough to allow sufficient motion of the piston, yet stiff enough to avoid introduction of excessive compliance into the system. The tethers have to be designed to allow maximum piezoelectric element compression for a given net fluid volume into the chamber, which occurs basically at every cycle during system operation. To analyze the tether structure, consider a simple hypothetical chamber which consists of a fluid chamber with rigid walls, a single layer piston attached to the wall with a single tether providing sealing, and a piezoelectric element. Figure 5-8 illustrates the hypothetical chamber and different tether designs. Figure 5-8(b) illustrates a good tether design where the tethers allow large piezoelectric element compression. Figure 5-8(c) illustrates a poor design where the tether is either too thin or the tether width, t_w , is very large ($t_w = [D_{ch} - D_{pis}]/2$). This results in low pressure in the chamber and small compression of the piezoelectric element since the compliance introduced by the tether is very large. In other words, pressure doesn't built up inside the chamber because of the excessive bending of the tether. Figure 5-8(d) illustrates another poor design where the tether is either too thick or the tether width, t_w , is very small. In this case the pressure in the chamber is high but the compression of the piezoelectric element is still very small since the very stiff tethers

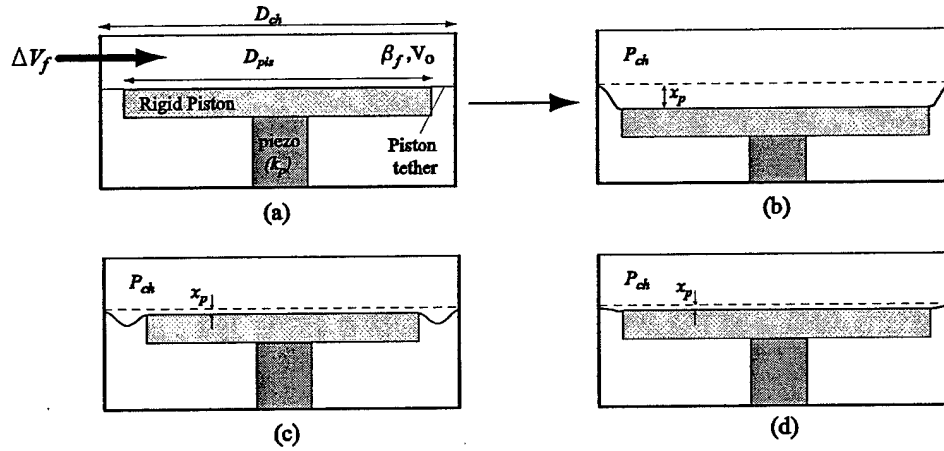


Figure 5-8: (a) Schematic illustrating the hypothetical chamber (b) good tether design providing large piezoelectric element compression (c) poor tether design, either too thin or large width, resulting in low chamber pressure and small piezoelectric element compression (d) poor tether design, either very thick or small width, resulting in large pressures but small piezoelectric element compression.

do not allow the piston to move although they introduce very small additional compliance into the system. This suggests that for a design where the chamber diameter(or piston diameter) is determined, the tether structure has to be optimized in conjunction with fabrication limitations, such as thickness of the tether, which is determined by the SOI wafer, or the maximum tether width which can be etched.

Consider a chamber of the following geometric parameters: $D_{ch} = 5mm$, $D_p = 1mm$, $L_p = 1mm$, and $H_{ch} = 200\mu m$. An additional fluid volume, $\Delta V_f = 10^{-11}m^3$, is introduced into the chamber. Figure 5-9 shows piston deflection/piezoelectric element deflection, pressure in the chamber and the compliance of the chamber for different tether thicknesses and widths. The tether width is varied by keeping the chamber diameter the same and changing the piston diameter. Since the tether width is very small compared to chamber or piston diameter, it doesn't matter which parameter is kept constant, i.e. the the piston diameter could be kept constant and the chamber diameter could be varied alternatively. Thus we can generalize this study for a nominal chamber diameter of $5mm$. It can be seen that for a tether thickness, there exists a range of values for tether widths where maximum deflection of the piston occurs. It

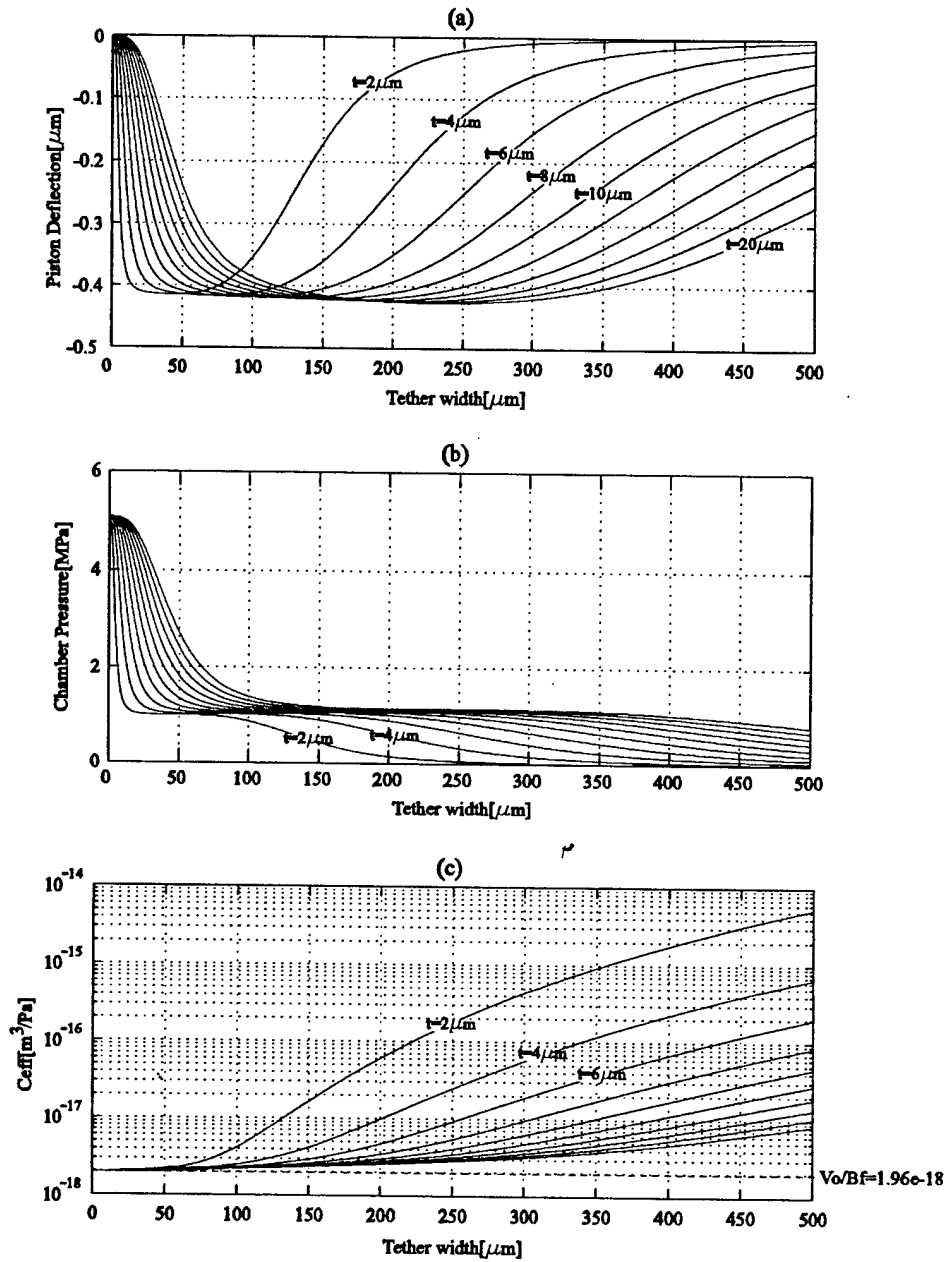


Figure 5-9: (a) Piston deflection for different tether thicknesses and widths, (b) corresponding pressures in the chamber (c) compliance of the chamber. The dashed line corresponds to the hypothetical case where piston diameter is equal to chamber diameter and there is perfect sealing.

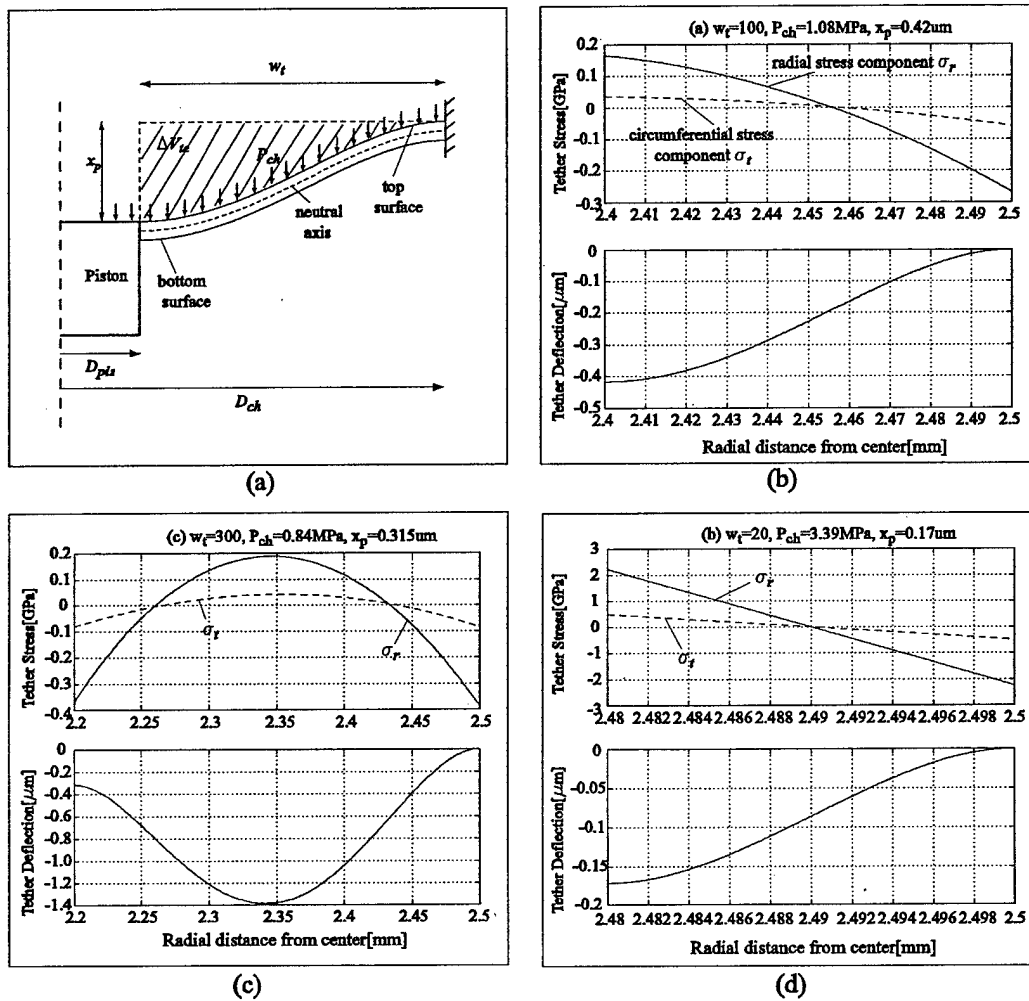


Figure 5-10: (a) Schetch illustrating tether deflection. (b),(c),and (d) show the stress components on the bottom surface and deflected shape of the tether for 3 different cases.(b) good tether design, (c) poor tether design where the tether is too compliant, and (d) poor tether design where the tether is too stiff.

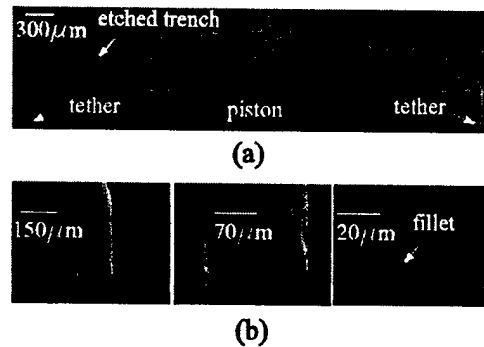


Figure 5-11: (a) SEM picture of micromachined piston structure [7](b) detailed view of the tether and the fillet.

can be also seen that for those values, the additional compliance introduced by the tethers is negligible.

Figure 5-10 illustrates the stresses and deflected shapes of the tether with a thickness of $10\mu\text{m}$ for three different cases. Figure 5-10(b) illustrates a good design where the tether width is optimized. Figure 5-10(c) illustrates a poor design where the tether width is very large and therefore the pressure in the chamber and piston deflection are small. Figure 5-10(d) illustrates another poor design where the tether width is small and therefore the tether is very stiff, which results in small piston deflection even though the pressure built up in the chamber is high. It can be also seen that the stresses in this case are very large compared to the previous two cases.

It should be noted that linear plate theory is used for this analysis which means that the neutral axis coincides with the central axis of the tether. In general, in a well-designed tether structure, the bottom surface of the tether experiences compressive stress near the chamber wall and tensile stress near the piston, which is the case in Figure 5-10(b), and the maximum stress occurs at the point where the tether is attached to the wall. The top surface experiences stresses with opposite signs.

It is also very important to consider the effect of the fillet on the stress and to note that the stresses calculated from the linear plate theory should be corrected using the proper stress concentration factor. However the stresses calculated using linear theory give a reasonable estimate and provide first order prediction about stresses during the design procedure. A

detailed study of the fillet radius and stress concentration factors can be found in [7]. A fabricated piston structure and the fillets are shown in Figure 5-11.

5.1.4 Operation Conditions and Trade-offs

In most of the analysis performed so far the basic parameters of the chamber, such as chamber diameter, and operation conditions such as reservoir pressures and operation frequency were fixed. This section will discuss how to choose chamber geometry and operation conditions for a given power requirement and will discuss trade-offs between operation conditions. The general design guidelines can be summarized as follows:

- The operation frequency should be kept as small as possible due to the bandwidth limitations imposed by the active valve structure,
- The flowrate should be kept as small as possible to minimize valve size and reduce power consumption in the valves,
- The maximum pressure in the chamber should be kept as small as possible in order to avoid high stresses in the tethers and active valve membranes.

For the analysis of this section, a relatively simple chamber structure will be assumed, namely the effect of the tethers, the deformation of the piston, and the deformation of the bottom plate will be ignored. This means that the effective compliance will be comprised of the fluidic compliance and structural compliance only due to the deflection of the top support structure. These assumptions are done for simplification of the analysis without loss of generality.

Fixed geometric parameters in this analysis are: chamber height, $H_{ch} = 200\mu$, length of piezoelectric element, $L_p = 1mm$, and top support structure thickness, $t_{top} = 1mm$. For each design point considered, piston area and cross-sectional area of the piezoelectric element satisfy the following relationship.

$$A_{pis} = \frac{\sigma_d A_p}{P_{HPR}} \quad (5.11)$$

which represents the static force balance between the piston and the piezoelectric element. The areas of the piston and the piezoelectric element are designed such that maximum stress on the piezoelectric element is equal to the depolarization stress, σ_d , for maximum power output.

It is assumed that the maximum and minimum pressures attained in the chamber are equal to the high and low pressure reservoirs respectively, where P_{LPR} is assumed to be zero for simplicity.

Required operation frequency for a given power requirement

The required frequency in order to generate a certain amount of power, W , for the case of the chamber attached to regular diode bridge is given by:

$$f = \frac{4W}{(s_{33}^E - s_{33}^D)\sigma_d^2 A_p L_p} \quad (5.12)$$

where s_{33}^E and s_{33}^D are the closed circuit and open circuit compliances of the piezoelectric element respectively. Figure 5-12 compares different piezoelectric materials in terms of required frequency for a $0.5W$ power requirement at different chamber diameters and reservoir pressures. It can be seen that, $PZT - 4S$ and $PZT - 8$ require lower frequencies because of their very high depolarization stress, even though they have smaller coupling coefficients compared to $PZT - 5H$ and $PZN - PT$. It should be noted that, the required frequency does not depend on the chamber compliance, as can be seen from equation 5.12.

It is important to note that there is a trade-off between the maximum chamber pressure (P_{HPR}) and the operation frequency. For lower chamber pressures, higher operation frequencies are needed. In fact, for a given piston diameter the required frequency is inversely proportional to the reservoir pressure, as can be easily seen from equations 5.11 and 5.12. It can be also seen that, for larger chamber diameters, the required operation frequency is smaller since for larger chamber diameters, piezoelectric elements having larger diameter are used to satisfy equation 5.11, which results in lower frequency requirement due to the increased piezoelectric element volume.

Required flowrate for a given power requirement

The required flowrate is given by the following equation, which was derived in Chapter 3:

$$Q = \frac{2(s_{33}^E + s_{33}^D)W}{(s_{33}^E - s_{33}^D)P_{HPR}} + C_{eff}P_{HPR}f \quad (5.13)$$

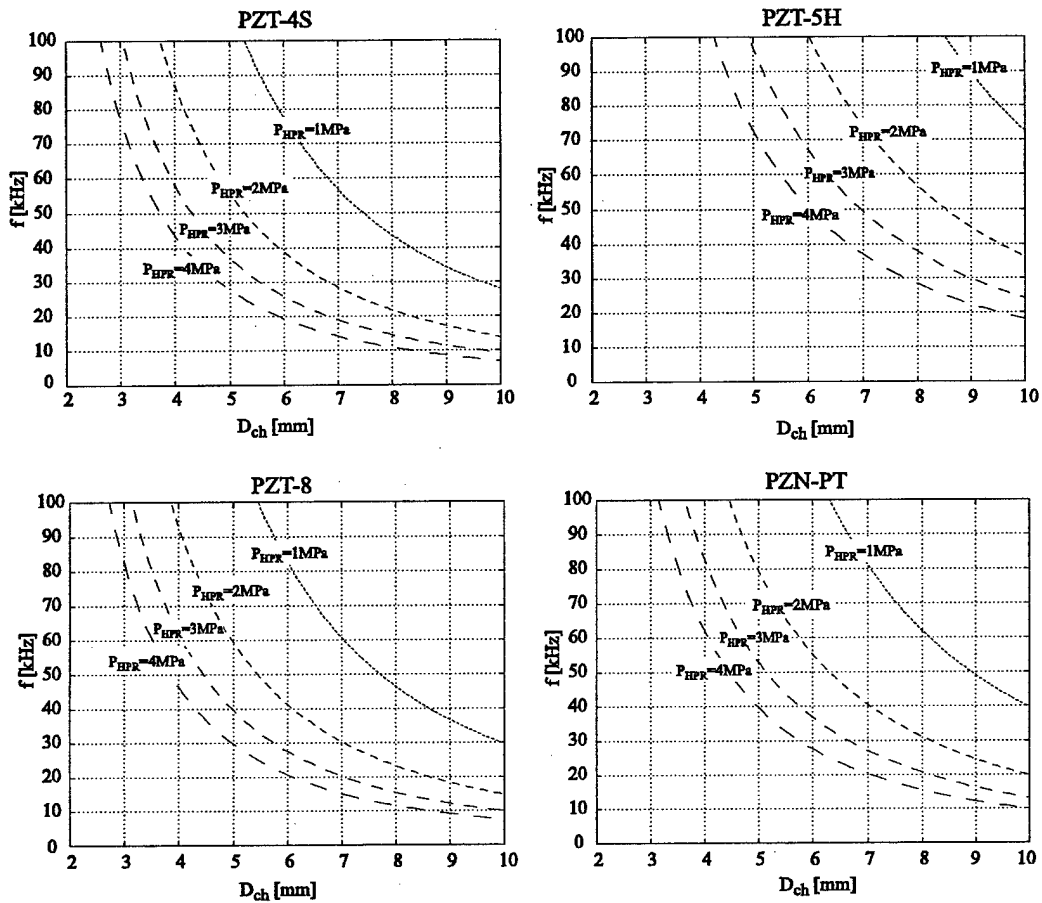


Figure 5-12: Comparison of different piezoelectric materials in terms of required operation frequency at different chamber diameters for a power requirement of 0.5W.

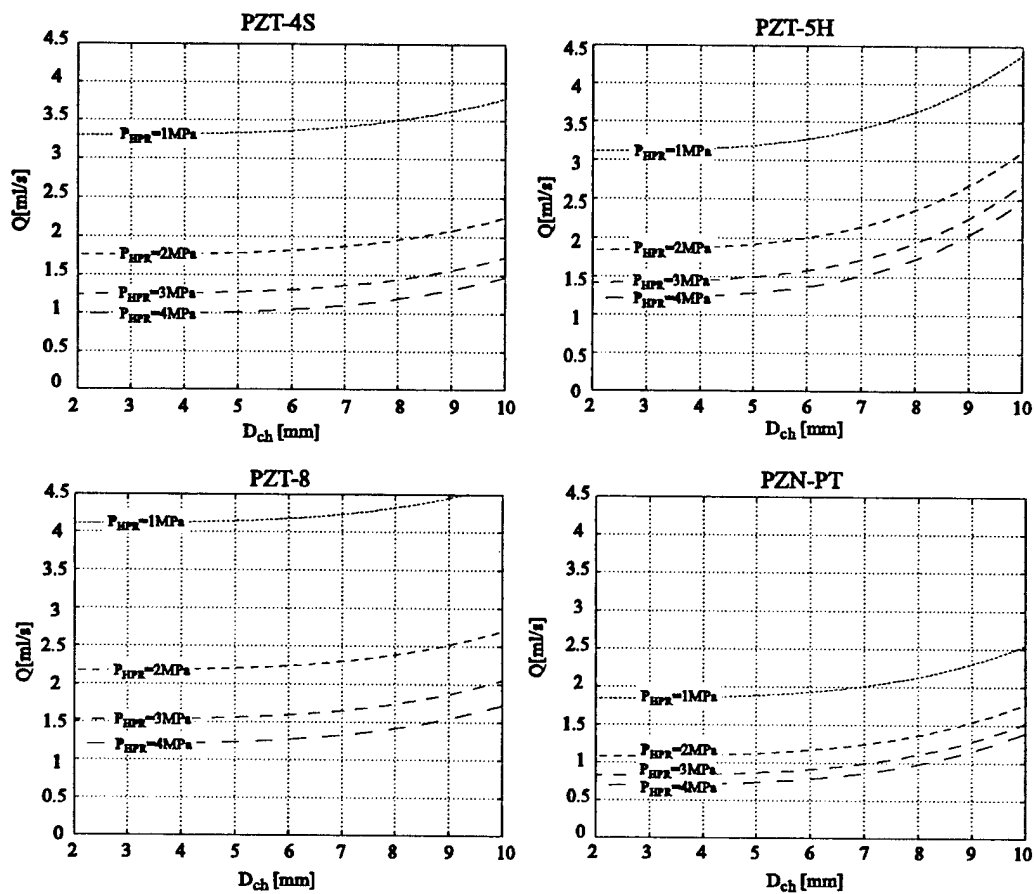


Figure 5-13: Comparison of different piezoelectric materials in terms of required flowrate at different chamber diameters for a power requirement of 0.5W.

where f is the required operation frequency corresponding to the power requirement at the particular chamber diameter and reservoir pressure, as discussed in the previous subsection. Figure 5-13 shows a comparison of different piezoelectric materials in terms of required flowrate at different reservoir pressures and chamber diameters.

It can be seen that $PZN - PT$ requires the least flowrates due to its high coupling coefficient, which translates into higher system efficiencies as discussed in Chapter 3. It can be also noted that, for larger chamber diameters, higher flowrates are required. This can be explained by considering equation 5.13. There are in fact two competing effects. For larger chamber diameters, lower frequencies are needed, as shown in Figure 5-12, which suggest lower flowrates. However, larger chamber diameters result in increased chamber compliance, which is the dominating factor resulting in higher flowrates.

In this case, a trade-off exists between the required flowrate and maximum chamber pressure, namely for lower chamber pressures, higher flowrates are required.

Efficiency

The efficiency of the system is given by:

$$\eta = \frac{W}{Q P_{HPR}} \quad (5.14)$$

where the power consumption in the active valves is not considered. Figure 5-14 shows a comparison of different piezoelectric elements in terms of system efficiency for different reservoir pressures and chamber diameters. It can be seen that $PZN - PT$ provides the most efficient power generation due to its high coupling coefficient. For larger chamber diameters, the efficiency is lower due to the fact that the flowrate is higher at larger chamber diameters, as shown in Figure 5-13. It is also important to note that the efficiency decreases as the reservoir pressure increases. This can be explained considering equations 5.11, 5.12 and 5.13. Combining these equations we get:

$$Q = \frac{2(s_{33}^E + s_{33}^D)W}{(s_{33}^E - s_{33}^D)P_{HPR}} + \frac{4C_{eff}W}{(s_{33}^E - s_{33}^D)\sigma_d A_{pis} L_p} \quad (5.15)$$

which is the explicit form of equation 5.13. Using equation 5.14 we get:

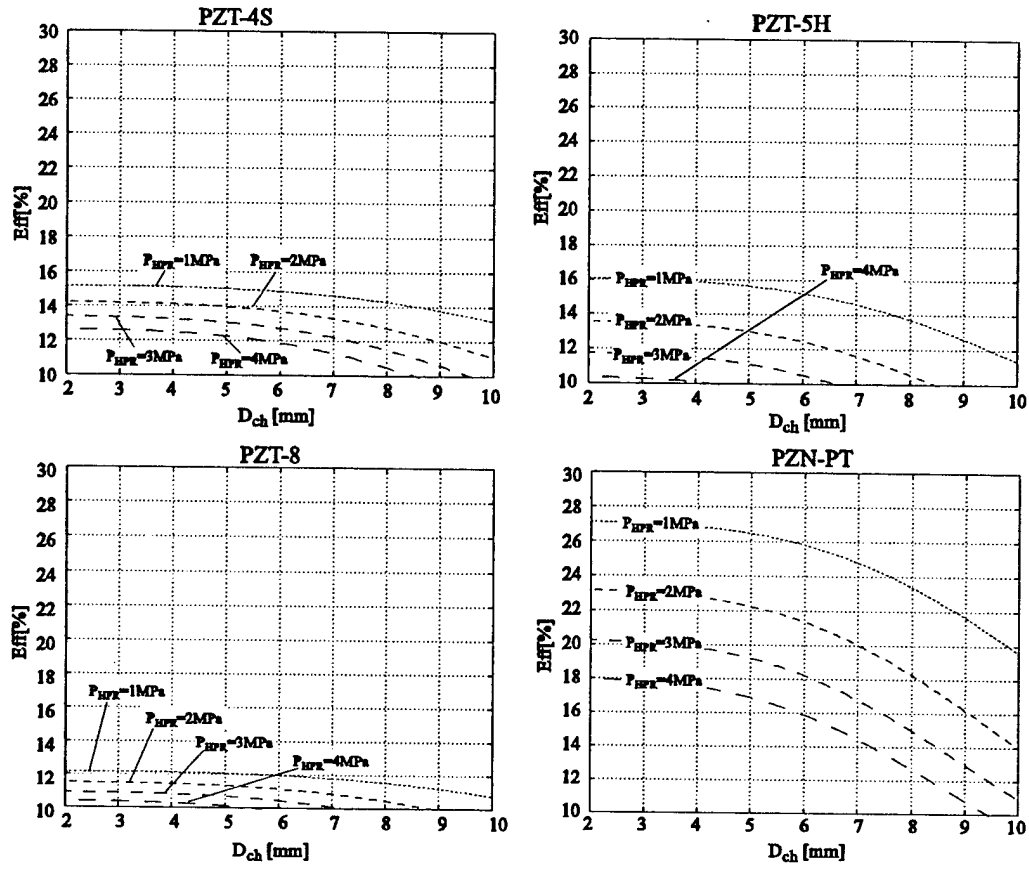


Figure 5-14: Comparison of different piezoelectric elements in terms of system efficiency for different reservoir pressures and chamber diameters.

$$\eta = \frac{W}{Q P_{HPR}} = \left(\frac{2(s_{33}^E + s_{33}^D)}{(s_{33}^E - s_{33}^D)} + \frac{4C_{eff} P_{HPR}}{(s_{33}^E - s_{33}^D) \sigma_d A_{pis} L_p} \right)^{-1} \quad (5.16)$$

from which it can be easily seen that at a certain chamber diameter, the efficiency decreases with increasing reservoir pressure. It is also possible to observe that efficiency does not depend on the generated power.

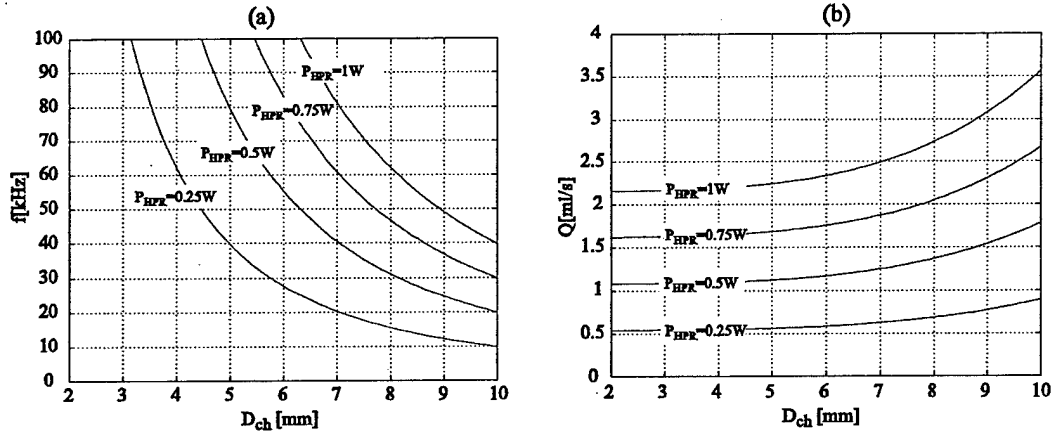


Figure 5-15: Required operation frequency and flowrate for different power requirements at different chamber diameters ($P_{HPR} = 2MPa$, piezoelectric material: $PZN - PT$).

Effect of power requirement

As can be seen from equations 5.12 and 5.16, the required operation frequency and flowrate are directly proportional to the generated power. Figure 5-15 illustrates the effect of power requirement on frequency and flowrate for the case where $P_{HPR} = 2MPa$ and piezoelectric material: $PZN - PT$.

5.1.5 Bias Pressure

As discussed in section 5.1.1, negative pressure in the chamber should be avoided due to cavitation. Even though the chamber is designed for positive pressure fluctuations, cavitation could occur due to unexpected fluidic resonances. Also the active valve design imposes minimum pressure requirements for the low pressure reservoir due to cavitation considerations inside the hydraulic amplification chamber. For a conservative design, the chamber pressure can be biased by a certain amount, by keeping the pressure differential $P_{HPR} - P_{LPR}$ the same, aiming for the same power as would be generated with $P_{LPR} = 0$. However, since the depolarization stress of the piezoelectric element cannot be exceeded, the effective stress band reduces, even though the pressure band remains the same. For the case where $P_{LPR} = 0$, the stress band, i.e. the difference between the maximum and minimum stress on the piezoelectric element is equal to

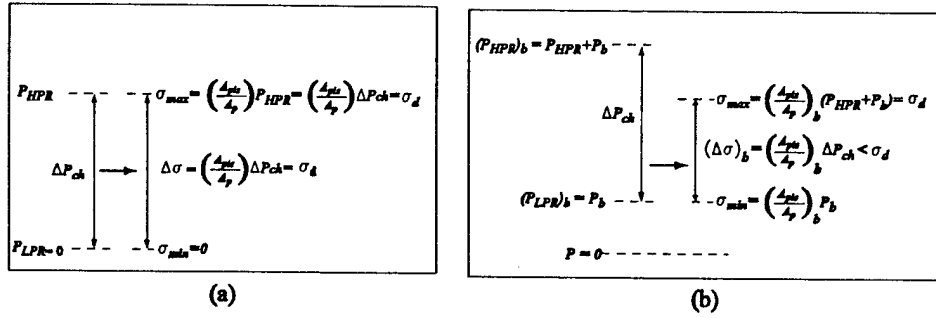


Figure 5-16: Schematic illustrating the effect of bias pressure.(a) not biased case (b) biased case

the depolarization stress, given by:

$$\Delta\sigma = \left(\frac{A_{pis}}{A_p} \right) \Delta P_{ch} = \sigma_d \quad (5.17)$$

However, for the biased case, where $P_{LPR} \neq 0$, the stress band is given by:

$$(\Delta\sigma)_b = \left(\frac{A_{pis}}{A_p} \right)_b \Delta P_{ch} < \sigma_d \quad (5.18)$$

which is smaller than the depolarization stress of the piezoelectric material. Figure 5-16 illustrates the effect of bias pressure. This means that for the same pressure differential, higher frequencies and flowrates are required, which can be seen from the following equations which are derived for the general case:

$$f_b = \frac{4W}{(s_{33}^E - s_{33}^D)(\Delta\sigma)_b^2 A_p L_p} \quad (5.19)$$

$$Q_b = \frac{2(s_{33}^E + s_{33}^D)W}{(s_{33}^E - s_{33}^D)\Delta P_{ch}} + C_{eff}\Delta P_{ch}f_b \quad (5.20)$$

or

$$Q_b = \frac{2(s_{33}^E + s_{33}^D)W}{(s_{33}^E - s_{33}^D)\Delta P_{ch}} + \frac{4C_{eff}W}{(s_{33}^E - s_{33}^D)(\Delta\sigma)_b A_{pis} L_p} \quad (5.21)$$

Figure 5-17 illustrates the effect of bias pressure on required frequency, flowrate and efficiency for the case of 0.5W power requirement, where $\Delta P_{ch} = P_{HPR} - P_{LPR} = 2MPa$, and

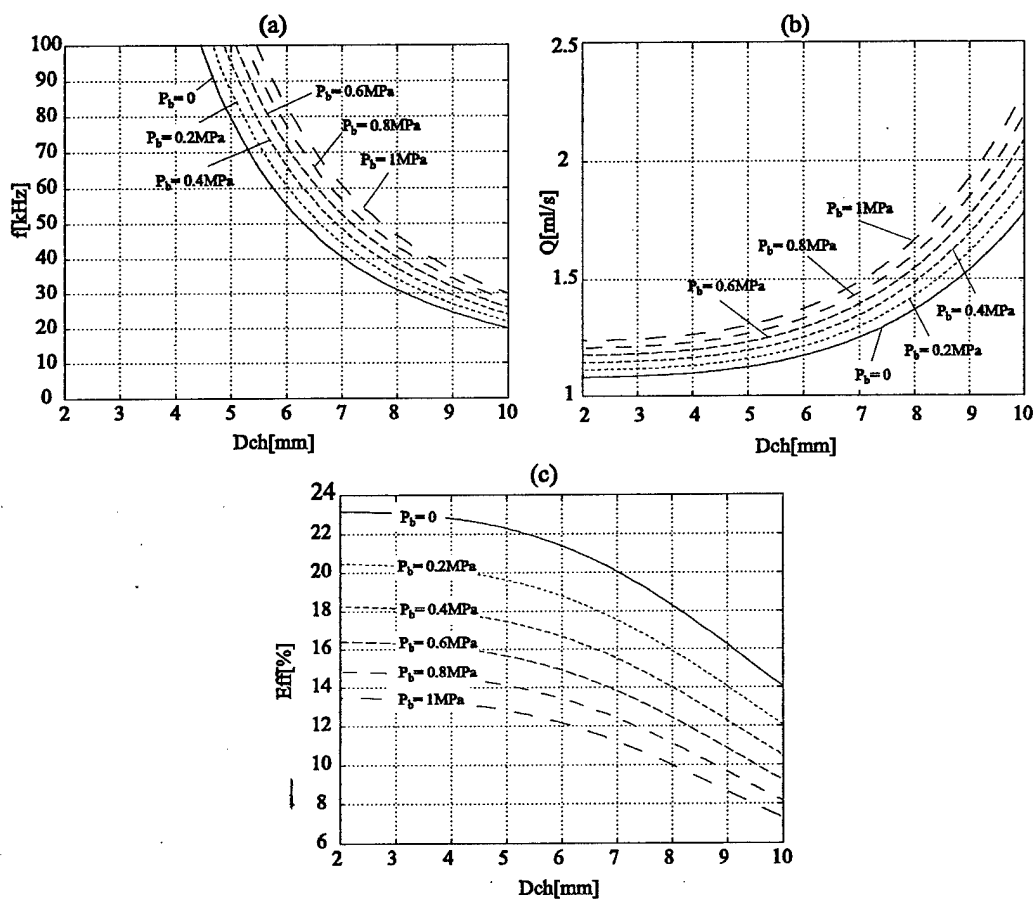


Figure 5-17: Effect of bias pressure on required frequency, flowrate and efficiency.

piezoelectric material is $PZN - PT$. It is important to note that the generated power is proportional to the square of stress band and therefore the bias pressure should be kept as small as possible. It can be easily shown that, for a given chamber diameter, the required frequency for the biased case and for the case where $P_{LPR} = 0$ are related by:

$$\frac{f}{f_b} = \left(\frac{\Delta P_{ch}}{\Delta P_{ch} + P_b} \right)^2 \quad (5.22)$$

where P_b is the bias pressure. It is assumed that in both cases the pressure differential in the chamber is the same. Equation 5.22 implies that if the bias pressure is much smaller than the pressure band in the chamber, its effect is negligible. However for typical MHT devices this is not the case and the effect of bias pressure should be considered.

5.1.6 Scaling Issues

One of the many advantages of MEMS devices is their ability to operate at very high frequencies. In other words, they allow operation with much larger bandwidth due to their high natural frequencies. For linear systems, the scaling law for natural frequency can be obtained by considering a very simple system consisting a cantilever beam and a proof mass attached to the tip of the beam. The stiffness corresponding to the tip deflection of the beam in response to a force applied to the tip can be obtained from beam theory:

$$k = \frac{EWH^3}{4L^3} \quad (5.23)$$

where E is the Youngs modulus, and W , H , and L are the width, the height and the length of the beam respectively. The natural frequency of this system can be calculated by:

$$\omega_n = \sqrt{\frac{k}{m}} \quad (5.24)$$

where m is the mass of the proof mass. If we define the scale factor, λ , as the ratio of the new scaled dimensions divided by the nominal, the dependence of the stiffness of the beam and the mass of the proof mass on the system scale are:

$$k \sim \lambda \quad \text{and} \quad m \sim \lambda^3 \quad (5.25)$$

where the scale dependence of the stiffness of the beam is obtained from equation 5.23.

The natural frequency of the system is then related to its size by:

$$f_n \sim \sqrt{\frac{\lambda}{\lambda^3}} = \frac{1}{\lambda} \quad (5.26)$$

which can be generalized to any linear structure.

Similarly we can obtain the scaling laws for the power generator considering the dependence of the natural frequency, required operation frequency and compliance of the system on system scale. Consider the simple chamber structure described in Section 4.1, which consists of a fluid chamber and a compliant top support structure. Here we assume that in the energy harvesting chamber the top support structure is the only compliant structure, and the piston is rigid and perfectly sealed to piston walls without tethers. The effective compliance for this case was derived in Section 4.1 as:

$$C_{eff} = \left(\frac{V_o}{\beta_f} + C_s \right) = \left(\frac{\pi D_{ch}^2 H_{ch}}{4\beta_f} + \frac{\pi D_{ch}^6 (1 - \nu^2)}{1024 E t_{top}^3} \right) \quad (5.27)$$

where D_{ch} is the chamber diameter, H_{ch} is the chamber height, and t_{top} is the thickness of the top support structure. The dependence of the effective chamber compliance on the system scale is then

$$C_{eff} \sim \lambda^3 \quad (5.28)$$

which suggests that as the system gets smaller, the compliance gets smaller. Lets consider a case where $P_{LPR} = 0$ and the effective chamber compliance is given by equation 5.27. For a certain power requirement, the required operation frequency can be calculated as:

$$f_{req} = \frac{4W}{(s_{33}^E - s_{33}^D) \sigma^2 A_p L_p} \quad (5.29)$$

where σ is the stress band on the piezoelectric element, which is equal to the maximum stress since $P_{LPR} = 0$. As discussed earlier, in a design procedure, the chamber diameter and the piezo diameter are chosen such that the maximum stress on the piezoelectric element is equal to the depolarization stress of the piezoelectric element. If we assume that for any design scenario

this condition will be satisfied, then the dependence of the required frequency on system scale can be obtained as:

$$f_{req} \sim \frac{1}{\lambda^3} \quad (5.30)$$

which suggests that as the system gets smaller, larger frequencies are required due to the reduced piezoelectric element volume. The required flowrate is given by:

$$Q = \frac{2(s_{33}^E + s_{33}^D)W}{(s_{33}^E - s_{33}^D)P_{HPR}} + C_{eff}P_{HPR}f_{req} \quad (5.31)$$

From equations 5.28 and 5.30 we can obtain the dependence of the required flowrate on the system scale as:

$$Q \sim \lambda^0 \quad (5.32)$$

which suggests that the required flowrate does not depend on the system scale. In smaller scale, although the system compliance reduces, the required frequency increases in the same amount which results in the same required flowrate. Since this results were derived for constant P_{HPR} and required power, W , the system efficiency does not depend on the system scale either, which can be expressed as:

$$\eta = \frac{W}{P_{HPR}Q} \sim \lambda^0 \quad (5.33)$$

It should be noted that this analysis relies on the assumption that the active valves can operate at very high frequencies and the valves and channels can provide the required flowrates even when the system gets very small.

Consider a design case where the operation frequency is equal to the maximum bandwidth of the device. If we make the system 10 times smaller and keep the required power and P_{HPR} the same, we will need 1000 times the frequency to generate the same power from the smaller device. However we can increase the operation frequency only 10 times since the natural frequency is inversely proportional to the system scale, which is expressed in equation 5.26. This implies that we can extract only one percent of the required power from the small device. However

we can fit 1000 small devices inside the original volume, which means that we can generate 10 times the original power from the same volume. This suggests that the power density is inversely proportional to the system scale, which can be expressed as:

$$PD \sim \frac{1}{\lambda} \quad (5.34)$$

This suggests that, as the system gets smaller, the power density increases. Again, it should be mentioned that, this analysis assumed that, in the smaller scale the valves and channels can provide the required flowrate regardless of the system scale. However, it is expected that viscous losses in the valves will begin to dominate beyond a certain scale and scaling further down will not be more efficient. In order to perform this study, more detailed fluid models are needed. Nevertheless, the above analysis provides a general understanding about the scaling of the system.

5.2 Design Procedure

This section will present a design procedure for designing the microhydraulic piezoelectric power generator. First, the design decisions made considering the issues discussed in previous sections as well as those imposed by the active valve design and fabrication process will be presented. Then, the design procedure will be described and two design examples will be presented along with simulation results.

5.2.1 Preliminary design decisions

As discussed in Chapter 3, the working fluid is chosen to be silicone oil due to its low viscosity and low density. It also has a comparable bulk modulus to that of water. Choice of piezoelectric element is done considering the results in sections 5.1.4, 5.1.4, and 5.1.4. From Figure 5-12 it can be seen that the piezoelectric material *PZT* – 5*H* has very high frequency requirements, *PZT* – 4*S*, *PZT* – 8 have lower and very similar frequency requirements, and *PZN* – *PT* has comparable frequency requirements to those of *PZT* – 4*S* and *PZT* – 8. If we examine Figures 5-13 and 5-14, we can see that *PZN* – *PT* requires much lower flowrates and provides much efficient power generation compared to other piezoelectric materials. In Chapter 2 it was

concluded that $PZN - PT$ has the smallest energy density among the piezoelectric elements considered, which is a result of its low depolarization stress. However due to its very high coupling coefficient it provides very efficient electromechanical energy conversion and requires the lowest flowrate for a given power requirement. It should be noted that, the implication of the low energy density of $PZN - PT$ is that, larger piezoelectric material volume is needed compared to other piezoelectric materials for the same power output. However, the weight of the piezoelectric element constitutes only a small fraction of the overall system weight and the increased efficiency of $PZN - PT$ due to its much higher coupling coefficient would still overwhelm the effect of increased weight in terms of the overall system power density. The chamber height is chosen to be $200\mu m$. A preliminary study has shown that chamber heights smaller than this could cause squeeze film damping effect inside the chamber and can result in undesired losses. And, larger chamber heights would increase the chamber compliance, which would decrease the efficiency of the system. The length of the piezoelectric element is chosen to be $1mm$. This parameter is basically determined considering the actuation in the active valves, since all the piezoelectric cylinders within the system, namely the ones in the active valves and the one in the energy harvesting chamber, have the same length because of the layered structure of the device, which was explained in Chapter 1. Larger lengths would decrease the stiffness of the piezoelectric elements inside the active valves, which reduces the actuation capability, and smaller lengths could cause dielectric breakdown.

5.2.2 Parameters imposed by active valve design

The basic limitation of the active valves is their bandwidth. Current active valve designs predict bandwidths in the order of $10 - 20kHz$. Typical trade-offs in the active valve design are stroke, bandwidth and force, which are detailed in [5]. Another important limitation is the pressures that the active valves can work against, which basically imposes the maximum high reservoir pressure possible. They can typically work against pressures of $2 - 3MPa$. Also the active valves impose a minimum pressure requirement due to cavitation considerations in the hydraulic amplification chamber(HAC) within the active valve structure. In the design example presented, the low pressure reservoir pressure, P_{HPR} is chosen as $0.5MPa$.

5.2.3 Parameters imposed by fabrication process

As briefly described in Chapter 1, the device consists of silicon and pyrex micromachined layers. The thickness of the layers basically dictate the thicknesses of individual components. For example, a double layer piston structure, which consist of two silicon layers bonded to each other, will have a thickness of $t_{pis} = 800\mu m$, which is the case in the design example. Since the tethers are created through deep reactive ion etching(DRIE) of a SOI wafer, the tether thickness is defined by the SOI layer. Also, the fillet radius control during the fabrication process imposes some limitations on the tether width. For example narrow tethers would be very stiff due to the relatively large fillet radius and the predictions of the linear theory used for the optimization would not valid beyond a certain tether width. The top tether thickness, t_{ttop} , is chosen to be $10\mu m$, whereas the bottom tether thickness is chosen to be thinner, namely, $5\mu m$, because the bottom tether does not have any functionality and therefore it should be kept as thin as possible so that it won't cause significant resistance to piston motion. The thicknesses of the top and bottom support structures are determined by the number of layers used, including the packaging layers on top and bottom portions of the device. As discussed in Chapter 3, the compliance of the system is very important in terms of system performance and they should be kept as small as possible. Therefore it is desirable to have very thick top and bottom support structures. The effective thickness would also depend on the structure of the auxiliary system in which the device is packaged. In the design examples, the top and bottom structures are assumed to have the same thicknesses, namely $t_{top} = t_{bot} = 2.5mm$, and they are assumed to comprise of all silicon layers.

5.2.4 Design Procedure

Figure 5-18 presents a design procedure, which will be followed after the initial design decisions are made using above considerations. The first part consists of analytical design calculations. The pressure band in the chamber is dictated by the bias pressure, P_b , and high pressure reservoir pressure, P_{HPR} . The piston diameter and piezo diameter are calculated using equations 5.11 and 5.19, and the battery voltage is calculated using equation 5.6.

These calculations are followed by the tether structure optimization, which determines the optimum tether width, w_t , for the given tether thicknesses and piston diameter. The designed

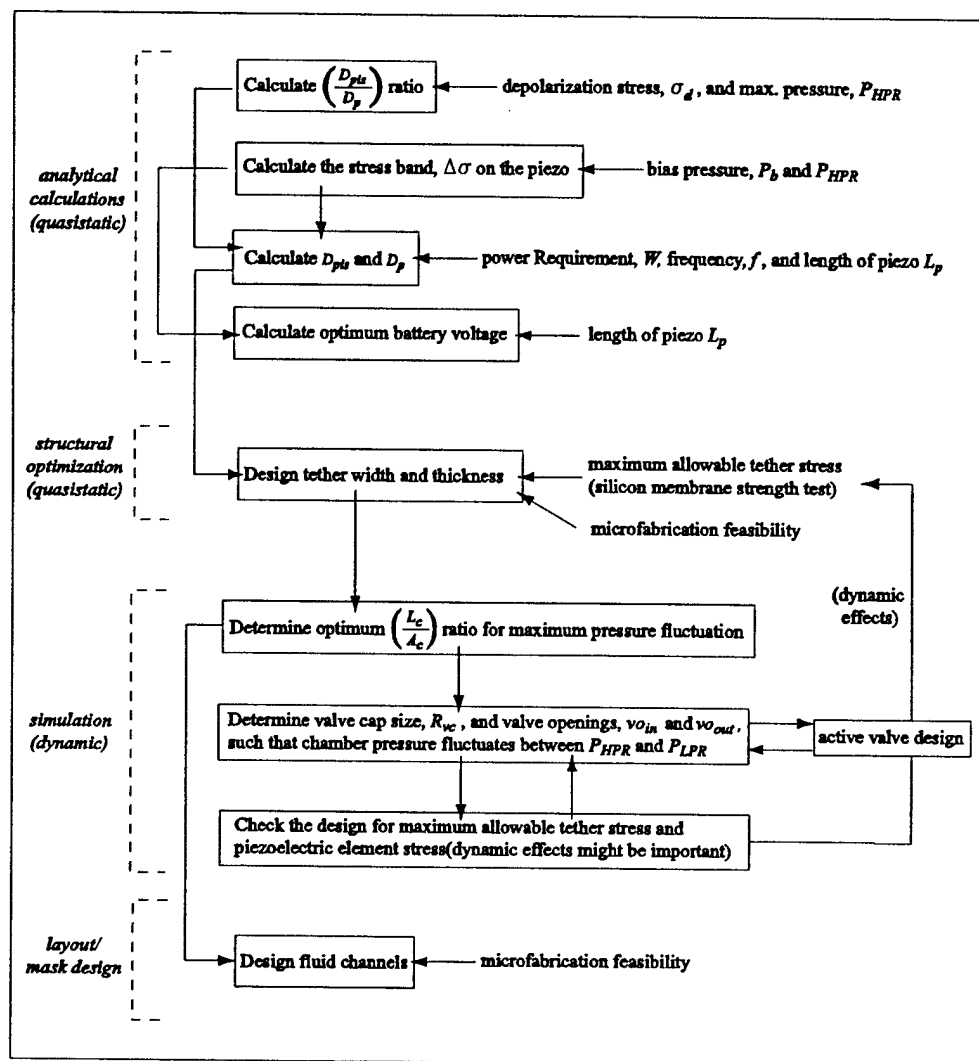


Figure 5-18: Design procedure.

tether width also determines the chamber diameter, D_{ch} . The geometric parameters along with the operation conditions are then fed to the system level simulation. The simulation architecture is shown 5-19 and the Simulink block diagrams are given in Appendix A.

First, simulations are performed to determine the optimum length to area ratio of the fluid channels, using arbitrary valve resistance, i.e. arbitrary valve cap size or valve openings. It is helpful to run these simulations with very small valve resistance, namely with very large valve opening or very large valve cap, since the fluidic oscillations are much more pronounced with lower valve resistances and it is easier to determine the optimum length to area ratio of the channels. Then, the valve cap size and valve opening are designed such that the chamber pressure fluctuates between reservoir pressures, namely between P_{HPR} and P_{LPR} . At this stage, it is important to consider structural limitations, which might be imposed by the active valves. For example, a large valve cap size requires a large membrane to allow sufficient valve motion, however this may cause excessive stresses in the membrane. Or, a very large valve opening can cause the same problem. Since the same effective valve resistance can be achieved with different combinations of valve opening and valve cap size, coupled iterations may be necessary with the active valve design procedure, which is not within the scope of this thesis. Detailed information about the active valve design procedure can be found in [5].

Finally, the system is simulated, stresses in the tethers and on the piezoelectric element are checked, and design iterations are performed if necessary. Although the valves are designed to achieve the desired pressure band in the chamber, the stress band may be a little bit different than expected. This can be explained by considering equation 5.11. This equation assumes static force balance between the piezoelectric cylinder and the piston. Also, the effect of the tether is neglected since the force exerted by the tethers on the piston is generally very small compared to the force exerted by the piezo and force due to chamber pressure. As will be seen in the design examples, the dynamics of the piston does not have a significant effect on system performance and it is reasonable to assume quasi-static force balance. However, if the operation frequency is much higher, the dynamics of the piston will be important and equation 5.11 will not be valid. The design procedure presented above is followed by the layout and mask design for the fabrication.

For the piston dynamics, a damping ratio of 5% is assumed, considering the piezoelectric

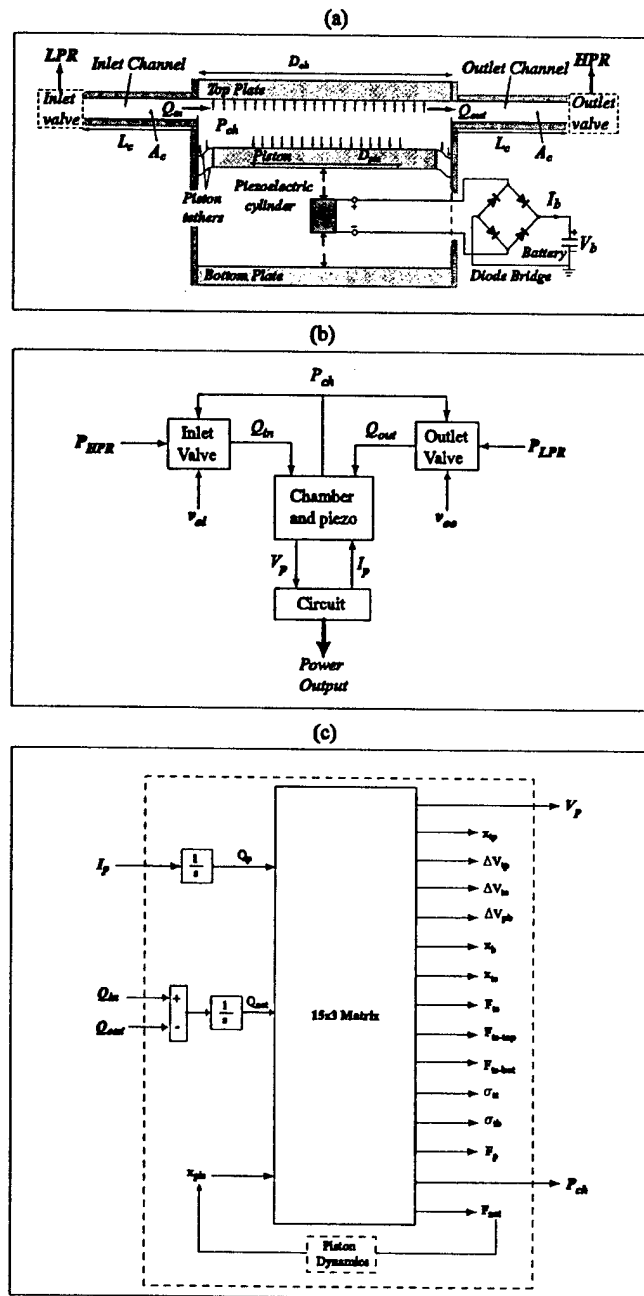


Figure 5-19: (a) System layout (b) System level simulation architecture (c) The chamber and piezo block in the overall system architecture which was developed in Chapter 4.

| | | |
|--|--------------|-----------------------------|
| Design Decisions | | |
| Piezoelectric material | PZN-PT | lowest flowrate requirement |
| Working fluid | silicone oil | low viscosity and density |
| Piezoelectric element length, L_p | 1mm | active valve actuation |
| Chamber height, H_{ch} | 200 μm | squeeze film damping |
| Parameters imposed by fabrication process | | |
| Piston thickness, t_{pis} | 800 μm | double layer piston |
| Top and bottom support structure thickness | 2.5mm | packaging layers |
| Top tether thickness, t_{tetop} | 10 μm | fabrication feasibility |
| Bottom tether thickness, t_{tebot} | 5 μm | fabrication feasibility |
| Material Limitations | | |
| Depolarization stress of piezoelectric element, σ_d | 10MPa | shouldn't be exceeded |
| Maximum allowable stress in tethers | 1GPa | shouldn't be exceeded |
| Damping | | |
| Damping ratio of piston | 5% | assumed |

Table 5.1: Summary of preliminary design decisions applied to the design examples.

element as the effective spring. Namely the damping coefficient is calculated as:

$$c = 2\zeta \sqrt{m_{pis} k_p} = 2\zeta \sqrt{m_{pis} \frac{A_p}{s_{33}^D L_p}} \quad (5.35)$$

where ζ is the damping ratio and s_{33}^D is the open circuit compliance of the piezoelectric element.

5.3 Design Examples

This section will present two design examples who have different operational requirements due to the limitations imposed by the active valves. The preliminary design decisions, parameters imposed by fabrication process and material limitations, which are valid for both examples are summarized in Table 5.1.

5.3.1 Design Example 1

The parameters imposed by the active valves, the design parameters obtained by applying the design procedure discussed in the previous section, and performance parameters are summarized in Table 5.2. Simulation results are shown in Figure 5-21, Figure 5-22 and Figure 5-23. The

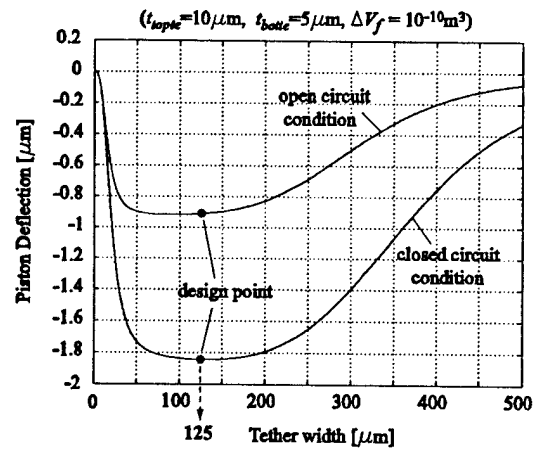


Figure 5-20: Tether structure design. Piston deflection shown for different tether widths.

tether structure optimization is shown in Figure 5-20 where the piston deflection is plotted as a function of the tether width for an added fluid volume of $\Delta V_f = 10^{-10} \text{ m}^3$.

Figure 5-22 shows simulation results for the deflections and swept volumes of individual structural components. It can be seen that, as expected, the deflection of the bottom support structure is much smaller than the piston deflection, which is desirable for maximum piezoelectric element compression. Also, it can be seen that the volume swept due to tether bending, piston deformation and top support structure deformation is much smaller than the volume swept by the piston motion, which is again desirable for maximum piezoelectric element compression.

5.3.2 Design Example 2

The parameters imposed by the active valves, design parameters and performance parameters are summarized in Table 5.3. In this example, the performance of the active valves are very limited, which results in very small power output compared to the first example. Simulation results are shown in Figure 5-24, Figure 5-25 and Figure 5-26. The observations done for the deflections and swept volumes of the individual structural members in the first design example are also valid for this example. Namely, the deflection of the bottom support structure is

| | | |
|---|---------------------|---|
| Power Requirement | 0.25W | Electrical power output |
| Parameters imposed by active valve design | | |
| Operation frequency, f | 20kHz | bandwidth of active valves |
| Bias Pressure, P_b | 0.5MPa | cavitation in HAC chamber |
| High Pressure Reservoir Pressure, P_{HPR} | 3MPa | membrane stress limitation |
| Important parameters resulting from operation conditions | | |
| Pressure band in the chamber, ΔP_{ch} | 2.5MPa | - |
| Stress band on piezoelectric element, $\Delta\sigma$ | 8.33MPa | - |
| Designed parameters | | |
| Piston Diameter, D_{pis} | 6.95mm | - |
| Piezoelectric cylinder diameter, D_p | 3.8mm | - |
| Battery voltage, V_b | 74.9V | - |
| Tether width, w_t | 125 μ m | optimization |
| Chamber diameter, D_{ch} | 7.2mm | - |
| Fluid channel length to area ratio, $\frac{L_c}{A_c}$ | 5000m ⁻¹ | same for inlet and outlet |
| Valve cap radius, R_{vc} | 400 μ m | same for inlet and outlet |
| Valve opening, vo_{in}, vo_{out} | 24 μ m | same for inlet and outlet |
| Performance parameters | | |
| Net flowrate, Q_{net} | 0.52ml/s | - |
| Hydraulic power input | 1.3W | $(P_{HPR} - P_{LPR})Q_{net}$ |
| Efficiency, η | 19.2% | $\frac{\text{Electrical power output}}{\text{Hydraulic power input}}$ |

Table 5.2: Summary of design and performance parameters of design example 1.

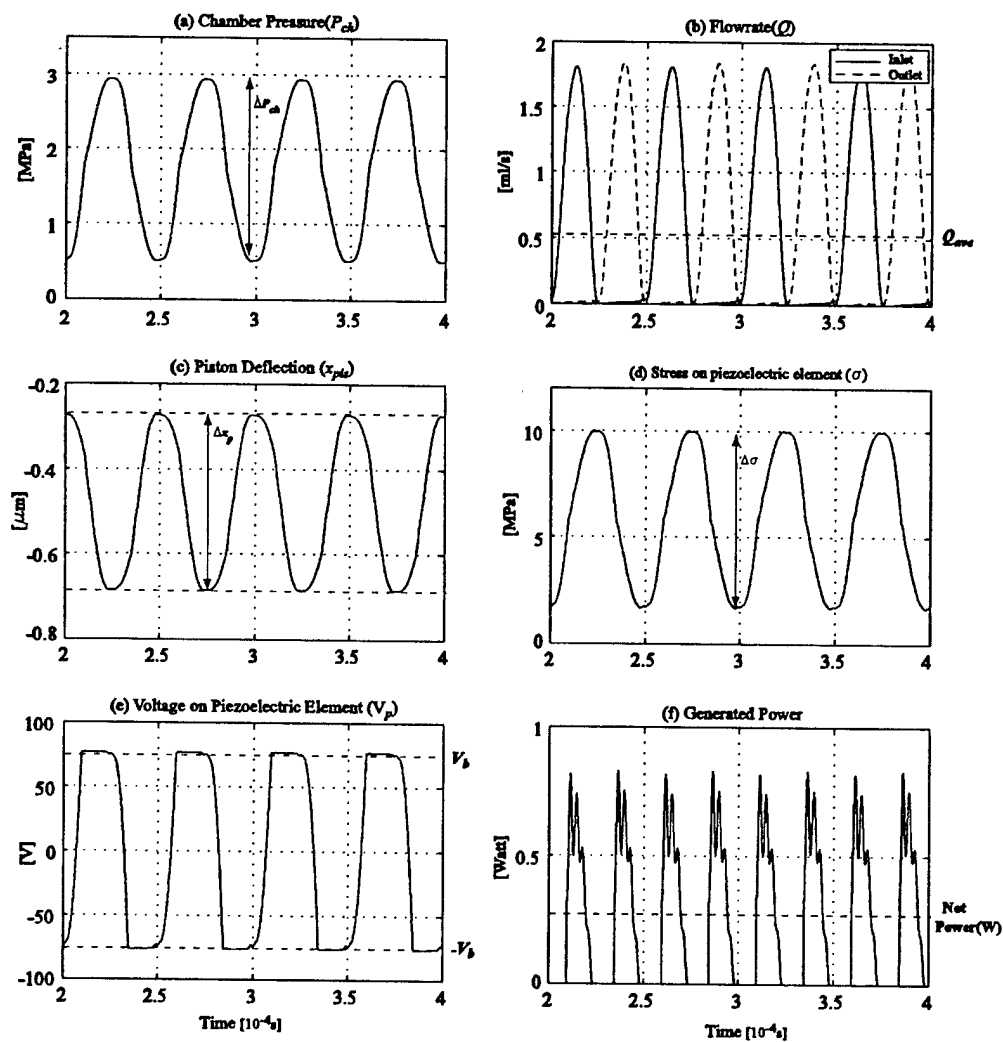


Figure 5-21: Simulation time histories of the design example 1.

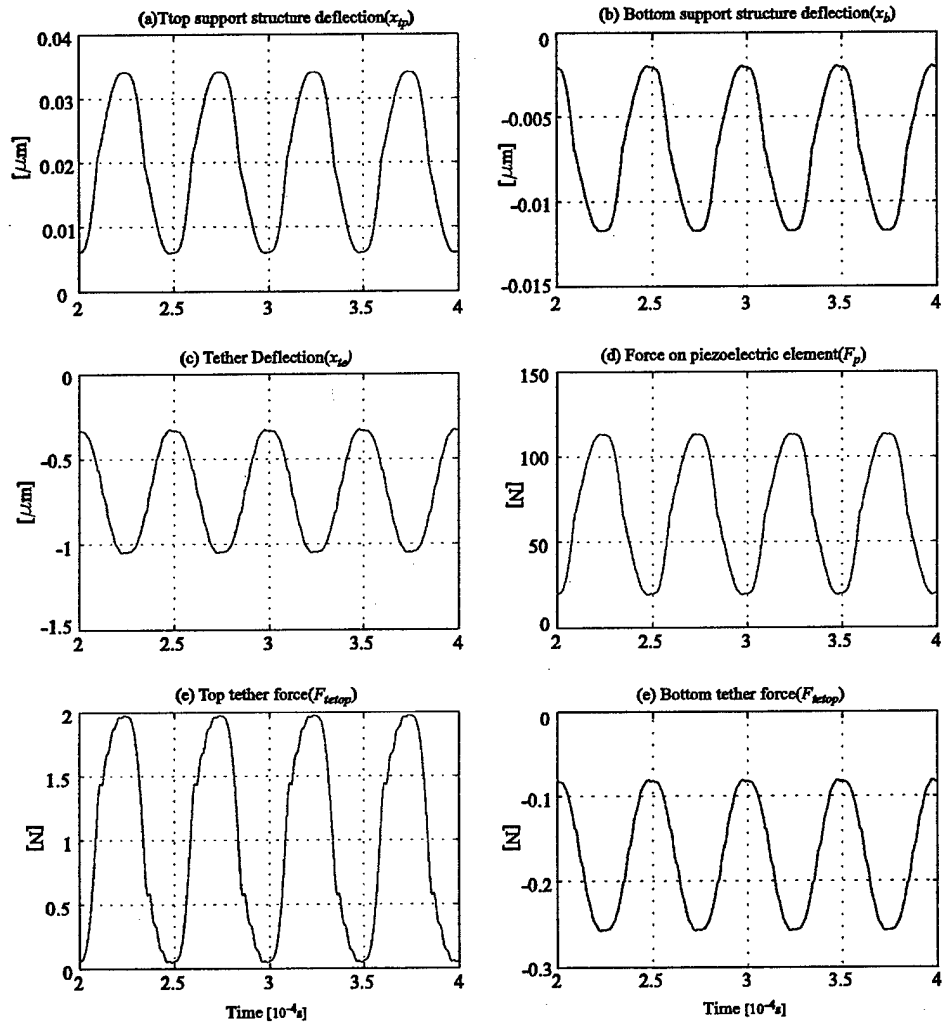


Figure 5-22: Simulation time histories of the design example 1.

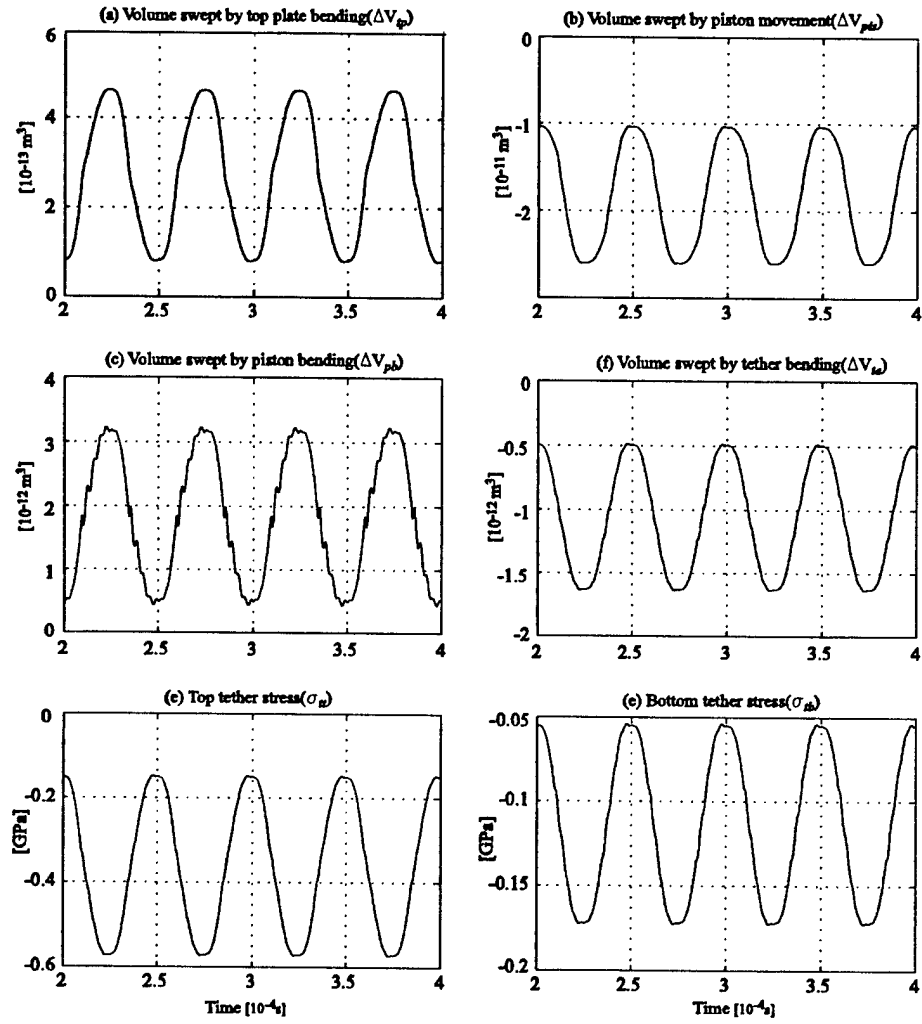


Figure 5-23: Simulation time histories of the design example 1.

| | | |
|---|-----------------------|---|
| Power Requirement | 0.01W | Electrical power output |
| Parameters imposed by active valve design | | |
| Operation frequency, f | 5kHz | bandwidth of active valves |
| Bias Pressure, P_b | 0.5MPa | cavitation in HAC chamber |
| High Pressure Reservoir Pressure, P_{HPR} | 1.5MPa | membrane stress limitation |
| Important parameters resulting from operation conditions | | |
| Pressure band in the chamber, ΔP_{ch} | 1MPa | - |
| Stress band on piezoelectric element, $\Delta \sigma$ | 6.67MPa | - |
| Designed parameters | | |
| Piston Diameter, D_{pis} | 4.89mm | - |
| Piezoelectric cylinder diameter, D_p | 1.89mm | - |
| Battery voltage, V_b | 59.9V | - |
| Tether width, w_t | 125 μm | optimization |
| Chamber diameter, D_{ch} | 5.19mm | - |
| Fluid channel length to area ratio, $\frac{L_c}{A_c}$ | 110000m ⁻¹ | same for inlet and outlet |
| Valve cap radius, R_{vc} | 150 μm | same for inlet and outlet |
| Valve opening, vo_{in}, vo_{out} | 9.3 μm | same for inlet and outlet |
| Performance parameters | | |
| Net flowrate, Q_{net} | 0.042ml/s | - |
| Hydraulic power input | 0.042W | $(P_{HPR} - P_{LPR})Q_{net}$ |
| Efficiency, η | 23.8% | $\frac{\text{Electrical power output}}{\text{Hydraulic power input}}$ |

Table 5.3: Summary of design and performance parameters of design example 2.

much smaller than the piston deflection, which is desirable for maximum piezoelectric element compression and the volume swept due to tether bending, piston deformation and top support structure deformation is much smaller than the volume swept by the piston motion, which is again desirable for maximum piezoelectric element compression.

As discussed in the previous chapters, the generated power is a strong function of the stress band on the piezoelectric element and the operation frequency. As the maximum operating frequency reduces due to active valve design limitations, much larger piezoelectric elements and chamber structures are needed to generate the same amount of power. In the second design example, in order to generate the same power as in design example 1, huge chamber diameters, larger than 20mm, is needed, which is not feasible due to the increased compliance and size constraints. As discussed earlier in Section 5.1.6, it is feasible to make smaller and multiple devices which would fit in the original volume. In section 5.1.6 it was concluded that the efficiency does not depend on system scale. As can be seen from Tables 5.2 and 5.3 the

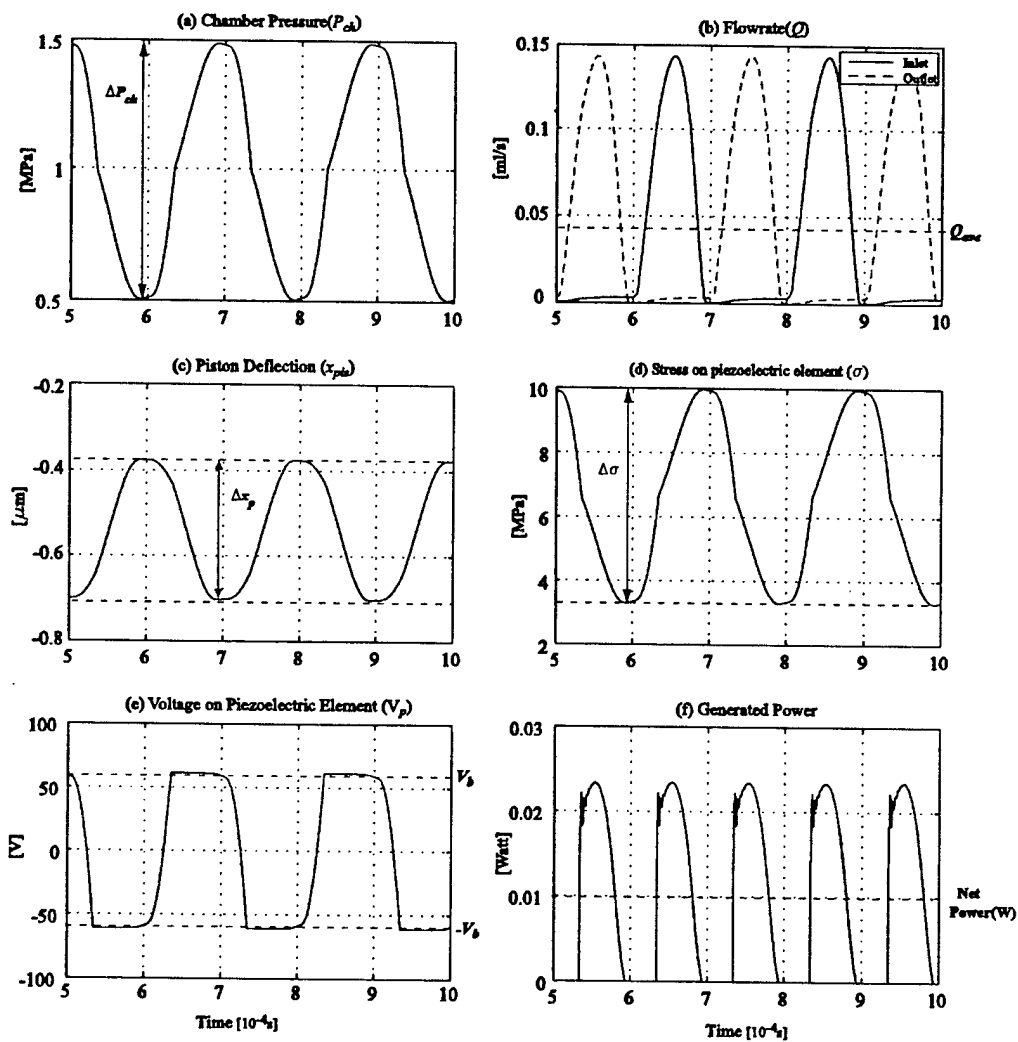


Figure 5-24: Simulation time histories of the design example 2.

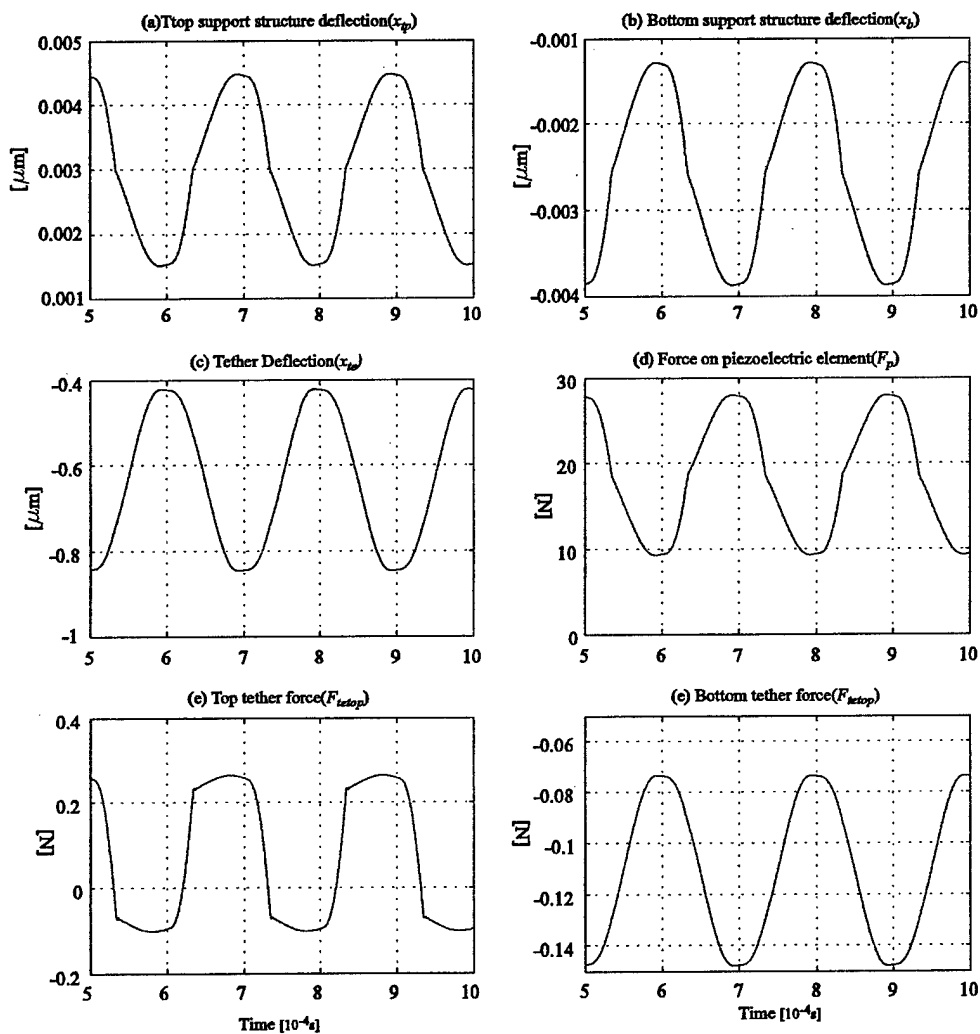


Figure 5-25: Simulation time histories of the design example 2.

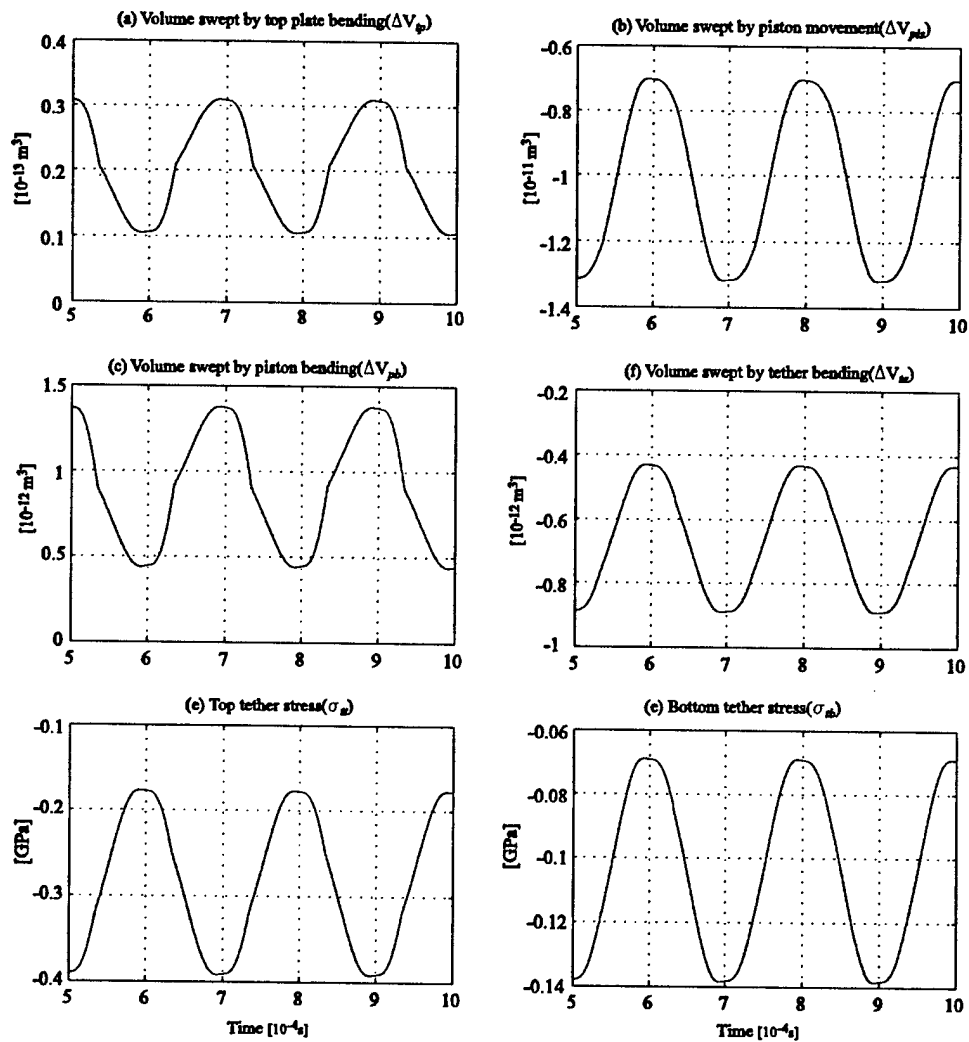


Figure 5-26: Simulation time histories of the design example 2.

second device, which is smaller than the first one, has higher efficiency. This is due to the fact that in the example, only the chamber diameter and piezo diameter are smaller. The length of the piezoelectric element, chamber height and structural thicknesses are kept constant. This resulted in a stiffer chamber compared to the case where all the dimensions were reduced. The explicit relationships and effect of geometric parameters on system scale can be seen in equation 5.27, which represents a simpler case than the actual chamber.

5.4 Summary

This chapter presented further design considerations and a design procedure along with two design examples. Fluidic oscillations within the system and conditions for sufficient chamber filling and evacuation is analyzed. An optimization procedure for the tether structure is presented. Trade-offs between operation conditions and their effect on the performance is discussed. Effect of system scale on the performance is discussed. Effect of the fabrication process and the active valves on the design is discussed.

Chapter 6

Conclusions and Recommendations for Future Work

6.1 Summary

The objectives of this thesis were:

- To develop a comprehensive system level model and simulation tool to analyze the main chamber and the associated fluid channels and valves of piezoelectric microhydraulic power generation devices
- To gain insight into system operation and understand the factors affecting the system performance
- Develop a design procedure, which should be complemented by the design of the active valves.

Chapter 1 presented the configuration, operation and motivation of microhydraulic-piezoelectric power generators. Primary challenges and preliminary design considerations is discussed.

Chapter 2 presented an analysis of piezoelectric power generation based on linear electromechanical energy conversion. Effect of circuitry and piezoelectric material on energy density and effective coupling factor is discussed. Models for two different circuit topologies are developed, simulations are performed and analytical expressions are derived for the generated power and effective coupling factor. Different piezoelectric materials are compared in terms of their energy densities and energy conversion efficiencies for different circuitry. It has been concluded

that, although the single crystal piezoelectric material(PZN-PT) has very high effective coupling factor, it has a very low energy density compared to PZT-8 or PZT-4S because of its small depolarization stress. Another important conclusion of this chapter is that, for a piezoelectric element, the energy density obtained with the diode bridge and voltage detector circuit is four times bigger than the energy density obtained with only the diode bridge. The effective coupling factor is a function of the coupling coefficient and the circuitry, whereas the energy density is a function of coupling coefficient, circuitry and the depolarization stress. Indeed, the effective coupling factor becomes an important criteria if the piezoelectric element is considered along with its surrounding system, for example the infrastructure which provides the force on the element, which is the energy harvesting chamber in the microhydraulic power generation device. It should be remembered that in the analysis presented in this chapter a prescribed force is imposed on the piezoelectric element. This issue is addressed in Chapter 3.

Chapter 3 presented a simple model of the energy harvesting chamber, simulations with the coupled circuitry and preliminary design considerations. The interaction of the energy harvesting chamber and the circuitry is discussed. The two circuits presented in Chapter 2 and different piezoelectric materials are compared in terms of the flowrate and frequency requirements for a given pressure differential and power requirement, and in terms of system efficiency. Analytical expressions are derived for the generated power, required flowrate, effective coupling factor and system efficiency. The most important conclusion of this chapter is that the performance of the energy harvesting chamber depends on

- Circuit topology
- Piezoelectric material(k_{33}, σ_d)
- Chamber compliance(C_{eff}).

It is also concluded that, as k_{33} approaches 1 and C_{eff} approaches 0, the system efficiency for the two circuits analyzed approaches 50%. This means that, even with a perfect piezoelectric material($k_{33} = 1$) and zero effective chamber compliance, which are not possible, the system efficiency cannot exceed 50%. It should be emphasized that the efficiency definition throughout the thesis corresponds only to the energy harvesting chamber. The electrical power consumption in the active valves is not considered.

Chapter 4 presented detailed modelling of the energy harvesting chamber. In Chapter 3,

an effective chamber compliance (C_{eff}) was assumed to be used in the simulation and in the following analysis. This chapter investigated the contribution of different structural components on the effective compliance of the chamber. Deformations of individual structural members are calculated using linear plate theory. It is assumed that the deflections due to bending are significantly larger than that due to shearing. A simulation architecture is presented to be included in overall system level simulation, which allows for inclusion of the elastic equations into dynamic simulation as well as monitoring important parameters.

Chapter 5 presented further design considerations in addition to the design issues discussed in Chapter 3. These were fluidic oscillations within the system, chamber filling and evacuation, tether structure optimization, effect of operation conditions on system performance and trade-offs, and scaling issues. The system is analyzed only for the case where the chamber is attached to the regular bridge. A design procedure along with two design examples is presented. The design decisions made considering the issues discussed in previous chapters as well as those imposed by the active valve design and fabrication process is discussed. Simulation results are shown. In Chapter 2 it was concluded that $PZN - PT$ has the smallest energy density among the piezoelectric elements considered, which is a result of its low depolarization stress. However due to its very high coupling coefficient it provides very efficient electromechanical energy conversion and requires lowest flowrate for a given power requirement. It should be noted that, the implication of the low energy density of $PZN - PT$ is that, larger piezoelectric material volume is needed compared to other piezoelectric materials for the same power output. However, the weight of the piezoelectric element constitutes only a small fraction of the overall system weight and the increased efficiency of $PZN - PT$ due to its much higher coupling coefficient would still overwhelm the effect of increased weight in terms of the overall system power density.

This thesis developed a framework to analyze piezoelectric microhydraulic power generators. Insight into system operation is gained and important factors affecting system performance are analyzed.

6.2 Recommendations for Future Work

Recommendations for future work in terms of modeling and design can be summarized in the following subgroups:

Piezoelectric Element

The analysis presented in this thesis is based on linear electromechanical energy conversion. More detailed analysis including nonlinear effects is required to obtain better predictions for system performance. Also, piezoelectric element coefficients only in 3-3 direction is used since the piezoelectric element is subjected to compression parallel to the polarization of the element and assuming that the element is free to expand in lateral directions, so that T_3 is the only nonzero stress component. However, this is not the case since the piezoelectric cylinder is bonded to the piston and bottom support structure. Finite element analysis is required to calculate the effective coefficients in 3-3 direction, namely effective d_{33} , s_{33}^E and s_{33}^D .

Fluid Structure Interaction

The system is analyzed for relatively low frequencies where the fluid channels were the only components whose dynamic behavior was important for system performance. At higher frequencies, the modal behavior of the piezoelectric element and the piston structure along with the fluid contained in the chamber might be important (added mass effect of the fluid). Detailed finite element models are needed to investigate the fluid structure interaction within the chamber.

Fluid model

In this thesis, a simple fluid model based on discharge coefficients taken from published data is used. These models do not provide accurate estimation of the power consumption in the valves since it is not possible to predict the force exerted on the valve cap and valve membrane by the flow. Detailed CFD analysis can provide more insight into the fluid flow in the valve. This is very important because of the complicated geometry of the valves.

Squeeze film damping

Squeeze film damping is a common problem in MEMS devices. Although not presented in this thesis, a preliminary analysis has shown that, for the chamber height used in the design, squeeze film effects are not important. However, for smaller devices, squeeze film damping can effect system performance significantly. Detailed analytical models and/or finite element studies are required to investigate this effect.

Scaling Study

As the system size gets smaller, the power density increases, however, only until a certain scale. Beyond that scale, it is expected that viscous losses in the valves will begin to dominate and scaling further down will not be more efficient. In order to perform this study, more detailed fluid models are needed as mentioned earlier.

System level analysis

This thesis concentrated on the main chamber, also called the energy harvesting chamber, of the piezoelectric microhydraulic power generators. System level simulations, including full active valve structure, should be performed to obtained better predictions about system performance and efficiency. However, it should be emphasized that, these simulations would provide realistic predictions provided that good fluid models exist, as discussed above.

Bibliography

- [1] N.W Hagood, D.C. Roberts, L. Saggere, K.S. Breuer, K.S.Chen, J.A. Carretero, H. Li, R. Mlcak, S. Pulitzer, M. A. Schmidt, S. M. Spearing, Y.H.Su. "Micro Hydraulic Transducer Technology for Actuation and Power Generation". *Proceedings of the SPIE Annual International Symposium on Smart Structures and Materials*, 7:680-688, 2000.
- [2] Seward Webb Pulitzer III, "Feasibility Assesment and Design of Micro Hydraulic Solid-State Transducers". *SM Thesis, Masssachusetts Institute of Technology*, 2001.
- [3] H.Q. Li, D.C. Roberts, J.L. Steyn, K.T. Turner, J. A. Carretero, O. Yaglioglu, Y.H. SU, L. Saggere, N.W. Hagood, S.M. Spearing, M.A. Schmidt, R. Mlcak, K.S. Breuer. "A High Frequency High Flow Rate Piezoelectrically Driven MEMS Micropump". *Solid-State Sensor and Actuator Workshop*, pp. 69-72, 2000.
- [4] J. A. Carretero. "Measurement and Modeling of the Flow Characteristics of Micro Disc Valves". *SM Thesis, Masssachusetts Institute of Technology*, 2001.
- [5] D. C Roberts, O. Yaglioglu, J. Carretero, Y.H Su, L. Saggere, N.W. Hagood. " Modeling, Design, and Simulation of a Piezoelectrically Driven Microvalve for High Pressure, High Frequency Applications, SPIE Proceedings, 4327:366-380, 2001
- [6] D. C. Roberts. "Design, Modeling, Fabrication, and Testing of a Piezoelectric Microvalve for High Pressure, High Frequency Hydraulic Applications". *PhD Thesis, Masssachusetts Institute of Technology*, 2002.

- [7] K. Turner, " An Evaluation of Critical Issues for Microhydraulic Transducers: Silicon Wafer Bonding, Strength of Silicon on Insulator Membranes and Gold-Tin Solder Bonding" , *SM Thesis, Massachusetts Institute of Technology*, 2001.
- [8] D.A. Berlincourt. "Piezoelectric and Ferroelectric Energy Conversion" .*IEEE Transactions on Sonics and Ultrasonics*, S-15(2):89-97,1968.
- [9] M. Umeda, K.Nakamura, S. Ueha. " Analysis of the Transformation of Mechanical Impact Energy to Electric Energy Using Piezoelectric Vibrator" .*Jpn. Journal of Applied Physics*, 35:3267-3273, 1996.
- [10] M. Umeda, K.Nakamura, S. Ueha. "Energy Storage Characteristics of a Piezo-Generator using Impact Induced Vibration " .*Jpn. Journal of Applied Physics*, 36:3146-3151, 1997.
- [11] C. N. Xu, M. Akiyama, K. Nonaka, T. Watanabe. " Electrical Power Generation Characteristics of PZT Piezoelectric Ceramics" . *IEEE Transactions on Ultrasonics, Ferroelectrics, and Frequency Control*, 45(4):1065-1070, 1998.
- [12] M. Goldfarb, L. D. Jones."On the Efficiency of Electric Power Generation With Piezoelectric Ceramic". *Journal of Dynamic Systems, Measurement, and Control*, Transactions of ASME, 121:566-571, 1999
- [13] P. G. Jones, S. P. Beeby, E. P. James, N. M. White."The Modelling of a Piezoelectric Vibration Powered Generator for Microsystems. In *Transducers '01*, 2001
- [14] D. J. Warkentin, N. W. Hagood. "Nonlinear Piezoelectric Shunting for Structural Damping". *Proceedings of SPIE*, 3041:747-757, 1997.
- [15] N. W. Hagood, A. von Flotow. " Damping of Structural Vibrations with Piezoelectric Materials and Passive Electrical Networks". *Journal of Sound and Vibration*, 146(2):243-268, 1991.
- [16] N. W. Hagood, W. H. Chung, A. von Flotow. " Modelling of Piezoelectric Actuator Dynamics for Active Structural Control". *Journal of Intelligent Material Systems and Structures*, 1(3):327-354, 1990.

- [17] W. P. Mason. "An Electromechanical Representation of a Piezoelectric Crystal Used as a Transducer". *Proceedings of the Institute of Radio Engineers*, 23(10):1252-1263, 1935.
- [18] IEEE Std 176-1987 IEEE Standard on Piezoelectricity, The Institute of Electrical and Electronics Engineers. 1987
- [19] Ching-Yu Lin. "Material Characterization and Modeling for Piezoelectric Actuation and Power Generation under High Electromechanical Loading". *PhD Thesis, Massachusetts Institute of Technology*, 2002
- [20] J. M. Hall, W. E. Dillon, W. C. Nunnally. "Thermo-Acoustic-Piezoelectric Power Generation". Proceedings of the 26th Intersociety Energy Conversion Engineering Conference-IECEC'91, 2001.
- [21] V. H. Schmidt. "Piezoelectric Energy Conversion in Windmills". Proceedings of IEEE: Ultrasonic Symposium, 2:897-904, 1992.
- [22] V. H. Schmidt. "Piezoelectric Wind Generator". *United States Patent #4,536,674*. August 20, 1985.
- [23] S. Nagao. "Electronic Wristwatch With Generator". *United States Patent #5,939,707*. Assignee: Seiko Epson Corporation, July 3, 1990.
- [24] O. Takahashi, Y. Hashimoto, E. Nagasaka, H. Miyazaki, T. Funasaka. "Piezoelectric Power Generator For a Portable Power Supply Unit and Portable Electronic Device Equipped With Same ". *United States Patent #5,751,091*. Assignee: Seiko Epson Corporation, May 12, 1998.
- [25] Y. Hashimoto, O. Takahashi, H. Miyazaki, T. Funasaka, M. Furahata. "Power Generation Method and Power Generator Using a Piezoelectric Element and Electronic Device Using The Power ". *United States Patent #5,835,996*. Assignee: Seiko Epson Corporation, November 10, 1998.
- [26] P. Smalser. "Power Transfer of Piezoelectric Generated Energy". *United States Patent #5,703,474*. Assignee: Ocean Power Technologies Inc., December 30, 1997.

- [27] G. W. Taylor, J. R. Burns. "Power Generation From Waves Near the Surface of Bodies of Water". *United States Patent #4,404,490*. September 13, 1983.
- [28] J. R. Burns. "Ocean Wave Energy Conversion Using Piezoelectric Material Members". *United States Patent #4,685,296*. August 11, 1987.
- [29] M. Y. Epstein, C. B. Carroll. "Piezoelectric Electric Energy Generator". *United States Patent #5,512,795*. Assignee: Ocean Power Technologies, Inc., April 30, 1996.
- [30] M. Y. Epstein. "Piezoelectric Generation of Electrical Power From Surface Waves on Bodies of Water Using Suspended Weighted Members". *United States Patent #5,578,889*. Assignee: Ocean Power Technologies, Inc., November 26, 1996.
- [31] M. Y. Epstein, G. W. Taylor. "Water Craft Using Piezoelectric Materials". *United States Patent #5,621,264*. Assignee: Ocean Power Technologies, Inc., April 15, 1997.
- [32] C. B. Carroll. "Frequency Multiplying Piezoelectric Generators". *United States Patent #5,814,921*. Assignee: Ocean Power Technologies, Inc., September 29, 1998.
- [33] J. R. Burns. "DC Bias Scheme For Field Induced Piezoelectric Power Generators". *United States Patent #6,201,336*. Assignee: Ocean Power Technologies, Inc., March 13, 2001.
- [34] E. A. Kolm, H. H. Kolm. "Piezoelectric Fluid-Electric Generator". *United States Patent #4,387,318*. Assignee: Piezo Electric Products, Inc., June 7, 1983.
- [35] H. H. Kolm, E. A. Kolm. "Piezoelectric Acousto-Electric Generator". *United States Patent #4,467,236*. Assignee: Piezo Electric Products, Inc., August 21, 1984.
- [36] P. A. Todd, B. R. Walker. "Piezoelectric Circuit". *United States Patent #5,065,067*. November 12, 1991.
- [37] M. Kimura. "Piezo-Electricity Generation Device". *United States Patent #5,801,475*. Assignee: Seiki Company, Ltd., September 1, 1998.
- [38] S. Yamashita. "Portable Piezoelectric Electric Generation Device". *United States Patent #4,091,302*. May 23, 1978.

- [39] C. G. Triplett. "Vehicular Mounted Piezoelectric Generator". *United States Patent* #4,504,761. March 12, 1985.
- [40] E. Dieulesaint, D. Royer, D. Mazerolle, P. Nowak. "Piezoelectric Transformers". *Electronic Letters*, 24(7):444-445, 1998.
- [41] G. Ivensky, I. Zafrany, S. B. Yaakov. "Generic Operational Characteristics of Piezoelectric Transformers". *Proceedings of IEEE: Power Electronics Specialists Conference*, 3:1657-1662, 2000.
- [42] S. H. Lee, J. Hong, J.H. Yoo, G. S. Gong. "Characteristics of Piezoelectric Transformer for Power Supply". *Proceedings of IEEE: Ultrasonics Symposium*, 1:971-975, 1998.
- [43] J. Navas, T. Bove, J.A. Cobos, F. Nuno, K. Brebol. "Miniaturised Battery Charger Using Piezoelectric Transformers". *Proceedings of IEEE: Applied Power Electronics Conference and Exposition*, 1:492-496, 2001.
- [44] A. M. Flynn, S. R. Senders. "Fundamental Limits on Energy Transfer and Circuit Considerations for Piezoelectric Transformers". *Proceedings of Power Electronic Specialists Conference, IEEE Transactions*, 2:1463-1471, 1998.
- [45] S. E. Park, V. Vedula, M. J. Pan, W. S. Hackenbauer, P. Pertsch, T. Shrout. "Relaxor Based Ferroelectric Single Crystals For Electromechanical Actuators". *Proceedings of the SPIE*, 3324:136-144, 1998.
- [46] Q. M. Zhang, J. Zhao, K. Uchino, J. Zheng. "Change of the Weak-Field Properties of $PB(ZrTi)O_3$ Piezoceramics With Compressive Uniaxial Stresses and Its Links to the Effect of Dopants on the Stability of the Polarizations in the Materials". *J. Mater. Res.*, 12(1):226-234, 1997.
- [47] V. D. Kugel, Q. M. Zhang, B. Xu, Q. M. Wang, S. Chandran, L.E. Cross. "Behavior of Piezoelectric Actuators under High Electric Field". *Proceedings of the Tenth IEEE International Symposium on Applications of Ferroelectrics*, 2:655-658, 1996.

- [48] J. Zhao, Q. M. Zhang. "Effect of Mechanical Stress on the Electromechanical Performance of PZT and PMN-PT Ceramics". *Proceedings of the Tenth IEEE International Symposium on Applications of Ferroelectrics*, 2:971-974, 1996.
- [49] G. Yang, W. Ren, S.F. Liu, A. J. Masys, B. K. Mukherjee. "Effects of Uniaxial Stress and DC Bias Field on the Piezoelectric, Dielectric, and Elastic Properties of Piezoelectric Ceramics". *Proceedings of IEEE: Ultrasonics Symposium*, 2:1005-1008 , 2000.
- [50] S. Timoshenko. "Theory of Plates and Shells". McGraw-Hill, NewYork, NY, 1940.
- [51] I.E. Idelchik. "Handbook of Hydraulic Resistance", FL, 1994
- [52] Y.H. Su. Personal communication. *Massachusetts Institute of Technology*, 2000
- [53] V. Caliskan. Personal communication. *Massachusetts Institute of Technology*, 2001

Appendix A

Simulink Block Diagrams

This section presents the simulink models used in this thesis. Figure A-1 shows the model of the piezoelectric element model used in Chapter 2 in order to simulate the case of applied force. Later in the thesis, namely in Chapter 4 and Chapter 5, the piezoelectric element constitutive equations are solved along with the elastic equations of the structural members of the main chamber and incorporated into the simulation architecture with a 15x3 matrix, as described in Chapter 4. Figures A-2 and A-3 present the simulink models of the regular diode bridge and the diode bridge attached to the voltage detector, respectively, used throughout the thesis. Figure A-4 presents the simulink blocks used to implement the function of the voltage detection circuit. Figure A-5 shows the simulink architecture of the full system including the main chamber, fluid models and circuitry, used in Chapter 5. Simulations in Chapter 3 are performed with a similar model. Figures A-6, A-7 and A-8 present the simulink models for the main chamber presented in Chapter 4 and the fluid models presented in Chapter 3. The circuit model used for the simulations in Chapter 5, where the system is simulated only with regular diode bridge, is the same as in Figure A-2.

Implementation of the voltage detector circuit and silicon controlled rectifier The operation of the voltage detection circuit was described in Chapter 2. The function of the voltage detector is implemented as follows: The voltage detector block in the Simulink model sends a signal to the switch/resistor block which is either 1 or zero depending on the detected voltage, V_2 . The logic is as follows:

$$\begin{aligned}
&\text{If } \frac{dV_2}{dt} < 0 \text{ and } V_2 > 0 \quad \text{signal}=1 \text{ (switch on)} \\
&\text{If } \frac{dV_2}{dt} > 0 \text{ and } V_2 > 0 \quad \text{signal}=0 \text{ (switch off)} \\
&\text{If } \frac{dV_2}{dt} < 0 \text{ and } V_2 < 0 \quad \text{signal}=0 \text{ (switch off)} \\
&\text{If } \frac{dV_2}{dt} > 0 \text{ and } V_2 < 0 \quad \text{signal}=0 \text{ (switch off)}
\end{aligned}$$

The switch function is implemented with a resistor in the place of the SCR, whose value depends on the signal. If the signal value is 1, the value of the resistor is very small and the switch is in "on" state. If the signal value is 0, the value of the resistor is very large and the switch is in "off" state. The following parameter values are used:

Large resistance: 10^6 Ohm , small resistance: 10^{-6} Ohm , capacitance value: 10^{-7} F , inductor value: 20 mH , $m = 5$, $K = 10^7$, $\omega = 5 \times 10^{12}$.

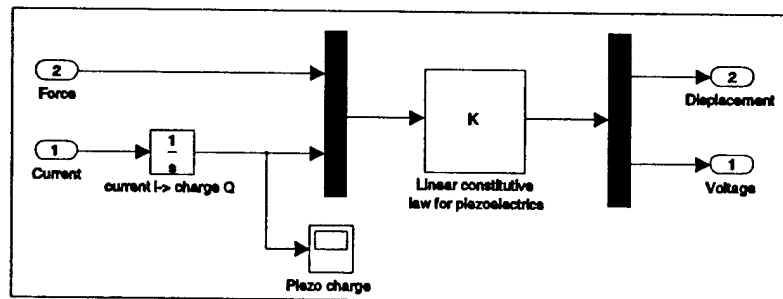


Figure A-1: Simulink model of the piezoelectric element.

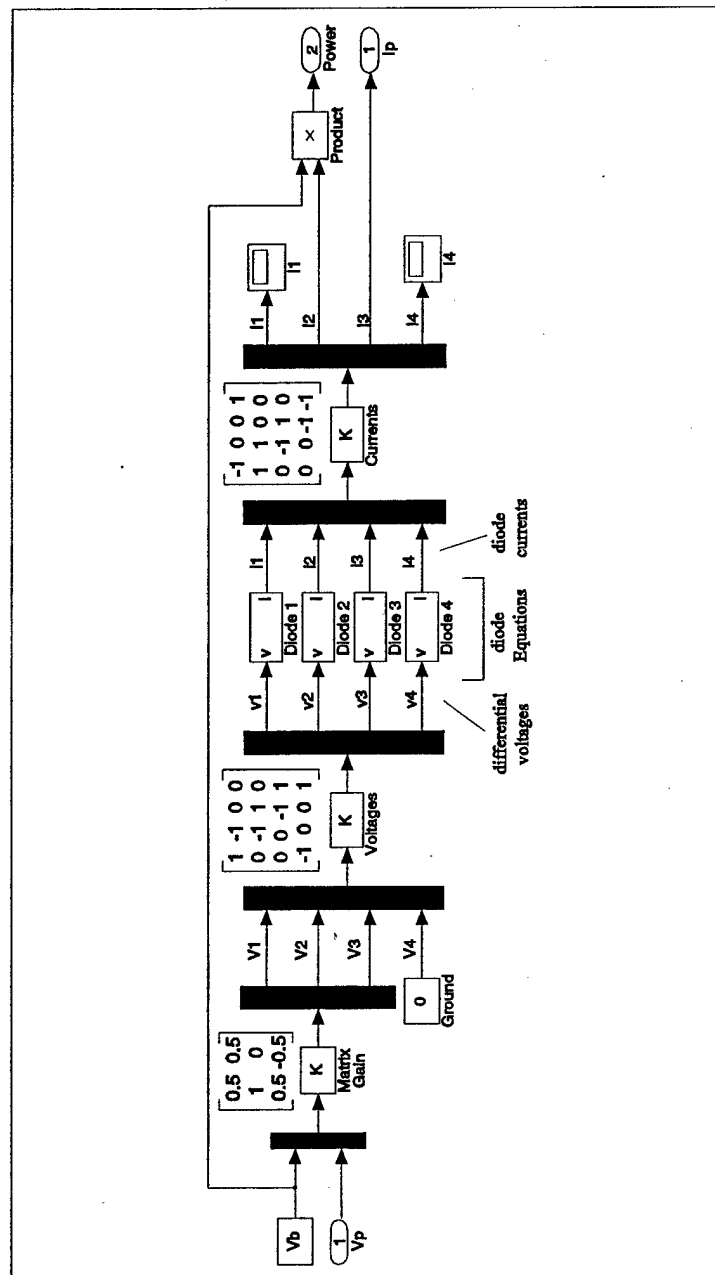


Figure A-2: Simulink model of the diode bridge.

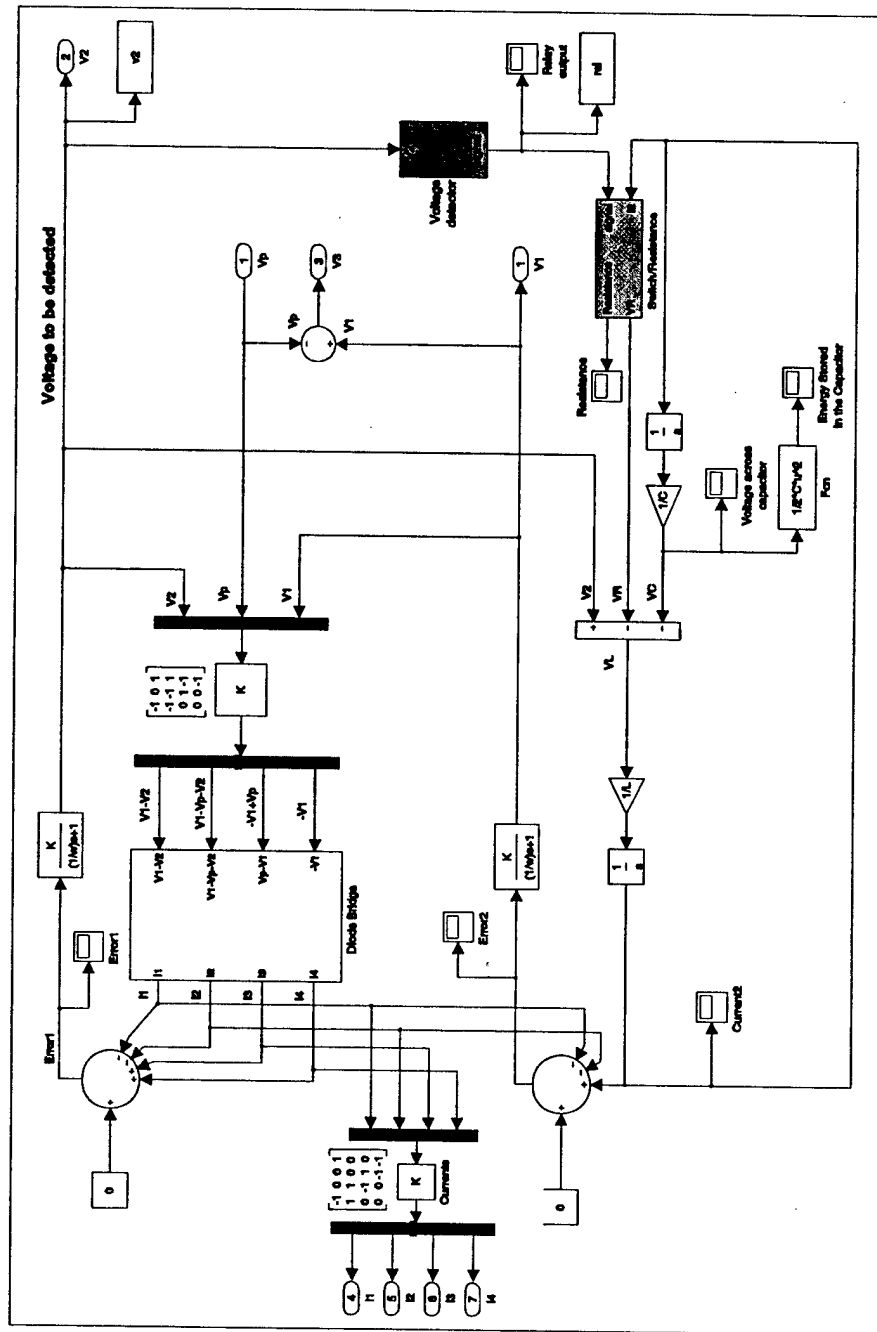


Figure A-3: Simulink model of the diode bridge attached to an inductor, voltage detector and SCR(Silicon Controlled Rectifier).

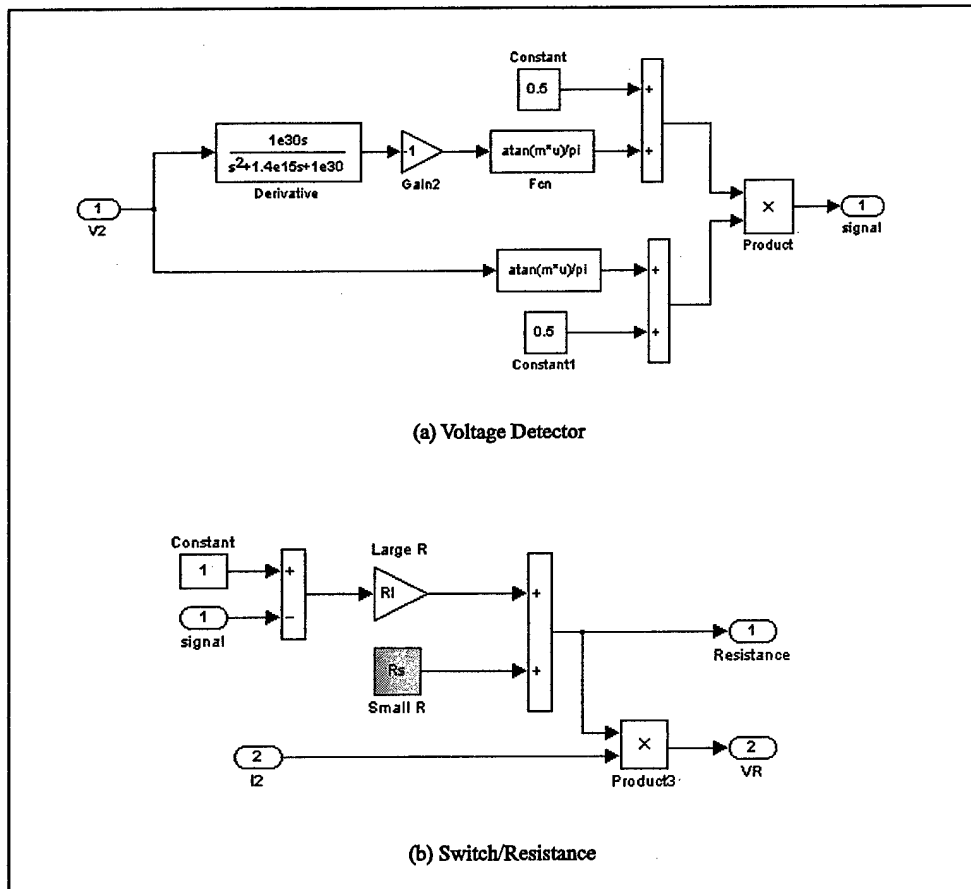


Figure A-4: Implementation of the voltage detector circuit.

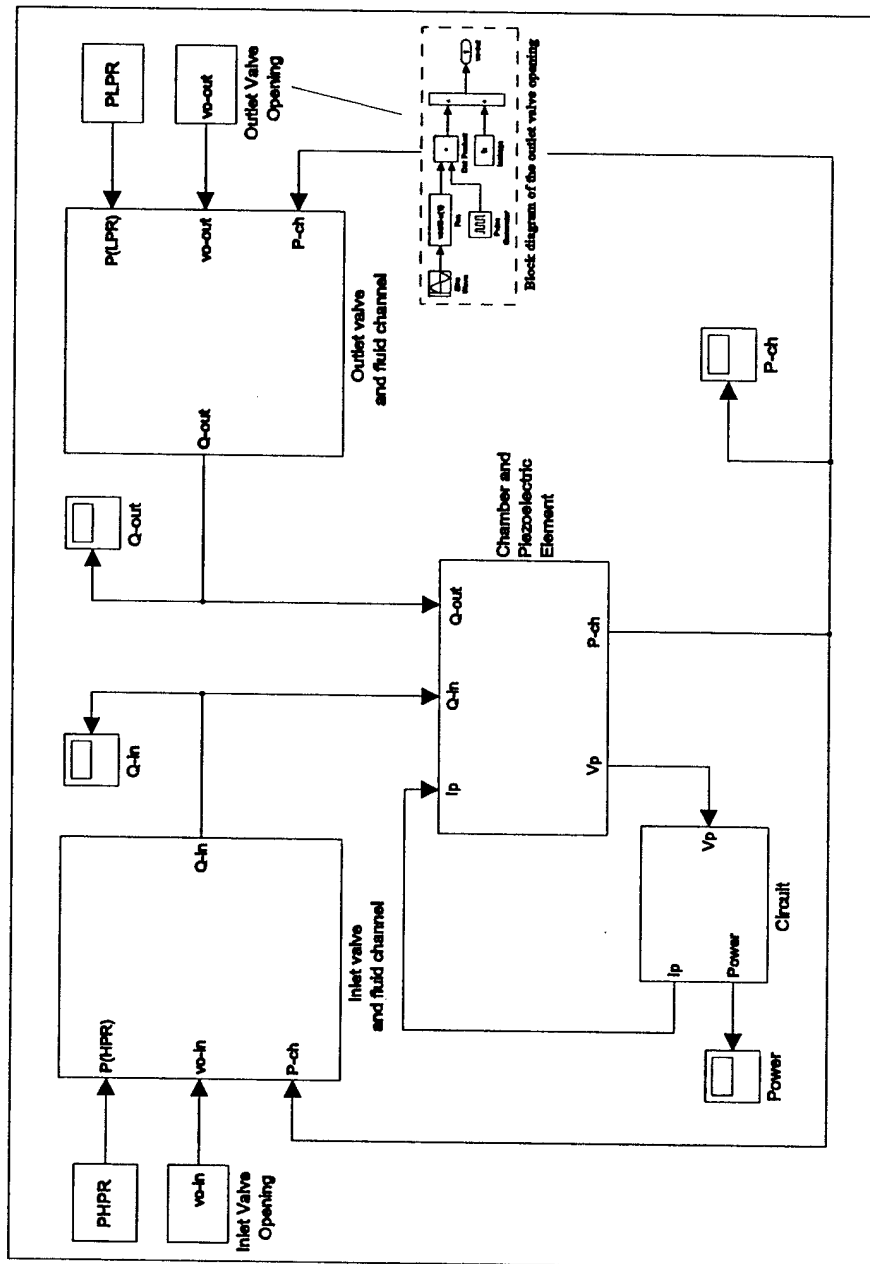


Figure A-5: Simulink model of the full system including the chamber, piezoelectric element, fluid models and circuitry.

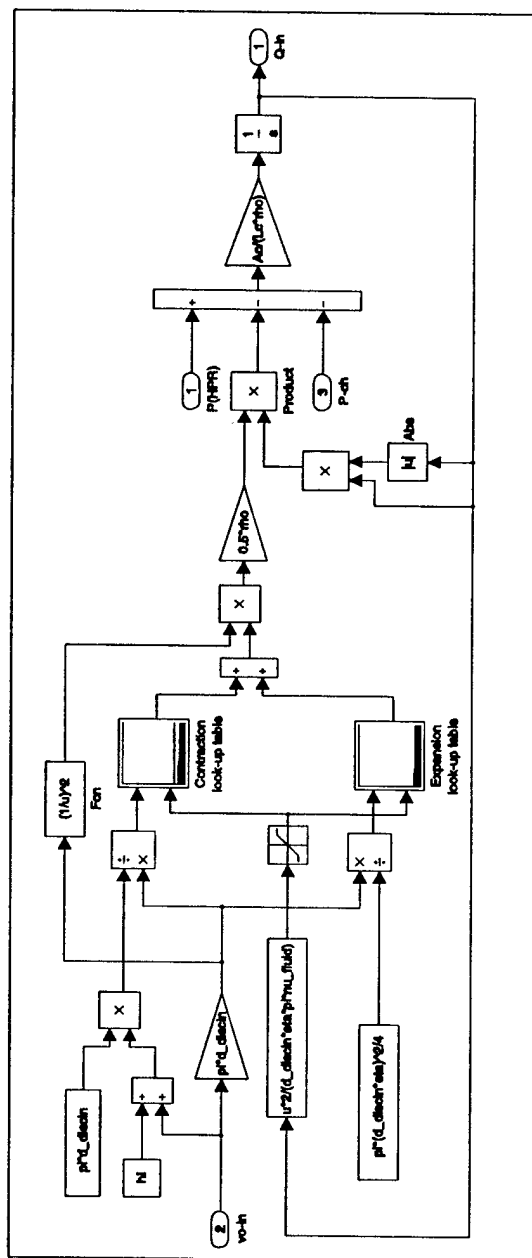


Figure A-7: Simulink model of the inlet valve and fluid channel.

Appendix B

Matlab Files

This section presents important Matlab codes used in the thesis.

Figure B-1 presents the code used in Chapter 3 to calculate the required frequency, flowrate and efficiency for different circuitry.

Figure B-2 presents the code used to calculate the required frequency, flowrate and efficiency of the system attached to regular diode bridge for different reservoir pressures and chamber diameters in Chapter 5.

Figure B-3 presents the Matlab code used in Chapter 5 for tether optimization. The elastic equations and equations governing the chamber behavior are solved in Maple, which is presented in Appendix C.

Figure B-4 presents the Matlab code used in Chapter 5 which writes the operational and some of the geometric parameters into the Matlab workspace, which can be read by the Simulink model for the system level simulation. Also, the 15x3 matrix required by the Simulink model (Appendix A) is generated, whose coefficients are calculated by Maple, which is presented in Appendix C.

```

% This code calculates the required frequency, flowrate and efficiency for two different circuitries.
% Effect of tethers is neglected and perfect sealing between the piston and the chamber walls is assumed.

clear all;

% Piezo properties (PZM-6.04PT)
a33R = 81e-12 ; % Closed circuit compliance
a33D = 17e-12 ; % Open circuit compliance
sd = 1e6 ; % Depolarisation stress
PMPR = 2e4 ; % High pressure reservoir
W = 0.5 ; % Power requirement

% Dimensions
Dpis = (4.5e-3) ; % Piston diameter (=chamber diameter since the effect of tethers is neglected)
Aps = (Dpis^2)*pi/4 ; % Piston area
Ap = Aps*PMPR/sd ; % Piezo area
Dp = sqrt(4*Ap/pi) ; % Piezo diameter
Lp = (1e-3) ; % Piezo length
Vp = Ap*Lp ; % Piezo volume

% Chamber stiffness
Keff = [1e15, 2e15, 3e15, 4e15, 5e15, 6e15, 7e15, 8e15, 9e15, 1e16, 2e16, 3e16, 4e16, 5e16, ...
        6e16, 7e16, 8e16, 9e16, 1e17, 2e17, 3e17, 4e17, 5e17, 6e17, 7e17, 8e17, 9e17, 1e18, 2e18, ...
        3e18, 4e18, 5e18, 6e18, 7e18, 8e18, 9e18, 1e19, 2e19, 3e19, 4e19, 5e19, 6e19, 7e19, 8e19, 9e19, 1e20];

% RECTIFIER
% Energy stored per cycle
Ee = ((a33R+a33D).*(sd).^2.*Vp)/4;

% Required frequency [kHz]
fr = W/Ee./1000;

% Required flowrate [ml/s]
Qr = (2.*(a33R+a33D).*W./((a33R+a33D).*(PMPR)+(PMPR.*fr.*1000./Keff)).*1e6 ;

% Efficiency
Royer = (W./((Qr.*1e-6).*(PMPR))).*100;

% RECTIFIER-VOLTAGE DETECTOR
% Energy stored per cycle
Ee = (-a33D.*sd.^2.*Lp.*Ap.*(a33R.*Lp.*Keff.*Apis.^2.*Ap).*(a33D.*Lp.*Keff.*Apis.^2.*Ap)/...
      (Ap.*3.*a33R.*Lp.*Keff.*Apis.^2.*a33D.*Lp.*Keff.*Apis.^2).^2);

% Required frequency [kHz]
fr = W/Ee./1000 ;

% Required flowrate [ml/s]
Qe = (W.*(PMPR.^2.*a33R.*Lp.*Keff.*sd.^2.*Ap.*a33D.*Lp.*Keff.*sd.^2.*Ap).*...
      (3.*a33R.*Lp.*Keff.*sd.^2.*Ap.*PMPR.^2.*a33R.*Lp.*Keff.^2.*sd.^4.*Ap.^2.*a33D.*PMPR.^4.*PMPR.^2.*a33D.*Lp.*Keff.*sd.^2.*Ap)/...
      (PMPR.*(a33R.*Lp.*Keff.*sd.^2.*Ap.*PMPR.^2).*(-a33D.*a33R).*Ap.*sd.^2.*Lp.*(PMPR.^2.*a33D.*Lp.*Keff.*sd.^2.*Ap).*Keff)).*1e6;

% Efficiency
Royer = ((a33R.*Lp.*Keff.*sd.^2.*Ap.*PMPR.^2).*(-a33D.*a33R).*Ap.*sd.^2.*Lp.*(PMPR.^2.*a33D.*Lp.*Keff.*sd.^2.*Ap).*Keff./...
      ((PMPR.^2.*a33R.*Lp.*Keff.*sd.^2.*Ap.*a33D.*Lp.*Keff.*sd.^2.*Ap).*...
      (3.*a33R.*Lp.*Keff.*sd.^2.*Ap.*PMPR.^2.*a33R.*Lp.*Keff.^2.*sd.^4.*Ap.^2.*a33D.*PMPR.^4.*PMPR.^2.*a33D.*Lp.*Keff.*sd.^2.*Ap)))*100;

Ceff=1./Keff; % Effective compliance

figure(1)
h=semilog(Ceff,Qr,'b--',Ceff,Qe,'r-');
set(h,'LineWidth',2)
title('Study9')
xlabel('Ceff[m^3/Pa]')
ylabel('Flowrate[ml/s]')
legend('Rectifier','Rectifier-Voltage Detector')
grid on
axis([1e-20 1e-18 0 10])

figure(2)
h=semilog(Ceff,fr,'b--',Ceff,fr,'r-');
set(h,'LineWidth',2)
xlabel('Ceff[m^3/Pa]')
ylabel('Frequency[kHz]')
grid on

figure(3)
h=semilog(Ceff,Royer,'b--',Ceff,Royer,'r-');
set(h,'LineWidth',2)
xlabel('Ceff[m^3/Pa]')
ylabel('System Efficiency[ml/s]')
legend('Rectifier','Rectifier-Voltage Detector')
grid on

```

Figure B-1: Matlab code used in Chapter 3 to calculate the required frequency, flowrate and efficiency for different circuitry.

```

% This code calculates the required frequency, flowrate and efficiency of
% the system for different reservoir pressures and chamber diameters

clear all;

% Power requirement
W = 0.5 ; % Power requirement

% Piezo properties(PZM-27)
s33E = 81e-12 ; % Closed circuit compliance
s33D = 17e-12 ; % Open circuit compliance
s4 = 10e6; % Depolarization stress

% Silicon material properties
v = 0.22; % Poissons ratio
E = 145e9 ; % Youngs modulus

% Silicon oil bulk modulus
Bf = 2e9 ; % Fluid bulk modulus

% Operation condition: varying PMPR
for PMPR = 1e6:1e6:4e6;

% Geometric dimensions
n = 1:0.1:10;
Dch = 1e-3*n ; % Chamber diameter

Hch = 20e-6 ; % Chamber height
Ach = (Dch.^2)*pi/4; % Chamber area
Ap = Ach.*PMPR./s4; % Piezo area
lp = 1e-3 ; % Piezo length
tp = 1e-3 ; % Top plate thickness

% Calculation of compliances
Cs = (16.*E.*tp.^3)/(pi.*(1-v.^2).*(Dch./2).^4).^-1; % Top plate compliance
Cf = (Bf./(Ach.*Hch)).^-1 ; % Fluidic compliance
Ceff = Cs+Cf; % Effective compliance

% Calculation of required frequency, flowrate and efficiency
f = 4.*W./((s33E-s33D).*s4.^2.*lp.*Ap); % Required frequency
Q = 2.*(s33E+s33D).*W./((s33E-s33D).*PMPR)+Ceff.*PMPR.*f; % Required flowrate
Hff = W./(Q.*PMPR); % Efficiency

% Plotting results
figure(1)
grid
plot(Dch/1e-3,f/1e3)
title('Required frequency vs. piston diameter')
xlabel('Dp[mm]')
ylabel('f[kHz]')
hold on

figure(2)
grid
plot(Dch/1e-3,Q/1e-6)
title('Required flowrate vs. piston diameter')
xlabel('Dp[mm]')
ylabel('Q[ml/s]')
hold on

figure(3)
grid
plot(Dch/1e-3,Hff*100)
title('Efficiency vs. piston diameter')
xlabel('Dp[mm]')
ylabel('Hff[%]')
hold on

end

```

Figure B-2: Matlab code used in Chapter 5 to calculate the required frequency, flowrate and efficiency of the system attached to regular diode bridge for different reservoir pressures and chamber diameters.

```

% Matlab code used in tether structure optimization (Double layer piston)
% The expressions for kxf, kxp, kvf, kvp, xpt, P, Ppt and Ceff are obtained using Maple.

clear all;

dVf = 1e-16; % Input flow volume into the chamber

Dch = 7.2e-3; % Chamber diameter
Dp = 3.6e-3; % Pieno diameter
Lp = 1e-3; % Pieno length
Ap = Dp^2*pi/4; % Pieno area
Hch = 200e-6; % Chamber height

E = 165e9; % Youngs modulus
nu = 0.22; % Poisson ratio
Bf = 2e9; % Bulk modulus
s33D = 81e-12; % Open circuit compliance

a = Dch/2;
kp = Ap/s33D/Lp; % Pieno stiffness
Vo = Hch*Dch^2*pi/4; % Initial volume of chamber

ttopta = 18e-6;
thotta = 5e-6;

d = E*ttopta^3/(12*(1-nu^2));
ds = E*thotta^3/(12*(1-nu^2));

for k= 1:1.2e3;

Dpis = (Dch)-k*0.0005e-3;

b = Dpis/2;
Aps = Dpis^2*pi/4;

% Top tether

kxf = -1/16*(b^4-2*b^2*a^2+a^4)*log(a/b)+a^4-4*a^2*log(a)^2+b^2+4*a^2*log(a)*b^2*log(b)/(d*pi*(b^2-a^2));
kxp = -1/64*(3*b^6-7*b^4*a^2+4*b^2*a^4+log(b)*a^2+5*b^2*a^4-4*b^4*a^2*log(a)-4*b^2*log(b)*a^4+16*b^4*log(b)*a^2*log(a/b)...
-a^6+4*a^4*b^2*log(a)-16*a^2*log(a)^2+b^4+16*a^2*log(a)*b^4*log(b)/(d*(b^2-a^2)));
kvf = 1/64*pi*(16*b^4*log(b)+a^2*log(a/b)+16*a^2*log(a)*b^4*log(b)+8*b^2*a^4-4*b^4*log(b)*a^2+4*b^4*a^2*log(a)+4*b^2*...
log(b)*a^4-4*a^4*b^2*log(a)-16*a^2*log(a)^2+b^4-4*b^4*a^2*log(a/b)+log(a)/(d*pi*(b^2-a^2)));
kvp = 1/16*pi*(24*a^4*b^4*log(a/b)+24*a^4*b^4-22*b^6*a^2+a^8+7*b^8-48*a^4*b^4*log(a/b)+log(a)-48*a^4*log(a)*b^4*log(b)...
+48*a^4*log(a)^2+b^4+48*b^6*a^2*log(a/b)+log(b)+48*b^6*a^2*log(a)*log(b)-48*b^6*a^2*log(a)^2-24*b^6*a^2*log(a/b)-...
16*a^6*b^2)/(d*(b^2-a^2));

% Bottom tether

kxfb = 1/8*b^2*log(b)/(pi*ds)-1/8*b^2/(pi*ds)+1/16*(-2*a^2*log(a)+a^2+2*b^2*log(b)-b^2)*b^2/(pi*ds*(a^2-b^2))+1/4*b^2*...
a^2*log(a/b)+log(b)/(pi*ds*(a^2-b^2))+1/16*a^2*(a^2-2*b^2*log(b)-b^2-4*b^2*log(a)^2+2*b^2*log(a)+4*b^2*log(a)*...
log(b))/(pi*ds*(a^2-b^2));

% Overall equations

xpie = -kxfb*(kxf*Apis-kxp)*dVf*Bf/(kxfb*Vo+kxfb*Bf*kvf*Apis-kxfb*Bf*kvp+kxf*Vo-kxf*Bf*kvp+kxf*kp+kxfb*Vo-kxf*kp+kxfb*...
Bf*kvp+kxf*Apis)+2*Bf*kxfb*kxp*Bf*kvf*kxp*Bf*kvf*kp+kxfb-kxp*Bf*kxfb*Apis);
P = Bf*dVf*(kxfb-kxf-kxfb*kxp)/(kxfb*Vo+kxfb*Bf*kvf*Apis-kxfb*Bf*kvp+kxf*Vo-kxf*Bf*kvp+kxf*kp+kxfb*Vo-kxf*kp+kxfb*Bf*...
*kvp+kxf*Apis)+Bf*kxfb-kxp*Bf*kvf*kxp*Bf*kvf*kp+kxfb-kxfb*kvp-kxf*kp+kxfb*kvp)/(kxfb+kxf+kxf*kp+kxfb);
Ceff = Vo/Bf*(kxfb*kvf*Apis+kxp*kvf*kp+kxfb-kxfb*kvp-kxf*kp+kxfb*kvp)/(kxfb+kxf+kxf*kp+kxfb);

xp(k) = xpie;
Pch(k) = P;
Comp(k) = Ceff;
Dpisn(k) = Dpis;

end

figure(2)
subplot(3,1,1)
plot((Dch-Dpisn)*1e6/2,xp/1e-6)
hold on
title('Dch fixed,Dpis varied')
ylabel('Piston Deflection(um)')
grid
subplot(3,1,2)
plot((Dch-Dpisn)*1e6/2,Pch/1e6)
hold on
ylabel('Chamber Pressure(DPa)')
grid
subplot(3,1,3)
semilogy((Dch-Dpisn)*1e6/2,Comp)
hold on
ylabel('Ceff(m^3/Pa)')
xlabel('tether width')
grid

```

Figure B-3: Matlab code used for tether optimization.

```

% This code writes the system parameters to the Matlab workspace to be read by Simulink.
% It also generates the 15x3 matrix used in Simulink, whose coefficients are calculated using Maple.

clear all;

% Fluid Properties
rho      = 740 ; % fluid density (kg/m^3);
mu_fluid = 0.65e-6; % viscosity (m^2/sec);
nu_fluid = rho/mu_fluid; % viscosity (Pa/sec);

% Valve geometry
d_discin = 2e40e-6 ; % inlet valve cap diameter[m];
d_discout = d_discin ; % outlet valve cap diameter[m];

hI = 100e-6;
eta = 0.945 ;

% Valve Channel Geometry
lk = 5e-7 ; % Leakage[m]
Lc = 5000; % Channel length
Ac = 1; % Channel area

% Note: since only L/A ratio is important in this study,
% no exact channel geometry is defined, only the ratio is determined.

% Diode Properties for the rectifier circuit
T = 300;
k = 1.38e-23;
eta = 17.25/S;
q = 1.6e-19;
Io = 1e-6;

% Operation Conditions
vol = 24e-6 ; % Inlet valve opening[m]
voo = 24e-6 ; % Outlet valve opening[m]
wm = 20000 ; % Operation frequency[Hz]
Vb = 74.5; % Battery Voltage[V]
PMPR = 3e6; % High Pressure Reservoir Pressure
PLPR = 0.5e6; % Low Pressure Reservoir Pressure

% Expansion look-up table
Re = [0, 0.05, 0.1, 0.2, 0.3, 0.4, 0.5, 0.6, 0.9] ;
Ce = [1, 10, 15, 20, 30, 40, 50, 100, 2e2, 5e2, 1e3, 2e3, 3e3, 1e4] ;
Te = [32, 3.1, 3.5, 3.04, 2.7, 2.42, 2.32, 1.92, 1.94, 2.07, 2.45, 1.92, 1.25, 0.98;
      22, 3.1, 3.3, 3.02, 2.86, 2.29, 2.33, 1.82, 1.79, 1.89, 2.23, 1.76, 1.13, 0.9;
      32, 3.1, 3.2, 3.2, 2.4, 2.19, 1.96, 1.7, 1.69, 1.72, 2.1, 1.6, 1, 0.81;
      32, 3.1, 3.2, 2.2, 2.2, 1.85, 1.65, 1.4, 1.3, 1.3, 1.6, 1.25, 0.7, 0.64;
      32, 3.1, 3.1, 2.6, 2, 1.6, 1.4, 1.3, 1.1, 1.1, 1.3, 0.95, 0.6, 0.5;
      32, 3.1, 3.0, 2.4, 1.8, 1.5, 1.3, 1.1, 1, 0.85, 1.05, 0.8, 0.4, 0.36;
      32, 3.1, 2.8, 2.3, 1.65, 1.35, 1.15, 0.9, 0.75, 0.65, 0.9, 0.65, 0.3, 0.25;
      32, 3.1, 2.7, 2.15, 1.55, 1.25, 1.05, 0.8, 0.6, 0.4, 0.4, 0.5, 0.2, 0.16;
      32, 3.1, 2.6, 2.1, 1.4, 1.1, 0.9, 0.4, 0.3, 0.1, 0.2, 0.2, 0.1, 0.08] ;

% Contraction look-up table
Rc = [0, 0.1, 0.2, 0.3, 0.4, 0.5, 0.6, 1] ;
Cc = [1, 10, 20, 30, 40, 50, 1e2, 2e2, 5e2, 1e3, 2e3, 4e3, 5e3, 1e4, 1e5] ;
To = [30, 8, 3.3, 2.5, 2.16, 1.98, 1.4, 1.11, 0.94, 0.77, 0.6, 0.97, 0.82, 0.4, 1;
      30, 5, 3.2, 2.4, 2.1, 1.8, 1.3, 1.04, 0.82, 0.64, 0.5, 0.8, 0.75, 0.50, 0.45;
      30, 5, 3.1, 2.3, 1.84, 1.62, 1.2, 0.85, 0.7, 0.5, 0.4, 0.6, 0.6, 0.4, 0.4;
      30, 5, 2.95, 2.15, 1.7, 1.5, 1.1, 0.85, 0.6, 0.44, 0.30, 0.55, 0.55, 0.35, 0.35;
      30, 5, 2.8, 2.0, 1.6, 1.4, 1.0, 0.78, 0.5, 0.35, 0.25, 0.45, 0.5, 0.3, 0.3;
      30, 5, 2.7, 1.8, 1.46, 1.3, 0.9, 0.65, 0.42, 0.3, 0.2, 0.4, 0.42, 0.25, 0.25;
      30, 5, 2.6, 1.7, 1.35, 1.2, 0.8, 0.56, 0.35, 0.24, 0.15, 0.35, 0.35, 0.20, 0.20;
      30, 5, 2.6, 1.7, 1.20, 0.8, 0.6, 0.40, 0.15, 0.01, 0.05, 0.15, 0.15, 0.10, 0.10] ;

% Preparation of the matrix to be fed into Simulink
ThesisSimMatrix; % Read in matrix values from ThesisSimMatrix.m
for i=1:15
    for j=1:3
        eval(['Amatrix(1,j)=A' num2str(i) num2str(j) ','']);
    end
end

```

Figure B-4: Matlab code used for writing system parameters into the workspace to be read by the Simulink model for the system level simulation.

Appendix C

Maple Files

This section presents important Maple files used in the Thesis.

The first two codes are the Maple files used for tether optimization in Chapter 5. The first one solves the elastic equations of the tether structures. The second one solves the governing equation for the chamber behavior. The coefficients calculated are then fed to the Matlab code used for tether optimization presented in Appendix B.

The third code solves the elastic equations of all the structural components within the system along with the equations governing the chamber continuity and piezoelectric element behavior. The equations are solved and the coefficients for the 15x3 matrix required by the Simulink model architecture, which is described in Chapter 4, are calculated. These coefficients are written in a Matlab m.file which are then read by another Matlab code (Appendix B) to generate the 15x3 matrix. The assumptions and derivation of these equations are presented in Chapter 4.

This file solves the elastic equations corresponding to the tether structure.
Double layer piston is considered.

It is assumed that everything except the tethers are rigid.

```
[ > restart;
[ > Digits:=40;
```

Top tether

Define governing DE for bending of circular plate and shear force

```
[ Governing DE
[ > eqn:='diff(1/x*diff(r*diff(w(x),x),x),x)=Q(x)/d';
[ Shear force in terms of Pch(chamber pressure) and Fpt (force applied by the piston on the top tether)
[ > Q(x):=Fpt/(2*pi*x) - (1/2)*P*(x^2-b^2)/x;
```

Integrate the DE

```
[ > Q1(x):=(int(Q(x)/d,x)+C1)*x;
[ > Q2(x):=(int(Q1(x),x)+C2)/x;
[ > w(x):=int(Q2(x),x)+C3;
```

Apply BC's

```
[ > BC1:=subs({x=a},w(x))=0;
[ > BC2:=subs({x=a},diff(w(x),x))=0;
[ > BC3:=subs({x=b},diff(w(x),x))=0;
[ > Set:=solve({BC1,BC2,BC3},{C1,C2,C3});
[ > W(x):=subs(Set,w(x));
```

Calculation of linear coefficients for deflection and swept volume

```
[ > kxf:=subs({P=0,Fpt=1},subs({x=b},W(x)));
[ > kxp:=subs({P=1,Fpt=0},subs({x=b},W(x)));
[ > kvf:=subs({P=0,Fpt=1},collect(simplify(int(2*pi*x*W(x),x=b..a)),{d,P}));
[ > kvp:=subs({P=1,Fpt=0},collect(simplify(int(2*pi*x*W(x),x=b..a)),{d,P}));
```

Bottom tether

Define governing DE for bending of circular plate and shear force

```
[ Governing DE
[ > eqn:='diff(1/x*diff(r*diff(w(x),x),x),x)=Q(x)/ds';
[ Shear force in terms of Fpb (force applied by the piston on the bottom tether)
[ > Q(x):=Fpb/(2*pi*x);
```

Integrate the DE

```
[ > Q1(x):=(int(Q(x)/ds,x)+C1)*x;
[ > Q2(x):=(int(Q1(x),x)+C2)/x;
[ >
[ > w(x):=int(Q2(x),x)+C3;
```

Apply BC's

```
[ > BC1:=subs({x=a},w(x))=0;
[ > BC2:=subs({x=a},diff(w(x),x))=0;
[ > BC3:=subs({x=b},diff(w(x),x))=0;
[ > Set:=solve({BC1,BC2,BC3},{C1,C2,C3});
[ > W(x):=subs(Set,w(x));
```

Calculation of linear coefficient for deflection

```
[ > kxfb:=subs({P=0,Fpb=1},subs({x=b},W(x)));
```



```

File: Comp1.mws
This file solves the overall equations governing the chamber behavior including piston deflection, swept volume, chamber pressure,
force on piezo and force on tethers.
Also the effective compliance of the system is calculated. The elastic equations governing the tether behavior are calculated using
another maple file.
The results of both maple files are then fed to Matlab for tether structure optimization.
[ > restart;
[ > Digits:=40:

Equations Governing top tether deflection
[ > eqn1:=xpis=kxf*Fpt+kxp*P:
[ > eqn2:=dVt=kvf*Fpt+kvp*P:

Equation Governing bottom tether deflection
[ > eqn3:=xpis=kxfb*Fpb:

Force Balance at piston-tether connection
[ > eqn4:=Fp=Fpt+Fpb:

Fluid Compliance
[ > eqn5:=P=((dVf+dVt+xpis*Apis)/(Vo))*Bf:

Piston and Piezo
[ > eqn6:=P*Apis+Fp+kp*xpis=0:

Solve equations for input dVf
[ > sys:=solve({eqn1,eqn2,eqn3,eqn4,eqn5,eqn6},{xpis,Fp,dVt,P,Fpt,Fpb}):
[ > assign(sys);
[ > Ceff:=collect(simplify((dVf+xpis*Apis)/P),{Vo,Bf}):

```

File: ThesisSimComp.mws

Within the simulink model, an 15×3 matrix is needed, which takes as inputs (Q_p , Q_{net} , x_{pis}) and solves for the outputs (V_p , x_{tp} , DV_{tp} , DV_{te} , DV_{pb} , x_b , x_{te} , F_{te} , F_{te-top} , F_{te-bot} , S_{tt} , S_{tb} , F_p , P_{ch} , F_{net}).

This code calculates the coefficients of this matrix.

```
[ > restart;
[ > Digits:=40;
```

Governing Equations

Top support structure

```
[ > EQN1 := x[tp]=k[dtb]*F[ch];
[ > EQN2 := DV[tp]=k[tp]*F[ch];
```

Bottom Support Structure

```
[ > EQN3 := x[b] = k[b]*F[p];
```

Piston

```
[ > EQN4 := x[pis]-x[te]=k[p1]*F[p]+k[p2]*F[ch];
[ > EQN5 := DV[pb]=k[p3]*F[p]+k[p4]*F[ch];
[ > EQN6 := F[net]=-A[pis]*P[ch]+F[p]-F[te];
```

Piston Tethers

```
[ > EQN7 := x[te]=k[tt1]*F[tetop]+k[tt2]*F[ch];
[ > EQN8 := DV[te]=k[tt3]*F[tetop]+k[tt4]*F[ch];
[ > EQN9 := Str[tt]=s[tt1]*F[tetop]+s[tt2]*F[ch];
[ > EQN10 := x[te]=k[tb]*F[tebot];
[ > EQN11 := Str[tb]=s[tb]*F[tebot];
[ > EQN12 := F[te]=F[tetop]+F[tebot];
```

Chamber continuity

```
[ > EQN13 := F[ch]=B[f]/V[o]*(Q[net]+x[pis]*A[pis]+DV[pb]+DV[te]-DV[tp]);
```

Piezoelectric Material

```
[ Linear constitutive relations.
[ > EQN14 := x[b]-x[pis] = L[p]/A[p]*(sD[33]*F[p]+d[33]/eT[33]*Q[p]);
[ > EQN15 := V[p] = L[p]/A[p]*(d[33]/eT[33]*F[p]-1/eT[33]*Q[p]);
```

Geometric and Material Parameters

Geometric Parameters:

```
[ > L[p]:=1e-3; d[p]:=3.8e-3; A[p]:=(Pi*d[p]^2)/4;
[ > d[pis]:=6.95e-3; w[t]:=125e-6; d[ch]:=d[pis]+2*w[t]; t[pis]:=800e-6;
[ > A[pis]:=(Pi*d[pis]^2)/4;
[ > t[tetop]:=10e-6; t[tebot]:=5e-6;
[ > t[tebot]:=2500e-6; t[top]:=2500e-6;
[ > H[ch]:=200e-6; V[o]:=Pi*(d[ch]^2/4)*H[ch];
[ Material Parameters:
[ > d[33]:=1780e-12; sD[33]:=17e-12; sE[33]:=81e-12; eT[33]:=d[33]^2/(sE[33]-sD[33]);
[ > E[sil]:=165e9; nu[sil]:=0.22; B[f]:=2e9; rho[sil]:=2230; M[pis]:=rho[sil]*A[pis]*t[pis];
```

Calculate Linear Plate Coefficients

Top Support Structure

```
[ Circular plate clamped at its outer radius(r=a).
[ Positive deflection is upward.
[ > eqn:='diff(1/x*diff(x*diff(z(x),x),x),x)=Q(x)/Ds';
[ > Q(x):=P[ch]*x/2;
```

Page 1

```
[ > Q1(x):=(int(Q(x)/Ds,x)+C1)*x:
[ > Q2(x):=(int(Q1(x),x)+C2)/x:
[ > wtp(x):=subs({C2=0},int(Q2(x),x)+C3):
[ > BC1:=subs({x=a},wtp(x))=0:
[ > BC2:=subs({x=a},diff(wtp(x),x))=0:
[ > Set:=solve({BC1,BC2},{C1,C3}):
[ > Wtp:=simplify(subs(Set,wtp(x))):
[ > DVtp:=int(2*Pi*x*Wtp,x=0..a):
[ > Wtpo:=subs({x=0},Wtp):
[ > k[dtpl]:=subs({P[ch]=1},Wtpo):
[ > k[dtpl]:=evalf(subs({a=d[ch]/2, Ds=E[s1]*t[top]^3/(12*(1-nu[s1]^2))},k[dtpl])):
[ > k[tp]:=subs({P[ch]=1},DVtp):
[ > k[tp]:=evalf(subs({a=d[ch]/2, Ds=E[s1]*t[top]^3/(12*(1-nu[s1]^2))},k[tp])):
```

Bottom Support Structure

Circular plate with a circular hole at the center which is clamped at its outer radius($r=a$) and guided at its inner radius($r=b$). Positive deflection is upward.

```
[ > eqn:=diff(1/x*diff(r*diff(Z(x),x),x),x)=Q(x)/Ds':
[ > Q(x):=-F[p]/2/Pi/r:
[ > Q1(x):=(int(Q(x)/Ds,x)+C1)*x:
[ > Q2(x):=(int(Q1(x),x)+C2)/x:
[ > wb(x):=int(Q2(x),x)+C3:
[ > BC1:=subs({x=a},wb(x))=0:
[ > BC2:=subs({x=a},diff(wb(x),x))=0:
[ > BC3:=subs({x=b},diff(wb(x),x))=0:
[ > Set:=solve({BC1,BC2,BC3},{C1,C2,C3}):
[ > Wb:=simplify(subs(Set,wb(x))):
[ > k[b]:=simplify(subs({F[p]=1},subs({x=b},Wb))):
[ > k[b]:=evalf(subs({a=d[ch]/2, b=d[p]/2, Ds=E[s1]*t[bot]^3/(12*(1-nu[s1]^2))},k[b])):
```

Piston

Circular plate with a circular hole at the center which is simply supported at its outer radius($r=a$) and guided at its inner radius($r=b$). Positive deflection is upward.

```
[ > eqn:=diff(1/x*diff(r*diff(Z(x),x),x),x)=Q(x)/Ds':
[ > Q(x):=-F[p]/2/Pi/x-P[ch]*x/2:
[ > Q1(x):=(int(Q(x)/Ds,x)+C1)*x:
[ > Q2(x):=(int(Q1(x),x)+C2)/x:
[ > wp(x):=int(Q2(x),x)+C3:
[ > BC1:=subs({x=a},wp(x))=0:
[ > BC2:=subs({x=a},diff(wp(x),x)+nu/r*diff(wp(x),x))=0:
[ > BC3:=subs({x=b},diff(wp(x),x))=0:
[ > Set:=solve({BC1,BC2,BC3},{C1,C2,C3}):
[ > Wp:=simplify(subs(Set,wp(x))):
[ > DVpb:=simplify(int(2*Pi*r*Wp,r=0..a)):
[ > k[p1]:=simplify(subs({P[ch]=0,F[p]=1},subs({x=b},Wp))):
[ > k[p1]:=evalf(subs({a=d[pis]/2, b=d[p]/2, Ds=E[s1]*t[pis]^3/(12*(1-nu[s1]^2)), nu=nu[s1]},k[p1])):
[ > k[p2]:=simplify(subs({P[ch]=1,F[p]=0},subs({x=b},Wp))):
[ > k[p2]:=evalf(subs({a=d[pis]/2, b=d[p]/2, Ds=E[s1]*t[pis]^3/(12*(1-nu[s1]^2)), nu=nu[s1]},k[p2])):
[ > k[p3]:=simplify(subs({P[ch]=0,F[p]=1},DVpb)):
[ > k[p3]:=evalf(subs({a=d[pis]/2, b=d[p]/2, Ds=E[s1]*t[pis]^3/(12*(1-nu[s1]^2)), nu=nu[s1]},k[p3])):
[ > k[p4]:=simplify(subs({P[ch]=1,F[p]=0},DVpb)):
[ > k[p4]:=evalf(subs({a=d[pis]/2, b=d[p]/2, Ds=E[s1]*t[pis]^3/(12*(1-nu[s1]^2)), nu=nu[s1]},k[p4])):
```

Drive Element Tethers

Top Tether

Annular plate clamped at outer radius ($r=a$) and guided at inner radius ($r=b$) with pressure applied downward over tether and concentrated force applied upward at inner radius ($r=b$).

```
[ > eqn='diff(1/r*diff(r*diff(Z(x),x),x),x)=Q(x)/Ds';
[ > Q(x):=F[tetop]/(2*pi*x)-P[ch]*(x^2-b^2)/(2*x);
[ > Q1(x):=(int(Q(x)/Ds,x)+C1)*x;
[ > Q2(x):=(int(Q1(x),x)+C2)/x;
[ > wtt(x):=int(Q2(x),x)+C3;
[ > BC1:=subs({r=a},wtt(x))=0;
[ > BC2:=subs({r=a},diff(wtt(x),x))=0;
[ > BC3:=subs({r=b},diff(wtt(x),x))=0;
[ > Set:=solve({BC1,BC2,BC3},{C1,C2,C3});
[ > Wtt:=simplify(subs(Set,wtt(x)));
[ > DVtt:=simplify(int(2*pi*x*Wtt,x=b..a));
[ > k[tt1]:=simplify(subs({P[ch]=0,F[tetop]=1},subs({x=b},Wtt)));
[ > k[tt1]:=evalf(subs({a=d[ch]/2, b=d[pi]/2,
[ > Ds=E[s1]*t[tetop]^3/(12*(1-nu[s1]^2)),k[tt1]));
[ > k[tt2]:=simplify(subs({P[ch]=1,F[tetop]=0},subs({x=b},Wtt)));
[ > k[tt2]:=evalf(subs({a=d[ch]/2, b=d[pi]/2,
[ > Ds=E[s1]*t[tetop]^3/(12*(1-nu[s1]^2)),k[tt2]));
[ > k[tt3]:=simplify(subs({P[ch]=0,F[tetop]=1,DVtt)));
[ > k[tt3]:=evalf(subs({a=d[ch]/2, b=d[pi]/2,
[ > Ds=E[s1]*t[tetop]^3/(12*(1-nu[s1]^2)),k[tt3]));
[ > k[tt4]:=simplify(subs({P[ch]=1,F[tetop]=0,DVtt)));
[ > k[tt4]:=evalf(subs({a=d[ch]/2, b=d[pi]/2,
[ > Ds=E[s1]*t[tetop]^3/(12*(1-nu[s1]^2)),k[tt4]));
[ > Stt:=simplify(6*(Ds*(diff(Wtt,x^2)+nu/x*diff(Wtt,x)))/(h^2));
[ > s[tt1]:=simplify(subs({P[ch]=0,F[tetop]=1},subs({x=a},Stt)));
[ > s[tt1]:=evalf(subs({a=d[ch]/2, b=d[pi]/2, Ds=E[s1]*t[tetop]^3/(12*(1-nu[s1]^2)),
[ > nu=nu[s1], h=t[tetop]},s[tt1]));
[ > s[tt2]:=simplify(subs({P[ch]=1,F[tetop]=0},subs({x=a},Stt)));
[ > s[tt2]:=evalf(subs({a=d[ch]/2, b=d[pi]/2, Ds=E[s1]*t[tetop]^3/(12*(1-nu[s1]^2)),
[ > nu=nu[s1], h=t[tetop]},s[tt2]));
```

Bottom Tether

Annular plate clamped at outer radius ($r=a$) and guided at inner radius ($r=b$) with concentrated force applied upward at inner radius ($r=b$).

```
[ > eqn='diff(1/r*diff(r*diff(Z(x),x),x),x)=Q(x)/Ds';
[ > Q(x):=F[tetot]/(2*pi*x);
[ > Q1(x):=(int(Q(x)/Ds,x)+C1)*x;
[ > Q2(x):=(int(Q1(x),x)+C2)/x;
[ > wtb(x):=int(Q2(x),x)+C3;
[ > BC1:=subs({r=a},wtb(x))=0;
[ > BC2:=subs({r=a},diff(wtb(x),x))=0;
[ > BC3:=subs({r=b},diff(wtb(x),x))=0;
[ > Set:=solve({BC1,BC2,BC3},{C1,C2,C3});
[ > Wtb:=simplify(subs(Set,wtb(x)));
[ > k[tb]:=simplify(subs({F[tetot]=1},subs({x=b},Wtb)));
[ > k[tb]:=evalf(subs({a=d[ch]/2, b=d[pi]/2, Ds=E[s1]*t[tetot]^3/(12*(1-nu[s1]^2)),
[ > nu=nu[s1]},k[tb]));
[ > Stb:=simplify(6*(Ds*(diff(Wtb,x^2)+nu/x*diff(Wtb,x)))/(h^2));
[ > s[tb]:=simplify(subs({F[tetot]=1},subs({x=a},Stb)));
[ > s[tb]:=evalf(subs({a=d[ch]/2, b=d[pi]/2, Ds=E[s1]*t[tetot]^3/(12*(1-nu[s1]^2)),
[ > nu=nu[s1], h=t[tetot]},s[tb]));
```

Solve Equations

In the Simulink model, the inputs to the matrix block are Q_0 , $Onet$ and x_{pis} . It is desired to solve for each of the output variables in

terms of these inputs. The output variables are Vp, xtp, DVtp, DVte, DVpb, xb, xte, Fte-top, Fte-bot, Stt, Stb, Fp, Pch, Fnet. Once solved, each of the coefficients is assigned to the proper location in the matrix. All the matrix coefficients are then fed to matlab matrix file, which is then called by a matlab preparation file to run the Simulink model.

```
> Solutions=solve({EQN1,EQN2,EQN3,EQN4,EQN5,EQN6,EQN7,EQN8,EQN9,EQN10,EQN11,EQN12,EQN13,
,EQN14,EQN15},{V[p],x[tp],DV[tp],DV[te],DV[pb],x[b],x[te],F[te],F[tetop],F[tebot],Str[
tt],Str[tb],F[p],P[ch],F[net]});
> A11=evalf(subs({Q[p]=1,Q[net]=0,x[pi]=0},subs(Solutions,V[p])));
> A12=evalf(subs({Q[p]=0,Q[net]=1,x[pi]=0},subs(Solutions,V[p])));
> A13=evalf(subs({Q[p]=0,Q[net]=0,x[pi]=1},subs(Solutions,V[p])));
> A21=evalf(subs({Q[p]=1,Q[net]=0,x[pi]=0},subs(Solutions,x[tp])));
> A22=evalf(subs({Q[p]=0,Q[net]=1,x[pi]=0},subs(Solutions,x[tp])));
> A23=evalf(subs({Q[p]=0,Q[net]=0,x[pi]=1},subs(Solutions,x[tp])));
> A31=evalf(subs({Q[p]=1,Q[net]=0,x[pi]=0},subs(Solutions,DV[tp])));
> A32=evalf(subs({Q[p]=0,Q[net]=1,x[pi]=0},subs(Solutions,DV[tp])));
> A33=evalf(subs({Q[p]=0,Q[net]=0,x[pi]=1},subs(Solutions,DV[tp])));
> A41=evalf(subs({Q[p]=1,Q[net]=0,x[pi]=0},subs(Solutions,DV[te])));
> A42=evalf(subs({Q[p]=0,Q[net]=1,x[pi]=0},subs(Solutions,DV[te])));
> A43=evalf(subs({Q[p]=0,Q[net]=0,x[pi]=1},subs(Solutions,DV[te])));
> A51=evalf(subs({Q[p]=1,Q[net]=0,x[pi]=0},subs(Solutions,DV[pb])));
> A52=evalf(subs({Q[p]=0,Q[net]=1,x[pi]=0},subs(Solutions,DV[pb])));
> A53=evalf(subs({Q[p]=0,Q[net]=0,x[pi]=1},subs(Solutions,DV[pb])));
> A61=evalf(subs({Q[p]=1,Q[net]=0,x[pi]=0},subs(Solutions,x[b])));
> A62=evalf(subs({Q[p]=0,Q[net]=1,x[pi]=0},subs(Solutions,x[b])));
> A63=evalf(subs({Q[p]=0,Q[net]=0,x[pi]=1},subs(Solutions,x[b])));
> A71=evalf(subs({Q[p]=1,Q[net]=0,x[pi]=0},subs(Solutions,x[te])));
> A72=evalf(subs({Q[p]=0,Q[net]=1,x[pi]=0},subs(Solutions,x[te])));
> A73=evalf(subs({Q[p]=0,Q[net]=0,x[pi]=1},subs(Solutions,x[te])));
> A81=evalf(subs({Q[p]=1,Q[net]=0,x[pi]=0},subs(Solutions,F[te])));
> A82=evalf(subs({Q[p]=0,Q[net]=1,x[pi]=0},subs(Solutions,F[te])));
> A83=evalf(subs({Q[p]=0,Q[net]=0,x[pi]=1},subs(Solutions,F[te])));
> A91=evalf(subs({Q[p]=1,Q[net]=0,x[pi]=0},subs(Solutions,F[tetop])));
> A92=evalf(subs({Q[p]=0,Q[net]=1,x[pi]=0},subs(Solutions,F[tetop])));
> A93=evalf(subs({Q[p]=0,Q[net]=0,x[pi]=1},subs(Solutions,F[tetop])));
> A101=evalf(subs({Q[p]=1,Q[net]=0,x[pi]=0},subs(Solutions,F[tebot])));
> A102=evalf(subs({Q[p]=0,Q[net]=1,x[pi]=0},subs(Solutions,F[tebot])));
> A103=evalf(subs({Q[p]=0,Q[net]=0,x[pi]=1},subs(Solutions,F[tebot])));
> A111=evalf(subs({Q[p]=1,Q[net]=0,x[pi]=0},subs(Solutions,Str[tt])));
> A112=evalf(subs({Q[p]=0,Q[net]=1,x[pi]=0},subs(Solutions,Str[tt])));
> A113=evalf(subs({Q[p]=0,Q[net]=0,x[pi]=1},subs(Solutions,Str[tt])));
> A121=evalf(subs({Q[p]=1,Q[net]=0,x[pi]=0},subs(Solutions,Str[tb])));
> A122=evalf(subs({Q[p]=0,Q[net]=1,x[pi]=0},subs(Solutions,Str[tb])));
> A123=evalf(subs({Q[p]=0,Q[net]=0,x[pi]=1},subs(Solutions,Str[tb])));
> A131=evalf(subs({Q[p]=1,Q[net]=0,x[pi]=0},subs(Solutions,F[p])));
> A132=evalf(subs({Q[p]=0,Q[net]=1,x[pi]=0},subs(Solutions,F[p])));
> A133=evalf(subs({Q[p]=0,Q[net]=0,x[pi]=1},subs(Solutions,F[p])));
> A141=evalf(subs({Q[p]=1,Q[net]=0,x[pi]=0},subs(Solutions,P[ch])));
> A142=evalf(subs({Q[p]=0,Q[net]=1,x[pi]=0},subs(Solutions,P[ch])));
> A143=evalf(subs({Q[p]=0,Q[net]=0,x[pi]=1},subs(Solutions,P[ch])));
> A151=evalf(subs({Q[p]=1,Q[net]=0,x[pi]=0},subs(Solutions,F[net])));
> A152=evalf(subs({Q[p]=0,Q[net]=1,x[pi]=0},subs(Solutions,F[net])));
> A153=evalf(subs({Q[p]=0,Q[net]=0,x[pi]=1},subs(Solutions,F[net])));
```

Generation of output matrix to Matlab file

[Output matrix coefficients values to a file which Matlab/Simulink can read.
> interface(echo=0);
> writeto('ThesisSimMatrix.m');

```

[ > printf("A11 = %+2.08e;", A11);
[ > printf("A12 = %+2.08e;", A12);
[ > printf("A13 = %+2.08e;", A13);
[ > printf("A21 = %+2.08e;", A21);
[ > printf("A22 = %+2.08e;", A22);
[ > printf("A23 = %+2.08e;", A23);
[ > printf("A31 = %+2.08e;", A31);
[ > printf("A32 = %+2.08e;", A32);
[ > printf("A33 = %+2.08e;", A33);
[ > printf("A41 = %+2.08e;", A41);
[ > printf("A42 = %+2.08e;", A42);
[ > printf("A43 = %+2.08e;", A43);
[ > printf("A51 = %+2.08e;", A51);
[ > printf("A52 = %+2.08e;", A52);
[ > printf("A53 = %+2.08e;", A53);
[ > printf("A61 = %+2.08e;", A61);
[ > printf("A62 = %+2.08e;", A62);
[ > printf("A63 = %+2.08e;", A63);
[ > printf("A71 = %+2.08e;", A71);
[ > printf("A72 = %+2.08e;", A72);
[ > printf("A73 = %+2.08e;", A73);
[ > printf("A81 = %+2.08e;", A81);
[ > printf("A82 = %+2.08e;", A82);
[ > printf("A83 = %+2.08e;", A83);
[ > printf("A91 = %+2.08e;", A91);
[ > printf("A92 = %+2.08e;", A92);
[ > printf("A93 = %+2.08e;", A93);
[ > printf("A101 = %+2.08e;", A101);
[ > printf("A102 = %+2.08e;", A102);
[ > printf("A103 = %+2.08e;", A103);
[ > printf("A111 = %+2.08e;", A111);
[ > printf("A112 = %+2.08e;", A112);
[ > printf("A113 = %+2.08e;", A113);
[ > printf("A121 = %+2.08e;", A121);
[ > printf("A122 = %+2.08e;", A122);
[ > printf("A123 = %+2.08e;", A123);
[ > printf("A131 = %+2.08e;", A131);
[ > printf("A132 = %+2.08e;", A132);
[ > printf("A133 = %+2.08e;", A133);
[ > printf("A141 = %+2.08e;", A141);
[ > printf("A142 = %+2.08e;", A142);
[ > printf("A143 = %+2.08e;", A143);
[ > printf("A151 = %+2.08e;", A151);
[ > printf("A152 = %+2.08e;", A152);
[ > printf("A153 = %+2.08e;", A153);
[ > printf("Ap = %+2.08e;", evalf(A[p]));
[ > printf("Api = %+2.08e;", evalf(A[pi]));
[ > printf("Mpi = %+2.08e;", evalf(M[pi]));
[ > writeto(terminal);

```